CODEN: JASMAN

ISSN: 0001-4966

The Journal of the Acoustical Society of America

Vol. 116, No. 5, November 2004

ACOUSTICAL NEWS—USA 2697

USA Meetings Calendar 2698

ACOUSTICAL STANDARDS NEWS 2699

Standards Meetings Calendar 2699

BOOK REVIEWS 2707

REVIEWS OF ACOUSTICAL PATENTS 2711

LETTERS TO THE EDITOR

Diffuse fields in open systems and the emergence of the Green's function (L) Richard L. Weaver, Oleg I. Lobkis 2731

Noise reduction through source rerouting (L) Rufin Makarewicz 2735

Differential intracochlear recordings of ensemble background activity (EBA) (L) Jianxun Zhou, John D. Durrant, Carey Balaban 2738

GENERAL LINEAR ACOUSTICS [20]

Full wave modeling of therapeutic ultrasound: Efficient time-domain implementation of the frequency power-law attenuation Marko Liebler, Siegfried Ginter, Thomas Dreyer, Rainer E. Riedlinger 2742

Singly focused backscattering from small targets in an Airy caustic formed by a curved reflecting surface Benjamin R. Dzikowicz, Philip L. Marston 2751

Propagation of sound in long enclosures K. M. Li, K. K. Iu 2759

On the interference between the two microphones in free-field reciprocity calibration Salvador Barrera-Figueroa, Knud Rasmussen, Finn Jacobsen, Lorenzo Muñíz 2771

Single-channel time reversal in elastic solids Alexander M. Sutin, James A. TenCate, Paul A. Johnson 2779

On the design of long T-shaped acoustic resonators Deyu Li, Jeffrey S. Vipperman 2785

A model for the radiated field of a plane piston after reflection from a curved surface Adrian Neild, David A. Hutchins, Toby J. Robertson, David W. Schindel 2793

The comb waveform as an efficient method for wideband transducer measurements Walter H. Boober, Gorham G. Lau, Kim C. Benjamin, Kenneth M. Walsh 2802

(Continued)

THE JOURNAL OF THE ACOUSTICAL SOCIETY OF AMERICA VOL. 116, NO. 5, NOVEMBER 2004

CONTENTS—*Continued from preceding page*

NONLINEAR ACOUSTICS [25]

Modeling of nonlinear shear waves in soft solids — Evgenia A. Zabolotskaya, Mark F. Hamilton, Yurii A. Ilinskii, G. Douglas Meegan — 2807

Optimized shapes of oscillating resonators for generating high-amplitude pressure waves — Xiaofan Li, Joshua Finkbeiner, Ganesh Raman, Christopher Daniels, Bruce M. Steinetz — 2814

Numerical simulation of acoustic streaming generated by finite-amplitude resonant oscillations in an enclosure — Murat K. Aktas, Bakhtier Farouk — 2822

Using light scattering to measure the response of individual ultrasound contrast microbubbles subjected to pulsed ultrasound *in vitro* — Jingfeng Guan, Thomas J. Matula — 2832

AEROACOUSTICS, ATMOSPHERIC SOUND [28]

Experimental study of the diffracted sound field around jagged edge noise barriers — Penelope Menounou, Jeong Ho You — 2843

Acoustic pulse propagation in an outdoor turbulent atmosphere — I. D. Mcleod, C. G. Don, G. G. Swenson — 2855

UNDERWATER SOUND [30]

Exact discrete nonlocal boundary conditions for high-order Padé parabolic equations — Dmitry Mikhin — 2864

Measurements of scattering by suspensions of irregularly shaped sand particles and comparison with a single parameter modified sphere model — Peter D. Thorne, Michael J. Buckingham — 2876

Environmental inversion and matched-field tracking with a surface ship and L-shaped receiver array — Michael Nicholas, John S. Perkins, Gregory J. Orris, Laurie T. Fialkowski, Garry J. Heard — 2891

ULTRASONICS, QUANTUM ACOUSTICS, AND PHYSICAL EFFECTS OF SOUND [35]

Guided wave propagation in three-layer pavement structures — Nils Ryden, Michael J. S. Lowe — 2902

Line source representation for laser-generated ultrasound in an elastic transversely isotropic half-space — David H. Hurley, James B. Spicer — 2914

A resonant, self-pumped, circulating thermoacoustic heat exchanger — G. W. Swift, S. Backhaus — 2923

TRANSDUCTION [38]

Modeling of viscous damping of perforated planar microstructures. Applications in acoustics — Dorel Homentcovschi, Ronald N. Miles — 2939

Cross-talk phenomena in a 1-3 connectivity piezoelectric composite — Mikaël Wilm, Raphaël Armati, William Daniau, Sylvain Ballandras — 2948

STRUCTURAL ACOUSTICS AND VIBRATION [40]

Analytical-numerical matching for fluid-loaded structures with discontinuities — Christopher D. Park, Linda P. Franzoni, Donald B. Bliss — 2956

NOISE: ITS EFFECTS AND CONTROL [50]

Sound field modeling in a street canyon with partially diffusely reflecting boundaries by the transport theory — Thierry Le Pollès, Judicaël Picaut, Michel Bérengier, Claude Bardos — 2969

(Continued)

THE JOURNAL OF THE ACOUSTICAL SOCIETY OF AMERICA VOL. 116, NO. 5, NOVEMBER 2004

CONTENTS—*Continued from preceding page*

ACOUSTIC SIGNAL PROCESSING [60]

Development of a time-frequency representation for acoustic detection of buried objects — Vincent Valeau, James Sabatier, R. Daniel Costley, Ning Xiang — 2984

PHYSIOLOGICAL ACOUSTICS [64]

Constructing a cochlear transducer function from the summating potential using a low-frequency bias tone — Chul-Hee Choi, Mark E. Chertoff, Lin Bian, David Lerner — 2996

Response of the cat eardrum to static pressures: Mobile versus immobile malleus — Hanif M. Ladak, Willem F. Decraemer, Joris J. J. Dirckx, W. Robert J. Funnell — 3008

Analytic treatment of the compound action potential: Estimating the summed post-stimulus time histogram and unit response — Mark E. Chertoff — 3022

PSYCHOLOGICAL ACOUSTICS [66]

Estimation of the level and phase of the simple distortion tone in the modulation domain — Aleksander Sek, Brian C. J. Moore — 3031

Sequential F0 comparisons between resolved and unresolved harmonics: No evidence for translation noise between two pitch mechanisms — Christophe Micheyl, Andrew J. Oxenham — 3038

Sample discrimination of frequency differences with distracters — Donna L. Neff, Eric C. Odgaard — 3051

The apparent immunity of high-frequency "transposed" stimuli to low-frequency binaural interference — Leslie R. Bernstein, Constantine Trahiotis — 3062

Cats exhibit the Franssen Effect illusion — Micheal L. Dent, Daniel J. Tollin, Tom C. T. Yin — 3070

Source localization in complex listening situations: Selection of binaural cues based on interaural coherence — Christof Faller, Juha Merimaa — 3075

Speech perception and talker segregation: Effects of level, pitch, and tactile support with multiple simultaneous talkers — Rob Drullman, Adelbert W. Bronkhorst — 3090

SPEECH PRODUCTION [70]

A comparison of vowel normalization procedures for language variation research — Patti Adank, Roel Smits, Roeland van Hout — 3099

SPEECH PERCEPTION [71]

Acoustic-phonetic correlates of talker intelligibility for adults and children — Valerie Hazan, Duncan Markham — 3108

Formant discrimination in noise for isolated vowels — Chang Liu, Diane Kewley-Port — 3119

Frequency-place compression and expansion in cochlear implant listeners — Deniz Başkent, Robert V. Shannon — 3130

The effect of overlap-masking on binaural reverberant word intelligibility — Brad Libbey, Peter H. Rogers — 3141

Hearing-aid automatic gain control adapting to two sound sources in the environment, using three time constants — Peter Nordqvist, Arne Leijon — 3152

Envelope-onset asynchrony as a cue to voicing in initial English consonants — Hanfeng Yuan, Charlotte M. Reed, Nathaniel I. Durlach — 3156

BIOACOUSTICS [80]

Geometry of locating sounds from differences in travel time: Isodiachrons — John L. Spiesberger — 3168

(Continued)

THE JOURNAL OF THE ACOUSTICAL SOCIETY OF AMERICA VOL. 116, NO. 5, NOVEMBER 2004

CONTENTS—*Continued from preceding page*

The effect of recording and analysis bandwidth on acoustic identification of delphinid species	Julie N. Oswald, Shannon Rankin, Jay Barlow	3178
Measurement of an individual silver perch *Bairdiella chrysoura* sound pressure level in a field recording	Mark W. Sprague, Joseph J. Luczkovich	3186
How to measure information carried by a modulated vocal signature?	Amanda Searby, Pierre Jouventin	3192
Drilling and operational sounds from an oil production island in the ice-covered Beaufort Sea	Susanna B. Blackwell, Charles R. Greene, Jr., W. John Richardson	3199
Improved scatterer property estimates from ultrasound backscatter for small gate lengths using a gate-edge correction factor	Michael L. Oelze, William D. O'Brien, Jr.	3212

ERRATA

Erratum: "A phenomenological model for the responses of auditory-nerve fibers: II. Nonlinear tuning with a frequency glide" [J. Acoust. Soc. Am. 114, 2007–2020 (2003)]	Qing Tan, Laurel H. Carney	3224

CUMULATIVE AUTHOR INDEX 3226

ACOUSTICAL NEWS—USA

Elaine Moran
Acoustical Society of America, Suite 1NO1, 2 Huntington Quadrangle, Melville, NY 11747-4502

Editor's Note: *Readers of this Journal are encouraged to submit news items on awards, appointments, and other activities about themselves or their colleagues. Deadline dates for news items and notices are 2 months prior to publication.*

New Fellows of the Acoustical Society of America

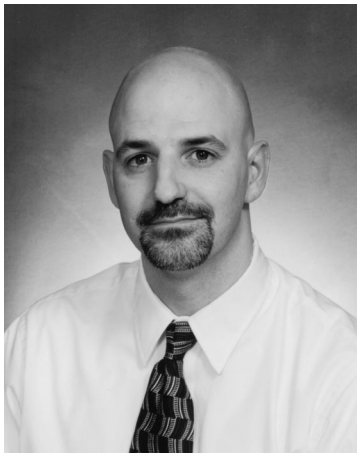

James Finneran—For contributions to understanding underwater hearing of marine mammals and fish.

Klaus Genuit—For application of binaural psychoacoustic principles to sound analysis and perception of sound quality.

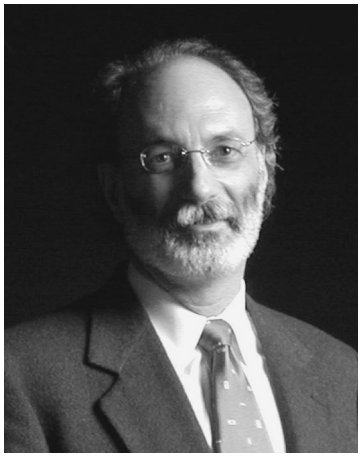

Robert Remez—For contributions to the understanding of perceptual organization of speech.

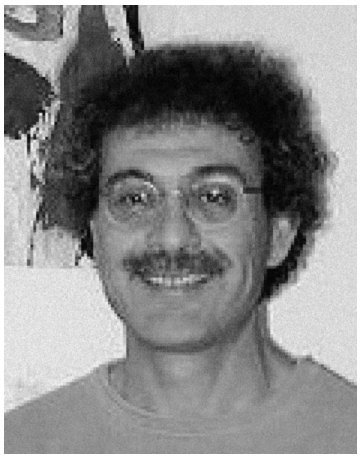

Shihab Shamma—For contributions to comutational modeling and cortical physiology of the mammalian auditory system.

Yoiti Suzuki—For contributions to equal-loudness contours and human response to continuous and impact noise.

Stephen C. Thompson—For contributions to acoustic transduction.

 0001-4966/2004/116(5)/2697/2/$20.00

USA Meetings Calendar

Listed below is a summary of meetings related to acoustics to be held in the U.S. in the near future. The month/year notation refers to the issue in which a complete meeting announcement appeared.

2004

15–19 Nov. 148th Meeting of the Acoustical Society of America, San Diego, CA [Acoustical Society of America, Suite 1NO1, 2 Huntington Quadrangle, Melville, NY 11747-4502; Tel.: 516-576-2360; Fax: 516-576-2377; E-mail: asa@aip.org; WWW:http://asa.aip.org].

2005

16–20 May 149th Meeting joint with the Canadian Acoustical Association, Vancouver, Canada [Acoustical Society of America, Suite 1NO1, 2 Huntington Quadrangle, Melville, NY 11747-4502; Tel.: 516-576-2360; Fax: 516-576-2377; E-mail: asa@aip.org; WWW:http://asa.aip.org].

16–19 May Society of Automotive Engineering Noise & Vibration Conference, Traverse City, MI [Patti Kreh, SAE International, 755 W. Big Beaver Rd., Ste. 1600, Troy, MI 48084, Tel.: 248-273-2474; E-mail: pkreh@sae.org].

18–22 July 17th International Symposium on Nonlinear Acoustics, State College, PA [Anthony Atchley, The Pennsylvania State University, 217 Applied Research Lab Building, University Park, PA 16802; Tel.: 814-865-6364; E-mail: ISNA17@outreach.psu.edu; WWW:http://www.outreach.psu.edu/c&i/isna17/].

17–21 October 150th Meeting joint with Noise-Con, Minneapolis, MN [Acoustical Society of America, Suite 1NO1, 2 Huntington Quadrangle, Melville, NY 11747-4502; Tel.: 516-576-2360; Fax: 516-576-2377; E-mail: asa@aip.org; WWW:http://asa.aip.org].

Cumulative Indexes to the Journal of the Acoustical Society of America

Ordering information: Orders must be paid by check or money order in U.S. funds drawn on a U.S. bank or by Mastercard, Visa, or American Express credit cards. Send orders to Circulation and Fulfillment Division, American Institute of Physics, Suite 1NO1, 2 Huntington Quadrangle, Melville, NY 11747-4502; Tel.: 516-576-2270. Non-U.S. orders add $11 per index.

Some indexes are out of print as noted below.

Volumes 1–10, 1929–1938: JASA and Contemporary Literature, 1937–1939. Classified by subject and indexed by author. Pp. 131. Price: ASA members $5; Nonmembers $10.

Volumes 11–20, 1939–1948: JASA, Contemporary Literature, and Patents. Classified by subject and indexed by author and inventor. Pp. 395. Out of Print.

Volumes 21–30, 1949–1958: JASA, Contemporary Literature, and Patents. Classified by subject and indexed by author and inventor. Pp. 952. Price: ASA members $20; Nonmembers $75.

Volumes 31–35, 1959–1963: JASA, Contemporary Literature, and Patents. Classified by subject and indexed by author and inventor. Pp. 1140. Price: ASA members $20; Nonmembers $90.

Volumes 36–44, 1964–1968: JASA and Patents. Classified by subject and indexed by author and inventor. Pp. 485. Out of Print.

Volumes 36–44, 1964–1968: Contemporary Literature. Classified by subject and indexed by author. Pp. 1060. Out of Print.

Volumes 45–54, 1969–1973: JASA and Patents. Classified by subject and indexed by author and inventor. Pp. 540. Price: $20 (paperbound); ASA members $25 (clothbound); Nonmembers $60 (clothbound).

Volumes 55–64, 1974–1978: JASA and Patents. Classified by subject and indexed by author and inventor. Pp. 816. Price: $20 (paperbound); ASA members $25 (clothbound); Nonmembers $60 (clothbound).

Volumes 65–74, 1979–1983: JASA and Patents. Classified by subject and indexed by author and inventor. Pp. 624. Price: ASA members $25 (paperbound); Nonmembers $75 (clothbound).

Volumes 75–84, 1984–1988: JASA and Patents. Classified by subject and indexed by author and inventor. Pp. 625. Price: ASA members $30 (paperbound); Nonmembers $80 (clothbound).

Volumes 85–94, 1989–1993: JASA and Patents. Classified by subject and indexed by author and inventor. Pp. 736. Price: ASA members $30 (paperbound); Nonmembers $80 (clothbound).

Volumes 95–104, 1994–1998: JASA and Patents. Classified by subject and indexed by author and inventor. Pp. 632. Price: ASA members $40 (paperbound); Nonmembers $90 (clothbound).

Volumes 105–114, 1999–2003: JASA and Patents. Classified by subject and indexed by author and inventor. Pp., Price: ASA members $50; Nonmembers $90 (paperbound).

BOOK REVIEWS

P. L. Marston
Physics Department, Washington State University, Pullman, Washington 99164

These reviews of books and other forms of information express the opinions of the individual reviewers and are not necessarily endorsed by the Editorial Board of this Journal.

Editorial Policy: *If there is a negative review, the author of the book will be given a chance to respond to the review in this section of the Journal and the reviewer will be allowed to respond to the author's comments. [See "Book Reviews Editor's Note," J. Acoust. Soc. Am.* ***81****, 1651 (May 1987).]*

Principles of Vibration and Sound, 2nd edition

Thomas D. Rossing and Neville H. Fletcher

Springer-Verlag, New York, 2004.
xiii +330 pp. Price: $49.95 (hardcover). ISBN: 0-387-40556-9

This book is designed to serve as a text for an introductory course in acoustics for physics or engineering students. Its primary focus is on the basic physical principles and associated mathematics underlying acoustics and some of its important applications.

The first edition of this text, published in 1995, consisted essentially of a separate publication of the foundation chapters on vibrating systems and sound waves contained in the first edition of *The Physics of Musical Instruments* (Springer-Verlag, New York, 1991) by the same authors (with the addition of an extra chapter on network analogs of acoustic systems, and some problems.) The first nine chapters of this new edition are, except for some slight revisions, the same as those in the first edition. However, in order to meet student needs for more applications of basic principles, the authors have added four new chapters.

In Part I of the book (Vibrating Systems), Chap. 1 focuses on simple vibrating systems and their mathematical representations, including responses to harmonic excitation, an introduction to some aspects of nonlinear vibrations, and two-dimensional harmonic motions (Lissajous figures). Chapter 2 gives a comprehensive introductory account of vibrating strings and bars, including the effects of stiffness, and motion of end supports. In Chap. 3, the vibrations of rectangular and circular plates and membranes are introduced, and in Chap. 4, the coupling of vibrating systems, including the example of string-plate coupling, is discussed. This chapter also contains very short descriptions of modal and finite element analyses and their literature. Part I is concluded by a very brief chapter on nonlinear systems.

Part II starts off with a fairly standard coverage of sound waves in air (Chap. 6), sound radiation (Chap. 7), and pipes and horns (Chap. 8). The presentation in these chapters is mostly confined to the frequency-domain case of steady-state harmonic excitation, but there is a brief summary of the time-domain analysis approach of Schumacher, McIntyre and Woodhouse, and Ayers at the end of Chap. 8. A leisurely introduction to acoustic network analysis in Chap. 9 is followed by one of the new chapters on microphones, loudspeakers, hydrophones, ultrasonic transducers, force transducers, and accelerometers. The book concludes with three new chapters on sound in three different environments—concert hall and studio, outdoor, and underwater.

On the basis of its clear and concise exposition of a mix of basic and applied subject matter, I would recommend this book for consideration as a text in an introductory acoustics course. However, in the spirit of wanting to see this text evolve into an even better one (perhaps in its next edition), I will make several recommendations.

First of all, several disconcerting statements, related to the fact that the first eight chapters are excised from a larger work, should certainly be removed. For example, on p. 70, in the discussion of the effect of air loading on the modal frequencies of a kettle drum, there is reference to a further discussion in Chap. 18 (a chapter in *The Physics of Musical Sounds*, but *not* in this book). In Chap. I, I would have liked to see the concept of a temporal Green's function introduced in the simple context of calculating the response of a harmonic oscillator to a general excitation. This introduction would have been a good entre to the later use of temporal Green's functions in Chap. 8. I also suggest adding a few lines of discussion to establish the simple general rules for reading off harmonic frequency ratios from Lissajous figures. In Chap. 2, the frequency analysis of plucked and struck strings should be made more general by calculating analytically the Fourier amplitudes of the string response for an *arbitrary* point of excitation (instead of just a point at $\frac{1}{5}$ of its length), and, for example, relating the general result to some of the ways that a guitarist is able to alter the timbre of a tone by changing the plucking position. I think that Chap. 5 on nonlinear systems is much too condensed to provide a good introduction to the various topics covered to typical students with no previous experience to the analysis of such systems. Also, there are no follow-up applications of the theory later in the book. This chapter should be expanded. Finally, I suggest giving a more fleshed-out development of the Sabine formula for reverberation time in Chap. 11.

As I emphasized above, these suggestions constitute only minor quibbles, and I again wish to acknowledge the overall excellence of *Principles of Vibration and Sound* as a solid text for introductory acoustics.

ARNOLD TUBIS
Purdue University
West Lafayette, Indiana 47907

Engineering Acoustics: An Introduction to Noise Control

Michael Möser

Springer-Verlag Berlin, 2004
xi+289 pp. Price: 69.95 EUR (hardcover) ISBN: 3-540-20236-6.

Engineering Acoustics is a translation from German into ''British'' English of Möser's *Technische Akustik*. That book is the 5th complete revision of Lothar Cremer's *Vorlesunden über Technische Akustik*. The result is a very readable and an excellent text.

The book is not a text book in the usual sense, with homework problems at the end of each chapter. Möser considers it a ''teaching text.'' He adequately covers a subject, then suggests references for further study.

The book is unique in several ways.

(1) His first chapter on the Perception of Sound includes the ear and its response and human response to stimulation. Then the need for filtering and types of filters is presented.
(2) Each subject is introduced with a qualitative description based on common observation. This is followed by a rigorous mathematical modeling of the phenomena.
(3) He uses figures that give good visualization of acoustic waves. This includes radiation of waves from directional sources and wave interaction with solids such as wall partitions.
(4) In presenting Intensity, he gives a very complete description and limitation of the two microphone probe.

The book provides an excellent coverage of acoustic fundamentals. Then, because of the need in noise control, he presents waves in solids and the means for vibration control. Sensors required for measurement of acoustic pressure and mechanical vibrations are discussed. In addition to the chapter on sound perception, other chapter headings are as follows:

Fundamentals of Wave Propagation
Propagation and Radiation of Sound
Structure-borne Sound
Elastic Isolation
Sound Absorbers
Fundamentals of Room Acoustics
Building Acoustics
Silencers
Diffraction
Electro-Acoustic Transducers for Air-Borne Sound

His Appendix presents ''Level Arithmetic'' to introduction logarithmic notation to newcomers to the field. Then he introduces ''Complex Pointers'' as his alternative to ''Phasor Notation.'' Complex arithmetic as applied to acoustics is covered in great detail. Finally, many references are given that applied to the theory and for further study. Many of these are from the German literature and may be difficult to obtain or read for the American reader.

The book is excellent in dealing with noise control in interior spaces. However, the author does not cover sound propagation in the atmosphere and the subject of community noise problems. This is an excellent book in the areas covered and it should be on the bookshelf of every noise control engineer.

ELMER L. HIXSON
University of Texas at Austin
Austin, Texas 78712-0240

Principles of Vibration and Sound, 2nd edition

Thomas D. Rossing and Neville H. Fletcher

Springer-Verlag, New York, 2004.
xiii +330 pp. Price: $49.95 (hardcover). ISBN: 0-387-40556-9

This book is designed to serve as a text for an introductory course in acoustics for physics or engineering students. Its primary focus is on the basic physical principles and associated mathematics underlying acoustics and some of its important applications.

The first edition of this text, published in 1995, consisted essentially of a separate publication of the foundation chapters on vibrating systems and sound waves contained in the first edition of *The Physics of Musical Instruments* (Springer-Verlag, New York, 1991) by the same authors (with the addition of an extra chapter on network analogs of acoustic systems, and some problems.) The first nine chapters of this new edition are, except for some slight revisions, the same as those in the first edition. However, in order to meet student needs for more applications of basic principles, the authors have added four new chapters.

In Part I of the book (Vibrating Systems), Chap. 1 focuses on simple vibrating systems and their mathematical representations, including responses to harmonic excitation, an introduction to some aspects of nonlinear vibrations, and two-dimensional harmonic motions (Lissajous figures). Chapter 2 gives a comprehensive introductory account of vibrating strings and bars, including the effects of stiffness, and motion of end supports. In Chap. 3, the vibrations of rectangular and circular plates and membranes are introduced, and in Chap. 4, the coupling of vibrating systems, including the example of string-plate coupling, is discussed. This chapter also contains very short descriptions of modal and finite element analyses and their literature. Part I is concluded by a very brief chapter on nonlinear systems.

Part II starts off with a fairly standard coverage of sound waves in air (Chap. 6), sound radiation (Chap. 7), and pipes and horns (Chap. 8). The presentation in these chapters is mostly confined to the frequency-domain case of steady-state harmonic excitation, but there is a brief summary of the time-domain analysis approach of Schumacher, McIntyre and Woodhouse, and Ayers at the end of Chap. 8. A leisurely introduction to acoustic network analysis in Chap. 9 is followed by one of the new chapters on microphones, loudspeakers, hydrophones, ultrasonic transducers, force transducers, and accelerometers. The book concludes with three new chapters on sound in three different environments—concert hall and studio, outdoor, and underwater.

On the basis of its clear and concise exposition of a mix of basic and applied subject matter, I would recommend this book for consideration as a text in an introductory acoustics course. However, in the spirit of wanting to see this text evolve into an even better one (perhaps in its next edition), I will make several recommendations.

First of all, several disconcerting statements, related to the fact that the first eight chapters are excised from a larger work, should certainly be removed. For example, on p. 70, in the discussion of the effect of air loading on the modal frequencies of a kettle drum, there is reference to a further discussion in Chap. 18 (a chapter in *The Physics of Musical Sounds*, but *not* in this book). In Chap. I, I would have liked to see the concept of a temporal Green's function introduced in the simple context of calculating the response of a harmonic oscillator to a general excitation. This introduction would have been a good entre to the later use of temporal Green's functions in Chap. 8. I also suggest adding a few lines of discussion to establish the simple general rules for reading off harmonic frequency ratios from Lissajous figures. In Chap. 2, the frequency analysis of plucked and struck strings should be made more general by calculating analytically the Fourier amplitudes of the string response for an *arbitrary* point of excitation (instead of just a point at $\frac{1}{5}$ of its length), and, for example, relating the general result to some of the ways that a guitarist is able to alter the timbre of a tone by changing the plucking position. I think that Chap. 5 on nonlinear systems is much too condensed to provide a good introduction to the various topics covered to typical students with no previous experience to the analysis of such systems. Also, there are no follow-up applications of the theory later in the book. This chapter should be expanded. Finally, I suggest giving a more fleshed-out development of the Sabine formula for reverberation time in Chap. 11.

As I emphasized above, these suggestions constitute only minor quibbles, and I again wish to acknowledge the overall excellence of *Principles of Vibration and Sound* as a solid text for introductory acoustics.

ARNOLD TUBIS
Purdue University
West Lafayette, Indiana 47907

REVIEWS OF ACOUSTICAL PATENTS

Lloyd Rice
11222 Flatiron Drive, Lafayette, Colorado 80026

The purpose of these acoustical patent reviews is to provide enough information for a Journal reader to decide whether to seek more information from the patent itself. Any opinions expressed here are those of reviewers as individuals and are not legal opinions. Printed copies of United States Patents may be ordered at $3.00 each from the Commissioner of Patents and Trademarks, Washington, DC 20231. Patents are available via the Internet at http://www.uspto.gov.

Reviewers for this issue:

GEORGE L. AUGSPURGER, *Perception, Incorporated, Box 39536, Los Angeles, California 90039*
JOHN M. EARGLE, JME Consulting Corporation, 7034 Macapa Drive, Los Angeles, California 90068
MARK KAHRS, *Department of Electrical Engineering, University of Pittsburgh, Pittsburgh, Pennsylvania 15261*
DAVID PREVES, *Starkey Laboratories, 6600 Washington Ave. S., Eden Prarie, Minnesota 55344*
DANIEL R. RAICHEL, *2727 Moore Lane, Fort Collins, Colorado 80526*
CARL J. ROSENBERG, *Acentech Incorporated, 33 Moulton Street, Cambridge, Massachusetts 02138*
NEIL A. SHAW, Menlo Scientific Acoustics, Inc., Post Office Box 1610, Topanga, California 90290
WILLIAM THOMPSON, JR., *Pennsylvania State University, University Park, Pennsylvania 16802*
ERIC E. UNGAR, *Acentech, Incorporated, 33 Moulton Street, Cambridge, Massachusetts 02138*
ROBERT C. WAAG, *Univ. of Rochester, Department of Electrical and Computer Engineering, Rochester, New York 14627*

6,748,815

43.20.Ye METHOD FOR DETERMINING PARTICLE SIZE

Malcolm J. W. Povey *et al.*, assignors to Baker Hughes, Incorporated
15 June 2004 (Class 73/865.5); filed 29 October 2002

''...[I]t has been discovered that the size, concentration, and size distribution of small particles in a fluid can be derived from measurements of acoustic speckle signals produced by the particles in response to input signals of acoustic energy. This...is especially significant because acoustic speckle, particularly for energy of ultrasonic wavelengths, can be measured

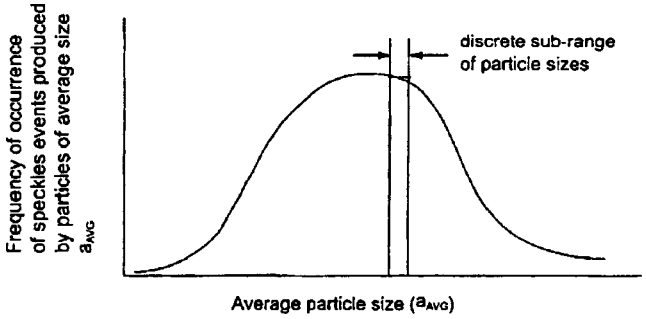

very quickly and can be transmitted and sensed in optically opaque fluids.'' This invention uses what has previously been seen as an annoyance in many applications to measure fluid flow and particle size and concentration in even opaque fluids. This technique can be used separately or in conjunction with other particle measurement techniques.—NAS

6,736,687

43.30.Nb METHOD FOR DISCHARGING WASTE GAS FROM SUBMARINES WITHOUT A SIGNATURE

Peter Hauschildt, assignor to Howaldtswerke-Deutsche Werft AG
18 May 2004 (Class 440/89 B); filed in Germany 9 December 2000

To obviate the problem of discharging exhaust gas from an onboard electrical energy producing system in an underwater vehicle and hence to reduce the radiated noise from that vehicle, the gas is dissolved inside a turbulent, water-filled pipe. That water is then discharged, at ambient pressure, back into the surrounding ocean.—WT

6,738,311

43.30.Vh SEABED SONAR MATRIX SYSTEM

Jacques Yves Guigné, assignor to Guigne International, Limited
18 May 2004 (Class 367/88); filed 26 October 2000

A sonar system for probing the seabed comprises a linear array of closely spaced transducers, each of which can be independently energized at a sufficiently high frequency to produce narrow beams. The echoes from the first beam are detected by an auxiliary sensor, whence another transducer in the array is energized to produce a second beam directed on an adjacent area of the seabed, etc. The array is moved perpendicularly to itself to implement raster scanning. The display of echoes enables an operator to detect anomalies indicating the presence of objects or a seabed condition of interest that can then be examined more extensively.—WT

6,741,381

43.35.Sx MODIFIED TUNABLE ACOUSTO-OPTIC FILTER

Marc Levenson and Robert Lodenkemper, assignors to Picarro, Incorporated
25 May 2004 (Class 359/285); filed 8 November 2002

This patent relates to acousto-optic filter systems for filtering a light beam by generating undiffracted and diffracted light beams within a birefringent filter and by suppressing the diffracted beam within or at the face of the crystal. When the two beams are noncollinear, an aperture provides diffracted beam suppression. In the case where the two beams possess different polarization directions, the diffracted beam is suppressed by a polarization analyzer, internal reflection of each beam in a Brewster angle at the surface, or a suitably oriented multilayer thin film at the source. Variation of the acoustic frequency provides tunability of the filter.—DRR

6,741,382

43.35.Sx ACOUSTO-OPTIC ACTIVITY FOR ACOUSTIC IMAGING

Milind M. Sonpatki, Wheeling, Illinois *et al.*
25 May 2004 (Class 359/285); filed 1 July 2003

Two acousto-optic media are combined to form a net medium having a net acousto-optical property activity greater than that of the first medium alone. The improvement is substantiated through measurements made at specific viewing conditions and by selection of the second medium due to its affect on at least one of three key properties of the net medium.—DRR

6,744,895

43.38.Dv LOUDSPEAKER

Kazumi Miyamoto and Masahito Furuya, assignors to Citizen Electronics Company, Limited
1 June 2004 (Class 381/182); filed in Japan 9 May 2001

If one can increase the density of the magnetic flux in a voice coil driving circuit, it is possible to increase the sound pressure from a loudspeaker design, the coil length and coil current remaining the same, that is, $F=Bli$. This is well known and expressly stated in the patent. When a loudspeaker assembly has two voice coils, each coil driving its own diaphragm, where one diaphragm **27** is used for a relatively broad-band signal,

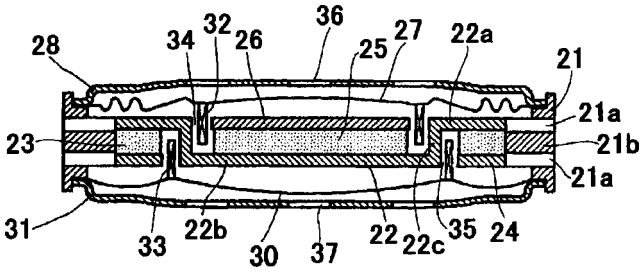

such as speech, and the other diaphragm **30** is used for a signal of more modest bandwidth, such as the ring signals used for cell phones, the sound pressure produced, by what is described as prior art, may not be sufficient for the intended use. This invention uses two magnets, **23** and **25**, and a novel pole piece **22** to increase the flux density in the voice coil gaps. The patent itself is extremely concise and to the point.—NAS

6,725,967

43.38.Ja LOW DISTORTION LOUDSPEAKER CONE SUSPENSION

Stefan R. Hlibowicki, assignor to Audio Products International Corporation
27 April 2004 (Class 181/172); filed 10 October 2002

The half-roll cone suspension used in many loudspeakers typically has a semicircular cross section. This patent argues that linearity can be improved by making the height substantially greater than half the width. Actually, for special applications, the idea can be carried much farther than is envisioned here, taking the form of a folded cuff. Such a transducer was designed and built by JBL more than a quarter-century ago.—GLA

6,735,320

43.38.Ja ANGLED PORT LOUDSPEAKER

Stephen J. Gertner, Jr., Allentown, Pennsylvania
11 May 2004 (Class 381/349); filed 25 March 1996

In theory, the vent output of a vented loudspeaker system has a bandpass characteristic, with response rolling off smoothly above resonance. In practice, all sorts of high-frequency garbage can come out of the vent open

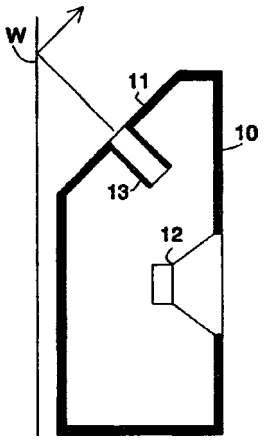

ing. From time to time, inventors try to make use of this energy instead of suppressing it. In the case at hand, ''...the direction of the angle of the port can be used to control the bass output. For more release of the upper notes, the port is directed at the center of the driver or speaker. For greater release of lower notes, the port is directed at the edge of the speaker cone, and for the deepest bass enhancement, the port is moved away from the cone or the steepness of the angle is increased.'' What could be more logical?—GLA

6,738,483

43.38.Ja OVERHEAD LOUDSPEAKER SYSTEMS

Robert W. Betts, assignor to Sonic Systems, Incorporated
18 May 2004 (Class 381/160); filed 11 October 2000

In this recessed ceiling speaker, woofer **24** and tweeter **25** are directed toward conical reflector **31**. Nothing new thus far. However, ''wave shaping

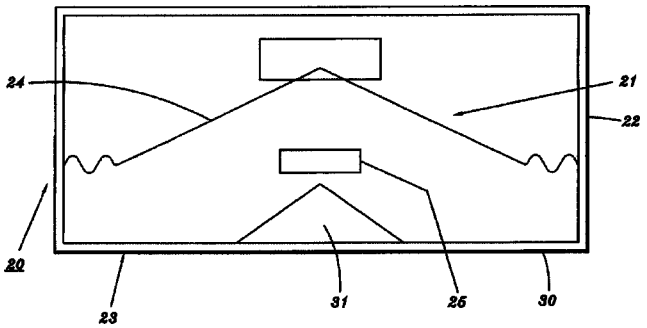

and controlling member'' **23** is actually a plate with numerous teardrop-shaped cutouts. Voila, ''...a synergistic interaction is realized which produces results heretofore believed to be unattainable.''—GLA

6,739,425

43.38.Ja EVACUATED ENCLOSURE MOUNTED ACOUSTIC ACTUATOR AND PASSIVE ATTENUATOR

Steven Griffin *et al.*, assignors to The United States of America as represented by the Secretary of the Air Force
25 May 2004 (Class 181/171); filed 5 April 2002

The air in the back chamber of a loudspeaker enclosure **20** is evacuated to decrease its effective spring constant. A nonlinear stiffness support

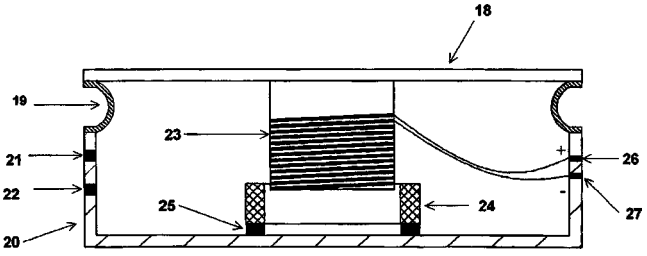

19 can support the large pressure loads across the diaphragm while simultaneously exhibiting a low stiffness on the order of that in conventional suspensions. By these means, the natural frequency of the system can be lowered so that the low-frequency response of the system is greatly enhanced. The patent is easy to follow, is straightforward in its presentation, makes reference to several standard texts, and provides a numerical example of the described improvement in response.—NAS

6,744,902

43.38.Ja PORTED LOUDSPEAKER ENCLOSURE

Lucio Proni, assignor to JL Audio, Incorporated
1 June 2004 (Class 381/386); filed 10 July 2002

The autosound aftermarket is a huge business which is very competitive. ''Among the objectives of this invention (is) to provide an enclosure for a loudspeaker which is visually acceptable in the environment of a vehicle, which is economical to fabricate, and which effectively transmits sound produced by loudspeakers mounted therein externally of the enclosure.'' Said invention is manifested by having a top panel, bottom panel, front panel, and opposed end panels defining a hollow interior in which a baffle is mounted to which a loudspeaker or loudspeakers are mounted. A port is formed that shares a common exit toward which said loudspeaker(s)

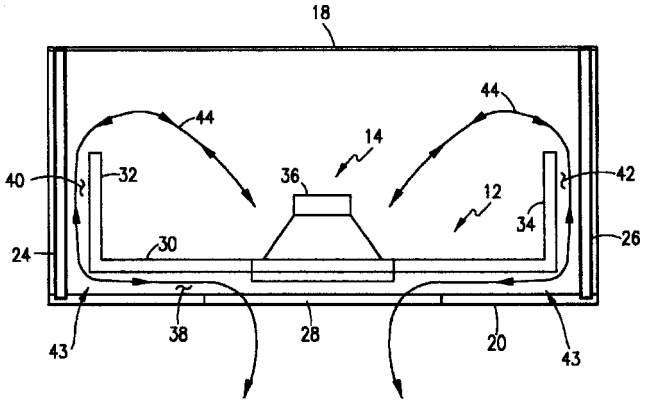

are also aimed. There are many variations of this type of box in existence, but the designer has made an astute application of construction. Specifically, such designs can use groove-folded laminate (vinyl covered particle board that folds using the vinyl as the hinge) for inner baffling and chambers and carpet covered panels for visible surfaces. Said design lends itself to cost-effective construction and compact size with significant commercial implications. It must also be said that the word ''said'' is the most common word in the claims.—NAS

6,717,524

43.38.Kb VOICE ACQUISITION SYSTEM FOR A VEHICLE

Jonathan E. DeLine *et al.*, assignors to Donnelly Corporation
6 April 2004 (Class 340/815.4); filed 15 October 2002

This disclosure involves methods of mounting microphones on a rear-view mirror or other mounting along the upper edge of the windshield of a car. Although multiple microphones are mentioned a couple of places in the patent text and in the claims and are shown in the figures, there is no mention of the well-developed technology for microphone array processing. Similarly, there is no particular emphasis on methods of signal processing,

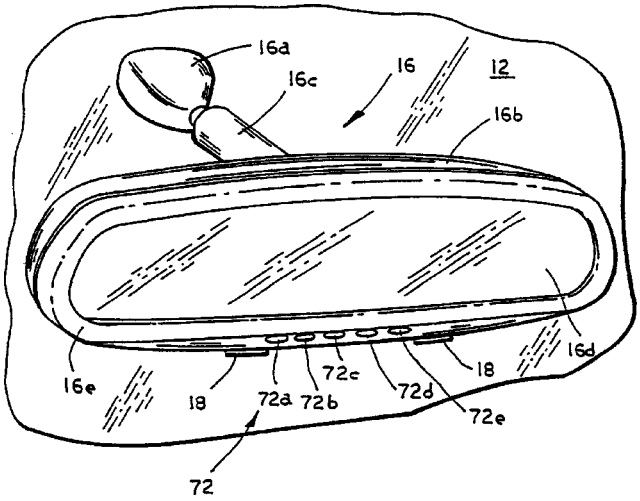

amplification, etc. A wide variety of mounts and attachments are described.—DLR

6,731,760

43.38.Lc ADJUSTING A LOUDSPEAKER TO ITS ACOUSTIC ENVIRONMENT: THE ABC SYSTEM

Jan A. Pedersen, assignor to Bang & Olufsen A/S
4 May 2004 (Class 381/59); filed in Denmark 2 November 1995

It is well known that a loudspeaker placed in a corner will produce more powerful bass than if it is located well away from room boundaries. Many powered loudspeaker systems include adjustable settings to modify low frequency response in relation to room placement. Why not include a sensor as part of the system and make such bass compensation automatic?

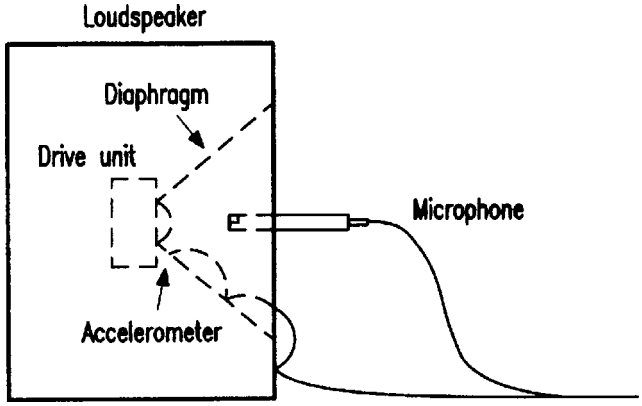

The advantage of such a method is that everything is included in a single package. The disadvantage is that equalization cannot be optimized for a particular listening location. This short, well-written patent describes an improved all-in-one equalization method that is said to ''...significantly increase the certainty that the customer will always experience the quality intended by the loudspeaker designer.''—GLA

6,748,085

43.38.Lc COMPUTER SYSTEM WITH A COMMON AUDIO INPUT FOR ITS AUDIO CIRCUITRY

Sung-Dong Yang, assignor to Samsung Electronics Company, Limited
8 June 2004 (Class 381/11); filed in the Republic of Korea 6 May 1998

The patent deals with the simplification of input circuits on personal computers. If a stereo signal is present (as with a ring-tip-sleeve connector),

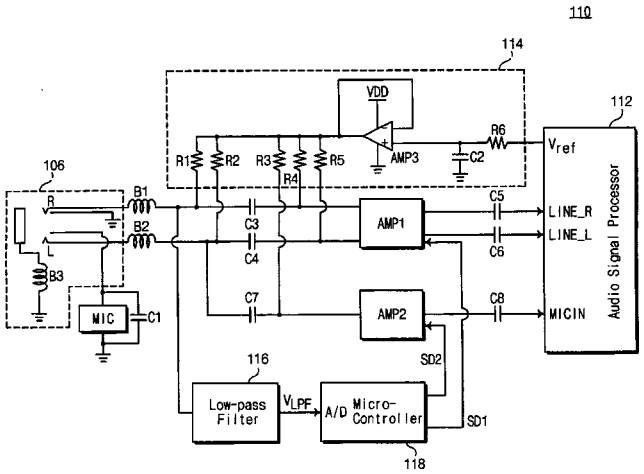

the stereo input is actuated and the mono preamplifier is defeated. If a mono device (e.g., a microphone) is detected, the stereo preamplifier is defeated. The intention is to save battery power and to conserve valuable space along the thin side edge of the PC case.—JME

6,704,706

43.38.Md METHOD AND SYSTEM FOR REDUCTION OF QUANTIZATION-INDUCED BLOCK-DISCONTINUITIES AND GENERAL PURPOSE AUDIO CODEC

Shuwu Wu and John Mantegna, assignors to America Online, Incorporated
9 March 2004 (Class 704/230); filed 4 February 2002

A transform-based audio coder must divide the data into fixed sized blocks. The block boundaries result in many audible artifacts. In this disclosure, the inventors aim to reduce the quantization error due to the ''Gibbs leakage'' at the window boundaries. Their solution is (a) to use bell shaped weighting on samples across the boundary, (b) to apply efficient quantization, and (c) to model any residual as stochastic noise. The algorithms are given clearly in MATLAB™ as well as text.—MK

6,728,585

43.38.Md PERSONAL ON-DEMAND AUDIO ENTERTAINMENT DEVICE THAT IS UNTETHERED AND ALLOWS WIRELESS DOWNLOAD OF CONTENT

Chong Lim Neoh, assignor to FreeSystems Pte, Limited
27 April 2004 (Class 700/94); filed 3 October 2001

This wireless headset includes digital memory and electronics cir-

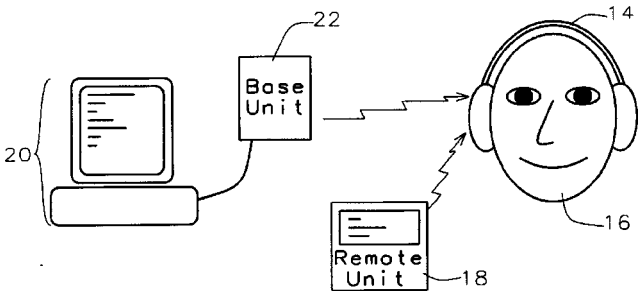

cuitry, allowing locally stored audio to be played at the same time that downloading is in process.—GLA

6,741,237

43.38.Md TOUCH SCREEN

David J. Benard *et al.*, assignors to Rockwell Automation Technologies, Incorporated
25 May 2004 (Class 345/173); filed 23 August 2001

A touch screen system is decribed in which surface acoustic waves are generated across a substrate of the screen. In a typical case, a single transmitter and at least two receivers are located along the edges of the substrate. When a finger or other object is placed on the screen, reflections at the point

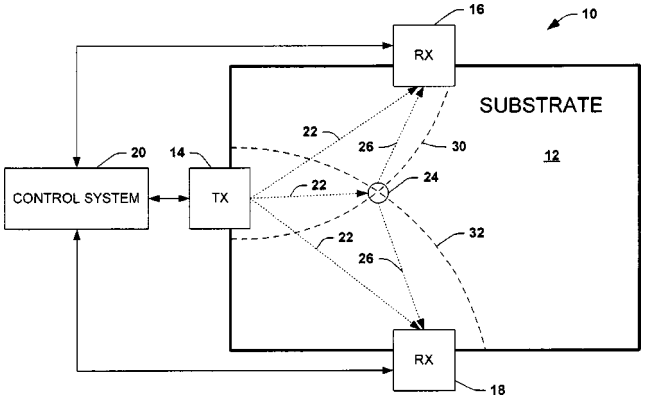

of contact disturb the reference pattern, allowing the specific location of the contact point to be identified. Other aspects of the patent deal with system accuracy and the logic involved in estimating the actual point of contact.—JME

6,744,703

43.38.Md CONTINUOUS RECORDING APPARATUS BY INTERPOLATING THE AUDIO SIGNAL DURING SEEKING OPERATION

Atsushi Saito *et al.*, assignors to Hitachi, Limited
1 June 2004 (Class 369/30.18); filed in Japan 27 February 2001

A modern disk generates noise when seeking from track to track as the head is pushed by the linear motor. This noise would be audible if the disk were close to the microphone. The inventors propose suspending audio recording while seeking and then interpolating. Given a seek time of approximately 4 ms for a modern disk, this would be 384 samples at 96 k samples/s. That's a sizable gap. They do note that this gap may be impossible to interpolate for some types of audio signals.—MK

6,744,971

43.38.Md INFORMATION SIGNAL RECORDING/ REPRODUCING APPARATUS AND METHOD THEREOF

Tadashi Noguchi, assignor to Pioneer Corporation
1 June 2004 (Class 386/95); filed in Japan 14 September 1999

Although commercial TV networks don't like it, video recorders can be used to skip over commercials. The question for the home viewer is: can the recorder automatically detect them? The inventor uses the time duration as a first threshold. If the time difference is less than 5 min, then see if it is a multiple of 30 s (due to network charges, commercial time is quantized). If so, then the playback can be advanced. Of course, this only works if the storage medium has a directory. In addition, you can use the audio channel status (stereo, mono) to make additional ''commercial judgements.''—MK

6,749,507

43.38.Md ENTERTAINMENT APPARATUS AND MONITOR DEVICE USED THEREIN

Ken Kutaragi *et al.*, assignors to Sony Computer Entertainment Incorporated
15 June 2004 (Class 463/31); filed in Japan 8 June 2000

This patent for the design of the Sony Playstation shows that a gaming console can be constructed with a lid **910** containing LCD display **911** with

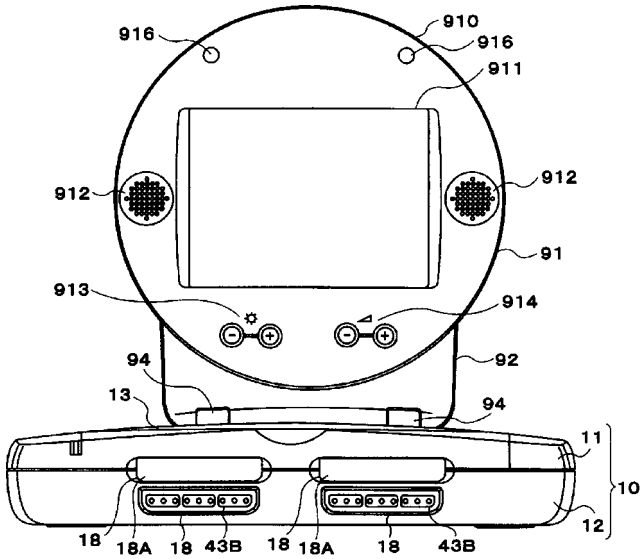

hinge **94** connected to the main box that has both audio and video output.—MK

6,751,167

43.38.Md INFORMATION PLAYBACK APPARATUS

Yoichi Yamada *et al.*, assignors to Pioneer Corporation
15 June 2004 (Class 369/30.19); filed in Japan 22 May 2001

Once again, a digital scratching player is described [see United States Patent 6,687,193, reviewed in J. Acoust. Soc. Am. **116**(1), 25 (2004)]. The patents describe how to use a large (64 Mbyte) ring buffer with read and write pointers and varying pointer increments and decrements to produce varying segments via a ''digital thumb.''—MK

6,728,374

43.38.Si TRANSMITTER/RECEIVER COMPRISING BONE-CONDUCTION SPEAKER

Takeshi Takeda, assignor to Temco Japan Company, Limited
27 April 2004 (Class 379/433.02); filed in Japan 25 May 1999

This hand-held handset for cellular telephones consists of a bone-conduction receiver, a microphone, and a housing for associated electronics. All three components are roughly the same size and the array can be disguised as a piece of costume jewelry. During operation, the receiver is held against the user's forehead or cheek bone with the microphone adjacent to the user's mouth. The entire assembly can be cupped in one's palm, facilitating inconspicuous, private voice communication—a feature that will puzzle American cell phone owners.—GLA

6,738,485

43.38.Si APPARATUS, METHOD AND SYSTEM FOR ULTRA SHORT RANGE COMMUNICATION

Peter V. Boesen, Des Moines, Iowa
18 May 2004 (Class 381/312); filed 7 November 2000

This patent is a continuation of eight previous filings extending over a five-year span. The inventor envisions a kind of intelligent two-way personal voice information system, ''...capable of receiving information, including, but not limited to voice sound information and providing actions

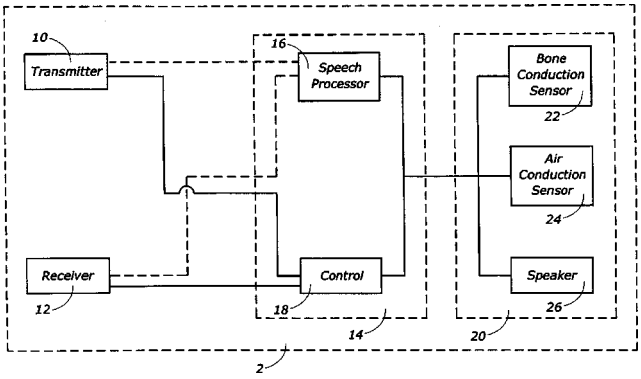

based upon the particular information.'' Numerous possible applications are described, but to this reviewer, exactly what is patented is difficult to pin down.—GLA

6,738,487

43.38.Si EARPHONE

Koji Nageno *et al.*, assignors to Sony Corporation
18 May 2004 (Class 381/322); filed in Japan 31 May 1999

The performance and comfort of an earbud type earphone depend on the particular ear in which it is inserted. This patent describes an improved design which incorporates a resistive air leak to counteract the effects of cavity resonances.—GLA

6,744,900

43.38.Si COMPLEX ACOUSTIC PATH AND GASKET FOR USE WITH MICROPHONES

Julia Carol Turner *et al.*, assignors to Mitel Knowledge Corporation
1 June 2004 (Class 381/355); filed in the United Kingdom 14 September 1999

This fairly simple and straightforward patent deals with telephone handsets and discusses improvements in transmitter construction and response.—JME

6,731,765

43.38.Vk LOUDSPEAKER DEVICE

Hiromi Sotome, assignor to Yamaha Corporation
4 May 2004 (Class 381/160); filed in Japan 26 September 1996

By using sophisticated digital filtering to compensate for interaural crosstalk, it is possible to reproduce multichannel stereo program material from two loudspeakers placed close together. This patent asserts that such close coupling provides an acoustical short circuit for certain signals that

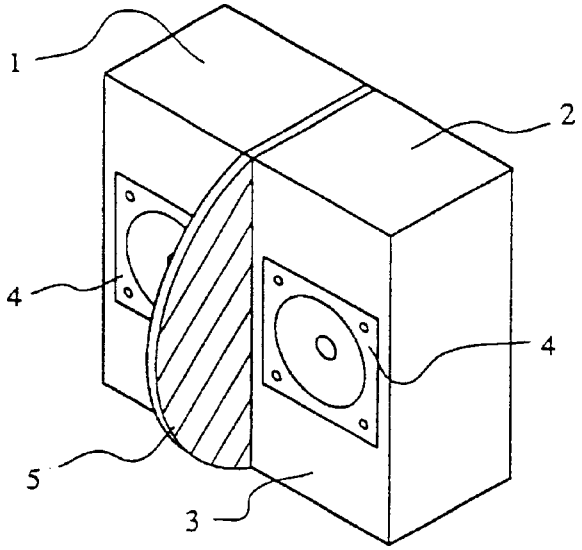

consequently fail to reach the listener's ears. The invention is a partial barrier **5** that is intended to reduce interaction between loudspeakers **4** and to stiffen the cabinet as well.—GLA

6,738,318

43.38.Vk AUDIO REPRODUCTION SYSTEM WHICH ADAPTIVELY ASSIGNS DIFFERENT SOUND PARTS TO DIFFERENT REPRODUCTION PARTS

Scott C. Harris, San Diego, California
18 May 2004 (Class 369/2); filed 5 March 2001

Individual channels of a multichannel recording system are assigned on the basis of sonic qualities rather than individual sources or source locations. During playback, channels are routed to the available loudspeakers best suited for the task.—GLA

6,741,273

43.38.Vk VIDEO CAMERA CONTROLLED SURROUND SOUND

Richard C. Waters and Franklin J. Russell, Jr., assignors to Mitsubishi Electric Research Laboratories Incorporated
25 May 2004 (Class 348/61); filed 4 August 1999

A video camera is used to record the positions of surround loudspeakers in a listening space. The data are subsequently used to compute and

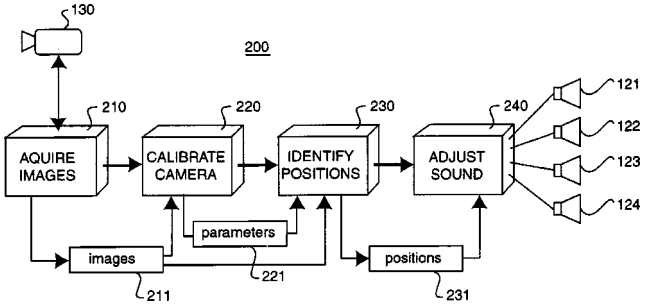

adjust signal level and delay values for each loudspeaker appropriate for the selected listening position.—JME

6,741,965

43.38.Vk DIFFERENTIAL STEREO USING TWO CODING TECHNIQUES

Osamu Shimoyoshi and Kyoya Tsutsui, assignors to Sony Corporation
25 May 2004 (Class 704/500); filed in Japan 10 April 1997

This very elaborate patent appears to combine the advantages of subband encoding and decoding with the basic simplicity of matrixing stereo channel pairs with their equivalent sum and difference components. The advantages lie partly in the fact that the difference channel normally has a lower signal amplitude than the sum channel and thus may be encoded at a lower data rate. With 37 figures and 61 claims, the patent makes for some heavy reading.—JME

6,741,706

43.38.Wl AUDIO SIGNAL PROCESSING METHOD AND APPARATUS

David Stanley McGrath *et al.*, assignors to Lake Technology Limited
25 May 2004 (Class 381/22); filed in Australia 25 March 1998

This patent deals with methods of delivering multichannel programs in a variety of reproducing formats and playback settings. The basic ''raw'' tracks are convolved as needed to meet the individual requirements of headphone or loudspeaker listening. The impulse data required for the various convolution operations can be simplified by a number of techniques described in the patent. The document is very well written and could easily serve as a guide for a workshop in digital signal processing.—JME

6,731,570

43.38.Zp SOUND DETECTION

Roger M. Langdon, assignor to BAE Systems Electronics Limited
4 May 2004 (Class 367/149); filed in the United Kingdom 6 February 1998

Enemy helicopter **110** is hidden from armored vehicle **112**, but it produces sound waves **117** that propagate into the atmosphere above. The invention is an improved opto-acoustical method of sensing such sound waves

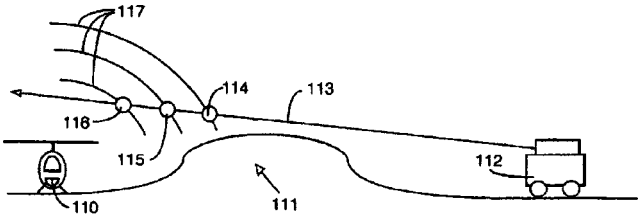

from a remote location by using a pulsed laser beam and then detecting scattered light from the beam. Those interested in the field will find the patent succinct and interesting.—GLA

6,742,960

43.40.Tm VIBRATORY COMPACTOR AND METHOD OF USING SAME

Paul T. Corcoran *et al.*, assignors to Caterpillar Incorporated
1 June 2004 (Class 404/117); filed 9 July 2002

According to this patent, vertical vibratory forces are produced in soil compactors by oscillating masses that are moved by electrodynamic means. The frequencies and amplitudes of the masses' vibrations can be controlled over much greater ranges than in compactors that rely on rotating unbalanced masses.—EEU

6,742,998

43.40.Tm LINEAR COMPRESSOR WITH VIBRATION CANCELING SPRING ARRANGEMENT

Sadao Kawahara *et al.*, assignors to Matsushita Electric Industrial Company, Limited
1 June 2004 (Class 417/416); filed in Japan 19 July 2001

A spring-mounted piston is driven electromagnetically to oscillate axially within a sealed housing. A spring-mounted sleeve that surrounds the piston and serves as its cylinder is similarly made to oscillate axially in the housing, but in opposite phase to the piston's vibration, resulting in reduced vibration of the housing.—EEU

6,742,381

43.40.Yq APPARATUS AND METHOD FOR EVALUATING DAMPING PERFORMANCE OF VIBRATION-DAMPING DEVICES

Hajime Maeno, assignor to Tokai Rubber Industries, Limited
1 June 2004 (Class 73/11.01); filed in Japan 12 March 2002

The system described in this patent appears to be intended for production testing of dynamic absorbers and inertial dampers. The item to be tested is mounted on the apparatus and an accelerometer is affixed to it. The item then is struck by a hammer that is dropped from a controlled height and caught so that it cannot rebound onto the test item. Performance of the test item is evaluated from the time trace of the accelerometer output or from its spectrum.—EEU

6,742,393

43.40.Vn VIBRATION CONTROL APPARATUS, VIBRATION CONTROL METHOD, EXPOSURE APPARATUS, AND DEVICE MANUFACTURING METHOD

Hiroshi Ito, assignor to Canon Kabushiki Kaisha
1 June 2004 (Class 73/662); filed in Japan 26 February 2002

This patent relates to systems in which high-speed, high-accuracy control is required, such as in semiconductor exposure apparatus, machine tools, and optical alignment devices. In such systems, the gain of the position control system is set as high as possible in order to obtain fast positioning, but this tends to induce elastic vibrations of key components. This leads to increased control error or servo system instability. To overcome this problem, the elastic and the rigid-body vibrations of a key component are controlled actively, using appropriate sensor, actuator, and controller arrangements.—EEU

6,745,149

43.50.Gf ACOUSTICAL NOISE REDUCING ENCLOSURE FOR ELECTRICAL AND ELECTRONIC DEVICES

Todd W. Beeten, Nashville, Tennessee
1 June 2004 (Class 702/132); filed 3 July 2001

Although there appear to be many commercially available examples of this type of device available (enter the appropriate keywords in your favorite search engine), a patent was issued nonetheless.—NAS

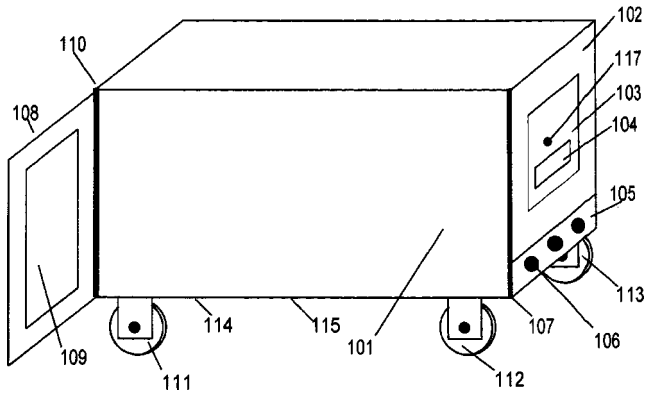

6,751,281

43.40.Yq MEASUREMENT SYSTEM OF TORSION VIBRATION FOR REACTOR INTERNAL PUMP

Naoto Hikida and Seiichi Matsumura, assignors to Hitachi, Limited
15 June 2004 (Class 376/372); filed in Japan 19 July 2002

The pumps to which this patent refers consist of relatively long cylindrical housings that penetrate through openings in reactor vessels. An impeller is located on the pump's end inside the vessel and a motor is located in the pump's cylindrical housing on the outside of the vessel. Torsional vibrations of the housing about its axis are monitored by means of two vibration sensors mounted near the housing's outer end: a velocity sensor senses motions perpendicular to the housing's surface, and an accelerometer, located at 90 degrees around the housing circumference from the first, senses motions tangential to the housing's surface. The accelerometer signal is integrated, low-pass filtered, and subtracted from the signal that is obtained from the velocity sensor to yield a measure of the housing's torsional vibrations.—EEU

6,749,939

43.55.Wk COMPOSITION HAVING SEALING AND SOUND DAMPENING PROPERTIES AND METHODS RELATED THERETO

Umesh C. Desai *et al.*, assignors to PPG Industries, Ohio, Incorporated
15 June 2004 (Class 428/413); filed 19 February 2002

The patent describes the composition of a sound damping coating that can be sprayed onto a metal sheet in an automotive body shop.—CJR

6,738,312

43.58.Dj ARRANGEMENT AND METHOD FOR MEASURING THE SPEED OF SOUND

Kah Chye Tan *et al.*, assignors to Addest Technovation Pte Limited
18 May 2004 (Class 367/89); filed 16 April 2003

This patent describes a low-cost system for measuring the speed of sound in air, suitable for high school science classes and demonstrations. A

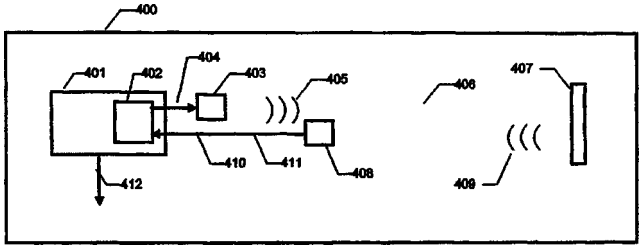

fairly simple device is connected to an ordinary personal computer. Microphone **408** picks up transmitted wave **405** and then reflected wave **409**. The signals are digitally generated and processed by the computer, which then derives sound speed from the round-trip transit time. Although the method described is intended to be more accurate than prior art, many science teachers may feel that it leaves much to be desired both in terms of accuracy and educational potential.—GLA

6,751,322

43.60.Dh ACOUSTIC MODELING SYSTEM AND METHOD USING PRE-COMPUTED DATA STRUCTURES FOR BEAM TRACING AND PATH GENERATION

Ingrid B. Carlbom *et al.*, assignors to Lucent Technologies Incorporated
15 June 2004 (Class 381/63); filed 2 October 1998

The technique of auralization has grown in importance over the last two decades as methods have been refined and the effects of diffraction and scattering have been more accurately modeled. The patent describes in copious detail a technique of beam tracing that makes use of a number of

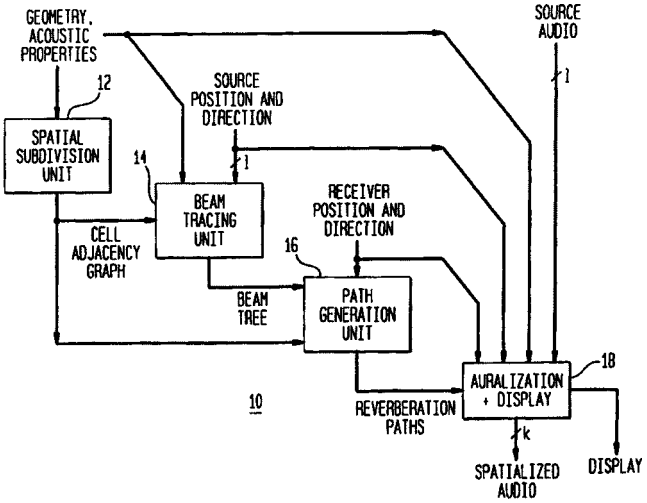

previously solved ''cells'' in the analysis structure. The method allows for ''real-time computation and auralization of propagation paths to an arbitrary receiver location.'' The patent is a model of organization and instruction.—JME

6,748,086

43.60.Fg CABIN COMMUNICATION SYSTEM WITHOUT ACOUSTIC ECHO CANCELLATION

Saligrama R. Venkatesh and Alan M. Finn, assignors to Lear Corporation
8 June 2004 (Class 381/71.4); filed 19 October 2000

The patent deals with the problems of providing speech reinforcement in the cabin of a multipassenger van via two or more loudspeakers. Using beamforming to produce a complex pattern of response peaks and nulls, the

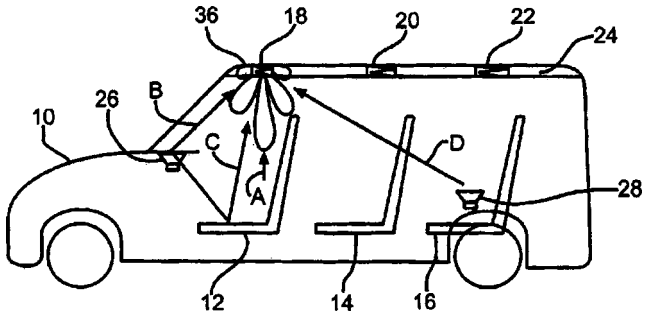

microphone array will track the primary signal from, say, the driver, while adaptively steering the delayed signals (from the loudspeakers) into null zones of the microphone array. The approach is distinctly different from that of echo cancellation.—JME

6,748,088

43.60.Fg METHOD AND DEVICE FOR OPERATING A MICROPHONE SYSTEM, ESPECIALLY IN A MOTOR VEHICLE

Klaus Schaaf, assignor to Volkswagen AG
8 June 2004 (Class 381/92); filed in Germany 23 March 1998

The patent deals with the synthesis of a primary talker's virtual microphone in an automotive environment. The virtual microphone is composed of the outputs of a set of noncollinear and noncoplanar microphone transducers spaced in the environment. When speech signals are received at these transducers, they are adaptively aligned in time, thus defining the virtual microphone. All other sounds originating in the environment will arrive at the transducers randomly, resulting in an improved signal-to-noise ratio for the primary talker. The ''virtual'' microphone's output can then be used for hands-free communication via cell phone.—JME

6,743,175

43.60.Qv VOICE-ENHANCED DIAGNOSTIC MEDICAL ULTRASOUND SYSTEM AND REVIEW STATION

Jeffrey M. Greenberg, assignor to Acuson Corporation
1 June 2004 (Class 600/437); filed 26 November 2002

This is a system designed to augment ultrasound diagnostic procedures by providing the user a voice-activated interaction with the imaging system or review station so that he/she can issue verbal commands instead of using

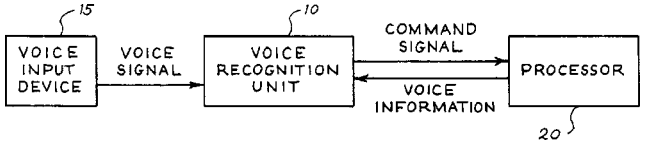

a mouse, keyboard, or other type of user interface that requires physical manipulation by the user. Voice feedback can also be used to allow the imaging system or review station to facilitate communication with a user.—DRR

6,704,413

43.66.Lj AUDITORY USER INTERFACE

William A. Weeks and Bruce E. Balentine, assignors to Plantronics, Incorporated
9 March 2004 (Class 379/374.01); filed 25 October 1999

This patent covers the idea of using sounds as user feedback for specific device functions, as an aid to using a device without having to look at a display. In essence, each major device action would have its own little ''theme song.'' The brief bits of sound are cleverly referred to as ''earcons.'' Patterns of device functions or modes would be represented by specific sound qualities, such as the musical scale, timbre, duration, loudness, and combinations of these. Uses would include eyes-busy tasks, such as driving a vehicle, and applications for the visually impaired.—DLR

6,741,712

43.66.Ts TIME-CONTROLLED HEARING AID

Nikolai Bisgaard, assignor to GN ReSound A/S
25 May 2004 (Class 381/312); filed in Denmark 8 January 1999

To facilitate a hearing aid leasing program, a counter and nonvolatile storage are used to keep track of the time for which the hearing aid has been in use. When this time reaches a preset limit signifying that the subscription has expired, a special function is initiated, such as deactivating the hearing aid. The wearer can reactivate the hearing aid and update its programs by contacting a dispenser via the Internet.—DAP

6,741,713

43.66.Ts DIRECTIONAL HEARING DEVICE

M. M. Boone *et al.*, assignors to Sonionmicrotronic Nederlan B.V.
25 May 2004 (Class 381/313); filed 17 December 1998

The outputs of two hearing aid microphones are fed to a summer hooked to a proportional amplifier and to a difference circuit connected to an

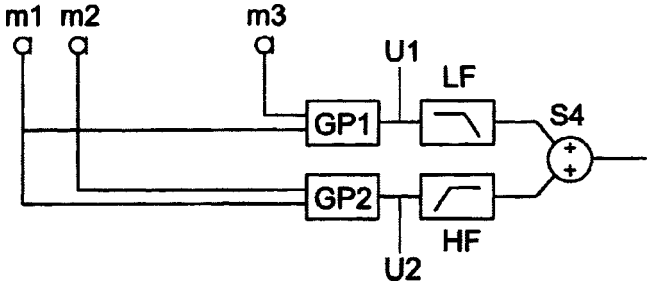

integrator. The proportional and integrator signal outputs are added in a third summer. The result is said to be a flat frequency response and a nearly constant directivity index across frequency. The invention may be used with a third microphone by providing another proportional-integral processor, low- and high-pass filters, and a fourth summer.—DAP

6,741,714

43.66.Ts HEARING AID WITH ADAPTIVE MATCHING OF INPUT TRANSDUCERS

Lars Baekgaard Jensen, assignor to Widex A/S
25 May 2004 (Class 381/313); filed in Denmark 4 October 2000

Signal processing in a hearing aid is modified depending on the type of

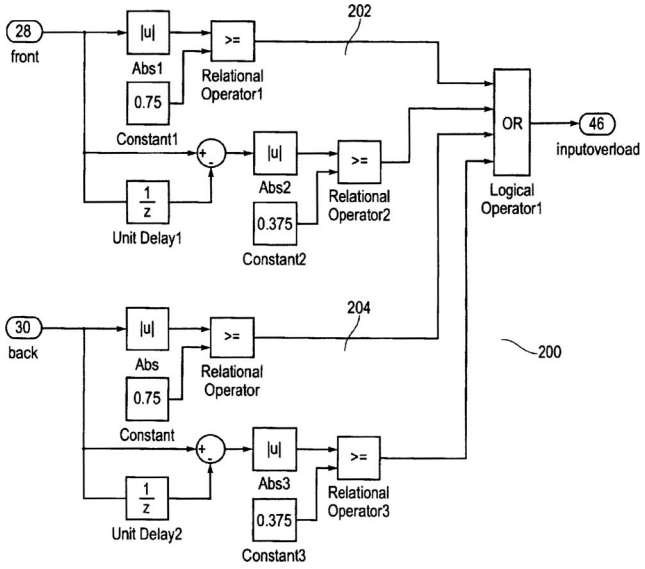

signal received by the hearing aid microphones. For example, if at least one of the microphone inputs is dominated by distortion produced by clipping or noise caused by wind, a correlation detector generates a control signal that temporarily switches the directional system formed by two omni-directional microphones to an omni-directional characteristic.—DAP

6,744,897

43.66.Ts HEARING AID

André Vonlanthen, assignor to Phonak AG
1 June 2004 (Class 381/322); filed in the World IPO 8 November 1999

Wax clogging up the output tubing of hearing aids and their speakers (receivers) is a major problem with current hearing aid fittings. This patent

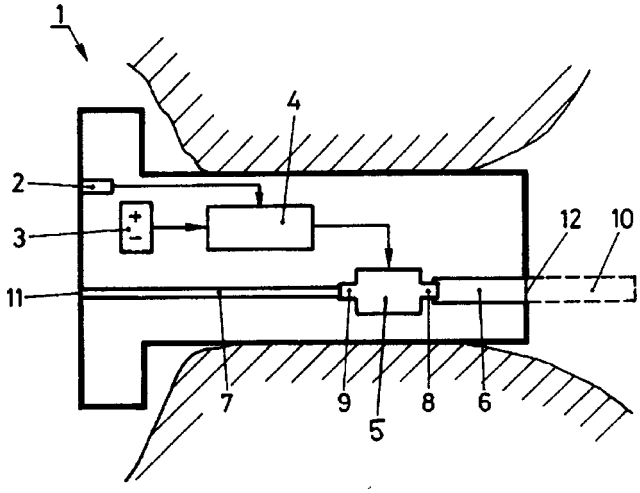

describes a special hearing aid receiver implemented with two ports so as to enable flushing out debris in the receiver and its tubings.—DAP

6,748,092

43.66.Ts HEARING AID WITH IMPROVED PERCENTILE ESTIMATOR

Lars Baekgaard, assignor to Widex A/S
8 June 2004 (Class 381/313); filed 1 December 1998

In prior art, intense noise input signals increase the percentile estimate on the input signal, thereby reducing the hearing aid gain for an elongated period, which may result in loss of audibility immediately after the signal level suddenly drops. A faster acting percentile estimation is achieved with a second control-integrator stage that sets up a predefined threshold for changes in the first control stage output. Thus gain and/or frequency response for speech signals is held constant even in rapidly changing acoustical environments.—DAP

6,741,716

43.66.Ts AFFIXED BEHIND-THE-EAR CHILD RESISTANT VOLUME CONTROL COVER

Nelson Morales and Kyle Ayen, assignors to Starkey Laboratories, Incorporated
25 May 2004 (Class 381/330); filed 19 February 2002

A cover protects the volume control on a hearing aid from being

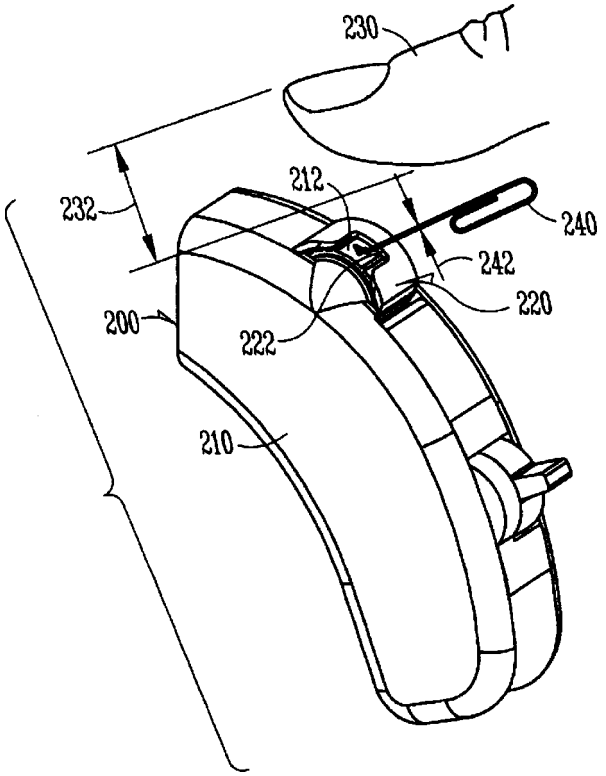

changed by preventing access of a human finger. The cover need not be removed for adjustment of the control by a tool.—DAP

6,741,715

43.66.Ts DIGITAL HEARING AID WITH A VOLTAGE CONVERTER FOR SUPPLYING A REDUCED OPERATION VOLTAGE

Henning Haugard Andersen, assignor to Widex A/S
25 May 2004 (Class 381/323); filed in Denmark 7 January 2000

To increase battery life, portions of digital hearing aid integrated circuitry that are less sensitive to supply voltage variations may be operated at lower voltage as long as the battery exceeds a certain minimum voltage. A switched step-down voltage converter connected to the power source produces the reduced supply voltage.—DAP

6,751,325

43.66.Ts HEARING AID AND METHOD FOR PROCESSING MICROPHONE SIGNALS IN A HEARING AID

Eghart Fischer, assignor to Siemens Audiologische Technik GmbH
15 June 2004 (Class 381/313); filed in Germany 29 September 1998

The directional characteristic of a hearing aid is modified adaptively depending on the microphone input signals received. For example, the lo-

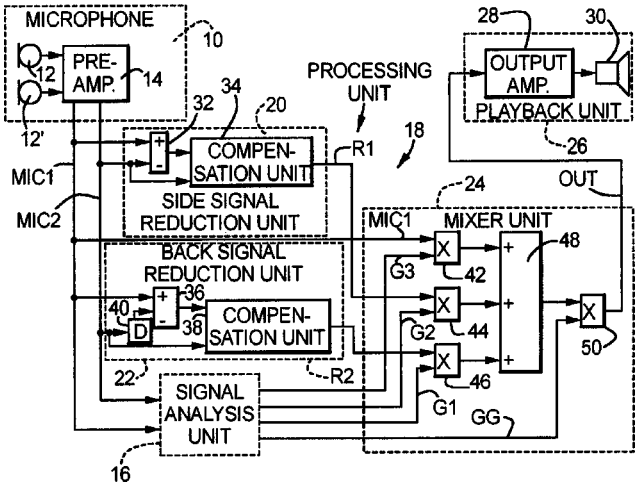

cation of a null in the directional polar pattern may be varied to reduce noise or a noise reduction algorithm may be performed by the signal processor.—DAP

6,751,326

43.66.Ts VIBRATION-DAMPENING RECEIVER ASSEMBLY

Henry G. Nepomuceno, assignor to Knowles Electronics, LLC
15 June 2004 (Class 381/322); filed 15 March 2001

A hearing aid receiver has an inner and outer case structure. The receiver structure is suspended on mounts made of damping material within the inner casing to reduce vibration conducted from the receiver to the hearing aid housing.—DAP

6,751,505

43.66.Ts METHOD AND APPARATUS FOR OPTIMIZING THE OPERATION OF A COCHLEAR IMPLANT PROSTHESIS

Chris Van Den Honert *et al.*, assignors to Cochlear Limited
15 June 2004 (Class 607/57); filed in Australia 3 March 1999

The operation of a cochlear implant is adjusted to maximize perfor-

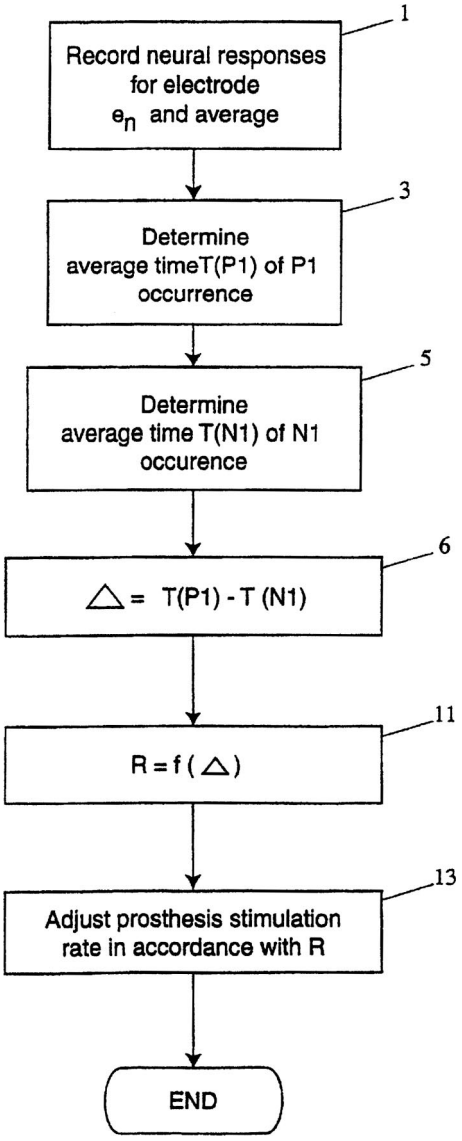

mance based on at least one neural response from at least one electrode.—DAP

6,745,162

43.72.Gy SYSTEM AND METHOD FOR BIT ALLOCATION IN AN AUDIO ENCODER

Fengduo Hu, assignor to Sony Corporation; Sony Electronics, Incorporated
1 June 2004 (Class 704/200.1); filed 23 October 2000

A method is proposed for allocating bits in an audio encoder which would reduce the frequency and magnitude of audio artifacts added by the encoding process. After the audio signal is filtered into subbands and a

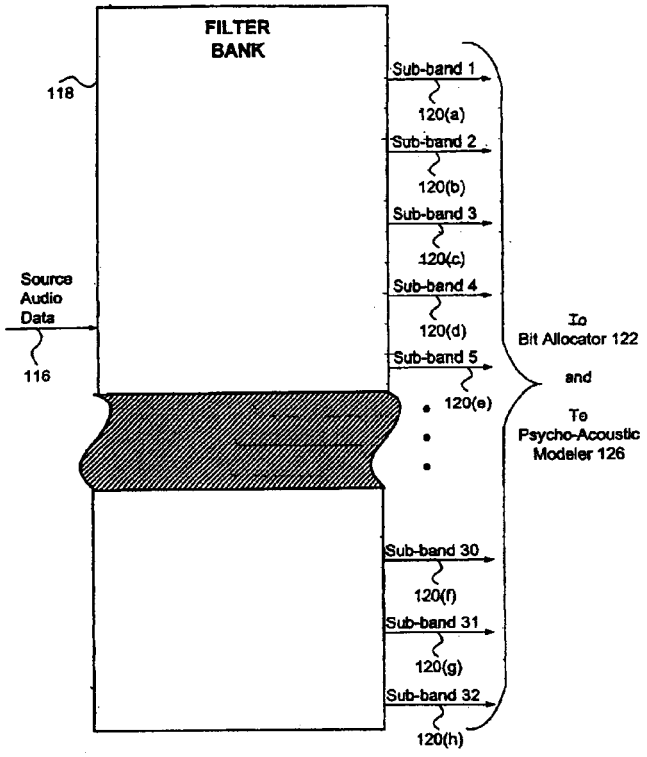

masking threshold is generated for each subband, bit allocation criteria are applied to each subband based on the signal to masking ratios of successive subbands.—DAP

6,697,780

43.72.Ja METHOD AND APPARATUS FOR RAPID ACOUSTIC UNIT SELECTION FROM A LARGE SPEECH CORPUS

Mark Charles Beutnagel *et al.*, assignors to AT&T Corporation
24 February 2004 (Class 704/258); filed 25 April 2000

High-quality speech synthesis by concatenation requires a very large database of fragments of speech to be joined at runtime into the final utterance. Information relating to specific pairs of fragments grows as the square of the database size. But substantial savings can be achieved by keeping such information for only the most frequently used pairs. Here, it is not the details of concatenation that are saved, but the cost of computing those

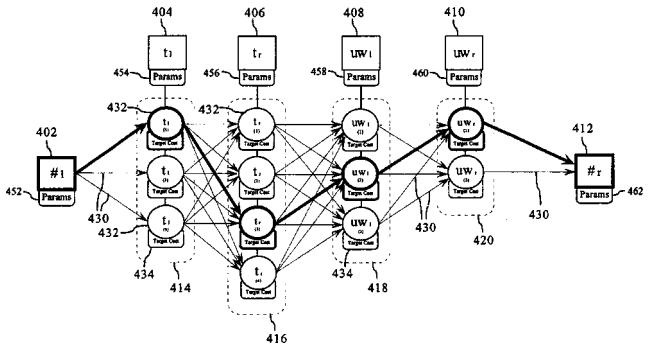

details, which itself is expensive to compute and enters into the selection of fragments to be used for a particular synthesis operation.—DLR

6,697,781

43.72.Ja METHOD AND APPARATUS FOR GENERATING SPEECH FROM AN ELECTRONIC FORM

William H. Sahlberg, assignor to Adobe Systems Incorporated
24 February 2004 (Class 704/260); filed 16 January 2001

Screen reader programs, designed to scan the text displayed on a computer screen and present that text in a form usable by other programs, have generally not been very successful in driving speech synthesizers when the application screen display involves a form to be filled out online. This patent describes a few extra layers of coding to interpret the contents of the form, to inquire what particular screen reader, if any, is active, what type of speech synthesis system, if any, is available, and to manage the conversion of items into the form of text suitable for the speech synthesizer.—DLR

6,701,295

43.72.Ja METHODS AND APPARATUS FOR RAPID ACOUSTIC UNIT SELECTION FROM A LARGE SPEECH CORPUS

Mark Charles Beutnagel *et al.*, assignors to AT&T Corporation
2 March 2004 (Class 704/258); filed 6 February 2003

This patent is nearly identical to United States Patent 6,697,780, filed three years earlier and reviewed above, except that the claims have been rewritten, breaking the process down into finer steps, apparently to broaden the coverage.—DLR

6,704,699

43.72.Ja LANGUAGE ACQUISITION AIDE

Einat H. Nir, Rosh Ha'Ayin, Israel
9 March 2004 (Class 704/2); filed 6 September 2001

This device is an assistant in learning a foreign language. It includes an OCR text scanner, a musical score reader, translation software, a phonetic dictionary for the target language, a sound recording device, and text-to-speech synthesis software. The user is supposedly able to learn proper pronunciation of the language by using the device.—DLR

6,707,985

43.72.Ja APPARATUS FOR RECORDING AND/OR PLAYING BACK CATALOG INFORMATION WITH AUDIO USING A RECORDING MEDIUM

Jung-wan Ko *et al.*, assignors to Samsung Electronics Company, Limited
16 March 2004 (Class 386/96); filed in the Republic of Korea 6 March 1998

This patent describes a system for organizing and creating a DVD disk which would contain the product catalog information for a company. Playing the DVD, perhaps in a user's home video system, would provide recorded audio descriptions of the products as they were viewed on the screen. Audio, video, and still snapshots are each stored in separate areas on the disk. Much of the short patent and the claims deal with how the various types of information about a product are managed to produce an attractive product presentation.—DLR

6,708,152

43.72.Ja USER INTERFACE FOR TEXT TO SPEECH CONVERSION

Mika Kivimäki, assignor to Nokia Mobile Phones Limited
16 March 2004 (Class 704/260); filed in the United Kingdom 30 December 1999

Intended for use in a PDA, cell phone, or similar small hand-held device, the patented concept here is a speech-playback-based system for navigating through a large amount of text displayed on a very small screen. Aids intended to make the method easier to use include control of the speech playback rate, backing up and stepping forward through the text, and jumping around in various ways through the text. Voice control of the device is not considered here.—DLR

6,711,539

43.72.Ja SYSTEM AND METHOD FOR CHARACTERIZING VOICED EXCITATIONS OF SPEECH AND ACOUSTIC SIGNALS, REMOVING ACOUSTIC NOISE FROM SPEECH, AND SYNTHESIZING SPEECH

Greg C. Burnett *et al.*, assignors to The Regents of the University of California
23 March 2004 (Class 704/223); filed 8 May 2001

While describing a system for speech synthesis, this patent also covers a method of vocal tract analysis using electromagnetic (EM) as well as acoustic sensors to recover articulatory information to be used in the synthesis. An EM sensor detects submillimeter motions of tissue boundaries in the sub- or supra-glottal regions. The resulting data can be processed to yield a glottal excitation function. Similar EM sensors detect voicing, pharynx enlargement, jaw motions, and other motions. Kalman filtering and other DSP techniques are used to remove noise and extract the speech functions. The information may then be adapted in various ways and used to synthesize speech.—DLR

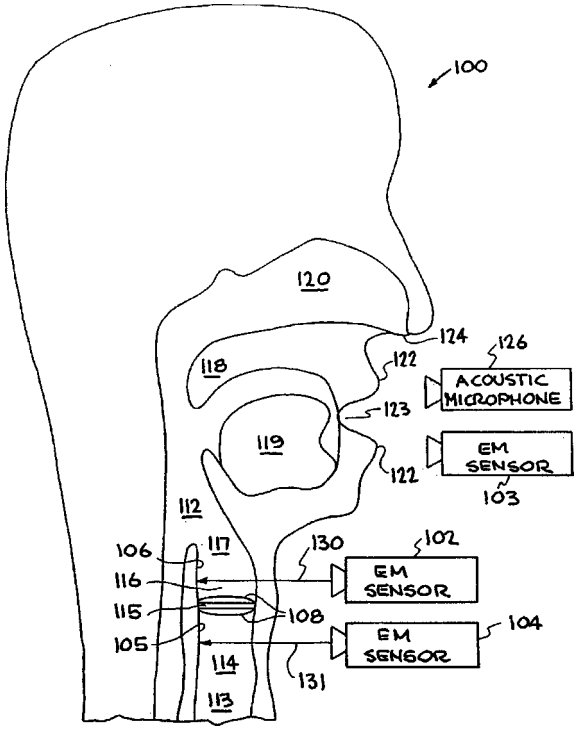

6,711,542

43.72.Ja METHOD OF IDENTIFYING A LANGUAGE AND OF CONTROLLING A SPEECH SYNTHESIS UNIT AND A COMMUNICATION DEVICE

Wofgang Theimer, assignor to Nokia Mobile Phones Limited
23 March 2004 (Class 704/257); filed in Germany 30 December 1999

This device receives text, such as from a network interface, and, based on single, 2-gram, and 3-gram letter-frequency statistics, determines the language represented by the text sample. A speech synthesizer is then configured to render the text into speech output in that language. Rating the observed letter frequencies according to statistics for the extant list of languages, the system determines when a previously untrained language is encountered or, if the language is already trained, uses the counts to update the stored reference data for that language.—DLR

6,704,709

43.72.Ne SYSTEM AND METHOD FOR IMPROVING THE ACCURACY OF A SPEECH RECOGNITION PROGRAM

Jonathan Kahn *et al.*, assignors to Custom Speech USA, Incorporated
9 March 2004 (Class 704/235); filed 26 July 2000

Intended to ease the task of preparing training speech materials for a recognizer, this device would allow iterative steps of recognizing a prepared voice recording and having the user check the result, correcting individual words as required. In this way, a database is gradually built up of correctly recognized speech together with files of the matching text. One notes that the system is to be implemented on a computer, requiring that the busy user, who didn't have time to record the training speech in the first place, now gets to sit and listen to the computer, correcting errors as it reads.—DLR

6,704,710

43.72.Ne ASSIGNING MEANINGS TO UTTERANCES IN A SPEECH RECOGNITION SYSTEM

Robert Don Strong, assignor to Apple Computer, Incorporated
9 March 2004 (Class 704/255); filed 12 October 2001

The term ''language model'' (LM), as used in this patent, refers to a finite state grammar constructed on the fly to cover the set of utterances which may be expected at a particular point in the user/machine dialogue at hand. The term ''speech rule'' (SR) is used for the system by which an utterance covered by a LM is associated with an action (or list of actions) to

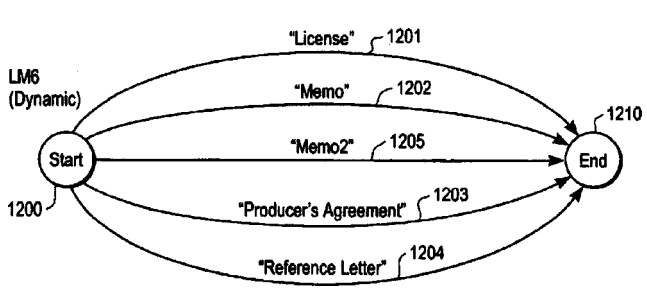

be performed by the system. SRs may be nested. For example, one SR would describe how to associate the number 43 with the utterance ''forty three.'' That SR could then be included within another SR. This reviewer found the descriptions of the basic word semantics to be somewhat sketchy, although, given the limited domain of computer operations as the intended subject matter, perhaps this reviewer was expecting too much.—DLR

6,718,303

43.72.Ne APPARATUS AND METHOD FOR AUTOMATICALLY GENERATING PUNCTUATION MARKS IN CONTINUOUS SPEECH RECOGNITION

Donald T. Tang *et al.*, assignors to International Business Machines Corporation
6 April 2004 (Class 704/235); filed in China 13 May 1998

One of the difficult aspects of speech-to-text recognition is the insertion of proper punctuation. Prior dictation systems have, at times, required the user to speak the punctuation marks explicitly, as in, ''left quote stop comma right quote he said period.'' This is very hard to do at all and nearly impossible to get right. This recognition system uses two approaches to insert punctuation. First, speech noises, such as breath and lip smack, are recognized and maintained as markers in the word stream. Similarly, the duration of silence between words is noted, including, when needed, a ''no pause'' marker. These annotations are referred to as ''pseudo noise.'' Second, a statistical analysis of a large amount of properly punctuated text results in a language model of punctuation usage probabilities within word usage patterns. Conditional probabilities are then computed for the occurrence of specific punctuation marks given the presence of a certain pseudo noise.—DLR

6,718,304

43.72.Ne SPEECH RECOGNITION SUPPORT METHOD AND APPARATUS

Mitsuyoshi Tachimori and Hiroshi Kanazawa, assignors to Kabushiki Kaisha Toshiba
6 April 2004 (Class 704/236); filed in Japan 30 June 1999

This voice-controlled vehicle navigation system first accepts a phrase in the user's speech input, then constructs a probable word sequence using the recognizer. The phrase is analyzed to determine a location on the map most likely intended as the speech referent. The distance from that point to a reference map point is computed and, if that distance exceeds a preset threshold, the user is asked for confirmation of the intended map location.—DLR

6,718,307

43.72.Ne SPEECH INPUT DEVICE WITH ATTENTION SPAN

Vincentius P. Buil *et al.*, assignors to Koninklijke Philips Electronics N.V.
6 April 2004 (Class 704/270); filed in the European Patent Office 6 January 1999

This patent involves methods for automatic shutdown of a speech recognition system when that system is not in use. A miminal recognition capability for some sort of startup command is maintained during the shutdown period. It should be clarified here that the shutdown mode is not intended as a power saving device, but rather as a way to insure that the system does not respond inappropriately to casual speech not directed to the recognition system. Shutdown may occur after a timeout as well as by recognition of a specific shutdown command. The system produces distinctive sounds marking the transitions to the active and inactive states.—DLR

6,741,791

43.72.Ne USING SPEECH TO SELECT A POSITION IN A PROGRAM

Ben S. Wymore *et al.*, assignors to Intel Corporation
25 May 2004 (Class 386/46); filed 31 January 2000

Spoken commands are recognized to select a position in an audio-

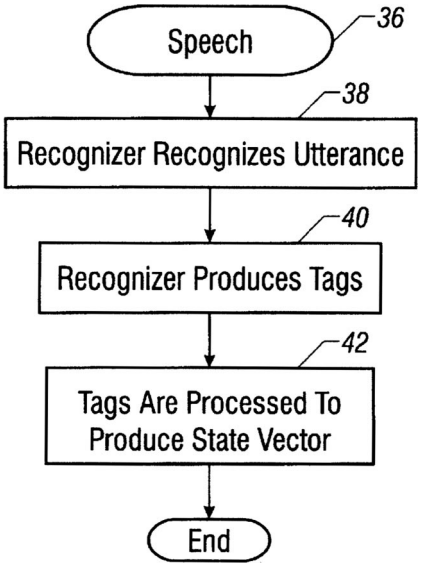

visual program, thereby improving on the control functions normally available with remote controls.—DAP

6,747,202

43.75.Gh SOUND GENERATING SYSTEM PRODUCING SOUND FROM VIBRATIONS IN MUSICAL INSTRUMENT THROUGH NATURAL MICROPHONE SIMULATION

Ryuichiro Kuroki, assignor to Yamaha Corporation
8 June 2004 (Class 84/737); filed in Japan 29 June 2001

The patent author wants to morph an electric guitar into an acoustic guitar. Without saying so, he employs a Schroeder style reverberator to emulate the resonance of the body. It's a pity that he didn't consider the actual body impulse response or the papers by Penttinen *et al.*, that show how to do it accurately.—MK

6,740,036

43.80.Qf OPTICAL AND ULTRASOUND PROBE FOR MONITORING BLOOD VOLUME CHANGES

Lian-Pin Lee and Jen-Shih Lee, both of Charlottesville, Virginia
25 May 2004 (Class 600/437); filed 18 October 2002

This is a multifunctional apparatus to evaluate the compressibility, density, and hematocrit of blood. The device incorporates an optical ultrasonic probe that is clipped onto tubing in which blood is flowing. The probe contains a combination of ultrasound transducers, a light-emitting diode, and photodiodes. An indicator medium is injected into the bloodstream at one or more points in time. A transducer emits ultrasound waves that pass through the bloodstream to be received by another transducer. The phase shift is assessed which results from the ultrasound's passing through the bloodstream. A linear relationship between compressibility and density and a calibration with two other fluid media allow changes in blood density to be calculated from changes in the phase shift. The optical aspect of the blood evaluates the hematocrit. Prior to clinical assessment, an on-line saline injection procedure and the resultant change in density are employed to calibrate the hematocrit in terms of optical density. This cardiovascular monitoring will reportedly be useful for evaluating how complications develop during hemodialysis or whether a post-trauma fluid replacement or therapy might help to mitigate the complications.—DRR

6,741,879

43.80.Qf ACOUSTIC GATING MONITOR FOR MAGNETIC RESONANCE IMAGING SYSTEM

Hsu Chang, assignor to Toshiba America MRI, Incorporated
25 May 2004 (Class 600/413); filed 6 May 2003

This device relates to magnetic resonance imaging (MRI) that is triggered and/or synchronized with sensors to detect physiological conditions such as a heartbeat, blood pulse, or respiration rate. The MRI system provides an audible feedback signal in the gantry room triggered by a physiological sensor on the patient. The feedback signal is a sound generated by one of the MRI gradient coils. The application of the sequence causes the coil to emit a sound that is indicative of the sensor output signal.—DRR

6,741,883

43.80.Qf AUDIBLE FEEDBACK FROM POSITIONAL GUIDANCE SYSTEMS

Philip L. Gildenberg, assignor to Houston Stereotactic Concepts, Incorporated
25 May 2004 (Class 600/429); filed 28 February 2002

Stereotactic surgery is a technique for localizing a target in surgical space. The use of stereotactic instrumentation based on tomographic imaging is conventional in surgery. When used for brain or other neurosurgery, such methods may entail attaching a headring apparatus to acquire imaging data where the data are spatially related to the headring. Current technology also allows the use of a frameless system to provide a visual reference in the operating room. Again, with brain surgery as an example, fiducial markers are placed around the patient's head so as to be apparent on the preoperative MRI or computerized tomography (CT) scans. A computer compares the marker information to that from previous images. The actual lo-

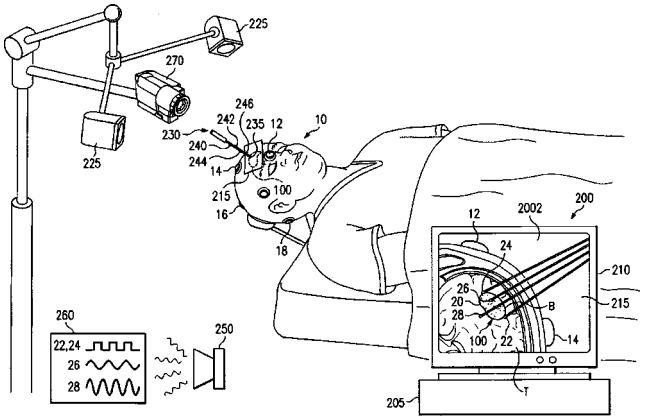

cation of the patient's head may thus be registered to, and correlated with the computerized three-dimensional head reconstruction. As described in this patent, a computer-based system generates audible feedback (to supplement visual and tactile feedback) to a surgeon moving the tip of a probe in a surgical field with respect to the volume of interest such as a tumor. Other surgical embodiments include generating audible feedback to assist with the precise insertion of a pedicle screw, inserting a biopsy cannula or electrode into the brain, and the like. The feedback may vary in numerous ways, such as tone, volume, pattern, and/or style, as the probe and/or instrument moves relative to the features of interest.—DRR

6,743,174

43.80.Qf ULTRASONIC DIAGNOSTIC IMAGING SYSTEM WITH AUTOMATICALLY CONTROLLED CONTRAST AND BRIGHTNESS

Gary Ng and Brian Hendee Smith, assignors to Koninklijke Philips Electronics N.V.
1 June 2004 (Class 600/437); filed 1 April 2002

In the process of imaging abdominal regions, a clinician will obtain dozens of ultrasonic images of different organs at different depths. Consequently, the ultrasonic echoes obtained by such scannings will result in various echo levels yielding images of differing brightness. This leads the clinician to make frequent adjustments of the display. For instance, if the deepest portion of an image is unusually dark, the clinician will adjust the time gain compensation (TGC) setting to provide more gain in the image of greater depths. If the image is too bright or too dark, the clinician will adjust the overall gain control. A noisy image (which occurs in fluid-filled regions such as the gall bladder), may lead to dynamic range adjustments. To ease

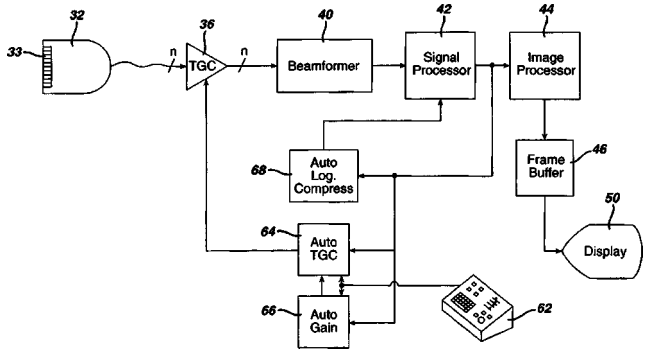

this task of constant adjustment, an ultrasonic system is provided which automatically compensates for variations in brightness or contrast by computing offsets to a nominal TGC curve to compensate for depth attenuation, then applying the offsets to the TGC curve to subsequent images. Image dynamic range is analyzed by comparison with a reference image. Overall system gain is adjusted for substantially uniform image production based on the compression function used to reduce the dynamic range.—DRR

6,743,177

43.80.Qf PUNCTURING NEEDLE GUIDE, ULTRASONIC PROBE, AND ULTRASOUND IMAGING APPARATUS

Hiroki Ito, assignor to GE Medical Systems Global Technology Company, LLC
1 June 2004 (Class 600/461); filed in Japan 10 April 2002

When a biopsy is performed on a patient's intracorporeal tissue, a puncturing needle penetrates at the site of a real-time, ultrasound-based tomographic image of the lesion. A needle guide attached to the ultrasonic probe has a through hole, i.e., a guide hole having an ultrasound transmitting/receiving member in its distal end. In this version of the device, the needle guide enables penetration in several directions, through a plate-like body whose width diminishes gradually from one end to the other. Multiple holes are formed at one end and a single hole is formed in an end surface of the plate-like body, through which a puncturing needle can be passed.—DRR

6,746,402

43.80.Qf ULTRASOUND SYSTEM AND METHOD

E. Tuncay Ustuner, assignor to E. Tuncay Ustuner
8 June 2004 (Class 600/462); filed 19 December 2002

This is a re-configuration of an ultrasonic system adapted for use by surgeons. In one embodiment, the system includes a wearable ultrasonic probe in combination with a display positioned within the sterile operable field and coupled through a processor to a probe. In one particular embodi-

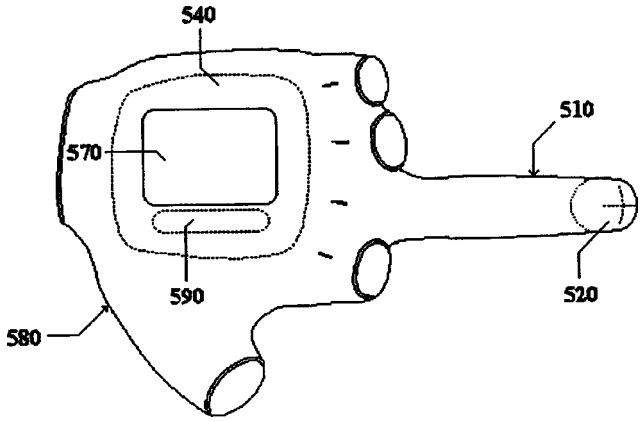

ment, the probe, display, and processor of a completely wearable ultrasound system are worn on the surgeon's hand. In other embodiments, the display is worn by the surgeon but not positioned within the sterile operable field, or the display is carried by an articulated arm and positioned near the surgical site.—DRR

6,749,572

43.80.Qf TRANSESOPHAGEAL ULTRASOUND PROBE HAVING A ROTATING ENDOSCOPE SHAFT

Stephen Dodge Edwardsen and Dag Jordfald, assignors to GE Medical Systems Global Technology Company, LLC
15 June 2004 (Class 600/459); filed 10 December 2002

This transesophageal ultrasound probe is used to image internal structures. The probe contains a rotating endoscope possessing an imaging element mounted on the distal end of the rotating shaft. The probe also incorporates a control handle for manipulating the imaging controls and a rotation

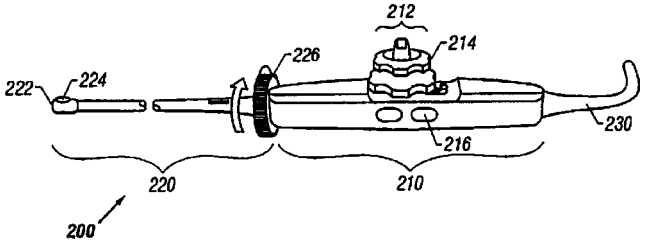

tube that extends through the rotating endoscopic shaft and into the control handle. The rotation control wheel is affixed to the rotating tube so that manual rotation of the control wheel causes the tube, the shaft, and thus, the imaging element to likewise rotate.—DRR

6,740,039

43.80.Sh METHODS AND APPARATUS FOR DISPLAYING INFORMATION RELATING TO DELIVERY AND ACTIVATION OF A THERAPEUTIC AGENT USING ULTRASOUND ENERGY

Patrick G. Rafter and Susan E. Beiter, assignors to Koninklijke Philips Electronics N.V.
25 May 2004 (Class 600/439); filed 17 May 2000

This apparatus delivers a therapeutic agent to a region of interest using a contrast agent and activates the therapeutic agent via ultrasound energy. An ultrasound imaging system generates an image of the region of interest and ultrasound energy destroys the microbubbles of the contrast agent. Parametric data are acquired indicative of the activation of the therapeutic agent in the region of interest and a parametric display is generated. One or more of the parameters may be adjusted, either manually based on the parametric display or automatically based on the acquired parametric data.—DRR

6,748,944

43.80.Sh ULTRASONIC DOSAGE DEVICE AND METHOD

Michael Anthony DellaVecchia, Berwyn and Claude Pezzopane, Honeybrook, both of Pennsylvania
15 June 2004 (Class 128/200.16); filed 3 May 2000

This ultrasonic dosage device is a portable, hand-held dosage dispenser and cartridge, which ultrasonically nebulizes a liquid, a gel, a powder, or a combination of such for inhalation by the user. The device contains an enclosure for providing medication in the form of a nebulized mist, with an energy source for applying electrical energy to a vibration device. An

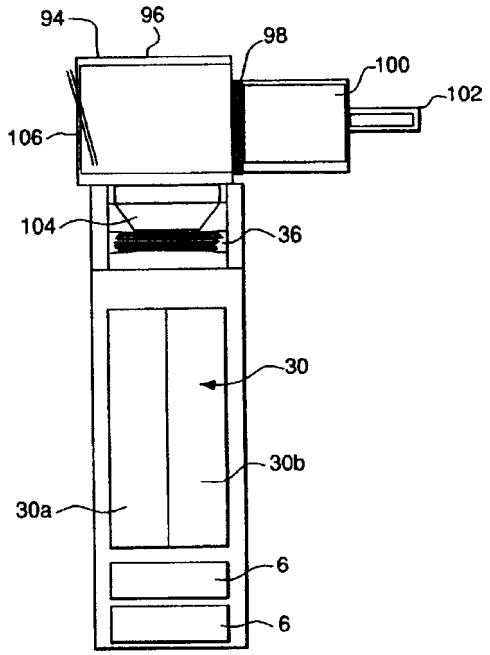

assembly attaches to the enclosure and has a membrane deployed between the vibration device and the medication. A switch-activated device vibrates the membrane, thereby converting the medication into a mist that is dispensed into the patient's respiratory system.—DRR

6,740,040

43.80.Sh ULTRASOUND ENERGY DRIVEN INTRAVENTRICULAR CATHETER TO TREAT ISCHEMIA

Evgenia Mandrusov *et al.*, assignors to Advanced Cardiovascular Systems, Incorporated
25 May 2004 (Class 600/439); filed 30 January 2001

This device is intended to improve blood flow to an ischemic region (a myocardial ischemia, for example). An ultrasonic transducer is placed near the ischemic region. Ultrasonic energy above 1 MHz is applied to create one or more thermal lesions in the ischemic region of the myocardium. The

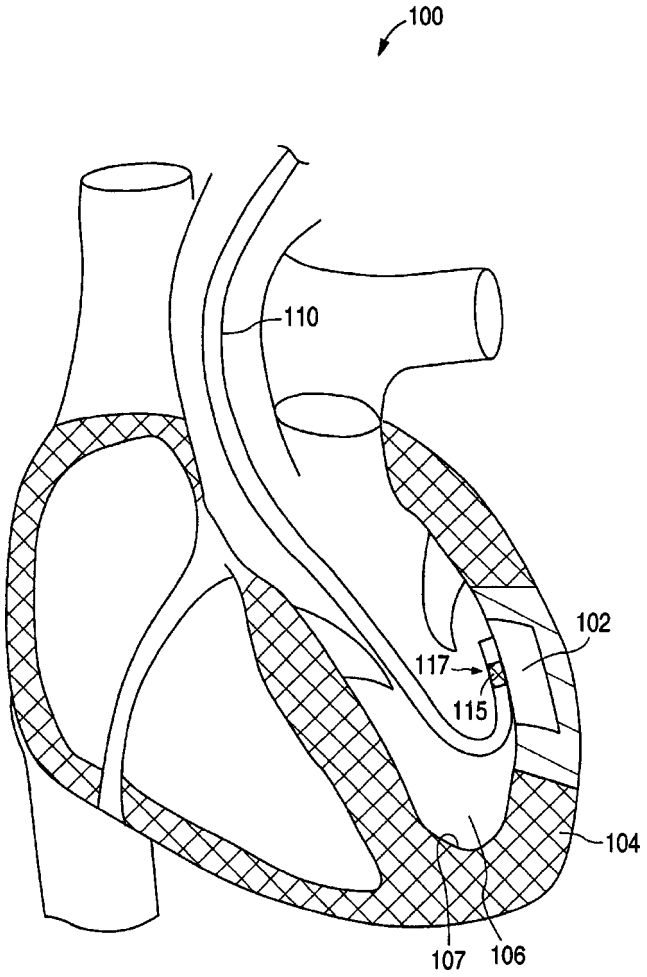

thermal lesions may constitute a series of different sizes. The transducer can have a curved shape so that the emitted ultrasound energy converges to a site within the myocardium so as to generate a lesion without injuring the epicardium or the endocardium.—DRR

6,730,033

43.80.Vj TWO DIMENSIONAL ARRAY AND METHODS FOR IMAGING IN THREE DIMENSIONS

Lin Xin Yao and Todor Sheljaskow, assignors to Siemens Medical Systems, Incorporated
4 May 2004 (Class 600/443); filed 16 May 2002

A transducer array without beamforming circuitry in the probe is used to achieve a high scan rate with a limited number of channels. A fan beam is transmitted in a scan plane from array elements that extend laterally along the aperture. Rows of these long elements in elevation permit electronic

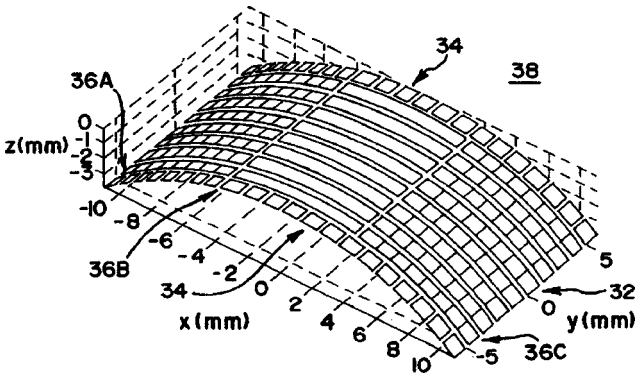

steering of the fan beam in the elevation dimension. One or more rows of smaller receive elements are used to form beams along scan lines in the lateral dimension. Resolution in elevation is provided primarily from transmit elements spaced in elevation and partially from rows of laterally spaced receive elements.—RCW

6,740,034

43.80.Vj THREE-DIMENSIONAL ULTRASOUND IMAGING SYSTEM FOR PERFORMING RECEIVE-FOCUSING AT VOXELS CORRESPONDING TO DISPLAY PIXELS

Jae Sub Hwang and Tai Kyong Song, assignors to Medison Company, Limited
25 May 2004 (Class 600/437); filed in the Republic of Korea 27 April 2001

Voxels to be displayed are spatially interpolated using signals from

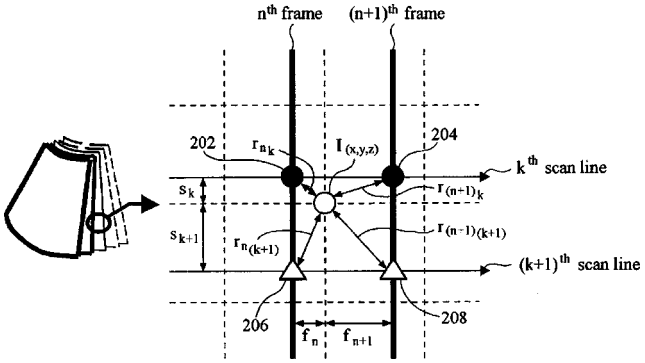

temporally and spatially adjacent frames.—RCW

6,740,037

43.80.Vj HIGH FREQUENCY ULTRASONAGRAPHY UTILIZING CONSTRUCTIVE INTERFERENCE

Myron R. Schoenfeld, Scarsdale, New York
25 May 2004 (Class 600/437); filed 10 December 2002

Discrete, narrow-beam ultrasound transducer elements are phased so that multiple single-frequency ultrasonic beams produced by the transducer add constructively at a focal point.—RCW

6,749,554

43.80.Vj MEDICAL TOOLS AND DEVICES WITH IMPROVED ULTRASOUND VISIBILITY

Robert Allen Snow *et al.*, assignors to Amersham PLC
15 June 2004 (Class 600/3); filed in the United Kingdom 17 June 1999

Enhanced ultrasonic visability is achieved using a coating that is ultrasonically discontinuous, using a matrix material with high ultrasonic contrast, or using a liquid or polymer that alters its ultrasonic properties at physiologic temperatures or as a result of change in pH.—RCW

6,749,569

43.80.Vj METHOD AND APPARATUS FOR ULTRASOUND IMAGING

Paolo Pellegretti, assignors to Esaote S.p.A.
15 June 2004 (Class 600/441); filed 7 January 2003

Echo signals are processed to produce a panoramic image of the region under examination and also to image a part of the region. The panoramic image is displayed using a gray scale and the regional image is displayed using color. The two images are shown on the same screen.—RCW

6,749,570

43.80.Vj ULTRASOUND METHOD AND APPARATUS FOR IMAGING BREAST

Kutay F. Üstüner *et al.*, assignors to Acuson Corporation
15 June 2004 (Class 600/443); filed 23 August 2002

A breast is positioned between an ultrasound transducer array and a plate with embedded point or line targets. Reflections from the targets are used to estimate corrections for tissue delay and amplitude aberration for

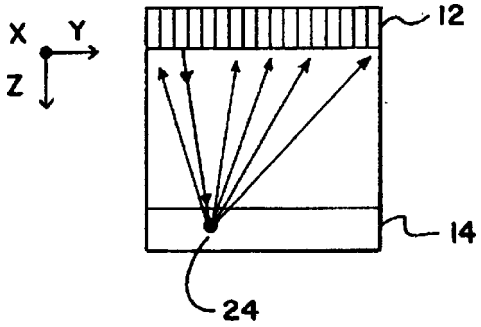

improved focusing. Images of sound speed and attenuation coefficient are also reconstructed to provide more information for diagnosis.—RCW

Diffuse fields in open systems and the emergence of the Green's function (L)

Richard L. Weaver[a] and Oleg I. Lobkis
Department of Theoretical and Applied Mechanics, University of Illinois, 104 South Wright Street, Urbana, Illinois 61801

(Received 21 May 2004; revised 3 August 2004; accepted 3 September 2004)

A definition of a diffuse field applicable to open heterogeneous systems is proposed. The identity between the Green's function of the structure and the diffuse field's correlations is proved. The Green's function that emerges from the correlation is found to be the full Green's function of the medium, symmetrized in time, with all reflections and scatterings and propagation modes. This is in contrast to suggestions that the correlation is the ballistic Green's function only, or the Green's function of a homogeneous effective medium. © *2004 Acoustical Society of America.*
[DOI: 10.1121/1.1810232]

PACS numbers: 43.20.Gp, 43.40.Qi, 43.40.Ph [JJM] Pages: 2731–2734

I. INTRODUCTION

Fully diffuse wave fields are often defined as ones which are globally equipartitioned, with all normal modes having uncorrelated amplitudes with equal mean squares.[1–4] They are also defined as in room acoustics as an uncorrelated and isotropic mix of plane waves of all propagation directions.[5–8] The former definition is awkward in open or infinite systems where the normal modes are problematic and where they are not equally excited or uncorrelated. Such a definition does, however, lend itself naturally to heterogeneous media. The latter definition is more intuitive, but fails to apply to heterogeneous media, to regions near boundaries, or to systems with more than one mode of propagation. There are numerous structures for which neither definition is satisfactory, and there remains a need for a concept of local equipartition, as opposed to a global one, and for a definition of a diffuse field applicable to open systems with scatterers or boundaries.

The need for more useful definitions has become especially apparent in the last couple of years. The recent proof, that diffuse fields have field–field correlation functions essentially equal to the Green's function,[9–13] depended on the notion of normal mode equipartition. Many applications, e.g., seismology,[14,15] ocean acoustics,[16] or ultrasonics,[17,18] however, are anticipated in open systems for which that proof does not apply. Open systems with diffuse wave fields are also common in optics and electronics.[19,20] Recently Snieder[21] has presented a proof for open systems. That proof depends on a notion of ballistic wave propagation[22] within the medium of interest, and does not apply to arbitrary geometries. Indeed, the conclusion there ''Passive imaging ... provides the superposition of the retarded and advanced *surface wave* Green's functions of the *ballistic* wave,'' (italics ours) is contradicted by experimental results[9–12] and by theoretical arguments indicating that the recovered waveform includes all waves and all multiple reflections and scatterings. Here we present a proof of emergence valid in any nondissipative wave system. We find that diffuse insonification from a surrounding homogenous region U (i.e., an incident field that conforms to the room acoustics notion of a diffuse field) onto a region V of arbitrary heterogeneity, generates within V a random field whose correlations are the full Green's function of that structure including all internal scatterings. Thus we not only compose an emergence proof applicable to open systems with scatterings, we also arrive at a definition of a local diffuse field as one with statistics identical to those that would apply if the region were in equilibrium with some other diffuse field. A diffuse field is a field in equilibrium with another diffuse field.

We begin in the next section with a short review of the basic features of diffuse fields, and the earlier argument for the emergence of the Greens' function. The new proof is presented in the third section.

II. DIFFUSE FIELDS

The most familiar notion of a fully diffuse field,[23] at frequency ω, is one consisting of an incoherent superposition of plane waves of all directions and phases, with delta-correlated amplitudes[5–8]

$$\psi(\mathbf{r},\omega) = \oint a(\hat{\mathbf{n}})\exp(-i\hat{\mathbf{n}}\cdot\mathbf{r}\omega/c)\,d^2\hat{\mathbf{n}} \tag{1}$$

with

$$\langle a(\hat{\mathbf{n}})\rangle = 0; \quad \langle a(\hat{\mathbf{n}})a(\hat{\mathbf{n}}')\rangle = 0;$$
$$\langle a(\hat{\mathbf{n}})a^*(\hat{\mathbf{n}}')\rangle = A\,\delta^2(\hat{\mathbf{n}}-\hat{\mathbf{n}}') \tag{2}$$

This definition is applicable for scalar waves in an isotropic medium. If required, it may be invoked within a finite region, albeit homogeneous and isotropic, of an open system. It has been found useful throughout room acoustics and structural acoustics[5–8] and in optics.[19,24] Equations (1) and (2) allow immediate construction of the field–field correlation function

$$\langle \psi(\mathbf{r},\omega)\psi^*(\mathbf{r}',\omega)\rangle = A \oint \exp(-i\hat{\mathbf{n}}\cdot(\mathbf{r}-\mathbf{r}')\omega/c)\,d^2\hat{\mathbf{n}}$$
$$= 4\pi A j_o(\omega/c|(\mathbf{r}-\mathbf{r}')|), \tag{3}$$

a result that is widely quoted. The spherical Bessel function j_o is of course the imaginary part of the Green's function for an isotropic scalar wave equation. The assumed statistics on

$a(\mathbf{n})$ also have implications for higher moments of the fields, and in particular for intensity–intensity correlations.

In heterogeneous or anisotropic or multi-mode media (e.g., elastic waves) Eq. (1) is inapplicable, though it can sometimes be generalized using concepts of equipartition[1,25] amongst the propagation modes. In many cases it is preferable to define a fully diffuse field as one with equipartitioned uncorrelated normal mode amplitudes. A field ψ may be written as an expansion in terms of the global normal modes $u^{(n)}(\mathbf{r})$. In the time domain, and while sources do not act, it may be written as

$$\psi(\mathbf{r},t)=\mathrm{Re}\sum_n a_n u^{(n)}(\mathbf{r})\exp\{i\omega_n t\}, \tag{4}$$

where the a_n are time-independent complex modal amplitudes.[26] If the field is diffuse, their statistics are taken to be

$$\langle a_n\rangle=0;\quad \langle a_n a_m\rangle=0;\quad \langle a_n a_m^*\rangle=F(\omega_n)\delta_{nm}. \tag{5}$$

This field is globally diffuse; the assumptions are correspondingly problematic when applied in ocean acoustics or seismology or any open system.

The field–field correlations of (4) are immediately derivable:

$$R(\mathbf{r},\mathbf{r}',t-t')=\langle\psi(\mathbf{r},t)\psi(\mathbf{r}',t')\rangle$$

$$=\sum_n F(\omega_n)u^{(n)}(\mathbf{r})u^{(n)}(\mathbf{r}')\cos\{\omega_n(t-t')\}. \tag{6}$$

This may be compared to the modal expansion for the time-dependent Greens function[27,9,10]

$$G(\mathbf{r},\mathbf{r}',\tau)=\sum_n u^{(n)}(\mathbf{r})u^{(n)}(\mathbf{r}')\frac{\sin\{\omega_n\tau\}}{\omega_n}\Theta(\tau). \tag{7}$$

Θ is the unit step function.

Except for a smooth frequency-dependent factor F, (6) is essentially the (time derivative) of the Green's function, symmetrized in time. F, representing the spectral power density of the diffuse field, may be thought of as a filter and the source of some distortion between the time derivative of the Green's function and the field–field correlation function.[28]

On Fourier transforming R with respect to $t-t'$, one constructs the correlation function in the frequency domain, between fields $\psi(\mathbf{r},\omega)$ and $\psi^*(\mathbf{r}',\omega)$[29]

$$R(\mathbf{r},\mathbf{r}';\omega)=\pi\sum_n u^{(n)}(\mathbf{r})u^{(n)}(\mathbf{r}')F(\omega_n)[\delta(\omega-\omega_n)$$

$$+\delta(\omega+\omega_n)], \tag{8}$$

which may be compared to

$$\mathrm{Im}\,G(\mathbf{r},\mathbf{r}',\omega)=\mathrm{Im}\sum_n u^{(n)}(\mathbf{r})u^{(n)}(\mathbf{r}')/[(\omega-i\varepsilon)^2-\omega_n^2]$$

$$=\sum_n u^{(n)}(\mathbf{r})u^{(n)}(\mathbf{r}')\frac{\pi}{\omega}$$

$$\times[\delta(\omega-\omega_n)+\delta(\omega+\omega_n)]. \tag{9}$$

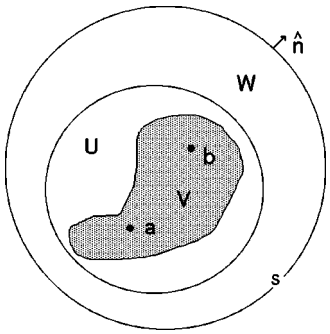

FIG. 1. A finite heterogeneous region V is embedded within a homogeneous isotropic region U and an exterior region W. We find that an incident diffuse field in U generates a field within V that has correlations Im G.

This is the basis for the statement, distortions due to F withstanding, that the correlation of a diffuse field is the imaginary part of the Green's function. The identity is seen to apply, not only to homogeneous isotropic media having diffuse fields that are incoherent superpositions of plane waves for which the correlation represents simple ballistic propagation as in Eq. (3), but to the more general case in which there may be heterogeneities and scatterers.

It was noted in Refs. 5, 12 that the modal amplitude statistics (5) can be obtained if one invokes delta-correlated sources. The mode amplitude a_n, after the action of a transient source $s(x)f(t)$, is given by

$$a_n=\int u^n(\mathbf{x})s(\mathbf{x})d^3\mathbf{x}f(\omega_n)/\omega_n. \tag{10}$$

If the source $s(\mathbf{x})$ is distributed over all $\mathbf{x}$ with statistics $\langle s\rangle=0$; $\langle s(\mathbf{x})s(\mathbf{x}')\rangle=\delta^3(\mathbf{x}-\mathbf{x}')$, $\langle f^2\rangle=0$, then the statistics of a_n are those of (5) above, with $\langle|f|^2\rangle=\mathrm{F}$. Thus one recognizes that an ensemble of incoherent sources, distributed throughout all space, generates a diffuse field.[30]

As noted above, these definitions and proofs have limited applicability. In the following section we show that a diffuse field may be defined locally, and in structures of arbitrary heterogeneity, as fields in equilibrium (i.e., in steady state contact) with other regions that are themselves diffuse. We further show that, with this definition, the field–field correlation functions are indeed the local Greens function.

III. PROOF OF EMERGENCE FOR OPEN SYSTEMS

Consider Fig. 1 of an unbounded homogeneous system with an embedded finite region (volume V) of arbitrary nonsingular heterogeneous real potential $v(\mathbf{x})$.[31] Circumscribe V by a surface, and label the intervening volume U. Label the exterior volume W, of large radius R and surface S. Label two points in V as $\mathbf{a}$ and $\mathbf{b}$.

Consider an integral over $\mathbf{x}$ within $U+V+W$,

$$I=\int_{V+U+W}\boldsymbol{\nabla}\cdot[G_{ax}\nabla G_{xb}^*-(\nabla G_{ax})G_{xb}^*]d^3\mathbf{x}$$

$$=\int_{V+U+W}[G_{ax}\nabla^2 G_{xb}^*-(\nabla^2 G_{ax})G_{xb}^*]d^3\mathbf{x}, \tag{11}$$

where G_{ax} refers to the Green's function between points $\mathbf{x}$ and $\mathbf{a}$, at a frequency $\omega-i\varepsilon$.[32] The spatial derivatives $\boldsymbol{\nabla}$ are

applied to the coordinate $\mathbf{x}$. Integrals like (11) are the basis for proofs of reciprocity theorems, such as have been used in discussions of field–field correlations by Wapenaar *et al.*[33] The divergence theorem allows (11) to be expressed as an integral over the outer surface S of W,

$$I=\int_S \hat{\mathbf{n}}\cdot[G_{ax}\nabla G^*_{xb}-(\nabla G_{ax})G^*_{xb}]d^2\mathbf{x}, \tag{12}$$

In the limit of a large radius R of the region W, each of the factors G entails propagation over a large distance R. At any finite ε, this integral thus vanishes like $\exp(-2\varepsilon R)$. We let R go to infinity, and find $I=0$. It is convenient to do this formally by letting $R\to\infty$ and $\varepsilon\to 0$ such that $\varepsilon\sim 1/\sqrt{R}$.

The governing equation for G,[27,31]

$$\nabla^2 G_{ax}+v(\mathbf{x})G_{ax}+(\omega-i\varepsilon)^2 G_{ax}=\delta^3(\mathbf{x}-\mathbf{a}), \tag{13}$$

allows the volume integral [the right-hand side of (11)] to be rewritten as

$$I=0=\varepsilon\int_{V+U+W} -4i\omega[G_{ax}G^*_{xb}]d^3\mathbf{x}+G_{ab}-G^*_{ab}. \tag{14}$$

The integral over $V+U$ is finite, so in the limit of small ε, we conclude

$$2\,\mathrm{Im}\,G_{ab}=4\varepsilon\omega\int_W G_{ax}G^*_{xb}\,d^3\mathbf{x}+O(\varepsilon). \tag{15}$$

The integral over W scales like $1/\varepsilon$ in the convenient limit $R\to\infty$, $\varepsilon\to 0$.

Now consider an ensemble of random delta-correlated sources $s(\mathbf{x})$ in W with strength St:

$$\begin{aligned}&\langle s(\mathbf{x})\rangle=0;\quad \langle s(\mathbf{x})s(\mathbf{x}')\rangle=0;\\ &\langle s(\mathbf{x})s^*(\mathbf{x}')\rangle=St\,\delta^3(\mathbf{x}-\mathbf{x}')\end{aligned} \tag{16}$$

A source $s(\mathbf{x})$ generates a field at $\mathbf{y}$ equal to

$$\psi(\mathbf{y})=\int_W G_{yx}s(\mathbf{x})d^3\mathbf{x}. \tag{17}$$

The ensemble mean of the field $\psi(\mathbf{y})$ is zero; the field's correlation $\langle\psi(\mathbf{a})\psi^*(\mathbf{b})\rangle$ is

$$\langle\psi(\mathbf{a})\psi^*(\mathbf{b})\rangle=St\int_W G_{ax}G^*_{xb}\,d^3\mathbf{x}. \tag{18}$$

On comparing with Eq. (15) we conclude that an ensemble of random sources in W of strength $St=2\varepsilon\omega$ generates an ensemble of random fields ψ with correlation in $U+V$ of $\mathrm{Im}\,G$. This conclusion is subtly different from that obtained earlier, where the ensemble of random sources was distributed over the entire volume.

We further note that the field ψ in U due to these sources consists of an incident field ψ^{inc} identical to what would be there if $v(\mathbf{x})=0$, plus a field of waves outgoing from the region V; $\psi=\psi^{\mathrm{incident}}+\psi^{\mathrm{scattered}}$. ψ^{incident} is a random field with correlations $\mathrm{Im}\,G^o\sim j_o$, i.e., it is a diffuse isotropic mix of plane waves. We conclude that an isotropic mix of incoherent plane waves incident from a surrounding region U upon a region V generates a field within V that has correlations $\mathrm{Im}\,G$. This is true regardless of the details of the sources or geometry outside of $V+U$, depending only on the assumed statistics of the field incident on V from U. The Green's function that emerges from that correlation is the Green's function of the region V embedded in a homogeneous matrix. We emphasize that this is not the ballistic Green's function as in Refs. 18, 21, 33, and 34, but includes all reflections and scatterings from heterogeneities $v(\mathbf{x})$ in V.

It is not difficult to generalize this proof to multi-mode systems, for example elastic waves, or to the presence of reflecting boundaries within V as might be present if interest was in correlations at the surface of a half-space.[14,15,33] In particular one can show that a properly weighted diffuse equipartitioned set of plane waves incident from a homogeneous elastic half-space towards a free surface (possibly stratified), together with their reflections and the appropriate diffuse set of guided surface waves, gives rise to correlations identical to those that would be obtained if one assumed equipartitioned global normal modes. That identity was shown long ago[35] for the special case of an unstratified isotropic elastic half-space.

This proof has shown that a diffuse field in a nondissipative structure, defined as an ensemble of steady-state fields with diffuse statistics in the field incident from a surrounding region U, will have the specified field-field correlation function in the internal region V. It has further shown that an ensemble of sources exterior to U can generate such a field. It is a far more difficult question to determine the extent to which a finite set of sources may be sufficient. In Ref. 10 it was found that a set of only eight sources was not fully adequate. Additional challenging questions will arise if it is desired to include the effects of significant amounts of absorption.

ACKNOWLEDGMENTS

This work was supported by grants from the National Science Foundation INT-0230312 and CMS-0201346. We thank Michel Campillo and Bart van Tiggelen for energetic discussions.

[a]Electronic mail: r-weaver@uiuc.edu

[1] R. Weaver, "On diffuse waves in solid media," J. Acoust. Soc. Am. **71**, 1608–1609 (1982).
[2] R. H. Lyon and R. G. DeJong, *Theory and Application of Statistical Energy Analysis* (Butterworths-Heimann, Boston, 1995).
[3] C. Kittel, *Thermal Physics* (Wiley, New York, 1969).
[4] R. L. Weaver, "Equipartition and mean square responses in large undamped structures," J. Acoust. Soc. Am. **110**, 894–903 (2001).
[5] K. J. Ebeling, "Statistical properties of random wave fields," in *Physical Acoustics*, edited by W. P. Mason (Academic, New York, 1984), Vol. 17, pp. 233–309.
[6] R. H. Lyon, "Statistical analysis of power injection and response in structures and rooms," J. Acoust. Soc. Am. **45**, 546 (1969).
[7] A. Pierce, *Acoustics, an Introduction to its Physical Principles and Applications* (McGraw–Hill, New York, 1981), Chap. 6.
[8] L. E. Kinsler, A. R. Frey, A. B. Coppens, and J. V. Sanders, *Fundamentals of Acoustics* (Wiley, New York, 1982), Chap. 13.
[9] R. L. Weaver and O. I. Lobkis, "Ultrasonics without a source, Thermal fluctuation correlations at MHz frequencies," Phys. Rev. Lett. **87**, 134301 (2001).
[10] O. I. Lobkis and R. L. Weaver, "On the emergence of the Greens function in the correlations of a diffuse field," J. Acoust. Soc. Am. **110**, 3011–3017 (2001).
[11] R. L. Weaver and O. I. Lobkis, "On the Emergence of the Greens Func-

tion in the Correlations of a Diffuse Field; Pulse-Echo using Thermal Phonons,'' Ultrasonics **40**, 435–439 (2002).
[12] R. L. Weaver and O. I. Lobkis, ''Elastic wave thermal fluctuations, ultrasonic waveforms by correlation of thermal phonons,'' J. Acoust. Soc. Am. **113**, 2611–2621 (2003).
[13] B. A. van Tiggelen, ''Green Function Retrieval and Time Reversal in a Disordered World,'' Phys. Rev. Lett. **91**, 243904 (2003).
[14] M. Campillo and A. Paul, ''Long range correlations in the diffuse seismic coda,'' Science **299**(5606), 547–549 (2003).
[15] N. M. Shapiro and M. Campillo, ''Emergence of broadband Rayleigh waves from correlations of the ambient seismic noise,'' Geophys. Res. Lett. **31**, L07614 (2004).
[16] P. Roux and M. Fink, ''Green's function estimation using secondary sources in a shallow water environment,'' J. Acoust. Soc. Am. **113**, 1406–1416 (2003).
[17] A. Derode, E. Larose, M. Campillo, and M. Fink, ''How to estimate the Green's function of a heterogeneous medium between two passive sensors? Application to acoustic waves,'' Appl. Phys. Lett. **83**(15), 3054–3056 (2003); E. Larose, A. Derode, M. Campillo, and M. Fink, ''Imaging from one-bit correlations of wideband diffuse wave fields,'' J. Appl. Phys. **95**, 8393–8399 (2004).
[18] A. E. Malcolm, J. A. Scales, and B. A. van Tiggelen, ''Retrieving the Green Function from Diffuse, Equipartitioned Waves,'' Phys. Rev. E **70**, 015601(R) (2004).
[19] M. J. Beran and G. B. Parrent, Jr., *Theory of Partial Coherence* (Prentice-Hall, Englewood Cliffs, N.J. 1964).
[20] J.-P. Fouque (ed), *Diffuse Waves in Complex Media*, Proceedings of the NATO Advanced Study Institute, Les Houches, 1998 (Kluwer, Boston, 1999); H.-J. Stockmann, *Quantum Chaos: An Introduction* (Cambridge U.P., Cambridge, 1999); P. Sheng, *Introduction to Wave Scattering, Localization, and Mesoscopic Phenomena* (Academic, San Diego, 1995).
[21] R. Snieder, ''Extracting the Greens' function from the correlation of coda waves: a derivation based on stationary phase,'' Phys. Rev. E **69**, 046610 (2004).
[22] The term ballistic refers to propagation without scattering.
[23] The word diffuse is used here to mean fully diffuse, with no net flux.
[24] S. Chandrasekhar, *Radiative Transfer* (Dover, New York, 1960).
[25] R. Hennino, N. Trégourès, N. M. Shapiro, L. Margerin, M. Campillo, B. A. van Tiggelen, and R. L. Weaver, ''Observation of equipartition of seismic waves,'' Phys. Rev. Lett. **86**, 3447–3450 (2001).
[26] In an open system one could take the u^n to be the normal modes of a finite region with suitable boundary conditions. These modes are complete and could be used to expand the field as in (4), but their amplitudes a_n would of course be time dependent.
[27] P. Morse and H. Feshbach, *Methods of Theoretical Physics* (McGraw-Hill, New York, 1953), Part I, Chap. 7.
[28] If $F \sim 1/\omega^2$, then one recovers the identity[9] between $\partial R/\partial t$ and G. This is discussed at greater length in Refs. 9–12.
[29] $\langle \psi(r,\omega)\psi^*(r',\omega')\rangle = \int R(r,r',t-t')\exp\{-i\omega t + i\omega' t')dtdt' = 2\pi\delta(\omega - \omega')R(r,r',\omega)$.
[30] This is the notion of a diffuse field imagined by Snieder[21] in a purely ballistic context.
[31] The scattering potential $v(x)$ may be thought of as a real frequency independent function, as in quantum mechanics. Alternatively, it may be identified as $v(x) = \omega^2 \delta\rho/\rho_0$ in terms of a material density fluctuation $\delta\rho(x)$ in acoustics. More complicated heterogeneities are encompassed by allowing $v(x)$ to be a local operator, perhaps with spatial derivatives.
[32] In the usual manner the real frequency ω has been analytically extended to the lower half plane with small positive ε in order to unambiguously define G even in the absence of dissipation; the process is equivalent to defining G as the Fourier transform of the response to an impulsive point load under quiescent initial conditions.
[33] K. Wapenaar, ''Synthesis of an inhomogeneous medium from its acoustic transmission response,'' Geophysics **68**, 1756–1759 (2003); K. Wapenaar, J. Thorbecke, and D. Draganov, ''Relations between reflection and transmission responses of three-dimensional inhomogeneous media,'' Geophys. J. Int. **156**(2), 179–194 (2004).
[34] T. L. Duvall, S. M. Jefferies, J. W. Harvey, and M. A. Pomerantz, ''Time-Distance Helioseismology,'' Nature (London) **362**, 430 (1993).
[35] R. L. Weaver, ''Diffuse elastic waves at a free surface,'' J. Acoust. Soc. Am. **78**, 131–136 (1983).

Noise reduction through source rerouting (L)

Rufin Makarewicz
Institute of Acoustics, A.Mickiewicz University, 61-614 Poznań, Umultowska 85, Poland

(Received 4 November 2003; revised 6 August 2004; accepted 6 August 2004)

Rerouting of a moving source can reduce noise exposure. For noise propagation governed by geometrical spreading and air absorption only, a lemniscate minimizes the A-weighted sound exposure. The route minimizing exposure in the presence of geometrical spreading and a simplified model for ground effects is found as well. © *2004 Acoustical Society of America.*
[DOI: 10.1121/1.1799271]

PACS numbers: 43.50.Lj [DKW] Pages: 2735–2737

I. INTRODUCTION

Many times noise is too high because the source path is too close to the receiver.[1] Unacceptably high noise exposure may result from the path of a moving source being too close to the receiver. The problem thus arises, how to reroute the source to minimize the A-weighted sound exposure E, i.e., the time integral of the squared A-weighted sound pressure

$$E=\int_{-\infty}^{+\infty} p_A^2(t)dt. \tag{1}$$

When a source S moves at the steady speed V along the straight line parallel to the x axis at distance D (Fig. 1), then

$$E=\frac{1}{V}\int_{-\infty}^{+\infty} p_A^2(x)dx. \tag{2}$$

To decrease its value at the receiver O, the straight segment of the path $-x_o<x<+x_o$ is substituted for the curved path $r(\phi)$ shown in Fig. 2. The A-weighted sound exposure for the original straight segment $-x_o<x<+x_o$ is as follows (Fig. 1):

$$E_s=\frac{1}{V}\int_{-x_o}^{+x_o} p_A^2(x)dx. \tag{3}$$

To calculate the A-weighted sound exposure for a new path, a polar coordinate system (r,ϕ) is introduced. When the source height H is small in comparison to the horizontal distance $r(\phi)$, one can write $r(\phi)\approx R(\phi)$ (Fig. 3), where R is the source–receiver distance. Thus, the noise coming from a source moving along the new path $r(\phi)$ is quantified by

$$E=\frac{1}{V}\int_{-\phi_o}^{+\phi_o} p_A^2(r)ds, \tag{4}$$

where the differential of the curve length is

$$ds=\sqrt{r^2+(\dot{r})^2}d\phi. \tag{5}$$

Here, $\dot{r}$ means the derivative with respect to the angle ϕ. The problem of this study is to determine the path $r(\phi)$ in such a way that the A-weighted sound exposure E [Eq. (4)] gets its minimal value and meets the condition $E<E_s$ [Eq. (3)].

II. EXCESS ATTENUATION

The study is limited to one receiver and refraction is neglected. In such a case air absorption and ground effect bring about attenuation in excess of geometrical spreading. For simplicity, it is assumed that the real noise source (e.g., aircraft) can be modeled by an omnidirectional point source. In a free field, without excess attenuation, the squared A-weighted sound pressure is as follows:

$$p_{A0}^2=\frac{W_A\rho c}{4\pi r^2}. \tag{6}$$

Here, ρc denotes the specific impedance of the air and W_A is the A-weighted sound power emitted by the source. The earth's atmosphere absorbs sound energy; therefore [Eq. (6)],

$$p_A^2=p_{A0}^2\cdot\tilde{F}_a(r). \tag{7}$$

The air absorption function $\tilde{F}_a$ depends on the source power spectrum, air temperature $\tau(°\mathrm{C})$, and humidity $h(\%)$. The explicit form of $\tilde{F}_a(r)$ is quite complicated. It has been shown that its approximation could be[2]

$$F_a=[1+\alpha(\tau,h)\cdot r]^{-1}. \tag{8}$$

As an example, under standard atmospheric conditions, with $\tau=25(°\mathrm{C})$ and $h=70$ (%), the air absorption of aircraft noise is characterized by $\alpha=2.5\cdot10^{-3}$ (1/m). For a wide range of temperature and humidity, within the distance $r<5000$ m, the approximation error $\Delta L=10\log(\tilde{F}_a/F_a)$ is less than 1.5 dB.

The lateral attenuation of the aircraft noise can be described by[3]

$$p_A^2=p_{A0}^2\cdot\tilde{F}_g(\psi), \tag{9}$$

where the ground effect function $\tilde{F}_g$ varies with the elevation angle $\psi=ctg^{-1}(r/H)$ (Fig. 3). Attenborough[4] has shown that above a homogeneous and flat surface $\tilde{F}_g$ decreases with r^{-2}. Under such circumstances, the exact function $\tilde{F}_g$ [Eq. (9)] can be approximated by

$$F_g=\beta\cdot\left[1+\gamma\frac{r^2}{H^2}\right]^{-1}, \tag{10}$$

where β describes the ground surface near the source ($r\rightarrow0$). The coefficient γ characterizes the long-distance behavior ($r\rightarrow\infty$) of the ground effect function. For example, the reflective- and absorbing ground is characterized by $\gamma\approx0.0001$ and 0.01, respectively. The validity of the above equation has been confirmed.[5] With the ground absorption coefficient $\gamma\approx0.01$, the function F_g [Eq. (10)] fits quite well

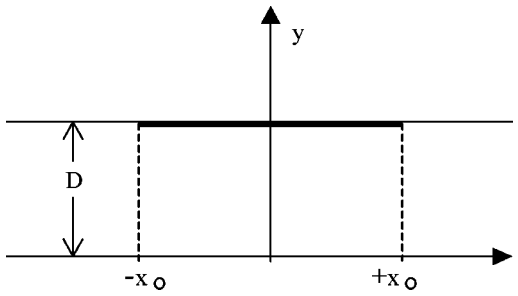

FIG. 1. The original straight segment, $-x_o<x<+x_o$, replaced by the new one.

to aircraft noise data.[6] For a small elevation angle ψ, such as $\gamma r^2 \gg H^2$, Eq. (10) simplifies to the form

$$F_g \approx \frac{\beta}{\gamma}\frac{H^2}{r^2}. \tag{11}$$

Taking into account the geometrical spreading and ground effect [Eqs. (6), (9), (11)], one obtains the squared A-weighted sound pressure as follows:

$$p_A^2 \propto \frac{1}{r^4}. \tag{12}$$

The above relationship corresponds to the 12-dB reduction of the A-weighted sound-pressure level L_A per doubling of the distance, $r \to 2r$. This prediction has been experimentally verified for airport noise (Fig. 19.32 in Ref. 3), so the hypothesis expressed by Eq. (11) seems to be feasible.

Formulas (7) and (9) are valid when noise propagates along straight lines in the homogeneous atmosphere being at rest. Although refraction creates curved ray paths, these formulas can be treated as a ''first approximation'' within 1-dB accuracy.[7]

III. CALCULATION OF VARIATIONS

With application of Eqs. (6)–(10), the A-weighted sound exposure for the new path $r(\phi)$ (Fig. 2) is as follows:

$$E \propto \int_{-\phi_o}^{+\phi_o} G(r,\dot{r})\, d\phi, \tag{13}$$

where

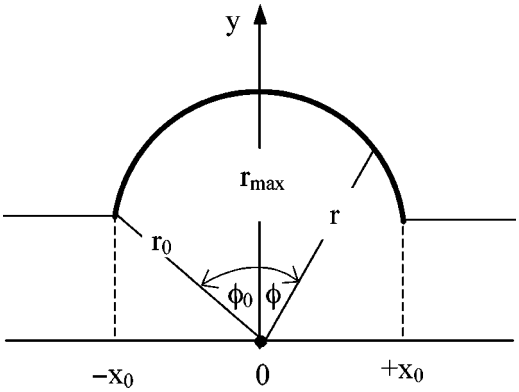

FIG. 2. The new route segment $r(\phi)$ which yields the minimal value of the A-weighted sound exposure E [Eq. (4)].

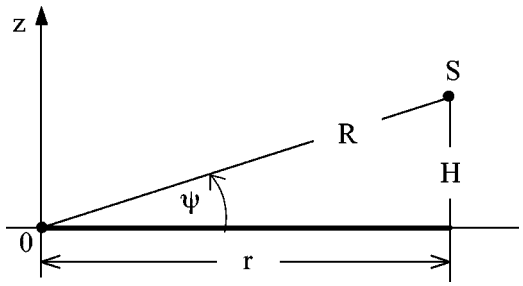

FIG. 3. Horizontal distance r and the elevation angle ψ of the source S and the receiver O in the vertical plane.

$$G(r,\dot{r}) = \frac{F_a(r)F_g(r)}{r^2}\sqrt{r^2+(\dot{r})^2}. \tag{14}$$

Integral (13) achieves its minimal value when the Euler variation principle is met[8]

$$G(r,\dot{r}) - \dot{r}\frac{\partial G(r,\dot{r})}{\partial \dot{r}} = \frac{1}{S}, \tag{15}$$

where S is a constant. Equation (13) and Eq. (14) yield

$$\frac{dr}{d\phi} = -\sqrt{S^2 F_a^2(r) F_g^2(r) - r^2}. \tag{16}$$

A. Air attenuation

For a large elevation angle ψ such as $\gamma r^2 \ll H^2$ (Fig. 3), the ground effect function is constant with distance, $F_g \approx \beta$ [Eq. (10)]. If the source–receiver distance is so large that $\alpha r \gg 1$, then the air attenuation function can be approximated by $F_a \approx 1/(\alpha r)$ [Eq. (8)]. Substitution of both F_a and F_g into Eq. (16) yields

$$\frac{dr}{d\phi} = -\sqrt{\left(\frac{\beta S}{\alpha r}\right)^2 - r^2}. \tag{17}$$

The integration gives the new path, which is a part of the lemniscate (Fig. 4)

$$r_a(\phi) = r_{\max}^{(a)} \cdot [\cos(2\phi)]^{1/2}, \tag{18}$$

where $-\pi/4 < \phi_o < \pi/4$. Here, the longest distance between the receiver and new path is

$$r_{\max}^{(a)} = \frac{r_o}{[\cos(2\phi_o)]^{1/2}} = \frac{D^2 + x_o^2}{[D^2 - x_o^2]^{1/2}}. \tag{19}$$

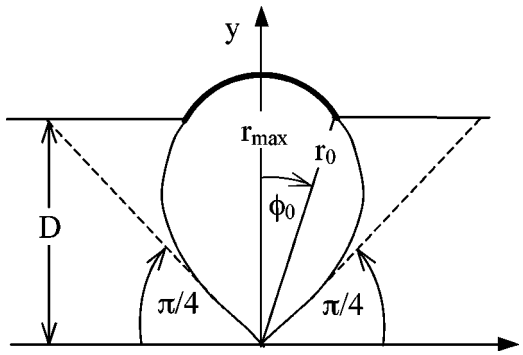

FIG. 4. The lemniscate $r_a(\phi)$ [Eqs. (18),(19)], which minimizes E [Eq. (4)] when noise propagation is governed mainly by air absorption.

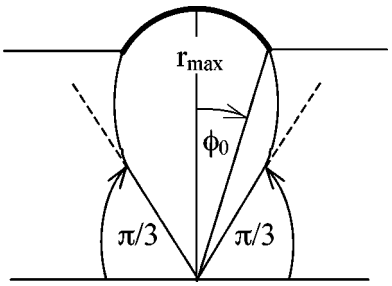

FIG. 5. The curve $r_g(\phi)$ [Eqs. (24),(25)] which minimizes E [Eq. (4)] when noise propagation is governed mainly by ground effect.

Application of the new path $r_a(\phi)$ is possible only when $D>x_o$. It corresponds to the above inequalities, $-\pi/4<\phi_o<\pi/4$.

Is this source rerouting rational? To answer this question, we calculate the A-weighted sound exposure [Eqs. (4)–(7), (9)] with $\tilde{F}_a\approx 1/(\alpha r)$ and $\tilde{F}_g\approx\beta$

$$E\propto\int_{-\phi_o}^{+\phi_o}\frac{\sqrt{r^2+(\dot{r})^2}}{r^3}d\phi, \tag{20}$$

for the original straight segment $-x_o<x<+x_o$ (E_s) and for the new path (E_a), respectively. The results of the integration are as follows:

$$E_s\propto\frac{\sin\phi_o}{\cos^2\phi_o}\quad\text{and}\quad E_a\propto\frac{1}{2}\sin(2\phi_o). \tag{21}$$

Using the definition of the sound exposure level, the noise decrease due to the source rerouting equals

$$\Delta L_{AE}^{(a)}=10\log\left(\frac{E_s}{E_a}\right)=-30\log[\cos\phi_o], \tag{22}$$

with $-\pi/4<\phi_o<\pi/4$. Taking $\phi_o\to\pi/4$ one obtains the maximum noise reduction: $\Delta L_{AE}^{(a)}\to 4.5$ dB.

B. Ground effect

For a small elevation angle ψ such as $\gamma r^2\gg H^2$ (Fig. 3), the ground effect function F_g decreases with the second power of the distance r [Eq. (11)]. Neglecting air attenuation $F_a\approx 1$ [Eq. (8)], combination of Eqs. (11) and (16) yields

$$\frac{dr}{d\phi}=-\sqrt{\left(\frac{\beta}{\gamma}SH^2\right)^2\frac{1}{r^4}-r^2}. \tag{23}$$

After a calculation similar to that in derivation of Eqs. (18), one gets (Fig. 5)

$$r_g(\phi)=r_{\max}^{(g)}\cdot[\cos(3\phi)]^{1/3}, \tag{24}$$

where $-\pi/6<\phi<+\pi/6$. Here, the longest distance between the receiver and the new path is

$$r_{\max}^{(g)}=\frac{r_o}{[\cos(3\phi_o)]^{1/3}}=\frac{D^2+x_o^2}{[D(D^2-3x_o^2)]^{1/3}}. \tag{25}$$

Application of the new path $r_g(\phi)$ is possible only when $D>\sqrt{3}x_o$, which corresponds to the inequalities: $-\pi/6<\phi<+\pi/6$.

To estimate the noise reduction due to the new path, the calculations of E_g with $r_g(\phi)$ [Eq. (24)] and E_s [Eq. (21)] for the original straight segment $-x_o<x<+x_o$ (Fig. 1) have to be done. Combination of Eqs. (4)–(7), (9) with $F_a\approx 1$ and F_g defined by Eq. (11) gives

$$E\propto\int_{-\phi_o}^{+\phi_o}\frac{\sqrt{r^2+(\dot{r})^2}}{r^4}d\phi. \tag{26}$$

The results of the integration are

$$E_s\propto\frac{2\phi_o+\sin(2\phi_o)}{\cos(3\phi_o)+3\cos(\phi_o)}\quad\text{and}\quad E_g\propto\frac{1}{3}\sin(3\phi_o). \tag{27}$$

Again using the sound exposure level, the noise decrease due to the source rerouting is

$$\Delta L_{AE}^{(g)}=10\log\left(\frac{E_s}{E_g}\right)=10\log\left[\frac{3(2\phi_o+\sin(2\phi_o))}{\sin(3\phi_o)(\cos(3\phi_o)+3\cos(\phi_o))}\right], \tag{28}$$

where $-\pi/6<\phi_o<\pi/6$. The maximum noise reduction occurs for $\phi_o\to\pi/6$: $\Delta L_{AE}^{(g)}\to 5.8$ dB.

IV. CONCLUSIONS

When the excess attenuation depends mainly on air absorption, the best shape for a minimum noise path is determined by the curve shown in Fig. 4. When ground effect dominates, the best shape is shown in Fig. 5. For practical purposes, the noise-minimizing curve $r(\phi)$ has to be smooth and without inflection points. It seems that the results presented here, though of preliminary nature, shed some light on the problem of noise reduction through source rerouting.

ACKNOWLEDGMENTS

The author would like to thank Dr. D. Keith Wilson (Associate Editor) and two anonymous reviewers for their helpful comments and suggestions.

[1] R. Makarewicz, "Theoretical foundations of some problems of environmental acoustics," J. Sound Vib. **81**, 271–286 (1982).
[2] R. Makarewicz, "Influence of air absorption and ground effect on aircraft noise," Third Joint Meeting of ASA and ASJ, Honolulu, Hawaii (1996).
[3] M.E. House, "Measurement and prediction of aircraft noise," in *Transportation Noise—Reference Book*, edited by Paul Nelson (Butterworths, London, 1987).
[4] K. Attenborough, "Review of ground effects on outdoor sound propagation from continuous broadband source," Appl. Acoust. **24**, 289–319 (1988).
[5] K. Attenborough, "A comparison of engineering methods for predicting ground effect," 2nd Convention of the European Acoustics Association, Forum Acusticum, Berlin (1999).
[6] H. Olsen, R. Ranberg, S. Storeheier, I. Granoien, and A. Ustad, "Validation of source distant propagation algorithms for aircraft noise prediction," Inter-Noise 2002, Dearborn, 2002.
[7] A.P. Dowling and J.E. Ffowcs Williams, *Sound and Sources of Sound* (Ellis Horwood, New York, 1983), pp. 119–121.
[8] I. Gelfand and S. Vomin, *Calculus of Variations* (Prentice-Hall, Englewood Cliffs, NJ, 1963).

Differential intracochlear recordings of ensemble background activity (EBA)[a] (L)

Jianxun Zhou[b] and John D. Durrant
Departments of Communication Science and Disorders and Otolaryngology, University of Pittsburgh, Forbes Tower 4033, Pittsburgh, Pennsylvania 15260

Carey Balaban
Departments of Otolaryngology, Communication Science and Disorders, and Neurobiology, University of Pittsburgh, Forbes Tower 4033, Pittsburgh, Pennsylvania 15260

(Received 20 April 2004; revised 28 June 2004; accepted 3 August 2004)

The ensemble background activity (EBA) recorded from the round window has a spectral peak near 900 Hz that is generally attributed to spontaneous eighth-nerve activity, but other frequency regions are less well understood, including the issue of contribution of hair cell (HC) potentials. To further investigate the EBA, an intracochlear electrode pair was employed to record from the basal turn in guinea pig, applying the principles of differential recording. Results confirmed 900 Hz to be the dominant feature of the EBA power spectrum in/near quiet, wherein this peak was more robust in the average derivation and readily suppressed by kainic acid, consistent with its presumptive neural origin. Another broad spectral prominence, centered around 3000 Hz, was more prominent in the difference derivation, dominated the spectrum with increasing external (white) noise, and was much less sensitive to kainic acid, implying a predominantly HC origin. The findings demonstrate efficacy of intracochlear EBA recording, potentially extend EBA utility via the differential recording method, and further validate the EBA for monitoring spontaneous activity of the eighth nerve. [DOI: 10.1121/1.1798291]

PACS numbers: 43.64.Nf, 43.64.Pg, 43.64.Ri [WPS] Pages: 2738–2741

I. INTRODUCTION

The ensemble background activity (EBA) recorded from the round window has a major spectral peak around 900 Hz (Dolan *et al.*, 1990; Costa *et al.*, 1997; McMahon and Patuzzi, 2002). Since each discharge of auditory-nerve fibers produces a unit waveform at the round window, this spectral feature may effectively reflect the convolution of the extracellular, single-unit action potential and the probability of spontaneous discharge (Kiang *et al.*, 1965; Dolan *et al.*, 1990; Costa *et al.*, 1997; McMahon and Patuzzi, 2002). Therefore, the recording/analysis of the EBA provides a minimally invasive means of testing spontaneous discharges over the population of neurons, and offers another useful approach to monitoring of cochlear nerve function. However, other background activity may contribute to this peak or produce others. It remains unclear, in particular, whether extracellular receptor potentials of the hair cells (HCs) contribute significantly to the spectral features of the EBA. Certainly, with increasing background or an applied noise, significant contribution from the HCs is expected.

A pair of differential intracochlear electrodes can be applied relatively easily and with minimal cochlear trauma to scala vestibuli (SV) and scala tympani (ST), especially at the base of the guinea-pig cochlea, a method of cochlear electrophysiology well established in the literature (Tasaki *et al.*, 1952). This system of intracochlear recording was designed specifically to permit substantial separation of hair cell and neural contributions to the electrocochleogram. Theoretically, the electrodes record the difference potential (DIF) across HC generators, but common mode potentials are generated ostensibly by the cochlear nerve. Since the summation of potentials from the electrodes will cancel much of the HC alternating-current potentials (i.e., cochlear microphonic, CM) and differential summating potential (DIF SP), the average (AVE) of the SV- and ST-recorded potentials is regarded as a best estimate of the whole-nerve potential (AP). Conversely, the difference between the potentials largely cancels the common mode, neural, contribution while emphasizing HC potentials (CM and DIF SP). The specific aim here, consequently, was to assess EBA via the differential recording method to further elucidate the makeup of the EBA spectrum.

II. METHOD

This study was a part of a larger work of which the focus was an investigation of the effects of cochlear perfusion on the EBA (which we intend to describe in a subsequent report). Young guinea pigs ($n=8$) were anesthetized using Nembutal (sodium pentobarbital; 25 mg/kg, intraperitoneal) and Innovar Vet (0.4 ml/kg, intramuscular injection). The bulla was widely opened via the ventral approach and an intracochlear electrode was introduced in ST, affixed along the perfusion tube (using a surgical adhesive, Vetbond [3M Corp., Minneapolis, MN]), of the miniature pump-and-syringe system employed in the main experiment. The elec-

[a]Portions of this report were presented at American Auditory Society 2003 Meeting, Scottsdale, AZ.

[b]Current address: Auditory Brainstem Physiology Laboratory, Kresge Hearing Research Institute, University of Michigan, 1301 E. Ann St., Ann Arbor, MI 48109-0506.

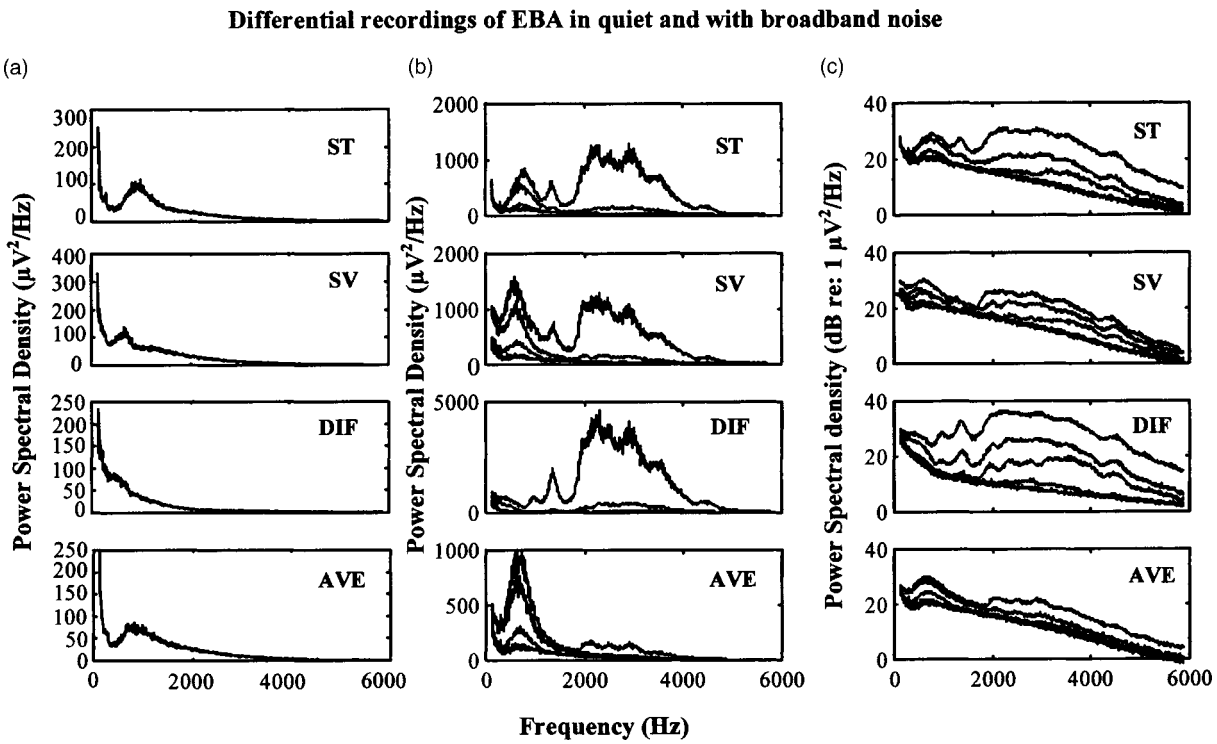

FIG. 1. Spectra of EBA in the intracochlear recordings in quiet and with broadband noise. (A) An example of differential recordings of EBA in quiet (GP 361). The difference (DIF) between SV and ST recordings largely canceled power in the 400–1500-Hz band, whereas the average (AVE) of SV and ST recordings augmented the spectral peak in the vicinity of 900 Hz. (B) and (C) Examples of differential recordings of EBA in quiet and with broadband noises from 66 to 106 dB SPL (GP 331). Panel (B) shows the changes of EBA spectra with noise in power, whereas panel (C) represents the corresponding spectra with values in dB. The DIF largely canceled the 900-Hz peak while enhancing the activity centered at 3000 Hz. In contrast, the AVE revealed increased power of the 900-Hz peak, with a concomitant decrease in higher frequency peak(s).

trode itself was formed of a thin tungsten wire covered by Teflon, except at the ends. A drainage hole was made at the cochlear apex. A second tungsten wire was supported in a glass pipette, heat sealed at the tip (Dallos, 1973), and used as the intracochlear electrode in the SV. Identical electrodes were not employed here, per the conventional method, apropos the objectives of the main study; thus, some electrode imbalance and/or dc difference between electrode half-cell potentials may have resulted. However, risk of potential adverse effects of yet another opening in ST seemed unwarranted, as all recordings were made using a high-impedance, ac-coupled recording amplifier. On the other hand, potential risks of intracochlear recordings, over the round-window approach of earlier EBA studies, were deemed warranted. First, intracochlear recording avoids the risk of round-window membrane rupture during the preparation and electrode short-circuiting caused by build-up of fluid in the round-window niche. Pilot studies indeed showed that the round-window recording, at least in combination with intracochlear perfusion, was neither less traumatic nor more stable than a strictly intracochlear recording. Furthermore, improved sensitivity and overall lower noise floor than that of the round-window recording were anticipated from electrocochleogaphy, i.e., recordings of stimulus-evoked cochlear/nerve potentials (Dallos, 1969). Last, two silver-wire electrodes were inserted into the skin at ''vertex'' and the neck muscles medial to the exposed bulla—reference and ground electrodes, respectively.

Background activity from the intracochlear electrodes was amplified (×20 000), filtered (30–10 000 Hz), sampled at 48 000 Hz, and stored for further off-line analysis (Cygnus CD-16, Cygnus Technology, Inc., Delaware Water Gap, PA), although an initial spectral analysis was performed for on-line verification of a viable recording and significant EBA. In *post hoc* analyses, the digitized data underwent more detailed spectral analysis—8192-point power spectral density (Welch's averaged periodogram method in MATLAB [MathWorks, Inc., Natick, MA]). As summarized above, it was assumed that the modes of DIF (SV-ST) and AVE ([SV + ST]/2) yield the best estimates of hair-cell activity and auditory-neural activity, respectively, from gross intracochlear recordings in the perilymphatic scalae. As described in more detail below, two major spectral components—a 900-Hz peak and a broad 3000-Hz peak (with applied background noise)—were observed and found to lie in the bands of 400–1500 Hz, and 2000–4000 Hz, respectively. Statistics of powers within these two bands was calculated to characterize input–output (I-O) functions of AVE versus DIF in these two frequency regions.

Intracochlear perfusion with kainic acid (KA, 1.5 nmol) was used at the end of the experiment in six animals to help validate further the interpretation of the EBA measured via intracochlear recording, somewhat replicating the study of Dolan *et al.* (1990). Since the perfusion of KA was used necessarily at the end of the experiment, some overall deterioration of the preparation often occurred. Hence, the overall reduction of the 3000-Hz peak of the EBA was observed and could not be attributed solely to a direct effect of KA. To

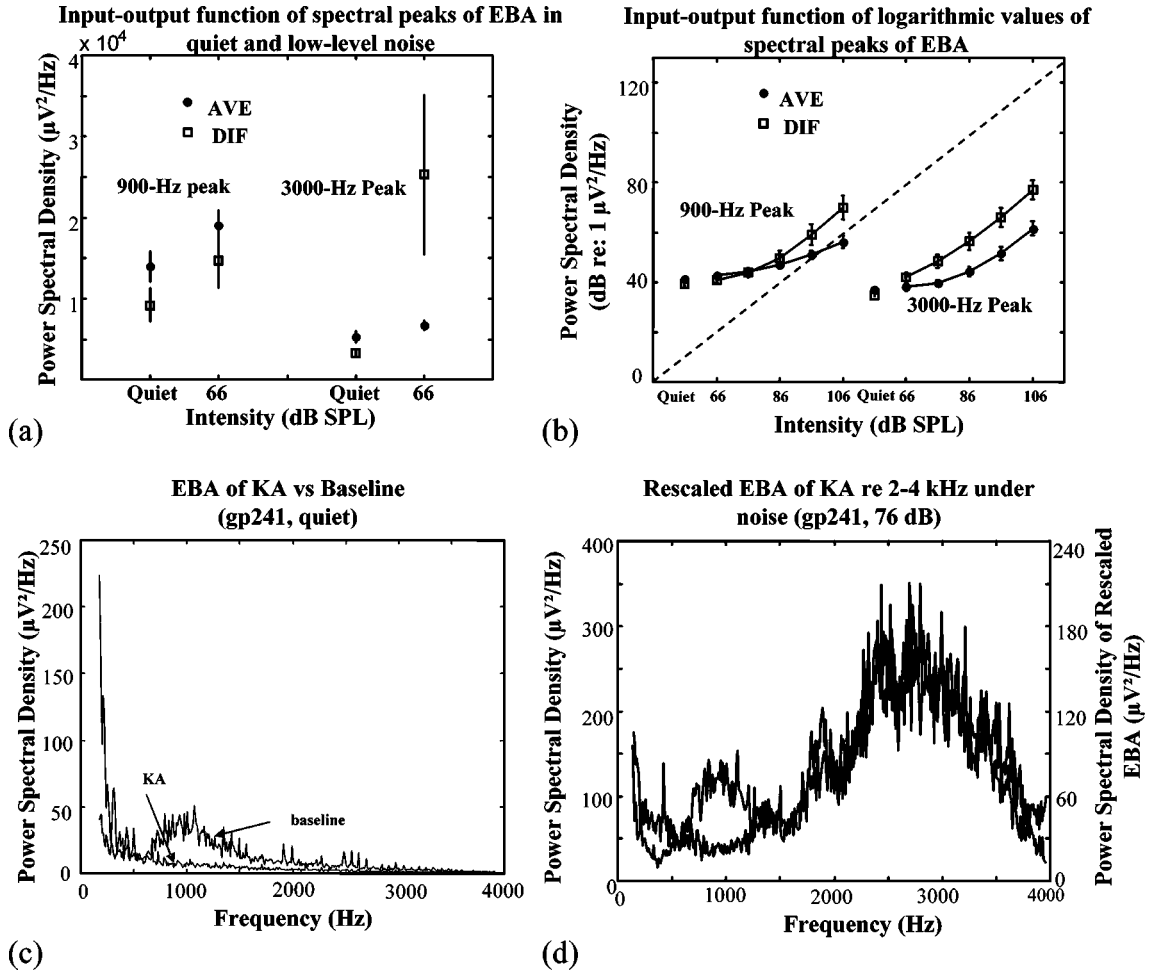

FIG. 2. Input–output function of the spectral peaks of the EBA and effect of kainic acid (KA) perfusion. (A) Spectral powers of the 900-Hz peak and the 3000-Hz peak in quiet and under low-level noise stimulation (66 dB SPL). (B) Logarithmic values of the spectral powers of the 900-Hz peak and the 3000-Hz peak in quiet and under low-to-high level noise conditions. The dashed line represents a linear growth in log–log (dB–dB) coordinates, for reference. KA application essentially eliminated the 900-Hz peak under both quiet condition (C) and noise stimulation (D), but did not eliminate the 3000-Hz peak (D). The KA data were rescaled to overlap the two spectral plots in the 2000 to 4000-Hz range (see the text), yet the EBA in the vicinity of 900 Hz falls well below the peak in the baseline plot.

evaluate the results further, a ratio of the power in the 2000–4000-Hz band after KA perfusion to that of baseline was calculated and applied to rescale the entire spectrum of the EBA after KA perfusion. For practical reasons, only the ST component was recorded during KA application, and the EBA was analyzed on-line (20 000-Hz sampling rate, rectangular window, and 2048-point FFT).

III. RESULTS AND DISCUSSION

A prominent spectral peak was seen in the ST recording, centered around 900 Hz, whereas the EBA from SV had a peak nearer 800 Hz. In either case, this spectral component was found to lie in a band of 400–1500 Hz [Fig. 1, panel (A)]. The average (AVE) of SV and ST recordings augmented the spectral peak in the vicinity of 900 Hz, whereas the difference (DIF) between SV and ST recordings largely canceled power in this band [Fig. 1, panel (A)]. From the theoretical bases of the method, the results are consistent with the assumption of a predominantly neural origin of the 900-Hz peak of EBA. Furthermore, introducing neural toxicity by KA largely eliminated the 900-Hz peak under either the quiet or stimulated-noise conditions described below [Figs. 2(C) and (D)].

Upon introducing and increasing broadband white noise, the EBA displayed increases in both the 900-Hz region and a band essentially from 2000–4000 Hz [Fig. 1, panels (B) and (C)]. The latter sometimes contained multiple small peaks, but that seemed to ride on a broad pedestal generally centered around 3000 Hz, referred to here for simplificity as the ''3000-Hz peak.'' This peak was small or undetectable under the quiet condition in all animals. It grew systematically in power, ultimately in step (see below), with increasing noise level. The AVE derivation also revealed increased power of the 900-Hz peak, with a concomitant decrease (relative to DIF) in higher frequency peak(s) in the vicinity of 3000 Hz. In contrast, the DIF derivation largely canceled the 900-Hz peak while enhancing the activity centered at 3000 Hz [Fig. 1, panels (B) and (C)]. Furthermore, the 3000-Hz peak was not eliminated by kainic acid [Fig. 2(D)]. Correspondingly, the stimulus-evoked AP was eliminated by KA application, but not CM (data not shown). These results argue strongly for a largely hair-cell origin of the 3000-Hz peak.

Further comparisons of DIF versus AVE EBA revealed that, under quiet and low-level noise conditions, the power of the DIF in the 400–1500-Hz band was uniformly lower than that of the AVE [Fig. 2(A)]. With increasing noise level, the DIF-recorded response grew rapidly at 900 Hz, overtaking the AVE response and growing in direct proportion to noise level [i.e., log–log coordinates, Fig. 2(B)]. Although the AVE ultimately followed similar direct-proportional growth, it is noteworthy that the slope of the AVE I–O function remained relatively shallow initially. The power of the DIF spectrum in the 2000–4000-Hz band was lower than that of the AVE in quiet, but exceeded the AVE from the first noise level on [see Figs. 2(A) and (B)]. During noise exposure, it always exceeded the power from both the AVE record and the corresponding 900-Hz DIF spectral power. The DIF response grew more nearly linearly at 3000 Hz than at 900 Hz. Still, the AVE fell nearly 20 dB below the DIF output at such levels.

Although the linear growth (dB/dB) of the magnitude of the DIF of the 3000-Hz component is consistent with the presumptive hair-cell origin of this spectral peak, such growth of the AVE also occurred under moderate to high noise levels. This could be due to increased neural activity (as seen typically in the input–output function of the whole-nerve AP, and/or the spread of excitation of hair-cell activity to other frequency regions) or the imbalance of the SV and ST electrode pairs across the cochlear partition, leading to a ''leakage'' effect that reflects imperfect cancellation of hair-cell potentials. Still, the power of the AVE for the 900-Hz component showed a rather shallow I–O function and was shallower than the AVE for the 3000-Hz component. The power of the AVE for the 3000-Hz component also fell substantially below the corresponding DIF power for the 900-Hz component. Furthermore, the power of the AVE for the 3000-Hz component fell substantially below the DIF at all levels, demonstrating nearly 20 dB of effective isolation of this component. These results are taken to suggest that neural and receptor origins can be assayed with a reasonable degree of isolation (as the differential method has classically been entrusted); differential intracochlear recording potentially extends the validity and basis of interpretation of the EBA analysis. Nevertheless, it would be interesting in future work to include high-pass noise stimulation to better delimit HC contribution, *per se*, namely by stimulating uniquely at frequencies well above the 900-Hz region.

Below 400 Hz, EBA was inconsistent. Although a slight prominence is suggested in the DIF spectrum in Fig. 1, such low-frequency areas varied greatly across animals, such that no systematic pattern of results was evident. Therefore, a peak as such in this frequency range was not evident in intracochlear recordings of EBA. Considering these results and comparing across studies (Schreiner and Snyder, 1987; Dolan, *et al.*, 1990; Martin, 1995; Costa *et al.*, 1997), the possibility of no significant low-frequency peaks in the EBA recorded within the guinea-pig cochlea might reflect either species differences or differences in the surgical preparation and recording techniques employed.

Lastly, as a pragmatic issue, differential recording *per se* (i.e., involving multiple intracochlear electrodes) may not be practical in a given experiment, for technical reasons. Still, the results of this study demonstrate intracochlear recording of EBA (e.g., from a single ST electrode) to be equally efficacious to RW-EBA recordings.

IV. SUMMARY

The differential intracochlear recording method in practice yields EBA results conforming to expectations from theory and serves to validate further the EBA as a research tool. Two spectral prominences are reliably observed in the analyses of the EBA in the guinea pig: (1) a 900-Hz peak emphasized by the AVE derivation, highly vulnerable to kainic acid perfusion, and thus attributable largely to activity of auditory neurons; (2) a broad peak centered around 3000 Hz, strongly represented in the DIF derivation—especially with applied noise, not eliminated by kainic acid, and thus dominated by electrical activity of the hair cells.

Costa, D. L. D., Erre, J. P., Sauvage, R. C. D., Popelar, J., and Aran, J. M. (**1997**). ''Bioelectrical cochlear noise and its contralateral suppression: Relation to background activity of the eighth nerve and effects of sedation and anesthesia,'' Exp. Brain Res. **110**, 259–269.

Dallos, P. (**1969**). ''Comments on the differential electrode technique,'' J. Acoust. Soc. Am. **45**, 999–1007.

Dallos, P. (**1973**). *The Auditory Periphery: Biophysics and Physiology* (Academic, New York and London).

Dolan, D. F., Nuttall, A. L., and Avinash, G. (**1990**). ''Asynchronous neural activity recorded from the round window,'' J. Acoust. Soc. Am. **87**(6), 2621–2627.

Kiang, N. Y.-S. (**1965**). ''Discharge patterns of single fibers in the cat's auditory nerve,'' Research Monograph 35 (MIT Press, Cambridge, MA).

Martin, W. H. (**1995**). ''Spectral analysis of brain activity in the study of tinnitus,'' in *Mechanisms of Tinnitus*, edited by J. A. Vernon and A. R. Moller (Allyn and Bacon, Baston), Chap. 13, pp. 163–180.

McMahon, C. M., and Patuzzi, R. B. (**2002**). ''The origin of the 900-Hz spectral peak in the spontaneous and sound-evoked round-window electrical activity,'' Hear. Res. **173**, 134–152.

Schreiner, C. E., and Snyder, R. L. (**1987**). ''A physiological animal model of peripheral tinnitus,'' in *Proceedings III International Tinnitus Seminar*, edited by H. Feldmann (Harsch, Karlsruhe), pp. 100–106.

Tasaki, I., Davis, H., and Legouix, J. P. (**1952**). ''The space-time pattern of the cochlear microphonic (guinea pig), as recorded by differential electrodes,'' J. Acoust. Soc. Am. **24**, 502–518.

Full wave modeling of therapeutic ultrasound: Efficient time-domain implementation of the frequency power-law attenuation

Marko Liebler,[a] Siegfried Ginter,[b] Thomas Dreyer, and Rainer E. Riedlinger
Institut für Höchstfrequenztechnik und Elektronik/Akustik, Universität Karlsruhe, Kaiserstrasse 12, 76128 Karlsruhe, Germany[c]

(Received 3 February 2004; revised 2 August 2004; accepted 2 August 2004)

For the simulation of therapeutic ultrasound applications, a method including frequency-dependent attenuation effects directly in the time domain is highly desirable. This paper describes an efficient numerical time-domain implementation of the power-law attenuation model presented by Szabo [Szabo, J. Acoust. Soc. Am. **96**, 491–500 (1994)]. Simulations of therapeutic ultrasound applications are feasible in conjunction with a previously presented finite differences time-domain (FDTD) algorithm for nonlinear ultrasound propagation [Ginter *et al.*, J. Acoust. Soc. Am. **111**, 2049–2059 (2002)]. Szabo implemented the empirical frequency power-law attenuation using a causal convolutional operator directly in the time-domain equation. Though a variety of time-domain models has been published in recent years, no efficient numerical implementation has been presented so far for frequency power-law attenuation models. Solving a convolutional integral with standard time-domain techniques requires enormous computational effort and therefore often limits the application of such models to 1D problems. In contrast, the presented method is based on a recursive algorithm and requires only three time levels and a few auxiliary data to approximate the convolutional integral with high accuracy. The simulation results are validated by comparison with analytical solutions and measurements. © *2004 Acoustical Society of America.*
[DOI: 10.1121/1.1798355]

PACS numbers: 43.20.Bi, 43.20.Hq, 43.35.Bf [RR] Pages: 2742–2750

I. INTRODUCTION

For simulation of medical ultrasound applications, diagnostics as well as therapeutics, the correct modeling of attenuation effects is crucial for the approximation quality of the acoustic field quantities inside the patient's body. Ultrasound wave propagation in lossy media, like biological tissue, is usually connected with dispersion. It is found empirically that acoustic attenuation typically exhibits a frequency dependence which can be described by a power law.[1] The most common approach today uses a splitting technique, where propagation and attenuation of ultrasound are calculated in different substeps. The propagation part is calculated in the time domain and the attenuation in the frequency domain using a Fourier transform. These models are simple but computationally very expensive, especially for broadband pulse propagation. Therefore, direct inclusion of attenuation effects in the time-domain equations is highly desirable. In this paper we focus on an efficient numerical implementation of attenuation effects according to a power law directly in the time domain. Simulations of therapeutic ultrasound applications can be performed combining this attenuation algorithm with a nonlinear propagation model, presented in the related paper of Ginter *et al.*[2]

In recent years a variety of time-domain attenuation models has been presented. Relaxation-dominated attenuation can be calculated by the use of multiple-relaxation models,[3,4] but these are computationally expensive[5] and further on there is a lack of knowledge in estimating the relaxation parameters needed for the simulation. Tavakkoli *et al.*,[6] presented a model based on an operator-splitting algorithm which includes the attenuation directly in the time domain. The frequency-dependent attenuation was implemented using a minimum-phase digital filter. However, the model is restricted to a linear function of frequency and has some disadvantages in propagation modeling since it neglects reflection and refraction and requires high numerical cost for the calculation of the diffraction substep.[7] Szabo[8] proposed the convolutional integral wave model which matches well with the empirically known frequency power-law attenuation.[9,10] Szabo introduced a causal convolutional operator, describing attenuation and dispersion directly in the time domain. This convolutional operator represents the memory effect of the medium, which depends on the past history of wave propagation.

The direct implementation of Szabo's model is limited by the numerical solution of the convolutional integral, which for an accurate calculation requires the complete time history of the acoustic field quantities. Because of limited memory space for practical problems, it is not feasible to store the complete field information of all discrete time levels.

Recently, Chen and Holm,[11] Ginter,[12] and Norton and Novarini[13] presented models to include Szabo's operator directly in the time domain. Chen and Holm modified Szabo's

[a]Electronic mail: marko.liebler@ihe.uka.de
[b]Now at: Richard Wolf GmbH, Pforzheimer Strasse 32, D-75438 Knittlingen, Germany.
[c]URL: http://www.ihe.uni-karlsruhe.de

original equation using the theory of fractional derivatives to avoid hypersingularity in the original convolution integral. The modified equations can be solved by standard numerical methods for fractional derivative equations. But, there still is the need to solve a convolutional integral and therefore to store a large amount of data in memory. Further on, for exponents higher than 1 in the power law, Chen's model requires initial conditions not readily available in many practical cases.[11] The approach of Ginter[12] is based on the method proposed by Wismer and Ludwig.[14] The original time-domain equations are transformed into frequency domain, converted into the complex discrete-time–frequency or Z domain, and then transformed back directly into discrete time operators. Then, the required number of discrete time steps for the calculation of the convolution has to be optimized, making a compromise between a sufficient approximation of the dispersion effects and the numerical effort. Norton and Novarini[13] use a similar approach. But, this approach cannot be used for practical 2D or 3D problems because of the enormous computational cost.

The main purpose of this paper is to describe an efficient numerical implementation of Szabo's model for the frequency-dependent power-law attenuation directly in the time domain, based on a recursive algorithm.

II. MATHEMATICAL MODEL

The full-wave propagation model combines an acoustic approximation of the original hydrodynamic equations for ideal fluids in inhomogeneous media with a broadband frequency power-law attenuation, typical for soft tissues. A detailed description of the nonlinear modeling of therapeutic ultrasound propagation in ideal homogeneous media is given in Ref. 2. In this paper we focus on the mathematical description and efficient numerical implementation of the attenuation algorithm directly in the time domain. Therefore, when describing the model equations, we limit the considerations to the case of linear ultrasound propagation. This means no general restriction. Using the presented splitting technique, calculating propagation and attenuation effects separately within one time step, the model can be easily extended to therapeutic applications where nonlinear effects occur. In that case the linear ultrasound propagation model has to be replaced by a nonlinear one, and the condition that nonlinear propagation effects are negligible within one time step has to be fulfilled. This is generally valid for most therapeutic ultrasound applications, where only weak shock waves occur.

With the acoustic variables pressure p, density ρ, and acoustic velocity $\mathbf{v}$, one gets the linear acoustic equations for conservation of mass and momentum

$$\frac{\partial \rho}{\partial t} = -\nabla(\rho_0 \mathbf{v}), \tag{1a}$$

$$\frac{\partial \mathbf{v}}{\partial t} = -\frac{1}{\rho_0}\nabla p. \tag{1b}$$

To close the system of equations for the ideal homogeneous fluid model, a linear equation of state $p=p(\rho)$ in the form

$$p = c_0^2 \rho, \tag{2}$$

has to be added. For inhomogeneous media, assuming $p_0(\mathbf{x})=$ const. and $\rho_0(\mathbf{x})$ to be independent of t, Eq. (2) must be replaced[15,16] by

$$\frac{\partial p}{\partial t} = c_0^2 \left(\frac{\partial \rho}{\partial t} + \mathbf{v}\nabla \rho_0 \right). \tag{3}$$

In biological media, an ultrasonic wave of initial amplitude $\hat{w}_0$ is attenuated exponentially with propagation distance Δx and by an attenuation according to a frequency power law

$$\hat{w}(x+\Delta x) = \hat{w}_0(x) e^{-\alpha(\omega)\Delta x}, \tag{4}$$

$$\alpha(\omega) = \frac{\alpha_0}{(2\pi)^y} |\omega|^y, \tag{5}$$

where $1 \leqslant y \leqslant 2$, which is typical for soft tissue.[1] Here, $\hat{w}$ represents the amplitude of an acoustic field variable w, such as pressure or velocity; $\alpha(\omega)$ is the attenuation coefficient; α_0 the attenuation constant; y the frequency-power exponent; and $\omega = 2\pi f$. Based on the description of Eq. (4), we derive the model equations considering the example of a one-dimensional plane-wave propagation in an ideal lossless medium in the positive x direction, described by

$$\frac{\partial w}{\partial t} + c_0 \frac{\partial w}{\partial x} = 0. \tag{6}$$

Transforming Eq. (6) into the frequency domain with a Fourier transform[8] leads to

$$\frac{\partial W(x,\omega)}{\partial x} + j\frac{\omega}{c_0} W(x,\omega) = 0. \tag{7}$$

With the dispersion relation $k(\omega)=\beta_0=\omega/c_0$, it follows from Eq. (7)

$$\frac{\partial W(x,\omega)}{\partial x} + jk(\omega) W(x,\omega) = 0. \tag{8}$$

In lossy media, the dispersion relation has to be extended[10] through

$$k(\omega) = \beta_0 + \beta'(\omega) - j\alpha(\omega) = \beta_0 + L_{\beta'}(\omega) - jL_\alpha(\omega), \tag{9}$$

where α and β' are related to the attenuation and the phase dispersion, respectively. Introducing $L_\gamma = L_\alpha(\omega) + jL_{\beta'}(\omega)$ as the dispersion loss operator leads to

$$\frac{\partial W(x,\omega)}{\partial x} + j\beta_0 W(x,\omega) + L_\gamma W(x,\omega) = 0, \tag{10}$$

or, in the time domain

$$\frac{\partial w(x,t)}{\partial x} + \frac{1}{c_0}\frac{\partial w(x,t)}{\partial t} + L_\gamma(t) * w(x,t) = 0. \tag{11}$$

Here, $*$ represents the convolution. Acoustic media satisfy the condition of causality, and by assuming linear propagation the attenuation and dispersion are linked by the Kramers–Kronig relations.[17,18] Using the Kramers–Kronig integral relations, phase dispersion can be calculated exactly at all frequencies if the attenuation is known at all frequencies. For an attenuation characteristic known over a limited

frequency range, like Eq. (5) for biological media, several models have been proposed to relate dispersion to attenuation in a local approximation. To determine the dispersive loss operator L_γ, we follow the approach of Szabo.[10] Szabo introduced the time-causal model, which has been shown to be the most accurate model in predicting the dispersion for nonlinear attenuation.[19] In the time-causal model the dispersion and attenuation are related by a Hilbert transform directly in the time domain

$$\begin{aligned} &L_{\beta'}(t) = -j\,\mathrm{sgn}(t) L_\alpha(t), \\ &L_\alpha(t) = j\,\mathrm{sgn}(t) L_{\beta'}(t), \\ &\rightarrow L_\gamma(t) = 2H(t) L_\alpha(t), \end{aligned} \tag{12}$$

with $H(t)$ as the Heaviside function and the loss operator L_α given by

$$\begin{aligned} L_\alpha(t) &= \mathcal{F}^{-1}\{L_\alpha(\omega)\} \\ &= \frac{1}{2\pi}\int_{-\infty}^{\infty}\left(-\frac{\alpha_0}{(2\pi)^y}\right)|\omega|^y \mathrm{e}^{-\mathrm{j}\omega t}\mathrm{d}\omega. \end{aligned} \tag{13}$$

With the help of the theory of generalized functions,[20] the inverse Fourier transform in Eq. (13) can be evaluated. Introducing the Riemann–Liouville definition of the fractional derivative[21] the dispersive loss operator $L_\gamma(t)$ now becomes

$$L_\gamma(t) * w(x,t) = \alpha_0 c_0 h_m \Gamma(-y) D^y w(x,t), \tag{14}$$

with h_m as a simple factor depending on the power-law exponent y as follows

$$h_m = \begin{cases} [(-1)^{y/2}], & \text{for } y = 0,2,4,... \\ \left[\dfrac{2(y+1)!(-1)^{(y+1)/2}}{\pi(y+1)}\right], & \text{for } y = 1,3,5,... \\ \left[\dfrac{2\Gamma(y+2)\cos\left[(y+1)\dfrac{\pi}{2}\right]}{\pi(y+1)}\right], & \text{for } y \text{ any real number'} \end{cases} \tag{15}$$

and with the definition of the fractional derivative[21] using the gamma function $\Gamma(x)$

$$D^y w(t) = \frac{1}{\Gamma(-y)}\int_0^t \frac{w(t')}{(t-t')^{y+1}}\mathrm{d}t'. \tag{16}$$

After the mathematical remodeling, one now has a convolution-type loss operator including dispersion effects according to Szabo's causal theory. In the last step the dispersive loss operator was rewritten using the fractional derivative. Doing this, the theory of fractional calculus can be applied to find an efficient numerical implementation of the convolution integral $D^y w(t)$.

III. NUMERICAL IMPLEMENTATION

For the numerical implementation of the ultrasound propagation model [Eq. (1) and Eq. (3)], a 2D explicit high-order FDTD algorithm is chosen. Depending on the application, Eqs. (1) and (3) are solved either in Cartesian or in cylindrical coordinates, assuming axisymmetry. A detailed description of the numerical treatment is given in Ref. 2. In the propagation substep the equations for propagation in an ideal lossless medium are applied. The incorporation of the dispersive loss operator into the FDTD ultrasound propagation algorithm works as a correction of the acoustic field variables w_{ideal}, calculated with the ideal propagation model. This correction is performed at every time step $t_n = n\Delta t$ in which the correction loss term $\Delta^n_{\text{loss}} w$ depends on the time history of the field variables

$$w^{n+1} = w^{n+1}_{\text{ideal}} - \underbrace{\frac{\alpha_0 c_0 h_m \Gamma(-y)}{\Delta t^y} D^{y,n} w}_{\Delta^n_{\text{loss}} w}. \tag{17}$$

In the following a derivation of an efficient FDTD implementation of the loss term $\Delta^n_{\text{loss}} w$ in Eq. (17) is presented. In a first step another definition of the fractional derivative[21] is used to get a time-discrete formulation of the convolution integral

$$D^y w(t) = \lim_{\Delta t \to 0} \frac{1}{\Delta t^y} \sum_{\ell=0}^{\infty} \frac{\Gamma(\ell - y)}{\Gamma(-y)\Gamma(\ell+1)} w(t - \ell\Delta t). \tag{18}$$

Including this formulation in a real FDTD algorithm, Δt remains finite and so Eq. (18) shows a low-pass behavior. Using the identity[21]

$$\frac{\Gamma(\ell - y)}{\Gamma(-y)\Gamma(\ell+1)} = (-1)^\ell \binom{y}{\ell}, \tag{19}$$

the coefficients of Eq. (18) can be expressed as binomial coefficients. For even-integer values of y only a finite number of coefficients are not zero and the fractional derivative expresses itself as an ordinary derivative with a local character in time. The sum in Eq. (18) remains finite. For all other values of y the sum remains infinite. The operator then exhibits its full convolutional behavior, requiring the entire history of field variables, which is referred to as nonlocal behavior in time in this paper. Due to the limited memory space and computational capacity, the time-discrete implementation on the basis of Eq. (18) is not a practical way to calculate the power-law attenuation in the time domain.

For $\ell \geqslant 2$ the coefficients for noninteger y as a function of ℓ behave as a monotonic decreasing function. The assumption that the coefficients are sufficiently low for large ℓ motivated the approaches in Refs. 12, 14, 22 to use only a finite number $l = 0,...,l_{de}$ $(20 < l_{de} < 50)$ of time steps in Eq. (18). But, the results show that the power-law damping behavior could not be modeled very well, mainly in the low-frequency regime. Further on, for 2D problems, the need to store more than 20 time levels leads to enormous costs in memory space and computational time.

Therefore, in this paper we introduce a new recursive implementation to overcome these problems. Using this algorithm we only need a finite number of three or four time levels of data and about four up to ten auxiliary fields of data, according to the approximation quality of the nonlocal part of the dispersive loss operator.

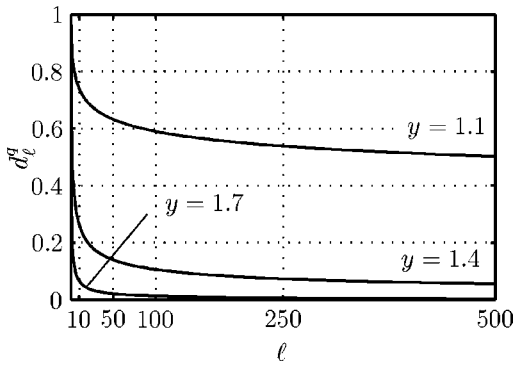

FIG. 1. The first 500 coefficients d_ℓ^q of the fractional derivative D^q for different values of $q=y-2$.

To get a recursive implementation, we first split the operator $D^y w(t)$ into a local and a nonlocal part. Applying the rule[21]

$$D^y w(t) = \frac{\partial^s}{\partial t^s} D^{y-s} w(t), \tag{20}$$

it follows from Eq. (18) at $t=n\Delta t$

$$D^{y,n} w = \frac{1}{\Delta t^y} \sum_{\ell=0}^{\infty} \underbrace{[w^{n-\ell} - 2w^{n-1-\ell} + w^{n-2-\ell}]}_{DQ2} \times \underbrace{\frac{\Gamma(\ell-q)}{\Gamma(-q)\Gamma(\ell+1)}}_{d_\ell^q},$$

where $s=2$ and $q=y-2$. At first glance there is not much of an improvement. The number of addends is still infinite. But, the nonlocal part from the index $\ell=0$ is now monotonically decreasing, as shown in Fig. 1. The idea of applying a recursive algorithm is to approximate this monotonic decreasing function of the coefficients d_ℓ^q by a sum of $N_e=4$ to about 10 monotonic decreasing exponential functions. For the ℓth coefficient d_ℓ^q we write

$$d_\ell^q = \frac{\Gamma(\ell-q)}{\Gamma(-q)\Gamma(\ell+1)} \approx \sum_{k=1}^{N_e} d_k^{q,a} \exp(-d_k^{q,e}\ell) = \tilde{d}_\ell^q. \tag{21}$$

For this approximation the values of the amplitudes $d_k^{q,a}$ and the exponents $d_k^{q,e}$ have to be calculated. This is performed by optimizing the approximation of these parameters to fit the given coefficient forming the nonlocal part of Eq. (21) in a huge range of several thousand time levels (ℓ). The number of exponential functions required for this approximation depends on the frequency-power-exponent y and the signal duration. As shown in Fig. 1, the influence of later time levels on the convolutional operator increases with decreasing y. The parameter optimization is performed using the commercial software package MATLAB in a least-square sense until a maximum difference of less than 10^{-4} between the approximated $\tilde{d}_\ell^q$ and the ideal coefficients d_ℓ^q is achieved. Because of this somewhat heuristic approach, the calculated coefficients $d_k^{q,a}$ and $d_k^{q,e}$ are validated by numerical test simulations, which will be described in Sec. IV. Approximated coefficients for the amplitudes $d_k^{q,a}$ and exponents $d_k^{q,e}$ are listed for some values of y in the Appendix.

The last step required to obtain the recursive algorithm takes advantage of the special properties of the exponential function. Similar approaches are known from modeling electromagnetic propagation through linear dispersive media.[23] Introducing the auxiliary variable Ψ_k at time step t_n

$$\begin{aligned}\Psi_k^n &= \sum_{\ell=0}^{\infty} d_k^{q,a}[w^{(n-\ell)} - 2w^{(n-1-\ell)} + w^{(n-2-\ell)}] \times \exp(-d_k^{q,e}\ell) \\ &= \underbrace{d_k^{q,a}[w^n - 2w^{n-1} + w^{n-2}]}_{\ell=0} + \underbrace{\exp(-d_k^{q,e})\Psi_k^{n-1}}_{\ell=1,\ldots\infty},\end{aligned} \tag{22}$$

one can split up the sum into the first summand and the remainder, where the remainder has the same form as the total sum before, replacing the index n by $n-1$. Thus, this variable can be calculated recursively, based on previous calculated values. Now, the fractional derivative $D^{y,n}w$ for noninteger y can be written in a recursive formulation

$$D^{y,n} w = \frac{1}{\Delta t^y} \sum_{k=1}^{N_e} d_k^{q,a} \underbrace{[w^n - 2w^{n-1} + w^{n-2}]}_{DQ2} + \exp(-d_k^{q,e})\Psi_k^{n-1}. \tag{23}$$

The difference to the original definition in Eq. (18) is that the summation now incorporates only the finite number of approximation functions and not the infinite number of time steps. To improve the approximation quality of this recursive algorithm, one can replace the local differential quotient of second order by a differential quotient of higher approximation level

$$\mathrm{DQ2} = [2w^n - 5w^{n-1} + 4w^{n-2} - w^{n-3}]. \tag{24}$$

Finally, the incorporation into the FDTD ultrasound propagation algorithm[2] works as given in Eq. (17).

IV. NUMERICAL VALIDATION

The numerical validation of the algorithm is performed by simulation of a plane-wave propagation in a 2D lossy medium. The simulation arrangement is shown in Fig. 2. For the numerical experiments a chirp signal with a frequency range from $f_s=100$ kHz to $f_e=3$ MHz and a pulse width of $t_p=10\,\mu$s according to Eq. (25) is used

$$p(t) = p_0 \cos\left(2\pi\left(\left(\frac{f_e - f_s}{2t_p}\right)t^2 + f_s t + 0.25\right)\right). \tag{25}$$

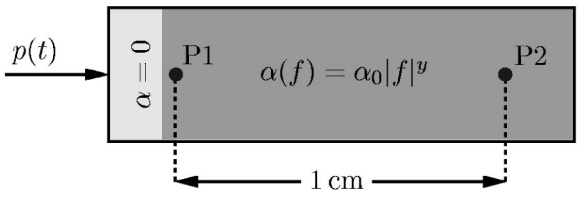

FIG. 2. Simulation arrangement for numerical validation.

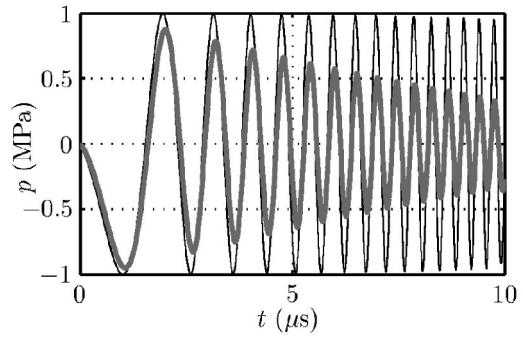

FIG. 3. Time-shifted pressure signals recorded at points P1 (thin) and P2 (bold) for $y=1.4$.

The plane wave with initial amplitude p_0 propagates from left to right (Fig. 2) and is recorded at the two points P1 and P2 with an intermediate distance of $d=1$ cm. The upper and lower boundaries of the computational domain are numerically treated as ideally rigid. At the right side an absorbing boundary condition is implemented, and at the left side a source condition based on characteristics is used.[2] The numerical calculations are performed with $\alpha_0=2.0\,\mathrm{dB/(cm\,MHz}^y)$ and different exponents y. In Fig. 3 the recorded pressure time signals for $y=1.4$ are plotted. With the related power spectral densities Φ_{P1} and Φ_{P2}, the numerically approximated attenuation coefficient α_{num} can be calculated

$$\alpha_{\mathrm{num}}(f)|_{\mathrm{dB/cm}}=-\frac{1}{d}10\log\frac{\Phi_{\mathrm{P2}}(f)}{\Phi_{\mathrm{P1}}(f)}. \tag{26}$$

Figure 4 demonstrates the excellent agreement between $\alpha_{\mathrm{num}}(f)$ and the predetermined $\alpha(f)=\alpha_0 f^y$ over the complete frequency range of the chirp signal for different exponents y. To give an impression of the benefit using the efficient recursive implementation, a calculation for $y=1.4$ using the standard convolution model with a limited time history as presented in Refs. 12, 14, 22, but requiring the same numerical effort with respect to memory space, is also plotted in Fig. 4.

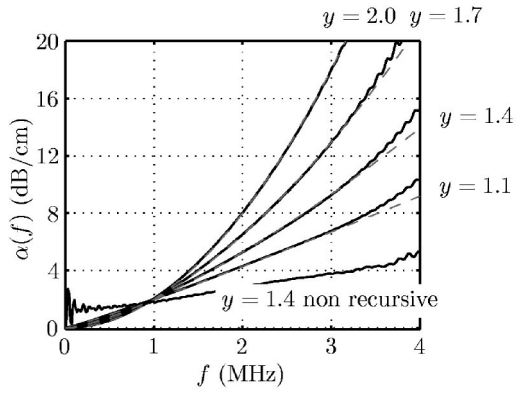

FIG. 4. Comparison of $\alpha(f)$ (--) and $\alpha_{\mathrm{num}}(f)$ (—) for different exponents y. Additionally, a calculation result for $y=1.4$ without the recursive algorithm but same numerical effort, with respect to the required memory space, is plotted.

V. EXPERIMENTAL VERIFICATION

For the experimental verification, we first consider the propagation of ultrasound from a plane piezoelectric transducer through water and a test material obeying a frequency power-law attenuation. To evaluate the accuracy of the attenuation model, pressure measurements are compared with simulation data. Furthermore, experiments are presented demonstrating the applicability of the presented model for a typical application of high-intensity focused ultrasound (HIFU), where nonlinear propagation effects occur. In a first step the acoustic parameters of the test materials are determined.

A. Determination of acoustic parameters for test materials

A broadband through-transmission technique according to Refs. 19, 24 is used to determine the sound-speed and acoustic attenuation parameters of the test materials. The densities of the materials are calculated using the measured mass and volume. Nonlinear propagation effects are assumed to be negligible in the transmission measurements because of small pressure amplitudes and short propagation paths. The experimental setup for sound-speed and attenuation measurement is shown schematically in Fig. 5. From a plane piezoelectric transducer (PIC 151, PI Ceramic, square, 7×7 cm, backed with brass), driven by an arbitrary waveform generator (AWG410, Tektronix) and a broadband power amplifier (model 2100, ENI) a chirp signal with a frequency range from 500 kHz to 3.5 MHz is emitted and recorded with a broadband PVDF hydrophone (25 μm PVDF, Piezotech S.A., circular, diameter=7 cm). The received signal is amplified and digitized for processing. To determine the sound speed or acoustic attenuation of a material, two measurements are performed: one reference water path measurement and one with the test material inserted between the piezoelectric transducer and the hydrophone. The attenuation of water ($\alpha_0=0.002$ dB/cm at $f=1$ MHz) is neglected, since for the considered experiment this introduces an error of less than 1% in pressure amplitude. Figure 6 shows the measured reference signal for ultrasound propagation in degassed water without a test material. Two different materials are used for the experimental verification, epoxy (Araldite CW 1195, Huntsman, Salt Lake City, UT) and castor oil (castor oil, pure, Carl Roth GmbH, Karlsruhe, Germany). The epoxy phantom is a cylindrical block with a diameter of 11 cm and a thickness of 2 cm. To make the second phantom, two ends of an aluminum tube (inner diameter=10 cm, thickness=3 cm) are sealed with a 38-μm-thin plastic film (Seal View™,

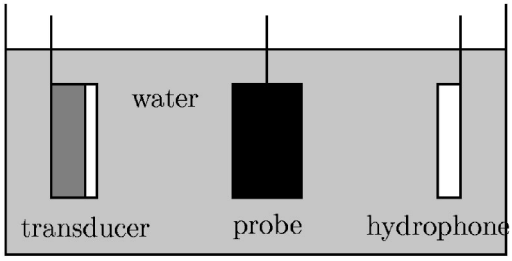

FIG. 5. Experimental setup for attenuation measurements.

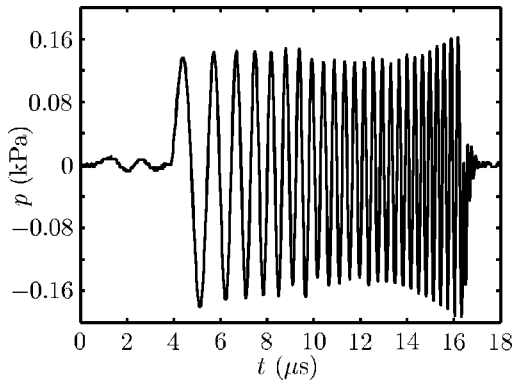

FIG. 6. Chirp signal used for attenuation measurements.

Norton Performance Plastics Corporation, Akron, OH) and filled with degassed castor oil. The water temperature is 20 °C. To determine the two attenuation parameters y and α_0 of the frequency power law, the experimentally obtained attenuation curves are least-square fitted. In Fig. 7 the measured and fitted attenuation curves for the two materials are plotted. For castor oil the two parameters are determined as $y=1.67$ and $\alpha_0=0.81\,\mathrm{dB/(cm\,MHz}^y)$, which is in good agreement with the values available in the literature.[19,25,26] The epoxy material shows a nearly linear frequency-dependent attenuation, and the determined parameters are $y=1.14$ and $\alpha_0=1.28\,\mathrm{dB/(cm\,MHz}^y)$. Regarding the uncertainty in determining the dimensions of the phantoms and digitizing errors, the relative error of the measured sound speed and acoustic density can be calculated to be less than 2%. Together with the curve fit, this leads to an uncertainty of less than 5% for the determined attenuation for frequencies above 2 MHz, whereas the relative error increases slightly for lower frequencies due to the influence of phantom thickness.

B. Comparison of simulation and measurement for 2D plane-wave propagation

A simulation arrangement corresponding to the experimental setup described in the previous section is used to compare simulation and experimental results. Two-dimensional linear ultrasound propagation through water and the attenuating test materials is calculated and compared to

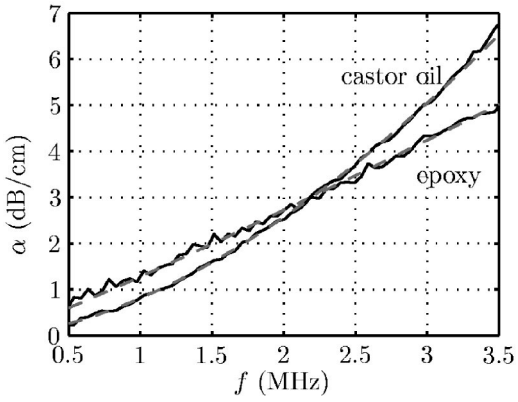

FIG. 7. Attenuation measured (—) and least-square fitted (--) for castor oil and epoxy.

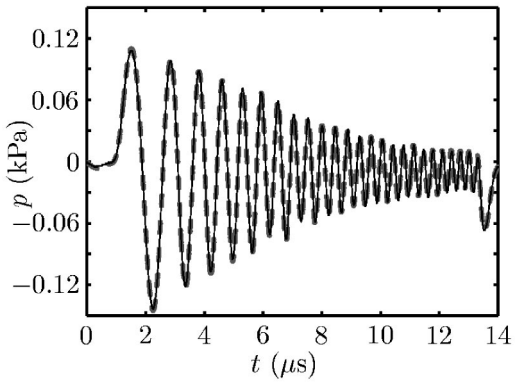

FIG. 8. Measured (—) and calculated (--) pressure time curves for propagation through 3-cm castor oil.

the measured pressure curves. The acoustic parameters used for simulations are summarized in Table I. Figure 8 demonstrates the excellent agreement between the calculated and measured pressure time signals for chirp signal propagation through castor oil. In Fig. 9 the results for epoxy are presented. Again, a very good agreement between simulation and experiment can be observed. Using the measured and simulated pressure curves shown in Fig. 8, the phase velocity dispersion $\Delta v(\omega)$ is calculated for propagation through castor oil

$$\Delta v(\omega)=v(\omega)-v(\omega_0), \tag{27}$$

$$\frac{1}{v(\omega_0)}-\frac{1}{v(\omega)}=\frac{\varphi_w(\omega)-\varphi_p(\omega)}{\omega d}-\frac{\varphi_w(\omega_0)-\varphi_p(\omega_0)}{\omega_0 d},$$

where φ_w and φ_p are the phase spectra for the propagation in water only and with material phantom, respectively; $v(\omega)$ is the phase velocity; d the phantom thickness; and ω_0 represents a reference frequency at which the recorded pulse has significant energy.[19] In Fig. 10 the calculated phase change from simulation and measurement is plotted and compared with the theoretical time-causal dispersion relation[10,19]

$$\frac{1}{v(\omega_0)}-\frac{1}{v(\omega)}=-\alpha_0\tan(y\pi/2)(\omega^{y-1}-\omega_0^{y-1}). \tag{28}$$

Figure 10 demonstrates that the presented model correctly predicts the phase dispersion. The figures shown for numeri-

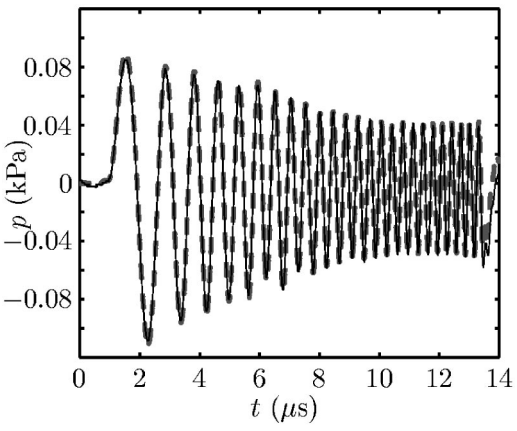

FIG. 9. Measured (—) and calculated (--) pressure time curves for propagation through 2-cm epoxy.

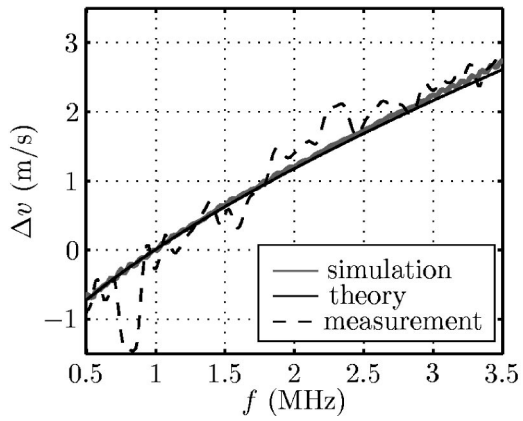

FIG. 10. Phase velocity change calculated from simulation and measurement data and compared with theory. The reference frequency is $f_0 = 1$ MHz.

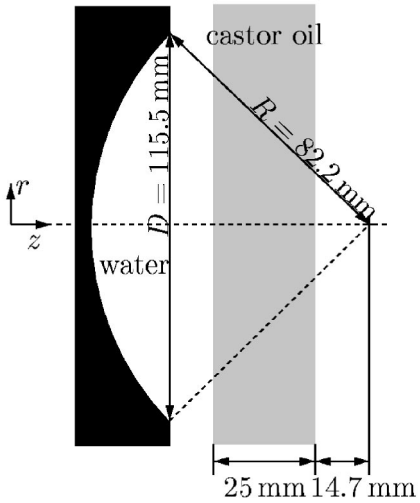

FIG. 11. Setup for HIFU application.

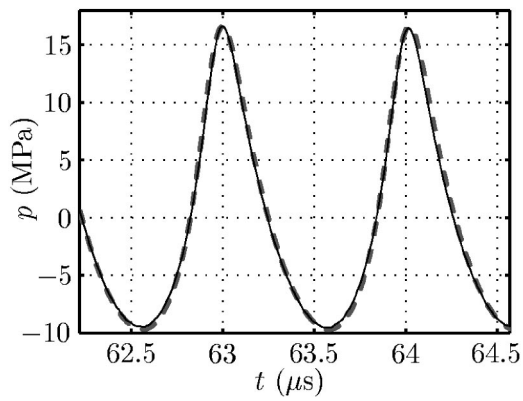

FIG. 12. Comparison of measured (—) and nonlinear calculated (--) pressure time curves in the acoustic focus for propagation in water.

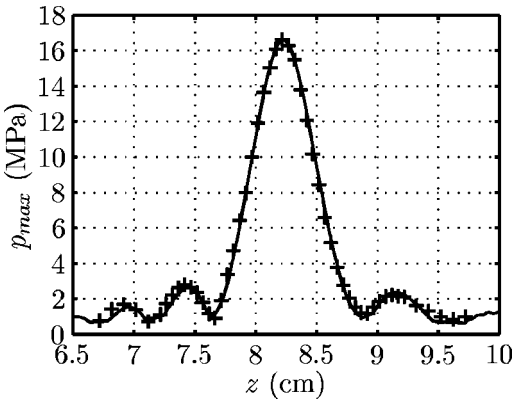

FIG. 13. Comparison of nonlinear calculated (solid line) and measured (+) axial distribution of maximal pressure amplitudes for propagation in water.

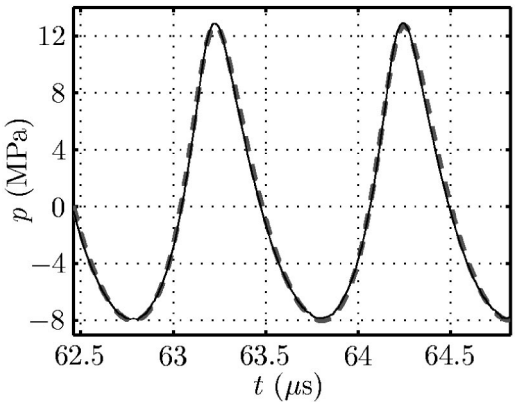

FIG. 14. Comparison of measured (—) and nonlinear calculated (--) pressure time curves in the acoustic focus for propagation in water and castor oil.

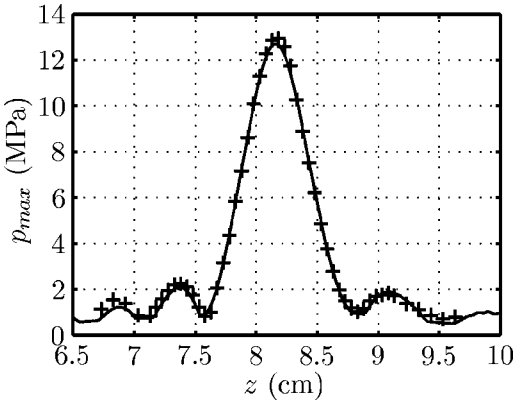

FIG. 15. Comparison of nonlinear calculated (solid line) and measured (+) axial distribution of maximal pressure amplitudes for propagation in water and castor oil.

TABLE I. Acoustic parameters of water (Ref. 26) and the two test materials at 20 °C used for simulations.

	Water	Castor oil	Epoxy
c_0 (m/s)	1482	1525	3117
ρ_0 (kg/m^3)	998	950	1734
α_0 (dB/(cm MHz^y))	0	0.81	1.28
y	2	1.67	1.14

cal validation and experimental verification of the attenuation algorithm demonstrate an excellent agreement of the simulation results with the analytical and measured ones for linear ultrasound propagation.

C. Comparison of simulation and measurement for therapeutic ultrasound application

To complete the experimental verification, a typical situation of therapeutic ultrasound application is considered. Measurements are compared with simulation results to validate the presented attenuation algorithm also for applications where nonlinear propagation effects are important. Therefore, the calculations are done combining the attenuation algorithm with the nonlinear ultrasound propagation model presented by Ginter *et al.*[2] Figure 11 shows the arrangement used for the experiments and simulations. A self-focusing piezoelectric transducer (P4, CeramTec) for HIFU applications with a focal distance of $R=82.2$ mm and a diameter of $D=115.5$ mm is used. The transducer operates at a resonant frequency of $f=980$ kHz. Experiments are performed for ultrasound propagation in degassed water only and with a 25-mm-thick castor oil phantom inserted into the propagation path. Pressure measurements in the focal area are done in water with a fiberoptical probe hydrophone[27] to investigate the effects of the attenuating castor oil layer. For the simulations the initial pressure amplitude at the transducers surface is set to $p_0=0.15$ MPa. The nonlinearity parameters (B/A) for water and castor oil are $B/A=5.1$[1] and $B/A=12.0$,[28] respectively. Figures 12 and 13 show the comparison between measurement and simulation of the pressure time curves in the focal point and axial distribution of the maximal pressure amplitudes for propagation in water only. For the calculations the attenuation of water is neglected. In Fig. 12 the steepening of the pressure wave due to nonlinear propagation effects can be cleary identified. The influence of the castor oil is demonstrated in Figs. 14 and 15, showing again the comparison between measurement and simulation for focal pressure curves and axial pressure distribution. The 25-mm castor oil layer, with an attenuation comparable to that of soft tissue, leads to a reduction in the maximal pressure amplitude of about 24%. These experiments demonstrate the applicability of the presented attenuation algorithm in combination with a nonlinear propagation model for therapeutic ultrasound applications.

VI. DISCUSSION AND CONCLUSIONS

We presented an efficient numerical algorithm for the broadband approximation of the typical soft-tissue power-law attenuation which is based on a recursive calculation method and thereby overcomes the problem of solving a convolutional integral in the time domain. It has been demonstrated that, using this algorithm, the information of only three (with standard second-order differential quotient) or four (with higher order approximation) time levels and a few auxiliary data are sufficient to approximate a convolutional loss operator with high accuracy. The computational results are validated by comparison with analytical solutions and measurements for situations of linear and nonlinear ultrasound propagation.

The presented algorithms provide the basis to simulate realistic scenarios of therapeutic ultrasound applications completely in the time domain with high efficiency. Numerical investigations on the interaction of nonlinear steepening effects and broadband power-law attenuation can be performed.[29] Especially for ultrasound thermotherapy, an accurate broadband calculation of this interaction is very important to be able to determine the absorbed ultrasound power in an accurate manner. Further, the extended model can be combined with the bio-heat-transfer-equation to investigate the role of such nonlinear propagation and attenuation behavior or the influence of temperature-dependent parameters on lesion formation in thermal therapies.[30,31]

ACKNOWLEDGMENTS

Parts of this work were supported by the Deutsche Forschungsgemeinschaft (DFG) under Grants No. Wi 1044/11-2 and Wi 1044/14-1.

APPENDIX: COEFFICIENTS OF THE APPLIED RECURSIVE ALGORITHM

In the following tables the coefficients $d^{q,a}$ and $d^{q,e}$ for amplitudes and exponents of the exponential function approximation are listed for three selected values of y.

TABLE II. Numerical coefficients of the recursive algorithm for $y=1.1$.

	$y=1.1$	
k	$d^{q,a}$	$d^{q,e}$
1	0.206 224 16	0.000 070 45
2	0.115 786 08	0.243 367 39
3	0.083 664 90	0.014 848 13
4	0.072 507 59	0.004 116 49
5	0.100 253 82	0.057 028 18
6	0.095 572 36	1.214 752 53
7	0.111 235 71	−0.000 054 74
8	0.138 198 13	0.000 050 03
9	0.076 482 35	0.001 054 30

TABLE III. Numerical coefficients of the recursive algorithm for $y=1.4$.

	$y=1.4$	
k	$d^{q,a}$	$d^{q,e}$
1	0.204 287 83	0.285 251 74
2	0.252 665 57	0.937 288 10
3	0.192 149 16	2.977 493 67
4	0.136 995 08	0.082 787 66
5	0.088 243 37	0.022 868 87
6	0.062 292 82	0.005 344 88
7	0.063 363 95	0.000 413 45

TABLE IV. Numerical coefficients of the recursive algorithm for $y = 1.7$.

$y = 1.7$		
k	$d^{q,a}$	$d^{q,e}$
1	0.027 180 97	0.007 319 30
2	0.236 869 00	0.795 357 20
3	0.569 258 93	3.089 802 85
4	0.112 460 54	0.232 596 81
5	0.027 115 23	0.060 155 48
6	0.027 115 23	0.060 155 48

[1] F. A. Duck, *Physical Properties of Tissue* (Academic, London, 1990).
[2] S. Ginter, M. Liebler, E. Steiger, T. Dreyer, and R. E. Riedlinger, ''Full wave modeling of therapeutic ultrasound: Nonlinear ultrasound propagation in ideal fluids,'' J. Acoust. Soc. Am. **111**(5), 2049–2059 (2002).
[3] A. I. Nachman, J. F. Smith, and R. C. Waag, ''An equation for acoustic propagation in inhomogeneous media with relaxation losses,'' J. Acoust. Soc. Am. **88**(3), 1584–1595 (1990).
[4] R. O. Cleveland, M. F. Hamilton, and D. T. Blackstock, ''Time-domain modeling of finite-amplitude sound beams in relaxing fluids,'' J. Acoust. Soc. Am. **99**(6), 3312–3318 (1996).
[5] X. Yuan, D. Borup, and J. Wiskin, ''Simulation of acoustic wave propagation in dispersive media with relaxation losses by using FDTD method with PML absorbing boundary condition,'' IEEE Trans. Ultrason. Ferroelectr. Freq. Control **46**(1), 14–23 (1999).
[6] J. Tavakkoli, D. Cathignol, and R. Souchon, ''Modeling of pulsed finite-amplitude focused sound beams in time domain,'' J. Acoust. Soc. Am. **104**(4), 2061–2072 (1998).
[7] R. J. Zemp, J. Tavakkoli, and R. S. C. Cobbold, ''Modeling of nonlinear ultrasound propagation in tissue from array transducers,'' J. Acoust. Soc. Am. **113**(1), 139–152 (2003).
[8] T. L. Szabo, ''Time domain wave equation for lossy media obeying a frequency power law,'' J. Acoust. Soc. Am. **96(1)**, 491–500 (1994).
[9] P. He, ''Simulation of ultrasound pulse propagation in lossy media obeying a frequency power law,'' IEEE Trans. Ultrason. Ferroelectr. Freq. Control **45**(1), 114–125 (1998).
[10] T. L. Szabo, ''Causal theories and data for acoustic attenuation obeying a frequency power law,'' J. Acoust. Soc. Am. **97**(1), 14–24 (1995).
[11] W. Chen and S. Holm, ''Modified Szabo's wave equation models for lossy media obeying frequency power law,'' J. Acoust. Soc. Am. **114**(5), 2570–2574 (2003).
[12] S. Ginter, ''Numerical simulation of ultrasound-thermotherapy combining nonlinear wave propagation with broadband soft-tissue absorption,'' Ultrasonics **37**, 693–696 (2000).
[13] G. V. Norton and J. C. Novarini, ''Including dispersion and attenuation in the time domain for wave propagation in isotropic media,'' J. Acoust. Soc. Am. **113**(6), 3024–3031 (2003).
[14] M. G. Wismer and R. Ludwig, ''An explicit numerical time domain formulation to simulate pulsed pressure waves in viscous fluids exhibiting arbitrary frequency power law attenuation,'' IEEE Trans. Ultrason. Ferroelectr. Freq. Control **42**(6), 1040–1049 (1995).
[15] A. D. Pierce, *Acoustics—An Introduction to its Physical Principles and Applications* (Acoustical Society of America, Woodbury, NY, 1991), Chap. 1.
[16] E. Skudrzyk, *The Foundations of Acoustics* (Springer, Wien, New York, 1971), Chap. 13.
[17] C. W. Horton, Sr., ''Dispersion relationships in sediments and sea water,'' J. Acoust. Soc. Am. **55**(3), 547–549 (1974).
[18] M. O'Donnell, E. T. Jaynes, and J. G. Miller, ''Kramers–Kronig relationship between ultrasonic attenuation and phase velocity,'' J. Acoust. Soc. Am. **69**(3), 696–701 (1981).
[19] P. He, ''Experimental verification of models for determining dispersion from attenuation,'' IEEE Trans. Ultrason. Ferroelectr. Freq. Control **46**(3), 706–714 (1999).
[20] M. J. Lighthill, *Einführung in die Theorie der Fourieranalysis und der verallgemeinerten Funktionen (An Introduction to Fourier Analysis and Generalised Functions)* (Bibliographisches Institut AG, Mannheim, 1966).
[21] K. B. Oldham and J. Spanier, *The Fractional Calculus* (Academic, New York, London, 1974).
[22] E. Steiger and S. Ginter, ''Numerical simulation of ultrasonic shock wave propagation in lossy liquids obeying a frequency power law,'' J. Acoust. Soc. Am. **105**(2), 1231 (1999).
[23] R. J. Luebbers and F. Hunsberger, ''FDTD for *N*th-order dispersive media,'' IEEE Trans. Antennas Propag. **40**(11), 1297–1301 (1992).
[24] W. Sachse and Y.-H. Pao, ''On the determination of phase and group velocities of dispersive waves in solids,'' J. Appl. Phys. **49**(8), 4320–4327 (1978).
[25] ICRU Report 61—''Tissue Substitutes, Phantoms and Computational Modeling in Medical Ultrasound,'' International Commission on Radiation Units and Measurements (ICRU), 1998.
[26] G. W. C. Kaye and T. H. Laby, *Tables of Physical and Chemical Constants*, 16th ed. (Longman Group, Harlow, UK, 1995).
[27] W. Eisenmenger, ''Fiber-optic probe hydrophone for ultrasonic and shock-wave measurements in water,'' Ultrasonics **31**, 267–273 (1993).
[28] R. Apfel, ''The effective nonlinearity parameter for immiscible liquid mixtures,'' J. Acoust. Soc. Am. **74**, 1866–1868 (1983).
[29] M. Liebler, S. Ginter, T. Dreyer, and R. Riedlinger, ''Simulation of enhanced absorption in ultrasound thermotherapy due to nonlinear effects,'' J. Acoust. Soc. Am. **109**(5), 2458 (2001).
[30] S. Ginter, *Selbstkonsistente Modellierung der Erhitzung von biologischem Gewebe durch hochintensiven Ultraschall (Self-consistent Modeling of Tissue Heating by High Intensity Ultrasound)*. Ph.D. thesis, Fakultät für Elektrotechnik und Informationstechnik der Universität Karlsruhe, 2002.
[31] M. Liebler, S. Ginter, T. Dreyer, and R. E. Riedlinger, ''Nonlinear FDTD-Modeling of Ultrasound Thermotherapy Including Temperature Dependent Tissue Parameters,'' in *Nonlinear Acoustics at the Beginning of the 21st Century*, ''Proceeding of the 16th Symposium on Nonlinear Acoustics, Moscow''Vol. 1, pp. 429–432, 2002.

Singly focused backscattering from small targets in an Airy caustic formed by a curved reflecting surface

Benjamin R. Dzikowicz[a] and Philip L. Marston
Department of Physics, Washington State University, Pullman, Washington 99164-2814

(Received 17 March 2004; recised 19 August 2004; accepted 22 August 2004)

When sound scatters off a curved-reflecting surface such as the ocean floor or surface, it can focus forming caustics in the water column. The simplest caustic is an Airy caustic formed by the merging of two rays. In a backscattering experiment with a target residing at or near an Airy caustic, a signal can be focused on the way to the target, upon return from the target, or in both directions. To investigate these processes, an experiment is conducted in which an Airy caustic is formed using a cylindrical half-pipe reflector. The backscattered echo focused only once, either to or from a spherical target, is examined here. These focused echoes can be significantly stronger than the simple direct echo. Approximations are examined where the echo amplitude changes with target position in proportion to an Airy function. The argument of the Airy function is calculated using the relative echo times of transient pulses. This result is extended by applying the uniform approximation method of Chester, Friedman, and Ursell. © *2004 Acoustical Society of America.*
[DOI: 10.1121/1.1805143]

PACS numbers: 43.20.El, 43.30.Gv, 43.20.Dk [JJM] Pages: 2751–2758

I. INTRODUCTION

Curved reflecting surfaces can reflect sound in such a way as to form caustics in the body of a fluid such as the ocean. Sound backscattered from targets lying near these caustics can show enhancements from echoes, which can be in excess of a direct echo that does not reflect from the aforementioned curved surface. When a target resides near the caustic in the insonified region it is expected to scatter much more sound than a target in a shadow region. Prior research associated with sound reflected from curved surfaces in water has typically emphasized the classification and parametrization of the caustics and associated wave fields[1–3] and the statistical properties of the intensity fluctuations.[4,5] The branch of singularity theory commonly known as catastrophe theory provides a framework for classifying and parametrizing the wave fields.[6–9] Caustics are also produced by refraction and reflection of sound associated with long-range propagation, and catastrophe theory has been successfully applied to those situations. Though in some situations the reverberation from these reflecting surfaces may be considered noise or interference, these reflections can be used to enhance the amplitude of the backscattering.

The goal of the present research is to extend the understanding of the aforementioned echo enhancement associated with placing a small target at (or close to) the bright region of a caustic wave field. For mathematical and experimental simplicity a circular, cylindrical half-pipe is chosen as a reflecting surface. The first step in the study of this problem will be to look at the ray picture of our simple system. A source located at one end of the half-pipe in the position shown in Fig. 1 gives rise to the caustic shown in that figure. (Note that the caustic is actually a surface extended from the line shown in the Z direction; only a slice of the surface in the $X-Y$ plane of P is shown.) At position P, on the illuminated side of the caustic, two rays reflect off the surface between the source and position P. Also shown is the direct ray that does not reflect off the surface but goes directly between the source and point P. If point P is moved closer to the caustic the two reflected rays move closer to each other, finally merging when point P is at the caustic, where they are the same length. With P on the other side of the caustic, the shadow region, there are no reflected rays connecting the source and P. The caustic formed by this type of ray merging is a fold or Airy caustic.[6–10] It is modeled using a cubic distance function to describe the incoming wave front.[7–11] For additional background information on reflections from concave cylindrical surfaces, some research related to microwaves is helpful.[12]

In this study, referring to Fig. 1, a target is placed at point P and echoes back to the source/receiver are measured. The target begins in the shadow region and moves to the illuminated region. Figure 2 shows the target (open circle) moving across the caustic formed by the source (closed circle). The signal coming from the target then forms a caustic at the source/receiver; this is also shown in Fig. 2. The caustic moves in the direction indicated by the arrow. Due to reciprocity, the target crosses the source's caustic at the same position that the target's caustic crosses the receiver. Thus, focusing in both directions can be important. The rays going between the source/receiver and a point target when the target is in the illuminated region are classified as follows.

(1) *Direct ray*. This is the trivial ray that passes directly from the source/receiver to the target and back without striking the surface.
(2) *Single bounce rays (SB)*. Four rays strike the surface only one time on their round-trip. Two of these strike the surface in the following order: source–surface–target–

[a]Now with: NSWC, Panama City, Code R-21, 110 Vernon Ave., Panama City, FL 32407; electronic mail: benjamin.dzikowicz@navy.mil

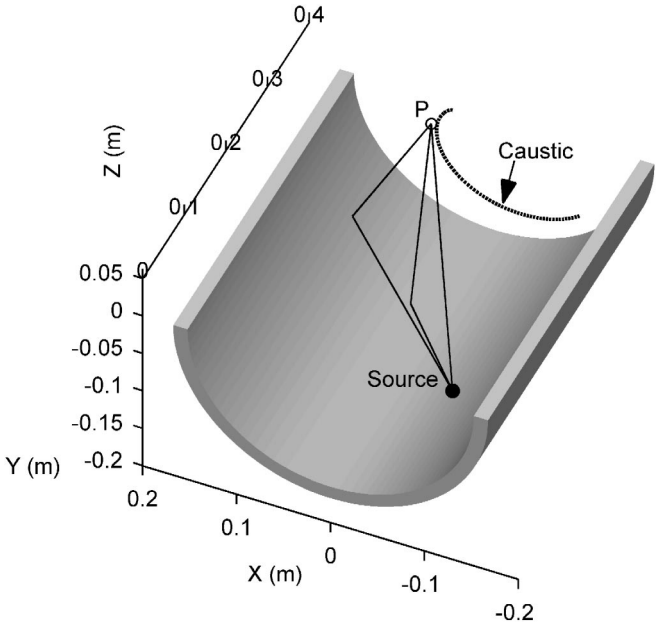

FIG. 1. An acoustic source in the presence of a cylindrical half-pipe reflecting surface. The point P lies on the illuminated side of the caustic. For P to the right of the caustic there are no reflected rays from the source.

receiver. The reverse of these paths are also valid rays, source–target–surface–receiver. This gives two pairs of degenerate rays.

(3) *Double bounce rays (DB).* There are also four rays striking the surface both to and from the target. Two of these strike the same location in each direction. The other two rays are degenerate and strike the curved surface at different locations each way.

When the target moves across the caustic the SB rays are singly focused and the DB rays focused twice. This paper concerns itself with the first case, the merging of the SB rays. It is important to note that the actual target is not a point but a finite sphere. A numerical model was developed to show that the SB merging takes place regardless of the size of the target. The rays simply merge also on the surface of the target. The effect of target size on the DB rays is more complicated,[13] and will be the subject of a different paper.

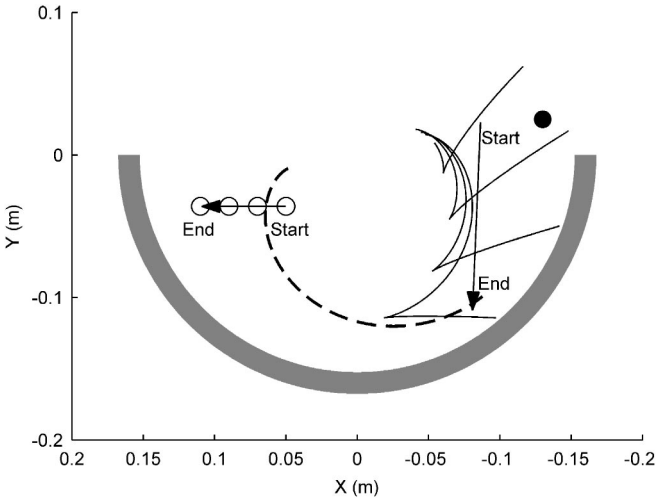

FIG. 2. This projection down the axis of the half-pipe shows the reciprocity of the caustics. As the target (open circle) moves to the left across the caustic formed by the source (dashed line), the caustic reflected back by the target (solid line) moves across the source (closed circle).

II. THEORY

In order to find the pressure at the receiver due to the merging of the returning rays, the following expression is used:

$$p(0,0,z) \approx \frac{ik}{2\pi z} \int_{-\infty}^{\infty} \int_{-\infty}^{\infty} A(x,y) e^{ik\phi(x,y)} dx dy. \tag{1}$$

This is a special case for a fixed receiver location of a general form given in the literature.[8] Throughout the paper, lowercase letters will be used to describe the Cartesian coordinates of a wave field, whereas the capital letters, X, Y, and Z, will be used to denote the Cartesian coordinates of the target. The convention $e^{-i\omega t}$ describing the time dependence is omitted. The field point at the receiver is chosen on the z axis. It is illuminated in the far field by an incoming wave that can be attributed to a virtual wave front defined by a distance function $\phi(x,y)$ and amplitude $A(x,y)$. The wave front is described as virtual since it is located beyond the curved reflecting surface and serves as a model for the real system. The function ϕ (sometimes described as the generating function) gives the distance from the receiver at $(X,Y,Z)=(0,0,Z)$ to a point on the wave front in some reference frame. Equation (1) is used to calculate the backscattered echo and this paper concerns itself with finding $\phi(x,y)$ and $A(x,y)$ for the merging of SB rays and comparing predictions based on Eq. (1) to experimental results. These functions also depend on the target coordinates X, Y, and Z.

Since the rays returning to the receiver number zero, two, or (exactly on the caustic) one, as the target is scanned through an Airy caustic, the simplest distance function describing the correct properties and parameters is

$$\phi(x,y) = \gamma x^3 + \alpha x + \beta y^2 + z_0. \tag{2}$$

Including a term linear in y does not alter the conclusions of the essential analysis. Figure 22 of Ref. 8 shows a section of the associated wave front. Making the substitutions $s=(3\gamma k)^{1/3}x$ and $w=-\alpha k^{2/3}(3\gamma)^{-1/3}$, separating variables and solving the integrals using standard solutions one is left with the form[8]

$$p(Q) \approx \frac{i\pi^{1/2}k^{1/6}p_0}{z_0(3\gamma)^{1/3}\beta^{1/2}} \exp\left[i\left(kz_0 + \frac{\pi}{4}\right)\right] \mathrm{Ai}(-w), \tag{3}$$

for the pressure of the receiver where the Airy function is defined as

$$\mathrm{Ai}(-w) = \frac{1}{2\pi} \int_{-\infty}^{\infty} \exp\left[i\left(\frac{s^3}{3} - ws\right)\right] ds. \tag{4}$$

The positions of the source/receiver and the target are indicated by the symbol Q. In the two-ray region w is positive. For this first approximation, it is assumed that the amplitude does not vary significantly over the wave front, thus $A(x,y)=p_0$.

A numerical ray finding algorithm is developed to find the exact location of each of the rays described in the introduction. From this model, the return times for pulses traveling along each of the rays can be found. The difference between the two return times associated with the SB rays can be used to calculate w in the illuminated region as follows. First, the stationary points are found by setting the derivative of $\phi(x,y)$ to 0,

$$\frac{d\phi}{dx}=3\gamma x^2-k^{-2/3}(3\gamma)^{1/3}w=0, \quad \frac{d\phi}{dy}=2\beta y=0, \tag{5}$$

giving

$$x_{\pm}=\pm(3k\gamma)^{-1/3}\sqrt{w}, \quad y_{\pm}=0 \tag{6}$$

for the locations of the stationary points. Then $x_{\pm}$ and $y_{\pm}$ can be put into Eq. (2) to give the distance function evaluated for the two rays. The difference between these distance functions may be given by the arrival time difference $\Delta t=[\phi(x_+,0)-\phi(x_-,0)]/c$, which may be used to express Airy argument $-w$,

$$w=(\tfrac{3}{4}\omega\Delta t)^{2/3}, \tag{7}$$

and hence a final solution for the form of the pressure is found by putting this into Eq. (3)

$$p(Q)\approx-\frac{i\pi^{1/2}k^{1/6}p_0}{z_0(3\gamma)^{1/3}\beta^{1/2}}\exp\left[i\left(kz_0+\frac{\pi}{4}\right)\right] \times \mathrm{Ai}\left(-\left(\frac{3}{4}\omega\Delta t\right)^{2/3}\right). \tag{8}$$

The coefficients γ and β affect the magnitude of the returns but their explicit determination is not central to the discussion that follows. The experiment described in the following section only gives the relative magnitude of the pressure. Thus, for comparison it is more helpful to write:

$$|p_{\mathrm{SB}}(Q)|=S\omega^{1/6}|\mathrm{Ai}(-(\tfrac{3}{4}\omega\Delta t)^{2/3})|. \tag{9}$$

Written in this form the frequency dependence is retained and the coefficient S found experimentally. S is in units of pressure$\times$time$^{1/6}$. The argument of the Airy function has been explained in terms of a time difference by various other researchers in acoustics.[14] This is the first approximation giving the pressure of the backscattered signal at the transducer for a point target moving through an Airy caustic. An improved approximation will now be described.

One of the approximations made in the previous argument was that the amplitude $A(x,y)$ has the same magnitude across the whole virtual wave front for all target positions. This approximation is needed if only the location of the stationary points is known. However, other information can be gleaned by numerical ray finding. The angle that the incoming (or outgoing) rays make as the target changes position can also be recovered using this technique. These are related to the geometrically determined ''classical'' scattering amplitude. As shown in the Appendix, this is proportional to

$$\rho=\left|\left(\frac{d\theta}{dX}\right)\right|^{1/2}, \tag{10}$$

where $d\theta$ is the change in return angle of a returning ray to the transducer resulting from the change, dX, in target position, (X,Y,Z), with respect to the fixed frame of the reflecting surface. The incoming ray angle, θ, is the angle measured between the direct ray and the SB ray. Since there are two SB rays, there will be two angles denoted θ_+ and θ_-. This measure of the ray density is proportional to the amplitude associated with the returning rays, *not* to the amplitude at the virtual wave front.

For two ray merging, the solution sought here always reduces to solving a diffraction integral of the form:

$$I=\int_{-\infty}^{\infty}A(u)\exp\left[i\left(\frac{u^3}{3}-wu\right)\right]du, \tag{11}$$

with stationary points at $u_{\pm}=\pm\sqrt{w}$. An approximation of the cubic wave term by taking a Taylor expansion about the two stationary points and keeping up to the quadratic term can be made. Then along with a linear expansion of wave front amplitude the integral can be written revealing the two incoming rays. This result is from Conner and Marcus[15] and is valid for large positive w,

$$I\approx A(u_+)\pi^{1/2}w^{-1/4}\exp\left[i\left(-\frac{2}{3}w^{3/2}+\frac{\pi}{4}\right)\right] +A(u_-)\pi^{1/2}w^{-1/4}\exp\left[i\left(\frac{2}{3}w^{3/2}-\frac{\pi}{4}\right)\right]. \tag{12}$$

Here $A(u_{\pm})$ is the virtual wave front amplitude at each of the stationary points. For large w ray contributions are separately expressed. Thus, the classical amplitude returning to the target can be identified in Eq. (12) as

$$\rho_{\pm}=\left|\left(\frac{d\theta_{\pm}}{dX}\right)\right|^{1/2}\propto w^{-1/4}A(u_{\pm}). \tag{13}$$

This gives the integral I with the following proportionality,

$$I\propto\rho_+\exp\left[i\left(-\frac{2}{3}w^{3/2}+\frac{\pi}{4}\right)\right]+\rho_-\exp\left[i\left(\frac{2}{3}w^{3/.2}-\frac{\pi}{4}\right)\right]. \tag{14}$$

As mentioned earlier these amplitudes will diverge at the caustic so a better approximation must be utilized, one which will not diverge at the caustic.

By using the complete form of the phase and a linear expansion of wave front amplitude Conner[15] uses the method of Chester *et al.*[16] to give a uniform approximation of the integral in Eq. (11):

$$I\approx\pi(A(u_+)w^{-1/4}+A(u_-)w^{-1/4})w^{1/4}\mathrm{Ai}(-w) -i\pi(A(u_+)w^{-1/4}-A(u_-)w^{-1/4})w^{-1/4}\mathrm{Ai}'(-w). \tag{15}$$

The derivative of the Airy function is defined

$$2\pi\mathrm{Ai}'(q)=i\int_{-\infty}^{\infty}s\exp\left[i\left(\frac{s^3}{3}+qs\right)\right]ds. \tag{16}$$

According to Connor[15] the approximation of Eq. (15) is exact if $A(u)$ is a linear function of u, which is not necessarily the case in the present application. In addition, the

form of the phase does not need to be exactly cubic to use this approximation, but it needs two roots and must go over to a cubic function for small argument. For discussion of an alternative approach, see Ludwig.[17]

In the present application, the relation in Eq. (13) can be used to rewrite Eq. (15) as follows:

$$I \propto \pi(\rho_+ + \rho_-) w^{1/4} \mathrm{Ai}(-w) - i\pi(\rho_+ - \rho_-) w^{-1/4} \mathrm{Ai}'(-w). \tag{17}$$

Finally, rewriting Eq. (9) in a more refined way:

$$|p_{\mathrm{SB}}(Q)| = S' \omega^{1/6} \left| \begin{array}{l} \left[\left| \left(\frac{d\theta_+}{dX} \right) \right|^{1/2} + \left| \left(\frac{d\theta_-}{dX} \right) \right|^{1/2} \right] \left(\frac{3}{4} \omega \Delta t \right)^{1/6} \mathrm{Ai}\left[-\left(\frac{3}{4} \omega \Delta t \right)^{2/3} \right] \\ -i \left[\left| \left(\frac{d\theta_+}{dX} \right) \right|^{1/2} - \left| \left(\frac{d\theta_-}{dX} \right) \right|^{1/2} \right] \left(\frac{3}{4} \omega \Delta t \right)^{-1/6} \mathrm{Ai}'\left[-\left(\frac{3}{4} \omega \Delta t \right)^{2/3} \right] \end{array} \right| \tag{18}$$

using Eq. (17) and Eq. (13). Here, S' is a different coefficient from S in Eq. (9) since the classical amplitude is specified to a multiplicative constant in that result. The coefficient S' has the units pressure$\times$time$^{1/6}\times$(distance/radians)$^{1/2}$ to account for the units of the derivatives. The form in Eq. (18) is the same as was found by Berry[18,19] by studying two-ray merging from a cylindrical wave front using purely geometric arguments. An important test of this method lies in the limits at the caustic. Each of the combined prefactors must be smooth, nonzero, and finite at the caustic. Each of these prefactors as well as the diverging classical ray amplitude is plotted for the smaller of the two target sizes in the experiment using the numerical estimates of $|(d\theta_\pm/dX)|^{1/2}$ in Fig. 3. The required ray angles, θ_+ and θ_-, along with their evolution with target location X, were determined using a ray tracing algorithm.[13]

It is important to note that although these results were derived considering the merging of SB rays returning from a point target in an Airy field, they can be applied to finite, smooth reflecting targets where the rays merge in a such a way that α, β, and z_0 vary little throughout the target positions of interest. Expressions formally similar to Eq. (18) were given by Tindle for a different problem in underwater acoustics.[14]

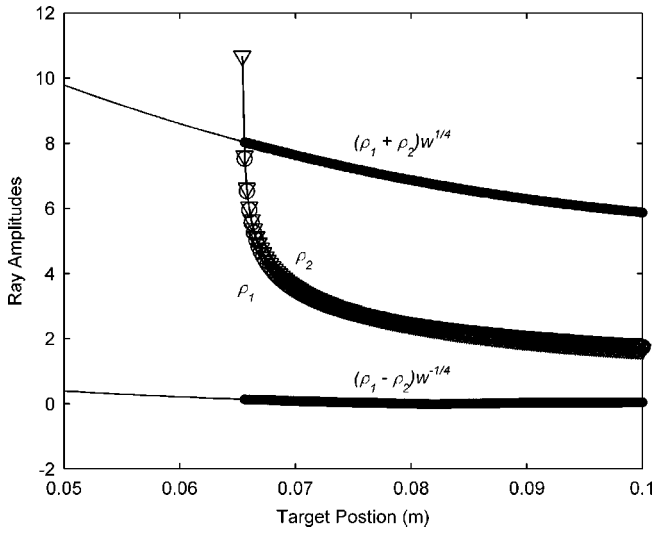

FIG. 3. A plot of the normalized classical ray amplitude ($\rho_\pm$) from Eq. (10) demonstrates their divergence. These are plotted as open squares and triangles and a polynomial fit appears as a solid line. However, the coefficients of Eq. (17), which are also plotted here as solid points (so close they appear as a thick line), are finite at the caustic and their fit moves smoothly into the two ray region. The data are taken from the numerical ray finding technique for the 9.95 mm radius target.

III. EXPERIMENTS

In order to create an Airy caustic a cylindrical half-pipe with a radius of 0.1524 m is used. The geometry is shown in Fig. 1. All the reflectors (the target and the surface) are made of closed-cell Styrofoam and are submerged in an 8-ft-diam water tank. This allows the approximation of reflections as perfectly soft. At one end of the foam, the composite transducer is aimed down the half-pipe approximately between the target and the expected direction of the returns. At the other end (approximately 0.34 m away) is a spherical target with a radius of $a=0.009\,95$ m. This gives $ka=10.55$ using the tone burst frequency of 250 kHz. These values put the target in a regime where the scattering is nearly isotropic in the backward hemisphere.[20] There is also a large forward scattering peak in both these cases but this is not of concern since the signal passes down the length of the half-pipe. The isotropic scattering, in all but the forward scattering direction, is important to simplify the classical ray amplitude as described in Sec. II. Even with the careful choice of targets, there is a creeping wave running around the back of the target causing a second, later signal.[21] Simple experiments with the transducer and targets used here confirm that these creeping wave contributions are small and are neglected in the discussions to follow.

The target is positioned in a plane perpendicular to the axis of the half-pipe using a mechanical positioning system. The source lies at $(-0.130, 0.032, 0)$ m and the target at $(X, -0.042, 0.275)$ m with the whole of the half-pipe lying below $Y=0$ and the Z axis running down the center of the cylinder. The target moves on a horizontal line as shown in Fig. 2. Data are taken at a position X and then the target is moved to a new position, $X+\delta$, and repeated until all the data points are collected. For the data shown here the target is moved from $X=0.0500$ m to $X=0.1000$ m with steps of

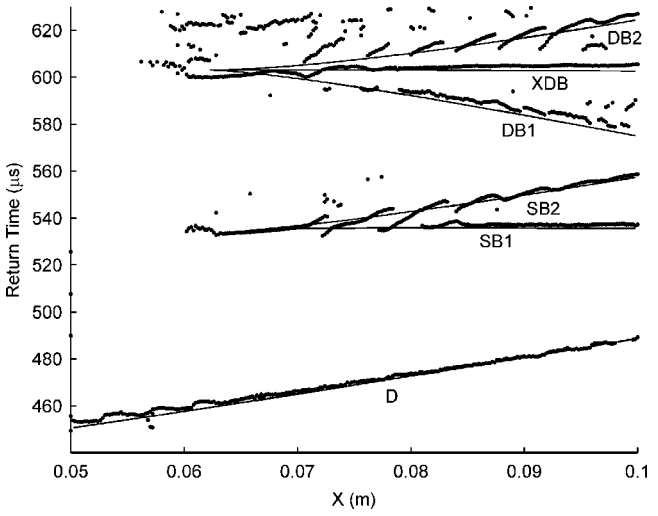

FIG. 4. Round trip return times for a short pulse plotted with respect to the target position as it moves across the caustic. The solid lines are the calculated return times using a numerical ray finding technique. Each of the different types of returns is labeled: the lone direct return (D), two single bounce (SB) returns, and the double bounce returns (DB and XDB). The target radius was 9.95 mm.

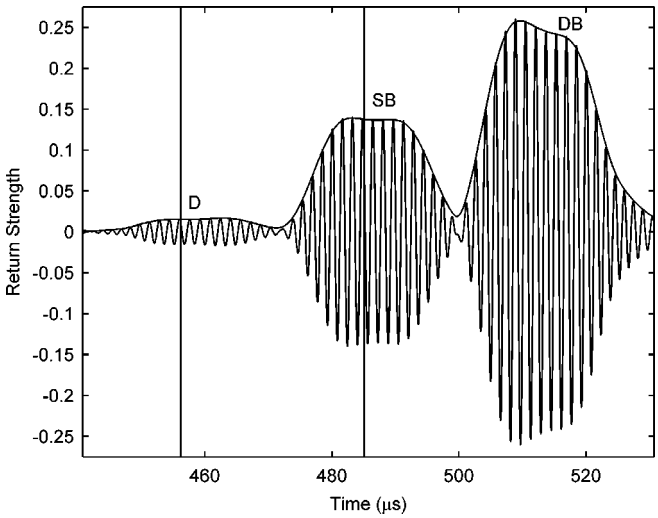

FIG. 5. A typical backscattered return with the target near the caustic. Each of the three types of return can be seen. The direct reflection (D), the singly focused returns (SB), and the doubly focused returns (DB) can be seen. Each focusing gives a greater return than the one before it. The Hilbert transform is used to find the envelope of the return also plotted here. The target radius was 9.95 mm and $ka=10.55$.

$\delta=0.0002$ m crossing from the zero-ray to the two-ray region in the process.

A straightforward send–receive trigger system is used. First, a pulse generator puts a Send–Receive Switch (RITEC clamped diplexer) into its send mode. Then, after a delay of 20 μs set by a digital delay generator, the transient pulse or tone burst is sent toward the transducer. The form of the outgoing signal is programmed into a function generator. On its way, it is amplified to about 185 V peak. The signal then passes through a diode circuit to prevent noise from the amplifier from interfering with the return signal. The function generator also triggers the oscilloscope as it releases its signal. The oscilloscope is set with a delay to crop out the signal until the returns of interest appear.

After reflecting off the target and surfaces, the backscattered signal returns to the transducer. By now, the transducer has been switched to receive mode by the rising end of the pulse from the pulse generator. A preamplifier amplifies the signal before passing it though an analog bandpass filter. The oscilloscope then records the signal at a sampling rate of 100 MHz. The data are then collected and recorded on a computer. After data collection, the signals are high and low pass filtered and the envelope amplitudes determined from the magnitude of the analytic signal constructed using the Hilbert transform.[13]

Since it is difficult to determine the exact position of the target and source/receiver in the water tank, a short transient pulse is used to determine return times of the echoes described in Sec. I. A Gaussian envelope burst of six cycles (the Gaussian is truncated at 5% of maximum amplitude) at 400 kHz is used. The return times for the peak transient echo are then matched to the return times calculated by the numerical ray technique. This is shown in Fig. 4. The surface, target, and source/receiver locations are adjusted in the numeric ray finding technique to optimize the agreement in the figure giving the locations previously noted. Although the DB merging is also shown, this paper only deals with the merging of the SB rays. Some imperfections evident in the comparisons are associated with the difficulty of automatically determining the peaks of the envelope in a superposition of closely spaced signals.[13] The extracted position of a peak is occasionally offset from the relevant arrival time as evident from some of the DB data. Once the numerical time differences and the angular changes are known from the model they are put into Eq. (18) to find the steady state amplitude.

To avoid interference with the returning direct and DB returns a steady state signal cannot be used to verify Eq. (18). Instead, a 70 μs tone burst at 250 kHz is smoothed with 25 μs rise and fall tails on either end is used. A tone burst of this length is long enough for the SB returns to overlap, but not too long to interfere with the DB or direct returns in most cases.[13] The tails are cosine-squared functions giving a true center width of 20 μs and an effective center width of 34.3 μs (the effective center width being the width where the amplitude of the envelope is greater than 90% of maximum). The amplitude of the SB focused returns is taken at the average time of the two SB return times from the numerical model.

IV. RESULTS AND DISCUSSION

Figure 5 shows the signal return of the tone burst when the target is near the caustic. The enhancement due to the focusing can clearly be seen. The singly focused return is larger than that of the direct return and the doubly focused return is even greater. The lines indicate the time where the amplitude was recorded. Plotting the measured amplitudes against the results of Eq. (18) is shown in Fig. 6. The result, Eq. (9), without the wave front amplitude correction is also shown; it also agrees with the measurements, but not as well as the complete solution. The Δt in Eqs. (9) and (18) was given by time differences between the predicted SB times in

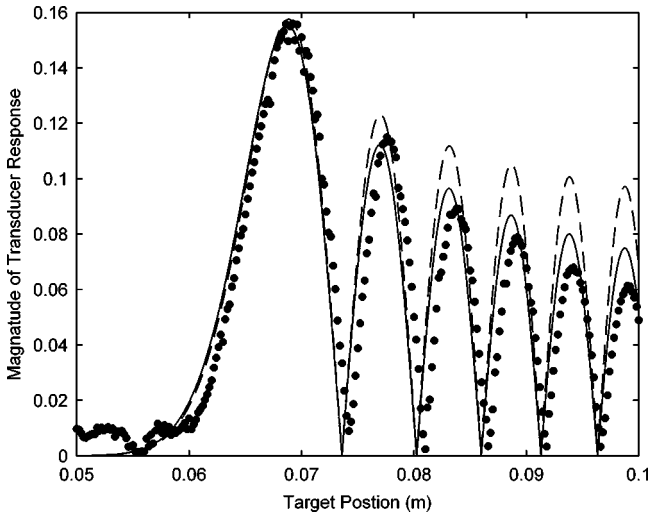

FIG. 6. The magnitudes of the center of the singly focused returns are shown for different target positions of a small target ($ka \approx 10.5$ and radius, 9.95 mm). The dashed line is the Airy fit from Eq. (9) and the solid line is the refinement from Eq. (18).

Fig. 4. The constant S in Eq. (9) was selected independently from S' in Eq. (18). When the target is in the shadow region of the Airy caustic, the arguments of $\mathrm{Ai}(w)$ and $\mathrm{Ai}'(w)$ in Eqs. (8) and (9) are extrapolated from the values in the illuminated region. A simple least-squares cubic polynomial fit is used. It is also necessary to use smooth extrapolations of the combined amplitude prefactors for the $\mathrm{Ai}(w)$ and $\mathrm{Ai}'(w)$ terms in Eq. (18). These are plotted in Fig. 3 and are given by polynomial fits.[13]

Figure 7 shows the result with a larger target (radius 0.030 m) and the theory matches here as well. For the large target experiment, the target is located at $(X, -0.036, 0.409)$ m and the source at $(-0.13, 0.025, 0)$ m. The target moves from $X=0.05$ to 0.11 m. The anomalous variation of the amplitude visible in the right near $X=0.109$ m is a consequence of a small amount of overlap with the double bounce echo specific to this target location.[13] Inspection of Figs. 6

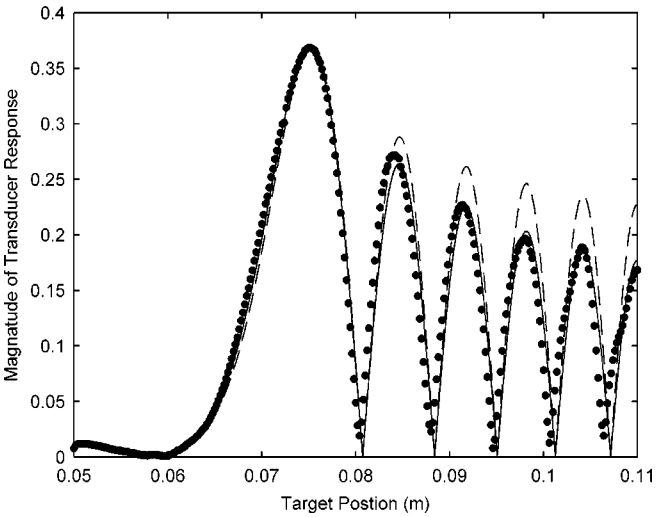

FIG. 7. The magnitudes of the center of the singly focused returns are shown for different target positions of a large target ($ka \approx 30$ and radius, 30 mm). The dashed line is the Airy fit from Eq. (9) and the solid line is the refinement from Eq. (18).

and 7 indicates that the model given by the solid curves from Eq. (18) is a significant improvement relative to the elementary Airy function model given by Eq. (9). This improvement is also evident in several other measurements obtained with the small target between 200 and 300 kHz.[13]

The method presented in this paper for analyzing the magnitudes of the backscattering of a target in a caustic field can be thought of as a blueprint for approaching and considering related problems. One can envision finding the echo amplitudes for targets passing through different types of caustic fields as well as focusing due to refraction due to sound speed variations. Although these types of wave fields have been characterized,[10,11,14] evidently less is known about the scattering by targets near the caustics. The models given here have a versatility that goes beyond locating a spherical target in a cylindrical half-pipe. The most direct application pertains to the evolution of echo amplitude near Airy caustics.

The qualitative results are also important: the simple enhancement of the backscattering when the target is on the caustic and the simple echo time relationships. Imagine a spherical source/receiver searching for a target in the presence of a rippled surface. The target would move in and out of caustic regions and thus the returns would focus and defocus. With knowledge of the simple time relationships between the direct echo and the single and double bounce echo times, one could confirm a target with more confidence than simply a direct echo from the target by applying the approximation in Eq. (9).

ACKNOWLEDGMENT

This work was supported by the Office of Naval Research.

APPENDIX: GEOMETRIC AMPLITUDE FACTOR

What follows is a summary of the derivation of the amplitude-scaling factor ρ in Eq. (10). For this derivation, reflectors in the system (including the target) are assumed to have isotropic reflection coefficients that do not depend on the angle of incidence. If this is true, conservation of energy and geometric arguments can be used. It is sufficient to consider two-dimensional propagation because the specific value of the coefficient β in Eq. (2) was not important in the analysis. A receiver is located a distance r from a virtual wave front, $W(x,\xi)$, which has a local radius of curvature r_0 at the stationary point. Here ξ is a parameter that affects the wave front shape. In the present application, this is the target position. By conservation of energy, the power through a small section $ds = r_0 d\psi$ of wave front at the stationary point is the same as the power after spreading to the receiver, where $ds' = (r + r_0) d\psi$. Thus, the spreading in two dimensions gives intensity with the following proportionality:

$$I \propto \frac{ds}{ds'} \propto \frac{r_0}{r_0 + r} \approx \frac{r_0}{r}, \tag{A1}$$

where the last approximation comes from the receiver being far from the wave front or $r \gg r_0$. Calculating the curvature,

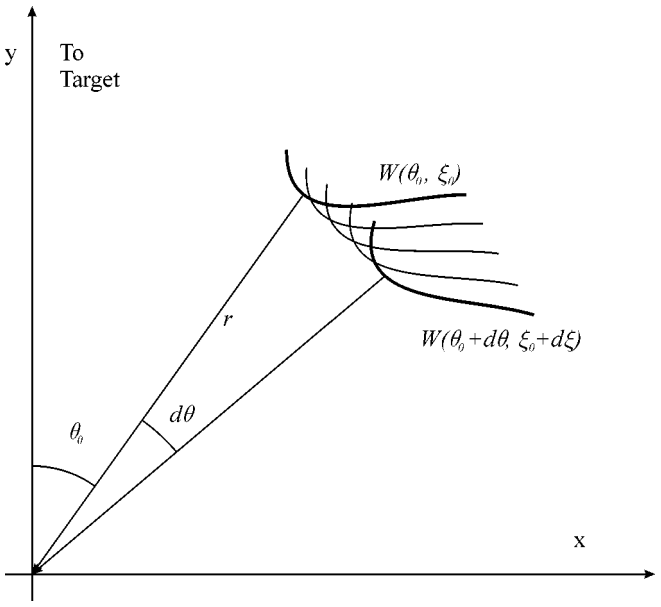

FIG. 8. This diagram shows the change in direction of a ray as the parameter ξ varies the virtual wave front.

$$\frac{1}{r_0} = \frac{W_{xx}}{(1+W_x^2)^{3/2}} = W_{xx}. \tag{A2}$$

W_x indicates the partial derivative of W with respect to x. At the stationary point, the first derivative with respect to x vanishes. The proportionality $I \propto |W_{xx}|^{-1}$ follows from Eq. (A1). To find W_{xx}, expand $W(x=0,\xi=\xi_0)$ in a Taylor series about $x=0$ and $\xi=\xi_0$. Since the ray meets the wave front perpendicularly, the Taylor expansion contains no linear term in x,

$$W(x,\xi) \approx r + W_\xi(\xi-\xi_0) + \frac{W_{\xi\xi}}{2}(\xi-\xi_0)^2 + \frac{W_{xx}}{2}(x)^2 + W_{x\xi}(x)(\xi-\xi_0) + \cdots. \tag{A3}$$

Then when $\xi=\xi_0$ there is a stationary point at $x=0$. When ξ is shifted from ξ_0 (as when the target position is shifted), the derivative, which must vanish for the ray condition, becomes

$$\frac{\partial W}{\partial x} = xW_{xx} + W_{x\xi}(\xi-\xi_0). \tag{A4}$$

For small deviations from $x=0$ and ξ_0, this becomes

$$W_{xx}dx + W_{x\xi}d\xi = 0. \tag{A5}$$

Giving, for W_{xx},

$$\frac{1}{W_{xx}} = -\frac{1}{W_{x\xi}}\left(\frac{dx}{d\xi}\right). \tag{A6}$$

Then Eqs. (19) and (20) give the following proportionality:

$$I \propto \frac{1}{r|W_{x\xi}|}\left|\left(\frac{dx}{d\xi}\right)\right|. \tag{A7}$$

It is helpful to introduce polar coordinates since the ray angles can be more easily specified. Let $x=r\sin\theta$ and $dx = r\cos\theta_0 d\theta + \sin\theta_0 dr$ where θ_0 is the angle from the y axis as shown in Fig. 8. Now the derivative is rewritten,

$$\left(\frac{dx}{d\xi}\right) = r\cos\theta_0\left(\frac{d\theta}{d\xi}\right) + \sin\theta_0\left(\frac{dr}{d\xi}\right). \tag{A8}$$

The radial derivative may be eliminated by selecting a coordinate system such that for a given ray $\sin\theta_0=0$. This leaves, once substituting into Eq. (25),

$$I \propto \frac{1}{|W_{x\xi}|}\left|\left(\frac{d\theta}{d\xi}\right)\right|. \tag{A9}$$

Finally, since the ray amplitude is proportional to the root of the intensity I, the desired property in Eq. (10) is found. Here the parameter ξ is taken to be the location of the target, X. When the curvature of the virtual wave front vanishes at a caustic, then $dx/d\xi$ in Eq. (A6) diverges and $d\theta/d\xi$ diverges, which becomes $d\theta/dX$ in the notation of Eq. (10). The other factor, $|W_{x\xi}|^{-1}$ in Eq. (A9) depends relativity weakly on the target position and is taken as constant.

[1] K. L. Williams, J. S. Stroud, and P. L. Marston, "High-frequency forward scattering from Gaussian spectrum, pressure release, corrugated surfaces. I. Catastrophe theory modeling," J. Acoust. Soc. Am. **96**, 1687–1702 (1994).

[2] C. K. Frederickson and P. L. Marston, "Transverse cusp diffraction catastrophes produced by the reflection of ultrasonic tone bursts from a curved surface in water: Observations," J. Acoust. Soc. Am. **92**, 2869–2877 (1992).

[3] C. K. Frederickson and P. L. Marston, "Travel time surface of a transverse cusp caustic produced by reflection of acoustical transients from a curved metal surface in water," J. Acoust. Soc. Am. **95**, 560–660 (1994).

[4] J. S. Stroud, "Twinkling of underwater sound reflected by one realization from a Gaussian spectrum population of corrugated surfaces: Experiments and comparisons with a catastrophe theory approximation," Ph.D. dissertation—Washington State University, 1995.

[5] J. S. Stroud, P. L. Marston, and K. L. Williams, "Intensity moments of underwater sound scattered by a Gaussian spectrum corrugated surface: Measurements and comparison with a catastrophe theory approximation," Proceedings from NATO SCLANTCEN, edited by N. G. Pace, E. Pouliquen, and O. Bergem, Lerici, Italy, 30 June–4 July 1997, pp. 535–1997.

[6] R. Thom, *Structural Stability and Morphogenesis* (*Benjamin/Cummings*, 1975).

[7] M. V. Berry, "Waves and Thom's Theorm," Adv. Phys. **25**, 1–26 (1976).

[8] P. L. Marston, "Geometrical and catastrophe optics methods in scattering," in *High Frequency and Pulse Scattering, Physical Acoustics*, edited by R. N. Thurston and A. D. Pierce (Academic, Boston, 1992), pp. 1–234.

[9] J. F. Nye, *Natural Focusing and Fine Structure of Light; Caustics and Wave Dislocations*, (IOP Bristol, 1999).

[10] M. G. Brown, "The transient wave fields in the vicinity of the cuspoid caustics," J. Acoust. Soc. Am. **79**, 1367–1384 (1986).

[11] M. G. Brown and F. D. Tappert, "Catastrophe theory, caustics and traveltime diagrams in seismology," Geophys. J. R. Astron. Soc. **88**, 217–229 (1987).

[12] E. D. Constantinides and R. J. Marhefka, "Plane Wave Scattering from 2-D Perfectly Conducting Superquadratic Cylinders," Trans. Antennas and Propagation **39**, 367–376 (1991).

[13] B. Dzikowicz, "Backscattering of sound from targets in an Airy caustic formed by a curved reflecting surface," Ph.D. dissertation—Washington State University, 2003.

[14] C. T. Tindle, "Wavefronts and waveforms in deep-water sound propagation," J. Acoust. Soc. Am. **112**, 464–475 (2002).

[15] J. N. L. Conner and R. A. Marcus, "Theory of Semiclassical Transition Probabilities for Inelastic and Reactive Collisions. II Asymptotic Evaluation of the S Matrix," J. Chem. Phys. **55**, 5636–5643 (1971).

[16] C. Chester, B. Friedman, and F. Ursell, "An extension of the method of steepest descent," Proc. Cambridge Philos. Soc. **54**, 533–370 (1957).

[17] D. Ludwig, "Uniform asymptotic expansions for wave propagation and

diffraction problems,'' SIAM Rev. **12**, 325–331 (1970).
[18] M. V. Berry, ''Uniform approximation for potential scattering involving a rainbow,'' Proc. Phys. Soc. London **89**, 479–490 (1966).
[19] M. V. Berry, ''Uniform approximation: A new concept in wave theory,'' S. Prog. Oxf. **57**, 43–64 (1969).
[20] J. J. Bowman, T. B. A. Senior, and P. L. E. Uslenghi, *Electromagnetic and Acoustic Scattering by Shapes* (North-Holland Publishing Company, Amsterdam, 1969), pp. 358–359.
[21] A. J. Rudgers, ''Acoustic Pulses Scattered by a Rigid Sphere Immersed in a Fluid,'' J. Acoust. Soc. Am. **45**, 900–910 (1969).

Propagation of sound in long enclosures

K. M. Li[a] and K. K. Iu
Department of Mechanical Engineering, The Hong Kong Polytechnic University, Hung Hom, Hong Kong

(Received 21 February 2004; revised 22 July 2004; accepted 4 August 2004)

The propagation of sound in long enclosures is addressed theoretically and experimentally. In many previous studies, the image source method is frequently used. However, these early theoretical models are somewhat inadequate because the effect of multiple reflections in long enclosures is often modeled by the incoherent summation of contributions from all image sources. Ignoring the phase effect, these numerical models are unlikely to be satisfactory for use in predicting intricate patterns of interference due to contributions from each image source. In the present paper, the effect of interference is incorporated by coherently summing the contributions from the image sources. To develop a simple numerical model, the walls of long rectangular enclosures are represented by either geometrically reflecting or impedance boundaries. Measurements in a one-tenth-scale model are conducted to validate the numerical model. In some of the scale-model experiments, the enclosure walls are lined with a carpet to simulate the impedance boundary condition. It has been shown that the proposed numerical model agrees reasonably well with experimental data. [DOI: 10.1121/1.1798351]

PACS numbers: 43.20.Fn, 43.20.Mv, 43.28.Js [SFW] Pages: 2759–2770

I. INTRODUCTION

Based on the assumption of a diffuse sound field, the classic room acoustics theory has been developed and used for more than a century.[1] In long enclosures, such as corridors and tunnels, the classic formulas are unsatisfactory, as the assumption of a diffuse field does not necessarily hold due to the extreme dimensions. Kang[2] conducted measurements showing that classical room acoustics was not applicable in a long enclosure. In general, it would be rather difficult to determine the reverberant levels in a long enclosure because the sound field is inhomogeneous and the level of sound will not be constant throughout.

We note that a number of investigations relating to the reverberation in long enclosures have been carried out since the 1960s. Yamamoto[3] was among the first to study the propagation of sound in corridors. Davies[4] and Redmore[5] were also interested in the subject in the 1970s and 1980s, respectively. The ray-tracing technique and image source method were used to predict the attenuation of sound in long corridors. In the late 70s, Sergeev[6] used an image source model to derive simple formulas to estimate the propagation of sound in city streets and long tunnels. A point source was considered in his study and the total sound field was evaluated by summing contributions from all rays incoherently. However, he offered no measurement results to support his model. In the 1990s, Kang[7,8] proposed theoretical expressions derived from the image source method to calculate reverberation times in long rectangular rooms with geometrically reflecting walls. In the late 1990s, Imaizumi *et al.*[9] used a conical beam method, which combined the advantages of the ray-tracing technique and the image source method, to predict the propagation of sound along a ''T''-shaped tunnel. In a recent study, Yang and Shield[10] developed a ray-tracing computer model for the detailed investigation of sound fields in long enclosures.

The effects of interference due to multiple reflections of sound rays from boundary walls were generally ignored in all of the previous studies mentioned above. It is important to point out that in the late 70s Gensane and Santon[11] considered the wave nature of sound in their study of sound fields in bounded and arbitrarily shaped spaces. Lemire and Nicolas[12] extended this approach by using a spherical-wave reflection coefficient instead of a plane-wave reflection coefficient to model the propagation of waves in a bounded space. In particular, they investigated the sound fields in a rectangular enclosure and in the region bounded by two infinite parallel planes. Their predicted results agreed very well with the standard normal-mode solutions, but no experimental validations were presented. It is also notable that the Acoustical Society of Japan published a simple numerical scheme to predict the propagation of road traffic noise in tunnels.[13] This numerical scheme is referred as the ASJ model in the following discussions and analysis.

The current study is motivated by the need to reduce the levels of noise inside a road traffic tunnel. A simple yet accurate model for prediction is required to assess the propagation of sound in tunnels with absorptive lining. In this paper, we wish to investigate the propagation of sound in long enclosures both theoretically and experimentally. A numerical scheme is developed using a complex image source theory according to Lemire and Nicolas.[12] Scale-model experiments are conducted to validate their theory. This preliminary study will provide a basis for assessing the propagation of sound in tunnels.

In Sec. II, we describe three models frequently used to model the propagation of sound in long enclosures: the incoherent model, the complex image source model (also known as the coherent model), and the ASJ model. Section III presents experimental results as well as theoretical predictions

[a]Electronic mail: mmkmli@polyu.edu.hk

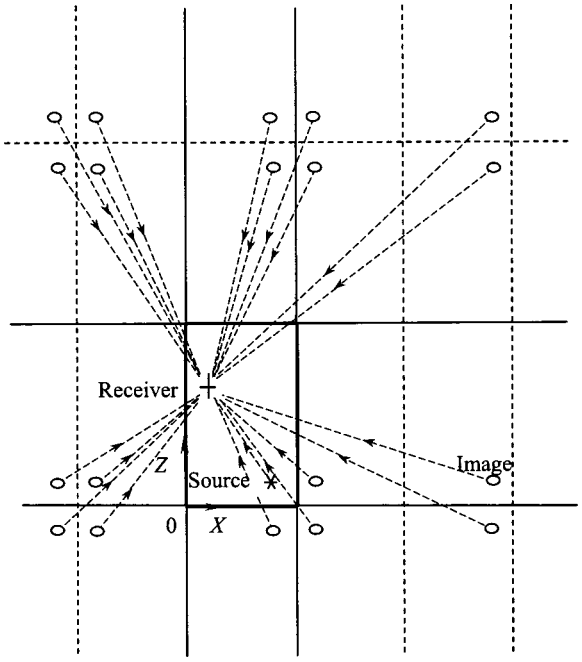

FIG. 1. Rows of image sources formed in a tunnel by reflections of four boundaries.

according to coherent and incoherent models for various impedance boundary conditions. Finally, conclusions are drawn in Sec. IV.

II. THEORETICAL MODELS

A. Ray model—Incoherent summation

In studying the effects of interference due to the direct ray and its reflected rays from the boundaries of long enclosures, the propagation model reviewed here was based on a typical case of rectangular long enclosures with geometrically reflecting boundaries (see Fig. 1). Diffusion is ignored and the absorption coefficient of the boundaries is assumed to be independent of the incident angle.

According to the acoustic ray models developed by Yamamoto[3] in the 1960s, by Davies[4] in the 1970s, by Redmore[5] in the 1980s, and by Kang[2] in the 1990s, the sound field at a particular receiver position is considered to be a summation of the intensities from the direct and each image source. Taking into consideration the absorption of the boundaries, the total intensity, I, can be obtained by incoherently summing all contributory components to yield

$$I = I_{\mathrm{ref}} d_{\mathrm{ref}}^2 \sum_N \frac{R_N}{d_N^2}, \tag{1}$$

where I_{ref} is the free-field sound intensity of the source at a reference distance of d_{ref} from the source, d_N is the length of the path from the image source to the receiver, and R_N is the reflection factor which represents the fraction of sound energy reflected from the boundaries. We remark that the attenuation due to the absorption of sound in air has been ignored in Eq. (1). The path length d_N can be determined in a straightforward manner by simple geometrical considerations. The reflection coefficient for each interaction with a boundary surface is simply given by

$$R_N = 1 - \alpha_j, \tag{2}$$

where α_j $(j=1,2,3,4)$ is the respective absorption coefficients of the walls of the rectangular enclosure. The reflection factor R_N is the combined reflection coefficient associated with the image source n. The amplitude of R_N is reduced by a factor $(1-\alpha_j)$ for each interaction with the corresponding boundary surface. An implicit assumption of the model given in Eq. (1) is that the mutual effects of the interference of direct and all reflected waves are ignored. We refer to this model as the incoherent model.

The absorption coefficients of the boundaries of long enclosures vary from case to case depending on the surface finish. Kang,[8] and Yang and Shield[10] conducted field measurements in an underground station, the surfaces along the length of which were all of concrete. They assumed in their models that the absorption coefficients of all boundaries were the same, ranging from 0.03 to 0.07 at octave bands of 125 to 4000 Hz. In our study, these parameters for absorption coefficients are used in our subsequent numerical analyses, unless otherwise stated.

B. Complex image source theory—Coherent model

Although the wave nature of sound fields in enclosed spaces was studied by Gensane and Santon,[11] and by Lemire and Nicolas,[12] they presented no experimental validations of their theoretical formulations. In a recent study, Dance *et al.*[14] have developed an interference model for calculating the total sound fields in an industrial space. However, their model is only accurate at receivers located close to the reflecting surfaces. We plan to explore these earlier models both theoretically and experimentally to investigate the effect of finite impedance on the overall sound fields in a long enclosure.

In previous publications, Iu and Li[15] derived an expression for the propagation of sound in a narrow city street. Lemire and Nicolas[12] formulated a solution for the propagation of sound in a bounded space. These two theoretical models are based on an analytic Green's function that was also a complex image source model. A spherical wave reflection coefficient was included in their numerical models to account for the reflection from the surface of an impedance boundary. In the current study, we follow Lemire and Nicolas in representing a long enclosure using two parallel vertical inwalls of infinite extent and two parallel horizontal planes, namely, the ground and ceiling. The width of the long enclosure is W, with the left vertical wall located at a plane of $x=0$. The height of the long enclosure is H, with the ground situated at a plane of $z=0$. Both the ground and ceiling are assumed to be perpendicular to the vertical walls. The schematic diagram in Fig. 1 shows a view of the plan of the posed problem, and illustrates formation of the first- and second-order image sources. The source and receiver are located at $(x_s,0,z_s)$ and (x,y,z), respectively. As the sound field is symmetrical at about the $y=0$ plane, we are interested in the region where $x \in [0,W]$, $y \in [0,\infty)$, and $z \in [0,H]$.

As can be seen from Fig. 1, the total sound field is composed of contributions from the direct source, and a series of image sources is produced by reflections of the two parallel walls from the source located at $(x_s,0,z_s)$. In addition, the total sound field is augmented by infinite rows of image sources due to the presence of a reflecting ceiling and the reflecting ground. The total sound field due to a monopole of unit strength can be computed by summing all contributions coherently to yield

$$P=\frac{1}{4\pi}\sum_{N=0}^{\infty} Q_{sN}\frac{e^{ikd_N}}{d_N}, \tag{3}$$

where d_N is the distance of the image source n and the receiver, and Q_{sN} is the combined complex wave reflection coefficient associated with the image source n. At each interaction with a boundary plane, the complex wave reflection coefficient, Q_N, is determined according to[16]

$$Q_N \equiv Q(d_N,\beta_i,\theta_N)=R_p+(1-R_p)F(w_N), \tag{4}$$

with the plane-wave reflection coefficient, R_p, given by

$$R_p=\frac{\cos\theta_N-\beta_j}{\cos\theta_N+\beta_j}, \tag{5}$$

where θ_N is the incident angle of the reflected wave of the image source n, and β_j ($j=1$, 2, 3, and 4 for the four boundary surfaces of the long enclosure) is the specific normalized admittance of the corresponding boundary surface. The term $F(w_N)$ is known as the boundary loss factor, which can be determined by

$$F(w_N)=1+i\sqrt{\pi}w_N e^{-w_N^2}\,\mathrm{erfc}(-iw_N), \tag{6}$$

with the parameter w, which is also known as the numerical distance, defined by

$$w_N=\sqrt{kd_N/2}(1+i)(\cos\theta_N+\beta_j). \tag{7}$$

The successive reflections of a spherical wave due to an image source n are then modeled by the product of the spherical wave reflection coefficient Q_N pertaining to each reflection in the sequence. This product, the overall complex wave-reflection coefficient, is labeled as Q_{sN} in Eq. (3). As pointed out by Lemire and Nicolas, Eq. (3) represents a first-order approximate solution, but Allen and Berkeley[17] have shown that this solution is an exact one when all of the boundary walls are rigid, i.e., $\beta_j=0$ and hence $Q_{sN}=1$. In this case, the solution can be written simply as

$$P=\frac{1}{4\pi}\sum_{n=0}^{\infty}\frac{e^{ikd_N}}{d_N}. \tag{8}$$

Hodgson *et al.*[18] revealed that the introduction of porous absorbers into a scale model of a factory led to unexpected effects. He found that the absorptive effect of boundaries was dependent on the shape of the enclosure and could not be measured in the usual way in a reverberation chamber. Recently, Kang[19] studied the effect of architectural acoustic treatments to improve the intelligibility of speech in a long enclosure. He pointed out that the attenuation of sound along the length of the enclosure is greater when the sound absorbers are along three or four boundaries rather than along one or two. However, at present, there is no validated theoretical model that takes into account the effects of mutual interference from all image sources for predicting the propagation of sound in a long enclosure with impedance boundary conditions.

C. The ASJ prediction model

The Research Committee on Road Traffic Noise of the Acoustical Society of Japan published a Prediction Model 1998 for Road Traffic.[13] Hereafter, we refer to this numerical scheme as the ASJ model. The model is used to predict the propagation of road traffic noise in tunnels. It is based on a sound energy balance inside the tunnel. Numerically, it is a simple model for the calculation of noise radiation in the tunnels, as two imaginary sources are assumed in the model. The first imaginary source represents the direct sound field in the tunnel. The residual sound field due to the effect of multiple reflections between the tunnel walls is calculated by the second imaginary source, which represents a distribution of surface sources.

The ASJ model was adopted by Kobayashi *et al.*[20] to predict noise propagation in a road tunnel. Attenuation at the straight and curved sections of the tunnel showed similar reduction characteristics, with a reduction rate of 4 dB per doubling of distance, up to a distance of 250 m. It was observed that the measured data over a distance of 300 m showed a greater reduction than predicted. The effect due to air absorption was ignored in the ASJ model.

Although the predicted tunnel attenuation agreed quite well with the experimental data, the measured decay rates at the 63-Hz and 125-Hz octave bands were rather irregular: no clear attenuation was observed. Kobayashi *et al.* indicated that this was possibly due to mode resonance at particular sections of the tunnel, or reflections at the open ends of the tunnel.

Tachibana *et al.*[21] carried out experimental measurements in a 1:40 scale-model tunnel to validate the ASJ model. Their experimental results showed that the propagation of sound was dependent on the source frequency. They concluded that the ASJ model could only be used as a first-order approximation for estimating the noise attenuation in tunnels.

In a recent study, Takagi *et al.*[22] demonstrated that the ASJ model was a simple and useful numerical scheme applicable to the prediction of road traffic noise in tunnels. To predict the road traffic noise in tunnels of a rectangular cross section, they derived a simple expression for the attenuation of sound energy as follows:

$$I=I_{\mathrm{ref}}\frac{2d_{\mathrm{ref}}^2}{wH}\tan^{-1}\left(\frac{wH}{\sqrt{(\alpha_t d)^4+(w^2+H^2)(\alpha_t d)^2}}\right), \tag{9}$$

where I is the predicted sound intensity at a horizontal distance d from the source, I_{ref} is the reference sound intensity at a reference distance of d_{ref} from the source in the free-field condition, H is the height of the tunnel, and $2w$ is the width of the tunnel. The absorption parameter, α_t is an empirical factor used to account for the acoustical characteristics of the tunnel walls. It vanishes when the tunnel has a perfectly

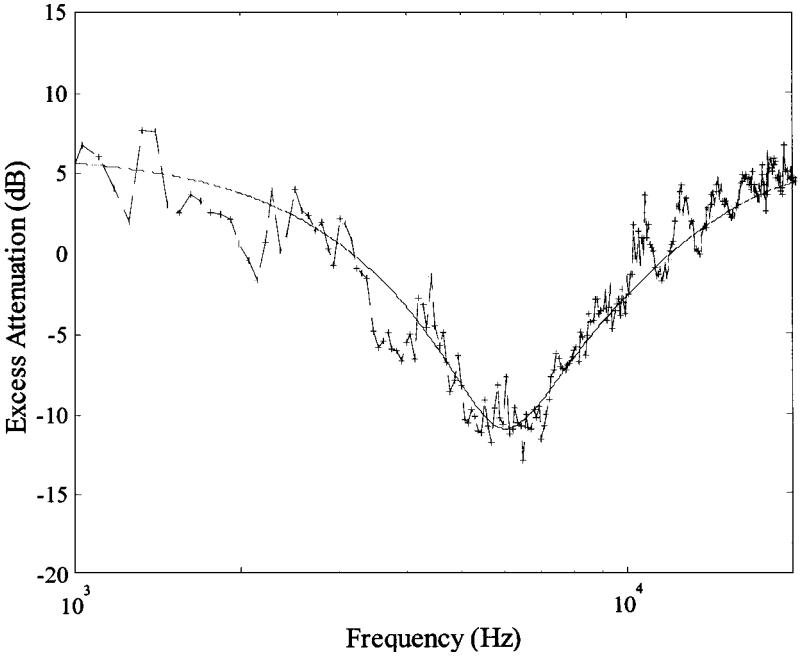

FIG. 2. Characterization of the impedance of a carpet. Both source and receiver are 0.065 m above the ground and are separated from each other at 1.0 m. (Measurement: dashed line with crosses; Theoretical prediction: solid line).

reflecting boundary. The absorption parameter was normally obtained by experimental measurements and a value of 0.04 was determined for the concrete walls.[22] Takagi *et al.*[22] proposed an empirical formula for the determination of α_t as follows:

$$1-\alpha_t=(1-\alpha)^{0.48}, \tag{10}$$

where α is the sound absorption coefficient of the material.

It is worth pointing out that the ASJ model offers a simpler formula than the incoherent model proposed by Redmore[5] and Kang[7] for predicting the sound field. Results of sound measurements in a highway tunnel showed good agreement with the ASJ model where discrepancies of less than 2 dB were reported between measured data and predictions.[22]

III. NUMERICAL SIMULATIONS AND EXPERIMENTAL RESULTS

A. Numerical simulations

The total sound field is composed of contributions from the direct source and from a series of image sources produced by multiple reflections of the two parallel walls due to the source located at $(x_s,0,z_s)$. In addition, the total sound field is also augmented by infinite rows of image sources due to the presence of a reflecting ceiling on the top and a ground surface on the bottom. The total sound field can be estimated by summing up the contributions from each of these sources.

In the presentation of numerical and experimental results, we use the term excess attenuation (EA). EA is defined as the ratio of the total sound field at various receiver locations, P, to the free-field sound pressure at 1 m from the source. Thus, EA is given by

$$\mathrm{EA}=20\log(P). \tag{11}$$

On the other hand, a comparable definition is needed for the excess attenuation if the incoherent model is used to predict the sound fields. In this case, the excess attenuation can be defined as the ratio of the total intensity level, I, to the free-field intensity level measured at 1 m from the source. It is simply given by

$$\mathrm{EA}=10\log(I), \tag{12}$$

where the total intensity level can be obtained from Eq. (1).

B. Scale-model experiments

To study the sound field in nondiffuse spaces, Hodgson *et al.*[18] used a 1:50 scale model to investigate factory sound fields with considerable success. However, it was found that the introduction of porous absorbers into the model resulted in unexpected effects. In the 1990s, Orlowski[23] built a model of an existing factory at a scale of 1:16. Comparisons of the measurements of field and scale models showed good agreement. In the late 90s, Orlowski[24] used scale modeling to study the intelligibility of speech in underground stations. Tachibana *et al.*[21] used a 1:40 scale model to predict the radiation of sound from the mouths of tunnels. Kang[25] developed a computer model to predict the temporal and spatial distribution of train noise in underground stations. In his study, a 1:16 scale physical model was constructed to validate the prediction model. To compensate for the effect of the absorption of air at high frequencies, measurements were carried out in a test tunnel filled with oxygen-free nitrogen at a concentration of 97% to 99%.

In the present study, a larger model tunnel at a scale of one-tenth was built for our experimental measurements. Experimental data were obtained to validate the theoretical models described in Sec. II. In fact, the use of a larger scale in the construction of a model tunnel proved to be a relatively simple and inexpensive technique, because the measurements can be carried out in normal atmospheric conditions without the need to fill the test tunnel with oxygen-free nitrogen. Sandwich-type steel panels 60 mm thick were used to build the model long duct with acoustically hard boundaries. The outer skin of the panel was made of 1.5-mm-thick

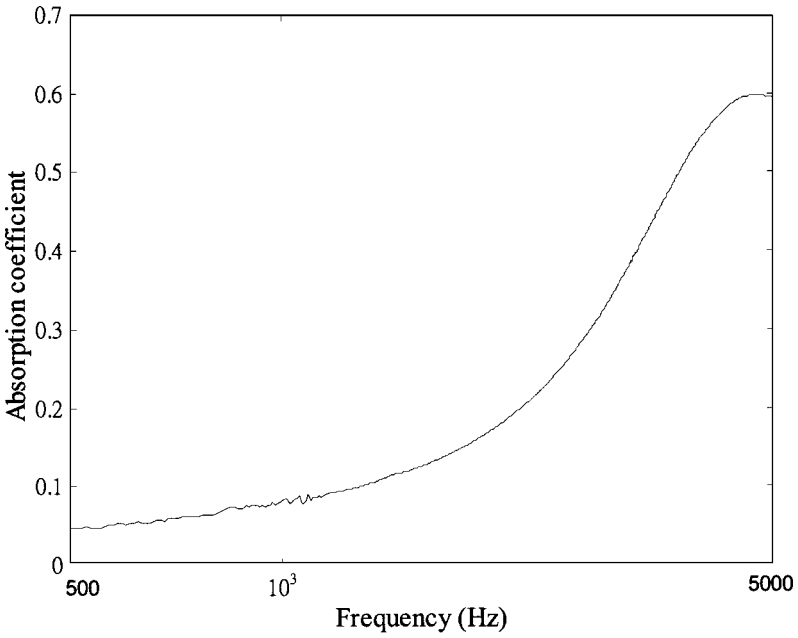

FIG. 3. The normal incidence absorption coefficient of the carpet measured using the impedance tube method.

galvanized steel sheet and the infill with 50-mm-thick fiberglass. To minimize the effects of vibration from the galvanized steel sheet, a 9-mm-thick gypsum board was stuck to the inside surface of the steel sheet. Due to the size of the model long duct, all measurements were conducted in an open space in a factory. During our measurements, the level of background noise was monitored to ensure that it was always below 60 dB, with typical signal levels inside the model long duct well above 75 dB. This precautionary step was necessary for all experimental measurements to minimize any effects from the background.

The steel panels were assembled to have an internal width and height of 1.0 and 0.6 m, respectively. To prevent the sound waves from reflecting back into the model long duct due to the effect of end reflection, an anechoic termination was designed according to ISO 7235-1996.[26] The anechoic termination was erected at the end of the test duct on the receiving side for all experimental measurements. The overall length of the model long duct was 8.5 m. At full scale, the model represents a cross section of a rectangular tunnel 10 m in width and 6 m in height. In the following paragraphs, we refer to all dimensions as scaled distances unless otherwise stated.

A Brüel & Kjær 1/2-in. condenser microphone and a Tannoy driver were used as a receiver and a point source, respectively. A PC-based maximum length sequence system analyzer (MLSSA)[27] was used both as a signal generator for the source and as an analyzer for the subsequent processing of data. The maximum length sequence (MLS) technique was chosen in the present study because Vörlander *et al.*[28] had confirmed the validity of applying MLS techniques to measure sound in highly reverberant sound fields. Indeed, the MLS technique was also chosen by Kang[8] to carry out his site measurements in an underground train station with a tunnel having a dimension of 20 m in width, 5.7 m in height, and 200 m in length.

In the current study, the MLS technique has the advantage that no correction of background noise is necessary for a signal-to-noise ratio of 0 dB. As MLSSA was operated in the time domain where the impulse response was measured, the chosen data for processing were based on the time between the arrival of the direct and the last order rays. The time-series data were converted to spectral data by the fast Fourier transform (FFT) technique. Each spectrum level was then normalized by the prerecorded direct field measurement taken at 1 m from the source at the free field. The final output was then the required excess attenuation spectrum.

In addition to hard duct walls, some measurements were conducted to model conditions when the boundary walls were covered with sound absorption materials. Carpets were fixed on one or both vertical panels of the model duct and were used to simulate a soft wall surface. Prior experiments were performed to characterize the acoustic impedance of the carpet at the open space of the factory. The MLS technique was again used for the characterization, with both the source and receiver set at a height of 0.065 m above the carpet and

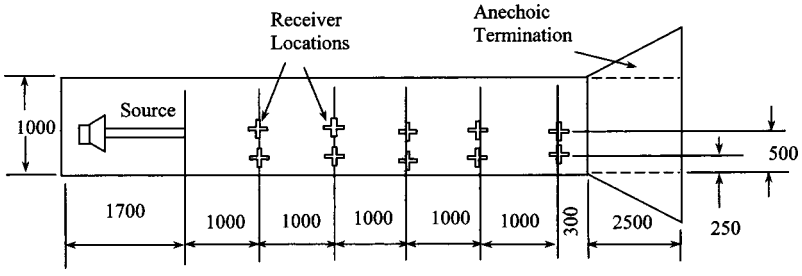

FIG. 4. The schematic sketch illustrates the model tunnel with anechoic termination.

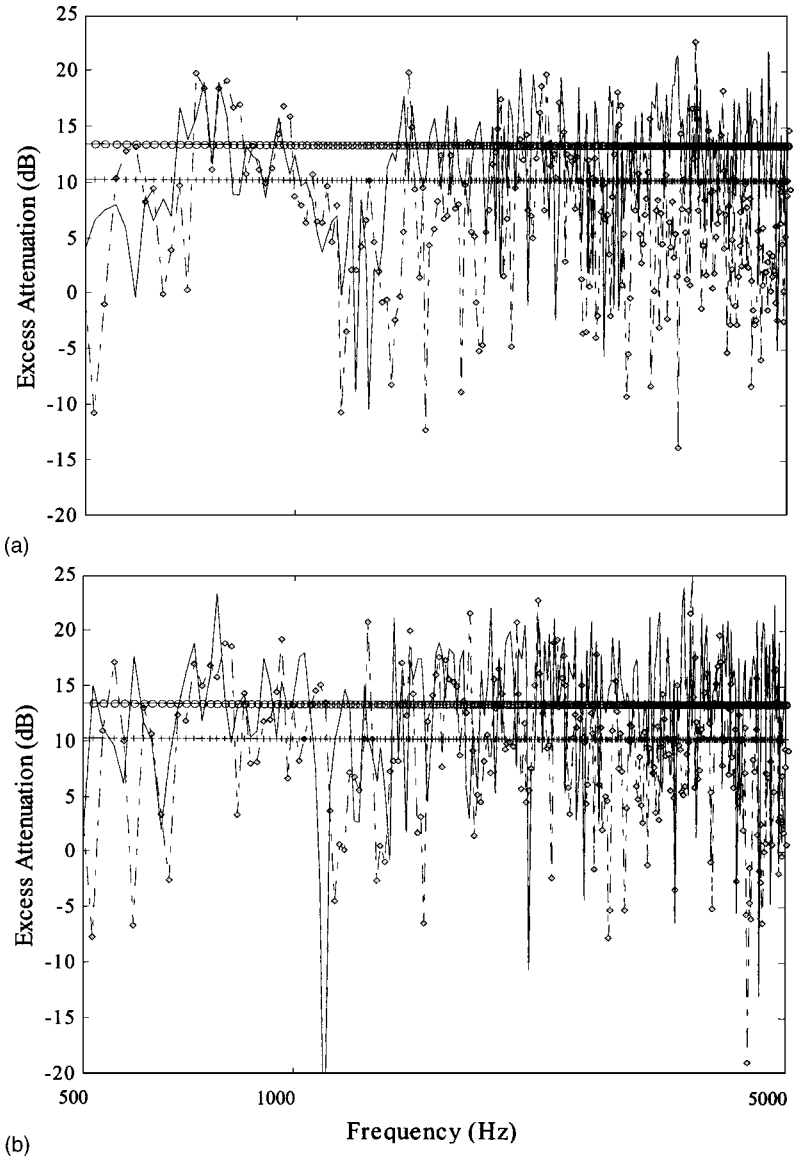

FIG. 5. Comparison of the measured spectrum of excess attenuation with the respective predictions by the coherent, incoherent, and ASJ models. Measurements were conducted in a model tunnel with hard boundaries. Both the source and receiver were located at 0.11 m above the ground. The source/receiver geometries are as follows: (a) source at (0.5,0,0.11) and receiver at (0.25,5,0.11), and (b) source at (0.25,0,0.11) and receiver at (0.25,5,0.11) (Measurement: dashed-dotted line with closed circles; Coherent prediction: solid line; Incoherent prediction: solid line with open circles; dotted line with crosses).

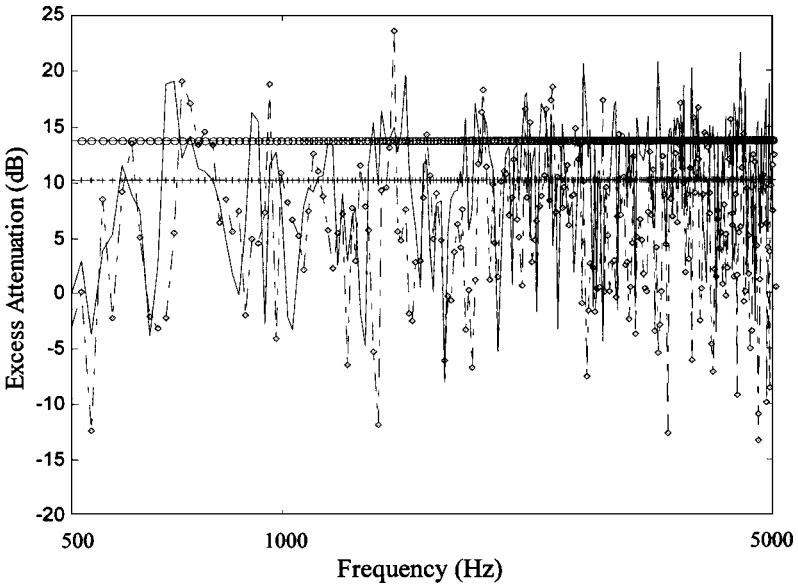

FIG. 6. Comparison of the measured spectrum of excess attenuation with the respective predictions by the coherent, incoherent, and ASJ models. Measurements were conducted in a model tunnel with hard boundaries. The source and receiver are located at different heights of 0.11 and 0.3 m, respectively. In addition, the source is situated at the centerline and the receiver at the offset line. They are separated by a horizontal distance of 4 m. The key of this figure is same as Fig. 5.

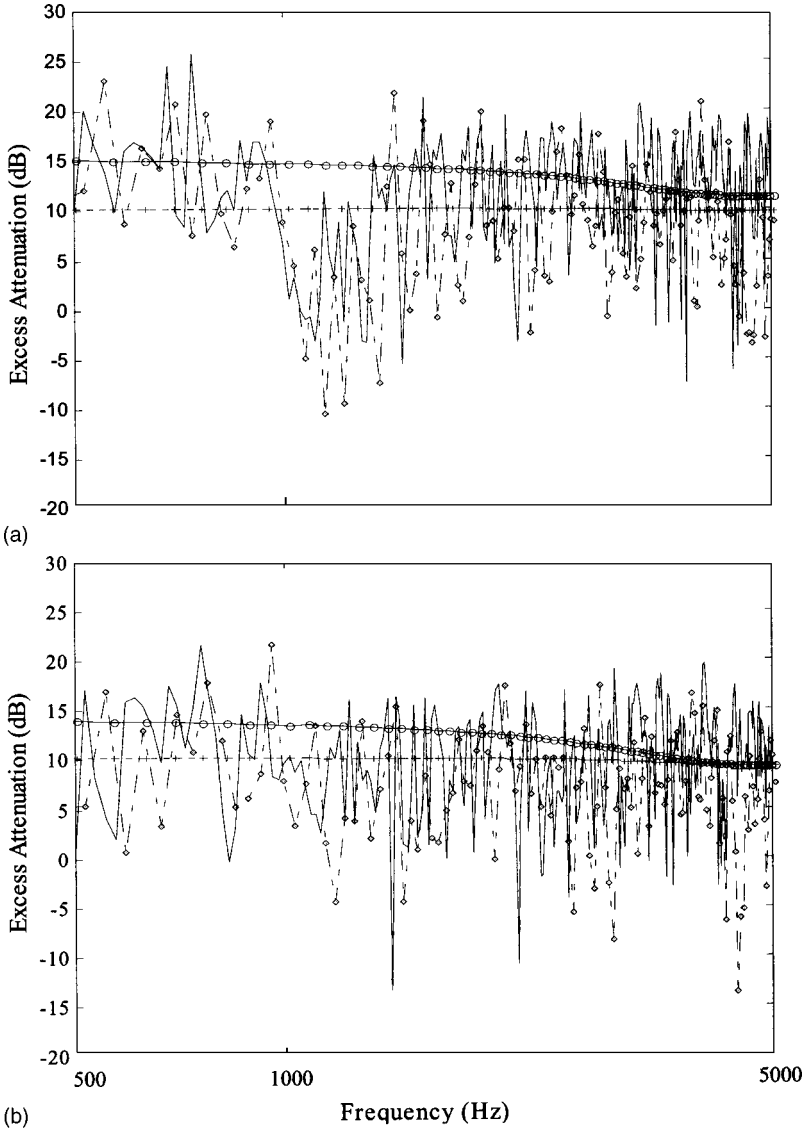

FIG. 7. Comparison of the measured spectrum of excess attenuation with the respective predictions by the coherent, incoherent, and ASJ models. Measurements were conducted in a model tunnel with an impedance wall and both the source and receiver were located at the offset line. The key of this figure is same as Fig. 5. The source/receiver geometries are as follows: source at (0.25,0,0.11) and receiver at (0.25,1,0.11); (b) source at (0.25,0,0.11) and receiver at (0.25,2,0.11).

their horizontal separation set at between 0.5 and 1.0 m.

A two-parameter model,[29] with respective best-fit parameter values for the effective flow resistivity σ_e and the effective rate of change of porosity with depth α_e of 250 kPa s m^{-2} and 300 m^{-1}, was used to calculate the impedance. A typical measurement of the excess attenuation spectrum with the horizontal separation set at 1 m was shown in Fig. 2. In the same figure, we also show the numerical predictions indicating a reasonably good fit with the experimental data for the given parameter values.

While the impedance characterized by the two-parameter model is used in the coherent ray model, an absorption coefficient at a normal incidence is used in the incoherent model. It is determined by means of the impedance tube method according to ASTM C384-98,[30] where the data acquisition system includes a Brüel & Kjær two-microphone impedance measurement tube type 4206, a power amplifier type 2706, two 1/4-in. microphones type 4187 with preamplifiers, a data acquisition front-end type 2827, and a personal computer with pulse software. Figure 3 shows the measured absorption coefficients versus the frequency. The measured absorption coefficient, α, of the carpet used in the experimental measurements varies from 0.05 to 0.6 at frequencies ranging from 500 to 5000 Hz.

The excess attenuation was measured experimentally at various receiver locations, with the source located 0.11 m above the ground. The height of the source was chosen to simulate the approximate locations of noise emitted from heavy vehicles at about 1.1 m (full scale) above the surface of tunnel roads. The source and receiver were located either at the centerline or on the side of the tunnel 0.25 m away from the centerline. In all measurements, the receivers were located at heights of either 0.11 or 0.3 m from the ground. The horizontal distances between the source and receivers ranged from 1 to 5 m (see Fig. 4 for the monitoring stations of the experimental setup).

In the numerical simulations, we can show that 30 to 50 reflections are generally required to give satisfactory results in this model long enclosure. The final choice of the number of reflections is dependent on the boundary condition of the enclosure and the source/receiver geometry. The path length from the 50th image sources to the receiver corresponds to about 30 m in our scale-model measurement. The absorption of sound in air was not significant at such a path length and

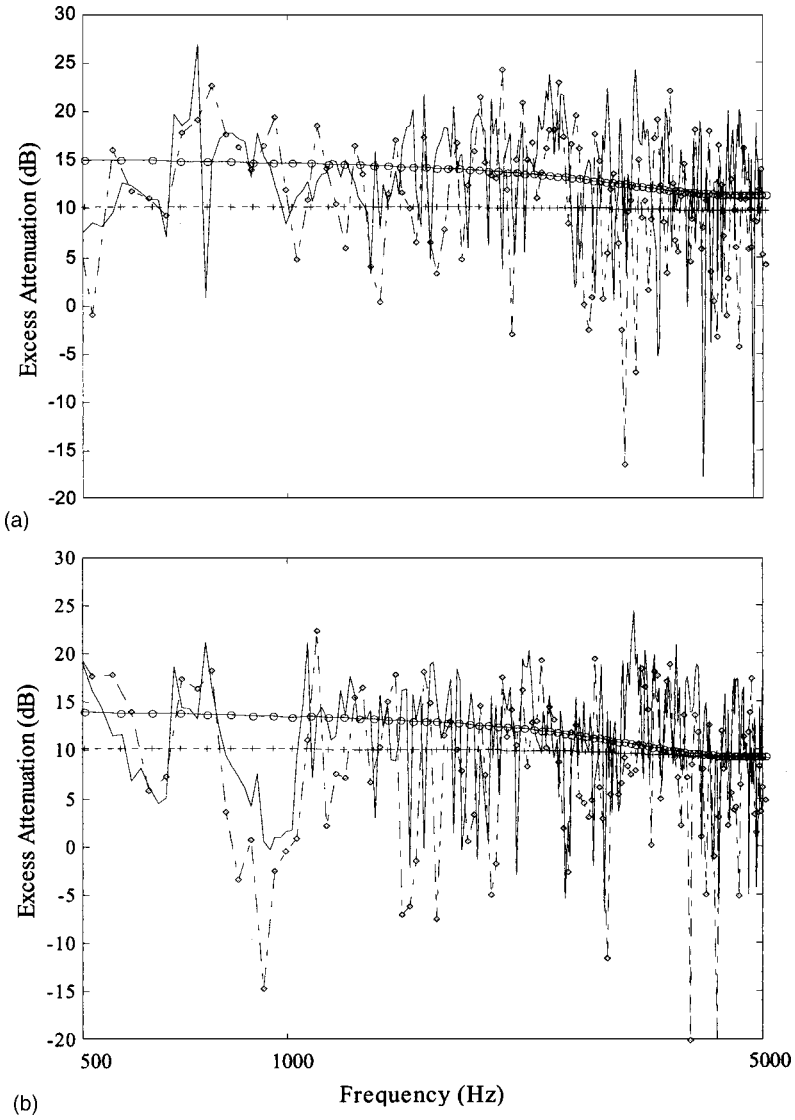

FIG. 8. Comparison of the measured spectrum of excess attenuation with the respective predictions by the coherent, incoherent, and ASJ models. Measurements were conducted in a model tunnel with an impedance wall and both the source and receiver were located at the centerline. The key of this figure is same as Fig. 5. The source/receiver geometries are as follows: (a) source at (0.5,0,0.11) and receiver at (0.5,1,0.11), and (b) source at (0.5,0,0.11) and receiver at (0.5,2,0.11).

at frequencies up to 10 kHz; hence, its effect was not included in our analyses.

1. Validations in the model tunnel with hard boundaries

To demonstrate the effect of mutual interference, the receiver was placed at the offset line and at a height of 0.11 m. Measurements were taken at a horizontal distance of 5 m in front of the source, which was also located at a height of 0.11 m above the ground. In the measurements, the source was placed at either the centerline or at the offset line located 0.25 m from the centerline. Figures 5(a) and (b) show the experimental results for the source located at the centerline and the offset line, respectively. The measured excess attenuation spectra fluctuate considerably as the source frequency increases. In Fig. 5(a), there is a distinct ''dip'' that occurs at a frequency of around 1250 Hz (125 Hz at full scale), while Fig. 5(b) illustrates no destructive interference effect occurs at the same frequency. The measured excess attenuations around 1250 Hz shown in Fig. 5(b) are increased by more than 5 dB when comparing with Fig. 5(a). In the same figure, predictions according to the incoherent model and ASJ model are also shown. We note that predictions by the incoherent model and ASJ model are only based on the path lengths between the source and receiver. Consequently, the same prediction of EA was obtained across the whole spectrum in Figs. 5(a) and (b). As shown in the comparisons, only the predictions by the coherent model give good agreements with the measurements. The incoherent model and ASJ model cannot predict such fluctuations in frequency. The results predicted by the incoherent model and ASJ model are independent of the frequency of sound and do not give good agreements with the measurements.

The pattern of the fluctuation in frequency spectrum is dependent on the relative positions of source and receiver. To illustrate this point, another measurement was taken with the source and receiver located at respective heights of 0.11 m and 0.3 m above the ground. The horizontal separation between the source and receiver was reduced to 4 m in this set of measurements. During the measurement, the source was situated at the centerline and the receiver at the offset line. In the measured results shown in Fig. 6, several distinct dips occur at frequency below 1000 Hz (100 Hz at full scale). The pattern of fluctuation in the frequency spectrum is quite different from that shown in Figs. 5(a) and (b).

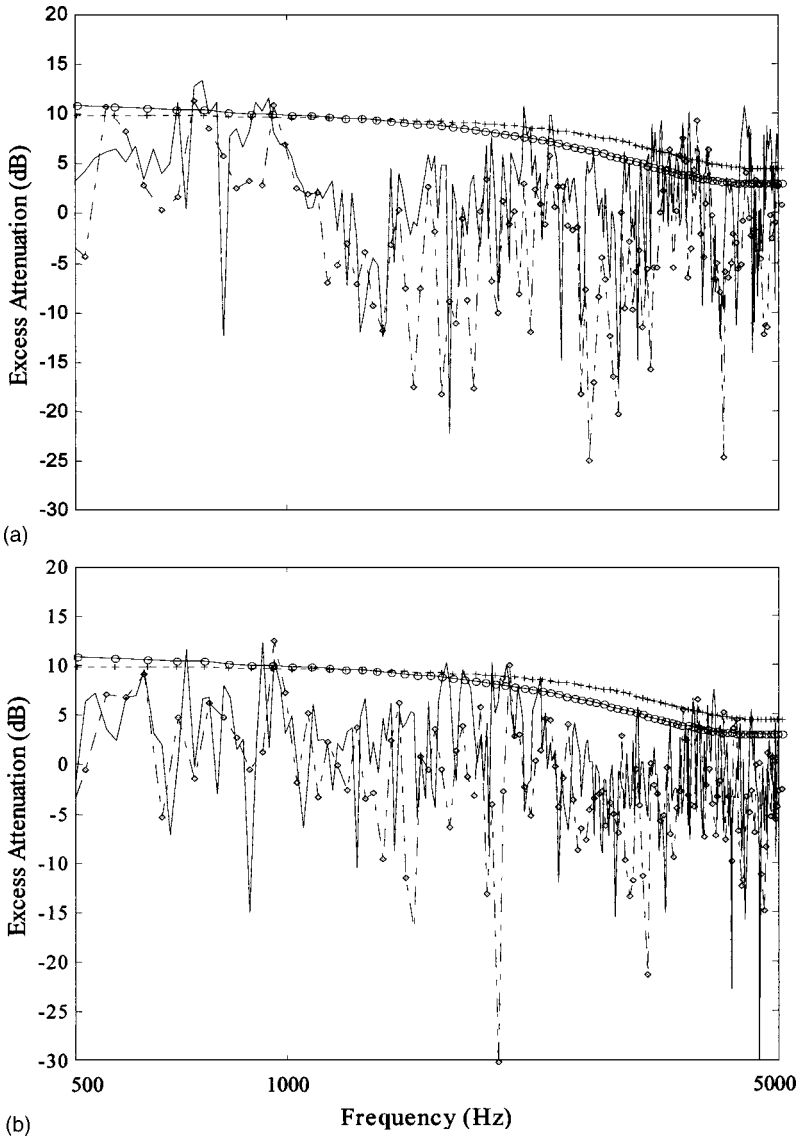

FIG. 9. Comparison of the measured spectrum of excess attenuation with the respective predictions by the coherent, incoherent, and ASJ models. Measurements were conducted in a model tunnel with two impedance walls and the receiver was located at the offset line. The key of this figure is same as Fig. 5. The source/receiver geometries are as follows: (a) source at (0.5,0,0.11) and receiver at (0.25,5,0.11), and (b) source at (0.25,0,0.11) and receiver at (0.25,5,0.3).

The effect of interference was also found when both the source and receiver were situated at other locations. These results were shown elsewhere,[31] and not repeated here. Again, only the predictions using the coherent model agree reasonably well with the measurements. The incoherent and ASJ models can only give an indication of the average levels of noise. These two models tend to give a better agreement in the average noise levels with measured results at frequencies higher than about 3000 Hz for the typical geometry used in the present study. However, the incoherent and ASJ models are unable to predict variations with frequency because they ignore the effects of the interference from all contributing rays.

2. Validations in the model tunnel with an impedance wall surface

The effect of mutual interference also occurs in tunnels with an impedance wall surface. Figure 7(a) illustrates that a distinct dip occurs at around 1100 Hz (110 Hz at full scale) when the receiver is located 1 m directly in front of and at the same height as the source. When the receiver is moved to a distance of 2 m in Fig. 7(b), the effect of destructive interference becomes less significant. We note that only the results of the prediction by the coherent model agree reasonably well with the measurements, while the incoherent model and ASJ model give an approximate mean value of the excess attenuations across the frequency spectra. In Figs. 7(a) and (b), both the source and receiver are located at the offset line close to the impedance wall. If the source and receiver are moved to the centerline, by locating the receiver at 1 m directly in front of and at the same height as the source, the dip at 1100 Hz disappears as shown in Fig. 8(a). Apparently, it seems that the impedance wall will reduce the levels of sound if both the source and receiver are located close to the impedance wall. However, by locating the receiver 2 m directly in front of and at the same height as the source at the centerline, Fig. 8(b) shows that there a distinct dip at around 900 Hz (90 Hz at full scale) while Fig. 7(b) displays a peak there. This shows that there is no simple relationship between the position of the impedance wall and the location of the source–receiver when predicting sound fields in long tunnels.

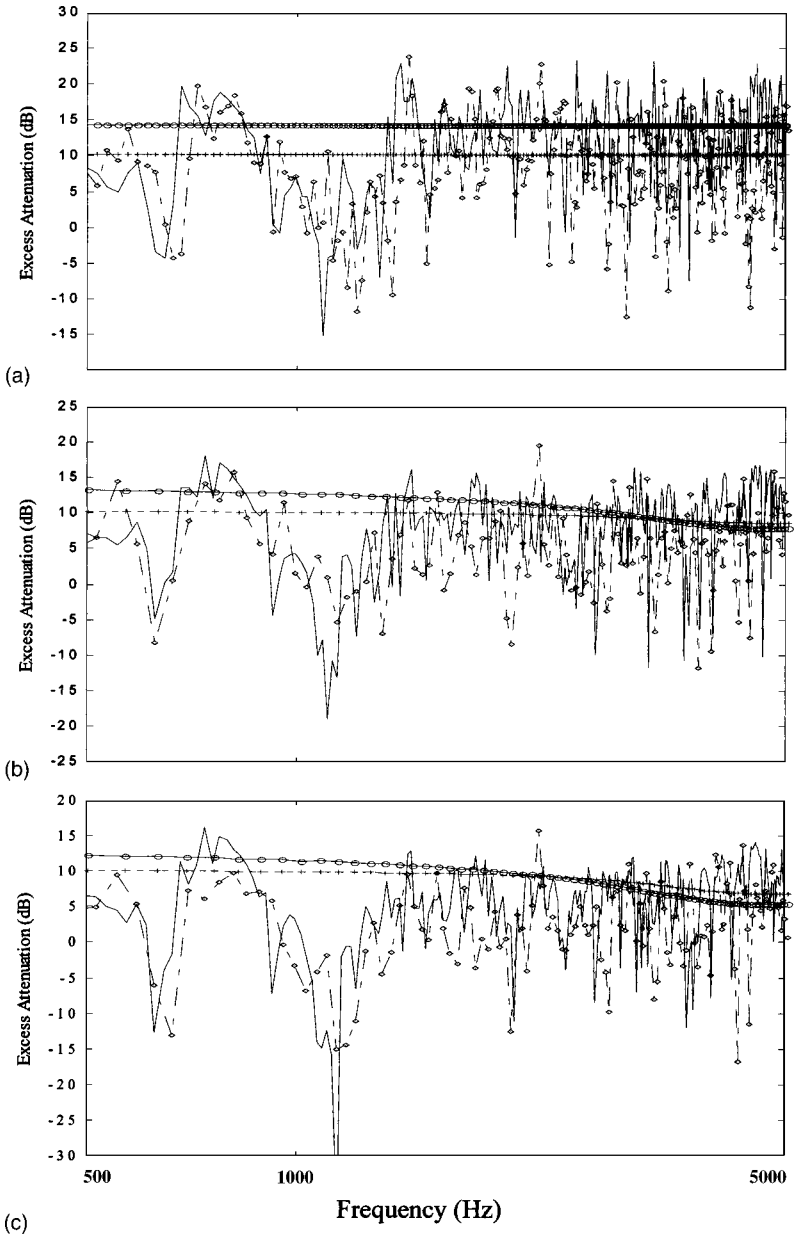

FIG. 10. Comparison of the measured spectrum of excess attenuation with the respective predictions by the coherent, incoherent, and ASJ models. Measurements were conducted in a model tunnel with different boundary conditions. The source was located at (0.25,0,0.11) and receiver at (0.5,3,0.11). The key of this figure is same as Fig. 5. The source/receiver geometries are as follows: (a) hard boundaries (no impedance wall); (b) one impedance wall; and (c) two impedance walls.

3. Validations in a model tunnel with two impedance wall surfaces

The coherent model can be used to predict the peaks and dips of the interference in the tunnel with impedance wall surfaces. The usefulness of the coherent model for predicting the sound field in a tunnel with an impedance wall has been demonstrated in the last section. Here, we extend the study to cover the situation where there are two parallel impedance wall surfaces in the long enclosure. To compare the numerical and experimental results, the predicted excess attenuations, together with the measured excess attenuations, are plotted against the frequency. Figures 9(a) and (b) illustrate two typical examples for the receiver located at the offset position and at a horizontal distance of 5 m from the source. Figure 9(a) displays the experimental results where both the source and receiver were located at 0.11 m above the ground but the source was located at the centerline. On the other hand, the configuration for Fig. 9(b) was the same as Fig. 9(a) except that the source was located at the offset line. Again, good agreements between the theoretical predictions by the coherent model and experimental measurements are evident from the results as shown in these two figures. We reiterate that the most important point to note is that the coherent model can well predict the general trend of the experimental data in the frequency spectrum, while the incoherent and ASJ models tend to give higher estimated excess attenuations and cannot predict the fluctuations in frequency caused by the effects of interference.

It is increasingly common to install sound absorption panels onto wall surfaces in tunnels to reduce the noise from traffic.[32] In this section, we explore the effects of adding an impedance wall or two parallel impedance walls in a tunnel with a stationary source, a point monopole source at a height of 0.11 m (1.1 m at full scale) above the ground. Figures 10(a)–(c) show the effect of the impedance wall on the level of sound produced by the source located at the offset line, which is 0.25 m away from the centerline of the tunnel. The receiver is located 0.11 m above the ground at the centerline

and at a horizontal distance of 3 m from the source. The impedance wall leads to decreased values in the levels of sound throughout the whole frequency range. Figures 10(a)–(c) compare the levels of sound in tunnels with reflecting hard surfaces, one impedance wall, and two impedance walls. By introducing an impedance wall, sound levels are reduced by about 3 dB across the whole frequency spectrum being displayed. By adding another impedance wall, the levels of sound are further reduced by about 2 to 3 dB.

In general, the theoretical predictions by the coherent model agree reasonably well with the measurements using experimental scale model. This suggests that the effect of interference should not be ignored when predicting the propagation of sound along tunnels. Although the measurements are conducted for a frequency range of 0.5 to 10 kHz (50 to 1000 Hz at full scale), for the sake of clarity all of the figures displayed are from 500 to 5000 Hz. We also wish to point out that the spectra of the excess attenuation are presented in the current study. These measured results allow detailed comparisons of experimental data with the numerical models in a more precise manner. The investigation of sound attenuation in octave bands in tunnels is a subject of future studies.

IV. CONCLUSIONS

In this paper, three prediction schemes, the coherent, incoherent, and ASJ models, were presented to predict the propagation of sound in long enclosures. The incoherent and ASJ models were based on a summation of the intensities from the direct and image sources without taking into account the effect of mutual interference. The coherent model, on the other hand, included the effects of the interference caused by the direct and reflected waves in the computation of sound fields. The total sound field was calculated by coherently summing the contributions from all image sources. An extensive set of one-tenth scale-model experiments were conducted in frequencies ranging from 500 to 5000 Hz and at a horizontal distance of up to 5 m in a model tunnel with a cross-sectional area of 1×0.6 m. It was shown that the theoretical predictions by the coherent model agree reasonably well with the results of the measurement, with an accuracy in most cases of well within 3 dB. However, the incoherent and ASJ models give less satisfactory agreement with the experimental measurements and their predictions are not able to match the peaks and dips caused by the effects of interference in the frequency spectra. They are only capable of predicting average noise levels at the high-frequency regime where the overall effect of multiple reflections becomes more significant. It is interesting to note that, as expected, the introduction of impedance walls resulted in a considerable increase in the attenuation of sound in the long enclosure.

ACKNOWLEDGMENTS

One of the authors (K.K.I.) was supported by a Teaching Company Scheme jointly sponsored by the Industry Department of the HKSAR Government and NAP Acoustics (Far East) Limited. The research described in this paper was supported by the Research Grants Council of the HKSAR Government and The Hong Kong Polytechnic University. The authors are grateful to NAP Acoustics (Far East) Limited for the provision of the model long duct.

[1] W. C. Sabine, *Collected papers on Acoustics* (Harvard University Press, Cambridge, MA, 1927).
[2] J. Kang, ''The unsuitability of the classic acoustical theory in long enclosures,'' Architect. Sci. Rev. **39**, 89–94 (1996).
[3] T. Yamamoto, ''On the distribution of sound in a corridor,'' J. Acoust. Soc. Jpn. **17**, 286–292 (1961).
[4] H. G. Davies, ''Noise propagation in corridors,'' J. Acoust. Soc. Am. **53**, 1253 (1973).
[5] T. L. Redmore, ''A theoretical analysis and experimental study of the behavior of sound in corridors,'' Appl. Acoust. **15**, 161–170 (1982).
[6] M. V. Sergeev, ''Scattered sound and reverberation on city streets and in tunnels,'' Sov. Phys. Acoust. **25**(3), (1979).
[7] J. Kang, ''Reverberation in rectangular long enclosures with geometrically reflecting boundaries,'' Acustica **82**, 509–516 (1996).
[8] J. Kang, ''A method for predicting acoustic indices in long enclosures,'' Appl. Acoust. **51**, 169–180 (1997).
[9] H. Imaizumi, S. Kunimatsu, and T. Isei, ''Sound propagation and speech transmission in a branching underground tunnel,'' J. Acoust. Soc. Am. **108**(2), 632–642 (2000).
[10] L. Yang and B. M. Shield, ''The prediction of speech intelligibility in underground stations of rectangular cross section,'' J. Acoust. Soc. Am. **109**(1), 266–273 (2001).
[11] M. Gensane and F. Santon, ''Prediction of sound fields in rooms of arbitrary shape: The validity of the image sources method,'' J. Sound Vib. **63**, 97–108 (1979).
[12] G. Lemire and J. Nicolas, ''Aerial propagation of spherical sound waves in bounded spaces,'' J. Acoust. Soc. Am. **86**, 1845–1853 (1989).
[13] Research Committee of Road Traffic Noise in Acoustical Society of Japan, ''ASJ Prediction Model 1998 for Road Traffic Noise,'' J. Acoust. Soc. Jpn. **55**(4), 281–324 (1999).
[14] S. M. Dance, J. P. Roberts, and B. M. Shield, ''Computer prediction of sound distribution in enclosed spaces using an interference pressure model,'' Appl. Acoust. **44**, 53–65 (1995).
[15] K. K. Iu and K. M. Li, ''The propagation of sound in narrow street canyons,'' J. Acoust. Soc. Am. **112**(2), 537–550 (2002).
[16] T. F. W. Embleton, ''Tutorial on sound propagation outdoors,'' J. Acoust. Soc. Am. **100**, 31–48 (1996).
[17] J. B. Allen and D. A. Berkeley, ''Image method for efficient simulating small-room acoustics,'' J. Acoust. Soc. Am. **65**, 943–950 (1979).
[18] M. R. Hodgson and R. J. Orlowski, ''Acoustic scale modeling of factories. II. 1:50 scale model investigations of factory sound fields,'' J. Sound Vib. **113**, 257–271 (1986).
[19] J. Kang, ''Scale modeling for improving the speech intelligibility from multiple loudspeakers in long enclosures by architectural acoustic treatments,'' Acustica **84**, 689–700 (1998).
[20] Y. Kobayashi, S. Seki, T. Kitamura, K. Mitsui, and S. Yamada, ''Study on the characteristics of noise propagation in tunnel and noise control with absorbing material of ceramics,'' Proc. Internoise **99**, 517–522 (1999).
[21] H. Tachibana, S. Sakamoto, and A. Nakai, ''Scale model experiment on sound radiation from tunnel mouth,'' Proc. Internoise **99**, 387–392 (1999).
[22] K. Takagi, T. Miyake, K. Yamamoto, and H. Tachibana, ''Prediction of road traffic noise around tunnel mouth,'' Proc. InterNoise **2000**, 3099–3104 (2000).
[23] R. J. Orlowski, ''Scale modeling for predicting noise propagation in factories,'' Appl. Acoust. **31**, 147–171 (1990).
[24] R. J. Orlowski, ''Underground station scale modeling for speech intelligibility prediction,'' Proc. Inst. Acoust. **16**, 167–172 (1994).
[25] J. Kang, ''Modeling of train noise in underground stations,'' J. Sound Vib. **195**(2), 241–255 (1996).
[26] British Standard BS EN ISO 7235, ''Acoustics—Measurement procedures for ducted silencers—Insertion loss, flow noise and total pressure loss,'' pp. 21–25 (1996).
[27] D. D. Rife and J. Van der Kooy, ''Transfer-function measurement with maximum-length sequences,'' J. Audio Eng. Soc. **37**(6), 419–443 (1989).
[28] M. Vorlander and M. Kob, ''Practical aspect of MLS measurements in building acoustics,'' Appl. Acoust. **52**(3/4), 239–258 (1997).

[29] K. Attenborough, ''Ground parameter information for propagation modeling,'' J. Acoust. Soc. Am. **92**, 418–427 (1992).
[30] ASTM Standard C384, ''Standard test method for impedance and absorption of acoustical materials by the impedance tube method,'' (1998).
[31] K. K. Iu, ''The prediction of noise propagation in street canyons and tunnels,'' M. Phil. thesis, The Hong Kong Polytechnic University (2003).
[32] H. Woehner, ''Sound propagation at tunnel openings,'' Noise Control Eng. J. **39**(2), 47–56 (1992).

On the interference between the two microphones in free-field reciprocity calibration

Salvador Barrera-Figueroa,[a] Knud Rasmussen,[b] and Finn Jacobsen[c]
Acoustic Technology, Ørsted·DTU, Technical University of Denmark, Building 352, DK-2800, Kgs. Lyngby, Denmark

Lorenzo Muñíz[d]
Centro Nacional de Metrología, División de Acústica y Vibraciones, Carretera a Los Cués km 4.5, El Marqués, Querétaro, México

(Received 19 January 2004; revised 12 May 2004; accepted 30 July 2004)

One of the fundamental assumptions in free-field reciprocity calibration of microphones is that the microphones can be substituted by point sources at the positions where the acoustic centers are located. However, in practice the microphones have finite dimensions and, at the distance and in the frequency range where the measurements are made, the direct wave and the subsequent reflections from the microphones interfere with each other, creating a ''standing wave.'' This interference effect gives rise to deviations from the inverse distance law, indicating that the free-field assumption is not strictly valid. The interference has been thought to be caused by specular reflection between the parallel diaphragms of the microphones, and a solution based on tilting the axis of one of the microphones a few degrees has been proposed, but never examined in practice. In this paper a time-selective technique is applied for analyzing the interference and for removing it in the time domain. It is shown that the phenomenon is due to multiple backscattering rather than specular reflection. Thus tilting one of the microphones does not alleviate the problem, as also demonstrated experimentally. However, the time-selective technique is quite effective in removing the interference effect and other disturbances from the direct wave between the microphones. [DOI: 10.1121/1.1795333]

PACS numbers: 43.20.Fn, 43.20.Ye, 43.38.Kb [AJZ] Pages: 2771–2778

I. INTRODUCTION

Free-field reciprocity calibration of condenser microphones is a well-established technique used for obtaining the absolute sensitivity of condenser microphones under free-field conditions. This is reflected in the fact that there is an international standard for such calibrations.[1] The theoretical foundation of the free-field reciprocity calibration of microphones was developed by MacLean[2] and Wathen-Dunn.[3] Descriptions of the practical implementation of the technique have been given, e.g., by Rudnick and Stein,[4] and more recently by researchers from a number of national metrology laboratories.[5–7] Some years ago an international comparison among several national metrology laboratories was carried out,[8] yielding results that have motivated further research on certain aspects of the calibration technique.

One of the basic assumptions of the underlying theory is that the microphones can be substituted by point sources/receivers with a given diffraction factor.[1–3] This greatly simplifies the procedure, and a quantity proportional to the product of the free-field sensitivities of the two microphones, the electrical transfer impedance, can be obtained.[1] The diffraction factor is the result of the finite size of the microphones.[9,10] However, another result of the finite size of the microphones, a phenomenon often referred to as a ''standing wave'' between the microphones, has been observed in some practical implementations of the technique.[3–5,8] This problem has been thought to be caused by ''specular'' reflections between the parallel diaphragms of the microphones. Since such an interference represents a deviation from the basic assumptions of the technique, it has a negative effect on the accuracy of the calibration.

One of the solutions proposed for solving this problem consists in finding the ''optimal'' distance where the magnitude of the ''standing wave'' becomes negligible.[3] However, as the distance between the microphones is increased, the influence of reflections from the walls of the (in practice less than perfect) anechoic chamber will be more serious, making this solution impractical. It has also been suggested to tilt the axis of one of the microphones a few degrees,[4,5] but this method has never been examined in practice because of the practical difficulties in the mechanical positioning of the microphones.

The interference problem has hitherto been analyzed in the frequency domain by comparing transfer impedances measured using different distances between the microphones.[5,8] However, a fast Fourier transform (FFT)-based, time-selective technique has recently been developed and applied to the free-field reciprocity calibration.[11] This technique makes it possible to determine the impulse response corresponding to the electrical transfer impedance and thus identify the direct impulse response between the microphones and responses resulting from unwanted reflections. Subse-

[a]Electronic mail: sbf@oersted.dtu.dk
[b]Electronic mail: kr@oersted.dtu.dk
[c]Electronic mail: fja@oersted.dtu.dk
[d]Electronic mail: lmuniz@cenam.mx

quently the undesirable components can be eliminated by means of time-windowing.

Quantifying the interference phenomenon is not easy. There is no analytical solution to the wave equation for the geometry of the two microphones facing each other. Numerical methods such as the boundary element method (BEM) can solve the problem, but substantial computer resources will be required. In a recent paper concerned with the scattering of an array of closely spaced microphones, Ihlárova and Jacobsen used a three-dimensional BEM formulation for simulating a 3×3 microphone array and added the pressure increase on the diaphragm of the microphone located in the center of the array caused by each of the surrounding microphones, one at a time.[12] Although this procedure does not give the complex interference that occurs when all the microphones are interacting at the same time, it gives a fairly good approximation. This approximate procedure was developed because of the large amount of computational resources required for direct modeling of the microphone array. Although there are only two microphones in the free-field reciprocity arrangement, it is specified in the standard that the length of the rods on which the microphones are mounted should be ''long compared to the diameter of the microphones,'' to avoid interference from the end of the rods,[1] and in practice rods more than 20 times longer than the diameter are used. Thus, the number of required elements of the BEM model would be as prohibitive as in case of the microphone array studied in Ref. 12. However, the case where the axes of the microphones are aligned can be modeled using a far more economical axisymmetric formulation.[13]

The problem of the interference between the transmitter microphone and the receiver microphone is not only relevant in a free-field reciprocity calibration, but also for comparison methods where the transducers under study are closely located in front of each other. Thus, our purpose in this paper is to analyze the interference between the source and the receiver in free-field calibration in general. The time-selective technique described in Ref. 11 is used for examining the ''standing wave'' when the microphones are aligned and for investigating the effect of tilting one of the microphones. The experiments are supplemented by BEM calculations.

II. THE INTERFERENCE MECHANISM

Consider a source with finite dimensions and another (passive) body, the receiver, some distance away in a free field. If a portion of the surface of the source moves with a given velocity distribution it will generate a sound wave that propagates away from the source. A fraction of the sound energy is scattered by the receiver back toward the source. When this backscattered wave impinges on the body of the source, it gives rise to yet another wave that propagates toward the receiver. Thus, the receiver will register the direct wave and the secondary reflection from the source.

In the case at hand the source and the receiver are condenser microphones in a free-field reciprocity calibration setup. As specified in the standard, the two microphones are mounted on long cylindrical rods with the same diameter and placed in front of each other in an anechoic room.[1] It would be interesting to estimate the ratio of the direct wave to the secondary reflection at the receiver microphone. To get an idea about this ratio three cases can be considered: pure specular reflection, scattering when the dimensions of the two bodies are much shorter than the wavelength, and scattering when the dimensions are much larger than the wavelength.

A. Specular reflection

Consider a point source located on an infinite, rigid baffle, and a second parallel, rigid baffle located at a distance d in front of the baffled source. The receiver is the point on the second baffle directly in front of the point source. A wave emitted by the source will travel the distance d toward the baffled receiver, where it will be reflected back. The reflected wave can be regarded as generated by an image source located at a distance d behind the reflecting baffle. The reflected wave will travel back to the baffle with the original source, where it is reflected once again. This second reflection can be thought to be caused by a second image source located at a distance of $2d$ behind the baffled source. Thus, when the second reflection reaches the receiver in front of the source, the sound wave has traveled three times the distance between the baffles. Note that the second image source has the same strength as the original source, because the energy is fully reflected from the infinite baffles. Therefore, the logarithmic ratio of the amplitude of the second reflection to the amplitude of the direct wave at the receiver position is

$$R = 20\log\left(\frac{d}{3d}\right) = -9.54 \text{ dB}. \tag{1}$$

The relation between the amplitudes of reflected waves at two different distances between the baffles can be expressed as the logarithmic ratio of the distances,

$$R' = 20\log\left(\frac{d_1}{d_2}\right). \tag{2}$$

B. Scattering

When the diameters of the source and the receiver are smaller than or comparable with the wavelength, specular reflection is not very realistic; it seems more reasonable to assume that the sound wave generated by the source is scattered by the second body. This means that the reflected energy will only be a fraction of the energy emitted by the source. This fraction may be expected to be related to the solid angle formed by the receiver, as seen from the source. The most adequate way of establishing the relation between the direct wave and the backscattering from the receiver microphone would be to solve the wave equation with the boundary conditions posed by the bodies of the microphones. However, this problem cannot be solved analytically. Therefore the simple case of scattering by a sphere is analyzed instead, on the assumption that it can, at least, illustrate the phenomenon and give an idea about orders of magnitude.

Assuming harmonic variation with the $e^{-j\omega t}$ sign convention, the sound pressure scattered by a solid sphere of radius a, centered at the origin of a spherical coordinate system, can be calculated from the expression[14]

$$p_s(r,\theta) = -A\sum_{m=0}^{\infty}\{(2m+1)j^{m+1}e^{-j\delta_m} \times \sin\delta_m P_m(\cos\theta)h_m(kr)\}, \quad (3)$$

where A is the amplitude of a plane wave incident in the direction $\theta=0$, $h_m(x)$ is the spherical Hankel function of first kind and order m, P_m is the Legendre function of order m, k is the wave number, r is the distance to the observation point, and the angle δ_m is defined as

$$\delta_m = \arctan\left\{\frac{(m+1)j_{m+1}(ka) - mj_{m-1}(ka)}{mn_{m-1}(ka) - (m+1)n_{m+1}(ka)}\right\}. \quad (4)$$

In this expression, j_m and n_m are the spherical Bessel and Neumann function of order m.

If the two transducers in a free-field calibration setup may be approximated by spheres, and if it can be assumed that the wave from one sphere may be regarded as locally plane when it arrives at the other sphere, it follows that the amplitude of the sound wave impinging on the receiving sphere after being scattered by both spheres in succession is

$$\begin{aligned} p_{s,2} &= -p_s\sum_{m=0}^{\infty}\{(2m+1)j^{m+1}e^{-j\delta_m} \times \sin\delta_m P_m(\cos\pi)h_m(kr)\} \\ &= A\left[\sum_{m=0}^{\infty}\{(2m+1)j^{m+1}e^{-j\delta_m} \times \sin\delta_m P_m(\cos\pi)h_m(kr)\}\right]^2, \end{aligned} \quad (5)$$

where the distance between the spheres is r. It is apparent that the ratio of the secondary reflection to the incident sound pressure depends on three quantities; the radius of the spheres (which is present in the angles δ_m), the distance between the spheres, and the frequency. When $ka \ll 1$ the infinite series in Eq. (5) can be truncated to the first two terms, $m=0$ and 1,[14] and thus

$$\begin{aligned} \frac{p_{s,2}}{A} &\approx (je^{-j\delta_0}\sin\delta_0 P_0(\cos\pi)h_0(kr) \\ &\quad - 3e^{-j\delta_1}\sin\delta_1 P_1(\cos\pi)h_1(kr))^2 \\ &= \left\{\frac{e^{jkr}}{kr}\left[e^{-j\delta_0}\sin\delta_0 + 3e^{-j\delta_1}\sin\delta_1\cos\pi\left(1+\frac{j}{kr}\right)\right]\right\}^2, \end{aligned} \quad (6)$$

which, with the asymptotic values of the spherical Bessel and Neumann functions for small arguments,[14] simplifies to

$$\frac{p_{s,2}}{A} = \left(\frac{e^{jkr}}{kr}\frac{(ka)^3}{3}\left(1+\frac{3}{2}\left(1+\frac{j}{kr}\right)\right)\right)^2. \quad (7)$$

When $ka \gg 1$, Eq. (3) becomes[14]

$$|p_s| = |A|\frac{a}{2r}, \quad (8)$$

and thus

$$\left|\frac{p_{s,2}}{A}\right| = \left(\frac{a}{2r}\right)^2. \quad (9)$$

Equation (7) shows that the scattered pressure is much lower than the direct pressure at low frequencies, but depends strongly on the frequency. It can also be seen that the ratio decreases roughly by 12 dB as the distance r is doubled. At high frequencies, Eq. (9) shows that the scattered pressure approaches a frequency-independent fraction of the direct pressure, and the ratio decreases by 12 dB when the distance is doubled.

Equation (3) shows that the scattered pressure depends on the cosine of the incidence angle, θ, which equals π for straight backscattering as in Eq. (6). The cosine is a slowly varying function for arguments around π. At high frequencies there is no influence of the angle at all (except at $\theta=0$ in the shadow zone behind the sphere).[14] Thus, insofar as one can draw conclusions about microphones from spheres, only a modest influence of small tilting angles in the calibration setup can be expected.

It seems reasonable to present the results of the foregoing considerations in the same way as Eqs. (1) and (2). Thus, from Eq. (7), the ratio of the secondary reflection to the direct sound is

$$R \approx 40\log\left(\frac{5}{6}\frac{k^2a^3}{d}\right), \quad (10)$$

at low frequencies, and, from Eq. (9),

$$R = 40\log\left(\frac{a}{2d}\right), \quad (11)$$

at high frequencies, and the ratio of the amplitudes of the secondary reflection at two different distances is

$$R' = 60\log\left(\frac{d_1}{d_2}\right), \quad (12)$$

at low as well as at high frequencies.

III. EXPERIMENTAL RESULTS

Some experiments have been carried out with a setup for free-field reciprocity calibration in an anechoic room using the measurement technique described in Ref. 11. The anechoic room used in these experiments was not the very small room described in Ref. 11, but DTU's ''small anechoic room,'' with free space dimensions $4.8\times4.1\times2.9$ m and a lower limiting frequency of about 100 Hz.[15] The microphones were mounted on long cylindrical rods. The electrical transfer impedance between two microphones was measured frequency by frequency, and the corresponding impulse response was calculated by an inverse fast Fourier transform. Two cases were studied, frontal incidence where the axes of the microphones coincided, and oblique incidence where one of the microphones was tilted a few degrees. The experimental arrangement is shown schematically in Fig. 1.

A. Frontal incidence

Although microphones are not spheres it is interesting to compare the experimental results with a prediction based on

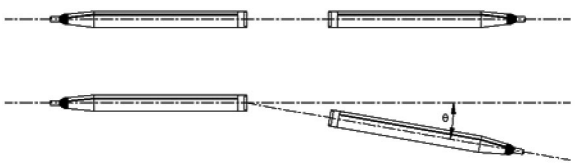

FIG. 1. A simplified sketch of the experimental arrangement. The top figure represents the case of frontal incidence, and the figure below represents the case where the axis of one of the microphones has been tilted at an angle θ.

Eq. (5). The electrical transfer impedance between two microphones represents the ratio of the output voltage of the receiver microphone to the input current through the transmitter microphone.[1] If microphones scatter sound as spheres then the electrical transfer impedance is modified as follows:

$$Z'_{e,12} = Z_{e,12}\left(1 + \frac{p_{s,2}}{A}\right), \tag{13}$$

where $Z_{e,12}$ is the ideal electrical transfer impedance and the second term in the parentheses represents the error due to the ''standing wave.'' The ideal transfer impedance is calculated as described in Ref. 11 on the basis of expressions given in Ref. 1.

Figure 2(a) shows the logarithmic modulus of the Hilbert envelope of two impulse responses between two 1-in. laboratory standard (LS1) microphones of type Brüel & Kjær (B&K) 4160 at two different distances, 200 and 280 mm. Figure 2(b) shows the corresponding theoretical impulse responses, calculated from Eq. (13), on the assumption that the microphones scatter sound as spheres with the same diameter.

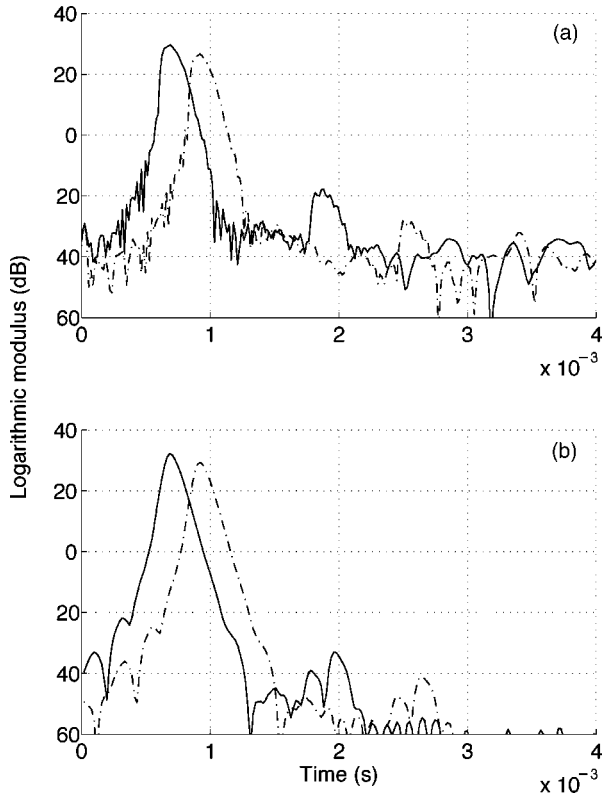

FIG. 2. The logarithmic modulus of the Hilbert envelope of the impulse response with two different distances between the microphones: —, 200 mm; –·–, 280 mm. (a) Experimental results; (b) the calculation in which the microphones are approximated by spheres.

Whereas it may be difficult to separate the direct sound from the reflections in the frequency response, these components are clearly differentiated in the time domain. The perturbation that occurs just after the direct impulse response is due to the ''standing wave'' between the microphones; as expected, it appears at an instant corresponding roughly to the time it takes a wave front to travel three times the distance between the microphones. Subsequent disturbances are caused by reflections from the walls; they appear at instants corresponding to the time it may take a wave to travel from the transmitter microphone through reflections from the walls to the receiver microphone.

According to the analysis in Sec. II the secondary reflection will decrease rapidly as the distance between the microphones is increased if the phenomenon essentially is scattering; according to Eq. (12) it should decrease by 8.8 dB when the distance is increased from 200 to 280 mm. On the other hand, if the phenomenon is specular, the reflection should decrease much less, only 2.9 dB according Eq. (2). It can be seen from Fig. 2 that the peak value of the secondary reflection decreases by about 10 dB both in the experimental case and in the theoretical prediction based on approximating the microphones with spheres. This demonstrates, perhaps not surprisingly, that the phenomenon is scattering rather than specular reflection. It also confirms that the amplitude of the ''standing wave'' is reduced more rapidly than the direct sound when the distance between the two microphones is increased. However, this may not be a practical solution because the signal-to-noise ratio becomes very poor as the distance is increased, and reflections from the walls become more serious.

At a distance of 200 mm between the objects the secondary reflection is about 15 dB stronger compared with the direct sound in the experimental results than in the case of scattering by spheres. This is not totally unexpected since backscattering depends on the shape of the scattering object. For example, at low frequencies the amplitude of a scattered wave from a sphere differs from the scattered wave from a disk by a factor of $5\pi/4$.[16] The shape of the pulse representing the secondary reflection also depends on the scattering object; for example, the double peak seen in Fig. 2(b) is due to the fact that the sound wave travels around the sphere. Furthermore, LS1 microphones have a small front cavity or recess that may act as a resonator, increasing the backscattering; see Fig. 3.

The influence of the front cavity has been examined experimentally by measuring the electrical transfer impedance between two microphones with and without the front cavity. Figure 4 shows the Hilbert envelope of the impulse response of measurements with a pair of microphones of type B&K 4160 and a pair of microphones of type B&K 4145 without a protection grid located 200 mm from each other. The impulse responses have been normalized to the same amplitude of the direct sound.

The first disturbance after the direct impulse response is the result of the ''standing wave,'' which appears at an in-

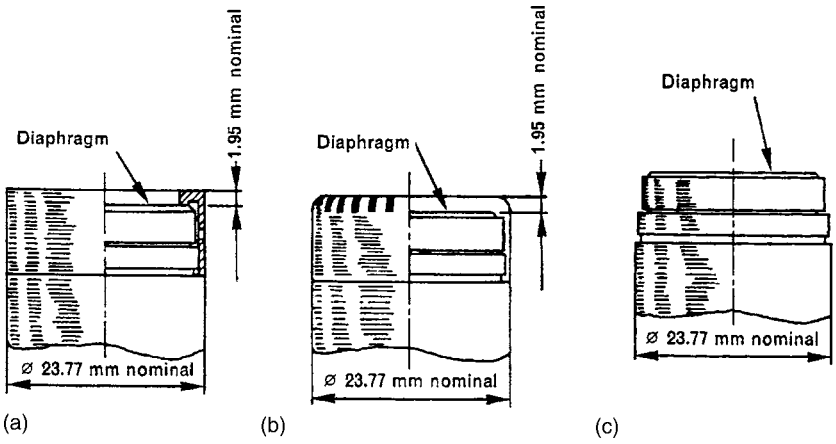

FIG. 3. (a) Microphone of type LS1 (B&K 4160); (b) the microphone of type B&K 4145 with a protection grid; (c) the microphone of type B&K 4145 without a protection grid.

stant corresponding to the time it takes a wave front to travel three times the distance between the microphones. Later reflections from the mounting setup can be neglected in this analysis. It can be seen that the amplitude of the secondary reflection of the microphones with a front cavity is nearly two times larger than that of the B&K 4145 microphones. This may be due to a transversal resonance of the front cavity, or the cavity may act as a focusing element that amplifies the backscattering.

B. Oblique incidence

Figure 5 shows the Hilbert envelope of the impulse responses between two LS1 microphones obtained from measurements where one of the microphones has been tilted 0°, 2°, 4°, and 8°. The amplitudes are normalized by the amplitude of the direct sound. Again there is first an echo at about 2 ms, which is the time it takes the secondary reflection to reach the receiver microphone. Subsequent reflections are caused by traverse rods of the mounting setup; they can be disregarded in this analysis. It can be seen that neither the amplitude nor the shape of the echo related to the ''standing wave'' between the microphones changes significantly for tilting angles up to 4°, and the impulse response with angles of 0° and 2° almost coincide. The most significant change occurs with an angle of 8°.

A similar experiment was made with microphones without the front cavity, type B&K 4145, without protection grid; Fig. 6 shows the results. As mentioned before, there is a geometrical difference between an LS1 microphone and the B&K 4145; the former has a front cavity and the latter has not. It is known that this difference has a significant effect on the free-field sensitivity.[17] The temporal positions of the echoes are the same as in the previous experiment, but the change in the amplitude and shape is much less pronounced. In fact, there is no significant change in the amplitude at any angle, although the shape of the echo seems to widen and split into two components at 8° in the same way as observed with the B&K 4160 microphones. Presumably the stronger backscattering of the B&K 4160 microphones and the larger effect of tilting the microphone can be attributed to a focusing effect due to the front cavity.

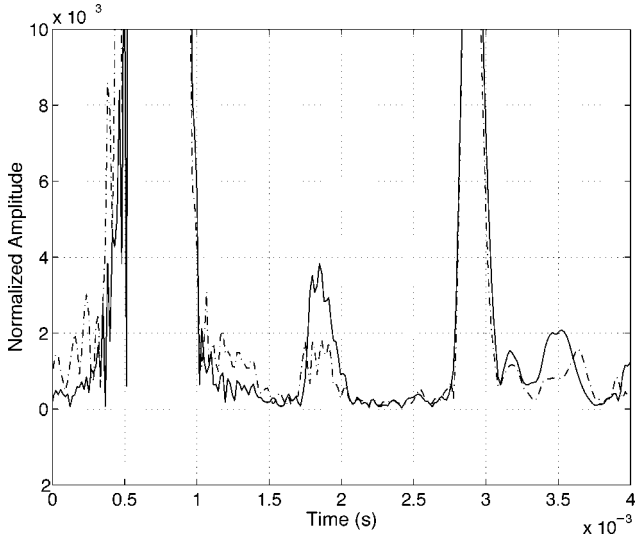

FIG. 4. A comparison between the Hilbert envelope of the normalized impulse response of the electrical transfer impedance between two microphones located at a distance of 200 mm from each other. —, LS1 microphones (type B&K 4160); –·–, microphones of type B&K 4145 without a protection grid.

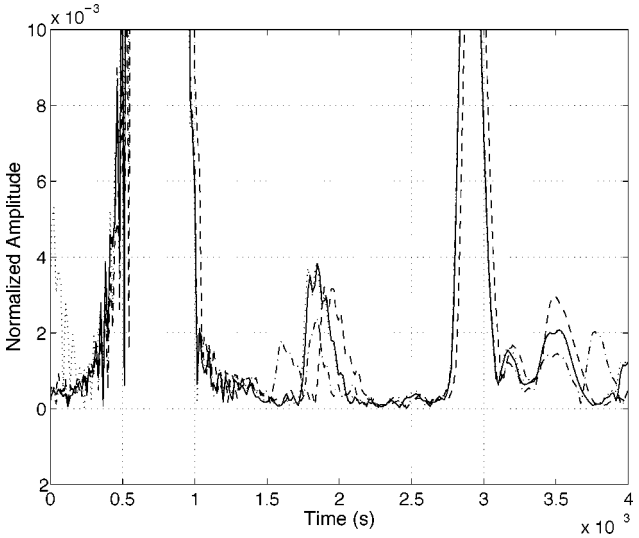

FIG. 5. The Hilbert envelope of the normalized impulse response corresponding to the electrical transfer impedance between two LS1 microphones (type B&K 4160), one of which is tilted at different angles. —, 0°; ···, 2°; –, 4°; –·–, 8°.

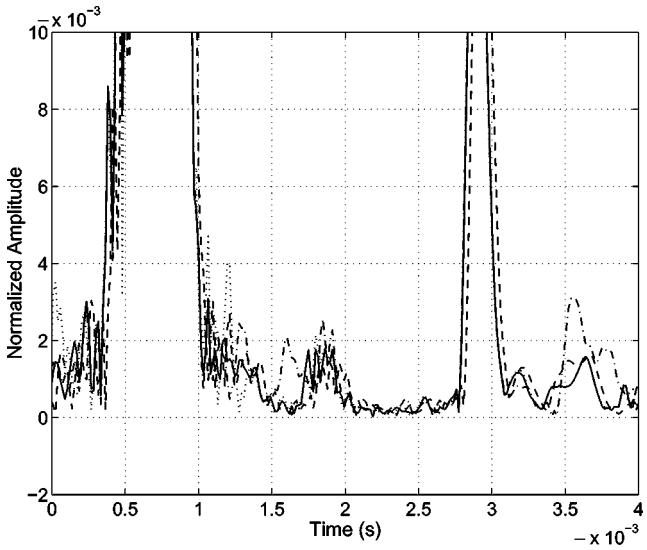

FIG. 6. The Hilbert envelope of the normalized impulse response corresponding to the electrical transfer impedance between two microphones of type B&K 4145 without a protection grid, one of which is tilted at different angles. —, 0°; ···, 2°; –, 4°; –·–, 8°.

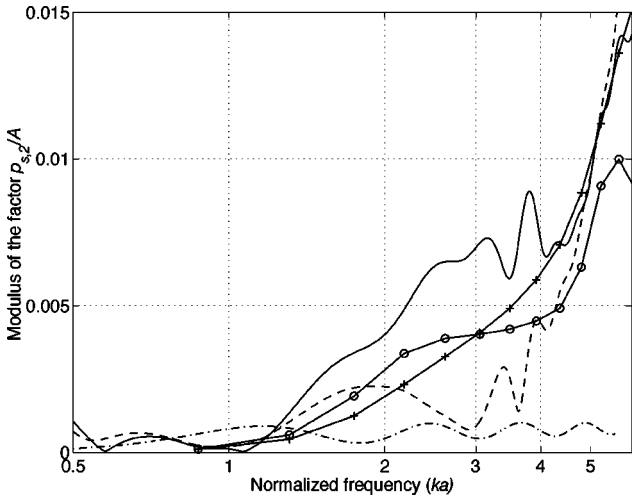

FIG. 7. The ratio of secondary reflection to direct sound at a distance of 200 mm between the objects. –○–, numerical results for LS1 microphones; –+–, numerical results for microphones of type B&K 4145 without a protection grid; –·–, spheres; —, experimental results for LS1 microphones (type B&K 4160); –, experimental results for microphones of type B&K 4145 without a protection grid.

IV. NUMERICAL RESULT

To obtain a more realistic estimate of the amplitude of the secondary reflection than provided by approximating the microphones with spheres, a numerical solution of the scattered field is needed. This can be obtained by applying the Boundary Element Method (BEM).

First, the problem of obtaining an estimate of the factor $(p_{s,2}/A)$ for frontal incidence is considered. For this purpose, an axisymmetric BEM formulation is used.[13] A plane wave is incident on the body of a microphone mounted on a long rod. The rod has a length of 60 cm and is rounded at the end. The finite length introduces a small disturbance in the simulated results because of the reflections from the end, but it is expected that the amplitude of such a disturbance is small. The highest frequency in the calculations is 30 kHz. The size of the smallest element in the axisymmetric mesh is 2.5 mm. Thus, there are at least four elements per wavelength at the highest calculation frequency.

It is well known that BEM solutions for exterior problems can be contaminated by spurious results associated with fictitious eigenfrequencies in the internal domain of the geometry.[18] This is also known as the nonuniqueness problem. In the case at hand this problem can occur above about 10 kHz. The nonuniqueness problem has been avoided by adding a random CHIEF point, as described in Ref. 18 and further checked by calculating the condition numbers of the BEM matrices[19] and by repeating calculations with small frequency shifts.

Figure 7 shows the modulus of the factor $(p_{s,2}/A)$ for the microphones with and without a front cavity. The modulus has been determined from the BEM calculations and, for a comparison, also from the experimental results shown in Fig. 5. The BEM calculations are based on the ratio of the direct wave to the backscattered wave. The experimental results have been determined by time windowing the direct impulse response and the disturbance caused by the ''standing wave'' using the technique described in Ref. 11, and then transforming them to frequency responses by applying the Fourier transform, and eventually calculating the ratio of the disturbance to the direct wave. The case of the sphere is also presented.

It can be seen that the ratio is significantly larger for microphones than for spheres. It is also apparent that there are substantial differences between the backscattering of the two types of microphones. Whereas the calculated ratio for the microphone without the front cavity increases nearly monotonously with the frequency, there is a change in the slope from ka values between 2.5 and 5 for the microphone with a front cavity. This more irregular behavior may be caused by the influence of the first radial resonance of the front cavity. The experimental results for the B&K 4160 microphones appear to be in tolerable agreement with the numerical calculations, considering the fact that they are experimental second-order data determined with a very poor signal-to-noise ratio. The experimental results for the B&K 4145 microphones are in poor agreement with the numerical results for ka values between 2 and 5.

Finally, it would be interesting to have an illustration of the sound field around the microphones. This can be determined by simulating two microphones in front of each other. The diaphragm displacement, η, of the transmitter microphone under uniform pressure conditions is

$$\eta(r) = \left[\frac{J_0(k_M r)}{J_0(k_M a)} - 1\right]\eta_0, \tag{14}$$

where J_0 is the Bessel function of zeroth order, η_0 is a constant that describes the amplitude of the movement, k_M is the wave number of the diaphragm, a is the radius of the diaphragm, and r is the radial coordinate. Equation (14) is expected to represent the actual distribution fairly well.[20] Thus, the simulated geometry consists of two microphones mounted on rods, facing each other. The same meshing parameters as in the previous calculations were used, but this

FIG. 8. The sound field between the two LS1 microphones, 20 cm apart in a free-field reciprocity setup at 20 kHz. The dark zones indicate minimum values, and the bright zones indicate the maximum values of the sound pressure.

time the sound pressure was calculated in a mesh around the microphones. Figure 8 shows the calculated sound field around for the LS1 microphones at 20 kHz. An interference pattern is apparent in front of the receiver microphone.

V. DISCUSSION

The term ''standing wave'' is somewhat misleading, and it would seem to be better to call the phenomenon an interference between the direct wave and the result of scattering by the two microphones. This interference cannot be eliminated by tilting the axis of one of the microphones a few degrees, as suggested; fairly large angles are required. However, this would introduce additional complications. For example, the acoustic center of a microphone, which is essential to know in free-field reciprocity calibration,[1] depends on the angle of incidence.

The interference problem is larger for LS1 microphones, which have a front cavity, than for microphones without a front cavity, such as B&K 4145 without a protecting grid, in agreement with the fact that the latter have a more uniform directional behavior as a function of frequency than microphones with a front cavity.[17]

VI. CONCLUSIONS

The interference between the two microphones in a free-field reciprocity calibration has been analyzed in some detail. The phenomenon is an interference effect due to multiple backscattering from the bodies of the transducers rather than a ''standing wave'' between the diaphragms. Therefore, tilting the axis of one of the microphones cannot eliminate the phenomenon. Time-selective techniques seem to be more appropriate.

ACKNOWLEDGMENT

The authors would like to thank Vicente Cutanda for his constructive criticism.

[1] IEC 61094-3 (1995-11), ''Measurement microphone Part 3: Primary method for free-field calibration of laboratory standard microphones by the reciprocity technique,'' 1995.
[2] W. R. MacLean, ''Absolute measurement of sound without a primary standard,'' J. Acoust. Soc. Am. **12**, 140–146 (1940).
[3] W. Wathen-Dunn, ''On the reciprocity free field calibration of microphones,'' J. Acoust. Soc. Am. **21**, 542–546 (1949).
[4] I. Rudnick and M. N. Stein, ''Reciprocity free field calibration of microphones to 100 Kc in air,'' J. Acoust. Soc. Am. **20**, 818–825 (1948).
[5] E. W. Burnett and V. Nedzelnitsky, ''Free-field reciprocity calibration of microphones,'' J. Res. Natl. Bur. Stand. **92**, 129–151 (1987).
[6] D. L. H. Gibbings and A. V. Gibson, ''Free-field reciprocity calibration of capacitor microphones at frequencies from 19.95 kHz to 316.2 Hz,'' Metrologia **20**, 85–94 (1984).
[7] J.-N. Durocher, ''Etalonnage des microphones à condensateur en champ libre,'' J. d'Acoust. **2**, 431–436 (1989).
[8] K. Rasmussen and E. Sanderman Olsen, ''Intercomparison on free-field calibration of microphones,'' The Acoustics Laboratory, Technical University of Denmark, Report PL-07, 1993.
[9] L. L. Foldy and H. Primakoff, ''A general theory of passive linear electroacoustic transducers and the electroacoustic reciprocity theorem. I,'' J. Acoust. Soc. Am. **17**, 109–120 (1945).
[10] R. J. Bobber, ''Diffraction constants of transducers,'' J. Acoust. Soc. Am. **37**, 591–595 (1965).
[11] S. Barrera-Figueroa, K. Rasmussen, and F. Jacobsen, ''A time-selective technique for free-field reciprocity calibration,'' J. Acoust. Soc. Am. **114**, 1467–1476 (2003).
[12] I. Ihlárova and F. Jacobsen, ''An approximate method of modelling scattering by composite bodies,'' J. Sound Vib. **262**, 1235–1241 (2003).
[13] P. M. Juhl, ''A numerical investigation of standard condenser microphones,'' J. Sound Vib. **177**, 433–446 (1994).
[14] P. M. Morse and K. U. Ingard, *Theoretical Acoustics* (McGraw-Hill, New York, 1968/1984). See Sec. 8.2.
[15] F. Ingerslev, O. J. Pedersen, P. K. Møller, and J. Kristensen, ''New rooms for acoustic measurements at the Danish Technical University,'' Acustica **19**, 187–199 (1967/68).
[16] A. D. Pierce, *Acoustics. An Introduction to Its Physical Principles and*

Applications (American Institute of Physics, New York, 1989). See Sec. 9.1.
[17] Brüel & Kjær technical documentation, ''Condenser microphones data handbook,'' Nærum, 1982.
[18] H. A. Schenck, ''Improved integral formulation for acoustic radiation problems,'' J. Acoust. Soc. Am. **44**, 41–58 (1968).
[19] P. M. Juhl, F. Jacobsen, V. Cutanda, and S. Quirós Alpera, ''On the non-uniqueness problem in a 2-D half-space BEM formulation,'' *Proceedings of the 9th International Congress on Sound and Vibration*, Orlando, FL, 2002 (CD-ROM).
[20] A. J. Zuckerwar, ''Theoretical response of condenser microphones,'' J. Acoust. Soc. Am. **64**, 1278–1285 (1978).

Single-channel time reversal in elastic solids

Alexander M. Sutin[a)]
Davidson Laboratory, Stevens Institute of Technology, Hoboken, New Jersey 07030

James A. TenCate[b)]
Geophysics, MS D443, Los Alamos National Laboratory, Los Alamos, New Mexico 87545

Paul A. Johnson[c)]
Geophysics, MS D443, Los Alamos National Laboratory, Los Alamos, New Mexico 87545

(Received 15 September 2003; revised 11 August 2004; accepted 12 August 2004)

Reverberant volume time reversal in 3D elastic solids (doped glass and Berea sandstone) using a single channel are presented. In spite of large numbers of mode conversions (compressional to shear wave conversions at the walls), time reversal works extremely well, providing very good spatial and time focusing of elastic waves. Ceramics were bonded to the surface as sources (100–700 kHz); a broadband laser vibrometer (dc—1.5 MHz) was used as detector. Temporal and spatial time-reversal focusing are frequency dependent and depend on the dissipation characteristics of the medium. Doped glass (inverse dissipation Q between 2000 to 3000) shows time-reversed spatial focal resolution at about half of the shear wavelength. The Berea sandstone ($Q=50$) yields a wider focusing width (a bit more than the shear wavelength) due to its lower Q. Focusing in the doped glass is better because the time-reversal (virtual) array created by wave reflections is larger than in the highly attenuating sandstone. These are the first results reported in granular media, and are a first step toward geophysical and field applications.
[DOI: 10.1121/1.1802676]

PACS numbers: 43.20.Gp, 43.20.Jr, 43.20.Ye, 43.35.Cg [DRD] Pages: 2779–2784

I. INTRODUCTION

Time-reversed acoustics (TRA) is unquestionably one of the most interesting topics to have emerged in modern acoustics. Most of the recent innovative research in this area has been carried out by the group at the Laboratoire Ondes et Acoustique at the Université Paris 7,[1] who have demonstrated the ability and robustness of TRA (using time-reversal mirrors) to provide spatial control and focusing of an ultrasonic beam. However, the topic of time reversal had its beginnings in ocean acoustics more than 40 years ago. In fact, Parvulescu[2] filed a patent application in 1962 for a time-reversal method (which he called a matched-signal technique) for underwater communication and underwater object detection. Some of the first experiments were conducted by Parvulescu and Clay,[3] who used their matched-signal technique to study the reproducibility of signal transmission in deep ocean water over a distance of 36 km. The results of current research to apply TRA for underwater communication in the field can be found in Refs. 4 and 5 and in highly reverberant conditions in the laboratory in Refs. 6 and 7. The ability to obtain highly focused signals with TRA has numerous other applications as well, including lithotripsy,[8] ultrasonic brain surgery,[9] and nondestructive evaluation.[10,11]

Notably, the study of time reversal in solids and in the earth is still relatively new and presents questions and challenges not seen in fluids. The work reported here on laboratory-scale solids was intended, in part, to be a prelude to trying time-reversal methods in the earth. For example, seismic imaging could benefit from using time-reversal techniques—concurrent with conventional imaging techniques—to focus energy only on the strongest scatterers (e.g., fault zones) to better classify interesting underground features. We have reported on similar ideas to develop time-reversal techniques for nondestructive testing (e.g., flaw detection in solids).[12] The problem of time reversal in the earth (and in all solids) is fundamentally different from the purely acoustic one due to the excitation and propagation of both compressional (bulk) and shear waves, conversions between the two types of waves, and the scattering and potentially high losses in the medium. In the preliminary laboratory experiments reported here, solids were chosen where internal scattering from the medium is not an issue. The results shown in this paper demonstrate that time reversal works both in solids and granular media where unwanted wave conversions and high losses could easily ruin the time-reversal process.

Draeger *et al.*[13] developed a simple theory describing a time-reversal (TR) process with elastic waves. Their paper nicely illustrates the potential problems of time reversal in solids. Draeger examined the case of a compressional (P) and vertically polarized shear (SV) wave—both generated simultaneously by a point source in a solid—propagating to a time-reversal mirror somewhere in a fluid surrounding the solid. When the time-reversal mirror sends the signals from the two waves back into the solid, there are now four waves generated in the solid, a shear and a compressional wave from each of the compressional and shear waves. The ''unwanted'' waves (i.e., those which will not properly time reverse) are simply thrown away in the analysis since they

[a)]Electronic mail: asutin@stevens-tech.edu
[b)]Electronic mail: tencate@lanl.gov
[c)]Electronic mail: paj@lanl.gov

''yield a low-level noise, they are not focused, and arrive at different times.'' [13] In the reverberant volume experiments described here, the initial wave may undergo hundreds of reflections (and corresponding wave conversions), yielding potentially hundreds of unwanted waves from all these reflections. Being able to see a reconstructed source signal in spite of significant mode conversion was not an obvious outcome. We chose to examine these ideas using a simplified numerical simulation of the experiment—these results have already been published and are reported elsewhere.[14] In that simulation, we made a first attempt to model and simulate the process numerically using the local interaction method known as LISA.[15] The initial results from that work (simulating just a few reflections) were encouraging. Now that the experiments reported here have demonstrated that time reversal in granular solids works very well, research continues on extending the simulation to multiple reflections and simulating more realistic situations.

A few experiments in solids have been reported already. In one experiment, an aluminum cylinder was a basic element in a TR system developed for lithotripsy.[8] Another experiment describes TR focusing in a 2D silicon wafer where only shear (Lamb) waves can propagate. Strong temporal and spatial focusing were demonstrated. The aperture of focus for their experiment had a radius of about half a wavelength and was highly focused in time. In another work, Prada *et al.*[11] studied TR scattering techniques for nondestructive testing applications in a sample composed of titanium billets and, unlike experiments described here, carefully avoided all reflections from the surfaces of the billet.

In this work we describe results from single-channel, 3D experiments in two solids, a doped glass and a fine-grained Berea sandstone. Both are essentially experiments in solid reverberant volumes with numerous wave conversions. These wave conversions were absent in the 2D silicon wafer experiments discussed above.[16,17] The doped-glass sample was used as a low dissipation standard and was chosen because it has a similar wave speed to compare with the sandstone (which has high dissipation). Unlike earlier experiments conducted with solids, submersion in a fluid to conduct TR studies is neither possible nor desirable in many solids. Thus, in these experiments, we also report on the first use of direct-coupled transducers on solids in tandem with a large-bandwidth laser detector. We show that despite the fact that the transducer radiates primarily compressional waves, the TRA spatial focusing has a width comparable with a half wavelength of the shear wavelength. We surmise that shear waves dominate the reverberant wave field due to numerous wave conversions for each reflection at each free surface. This paper begins with a description of the experimental procedure, followed by a description of experimental results, discussion, and conclusions.

II. EXPERIMENTAL PROCEDURE

In experiments conducted in fluids, the same device is frequently used for both source and receiver, either by itself or as part of an array.[13,16,17] In the experiments in solids described here, a single piezoelectric ceramic disk directly bonded to the sample surface was used as a source for both the initial waves and also for the time-reversed waves (Fig. 1). The ceramic operated in thickness mode and thus generated primarily compressional waves. The received signal—specifically the motion normal to the surface—was detected at various places on the solid by a laser vibrometer which measured surface velocity (a Polytec 301 with 303 laser head). The laser vibrometer is a noncontact measurement device and thus experiences no coupling effects, and has a flat, broadband response from near-dc to 1.5 MHz. The sample was placed on an optical table and the laser vibrometer was placed on a translation stage.

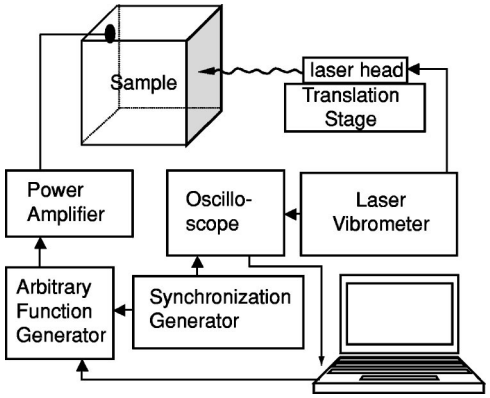

FIG. 1. Experimental setup for measurements of single channel, time reversal in solids.

A typical time-reversal experiment in these solids was carried out in the following way. A short, triangular pulse (see Fig. 2) was generated by an arbitrary waveform signal generator (HP 33120A), amplified by a power amplifier (Krohn-Hite 7500), and applied to the transducer. The transducer generated a fairly broad, multifrequency tone burst into the sample. The laser vibrometer was then aimed at one of several arbitrary points on the opposite wall of the block being tested. The recorded signal—a fairly long wave train consisting of the initial arrival and its reverberation or *coda*[18]—was time reversed and then fed into the arbitrary waveform generator and radiated *from the original source* as done by Draeger *et al.*[17] The time-reversed signal then propagates through the sample and is detected by the laser vibrometer. The focusing aperture was obtained by conducting repeated measurements across the sample face with the laser mounted on a translation stage. We note that these time-reversal experiments were conducted for several different receiver locations—although not near an edge or corner—in each block and, somewhat surprisingly, *qualitatively the time-reversal focus does not depend on the where the receiver is placed*. A quantitative study of the influence of receiver location is beyond the scope of this paper, but should be conducted.

III. OBSERVATIONS AND RESULTS

A. Doped-glass block

The first experiment was carried out in a $101\times89\times89$-mm doped glass parallelepiped. The bulk wave speed in the sample was approximately 3000 m/s with a quality factor Q (inverse dissipation) between 2000 and 3000 in the

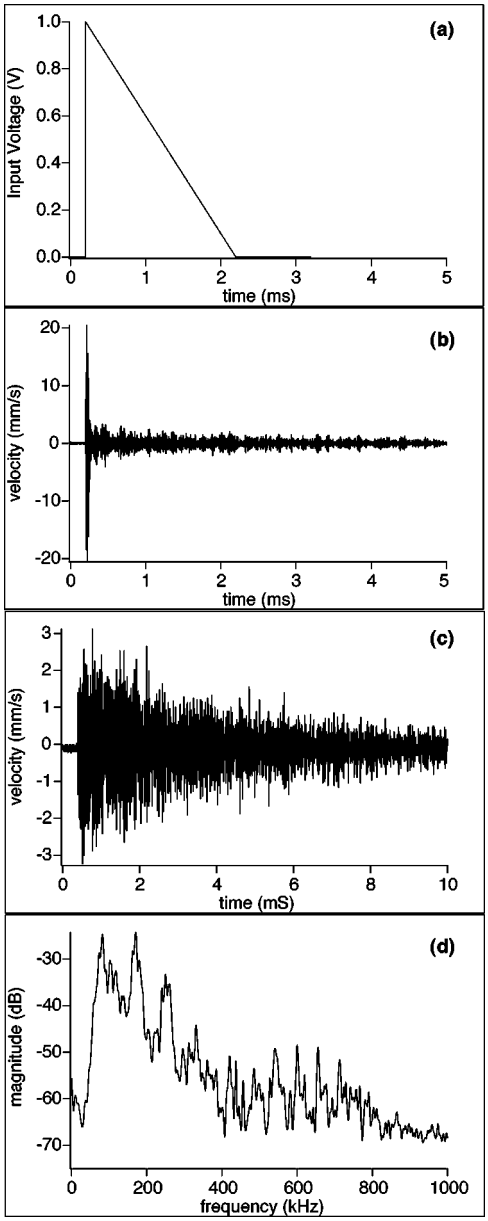

FIG. 2. Input and detected waves in the doped glass sample: (a) the electrical input into the ceramic; (b) the signal detected using the laser vibrometer on the back side of the ceramic; (c) the detected signal after traversing the sample, measured with the laser vibrometer and (d) the spectrum of the detected signal.

frequency bands used. The wave speed was measured by a standard time-of-flight method, and the Q from resonance peak width. The doped-glass sample was selected as a standard to compare with the (granular) sandstone because the wave speeds are similar but the structure is much less complex. A 50-mm-diameter, 2.8-mm-thick piezoceramic disk was epoxied with its center 28 mm from the corner of two sides of the sample, as shown in Fig. 1.

A short, triangular-shaped pulse was applied to the transducer [Fig. 2(a)]. The resulting signal broadcast into the solid was measured on the backside of the transducer using the laser vibrometer and is shown in Fig. 2(b). The signal that arrived on the opposite side (not far from the sample center in this particular case) was measured by the laser vibrometer and is shown in Fig. 2(c). The detected signal was then bandpass filtered from 100–700 kHz to eliminate low- and high-frequency noise; its frequency spectrum is shown in Fig. 2(d). Notice that the direct signal consists of the first few arrivals and almost 10 ms of coda (which includes over 300 reflections directly back and forth within the sample and a host of side-wall reflections as well). It is known that coda consists of primarily shear wave energy[18] and, as mentioned later, appears to be the case in these experiments as well.

The recorded signal was time reversed, Fig. 3(a), normalized to 1 V p-p, and rebroadcast using a $\times 100$ fixed amplification. The resulting refocused signal [shown in Fig. 3(b); zoom shown in Fig. 3(c)] was nicely reconstructed. The refocused signal was also highly compressed, 50 μs in contrast with the 6000-μs-long time-reversed signal. The noticeable ''echoes'' shown on either side of the refocused signal are possibly due to the geometry of the sample or perhaps due to the size of the transmitter. It is also well known that with additional transducers the echoes will be minimized, but that is not the purpose of these experiments. In any case, it is normal that one does not recreate a perfect pulse, since the TR field is not recorded everywhere. For instance, similar, but much smaller, echoes are shown in results in Draeger and Fink.[16]

Identical measurements were carried out for several different receiver points (on the remaining five sides), and it was found that the TRA focusing did not depend on the point of measurement. In fact, we have shown elsewhere that TRA focusing does not depend on the form of the resonator either; TRA focusing was observed in cylinders, diamond shapes, and other complex forms of acoustical resonators being tested for various medical applications.[19]

Application of a filter with center frequency near one of the coupled source/sample resonances on either the time-reversed signal or the final refocused signal greatly improved the amplitude and signal-to-noise ratio of the time reversal as one might anticipate from the spectrum shown in Fig. 2(d). When we chose to bandpass filter the received signal before reinjecting it at two of the spectral peaks—210 to 310 kHz (center frequency 260 kHz) and 700 to 800 kHz (center frequency 750 kHz)—time reversal was improved for the higher frequency bandpass-filtered signal [see Figs. 3(d)–(i)]. The resulting refocused pulses have durations of 15 μs for the 260-kHz bandpass filter and 10 μs for 750-kHz bandpass filter. The spatial distribution of the TR focused signal amplitude is presented in Fig. 4 for the horizontal [4(a) and vertical 4(b)] directions using the three bandpass filters. Amplitudes are measured peak amplitudes of the TR signal at each position, normalized to the maximum measured amplitude. The points are the actual data values and the lines are smooth fits to each measurement group. The width measured at -3 dB is approximately 3.6 mm for the 100–700-kHz bandpass signal, 2.8 mm for the signal bandpass filtered at a center frequency of 260 kHz, and about 1.2 mm for the signal bandpass filtered at a center frequency of 750 kHz. Note that the longitudinal (compressional) and shear wavelengths for these two frequencies are 12 mm (6.4 mm shear) and 4 mm (2.3 mm shear), respectively. Since the field of a symmetric spherical converging wave is described by $\sin(kr)/kr$, where the wave number $k=2\pi/\lambda$, the diffraction limit of the

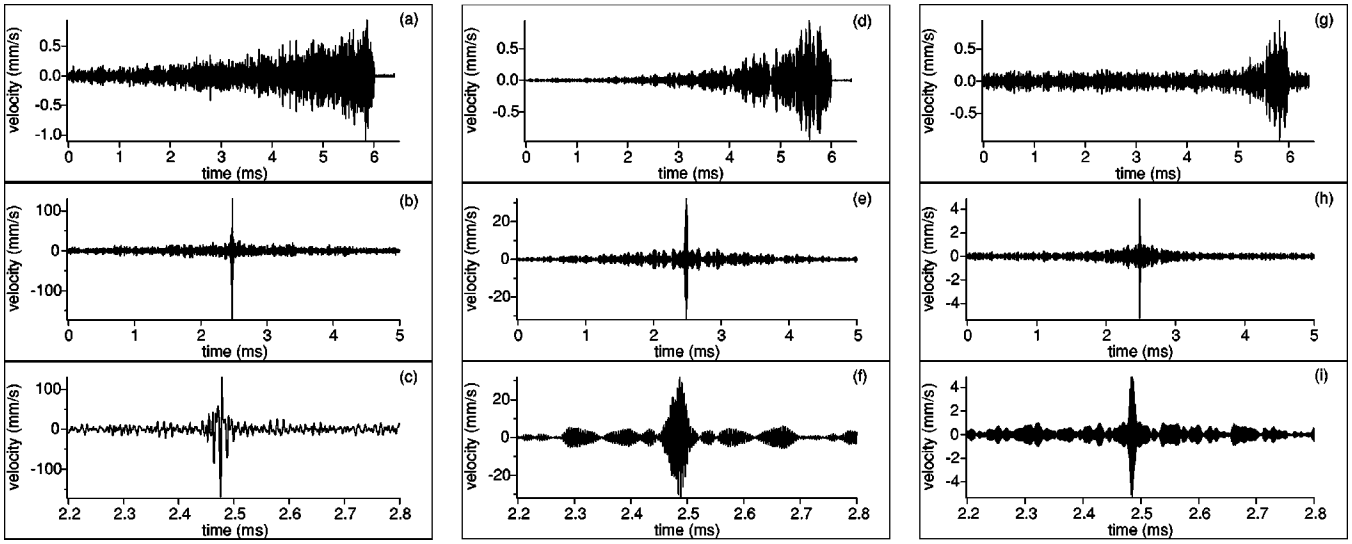

FIG. 3. Time-reversal results in doped glass for select frequency bands. Column 1 shows the (a) detected signal (time reversed); (b) the resulting time-reversed signal; and (c) its zoom for 100–700-kHz bandwidth. Column 2 (d)–(f) shows the same results for a 220–280-kHz bandwidth. Column 3 (g)–(i) shows the same results for a 700–800-kHz bandwidth.

focal spot is 0.44λ, quite close to what is observed in the experiment in all frequency bands studied.

The observed high degree of focusing is due to the numerous reflections of the acoustic signal from the walls of the solid, and is surprisingly good. We assume that the focusing is due to the large number of virtual sources from back-wall and side-wall reflections that exist in the material, and may well have to do with the fact that shear waves dominate in the coda.

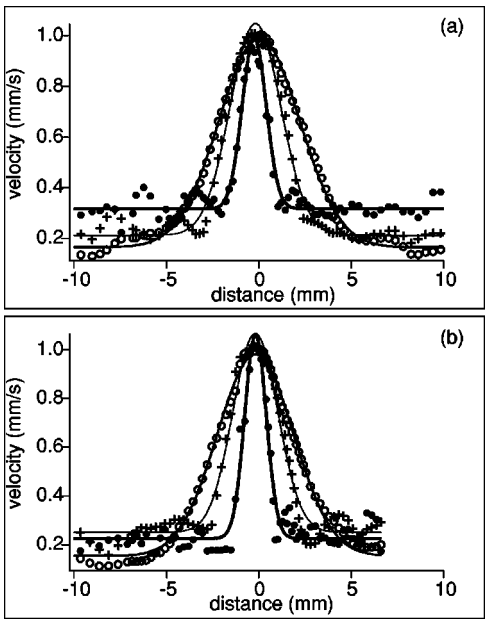

FIG. 4. Time-reversal spatial focusing pattern from time-reversal experiment in the doped glass for three different bandwidths: (a) shows the horizontal patterns and (b) shows the vertical patterns. The open circles correspond to a 100–700-kHz bandwidth, the crosses correspond to a 220–280-kHz bandwidth, and the solid circles represent a 700–800-kHz bandwidth. The solid lines are Gaussian fits to the beam patterns. Amplitudes were obtained by measuring the peak amplitude of the detected, time-reversed signal in each case. All values are normalized to the maximum detected amplitude for each bandpass interval.

B. Berea sandstone

A similar experiment was conducted for a sample of slightly different geometry and much larger dissipation, a long rough parallelepiped of Berea sandstone of dimensions $75\times75\times254$ mm. The Berea sandstone sample is a porous material composed primarily of quartz (85%) and a small fraction of feldspar (8%) grains, with kaolinite and other clays in the interstices. The wavelength in this sandstone was nearly 13 mm at the frequencies of interest, much greater than the average grain size of 100 μm, so scattering from the medium was not an issue. The bulk wave speed was around 2.2 km/s and the Q is 50—an equivalent attenuation much larger than that of the glass block.

The source signal was identical to that of the glass, and the signal emitted at the source is shown in Fig. 5(a). Figure 5(b) shows the received signal—much smaller in amplitude and shorter in duration because of high attenuation in the sample—corresponding in time to only 20 back and forth transversal before the signal is overcome by noise; the corresponding frequency spectrum is shown in Fig. 5(c). The time-reversed signal for a frequency band between 70 and 700 kHz is shown in Fig. 6(a), and the refocused signal is shown in Fig. 6(b) with its zoom in Fig. 6(c). Time reversal worked well even in the case of extremely large attenuation. As in the glass block, the spatial distribution of the TR focused signal—filtered in the frequency band between 130–200 kHz—in the sandstone was also measured and is shown in Fig. 7. The focal width at -3 dB was about 8 mm, wider than that in the glass sample and almost equal to the shear wavelength in this sample (7.8 mm). It is clear that higher attenuation and fewer reflections—and thus fewer virtual sources—restricted the focusing properties of the TR system in the sandstone, and, one can assume, in low-Q materials in general.

It is remarkable that one can virtually ignore the complications of mode conversion and treat the TR process blindly. Due to mode conversion between compressional and

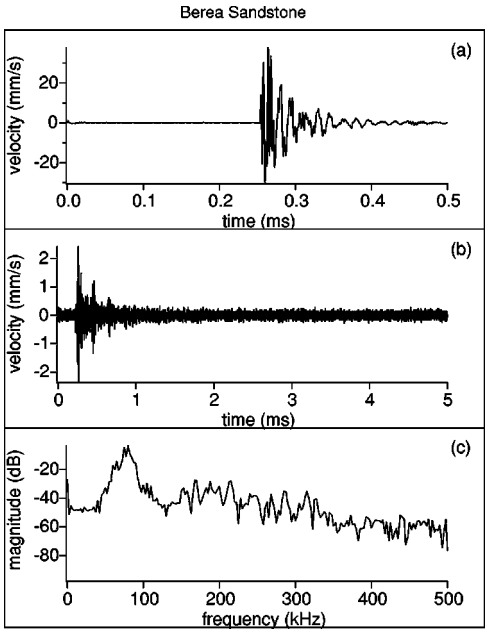

FIG. 5. Input and detected waves in Berea sandstone [the electrical input was identical to that shown in Fig. (2a)]: (a) the signal measured on the backside of the source ceramic with the laser vibrometer without filtering; (b) the direct signal that has propagated across the sandstone sample; (c) the unfiltered spectrum of the detected signal.

shear waves, reciprocity may not hold as it does in acoustical media;[20] however, this point still needs rigorous study. Nonetheless, time reversal works remarkably well in terms of spatial and temporal focusing. This is an extremely promising result because it implies that solids can be treated without concern for mode conversion that might normally be expected to complicate the problem.

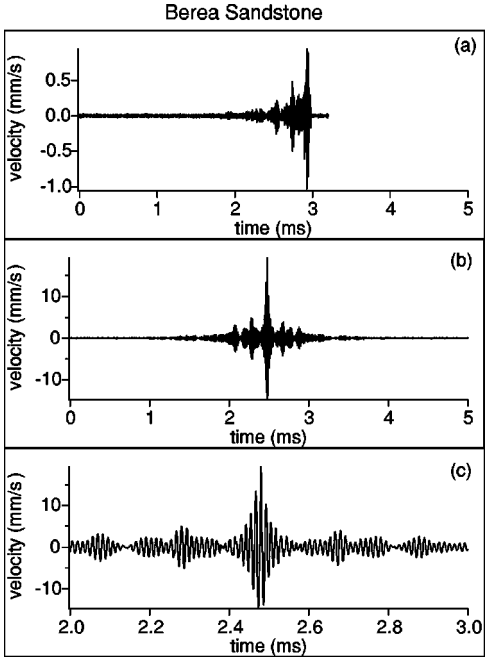

FIG. 6. Time-reversal results in Berea sandstone. (a) The detected, bandpassed (70–700 kHz) signal that has been time-reversed; (b) the resulting time-reversed signal, and its zoom (c).

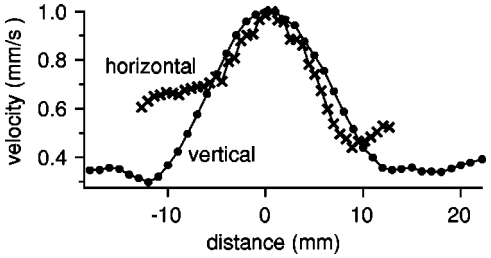

FIG. 7. The spatial distribution of the time-reversed signal amplitude in the sandstone for the vertical (closed circles) and horizontal (x's) directions. Lines serve to connect the points. Amplitudes were obtained by measuring the peak amplitude of the detected, TR signal in each case. All values are normalized to the maximum detected amplitude for each bandpass interval.

IV. SUMMARY AND CONCLUSIONS

The single-channel time-reversal experiment demonstrated extremely effective focusing of acoustic energy in time and space at an arbitrary point in three-dimensional solids where multiple compressional to shear wave conversions could have potentially destroyed the process. The role of frequency is extremely important as one might expect: filtering the TR signal, we observe focusing to a degree that is surprising (better than one would expect using the diffraction limit set by the compressional wavelength). Focusing in a lower-Q material (sandstone) is still very good, in between the compressional and shear wavelength. To our knowledge these are the first demonstrations of time reversal in granular solids.

ACKNOWLEDGMENTS

We thank Clarence Clay for pointing us to the early work on matched filtering and time reversal. We also thank Arnaud Derode, Marco Scalerandi, and Robert Guyer for reviews, discussion, and helpful comments. This work was supported by Los Alamos National Laboratory Institutional Support (LDRD).

[1] For additional references and an excellent overview, see M. Fink, "Time reversed acoustics," Sci. Am. **281**, 91–113 (1999).
[2] A. Parvulescu, Correlation system using matched signals, United States Patent #3,939,461. Filed 19 November 1962.
[3] See the discussion in I. Tolstoy and C. S. Clay, *Ocean Acoustics: Theory and Experiment in Underwater Sound* (McGraw-Hill, New York, 1966).
[4] W. A. Kuperman, W. S. Hodgkiss, H. C. Song, T. Akal, C. Ferla, and D. R. Jackson, "Phase conjugation in the ocean: Experimental demonstration of an acoustic time-reversal mirror," J. Acoust. Soc. Am. **103**, 25–40 (1998).
[5] S. Kim, G. F. Edelmann, W. A. Kuperman, W. S. Hodgkiss, H. C. Song, and T. Akal, "Spatial resolution of time-reversal arrays in shallow water," J. Acoust. Soc. Am. **110**, 820 (2001).
[6] M. G. Heinemann, A. Larraza, and K. B. Smith, "Acoustic communications in an enclosure using single-channel time-reversal acoustics," Appl. Phys. Lett. **80**, 694 (2002).
[7] A. Derode, A. Tourin, J. de Rosny, M. Tanter, S. Yon, and M. Fink, "Taking advantage of multiple scattering to communicate with time reversal antennas," Phys. Rev. Lett. **90**, 014301-1–014301-4 (2003).
[8] G. Montaldo, P. Roux, A. Derode, C. Negreira, and M. Fink, "Generation of very high pressure pulses with 1-bit time reversal in a solid waveguide," J. Acoust. Soc. Am. **110**, 2849–2857 (2001).
[9] M. Tanter, J. L. Thomas, and M. Fink, "Focusing and steering through absorbing and aberrating layers: Application to ultrasonic propagation through the skull," J. Acoust. Soc. Am. **103**, 2403–2410 (1998).
[10] E. Kerbrat, C. Prada, D. Cassereau, and M. Fink, "Ultrasonic nondestructive testing of scattering media using the decomposition of the time rever-

sal operator,'' IEEE Trans. Ultrason. Ferroelectr. Freq. Control **49**, 1103–1113 (2002).
[11] C. Prada, E. Kerbrat, D. Cassereau, and M. Fink, ''Time reversal techniques in ultrasonic nondestructive testing of scattering media,'' Inverse Probl. **18**, 1761–1773 (2002).
[12] A. Sutin, P. Johnson, and J. TenCate, ''Development of nonlinear time reverse acoustics (NLTRA) for applications to crack detection in solids,'' Proceedings of the 5th World Congress on Ultrasonics, Paris, France, pp. 121–124 (2003).
[13] C. Draeger, D. Cassereau, and M. Fink, ''Theory of the time-reversal process in solids,'' J. Acoust. Soc. Am. **102**, 1289–1295 (1997). A related paper is C. Draeger, D. Cassereau, and M. Fink, ''Acoustic time reversal with mode conversion at a solid–fluid interface,'' Appl. Phys. Lett. **72**, 1567–1569 (1998).
[14] P.-P. Delsanto, P. A. Johnson, M. Scalerandi, and J. A. TenCate, ''LISA simulations of time-reversed acoustic and elastic wave experiments,'' J. Phys. D **35**, 3145–3152 (2002).
[15] P. P. Delsanto, T. Whitcombe, H. H. Chaskelis, and R. B. Mignona, ''Connection machine simulation of ultrasonic wave propagation in materials. I. The one-dimensional case,'' Wave Motion **16**, 65–80 (1992).
[16] C. Draeger and M. Fink, ''One-channel time reversal of elastic waves in a chaotic 2D-silicon cavity,'' Phys. Rev. Lett. **79**, 407–410 (1997).
[17] C. Draeger, J.-C. Aime, and M. Fink, ''One channel time-reversal in chaotic cavities: Experimental results,'' J. Acoust. Soc. Am. **105**, 618–625 (1999).
[18] M. Fehler and H. Sato, ''Coda,'' Pure Appl. Geophys. **160**, 541–554 (2003).
[19] A. Sutin and A. Sarvazyan, ''Spatial and temporal concentrating of ultrasound energy in complex systems by single transmitter using time reversal principles,'' Proceedings of the 5th World Congress on Ultrasonics, Paris, France, pp. 863–866 (2003).
[20] See K. Aki and P. Richards, *Quantitative Seismology* (Freeman, San Francisco, 1980) Vol. 1, for a general discussion of reciprocity in solids.

On the design of long T-shaped acoustic resonators

Deyu Li and Jeffrey S. Vipperman[a)]
Department of Mechanical Engineering, University of Pittsburgh, Pittsburgh, Pennsylvania 15261

(Received 23 February 2004; revised 19 July 2004; accepted 29 July 2004)

In this work we present a more general mathematical model for the calculation of resonance frequencies for long, T-shaped acoustic resonators. The method is based upon wave propagation and, unlike previous theories, no constraints on the geometry of the resonator are imposed. In addition, a new end-correction model based upon Rayleigh's end corrections is proposed and evaluated. The theory is used to develop a plane-wave multimodal-based design theory, which permits higher-order 1-dimensional modes of the T-shaped acoustic absorber to be used for absorbing high-frequency noise within enclosures. A series of experiments are conducted on round and square cross section resonators to validate the theory, evaluate the end correction models, and demonstrate design examples. © *2004 Acoustical Society of America.* [DOI: 10.1121/1.1795336]

PACS numbers: 43.20.Ks, 43.20.Mv, 43.50.Gf [LLT] Pages: 2785–2792

I. INTRODUCTION

Since Helmholtz[1] first presented the theory of the acoustic cavity resonator, numerous articles related to Helmholtz resonator design and resonance frequency prediction have been published. The currently used formula[2,3] for the Helmholtz resonator design and Helmholtz frequency prediction was developed by Lord Rayleigh[4] and Sondhauss[5] over 100 years ago. These authors are credited with first developing the inertial end corrections, which were obtained by comparing the energy of motion with the square of the total current through the aperture plane. Ingard[6] investigated the Helmholtz resonator design theory in great detail, including scattering and absorptive mechanisms, inertial end corrections, interaction of close apertures, nonlinear and flow effects, and optimal design of the resonators. The inertial end corrections of regular geometric resonators were also investigated by Ih[7] in some detail. Alster[8] considered effects of both resonator cavity shape and mass particles' motion inside the resonator, and gave a general formula for resonance frequency predication. Panton and Miller[9] and Li and Vipperman[10,11] presented transcendental equations for the frequency calculation of a cylindrical Helmholtz resonator based on acoustic impedance matching. Chanaud[12] derived an explicit interior end correction formula based on the wave equation, in which the influence of cavity and orifice geometries was included. Bigg[13] used matched asymptotic expansions to predict the complete response curve of a cavity resonator. Note that with the exception of references,[9–11] all of the above references are based upon the classical Helmholtz resonator design, where the dimensions of the resonator cavity are assumed to be small with respect to the wavelength of the incident wave and none of them addresses the T-shaped resonator. Further, in Ref. 9, the assumptions require that the neck length be very short.

Classical Helmholtz resonators are often used to control undesired sound in large enclosures, such as concert halls or buildings. For noise control in smaller enclosures, such as cars, helicopter nacelles, aircraft cabins, and payload fairings,[10,11,14,15] the resonators are often integrated into the structure to conserve space occupied by the resonators. In fact, the US Air Force has developed a new type of composite structure[16] that has vertical wall chambers that can be used to form the volume of an acoustic resonator. The classical Helmholtz resonator is hard to integrate because of its bulbous structure. Moreover, when using Helmholtz resonators to control relatively low-frequency noise, the cavity volume or the neck length must be very large for a given opening, which also will not easily fit into a small enclosure. On the other hand, if the targeted frequency is relatively high, the designed cavity volume or the neck length of the classical resonator must be very small for the given opening, which degrades the ability of the resonator to absorb noise from an enclosure.

Our major purpose in the present paper is to discuss the design theory for a practical long, T-shaped acoustic resonator (see Fig. 1) that can be easily integrated into the structure of an enclosure, and is applicable to noise control in either small or large enclosures. Here, it is called an ''acoustic resonator'' rather than a Helmholtz resonator because the lengths of the T-shaped resonator branches may be comparable to the wavelength or longer than the wavelength of the impinging sound. Miles[17] represented a model to calculate the sound pressure and velocity distribution in a T-joint rectangular tube by using the transmission line and impedance analogy circuit. Such a T-joint rectangular tube is similar to models of woodwind musical instruments that have two open ends for each branch[18,19] (although the two coaxial branches of the T-shaped resonator have one open end and one closed end). This analytical model is useful to predict plane wave propagation (pressure response) in three branches of the T-shaped tubes at a given incident wave, but cannot be used to predict resonances of a T-shaped resonator, nor be used to design a T-shaped acoustic resonator for a given resonance frequency. A previous report by Merkli[20] proposed a model for the calculation of resonant frequencies of a T-shaped resonator

[a)]Corresponding author: Jeffrey S. Vipperman, Department of Mechanical Engineering, 648 Benedum Hall, 3700 O'Hara Street, University of Pittsburgh, Pittsburgh, Pennsylvania 15261. (412) 624-1643 (voice); (412) 624-4846 (fax).

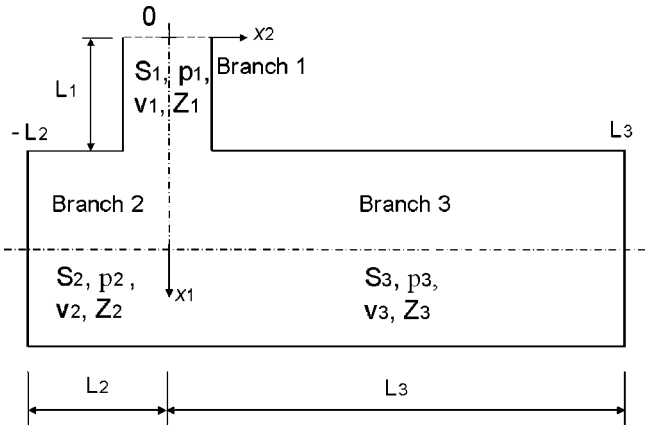

FIG. 1. Long T-shaped acoustic resonator and coordinate system.

based on the wave propagation principles in a T-shaped waveguide. However, this model is limited to the special case where the cross sections of the three branches are circular and of the same diameter, and the two collinear branches are of the same length. Moreover, his model cannot be used to directly design a T-shaped acoustic resonator because his end corrections depend on the lengths of the three branches themselves.

In this work, a more general model for the long, T-shaped acoustic resonator design and resonance frequency predication is developed, including the inertial end corrections for the three branches. The paper is organized as follows. In the second section we describe a general mathematical model of the T-shaped resonator that is based on the wave propagation theory in a waveguide. The resulting equation for the prediction of resonance frequencies is derived, along with an approach to analytically design multimodal T-shaped resonators. In Sec. III, a new model for the calculation of inertial end corrections is proposed. In Sec. IV we present the experimental validation of prediction and design formulas, including comparisons of the proposed new end corrections. Some conclusions are given in the final section.

II. DEVELOPMENT OF THE MATHEMATICAL MODEL

A long T-shaped acoustic resonator is shown in Fig. 1. All boundaries are assumed to be rigid, and the axial cross section of each branch is assumed to be uniform. There are no sources inside the resonator, and the effects of mean flow are neglected. The fluid contained in the resonator is assumed to be stationary, homogeneous, inviscid, and nonheat conducting. The temperature distribution in the resonator is assumed to be same everywhere (20 °C). The resonator consists of three branches: Branch 1, Branch 2, and Branch 3 as labeled in Fig. 1. Branch 1 is perpendicular to Branch 2 and Branch 3, which are coaxial. It is assumed in the analysis that only plane waves propagate in each branch. Since the dynamic properties of the resonator do not change with the wave propagation direction and the coordinate system, it is also assumed that the incident plane wave is from the opening of Branch 1, and that it transmits down to Branch 2 and Branch 3. Thus, the axis origin is set at the outside opening of the resonator. In Fig. 1, L_1, L_2, and L_3 are the effective lengths of Branch 1, Branch 2, and Branch 3, respectively, S_1, S_2, and S_3 are the cross-sectional areas of Branch 1, Branch 2, and Branch 3, respectively, and $Z_1(x_1)$, $Z_2(x_2)$, and $Z_3(x_2)$ are the acoustic impedance at the position x_1 of Branch 1, and the position x_2 of Branch 2 and Branch 3, respectively.

A. Calculation of resonance frequencies

The general expression for the acoustic pressure in the resonator is

$$p(x,t)=Ae^{j(\omega t-kx)}+Be^{j(\omega t+kx)}, \tag{1}$$

where x is the position coordinate, $k=\omega/c=2\pi f/c$ the wave number, and ω the sound frequency of the incident plane wave. Constants A and B are determined by acoustic boundary conditions. The general relationship of the acoustic impedance at the two ends of a tube is expressed as[2,3]

$$Z(0)=\frac{Z(L)+j\dfrac{\rho c}{S}\tan(kL)}{1+j\dfrac{S}{\rho c}\tan(kL)}. \tag{2}$$

The continuity equation holds at the junction of three branches as

$$\nu_1(L_1)\rho S_1=\nu_2(0)\rho S_2+\nu_3(0)\rho S_3, \tag{3}$$

where ν is the acoustic velocity, and ρ the air density.

The boundary conditions are

$$p_1(L_1)=p_2(0)=p_3(0), \tag{4}$$

$$Z_1(0)=0, \tag{5}$$

$$Z_2(-L_2)=\infty, \tag{6}$$

$$Z_3(L_3)=\infty. \tag{7}$$

In terms of the acoustic impedance ($Z=p/\nu S$), Eq. (3) and Eq. (4) are combined to give

$$\frac{1}{Z_1(L_1)}=\frac{1}{Z_2(0)}+\frac{1}{Z_3(0)}. \tag{8}$$

Using Eqs. (2), (5), (6), and (7), the acoustic impedance of $Z_1(L_1)$, $Z_2(0)$, and $Z_3(0)$ are solved. Substituting these impedances into Eq. (8), and simplifying, the equation for the calculation of resonance frequencies of the long T-shaped acoustic resonator is obtained as

$$S_1\cot(kL_1)=S_2\tan(kL_2)+S_3\tan(kL_3). \tag{9}$$

Note that there are no limitations given during the derivation of Eq. (9), providing the plane wave assumptions are met. Unlike previous theories,[20] Eq. (9) permits resonators having various cross-sectional areas to be analyzed. Further, the branch lengths may be comparable to a resonance wavelength or longer. When the area of the three branches is equal and the effective lengths of the three branches satisfy $L_1=l_{\text{eff}}$ and $L_2=L_3=L_{\text{eff}}$, then Merkli's formula is obtained from Eq. (9):

$$\cot(kl_{\text{eff}})=2\tan(kL_{\text{eff}}), \tag{10}$$

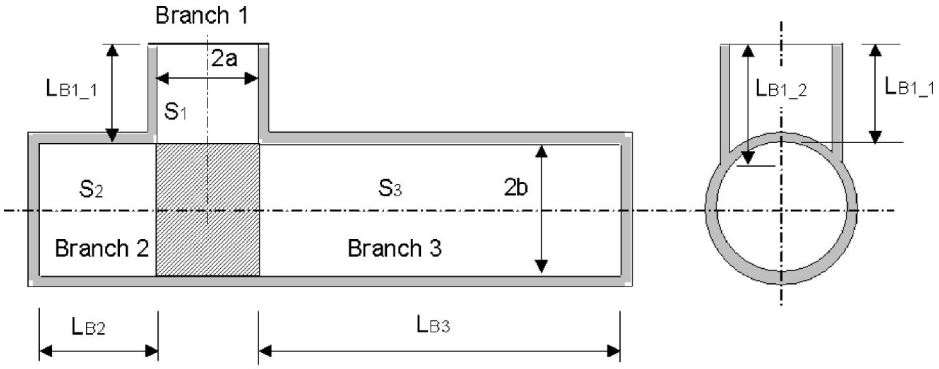

(a)

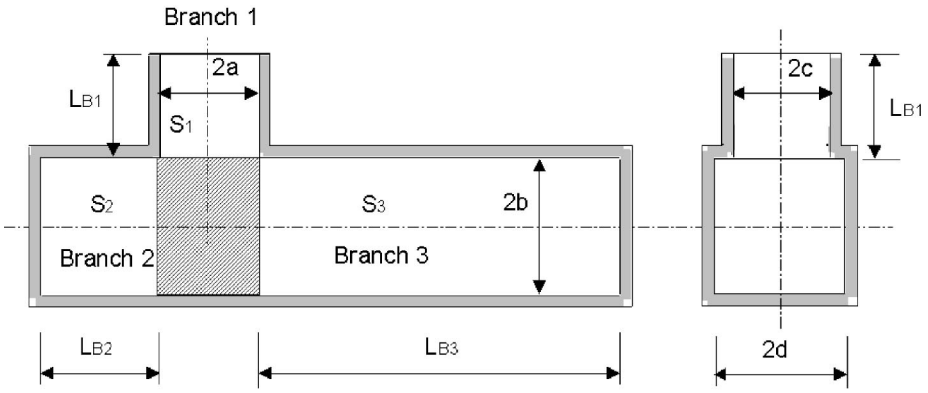

(b)

FIG. 2. Geometry of a two-dimensional T-shaped acoustic resonator.

where l_{eff} is the effective length of Branch 1, and L_{eff} is the effective length for Branch 2 and Branch 3 in Merkli's formula.

Equation (9) is rearranged to obtain the following function:

$$F(f)=\frac{S_2}{S_1}\tan\left(\frac{2\pi f L_1}{c}\right)\tan\left(\frac{2\pi f L_2}{c}\right)+\frac{S_3}{S_1}\tan\left(\frac{2\pi f L_1}{c}\right)\tan\left(\frac{2\pi f L_3}{c}\right)-1. \tag{11}$$

The resonant frequencies are found from the intersection of $F(f)$ from Eq. (11) with the abscissa. The first root is the Helmholtz frequency, and succeeding resonances are the higher mode frequencies.

B. Multimodal plane-wave model for the long T-shaped acoustic resonator design

In order to study the problems of design and inertial end corrections, more detailed geometric dimensions of the long T-shaped acoustic resonator are defined in Fig. 2. In Fig. 2(a), the three branches are cylindrical tubes, where $L_{\text{B1\_1}}$ and $L_{\text{B1\_2}}$ are the smallest and largest heights of the Branch 1, L_{B2} and L_{B3} are the lengths of Branch 2 and Branch 3, respectively. The shaded part is the common junction area. In Fig. 2(b), Branch 1 may be a rectangular or circular cross section, while Branch 2 and Branch 3 are rectangular in cross section, and L_{B1}, L_{B2}, and L_{B3} are the lengths of Branch 1, Branch 2, and Branch 3, respectively.

In order to control a particular mode in an acoustic cavity or frequency component of noise spectrum, the resonator must be placed in an optimal position that corresponds to the sound pressure maximum at the targeted acoustic mode or frequency. Such placement can constrain the length of Branch 2 and/or Branch 3. However, in Merkli's model, the lengths of Branch 2 and Branch 3 are assumed to be equal. This assumption restricts the resonator placement in a small enclosure, often making the integration of acoustic resonators directly into structures impractical. Further, it is preferable that the T-shaped acoustic resonator theory should permit any one variable of S_1, S_2, S_3, L_{B1}, L_{B2}, and L_{B3} to be calculated for a designated resonant frequency to facilitate the design process. This issue raises another limitation of Merkli's model concerning the length correction calculation. He defined an ''intersection volume'' formed by intersecting the three equal cross-sectional branches of the acoustic resonator, which was then transformed geometrically into cylinders of the same radius as the branches. The calculation of the length corrections is based on the linear ratio (weight) of each branch length to the sum of the three branch lengths (see Sec. III B). The coupling of lengths in Merkli's end correction model makes the design of T-shaped acoustic resonators complex, requiring iterative methods. Thus, a more direct approach for the design of T-shaped acoustic resonators and the calculation of the end correction is desired.

The two considerations for integrating T-shaped acoustic resonators into small enclosures are minimizing the space occupied by resonators and placing the resonator opening in an optimal position. The first consideration dictates that the

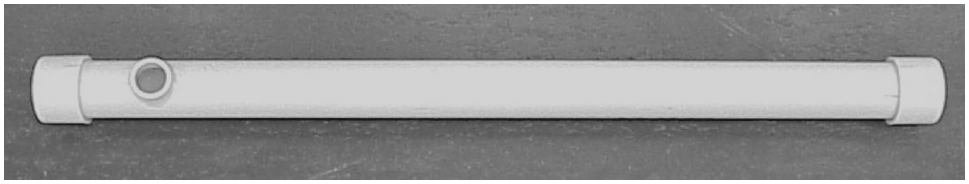

FIG. 3. Picture of an acoustic resonator constructed from PVC pipe.

length of Branch 1 be as short as possible, and the second consideration requires that either L_{B2} or L_{B3} be selected such that the resonator opening lies at a pressure maximum for the particular controlled acoustic mode or frequency, which will always occur at the boundaries of the walls of an enclosed space. The limitations in Ref. 20 can prohibit proper placement for integrated resonators. Assuming that L_1 and L_2 are given, as well as the areas of the three branches, then Eq. (9) is rearranged to permit one to solve L_3:

$$L_3 = \frac{a\tan\left(\frac{S_1}{S_3}\cot(kL_1) - \frac{S_2}{S_3}\tan(kL_2)\right) + (i-1)\pi}{k}, \quad (12)$$

where $i(=1,2,3,4,...)$ is the chosen harmonic of the acoustic resonator. In order to control the low-frequency cavity mode of an enclosure, the fundamental acoustic resonator mode $(i=1)$ is typically used. For higher-order acoustic resonator modes, $i>1$ should be considered to prevent L_3 from becoming too small to effectively absorb energy. Note that Eq. (12) could just as easily be rearranged to solve for the length of L_1 or L_2 branches or any of the three cross-sectional areas, S_1, S_2, or S_3.

III. INERTIAL END CORRECTIONS

End corrections are very important in design and analysis of acoustic resonators, and play a particularly decisive role in analyzing the acoustic performance of the T-shaped resonators when the branch dimensions become small. As described in Sec. I, the end corrections are well established and extensively documented for classical Helmholtz resonators.[4,6–8,12] However, these end corrections were found not to produce suitable results for the design of T-shaped acoustic resonators. In this section, a new model for the calculation of end corrections is proposed and compared with Merkli's model.[20] Two other variations of the proposed end correction model were also developed and evaluated, which are not presented for brevity.[10] Although they provided better results than Merkli's model, they were less accurate than the Hybrid Rayleigh End Corrections, which are presented next.

A. Model 1 (Hybrid Rayleigh's end corrections)

Model 1 is a novel model for the calculation of acoustic resonator end corrections and effective lengths. In the development of this model, Branch 1 is assumed to be a circular tube of radius a. It is found that if the end correction of Branch 1 is the summation of its outer and interior end corrections,[3] and the other two branches use Rayleigh's outer end correction,[4] the predicted Helmoholtz frequency is higher than the measured one.[10] This result indicates that the corrected length of Branch 1 is too long. Therefore, Branch 1 will use only an outer Rayleigh's end correction, ΔL_1, while the interior end correction of Branch 1 is combined into the end corrections of Branch 2 and Branch 3. Thus, the end correction of Branch 1 is expressed as

$$\Delta L_1 = \frac{8}{3\pi}a. \quad (13)$$

For the development of the end corrections of Branch 2 and Branch 3, the special case in which the three branches have the same circular cross section of radius a is first considered. Rayleigh's end corrections [Eq. (13)] are also considered for Branch 2 and Branch 3, however, the interior end correction for Branch 1 is divided equally between Branch 2 and Branch 3, yielding

$$\Delta L_2 = \Delta L_3 = 1.5\frac{8}{3\pi}a. \quad (14)$$

The effective length of the three branches are then calculated as

$$L_1 = L_{B1\_1} + \Delta L_1, \quad (15)$$

$$L_2 = L_{B2} + \Delta L_2, \quad (16)$$

$$L_3 = L_{B3} + \Delta L_3. \quad (17)$$

Although Model 1 is developed for the special case where all branches are circular and of the same cross-sectional area, experimental results have shown that the model also works well for more general cases, such as different radii for Branch 1, Branch 2, and Branch 3, or square cross sections for Branch 2 and Branch 3.

B. Model 2 (Merkli's model)

When the three branches of T-shaped resonators have the same circular cross sections with radius a, Merkli's model[20] for the end corrections of Branches 1, 2, and 3, can be computed as

$$\Delta L_1 = \Delta L_{1\_1} + \Delta L_{1\_2} + \Delta L_{out}, \quad (18)$$

$$\Delta L_2 = \Delta L_{2\_1} + \Delta L_{2\_2}, \quad (19)$$

$$\Delta L_3 = \Delta L_{3\_1} + \Delta L_{3\_2}, \quad (20)$$

where ΔL_{1_1}, ΔL_{2_1}, and ΔL_{3_1} are the end corrections induced by the common volume for Branch 1, Branch 2, and Branch 3, respectively, and ΔL_{1_2}, ΔL_{2_2}, and ΔL_{3_2} are the end corrections induced by the intersection volume for Branches 1, 2, and 3, respectively.[20] ΔL_{out} is the end correction of the open end of Branch 1. These terms are calculated by the following equations:[20]

$$\Delta L_{1\_1} = \Delta L_{2\_1} = \Delta L_{3\_1} a\left(1 - \frac{8}{3\pi}\right), \quad (21)$$

TABLE I. Geometric dimensions of circular cross-section acoustic resonators AR1–AR5.

		AR1	AR2	AR3	AR4	AR5
Branch 1	Radius: a (mm)	20.13	25.78	25.78	13.20	13.20
	Length: L_{B1_1} (mm)	10.24	23.70	22.82	18.71	17.49
Branch 2	Radius: b (mm)	20.13	25.78	25.78	20.13	20.13
	Length: L_{B2} (mm)	20.75	47.36	51.42	20.62	22.62
Branch 3	Radius: b (mm)	20.13	25.78	25.78	20.13	20.13
	Length: L_{B3} (mm)	377.52	501.32	543.28	392.62	391.62

$$\Delta L_{\text{out}} = \begin{cases} \dfrac{8a}{3\pi} & (2ka < 1), \\ \dfrac{c^2}{\pi^3 f^2 a} & (ka \gg 1), \end{cases} \tag{22}$$

$$\Delta L_{1\_2} = \frac{16a}{3\pi} \frac{L_{B1\_1}}{L_{B1\_1} + L_{B2} + L_{B3}}, \tag{23}$$

$$\Delta L_{2\_2} = \frac{16a}{3\pi} \frac{L_{B2}}{L_{B1\_1} + L_{B2} + L_{B3}}, \tag{24}$$

$$\Delta L_{3\_2} = \frac{16a}{3\pi} \frac{L_{B3}}{L_{B1\_1} + L_{B2} + L_{B3}}. \tag{25}$$

The effective lengths of the three branches can be calculated from Eqs. (15)–(17).

IV. EXPERIMENTAL VALIDATION AND VERIFICATION

As derived above, the design equation [Eq. (12)] is based on the assumption of plane waves. Thus, the frequency range covered by the model must always be below the internal critical frequency[10,21] of the T-shaped acoustic resonator. If the maximum radius of a circular resonator is $a_{\max} = 25.4$ mm, the critical frequency of the resonator is $f_{\text{cr}} = 1.84c/(2\pi a_{\max}) = 3955$ Hz, below which the plane-wave assumption is still valid. This is a rather high frequency, whose value would increase further as the radius decreases meaning that the plane-wave assumption is valid for a wide range of problems.

Typically the T-shaped acoustic resonators are used for noise control in a small enclosure at low frequencies (<1000 Hz), where absorptive treatments are impractical.[10,14,15] However, the control study are not presented in detail since they are beyond the scope of this paper, and hence the emphasis of this section will be placed on the experimental validation and evaluation of the design equations developed previously. Two sets of experiments are performed. The first set serves to validate the new resonator models, including the end corrections. The second set serves to demonstrate the use of Eq. (12) in the design T-shaped acoustic resonators, which target selected modes in an enclosure.

TABLE II. Geometric dimensions of square cross-section acoustic resonators AR6 and AR7.

		AR6	AR7
Branch 1	Radius: a (mm)	13.20	13.20
	Length: L_{B1} (mm)	14.26	8.46
Branch 2	Width: w_2 (mm)	28.29	28.29
	Height: h_2 (mm)	28.44	28.44
	Length: L_{B2} (mm)	25.50	10.00
Branch 3	Width: w_3 (mm)	28.29	28.29
	Height: h_3 (mm)	28.44	28.44
	Length: L_{B3} (mm)	356.00	365.00

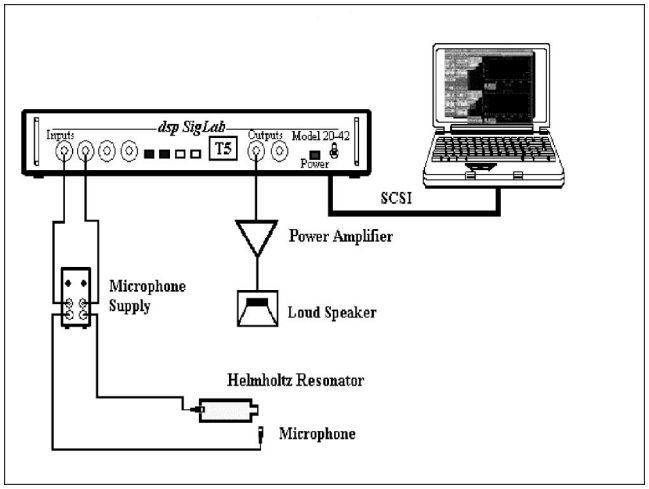

FIG. 4. Measurement system for acoustic resonators.

A. Experimental model validation

For the purpose of experimental validation end correction models, five long, T-shaped acoustic resonators (AR1–AR5) with arbitrarily chosen dimensions were constructed from PVC tubing and fittings (see Fig. 3), and two square cross-section T-shaped acoustic resonators (AR6 and AR7) were constructed from medium density fiber boards. In order to match the requirement of Merkli's model, the first three

TABLE III. Measured and predicted frequencies of T-shaped acoustic resonators. Model 1 is the proposed new model and Model 2 is Merkli's model (Ref. 20).

Group	Measured (Hz)	Model 1 (Hz)	Error (%)	Model 2 (Hz)	Error (%)
	199.60	198.98	0.31	193.27	3.17
AR1	591.87	590.63	0.21	576.32	2.63
	958.75	949.87	0.93	947.51	1.17
	148.13	147.59	0.36	143.91	2.85
AR2	433.75	432.35	0.32	424.94	2.03
	671.88	659.61	1.83	680.07	1.22
	888.75	852.72	4.05	906.93	2.05
	138.80	137.88	0.66	134.65	2.99
AR3	410.00	405.70	1.05	398.57	2.79
	638.88	625.75	2.06	640.52	0.26
	831.25	798.80	3.90	850.86	2.36
	178.75	178.65	0.06		
AR4	532.50	527.84	0.88		
	875.63	860.63	1.71		
	179.38	180.06	0.38		
AR5	535.63	531.01	0.86		
	881.88	861.75	2.28		
AR6	208.75	208.64	0.05		
	621.83	615.34	1.04		
AR7	208.75	208.65	0.05		
	626.25	622.48	0.60		
Average			1.21		2.14

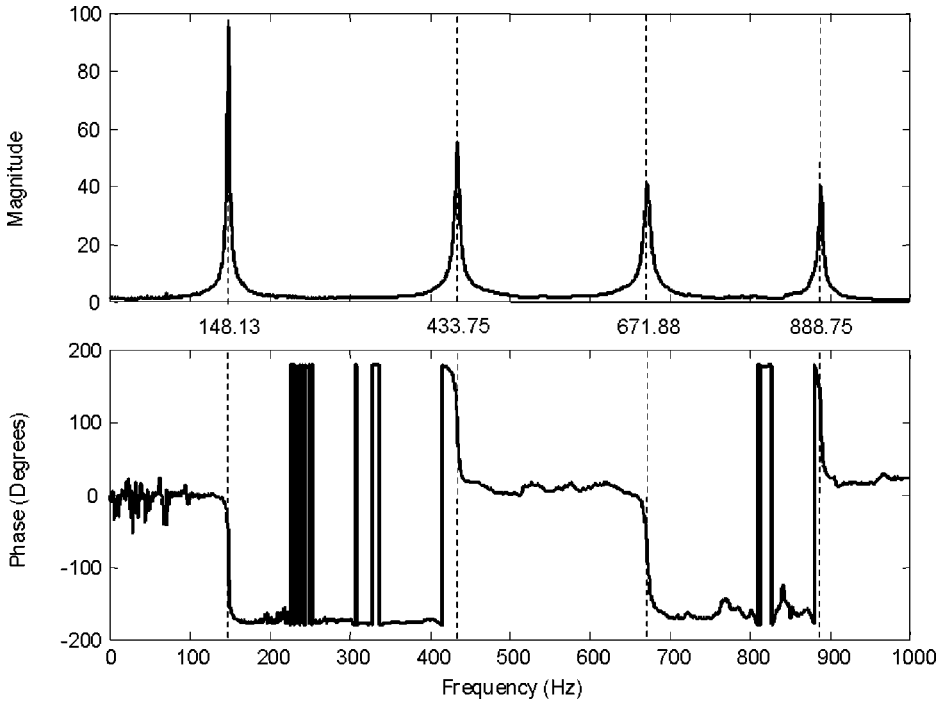

FIG. 5. Measured frequency response function (FRF) for AR2.

acoustic resonators (AR1, AR2, and AR3) were fabricated from circular tubes with the same radius. The geometric dimensions of the resonators are listed in Tables I and II. An experiment was designed to measure the frequency response function (FRF) of the acoustic resonators. The measurement system is shown in Fig. 4. One microphone was placed near the external opening of the resonator to measure the input, and another microphone was installed in the end of the resonator to measure the inside response. An external speaker driven with a white noise source was used to excite the acoustic resonator. Measurements were made with a SigLab 2042 signal analyzer, which also generated the white noise.

A representative FRF curve between the two measurement microphones for AR2 is shown in Fig. 5. The phase lag curve is also shown along with the FRF curve to help one accurately determine the resonance frequencies. It is observed from the figure that AR2 has four resonant frequencies in the frequency range of [0,1,000] Hz: 148.13, 433.75, 671.88, and 888.75 Hz. The measured and predicted natural frequencies between 0–1000 Hz for all of the resonators are given in Table III, along with the rms (unsigned magnitude) error between measured and predicted resonant frequencies for the two end correction models. The last row of Table III gives the average (rms, unsigned) error summed across all modes between 0–1000 Hz for all seven resonators.

From Table III, it is observed that the end corrections for Model 1 give accurate results for the prediction of resonant frequencies under 1000 Hz for long T-shaped acoustic resonators. The discrepancies are likely due to the fact that the end corrections for Merkli's model are based solely on the geometric considerations, and do not take into account the acoustic effects. From the results, Model 1 is found to work not only on the circular (AR1–AR5) and the same radius case (AR1–AR3) but also on the different radius case (AR4,AR5) and square cross section case (AR6,AR7). Further, note that the maximum errors for the first and second predicted resonant frequencies for Model 1 are only 0.66% and 1.05%, respectively, which are typically the modes selected for control. This is in contrast to 3.0% and 2.5% error, respectively, for Merkli's model. The model also performs well at predicting the resonant frequencies of higher modes, as seen by the average error (1.21% vs 2.14%) given in the last row of Table III. Consequently, Model 1 is chosen for use with Eq. (12) for the subsequent design of long, T-shaped

TABLE IV. Geometric dimensions of designed T-shaped acoustic resonators.

		AR228		AR398		AR452	AR458
	Group	1	2	1	2		
	Radius: a (mm)	13.2	13.2	13.2	13.2	13.2	13.2
Branch 1	Area: S_1 (mm^2)	547.4	547.4	547.4	547.4	547.4	547.4
	Length: L_{B1_1} (mm)	10.0	10.0	10.0	10.0	10.0	10.0
	Radius: b (mm)	20.2	20.2	20.2	20.2	20.2	20.2
Branch 2	Area: S_2 (mm^2)	1281.9	1281.9	1281.9	1281.9	1281.9	1281.9
	Length: L_{B2} (mm)	63.2	43.2	63.2	43.2	63.2	43.2
	Radius: b (mm)	20.2	20.2	20.2	20.2	20.2	20.2
Branch 3	Area: S_3 (mm^2)	1281.9	1281.9	1281.9	1281.9	1281.9	1281.9
	Length: L_{B3} (mm)	306.5	307.5	568.1	572.7	485.8	485.1

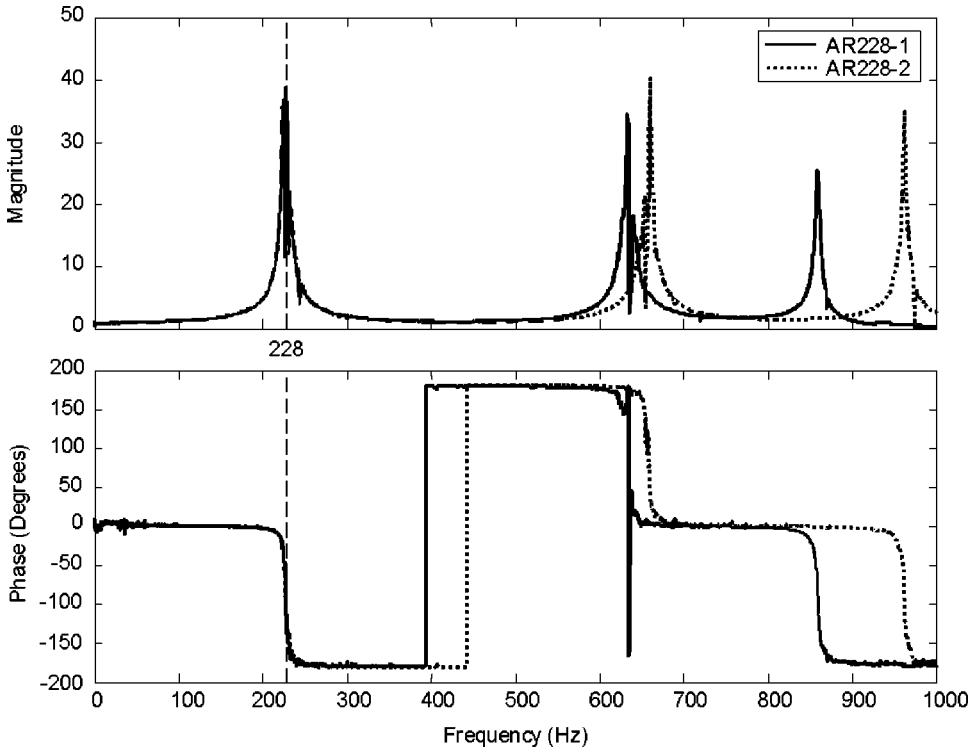

FIG. 6. Measured FRFs for AR228-1 and AR228-2.

acoustic resonators. Note that the resulting equations are more tractable and have a closed-form solution.

B. Design examples and verification

The second part of the experimental study focuses on the design, fabrication, and testing of a set of long, T-shaped acoustic resonators, which were used for a related noise control study in a small enclosure.[10,14,15] The enclosure was found to have resonances at 228, 398, 452, and 458 Hz, and one or more resonators were designed for each of these frequencies. Two AR228's, two AR398's, one AR452, and one AR458 resonator were designed using design Eq. (12) and the end corrections given in Eqs. (13)–(14). The desired resonance frequency of each resonator is included in its name (e.g., AR228 is designed to produce control at 228 Hz). The AR228 resonators were designed for the fundamental resonator mode [$i=1$ in Eq. (12)], while the AR398, AR452, and AR458 were designed for the second resonator mode [$i=2$ in Eq. (12)]. The geometric dimensions for all resonators are given in Table IV. The six T-shaped acoustic reso-

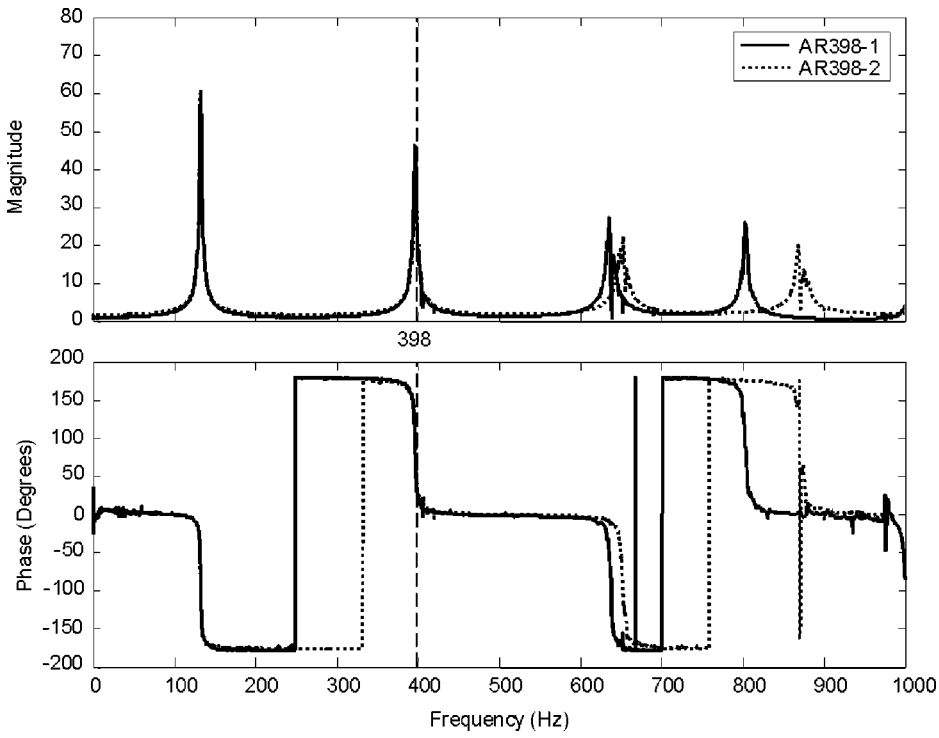

FIG. 7. Measured FRFs for AR398-1 and AR398-2.

TABLE V. Measured and designed resonance frequency of acoustic resonators.

Group		Measured (Hz)	Designed (Hz)	Error (Hz)	Error (%)
AR228	1	227.5	228.0	−0.5	0.22
	2	228.4	228.0	+0.4	0.18
AR398	1	396.6	398.0	−1.4	0.35
	2	397.2	398.0	−0.8	0.20
AR452		450.3	452.0	−1.7	0.38
AR458		458.8	458.0	+0.8	0.17

nators were also constructed from commercially available, circular cross-sectional PVC tubing and fittings (see Fig. 3). The measured representative FRFs for resonator AR228's and AR398's are given in Figs. 6 and 7. Figure 6 shows the FRFs for both AR228 resonators. A vertical line is drawn at the desired resonance frequency of 228 Hz, and the Helmholtz mode of both resonators is observed to occur there. Some small discrepancies are observed in the higher-order resonator modes above 228 Hz. Similar plots for the AR398 resonators are given in Fig. 7, although the desired 398 Hz resonance matches at the second resonator mode, as desired. The measured and designed resonance frequencies for all six resonators are listed in Table V, along with the error between the designed (using end correction Model 1) and measured frequencies. As shown in Table V, the maximum error at the design frequencies is 0.38%, which occurs for AR452. The accuracy of the designs was sufficient such that the resonators did not require tuning.

V. CONCLUSIONS

A general model for the calculation of resonant frequencies of long T-shaped acoustic resonators has been derived in Sec. II. The novel model is amenable for directly designing long T-shaped acoustic resonators. A new end correction model has been proposed and experimentally validated for circular and square cross sections. The model is referred to as the ''Hybrid Rayleigh's End Correction'' method, and was found to give roughly half the error in the frequency prediction and resonator design when compared to Merkli's model. This new model uses the Rayleigh end correction for the three branches of the resonator, and the interior end correction of Branch 1 is divided into two equal parts and added to the other branches. Unlike the previous model for T-shaped resonators,[20] the new models proposed in Sec. II are simple and have no inherent limitations for the cross-sectional shape and length of the three branches, providing the plane wave assumption is not violated.

As we have explained in the paper, one advantage of the T-shaped acoustic resonators is that they offer the promise of compact, integrated noise absorbers. Currently, the long T-shaped acoustic resonators have been successfully used in an Air Force project concerning noise transmission control through a cylindrical ChamberCore composite fairing (3–6 dB),[10,14,15] in an unpublished Army vehicle structural born noise control project (3–4 dB A), and in civil noise transmission control projects (such as noise transmission control through two-partition windows, 5–6 STC). Noise control was observed, not only at the targeted frequencies but also at other higher frequencies because of the modal coupling.

ACKNOWLEDGMENTS

The work was sponsored by the Air Force Research Laboratory, Space Vehicles Directorate (AFRL/VSDV). The POC for this effort is Dr. Steven A. Lane, and can be contacted at (505) 846–9944.

[1] H. Helmholtz, ''Theorie der luftschwingungen in röhren mit offenen offenen enden,'' (''Theory of air oscillations in tubes with open ends''), J. Reine Angew. Math. **57**, 1–72 (1859).
[2] P. M. Morse, *Vibration and Sound*, The Acoustical Society of America through the American Institute Physics, Woodbury, NY, 1964.
[3] L. E. Kinsler and A. R. Frey, *Fundamentals of Acoustics* (Wiley, New York, 1962).
[4] Lord Rayleigh, ''On the theory of resonators,'' Philos. Trans. R. Soc. London **CLXI**, 77–118 (1870).
[5] V. Sondhauss, Ann. Phys. (Leipzig) **LXXXI**, 235 (1850).
[6] K. Uno Ingard, ''On the theory and design of acoustic resonators,'' J. Acoust. Soc. Am. **25**, 1037–1061 (1953).
[7] J.-G. Ih, ''On the inertial end corrections of resonators,'' Acustica **78**, 1–15 (1993).
[8] M. Alster, ''Improved calculation of resonant frequencies of Helmholtz resonators,'' J. Sound Vib. **24**, 63–85 (1972).
[9] R. L. Panton and J. M. Miller, ''Resonant frequencies of cylindrical Helmholtz resonators,'' J. Acoust. Soc. Am. **57**, 1533–1535 (1975).
[10] D. Li, ''Vibroacoustic behavior and noise control studies of advanced composite structures,'' Ph.D. dissertation, School of Engineering, University of Pittsburgh, 2003.
[11] D. Li and J. S. Vipperman, ''Noise control of a ChamberCore cylinder using cylindrical Helmholtz resonators,'' IMECE03-41978, New York, 2003.
[12] R. C. Chanaud, ''Effects of geometry on the resonance frequency of Helmholtz resonators,'' J. Sound Vib. **178**, 337–348 (1994).
[13] G. R. Bigg, ''The three dimentional cavity resonator,'' J. Sound Vib. **85**, 85–103 (1982).
[14] D. Li and J. S. Vipperman, ''Noise control for a chamber core composite structure using long T-shaped acoustic resonators,'' 146th Meeting of ASA, Austin, Texas, 10–14 November, 2003.
[15] D. Li and J. S. Vipperman, ''Noise transmission control for a ChamberCore fairing by using integrated acoustic resonators,'' submitted to Noise Control Eng. J.
[16] E. Herup, S. Huybrechts, S. Griffin, and S. Tsai, ''Method of making composite ChamberCore sandwich-type structure with inherent acoustic attenuation,'' U.S. Patent No. 6,231,710 B1, 2001.
[17] J. W. Miles, ''The diffraction of sound due to right-angled joints in rectangular tubes,'' J. Acoust. Soc. Am. **19**, 572–579 (1947).
[18] D. H. Keefe, ''Theory of the single woodwind tone hole,'' J. Acoust. Soc. Am. **72**, 676–687 (1982).
[19] C. J. Nederveen, ''Corrections for woodwind tone-hole calculations,'' Acustica **84**, 957–966 (1998).
[20] P. Merkli, ''Acoustic resonance frequencies for a T-tube,'' J. Appl. Math. Phys. (ZAMP) **29**, 486–498 (1978).
[21] F. Fahy, *Sound Structural Vibration* (Academic Press, New York, 1987).

A model for the radiated field of a plane piston after reflection from a curved surface

Adrian Neild,[a] David A. Hutchins,[b] and Toby J. Robertson
School of Engineering, University of Warwick, Coventry CV4 7AL, United Kingdom

David W. Schindel
MicroAcoustic Instruments Inc., 460 Wilbrod Street, Suite 2, Ottawa, Ontario K1N 6M8 Canada

(Received 14 June 2003; revised 19 July 2004; accepted 13 August 2004)

A theoretical model is described for the field resulting from reflection of a plane piston source from a curved surface. The approach is based on an impulse response model, which treats the surface of the mirror as a grid of point reflectors to give an overall reflective response. The model was verified by comparison to experimental measurements in air, using a polymer-filmed capacitive transducer source fitted with an optical-grade mirror, at frequencies up to 1 MHz. The design parameters of such a device were investigated in order to determine the effect on the focal area, and to indicate how this model could be used to optimize the focusing effect of such a system. © *2004 Acoustical Society of America.* [DOI: 10.1121/1.1808457]

PACS numbers: 43.20.Rz [LLT] Pages: 2793–2801

I. INTRODUCTION

There have been many papers published that describe the radiated field of plane pistons, in both the nearfield and farfield regions.[1–5] The resulting models can be used for either single frequency (continuous-wave) or transient excitation. In the most common approach, the impulse response of the source is first evaluated for the particular geometry and medium of operation. The pressure waveform at any point in the radiated field can then be determined by convolution of the impulse response with the acceleration of the piston face.

Of particular interest in the present work is the prediction of focused fields that result from reflection at an external mirror. Note, however, that focusing can be achieved using curved radiators, such as spherical bowl transducers, which can be modeled either directly[6] or as a series of annuli.[7] There has also been interest in conical sources,[8] which can be modeled in a similar way. Experimental work has been reported on the use of external focusing elements, such as Fresnel zone-plates,[9,10] and reflective mirrors.[11,12] However, there does not appear to be any description in the literature of theoretical predictions of the resulting field from such an approach. In this paper, a model is presented which analyzes the use of a parabolic mirror, which reflects ultrasound produced by a circular plane piston source. While it would have been simpler to model the focus produced by reflection of a plane wave, practical devices use sources of finite diameter, and hence it was felt important to model the piston source properly. Deviations of the sound field from a piston, which may be only a few wavelengths in diameter, from a plane wave might have a large effect on the detailed focal region, and hence the piston source has been modeled fully. Such devices have been used increasingly for imaging surfaces of solids in air for metrology and other applications.[12]

The model presented here approximates the mirror surface to a grid of point reflectors. Each of these point reflectors will have an incoming waveform, which can be found from the impulse response method.[3] This incoming waveform is reflected. The reflected pressure waveform, which arrives at a point in the field, can be found by summing these reflected waveforms once the variation in pathlength is accounted for by a time shift.

The results predicted by the theoretical model have been compared to those measured experimentally, using an ultrasonic transducer system designed for use in air.[12] This used a polymer-filmed capacitive source, with a fitted parabolic mirror, which focused signals in air at a known location. It was designed to operate over the 500-kHz to 1-MHz frequency range, and to give a focal region with a spot size of <1 mm. A schematic diagram of the device, fitted with a parabolic mirror, is shown in Fig. 1. Signals from the circular source, of 22-mm diameter, were focused using the off-axis parabolic optical reflector. This was of metal-coated glass, and was made from optical grade material. Because of the large acoustic impedance mismatch to air, it acted as an excellent acoustic reflector. This device was shown to focus ultrasonic signals to a well-defined focal region.[13] It was thought to be a good example of a situation where a theoretical prediction of the reflected field would be useful, as it could help in the design of the device for optimal focusing performance. Predictions of the model could also be compared to the field measured experimentally, so that the theory could be tested against real data.

Many ultrasonic and acoustic instruments use a signal that has been reflected to make a measurement, but it would appear that little theoretical work exists in the literature for the case of reflection and focusing of a beam from a plane piston. This paper considers this problem for the particular case of reflection of a circular plane piston from a parabolic mirror, although any shape of mirror can be modeled.

[a]Present address: Institute of Mechanical Systems, Center of Mechanics, ETH Zürich, CH-8092 Zürich, Switzerland.
[b]Author to whom correspondence should be addressed. Electronic mail: d.hutchins@warwick.ac.uk

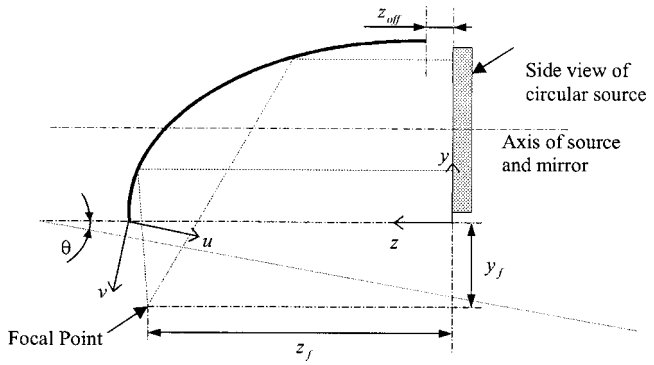

FIG. 1. Schematic diagram of the cross-section through a device containing a plane piston source and an off-axis parabolic mirror.

II. THE THEORETICAL APPROACH

The model presented here approximates the mirror surface to a grid of point reflectors. The incoming acoustic pressure field from the plane piston radiator, positioned at some distance from the mirror, can be predicted theoretically at each of these point reflectors. The resulting pressure waveform at some field position after reflection can then be found by summing the contributions from each individual location on the reflector surface.

There are many methods for predicting the radiated field from a circular plane piston source. In this work, the impulse response model, which uses a convolution approach, has been used.[5] It is assumed that an infinite rigid baffle surrounds the planar source, and that the propagation medium is nondissipative, isotropic and homogeneous, so that the only attenuation mechanism considered is diffraction. Rayleigh[14] stated that the time-dependant velocity potential, $\phi(\bar{r},t)$ could be written as

$$\phi(\bar{r},t)=\int_s \frac{v(t-r'/c)}{2\pi r'}\,dS, \tag{1}$$

where $v(t)$ is the uniform normal acoustic velocity waveform on the face of the plane piston (although the equation can also be used in the general case where the normal velocity is a function of space and time), $\bar{r}$ defines the location of the reception point relative to the center of the piston, t is time, and r' is the distance from an element of surface area

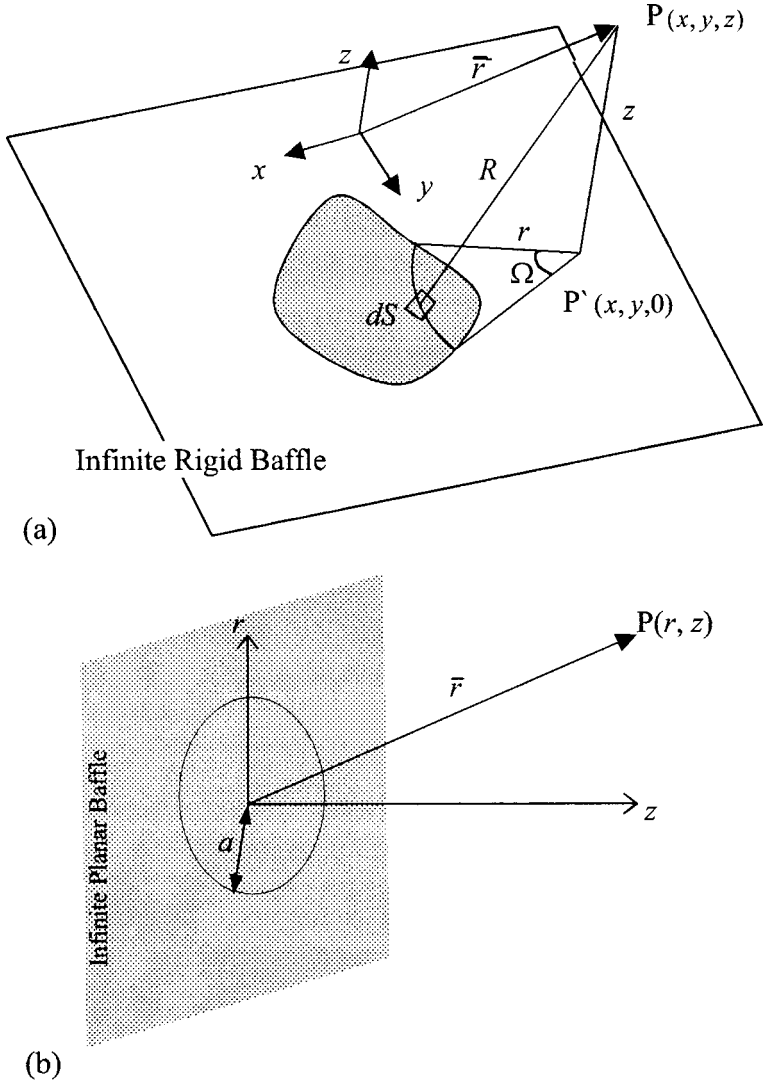

FIG. 2. (a) Coordinate system for an arbitrarily shaped source in an infinite baffle and (b) the variables used to model a circular plane piston source.

on the piston face, δS, to the reception point. The acoustic pressure $p(r,t)$ can be found from the velocity potential using

$$p(\bar{r},t)=\rho\frac{\delta\phi(\bar{r},t)}{\delta t}. \tag{2}$$

The impulse response method solves the problem by assuming that $v(t)$ is a Dirac delta function (or "impulse"), and establishing an expression for the scalar velocity potential. The result is known as the scalar impulse response, $h(\bar{r},t)$, which can then be convolved with the actual form of $v(t)$ to model the real situation. A solution for the pressure can then be written as

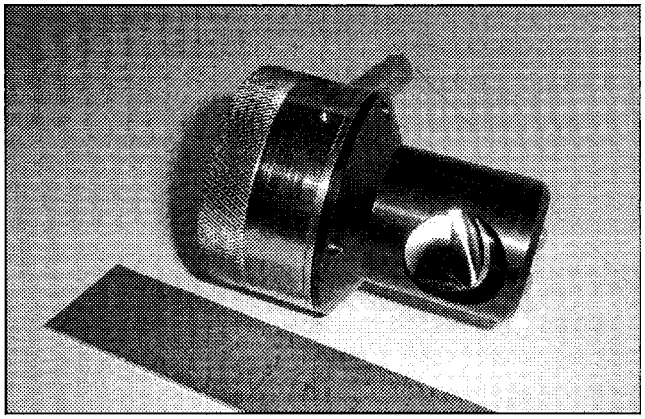

FIG. 3. A photograph of the transducer used experimentally for focusing ultrasound in air with a parabolic mirror.

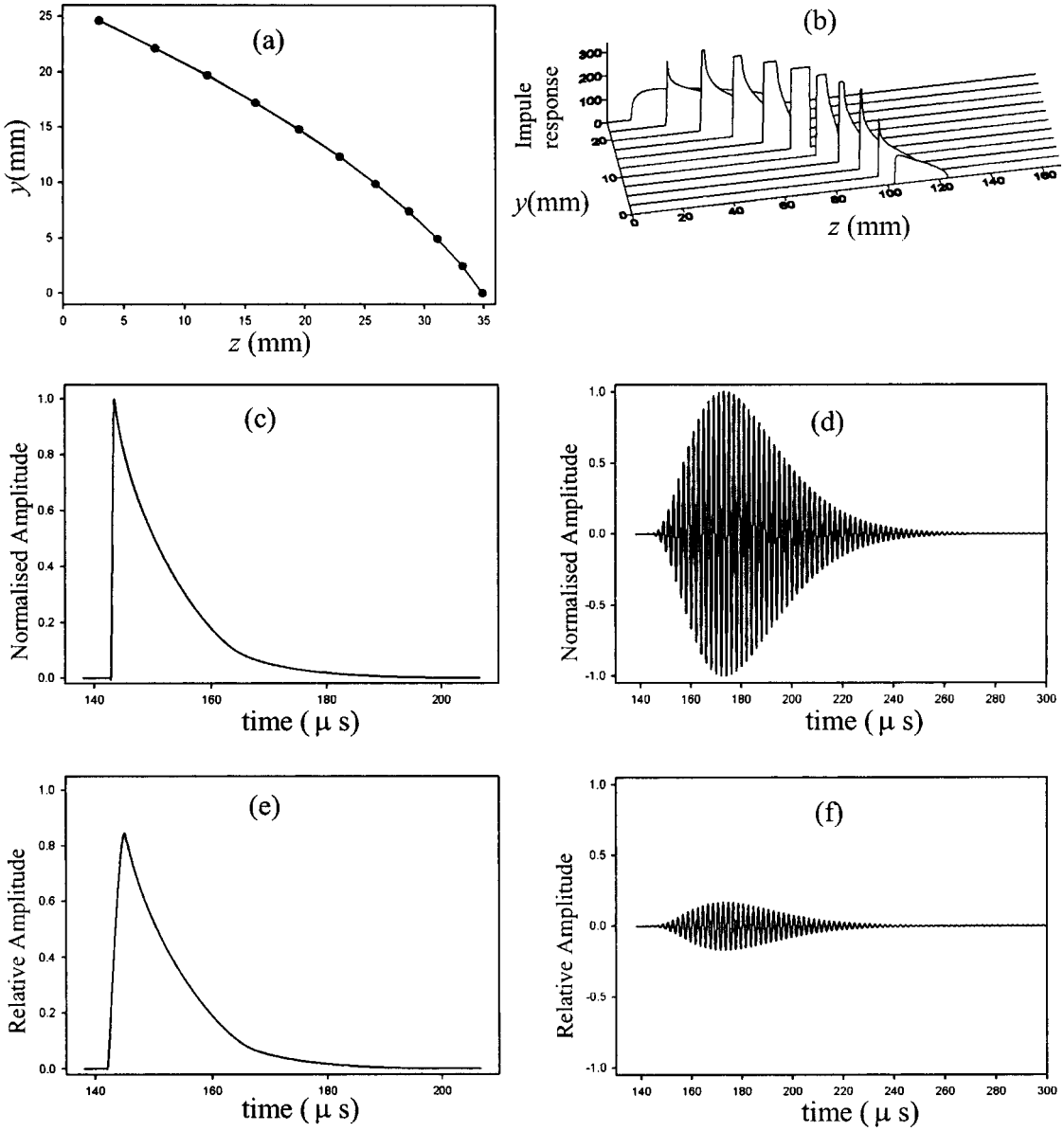

FIG. 4. The impulse response at 11 points on the mirror, and the resulting total scalar response and pressure waveforms at two points in the field (the focal point, and one displaced from there by 1 mm). (a) The 11 positions on the mirror being modeled and (b) the scalar impulse response from each of these at the focal point. (c) The total impulse response at the focal point and (d) the resulting pressure waveform. (e) The total impulse response at 1 mm from the focal point in the *u* direction and (f) the corresponding pressure waveform.

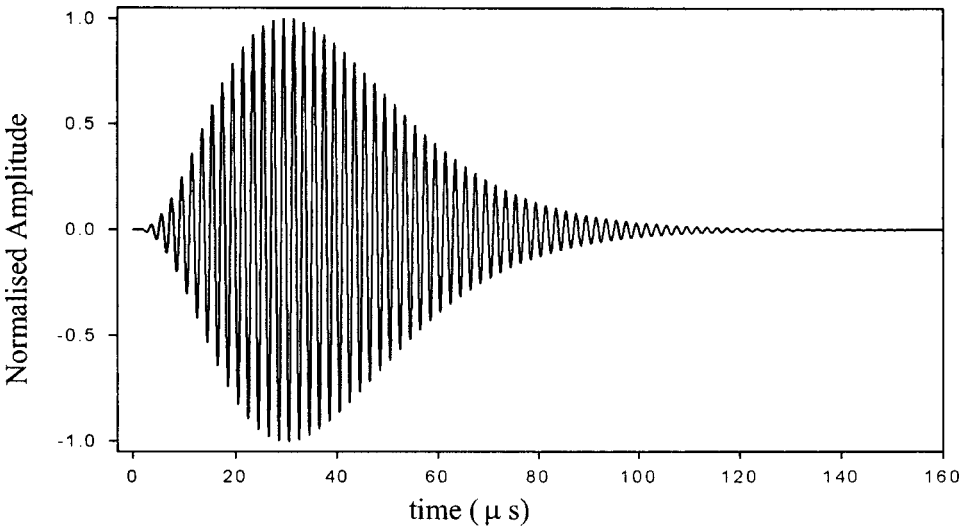

FIG. 5. The velocity waveform of the piston used in the simulation of a 500-kHz toneburst.

$$p(\bar{r},t)=\rho\frac{\partial[v(t)*h(\bar{r},t)]}{\partial t}=\rho\frac{\partial[v(t)]}{\partial t}*h(\bar{r},t)$$

$$=\rho\cdot v(t)*\frac{\partial[h(\bar{r},t)]}{\partial t}. \tag{3}$$

Equation (1) can then be modified to give the necessary form of the scalar impulse response to be used in Eq. (3), which is given by

$$h(\bar{r},t)=\int_s\frac{\delta(t-R/c)}{2\pi R}dS. \tag{4}$$

San Emeterio[4] stated that geometrical considerations can be used to rewrite Eq. (4) in an alternative form, which can be written as

$$h(\bar{r},t)=c\cdot\frac{\Omega(\bar{r},t)}{2\pi}, \tag{5}$$

where $\Omega(\bar{r},t)$ is the angle subtended by the piston in the plane of the source, as shown in Fig. 2(a). Stepanishen[3] has found this angle as a time-stepped function for a uniform circular source operating in a homogenous propagation medium. The variables used are shown in Fig. 2(b).

The point $P(r,z)$, located at $\bar{r}$, can be defined using radial and axial cylindrical coordinates r and z, respectively, relative to the center of the circular plane piston source of radius a. The value of $h(\bar{r},t)$ for the case of $a>r$ [i.e., where point $P(r,z)$ is geometrically within the radius of the source] is given by several authors (e.g., Refs. 2, 4, and 5) as

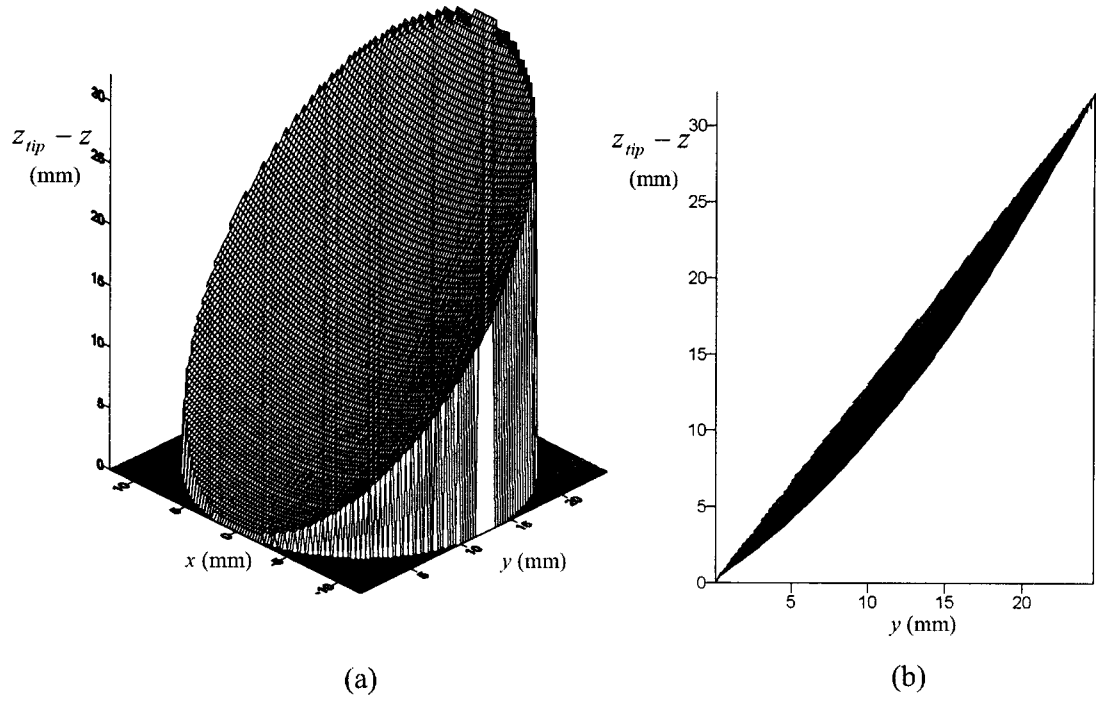

FIG. 6. Mirror shape used to simulate the experimental device. (a) A wireframe view showing the points at which the impulse response was calculated and (b) a cross section through the $x=0$ plane.

$$h(\bar{r},t)=\begin{cases}0, & ct<z,\\ c, & z<ct<R,\\ \dfrac{c}{\pi}\cos^{-1}\left\{\dfrac{(ct)^2-z^2+r^2-a^2}{2r[(ct)^2-z^2]^{1/2}}\right\}, & R<ct<R,\\ 0, & ct>R,\end{cases} \tag{6}$$

where c is the speed of sound in the propagation medium, $R=[z^2+(a-r)^2]^{1/2}$, and $R=[z^2+(a+r)^2]^{1/2}$. For the case where $a\leqslant r$, then $h(\bar{r},t)$ is given by

$$h(\bar{r},t)=\begin{cases}0, & ct<R,\\ \dfrac{c}{\pi}\cos^{-1}\left\{\dfrac{(ct)^2-z^2+r^2-a^2}{2r[(ct)^2-z^2]^{1/2}}\right\}, & R<ct<R,\\ 0, & ct>R.\end{cases} \tag{7}$$

Using these two sets of equations, the scalar impulse response at any point, $\mathrm{P}(r,z)$, in the field can be found, and consequently the pressure waveform can be found from a given piston source velocity waveform.

The above can be used to plot the radiated field of a circular plane piston, e.g., in terms of spatial variations in the amplitude of the pressure waveform. The task now is to derive a method for calculating the resultant pressure distribution when the field of a planar piston is reflected at a boundary.

Consider the case where the reflector is a single point. Here, the scattered pressure wave results in a drop of pressure amplitude proportional to $1/R$, where R is the distance from the point reflector.[15] The basis of the model presented here is that the finite-sized mirror can be modeled as a fine grid of such point reflectors. The pressure waveform at any one of these points can be calculated using the theory above for the circular plane piston, and this waveform then forms the pressure variations of the secondary source at that point on the mirror. An assumption is made that no component of the original field from the circular piston is present when calculating the reradiated field, and that any phase change that occurs during reflection it is a constant factor. The particular case of a parabolic mirror, which can be used for focusing, will be used as an illustration of the technique, and a comparison will be presented to experimental scans of such a reflector. The geometry of the actual device to be studied was shown earlier in Fig. 1, and a photograph is presented in Fig. 3. This device, obtained from MicroAcoustic Instruments Inc., used a planar polymer-membrane capacitive transducer,[16,17] fitted with an off-axis parabolic mirror with a diameter of 24.6 mm. The shape of this mirror is dictated by the criteria that the propagation distance of parallel rays from the source to the focal point must be equal for all ray paths.

For simplicity of calculation, the mirror geometry is defined in terms of a new set of axes (u and v). Each point on the mirror surface is defined using orthogonal x, y and z axes, as shown in Fig. 1. The $x=0$ plane intersects both the source and the mirror thorough their centers, and hence is a plane of symmetry. The source face lies in the $z=0$ plane. The point on the mirror surface most distant from the source is defined as occurring at $y=0$. The mirror and source are aligned coaxially, and have diameters of d_{mirror} and d_{source}, respectively. A second set of axes, u and v, are respectively parallel and perpendicular to the line from the center of the mirror to the focal point, with a further axis w being orthogonal to those two (not shown). The distances z_f and y_f shown define the location of the focal point. The distance z_{off} is the distance from the surface of the transducer to the nearest point on the mirror, that is the value of z when $x=0$, and $y=d_{mirror}$. It is assumed that the values z_f and y_f are specified design criteria for the mirror and as such are known. In addition the values of d_{mirror}, d_{source} and z_{off} must be specified.

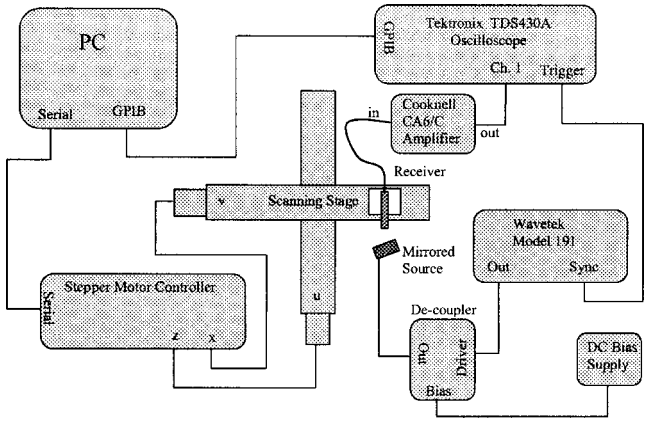

FIG. 7. Experimental apparatus used to measure the ultrasonic fields reflected by the mirror.

For a parabolic mirror, the path length to the focal point will be constant for all x, y, z coordinates on the mirror surface. It can be shown from Fig. 1 that the path length to the focal point is given by

$$pl_f=z_{off}+\sqrt{(z_f-z_{off})^2+(y_f+d_{mirror})^2}. \tag{8}$$

If x and y define a line passing through the mirror, then the value of z such that the point (x,y,z) lies on the mirror surface can be found from the path length using

$$z=\frac{pl_f^2-z_f^2-(y_f+y)^2-x^2}{2(pl_f-z_f)}. \tag{9}$$

Using this method, any point on the surface of the mirror can be found.

The dimension z_{tip} is defined as the length, in the z direction, to the further most tip of the mirror, and occurs at $x=y=0$ (see Fig. 1), and can be obtained from Eq. (9) to give

$$z_{tip}=\frac{pl_f^2-z_f^2-y_f^2}{2(pl_f-z_f)}. \tag{10}$$

It has been stated that the reflecting surface will be modeled by an approximation to a grid of point reflectors on the surface of the mirror. The grid which is used is of constant pitch in the x and y directions, at x_p and y_p, respectively. The values of y will range between 0 and d_{mirror}; consequently, y is incremented at steps of y_p within this range. For a given value of y, then x will range between the following values:

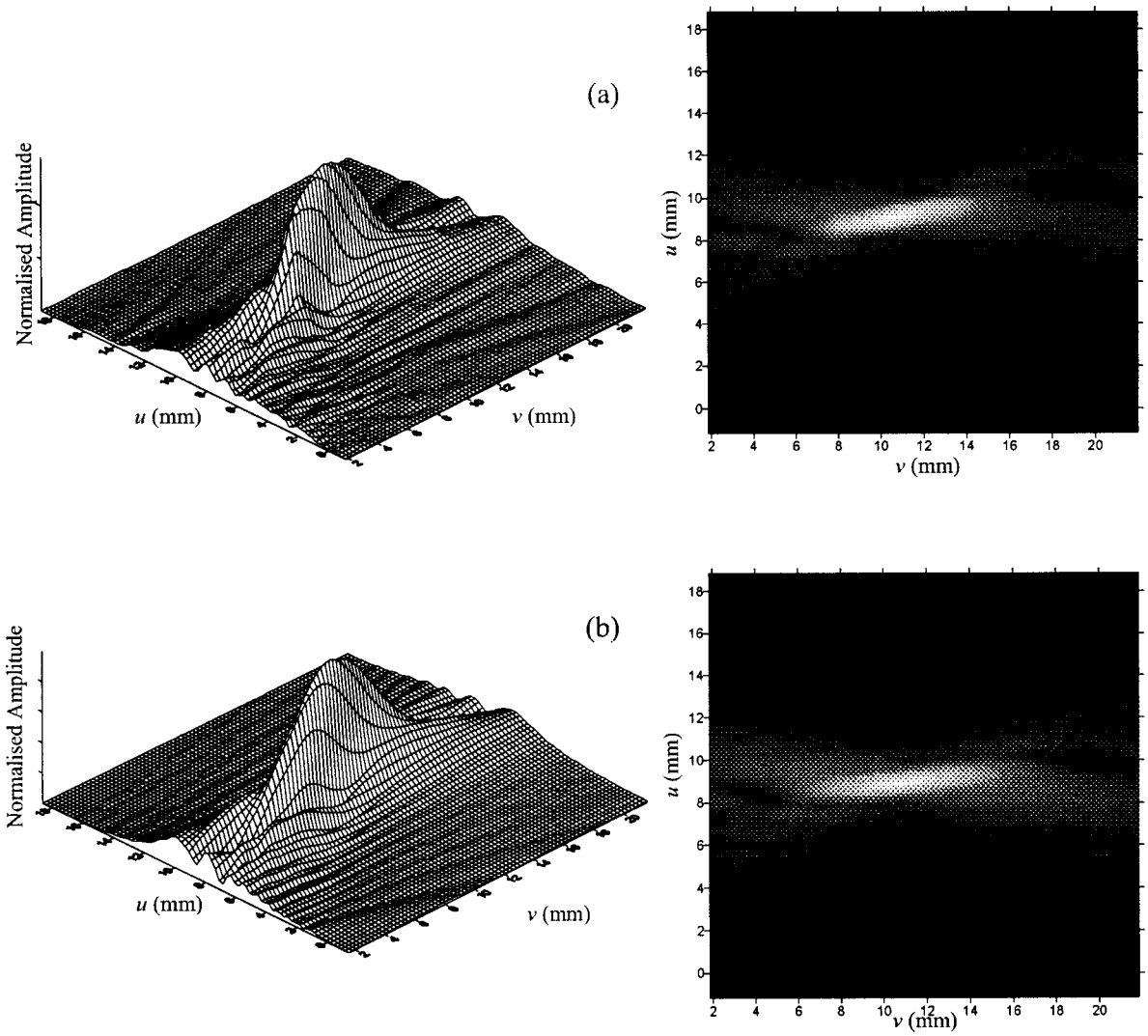

FIG. 8. Comparison of (a) experimental and (b) theoretical reflected pressure fields for excitation of the plane piston with a 500-kHz tone-burst voltage drive signal.

$$x_{\max}^{\min} = \frac{-}{+} \sqrt{\left(\frac{d_{mirror}}{2}\right)^2 - \left(\frac{d_{mirror}}{2} - y\right)^2}. \tag{11}$$

For each of these (x,y) combinations, the value of z can be found using Eq. (9). At each of these points on the mirror surface, the pressure amplitude can be found from the scalar impulse response using Eqs. (6) and (7), where $r = d_{mirror}$, and $a = \sqrt{(y - d_{mirror})^2 + x^2}$.

The pressure waveform at any point in the field is proportional to the sum of the reflected signals from the mirror. As stated previously, the pressure amplitude of a point source drops with $1/R$, where R is the distance from the source. Consequently, the pressure waveform emerging from one of the grid points, (x,y,z), which arrives at a field point (u,v,w), is proportional to the reflected pressure waveform divided by R, where R is given by

$$R = \sqrt{(w-x)^2 + (y + u \sin\theta + v \cos\theta)^2 + (z_{tip} - u \cos\theta + v \sin\theta - z)^2}, \tag{12}$$

where θ is the angle shown in Fig. 1.

It is also necessary to calculate the total path length from the source to the field point (u,v,w), via a given point on the mirror surface (x,y,z), and this is given by

$$pl = z + R. \tag{13}$$

The change in the actual path length, from point to point, can be used to find a time shift by dividing by the speed of sound, c. In addition, the length pl can be used to account for absorption in the propagation medium, as this is the total distance traveled from the source to the point in the field. However, in the predictions shown here, the absorption has

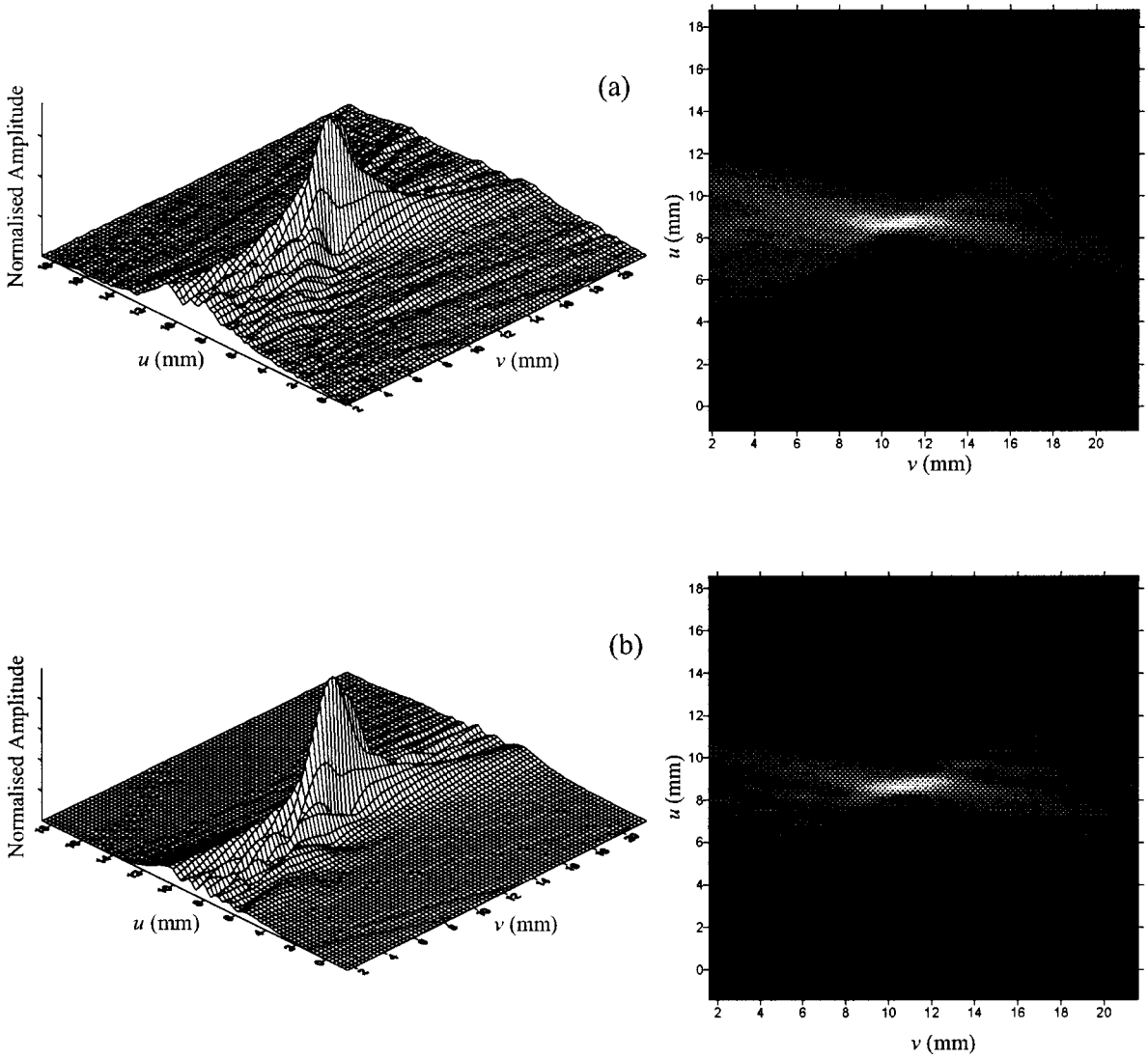

FIG. 9. Comparison of (a) experimental and (b) theoretical reflected pressure fields for excitation of the plane piston with a 1-MHz tone-burst voltage drive signal.

been ignored, as the path length differences are not great, and the pressure field is in any case normalized. Note that if a field in the uv plane is considered, it is possible to use the symmetry of the system, and consider only points on the mirror which have a positive x value. Under such conditions, $x^{\min}$ in Eq. (11) becomes zero. Symmetry can also be used when the pressure arriving in points in the uw plane is considered, as here it is only necessary to consider field points in which w is positive.

As an illustration of the technique, consider the simplified case with 11 point reflectors only along the curved parabolic reflector, as shown in Fig. 4(a) as a plot of y against z. The points are at $x=0$ and $y=0:22.4$ mm in 2.24-mm steps. Figure 4(b) shows the scalar impulse response $(h(\bar{r},t))$ that results from the circular plane piston at each of the 11 points on the surface of the mirror described above. The total scalar impulse response of the whole mirror can then be calculated at the focal point, and is shown in Fig. 4(c). This is then convolved with the time differential of the piston velocity waveform (or acceleration), to give the pressure waveform arriving at the focal point. This is shown in Fig. 4(d) for a piston velocity waveform in the form of a 500-kHz tone-burst (see Fig. 5). This can be repeated for a field point 1 mm from the focal point in the positive u direction, and the resultant scalar impulse response and pressure waveform are shown in Figs. 4(e) and 4(f), respectively. The scalar impulse response at the focal point has been normalized to unity. Note the expected reduction in the amplitude of the pressure waveform as the field point moves out of the focal region, even though there was a much smaller change in the impulse response.

It should be noted that the number of points taken across the reflector had to be sufficient to guarantee convergence to a reasonable scalar impulse response. In the example shown above, the points were chosen to give sufficiently small changes in path length to the receiver position from adjacent points on the mirror (and hence sufficiently small changes in arrival time to the receiver point) at 500 kHz. This allowed the subsequent convolution to be performed adequately. Each case for simulation needs to bear this in mind when fixing the number of points across the reflector.

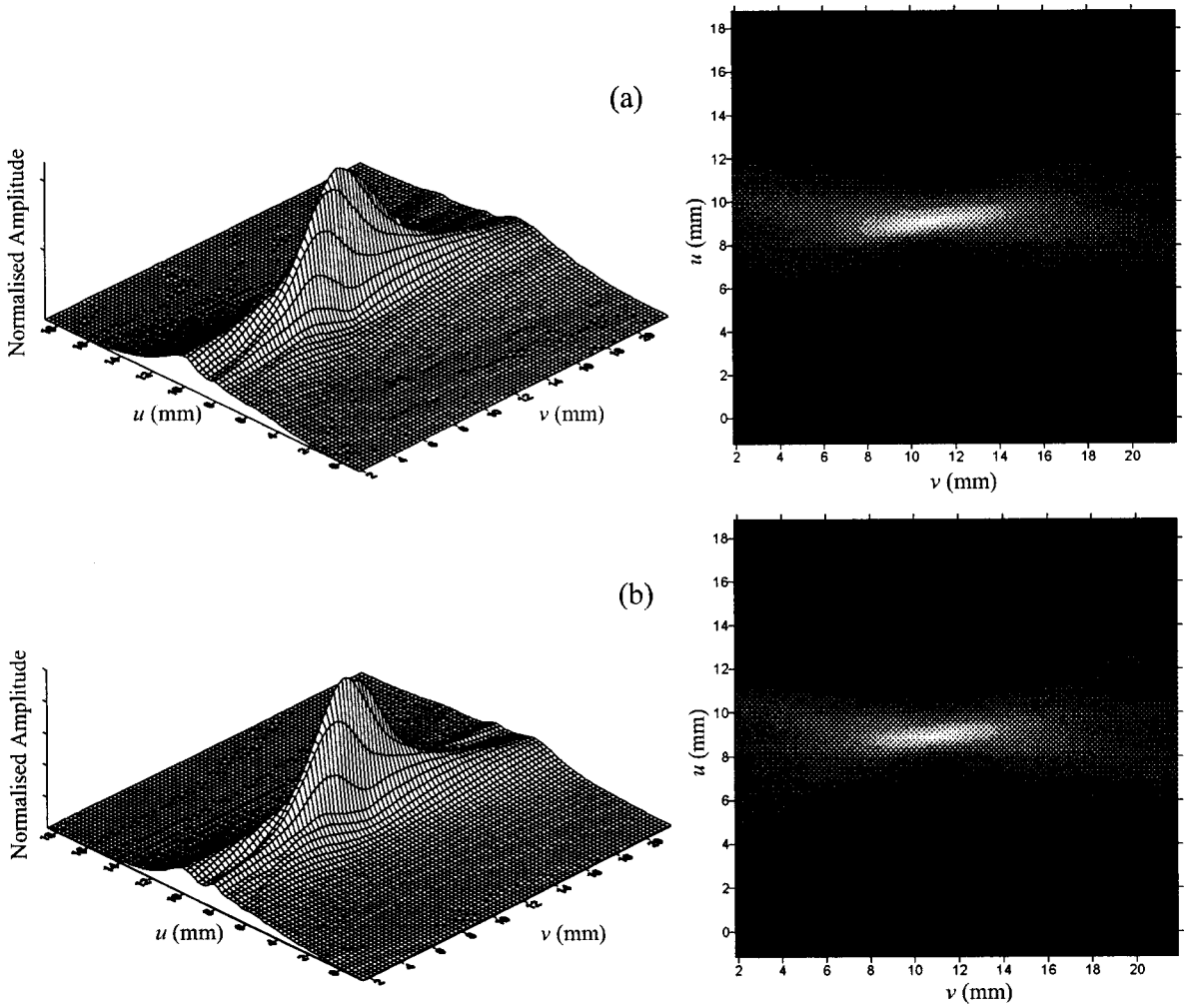

FIG. 10. Comparison of (a) experimental and (b) theoretical reflected pressure fields for excitation of the plane piston with a broad bandwidth voltage drive signal centered at 625 kHz.

III. COMPARISON OF THEORETICAL PREDICTIONS TO EXPERIMENTAL RESULTS

The theoretical model has been used to predict the fields from the actual device shown earlier in Fig. 4, using Eqs. (8) and (9). The mirror shape that was modeled is illustrated in Fig. 6 as (a) a three-dimensional view, and (b) as a cross-section through the $x=0$ plane. The predictions used a series of grid points across the reflector, separated by 0.06 mm, as indicated in Fig. 6(a). Note that a capacitive transducer of the type used to generate the incident field has been previously shown to operate very much like a plane-piston, and hence it is a useful device to help study theoretical models and so aid theoretical understanding.

The experimental apparatus used to measure the radiated field experimentally is shown in Fig. 7. The peak-to-peak pressure was measured experimentally using a miniature capacitive detector, which was 0.5 mm square. This was of a type described elsewhere,[18] and had a silicon nitride membrane fabricated using silicon micromachining. The characteristics of this device were measured, and it was shown that the reception bandwidth in air was sufficiently wide to be used with the focused source. It should, however, be noted that the wavelength in air at a frequency of 1 MHz was ~0.34 mm, and hence at the highest frequencies used in the experiment, the detector was approximately one acoustic wavelength wide. It would thus be expected that some modifications to the received waveforms would result from spatial filtering, when this finite-sized receiver is used at higher frequencies. These effects have been simulated by the authors, and results for typical air-coupled transducers of this type have again been presented elsewhere.[19] These studies indicate that the resultant effect on spatial amplitude scans presented here would be small.

The miniature detector was scanned in the u and v directions with respect to the mirror, in the $w=0$ plane, and waveforms recorded at regular spatial intervals. The focused source was driven using tone-bursts of 30-V amplitude from the Wavetek signal generator, and the radiated field measured at 0.25-mm intervals by scanning the miniature detector using stepper motors, controlled by the PC. The Cooknell CA/6 charge amplifier was used to supply the necessary dc voltage to the detector, and to provide amplification, before the signal was digitized by the oscilloscope under PC control.

Figure 8(a) shows the normalized peak-to-peak pressure amplitude variations that were measured when the source was driven by a 500-kHz tone-burst (the form of which was shown earlier in Fig. 5). The field is plotted using both as a three-dimensional wire plot, and as a gray-scale image

(where a darker region represents a lower amplitude) for clarity. As can be seen, the resulting field has the expected maximum at the focal region. As stated above, the theoretical results were produced using a grid of points on the mirror surface at a pitch of $x_p = y_p = 0.06$ mm (which for the case of the 1-MHz drive waveform, the highest frequency simulated here, corresponds to approximately one-fifth of a wavelength). The resulting pressure field is presented in Fig. 8(b), where it can be seen that the correlation between theoretical and experimental results is very good. Note the structure within the field to the left of the focal region in the plots (i.e., closer to the mirror), which arises from diffraction effects from the narrow-bandwidth tone-burst.

The above procedure was now repeated for a tone burst at a frequency of 1 MHz, and the results are shown in Fig. 9. It can be seen that the focal point in this case is narrower in width than in the case of the 500-kHz drive signal, as would be expected for a shorter wavelength. In addition, Fig. 10 shows a comparison of theory to experiment when a broad bandwidth impulsive drive signal was used to drive the source. The apparatus used in this experiment was the same as that shown in Fig. 7, except that the Wavetek signal generator was replaced by a Panametrics PR5055 pulser. The response of the transducer was found to be centered at 625 kHz, and hence the theoretical simulation used a damped signal with a spectrum centered at the same frequency. It can be seen that with this broader bandwidth waveform there were less amplitude variations in the field regions close to the focal spot than was the case with the longer tone-burst signals, and that the size of the focal point was intermediate in size between those for the 500-kHz and 1-MHz tone-bursts.

IV. CONCLUSIONS

A theoretical model has been produced which predicts the emerging pressure field from a mirror place in the radiated field of a plane piston. The approach of this model is to approximate the reflective surface of the mirror to a grid of point reflectors, and to treat each one as secondary acoustic source with a pressure waveform that can be calculated. This was done for the field from the source in the form of a plane piston, whose field was calculated separately. In this way, the full diffraction pattern following reflection could be calculated. The approach was compared to the results of experiments on a real device working in air, and the main features of the theoretical prediction were observed experimentally. This demonstrated that the theoretical approach had some merit. Note that the technique presented here could be applied to other reflective surfaces, such as flat plates, and appears to be the first such model to be described. In addition, it may be possible to use this model to investigate how the surface roughness of the mirror affects the focal region, by introducing a scaled random variation in the calculation of each point on the mirror surface. This is likely to be the subject of further work.

[1] A. Freedman, ''Sound field of a rectangular piston,'' J. Acoust. Soc. Am. **32**, 197–209 (1960).
[2] J. C. Lockwood and J. G. Willette, ''High-speed method for computing the exact solution for the pressure variations in the nearfield of a baffled piston,'' J. Acoust. Soc. Am. **53**, 735–741 (1973).
[3] P. R. Stepanishen, ''Transient radiation from pistons in an infinite planar baffle,'' J. Acoust. Soc. Am. **49**, 1629–1638 (1971).
[4] J. L. San Emeterio and L. G. Ullate, ''Diffraction impulse-response of rectangular transducers,'' J. Acoust. Soc. Am. **92**, 651–662 (1992).
[5] G. R. Harris, ''Review of transient field-theory for a baffled planar piston,'' J. Acoust. Soc. Am. **70**, 10–20 (1981).
[6] L. W. Schmerr, Jr., A. Sedov, and T. P. Lerch, ''A boundary diffraction wave model for a spherically focussed ultrasonic transducer,'' J. Acoust. Soc. Am. **101**, 1269–1277 (1997).
[7] T. Gudra, M. Pluta, and Z. Kojro, ''The measurement and numerical modelling of the diffraction field of a spherical ultrasonic transducer working in the air at the frequency of 1.3 MHz,'' Ultrasonics **38**, 794–798 (2000).
[8] T. J. Robertson, D. A. Hutchins, and D. R. Billson, ''An air-coupled line focused capacitive ultrasonic transducer,'' Proc. 2000 IEEE Ultrasonics Symposium, San Juan, Puerto Rico, Vol. 2, pp. 1061–1064.
[9] D. W. Schindel, A. G. Bashford, and D. A. Hutchins, ''Focusing of ultrasonic waves in air using a micromachined Fresnel zone-plate,'' Ultrasonics **35**, 275–285 (1997).
[10] D. W. Schindel, ''Ultrasonic imaging of solid surfaces using a focussed air-coupled capacitance transducer,'' Ultrasonics **35**, 587–594 (1998).
[11] G. R. Lockwood, L. K. Ryan, and F. S. Foster, ''A 45 to 55 MHz Needle-based ultrasound system for invasive imaging,'' Ultrason. Imaging **15**, 1–13 (1993).
[12] T. J. Robertson, D. A. Hutchins, D. R. Billson, and J. H. Rakels, ''Surface metrology using reflected ultrasonic signals in air,'' Ultrasonics **39**, 479–486 (2002).
[13] T. J. Robertson, ''Advances in ultrasonic capacitive transducer technology,'' Ph.D. thesis, University of Warwick, 2001.
[14] J. W. S. Rayleigh, *The Theory of Sound* (Dover, New York, 1945), Vol. 1.
[15] J. Krautkrämer and H. Krautkrämer, *Ultrasonic Testing of Materials*, 4th ed. (Springer-Verlag, New York, 1990).
[16] D. W. Schindel, D. A. Hutchins, L. Zou, and M. Sayer, ''The design and characterization of micromachined air-coupled capacitance transducers,'' IEEE Trans. Ultrason. Ferroelectr. Freq. Control **42**, 42–50 (1995).
[17] D. A. Hutchins, D. W. Schindel, A. G. Bashford, and W. M. D. Wright, ''Advances in ultrasonic electrostatic transduction,'' Ultrasonics **36**, 1–6 (1998).
[18] R. A. Noble, A. D. R. Jones, T. J. Robertson, D. A. Hutchins, and D. R. Billson, ''Novel, wide bandwidth, micromachined ultrasonic transducers,'' IEEE Trans. Ultrason. Ferroelectr. Freq. Control **48**, 495–1507 (2001).
[19] A. Neild and D. A. Hutchins, ''A theoretical model for the effect of a finite size acoustic receiver,'' J. Acoust. Soc. Am. **115**, 1546–1556 (2004).

The comb waveform as an efficient method for wideband transducer measurements

Walter H. Boober, Gorham G. Lau, and Kim C. Benjamin[a)]
Naval Sea Systems Command Division Newport, Newport, Rhode Island 02841

Kenneth M. Walsh
K & M Engineering LTD, 51 Bayberry Lane, Middletown, Rhode Island 02842

(Received 17 May 2004; revised 22 August 2004; accepted 24 August 2004)

An efficient acoustic calibration technique based on a uniformly weighted comb waveform is presented. The method takes advantage of the linear, time invariant nature of the measurement configuration and the comb's wide bandwidth to capture all spectral components of interest for a device under test in a single ping. Measured results comparing single ping comb measurements with conventionally obtained tonal measurements are presented. The examples given illustrate the accuracy and utility of this technique for the calibration of broadband systems. © *2004 Acoustical Society of America.* [DOI: 10.1121/1.1808222]

PACS numbers: 43.20.Ye, 43.30.Xm, 43.58.Vb [EJS] Pages: 2802–2806

I. INTRODUCTION

For acoustic calibrations being performed in a stationary tank environment, the comb pulse provides an efficient way to measure the device(s) under test by reducing the number of discrete tonal signals, required to cover the frequency range of interest, to one.

Background information on the use of comb pulses in sonar applications emphasizes its use as a wideband sonar waveform due to its Doppler sensitivity.[1–3] For a moving target/platform scenario such wideband signals improve signal-to-noise ratio in littoral environments. As a result, several comb constructs have been examined for optimal range and Doppler resolution in terms of their ambiguity functions. Parametric studies have included amplitude weighting and nonlinear spacing of comb tines as well as superposing multiple combs within a single pulse.

By using the comb-based technique described below, one can condense hours of testing into a very short span of time. For example, a comb pulse waveform was successfully used to calibrate a system at 5000-Hz increments from 5 to 100 kHz over ±58° in the *XY* plane. This evaluation required the system under test to acquire and store the data, a process taking about 155 s for the ±58°. Using conventional techniques, this would require 20 measurements to acquire each discrete frequency and would take >60 min. The comb pulse method reduced this by a factor of >20, to ~2.5 min. Add to this that each run had to be repeated at 18 different roll angles and one can see the efficacy of the comb quite clearly.

The comb waveform allows one to sample the frequency band of interest at a set of desired frequencies (narrow spectral bands) that are transmitted simultaneously. The shape of these stacked pass bands resemble the tines of a comb in the frequency domain. A single tine component in the time domain, shown in Fig. 1, is developed at the four desired frequencies and summed to form a comb pulse. For example, four separate tines of a comb centered at 1-kHz increments are shown in the Fig. 2 spectrum.

Due to the linear, time invariant nature of the acoustic signals considered here, the comb pulse can be initially generated in either the time or frequency domain. However, in this paper, the example given creates the comb pulse in the time domain by creating and summing the individual pulsed waveforms at the frequencies of interest. In practice it is much simpler to work in the time domain where quantities are real-valued. Also, working in the time domain makes amplitude weighting versus time easier. Amplitude weighting versus time (cosine tapering) is used to reduce the influence of leading and trailing edge slopes that increase the pulse bandwidth. Amplitude shading in the time domain reduces the coupling between adjacent tines to −80 dB in the frequency domain (see Fig. 2).

Variations such as 12 dB/oct below, or 6 dB/oct above, resonance, typical for most transducers, are readily compensated for through weighting versus frequency prior to application of the signal to the unit under test. In some cases it is desirable to generate a sound pressure level that is constant with respect to frequency. One caveat to keep in mind is that, due to the range of frequencies being covered, one must be conscious of the fidelity of voltage, current, and sound field over the range of interest. Thus signal-to-noise ratio (SNR) at some frequencies does come into play over very wide bands of interest where the requirement for lower drive levels at some frequencies will appreciably attenuate others. But, the beauty of a comb is one can put an inverse slope on the signal to mitigate such effects.

The background noise in the acoustic calibration tank is relatively low; 25 dB re 1 μPa up to 80 kHz, rising to 38 dB re 1 μPa at 120 kHz. With source levels for acoustic test signals ranging 150–160 dB re 1 μPa, SNR values around 125 dB are typical. If a ten tone comb is used, the pulse components are 20 dB down resulting in 105 dB SNR. Techniques to modify the phase of the signals (i.e., parabolic phase) will reduce the peak effects among the tones.

[a)]Author to whom correspondence should be addressed. Electronic mail: benjaminkc@npt.nuwc.navy.mil

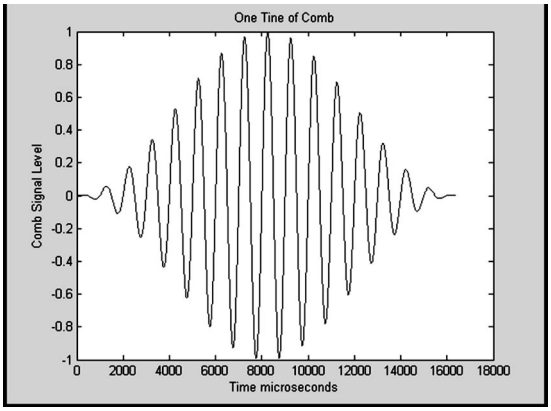

FIG. 1. Time domain plot of one comb tine.

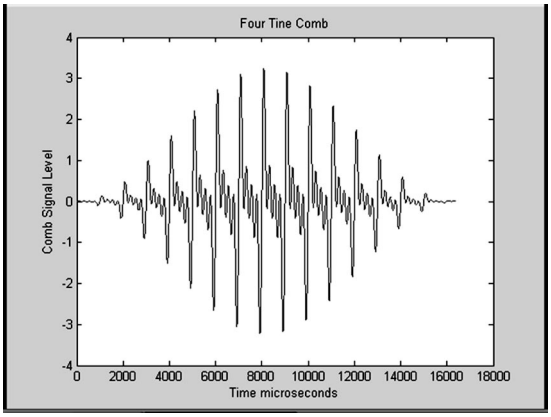

FIG. 3. Time domain plot for four tines in one comb pulse.

Figure 3 shows a four tine comb waveform in the time domain. This signal is represented digitally with an arbitrary waveform generator or a digital computer interface coupled to the analog test electronics.

The use of a uniform weighted comb for calibrating sonar transducers and arrays seems to be relatively ignored and perhaps categorized as another complex waveform that is easily described mathematically but difficult to realize in practice. Yet recent developments in broadband piezocomposite-based acoustic standards,[4,5] that provide usable bandwidths, on the order of a decade, have enhanced the viability and effectiveness of the comb measurement approach.

Other broadband signals such as FM chirps, pulsed white noise, or impulse spikes have been used for acoustic calibration purposes. The FM chirp, in contrast to the comb pulse, possesses a continuous spectrum, and separation of the spectral components requires slightly more complicated matched-filter processing. Both pulsed white noise and impulsive waveforms are of limited use for high Q devices due to the insufficient time duration and/or energy content of their spectral components. As a rule,[6] Q cycles of build-up time in the signal are required before capturing data, where Q is the mechanical quality factor of the transducer.

The comb pulse can be used in a research and development environment requiring prodigious amounts of testing for limited amounts of funds, or in a production setting where time savings and product consistency are important. The technique also allows one to vary the sampling resolution; increasing it in some regions, decreasing it in others, providing for more in-depth data collection.

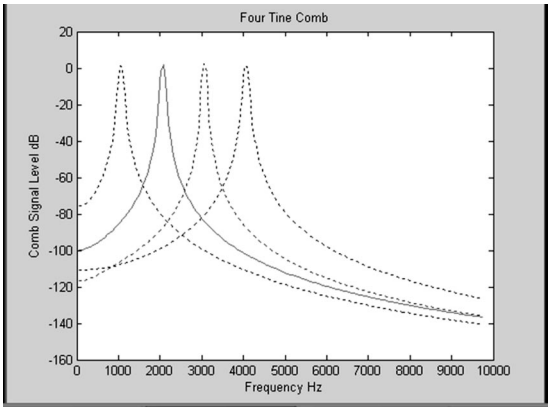

FIG. 2. Spectrum of four tines plotted on the same graph with 1 kHz between tine centers.

The comb pulse was first proposed in October of 2000 for use at the Navy's Acoustic Test Facility, Code 8211, in Newport, RI as a way of saving money during acoustic tank tests of a broadband sparse array hydrophone system as was described earlier. Essentially all of the standard acoustic calibrations made by stepping frequency or amplitude can easily be done with a single comb pulse. Examples include frequency responses, impedance/admittance, spatial response measurements, and power linearity measurements.

The next section algorithmically describes the comb calibration technique. Measured results comparing comb to tonal measurements and conclusions are presented in Secs. III and IV, respectively. The MATLAB code used to generate and process the comb waveforms used in this paper is available from the authors upon request.

II. COMB PULSE GENERATION AND PROCESSING

A. Comb pulse algorithm (Transmit)

The comb pulse given by Eq. (1) (Figs. 2 and 3) may be obtained by summing the product of a time dependent window function env (t) and a uniform weighted sinusoidal pulse TimeSeries (i,t) as defined by Eqs. (2) and (3), respectively, over a series of frequencies of interest.

$$\text{CombPulse}(t)=\sum\ (\text{Env}(t)*\text{TimeSeries}(i,t)),$$
$$i=1-4, \tag{1}$$

$$\text{Env}(t)=0.5-0.5*\cos(2*\pi*t/T), \tag{2}$$

where t is in microseconds and $T=16\,384\,\mu$,

$$\text{TimeSeries}(i,t)=\sin(2*\pi*F(i)*t)$$
$$F(i)=1-4\ \ \text{kHz}. \tag{3}$$

TimeSeries (i,t) and env (t) represent the ith uniformly weighted sinusoidal pulse and corresponding time window function where i is an integer-valued index corresponding to the frequency of interest.

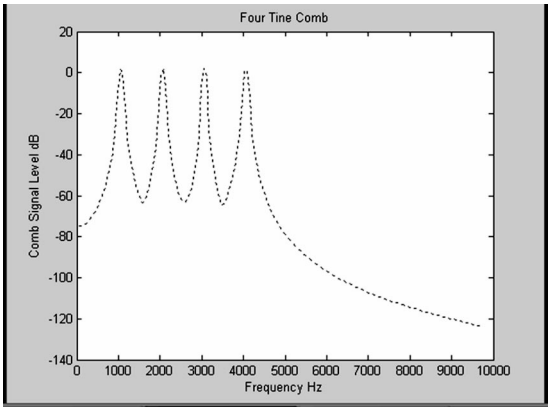

FIG. 4. FFT of four tine comb pulse.

The four tine transmit pulse generated by Eqs. (1)–(3) has a time domain representation that is shown in Fig. 3. It can be Fourier transformed on receive as depicted in Fig. 4. Note the shape of the spectrum is essentially the same as the sum of the individual components plotted in Fig. 2.

Comb pulses of up to 96 tines have been used successfully to calibrate underwater transducers at the Naval Undersea Warfare Center's Acoustic Test Facility, Code 8211, in Newport, RI.

B. Comb pulse algorithm (Receive)

On reception, the composite comb time signal is transformed using the fast Fourier transform (FFT) according to Eq. (4), and the real and imaginary parts of the positive frequency components are retained for processing as indicated in Eq. (5):

$$\text{COMB PULSE Spectrum} = \text{FFT}\{\text{Comb Pulse}(t)\}, \quad (4)$$

$$\text{COMB PULSE Spectrum Pos} = C_{\text{Real}}(f) + jC_{\text{Imag}}(f). \quad (5)$$

These are then converted to magnitude and phase according to Eqs. (6) and (7), respectively:

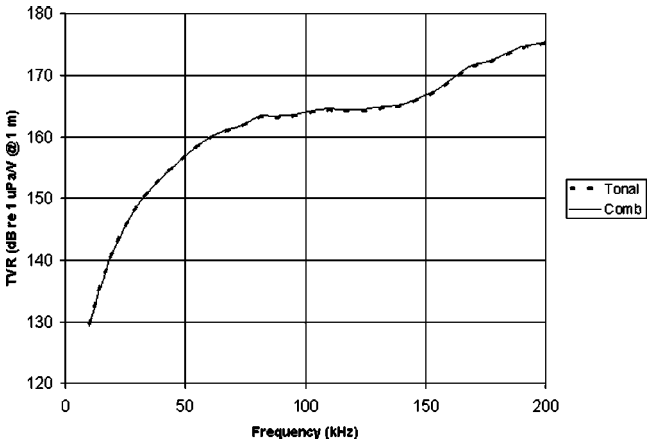

FIG. 5. Comparison between comb pulse and conventional CW methods: transmit voltage response (TVR).

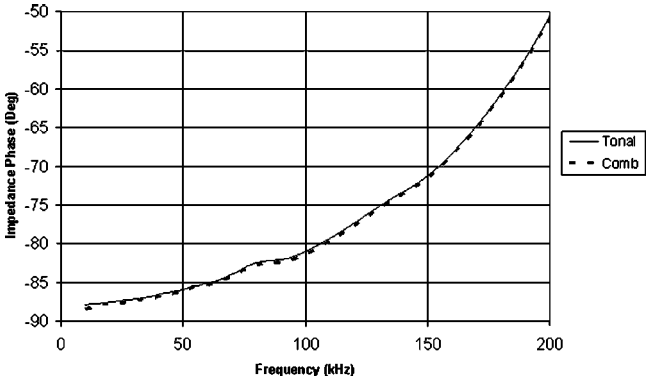

FIG. 6. Comparison between comb pulse and conventional CW methods: impedance phase angle.

$$\text{Magnitude (dB)} = 20\,\text{Log}_{10}\{\text{abs(COMB PULSE Spectrum Pos)}\} - 3, \quad (6)$$

$$\text{Phase (Deg.)} = \text{ArcTangent2}\{(C_{\text{Imag}}(f))/(C_{\text{Real}}(f))\} * 180/\pi. \quad (7)$$

In the case of the magnitude, 3 dB is subtracted from the value returned from the FFT to convert it from peak to rms. Three one-dimensional arrays are formed to store frequency, magnitude, and phase data. For each frequency of interest (comb tine), an integer-valued index is calculated, which is used to locate the corresponding magnitude and phase values within the spectrum returned by the FFT routine. This index will range from 1 to N where N is the number of frequency components in the comb. The index values are calculated using Eq. (8),

$$\begin{aligned} &\text{Index (1)} = \text{f1/FFT bin width},\\ &\text{Index (2)} = \text{f2/FFT bin width},\\ &\quad .\\ &\quad . \\ &\text{Index } (N) = \text{f}N\text{/FFT bin width}, \end{aligned} \quad (8)$$

where the

$$\text{FFT bin width} = \text{Sampling Frequency/Time record length}, \quad (9)$$

f1,...,fN are the frequencies of interest (tops of the tines).

The frequencies of interest (tines) do not necessarily have to be linearly spaced. However, the sampling frequency should be selected such that each frequency of interest divided by FFT bin width is integer-valued. This will facilitate accurate recovery of data corresponding to the frequencies of interest.

For a frequency response measurement, these data values can be used directly in the various data reduction formulas and graphically displayed as if a normal test had been run.

For a spatial response (beam pattern) measurement, the magnitude and phase values of each of the comb frequencies must be stored into a $3 \times n$ array for each of the n bearings.

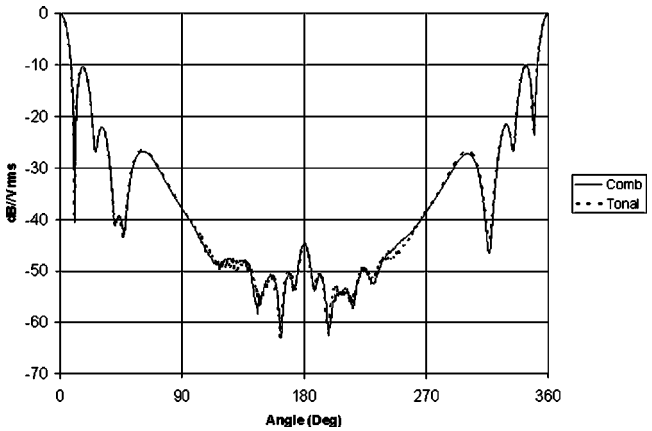

FIG. 7. Comparison between comb pulse and conventional CW methods: 10-kHz beam pattern.

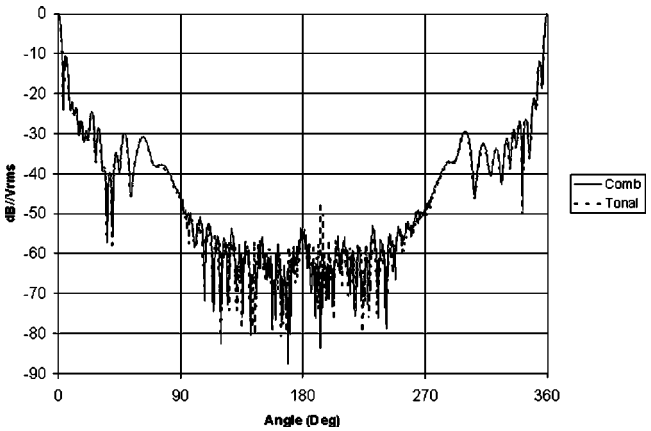

FIG. 9. Comparison between comb pulse and conventional CW methods: 30-kHz beam pattern.

When displaying the beam patterns, only one can be displayed at a time. The user selects the frequency to be displayed. The program will then use the index array to retrieve the angular data related to that frequency and display the desired plot.

III. TEST DATA COMPARISON

The following measured acoustic responses were generated using both the standard CW pulse method,[6] and the comb pulse approach described above. The MATLAB Scripts (available to interested readers upon request) were used to generate and process the pulses.

The frequency response data, transmitting voltage response (TVR) and impedance and phase, were obtained using a broadband US Navy standard,[5] whereas the spatial response data were measured on a commercially available transducer.

A. Frequency response measurements

Figure 5 shows a comparison of the transmit voltage response obtained by the two methods. The tonal pulse method required 96 individual measurements (10–200 kHz with 1-kHz steps) of voltage, current, and hydrophone output, while the comb method required only one. The impedance phase was also measured using both methods and the comparison is shown in Fig. 6. Note the traces overlay near perfectly for these cases.

The results differ by less than 0.2 dB (200 mdB) for the TVR measurement and 0.4° (380 mDeg.).

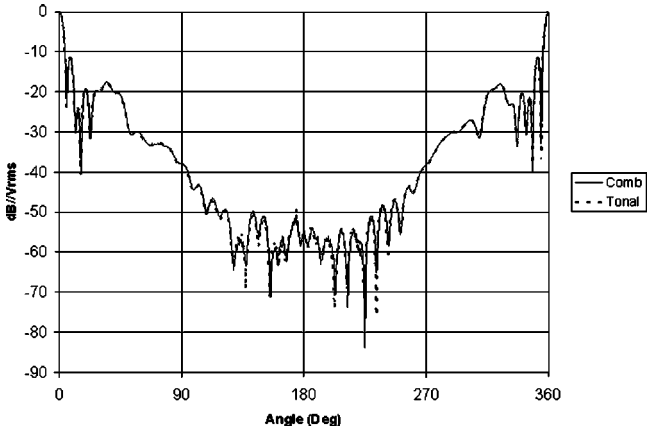

FIG. 8. Comparison between comb pulse and conventional CW methods: 20-kHz beam pattern.

B. Spatial response measurements

Figures 7–9 are radiation pattern overlays which illustrate the extreme fidelity of the tonal pulse and the comb waveform. In this case the comb covered a band from 10 to 30 kHz. The slight variations between patterns, in the worst example, do not appear until >25 dB below the mean response axis (MRA) of the 10-kHz pattern. At 30 kHz irregularities do not appear until levels are >35 dB below the MRA. As in the transfer functions, upon careful examination the differences at those levels can be seen to be <0.5 dB, which at those levels is equivalent to 0.992 mV. This could be attributed to changes due to the nearly 3 h of time difference between the acquisitions of the patterns. Therefore, it is noted that utilizing a comb pulse approach for beam patterns, or any other test requiring physical movement, mitigates problems related to repeatability of position that are often the case for discrete successive frequency increments run over time.

IV. CONCLUSIONS

An efficient acoustic calibration technique based on a uniformly weighted comb waveform has been experimentally demonstrated. The method takes advantage of the linear, time invariant nature of the measurement configuration and the comb's wide bandwidth to capture all spectral components of interest for a device under test in a single ping. Measured results comparing single ping comb measurements with conventionally obtained CW measurements have shown excellent agreement. The examples given illustrate the accuracy and utility of this technique for the calibration of broadband systems.

ACKNOWLEDGMENTS

The measurement technique described in this article was sponsored by the U.S. Navy, NUWCDIVNPT, Code 8211

Acoustic Test Facility and K&M Engineering LTD. The authors thank the following individuals for their valuable support in performing the required validation tests for the ''comb'' measurement technique reported: Rene Lafleur and Hugo Mendoza (Code 8211). Also, special thanks to Steve Tomaszewski, Senior Systems Engineer for Advanced Acoustics Concepts, whose test requirements and willingness provided the impetus for developing and utilizing the ''comb'' as a testing tool.

[1] J. M. Alsup, ''Comb waveforms for sonar,'' in Proceedings of 33rd Asilomar Conference on Signals, systems, and computers (1999), Vol. Pt. 2, pp. 864–869.

[2] T. Collins and P. Atkins, ''Doppler-sensitive active sonar pulse design for reverberation processing,'' in IEE Proc. Radar, Sonar Navig. (1998), Vol. 145(6), pp. 347–353.

[3] H. Cox and H. Lai, ''Geometric comb waveforms for reverberation suppression,'' in Proceedings of 28th Asilomar Conference on Signals, systems, and computers (1994), Vol. Pt. 2, pp. 1185–1189.

[4] K. C. Benjamin and S. Petrie, ''The design, fabrication, and measured acoustic performance of a 1–3 piezocomposite-based Navy calibration standard transducer,'' J. Acoust. Soc. Am. **109**(5), 1973–1978 (2001).

[5] K. C. Benjamin, A. L. Van Buren, and S. Petrie, ''The development of affordable constant beamwidth transducers using injection molded 1-3 piezoelectric composite,'' presented at the 135th Meeting of the Acoustical Society of America, Seattle, WA (June 1998).

[6] ANSI Std S1.20-1988, reaffirmed by ANSI 5/28/98.

Modeling of nonlinear shear waves in soft solids

Evgenia A. Zabolotskaya, Mark F. Hamilton, Yurii A. Ilinskii, and G. Douglas Meegan
Applied Research Laboratories, The University of Texas at Austin, Austin, Texas 78713-8029

(Received 17 December 2003; revised 12 August 2004; accepted 12 August 2004)

An evolution equation for nonlinear shear waves in soft isotropic solids is derived using an expansion of the strain energy density that permits separation of compressibility and shear deformation. The advantage of this approach is that the coefficient of nonlinearity for shear waves depends on only three elastic constants, one each at second, third, and fourth order, and these coefficients have comparable numerical values. In contrast, previous formulations yield coefficients of nonlinearity that depend on elastic constants whose values may differ by many orders of magnitude because they account for effects of compressibility as well as shear. It is proposed that the present formulation is a more natural description of nonlinear shear waves in soft solids, and therefore it is especially applicable to biomaterials like soft tissues. Calculations are presented for harmonic generation and shock formation in both linearly and elliptically polarized shear waves.
 [DOI: 10.1121/1.1802533]

PACS numbers: 43.25.Dc [JJM] Pages: 2807–2813

I. INTRODUCTION

While the canonical form of the evolution equation for nonlinear shear waves in isotropic solids is well known,[1,2] explicit expressions for the coefficient of nonlinearity are rarely presented and, to our knowledge, yet to be interpreted. We are aware of only two articles that provide such expressions. In the first, by one of the present authors,[3] the coefficient is expressed in terms of elastic constants in an extension of the strain energy expansion introduced by Landau and Lifshitz[4] for isotropic solids. In the second, by Jiang *et al.*,[5] the coefficient is expressed in terms of the general elastic constants used by Thurston and Shapiro.[6]

An expansion introduced recently[7] for the strain energy density allows separation of the effects associated with compressibility and pure shear deformation. The expansion was motivated by attempts to interpret measurements of nonlinear shear waves in tissuelike media.[8] It was shown that for pure shear deformation, the expansion requires only three elastic constants through fourth order, one at second order (the shear modulus), one at third order (the constant A of Landau and Lifshitz), and a new constant at fourth order. These three constants are of the same order of magnitude for shear deformation in tissuelike media. In contrast, the individual elastic constants in earlier expressions for nonlinear shear waves[3,5] differ by five to six orders of magnitude in such media.[8] Measured values of second-order elastic constants in soft biological tissues may be found in articles on this subject that are cited by Sarvazyan *et al.*[9]

The problem is that conventional expansions[4,6] of the strain energy density yield elastic constants that account individually for both compression and shear. For soft solids, these constants contain very large parts associated with compression, and very small parts associated with shear, with small and large reflecting the difference in magnitudes described in the previous paragraph. Using these expansions it is difficult, if not currently impossible, to determine the very small parts of the third- and fourth-order coefficients that contribute to shear deformation alone.

Although the motivation for the present paper is the recent measurements of fourth-order elastic constants in tissuelike media,[8] this paper does not focus specifically on, nor is it restricted to, propagation in tissuelike media. The analysis is advantageous for soft solids in general because the speeds of the shear and longitudinal waves differ so greatly that coupling of these modes of propagation can be ignored. In this case the expansion of the strain energy density used below is especially convenient. Measurements of odd-harmonic generation and shock formation in nonlinear shear waves propagating in a soft tissue phantom were reported recently by Catheline *et al.*[10] We note that the present analysis can also be used for shear waves in hard solids provided longitudinal disturbances are avoided. For example, measurements of third-harmonic generation in piezoelectric (PZT) ceramics were reported recently by Jiang *et al.*[5] For their experiments on unpoled PZT the medium may be treated as isotropic, in which case the theory presented below may be applied. Comparison of our result with theirs for the coefficient of nonlinearity in this case is made in Sec. IV.

The purpose of the present paper is to develop an evolution equation for nonlinear shear waves, based on first principles, using the expansion of the strain energy density described in Ref. 7. It is proposed that the present formulation offers considerable advantage over previous formulations for determining the third- and fourth-order elastic constants that contribute most to the nonlinear distortion of shear waves.[3,5] Both linearly and elliptically polarized shear waves are considered, and calculations are presented in each case for harmonic generation and shock formation.

II. BASIC EQUATIONS

The strain energy density of an isotropic solid can be expanded with respect to three independent invariants. As shown previously,[7] if ρ_0^2/ρ^2 (the third principal invariant of the Green deformation tensor) and two Lagrangian strain

tensor invariants I_2 and I_3 are taken as independent invariants, then the strain energy density can be expanded through cubic order as follows:

$$\mathcal{E}=\mathcal{E}_0(\rho)+\mu(\rho)I_2+\frac{1}{3}A(\rho)I_3+DI_2^2. \tag{1}$$

Here

$$I_2=u_{ik}u_{ki}, \quad I_3=u_{ik}u_{kl}u_{li}, \tag{2}$$

are the invariants used by Landau and Lifshitz,[4] and

$$u_{ik}=\frac{1}{2}\left(\frac{\partial u_i}{\partial x_k}+\frac{\partial u_k}{\partial x_i}+\frac{\partial u_l}{\partial x_i}\frac{\partial u_l}{\partial x_k}\right) \tag{3}$$

is the Lagrangian strain tensor, where u_i are components of the particle displacement vector. The first term in Eq. (1), $\mathcal{E}_0(\rho)$, accounts only for effects associated with compression, and subsequent terms account for shear deformation and its coupling with compression. In general, the parameters μ and A are functions of the density ρ, and D is the fourth-order elastic constant. This expansion of the strain energy thus permits separation of effects due to compression and shear deformation.

In particular, for the case of soft solids, Eq. (1) permits longitudinal and shear waves to be considered separately. For describing longitudinal waves it is sufficient to let $\mathcal{E}=\mathcal{E}_0(\rho)$, whereas for shear waves Eq. (1) reduces to

$$\mathcal{E}=\mu I_2+\frac{1}{3}AI_3+DI_2^2, \tag{4}$$

where μ is the shear modulus, and A is one of the third-order elastic constants introduced by Landau and Lifshitz.[4] It is Eq. (4) that we use here to develop an explicit expression for the coefficient of nonlinearity for shear waves of finite amplitude. The advantage of the present approach is discussed in Sec. IV.

The equation of motion in the medium is[4]

$$\rho_0\frac{\partial^2 u_i}{\partial t^2}=\frac{\partial \sigma_{ik}}{\partial x_k}, \tag{5}$$

where ρ_0 is the density of the material in its undeformed state and σ_{ik} is the stress tensor, defined by

$$\sigma_{ik}=\frac{\partial \mathcal{E}}{\partial(\partial u_i/\partial x_k)}. \tag{6}$$

Substitution of Eq. (3) in Eq. (2) yields

$$I_2=\frac{1}{2}\left(\frac{\partial u_i}{\partial x_k}\frac{\partial u_i}{\partial x_k}+\frac{\partial u_i}{\partial x_k}\frac{\partial u_k}{\partial x_i}+\frac{\partial u_i}{\partial x_k}\frac{\partial u_l}{\partial x_i}\frac{\partial u_l}{\partial x_k}+\frac{\partial u_k}{\partial x_i}\frac{\partial u_l}{\partial x_i}\frac{\partial u_l}{\partial x_k}+\frac{1}{2}\frac{\partial u_l}{\partial x_i}\frac{\partial u_l}{\partial x_k}\frac{\partial u_s}{\partial x_i}\frac{\partial u_s}{\partial x_k}\right), \tag{7}$$

$$I_3=\frac{1}{4}\left(\frac{\partial u_i}{\partial x_k}\frac{\partial u_k}{\partial x_m}\frac{\partial u_m}{\partial x_i}+3\frac{\partial u_i}{\partial x_k}\frac{\partial u_k}{\partial x_m}\frac{\partial u_i}{\partial x_m}+3\frac{\partial u_i}{\partial x_k}\frac{\partial u_s}{\partial x_k}\frac{\partial u_s}{\partial x_m}\frac{\partial u_m}{\partial x_i}+\frac{3}{2}\frac{\partial u_i}{\partial x_k}\frac{\partial u_s}{\partial x_k}\frac{\partial u_s}{\partial x_m}\frac{\partial u_i}{\partial x_m}+\frac{3}{2}\frac{\partial u_k}{\partial x_i}\frac{\partial u_s}{\partial x_k}\frac{\partial u_s}{\partial x_m}\frac{\partial u_m}{\partial x_i}\right), \tag{8}$$

$$I_2^2=\frac{1}{4}\left[\left(\frac{\partial u_i}{\partial x_k}\frac{\partial u_i}{\partial x_k}\right)^2+\left(\frac{\partial u_i}{\partial x_k}\frac{\partial u_k}{\partial x_i}\right)^2+2\frac{\partial u_i}{\partial x_k}\frac{\partial u_i}{\partial x_k}\frac{\partial u_m}{\partial x_s}\frac{\partial u_s}{\partial x_m}\right]. \tag{9}$$

For pure shear deformation, we may now substitute Eqs. (7)–(9) in Eq. (4), and the latter in Eq. (6), to obtain the following expression for the stress tensor:

$$\sigma_{ik}=\mu\left(\frac{\partial u_i}{\partial x_k}+\frac{\partial u_k}{\partial x_i}+\frac{\partial u_l}{\partial x_i}\frac{\partial u_l}{\partial x_k}+\frac{\partial u_i}{\partial x_l}\frac{\partial u_k}{\partial x_l}+\frac{\partial u_i}{\partial x_l}\frac{\partial u_l}{\partial x_k}+\frac{\partial u_i}{\partial x_l}\frac{\partial u_s}{\partial x_l}\frac{\partial u_s}{\partial x_k}\right)+\frac{A}{4}\left(\frac{\partial u_k}{\partial x_m}\frac{\partial u_m}{\partial x_i}+\frac{\partial u_k}{\partial x_m}\frac{\partial u_i}{\partial x_m}+\frac{\partial u_m}{\partial x_i}\frac{\partial u_m}{\partial x_k}+\frac{\partial u_i}{\partial x_s}\frac{\partial u_s}{\partial x_k}\right.$$
$$\left.+\frac{\partial u_s}{\partial x_k}\frac{\partial u_s}{\partial x_m}\frac{\partial u_m}{\partial x_i}+\frac{\partial u_j}{\partial x_k}\frac{\partial u_i}{\partial x_m}\frac{\partial u_m}{\partial x_j}+\frac{\partial u_j}{\partial x_l}\frac{\partial u_i}{\partial x_l}\frac{\partial u_k}{\partial x_j}+\frac{\partial u_k}{\partial x_l}\frac{\partial u_s}{\partial x_l}\frac{\partial u_s}{\partial x_i}+2\frac{\partial u_s}{\partial x_k}\frac{\partial u_s}{\partial x_m}\frac{\partial u_i}{\partial x_m}+\frac{\partial u_s}{\partial x_i}\frac{\partial u_s}{\partial x_m}\frac{\partial u_m}{\partial x_k}+\frac{\partial u_i}{\partial x_m}\frac{\partial u_k}{\partial x_j}\frac{\partial u_m}{\partial x_j}\right)$$
$$+D\left(\frac{\partial u_m}{\partial x_j}\frac{\partial u_m}{\partial x_j}\frac{\partial u_i}{\partial x_k}+\frac{\partial u_m}{\partial x_j}\frac{\partial u_j}{\partial x_m}\frac{\partial u_k}{\partial x_i}+\frac{\partial u_i}{\partial x_k}\frac{\partial u_m}{\partial x_j}\frac{\partial u_j}{\partial x_m}+\frac{\partial u_m}{\partial x_j}\frac{\partial u_m}{\partial x_j}\frac{\partial u_k}{\partial x_i}\right). \tag{10}$$

III. LINEARLY POLARIZED SHEAR WAVE

Considerable simplification of the equation of motion is obtained for linearly polarized plane shear waves. We consider a plane wave that propagates along the x_3 axis, with particle motion restricted to the x_1 axis. The particle displacement in the wave is expressed as $u_1(x_3,t)$, and the only nonzero component of the stress tensor is thus

$$\sigma_{13}=\mu\frac{\partial u_1}{\partial x_3}+\left(\mu+\frac{A}{2}+D\right)\left(\frac{\partial u_1}{\partial x_3}\right)^3. \tag{11}$$

Substitution of Eq. (11) in Eq. (5) yields

$$\rho_0\frac{\partial^2 u}{\partial t^2}=\mu\frac{\partial^2 u}{\partial z^2}+\gamma\frac{\partial}{\partial z}\left(\frac{\partial u}{\partial z}\right)^3, \tag{12}$$

where we have let $u=u_1$, $z=x_3$, and

$$\gamma=\mu+\frac{1}{2}A+D. \tag{13}$$

Standard methods may now be used to simplify Eq. (12) for progressive waves, assumed here to propagate in the $+z$ direction. Specifically, the following coordinate transformation is introduced:

$$z_s=\epsilon^2 z, \quad \tau=t-z/c, \tag{14}$$

where τ is a retarded time corresponding to a reference frame travelling at the small-signal wave speed $c=(\mu/\rho_0)^{1/2}$. With ϵ a small dimensionless parameter of order u, distance z_s is a slow scale corresponding to the variation of u in the retarded time frame. We thus have

$$\frac{\partial}{\partial z}=\epsilon^2\frac{\partial}{\partial z_s}-\frac{1}{c}\frac{\partial}{\partial \tau}, \quad \frac{\partial}{\partial t}=\frac{\partial}{\partial \tau}. \tag{15}$$

Substitution in Eq. (12) and discarding terms of higher order than ϵ^3 gives

$$\epsilon^2\frac{2\mu}{c}\frac{\partial^2 u}{\partial z_s \partial \tau}=\frac{\gamma}{c^4}\frac{\partial}{\partial \tau}\left(\frac{\partial u}{\partial \tau}\right)^3. \tag{16}$$

Reinstating the coordinate z in place of z_s and introducing the particle velocity

$$v=\frac{\partial u}{\partial \tau} \tag{17}$$

yields

$$\frac{\partial v}{\partial z}=\frac{\gamma}{2\mu c^3}\frac{\partial v^3}{\partial \tau}, \tag{18}$$

or equivalently

$$\frac{\partial v}{\partial z}=\frac{\beta}{c^3}v^2\frac{\partial v}{\partial \tau}, \tag{19}$$

where

$$\beta=\frac{3}{2}\left(1+\frac{\frac{1}{2}A+D}{\mu}\right) \tag{20}$$

is the coefficient of nonlinearity. Equation (19) is the desired evolution equation for nonlinear shear waves, expressed in terms of $v(z,\tau)$.

The general solution of Eq. (19) is well known.[2] If $v(0,\tau)=f(\tau)$, where $f(t)$ is an arbitrary waveform at $z=0$, the implicit solution is

$$v=f(\tau+\beta z v^2/c^3) \tag{21}$$

or, in parametric form,

$$v=f(\phi), \quad \phi=\tau+\beta z v^2/c^3. \tag{22}$$

The solution is valid up to the point of shock formation, beyond which it becomes multivalued.

The shock formation distance is determined by writing

$$\frac{\partial v}{\partial \tau}=f'(\phi)\frac{\partial \phi}{\partial \tau}=f'(\phi)\left(1+\frac{2\beta z}{c^3}v\frac{\partial v}{\partial \tau}\right) \tag{23}$$

and rearranging to solve for $\partial v/\partial \tau$:

$$\frac{\partial v}{\partial \tau}=\frac{f'(\phi)}{1-(2\beta z/c^3)f(\phi)f'(\phi)}, \tag{24}$$

where $f'(\phi)=df/d\phi$. The shock formation distance $\bar{z}$ is the minimum value of z for which $\partial v/\partial \tau=\infty$, where the denominator vanishes:

$$\bar{z}=\frac{c^3}{2\beta \max[f(t)f'(t)]}, \tag{25}$$

expressed here in terms of the source waveform $f(t)$.

For example, given the sinusoidal source condition

$$v(0,t)=v_0 \sin \omega t \equiv f(t), \tag{26}$$

Eq. (25) yields

$$\bar{z}=\frac{c^3}{\beta \omega v_0^2}, \tag{27}$$

obtained by noting that $f(t)f'(t)=\frac{1}{2}\omega v_0^2 \sin 2\omega t$. In a given period of the source waveform, say $-\pi \leq \omega t \leq \pi$, there are two points at which shock formation occurs. These are the points where $\sin 2\omega t=1$ within the same interval, i.e., $\omega t=-3\pi/4$ and $\omega t=\pi/4$. Lee-Bapty and Crighton[1] developed a weak shock theory that determines the waveforms beyond the shock formation distance.

IV. COMPARISON WITH OTHER APPROACHES

Here we compare our approach with previous formulations. This is done most conveniently in terms of the coefficient of the cubic terms in Eqs. (11) and (12), as defined in Eq. (13) and rewritten here for convenience:

$$\gamma=\mu+\frac{1}{2}A+D. \tag{28}$$

Its relation to the coefficient of nonlinearity used above is $\beta=3\gamma/2\mu$.

If instead of Eq. (4) the standard expansion

$$\mathcal{E}=\frac{1}{2!}c_{ijkl}u_{ij}u_{kl}+\frac{1}{3!}c_{ijklmn}u_{ij}u_{kl}u_{mn}+\frac{1}{4!}c_{ijklmnpq}u_{ij}u_{kl}u_{mn}u_{pq} \tag{29}$$

is used, then for an isotropic solid one obtains

$$\gamma=\frac{1}{2}c_{11}+c_{155}+\frac{1}{6}c_{5555}, \tag{30}$$

in which the abbreviated Voigt notation for the elastic constants is employed.[11] Equation (30) is the result obtained by Jiang *et al.*[5] (see the expression for M_4 in their Table I; differences in subscripts are due to different axes used for propagation direction and particle displacement).

Alternatively, the following expansion for an isotropic solid can be used:[3]

$$\mathcal{E}=\mu I_2+\frac{1}{2}\lambda I_1^2+\frac{1}{3}AI_3+BI_1I_2+\frac{1}{3}CI_1^3+EI_1I_3+FI_1^2I_2+GI_2^2+HI_1^4, \tag{31}$$

where $I_1=u_{ii}$ is an invariant, I_2 and I_3 are defined in Eq. (2), λ is a Lamé constant (often expressed as $\lambda=K-\frac{2}{3}\mu$, where K is the bulk modulus), A, B, and C are third-order

elastic constants[4] [with A the same as in Eq. (4)], and E, F, G, and H are fourth-order elastic constants. Equation (31) is equivalent to Eq. (12) in Ref. 3 with D set to zero in the latter (see Ref. 7 for discussion of this difference). One now obtains[3]

$$\gamma = \mu + \frac{1}{2}\lambda + \frac{1}{2}A + B + G, \tag{32}$$

which can be shown to be equivalent to Eq. (30). We therefore focus on the comparison of Eqs. (28) and (32).

Given independent measurements of the second- and third-order elastic constants, consider the problem of using measurements of shear wave distortion, such as third-harmonic generation, to determine the fourth-order elastic constants for a soft solid such as tissue or tissue-phantom. For such materials it is known from measurements[8] and from comparison with relations for liquids[7] that μ, A, and D are of the same order, λ, B, and G are the same order, and that μ, A, and D are five to six orders of magnitude less than λ, B, and G.

If μ and A are known, then measurement of the third harmonic, whose rate of growth is initially proportional to γ, should provide a reasonable determination of the fourth-order constant D via Eq. (28) because all three elastic constants are of the same order. Now suppose μ, λ, A, and B are known, and we wish to use third harmonic generation to measure the fourth-order constant G via Eq. (32). From Eq. (28) we know that γ is of order μ, and therefore the sum $\frac{1}{2}\lambda + B + G$ in Eq. (32) must add up to a value that is five to six orders of magnitude less than the value of any one of the individual elastic constants. However, since measurements of third-order elastic constants such as B are typically known to at best one or two significant figures, it would be impossible to use this information to determine a quantity that is smaller by five to six orders of magnitude.

At issue is the fact that for soft solids the constant G consists of a large part G_0 (of order λ and B) associated with compressibility, and a small part D (of order μ) associated with shear. These components cannot be separated using the expansion in Eq. (31). For a medium free of shear, i.e., a liquidlike medium, the three large constants in Eq. (32) sum identically to zero as follows:[7]

$$\frac{1}{2}\lambda + B + G = \frac{1}{2}A_l - A_l + \frac{1}{2}A_l = 0, \tag{33}$$

where $A_l = \rho c_l^2$ is a standard coefficient in the expansion of the pressure-density relation for a liquid, c_l being the longitudinal wave speed.

V. DISSIPATION

Viscous dissipation can be taken into account by augmenting the stress tensor to include the component[4]

$$\sigma'_{ik} = 2\eta\left(\dot{u}_{ik} - \frac{1}{3}\delta_{ik}\dot{u}_{ll}\right) + \zeta\delta_{ik}\dot{u}_{ll}, \tag{34}$$

where the dots indicate time derivatives, η is the shear viscosity, and ζ is the bulk viscosity. Thermal conductivity can be taken into account by augmenting the definition of ζ.[11] For the case at hand, with propagation in the $+x_3$ direction and the single displacement component u_1, we have $u_1 = u_1(x_3,t)$ and Eq. (34) reduces to

$$\sigma'_{13} = 2\eta\frac{\partial u_{13}}{\partial t}. \tag{35}$$

Instead of Eq. (12) we now have, again with $u = u_1$ and $z = x_3$,

$$\rho_0\frac{\partial^2 u}{\partial t^2} = \mu\frac{\partial^2 u}{\partial z^2} + \gamma\frac{\partial}{\partial z}\left(\frac{\partial u}{\partial z}\right)^3 + \eta\frac{\partial^3 u}{\partial z^2 \partial t}. \tag{36}$$

Using the slow scale in Eq. (14) and considering η to be of order ϵ^2 one obtains

$$\frac{\partial v}{\partial z} = \frac{\beta}{c^3}v^2\frac{\partial v}{\partial \tau} + \delta\frac{\partial^2 v}{\partial \tau^2}, \tag{37}$$

where

$$\delta = \frac{\eta}{2\rho_0 c^3}. \tag{38}$$

Equation (37) is the modified Burgers equation analyzed by Lee-Bapty and Crighton[1] to investigate shock formation.

An exact solution of Eq. (37) is not available. We therefore consider here a harmonic source excitation and the resulting third-harmonic generation. Given the source condition

$$v(0,t) = v_0\cos\omega t \tag{39}$$

we express the fundamental- and third-harmonic components as follows:

$$\begin{aligned} v_1(z,\tau) &= \mathrm{Re}\{\tilde{v}_1(z)e^{j\omega\tau}\} = \frac{1}{2}\tilde{v}_1(z)e^{j\omega\tau} + \text{c.c.},\\ v_3(z,\tau) &= \mathrm{Re}\{\tilde{v}_3(z)e^{j3\omega\tau}\} = \frac{1}{2}\tilde{v}_3(z)e^{j3\omega\tau} + \text{c.c.}, \end{aligned} \tag{40}$$

where $v = v_1 + v_3$ for $|v_3| \ll |v_1|$, and c.c. designates complex conjugate of the preceding term. From Eq. (37) we have, by successive approximations,

$$\begin{aligned} &\frac{d\tilde{v}_1}{dz} + \alpha\tilde{v}_1 = 0,\\ &\frac{d\tilde{v}_3}{dz} + 9\alpha\tilde{v}_3 = \frac{j\omega\beta}{4c^3}\tilde{v}_1^3, \end{aligned} \tag{41}$$

where $\alpha = \delta\omega^2$. Sequential solution of these equations, satisfying the source conditions $v_1(0,\tau) = v_0\cos\omega\tau$ and $v_3(0,\tau) = 0$, one obtains in a straightforward way

$$\begin{aligned} v_1 &= v_0 e^{-\alpha z}\cos\omega\tau,\\ v_3 &= -\frac{\beta\omega v_0^3}{24c^3\alpha}(e^{-3\alpha z} - e^{-9\alpha z})\sin 3\omega\tau. \end{aligned} \tag{42}$$

When effects of dissipation are negligible these equations reduce to

$$v_1 = v_0\cos\omega\tau, \quad v_3 = -\frac{\beta\omega v_0^3}{4c^3}z\sin 3\omega\tau. \tag{43}$$

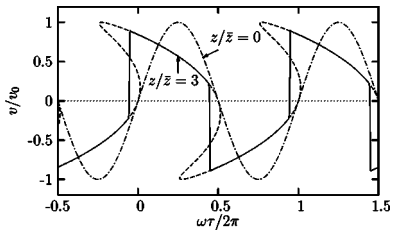

FIG. 1. Distortion of a linearly polarized sinusoid, calculated using Eq. (45). Dot-dash curve is source waveform, solid curve is waveform at $z=3\bar{z}$, and dashed line is the multivalued solution at $z=3\bar{z}$ given by Eq. (21).

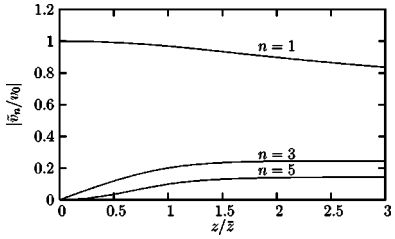

FIG. 2. Harmonic amplitudes corresponding to waveform distortion depicted in Fig. 1.

Equations (42) and (43) resemble very closely the results for second harmonic generation in a fluid,[12] and the corresponding physical interpretation is likewise very much the same for the two phenomena. The lossless result, Eq. (43), is presented to facilitate this comparison. As noted in the previous section, if the second- and third-order elastic constants μ and A, respectively, are known by other means, measurement of the third harmonic can be used to determine the fourth-order elastic constant D via Eq. (20).

VI. NUMERICAL SIMULATION

Numerical simulations of waveform distortion and shock formation based on Eq. (37) may be obtained by letting

$$v=\frac{1}{2}\sum_{n=-\infty}^{\infty}\tilde{v}_n(z)e^{jn\omega\tau}. \tag{44}$$

Substitution in Eq. (37) yields the coupled spectral evolution equations

$$\frac{d\tilde{v}_n}{dz}+\alpha_n\tilde{v}_n=\frac{jn\omega\beta}{12c^3}\sum_{m=-\infty}^{\infty}\tilde{v}_{n-m}\sum_{l=-\infty}^{\infty}\tilde{v}_l\tilde{v}_{m-l}, \tag{45}$$

where $\alpha_n=\delta n^2\omega^2$. The spectral equations are solved by standard techniques.

In the first example the sinusoidal source condition in Eq. (26) is used, for which the shock formation distance in the absence of losses is given by Eq. (27). The attenuation coefficients may be expressed as $\alpha_n=n^2\alpha_1$, and we set $\alpha_1\bar{z}=0.005$ so that attenuation is very weak except at the shocks. The resulting waveform distortion is shown in Fig. 1. The dot-dash curve is the source waveform, and the solid curve is the waveform at $z=3\bar{z}$, in agreement with the result obtained by Lee-Bapty and Crighton[1] using weak shock theory (and for a negative value of β). For comparison, the (multivalued) analytic solution given by Eq. (21) is shown as the dashed line. In Fig. 2 are shown the harmonic amplitudes corresponding to the waveform distortion in Fig. 1.

Figure 3 depicts the distortion of a shear wave pulse, described by

$$v=v_0e^{-(\omega t/a)^2}\cos\omega t$$

at the source. In numerical calculations we set $a=5$ and $\alpha_1\bar{z}=0.025$. The dot-dash curve is the source pulse, and the solid curve is the pulse at $z=3\bar{z}$. The analytic solution given by Eq. (21) is also shown as the dashed line for comparison. The solid line in Fig. 3 is similar to a measurement of shear wave distortion in a tissue phantom reported recently by Catheline *et al.*[10]

VII. SHEAR WAVE WITH TWO DISPLACEMENT COMPONENTS

For completeness we conclude by considering a plane shear wave propagating in the $+x_3$ direction with two displacement components, $u_1(x_3,t)$ and $u_2(x_3,t)$. Particle displacement is no longer along a single coordinate axis but instead follows an elliptical path in the plane perpendicular to the axis of propagation. In linear acoustics the two components propagate independently (in homogeneous media) and couple only at boundaries. In nonlinear acoustics the two components couple during propagation. Here we show the nature of this coupling, and we present a special case in which the coupling vanishes. Finally, we present calculations of third-harmonic generation and shock formation.

There are now two components of the stress tensor:

$$\sigma_{13}=\mu\frac{\partial u_1}{\partial x_3}+\left(\mu+\frac{A}{2}+D\right)\left[\left(\frac{\partial u_1}{\partial x_3}\right)^3+\frac{\partial u_1}{\partial x_3}\left(\frac{\partial u_2}{\partial x_3}\right)^2\right], \tag{46}$$

$$\sigma_{23}=\mu\frac{\partial u_2}{\partial x_3}+\left(\mu+\frac{A}{2}+D\right)\left[\left(\frac{\partial u_2}{\partial x_3}\right)^3+\frac{\partial u_2}{\partial x_3}\left(\frac{\partial u_1}{\partial x_3}\right)^2\right]. \tag{47}$$

Substitution in Eq. (5) gives

$$\rho_0\frac{\partial^2u_1}{\partial t^2}=\mu\frac{\partial^2u_1}{\partial x_3^2}+\gamma\frac{\partial}{\partial x_3}\left[\left(\frac{\partial u_1}{\partial x_3}\right)^3+\frac{\partial u_1}{\partial x_3}\left(\frac{\partial u_2}{\partial x_3}\right)^2\right], \tag{48}$$

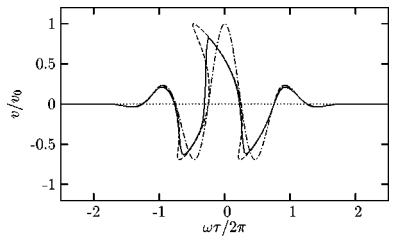

FIG. 3. Distortion of a linearly polarized pulse, calculated using Eq. (45). Dot-dash curve is source waveform, solid curve is waveform at $z=3\bar{z}$, and dashed line is the multivalued solution at $z=3\bar{z}$ given by Eq. (21). The value of a and attenuation are taken as $a=5$ and $\alpha_1\bar{z}=0.025$.

$$\rho_0 \frac{\partial^2 u_2}{\partial t^2} = \mu \frac{\partial^2 u_2}{\partial x_3^2} + \gamma \frac{\partial}{\partial x_3}\left[\left(\frac{\partial u_2}{\partial x_3}\right)^3 + \frac{\partial u_2}{\partial x_3}\left(\frac{\partial u_1}{\partial x_3}\right)^2\right], \quad (49)$$

which, following introduction of the slow scale, reduce to

$$\frac{\partial u_x}{\partial z} = \frac{\gamma}{2\rho_0 c^5}\left[\left(\frac{\partial u_x}{\partial \tau}\right)^3 + \frac{\partial u_x}{\partial \tau}\left(\frac{\partial u_y}{\partial \tau}\right)^2\right], \quad (50)$$

$$\frac{\partial u_y}{\partial z} = \frac{\gamma}{2\rho_0 c^5}\left[\left(\frac{\partial u_y}{\partial \tau}\right)^3 + \frac{\partial u_y}{\partial \tau}\left(\frac{\partial u_x}{\partial \tau}\right)^2\right], \quad (51)$$

where $u_x = u_1$, $u_y = u_2$, and $z = x_3$. Introducing the particle velocities

$$v_x = \frac{\partial u_x}{\partial \tau}, \quad v_y = \frac{\partial u_y}{\partial \tau}, \quad (52)$$

one obtains

$$\frac{\partial v_x}{\partial z} = \frac{\beta}{3c^3}\frac{\partial}{\partial \tau}[v_x(v_x^2 + v_y^2)], \quad (53)$$

$$\frac{\partial v_y}{\partial z} = \frac{\beta}{3c^3}\frac{\partial}{\partial \tau}[v_y(v_x^2 + v_y^2)]. \quad (54)$$

An analytic solution of these coupled equations is not available. For $v_y = 0$ (linear polarization), the second equation vanishes and the first reduces to Eq. (19).

We consider first the special case in which the particle motion is circular, such that

$$v_x^2 + v_y^2 = v_0^2, \quad (55)$$

where v_0 is a constant. In this case Eqs. (53) and (54) decouple as follows:

$$\frac{\partial v_x}{\partial z} = \frac{\beta v_0^2}{3c^3}\frac{\partial v_x}{\partial \tau}, \quad \frac{\partial v_y}{\partial z} = \frac{\beta v_0^2}{3c^3}\frac{\partial v_y}{\partial \tau}. \quad (56)$$

Perhaps even more interesting is that the equations are linear, and the nonlinearity is manifest only as an amplitude-dependent phase speed. For either component the dispersion relation may be obtained by writing $v = v_0 e^{j(\omega\tau + \kappa z)}$ to find that $\kappa = \beta\omega v_0^2/3c^3$. Setting $e^{j(\omega\tau+\kappa z)} = e^{j\omega(t - z/c_{\mathrm{ph}})}$, where c_{ph} is the phase speed and $\tau = t - z/c$, we have

$$c_{\mathrm{ph}} = c\left(1 - \frac{\beta v_0^2}{3c^2}\right)^{-1} \simeq c + \frac{\beta v_0^2}{3c}. \quad (57)$$

The phase speed thus increases (very slightly) with wave amplitude.

We now calculate third-harmonic generation for a shear wave with arbitrary elliptical particle motion. The primary wave is given here by

$$v_{x1}(z,\tau) = v_{x0}\cos\omega\tau = \mathrm{Re}\{v_{x0}e^{j\omega\tau}\}, \quad (58)$$

$$v_{y1}(z,\tau) = v_{y0}\sin\omega\tau = \mathrm{Im}\{v_{y0}e^{j\omega\tau}\}, \quad (59)$$

and the corresponding third-harmonic components by

$$\begin{aligned} v_{x3}(z,\tau) &= \mathrm{Re}\{\tilde{v}_{x3}(z)e^{j3\omega\tau}\}, \\ v_{y3}(z,\tau) &= \mathrm{Im}\{\tilde{v}_{y3}(z)e^{j3\omega\tau}\}. \end{aligned} \quad (60)$$

Substitution in Eqs. (53) and (54) gives for the third harmonic

$$\frac{d\tilde{v}_{x3}}{dz} = \frac{j\omega\beta v_{x0}}{4c^3}(v_{x0}^2 - v_{y0}^2), \quad (61)$$

$$\frac{d\tilde{v}_{y3}}{dz} = \frac{j\omega\beta v_{y0}}{4c^3}(v_{x0}^2 - v_{y0}^2). \quad (62)$$

Subject to the source conditions $\tilde{v}_{x3}(0) = \tilde{v}_{y3}(0) = 0$, the solutions are thus

$$v_{x3} = -\frac{\beta\omega v_{x0}}{4c^3}(v_{x0}^2 - v_{y0}^2) z \sin 3\omega\tau, \quad (63)$$

$$v_{y3} = \frac{\beta\omega v_{y0}}{4c^3}(v_{x0}^2 - v_{y0}^2) z \cos 3\omega\tau. \quad (64)$$

These solutions are seen to resemble Eq. (43) very closely, and they reduce (in magnitude) to Eq. (43) if either component is zero at the source.

To calculate waveform distortion and in particular shock formation we introduce the expansions

$$v_x = \frac{1}{2}\sum_{n=-\infty}^{\infty} \tilde{v}_{x,n}(z)e^{jn\omega\tau}, \quad v_y = \frac{1}{2}\sum_{n=-\infty}^{\infty} \tilde{v}_{y,n}(z)e^{jn\omega\tau}. \quad (65)$$

Substitution in Eqs. (53) and (54) and introducing attenuation ad hoc yields, in place of Eqs. (45),

$$\frac{d\tilde{v}_{x,n}}{dz} + \alpha_n \tilde{v}_{x,n} = \frac{jn\omega\beta}{12c^3}\sum_{m=-\infty}^{\infty} \tilde{v}_{x,n-m}\sum_{l=-\infty}^{\infty}(\tilde{v}_{x,l}\tilde{v}_{x,m-l} + \tilde{v}_{y,l}\tilde{v}_{y,m-l}), \quad (66)$$

$$\frac{d\tilde{v}_{y,n}}{dz} + \alpha_n \tilde{v}_{y,n} = \frac{jn\omega\beta}{12c^3}\sum_{m=-\infty}^{\infty} \tilde{v}_{y,n-m}\sum_{l=-\infty}^{\infty}(\tilde{v}_{x,l}\tilde{v}_{x,m-l} + \tilde{v}_{y,l}\tilde{v}_{y,m-l}). \quad (67)$$

The equations couple the harmonic amplitudes of the x and y velocity components. For the source condition we choose the harmonic excitation

$$v_x = v_0 \sin\omega t, \quad v_y = s v_0 \cos\omega t. \quad (68)$$

The calculations are presented for $z = 3\bar{z}$, where $\bar{z}$ corresponds to the case $s = 0$, and the attenuation coefficient is the same as that used in Fig. 1. For $s = 0$ the wave is linearly polarized, and Fig. 1 is obtained. For $s = 1$ the wave is circularly polarized, and Fig. 4(a) is obtained (solid line is the x component, dashed line is the y component). Note that only phase shift, and no nonlinear distortion, occurs for circular polarization, in agreement with Eqs. (56). For intermediate values of s the wave is elliptically polarized. Figure 4(b) reveals the distortion for $s = 0.25$. In this case the waveform of the stronger component v_x resembles that for linear polarization (Fig. 1). The waveform of the weaker component v_y is considerably different. It exhibits cusps rather than shocks. Moreover, whereas v_y is one quarter the amplitude of v_x at $z = 0$, the peak amplitudes of the two waveforms are comparable at $z = 3\bar{z}$.

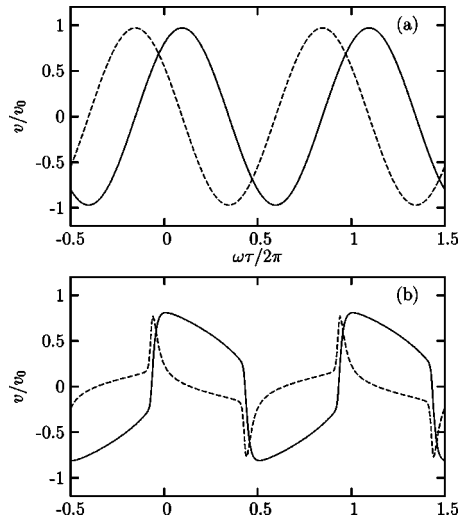

FIG. 4. Distortion of elliptically polarized shear waves corresponding to source condition in Eqs. (68). Waveforms are shown at $z=3\overline{z}$ as calculated for $s=0$. Solid line is v_x and dashed line is v_y. (a) $s=1$ (circular polarization); and (b) $s=0.25$ (elliptical polarization).

VIII. CONCLUSION

A model for nonlinear shear waves has been developed using a formulation of the strain energy function. The model is particularly useful for soft elastic solids because harmonic generation and waveform distortion are expressed in terms of elastic constants that are of comparable order of magnitude. Earlier descriptions of nonlinear shear waves are expressed in terms of elastic constants that for soft solids differ by many orders of magnitude. Using earlier models to determine the values of the relevant elastic constants by measuring nonlinear distortion of shear waves is all but impossible for soft solids. The present model is therefore suitable for using nonlinear shear waves to determine the fourth-order elastic constant in soft tissue. Sample calculations are presented for various features of nonlinear shear waves, including shear waves manifesting elliptical particle motion.

ACKNOWLEDGMENTS

This work was supported by the Office of Naval Research, and by the Internal Research and Development Program at Applied Research Laboratories, The University of Texas at Austin.

[1] I. P. Lee-Bapty and D. G. Crighton, "Nonlinear wave motion governed by the modified Burgers equation," Philos. Trans. R. Soc. London, Ser. A **323**, 173–209 (1987).
[2] K. Naugolnykh and L. Ostrovsky, *Nonlinear Wave Processes in Acoustics* (Cambridge University, New York, 1998), pp. 74–77.
[3] E. A. Zabolotskaya, "Sound beams in a nonlinear isotropic solid," Sov. Phys. Acoust. **32**, 296–299 (1986).
[4] L. D. Landau and E. M. Lifshitz, *Theory of Elasticity*, 3rd ed. (Pergamon, New York, 1986), p. 107.
[5] W. Jiang, W. Cao, and G. Du, "Third harmonic generation of transverse acoustic waves in crystals and ceramics," Acta Acust. (Beijing) **88**, 163–169 (2002).
[6] R. N. Thurston and M. J. Shapiro, "Interpretation of ultrasonic experiments on finite-amplitude waves," J. Acoust. Soc. Am. **41**, 1112–1125 (1967).
[7] M. F. Hamilton, Yu. A. Ilinskii, and E. A. Zabolotskaya, "Separation of compressibility and shear deformation in the elastic energy density," J. Acoust. Soc. Am. **116**, 41–44 (2004).
[8] S. Catheline, J.-L. Gennisson, and M. Fink, "Measurement of elastic nonlinearity of soft solid with transient elastography," J. Acoust. Soc. Am. **114**, 3087–3091 (2003).
[9] A. P. Sarvazyan, A. R. Skovoroda, S. Y. Emelianov, J. B. Fowlkes, J. G. Pipe, R. S. Adler, R. B. Buxton, and P. L. Carson, "Biophysical bases of elasticity imaging," in *Acoustical Imaging*, Vol. 21, edited by J. P. Jones (Plenum, New York, 1995), pp. 223–240.
[10] S. Catheline, J.-L. Gennisson, M. Tanter, and M. Fink, "Observation of shock transverse waves in elastic media," Phys. Rev. Lett. **91**, 164301 (2003).
[11] A. N. Norris, "Finite-amplitude waves in solids," in *Nonlinear Acoustics*, edited by M. F. Hamilton and D. T. Blackstock (Academic Press, San Diego, 1998), Chap. 9, pp. 263–277.
[12] D. T. Blackstock, M. F. Hamilton, and A. D. Pierce, "Progressive waves in lossless and lossy fluids," in *Nonlinear Acoustics*, edited by M. F. Hamilton and D. T. Blackstock (Academic Press, San Diego, 1998), Chap. 4, pp. 65–150. See especially pp. 134–136.

Optimized shapes of oscillating resonators for generating high-amplitude pressure waves

Xiaofan Li[a)]
Department of Applied Mathematics, Illinois Institute of Technology, Chicago, Illinois 60616

Joshua Finkbeiner[b)] and Ganesh Raman
Department of Mechanical, Materials and Aerospace Engineering, Illinois Institute of Technology, Chicago, Illinois 60616

Christopher Daniels[b)]
University of Akron, Akron, Ohio 44325

Bruce M. Steinetz
NASA Glenn Research Center, Cleveland, Ohio 44135

(Received 6 January 2004; revised 27 August 2004; accepted 5 September 2004)

Several studies have proved that the geometry of an oscillating acoustic resonator strongly influences its resonance frequencies and the nonlinear standing pressure waveform generated within the cavity. The research presented herein uses a quasi-one-dimensional numerical model to solve the acoustic field and is validated by comparing with experimental results. A quasi-Newton type numerical scheme is used to optimize the axisymmetric cavity contour by maximizing the pressure compression ratio, defined as the ratio of maximum to minimum gas pressure at one end of the oscillating resonator. Cone, horn-cone, and cosine resonator contours are each optimized for a fixed amplitude of the periodic external force oscillating the cavity. Different optimized shapes are found when starting with different initial guesses, indicating multiple local extrema. The maximum pressure compression ratio value of 48 is found in an optimized horn-cone shape. This represents a 241% increase in the compression ratio over any previously published results. © *2004 Acoustical Society of America.* [DOI: 10.1121/1.1810139]

PACS numbers: 43.25.Gf, 43.25.Cb [MFH] Pages: 2814–2821

I. INTRODUCTION

The waveform of the standing wave in an oscillating closed cavity is strongly influenced by the geometry of the resonator cavity. It is well known that shocks form in a cylindrical tube when the interior gas is oscillating at its resonance frequency. Lawrenson *et al.*[1] at MacroSonix Corp first exploited the shape dependence and obtained high-amplitude and shock-free acoustic pressures in axisymmetric tubes of varying cross sections, referred to as resonant macrosonic synthesis (RMS). Peak acoustic pressures that measure three to four times ambient pressure and maximum to minimum pressure ratios of 27 were observed in shaped cavities. The size of the demonstrated overpressure reached the level that is required by commercial applications such as acoustic pumps or compressors. The researchers considered these types of axisymmetric shapes: cylinder, cone, hone-cone, and bulb. They concluded that the hone-cone resonator shape generated the highest overpressure for a given input power. They also demonstrated that the overall characteristics of the waveform does not change when a resonator is filled with different gases.

A companion paper by Ilinskii *et al.*[2] developed a one-dimensional frequency-domain model for studying the RMS numerically. The results confirmed the nonlinear standing waveform and the related characteristics such as shape-induced resonance hardening and softening observed in the experiments by Lawrenson *et al.*[1] To account for the energy losses in the boundary layer along cavity wall, Ilinskii *et al.*[3] later modified the one-dimensional model by introducing an additional term in the continuity equation and used a turbulence model. Hamilton *et al.*[4] analytically investigated the relationship between the natural frequency of a nonlinear acoustic resonator and its shape as well as the nonlinear interactions of modes in the resonator. Chun and Kim[5] numerically investigated cosine shaped resonators in addition to cylindrical and conical shapes using high-order finite-difference approximations. They concluded that the half cosine-shape is more suitable to induce high compression ratio than other shapes under certain assumptions. Recently, Erickson and Zinn[6] used the Galerkin method to solve the one-dimensional model and found a nonmonotonic increase in compression ratio when the flare constant is raised for a class of horn-shaped resonators. To serve commercial needs, such as in an acoustic gas compressor and an acoustic liquid pump, the objective is to find an optimized shape for generating the greatest overpressure. However, the optimization procedure and results have not yet been discussed.

In this article, the numerical schemes are introduced and the results are presented for optimizing the shape parameters that yield the highest maximum-to-minimum pressure ratio in each of the following resonator shapes: cone, horn-cone, and cosine-shape. In Sec. II, the modeling equations are pre-

[a)]Electronic mail: lix@iit.edu
[b)]Current address: NASA Glenn Research Center, Cleveland, Ohio 44135.

sented; in Sec. III, the numerical schemes are described; in Sec. IV, the numerical model and experiment results are compared and the resulting optimized shapes are discussed.

II. GOVERNING EQUATIONS

In the following section we briefly describe the one-dimensional model for computing the acoustic wave field in an axisymmetric resonator. The equations are presented for completeness and the details of the derivation are given in the work by Ilinksii *et al.*[2] The possible effects of the boundary layer along the resonator wall and the acoustically generated turbulence on the acoustical field are neglected in this model.

Consider the acoustic field in an oscillating resonator of length l driven by an external force. The resonator is axisymmetric with the inner radius given by $r=r(x)$, $0<x<l$, where x is the coordinate along the axis of symmetry. The density of the gas ρ, the velocity u, and the pressure p satisfy the conservation of mass,

$$\frac{\partial \rho}{\partial t}+\frac{1}{r^2}\frac{\partial}{\partial x}(r^2\rho u)=0, \tag{1}$$

and the conservation of momentum,

$$\frac{\partial u}{\partial t}+u\frac{\partial u}{\partial x}=-\frac{1}{\rho}\frac{\partial p}{\partial x}-a(t)+\frac{(\zeta+4\eta/3)}{\rho}\frac{\partial}{\partial x}\left(\frac{1}{r^2}\frac{\partial}{\partial x}(r^2u)\right), \tag{2}$$

where $a(t)$ is the acceleration of the resonator enforced by the external force; ζ and η are coefficients of viscosity. Shear viscosity is denoted as η, and ζ is the bulk viscosity that results from nonequilibrium deviations between the actual local pressure and the thermodynamic pressure. The no-penetration boundary conditions at the two ends require that the velocity vanish at $x=0$ and l. The state equation is specified by that of an ideal gas,

$$p=p_0(\rho/\rho_0)^{\gamma}, \tag{3}$$

where p_0 and ρ_0 are the ambient pressure and density, respectively, and γ is the ratio of specific heats of the gas.

The quasi-one-dimensional compressible Navier–Stokes equations (1)–(3) are solved using a frequency-domain method, where the unknown variables are expressed in terms of finite Fourier series in time. The Fourier coefficients are determined using a shooting method. Both the experimental and numerical results show that the time harmonics of the dependent variables, such as the pressure p, decay rapidly as the frequency increases. This ensures that the number of time harmonics, N, needed for accurate results is small. In the present numerical simulations, the value of N is twenty and it can be shown that increasing N does not change the results.

Following Ilinksii *et al.*[2] by expressing the variables in Fourier series, Eqs. (1) and (2) can be reduced to a system of Ordinary Differential Equations (ODEs) for the Fourier coefficients of the velocity potential φ, defined as $u=\nabla\varphi$:

$$\frac{d\hat{\varphi}_k}{dx}=\frac{\hat{v}_k}{r^2},\qquad \sum_l D_{kl}\frac{d\hat{v}_l}{dx}=f_k, \quad \text{for } k=1,2,\ldots,N, \tag{4}$$

where $v=r^2(\partial\varphi/\partial x)$, and $\hat{\varphi}_k$, $\hat{v}_k$, and $\hat{a}_k$ are the Fourier coefficients defined as $\varphi=\Sigma_{k=-N}^{N}\hat{\varphi}_k e^{ik\omega t}$, $v=\Sigma_{k=-N}^{N}\hat{v}_k e^{ik\omega t}$, $a=\Sigma_{k=-N}^{N}\hat{a}_k e^{ik\omega t}$. ω is the frequency of the periodic force exerted on the resonator by the shaker. The detailed expressions for $D_{kl}=D_{kl}(\hat{v}_k,\hat{\varphi}_k,x)$ and $f_k=f_k(\hat{v}_k,\hat{\varphi}_k,x)$ are given by

$$D_{kl}=(c_0^2+ik\omega\delta)\delta_{kl}+D'_{k-l},$$

$$f_k=-k^2\omega^2r^2\hat{\varphi}_k+ik\omega r^2x\hat{a}_k+\frac{ik\omega[v^2]_k}{r^2}+\sum_{l=-N+k}^{N}\hat{a}_{k-l}\hat{v}_l-\frac{\frac{dr^2}{dx}}{r^6}\sum_{l=-N+k}^{N}[v^2]_{k-l}\hat{v}_l,$$

where $\delta=(\zeta+4\eta/3)/\rho_0$ is the viscosity, $c_0=\sqrt{\gamma p_0/\rho_0}$ is the reference speed of sound, D'_m is given by $D'_m=-(\gamma-1)x\hat{a}_m-im\omega(\gamma-1)\hat{\varphi}_m-[(\gamma+1)/2r^4][v^2]_m$, and $[v^2]_k=\Sigma_{l=-N+k}^{N}\hat{v}_{k-l}\hat{v}_l$. The no-slip boundary conditions at the two ends are translated to the equivalent conditions in Fourier space: $\hat{v}_k=0$ at $x=0$, l.

After the Fourier coefficients $\{\hat{\varphi}_k\}$ and $\{\hat{v}_k\}$ are obtained by solving the boundary-value problem, Eq. (4), the velocity potential φ and the modified velocity v are computed from the inverse FFT. The density ρ is given by the momentum equation,

$$\frac{\rho}{\rho_0}=\left(1-\frac{\gamma-1}{c_0^2}\left[\frac{\partial\varphi}{\partial t}+\frac{1}{2r^4}v^2+ax-\frac{\delta}{r^2}\frac{\partial v}{\partial x}\right]\right)^{1/(\gamma-1)}, \tag{5}$$

and the pressure p can be obtained from the state equation (3).

III. NUMERICAL METHODS

The procedures for finding the optimal shape parameters are described as follows. Given an initial resonator shape and a fixed value of maximum external force, the resonance frequency of the resonator is determined and the compression ratio, defined as the maximum-to-minimum pressure ratio at the narrow end of the cavity, is computed. Then, the optimization step is performed yielding the next resonator shape candidate. The first and the second steps are repeated until incremental changes in the resonator contour no longer produce higher compression ratios and the local optimal design is determined.

To simplify the discussion, the following dimensionless variables are introduced:

$$X=\frac{x}{l},\quad T=\omega t,\quad R=\frac{r}{l},\quad R_0=\frac{r_0}{l},\quad A=\frac{a}{l\omega_0^2}, \tag{6}$$

where ω is the frequency of the periodic force acted on the resonator, $\omega_0 = \pi c_0 / l$ is the fundamental frequency of a cylindrical resonator of length l.

In this work, the acceleration of the resonator induced by external force is assumed to be harmonic, $A(T) = \tilde{A}\cos(T)$. The physical parameters that determine the acoustic wave field in the resonator are as follows: the acceleration amplitude $\tilde{A}$, the ratio of specific heats γ, the attenuation coefficient $G = \pi(\zeta + 4\eta/3)\omega_0 / c_0^2 \rho_0$, and the resonator oscillating frequency $\Omega = \omega/\omega_0$.

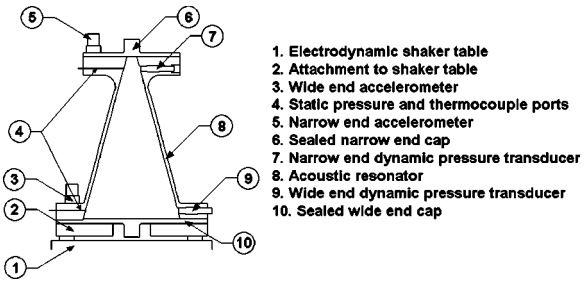

FIG. 1. Experimental apparatus.

A. Shape optimization

Suppose the resonator shape $R(X)$ is determined by a number of shape parameters, $S_0, S_1, \ldots, S_n$. For example, a cone is given by $R(X) = S_0 + S_1 X$. To determine the shape producing the highest value of the pressure compression ratio R_c, i.e.,

$$R_c(S_0, S_1, \ldots, S_n) = \frac{p_{\max}}{p_{\min}}, \quad \text{at } X = 0, \tag{7}$$

gradients of the pressure compression ratio value are compared with the gradients of the shape parameters to indicate the next contour iteration. $p_{\max}$ and $p_{\min}$ denote the maximum and minimum pressure at the narrow end of the resonator during one period of oscillation, respectively. The compression ratio R_c is a function of the shape parameters, the dimensionless frequency Ω and the history of Ω (due to the existence of hysteresis effects). The method for obtaining R_c for a fixed resonator shape is explained later in the section.

The optimization method begins by specifying the practical conditions and constraints. The original experiments by Lawrenson *et al.*[1] and some commercial applications use refrigerant R-134a as the gas contained within the resonators. Therefore, the specific heat ratio $\gamma = 1.2$ is used to match the gas properties of the refrigerant. The viscosity-related parameter G is fixed at 0.010, which was found appropriate in the separate studies.[2,7,8] The dimensionless radius of the resonator at the narrow end, $R(X=0)$, is restricted to be greater than 0.020833. This is the minimum value that would allow for a mechanical connection to the resonator required for real world applications.

Since the electrodynamic shaker system used in this study[1,7,8] is force-limited, the resonator shape is optimized by holding constant *the maximum inertial force required to establish the periodic oscillation*. This stipulation is justified by the experimental results that the force acting on the resonator surface by the acoustic field is negligible even at resonance.[7] This imposed constraint limits the acceleration of the resonator, $\tilde{A}$, and reduces $\tilde{A}$ when additional weight is added with changing resonator geometry. Previous studies held the acceleration amplitude constant, resulting in an optimal conical resonator shape that has a very small narrow end and very large wide end.[9] This geometry is not practical since it results in heavy weight experimental hardware. Upon application, the heavy weight resonator could not produce high compression ratios due to the low acceleration generated by the shaker system. A greater compression ratio would be obtained from lighter weight hardware oscillated at higher acceleration amplitude. In this study, therefore, the maximum external force delivered to the resonator oscillation is fixed during the optimization, effectively favoring lighter weight resonators and more closely modeling the real system.

Using Newton's Second Law, for a fixed amount of maximum dimensionless external force $F_{\max}$, the dimensionless acceleration amplitude $\tilde{A}$ is easily deduced from

$$\tilde{A} = F_{\max}/(M + M_a), \tag{8a}$$

where M is the dimensionless mass of the resonator given by

$$M = \int_0^1 \pi[(R(X) + D_w)^2 - R^2(X)]\,dX + \pi[R^2(0) + R^2(1)]D_w, \tag{8b}$$

and M_a is the mass due to the fixture and armature attached to the shaker as shown in Fig. 1. From the data in our experiments, M_a is set to the dimensionless value of 0.89295, equivalent to twice the weight of the conical resonator in our experiment. D_w is the thickness of the resonator wall nondimensionalized by the length of the resonator and is chosen to be 0.020941 matching the dimension of the conical resonator in the experiments. The second term of Eq. (8b) accounts for the mass of the two end caps of the resonator.

A quasi-Newton method, BFGS (Broyden-Fletcher-Goldfarb-Shanno),[10] then is used for maximizing the multi-variable nonlinear function $R_c(S_0, S_1, \ldots, S_n)$. BFGS is an iterative method, approximating the objective function by a quadratic function at each iteration. At each major iteration step, k, a line search is performed in the direction

$$d^{(k)} = H_k^{-1} \cdot \nabla R_c(S^{(k)}),$$

where $S^{(k)} = (S_0^{(k)}, S_1^{(k)}, \ldots, S_n^{(k)})$ is the vector of the shape parameters at the k-th iteration of BFGS. H_k is the BFGS approximation to the Hessian matrix of R_c with respect to S, defined by

$$H_k = H_{k-1} + \frac{q_{k-1} q_{k-1}^{\mathrm{T}}}{q_{k-1}^{\mathrm{T}} q_{k-1}} - \frac{H_{k-1}^{\mathrm{T}} t_{k-1}^{\mathrm{T}} t_{k-1} H_{k-1}}{t_{k-1}^{\mathrm{T}} H_{k-1} t_{k-1}},$$

where $t_{k-1} = S^{(k)} - S^{(k-1)}$, $q_{k-1} = \nabla R_c(S^{(k)}) - \nabla R_c(S^{(k-1)})$ and $H_0 = I$.

The evaluation of the objective function R_c involves solving many iterations of a nonlinear system of ODEs given in Eq. (4), since the gradient information of R_c required for the BFGS method is not available analytically. Using a numerical differentiation method via finite differences, the gra-

dient information is determined by perturbing each design variable, S_i, in turn and calculating the rate of change in the objective function $R_c(S_0, S_1, \ldots, S_n)$. For two shape parameters, the optimization takes 4 to 48 hours of CPU time (depending on the type of the resonator shape and initial guess for the shape parameters) on a 1.3 GHz Athlon T-Bird PC with the Lahey-Fujitsu FORTRAN compiler.

B. Boundary value problem

For a given shape of the resonator, the boundary value problem, Eq. (4), is solved numerically by a Multiple Shooting Method. Since the amplitude of the pressure in a resonator strongly depends on the oscillating frequency Ω, the quantity to be optimized is the maximum pressure compression ratio R_c over the entire range of Ω for a given resonator shape. Because of the hysteresis effects, the solution is *not* unique near the resonance frequency and the Multiple Shooting Method will not converge unless a good initial guess of the solution is provided. To circumvent the difficulty, a continuation method is implemented. The system of ODEs is solved starting from a frequency Ω that is away from the resonance frequency and the solution is used as an initial guess for solving the ODEs for increased or decreased Ω. The steps are repeated until all branches of the solution for all values of Ω near the resonance is completed. The maximum ratio R_c among different values of Ω, and among the increasing and decreasing frequency branches (if hysteresis is present), is chosen as the compression ratio corresponding to the resonator contour.

IV. RESULTS

A. Experimental validation of the numerical method

While the numerical model by itself provides insight into the physics of the nonlinear acoustic standing waves in oscillating resonators, experimental verification is required to ensure the model's accuracy. Experimental conditions are used as inputs to the numerical model, and the numerical predictions are then compared to the experimental results.

The acceleration input to the numerical model is generated using measured signals from the experimental data. Recall that the model assumes that the resonator is excited using a simple sinusoidal acceleration. In addition, the resonator is assumed to be ideally rigid so that the acceleration is constant across the length of the resonator body. The arguments made in Finkbeiner *et al.*[11] allow the measured acceleration signals to be input to the model by isolating the fundamental acceleration harmonic as the driving function for the model.

The value for G, the effective viscosity parameter, is based in part upon the second coefficient of viscosity due to the high-pressure gradients and frequencies due to the acoustics. Previous work[2] assumed a value of $G=0.010$, although no justification was given for this value. To estimate this parameter, the pressure results from the numerical model are computed for several values of G, and are plotted together with the experimental data.[8,12] A single comparison between experimental and numerical data is presented here, but is characteristic of several comparisons.

A representative experimental configuration is shown in Fig. 1, with a resonator rigidly mounted on a Labworks ET-127 shaker system. PCB Piezotronics 353B03 accelerometers are mounted at both ends of the resonator. PCB Piezotronics dynamic pressure transducers are mounted in the side wall of the resonator at axial positions of $X=0.05$ and $X=0.95$. Thermocouples and Druck PDCR 130 static pressure transducers are mounted at the same axial positions as the dynamic pressure transducers. The dynamic pressure transducers are acceleration compensated, designed for high frequency measurements, and are incapable of measuring static pressure. The static pressure value is measured with static transducers and is combined with the dynamic measurements to complete the pressure measurement. The value of the maximum force limit, $F_{\max}$, adopted in this work corresponds to an electrodynamic shaker with 500 lbf maximum capacity and about 6 lbm armature and fixture.

At the acoustic resonance of the working fluid, the acceleration signals measured near the two ends have small difference in amplitude as graphed in Fig. 2. The dimensionless acceleration based on the signal measured at the wide and the narrow ends of the resonator is given by $\tilde{A}=9.76\times10^{-5}$ and $\tilde{A}=1.03\times10^{-4}$, respectively. The difference in the amplitude at the two ends is due to elasticity of the resonator. The dynamic pressure frequency response measured at the narrow end of the horn-cone resonator is displayed in Fig. 3 along with the curves which are computed for varying values of G with a dimensionless acceleration level, $\tilde{A}=1.03\times10^{-4}$, matching the acceleration measured at the resonator narrow end. The computational pressure amplitude is measured at the axial location of $X=0.05$. The result shows that the model over-predicts the resonance frequency of the horn-cone resonator by roughly 2.6%. However, in terms of amplitude and wave form, the model predicts the pressures generated in the resonator very well. The matching value of G is between 0.011 and 0.012 with acceleration referenced at the narrow end. A similar comparison shows, when the computed pressure frequency response curves are calculated based on the dimensionless acceleration at the wide end, $\tilde{A}=9.76\times10^{-5}$, the matching value of G is found to lie in (0.010, 0.011). These values of G are, for all intents and purposes, close to those assumed in previous studies.[2]

B. Optimal resonator shapes

In the following subsections, the results are shown from optimizing each type of resonator shapes to achieve maximum compression ratio R_c at one end of the resonators. The ratio of specific heats is held at $\gamma=1.2$ and the attenuation coefficient $G=0.01$ which is identical to the value used in Ilinskii *et al.*[2] and closely matching the value determined by the experiments discussed previously. The acceleration $\tilde{A}$ for a given shape is calculated from Eq. (8), where the value of the maximum inertial force $F_{\max}$ is deduced from that for a reference conical resonator accelerated at the amplitude $\tilde{A}=5\times10^{-4}$.

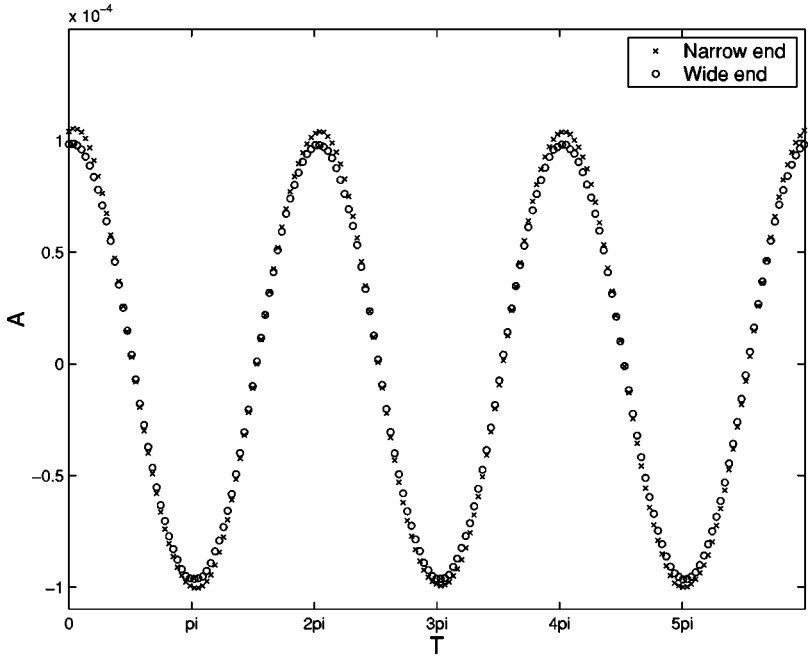

FIG. 2. The dimensionless acceleration signals measured at the two ends of the horn-cone resonator by PCB accelerometers.

1. Optimal conical shaped resonator

The conical resonator contour can be written as

$$R(X)=S_0+S_1X, \quad \text{for } 0\leqslant X\leqslant 1. \tag{9}$$

The conical resonator studied in Lawrenson *et al.*[1] and Ilinksii *et al.*[2] with $S_0=0.032941$ and $S_1=0.26800$ is chosen to be the reference resonator, shown in Fig. 4(a). For the reference resonator, the compression ratio reaches its maximum value of $R_c=5.0475$ when the oscillation frequency is raised to $\Omega=1.3134$.

Using the optimization procedure described in Sec. III and starting with the reference conical shape, the optimal conical resonator is found to have the shape parameters $S_0=0.020833$ and $S_1=0.17211$. The compression ratio R_c of the conical resonator reaches a value of 5.8932, which is about 17% higher than that of the reference resonator. Recall that, due to hysteresis, the entire branch must be traced by incrementing the frequency Ω. The compression ratio reaches the value when the frequency is increased to 1.3200. The corresponding acceleration that achieves such a compression ratio has the amplitude $\tilde{A}=5.7470\times10^{-4}$. According to our assumption (8), accelerating the optimal resonator at this level requires the same amount of maximum inertial force that oscillates the reference conical resonator at $\tilde{A}=5\times10^{-4}$. As stated before, to find realistic dimensions of the resonator, the optimization scheme limits the lower bound for the dimensionless radius of the resonator at the narrow end to be $R(X=0)=0.020833$. From the dimensions of the optimal conical resonator, the smaller narrow end, S_0, generates a larger compression ratio. Due to the fixed external

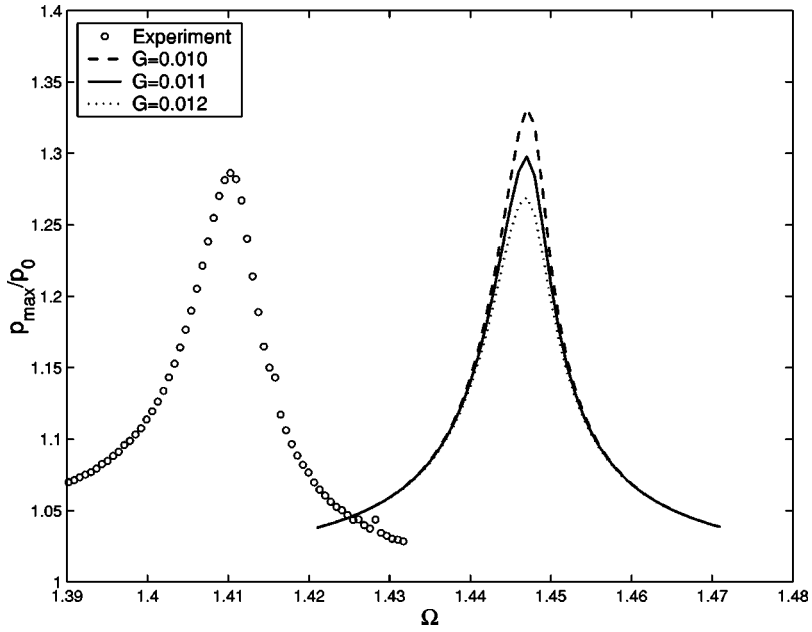

FIG. 3. The dynamic pressure frequency response measured at the narrow end of the horn-cone resonator and the pressure responses predicted by the numerical model computed for varying values of G with a dimensionless acceleration level, $\tilde{A}=1.03\times10^{-4}$, matching the acceleration measured at the resonator narrow end.

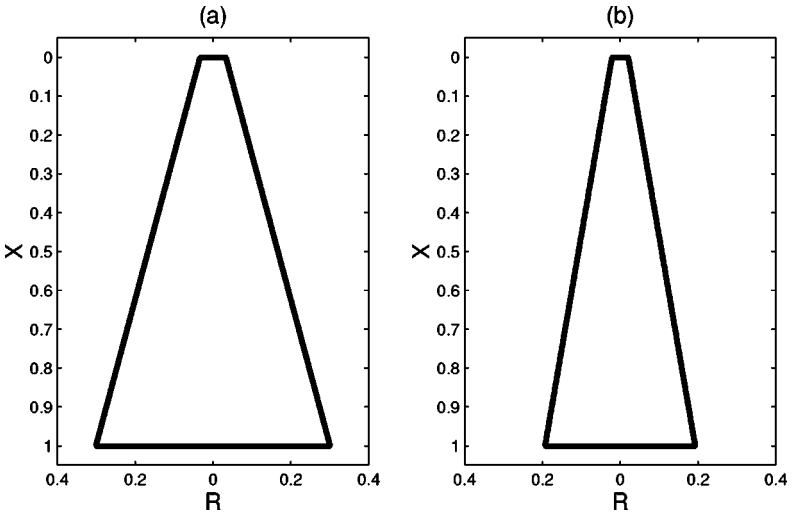

FIG. 4. Conical shapes: (a) the reference conical resonator; (b) the optimized conical resonator. For the same maximum external force, the compression ratios corresponding to the shapes in (a) and (b) reach the values of 5.0475 and 5.8932, respectively. For shape parameters, see the text.

force constraint, the slope of the optimal cone S_1 is finite. The reference resonator and the optimal conical resonator are shown in Fig. 4. The second cone [Fig. 4(b)] has a smaller narrow end and smaller slope than the reference [Fig. 4(a)].

2. Optimal horn-cone shaped resonator

The horn-cone resonator shape is described by

$$R(X)=\begin{cases} S_0\cosh(S_1X), & \text{for } 0\leqslant X\leqslant S_2, \\ \alpha+\beta X, & \text{for } S_2\leqslant X\leqslant 1, \end{cases} \tag{10}$$

where $\alpha=S_0\cosh(S_1S_2)$ and $\beta=S_0S_1\sinh(S_1S_2)$. The three shape parameters S_0, S_1 and S_2 are optimized. The first optimization attempt starts with the dimensions of the horn-cone given in Lawrenson *et al.*,[1] $S_0=0.028333$, $S_1=5.7264$ and $S_2=0.25$ [shown in Fig. 5(a)]. Using these original shape parameters, the compression ratio $R_c=14.059$ is achieved when the horn-cone resonator is accelerated at $\tilde{A}=5.1516\times10^{-4}$ and the frequency is increased to $\Omega=1.4678$. In searching for the optimal horn-cone design, the lower bound of the radius of the narrow end S_0 is limited to be 0.020833 for practical reasons. The separation point between the horn section and the cone section, S_2, could be any value between 0 and 1. The result of optimization finds that the compression ratio reaches a maximum value of 19.115, which is 36% higher than that of the horn-cone of Lawrenson *et al.*,[1] when the shape has $S_0=0.20833$, $S_1=5.7044$ and $S_2=0.25246$. This optimal horn-cone achieves the value of the compression ratio when its acceleration has the amplitude $\tilde{A}=5.6730\times10^{-4}$ and it is oscillating at its resonance frequency $\Omega=1.4716$. The value of the acceleration satisfies the requirement of fixed inertial force $F_{\max}$ formulated in Eq. (8). For horn-cone shapes, the principle that higher compression ratio is obtained with smaller narrow end is valid, as in the case of conical shapes.

The optimization scheme BFGS is designed for finding a local extreme of a multivariable function. Our numerical simulations indicate that the compression ratio, as a function of the shape parameters, usually has many local extrema. Our second optimization attempt started with a different initial geometry of the horn-cone and a substantially larger value of the compression ratio $R_c=47.975$ is obtained when the shape parameters are $S_0=0.020833$, $S_1=6.1698$ and $S_2=0.27704$ [shown in Fig. 5(b)]. For this compression ratio, the resonator is oscillated at the acceleration amplitude $\tilde{A}=5.1814\times10^{-4}$ and the frequency $\Omega=1.5603$. Comparing with the compression ratio for the horn-cone in Lawrenson *et al.*,[1] the second optimal horn-cone improves the compression ratio by *more than 241%* at the same value of $F_{\max}$. Comparing the dimensions of the two horn-cones, the volumes of the shapes are similar but the optimal horn-cone has a relatively shorter cone section than that of the horn-cone used in Lawrenson *et al.*[1] In Fig. 5(c), the pressure waveform at the narrow end is presented for both the Lawrenson and the optimized horn-cone resonators. The two pressure waves

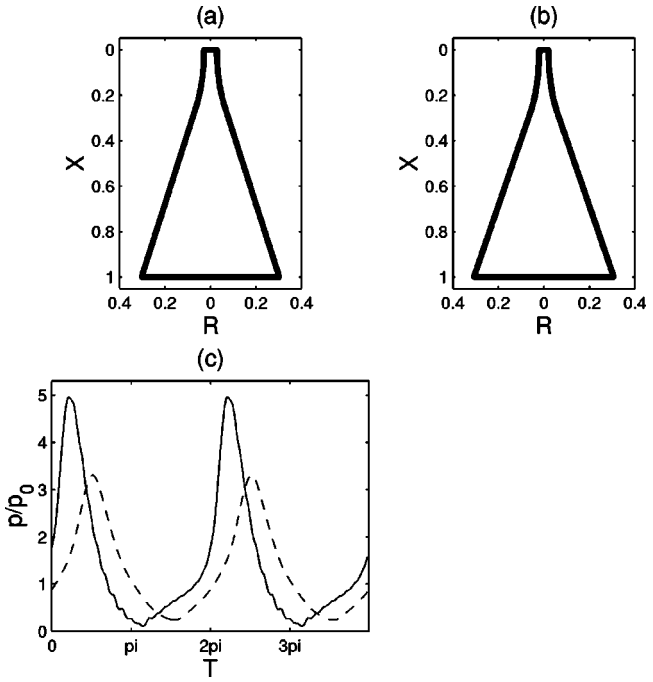

FIG. 5. (a) The horn-cone shape in Lawrenson *et al.* (Ref. 1). (b) Optimized horn-cone shape. For shape parameters, see the text. (c) The pressure waveform at the narrow end for the horn-cone in Lawrenson *et al.* (Ref. 1) (the dashed line) and that for the second optimized horn-cone (the solid line) are shown.

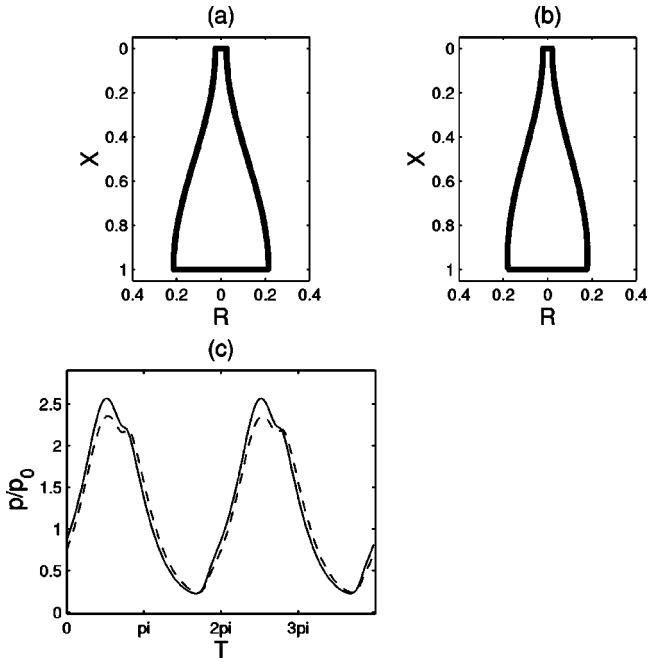

FIG. 6. (a) The $\frac{1}{2}$-cosine shape as in Chun and Kim (Ref. 5). (b) The optimized cosine shape. (c) The pressure waveform at the narrow end for the $\frac{1}{2}$-cosine resonator in Chun and Kim (Ref. 5) (the dashed line) and that for the optimized cosine shape (the solid line) are shown.

corresponding to the two horn-cone resonators also have different phases. Under the prescribed conditions, the peak of the pressure is about 5.0 times the ambient pressure in the optimal horn-cone while the peak is about 3.3 times for the horn-cone in Lawrenson *et al.*[1]

3. Optimal cosine shaped resonator

The cosine shape is defined as

$$R(X)=S_0+S_1(1-\cos(S_2X)), \quad \text{for } 0\leqslant X\leqslant 1. \tag{11}$$

Assuming that the input power is entirely determined by the interior gas pressure, Chun and Kim[5] compared three individual resonators of the same volume: one conical shape, one $\frac{1}{2}$-cosine shape ($S_2=\pi$) and one $\frac{3}{4}$-cosine shape ($S_2=3\pi/2$). They found that the $\frac{1}{2}$-cosine resonator produces the highest compression ratio among the three resonators. Imposing our optimization constraint of external force-limit, for the $\frac{1}{2}$-cosine dimensions reported in Chun and Kim,[5] $S_0=0.025$, $S_1=0.095$, $S_2=\pi$, the compression ratio reaches the value 11.216 when $\tilde{A}=5.5775\times10^{-4}$ and $\Omega=1.4834$. Starting with this shape, the resulting optimal cosine shape parameters are given by $S_0=0.020833$, $S_1=0.10462$ and $S_2=3.2490$, and the corresponding compression ratio increases to $R_c=11.865$ at the acceleration $\tilde{A}=5.4680\times10^{-4}$ and the frequency $\Omega=1.5552$, which is about 6% better than that of Chun and Kim[5] at the same level of force-limit. Using different initial guesses of the shape parameters for cosine resonators, the optimization scheme produced results that yielded a higher compression ratio of $R_c=11.954$, 7% higher than that of Chun and Kim.[5] The higher performance is achieved at $\tilde{A}=5.9209\times10^{-4}$ and $\Omega=1.4837$ when the cosine resonator described by Eq. (11) has the following shape parameters: $S_0=0.020833$, $S_1=0.070327$ and $S_2=3.3553$. The shape is displayed in Fig. 6(b). As shown in Fig. 6(c), the pressure waveform of the optimal cosine design is smoother compared to that of Chun and Kim[5] with a greater pressure peak and a different phase.

Under the specified conditions (the same force-limit $F_{\max}$, the ratio of specific heats γ and the viscosity-related parameter G), the horn-cone shape is found to be better than the cosine shape in generating higher compression ratio at the narrow end, different than the findings of Chun and Kim[5] under a different set of criteria. The resonance frequency of the optimal horn-cone shape $\Omega=1.5603$ is higher than that of the optimal cosine shape $\Omega=1.4837$, and the acceleration amplitudes for achieving the corresponding compression ratios are comparable: $\tilde{A}=5.1814\times10^{-4}$ for the horncone resonator and $\tilde{A}=5.9209\times10^{-4}$ for the cosine resonator.

V. CONCLUSIONS

A local optimization scheme is presented for determining the axisymmetric resonator contours that maximize the pressure compression ratio at one end of an oscillating acoustic resonator. The optimal dimensions under a limiting constraint of external periodic force are reported for cone, horn-cone, and cosine shaped resonators. The results are summarized in Table I, including the shape parameters, corresponding acceleration amplitude, resonance frequency, and compression ratio.

TABLE I. A summary of the shape parameters and compression ratios of previous studies compared with the optimum geometries. For reference, the corresponding acceleration levels and fundamental resonance frequency are listed.

	S_0	S_1	S_2	$\tilde{A}(\times10^{-4})$	Ω	R_c
Cone:						
Ilinskii *et al.* (Ref. 2)	0.032941	0.26800	N/A	5.0000	1.3134	5.0475
Optimal	0.020833	0.17211	N/A	5.7470	1.3200	5.8932
Horn-cone:						
Lawrenson *et al.* (Ref. 1)	0.028333	5.7264	0.25	5.1516	1.4678	14.059
Optimal	0.020833	6.1698	0.27704	5.1814	1.5603	47.975
Cosine-shape:						
Chun and Kim (Ref. 5)	0.025	0.095	3.1416	5.5775	1.4834	11.216
Optimal	0.020833	0.070327	3.3553	5.9209	1.4837	11.954

For each type of resonator, a smaller narrow end is found to give a larger pressure peak-to-peak ratio. This finding suggests that the number of shape parameters in an optimization can be reduced by holding the diameter of the narrow end fixed at a value as small as practical. For the types of horncone and cosine shapes, there are many different designs that achieve local extrema. However, using different initial guesses a more global optimum can be determined and a 241% improvement of in compression ratio can be achieved. For the shapes considered herein, the horncone shape is found to generate the highest compression ratio. The acoustic field in a resonator is a continuous function of the resonator shape, the ratio of specific heats and the viscosities. Consequently, the dimensions of optimal resonator shape reported herein will undergo change as the specific heats and/or the viscosities change. The optimized shapes depend on the capacity and the fixture/armature mass of the force-limited shaker, the mass of the resonator, and other possible constraints that a particular application demands.

The quasi-one-dimensional model in this paper does not include the possible effects due to the boundary layer along the resonator wall and acoustically generated turbulence at high amplitudes. Nevertheless, a direct comparison is made between the results from our model and those from Ilinskii *et al.*[3] which include both of these effects. We find that, for the horncone studied in Ilinskii *et al.*,[3] the combined influence of the boundary layer attenuation and possible turbulence on the acoustical field, in particular, on the compression ratio of the pressure wave, is small (less than 5%) at $\tilde{A}=5\times10^{-4}$, approximately the highest acceleration level considered in this paper.

[1] C. C. Lawrenson, B. Lipkens, T. S. Lucas, D. K. Perkins, and T. W. Van Doren, ''Measurements of macrosonic standing waves in oscillating closed cavities,'' J. Acoust. Soc. Am. **104**, 623–636 (1998).

[2] Y. A. Ilinskii, B. Lipkens, T. S. Lucas, T. W. Van Doren, and E. A. Zabolotskaya, ''Nonlinear standing waves in an acoustical resonator,'' J. Acoust. Soc. Am. **104**, 2664–2674 (1998).

[3] Y. A. Ilinskii, B. Lipkens, and E. A. Zabolotskaya, ''Energy losses in an acoustical resonator,'' J. Acoust. Soc. Am. **109**, 1859–1870 (2001).

[4] M. F. Hamilton, Y. A. Ilinskii, and E. A. Zabolotskaya, ''Linear and nonlinear frequency shifts in acoustical resonators with varying cross sections,'' J. Acoust. Soc. Am. **110**, 109–119 (2001).

[5] Y.-D. Chun and Y.-H. Kim, ''Numerical analysis for nonlinear resonant oscillations of gas in axisymmetric closed tubes,'' J. Acoust. Soc. Am. **108**, 2765–2774 (2000).

[6] R. R. Erickson and B. T. Zinn, ''Modeling of finite amplitude acoustic waves in closed cavities using the Galerkin method,'' J. Acoust. Soc. Am. **113**, 1863–1870 (2003).

[7] J. Finkbeiner, ''Nonlinear acoustic standing waves in oscillating closed containers,'' Master's thesis, Illinois Institute of Technology, May 2003.

[8] C. Daniels, J. Finkbeiner, B. Steinetz, X. Li, and G. Raman, ''Determination of dimensionless attenuation coefficient in shaped resonators,'' presentation 4aPAa3, *145th Meeting of the Acoustical Society of America*, May 2003, Nashville, TN.

[9] X. Li, J. Finkbeiner, G. Raman, C. Daniels, and B. Steinetz, ''Nonlinear resonant oscillations of gas in optimized acoustical resonators and the effect of central blockage,'' *41st AIAA Aerospace Sciences Meeting and Exhibit*, AIAA Paper No. 2003-0368, 2003, Reno, Neveda.

[10] P. E. Gill, W. Murray, and M. H. Wright, *Practical Optimization* (Academic, New York, 1981).

[11] J. Finkbeiner, X. Li, C. Daniels, G. Raman, and B. Steinetz, ''Effect of forcing function on nonlinear acoustic standing waves,'' presentation 4aPAa2, 145th Meeting of the Acoustical Society of America, May 2003, Nashville, TN.

[12] C. Daniels, J. Finkbeiner, B. Steinetz, X. Li, and G. Raman. ''Nonlinear oscillations and flow of gas within closed and open conical resonators,'' *American Institute of Aeronautics and Astronautics 42st Aerospace Sciences Meeting*, AIAA-2004-0677, Reno, Nevada, 2004, and NASA TM-2004-212902.

Numerical simulation of acoustic streaming generated by finite-amplitude resonant oscillations in an enclosure

Murat K. Aktas and Bakhtier Farouk[a)]
Department of Mechanical Engineering and Mechanics, Drexel University, Philadelphia, Pennsylvania 19104

(Received 20 March 2004; revised 23 July 2004; accepted 27 July 2004)

Acoustic streaming motion in a compressible gas filled two-dimensional rectangular enclosure is simulated and the effects of the sound field intensity on the formation process of streaming structures are investigated numerically. The oscillatory flow field in the enclosure is created by the vibration of the left wall of the enclosure. The frequency of the wall vibration is chosen such that the lowest acoustic mode propagates along the enclosure. The fully compressible form of the Navier–Stokes equations is considered and an explicit time-marching algorithm is used to track the acoustic waves. The formation of the wave field in the enclosure is computed and fully described and the acoustic boundary layer development is predicted. The interaction of the wave field with viscous effects and the formation of streaming structures are revealed by time-averaging the solutions over a given period. The strength of the pressure waves associated with the acoustic effect and the resulting streaming flow pattern is found to be strongly correlated to the maximum displacement of the wall during a vibration cycle. The wave form determines the shape of the steady streaming structures in the oscillatory flow field.
[DOI: 10.1121/1.1795332]

PACS numbers: 43.25.Nm [MFH] Pages: 2822–2831

I. INTRODUCTION

Interaction of acoustic waves in compressible fluids and solid boundaries creates challenging problems. One of these problems is *the acoustic streaming*. It is a well-known fact that sound sources may generate a flow field in which the particle velocities are not simply sinusoidal and a pattern of time-independent vortical flows or steady circulations is often found in the body of compressible media.[1] Sound at high intensity levels in gases and liquids is accompanied by these second-order steady flow patterns known as ''acoustic streaming.'' These steady flows always have rotational character and their velocity increases with the sound intensity. But, even at the high intensity levels, the secondary streaming velocity magnitude remains smaller than the primary oscillatory particle velocity magnitude.

Acoustic streaming may be effective in accelerating certain kinds of rate processes and has applications in localized micromixing of polymers, and convective cooling in reduced gravity environment. These streaming flows may also appear in devices like acoustic compressors, thermoacoustic refrigerators, and in processes like containerless material processing via acoustic levitation, ultrasonic medical diagnostic devices, and ultrasonic cleaning of contaminated surfaces. Proper knowledge of the flow structure is important for the successful design and execution of these applications.

While various analytical models are available for describing acoustic streaming phenomena, they are usually based on substantial approximations and the solutions are often limited to idealized conditions. The study of acoustic streaming started with the theoretical work of Lord Rayleigh.[2] He considered vortex flows occurring in a long pipe (Kundt's tube) as a result of the presence of a longitudinal standing wave. Westervelt[3] obtained a general vorticity equation and developed a general procedure for evaluating the streaming velocity induced by acoustical disturbances that can be specified in a first-order manner by a wave equation—linear in the field variables. The treatment presented in the above study was not applicable to problems where the wave amplitudes are large and the field values cannot be described by a linear wave equation because of the fact that no first-order specification of the field exists. The vorticity equation was thus subject to the restrictions: solenoidal first-order motion and irrotational first-order motion. Andres and Ingard investigated low[4] and high[5] Reynolds number acoustic streaming analytically and discussed the distortion of the streaming flow patterns as a function of sound intensity. Nyborg[6] reviewed the theories for calculating steady streaming associated with sound fields. He worked out two illustrative problems, both for rectilinear flow due to irrotational sound fields: the first deals with a single attenuated plane wave traveling down a tube and the second one deals with a pair of crossed plane waves. An approximate solution was also developed by Nyborg[7] for sonically induced steady flow near a fluid–solid interface subjected to the condition of known irrotational oscillatory velocity distribution in the vicinity of the interface. The previously developed theoretical approaches are based on successive approximations to solutions of nonlinear hydrodynamic equations, where the first- and second-order solutions in each approximation must satisfy the boundary conditions. Accurate solutions exist only for the cases where the boundaries are planes, cylinders, or spheres and where the specified velocity distributions on these boundaries are as simple. When the geometry is complex, the method will not work.

a)Author to whom correspondence should be addressed. Electronic mail: bfarouk@coe.drexel.edu

The effect of compressibility on acoustic streaming near a rigid boundary was investigated by Qi[8] with a theoretical study. In this study, the goal was to resolve an existing inconsistency: while the compressibility is a necessary condition for the propagation of acoustic waves, past analysis of acoustic streaming are limited to incompressible fluids. It appears that this inconsistent description results from adapting the incompressible boundary layer solutions obtained by Schlichting to acoustic streaming near rigid boundaries. It was shown that the consideration of compressibility leads to a larger streaming velocity outside the boundary layer. The effect was found to be significant in gases, but not in liquids. However, Hamilton *et al.*[9] noted that the interpretation proposed by Qi[8] on the effect of compressibility is misleading since Qi's solution[8] reduces to the classical solution of Rayleigh in the absence of heat conduction. Qi extended this study[8] to investigate acoustic streaming in a circular tube.[10] Vainshtein[11] combined the problems of Rayleigh streaming and Couette flow and investigated the effect of streaming on shear flows. Menguy and Gilbert[12] studied nonlinear acoustic streaming in a cylindrical waveguide with a perturbation scheme using asymptotic expansions. A noticeable distortion of the acoustic field due to the fluid inertia was demonstrated and a comparison of slow and nonlinear acoustic streaming was presented. Hamilton *et al.*[13] derived an analytic solution for the average mass transport velocity generated by a standing wave confined by parallel plates. In this study both the outer, Rayleigh streaming vortices and the inner, boundary layer vortices were described. They found that as the channel width is reduced, the inner vortices increase in size relative to the Rayleigh vortices and for sufficiently narrow channels the Rayleigh vortices disappear and only inner vortices exist. Hamilton *et al.*[9] recently extended this analysis to a gas in which heat conduction and the dependence of viscosity on temperature are taken into account.

Kawahashi and Arakawa[14] performed a numerical analysis of acoustic streaming induced by finite-amplitude oscillation in a closed duct driven by a piston applying a fourth-order spatial difference method. The results obtained showed velocity distributions in the oscillatory boundary layer and the change of the streaming profile owing to the increase in the amplitude of oscillation and the existence of a double layer in the vicinity of the duct wall. Gopinath and Mills[15] investigated the convective heat transfer due to acoustic streaming across the ends of a tube supporting a standing wave, numerically. A parametric study of the effects of the controlling acoustic and geometric variables was conducted, and Nusselt number correlations were developed for air. Yano[16] investigated acoustic streaming excited by resonant oscillations with periodic shock waves in a gas-filled closed tube. His computational predictions demonstrated strong vortices localized near the tube wall that are quite different from Rayleigh streaming. For high streaming Reynolds numbers $(=\pi X_{\mathrm{MAX}} c_0/\nu)$, turbulent streaming appears in the form of irregular vortical flow structures in the tube. Alexeev and Gutfinger[17] studied resonant gas oscillations in closed tubes numerically and experimentally. They considered a two-dimensional axisymmetric flow for a compressible gas with a turbulence model and reported shock waves traveling back and forth along the tube. They reported streaming motion at resonance having an opposite direction with that in nonresonant oscillations.

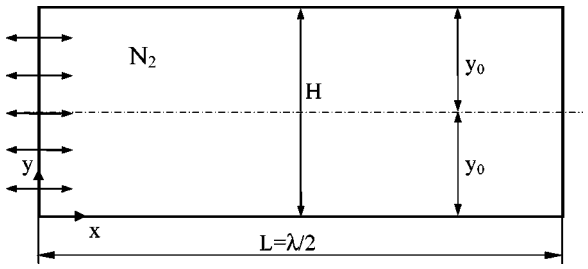

FIG. 1. Schematic of the problem.

The above survey indicates that, in most of the analytical and numerical studies cited in the literature, the formation of acoustic streaming is analyzed with a simplified approach. In these studies, a perfectly sinusoidal primary standing wave field in the domain of interest is assumed and the investigation is started from this point. In other terms, the formation of the sound field and streaming processes are not modeled. The current study is specifically concerned with the modeling of the actual physical processes, i.e., the formation of the sound field and streaming processes in a resonator. We do not employ any pre-defined sound field in the computational domain for the simulation of acoustic streaming. Instead, we directly compute and fully describe the formation of the acoustic field in the domain. A rectangular enclosure filled with a compressible fluid is considered. The left wall of the enclosure is modeled as a rigid boundary that vibrates harmonically in time representing the motion of a loudspeaker diaphragm or vibration of a commercial ultrasonic mixer probe. The vibrating boundary is the acoustic source in this geometry and a sound field in the enclosure is created by this source. We are able to model the physical processes including the compression of the fluid and the generation of the wave, acoustic boundary layer development, and finally the interaction of the wave field with viscous effects and the formation of streaming structures. A similar approach was also followed by Kawahashi and Arakawa[14] in their study and the simulations were performed for a single enclosure height (aspect ratio, $H/L=0.036$) and three wall displacement values. We consider five different enclosure heights with various wall displacement values for the geometries considered in this study. This present model is a flexible tool that can analyze acoustic streaming in various geometries, and with different fluids. The results of the current study will also be a good reference and starting point for more advanced studies involving heat transfer analysis in acoustically induced flow fields with streaming.

II. THE MODEL AND GOVERNING EQUATIONS

To investigate the formation of streaming flow structures, a rectangular enclosure filled with nitrogen having thermally insulated and no-slip walls is considered as illustrated in Fig. 1. The vibration frequency of the enclosure left wall is chosen as $f=20\,\mathrm{kHz}$ since this value is a typical operating frequency for ultrasonic mixer probes. The corresponding wavelength of the sound waves at this frequency is

$\lambda = 17.65$ mm for the value of sound speed in nitrogen at 300 K being $c_0 = 353$ m/s. The harmonic displacement and the velocity of the vibrating wall are given by $X = X_{\mathrm{MAX}} \sin(\omega t)$ and $v_w = \omega X_{\mathrm{MAX}} \cos(\omega t)$, respectively. Here, X_{MAX} is the maximum displacement of the wall, ω is the angular frequency of the vibration ($\omega = 2\pi f$), and ωX_{MAX} represents the maximum velocity of the wall. The length of the enclosure was chosen as $L = \lambda/2 = 8.825$ mm while five different values were considered for the enclosure height. Chosen height values give dimensionless enclosure height (y_0/δ_ν) as 10, 20, 30, 40, and 50 varying from a narrow geometry to wider enclosures. Here δ_ν represents the acoustic boundary layer thickness, given by $\delta_\nu = (2\nu/\omega)^{1/2}$ and ν is the kinematic viscosity of the fluid.

Acoustic streaming formation is described by the full two-dimensional Navier–Stokes and energy equations for a compressible fluid. In a Cartesian coordinate system, these equations are expressed as

$$\frac{\partial \rho}{\partial t} + \frac{\partial(\rho u)}{\partial x} + \frac{\partial(\rho v)}{\partial y} = 0, \tag{1}$$

$$\rho \frac{\partial u}{\partial t} + \rho u \frac{\partial u}{\partial x} + \rho v \frac{\partial u}{\partial y} = -\frac{\partial p}{\partial x} + \frac{\partial \tau_{xx}}{\partial x} + \frac{\partial \tau_{xy}}{\partial y}, \tag{2}$$

$$\rho \frac{\partial v}{\partial t} + \rho u \frac{\partial v}{\partial x} + \rho v \frac{\partial v}{\partial y} = -\frac{\partial p}{\partial y} + \frac{\partial \tau_{yy}}{\partial y} + \frac{\partial \tau_{xy}}{\partial x}, \tag{3}$$

$$\frac{\partial E}{\partial t} + \frac{\partial}{\partial x}[(E+p)u] + \frac{\partial}{\partial y}[(E+p)v] = \frac{\partial}{\partial x}[u\tau_{xx} + v\tau_{xy}] + \frac{\partial}{\partial y}[u\tau_{xy} + v\tau_{yy}] - \frac{\partial q_x}{\partial x} - \frac{\partial q_y}{\partial y}. \tag{4}$$

Here t is time, x and y refer to the Cartesian coordinates, ρ is density, p is pressure, u and v are the velocity components, and E is the total energy:

$$E = \frac{p}{\gamma - 1} + \frac{1}{2}\rho(u^2 + v^2). \tag{5}$$

Here $\gamma\,(=1.4)$ is the ratio of specific heats. The components of the stress tensor τ are

$$\tau_{xx} = \frac{4}{3}\mu\frac{\partial u}{\partial x} - \frac{2}{3}\mu\frac{\partial v}{\partial y}, \quad \tau_{yy} = \frac{4}{3}\mu\frac{\partial v}{\partial y} - \frac{2}{3}\mu\frac{\partial u}{\partial x}, \quad \tau_{xy} = \mu\left(\frac{\partial u}{\partial y} + \frac{\partial v}{\partial x}\right), \tag{6}$$

where μ is the dynamic viscosity. The components of the heat-flux vector are written as

$$q_x = -k\frac{\partial T}{\partial x}, \quad q_y = -k\frac{\partial T}{\partial y}, \tag{7}$$

where T is temperature and k is thermal conductivity. Since the temperature fluctuations for the cases considered are significant and vary in the range of 10 °C to 30 °C, the temperature dependence of the viscosity and thermal conductivity[18] are taken into account using the following polynomial expressions:

$$\mu(T) = -1.253\times10^{-6} + 8.983\times10^{-8}T - 1.139\times10^{-10}T^2 + 9.101\times10^{-14}T^3, \tag{8}$$

$$k(T) = 1.494\times10^{-4} + 1.108\times10^{-4}T - 1.045\times10^{-7}T^2 + 6.958\times10^{-11}T^3. \tag{9}$$

The temperature is related to the density and pressure through the ideal-gas law:

$$p = \rho R T, \tag{10}$$

where $R\,(=296.8$ J/kg K) is the specific gas constant of the medium.

III. NUMERICAL SCHEME

The governing equations (except for the diffusion terms) are discretized using a control-volume-based finite-volume method based on the flux-corrected transport (FCT) algorithm. FCT is a high-order, nonlinear, monotone, conservative, and positivity-preserving scheme designed to solve a general one-dimensional continuity equation with appropriate source terms.[19] This scheme has fourth-order phase accuracy and is able to resolve steep gradients with minimum numerical diffusion. We have successfully used the algorithm in predicting the generation and propagation of thermoacoustic waves in gases.[20,21] In this algorithm, when a flow variable such as a density is initially positive, it remains positive during the computations and no new minimum or maximum values are introduced due to numerical errors in the calculation process. To ensure positivity and stability, a minimum amount of numerical diffusion over the stability limit is added at each time step. The time-step splitting technique is used to solve the two-dimensional problem addressed here. Further details of the FCT algorithm used here are documented by Boris *et al.*[22] The diffusion terms (the viscous term in the momentum equations and the conduction and viscous dissipation terms in the energy equation) were discretized using the central-difference approach and the time-step splitting technique was used to include the terms in the numerical scheme.

No-slip and zero-gradient temperature boundary conditions were used for all the solid walls. A high-order nondissipative algorithm such as FCT requires a rigorous formulation of the boundary conditions. Otherwise, numerical solutions may show spurious wave reflections at the regions close to boundaries and nonphysical oscillations arising from instabilities. In the present computational method, the treatment proposed by Poinsot and Lele[23] was followed for implementing the boundary conditions for the density. This method avoids incorrect extrapolations and overspecified boundary conditions. Along any stationary solid wall, the density is calculated from

$$\left(\frac{\partial \rho}{\partial t}\right)_M + \frac{1}{c_M}\left(\frac{\partial p}{\partial n} + \rho c \frac{\partial u_n}{\partial n}\right)_M = 0, \tag{11}$$

where c_M is the acoustic speed, M indicates the location of the wall, and n is the direction normal to the wall. Since the current problem involves a moving boundary and a time-dependent boundary velocity, a modification in this part of

TABLE I. Summary of cases considered for acoustic streaming analysis.

Case	y_0/δ_ν	X_{MAX} (μm)	H/L
A	10	10	0.0358
B-1	20	10	0.0716
B-2	20	3	0.0716
C-1	30	10	0.1074
C-2	30	2	0.1074
C-3	30	1	0.1074
D-1	40	10	0.1432
D-2	40	0.5	0.1432
E-1	50	10	0.1790
E-2	50	0.5	0.1790
E-3	50	0.2	0.1790

the scheme is required. Along the vibrating wall, the density is calculated from

$$\frac{\partial \rho}{\partial t}=\frac{\rho\gamma}{c_L}\frac{\partial u_W}{\partial t}+\frac{\rho\gamma(u_W-c_L)}{c_L}\frac{\partial u}{\partial x}-\frac{\gamma(u_W-c_L)}{c_L^2}\frac{\partial p}{\partial x}, \tag{12}$$

where c_L is the acoustic speed.

Since the formation of acoustic streaming structures results from the interaction between the wave field and the viscous boundary, resolving the acoustic boundary layer thickness in the computational method is a required condition to accurately predict the acoustic streaming structures. Due to symmetry of the geometry, we consider the bottom half of the enclosure as the computational domain and employ mesh sizes varying between 121×55 to 121×110 for the five different enclosure heights considered in these simulations. The simulations performed using even denser computational grids did not change the results significantly and chosen meshes were found to be sufficient for the present computations. The computational cells are uniformly distributed in the x direction and are found sufficient to capture wave propagation and reflection accurately. The grid has nonuniformly distributed cells in the y direction with fine grids in the vicinity of the bottom wall of the enclosure. In this grid structure, the variation of the left wall position and the size changes for the first column of cells were also taken into account since the problem involves the modeling of a vibrating wall.

IV. RESULTS AND DISCUSSION

The pressure amplitude in the enclosure (see Fig. 1) is determined by adjusting the maximum displacement of the wall (X_{MAX}). The calculations were started with the vibration of the left wall at $x=0$ and with uniform values of pressure (101 325 Pa), temperature (300 K), and density (1.138 kg/m^3) within the quiescent medium. For the duration of each cycle of the vibration of the wall, about 25 000 time steps were used.

We considered five different values of the enclosure height. The cases considered are summarized in Table I. The dimensionless channel width (y_0/δ_ν), the maximum displacement of the left wall (X_{MAX}), and the aspect ratio of the enclosure ($H/L=2y_0/L$) are included in Table I for each case.

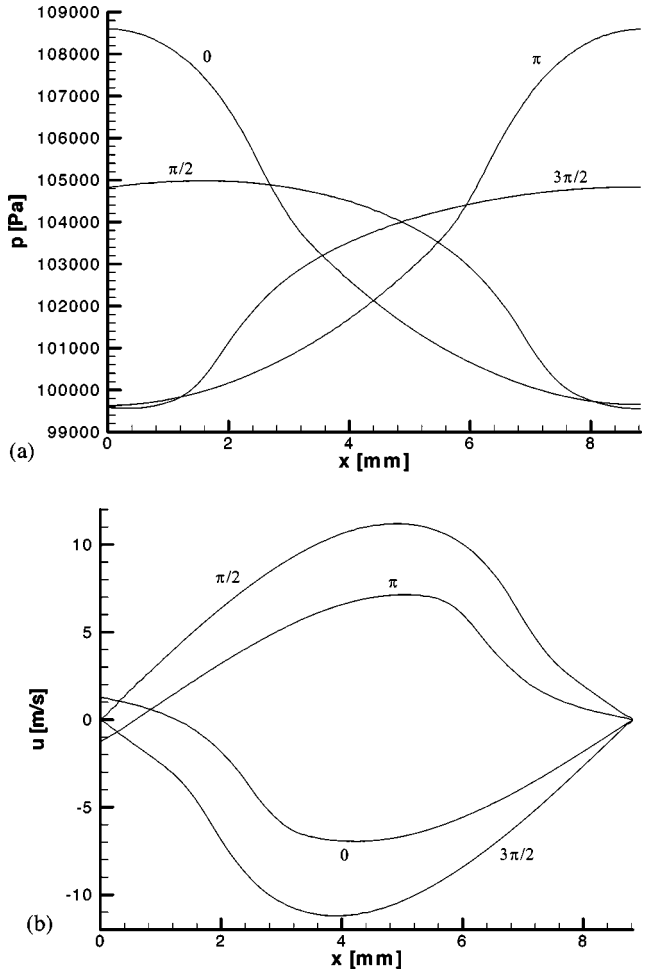

FIG. 2. Variation of (a) pressure; (b) u velocity along the symmetry axis of the enclosure at four different instants ($\omega t=0,\pi/2,\pi,3\pi/2$) during the acoustic cycle #100 (Case A).

In the first case considered (Case A), the enclosure half-width is the smallest ($y_0/\delta_\nu=10$) and the maximum displacement of the wall was set to $X_{\mathrm{MAX}}=10\,\mu$m. Figures 2(a) and 2(b) show the pressure and velocity distributions, respectively, along the symmetry axis ($y=y_0$) of the enclosure at $\omega t=0$, $\pi/2$, π, $3\pi/2$ for Case A (during cycle #100). Pressure distribution for $\omega t=2\pi$ (not shown here) is identical to the curve given for $\omega t=0$. The perfectly sinusoidal profile of the emitted wave by the oscillating wall is weakly distorted due to viscous and nonlinear effects. At $\omega t=0$ and $\omega t=\pi$, the amplitude of the pressure waves reach a maximum value in the enclosure. At the beginning of the cycle ($\omega t=0$), the pressure is maximum on the vibrating wall of the enclosure and decreases with distance from the wall and reaches a minimum at the opposite wall ($x=L$). In the middle of the cycle ($\omega t=\pi$) the pressure profile is fairly symmetric with respect to the vertical midplane ($x=L/2$) to the profile given for $\omega t=0$, and reaches a maximum at the right wall. The pressure profiles given for different time levels intersect at approximately $x=L/2$ and creates a pressure node. The corresponding u-velocity profile for this case is given in Fig. 2(b). Unlike the pressure field, velocity maximums and minimums are observed at $\omega t=\pi/2$ and $\omega t=3\pi/2$. The left wall is stationary at $\omega t=\pi/2$ and $\omega t=3\pi/2$. The primary oscil-

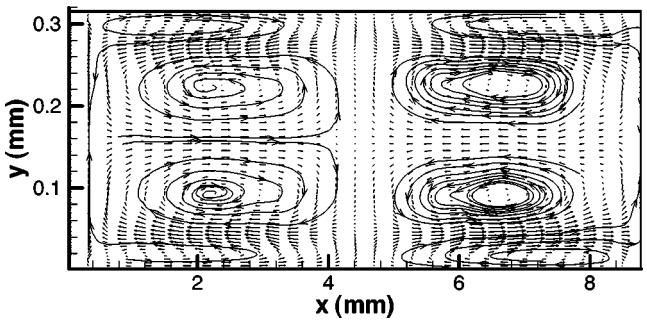

FIG. 3. Mean flow field in the enclosure at $t=0.005$ s (Case A).

latory flow is periodic and the maximum value of the velocity is predicted to be approximately 12 m/s. Due to attenuation caused by viscous and nonlinear effects, both pressure and velocity profiles slightly differ from a perfect sinusoidal wave field.

The predicted secondary flow field for Case A is shown in Fig. 3 for the enclosure. This flow field is based on the average mass transport velocity values in the enclosure. The average mass transport velocity was given by

$$u_{\mathrm{st}}=\frac{\langle \rho u\rangle}{\langle \rho\rangle}, \quad v_{\mathrm{st}}=\frac{\langle \rho v\rangle}{\langle \rho\rangle}, \tag{13}$$

and describes the x and y components of the streaming velocities, respectively. Here $\langle\ \rangle$ indicates the time-averaged quantities. The time averaging was applied during the 100th vibration cycle (between cycle #99 and #100) and gives the streaming velocity values near $t=5$ ms. The streaming velocities calculated based on the time averaging during 150th ($t=7.5$ ms) and 200th ($t=10$ ms) cycles do not differ significantly from the values computed at $t=5$ ms. Hence, the average mass transport velocities were assumed to be cycle independent by this time ($t=5$ ms). The maximum streaming velocity value is found to be approximately 0.06 m/s while the maximum instantaneous velocities reach 12 m/s in the primary oscillatory flow field in the enclosure. Four clockwise and four counterclockwise circulations are observed in the enclosure. Two of these vortical structures, namely inner streaming structures, formed at the vicinity of the bottom wall. The height of the circulatory flow structures (inner streaming) observed in the vicinity of the horizontal walls is characterized by the thickness of the acoustic boundary layer. The streaming structures seen in the middle section of the enclosure (outer streaming) have larger sizes. The horizontal length of both the inner and the outer streaming vortices is characterized by a quarter-wavelength ($\lambda/4$). The predicted streaming structures are in good agreement with the results reported by Hamilton *et al.*[9,13] in their recent studies.

Figure 4(a) shows the variation of the x component of streaming velocity along the enclosure semiheight at $x=3L/4$ for Case A. In this figure, the vertical axis is the x component of the dimensionless streaming velocity (u_{st}/u_R) and u_R is the reference velocity given by $u_R=3u_0^2/16c_0$, where u_0 is the maximum oscillatory velocity. This reference velocity value represents the maximum streaming velocity in case of a perfect sinusoidal wave form obtained by Rayleigh.

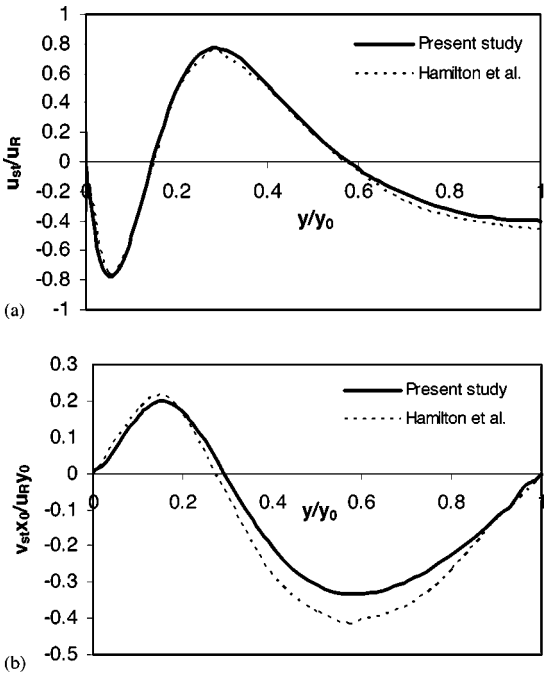

FIG. 4. Variation of the streaming velocity along the semiheight of the enclosure (Case A). (a) u component of the streaming velocity at $x=3L/4$ and (b) v component of the streaming velocity at $x=L/2$.

Results from Hamilton *et al.*[13] are also included in the same figure (dashed curve). The predictions of the current study for Case A compare well with the results from Hamilton *et al.*[13] Figure 4(b) shows the variation of the y component of streaming velocity along the enclosure semiheight at $x=L/2$. The vertical axis represents the y component of the nondimensional streaming velocity ($v_{\mathrm{st}}x_0/u_Ry_0$). The maximum difference between the predictions of the current study and the reference solution (dashed curve)[13] is approximately 10%. The results given in the reference solution are for a resonator in which the sound field is assumed to be formed by shaking the system with a harmonic excitation. Since the present study considers a resonator with a vibrating boundary, the resulting velocity fields slightly differ.

In the next case considered (Case B-1), the enclosure height ($y_0/\delta_\nu=20$) was doubled compared to Case A and the maximum wall displacement was kept the same ($X_{\mathrm{MAX}}=10\,\mu$m). Figure 5 shows the pressure distribution in the enclosure for this case during acoustic cycle #100. Pressure waves emanating from the sinusoidal displacement of the oscillating wall are strongly distorted by the nonlinear effects. Since we have a wider system ($y_0/\delta_\nu=20$), the viscous effects are weaker and shear forces along the top and the bottom walls have less effect on the bulk of the gas. This leads to higher pressure amplitudes and ''shock wave''-type profiles in the enclosure due to less attenuation. Similar wave profiles were reported by Chester[24] and several other researchers[17,25–29] for resonant gas oscillations in closed tubes. Corresponding flow structures based on the average mass transport velocity in the enclosure is shown in Fig. 6. The figure depicts the flow field in the bottom half of the enclosure. For this case, the secondary flow patterns are observed in the shape of irregular vortical structures. Several second-order vortices form the streaming flow field. Circula-

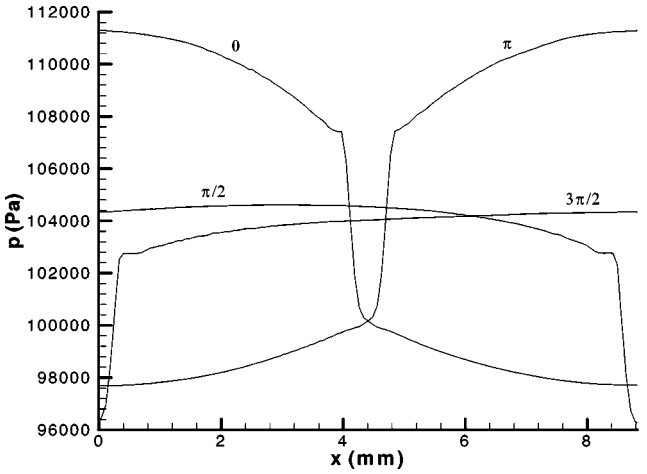

FIG. 5. Variation of the pressure along the symmetry axis of the enclosure at four different instants ($\omega t = 0, \pi/2, \pi, 3\pi/2$) during the acoustic cycle #100 (Case B-1).

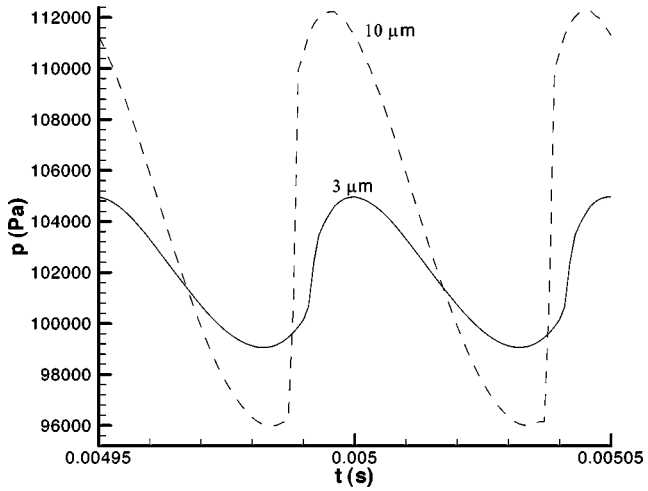

FIG. 7. Time evolution of left wall pressure at the midpoint (Cases B-1, B-2).

tion loops apparently become unstable and nonsymmetric vortex patterns are observed. The inner streaming structures are destructed but visible. The maximum primary oscillatory flow velocity is predicted as 20 m/s while the maximum flow speed is 0.54 m/s in the secondary quasisteady streaming flow field. For this case, we qualitatively compare our results with the predictions of Yano.[16] The aspect ratio of the enclosure 0.07 is quite close to that of 0.1, considered by Yano.[16] Yano's definition[16] of the streaming Reynolds number can be expressed as $\pi X_{\mathrm{MAX}} c_0 / \nu$ using the present nomenclature. Based on this definition, streaming Reynolds number for Case B-1 is 699. This value is close to the minimum streaming Reynolds number (560) considered by Yano. However, the pressure amplitudes and the oscillatory flows are much stronger in Case B-1, compared to those addressed by Yano. Yano's computations demonstrate streaming structures localized near the tube wall. A number of vortices are visible in the bottom half of the tube distributed nonhomogeneously and in skewed form. The streaming currents are not strong enough to position the vorticity in the vicinity of two ends of the tube. The present computations show more homogeneous streaming pattern distribution in the enclosure due to larger streaming velocities.

In the next case considered (Case B-2), we decreased the maximum wall displacement value to $X_{\mathrm{MAX}} = 3\ \mu$m to reduce the sharp pressure and velocity gradients observed for Case B-1 in the enclosure. The enclosure height is kept the same ($y_0 / \delta_\nu = 20$) as in Case B-1. Figure 7 compares the temporal variation of the pressure for Cases B-1 and B-2 at the midpoint of the left wall at the end of 100th vibration cycle. The pressure amplitude reaches approximately 16 kPa with 10 μm maximum wall displacement (Case B-1) while it is 6 kPa with 3 μm maximum wall displacement (Case B-2). Also, with a higher wall displacement value (10 μm), the pressure wave form is much sharper and shock wave-type profile is observed. For the smaller wall displacement (3 μm), the pressure profile is near-sinusoidal. The temporal variation of the pressure at the left wall is characterized by a sudden amplitude increase for Case B-1 while a more gradual increase is observed for Case B-2. The corresponding quasisteady (time-averaged) flow structure in the bottom half of the enclosure for Case B-2 is shown in Fig. 8 at $t = 5$ ms. For this case, the flow patterns are observed in the shape of regular structures. The inner and outer acoustic streaming structures are clearly visible. The maximum primary oscillatory flow velocity is computed as 7 m/s while the maximum flow speed is 0.03 m/s in the secondary steady streaming flow field.

For the next three cases considered the enclosure height increased further ($y_0 / \delta_\nu = 30$). In this geometry we consider $X_{\mathrm{MAX}} = 10\ \mu$m, $X_{\mathrm{MAX}} = 2\ \mu$m, and $X_{\mathrm{MAX}} = 1\ \mu$m as maximum wall displacement values for Cases C-1, C-2, and C-3, respectively. The instantaneous pressure profiles obtained for these three cases along the symmetry line are presented in Fig. 9. Larger wall displacement creates higher pressure amplitudes. Also, the pressure gradients in the flow field increases with a larger wall displacement. Sharp wave profile indicates the presence of higher harmonics in the wave field

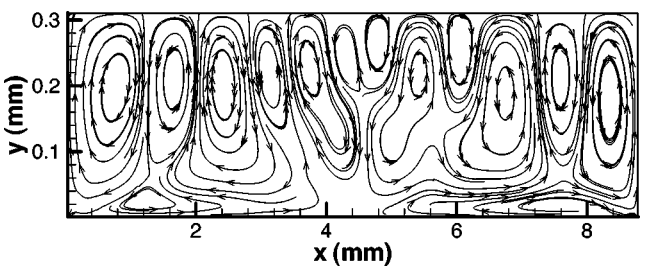

FIG. 6. Mean flow field in the enclosure at $t = 0.005$ s (Case B-1).

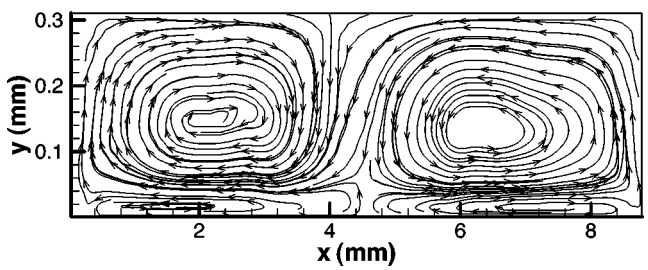

FIG. 8. Mean flow field in the enclosure at $t = 0.005$ s (Case B-2).

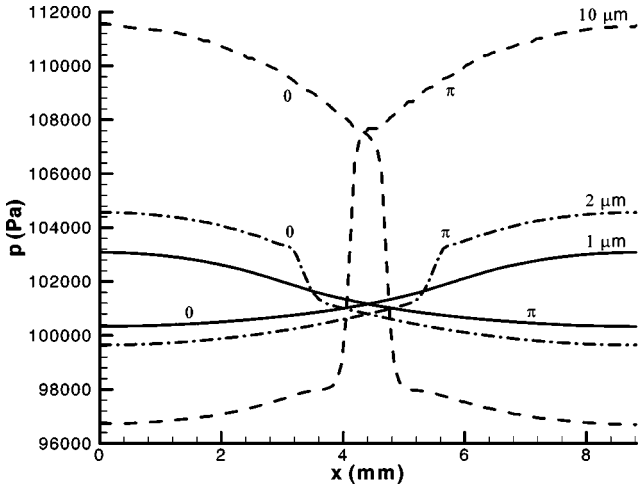

FIG. 9. Variation of the pressure along the symmetry axis of the enclosure at two different instants ($\omega t = 0, \pi$) during the acoustic cycle #100 for Case C-1 ($X_{MAX} = 10\ \mu$m), Case C-2 ($X_{MAX} = 2\ \mu$m), and Case C-3 ($X_{MAX} = 1\ \mu$m).

in addition to the fundamental component. The maximum pressure amplitudes are approximately 19.2, 5.2, and 3.1 kPa for Cases C-1, C-2, and C-3, respectively. Figures 10(a), 10(b), and 10(c) show the instantaneous flow fields in the

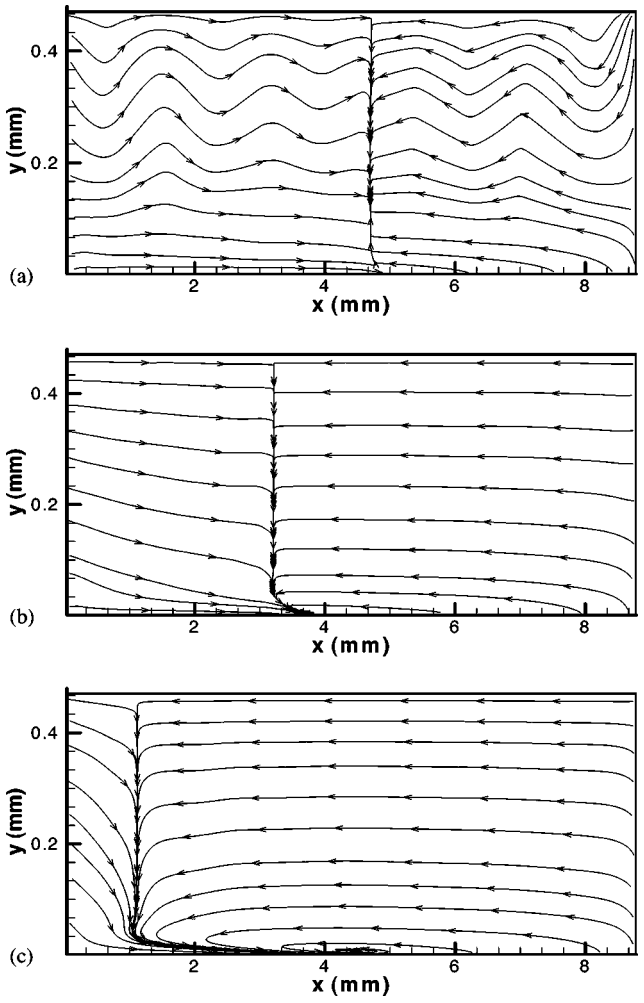

FIG. 10. Oscillatory flow fields (instantaneous) in the enclosure at $t = 0.005$ s for (a) Case C-1, (b) Case C-2, and (c) Case C-3.

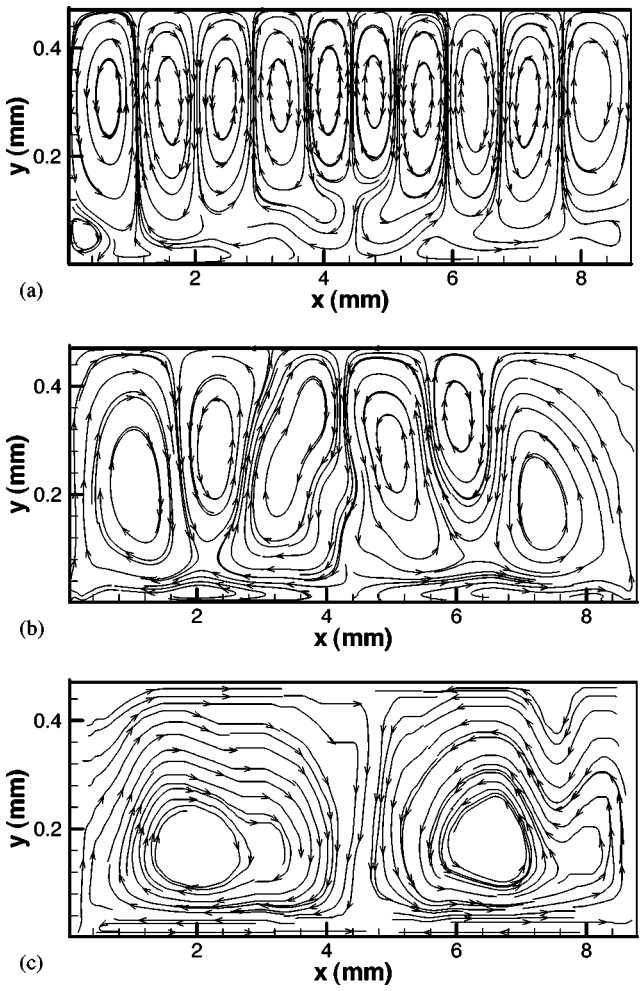

FIG. 11. Mean flow field in the enclosure at $t = 0.005$ s for (a) Case C-1, (b) Case C-2, and (c) Case C-3.

enclosure for these cases at $t = 5$ ms that corresponds to the beginning of acoustic cycle #101 ($\omega t = 0$). These are representative figures and although the flow directions change during the acoustic cycle due to periodic oscillations, the nature of the flow field is preserved. The maximum instantaneous flow velocities are 25, 6.8 and 3.6 m/s for cases C-1, C-2, and C-3, respectively. In Fig. 10(a), a strongly two-dimensional flow pattern is observed. In the vicinity of the bottom wall, flow is fairly uniform. As the wall displacement amplitude decreases (Case C-2), the transient flow field is an almost one-dimensional form [Fig. 10(b)], except a circulation pattern resulting from viscous interactions at $x \cong 4$ mm. For case C-3, the flow field is mostly one-dimensional, again except regions close to the bottom wall [Fig. 10(c)].

The time-averaged (over one cycle) flow fields in the bottom half of the enclosure for these three cases are given in Figs. 11(a), 11(b), and 11(c). In Fig. 11(a), the flow pattern in the bottom half of the enclosure is in the form of a number of vortical structures and five streaming structures are observed per quarter-wavelength. This irregular streaming flow pattern is the result of the two-dimensional transient (periodic) flow field [Fig. 10(a)]. The maximum streaming flow speed in Fig. 11(a) is 2.1 m/s. In Fig. 11(b), three outer streaming structures are observed per quarter-wavelength while one inner

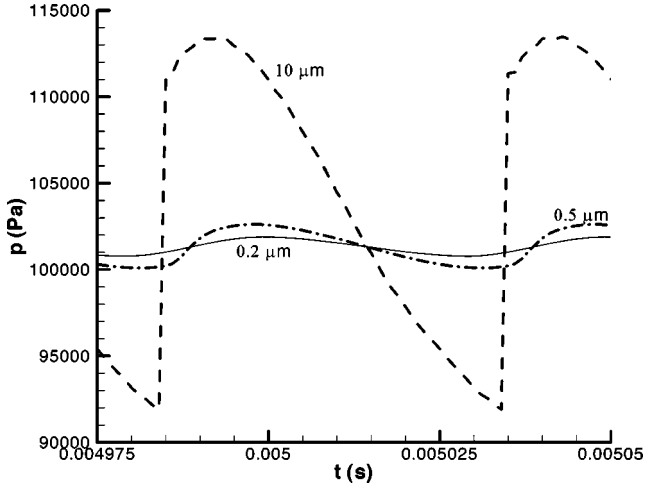

FIG. 12. Time evolution of left wall pressure at the midpoint for Case E-1 ($X_{MAX}=10\,\mu$m), Case E-2 ($X_{MAX}=0.5\,\mu$m), and Case E-3 ($X_{MAX}=0.2\,\mu$m).

streaming structure exists per quarter-wavelength. The change of the oscillatory flow field from a two-dimensional form to a near-one-dimensional form reduces the number of streaming structures and the irregularity of the streaming field. The streaming pattern in Fig. 11(b) is still quite different from that of classical Rayleigh streaming. The maximum streaming flow speed here is 0.044 m/s. In Fig. 11(c), two inner and two outer streaming structures are present in the system and the maximum streaming flow speed is 0.008 m/s.

In the last three cases considered (Cases E-1, E-2, E-3), the dimensionless enclosure height was chosen as $y_0/\delta_\nu=50$. In this geometry we consider $X_{MAX}=10\,\mu$m, $X_{MAX}=0.5\,\mu$m, and $X_{MAX}=0.2\,\mu$m as maximum wall displacements for Cases E-1, E-2, and E-3, respectively. Figure 12 compares the temporal variation of the pressure for these three cases at the midpoint of the left wall at the end of the 100th vibration cycle. The pressure amplitude reaches a value of approximately 21.2 kPa for the 10 μm wall displacement (Case E-1), 2.5 kPa for 0.5 μm (Case E-2) and 1.1 kPa for 0.2 μm (Case E-3) wall displacements. Also, with a higher wall displacement value, the pressure wave form is much sharper and distorted. The temporal variation of pressure at the left wall is characterized by sudden amplitude increase for Case E-1 while a more gradual increase is observed for Cases E-2 and E-3. Corresponding streaming structures in the bottom half of the enclosure for all three cases are shown in Figs. 13(a), 13(b), and 13(c). All three figures demonstrate highly irregular flow structure for the nonlinear sound fields. For Case E-1, approximately four outer streaming rolls are observed per quarter-wavelength. In Fig. 12 the pressure profiles seem fairly linear for Case E-2 ($X_{MAX}=0.5\,\mu$m) and for Case E-3 ($X_{MAX}=0.2\,\mu$m) though the (weak) attenuation effects are present. However, the corresponding flow structures do not contain the classical streaming field having two inner and two outer vortices per half-wavelength. Approximately four and one-half streaming rolls are observed per quarter-wavelength for Cases E-2 and E-3. The pressure variations (Fig. 12) are weaker in the domain for Cases E-2 (pressure amplitude: 2.5 kPa) and E-3

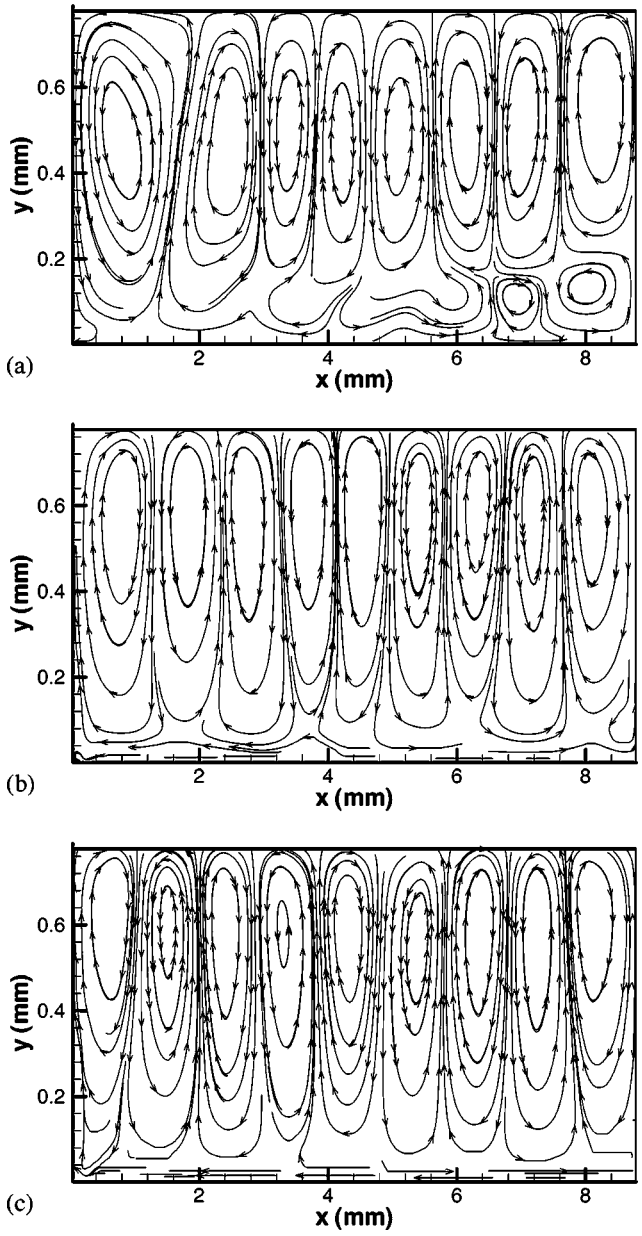

FIG. 13. Mean flow field in the enclosure at $t=0.005$ s for (a) Case E-1, (b) Case E-2, and (c) Case E-3.

(pressure amplitude: 1.1 kPa) compared to the pressure variations in classical streaming cases A (Fig. 2, pressure amplitude: 9.6 kPa), B-2 (Fig. 7, pressure amplitude: 6 kPa), and C-3 (Fig. 9, pressure amplitude: 3.1 kPa). Similar behavior is observed also for the maximum u-velocity values (u_{MAX}) in the oscillatory flow fields (Table II). These two points, viz., the two-dimensional oscillatory flow field and weak pressure variations appear to be the major factors resulting in irregular streaming motion.

When the enclosure is sufficiently high ($H/L>0.14$) Rayleigh streaming patterns are not observed even for small vibration amplitudes. Compared to narrow enclosures having oscillatory velocity amplitudes of the same order, wide systems are associated with larger streaming velocities and irregular flow structures. The maximum oscillatory flow velocities are 28, 3, and 1.3 m/s for Cases E-1, E-2, and E-3, respectively, while the maximum streaming flow speeds are

TABLE II. Characteristic results for the cases studied.

Case	u_{MAX} (m/s)	$v_{st\,MAX}$ (m/s)	Re_s	Streaming structure
A	12	0.06	73	Classical
B-1	20	0.51	203	Irregular
B-2	7	0.03	24.8	Classical
C-1	25	2.1	317	Irregular
C-2	6.8	0.044	23.4	Irregular
C-3	3.6	0.008	6.6	Classical
D-1	26.5	3.17	356	Irregular
D-2	2.5	0.005	3.2	Irregular
E-1	28	4.25	397	Irregular
E-2	3	0.047	4.5	Irregular
E-3	1.3	0.02	0.86	Irregular

4.5, 0.047, and 0.02 m/s. Since the thickness of the acoustic boundary layer is small compared to the enclosure height, inner streaming structures diminish.

Figure 14 shows the variation of the normalized pressure amplitude ($\Delta p/\Delta p_1$) calculated at resonance with the modified acoustic Reynolds number ($\mathrm{Re}_a^{1/3}/\Lambda$). Here Δp indicates the amplitude of the pressure variation at the right wall ($\Delta p = p_{max} - p_{min}$) and $\Delta p_1 = 8\gamma\epsilon p_0/[\pi(\gamma+1)]^{1/2}$, where $\epsilon = (\pi X_{MAX}/L)^{1/2}$, and p_0 is the initial pressure. The acoustic Reynolds number is defined as $\mathrm{Re}_a = c_0 X_{MAX}/\nu$ and $\Lambda = L/H$ is the dimensionless length of the enclosure. In this figure, the dashed curve indicates the values computed based on the correlation suggested by Alexeev and Gutfinger.[17] This correlation is given for $0.05 < \epsilon < 0.25$. The data from the present study (symbols in the figure) are in the range of $0.03 < \epsilon < 0.06$. The pressure amplitude predictions of the present study compare well with the above correlation.[17] The authors[17] also reported recirculating flow patterns at each half of the tube resulting from acoustic streaming for $\epsilon = 0.137$ and $H/L = 0.016$. In their predictions, the direction of streaming at resonance was opposite to that at nonresonance frequencies. In the present computations, we did not observe any flow reversal for the streaming structures (having a width of quarter-wavelength for $\epsilon \leqslant 0.06$ and $H/L \geqslant 0.036$) for resonant and nonresonant conditions.

In another study Merkli and Thomann[30] observed similar irregular circulations resulting from the transition to turbulence in their experiments. They considered gas oscillations excited with nonresonant frequencies (the flow properties varied sinusoidally in time) in a tube and they

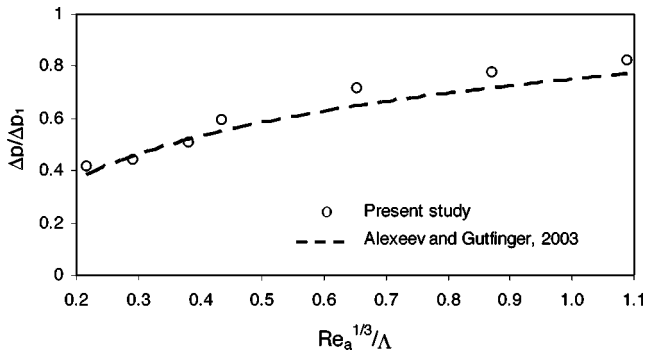

FIG. 14. Normalized pressure amplitude at resonance versus dimensionless parameter $\mathrm{Re}_a^{1/3}/\Lambda$.

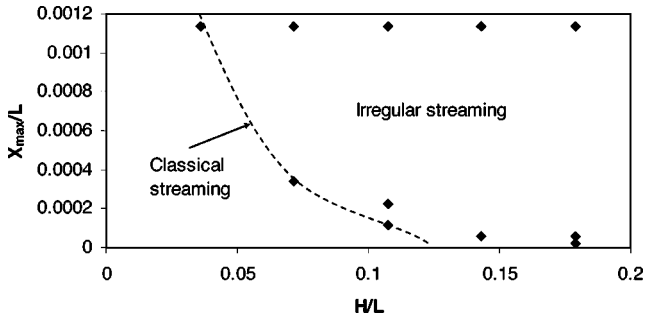

FIG. 15. Map of the cases considered as a function of the normalized maximum wall displacement and the enclosure aspect ratio. The symbols (♦) indicate the cases considered in terms of the geometrical condition and the normalized maximum wall displacement.

reported a number of vortices nonuniformly distributed in the tube for $H/L \cong 0.01$. In this study, the critical Reynolds number for transition was found as $A_c = 2u_{MAX}/(\nu\omega)^{1/2} \cong 400$. However, for the present computations the maximum value of A_c is 40.

Some characteristic results obtained for each case and the forms of streaming fields are summarized in Table II. The maximum velocity in the oscillatory flow field (u_{MAX}), the maximum acoustic streaming velocity, and the streaming Reynolds number ($\mathrm{Re}_s = u_{MAX}^2/\nu\omega$) are included in the table. An observation from these results is that the relative magnitude of the streaming velocity with respect to the oscillatory flow velocity ($v_{st\,MAX}/u_{MAX}$) is much larger for irregular streaming conditions compared to the relative magnitude of the streaming velocity for classical streaming.

Finally, we attempt to map the regions (defined by the aspect ratio of the enclosure and the maximum displacement of the wall amplitude) for which classical streaming patterns are obtained. The symbols in Fig. 15 indicate the cases considered in terms of the enclosure aspect ratio and the normalized maximum wall displacement. The dashed line indicates the combinations of the aspect ratios and wall vibrational amplitudes that result in the formation of the classical acoustic streaming flow patterns characterized by two outer streaming vortices per half-wavelength. Based on our results, the line defines the upper bound of the geometrical and vibrational amplitude conditions where the classical Rayleigh streaming patterns form. Clearly, both the vibrational amplitude and the height of the enclosure (wall-induced viscous effects) play roles in the formation of the classical Rayleigh streaming structures. On the right-hand side of the line, the acoustic streaming structures appear in complex and irregular forms. The number of streaming rolls increases as the enclosure height and the wall displacement increases.

V. CONCLUSIONS

The formation of pressure (acoustic) waves, acoustic-viscous boundary layer interactions, and associated flows in a rectangular enclosure are studied by solving the unsteady compressible Navier–Stokes equations in a two-dimensional (2-D) Cartesian coordinate system. The acoustic field in the enclosure is created due to the harmonic vibration of the left wall. The effects of the maximum amount of wall displacement on the wave field and the formed flow structures are

determined by utilizing a highly accurate flux corrected transport (FCT) algorithm. Observed primary oscillatory and secondary steady flow fields demonstrate the significant effects of the wall displacement and the enclosure height. The flow structure is strongly dependent on the pressure wave form in the enclosure. For a given enclosure height, increasing pressure amplitude induces stronger streaming motion (large u_{st}/u_R) and greatly changes the flow structures. Up to a certain enclosure height, the vibrational motion causes steady streaming flows that usually appear as two streaming rolls per half-wavelength, as reported in previous studies. However, when the enclosure height is increased beyond this limit, the streaming structures become irregular and complex.

[1] W. L. Nyborg, in *Physical Acoustics; Vol. 2B*, edited by W. P. Mason (Academic, New York, 1965), pp. 265–331.
[2] Lord Rayleigh, ''On the circulation of air observed in Kundt's tubes,'' Philos. Trans. R. Soc. London, Ser. A **175**, 1–21 (1884).
[3] P. J. Westervelt, ''The theory of steady rotational flow generated by a sound field,'' J. Acoust. Soc. Am. **25**, 60–67 (1953).
[4] J. M. Andres and U. Ingard, ''Acoustic streaming at low Reynolds numbers,'' J. Acoust. Soc. Am. **25**, 932–938 (1953).
[5] J. M. Andres and U. Ingard, ''Acoustic streaming at high Reynolds numbers,'' J. Acoust. Soc. Am. **25**, 928–932 (1953).
[6] W. L. Nyborg, ''Acoustic streaming due to attenuated plane waves,'' J. Acoust. Soc. Am. **25**, 68–75 (1953).
[7] W. L. Nyborg, ''Acoustic streaming near a boundary,'' J. Acoust. Soc. Am. **30**, 329–339 (1958).
[8] Q. Qi, ''The effect of compressibility on acoustic streaming near a rigid boundary for a plane traveling wave,'' J. Acoust. Soc. Am. **94**, 1090–1098 (1993).
[9] M. F. Hamilton, Y. A. Ilinskii, and E. A. Zabolotskaya, ''Thermal effects on acoustic streaming in standing waves,'' J. Acoust. Soc. Am. **114**, 3092–3101 (2003).
[10] Q. Qi, R. E. Johnson, and J. G. Harris, ''Boundary layer attenuation and acoustic streaming accompanying plane-wave propagation in a tube,'' J. Acoust. Soc. Am. **97**, 1499–1509 (1995).
[11] P. Vainshtein, ''Rayleigh streaming at large Reynolds number and its effect on shear flow,'' J. Fluid Mech. **285**, 249–264 (1995).
[12] L. Menguy and J. Gilbert, ''Non-linear acoustic streaming accompanying a plane stationary wave in a guide,'' Acustica **86**, 249–259 (2000).
[13] M. F. Hamilton, Y. A. Ilinskii, and E. A. Zabolotskaya, ''Acoustic streaming generated by standing waves in two-dimensional channels of arbitrary width,'' J. Acoust. Soc. Am. **113**, 153–160 (2003).
[14] M. Kawahashi and M. Arakawa, ''Nonlinear phenomena induced by finite-amplitude oscillation of air column in closed duct,'' JSME Int. J. **39**, 280–286 (1996).
[15] A. Gopinath and A. F. Mills, ''Convective heat transfer due to acoustic streaming across the ends of a Kundt tube,'' J. Heat Transfer **116**, 47–53 (1994).
[16] T. Yano, ''Turbulent acoustic streaming excited by resonant gas oscillation with periodic shock waves in a closed tube,'' J. Acoust. Soc. Am. **106**, L7–L12 (1999).
[17] A. Alexeev and C. Gutfinger, ''Resonance gas oscillations in closed tubes: Numerical study and experiments,'' Phys. Fluids **15**, 3397–3408 (2003).
[18] W. M. Kays and M. E. Crawford, *Convective Heat and Mass Transfer*, 3rd ed. (McGraw-Hill, New York, 1993).
[19] E. S. Oran and J. P. Boris, *Numerical Simulation of Reactive Flow*, 2nd ed. (Cambridge University Press, Cambridge, 2000).
[20] B. Farouk, E. S. Oran, and T. Fusegi, ''Numerical study of thermoacoustic waves in an enclosure,'' Phys. Fluids **12**, 1052–1061 (2000).
[21] M. K. Aktas and B. Farouk, ''Numerical simulation of developing natural convection in an enclosure due to rapid heating,'' Int. J. Heat Mass Transfer **46**, 2253–2261 (2003).
[22] J. P. Boris, A. M. Landsberg, E. S. Oran, and J. H. Gardner, ''LCPFCT—A flux-corrected transport algorithm for solving generalized continuity equations,'' Report No. NRL/MR/6410-93-7192, 1993.
[23] T. J. Poinsot and S. K. Lele, ''Boundary conditions for direct simulations of compressible viscous flows,'' J. Comput. Phys. **101**, 104–129 (1992).
[24] W. Chester, ''Resonant oscillations in closed tubes,'' J. Fluid Mech. **18**, 44–64 (1964).
[25] M. A. Ilgamov, R. G. Zaripov, R. G. Galiullin, and V. B. Repin, ''Nonlinear oscillations of a gas in a tube,'' Appl. Mech. Rev. **49**, 137–154 (1996).
[26] R. A. Saenger and G. E. Hudson, ''Periodic shock waves in resonating gas column,'' J. Acoust. Soc. Am. **32**, 961–971 (1960).
[27] D. B. Cruikshank, ''Experimental investigation of finite-amplitude acoustic oscillations in closed tubes,'' J. Acoust. Soc. Am. **52**, 1024–1034 (1972).
[28] S. Temkin, ''Nonlinear gas oscillations in a resonance tube,'' Phys. Fluids **11**, 960–963 (1968).
[29] A. Goldshtein, P. Vainshtein, M. Fichman, and C. Gutfinger, ''Resonance gas oscillations in closed tubes,'' J. Fluid Mech. **322**, 147–163 (1996).
[30] P. Merkli and H. Thomann, ''Transition to turbulence in oscillating pipe flow,'' J. Fluid Mech. **68**, 567–575 (1975).

Using light scattering to measure the response of individual ultrasound contrast microbubbles subjected to pulsed ultrasound *in vitro*

Jingfeng Guan and Thomas J. Matula[a)]
Applied Physics Lab, University of Washington, 1013 NE 40th Street, Seattle, Washington 98115

(Received 19 February 2004; revised 6 July 2004; accepted 26 July 2004)

Light scattering was used to measure the radial pulsations of individual ultrasound contrast microbubbles subjected to pulsed ultrasound. Highly diluted Optison® or Sonazoid® microbubbles were injected into either a water bath or an aqueous solution containing small quantities of xanthan gum. Individual microbubbles were insonified by ultrasound pulses from either a commercial diagnostic ultrasound machine or a single element transducer. The instantaneous response curves of the microbubbles were measured. Linear and nonlinear microbubble oscillations were observed. Good agreement was obtained by fitting a bubble dynamics model to the data. The pulse-to-pulse evolution of individual microbubbles was investigated, the results of which suggest that the shell can be semipermeable, and possibly weaken with subsequent pulses. There is a high potential that light scattering can be used to optimize diagnostic ultrasound techniques, understand microbubble evolution, and obtain specific information about shell parameters. © *2004 Acoustical Society of America.* [DOI: 10.1121/1.1795334]

PACS numbers: 43.25.Yw, 43.35.Wa [AJS] Pages: 2832–2842

I. INTRODUCTION

Gas-filled microbubbles with an encapsulating shell, called ultrasound contrast agents (UCAs), are used regularly in diagnostic ultrasound, and are becoming important in therapeutic ultrasound applications. However, there is a need to better understand the physical interaction of ultrasound with UCAs so that diagnostic and therapeutic techniques are successful. Toward this goal researchers have used (acoustic) scattering, attenuation, noise emission, and optical microscopy to study ultrasound/bubble interaction. In this paper we show how light scattering can be used to measure the pulsations of an individual UCA (throughout this paper, we refer to ultrasound contrast agents by their acronym, or by the common terms ''microbubble'' and ''encapsulated microbubble'').

A basic characterization of UCAs typically involves attenuation (scattering and absorption) measurements.[1–5] These measurements provide information about the resonance frequency of the bubbles, and their damping. Some information about bubble populations[6] can also be inferred. However, there is no correlation between attenuation and UCA performance or functionality.

Broadband noise has also been used to obtain information about UCAs and their effect on the environment. Chen *et al.*[7] found that cavitation dose (a measure of initial cavitation activity) correlated very well with hemolysis (the destruction of red blood cells and associated release of hemoglobin) *in vitro*, suggesting that hemolysis can potentially be used as a measure of cavitational activity. Chen *et al.*[8] also compared the inertial cavitation thresholds of various UCAs by examining noise spectra, although thresholds obtained in this way only describe relatively violent collapses, and not less-violent microbubble fragmentation mechanisms. Porter *et al.*[9] showed how cavitational activity depended on pulse parameters *in vivo*, suggesting that optimal imaging is obtained when cavitation is reduced. As with attenuation measurements, noise emissions do not necessarily correlate with UCA performance or functionality.

A more direct approach to UCA performance characterization involves backscattering, especially since diagnostic ultrasound is based on backscattered signals. A variety of detection modalities have been used, including subharmonic,[10,11] second-harmonic,[12,13] and super-harmonic[14,15] detection. In addition, various pulse schemes have increased the signal-to-noise ratio (SNR) of the system.[16] Such modalities, however, are limited because of a fundamental lack of understanding in the physics of ultrasound/microbubble interaction. For example, backscattering signatures are often machine dependent, or concentration dependent.[17]

Recently, fundamental information about the interaction of ultrasound with UCAs has been obtained by using high-speed cameras. Single UCAs were insonified with pulses from a single element transducer, and imaged with the camera, providing direct information about their response.[18–20] Although the image quality is high, and important information about bubble response and bubble destruction is obtained, high-speed cameras are expensive, and the amount of data obtained is small. Usually only one, or at most a few acoustic cycles of data can be collected, often splicing together data from multiple experiments.

In this article we show that light scattering has the potential of obtaining significant information about the fundamental interaction of ultrasound with UCAs. Light scattering has previously been used to size air bubbles[21,22] and to measure unshelled bubble oscillations.[23–25] For our application, it offers several advantages (and some disadvantages) over im-

a)Electronic mail: matula@apl.washington.edu

aging and acoustic techniques. Compared to high-speed optical imaging, the major advantage is in data collection.

Light scattering signals can be collected in real time, over tens, hundreds, and even thousands of acoustic pulses, allowing us to monitor the evolution of UCAs with successive acoustic pulses. It is also inexpensive, and can be incorporated easily into an experimental setup. The major disadvantage to high-speed imaging is that light scattering cannot give direct *visual* information regarding UCA dynamics and destruction.

The major advantage over acoustic scattering is in monitoring the instantaneous motion of a microbubble. The disadvantage is a low signal/noise compared to the highly echogenic bubble.

We begin with a description of light scattering from coated bubbles, where we show that for thin coatings, the scattered light intensity is minimally affected. We then explore a contrast agent parameter space using a published bubble dynamics model that incorporates shell parameters, in order to show that unique solutions can be obtained for fitting to the data. It is not our intent in this paper to determine whether or not the model is the *correct* model, or the *only* model that can, or should be used. Rather, by fitting the model to the data, we show that light scattering can be used to obtain information from encapsulated microbubbles, with a potential for understanding microbubble evolution, optimizing bubble-specific diagnostic ultrasound modalities, and obtaining shell parameters. Experimental details for collecting light scattering data from individual UCAs are then described, and several results for Optison® and Sonozoid® microbubbles are shown.

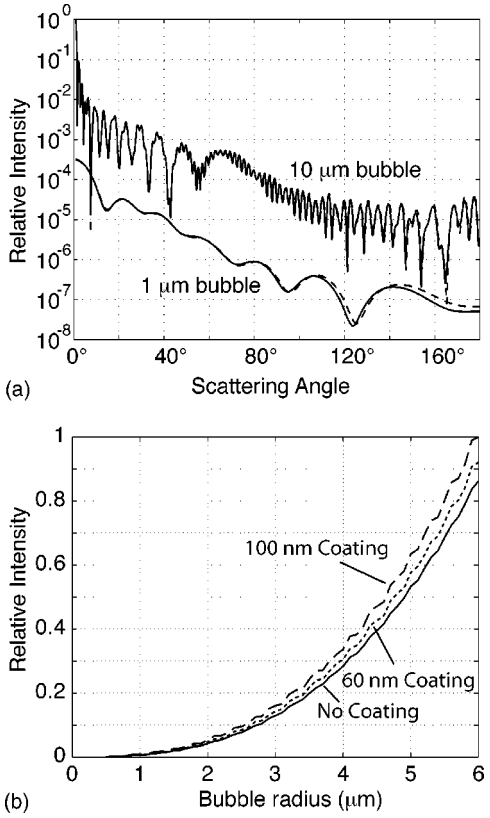

FIG. 1. Light scattering calculations for the electric field polarized perpendicular to the scattering plane. (a) Relative scattered light intensity as a function of scattering angle for a shelled (dashed line) and unshelled (solid line) gas bubble. The shell thickness $\epsilon=15$ nm and index of refraction $n=1.5$. (b) The relative scattering intensity as a function of bubble radius at 80° with a ±10° aperture. For $\epsilon<30$ nm, there is little difference between the shelled and unshelled case.

II. THEORY

A. Light scattering

We begin with a brief discussion on the Mie theory of light scattering from homogeneous spheres (bubbles in our case) in a homogeneous environment. Because the mathematics is cumbersome, it is not described here. Interested readers can refer to the references for details.[26,27] Modifications of Mie scattering for a coated sphere (such as contrast agents) were developed by Aden and Kerker[28] and applied to coated bubbles by Marston.[29,30] Our implementation of the model for a coated sphere is based on the mathematics in the book by Bohren and Huffman.[27]

In essence, the intensity of scattered light depends strongly on the observation angle. Marston[31,32] recommended that for an air bubble in water, the observation angle be near the critical angle $\theta_c \approx 82.8°$ from forward scattering.[23] The recommendation was based on a physical-optics approximation, which suggested that the scattered light intensity would be a monotonic function of bubble size, with a nearly R^2 dependence.[33] The approximation apparently breaks down near a minimum size parameter of $ka=25$.[21] In our experiments, $ka \approx 10$, where k is the optical wave number and a is the bubble radius; nevertheless, we also choose the scattering region near the critical angle. This scattering region is *a posteriori* justified by the calculations below. It will be shown that the scattered light intensity remains a monotonic function of bubble size, even for UCAs. However, the R^2 dependence does not hold for these small bubbles, so the full Mie scattering algorithm is used.

The critical angle apparently is also a function of the optical properties of the shell and its thickness. Marston showed that for thin bubble coatings, the net effect of the coating is to shift the course structure of the interference fringes.[29,30] In particular, the coating shifts the critical angle by an approximate amount $\Delta = 2h/a[(n_w^2-1)^{-1/2}-(n_s^2-1)^{-1/2}]$ (in radians), where the coating thickness-to-radius ratio is h/a, and n_s and $n_w=1.33$ are the indices of refraction for the shell and water, respectively.

By calculating the shift in the critical angle, we can estimate the sensitivity to scattering angle: The refractive indices of lipids and albumin are $n_s=1.48$[34] and $n_s=1.50$,[35] respectively. For a shell thickness of 10 nm (presumably about the thickness of Optison®), and for a 1 μm radius bubble, the shift in the critical angle is quite small, approximately 0.25°. Therefore, because of the relative insensitivity of the coating on the critical angle (and presumably also on the course structure of the interference fringes), one can argue that including a coating in the calculations is not necessary. One can also argue that because $\lambda(=633\,\text{nm}) \gg h$, thin shells should not have a particularly strong effect on the scattered intensity. As an example, Fig. 1(a) shows the relative scattered intensity as a function of scattering angle for two dif-

ferent sized bubbles, with, or without a 15 nm albumin coating. Near the critical angle it is difficult to distinguish between the coated and uncoated bubble, as expected (all calculations in this paper were performed using MATLAB software).

The more important calculation is to fix the angle and calculate the relative intensity as a function of bubble size, a natural experimental configuration. However, one must also take into account that the detector collects light from a finite angular distribution, not just at a single angle. Our experimental procedure in particular, makes use of a collecting lens to increase the light intensity onto the detector (and also helps smooth out the fine structure in the scattered intensity). This angular span ranges from approximately 70° to 90°. In Fig. 1(b) we show the relative integrated intensity over this span, as a function of bubble size. There is little to no deviation from the uncoated bubble for coating thicknesses of less than 30 nm. Therefore, we can neglect the coating to simplify the calculations. Also, as expected, there is a monotonic relationship between bubble size and scattered light intensity, *a posteriori* justification for scattering near the critical angle. Because of this relationship, it is straightforward to convert the light scattered intensity into a radius.

One final note: Our experiments utilized a red HeNe laser source ($\lambda = 633$ nm). One might expect that a thin coating might be better resolvable using a shorter wavelength source. Unfortunately, even for wavelengths on the order of 488 nm (blue light), the distinction is too small to observe for the thin coatings we have explored.

B. Bubble dynamics

Dynamic modeling of UCA bubbles is an important aspect to this study. Comparisons with experimental results will be performed, so it is important that we consider bubble dynamics models that incorporate shell properties. There are several approaches for modeling a coated bubble. *Ad hoc* extensions to simple Rayleigh–Plesset models were first introduced by de Jong and Hoff using a linear model.[1,36] Later, Church modeled the shell as a continuous, damped, elastic solid.[37] His results agree with de Jong and Hoff for the scattering and attenuation of Albunex microbubbles. Thin-shell assumptions to this model were incorporated by Hoff *et al.*[38] A newer Newtonian interface model has also recently been published,[39] while even more models are currently under development.

The choice of which bubble dynamics model we use is not based on the relative accuracy of any particular model. We are working with thin-shelled agents, and thus thin-shell approximations are appropriate. However, we wish to verify the ability of this technique to measure encapsulated microbubble dynamics. To do so, we have chosen a simplified model that has previously been used in comparisons with high-speed camera images of encapsulated microbubble dynamics, the Morgan *et al.* model.[40] The major advantage to us is that it has a reduced set of fitting parameters. In the future, a refinement of this technique may be useful in distinguishing the accuracy of various models.

The implementation of Morgan *et al.* is

$$\rho R\ddot{R} + \frac{3}{2}\rho\dot{R}^2 = \left(P_0 + \frac{2\sigma}{R_0} + \frac{2\chi}{R_0}\right)\left(\frac{R_0}{R}\right)^{3\gamma}\left(1 - 3\frac{\dot{R}}{c}\right) - \frac{4\mu\dot{R}}{R} - \frac{2\sigma}{R}\left(1 - \frac{\dot{R}}{c}\right) - \frac{2\chi}{R}\left(\frac{R_0}{R}\right)^2\left(1 - 3\frac{\dot{R}}{c}\right) - 12\epsilon\mu_{\mathrm{sh}}\frac{\dot{R}}{R(R-\epsilon)} - (P_0 + P_{\mathrm{drive}}(t)), \quad (1)$$

where R is radius of the bubble, R_0 is initial radius of the bubble, $P_0 = 1.01 \times 10^5$ Pa is the ambient pressure, $P_{\mathrm{drive}}(t)$ is the acoustic driving pressure, $\rho = 1000$ kg/m^3 is the liquid density, $\gamma \approx 1$ is the ratio of specific heats,[41] $c = 1500$ m/s is the sound speed in the liquid, $\sigma = 0.051$ N/m^2 is the surface tension coefficient, $\chi = 0$ (see below) is the shell elasticity, $\mu = 0.001$ Pa s is fluid shear viscosity, μ_{sh} is the UCA shell shear viscosity, and ϵ is the UCA shell thickness.

Using Eq. (1), we examined the relevant parameter space to determine the relationship between the various parameters. This was done in order to determine if a fit to the data would be unique. For UCAs, this parameter space covers $0.1 \leqslant R_0 \leqslant 6\ \mu$m, $0 \leqslant \epsilon\mu_{\mathrm{sh}} \leqslant 8$ nm Pa s, and $0.0235 \leqslant P_{\mathrm{drive}}(t) \leqslant 1.2$ MPa (peak negative), relevant for thin-shelled agents. Because we are assuming isothermal behavior, the elasticity terms cancel. We have also assumed that $R \gg \epsilon$ (Morgan *et al.* also made this assumption) so that the only term with shell parameters is given by $12\epsilon\mu_{\mathrm{sh}}\dot{R}/R^2$. Hence, when referring to the shell parameter, we refer to the product $\epsilon\mu_{\mathrm{sh}}$. Note that there are initially three unknowns: R_0, $P_{\mathrm{drive}}(t)$, and the product $\epsilon\mu_{\mathrm{sh}}$.

Now let us focus on the driving pressure $P_{\mathrm{drive}}(t)$. Using a calibrated needle hydrophone (NTR, Seattle, WA), we were able to use the measured acoustic driving pressure as an input to the bubble dynamics model, thereby decreasing the unknowns by one. Most of the data described here was obtained from the M mode of a diagnostic ultrasound system (ATL Ultramark 4Plus), and so the parameter space we explored later in Fig. 3 is based on this pressure profile, shown in Fig. 2(a). We will also show preliminary measurements using longer tone bursts from a single element focused ultrasound source. The measured waveform from that source is shown in Fig. 2(b). For brevity, the parameter space for that source is not shown.

We are now set to examine the parameter space for the unknown parameters R_0 and $\epsilon\mu_{\mathrm{sh}}$, using the measured driving pressure (we emphasize that examining this parameter space is necessary in order to ensure that the fits will be unique). Figure 3(a) shows a simulation for microbubbles with a varying shell parameter, for an initial bubble size of $R_0 = 1\ \mu$m radius, and $P_{\mathrm{drive}}(t) = 235$ kPa peak negative pressure. Figure 3(b) shows a waterfall plot of the simulated response curve $R(t)$ for various initial bubble sizes and a fixed shell parameter (same drive amplitude). The resonant bubble size is darkened. Figure 3(c) plots a simulation contour map of $(R_{\max} - R_0)$ vs R_0 and $\epsilon\mu_{\mathrm{sh}}$ (same drive amplitude). Finally, Fig. 3(d) shows the peak in the power spectral density (the main frequency component) of the simulation in (a).

These figures deserve a few comments. First, the reso-

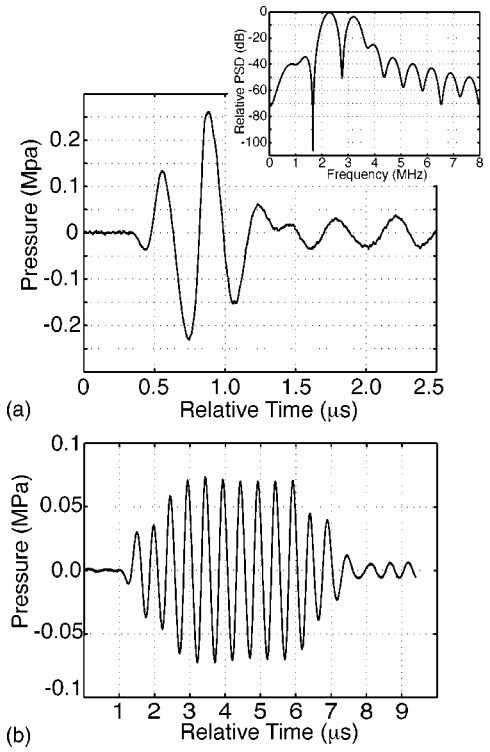

FIG. 2. (a) Measured pulse from an Ultramark 4Plus operated in the M mode. Inset: Power spectral density (PSD). (b) Measured ten-cycle burst from a single element transducer.

nant bubble size can be seen in (b), where the curves appear to bunch together. As expected, the response curve $R(t)$ has significant fluctuations near resonance. In (c), the resonant bubble size is seen to grow with increasing shell parameter, from about 1.3 μm to 2.1 μm. This is also expected behavior, consistent with the (thin) shell behaving as a damping mechanism. That is, an increase in damping results in a decrease in resonant frequency, or, equivalently, an increase in resonant size. Also, (c) shows that near resonance there is a strong dependence on the shell parameter (as one moves from contour to contour). However, for bubbles larger than about 3 μm, the dependence is weak at best (vertical contour lines). Thus, for larger UCAs, this model would not be useful for fitting shell parameters to the data.

Notice also that the maximum amplitudes of the two main peaks in Fig. 3(a) change relative to each other as the shell parameter increases. The first peak, initially smaller than the second peak, becomes the largest peak for $\epsilon\mu_{\mathrm{sh}} > 0.4$ nm Pa s. This is most probably a consequence of the specific pressure pulse used. That is, our pressure pulse has apparently two resonant peaks, near 2.3 and 3.2 MHz [see the inset to Fig. 2(a)]. Because the resonance size depends on the shell parameter, as the shell parameter increases it is possible that first one, and then the other of these resonances are being manifest, resulting in a change in the bubble response.

The power spectral density (PSD) of (a) is shown in (d). The peak in the PSD decreases with increasing shell parameter, but levels off quickly. It would be difficult to distinguish between two bubbles with different shell parameters for $\epsilon\mu_{\mathrm{sh}} > 3$ nm Pa s using only the PSD; however, the PSD might be used to determine when the shell breaks.

The PSD is the frequency response of the system driven by the measured pressure pulse, and thus includes the spectral characteristics of the driving pulse. It is nevertheless instructive to compare it to the bubble's resonance frequency, obtained from linearizing the equation of motion, setting $R \rightarrow R_0(1+\epsilon)$, expanding relevant terms in a binomial expansion, and neglecting second-order and higher terms. We then arrive at the frequency of oscillation,

$$f_r = \frac{1}{2\pi}\sqrt{\frac{3\gamma}{\rho R_0^2}\left(P_0 + \frac{2\sigma}{R_0} + \frac{2\chi}{R_0}\right) - \frac{2\sigma + 6\chi}{\rho R_0^3} - \frac{(4\mu + 12\epsilon\mu_{\mathrm{sh}}/R_0)^2}{\rho^2 R_0^4}}. \tag{2}$$

Using the parameters above ($R_0 = 1$ μm, $\gamma = 1$), and considering the undamped case ($\epsilon\mu_{\mathrm{sh}} = \mu = 0$), the linear resonance frequency is $f_r \approx 3.5$ MHz.

The frequency of oscillation, Eq. (2), does not follow the PSD curve (because the PSD includes the driving pulse spectral characteristics). Instead, it drops quickly to zero near $\epsilon\mu_{\mathrm{sh}} = 1.6$ nm Pa s (for a 1 μm bubble). Apparently, this implies that smaller bubbles are overdamped and do not resonate.[42]

Until now, the discussion has been limited to resonances and the relationship with a particular pressure pulse. However, the most important reason for mapping the parameter space is to determine if a solution is unique, because as mentioned above, there are two unknown parameters to be fitted, namely R_0 and $\epsilon\mu_{\mathrm{sh}}$. To help answer this question, we focus on Fig. 3(c), the contours of $(R_{\max} - R_0)$ vs R_0 and $\epsilon\mu_{\mathrm{sh}}$. Keep in mind that we have measured the pressure amplitude, which constrains us in the amplitude of $R(t)$.

If $R_0 > 3$ μm, the quantity $(R_{\max} - R_0)$ is not as sensitive to the shell parameter, making unique fits difficult. Fortunately, with UCAs, the majority of bubbles are in the size range from about $R_0 = 1 - 2.5$ μm. In this range, the contours show sensitive dependences. Consider the darkened contour line. If we initially set $\epsilon\mu_{\mathrm{sh}} = 2$ nm Pa s, there will be two possible solutions for R_0 that would give us the same $(R_{\max} - R_0)$ value, near 1 and 2.4 μm. However, $R_{\max}$ by itself is different for these two values. For example, if we chose $R_0 = 1$ μm, then $R_{\max} = 1.6$ μm, and if $R_0 \approx 2.4$ μm, then $R_{\max} \approx 3.0$ μm. Our data would constrain us to only one of these values. In Sec. IV, we will discuss the sensitivity of these parameters.

In conclusion, although we have a two-parameter fit, the

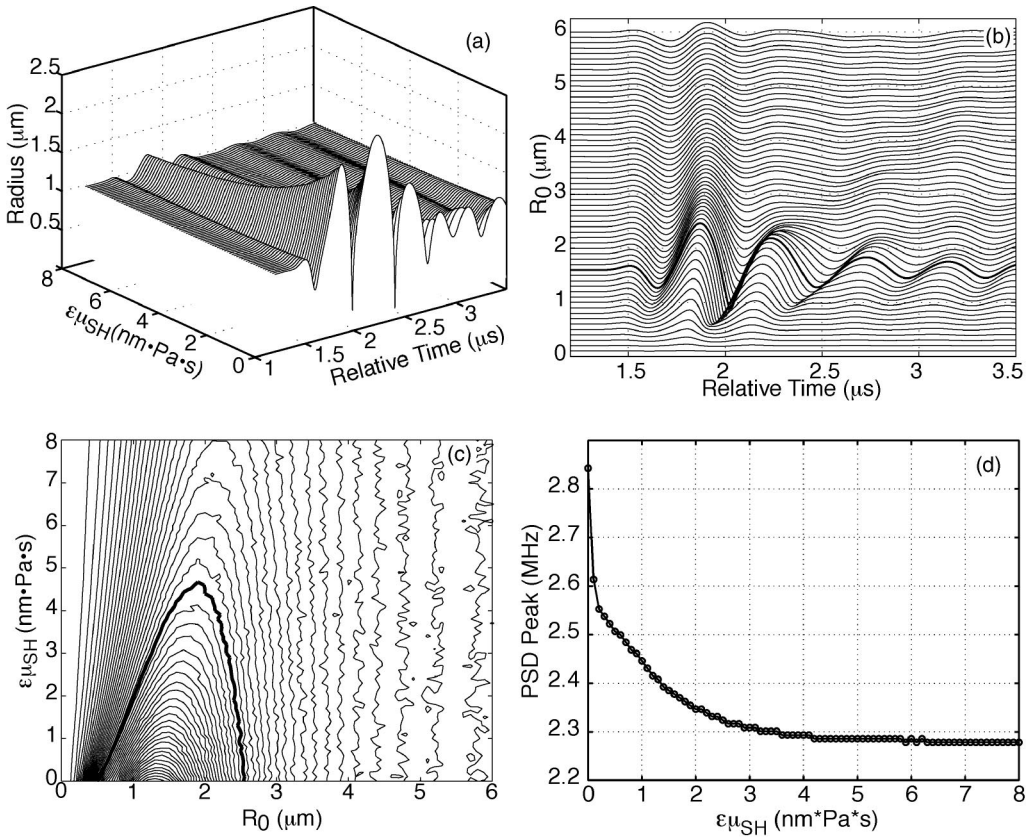

FIG. 3. Parameter space simulations based on the Ultramark 4Plus pulse [from Fig. 2(a)]. (a) $R(t)$ curves as a function of shell parameter $\epsilon\mu_{sh}$ [$R_0 = 1\ \mu$m, $P_{drive}(t) = 235$ kPa, peak negative]. The particular form of this plot depends strongly on R_0. (b) $R(t)$ plot versus R_0 for $\epsilon\mu_{sh} = 2$ nm Pa s. The resonant radius is darkened. (c) Contour plot of $(R_{max} - R_0)$. Contour values begin at the leftmost side at 0.028 μm, and progress in 0.026 μm increments up to 1.313 μm. For larger bubbles, $(R_{max} - R_0)$ is not affected by the shell parameter. The resonant radius increases with shell parameter. A particular contour is darkened to facilitate discussion in the text. (d) A plot of the main peak in the power spectral density of (a). There is only a small change in the shell parameter for $\epsilon\mu_{sh} > 3$.

data constrains our solutions. In this model, the shell parameter is not important for larger bubbles, but for microbubbles of interest, it is a sensitive parameter; thus, unique fitting to the data should be possible.

III. EXPERIMENTAL SETUP

The experiment is performed by (1) the injection of individual microbubbles into the region of interest, (2) insonifying the microbubble with ultrasound, and (3) scattering light off the microbubble. This arrangement is shown in Fig. 4(a).

The region of interest is the small volume of liquid where the ultrasound and laser illumination intersect with microbubble location. For most studies, the liquid was filtered ($<0.2\ \mu$m) deionized ($>18\ M\Omega$) water. The gas concentration was not measured; however, based on previous similar studies it was approximately 90%–95% saturated.

A. UCA injection

Two methods were used to inject UCAs into the region of interest. Most often, a highly diluted UCA solution (calculated to be on the order of 10^5/ml) was injected into a rectangular water tank (3.5 cm^2 cross section, filled to 4 cm height) by a syringe pump (rate=10 ml/h) with a 0.5 mm inner-diameter tube. The ejection of the microbubble was approximately one-half cm from the laser beam path. Based on the numbers given above, one would anticipate that subsequent bubbles would generate a scattering ''event'' every 3 ms. However, the actual number of events was much smaller (approximately one event over several seconds). The most probable reasons for this are due to UCA congregation within the syringe, and at curves in the tubing, especially where the tubing goes up and over a lip, as is the case in our setup. Also, bubbles ejected from the tip may move away from the laser beam, and not into it.

To verify that the measured response curves were for single microbubbles, we sometimes injected the UCAs manually into the water-filled vessel that contained a small amount of a water soluble gum, xanthan gum. The xanthan gum increased the viscosity of the liquid slightly, so that after injection the microbubble came to rest and remained relatively stationary. We could then image the microbubble with a back-lit LED, microscope, and CCD camera to verify that it was indeed a single bubble. The vessel would then be moved into position so that the bubble was at the center of the laser beam/ultrasound probe focus. We will show below that there was no major difference in measurements between experiments conducted in water or xanthan gum mixtures, except that the added xanthan gum yielded higher noise levels.

The gel preparation is based on that used by McCormick

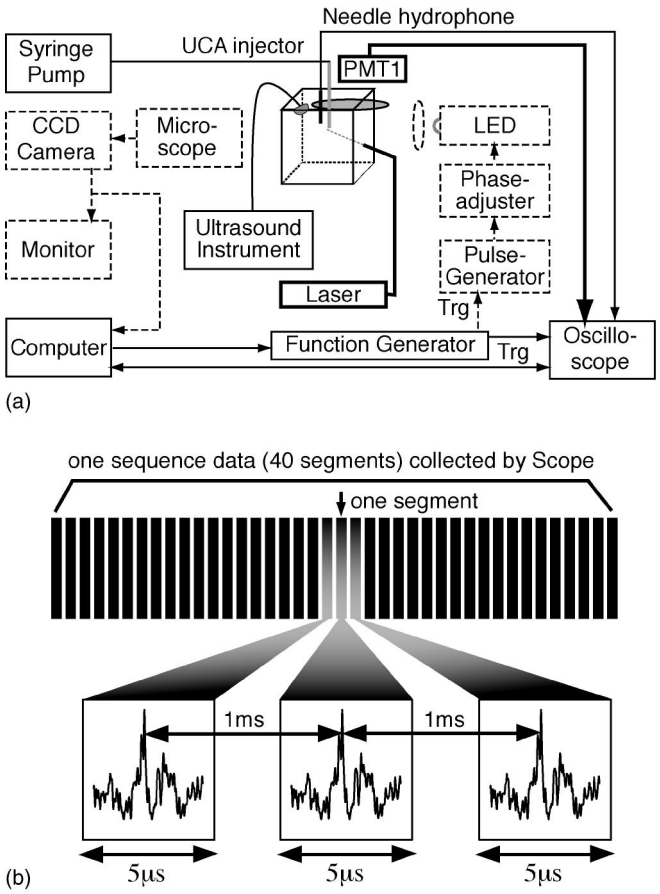

FIG. 4. (a) Experimental setup. The items with dashed lines represent the imaging system; the items with dark lines represent the light-scattering system (E-field polarized perpendicular to the scattering plane). The UCAs can be injected with a syringe pump, or manually. The Ultramark4 Plus probe is inserted from the top; the single element transducer is inserted through the bottom (not shown). (b) Data is collected from the scope using sequence acquisition, whereby 5 μs intervals are collected during each pulse, but not during the $\approx$1 ms quiescent period between pulses.

for his Masters project,[43] with some modifications. The recipe used in this research consists of 2.6 grams BT food grade Xanthan Gum powder (from CP Kelco), 12 g glycol (from Aldrich), and 600 g water. The water is initially slightly degassed. The powder and glycol are mixed and poured into a beaker. The water is then poured into the beaker very slowly over a stick to minimize the trapping of bubbles. The mixture is stirred slowly for up to an hour using a magnetic stir bar to make it homogeneous. The gel is finally poured slowly into the experiment vessel. Because of the possible contamination and bacterial growth, a new gel is made prior to each experiment. Parenthetically, in other research, we sometimes use a more viscous gel preparation. Removing trapped bubbles becomes much more difficult, and requires centrifuging the solution for up to 3 h.

One final note about xanthan gum gel: It is a non-Newtonian fluid, and thus there is some uncertainty as to its effect on microbubble pulsation. Because of the ubiquitous use of xanthan gum in the food industry, there is a high quantity of data regarding its properties. The properties, however, are measured at low frequencies ($<$10 kHz). At low concentrations and at high frequencies (in the MHz range), the properties may be similar to water.[44]

B. Laser system

Some details in the laser system in Fig. 4(a) were not shown in order to keep the figure from being cluttered. In particular, we used a 30 mW HeNe laser (Melles Griot) to illuminate the microbubbles. With a lens, the beam waist at the microbubble location was focused to less than 100 μm (some scattering occurs through the plastic water tank and through the water, so that it is impossible to accurately measure the beam waist). The light scattered off the bubble was then focused with a 5 cm lens onto a photomultiplier tube (PMT) detector (Hamamatsu, model 2027). The main purpose for the collecting lens was to increase the signal/noise (covering the angles 70°–90°). The PMT was biased at $-$1000 V. A HeNe line filter was placed against the PMT cathode window to block other sources of light. The output of the PMT was sent directly to a high-speed digital oscilloscope (LeCroy), and then to a PC for post-processing.

Data collection was performed in sequence mode, where high-resolution data files can be collected each and every pulse. The total data collected is limited by the available memory in the oscilloscope. For these experiments we collected data sequence records of 40 consecutive acoustic pulses before transferring the file to a PC [diagrammed in Fig. 4(b)]. Each segment consisted of a 5 μs long window with a resolution of 4 ns. The segments were separated by about 1 ms (triggered by the source transducer). Appropriate delays in triggering were used to ensure that the bubble response was centered in the segment window.

C. Ultrasound probes

Two transducers were used as sources in this research. The first was a diagnostic ultrasound instrument (Ultramark 4Plus) operated in the M mode at about 1 kHz PRF. A NTR calibrated needle hydrophone monitored the acoustic pressure. Figure 2(a) shows an example of the pulse from the Ultramark 4Plus. The response of microbubbles to this pulse is described in the theory section.

In actual experiments, the hydrophone was placed at an angle relative to the pulse. Thus, we had to measure the relative angle between the transducer and hydrophone, and then set up a separate water tank to determine the hydrophone response as a function of angle to the ultrasound probe. This multiplicative factor was then used in all subsequent data analyses.

In experiments using the single element transducer (Ultran Labs, Boalsburg, PA), the transducer was inserted through the bottom of the vessel, and the hydrophone was positioned directly above it, so that the angle problem described above was not an issue (the diagram for this setup is not illustrated). For this configuration, relevant transducer parameters are center frequency $f=1.8$ MHz, focal length$=$63 mm, $-$6 dB bandwidth$=$500 kHz, 2.5 cm active area, 10 cycle bursts, 10 kHz pulse repetition frequency (PRF).

IV. RESULTS AND DISCUSSION

In the following figures, we show data and model fits for Optison® and Sonazoid®, in water and diluted aqueous xan-

than gum gel. There are two important points to note. First, the light scattering model and data both produce an intensity versus time $I(t)$ that must be converted into a radius versus time $R(t)$. For the experimental data, the scattered intensity is found by subtracting the background intensity from the total intensity. The model generates a relative value, so a multiplicative scaling factor must be found to match the model to the data. Once the scaling factor is found, it is unchanged for all subsequent experiments. We can then use Fig. 1(b) to convert the relative intensity to a radius.

The second point to note is that we had to perform best-fit studies in order to constrain the two unknowns (R_0 and $\epsilon\mu_{\mathrm{sh}}$). As described in Sec. II, our search was facilitated by knowing what range of values are expected for R_0 and $\epsilon\mu_{\mathrm{sh}}$. Within this range, we found that a deviation of $\pm 5\%$ in R_0 would generate good fits. In addition, we found that the shell parameter values published in the literature would give good fits.[40] Therefore, for these studies we set the initial shell parameter for Optison® to $\epsilon\mu_{\mathrm{sh}} = 6.0\,\mathrm{nm\,Pa\,s}$, and for Sonazoid® $\epsilon\mu_{\mathrm{sh}} = 2.0\,\mathrm{nm\,Pa\,s}$. Deviations of up to about ± 1 nm Pa s would also generate good fits.

A. Response curves from relatively stable bubbles

We often found that UCA oscillations from pulse to pulse were relatively regular, so we grouped (averaged) several pulses together to improve our SNR. In the next series of figures, we examine individual groups, and call the bubbles ''relatively'' stable, realizing that small changes can be occurring within a group.

1. Ultramark 4Plus

A response curve from an Optison® UCA to the Ultramark 4Plus pulse is shown in Fig. 5(a). Ten consecutive pulses (segments) were averaged together to increase the signal/noise ratio. The measured peak negative pressure and fitted initial bubble radius are 210 kPa and 1.47 μm, respectively. For these parameters, the data and simulations exhibit quasilinear motion. For this, and other data, very good agreement with the major oscillations is obtained. The smaller ring-down oscillations are more difficult to fit because of the lower signal strength.

Although the model we have employed is not the most accurate model to use for encapsulated microbubbles, the overall good fit to the data suggests that we are indeed measuring the pulsations of individual encapsulated microbubbles. Nevertheless, we felt that these (and our other) data did not necessarily prove that light scattering was being performed on *single* bubbles, and/or that the bubbles were *shelled*. Therefore, we repeated the experiments in the diluted aqueous gel mixture. As described above, the diluted gel mixture allowed us to manually inject UCA bubbles into the region of interest. We could then examine the UCAs under a microscope to ensure that the agents were individual microbubbles (although the resolution was not high enough to make size measurements). The UCAs would not move out of the region of interest over several minutes, a demonstration that the bubbles were shelled and stable. As can be seen in Fig. 5(b), apparently the diluted gel did not affect the dynamics adversely, for the fit is remarkably good (we assumed parameters for water). The measured peak negative pressure and fitted initial bubble radius R_0 are 340 kPa and 1.5 μm, respectively. As with the previous data, these bubbles also exhibit nearly linear oscillations. In the next series of data, and later, we will show cases of nonlinear behavior.

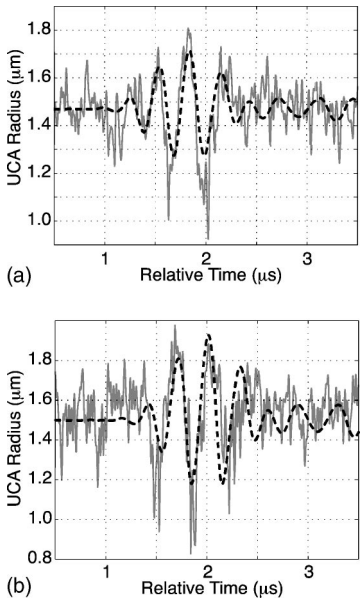

FIG. 5. Optison® response to a diagnostic ultrasound pulse in (a) water and (b) diluted aqueous (xanthan gum) gel. Ten consecutive pulses were averaged together to generate the figure. The experimental results are solid lines, and the simulated results are dashed lines. Relevant parameters are given in the text and Table I.

2. Single element transducer

Sample response curves from the single element transducer are shown in Figs. 6 and 7. These experiments were performed both in water and aqueous xanthan gum gel mixtures. In Fig. 6, (Optison®) we averaged 37 and 40 pulses, respectively; in Fig. 7 (Sonazoid®) there are 5 and 40 pulses averaged, respectively. The measured peak negative pressures and fitted ambient bubble sizes are summarized in Table I. The relative poor signal/noise in Fig. 6(a) may be due to the bubble not being in the center of the laser beam. Nonlinear bubble oscillations were especially present in Figs. 6(b) and 7(b), presumably due to the increased pressure amplitudes.

Although these longer tone bursts are not very relevant to imaging applications (which utilize short diagnostic pulses), variable pulse lengths can be used to explore issues such as shell fatigue and microbubble stability.

The fitted ambient sizes (from Table I) are consistent with known UCA bubble sizes. From Figs. 5–7, we can conclude that the good fit of the model to the experimental data, both in water and diluted gel, is evidence that light scattering can be highly successful at measuring individual UCA dynamics. Apparently, these results are the first that show how UCAs respond from actual diagnostic ultrasound pulses. We believe that this technique may also be very useful with UCA

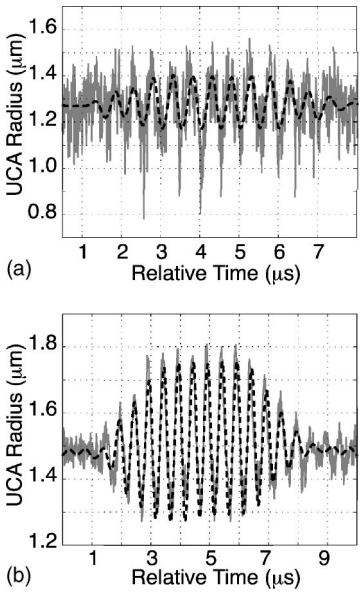

FIG. 6. The response of an Optison® bubble subjected to a ten-cycle tone burst from a single element transducer in (a) water and (b) diluted aqueous (xanthan gum) gel. The experimental results are solid lines, and the simulated results are dashed lines. Relevant parameters are given in the text and Table I.

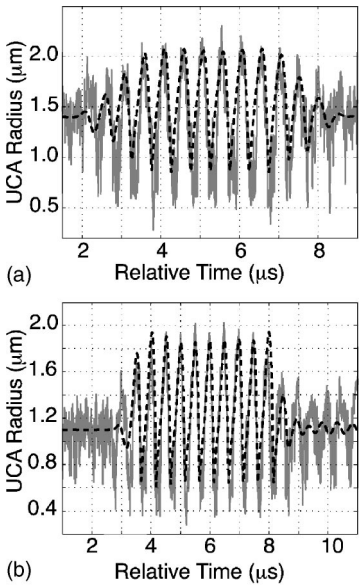

FIG. 7. The response of a Sonazoid® bubble subjected to a ten-cycle tone burst from a single element transducer in (a) water and (b) diluted aqueous (xanthan gum) gel. The experimental results are solid lines, and the simulated results are dashed lines. Relevant parameters are given in the text and Table I.

clusters, not just individual bubbles. We will describe such measurements in a future publication.

B. Response curves from evolving bubbles

One of the strengths of light scattering is in its ability to make high temporal resolution measurements over long time scales. In this section we describe observations that show the evolution of UCA microbubbles subjected to consecutive pulses from the Ultramark 4Plus. For slowly evolving microbubbles, we combined the data in groups of ten (as we did in averaging). For quickly evolving microbubbles, we examined the data from each individual pulse.

When fitting these data to the model, there is always the question of which parameter to change in order to obtain a good fit. We have a choice between the two unknowns: R_0, and the product $\epsilon\mu_{\mathrm{sh}}$. Because the shell may be compromised (e.g., from dislodging, or crumpling, or via changes in permeability) we must be able to vary the shell parameter.

1. Slowly evolving agents

To follow the slow evolution of UCAs, our pressure amplitude was approximately 130 kPa. This pressure amplitude is lower than the fragmentation thresholds found in the literature.[8,45] Those studies, however, were looking at relatively fast destruction mechanisms, not slow decay mechanisms. A more relevant comparison may be with the experiment from Moran *et al.*,[46] which shows the slow decay of backscatter signals for UCAs subjected to clinical ultrasound.

Figure 8 shows an example of the slow evolution of a Sonazoid microbubble in water, collected in three successive groups of ten pulses. What is interesting about this figure is that a good fit was obtained without having to change the shell parameter; it was kept constant at 2.0 nm Pa s. However, we did have to increase R_0 between groups (from 1.2 to 1.9 μm; see Table II). That is, the Sonazoid microbubble appears to be growing with successive pulses. We did not observe this slow growth phenomenon with Optison.

Two physical interpretations can be made: The lipid shell may have been partially compromised before the experiment began. Although possible, we have often observed this trend in other data. Alternatively, during expansion or compression, the lipid shell may become semipermeable. If we assume that the bubble is filled initially with perfluorobu-

TABLE I. Response curve parameters. P^-_{peak} is the measured peak negative pressure, $\epsilon\mu_{\mathrm{sh}}$ is the assumed shell parameter, R_0 is the fitted ambient radius, and R_{max} is the resultant maximum radius.

Figure	Agent	$\epsilon\mu_{\mathrm{sh}}$ (nm Pa s)	Media	Source	P^-_{peak} (kPa)	R_0 (μm)	R_{max} (μm)	R_{max}/R_0
Fig. 5(a)	Optison®	6	Water	UM4+[a]	210	1.47	1.71	1.2
Fig. 5(b)	Optison®	6	Gel	UM4+[a]	340	1.50	1.93	1.3
Fig. 6(a)	Optison®	6	Water	SET[b]	70	1.27	1.4	1.1
Fig. 6(b)	Optison®	6	Gel	SET[b]	100	1.48	1.8	1.2
Fig. 7(a)	Sonazoid®	2	Water	SET[b]	130	1.4	2.1	1.5
Fig. 7(b)	Sonazoid®	2	Gel	SET[b]	190	1.1	2.0	1.8

[a]Ultramark 4Plus.
[b]Single element transducer.

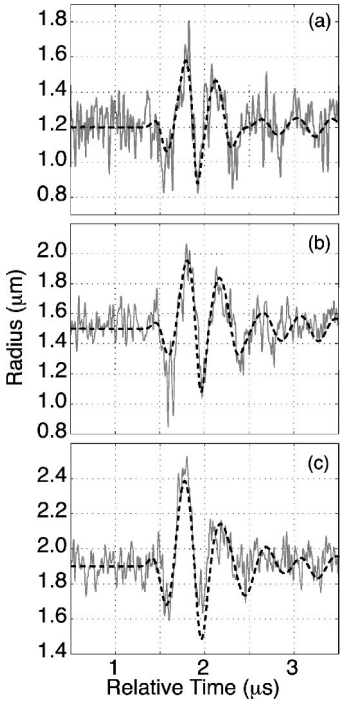

FIG. 8. The evolution of a Sonazoid® microbubble in water. For each subplot, the shell parameter was kept constant at $\epsilon\mu_{sh}=2.0$ nm Pa s. (a) Average of consecutive pulses 1–10. (b) Average of consecutive pulses 11–20. (c) Average of consecutive pulses 21–30. Good fits were obtained provided that R_0 was increased from 1.2→1.5→1.9 μm, respectively. The spectra of these curves are shown in Fig. 11.

tane (PFB) and the water contains air; then because of the higher diffusivity of air, diffusion of air into the bubble will occur at a faster rate than diffusion of PFB out of the bubble. Thus, at least initially, the bubble can grow. Again, we emphasize that these three plots are successive segments in one sequence of data. At about 1 ms between segments (equal to the burst PRF), the total experiment time is about 30 ms. A summary of the parameters for this figure is given in Table II.

These results are different than the experimental results of Chomas *et al.*, in which their well-performed optical experiments showed that the bubble dissolves after each pulse, a trend they termed ''acoustically-driven diffusion.[47]'' However, it should be noted that their experiment used about twice the pressure amplitude. We speculate that at those higher pressures, gas may be forced through the shell during compression.

2. Quickly evolving agents

For this study, we increased the pressure amplitude to 340 kPa for Optison® and 390 kPa for Sonazoid®. Moran

TABLE II. Response curve parameters for evolving Sonazoid® microbubble in water. $\epsilon\mu_{sh}$ is the assumed shell parameter, P^-_{peak} is the measured peak negative pressure, R_0 is the fitted ambient radius, and R_{max} is the resultant maximum radius.

Figure	$\epsilon\mu_{sh}$ (nm Pa s)	P^-_{peak} (kPa)	R_0 (μm)	R_{max} (μm)	R_{max}/R_0
Fig. 8(a)	2	130	1.20	1.58	1.32
Fig. 8(b)	2	130	1.50	1.96	1.31
Fig. 8(c)	2	130	1.90	2.39	1.26

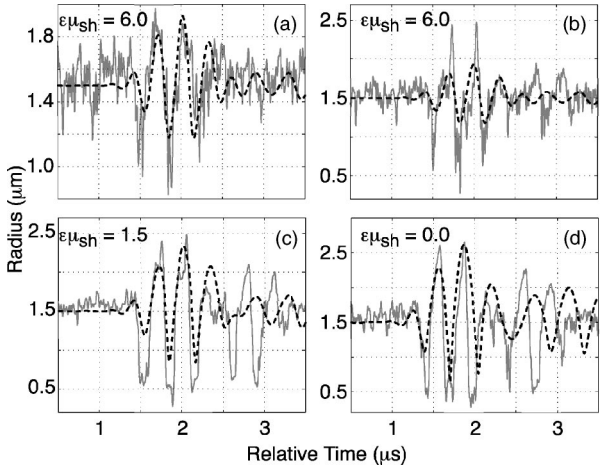

FIG. 9. The evolution of an Optison bubble manually injected into a diluted aqueous xanthan gum mixture. Plots (a)–(d) correspond to a bubble's response to pulses 1, 2, 3, and 5, respectively. $R_0=1.5$ μm for all plots. (a) Response curve from the first pulse. (b) We used the same parameters as in (a), but note the large spikes. We often observed spikes during bubble destruction. (c) The shell parameter was reduced in order to obtain a relatively good fit. (d) Even with a shell parameter at 0, a good fit is difficult to obtain. Also note the additional signal growing with each pulse near 2.7 μs. This signal may be due to a second bubble entering the region.

et al. found the decay rate of the backscattered signal for Optison® increased at these higher pressures; Sonazoid® also showed a decay, although at a slower rate.[46] In addition, Chen's data shows that these pressures are above the fragmentation threshold.[8]

Figure 9 shows examples of Optison® response curves to *individual* (nonaveraged) pressure pulses from the Ultramark 4Plus in the diluted aqueous gel. In (a) to (c), the microbubble response comes from consecutive pulses. A single pulse is skipped, and then (d) is shown. In terms of pulses, we are showing the dynamical response from pulses 1, 2, 3, and 5.

There appears to be a second series of oscillations developing in (b)–(d). These signals may be due to the arrival of a second microbubble. We focus on the first major signal. In Fig. 9(a), the model represents the data rather well. The fit is for a 1.5 μm radius bubble with a shell parameter of 6.0 nm Pa s. In Fig. 9(b), the fit is still acceptable, however, there are large amplitude ''spikes'' in the dataset. We often observe these spikes immediately before, or during microbubble destruction. They may be related to caustics from a crumpling of the shell (shell crumpling has been previously observed[18]). In (c) and (d) the model must be adjusted by decreasing the shell parameter (keeping the radius fixed). That is, the shell of this microbubble appears to be compromised. The parameters for this dataset are summarized in Table III.

We show in Fig. 10 another experiment, in this case a Sonazoid® bubble in water is undergoing an evolution during consecutive pulses (one pulse is not shown between the last two pulses). In (a) through (d), the shell parameter is fixed, but the ambient bubble radius must be increased from 0.8 to 1.2 μm to maintain a good fit. As with Fig. 8, the Sonazoid® bubble appears to absorb air from its surroundings before the shell is broken. By pulse #5, the shell is compromised. Also

TABLE III. Response curve parameters for evolving Optison® microbubble in an aqueous xanthan gum mixture. P^-_{peak} is the measured peak negative pressure, $\epsilon\mu_{sh}$ is the fitted shell parameter, R_0 is the fitted ambient radius, and R_{max} is the resultant maximum radius.

Figure	P^-_{peak} (kPa)	$\epsilon\mu_{sh}$ (nm Pa s)	R_0 (μm)	R_{max} (μm)	R_{max}/R_0
Fig. 9(a)	340	6	1.50	1.93	1.29
Fig. 9(b)	340	6	1.50	1.93	1.29
Fig. 9(c)	340	1.5	1.50	2.33	1.55
Fig. 9(d)	340	0	1.50	2.61	1.68

note the apparent nonlinearity of the bubble motion. The parameters for this data set are summarized in Table IV.

To conclude this section, we find that at these modest pressures, Sonazoid® microbubbles appear to have a semipermeable shell when insonified, allowing air to be absorbed, and causing the bubble to grow. In future experiments we plan to adjust the air concentration in the water to better resolve this issue. Both Optison® and Sonazoid® appear to show compromises in the shell after two or more pulses. We emphasize that these results are examples involving individual microbubbles; it would be necessary to examine many such cases before a conclusion could be drawn as to the ''average'' response of a particular microbubble.

C. Spectral analysis

Light scattering data may also be suited to fast analysis by examining the spectrum of the signals. Toward this eventual goal, we examined the power spectral density (PSD) of the $R(t)$ curves in this paper. We show in Fig. 11 an example

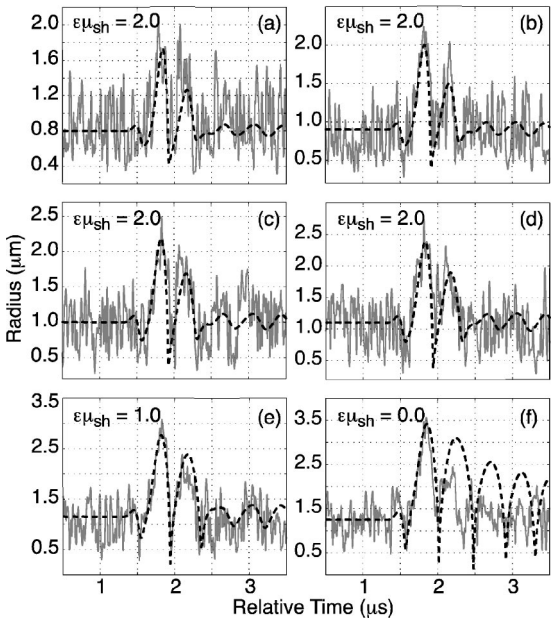

FIG. 10. An example of a Sonazoid bubble's destruction. The six subplots are the Sonazoid bubble's response to consecutive pulses [there is one plot omitted between (e) and (f)]. In (a)–(d), the bubble is modeled with an R_0 of 0.8, 0.9, 1.0, and 1.1 μm, and shell parameter $\epsilon\mu_{sh}=2.0$ nm Pa s. That is, the Sonazoid bubble is increasing its ambient size, apparently after each pulse. Similar results are seen in Fig. 8. In (e), a better fit is obtained by reducing the shell parameter to $\epsilon\mu_{sh}=1.0$ nm Pa s. In (f), we have removed the shell parameter in order to get a good fit to the first portion of the bubble growth; however, the rest of the oscillations do not fit as well.

TABLE IV. Response curve parameters for evolving Sonazoid® microbubble in water. P^-_{peak} is the measured peak negative pressure, $\epsilon\mu_{sh}$ is the fitted shell parameter, R_0 is the fitted ambient radius, and R_{max} is the resultant maximum radius.

Figure	P^-_{peak} (kPa)	$\epsilon\mu_{sh}$ (nm Pa s)	R_0 (μm)	R_{max} (μm)	R_{max}/R_0
Fig. 10(a)	390	2	0.80	1.74	2.18
Fig. 10(b)	390	2	0.90	1.99	2.21
Fig. 10(c)	390	2	1.00	2.19	2.19
Fig. 10(d)	390	2	1.10	2.38	2.16
Fig. 10(e)	390	1	1.15	2.77	2.41
Fig. 10(f)	390	0	1.25	3.42	2.74

of the normalized power spectral densities (PSD) from Fig. 8. There are significant fundamental peaks in the PSDs, related to the (real) resonance frequency of the system. Furthermore, we often observe apparent subharmonic and harmonic components. A more thorough analysis of these signals may eventually lead to better information about the response curves, or $R(t)$ that could be used to optimize the agents for imaging and therapy.

V. CONCLUSIONS

We evaluated the feasibility of using light scattering to measure the radial pulsations of individual ultrasound contrast microbubbles (Optison® or Sonazoid®) subjected to pulsed ultrasound. Experiments performed in a highly diluted xanthan gum mixture were used to verify that individual encapsulated microbubbles could be investigated. The evolution of individual contrast microbubbles was observed over several consecutive acoustic pulses, suggesting that shell permeablization and/or shell fatigue are important consequences in the evolution of microbubbles. We believe that light scattering can be used to better understand the physical interaction between ultrasound pulses and contrast agents, and eventually be used to evaluate shell parameters and explore shell fatigue, leading to better agent design.

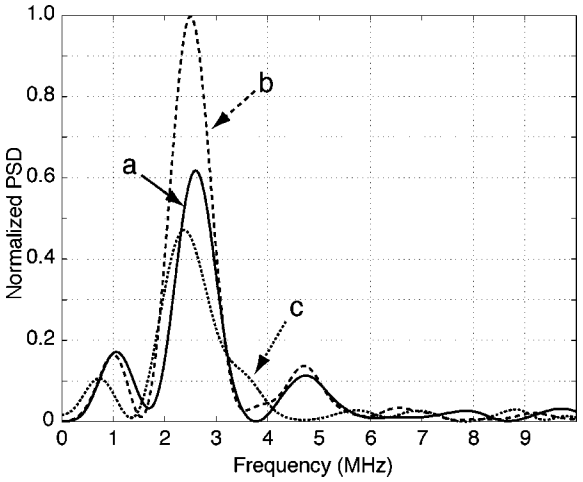

FIG. 11. Power spectral densities (PSDs) from light scattering data. The letters correspond to the subplots in Fig. 8.

ACKNOWLEDGMENTS

We wish to thank L. A. Crum, S. G. Kargl, and P. L. Marston for numerous discussions, and P. Hilmo for help in the lab. This research is funded by NIH 8RO1 EB00350-2.

[1] N. de Jong, L. Hoff, T. Skotland, and N. Bom, ''Absorption and scatter of encapsulated gas filled microspheres: theoretical considerations and some measurements,'' Ultrasonics **30**, 95–103 (1992).
[2] L. Hoff, *Acoustic Characterization of Contrast Agents for Medical Ultrasound Imaging* (Kluwer Academic, Boston, 2001).
[3] J. N. Marsh, M. S. Hughes, G. H. Brandenburger, and J. G. Miller, ''Broadband measurement of the scattering-to-attenuation ratio for Albunex (*R*) at 37 degrees C,'' Ultrasound Med. Biol. **25**, 1321–1324 (1999).
[4] D. Zhang, X. F. Gong, J. H. Liu, L. Z. Shao, X. R. Li, and Q. L. Zhang, ''The experimental investigation of ultrasonic properties for a sonicated contrast agent and its application in biomedicine,'' Ultrasound Med. Biol. **26**, 347–351 (2000).
[5] J. M. Correas, E. Kurtisovski, S. L. Bridal, A. Amararene, O. Helenon, and G. Berger, ''Optimizing an ultrasound contrast agent's stability using in vitro attenuation measurements,'' Invest. Radiol. **37**, 672–679 (2002).
[6] H. Medwin, ''Counting bubbles acoustically: a review,'' Ultrasonics **15**, 7–13 (1977).
[7] W.-S. Chen, A. A. Brayman, T. J. Matula, and L. A. Crum, ''Inertial cavitation dose and hemolysis produced *in vitro* with or without Optison,'' Ultrasound Med. Biol. **29**, 725–737 (2003).
[8] W.-S. Chen, T. J. Matula, A. A. Brayman, and L. A. Crum, ''A comparison of the fragmentation thresholds and inertial cavitation doses of different ultrasound contrast agents,'' J. Acoust. Soc. Am. **113**, 643–651 (2003).
[9] T. R. Porter, C. Everbach, D. Kricsfeld, and F. Xie, ''Myocardial cavitational activity during continuous infusion and bolus intravenous injections of perfluorocarbon-containing microbubbles,'' J. Am. Soc. Echocardiogr **14**, 618–625 (2001).
[10] W. T. Shi, F. Forsberg, A. L. Hall, R. Y. Chia, J. B. Liu, S. Miller, K. E. Thomenius, M. A. Wheatley, and B. B. Goldberg, ''Subharmonic imaging with microbubble contrast agents: Initial results,'' Ultrason. Imaging **21**, 79–94 (1999).
[11] F. Forsberg, W. T. Shi, and B. B. Goldberg, ''Subharmonic imaging of contrast agents,'' Ultrasonics **38**, 93–98 (2000).
[12] P. H. Chang, K. K. Shung, and H. B. Levene, ''Second harmonic imaging and harmonic Doppler measurements with Albunex,'' IEEE Trans. Ultrason. Ferroelectr. Freq. Control **42**, 1020–1027 (1995).
[13] P. D. Krishna and V. L. Newhouse, ''Second harmonic characteristics of the ultrasound contrast agents,'' Ultrasound Med. Biol. **23**, 453–459 (1997).
[14] W. T. Shi and F. Forsberg, ''Ultrasonic characterization of the nonlinear properties of contrast microbubbles,'' Ultrasound Med. Biol. **26**, 93–104 (2000).
[15] R. Basude and M. A. Wheatley, ''Generation of ultraharmonics in surfactant based ultrasound contrast agents: use and advantages,'' Ultrasonics **39**, 437–444 (2001).
[16] P. J. A. Frinking, A. Bouakaz, J. Kirkhorn, F. J. Ten Cate, and N. de Jong, ''Ultrasound contrast imaging: Current and new potential methods,'' Ultrasound Med. Biol. **26**, 965–975 (2000).
[17] V. Sboros, K. V. Ramnarine, C. M. Moran, S. D. Pye, and W. N. McDicken, ''Understanding the limitations of ultrasonic backscatter measurements from microbubble populations,'' Phys. Med. Biol. **47**, 4287–4299 (2002).
[18] P. A. Dayton, K. E. Morgan, A. L. Klibanov, G. Brandenburger, and K. W. Ferrara, ''Optical and acoustical observation of the effects of ultrasound on contrast agents,'' IEEE Trans. Ultrason. Ferroelectr. Freq. Control **46**, 220–232 (1999).
[19] B. Wolfrum, R. Mettin, T. Kurz, and W. Lauterborn, ''Observations of pressure-wave-excited contrast agent bubbles in the vicinity of cells,'' Appl. Phys. Lett. **81**, 5060–5062 (2002).
[20] N. de Jong, P. J. A. Frinking, A. Bouakaz, M. Goorden, T. Schourmans, X. Jingping, and F. Mastik, ''Optical imaging of contrast agent microbubbles in an ultrasound field with a 100-MHz camera,'' Ultrasound Med. Biol. **26**, 487–492 (2000).
[21] D. L. Kingsbury and P. L. Marston, ''Mie scattering near the critical angle of bubbles in water,'' J. Opt. Soc. Am. **71**, 358–361 (1981).
[22] G. M. Hansen, ''Mie scattering as a technique for the sizing of air bubbles,'' Appl. Opt. **24**, 3214–3220 (1985).
[23] R. G. Holt and L. A. Crum, ''Mie scattering used to determine spherical bubble oscillations,'' Appl. Opt. **29**, 4182–4191 (1990).
[24] B. P. Barber and S. J. Putterman, ''Light scattering measurements of the repetitive supersonic implosion of a sonoluminescing bubble,'' Phys. Rev. Lett. **69**, 3839–3842 (1992).
[25] T. J. Matula, ''Inertial cavitation and single bubble sonoluminescence,'' Philos. Trans. R. Soc. London, Ser. A **357**, 225–249 (1999).
[26] M. Kerker, *The Scattering of Light and Other Electromagnetic Radiation* (Academic, New York, 1969).
[27] C. F. Bohren and D. R. Huffman, *Absorption and Scattering of Light by Small Particles* (Wiley, New York, 1998).
[28] A. L. Aden and M. Kerker, ''Scattering of electromagnetic waves from two concentric spheres,'' J. Appl. Phys. **22**, 1242–1246 (1951).
[29] P. L. Marston, S. C. Billette, and C. E. Dean, ''Scattering of light by a coated bubble in water near the critical and Brewster scattering angles,'' Ocean Optics IX, M. A. Blizzard ed., Proc. SPIE **925**, 308–316 (1988).
[30] P. L. Marston, ''Colors observed when sunlight is scattered by bubble clouds in sea water,'' Appl. Opt. **30**, 3479–3484+3549 (1991).
[31] P. L. Marston and D. L. Kingsbury, ''Scattering by a bubble in water near the critical angle: Interference effects,'' J. Opt. Soc. Am. **71**, 917 (1981); **71**, 192–196 (1981).
[32] D. S. Langley and P. L. Marston, ''Critical-angle scattering of laser light from bubbles in water: measurements, models, and application to sizing of bubbles,'' Appl. Opt. **23**, 1044–1054 (1984).
[33] C. E. Dean and P. L. Marston, ''Critical angle light scattering from bubbles: an asymptotic series approximation,'' Appl. Opt. **30**, 4764–4776 (1991).
[34] J. Beuthan, O. Minet, J. Helfmann, M. Herrig, and G. Muller, ''The spatial variation of the refractive index in biological cells,'' Phys. Med. Biol. **41**, 369–382 (1996).
[35] M. Kohl and M. Cope, ''Influence of glucose concentration on light scattering in tissue,'' Opt. Lett. **19**, 2170–2172 (1994).
[36] N. de Jong and L. Hoff, ''Ultrasound scattering properties of Albunex microspheres,'' Ultrasonics **31**, 175–181 (1993).
[37] C. C. Church, ''The effects of an elastic solid surface layer on the radial pulsations of gas bubbles,'' J. Acoust. Soc. Am. **97**, 1510–1521 (1995).
[38] L. Hoff, P. C. Sontum, and J. M. Hovem, ''Oscillations of polymeric microbubbles: Effect of the encapsulating shell,'' J. Acoust. Soc. Am. **107**, 2272–2280 (2000).
[39] D. Chatterjee and K. Sarkar, ''A newtonian rheological model for the interface of microbubble contrast agents,'' Ultrasound Med. Biol. **29**, 1749–1757 (2003).
[40] K. E. Morgan, J. S. Allen, P. A. Dayton, J. E. Chomas, A. L. Klibanov, and K. W. Ferrara, ''Experimental and theoretical evaluation of microbubble behavior: Effect of transmitted phase and bubble size,'' IEEE Trans. Ultrason. Ferroelectr. Freq. Control **47**, 1494–1508 (2000).
[41] C. L. Yaws, *Matheson Gas Data Book*, 7th ed. (McGraw-Hill, New York, 2001).
[42] D. B. Khismatullin and A. Nadim, ''Radial oscillations of encapsulated microbubbles in viscoelastic liquids,'' Phys. Fluids **14**, 3534–3557 (2002).
[43] R. D. McCormick, Masters thesis, Boston University, 44 Cummington Street Boston, MA, 02215, 2002.
[44] R. Clark (personal communication).
[45] J. E. Chomas, P. Dayton, D. May, and K. W. Ferrara, ''Threshold of fragmentation for ultrasonic contrast agents,'' J. Biomed. Opt. **6**, 141–150 (2001).
[46] C. M. Moran, T. Anderson, S. D. Pye, V. Sboros, and W. N. McDicken, ''Quantification of microbubble destruction of three fluorocarbon-filled ultrasonic contrast agents,'' Ultrasound Med. Biol. **26**, 629–639 (2000).
[47] J. E. Chomas, P. Dayton, J. Allen, K. Morgan, and K. W. Ferrara, ''Mechanisms of contrast agent destruction,'' IEEE Trans. Ultrason. Ferroelectr. Freq. Control **48**, 232–248 (2001).

Experimental study of the diffracted sound field around jagged edge noise barriers

Penelope Menounou
Department of Mechanical Engineering, The University of Texas at Austin, 1 University Station C2200, Austin, Texas 78712-0292

Jeong Ho You
Department of Mechanical and Industrial Engineering, The University of Illinois at Urbana-Champaign, Illinois 61801

(Received 27 February 2004; revised 11 August 2004; accepted 17 August 2004)

Noise barriers are commonly used to protect communities from transportation noise. In the present study, three types of barriers, modeled as half planes, have been tested in the laboratory: a conventional rigid barrier with a straight top edge, a straight top edge barrier covered with sound absorbing material, and a rigid barrier with a jagged top edge. Measurements were taken not just behind the barriers, but around them on a plane perpendicular to their top edge. Measured signals were compared against theoretical predictions contributing to further validation of a theoretical model. The sound absorbing material was found to affect the diffracted field more in the front of the barrier than behind it. The diffracted field in front of a jagged edge barrier, similar to the field behind it, was found to depend on the geometry of the edge in the area where the shortest diffraction path intersects the edge profile. Last, the performance of the three barriers was compared with one another in all areas around the barrier. It was found that the jagged edge barrier provides shielding similar to the sound absorbing barrier but at a fraction of the cost. © *2004 Acoustical Society of America.* [DOI: 10.1121/1.1804633]

PACS numbers: 43.28.En, 43.28.Js [LCS] Pages: 2843–2854

I. INTRODUCTION

A barrier placed between a sound source and the receiver, puts the receiver into an acoustical shadow zone. However, sound still reaches the receiver primarily as it diffracts from the barrier's edges. The everyday equivalent is a noise barrier built alongside highways, railroads, airplane runways, or factories to shield the nearby communities from the noise. In these cases, sound reaches the receiver primarily by diffraction at the top edge of the noise barrier.

Recent public awareness of noise pollution has intensified the research on noise barriers and on ways to improve their shielding effect. References 1–19 are a portion of published work on improving the shielding effect of a barrier by modifying its top edge or by using sound absorbing material on the barrier's surface.

Our motivation came from work on jagged edge noise barriers[18,19] and on its possible use as parallel noise barriers built along opposite sides of the road. Jagged edge barriers are a new design of barriers that have been shown to improve the shielding effect compared to a straight edge barrier having the same average height. A theoretical model termed directive line source model (DLSM) has also been developed to predict the shielding effect of such a barrier design.[20] The performance of jagged edge barriers has been investigated only in the shadow region behind them. No measured data exist for receivers in front of them. Similarly, the theoretical model, applied to both straight and jagged edge barriers, has been validated through comparisons with experimental data only in the shadow region behind the barriers.

Knowledge of the diffracted field outside the shadow zone is important in certain noise control applications, for example, in the study of parallel noise barriers. In order to compute the effective noise source in these cases, one must add to the sound field coming directly from the noise source two more sound field components: (i) the reflected field coming from reflections on the barriers' surface and (ii) the diffracted field that penetrates back into the area in front of the barriers (i.e., that facing the source) after sound diffracts on the barriers' top edges. Knowledge of the diffracted field directivity is also of interest. Consider the diffracted field on a plane perpendicular to the top edge of the barrier. Far from being omnidirectional, the diffracted field undergoes jump discontinuities at certain locations, vanishes completely at others, and has a different sign at different areas on that plane. For medical applications, for example, knowledge of the polarity of a diffracted signal can be important (a strong positive pulse can be harmful).

In the present study, measurements were taken in the laboratory around the barriers on a plane perpendicular to its top edge, thus covering areas not only behind the barrier but in front of and above it, as well. Specifically, three types of barriers were tested: a straight-edge/rigid barrier (the reference case), a straight-edge/sound absorbing barrier, and a jagged-edge/rigid barrier. Because the experiments were conducted using a spark that produces pulses of short duration, we were able to capture diffracted signals resolved from reflections. We were, therefore, able to investigate the directivity of the diffracted field without any interference from the reflected and/or incident field that co-exist with the diffracted field in front of the barrier.

The problem of edge diffraction is described in Sec. II of

this work. The experimental setup is described in Sec. III and the particular problems encountered are discussed. In Sec. IV, the experimental signals are compared with solutions predicted by DLSM, the directivity of the measured diffracted field is examined, and finally the types of barriers tested are compared with one another.

The experimental investigation presented here contributes the following: (i) The validation of the theoretical model DLSM is extended to areas where it had not been validated before. Previously, we had results in the shadow zone behind the barrier. In this paper, we validate the model, as applied to both straight and jagged edge barriers, in front of the barrier and above it. (ii) The effectiveness of the jagged edge barrier (its shielding improvement compared to a straight edge barrier with the same average height) is investigated for receiver locations outside the shadow region. As mentioned earlier, the performance of the jagged edges has been investigated only in the shadow region. (iii) Finally, the jagged edge profile, as a method to improve the shielding effect of the conventional straight edge barrier, is compared with, perhaps, the most obvious alternative: to cover the barrier with sound absorbing material. No measured data exist to compare the shielding effect of the jagged edge to other means of improving the barriers' performance. The results can be important to retrofit studies of existing barriers and to the final acceptance of the jagged edge barriers by the community.

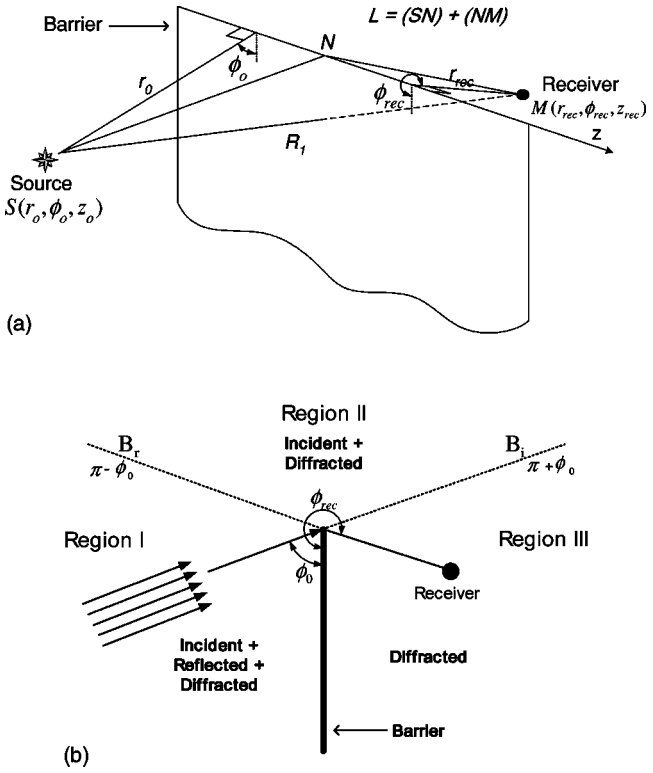

FIG. 1. Barrier geometry.

II. GEOMETRY OF THE PROBLEM AND NATURE OF THE SOLUTION

In the present study the following simplifying assumptions have been made. The incident signal comes from a simple point source. The barrier itself is assumed to be very thin, compared to the spatial duration of the incident signal, and is modeled as a semi-infinite plane. Therefore, reflections from the ground, diffraction from the side edges of the barrier, the thickness of the barrier and, thus, diffraction from the second top edge of a thick barrier are ignored. Also, the surrounding medium is considered to be homogeneous and quiet. It should be noted that the above simplifying assumptions have been made in order to focus our attention to the effect of sound diffraction by the different top edges tested. The excluded effects are by no means unimportant to the study of the real life problem with the effect of ground being, perhaps, the most important among them.

The typical geometry for the half-plane diffraction problem is shown in Fig. 1(a), where the sound field is produced by a point source S located at (r_0, ϕ_0, z_0) and the receiver M with coordinates $(r_{\mathrm{rec}}, \phi_{\mathrm{rec}}, z_{\mathrm{rec}})$ can be any point. The notation is based on a cylindrical coordinate system having the edge of the half plane as its z axis. The radial distances r_0 and r_{rec} are measured from the edge of the half plane and the angles, ϕ_0 and ϕ_{rec}, are measured from the surface of the half plane facing the source. The sound from the source can be either normally incident on the half plane [S and M on the same plane normal to the z axis $(z_0 = z_{\mathrm{rec}})$] or obliquely incident $[(z_0 \neq z_{\mathrm{rec}})]$. In all cases presented here, the incidence is normal. The shortest distance that the sound travels to reach the receiver by diffraction is $L = (SN) + (NM)$, where N is the point on the edge of the barrier, where the least diffraction path intersects the edge. This point will be called in the following *point of first contact*.

Based on geometrical acoustics, in region I [shown in Fig. 1(b)] both incident (p_i) and reflected (p_r) waves are present, in region II only the incident wave is present, and region III is a shadow zone. The dividing line at $\pi + \phi_0\,(B_i)$ that separates regions II and III, establishes the *shadow boundary for the incident wave* and the dividing line at $\pi - \phi_0$ establishes the *shadow boundary for the reflected wave*. If diffraction is taken into account, a diffracted wave (p_d) should be added in all three regions. The diffracted sound (p_d) may be considered as having two components $(p_d = p_{di} + p_{dr})$; one associated with the incident field (p_{di}) and one with the reflected field (p_{dr}). At B_r the disappearance of the reflected signal is compensated by a discontinuity in p_{dr}, while the disappearance of the incident signal at B_i is compensated by a discontinuity in p_{di}. Therefore, the total solution remains continuous throughout the domain.

III. EXPERIMENTAL STUDY

A. Experimental setup and apparatus

All the experiments were conducted in the laboratory in air using a spark as the sound source. The experimental setup is presented in Fig. 2. The entire apparatus was placed on a dense, thick wood table that served as the ground plane. The frequency range of the spark source was 4–20 kHz, which is approximately 10 times the frequency of traffic noise (400–2000 Hz). The experiment can, therefore, be viewed as a 1/10 model experiment of a real traffic noise barrier.

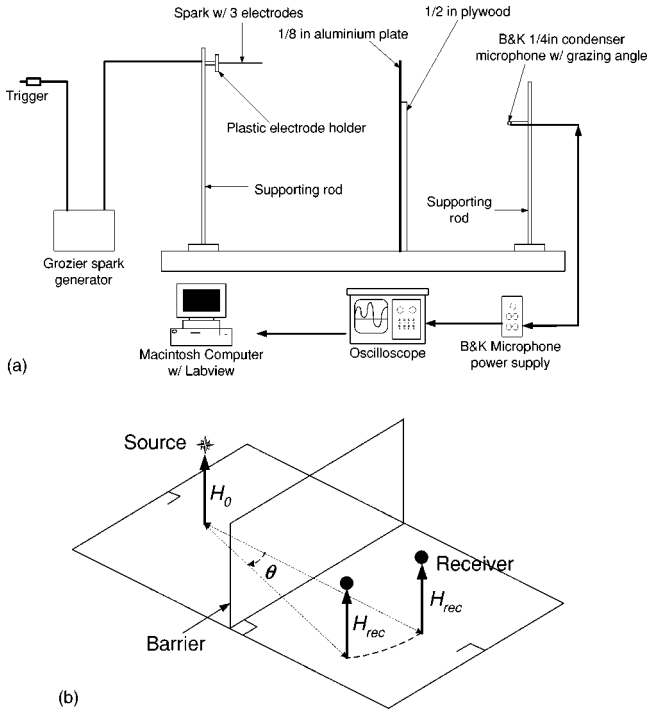

FIG. 2. Experimental setup.

The experimental apparatus consists of: (i) a spark source system with three electrodes, a plastic plate holder and a Grozier spark generator, (ii) a 1/8 in. (0.32 cm) aluminum plate supported by a 1/2 in. (1.27 cm) plywood (barrier), (iii) a 1/4 in. Brüel and Kjær condenser microphone connected to a microphone power supply, and (iv) an oscilloscope and a computer using Labview software to store and postprocess the measured signals.

1. Sound source

The spark generator contains a 1 μF capacitor and the resulting voltage across the electrodes reaches about 4000 V. The spark source produces a blast type waveform[21] as shown in Fig. 3. The time duration of the signal is about $T = 100\,\mu$s, which corresponds to 3.45 cm spatial duration assuming sound velocity $c_o = 345$ m/s at 23 °C.

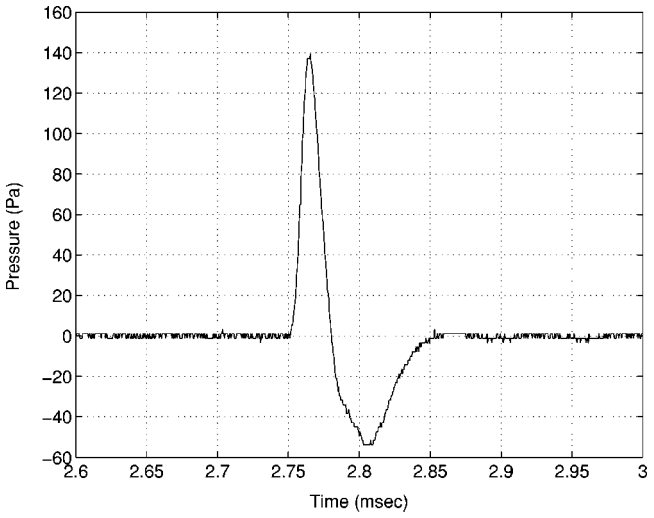

FIG. 3. Free-field measurement at 95 cm away from the source.

For the analysis in the present work it is assumed that the spark source is a point source that produces repeatable incident signals. Both assumptions have been tested experimentally and have been found to hold reasonably well. First, for all sets of measurements free-field measurements were taken at the beginning and at the end of each session. It was found that the incident signal remained reasonably the same throughout. A 4% change in the peak amplitude was the largest ever encountered. Finally, the gap between the electrodes, where the sparks are generated, is less than 1 mm. Because the electronic discharging length is much smaller than any length in the geometry of the problem, the spark source can be considered a point source. Free-field measurements were taken at various receiver positions, all located 95 cm away from the source but at different angles θ [see Fig. 2(b)] to verify the point source assumption. It was found that the measured signals were effectively the same at all receiver locations. The maximum encountered change in the peak amplitude was less than 1%.

2. Receiver

The effect of the orientation of the microphone was studied before the microphone orientation for the present set of measurements was determined. It was shown that different microphone orientations can result in substantially different amplitudes and shapes of the captured signals. Figures 4(a) and 4(b) show the freefield signal captured by the microphone oriented at grazing and normal incidence, respectively. The change in the peak amplitude, as well as the ringing of the microphone can be observed. For our experiments, the microphone was placed at grazing angle, as shown in Fig. 4(c). With the barrier present, the diffraction contributions coming from the 120 cm long barrier arrive at the microphone at angles that range from grazing angle (contributions from the center portion of the top edge) to 30.26° from the normal incidence (contributions from the farthest portions of the top edge). In our study the dominant contributions to the diffracted signals come from the portions of the edge that are close to the receiver location, and arrive almost at grazing incidence to the diaphragm of the microphone.

3. Three different types of barriers

To model the barriers, a 1/8 in. (0.32 cm) aluminum plate was used for all types of barriers tested. It was attached to a 1/2 in. (1.27 cm) plywood, which was clamped to the ground table, so that it could stand firmly. The length of the barrier is 120 cm, which was found to be long enough to separate the diffracted signals from the top edge from diffracted signals from the side edges of the barrier in certain time ranges. (For all source-edge-receiver configurations in the experiments, the diffracted signal from the top edge can be observed in the time interval between 2.7 and 3 ms, while any diffracted signal from the side edges arrives at the receiver after 4.5 ms). The three different types of barriers used were: (i) a straight top edge barrier with acoustically rigid material (straight-edge/rigid barrier), (ii) a straight top edge

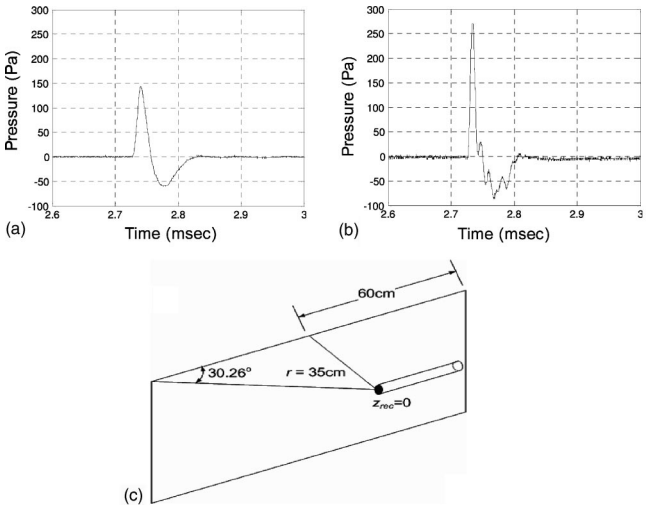

FIG. 4. Effect of the microphone orientation. Freefield signal at grazing incidence on the microphone [(a)] and at normal incidence [(b)]. Microphone orientation chosen for the experiments [(c)].

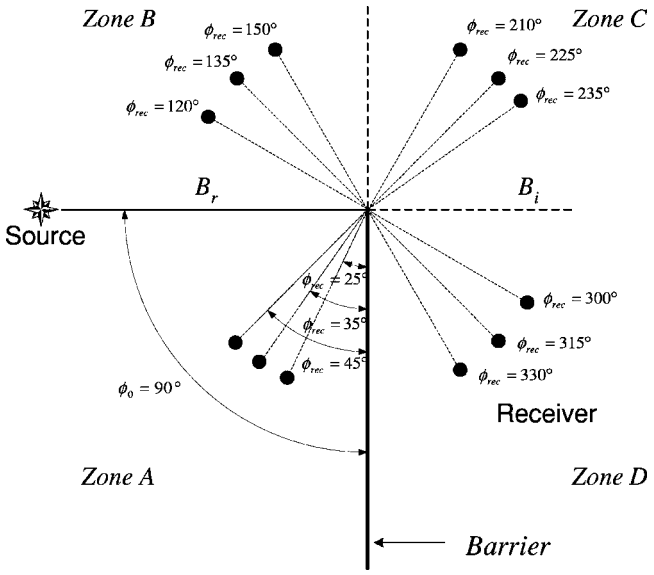

FIG. 6. Source and receiver positions for the set of experiments.

barrier with sound absorbing material (straight-edge/sound absorbing barrier), and (iii) a jagged top edge barrier with acoustically rigid material (jagged-edge/rigid barrier) as shown in Fig. 5. The straight-edge/rigid barrier was investigated first and used as a reference. A 60 cm by 120 cm aluminum plate with 1/8 in. thickness was cut and simply attached to the plywood. For the soft edge barrier, a 1.5 in. innerdiameter and 0.25 in. thick PVC pipe was put on the top edge of the aluminum plate and a 1.5 in. thick layer of fiberglass was attached around the pipe. For the jagged-edge/rigid barrier, two simple jags were cut on the top edge of aluminum in the shape of triangles, as shown in Fig. 5(d). The height (2.5 cm) and the width (5 cm) of the triangles, as well as the horizontal spacing between them (5 cm) are comparable to the spatial duration of the incident wave (3.45 cm), while the average height of the barrier remained unchanged. The jagged edge was tested at two source-edge-receiver configurations. In the first configuration, source and receiver were placed at $z_0 = z_{\mathrm{rec}} = 0$, while in the second source and receiver were placed at $z_0 = z_{\mathrm{rec}} = +5$ cm [see Fig. 5(d)]. Each of the configurations has its own characteristics as will be explained next.

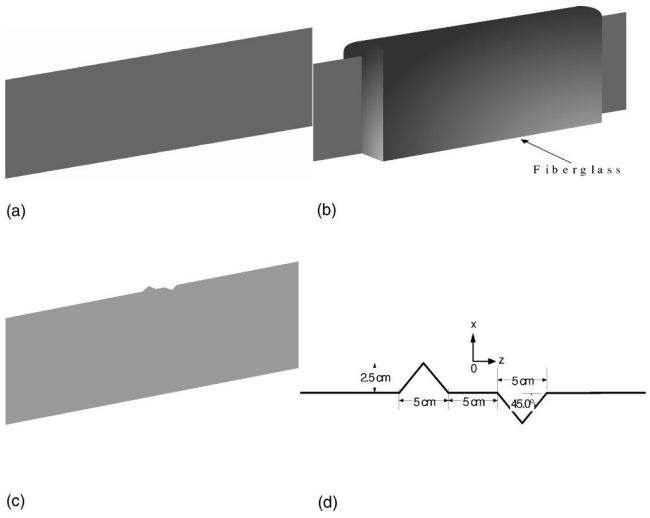

FIG. 5. Three different types of barrier: (a) straight-edge/rigid barrier; (b) straight-edge/sound absorbing barrier (thickness of fiberglass not in scale); (c) jagged-edge/rigid barrier; (d) top-edge profile of the jagged edge barrier.

B. Description of the experiments

For all measurements the angular position of the source was kept at $\phi_0 = 90°$, its distance from the top edge of the barrier at $r_0 = 60$ cm, and its horizontal position (the direction along the edge of the barrier) on the same vertical plane with the receiver ($z_0 = z_{\mathrm{rec}}$). Figure 6 indicates that by positioning the source at $\phi_0 = 90°$, the two shadow boundaries, the barrier, and the continuation of the barrier in the free space above it divide the area around the barrier into four equal zones, called zones A, B, C, and D.

For all cases, except for the second set of measurements with the jagged edge barrier, the horizontal positions of source and receiver were kept at the center of the barrier ($z_0 = z_{\mathrm{rec}} = 0$). In the case of the jagged-edge/rigid barrier, measurements were also taken on a different vertical plane, off center. For this set of measurements source and receiver were placed at $z_0 = z_{\mathrm{rec}} = +5$ cm. This was done in order to study two jagged edge configurations. In the former, the point of first contact lies for all receiver locations on the horizontal segment between the two triangles [see Fig. 5(d)]. All receivers should, therefore, ''see'' the jagged edge as a straight edge. In the second configuration, the point of first contact lies on the horizontal segment or at the dip of the right triangle depending on the receiver location.

The microphone was placed at various locations around the barrier, as shown in Fig. 6, all having the same distance from the top edge, $r_{\mathrm{rec}} = 35$ cm, but different angular positions $0 < \phi_{\mathrm{rec}} < 2\pi$. The positions of the receiver were chosen based on two considerations: (i) to be away (at least 30°) from the two shadow boundaries B_r and B_i, where the DLSM solution is not valid and (ii) diffracted signals to be resolved from incident and reflected signals, wherever the

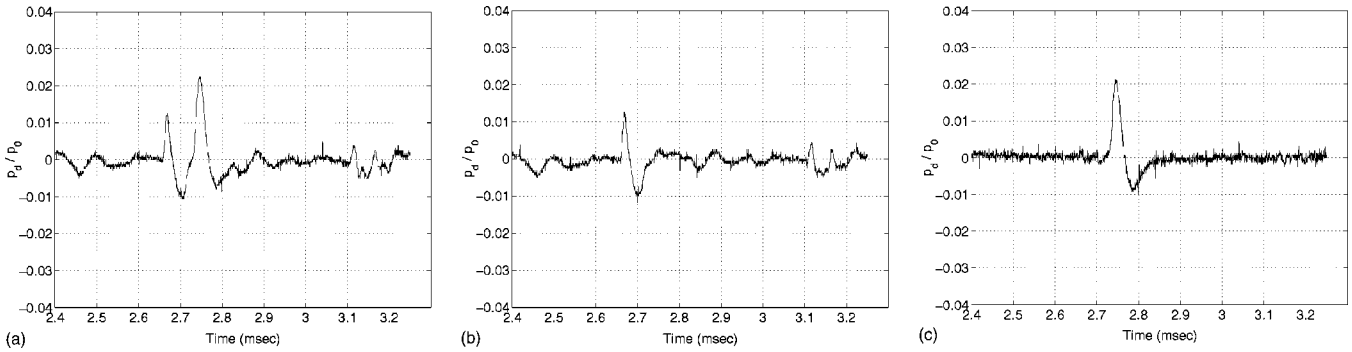

FIG. 7. Application of the subtraction method. Measured signal with the barrier present [(a)]: the first peak at 2.67 ms is a reflected signal from the electrode holder, the second peak is the diffracted signal. Measured signal without the barrier present [(b)]: peak at 2.67 ms is the reflected signal from the electrode holder. Subtraction results [(c)]: signal produced by subtracting signals in (a) and (b), only the diffracted signal can observed the reflected signal has been eliminated.

latter are present. One of the main concerns was to avoid reflected signals from the experimental equipment. Especially measurements in zone A required great care, as reflected signals from the plastic holder of the source arrive very close in time with the diffracted wave. Whenever necessary, measurements were taken with and without the barrier present and then were subtracted (the subtraction method). The signal resulted from the subtraction method contained only signals originating from the barrier. This subtraction method provided good results and was feasible, because our source signals were repeatable. Figure 7 shows an example. The subtraction method is applied to a case where a signal reflected from the plastic electrode holder arrives very close in time to the diffracted signal from the top edge of the barrier. Figure 7(a) shows the measurement with the barrier present. The first peak at around 2.67 ms is the signal from the apparatus, while the second is the diffracted signal. The same measurement was taken without the barrier present and is depicted in Fig. 7(b), where only the signal from the plastic holder can be observed. The two measurements are subtracted to eliminate the signal from the apparatus and leave only the diffracted signal, as shown in Fig. 7(c).

IV. RESULTS

A. Comparisons with analytical solutions

In this section the experimental data for the straight-edge/rigid barrier and the jagged-edge/rigid barrier are compared with analytical solutions obtained from the DLSM.[20] For the reference case of the straight-edge/rigid-barrier, the Biot–Tolstoy–Medwin (BTM) solution is also employed for the comparisons. (Biot and Tolstoy derived the solution for an impulsive spherical wave incident on a half plane as an application to their method for wave propagation in infinite media.[22] Years later, Medwin revisited the Biot–Tolstoy results and used them in various acoustical applications.[23] Since then, the solution has been used with great success in many areas of acoustics.[24] Because of this wide acceptance, it is employed here for comparisons with our experimental data.)

A brief overview of the DLSM is given before we proceed to the comparisons. The DLSM was developed to predict the diffracted field (pressure time waveform) caused by a sound wave incident on a half plane. In this method the edge of the half plane is modeled as an infinite set of directive point sources continuously distributed along the edge. It can be applied for several types of incident radiation: omnidirectional cylindrical and spherical waves, plane waves, as well as waves from directional sources incident on a barrier having a straight or jagged edge. It is shown that the diffracted field is equivalent to re-radiation from the edge of the barrier, but modified by a certain directivity function. The straight or jagged edge of the barrier is modeled as a directive line source, straight, or jagged, respectively.

For a spherically spreading pulse $f(t)$ incident on a straight barrier, as the cases studied in this paper, the mathematical expression for the DLSM becomes:

$$P_d = -\frac{AF_t}{4\pi}\int_{\text{edge}} \frac{f\left(t-\frac{\sqrt{\rho^2+z^2}}{c}\right)}{\sqrt{\rho^2+z^2}} D(\phi_{\text{rec}};\phi_0)\,dz, \qquad (1)$$

where AF_t is an amplitude factor that depends on the radial distances of source (r_0) and receiver (r_{rec}) and on the type of the incident wave, ρ is an effective distance that depends on the type of the incident wave, and $D(\phi_{\text{rec}};\phi_0)$ is the directivity function, a simple function of the angular position of source (ϕ_0) and receiver (ϕ_{rec}), which remains the same regardless of the type of incident radiation. The integration is performed along the edge of the barrier and represents the summation of contributions from directive point sources.

The corresponding form for a jagged edge barrier consisting of inclined or horizontal finite-length segments is:

$$P_d = -\sum_{j=1}^{N} (AF_t)^{(j)} \frac{I^{(j)}(RC^{(j)})}{4\pi} D^{(j)}(\phi_{\text{rec}}^{(j)};\phi_0^{(j)}), \qquad (2)$$

where N is the number of the finite-length segments, $I^{(j)}$ is the integral along the segment j, $D^{(j)}$ is the directivity function of segment j, $RC^{(j)}$ is the position at which the receiver is presumed to be relocated for the diffraction problem to be transformed into a radiation problem (the relocated receiver is called virtual receiver), $(AF_t)^{(j)}$ is the amplitude factor, and $\rho^{(j)}$ is the distance between the segment and its corresponding virtual receiver. Each segment of the edge behaves

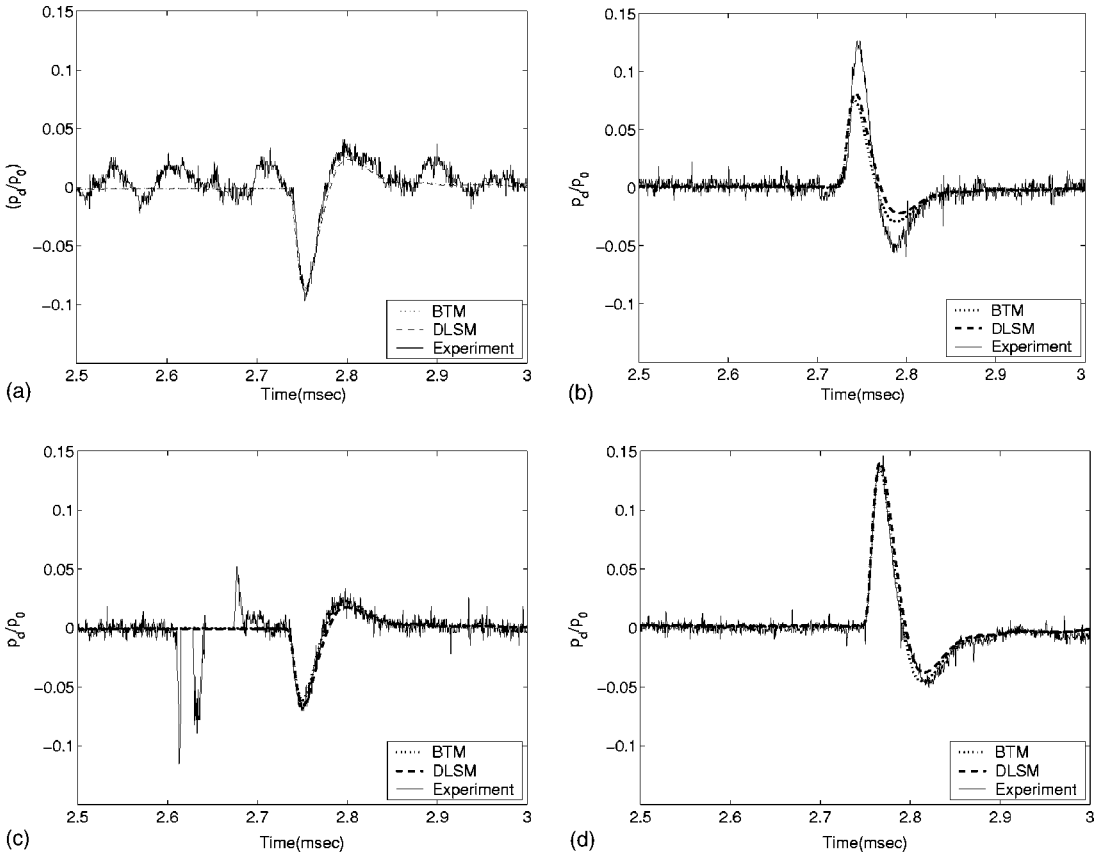

FIG. 8. Comparison between experimental data (solid line) and predictions from DLSM method (dashed line) and BTM solution (dotted line); straight-edge/rigid barrier; source at $\phi_0=90°$, $r_0=60$ cm, $z_0=0$ cm; receiver at $r_{\text{rec}}=35$ cm, $z_{\text{rec}}=0$, and $\phi_{\text{rec}}=25°$ (zone A) [(a)], $\phi_{\text{rec}}=120°$ (zone B) [(b)], $\phi_{\text{rec}}=225°$ (zone C) [(c)], $\phi_{\text{rec}}=300°$ (zone D) [(d)]. Data normalized so that the free-field signal has unity peak amplitude at 1 m away from the source.

as a part of an overlying infinitely long straight edge. The relative position of each segment to source and receiver results in a different value of $r_{\text{rec}}^{(j)}$, $r_0^{(j)}$, $\phi_{\text{rec}}^{(j)}$, $\phi_0^{(j)}$ and in turn in a different value of $AF_t^{(j)}$, $D^{(j)}$, and $RC^{(j)}$ for each segment. The position of the virtual receiver for each segment is determined so that the travel distance of the point-source-edge-receiver path in the diffraction problem is the same as the travel distance of line-source-virtual-receiver path in the radiation problem.

For the model to be valid two conditions must be met: (i) the receiver must be away from the two shadow boundaries B_i and B_r (see Fig. 1), and (ii) both source and receiver must be at least one wavelength away from all points on the top edge of the barrier. The proximity to the edge is measured in wavelengths for time harmonic source signals; other characteristic distances are used for non-time harmonic signals (for example, the spatial duration of a transient source signal, or the correlation length of a noise source signal).

Let us now resume our comparisons. It should be noted that the entire time waveform is compared, not just the energy contained in the signal. Signals containing the same acoustical energy, may differ substantially in shape, peak amplitude, duration, etc. Therefore, the time waveform comparisons employed here are more rigorous. In all cases the results are normalized, so that the free-field signal has unity peak amplitude at 1 m away from the source.

Representative comparisons are shown in Fig. 8 for the straight edge barrier and in Fig. 9 for the jagged edge barrier. The comparisons are presented for receivers in each of the zones A, B, C, and D, as indicated in Fig. 6. In Fig. 8 it can be observed that the analytical predictions obtained from DLSM are in reasonably good agreement with the BTM solution and the experimental data. Looking more closely, a negative peak followed by a positive peak can be observed in zone A [Fig. 8(a)], that is a polarity opposite the incident signal (see Fig. 3). Figure 8 shows that the polarity of the diffracted signal changes three times as we move the receiver on a circle around the barrier: (i) when we cross the shadow boundary for the reflected wave B_r, i.e., moving from zone A to zone B [Figs. 8(a) and 8(b)], (ii) when we cross the continuation of the barrier in the half space above it, i.e., moving from zone B to zone C [Figs. 8(b) and 8(c)], and (iii) when we cross the shadow boundary for the incident wave B_i, i.e., moving from zone C to zone D [Figs. 8(c) and 8(d)]. The noise observed in the signal in zone A [Fig. 8(a)] is attributed to the reflections from the experimental equipment. Signals in zone B are much cleaner, as the reflections from the equipment arrive later and are resolved from the diffracted signal. For signals in zone C the subtraction method (described in Sec. III) was used. The spikes in Fig. 8(c) are errors from the subtraction method. Finally, in the zone behind the barrier, there are no interfering signals and

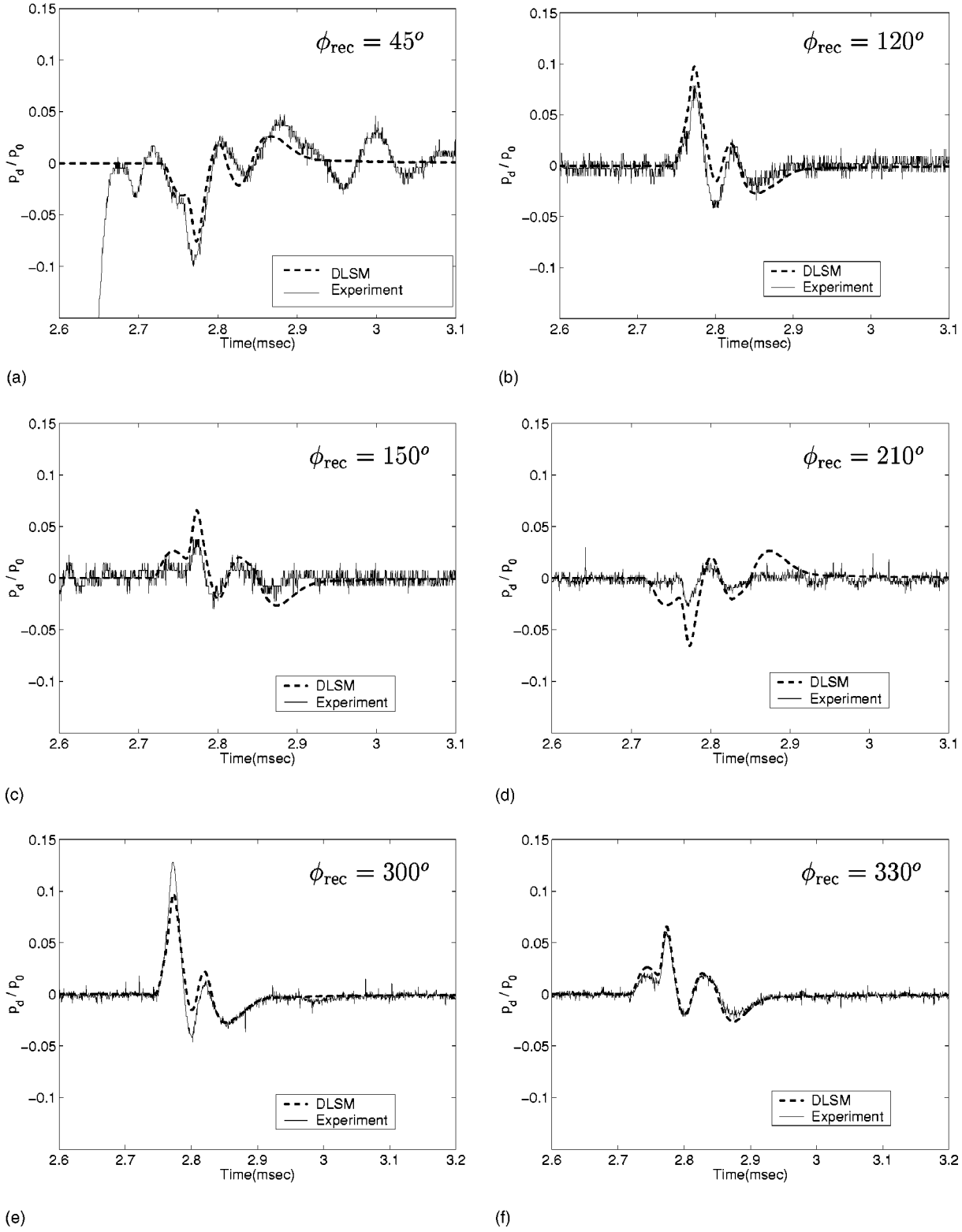

FIG. 9. Comparison between experimental data (solid line) and predictions from DLSM method (dashed line); jagged-edge/rigid barrier; source at $\phi_0 = 90°$, $r_0 = 60$ cm, $z_0 = 0$ cm; receiver at $r_{\rm rec} = 35$ cm, $z_{\rm rec} = 0$, and $\phi_{\rm rec} = 45°$ [(a)], $\phi_{\rm rec} = 120°$ [(b)], $\phi_{\rm rec} = 150°$ [(c)], $\phi_{\rm rec} = 210°$ [(d)], $\phi_{\rm rec} = 300°$ [(e)], $\phi_{\rm rec} = 330°$ [(f)]. Data normalized so that the free-field signal has unity peak amplitude at 1 m away from the source.

very clean diffracted signals were captured. Figure 9 shows the time waveform comparisons for the set of measurements conducted with the first configuration of the jagged edge barrier. Again here, a reasonably good agreement can be observed with the predictions from the DLSM.

In conclusion, DLSM seems to be as good as the established BTM solution in predicting the diffracted signal around a straight edge barrier. Also, DLSM seems to yield predictions that agree reasonably well with experimental data behind straight and jagged edge barriers, in the shadow zone behind them, as well as in front of and above them.

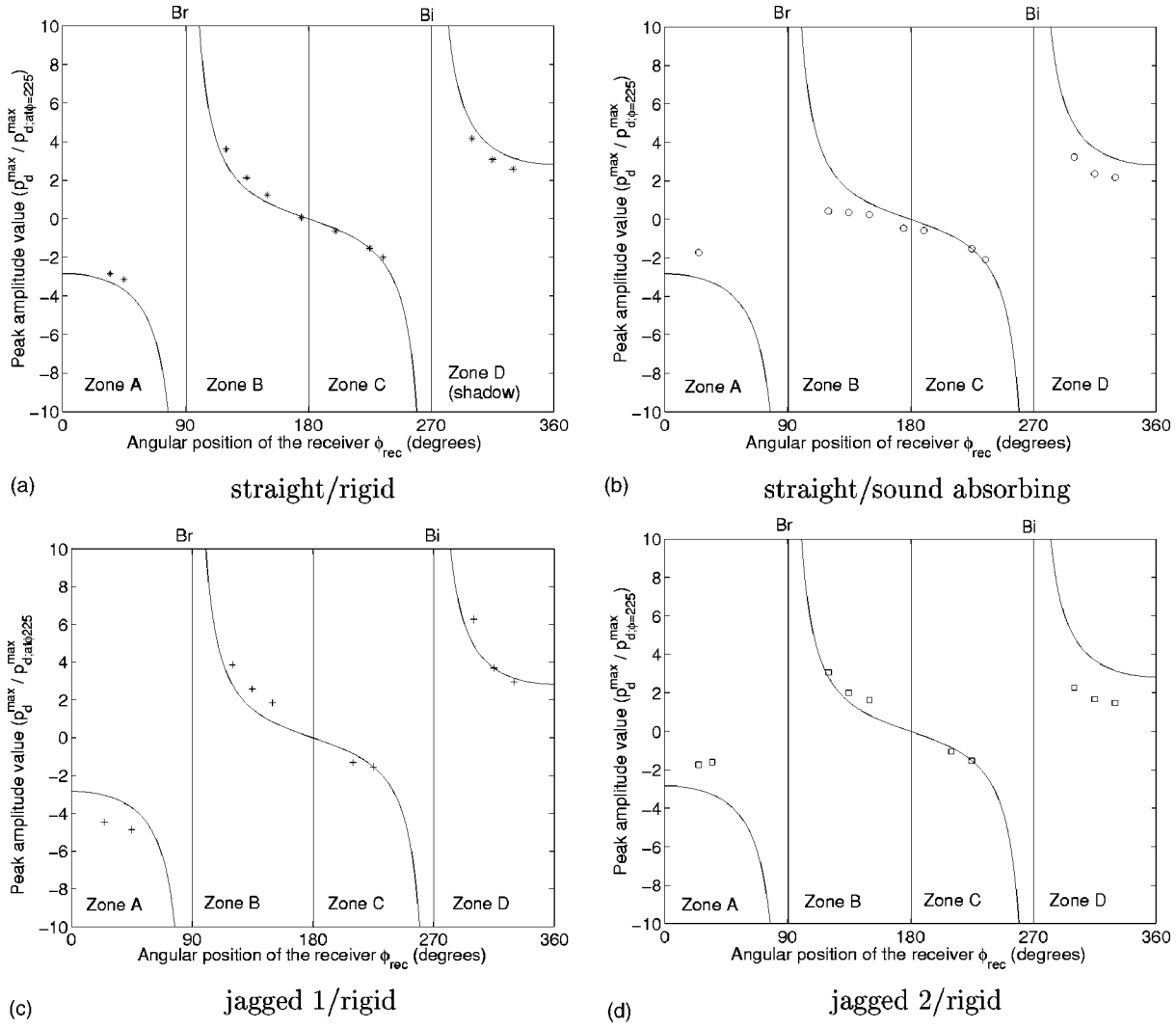

FIG. 10. Comparison between the theoretical directivity of the diffracted field around a straight-edge/rigid barrier as obtained by Eq. (3) (solid line) and the measured directivity (data points) around: the straight-edge/rigid barrier [(a)], the straight-edge/sound absorbing barrier [(b)], the first configuration of the jagged-edge/rigid barrier [(c)], and the second configuration of the jagged-edge/rigid barrier [(d)]. Data points correspond to the peak amplitude value of the measured diffracted signal normalized by the peak amplitude value of the signal at $\phi_{\text{rec}}=225°$ (an arbitrarily selected receiver location).

B. Effects on the directivity of the diffracted field: Deviations from the directivity of a straight edge rigid barrier

In this subsection, the measured data are used to construct the directivity of the diffracted field on a plane perpendicular to the barriers' top edge for each barrier type tested. The directivity of the field provides information about the locations where the diffracted field undergoes jump discontinuities, vanishes completely, or changes signs. It also shows the performance of the barrier in all areas around it, behind, above, and in front of it.

The directivity around a straight-edge/rigid barrier has a known analytical expression and is briefly outlined later herein. For details the reader is referred to Ref. 20 and to references therein. For the straight-edge/sound absorbing barrier the reader is referred to Refs. 11 and 24–30 and in references therein, as an indicative list of the available solutions, from which an analytical expression for the directivity can be extracted. There is no analytical solution for the directivity of the diffracted field around a jagged edge barrier. Each segment of the jagged edge has its own directivity as a result of the different angular positions of source and receiver relative to each inclined segment.

In the following the directivity of the diffracted field around a straight edge rigid barrier is presented and the measured directivities for each barrier are compared with it in Fig. 10. If the receiver is away from the two shadow boundaries B_i and B_r, and both source and receiver are at least one wavelength away from all points on the edge of the barrier, then the directivity of the diffracted field can be described, regardless of the type of incident radiation,[20] by the following directivity function:

$$D(\phi_{\text{rec}};\phi_0)=\frac{1}{2}\left[\sec\left(\frac{\phi_{\text{rec}}-\phi_0}{2}\right)+\sec\left(\frac{\phi_{\text{rec}}+\phi_0}{2}\right)\right]. \quad (3)$$

It should be emphasized that the above directivity function is the same for all types of incident radiation (omnidirectional cylindrical and spherical waves, plane waves, as well as waves from directional sources) and it can be recovered from solutions in the time domain, as well as in the frequency

domain, and from solutions derived by totally different methods. The directivity function is a simple relation of the angular position of source (ϕ_0) and receiver (ϕ_{rec}). Unlike other directivity functions, as, for example, the directivity function of a piston, $D(\phi_{\text{rec}};\phi_0)$ does not depend on the frequency of the incident wave. Finally, it should be noted that Eq. (3) predicts infinite values of the directivity function (and thus of the solution) at the two shadow boundaries (B_r at $\phi=\pi-\phi_0$ and B_i at $\phi=\pi+\phi_0$). The infinite values are an artifact of the assumptions used for the derivation.

Figure 10(a) shows, as expected, that the measured directivity for the straight-edge/rigid barrier is as predicted by the theory. The measured directivity for the first configuration of the jagged edge barrier also seems to follow the theoretical directivity of the straight edge barrier [Fig. 10(c)]. It should be recalled that for this configuration the point of first contact lies on the horizontal segment between the two triangles [see Fig. 5(d)] for all receiver locations. As a result, all receivers ''see'' the jagged edge barrier as a straight edge barrier and the measured directivity does not deviate from the theoretical one.

In the case of a sound absorbing barrier [shown in Fig. 10(b)], however, a considerable change in the directivity of the diffracted field can be observed. The deviations are more pronounced in front of the barrier than behind it. It should be emphasized that these deviations are not attributed to the interference between incident, reflected and diffracted signals in front of the barrier. Our measurements regard only the diffracted signals and resolve them from any other signal. A final observation for the sound absorbing barrier is that the diffracted signal does not vanish at $\phi=\pi$, as in the reference case of a rigid barrier, but at a smaller angle [compare Figs. 10(a) and 10(b) in the vicinity of $\phi=\pi$].

Finally, Fig. 10(d) shows that the directivity of the diffracted field around the second configuration of the jagged edge barrier follows the directivity of the straight edge barrier in zones B and C, but deviates considerably from it in zones A and D. This can be explained by the fact that the point of first contact lies on the horizontal segment for receivers in zones B and C, but at the junction of two inclined segments for receivers in zones A and D. As a result, receivers in the latter zones are more affected by the presence of the inclined segments in the edge profile. It should be noted, that the observation reenforces conclusions of a previous study on jagged edge barriers,[18] where it has been discovered that the part of the jagged edge close to the point of first contact plays a crucial role. This had been experimentally verified in the shadow zone behind the barrier. It can now be extended to all areas around the jagged edge barrier. Another conclusion from the same numerical investigation on jagged edge noise barriers had shown that changes of the directivity function along a jagged edge affect the diffracted field at receiver locations far from the edge considerably less than changes in the shape of the effective line source (from a straight line source to a jagged line source). In the particular case tested here, the relative angular position of the source is 90° for the straight segments and 92° for the inclined, which makes their respective directivity functions approximately the same. The drastic changes in zones A and D compared to zones B and C are not attributed to the change of the directivity between the straight and the inclined segments, but to the position of the point of first contact. Again, with the present study the previous conclusion is extended to all areas around the jagged edge barrier. Finally, it should be noted that the observed deviations in zones A and D seem to relate more to the amplitude than to the shape of the directivity function.

C. Comparison of the three types of barriers

In this subsection we compare the performance of the barriers with one another. First, let us take a look at the shape of the diffracted signals that each type of barrier produces (shown in Fig. 11). The straight edge barriers, regardless of the barrier surface treatment, produce smooth diffracted signals of small duration that, except for polarity inversion, maintain their shape at all receiver locations [compare Figs. 11(a) and 11(b) and 11(c) and 11(d)]. In the case of jagged edge barriers, however, the shape changes considerably [compare Figs. 11(e) and 11(f)] and at certain receiver locations smeared out signals of smaller amplitude are produced [see Fig. 11(e)].

Figure 12 presents the performance of the barriers by comparing the peak amplitude values of all the signals measured. Figure 12(a) shows that the sound absorbing material increases the shielding effect of the rigid barrier, in almost all receiver locations, with the exception of receivers in zone C, where the rigid barrier outperforms the sound absorbing barrier. The first configuration of the jagged edge barrier outperforms the straight edge barrier in all receiver locations, with its shielding effect more pronounced in the shadow zone behind the barrier [see Fig. 12(b)]. The second configuration of the jagged edge barrier, however, has a more spectacular performance than the first [see Figs. 12(c) and 12(d)]. It outperforms the straight one in all receiver locations, with its maximum performance in the shadow zone (zone D) and in the area in front of the barrier (zone A). The second jagged edge configuration reduces the peak amplitude of the diffracted signal by almost two thirds in the shadow zone behind the barrier (compared to a straight edge barrier) Finally, Fig. 12(e) compares two possible alternatives of retrofitting a straight-edge/rigid barrier to improve its effect: (i) modify its top edge or (ii) cover its surface with sound absorbing material. It can be seen that the improvement is quite comparable. However, because covering the barrier surface is a far more costly proposition, the jagged edge approach might be a viable alternative.

V. SUMMARY AND CONCLUSIONS

In the present work three different types of barrier have been tested experimentally: straight-edge/rigid-barrier, straight-edge/sound-absorptive-barrier, and jagged-edge/rigid-barrier. The experiments were conducted in the laboratory in air using a spark as the sound source. The diffracted signals were measured at various positions around the barriers on a plane perpendicular to their top edge and were resolved from any interference with incident and/or reflected

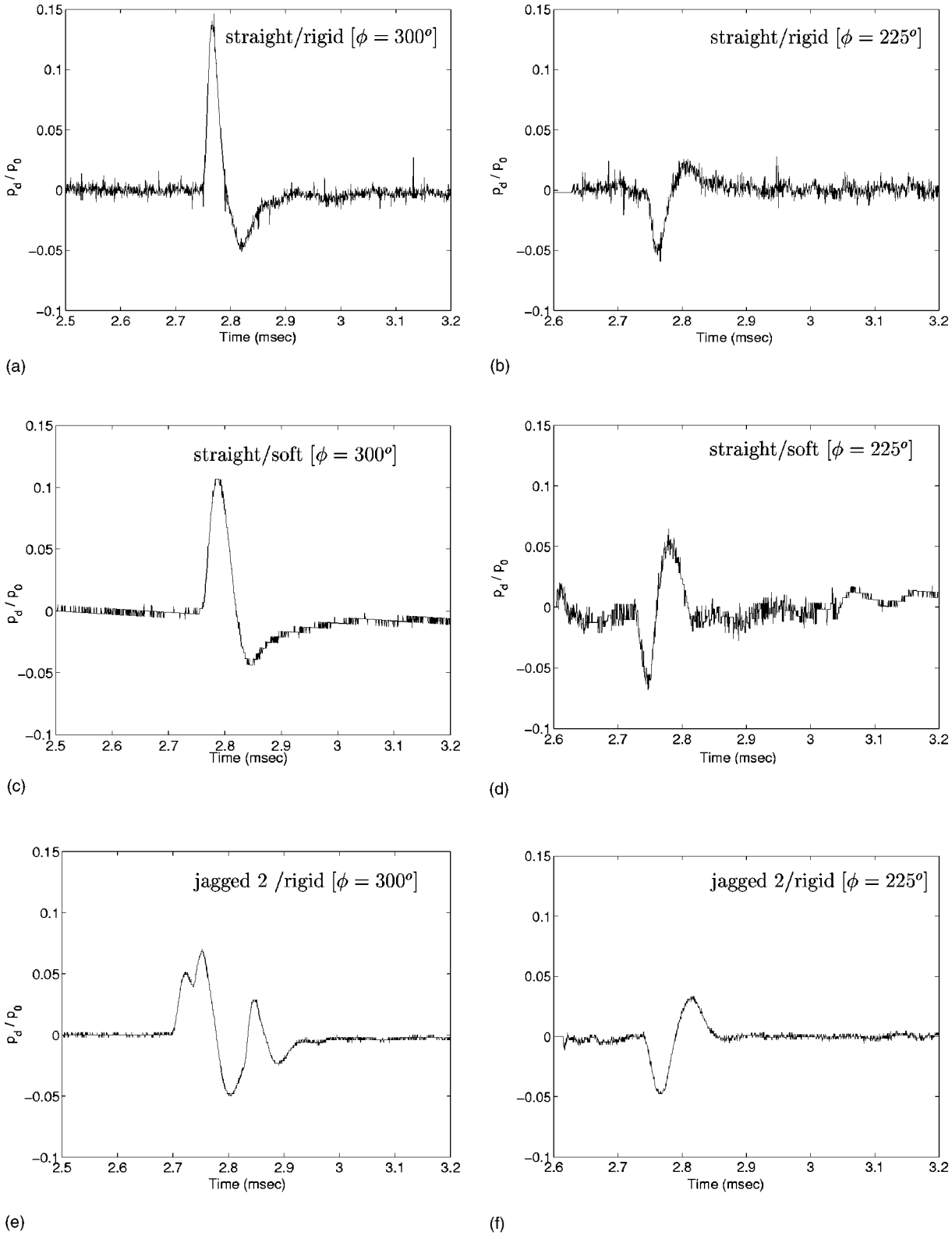

FIG. 11. Measured diffracted signals behind the three barrier types at two receiver locations: in the shadow zone behind the barrier at $\phi_{\text{rec}} = 300°$ and in the illuminated zone behind the barrier at $\phi_{\text{rec}} = 225°$. Data normalized so that the free-field signal has unity peak amplitude at 1 m away from the source.

signals. The measured data were presented, compared with analytical solutions and with one another. The results were as follows:

(1) DLSM validation

(a) The validation of the DLSM, formerly restricted to receiver locations in the shadow zone behind the barrier, was extended to areas in front of and above the barrier. The DLSM was found to yield accurate predictions in all regions around the barrier for the cases it was employed (straight-edge/rigid barrier and jagged-edge/rigid barrier).

(b) The portion of the jagged edge that is in the vicinity of the ''point of first contact'' plays a crucial role in deter-

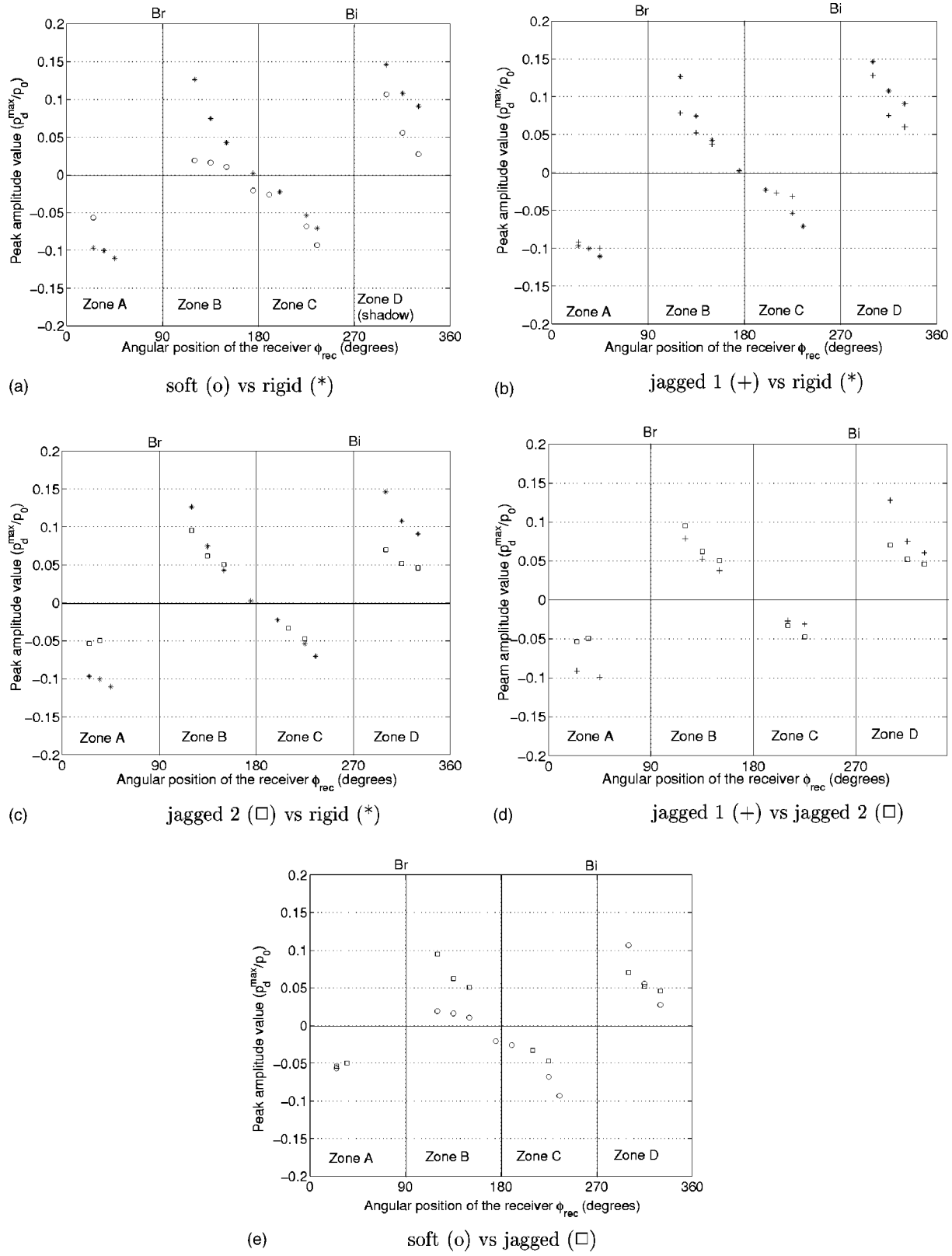

FIG. 12. Comparison between the types of barrier tested. Measured data. Peak amplitude values of the diffracted signals around the straight-edge/rigid barrier (∗), the straight-edge/sound absorptive (○), the jagged-edge/rigid barrier configuration 1 (+), and the jagged-edge/rigid barrier configuration 2 (□). Data normalized so that the freefield signal has unit peak amplitude value at 1 m away from the source.

mining the diffracted signal in all areas around the barrier. The fact that the directivity function changes along the jagged edge (it remains constant along a straight edge barrier) plays a secondary role. These qualitative observations extend previous conclusions that were restricted to the shadow zone behind the barrier.

(2) Directivity of the diffracted field

(a) In all cases tested, it was observed that the diffracted

signal changes its polarity three times as we move the receiver in a circle around the barrier: (i) when we cross the shadow boundary for the reflected field (B_r), (ii) when we cross the continuation of the half plane in the free space above it, and (iii) when we cross the shadow boundary for the incident field (B_i).

(b) Applying a sound absorbing material changes substantially the directivity of the diffracted field compared to the directivity around a rigid barrier. The most significant changes in the diffracted field can be observed in front of the barrier than behind it. This effect is not attributed to the interference of the diffracted signal with reflected and incident signals that are present in front of the barrier. In our study the diffracted signals were resolved from incident and/or reflected signals.

(c) For the jagged edge cases studied in the present work the following have been observed: The jagged edge leaves the directivity of the diffracted field almost unchanged (same as with a straight edge barrier), if the point of first contact lies on the horizontal segment of the edge profile but it does change the directivity (more the amplitude than the shape), if the point of first contact lies on different segments of the edge profile for different positions of the receiver.

(3) Barriers comparison

(a) The jagged edge reduced the peak amplitude of the diffracted signal by almost two thirds in the shadow zone behind the barrier (compared to a straight edge).

(b) The diffracted pressure signal for the straight-edge/rigid barrier, and straight-edge/sound-absorptive barrier is a smooth signal that considerably maintains its shape in all areas around the barrier. The diffracted signal produced by a jagged edge barrier is a smeared out signal of long duration and has different shapes at different receiver locations around the barrier.

(c) Comparing the application of sound absorbing material on the barrier and the introduction of jaggedness into its top edge as two means of improving the barrier's performance, the jagged edge appears to be a viable alternative. The jagged edge produced comparable results with only a fraction of the cost.

ACKNOWLEDGMENTS

The work presented here was supported by the Texas Advanced Technology Program. The authors are indebted to Dr. W. M. Wright for his valuable advice in the experiments.

[1] G. R. Watts, ''Acoustic performance of a multiple-edge noise barrier profile at motorway sites,'' Appl. Acoust. **47**, 47–66 (1996).
[2] G. R. Watts and P. A. Morgan, ''Acoustic performance on an interference type noise barrier profile,'' Appl. Acoust. **49**, 1–16 (1996).
[3] G. R. Watts, D. H. Crombie, and D. C. Hothersall, ''Acoustic performance of new designs of traffic noise barriers: Full-scale tests,'' J. Sound Vib. **177**, 289–305 (1994).
[4] D. C. Hothersall, D. H. Crombie, and S. N. Chandler-Wilde, ''The performance of T-profile and associated noise barriers,'' Appl. Acoust. **32**, 269–287 (1991).
[5] C. Wassilief, ''Improving the noise reduction of picket barriers,'' J. Acoust. Soc. Am. **84**, 645–650 (1988).
[6] L. S. Wirt, ''The control of diffracted sound by means of thnadners (shaped noise barriers),'' Acustica **42**, 73–88 (1979).
[7] D. A. Hutchins, H. W. Jones, and L. T. Russell, ''Model studies of barrier performance in the presence of ground surfaces. Part I: Thin, perfectly-reflecting barriers,'' J. Acoust. Soc. Am. **75**, 1807–1816 (1984).
[8] D. A. Hutchins, H. W. Jones, and L. T. Russell, ''Model studies of barrier performance in the presence of ground surfaces. Part II: Different shapes,'' J. Acoust. Soc. Am. **75**, 1817–1826 (1984).
[9] D. N. May and M. M. Osman, ''Highway noise barriers: new shapes,'' J. Sound Vib. **71**, 73–101 (1980).
[10] D. N. May and M. M. Osman, ''The performance of sound absorptive, reflective, and T-profile noise barriers in Toronto,'' J. Sound Vib. **71**, 65–71 (1980).
[11] S. I. Hayek, ''Mathematical modeling of absorbent highway noise barrier,'' Appl. Acoust. **31**, 77–100 (1990).
[12] C. D. Hothersall, S. N. Chandler-Wilde, and M. N. Hajmirzae, ''Efficiency of single noise barriers,'' J. Sound Vib. **146**, 303–322 (1991).
[13] K. Fujiwara and N. Furuta, ''Sound shielding efficiency of a barrier with a cylinder at the edge,'' Noise Control Eng. J. **37**, 5–11 (1991).
[14] K. Fujiwara, ''Noise control by barriers. Part 2: Noise reduction by an absorptive barrier,'' Appl. Acoust. **10**, 167–179 (1977).
[15] K. Fujiwara, D. H. Hothersall, and C. Kim, ''Noise barriers with reactive surfaces,'' Appl. Acoust. **53**, 255–272 (1998).
[16] T. Okubo and K. Fujiwara, ''Efficiency of a noise barrier with an acoustically soft cylindrical edge for practical use,'' J. Acoust. Soc. Am. **106**, 3049–3060 (1999).
[17] M. Moeser and R. Volz, ''Improvement of sound barriers using headpieces with finite acoustic impedance,'' J. Acoust. Soc. Am. **106**, 3049–3060 (1999).
[18] P. Menounou and I. J. Busch-Vishniac, ''Jagged edge noise barriers,'' J. Building Acoust. **7**, 179–200 (2000).
[19] S. T. Ho, I. J. Busch-Vishniac, and D. T. Blackstock, ''Noise reduction by a barrier having a random edge profile,'' J. Acoust. Soc. Am. **101**, 2669–2676 (1997).
[20] P. Menounou, I. J. Busch-Vishniac, and D. T. Blackstock, ''Directive line source model: A new method for sound diffraction by half planes and wedges,'' J. Acoust. Soc. Am. **107**, 2973–2986 (2000).
[21] M. J. Crocker and L. C. Sutherland, ''Instrumentation requirements for measurements of sonic boom and blast waves: A theoretical study,'' J. Sound Vib. **7**, 351–370 (1968).
[22] M. A. Biot and I. Tolstoy, ''Formulation of wave propagation in infinite media by normal coordinates with an application to diffraction,'' J. Acoust. Soc. Am. **29**, 381–391 (1957).
[23] H. Medwin, ''Shadowing by finite noise barriers,'' J. Acoust. Soc. Am. **69**, 1060–1064 (1981).
[24] H. Medwin and C. S. Clay, *Fundamentals of Acoustical Oceanography* (Academic, San Diego, 1998).
[25] A. L. Esperance, J. Nicolas, and G. A. Daigle, ''Insertion loss of absorbent barriers on ground,'' J. Acoust. Soc. Am. **86**, 1060–1064 (1989).
[26] A. D. Rawlins, ''Diffraction of sound by a rigid screen with a soft or perfectly absorbing edge,'' J. Sound Vib. **45**, 53–67 (1976).
[27] A. D. Rawlins, ''Diffraction of sound by a rigid screen with an absorbent edge,'' J. Sound Vib. **47**, 523–541 (1976).
[28] H. G. Jonasson, ''Diffraction by wedges of finite acoustics impedance with applications to depressed roads,'' J. Sound Vib. **25**, 577–585 (1972).
[29] A. D. Pierce and W. J. Hadden, Jr., ''Plane wave diffraction by a wedge with finite impedance,'' J. Acoust. Soc. Am. **86**, 17–27 (1978).
[30] T. B. A. Senior, ''Diffraction by a semi-infinite metallic sheet,'' Proc. R. Soc. London, Ser. A **212**, 436–458 (1952).
[31] W. E. Williams, ''Diffraction by an *E*-polarized plane wave by an imperfectly conducting wedge,'' Proc. R. Soc. London, Ser. A **252**, 376–393 (1959).

Acoustic pulse propagation in an outdoor turbulent atmosphere

I. D. Mcleod,[a] C. G. Don, and G. G. Swenson[b]
School of Physics and Materials Engineering, Monash University, Clayton, Victoria 3168, Australia

(Received 2 August 2003; revised 9 April 2004; accepted 17 June 2004)

In a series of short-range experiments, attempts were made to relate the prevailing meteorological conditions to significant wave shape changes in a 2 ms acoustic pulse propagating over distances from 0.5 to 16 m. Unlike the findings in long-range studies involving time and spatial averages, no meaningful correlations between wind speed and acoustic pulse shape parameters were obtained. Pulse delays could be predicted provided detailed measurements of the wind speed were obtained. Observations showed that two adjacent paths could experience quite different propagation regimes. The geometry and pulse nature of the experiments described here restrict the scale of turbules in any cascade suggesting that a single turbule model may be applicable. Indeed using one or two effective turbules was capable of explaining many of the observations. One model approach used typical parameter values obtained from the literature or from measurements and by locating a single turbule at an appropriate distance from the source receiver axis, correctly generated the observed variety of wave forms. Alternatively, relying on measured data from one distorted pulse and the spatial wind profile, the model was used to determine subsequent pulse distortions. This was successful in predicting behavior in 76% of cases.
[DOI: 10.1121/1.1781618]

PACS numbers: 43.28.Gq, 43.28.Js [DKW] Pages: 2855–2863

I. INTRODUCTION

Previously, understanding how turbulence causes changes to sound propagation has been limited to averaged effects. Generally, the variations in sound levels over a period of time have been related to fluctuations in the meteorological conditions. Both theoretical and experimental studies[1,2] of continuous wave propagation have shown that usually a correlation exists between the variance of the sound pressure level and the variance of the corresponding wind-dominated conditions. As they are time and spatial averages, such parameters are particularly relevant when dealing with long distance propagation over a period of time. Sonic booms are influenced by the snapshot of the atmospheric conditions present as the boom passes but, typically, this involves spatial averages over distances of kilometers. Both situations can be modeled by filling the source-receiver space with a distribution of turbules, with characteristics based on a measured power spectrum. This allows the number, size, and strength of the turbules to be determined, but not their location. Then a statistical approach, using arrays of turbules positioned along the propagation path, has been used with reasonable success, to estimate either the variations in the sound field[3–5] or the distribution of sonic boom wave forms and rise times.[6,7] The classic *N* wave of a sonic boom can display a wide variety of wave forms at a distant receiver[8] and these shapes can often be explained using the above-mentioned models.

In contrast, to avoid averaging effects, the current study used acoustic pulse propagation together with a snapshot of the meteorological conditions in the traversed region. A detailed knowledge of the wind structure over hundreds of meters was difficult to obtain. However, for the pulses used in this investigation, significant shape changes occur over short paths, for example, 16 m, and it was anticipated that the wind speed characteristics could be adequately determined over this distance. Initially, simple relationships between the meteorological and acoustic variables were expected. As discussed in the following, this did not occur. One advantage of using an impulse technique compared to cw measurements was that the direct and ground reflected components could be time isolated to investigate whether they experienced the same turbulent field. Because of the constraints imposed by this pulse experiment it seemed inappropriate to apply concepts based on cascade statistical parameters[9] so an attempt was made to test the validity of a simple isolated effective turbule model.

II. MEASUREMENT OF PULSE CHARACTERISTICS

A. Experimental systems: Circular and linear arrays

A circular array, Fig. 1, had six microphones positioned around the circumference of a 4 m diam. circle, at right angles to and coaxial with the source axis, on flat grass-covered ground. Each microphone was fixed to the end of a thin rod which was mounted horizontally from slender vertical masts. These uprights were stayed by a number of thin string supports, so that the rig did not move in the wind yet there was a minimum of reflecting surfaces. Impulses were generated by discharging shot-shell primers down a tube,[10] and were captured using 6 mm (1/4 in.) diameter Bruel & Kjaer type 4135 microphones and a Data Precision 6100 wave form analyzer with a dynamic range of 90 dB using a 5 μs sampling interval.[10,11] Because of the cylindrical symmetry of the source, in the absence of wind this arrangement

[a]Present address: Airservices Australia, 25 Constitution Avenue, Canberra 2601, Australia
[b]Electronic mail: gswenson@connexus.net.au

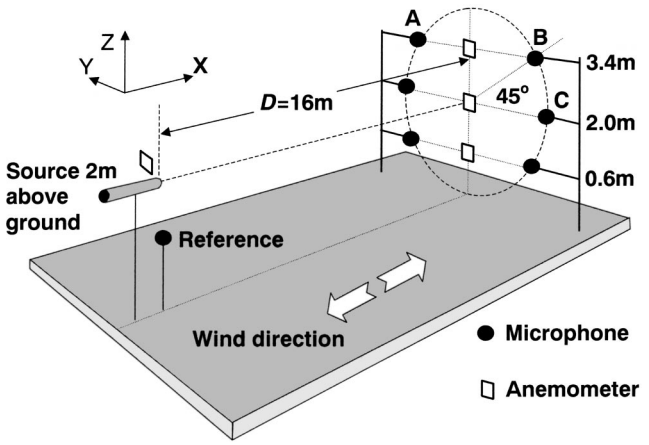

FIG. 1. Experimental geometry, with microphone and anemometer positions in the circular array. The three labeled microphones, A–C, are those used to obtain the data discussed in the text.

produced essentially identical pulse shapes[10] at each of the receiver microphones after subtracting any ground reflections. Peak receiver levels were typically around 120 dB at 1 m in front of the source. To eliminate source variations, a reference microphone was placed off axis 0.5 m from the source where effects due to turbulent changes had been shown experimentally to be negligible, as discussed in the next section.

Alnor type GGA-26 thermo-anemometers were positioned near the source and in a vertical line through the center of the array. Their response time of 100 ms was adequate as comparison measurements with a single anemometer of much higher frequency response gave near-identical results. The anemometers were aligned to measure the *X* component of the wind speed, with their outputs sampled at 10 ms intervals and stored on computer disk. Data were only collected when the wind direction was aligned with the *X* axis of the system, as judged by the average attitude of a series of light cloth flags positioned around each site. In some experiments, an additional anemometer was orientated at right angles to the *X* axis to measure the off-axis wind component. During the flight time of a pulse, the observed fluctuations in temperature were significantly less or negligible compared to those in wind speed, with no appreciable change between source and receiver temperatures. These findings were consistent with those of other studies[8,12] and so the effects of temperature were not considered further. To obtain upwind and downwind measurements, the source could be moved to the other side of the array or a second source employed.

In separate experiments, a 15 m linear array was used to observe the spatial evolution of the pulse wave form, with the source and three microphones uniformly spaced 5 m apart horizontally, slightly offset to avoid blocking sound reaching the more distant microphones. Anemometers were positioned adjacent to the source and microphones, although care was taken to minimize reflections into the microphones. As in the circular array experiments, a 0.5 m off axis reference microphone was used near the source.

B. Indoor measurements of pulse pressure values

To establish the degree of variation in the source, measurements were undertaken in a large hall following the geometry of Fig. 1, to check the symmetry and reproduction of the source. Indoors, with no wind present, the flight times of successive pulses were reproducible to one or two data points on the time axis, i.e., ± 10 μs, and floor reflection occurred at a constant delay. None of the data or wave forms presented in this paper include the ground reflection, unless specifically noted. At 0.5 m pulses exhibit different peak heights due to source variations, however, when adjusted to have the same peak height, their shapes essentially overlapped. Consequently for all further measurements the peak height of a pulse recorded by an off axis reference microphone at 0.5 m was used to normalize all pulses from that discharge to that of the first measured pulse. This procedure was termed source normalization. After applying this adjustment, ensemble averages of 30 individual shots at the various microphone positions on the measurement circle shown in Fig. 1 closely agreed with each other and with those of repeated data sets. From such measurements an average indoor benchmark wave form at each required range was determined whose peak height was then used to standardize all individual pulses. Consequently, all standardized indoor pulse heights have a value close to one, whereas meteorologically affected outdoor pulse heights diverged from unity. Also, contours corresponding to 1.5 standard deviations away from the mean at 16 m were determined, shown as the two thin lines in Fig. 2(a), and were found to be independent of microphone position.

To eliminate the possibility that the received pulse changes observed outdoors were due to wind–source interactions, measurements were taken indoors with fans blowing across the end of the source tube. These produced no significant distortions outside the contours obtained indoors without the fans.

A relative measure of the total energy content of a pulse was obtained by summing the square of successive instantaneous pressure values until the increase from the sum of the next five adjacent channels was less than 0.01%. The energy content of an outdoor pulse was then standardized by dividing by the corresponding value for that of the benchmark indoor pulse. For indoor pulses the maximum variations in the standardized peak height and energy content are 2% and 5%, respectively. Less than 5% of the total energy occurred in the tail, Fig. 2(a).

C. Variation in pulse properties outdoors

Measurements at 0.5 m indicated that the outdoor distributions of wave forms and peak heights were identical with those obtained indoors at this distance. This justified the use of the peak height at this microphone as an adjusting factor, for source normalization, of each shot. Importantly, the similarity of indoor and outdoor results at 0.5 m implies that turbulence effects at this distance on these pulses are negligible.

The six-microphone circular array allowed the influence of turbulence on a single impulse arriving at a number of equal range microphones to be investigated. Although propagating nearly parallel to the wind direction through a distance of only 16 m, pulses from a single shot often arrived at two microphones on the circle at times differing by as much

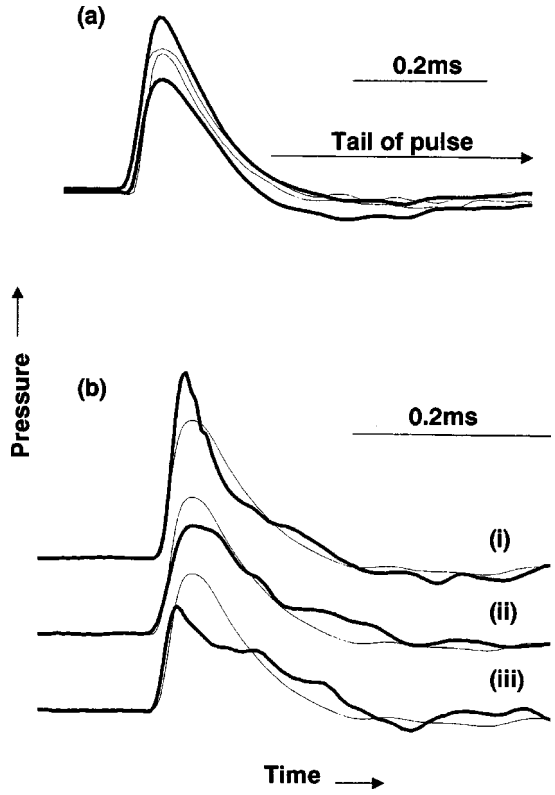

FIG. 2. (a) Ensemble averaged indoor (thin lines) and outdoor (thick lines) pulse wave shapes, each 1.5 standard deviations from the mean. The indoor peak value is scaled to one. (b) Three examples of outdoor pulse shapes (thick lines) compared with the indoor reference pulse (thin lines).

as ± 0.2 ms, the duration of the pulse head, indicating that two flight paths diverging by as little as 6° could experience quite different wind regimes.

Further, pulses derived from a single shot often showed little correlation between peak heights and shapes, even for two microphones only 1.5 m apart on the circular array, i.e., flight paths diverging by 6° at the source. The shot to shot variation in standardized peak height between three microphones is apparent from Fig. 3 where 80% differ well beyond the experimental uncertainty, indicated by the symbol size. In some cases, a 10% change in peak height could occur between two wave forms with a change of similar magnitude but of opposite sense occurring in the third wave form originating from the same initial discharge.

Figure 2(a) shows the ± 1.5 standard deviation contours

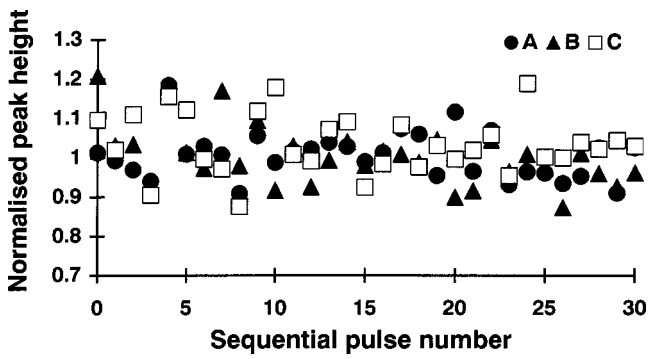

FIG. 3. Standardized peak values for 30 consecutive pulses at microphones A, B, and C of Fig. 1.

generated by ensemble averaging many hundreds of outdoor pulses obtained at 16 m. Many individual pulses, however, exhibit much greater deviations than indicated by the averaged contours. Figure 2(b) shows examples of (i) a pulse with enhanced peak height, (ii) a pulse with reduced peak height, and (iii) a pulse with a very irregular shape. A strong relationship exists between standardized energy and the corresponding standardized peak height, giving essentially the same result for pulses propagating either up or down wind. This implies that it is immaterial whether energy or peak height is used as the acoustic parameter when seeking correlations with meteorological data.

It might be expected that enhanced or diminished pulses would have a corresponding increased or decreased energy content. While this was generally true, 2% of 260 outdoor cases examined were inconsistent with this hypothesis. These atypical examples were associated with highly distorted pulse shapes, as in example (iii) of Fig. 2(b). Overall, the energy of the main peak could change by more than 15%. At 0.6 m, the partially inverted ground reflection could cause the standardized energy to reach 1.8 with 6% of cases exceeding 1.5, whereas there were no examples of such extreme increases at either of the other heights. These ground reflection cases were excluded from the following considerations.

At 2 and 3.4 m the direct and ground reflected pulses were well separated, however, there was no correlation between the corresponding peak heights. This implies that the two paths generally experience different turbulent regimes. However, the ensemble average of the direct and of the reflected pulses were very similar, indicating that the long-term averaged effect was independent of the path, i.e., the local turbulence. This has implications for continuous wave calculations involving direct and reflected components where it is assumed that both rays experience the same turbulence.[13] Further, the fact that two pulses simultaneously traveling along nearby paths are subject to quite different wind regimes highlights the difficulty of trying to categorize the nature of the turbulence from measurements at a few anemometer positions.

Over 80% of pulse wave shapes were altered significantly in a turbulent atmosphere in either up- or downwind propagation.[14] Of those with a reduced amplitude, 61% were broader with very few narrower, while 55% of the increased amplitude peaks were narrower with only 4% marginally wider than the average wave form. Here, pulse widths at half height were assumed to be the same as the indoor value if they were within $\pm 2\%$ of it. Small broad irregularities were often observable in the tail region, about 25% being in the same direction as the peak, and 44% in the opposite direction. Generally, the magnitude of this scattered energy diminished as the delay increased. All the observed irregularities occurred within 1.3 ms from the onset of the main peak, suggesting that the maximum deviation of significant sound energy from the direct source-receiver path was less than 2 m. In additional experiments, a receiver height of 4 m was used to give a 2.5 ms clear region before the ground reflection arrived. Once again, no additional scattered energy could be detected beyond 1.3 ms, confirming that the signifi-

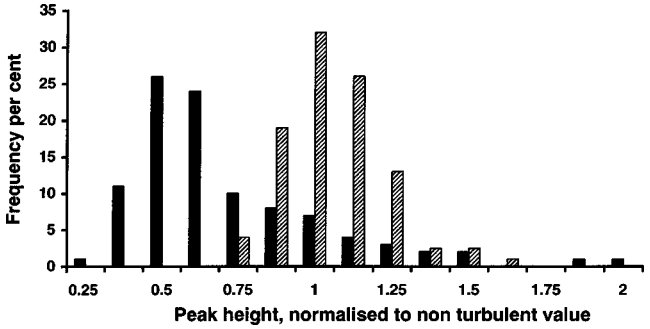

FIG. 4. Histograms of peak height for sonic booms (solid) compared to that of pulse data obtained in this work (hatched).

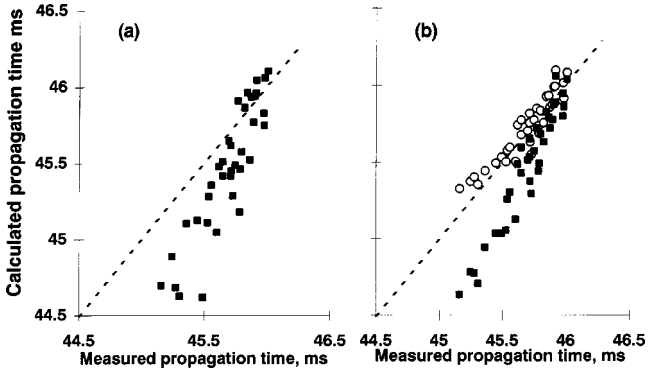

FIG. 5. Two examples of calculated vs measured propagation time (squares) using (a) mean of two readings (correlation coefficient, $r=0.90$) and (b) a cubic fit to four anemometer readings, ($r=0.96$) showing the improved fit. Note the data do not follow the 1:1 line, shown dashed, unless a correction is made for wind shear (circles).

cant scattering regions lie close to the direct path.

Our data show there are almost as many enhanced as attenuated pulses, consistent with the average indoor pulse being almost identical to the ensemble averaged outdoor pulse. However, when sonic boom measurements[7,8] are standardized to eliminate attenuation with distance effects, the distribution is skewed as the majority of pulses are markedly attenuated (Fig. 4). Skewed distributions were also found in model experiments using high frequency sparks.[15] Our symmetric result may arise because of the different scales involved. If the range of our outdoor experiments was extended, the acoustic pulse histogram may become skewed, and so the near identicality between indoor and outdoor average pulses would no longer hold.

III. PULSE AND METEOROLOGICAL INTERACTION

Initially a relationship was sought between pulse flight time and a measure of the wind speeds along the path. The additional delay, Δt, due to an effective wind speed, v_{wind}, acting over a distance D is given by,[16] $\Delta t = \mp D v_{\text{wind}}/c_0^2$, where c_0 is the speed of sound in still air and the minus and plus signs apply to downwind and upwind propagation, respectively. Wind speeds in the current experiments averaged $\pm 3.4\ \text{m s}^{-1}$ with maximum instantaneous values up to $10\ \text{m s}^{-1}$ but even during the short flight time of a single pulse, the wind speed varied along the path, so the problem was to choose the appropriate value for v_{wind}. Time-averaged wind speeds were measured over an interval exceeding the flight time at four anemometers equally spaced along the flight path. When the measured propagation time was compared to the calculated propagation time using just the source anemometer measurement a weak correlation was obtained. However, including the additional anemometer data along the path to estimate v_{wind} improved the correlation (Fig. 5). If the curvature of the flight path due to wind shear was also included, the data points fitted closely on a 1:1 line, indicating that there was no extra delay due to multiple scattering or other processes. The difficulty of determining an appropriate v_{wind} emphasizes the need for a detailed knowledge of the meteorological information.

Unlike the results from long-range and time-averaged continuous wave propagation studies, where correlations exist between meteorological and acoustic variables,[1,2] no correlation was found in our measurements between pulse height or energy and a variety of wind speed measures. These included instantaneous and averaged values from multiple anemometers, the variance of the wind speed or mean measures calculated from the application of Taylor's ''frozen turbulence'' hypothesis, i.e., that the wind speed pattern propagates at a constant velocity,[17] to generate a spatial wind speed trace at the time of shot. Instead of considering individual pulse properties, groupings of pulses were used following the approach of continuous wave analyses where the variance of the acoustic signal is often considered. Data for over 2400 pulses were sorted into 14 groups, with each group of about 170 pulses having approximately the same wind speed spread. The variance for peak heights was determined for each group and plotted against the various wind speed parameters described earlier, again with no improvement in the correlation.

As alternative measures of the wind speed variation, Tatarskii[18] used the product of the correlation length, L, and the variance in the refractive index, $\langle \mu^2 \rangle$, and also the structure parameter C_v. Using the method in Ref. 19, L was estimated from a 20 s wind trace centered on the shot. More than 180 individual wind traces were recorded simultaneously at both source and receiver. Rarely did the curves fit the Gaussian displacement function expected for frozen turbulence. Figure 6(a) shows an example where both source and receiver autocorrelation functions are initially consistent within themselves and with the Gaussian model, while a commonly occurring divergent case is shown in Fig. 6(b). In general the correlation lengths fell between 1 and 10 m with the two corresponding values often closely agreeing, although 50% of them differed by more than 1 m. Whilst the estimation of L is questionable,[9] it was used to allow application of the Tatarskii model and to estimate turbule size as discussed shortly. Figure 6(c) shows a plot of the variance in peak height against the parameter $\langle \mu^2 \rangle L$. The size of the error bars in Fig. 6(c) was calculated from the variation of L occurring within the group. Again, no strong correlation was observed. Correlation lengths estimated from a 50 ms segment of the wind speed did not improve the result. Similar results were obtained when C_v was utilized. The general lack of correlation amongst the various attempts to relate the me-

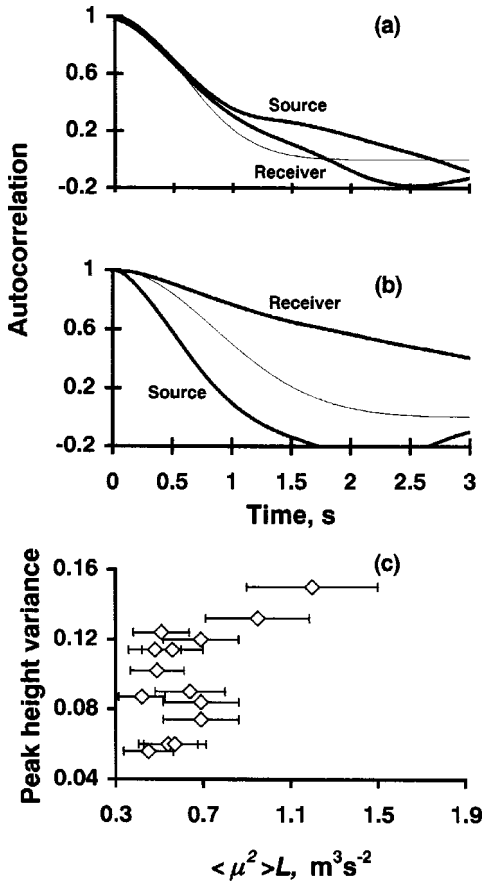

FIG. 6. Autocorrelation functions at the source, receiver (thick lines) and for a Gaussian fit (thin line) where (a) the wind initially conformed with Taylor's hypothesis and (b) where it disagreed. Such L values were used in the plotting of the peak height data as a function of $\langle\mu^2\rangle L$ shown in (c).

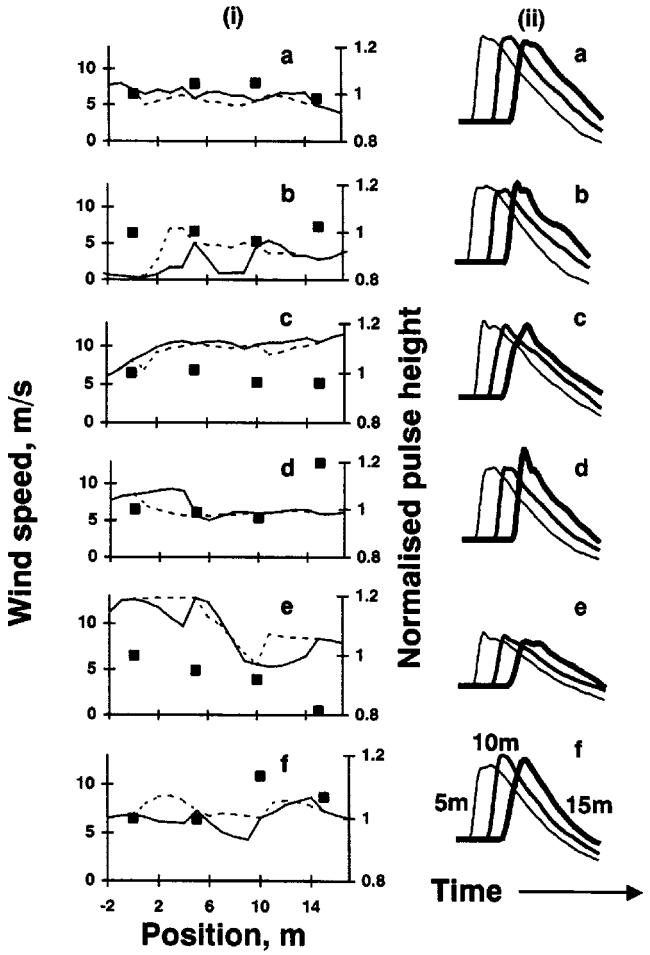

FIG. 7. (i) Six examples of spatial wind speed variation at time of shot for upwind (solid curve) and downwind (dashed curve) conditions. The squares show the standardized pulse heights at 5, 10, and 15 m, while (ii) shows the corresponding pulse shapes at the same ranges.

teorological and acoustic parameters outlined here led us to consider an alternative course.

IV. A TURBULE APPROACH

An attempt was made to follow the evolution of a single pulse over a 15 m range. Experimentally, pulse shape changes were observed by 5 m while none were detected at the 0.5 m reference microphone suggesting that scales between these limits were largely responsible for the distortions. For this narrow size range we assumed that, for simplicity, the turbulent cascade could be modeled by one effective turbule. Because of the simple nature of the model, the use of nonspherical turbules[20] was considered unnecessary. Initially typical literature values were used to specify the turbule parameters but then two subsequent approaches made increasing use of the measured meteorological and acoustical data.

Of 200 wind traces, 20 s long, taken at both source and receiver positions 15 m apart, only 8% conformed to Taylor's hypothesis after time shifting. Generally, the average wind speed at the source and at the receiver differed by about 0.6 $m\,s^{-1}$. However, instantaneous differences in speed between the two aligned Taylor's plots could exceed 2 $m\,s^{-1}$. In about 8% of cases there were gross discrepancies. It was postulated that a significant difference between the time shifted profiles may indicate the presence of a disturbed region, or turbule, which could distort the acoustic pulse.

Using the linear array, 4 s wind speed traces, centered on the shot time were used to deduce the local mean wind speed at each anemometer. Spatial wind speed profiles were determined using Taylor's hypothesis by projecting at 1, 2, 3, and 4 m intervals in both the forward and backward directions from each anemometer along the array. The 5 m value was assumed to be equal to that actually measured at the next anemometer. Upwind and downwind predictions of the profiles in Fig. 7(i) can agree quite well, over limited regions or not at all.

Superimposed on the wind profiles in Fig. 7(i)a–(i)f are the measured pulse peak height values at each position after standardization. There is little change in the peak height with distance in cases (i)a to (i)c, although in (i)b there are quite marked variations in the wind speed around the 5 m microphone position. In case (i)d the peak height has marginally decreased at 10 m but then increases markedly by the 15 m position, yet there is almost no wind speed fluctuation evident after the 5 m position, where the peak level is unaltered from its initial value. In case (i)e there is a steady decrease in peak height over the whole range although the wind speed has its greatest change around the 7 m mark. In (i)f, discrep-

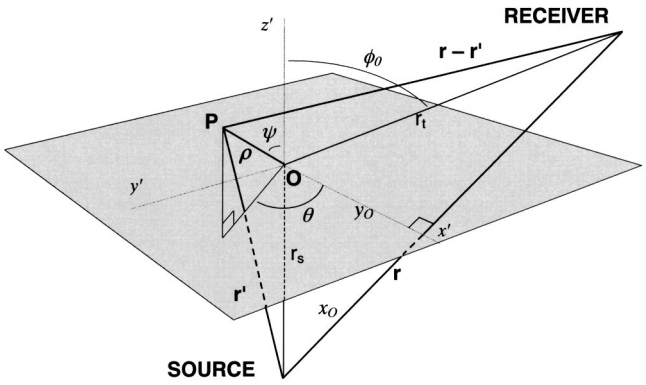

FIG. 8. Scattering geometry for a soft turbule.

ancies between the wind speed traces up to 10 m may be the cause of the increased pulse height at the 10 m position but there is no equivalent explanation for the decrease recorded at 15 m.

The corresponding pulse wave forms recorded at the 5, 10, and 15 m positions are presented in Fig. 7(ii)a–f. The zero position wave form is essentially the same in all cases and is not shown here. While the peak values change only slightly in cases (ii)a to (ii)c, there are significant alterations to the wave forms. At the 10 m mark, the start of the pulse has been reduced in (ii)b and enhanced in (ii)f, although the wind traces are relatively flat around these sites in both cases. Overall, there is no obvious, consistent pattern in the wind traces which correlates with pulse distortion. By monitoring the wind conditions at closer spacings, say 1 m as compared to 5 m, more precise values of the profiles could be obtained resulting in more reliable estimates of the correlation length L and derived turbule parameters.

De Wolf [21] suggested that an isotropic, nearly transparent turbulent medium could be modeled as an agglomeration of turbulent eddies with random positions and velocities. Each turbule is characterized by a Gaussian refractive index profile,

$$\mu(r) = q \exp[-(\mathbf{r}-\mathbf{r}_s)^2/s^2], \tag{1}$$

where s denotes the effective size of the turbule in Fig. 8. When $q>0$, the wave speed decreases as the center of the turbule is approached, while $q<0$ corresponds to an increasing wave speed. The magnitude of q depends on the standard deviation of the refractive index variation, $\langle \mu^2 \rangle$, and the number of turbules, N_0, such that

$$|q| = [8\langle \mu^2 \rangle / (\pi \sqrt{\pi} N_0 L^3)]^{1/2}, \tag{2}$$

where $L=\sqrt{2}s$ is the correlation length. Assuming the above-noted Gaussian profile for $\mu(r)$, the scattered pressure component $\Delta P(\mathbf{r})$ is given in Eq. (A1). Depending on the choice of coefficients (Table I), a small angle approximation may be made,[3] however, the full second-order calculation was utilized here.

The resultant distorted pulse is assumed to be the sum of a direct undistorted pulse and one scattered from a single spherical turbule positioned at a distance x_0 along, and y_0 normal to, the source–receiver axis. Both pulses are attenuated according to the inverse square law. The indoor pulse wave shape at the appropriate range is used as the direct pulse. To obtain the scattered pulse, the indoor wave shape is Fourier transformed, then Eq. (A3) with the full second-order coefficients is applied to each frequency component, before inverse transforming to obtain the time domain resultant. Initially, for calculation purposes, it was assumed that $L=2.5\,\mathrm{m}$ and $\langle \mu^2 \rangle = 5\times 10^{-6}$, typical of meteorological data quoted in the literature and $N_0 = 1/15\ \mathrm{turbule\,m^{-3}}$, corresponding to one turbule in a cylinder 1 m^2 in cross section between the source and receiver. For negative q, enhancement and peak narrowing occurs, the extent decreasing as y_0 (Fig. 8) increases [Figs. 9(a) and (b)]. By contrast, for positive q, the negative going scattered pulse can either enhance or decrease the direct pulse depending on the y_0 offset. In Fig. 9(c), the scattered pulse effectively delays the resultant pulse while in (d) it has been diminished and broadened. Thus this model can generate many of the observed pulse waveforms.

To achieve a more specific test, pulse wave forms and the corresponding speed profiles were recorded to estimate L and hence $|q|$ and s. Three examples of the calculated wave forms are shown in Fig. 10, where y_0 has been chosen to give the best fit with the observed pulse, assuming a single turbule located half way between the source and receiver. These examples show it is possible to generate the observed wave form but a better knowledge of the parameters is required to match magnitudes. Further studies maintained the value of y_0, but allowed s to vary by doubling or halving the measured value of L. Additionally, both x_0 and y_0 were al-

TABLE I. Coefficients to be used in Eq. (A3), depending on the approximation applied.[a]

	First order	Second-order small angle	Second-order full		First order	Second-order small angle	Second-order full
s_x^2	$\frac{s^2}{1-ia}$	$\frac{s^2}{1-ia}$	$\frac{s^2}{1-i(a-b)}$	$\mathbf{K_x}$	$-k\sin\phi_0$	$-k\sin\phi_0$	$-k\sin\phi_0$
s_y^2	$\frac{s^2}{1-ia}$	$\frac{s^2}{1-ia}$	$\frac{s^2}{1-ia}$	$\mathbf{K_y}$	0	0	0
s_z^2	$\frac{s^2}{1-ia}$	s^2	$\frac{4D^2}{4+B^2s_x^2D^2}$	$\mathbf{K_z}$	$k(1-\cos\phi_0)$	$k(1-\cos\phi_0)$	$k(1-\cos\phi_0)-\frac{ikBs_x^2}{2}$

[a] $a=(ks^2/2)(1/(r_s+r_t))$, $b=ks^2\sin^2\phi_0/2r_t$, $B=k\sin\phi_0\cos\phi_0/r_t$, $D^2=s^2/(1-ib)$.

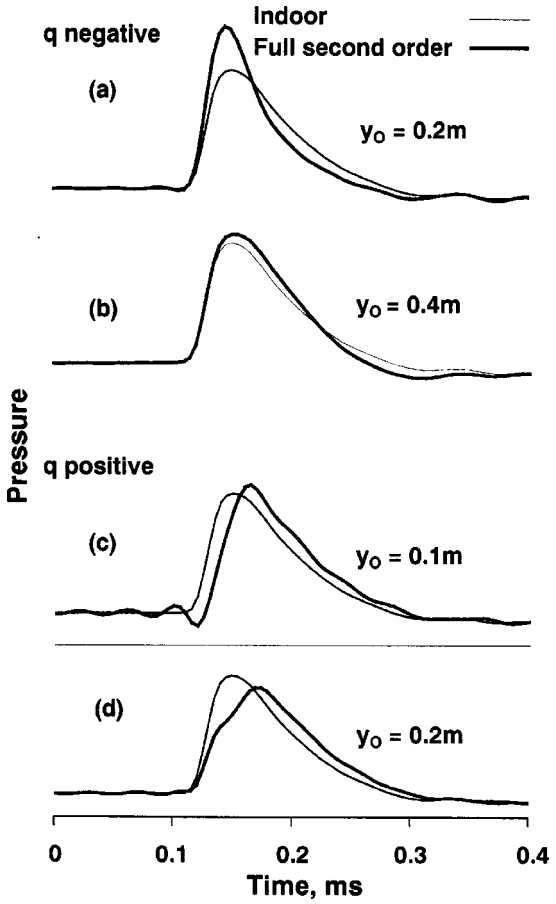

FIG. 9. Calculated pulse wave forms using the full second-order approximation for negative and positive q at two turbule offsets, y_O, assuming $L=2.5$ m, $\langle \mu^2 \rangle = 5\times10^{-6}$, and a density of 1 turbule per 15 m^3.

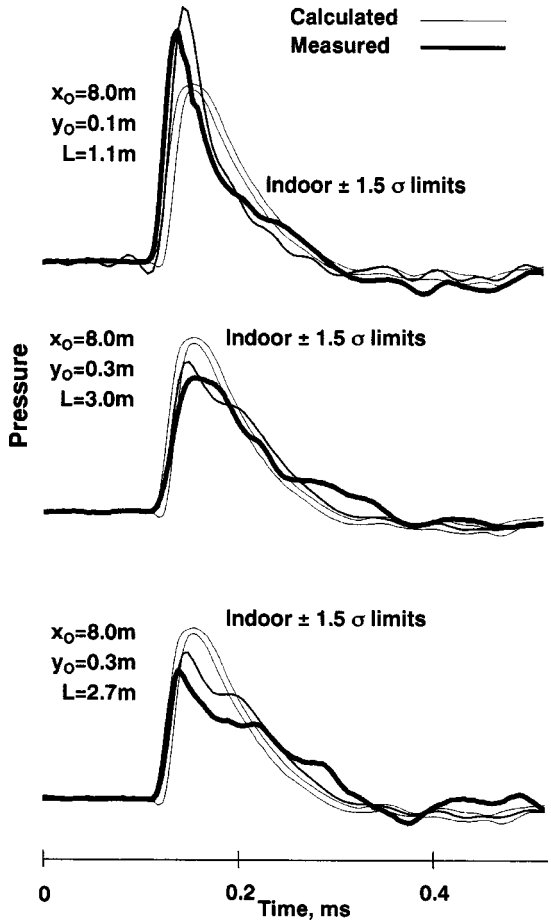

FIG. 10. Calculated pulse wave forms using the full second-order approximation where L, $|q|$, and s were obtained from measured spatial wind speed profiles, compared with measured wave forms. For reference, also shown are the indoor 1.5 standard deviation lines.

lowed to alter, while keeping the delay of the scattered component constant. None of these variations improved the match between the calculated and measured pulse wave forms and in some cases was detrimental.

A third test of the turbule theory, which relies almost entirely on measured data, involves using both wind speed profiles and one of the pulse wave forms obtained simultaneously, e.g., one of the data sets from Fig. 7. In this approach, a turbule is assumed to be located at an x position where there is a significant difference between upwind and downwind profiles, i.e., where Taylor's hypothesis has failed, such as at $x=3$ m in Fig. 11(a). L and $\langle \mu^2 \rangle$ were determined from the average of the values at the two measuring stations nearest to the turbule. The sign of q was found from the change in peak height of a measured wave form, in this case the pulse at 5 m. The optimum y value was obtained from the best fit between the reconstructed and measured wave form, again at the 5 m position. Using this information, the expected pulse shapes at 10 and 15 m were predicted and compared with the measured wave forms, as shown in Fig. 11(b). The optimum offset was 0.1 m at $x=3$ m, however, these choices give a reasonable but not exact fit to the 5 m wave form. At the 10 and 15 m positions, a noticeable scattered pulse is predicted to arrive almost simultaneously with the direct peak. Overall, the calculated wave forms match the measured wave form at 15 m but not at the 10 m position, where experimentally no significant change was observed from the 5 m wave form. In terms of the analysis, the wave form at 15 m was considered as a ''match'' whilst the pulse at the 10 m position was considered a ''no-match'' result.

The possibility of effectively having two spherical turbules along the flight path was also considered. In 3 of the 19 wind speed profiles investigated in detail, the velocity profile suggested it was necessary to invoke a two-turbule structure. In these cases, two of the three available wave forms had to be used to generate the turbule parameters, leaving only one pulse shape to be predicted. Of the 7 cases where the wind profiles suggest that no turbule was present, there were only three cases where all the wave shapes, i.e., at 5, 10 and 15 m, showed no significant distortion. However, in the other four cases considerable changes were observed at one microphone and, in one case, at all three microphones. In a different case a turbule was apparently present at 3 m yet there was no observable difference to the wave forms at either 5 or 10 m. So the technique of using wind profile differences to predict the presence of a turbule is limited. Of the remaining 11 cases where calculations were possible, 3 required a two turbule model leaving 19 wave shapes to be predicted. Of these 7 out of the 8 were correctly matched at 10 m and all at 15 m. This high predictability is, however, reduced to 76% if

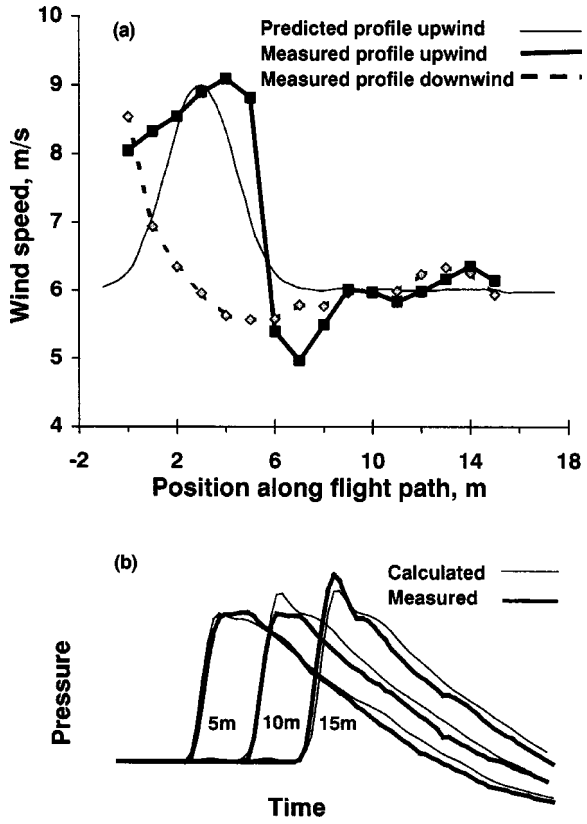

FIG. 11. (a) Measured spatial wind profiles and predicted profile for the case of Fig. 7(i)d. (b) Predicted pulse shapes at 10 and 15 m for this case. The 5 m curve is not a prediction but is the best fit based on optimum parameter values.

the 7 cases where no turbule seemed to be present, are included.

V. CONCLUSION

Over 80% of the thousands of recorded outdoor pulses at 16 m were distorted, however, the ensemble averaged outdoor pulse wave forms agreed quite closely with the undistorted indoor wave form. Results outdoors depended very much on the meteorological conditions along the particular flight path, as evidenced by the different distortions suffered by rays diverging by only a few degrees. This applied to both direct transmissions and those reflected from the ground. Average results were independent of the propagation direction either upwind or downwind.

Despite the pulse flight time measurements indicating that the measured wind conditions along the flight path were relevant to the behavior of the individual pulse, no significant correlation was found between the changes in peak height or the energy content of individual pulses and many different measures of the fluctuations in the wind speed. The weak trend possibly apparent in Fig. 6(c) was by far the most significant relationship detected. Nearly adjacent paths may experience different turbulent regimes. This finding has implications for continuous wave calculations.

Attempts to predict up- and downwind speed profiles from anemometers spaced 5 m apart met with limited success, indicating the space sampling was not fine enough. This is compounded by the need to involve off axis measurements. Future characterization of outdoor wind speed regimes will require very comprehensive instrumentation to obtain meaningful data. The need for adequate wind speed information could also be relevant to applications such as computer tomography where relative pulse flight times are used to identify a source location.[22]

An effective single turbule model predicted almost all of the observed outdoor peak distortions and allowed all the turbule parameters to be predicted, except for the sign of q which had to be determined from whether the pulse was enhanced or reduced. Alternatively, the turbule parameters can be found by matching the wind speed profile. From our preliminary investigation, when differences in wind speed traces and corresponding changes to the pulse wave form can be linked, the scattering calculations reliably predict pulse behavior along the propagation path. The major limitation lies in reliably establishing the presence of a turbule. Perhaps a closer anemometer spacing would allow a more precise location and determination of the number of turbules, though it should be noted that the spacing was related to the size of the turbule that would be detected. The model predictions were based on the questionable estimates of μ and L, which gave turbule diameters between 1 and 3 m. The success of the calculations suggest that these values are not critical.

While the current single effective turbule model can explain many of the peak distortions it does not successfully explain the delayed irregularities, either upright or inverted, observed in the tail of many pulses. To get such long delays, a turbule has to be located well away from the direct path, implying relatively large scattering angles. For this condition a turbule is a very inefficient scatterer giving rise to amplitudes much less than those observed. However, more complex mechanisms[20] may prove useful in explaining these long delayed components.

Measurements by others over long ranges have invoked large arrays of turbules of various symmetries.[7,20] However, the current experiments are quite different as they involve much shorter times and distances. No significant distortions were observed at the reference microphone suggesting that scales less than 0.5 m do not contribute strongly to scattering in these experiments. Distortions are evident at 5 m implying that such scales are important. This limited scale range suggests that for our pulse experiments a single effective turbule model may be sufficient. Indeed, many of our results are consistent with turbule sizes of the order of 1 to 2 m. Furthermore, the experimental observation that the direct and ground reflected pulses experience quite different turbulent regimes is consistent with turbule scales around a meter. Moreover the dominant energy of our pulses[10] corresponds to a wavelength around a meter, suggesting that the pulses will interact with turbules of this scale.[9] Thus we were concerned with predicting the properties and position of an effective turbule, not with ensemble averages. Whilst by no means completely successful, this work supports the potential of this approach in estimating the turbule parameters. Further development would require much more detailed knowledge of the meteorological conditions.

APPENDIX

Following Eq. (A7) of McBride *et al.*,[3] the change in pressure at the receiver due to scattered energy from a turbule located at $\mathbf{r}'$ can be shown to be

$$\Delta P(\mathbf{r}) = -\frac{Ak^2}{2\pi}\int_{\mathrm{Vol}}\frac{\mu(\rho)}{|\mathbf{r}-\mathbf{r}'|}\frac{e^{ik(|\mathbf{r}-\mathbf{r}'|+|\mathbf{r}'|)}}{|\mathbf{r}'|}d^3r', \qquad \text{(A1)}$$

where A is amplitude of the unperturbed source, $\mu(\rho)$ is the Gaussian refractive index profile of the turbule, located at O in Fig. 8. In terms of r_s, r_t and ϕ_0, $|\mathbf{r}-\mathbf{r}'||\mathbf{r}'| \approx r_s r_t$ and $|\mathbf{r}'|+|\mathbf{r}-\mathbf{r}'|$, to second order in ρ/r_s or ρ/r, is

$$\begin{aligned}|\mathbf{r}'|+|\mathbf{r}'-\mathbf{r}| = r_s + r_t + \frac{\rho^2}{2}\left(\frac{1}{r_s}+\frac{1}{r_t}\right)\sin^2\psi + \rho\cos\psi \\ \times(1-\cos\phi_0) - \rho\sin\psi\cos\theta\sin\phi_0 \\ -\frac{\rho^2}{2r_s}\cos^2\psi - \frac{\rho^2}{2r_t}(\sin\psi\cos\phi_0\sin\phi_0 \\ -\cos\psi\cos\phi_0)^2. \qquad \text{(A2)}\end{aligned}$$

If these expressions are substituted into Eq. (A1) we obtain

$$\begin{aligned}\Delta P(\mathrm{r}) = -A\frac{\sqrt{\pi}}{2}qk^2\frac{e^{ik(r_s+r_t)}}{r_s r_t} \\ \times s_x s_y s_z e^{-\{K_x^2 s_x^2/4 + K_y^2 s_y^2/4 + K_z^2 s_z^2/4\}}. \qquad \text{(A3)}\end{aligned}$$

The coefficients are shown in Table I when Eq. (A2) (a) simplifies to first order, (b) retains the second-order terms but applies the small angle approximations such that $\sin\phi_0\cos\phi_0$ and $\sin^2\phi_0$ are zero and $\cos^2\phi_0$ is 1 (which leads to the expression used by McBride *et al.*[3]), and (c) remains at the full second order. The first-order results are significantly less than those of the other two at small y offsets but diminish only slowly as y increases. The McBride and full second order almost agree at low offsets but the full scattering magnitude diminishes rapidly as y increases compared to the McBride approximation. In terms of dispersion, the full second-order result indicates that only the lowest frequencies are scattered toward the receiver at larger offsets.

[1] G. A. Daigle, J. E. Piercy, and T. F. W. Embleton, "Line of sight propagation through atmospheric turbulence near the ground," J. Acoust. Soc. Am. **74**, 1505–1513 (1983).

[2] R. Grosse, V. Mellert, M. S. Glahn, and A. Sill, "Sound propagation in the turbulent atmosphere: A comparison of approximation methods," Proceedings of the Eighth FASE Symposium, Zaragoza, Spain, April 1989, pp. 53–56.

[3] W. McBride, H. E. Bass, R. Raspet, and K. E. Gilbert, "Scattering of sound by atmospheric turbulence: A numerical simulation above a complex impedance boundary," J. Acoust. Soc. Am. **90**, 3314–3325 (1991).

[4] G. H. Goedecke and H. J. Auvermann, "Acoustic scattering by atmospheric turbules," J. Acoust. Soc. Am. **102**, 759–771 (1997).

[5] G. H. Goedecke, R. C. Wood, H. J. Auvermann, V. E. Ostashev, D. I. Havelock, and C. Ting, "Spectral broadening of sound scattered by advecting atmospheric turbulence," J. Acoust. Soc. Am. **109**, 1923–1934 (2001).

[6] R. Raspet, H. E. Bass, L. Yao, and P. Boulanger, "Statistical and numerical studies of the relationship between turbulence and sonic boom characteristics," J. Acoust. Soc. Am. **96**, 3621–3626 (1994).

[7] P. Boulanger, R. Raspet, and H. E. Bass, "Sonic boom propagation through a realistic turbulent atmosphere," J. Acoust. Soc. Am. **98**, 3412–3417 (1995).

[8] P. Blanc-Benon, B. Lipkens, L. Dallois, M. F. Hamilton, and D. T. Blackstock, "Propagation of finite amplitude sound through turbulence: Modeling with geometrical acoustics and the parabolic equation," J. Acoust. Soc. Am. **111**, 487–498 (2002).

[9] D. K. Wilson, J. G. Brasseur, and K. E. Gilbert, "Acoustic scattering and the spectrum of atmospheric turbulence," J. Acoust. Soc. Am. **105**, 30–24 (1999).

[10] C. G. Don, A. J. Cramond, I. D. McLeod, and G. G. Swenson, "Shotshell primer impulse sources," Appl. Acoust. **42**, 85–93 (1994).

[11] A. I. Papadopoulos and C. G. Don, "A study of barrier attenuation by using acoustic impulses," J. Acoust. Soc. Am. **90**, 1011–1018 (1991).

[12] B. G. Ferguson, L. G. Criswick, and K. W. Lo, "Locating far field impulsive sound sources in air by triangulation," J. Acoust. Soc. Am. **111**, 104–117 (2002).

[13] E. M. Salomons, V. E. Ostashev, S. F. Clifford, and R. J. Lataitis, "Sound propagation in a turbulent atmosphere near the ground: An approach based on the spectral representation of refractive-index fluctuations," J. Acoust. Soc. Am. **109**, 1881–1893 (2001).

[14] C. G. Don, A. J. Cramond, I. D. McLeod, and G. G. Swenson, "Impulse propagation in a turbulent atmosphere," ICA 95, Trondheim, Norway, June 1995, pp. 73–76.

[15] B. Lipkens and D. T. Blackstock, "Model experiment to study sonic boom propagation through turbulence. I. General results," J. Acoust. Soc. Am. **103**, 148–158 (1998).

[16] M. Karweit, D. Blanc-Benon, and G. Comte-Bellot, "Simulation of the propagation of an acoustic wave through a turbulent velocity field: A study of phase variance," J. Acoust. Soc. Am. **89**, 52–62 (1991).

[17] G. I. Taylor, "The Spectrum of Turbulence," Proc. R. Soc. London, Ser. A **164**, 476–490 (1938).

[18] V. I. Tatarskii, *The Effects of the Turbulent Atmosphere on Wave Propagation* (Keter Press Binding, Jerusalem, 1971).

[19] G. A. Daigle, J. E. Piercy, and T. F. W. Embleton, "Effects of atmospheric turbulence on the interference of sound waves near a hard boundary," J. Acoust. Soc. Am. **64**, 622–630 (1978).

[20] M. Kelly, R. Raspet, and H. E. Bass, "Scattering of sonic booms by anisotropic turbulence in the atmosphere," J. Acoust. Soc. Am. **107**, 3059–3064 (2000).

[21] D. A. de Wolf, "A random motion model of fluctuations in a nearly transparent medium," Radio Sci. **18**, 138–142 (1975).

[22] J. L. Spiesberger, "Locating animals from their sounds and tomography of the atmosphere; Experimental demonstration," J. Acoust. Soc. Am. **106**, 837–846 (1999).

Exact discrete nonlocal boundary conditions for high-order Padé parabolic equations

Dmitry Mikhin[a)]
Acacia Research Pty. Ltd., Adelaide, Australia

(Received 22 January 2004; revised 3 August 2004; accepted 13 August 2004)

The nonlocal boundary conditions (NLBCs) for high-order finite-difference parabolic equations (PEs) are obtained by Z transformation of the discrete PE in a homogeneous medium. The considered NLBCs include the free-space radiation condition, possibly with a density jump at the NLBC interface, the NLBC at an arbitrary impedance interface, and the NLBCs for sources and the starting field beyond the NLBC interface. The derivation is presented for the multiterm Padé PE model OWWE (one-way wave equation), but the developed technique is applicable to a broad class of finite-difference PEs. The obtained NLBCs are exact for the given finite-difference scheme. They are not limited by the order of Padé approximation or by the PE steps in range and depth. The NLBC convolution coefficients are calculated by the numerical inverse-Z transformation. The accuracy and performance of the algorithm are analyzed for several benchmark problems. The solution is robust for the range steps over 25 wavelengths and/or the approximations up to the tenth order. The NLBCs are faster and more accurate for large steps because fewer previous range steps contribute to the convolution. Precomputation of the NLBC coefficients may be required in time-demanding applications. The results are compared with earlier proposed NLBCs for high-order PEs. © *2004 Acoustical Society of America.* [DOI: 10.1121/1.1802811]

PACS numbers: 43.30.Dr, 43.30.Gv, 43.30.Ma [JBS] Pages: 2864–2875

I. INTRODUCTION

An acoustic field is defined by the propagation equation(s) along with the appropriate initial and boundary conditions (BCs). The boundary could be a physical limit of the spatial domain or a discontinuity in acoustic properties between two adjacent media. The radiation condition[1] is a special kind of BC that is applied at the infinity to ensure that the field consists of outgoing waves only. Similar interface and radiation conditions appear in the exact two-way propagation problems and in one-way approximations.

The interface conditions are commonly expressed in terms of spectral components of the field. The examples are an interface between two liquids,[2] a wind-driven sea surface, and a rough underside of ice.[3,4] Finite-difference PE models operate with the entire field without splitting it into spectral components. Therefore, many spectral BCs cannot be used directly in such algorithms.

The radiation conditions are applied when the spatial domain of the problem is unbounded. The model truncates the computational domain, and the BC(s) imposed at the artificial boundary must imitate the original problem. Usually, PE models implement the radiation condition by appending an absorbing layer to the medium and setting the field to zero at the opposite boundary of the layer.[3] This technique introduces the additional adjustable parameters such as the attenuation and thickness of the absorber. With the appropriate parameters, the method produces accurate results at the expense of increased computational domain, hence, time.

In underwater acoustics, the unbounded medium is the ocean bottom and the attenuating layer is commonly referred to as false bottom. Applicability of the false-bottom approach is facilitated by the absorbing nature of the physical bottom. As a rule of thumb, the thickness of the attenuating layer is one third of the water column;[5] hence, the computational overhead is about 30%. The overhead is substantially larger for wide-angle shallow-water problems, reaching the order of 15 in some cases.[6,7] The substantial overhead is typical in the acoustics of atmosphere and radio wave propagation.[8–10]

Both the spectral and radiation BCs can be incorporated into the PE models using the technique of nonlocal boundary conditions (NLBCs) introduced independently by Papadakis,[11–13] Baskakov and Popov,[14] and Marcus.[15] The first NLBCs[11,12] replaced the approximate false-bottom radiation condition in the standard PE with a homogeneous acoustic bottom. The PE problem in the infinite domain was transformed into an equivalent problem in a bounded domain. Similar results were obtained for diffraction problems.[14] The NLBC approach was generalized to treat elastic boundaries.[12,13] In the early NLBCs, the medium behind the artificial boundary was assumed homogeneous. Later, NLBCs were obtained for media with linear depth dependence of the refraction index and for simple quasistratified media.[9,16,17] Several NLBC generalizations for higher-order PEs were considered.[13,17–23]

Most of the proposed NLBCs are derived by Laplace or Fourier transformation of the parabolic differential equations, substitution of the spectral BCs, and then inverse Laplace or Fourier transformation. The resulting NLBC is a convolution integral of the field along the boundary at the previous ranges. The convolution kernel is obtained from the inverse transformation that can be performed analytically in some cases.[12,13,17] Numerical inverse transformation is required for more complicated boundaries.[12,13]

a)Electronic mail: dmitrym@acres.com.au

A group of alternative NLBCs was obtained directly for the discrete implicit finite-difference (IFD) PEs using the Z transformation[21] or decomposition of the boundary conditions into a series of the translational operator.[18,24] These techniques are closely related as shown below.

Despite significant research efforts, the available NLBCs are inadequate for the state-of-the-art PE models. Most NLBCs were obtained for low-order PEs: the standard PE,[11,15,18,20] the Claerbout PE,[15,18,20] and IFD PE based on a general [1,1] Padé approximation,[13,21] or a high-angle PE.[15] The wide-angle capabilities of these NLBCs are the same as those of the underlying equations and are insufficient for many shallow-water problems.

Papadakis[13] derived an NLBC directly for the one-way Helmholtz equation. Formally, his NLBC has unlimited wide-angle capability. However, it was not implemented in a computer model. A similar NLBC that was proposed in Ref. 20 revealed computational instability.

NLBCs derived for the standard and Claerbout PEs can be applied to a wider-angle multiterm Padé PE.[18,20] In doing so, the original unbounded problem is only approximately transformed into a bounded problem. No analytic estimates are available for the accuracy of such approximation. The examples in Refs. 18 and 20 refer to relatively narrow-angle problems that are presumably within the angular limitations of the low-order PEs. The unconditional stability of the original multiterm Padé IFD equations was violated because the obtained numerical schemes proved unstable for large range steps.

Almost all NLBCs were obtained for the differential PEs and not for the discrete PEs (but see Refs. 18, 21, and 24, and the *semidiscrete* approach of Refs. 23 and 25). The NLBCs were expressed as convolution integrals and then discretized. However, the PE and the integral NLBC must be discretized consistently. Independent discretization produces NLBCs that are no longer exact and can render the numerical scheme only conditionally stable.[21] The discretization may have lower asymptotic accuracy than the discrete PE.

The present paper is aimed at constructing *exact discrete* NLBCs for arbitrary high-order PEs with rational (e.g., Padé) approximations of the square root or exponential operators. Such conditions provide exact transformation of the semi-infinite *discrete* problem into a finite computational grid. Thus, the numerical scheme with NLBCs has the same energy-conservation, wide-angle, and accuracy properties as the original PE solution. The approach is largely inspired by Arnold and Ehrhardt.[21] The discrete NLBCs are necessarily specific for a discrete finite-difference algorithm. The analysis below uses the recursive multiterm Padé scheme of the model OWWE.[26]

II. THE IFD SCHEME OF OWWE MODEL

The OWWE model is based on an innovative one-way wave equation by Godin;[27] hence, the acronym. Mikhin[26] generalized the equation to include the source terms and to account for the medium motion. The solutions of the differential OWWE are strictly energy conserving and reciprocal. These properties are preserved in the numerical model.[26,28]

The Godin's equation for a 2D propagation problem in Cartesian coordinates range x and depth z is

$$\frac{\partial}{\partial x}[\rho^{-1/2}\hat{\mathbf{G}}_2\Psi]=ik_0\rho^{-1/2}\hat{\mathbf{G}}\hat{\mathbf{G}}_2\Psi. \tag{1}$$

Here, Ψ is the complex pressure envelope, $k_0=\omega c_0^{-1}$ is the reference wave number, c_0 is the reference sound speed, $\omega=2\pi f$, and f is the sound frequency. The medium density ρ may depend on both coordinates. The operators are $\hat{\mathbf{G}}=(1+\hat{\mathbf{X}})^{1/2}-1$, $\hat{\mathbf{G}}_2=(1+\hat{\mathbf{X}})^{1/4}$, and

$$\hat{\mathbf{X}}=\frac{1}{k_0^2}\left\{\rho\frac{\partial}{\partial z}\left[\frac{1}{\rho}\frac{\partial}{\partial z}\right]+k^2-k_0^2\right\}.$$

To simplify the formulas, the medium is assumed at rest. Generalization to moving media is considered below. In a stratified medium, OWWE (1) is equivalent to the one-way Helmholtz equation by Tappert.[29] In general range-dependent media, the two equations are essentially different and OWWE has better asymptotic accuracy.[27]

The available numerical solutions of OWWE (1) use the Crank–Nicolson scheme in range[26] or the exponential propagator[28] by Collins.[30] The second algorithm is outlined below. Equation (1) is first rewritten in terms of the local energy flux $U=\rho^{-1/2}\hat{\mathbf{G}}_2\Psi$

$$\frac{\partial U}{\partial x}=ik_0\rho^{-1/2}\hat{\mathbf{G}}\rho^{1/2}U. \tag{2}$$

This equation is solved at a uniform discrete mesh $x_n=n\Delta x$, $z_j=j\Delta z$. Assume that the medium is layered over a range step Δx. In range-dependent problems, the medium properties are taken in the middle of the step at $x=x_n+\Delta x/2$. The analytic solution of Eq. (2) is

$$U^{n+1}=\rho^{-1/2}\hat{\mathbf{S}}[\rho^{1/2}U^n],\quad \hat{\mathbf{S}}=\exp(ih_x\hat{\mathbf{G}}), \tag{3}$$

where $U^n=U(x_n)$ and $h_x=k_0\Delta x$. The product Padé approximation of the exponential propagator $\hat{\mathbf{S}}$ yields

$$U^{n+1}=\rho^{-1/2}\left[\prod_{l=0}^{L-1}\frac{1+\dot{w}_l\hat{\mathbf{X}}}{1+w_l\hat{\mathbf{X}}}\right]\rho^{1/2}U^n. \tag{4}$$

Calculation of coefficients w_l, $\dot{w}_l$ was considered in Ref. 30. The recursive solution of Eq. (4) is

$$\left[1+\frac{w_l}{\rho^{1/2}}\hat{\mathbf{X}}\rho^{1/2}\right]U^{n,l+1}=\left[1+\frac{\dot{w}_l}{\rho^{1/2}}\hat{\mathbf{X}}\rho^{1/2}\right]U^{n,l}. \tag{5}$$

Here, $U^{n,l}$, $l=0,...,L-1$ is the energy flux on the l^{th} partial step of the n^{th} complete step of the PE; $U^{n,0}=U^n$ and $U^{n,L}=U^{n+1}$. As in Ref. 30, the IFD scheme (3)–(5) allows large range steps and fast advance of the solution. The discrete equations (5) are solved by introducing new unknown functions[26,28]

$$\Theta^{n,l}=\frac{1}{2}(1+\gamma_l\hat{\mathbf{X}})^{-1}\{\rho^{1/2}(U^{n,l+1}+U^{n,l})\}.$$

Here, $\gamma_l=(w_l+\dot{w}_l)/2$. The quantities $\Theta^{n,l}$ represent the partial acoustical pressures at the corresponding substeps of the IFD scheme.[26,28] In terms of $\Theta^{n,l}$, each partial equation (5) is transformed into a system

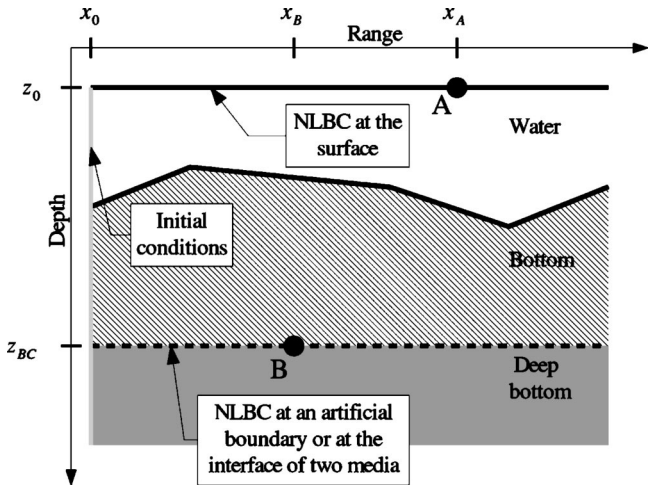

FIG. 1. The environmental layout of the problem.

$$U^{n,l}=\rho^{-1/2}[1+w_l\hat{\mathbf{X}}]\Theta^{n,l},$$
$$U^{n,l+1}=\rho^{-1/2}[1+\dot{w}_l\hat{\mathbf{X}}]\Theta^{n,l}. \tag{6}$$

The first equation is solved for $\Theta^{n,l}$; the result is substituted into the second equation to find the energy flux on the next substep. The depth operator is discretized as[26]

$$(\hat{\mathbf{X}}\Theta)_j=\rho_j h_z^{-2}\{\tau_j(\Theta_{j+1}-\Theta_j)-\tau_{j-1}(\Theta_j-\Theta_{j-1})\}+(k_j^2k_0^{-2}-1)\Theta_j. \tag{7}$$

Here, $\tau_j=0.5(\rho_{j+1}^{-1}+\rho_j^{-1})$ and $h_z=k_0\Delta z$.

The Crank–Nicolson scheme[26] results in the same finite-difference equations (6) with the coefficients $w_l=\gamma_l-ih_x\alpha_l$ and $\dot{w}_l=\gamma_l+ih_x\alpha_l$. Here, α_l, γ_l are the Padé coefficients in the sum approximation of the operator $\hat{\mathbf{G}}$. When the model uses the Padé coefficients from Ref. 30, the solution corresponds to the exponential propagator (3). Alternatively, the solutions with various Padé approximations of $\hat{\mathbf{G}}$ (Refs. 26 and 31–33) correspond to the Crank–Nicolson scheme. The IFD solver is the same in both cases.

III. DISCRETE NONLOCAL BOUNDARY CONDITIONS

The typical environment consists of the water column, the bottom, and the homogeneous deep bottom (Fig. 1). The water and bottom properties may depend on range and depth. Two types of NLBCs may be required. The first corresponds to the BC at the surface that may describe the finite impedance of the water–air interface or the sound scattering by waves. The NLBC at a point x_A depends on the field history along the surface for $x<x_A$.

The second NLBC replaces the radiation condition in the deep bottom. It is applied along the artificial boundary $z=z_{\mathrm{BC}}$ in the homogeneous bottom. Alternatively, this boundary may correspond to a horizontal interface between two media, e.g., a sediment layer and the deep bottom. Such NLBC should account for both discontinuities in the medium properties and the radiation condition. The starting field for the PE model at a range x_0 may be nonzero below the NLBC interface. Such initial conditions may be produced by an external program or by sources located below the interface. Then, the NLBC at point x_B depends on the field history for $z=z_{\mathrm{BC}}$, $x<x_B$, *and* on the initial field for $x=x_0$, $z<z_{\mathrm{BC}}$. Similarly, an initial field or sources above the surface would contribute to the surface NLBC at the point x_A. The contributions from the initial and near-boundary fields into the NLBCs are additive and allow independent analysis.

A. An artificial boundary within a homogeneous bottom

This type of NLBC was the first to appear in underwater acoustics. An artificial boundary $z_{\mathrm{BC}}=(J+1/2)\Delta z$ is placed in the homogeneous bottom with the refraction index N_b. The starting field is zero below the boundary. In particular, this is true in the most common case when the field is produced by a source located in the water. For $|\zeta|>R_L>=1$, where R_L is a convergence radius, the Z transformation[34] in range is defined as

$$Z\{F^{n,l}\}=\sum_{n=0}^{\infty}F^{n,l}\zeta^{-n}. \tag{8}$$

The transformation uses the function values $F^{n,l}$ at the same substeps of the subsequent full steps of the PE. The transformation variable is denoted ζ to reserve the common notation z for the depth coordinate. The Z transform of Eqs. (6) is

$$u^l=\frac{1}{\sqrt{\rho}}[1+w_l\hat{\mathbf{X}}]\vartheta^l,\quad u^{l+1}=\frac{1}{\sqrt{\rho}}[1+\dot{w}_l\hat{\mathbf{X}}]\vartheta^l, \tag{9}$$

where $u^l(\zeta)=Z\{U^{n,l}\}$ and $\vartheta^l(\zeta)=Z\{\Theta^{n,l}\}$. Recursive solution of these equations for $l=0,...,L-1$ gives a relationship between u^L and u^0. Alternatively, they are related by the Z transformation shift rule: $u^L=Z\{U^{n,L}\}=\zeta Z\{U^{n-1,L}\}=\zeta Z\{U^{n,0}\}=\zeta u^0$. Therefore

$$\zeta u^0=\prod_{l=0}^{L-1}\frac{1+\dot{w}_l\hat{\mathbf{X}}}{1+w_l\hat{\mathbf{X}}}u^0. \tag{10}$$

The discretization (7) transforms Eq. (10) into a difference equation with constant coefficients. Its solution has the form $u_j^0=\mu^{j-J}$, and $\hat{\mathbf{X}}u^0=su^0$, where $s=h_z^{-2}[\mu-2+\mu^{-1}]+m_b$, $m_b=N_b^2-1$. Together this yields the dispersion relationship for the plane waves in the finite-difference OWWE

$$\zeta=\prod_{l=0}^{L-1}\frac{1+\dot{w}_l s(\mu)}{1+w_l s(\mu)}. \tag{11}$$

This L^{th}-order polynomial equation has L complex roots $s_m(\zeta)$. The discrete vertical wave numbers are obtained by solving

$$\mu-2+\mu^{-1}=h_z^2[s_m(\zeta)-m_b]. \tag{12}$$

For any root $s_m(\zeta)$, there are two wave numbers $\mu_m^{(1,2)}(\zeta)$. If μ satisfies (12), then μ^{-1} also satisfies (12). Hence, one of the wave numbers is by modulo less than 1 or, if $|\mu_m^{(1,2)}|=1$, one of the wave numbers has a positive phase. This wave number further denoted as μ_m corresponds to a wave propagating downward away from the boundary; the other corresponds to a wave propagating upward. For any horizontal wave number, the discrete solution has L downward-propagating waves. There is only one such wave in the

pseudodifferential OWWE (1). The difference occurs when the operator $\hat{\mathbf{S}}$ (or $\hat{\mathbf{G}}$) is replaced by its multiterm Padé approximation.

The stability conditions on the Padé approximation of the operator $\hat{\mathbf{S}}$ require that the product in Eq. (11) by modulo does not exceed 1 for any s with a non-negative imaginary part. Given that $|\zeta|>1$, the solution of Eq. (11) is possible only for $\Im(s)<0$. The bottom absorption is non-negative. Hence, the right-hand side of (12) has a negative imaginary part and $|\mu_m|=1$ cannot be a solution. Physically, this means that the downward-propagating waves strictly attenuate in the energy-conserving scheme and/or in absorbing media.

Any solution of Eq. (9) satisfying the radiation condition is a linear combination of the L downward-propagating waves

$$u_j^l=\rho^{-1/2}\sum_{m=0}^{L-1} B_m^l \mu_m^{j-J}, \quad \vartheta_j^l=\sum_{m=0}^{L-1} A_m^l \mu_m^{j-J}. \tag{13}$$

The coefficients in these series are related by (9) as

$$B_m^{l+1}=\frac{1+\dot{w}_l s_m}{1+w_l s_m}B_m^l, \quad A_m^l=\frac{B_m^l}{1+w_l s_m}; \tag{14}$$

therefore

$$A_m^l=r_{lm}B_m^0, \text{ where } r_{lm}=\frac{\Pi_{j=0}^{l-1}(1+\dot{w}_j s_m)}{\Pi_{j=0}^{l}(1+w_j s_m)}.$$

The discrete BCs for the scheme (6) are written in terms of partial pressures $\Theta_J^{n,l}$, $\Theta_{J+1}^{n,l}$ at the near-boundary nodes of the discrete mesh. Hence, the NLBC should give a relationship between these quantities or, equivalently, between ϑ_{J+1}^l and ϑ_J^l. Using Eq. (13) for ϑ_J^l and ϑ_{J+1}^l, the Z-transformed NLBC is obtained as

$$\boldsymbol{\vartheta}_{J+1}=\mathbf{RMR}^{-1}\boldsymbol{\vartheta}_J. \tag{15}$$

Here, $\mathbf{R}=\|r_{lm}\|$, $\boldsymbol{\vartheta}_j=(\vartheta_j^0\cdots\vartheta_j^{L-1})^T$ for $j=J$, $J+1$, and $\mathbf{M}$ is a diagonal matrix of the wave numbers μ_m. The NLBC in the original coordinate space is given by the inverse Z transformation of (15)

$$\boldsymbol{\Theta}_{J+1}^n=\sum_{m=0}^{n}\mathbf{T}_{n-m}\boldsymbol{\Theta}_J^m. \tag{16}$$

The matrix sequence $\mathbf{T}_m$ is the inverse Z transform of the matrix $\mathbf{T}(\zeta)=\mathbf{RMR}^{-1}$, and the vectors are $\boldsymbol{\Theta}_j^n=(\Theta_j^{n,0}\cdots\Theta_j^{n,L-1})^T$, $j=J$, $J+1$. For the special case of $L=1$, the NLBC (16) coincides with the discrete NLBC of the Claerbout PE.[21]

The convolution (16) gives the exact discrete NLBC for the considered problem. Calculation of the inverse Z transformation of $\mathbf{T}(\zeta)$ is considered in Sec. IV. Now, consider only the first element $\mathbf{T}_0$ that equals the limit of $\mathbf{T}$ for $|\zeta|\to\infty$. According to (11), $s_m\approx -w_m^{-1}$ for large $|\zeta|$. Hence, $r_{lm}=O(\zeta)$ for $l\geqslant m$ and $r_{lm}=O(1)$ for $l<m$; i.e., $\mathbf{R}\approx\zeta\mathbf{L}$ and $\mathbf{R}^{-1}\approx\zeta^{-1}\mathbf{L}^{-1}$, where $\mathbf{L}$ is a lower triangular matrix. The wave numbers μ_m and the matrix $\mathbf{M}$ have no singularities for large $|\zeta|$. Therefore, $\mathbf{T}_0$ is also a lower triangular matrix. This establishes the causality of the NLBC (16). The partial pressure $\Theta_{J+1}^{n,l}$ on the substep l of the step n depends on the already known quantities: the partial pressures $\Theta_J^{m,k}$ on all the substeps $k=0,...,L-1$ of the previous steps $m<n$ and the partial pressures $\Theta_J^{n,k}$ on this and the previous substeps $k=0,...,l$ of the current step.

B. An interface between two media

The previous subsection assumed that both depth nodes $j=J$, $J+1$ used in the NLBC are located within the same homogeneous layer. Now, consider a modified problem when the NLBC is applied at an interface of two media. The node J is in the upper medium, whereas the node $J+1$ is in the homogeneous lower medium. The upper medium has constant sound speed and density along the boundary. As earlier, the initial field is assumed zero below the NLBC boundary.

The partial pressures at the boundary nodes are related by the discrete boundary conditions[26]

$$\begin{gathered}\tau_{J,<}(\Theta_{J+1,<}^{n,l}-\Theta_{J,<}^{n,l})=\tau_{J,>}(\Theta_{J+1,>}^{n,l}-\Theta_{J,>}^{n,l}),\\ \Theta_{J+1,<}^{n,l}+\Theta_{J,<}^{n,l}=\Theta_{J+1,>}^{n,l}+\Theta_{J,>}^{n,l}.\end{gathered} \tag{17}$$

The indexes $<$ and $>$ refer to the respective quantities in the lower and upper media. In the lower medium, the transformed partial pressures are linear combinations (13) of the downward-propagating waves. The same NLBC (15) is valid: $\boldsymbol{\vartheta}_{J+1,<}=\mathbf{T}_<(\zeta)\boldsymbol{\vartheta}_{J,<}$. Substitution of this relationship into the Z transformation of (17) gives the NLBC for the considered problem

$$\boldsymbol{\vartheta}_{J+1,>}=[g\mathbf{T}_<+\mathbf{E}][\mathbf{T}_<+g\mathbf{E}]^{-1}\boldsymbol{\vartheta}_{J,>}. \tag{18}$$

Here, $g=(\tau_{J,>}+\tau_{J,<})/(\tau_{J,>}-\tau_{J,<})$ and $\mathbf{E}$ is a unit $L\times L$ matrix. The inverse-Z transformation of (18) gives the NLBC in the coordinate space that is analogous to (16).

In the limit of identical media, the NLBC (18) coincides with (15). If the density of the lower medium tends to infinity, then $g\to 1$ and $\boldsymbol{\vartheta}_{J+1,>}\to\boldsymbol{\vartheta}_{J,>}$. The inverse-$Z$ transformation of this relation gives the expected local BC at a rigid surface. For the opposite limit of infinitely small density of the lower medium, $\boldsymbol{\vartheta}_{J+1,>}\to-\boldsymbol{\vartheta}_{J,>}$, which transforms into the local BC at a pressure-release surface.

C. A general impedance boundary

Assume that the medium is bounded by a horizontal interface with a known impedance Γ. The interface may be a rough sea surface, or a boundary of a bottom layer. The derivation is presented for the lower boundary. The acoustical field within the upper medium is described by Eqs. (6) and (7). The propagation equations might differ in the lower medium; e.g., this medium can support elastic waves not described by the acoustical OWWE. The upper medium is homogeneous along the interface. Below the interface, the initial field is zero. The problems considered above are special cases of this general problem.

The last depth horizon in the upper medium has an index J. The node $J+1$ is on the other side of the interface. The Z-transformed partial pressures and energy fluxes in the upper medium near the interface are linear combinations of plane waves

$$u_j^l=\rho^{-1/2}\sum_{m=0}^{L-1}(B_m^{l,+}\mu_m^{j-J}+B_m^{l,-}\mu_m^{J-j}),$$
$$\vartheta_j^l=\sum_{m=0}^{L-1}(A_m^{l,+}\mu_m^{j-J}+A_m^{l,-}\mu_m^{J-j}). \tag{19}$$

The amplitudes $A_m^{l,\pm}$, $B_m^{l,\pm}$ are related by Eqs. (14). The amplitudes of waves propagating to and from the interface are related by the impedance BCs for the corresponding vertical wave numbers. Consider a pair of incident and reflected plane waves, $\phi_j^m=A_m^+\mu_m^{j-J}+A_m^-\mu_m^{J-j}$. The discrete impedance BC for this field is

$$\Gamma_m=-i\omega\rho_J\frac{0.5(\phi_{J+1}^m+\phi_J^m)}{(\Delta z)^{-1}(\phi_{J+1}^m-\phi_J^m)}$$
$$=\frac{-i\omega\Delta z}{2\tau_J}\frac{A_m^+(\mu_m+1)+A_m^-(\mu_m^{-1}+1)}{A_m^+(\mu_m-1)+A_m^-(\mu_m^{-1}-1)}.$$

Hence, $A_m^-=\Omega_m A_m^+$, where

$$\Omega_m=\mu_m\frac{\Gamma_m'(1-\mu_m)+1+\mu_m}{\Gamma_m'(1-\mu_m)-1-\mu_m}, \tag{20}$$

and $\Gamma_m'=2i\tau_J\Gamma_m/\omega\Delta z$. Together with (14) and (19), this yields a relationship between the transformed partial pressures at the near-boundary horizons

$$\boldsymbol{\vartheta}_{J+1}=\mathbf{R}[\mathbf{M}+\boldsymbol{\Omega}\mathbf{M}^{-1}][\mathbf{E}+\boldsymbol{\Omega}]^{-1}\mathbf{R}^{-1}\boldsymbol{\vartheta}_J. \tag{21}$$

Here, $\boldsymbol{\Omega}$ is a diagonal matrix of the reflection coefficients (20). The inverse-Z transformation of (21) gives the NLBC in the coordinate space.

D. The initial conditions

A nonzero initial field on the other side of the NLBC interface contributes to the BCs. The contribution has been typically ignored in underwater acoustics, which is partially justified as most proposed NLBCs replaced the radiation condition in the deep bottom where the field is low. In some cases, however, the contribution of the starting field is important. If the initial field is taken from an external model, and one looks for the NLBCs at the water–bottom interface, the initial field is appreciable shallow in the bottom. Another example is generation of sound in the water by an airborne source located above the NLBC boundary at the sea surface. The proper account for a nonzero initial field may be important in atmospheric acoustics, quasioptics, and radio wave propagation.[8–10,17]

Assume that the PE solution on the first step is initialized by the energy flux $U_j^{0,0}$. To obtain the contribution of this initial field to the NLBCs, consider an auxiliary problem of calculating the field in the quadrant $n\geqslant 0$, $j\geqslant J$ from the starting field $U_j^{0,0}$, $j>J$, and known partial pressures $\Theta_J^{m,k}$, $m\leqslant n$, $k=0,...,L-1$ at the boundary (cf. Refs. 9 and 17). The resulting expression for calculating the partial pressures $\Theta_{J+1}^{n,l}$ from $\Theta_J^{m,k}$ and $U_j^{0,0}$ will give the NLBC for the considered problem.

The solution U, Θ of the auxiliary problem can be represented as $U=V+W$, $\Theta=\Phi+\Xi$. Here, V, Φ is the solution produced by the initial field under zero boundary conditions $\Phi_J^{m,k}=0$, whereas W, Ξ is the solution for zero initial field and boundary conditions $\Xi_J^{m,k}=\Theta_J^{m,k}$. The solution of the second problem at the depth node $J+1$ is given by the NLBCs from the previous subsections. To find $\Phi_{J+1}^{n,l}$, the discrete OWWE solution for an elementary initial field of energy flux (see the Appendix) is applied. The Z-transformed solution for the initial field $U_k^{0,0}\delta_{jk}$ *and* zero boundary conditions is

$$\phi_j^l=U_k^{0,0}\sum_{m=0}^{L-1}A_m^l(\mu_m^{|j-k|}-\mu_m^{|j-2J+k|}). \tag{22}$$

Here, ϕ is the Z transform of Φ and the coefficients A_m^l are given by (A3)–(A5) and (14). The solution for an arbitrary $U_j^{0,0}$ is a superposition of the fields (22)

$$\phi_{J+1}^l=\sum_{m=0}^{L-1}A_m^l(\mu_m^{-1}-\mu_m)\left[\sum_{k=J+1}^{\infty}U_k^{0,0}\mu_m^{k-J}\right]. \tag{23}$$

The inverse Z transformation of (23) yields the contribution of the initial energy flux into the NLBCs.

Alternatively, the OWWE solution may be initiated by acoustical source(s) located behind the NLBC interface, or by a starting field of acoustical pressure, or by both the sources and some starting field. The NLBCs for all these problems are obtained similar to (23) using the elementary solutions of OWWE obtained in the Appendix.

The NLBC (23) implies that sound propagation in the quadrant $n\geqslant 0$, $j\geqslant J$ is described by the IFD scheme (6). The medium homogeneity in the quadrant allows a direct solution of the differential OWWE or of the wave equation for the given initial and zero boundary conditions. However, the BCs for the PE in the upper medium are written in terms of partial pressures, and no technique is available to partition the obtained full acoustic pressure into the partial pressures.

E. NLBCs for moving media

To the author's knowledge, NLBCs have never been considered for sound fields in heterogeneous moving media. This agrees with the original purpose of the NLBC[12] to reproduce the radiation condition in the motionless ocean bottom. However, the medium motion may be important in other NLBC applications. For example, sound scattering at a rough sea surface may depend on the near-surface flow. Sound propagation in atmosphere is strongly affected by the wind. The wind must be accounted for in both the impedance NLBC at the surface and the radiation NLBC at the artificial upper boundary.

Fortuitously, the NLBCs for moving media are similar to those for media at rest. Following Sec. III C, consider the NLBC at a horizontal interface with a known impedance. The discrete propagation equations for moving media are given by Eqs. (3.5,3.6,4.4) of Ref. 26 (further, the notation (3.5)[26] is used for formulas in the referenced literature). In a homogeneous medium, their Z transformation is

$$u^l=\frac{1}{\sqrt{\sigma}}[1+w_l\hat{\mathbf{X}}]\vartheta^l,\quad u^{l+1}=\frac{1}{\sqrt{\sigma}}[1+\dot{w}_l\hat{\mathbf{X}}]\vartheta^l. \tag{24}$$

Here, $\sigma=\rho\beta^3$ and $\beta=1-vc_0^{-1}$ is the local Doppler factor of the in-plane current component v. The operator $\hat{\mathbf{X}}$ for moving media is given by (2.2).[26] The partial pressures are now defined as

$$\Theta^{n,l}=\frac{1}{2}(1+\gamma_l\hat{\mathbf{X}})^{-1}\{\sigma^{1/2}(U^{n,l+1}+U^{n,l})\}.$$

Equations (24), the boundary conditions $U^{n,L}=U^{n+1,0}$, and the Z-transformation shift rule produce the same dispersion relationship (11). The vertical wave numbers are now obtained from

$$\mu-2+\mu^{-1}=h_z^2[s_m(\zeta)-\beta(N_b^2\beta^2-1)]. \tag{25}$$

The transformed partial pressures and energy fluxes near the surface are given by the linear combinations (19) with the wave numbers from (25) and the factor $\rho^{-1/2}$ replaced by $\sigma^{-1/2}$. The same derivation as in Sec. III C again results in the NLBC (21) with the reflection coefficients Ω_m given by (20) and $\tau_J=0.5(\sigma_J^{-1}+\sigma_{J+1}^{-1})$.

The other proposed NLBCs are generalized to the moving media similarly.

IV. NUMERICAL IMPLEMENTATION AND EXAMPLES

The previous section left out the problem of calculating the inverse-Z transformation of the NLBCs (15), (18), etc. The NLBCs of the standard, Claerbout, and the pseudodifferential PEs[11–13,17,21] in a homogeneous bottom allowed exact analytic evaluation of the inverse Laplace (or Fourier, or Z) transformations. No analytic inverse transformation is available for more complicated impedance boundaries.[12] The transformation matrices $\mathbf{T}$ for the proposed NLBCs of multiterm PEs can be found explicitly for the schemes with $L\leqslant 4$, but the results are cumbersome. For higher-order Padé approximations, the dispersion equation (11) cannot be solved analytically.

The matrices in the convolution series (16) can be found by the numerical inverse-Z transformation.[35] The algorithm implemented in a subroutine ENTCAF evaluates the Taylor coefficients of an analytic function $f(\eta)=\Sigma_{j=0}^{\infty}a_j(\eta-\eta_0)^j$ for $|\eta-\eta_0|<R_c$. Here, R_c is the radius of convergence of the Taylor series. The Cauchy's theorem gives the integral representation of the coefficients a_j through contour integrals over a circle $|\eta-\eta_0|=r$, $r<R_c$. ENTCAF calculates the normalized Taylor coefficients $\tilde{a}_j=r^j a_j$ that are conveniently evaluated to the same absolute accuracy; the desired accuracy ε_r is provided by the user. The algorithm returns the number of estimated coefficients K, the approximations $\tilde{a}_j^{(K)}$, and the estimated accuracy ε_e. Supposedly, they satisfy $|\tilde{a}_j-\tilde{a}_j^{(K)}|<\varepsilon_e$ for $0\leqslant j<K$, $|\tilde{a}_j|<\varepsilon_e$ for $j\geqslant K$, and $\varepsilon_e<\varepsilon_r$. The requested accuracy may not be achieved, e.g., due to computational errors in the function values.

The change of variables $\eta=\zeta^{-1}$ transforms the Laurent series (8) into the Taylor series at the point $\eta_0=0$. ENTCAF evaluates the Taylor coefficients of a scalar function, whereas Eq. (16) needs the series of a matrix. The transformation matrix $\mathbf{T}$ of the respective NLBCs is precomputed at K_L points of a circle. Then, ENTCAF is invoked to calculate the Laurent series $\mathbf{T}_m$ (16) for one matrix element at a time using the precomputed values. To improve the accuracy and allow larger K, the routine was rewritten to use double-precision variables.

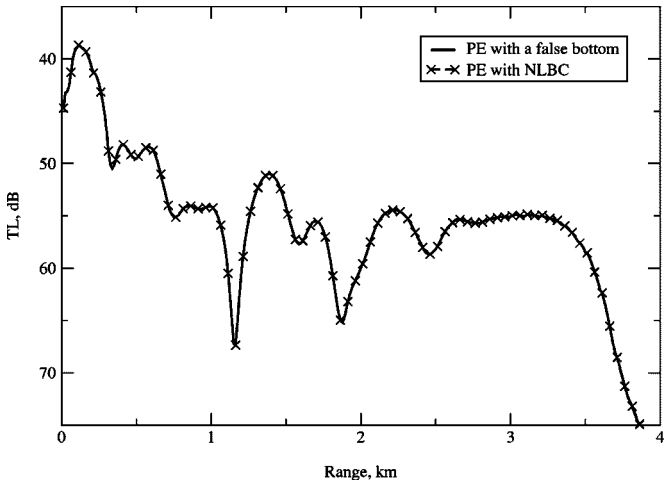

FIG. 2. Comparison of OWWE solutions for the ASA benchmark wedge using the absorbing false bottom (solid line) and the radiation NLBC (dashed line with markers). On this and the subsequent plots, the range resolution better than Δx is achieved using the range sampling technique of Ref. 28.

The convolution kernels of low-order NLBCs[11,17,20] decay with range as $r^{-1/2}$. Some NLBCs have a slower decay rate of $\log(r)$, or even tend to a constant for $r\to\infty$.[17] There are no analytic estimates for the NLBCs proposed in this paper. Assuming the same typical behavior, the convergence radius R_c should be about 1. The slow asymptotic decay also means that the convolution matrices $\mathbf{T}_m$ are required up to a high-order N_x. The upper estimate is $N_x\sim X/\Delta x$, where X is the maximal propagation range, yielding $N_x\sim 1000$ for $X=10\,\mathrm{km}$ and $\Delta x=10\,\mathrm{m}$. The number of precomputed function values should be $K_L>N_x$. To obtain the coefficients of such order, the circle radius r must be close to the convergence radius R_c; otherwise, the normalized coefficients $\tilde{a}_j$ would quickly decrease below the accuracy limit ε_r. Yet, the circle radius too close to R_c may result in larger numerical errors.[36]

Numerical tests revealed that $r=0.99$ provided reliable results up to the order of $K=2000$ for the requested accuracy $\varepsilon_r=10^{-12}$ and $K_L\sim 2K$. The estimated accuracy ε_e was below 10^{-13}. For such parameters, the higher-order nonnormalized coefficients a_j were by modulo $<5\cdot 10^{-5}$, so the contribution of the respective terms $m<n-K$ into the convolution (16) was small.

To show the NLBCs in action, the developed technique was applied to two common benchmark problems of underwater propagation. The results for the ASA penetrable wedge test[37] are shown in Fig. 2. The problem was solved using the false-bottom technique and the radiation NLBC (15) applied at 210-m depth. The two solutions are not discernible at the plot scale and agree with the reference result.[37] The model uses fourth-order Padé approximation of the exponential propagator with the coefficients due to Collins;[30] $\Delta x=100\,\mathrm{m}$ and $\Delta z=0.5\,\mathrm{m}$.

The second example is the Bucker waveguide that was often used for testing the NLBC approach.[12,13,18,20] As in the

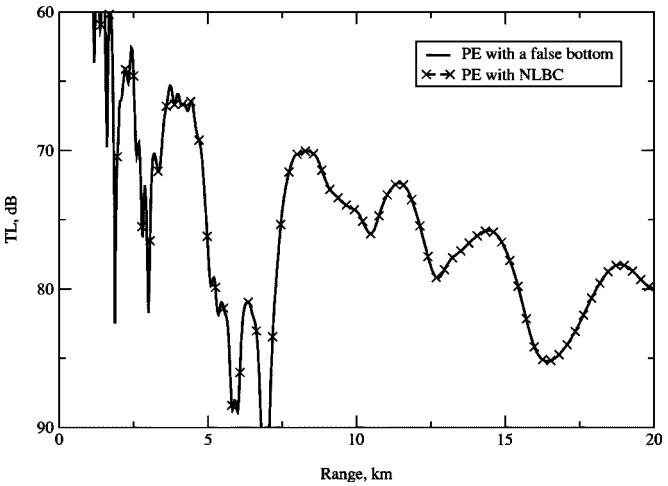

FIG. 3. Comparison of OWWE solutions for the Bucker waveguide using the absorbing false bottom (solid line) and the radiation NLBC (dashed line with markers).

referenced papers, the calculations were done for a 100-Hz point source located at 30-m depth and the receiver depth of 90 m. The nonlocal radiation condition (18) is applied at the water–bottom interface. The model uses eighth-order Padé approximation of Ref. 30 for $\Delta x = 400$ m, i.e., over 25 sound wavelengths; $\Delta z = 1$ m. OWWE results for the false-bottom and NLBC techniques (Fig. 3) are identical. They also agree with the reference solution of this problem by a full-field model.[18,20]

V. ERROR AND PERFORMANCE ANALYSIS

The absolute accuracy of the developed NLBCs was tested for a range-independent shallow-water environment. The sound speed in the water varied linearly from 1.52 km/s at the surface to 1.5 km/s near the bottom at 0.25-km depth. In the bottom, the sound speed was 1.8 km/s, the density was 1.5 g/cm^3, and the attenuation was 0.5 dB per wavelength. The problem was solved using a large computational domain (total depth 4 km) that eliminated any spurious reflections from below. At every step the obtained partial pressures were compared with the NLBC predictions. The simulations used two types of Padé approximations of the fourth order: by Milinazzo *et al.*[33] and by Collins.[30] The first set of coefficients approximates the operator $\hat{\mathbf{G}}$ for the rotated branch cut of the square root (the rotation angle was 45°). This Crank–Nicolson solution used $\Delta x = 2$ m. The second set of coefficients describes the exponential propagator (3–4) for $\Delta x = 40$ m and one stability constraint. The other parameters were $f = 200$ Hz, $\Delta z = 1$ m, and $c_0 = 1.5$ km/s.

Six NLBC problems were considered for the different initial conditions, the depth and type of the NLBC interface, and the Padé approximation (Table I). The NLBC interface at 260 m (the problems 1, 2, and 4–6) is within the homogeneous bottom, whereas the interface at 250 m (the problem 3) corresponds to the water–bottom boundary. The external field of energy flux was taken from the previous run of the model. For the problems 1 and 6, the initial field was set to zero below the NLBC interface.

The last column shows the relative errors of the respective NLBCs averaged over the first 1-km interval from the source or the initial field. This range corresponds to 500 steps of the Crank–Nicolson scheme or to 25 steps of the exponential scheme. The two values of the error were obtained from calculations on a Linux PC with GNU g77 compiler (first value) and an SGI O2 workstation with MIPS compiler. In the problem 5, the algorithm for calculating the Laurent series converged, but the achieved accuracy was slightly worse than the requested $\varepsilon_r = 10^{-12}$.

All NLBCs showed excellent accuracy. The magnitudes of errors and the differences between the two platforms indicate that the mismatches are due to round-off errors. In this sense, all the developed NLBCs are *exact*. Their applicability is not limited by the PE range step and/or the type and order of the Padé approximations.

The error estimates above are local because the NLBC predictions were never used by the false-bottom PE solution. When the model incorporates the NLBCs into the solution, the small errors in boundary conditions accumulate with range and may result in larger errors in the predicted acoustic pressure. The error accumulation was analyzed for the conditions of the Bucker waveguide. The original problem was modified by introducing the bottom absorption of 0.1 dB per wavelength. Without that, the false-bottom solution was contaminated by spurious reflections from the upper boundary of the absorbing layer.

TABLE I. Tests of NLBC accuracy for six problems in a layered medium.

#	Initial conditions	Interface depth	Propagator	NLBC equations	rms relative error
1	External energy flux that is zero below the NLBC interface	260 m	Crank–Nicolson	(15)	$0.66\cdot10^{-13}/0.10\cdot10^{-12}$
2	Self-starter at 100 m	260 m	Crank–Nicolson	(15)	$0.55\cdot10^{-13}/0.63\cdot10^{-13}$
3	Self-starter at 100 m	250 m	Crank–Nicolson	(18)	$0.39\cdot10^{-13}/0.38\cdot10^{-13}$
4	External energy flux that is not zero below the NLBC interface	260 m	Crank–Nicolson	(15), (23)	$0.86\cdot10^{-12}/0.19\cdot10^{-12}$
5	Five self-starters at 100 m and from 261 to 280 m	260 m	Crank–Nicolson	(15), (22), (A6)	$0.15\cdot10^{-12}/0.29\cdot10^{-12}$
6	External energy flux that is zero below the NLBC interface	260 m	Exponential	(15)	$0.31\cdot10^{-13}/0.33\cdot10^{-13}$

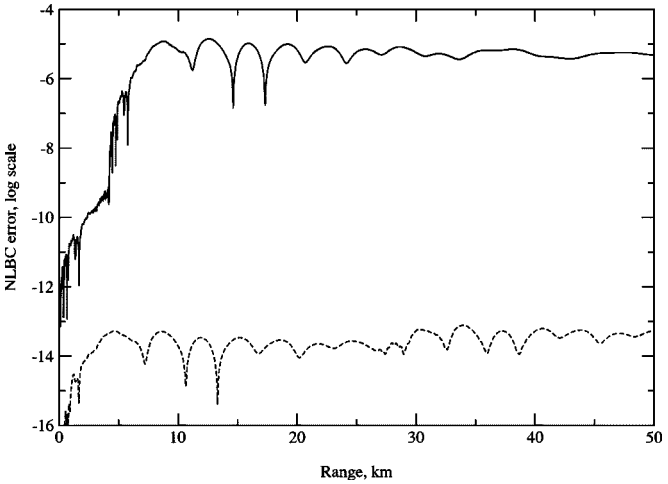

FIG. 4. The mismatch of OWWE solutions obtained for the modified Bucker problem with the absorbing false bottom and the radiation NLBC. The model used the Crank–Nicolson (solid line) and exponential (dashed line) propagators.

The simulations were performed for two Padé approximations of the order eight: the exponential propagator with the coefficients of Ref. 30 and the Crank–Nicolson propagator with the coefficients of Ref. 33 (the rotation angle was 45°). The range steps were 400 and 4 m, respectively. The convolution matrices computed for $\varepsilon_r = 10^{-12}$ had the estimated accuracy of about 10^{-14}. The lengths of the convolution series (16) determined by ENTCAF were $K = 64$ for the exponential propagator and $K = 1024$ for the Crank–Nicolson propagator.

The length is related to the range step because the norm $|\mathbf{T}_{n-m}|$ decays depending on the range lag $\Delta x(n-m)$ rather than on the index difference $n-m$. For a larger step, the coefficients decrease faster with index and fewer terms of the convolution series are essential. The NLBC is determined by the field history over some interval ΔX defined by the propagation conditions. The interval does not depend on the PE model; hence, the product $K\Delta x \sim \Delta X$ should be the same for all Padé approximations. For the Crank–Nicolson scheme above, this rule predicts $K = 6400$. Such a length is beyond the ENTCAF capabilities and the convolution is truncated early.

The mismatches between the acoustic fields predicted for the false-bottom and the radiation NLBC for the two Padé approximations are shown in Fig. 4. The convolution series in the exponential scheme is truncated at $K\Delta x \approx 25$-km range. The NLBC is approximate at larger distances. The mismatch (dashed line in Fig. 4) shows some increase at this range, but remains negligible. The truncation range is only 4.1 km for the Crank–Nicolson scheme. The corresponding plot reveals a large increase of the mismatch after this range due to the insufficient convolution length. Yet, there is no further growth of the mismatch with distance. The relative error of the truncated NLBC solution remains within 10^{-3} (cf. 10^{-11} in the exponential scheme). Before 4.1 km, the mismatch in the Crank–Nicolson scheme is over 1000 times larger than in the exponential scheme, likely due to accumulation of numerical errors in a longer convolution.

The numerical overhead of using NLBCs consists of two parts: calculation of the convolution matrices $\mathbf{T}_m$ and of the convolution itself. OWWE model requires about $9LN_z$ complex double-precision operations for each step in range (for simplicity, the difference between the multiplication and addition operations is ignored). Here, N_z is the total number of the PE depth nodes. Assume that the lower fraction H of the grid describes the false bottom that can be replaced by the NLBC (15). Computation of the convolution (16) over N_x range steps takes about $2L^2N_x$ operations. The NLBC is more efficient than the false bottom if $N_z > 2LN_x/9H = 2\Delta X/9H \cdot L/\Delta x$. The first multiplier in this formula depends on the environment, the second on the PE model. For $\Delta X = 5$ km, $H = 1/3$, $L = 8$, and $\Delta x = 100$ m, the condition $N_z > 270$ is commonly satisfied. The values used for this estimate are quite conservative. The condition is more relaxed for many other problems.

If the range step is fixed, the NLBC computations slow down for larger L. However, high-order Padé approximations may use larger steps in range. Let Δx be chosen as the maximal step of the exponential propagator (3) that is possible for the given wide-angle and accuracy requirements. The ratio $L/\Delta x$ decreases with the increase of L that makes both the exponential scheme and the NLBC more efficient for larger L.

Applying the NLBC at the ocean surface always increases the calculation time. The growth factor is about $1 + 2\Delta X/9N_z \cdot L/\Delta x$, which is typically small. Again, it decreases for larger L with optimally chosen Δx. The NLBCs for nonzero initial fields behind the NLBC interface are presented mainly for completeness. They are quite inefficient numerically because of the long inner sum.

Surprisingly, both the accuracy and the performance of the developed NLBCs *benefit* from using large steps in range. The required convolution length decreases for larger Δx. Hence, fewer coefficients must be calculated and stored and the convolution is faster. The accuracy also improves because the NLBC accounts for more distant field history along the interface and the accumulating numerical errors are smaller in the shorter convolution. On the contrary, the NLBCs proposed in Refs. 18 and 20 exhibit accuracy and stability problems for large steps.

The task of computing the convolution matrices is numerically demanding. Even for low-order NLBCs,[18] the time of calculations was comparable to the total run time of the PE model. The time is typically longer for the high-order NLBCs presented in this paper, although little effort was made to optimize this part of the code. The exact NLBCs are ideally suited for benchmark calculations when the extra CPU load is affordable. PE applications may require better performance. An efficient implementation of the high-order NLBCs may precompute the convolution matrices for a set of the medium parameters. For the radiation NLBC in the bottom, the tabulation is facilitated by the usual uncertainties in the bottom sound speed and density.

VI. COMPARISON WITH OTHER NLBCs

Discrete NLBCs for IFD PEs were considered earlier in Refs. 18 and 21. The NLBC of Ref. 21 is also based on the

Z transformation and is identical to (15)–(16) in the special case $L=1$ [except for some typos in the definitions following Eq. (3.6)].[21] The technique of Ref. 18 formally differs, but the difference proves to be superficial. Consider the Crank–Nicolson solution of the standard PE (SPE) given by Eq. (10).[18] Its Z transformation gives

$$\{k_0^2(\nu^2+m_b)+\partial^2/\partial z^2\}\zeta\phi=\{k_0^2(\nu^2-m_b)-\partial^2/\partial z^2\}\phi.$$

Here, $\nu^2=4ih_x^{-1}$ and ϕ is the Z transform of the pressure envelope ψ. The Z-transformation shift rule $Z\{\psi(x+\Delta x)\}=Z\{\psi^{n+1}\}=\zeta Z\{\psi^n\}$ was applied in the left-hand side. The above equation is equivalent to

$$\left\{\partial^2/\partial z^2+\Gamma_0^2\right\}\phi=0, \quad \text{where}$$

$$\Gamma_0^2=k_0^2[N_b^2-1+\nu^2(1-\zeta^{-1})/(1+\zeta^{-1})].$$

These equations coincide with Eqs. (13)–(14) (Ref. 18) except for the substitution of the translation operator R (11)–(12)[18] with ζ^{-1}. The similarity exists because the definition of the translation operator R is equivalent to the Z-transformation shift rule. After this correspondence is established, Eq. (17)[18] is recognized as the Z-transformed NLBC. The decomposition of Γ_0 into a power series of R is equivalent to the calculation of the Laurent series, and the NLBC (18) (Ref. 18) is an inverse-Z transform of Eq. (17).[18]

Similarly, consider the IFD scheme (6) in a homogeneous bottom. For the Padé approximation with $L=1$, $w=(1-ih_x)/4$, and $\dot{w}=(1+ih_x)/4$, this scheme coincides with the Crank–Nicolson solution of the Claerbout PE (8), (9), (20).[18] Its Z transformation produces Eqs. (21)–(22)[18] with the operator R replaced by ζ^{-1}. Discretization of the NLBC (21) (Ref. 18) in depth gives the fully discrete NLBC (18), which coincides with the results of Ref. 21 in a special case of no density jump across the interface.

Yevick and Thomson[18] also differ in the approach for calculating the coefficients of the convolution series in coordinate space from the Z-transformed NLBCs (or their equivalents in terms of R). Their algorithm calculates the Taylor series of the separate terms in the Z-transformed NLBCs and then the convolution of these series. Despite its appealing simplicity, this convolution method proved inadequate for the NLBCs of high-order PEs. Consider the Z-transformed NLBC (15). A Laurent series of the transformation matrix $\mathbf{T}=\mathbf{RMR}^{-1}$ is a convolution of the Laurent series $\mathbf{R}_m$, $\mathbf{M}_m$, and $(\mathbf{R}^{-1})_m$. The norms of these $L\times L$ matrices typically exponentially grow with the order m (Fig. 5), whereas the norm of the elements $\mathbf{T}_m$ must decrease with m. The example uses the environment of the Bucker problem and the coefficients of Ref. 33 for $L=4$ and the rotation angle 45°. The Laurent series for $\mathbf{R}$, $\mathbf{M}$, and $\mathbf{R}^{-1}$ were obtained independently by the inverse-Z transformation (lines) and by recursive solution of Eqs. (11), (12), and (14) (symbols). The convolution of three growing series cannot produce a decreasing series because of precision limitations. The norm of the elements of the convolution initially decreases with index (triangles), but then grows alongside the norms of $\mathbf{R}_m$ and other matrices. The maximal number of elements that can be calculated by this method depends on the floating-point accuracy. It is of order 20 for 64-bit floating-point arithmetic. For comparison, the required number of elements varied from 64 to a few thousand in the examples above.

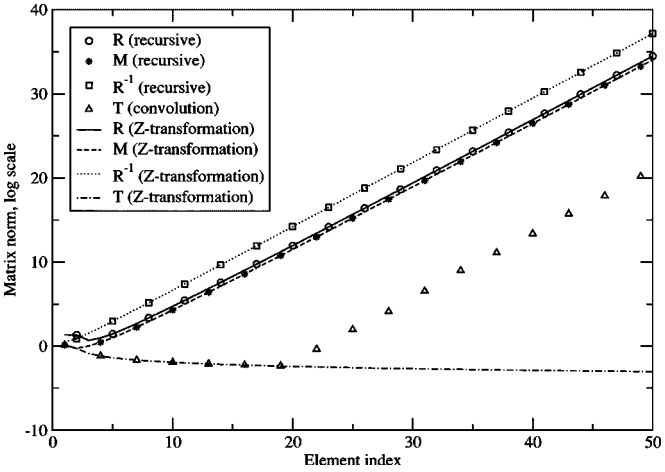

FIG. 5. The norm of the elements of the Laurent series for the NLBC convolution matrix **T** and its components calculated by different methods.

High-order Padé schemes may implement NLBCs of a low-order (standard or Claerbout) PE.[18,20] This approach was reproduced for evaluation. The analysis is performed for the Pekeris problem: a 1500-m/s water layer over a flat homogeneous bottom with $c=1590$ m/s and $\rho=1.2$ g/cm^3. A 250-Hz point source and the receiver are at 50-m depth. The PE model combined the radiation NLBC of the Claerbout PE with the IFD scheme of OWWE. The model used the exponential propagator with the Padé coefficients of Ref. 30. The NLBC is applied at the water–bottom interface at 100-m depth.

The mismatches in the predicted TL for various range steps and orders of the Padé approximation are shown in Fig. 6. The reference solution is obtained using the false-bottom approach, $\Delta x=5$ m and $L=8$. The mismatch is averaged over the distances from 2 to 10 km from the source. The errors in the high-order NLBC solutions are due to the de-

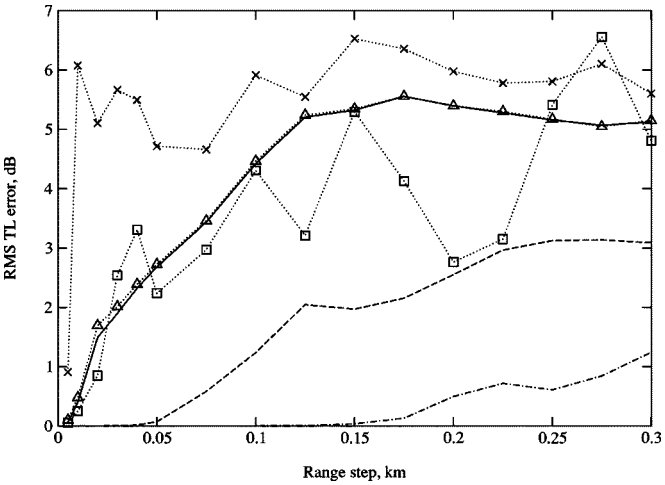

FIG. 6. The errors in the TL predicted for the Pekeris waveguide for various Δx using the exact (lines without markers) and low-order NLBCs (dotted lines with markers) for $L=2$ (solid line; triangles), 4 (dashed line; squares), and 8 (dash-dotted line; crosses).

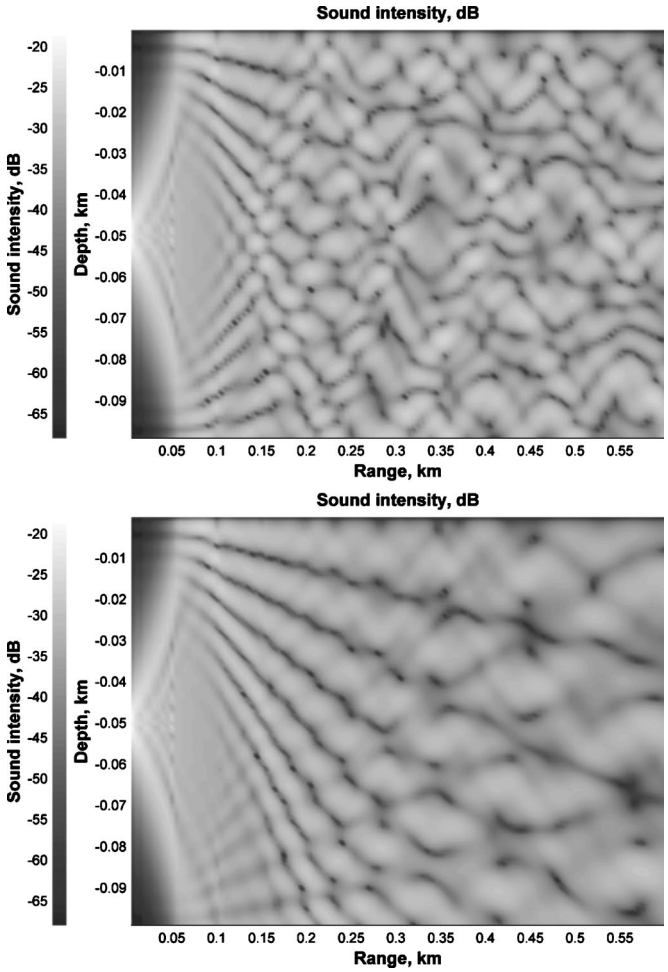

FIG. 7. The acoustical fields for the Pekeris waveguide predicted using the exact (bottom) and low-order (top) NLBCs at the water–bottom interface.

creasing accuracy of the PE propagator for large steps; the NLBCs themselves are exact.

The low-order NLBC provides fair accuracy only for small Δx and low-to-medium orders of Padé approximation. Large mismatches are observed when any of these conditions is violated. The Claerbout PE is applicable for grazing angles not exceeding 40°. The NLBC for this PE inherits these angle limitations. When applied to a high-order PE, the low-order NLBC gives wrong reflection coefficients for steeper waves (see false-bottom reflections of high-angle beams in Fig. 7; the model used the exponential propagator with $\Delta x = 50\,\mathrm{m}$ and $L=8$). The corresponding normal modes cause errors in the long-range field.

The false reflections generally increase with Δx because the Crank–Nicolson scheme of the Claerbout PE is valid only for small range steps. However, the dependence is complicated. For $L=2$, the mismatch quickly grows with Δx due to the insufficient accuracy of the PE propagator. The error is not NLBC-specific. For $L=4$ or 8, the propagator is accurate for larger steps. The TL error of the combined model is dominated by the approximate NLBC. The error is smaller for $L=4$ because some of the false reflections are beyond the wide-angle limits of the PE propagator. For $L=8$, OWWE supports such waves resulting in the largest long-range TL errors. Note that the successful examples of applying low-order NLBCs[18,20] used low-order Padé approximations.

The combination of the discrete low-order NLBC and the high-order propagator always produced stable solutions. The accuracy was fair for small range steps and paraxial waves, but unacceptable for larger Δx and L. This limits the performance and wide-angle properties of the combined model. The observed complex dependence of the TL error on the PE parameters prevents estimation of the applicability of the low-order NLBC in a general range-dependent problem. Calculations of the convolution coefficients are easier and faster for the low-order NLBC than for the high-order NLBCs proposed here. However, there is little difference in performance if the high-order NLBCs use precomputed coefficients.

VII. SUMMARY

The paper presents an approach for deriving NLBCs for finite-difference PEs. The Z transformation of the discrete PE in a homogeneous medium is applied to obtain a dispersion relationship for plane waves. Then, the Z-transformed acoustic field is expressed as an appropriate linear combination of plane waves. Their amplitudes are related by the propagation equations and the respective radiation or impedance BCs. This yields a relationship between the transformed partial pressures at the depth nodes around the interface. The NLBC in coordinate space is the inverse Z transformation of this relationship. The method inherently accounts for the Padé approximation of the propagation operator and for arbitrary PE steps in range and depth. The obtained NLBCs are exact for the given IFD scheme.

The discrete NLBCs depend on the specific discrete representation of the pseudodifferential operators and BCs. The NLBCs for other multiterm PEs will differ from those presented here, but can be obtained using the same approach. The technique is applicable for any finite-difference PE that approximates the square root (or exponential) propagator by a rational function of the vertical operator $\hat{\mathbf{X}}$ and represents $\hat{\mathbf{X}}$ by a three-point scheme. A similar solution is possible for higher-order discretizations of $\hat{\mathbf{X}}$. The overall structure of such NLBCs will coincide with (15)–(16), (18), etc., and the same numerical methods can be used for implementation.

APPENDIX: DISCRETE OWWE SOLUTIONS IN A HOMOGENEOUS MEDIUM

First, assume that there are no sources and the initial energy flux on the first step of the PE is $U_j^{0,0}=\delta_{j0}$. The Z-transformation shift rule for a nonzero initial energy flux is $u^L=\zeta(u^0-U^{0,0})$. For nonzero depth indexes $U_j^{0,0}=0$; hence, the shift rule and Eq. (9) yield the dispersion equation (10). Its roots and the vertical wave numbers are given by (11)–(12). To satisfy the radiation conditions, the solutions above and below $j=0$ should be linear combinations of waves attenuating towards $j\to\mp\infty$, respectively

$$u_j^l=\frac{1}{\sqrt{\rho}}\sum_{m=0}^{L-1}B_m^l\mu_m^{|j|}+\frac{D^l\delta_{j0}}{\sqrt{\rho}},\qquad \vartheta_j^l=\sum_{m=0}^{L-1}A_m^l\mu_m^{|j|}. \quad \text{(A1)}$$

The corresponding downward- and upward-propagating waves have the same amplitudes due to the up/down sym-

metry of the problem. Substitution of (A1) into (9) for $j \neq 0$ gives the relations (14). The same procedure for $j=0$ yields the equations for the remaining unknowns (assuming $m_b=0$ for simplicity)

$$D^l=\frac{w_l}{h_z^2}\sum_{m=0}^{L-1} r_{lm}(\mu_m-\mu_m^{-1})B_m^0, \quad 0\leqslant l<L,$$

$$D^{l+1}=\frac{\dot{w}_l}{h_z^2}\sum_{m=0}^{L-1} r_{lm}(\mu_m-\mu_m^{-1})B_m^0, \quad 0\leqslant l<L-1, \quad \text{(A2)}$$

$$D^0=\sqrt{\rho}+\frac{\dot{w}_{L-1}}{\zeta h_z^2}\sum_{m=0}^{L-1} r_{L-1,m}(\mu_m-\mu_m^{-1})B_m^0.$$

Comparison of the first two equations gives

$$D^l=D^0\mathfrak{P}^{l-1}, \text{ where } \mathfrak{P}^l=\prod_{k=0}^{l}(\dot{w}_k/w_k). \quad \text{(A3)}$$

Then, the first and the last equations in (A2) yield

$$D^0=\rho^{1/2}[1-\zeta^{-1}\mathfrak{P}^{L-1}]^{-1}. \quad \text{(A4)}$$

The remaining unknown coefficients B_m^0 satisfy

$$\sum_{m=0}^{L-1} r_{lm}(\mu_m-\mu_m^{-1})B_m^0=\frac{h_z^2}{w_l}D^0\mathfrak{P}^{l-1}, \quad 0\leqslant l<L. \quad \text{(A5)}$$

The solutions for an OWWE self-starter (describing a 2D point source) and for an elementary starting field of sound pressure are obtained similarly. The discrete OWWE schemes with the respective initial conditions are given by Eqs. (3.2)[28] and (3.18).[28] The point source is a discrete approximation of the Dirac's delta function with unit amplitude $\mathcal{B}_j^n=\delta_{n0}\delta_{j0}(\Delta x\Delta z)^{-1}$. The starting pressure is $P_j^n=\delta_{n0}\delta_{j0}(\Delta x)^{-1}$. The solutions are assumed in the form (A1) with the extra assumption $D^l\equiv 0$. Substitution of (A1) into the Z transformations of the respective systems for $j\neq 0$ gives Eq. (14) and for $j=0$ the remaining equations

$$\sum_{m=0}^{L-1} r_{lm}(\mu_m-\mu_m^{-1})B_m^0=\frac{\nu_l\Delta z}{4\alpha_l\Delta x}, \quad 0\leqslant l<L, \quad \text{(A6)}$$

$$\sum_{m=0}^{L-1} r_{lm}(\mu_m-\mu_m^{-1})B_m^0=i\frac{\kappa_l h_z^2}{2h_x\alpha_l}, \quad 0\leqslant l<L, \quad \text{(A7)}$$

for the self-starter and the elementary pressure field, respectively. The Padé coefficients ν_l and κ_l are defined in Ref. 28.

The solution in the coordinate domain is the inverse-Z transformation of (A1) with the respective coefficients. The solution for an arbitrary depth index of the starting field or self-starter is obtained by a shift of indexes. The solution for an arbitrary starting field or a combination of self-starters is a superposition of the fields produces by all the nodes.

[1] L. M. Brekhovskikh and O. A. Godin, *Acoustics of Layered Media. 1: Plain and Quasi-plane Waves*, Vol. 5 of Springer Series on Wave Phenomena (Springer, Berlin, 1990).

[2] L. M. Brekhovskikh and O. A. Godin, *Acoustics of Layered Media. 2: Point Sources and Bounded Beams*, Vol. 10 of Springer Series on Wave Phenomena (Springer, Berlin, 1992).

[3] F. B. Jensen, W. A. Kuperman, M. B. Porter, and H. Schmidt, *Computational Ocean Acoustics* (AIP, New York, 1994).

[4] W. A. Kuperman and H. Schmidt, "Rough surface elastic wave scattering in a horizontally stratified ocean," J. Acoust. Soc. Am. **79**, 1767–1777 (1986).

[5] J. A. Davis, D. White, and R. C. Cavanagh, "NORDA Parabolic Equation workshop," NORDA Technical Note 143, Naval Ocean Research and Development Activity, Stennis Space Center, MS (1982).

[6] R. B. Evans and K. E. Gilbert, "Acoustic propagation in a refracting ocean waveguide with an irregular interface," Comput. Math. Appl. **11**, 795–805 (1985).

[7] R. B. Evans and K. E. Gilbert, "The periodic extension of stepwise coupled modes," J. Acoust. Soc. Am. **77**, 983–988 (1985).

[8] K. E. Gilbert and M. J. White, "Application of the parabolic equation to sound propagation in a refracting atmosphere," J. Acoust. Soc. Am. **85**, 630–637 (1989).

[9] M. F. Levy, "Transparent boundary conditions for parabolic equation solutions of radiowave propagation problems," IEEE Trans. Antennas Propag. **45**, 66–72 (1997).

[10] M. F. Levy, "Horizontal parabolic equation solution of radiowave propagation problems on large domains," IEEE Trans. Antennas Propag. **43**, 137–144 (1995).

[11] J. S. Papadakis, "Impedance formulation of the bottom boundary condition for the parabolic equation model in underwater acoustics," NORDA Technical Note 143, Naval Ocean Research and Development Activity, Stennis Space Center, MS (1982).

[12] J. S. Papadakis, M. I. Taroudakis, P. J. Papadakis, and B. Mayfield, "A new method for a realistic treatment of the sea bottom in the parabolic approximation," J. Acoust. Soc. Am. **92**, 2030–2038 (1992).

[13] J. S. Papadakis, "Exact, non-reflecting boundary conditions for parabolic-type approximations in underwater acoustics," J. Comput. Acoust. **2**, 83–98 (1994).

[14] V. A. Baskakov and A. V. Popov, "Implementation of transparent boundaries for numerical solution of the Schrödinger equation," Wave Motion **14**, 123–128 (1991).

[15] S. W. Marcus, "A generalized impedance method for application of the parabolic approximation to underwater acoustics," J. Acoust. Soc. Am. **90**, 391–398 (1991).

[16] A. V. Popov, "Artificial transparent boundaries in computational quasi-optics," in *11th Annual Review of Progress in Applied Computational Electromagnetics* (Applied Computational Electromagnetics Society, Monterey, CA, 1995), pp. 195–201.

[17] A. V. Popov, "Accurate modeling of transparent boundaries in quasi-optics," Radio Sci. **31**, 1781–1790 (1996).

[18] D. Yevick and D. J. Thomson, "Nonlocal boundary conditions for finite-difference parabolic equation solvers," J. Acoust. Soc. Am. **106**, 143–150 (1999).

[19] D. J. Thomson and M. E. Mayfield, "An exact radiation condition for use with the *a posteriori* PE method," J. Comput. Acoust. **2**, 113–132 (1994).

[20] G. H. Brooke and D. J. Thomson, "Nonlocal boundary conditions for high-order parabolic equation algorithms," Wave Motion **31**, 117–129 (2000).

[21] A. Arnold and M. Ehrhardt, "Discrete transparent boundary conditions for wide angle parabolic equations in underwater acoustics," J. Comput. Phys. **145**, 611–638 (1998).

[22] R. A. Dalrymple and P. A. Martin, "Perfect boundary conditions for parabolic water-wave models," Proc. R. Soc. London, Ser. A **437**, 41–54 (1992).

[23] F. Schmidt, T. Friese, and D. Yevick, "Transparent boundary conditions for split-step Padé approximations of the one-way Helmholtz equation," J. Comput. Phys. **170**, 696–719 (2001).

[24] F. Schmidt and D. Yevick, "Discrete transparent boundary conditions for Schrödinger-type equations," J. Comput. Phys. **134**, 96–107 (1997).

[25] D. Yevick, T. Friese, and F. Schmidt, "A comparison of transparent boundary conditions for the Fresnel equation," J. Comput. Phys. **168**, 433–444 (2001).

[26] D. Yu. Mikhin, "Energy-conserving and reciprocal solutions for higher-order parabolic equations," J. Comput. Acoust. **9**, 183–203 (2001).

[27] O. A. Godin, ''Reciprocity and energy conservation within the parabolic approximation,'' Wave Motion **29**, 175–194 (1999).
[28] D. Yu. Mikhin, ''Generalizations of the energy-flux parabolic equation,'' J. Comput. Acoust. (to be published).
[29] F. D. Tappert, ''The parabolic approximation method,'' in *Wave Propagation and Underwater Acoustics*, Vol. 70 of Lecture Notes in Physics, edited by J. B. Keller and J. S. Papadakis (Springer, New York, 1977), pp. 224–284.
[30] M. D. Collins, ''A split-step Padé solution for the parabolic equation method,'' J. Acoust. Soc. Am. **93**(4), 1736–1742 (1993).
[31] A. Bamberger, B. Engquist, L. Halpern, and P. Joly, ''Higher order parabolic wave equation approximations in heterogeneous media,'' SIAM (Soc. Ind. Appl. Math.) J. Appl. Math. **48**(1), 129–154 (1988).
[32] M. D. Collins, ''Higher-order Padé approximations for accurate and stable elastic parabolic equations with application to interface wave propagation,'' J. Acoust. Soc. Am. **89**(3), 1050–1057 (1991).
[33] F. A. Milinazzo, C. A. Zala, and G. H. Brooke, ''Rational square-root approximations for parabolic equation algorithms,'' J. Acoust. Soc. Am. **101**, 760–766 (1997).
[34] G. A. Korn and T. M. Korn, *Mathematical Handbook for Scientists and Engineers* (McGraw-Hill, New York, 1968).
[35] J. N. Lyness and G. Sande, ''Algorithm 413. ENTCAF and ENTCRE: Evaluation of normalized Taylor coefficients of an analytic function,'' Commun. ACM **14**, 669–675 (1971).
[36] C. Lubich, ''Convolution quadrature and discretized operational calculus II,'' Numer. Math. **52**, 413–425 (1988).
[37] F. B. Jensen and C. M. Ferla, ''Numerical solutions of range-dependent benchmark problems,'' J. Acoust. Soc. Am. **87**, 1499–1510 (1990).

Measurements of scattering by suspensions of irregularly shaped sand particles and comparison with a single parameter modified sphere model

Peter D. Thorne[a)]
Proudman Oceanographic Laboratory, Joseph Proudman building, 6 Brownlow Street, Liverpool L3 5DA, United Kingdom

Michael J. Buckingham
Marine Physical Laboratory, Scripps Institution of Oceanography, University of California, San Diego, 9500 Gilman Drive, La Jolla, California 92093-0238

(Received 12 August 2003; revised 4 August 2004; accepted 30 August 2004)

Measurements are presented of multi-frequency underwater acoustic backscattering from suspensions of glass spheres and sands. The data were collected in a sediment tower, specifically designed for such measurements and capable of generating a homogeneous suspension over a distance of approximately 1 m. The glass sphere data were collected to assess the capability of the system and for calibration. The measurements on suspensions of sands were obtained as part of on-going studies into the measurement of nearbed sediment transport processes using acoustics. Utilizing the backscattered sound from sand suspensions, both the form function and total scattering cross section of the sediments have been measured for a range of sediments and particle sizes. Interpretation of the observations has been carried out within a framework of sphere scattering. The results show enhanced scattering for suspensions of sand grains, relative to that of similar size spherical scatterers and the enhancement can be described by a function dependent on the particle size and the wave number of the insonifying sound, with one free parameter. © *2004 Acoustical Society of America.* [DOI: 10.1121/1.1808458]

PACS numbers: 43.30.Ft, 43.30.Gv, 43.30.Pc [KGF] Pages: 2876–2889

I. INTRODUCTION

The development of our understanding of sediment transport processes, over sandy beds, has benefitted greatly from recent developments in the application of acoustics to this problem.[1] The potential of acoustics to provide co-located, simultaneous measurements of the seabed morphology, the sediment field, and the hydrodynamics, provides opportunities to examine how these three mutually interactive and interdependent components interrelate with each other. The idea of using acoustics for such studies is attractive and straightforward. A pulse of high frequency directional sound, typically in the range 0.5–5 MHz and centimetric in length, is transmitted from a source usually mounted around a metre above the bed. As the pulse propagates down towards the bed, sediment in suspension backscatters a proportion of the sound and the bed generally returns a strong echo. This signal has the potential to provide information on profiles of suspended sediment parameters, the flow, and the time history of the bedforms. The aim of such measurements is to provide sedimentologists and coastal engineers with new measuring capabilities for studying sediment entrainment and transport.

In the present study the focus is on the measurement and description of the scattering characteristics of suspensions of glass spheres and sands. The backscattering characteristics are formulated in terms of the form function and the attenuation through the total scattering cross section. These descriptions are at the kernel of the inversion to extract the suspended sediment component from the backscattered signal. Also, generically, although the scattering properties of a number of canonically shaped bodies are reasonably well understood, there are many natural scatterers that are irregular in shape and a description of such bodies is required. To date the data published on the backscattering characteristics of suspensions of irregularly shaped sand particles have been limited to the works of Hay.[2,3] These works form the basis of our current description of the backscattering properties of suspensions of marine sands. A further work has supported this general description.[4] However, a more recent detailed study on the attenuation characteristics[5] of sand suspensions showed significantly higher attenuation values than predicted by the commonly employed sphere-based scattering models[6] and somewhat larger than may have been anticipated on the basis of the previous scattering measurements.[2,3,7] This result led the present authors to revisit the form function and total scattering cross section characteristics for suspensions of sand and to this end a series of measurements were collected on different sand samples to examine their scattering properties. With the exception of one reported data set,[2] the measurements on the scattering properties of sediments have either measured the form function or the total scattering cross section; however, in the present study, both scattering prop-

[a)]Current address: Proudman Oceanographic Laboratory, Joseph Proudman Building, 6 Brownlow Liverpool L3 5DA, United Kingdom. Electronic mail: pdt@pol.ac.uk

erties were measured from the backscattered signal. The ability to measure both scattering parameters simultaneously provided an opportunity to assess the consistency of the descriptions of the form function and the total scattering cross section.

To provide a description of the scattering properties of the irregularly shaped sand sediments, calculations based on a simple analytical shape, the sphere, have been used. This approach of using canonically shaped representations with analytical solutions is common and has been used for both sediment[2–8] and biological scatterers.[9–11] The results from this study show both the form function and total scattering cross section can be reasonably well represented by a quartz sphere model, modified by an enhanced scattering function, dependent on the suspension particle "radius," a_s, and the wave number, k, of the sound in water, with one free parameter. The word radius is placed in quotation marks to indicate the definition of particle radius has a degree of ambiguity for irregularly shaped particles and this is considered later. The justification for using an enhancement factor which is dependent on ka_s is based on two premises. The first is that, in the Rayleigh region,[12] $ka_s \ll 1$, scattering is considered to be independent of the shape of the scatter. Though this is only strictly true for a fluid scatterer, one might anticipate elastic spherical and irregularly shaped scatterers may have similar scattering characteristics.[13] For $ka_s \gg 1$, sometimes known as the geometric regime, there is a theorem that states the geometric cross section of a convex particle, averaged over all orientations, is equal to a quarter of the surface area of the particle.[14,15] Given that a sphere has the minimum surface area to volume, then a particle of irregular shape, having a similar volume to a sphere, would have a larger surface area and hence a higher geometric and scattering cross section. This, therefore, leads straightforwardly to the expectation that there will be a functional dependence on ka_s of the scattering characteristic of a suspension of sand, relative to spheres having the same volume, and, as will be shown later, this approach requires only one free parameter to account for the difference between sphere and sand grain scattering. This methodology differs from that of Ref. 5 which used a two parameter equivalent sphere model. Two parameters were required to fit their observations to a sphere model because the functional dependence on ka_s, of irregularly shaped particle scattering relative to a sphere, was not considered. It will be shown here that the data in Ref. 5 can be represented by the approach adopted in the present paper.

II. SUSPENSION SCATTERING

For incoherent scattering, when the scattered phase is random and uniformly distributed over 2π, the recorded root-mean-square backscattered voltage, V, from a suspension of sediments, insonified with a piston source transducer, can be written[1,2,6,8] as

$$V = \frac{K_s K_t M^{1/2}}{r\psi} e^{-2r\alpha},$$

$$K_s = \frac{f_m}{(\rho\langle a_s\rangle)^{1/2}}, \quad K_t = P_o r_o \Re T_v \left\{\frac{3c\tau}{16}\right\}^{1/2} \frac{0.96}{ka_t}, \tag{1}$$

$$\alpha = \alpha_\omega + \frac{3}{4\rho_s r}\int_o^r \frac{\chi_m}{\langle a_s\rangle} M\, dr.$$

The term K_s represents the sediment backscattering properties, ρ_s is the sediment grain density, $\langle a_s\rangle$ is the mean particle radius of the sediment in suspension and $f_m = \{\langle a_s\rangle\langle a_s^2 f^2\rangle/\langle a_s^3\rangle\}^{1/2}$, where f is the form function in the backscatter direction and describes the backscattering characteristics of the scatterers. $\chi_m = \{\langle a_s\rangle\langle a_s^2\rangle\chi/\langle a_s^3\rangle\}$, χ is known as the total scattering cross section and describes the scattering attenuation characteristics of the scatterers. $\langle\ \rangle$ represents an average over the particle size distribution of the sediments in suspension. The term α_ω is the sound attenuation due to water absorption, M is the concentration of sediment in suspension, r is the range from the transducer, and ψ accounts for the departure from spherical spreading within the transducer nearfield.[16] For fixed settings K_t is a system constant. This comprises of the reference pressure, P_o, normally defined at $r_o = 1$ m, $\Re$ is the receive sensitivity, T_v is the voltage transfer function for the system, $c\tau$ is the pulse length, where τ is the pulse duration and c is the velocity of sound in water, k is the wavenumber of the sound in water, and a_t is the radius of the transducer.

To evaluate Eq. (1) the magnitude of the backscatter form function and the total scattering cross section are required. For a sphere these can be expressed[8,17] as

$$f = \left|\frac{2}{ix}\sum_{n=0}^{n=\infty}(-1)^n(2n+1)b_n\right|, \tag{2a}$$

$$\chi = \left|\frac{-2}{x^2}\sum_{n=0}^{n=\infty}(2n+1)\mathrm{Re}(b_n)\right|, \tag{2b}$$

where b_n is a function of spherical Bessel and Hankel functions of the first kind and their derivatives, Re denotes taking the real part of the complex expression, and $x = ka$, where a is the radius of the sphere. For the scattering of suspensions of sand a definition is required for the particle size and, from the discussion at the end of the Introduction, ascribing an equivalent sphere dimension is not readily defined. Even if one were to adopt the radius of a sphere with the equivalent surface area to that of the grains, obtaining such measurements for a suspension of sand grains would seem problematic. Therefore a pragmatic approach was taken and the size measured by sieving the sediments into relatively narrow size fractions was taken to define the particle size. Such an approach is not arbitrary, since most sedimentologists use sieving to define the particle size of sands and the end product of the application of acoustics to sediment processes is to deliver to the sedimentologist measurements of parameters they can readily utilize. In the present study the experimental expressions for the scattering parameters were

chosen to be independent of particle size. Taking the natural logarithm of Eq. (1), we can write for a homogenous suspension (as was the case in the present study, see Figs. 3 and 4)

$$\ln(Vr\psi)=\ln\left(f_m K_t\sqrt{\frac{M}{\rho_s\langle a_s\rangle}}\right)-2r\left(\alpha_w+\frac{3\chi_m M}{4\rho_s\langle a_s\rangle}\right). \tag{3}$$

This is now a simple linear equation in $\ln(Vr\psi)$ and r, and allows the following to be written

$$f_x=\frac{e^{\eta}}{K_t}\sqrt{\frac{\rho_s}{kM}}, \tag{4a}$$

$$\chi_x=\frac{2\rho_s}{3kM}(\kappa-2\alpha_w), \tag{4b}$$

where η and κ are respectively the intercept and the magnitude of the gradient obtained from the measurements as expressed in Eq. (3). Here we have used $f_x=f_m/\sqrt{x}$ and $\chi_x=\chi_m/x$, and for the measured values $x=k\langle a_s\rangle$ and $\langle a_s\rangle$ was the sieved sediment radius. The advantage of this form of expression is the rhs of Eqs. (4a) and (4b) do not depend on a definition of particle size.

To compare a sphere based scattering model with the measurements collected on suspensions of sands a simple modification to Eq. (2) was applied for consistency with the experimental definitions of f_x and χ_x. These equations are now written as

$$f_s=\gamma\langle f/\sqrt{x}\rangle, \tag{5a}$$

$$\chi_s=\gamma\langle\chi/x\rangle, \tag{5b}$$

where $\langle\ \rangle$ represents an average over a range of x. This essentially operates as a low pass filter and reduces the variation in f_s and χ_s associated with the acoustic resonances of a sphere (see Refs. 1–6). γ is the function in Eq. (5) which will be used to account for the difference in the scattering level, with x, between the low pass sphere model [i.e., Eq. (5) with $\gamma=1$] and the measured values for suspensions of sand, obtained from Eq. (4).

III. SEDIMENTS USED IN THE STUDY

A series of measurements was taken on glass spheres and seven different sands collected from estuarine, beach, and quarried locations. In Fig. 1 are scanning electron micrographs of the sediments used. The sand sediments labelling of (a) to (g) is consistent and is used in Fig. 1, Table I and Figs. 9 and 10. The glass spheres can be seen to be nominally spherical in shape, although it can be readily observed there was some departure from perfect sphericity. Although the glass sediments were not ideally spherical, studies on such suspensions[2,5,8,18] have shown their scattering characteristics are well represented by the theoretical description of a sphere. For the sphere calculations of the form function and total scattering cross section, the material properties chosen were based on measurements.[19] The values used for the compressional and shear wave velocities were respectively 5550 and 3545 ms^{-1}, with a density of 2500 $\mathrm{kg\,m}^{-3}$. For water the values used for density and sound velocity were 1000 $\mathrm{kg\,m}^{-3}$ and 1480 ms^{-1}. The comparison of the glass sphere prediction and measured form function is not highly sensitive to the sphere velocities chosen, within approximately $\pm 5\%$ of the above values, since they primarily control the resonance structure of the form function and, as will be seen later, these are only weakly observed when there is even a small departure from a uniform particle size in suspension.

The seven scanning electron micrographs of the sediments show in detail the size and shape of the sediments used in the study. None of the particles are particularly spherical; in fact, it would be difficult to formulate a geometric shape which accurately represents the profiles of the particles. Generically they could be described as irregular in form, with curved surfaces, facets, and edges. It does appear that some sediments are more rounded than others, for example, sample "*a*" sediments look as if they are somewhat smoother than the sediments "*b*," which appear more angular. Also sediment "*f*" has some particle shapes which were relatively flat in form. The effect these changes in particle shape have on the acoustic scattering properties of suspended sediments will influence whether or not a general description of the form function and total scattering cross-section can be obtained, which has wide-ranging applicability. All the sediments studied were sand grains, primarily composed of quartz and, for the calculations to follow, the density, compressional, and shear wave velocities were taken[20] to be respectively 2650 $\mathrm{kg\,m}^{-3}$, 5980 ms^{-1}, and 3760 ms^{-1}. Again the choice of velocities was not critical because variations of up to $\pm 10\%$ did not significantly alter the modified low pass sphere solution given by Eq. (5).

To study both the suspensions of glass spheres and sand grains, the sediments were sieved into $\frac{1}{4}\ \varphi$ ($\phi=-\log_2 d$ where d is the particle diameter in millimeters) narrow size fractions. Table I shows the values of $\langle a_s\rangle$ for the sediments studied and the number of experiments conducted on each sediment and each size fraction.

IV. DESCRIPTION OF THE SEDIMENT TOWER

The experimental arrangement used to measure the scattering properties of glass sphere and sand suspensions is shown in Fig. 2. The sediment tower was constructed from Perspex, with the main component being a vertical 2.15 m tube, with an inner diameter of 0.3 m and wall thickness of 0.01 m. Once the tower was filled with a suspension, bilge pumps were used to extract water and sediment from the bottom of the tower and deliver it back to the top of the tower through a 0.05-m-diam pipe. Two bilge pumps, pumping side by side, operating at approximately 50% of their maximum capacity, were chosen for this function. Operating in this mode prevented pump cavitation and thereby reduced the possibility of introducing air into the system through the pumping mechanism. Also two pumps generated sufficient flow in the return pipe to ensure the sediments extracted with the water from the bottom of the tower were returned to the top. At the top of the tower the suspension was reintroduced below the upper water surface, open to the atmosphere, through a mixing chamber, designed to homogenize the suspended sediments within the tower, without the entrainment of air. Further to assist with the homogeneity of the suspension, a unit near the base of the tower, consisting of a turbu-

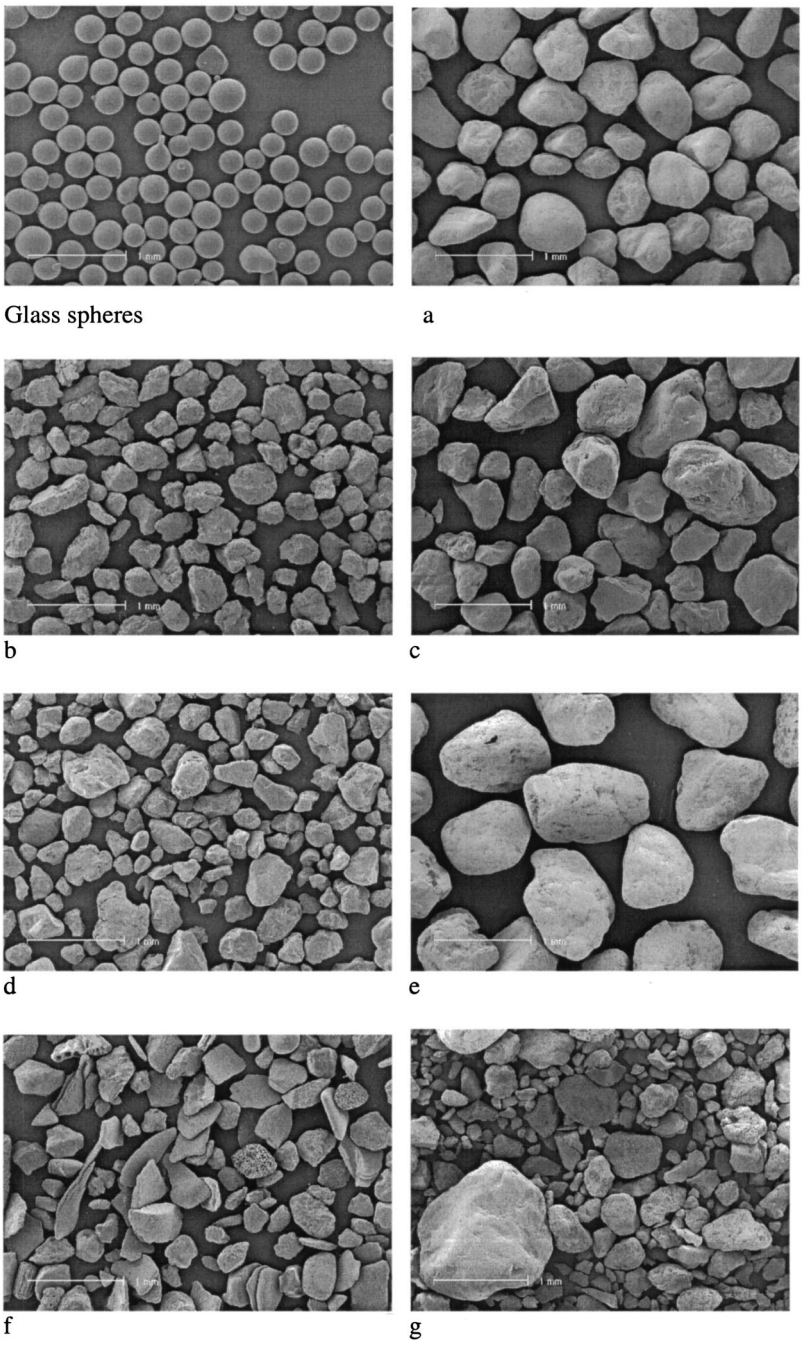

FIG. 1. Scanning electron micrographs of the glass spheres and sands used in the study.

lence grid, impeller, and propeller, was rotated to generate an upward mixing turbulent flow. This combination of mixing elements was designed to generate a uniform suspension throughout the tower.

To assess the homogeneity of the suspension in the tower three experiments were conducted using suspensions. The sediments used were glass spheres with $\langle a_s \rangle = 115.5\,\mu$m and $\langle a_s \rangle = 195\,\mu$m, and sand with $\langle a_s \rangle = 195\,\mu$m. Pumped samples of the sediments were collected between 0.1 and 0.8 m below the transducers, and located on the central vertical axis of the tower, at 0.07 m from the axis, and at 0.14 m from the axis; the latter was within 0.01 m of the tower wall. Know volumes of water were extracted, passed through a filter, and the retained sediments dried and weighed. The concentration was then calculated as the dried mass divided by the volume of water extracted. The resultant measured concentrations are given in Fig. 3. The data clearly show the suspended sediments were homogeneous both across the tower and vertically. There was no significant difference with sediment size or between the glass spheres and the sand. These measurements clearly show the sediments in suspension were homogeneous and uniform with range below the transducers.

To obtain the scattering measurements a triple frequency acoustic backscatter system operating at 1.0, 2.0, and 4 MHz was mounted in the upper section of the tower. The transducers had respective nominal −3-dB half beamwidths of 3.1°, 2°, and 1.2°. The system measured the envelope of the backscattered signal at 0.01-m intervals over a range of 1.28 m. For data collection a low pulse repetition frequency of 4 Hz was used to allow the sound from one transmission to dissipate before the following transmission. For each measure-

TABLE I. The table shows the number of experiments conducted, at each sediment size, for the different sediments. The total column and row respectively give the number of experiments conducted on each sediment and for each size. β_f and β_χ respectively give the values for β in Eq. (7) for calculating f_s and χ_s.

$\langle a_s \rangle$ (μm)	Glass	a	b	c	d	e	f	g	Total
45.0								2	2
57.75	3				2		7	2	11
68.75	3				2		3	2	7
82.5	3		3	1	2	3	5	4	18
98.0	5			2	1	1	3	2	9
115.5	16		1	2	1	1	4	2	11
137.5	11		2	3		1	3	4	13
163.75	2	5		4		1	5	2	17
195.0	9	5	1	3		1	6	6	22
231.25	5	8		3		1	5	4	21
275.0	3	5		5					10
327.5	3	3		4		2			9
390	3			1					1
Total	66	26	7	28	8	11	41	30	151
β_f		2.1	1.7	2.4	1.6	2.0	2.4	1.4	1.9±0.4
$\sigma(\beta_f)$		0.4	0.3	0.5	0.2	0.2	0.3	0.2	
β_χ		1.6	1.9	1.8	1.7	1.8	1.7	1.4	1.7±0.2
$\sigma(\beta_\chi)$		0.4	0.2	0.5	0.3	0.3	0.4	0.3	

ment run 320 backscatter profiles were collected at each frequency. These profiles were averaged and the scattering levels calculated. Four runs were conducted to provide a mean form function and total scattering cross section with

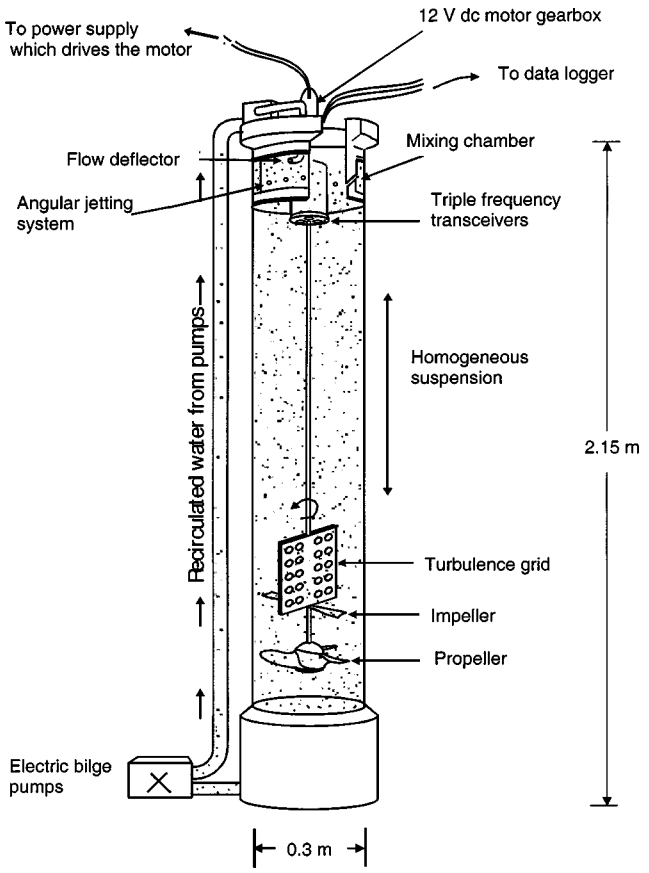

FIG. 2. The sediment tower used to measure the suspension scattering properties of glass spheres and sands.

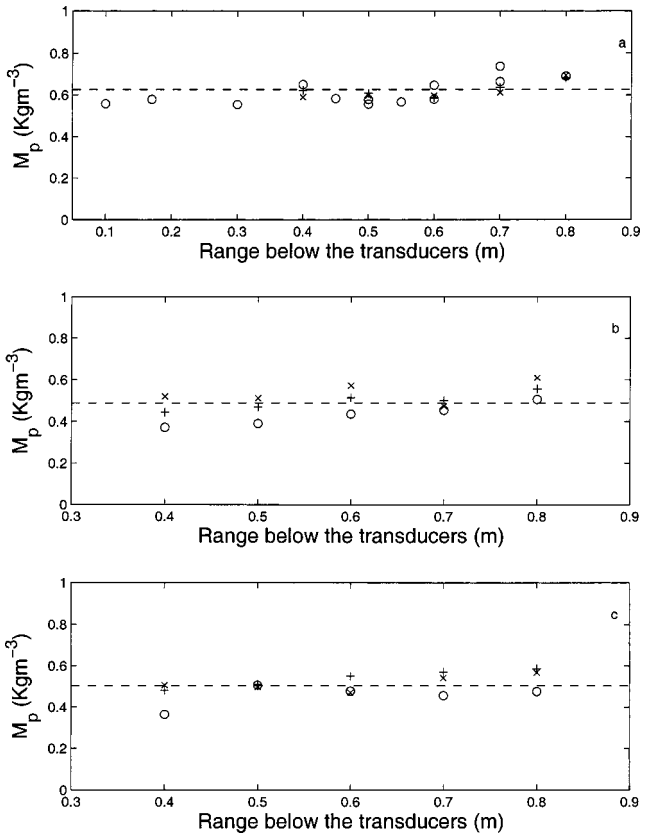

FIG. 3. Pumped sample measurements in the tower of the suspended sediment concentration with range below the transducers. Data were collected on the central axis of the tower (○), at 0.07 m from the axis (×), and at 0.14 m from the axis (+) for sediment sizes; (a) glass spheres with $\langle a_s \rangle = 115.5\ \mu$m, (b) sand with $\langle a_s \rangle = 195\ \mu$m, and (c) glass spheres with $\langle a_s \rangle = 195\ \mu$m.

error bars. This averaging was required to offset the effects of configurational noise[21] associated with the random position of the scatterers within the insonified volume and short-term fluctuations in the homogeneity of the suspension.

V. SPHERE BACKSCATTERING AND SYSTEM CALIBRATION

For all the scattering measurements, glass spheres, and sands, a common measurement procedure was adopted and this is briefly described here. After the tower had been filled with water from the mains supply, a period of several hours to days was provided, with the pumps and mixing systems running, to allow time for any bubbles present in the water to vent through the upper open water surface into the atmosphere. Acoustic backscatter data were collected over this period, and this degassing process continued until signals reduced to background levels. These varied between 1% and 10% of the levels recorded when sediment was in suspension, depending on particle size, range, frequency, and concentration. The background levels, due to detritus, residue micro-bubbles, and possibly turbulence scattering, were accounted for in the data processing procedure. Water-saturated degassed sediments were added to the tower and a period of several hours was allowed for the suspension to become homogeneous throughout the tower. Four acoustic runs were then carried out separated by approximately 5 min, with 320

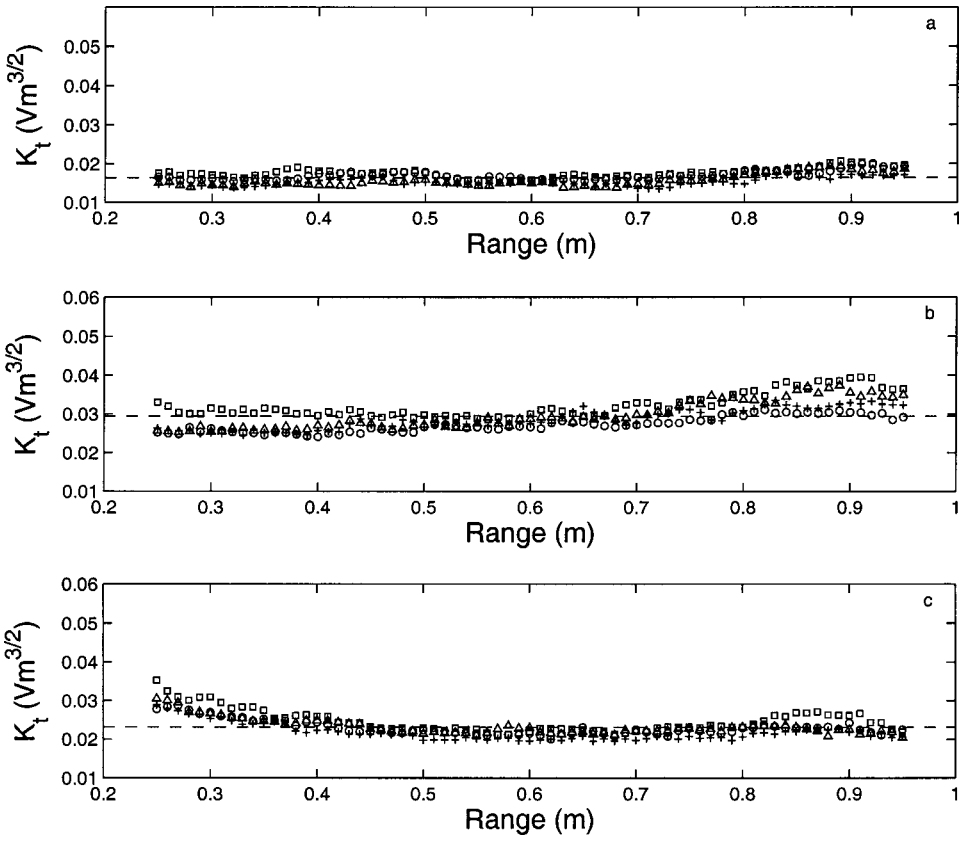

FIG. 4. Measurement of the system constant, K_t, at (a) 1.0 MHz, (b) 2.0 MHz, and (c) 4.0 MHz. The measurements were from data collected on glass spheres having mean radii of (○) 98 μm, (+) 115 μm, (△) 137 μm, and (□) 195 μm.

profiles being collected at each frequency on each run. Nominally this was repeated four times, with about 1 h between each set of four runs. At the end of the last run, pumped sampling at 0.4 and 0.75 m below the transducers was carried out to establish the concentration and homogeneity of the suspension. This series of measurements, 16 runs, constituted one experiment on one particular particle size. At the end of the experiment the sediments were extracted from the tower by placing a fine gauze net within the body of the tower. This extraction continued until acoustic background measurements showed there was no significant residue of sediment in the tower. A different sediment sample was then introduced into the tower and new acoustic and pumped sample data collected. The experiments were inter-

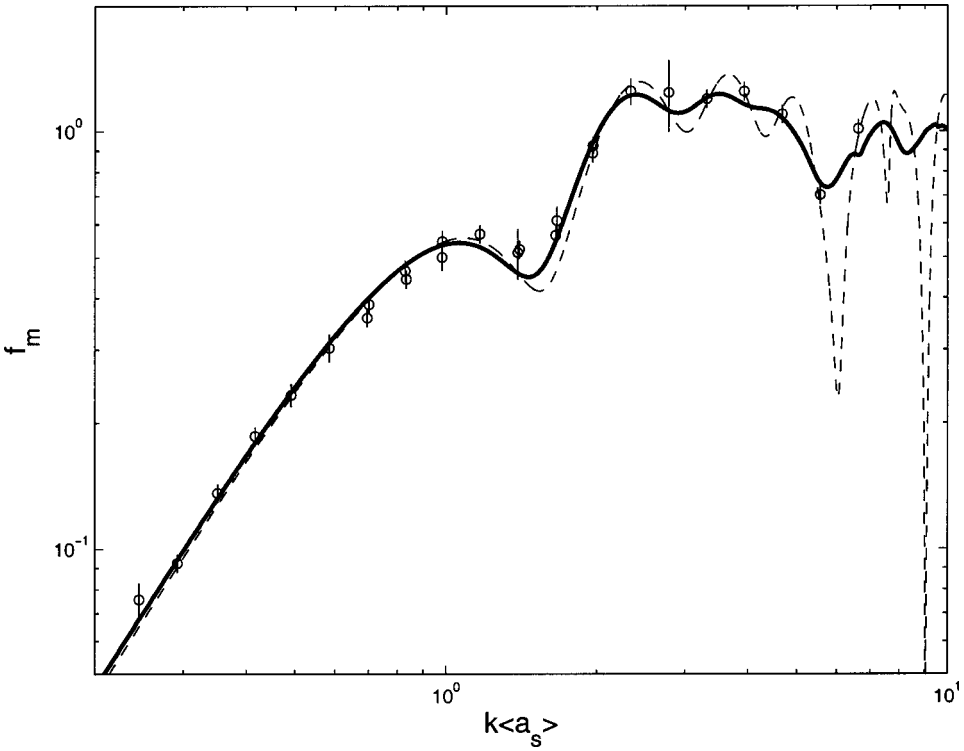

FIG. 5. Predicted and measured (○) backscatter form function for a suspension of glass spheres. The lines show the form function for the case of a single particle size in suspension (--) and for the size distribution due to the $\frac{1}{4}$ ϕ sieves used (———).

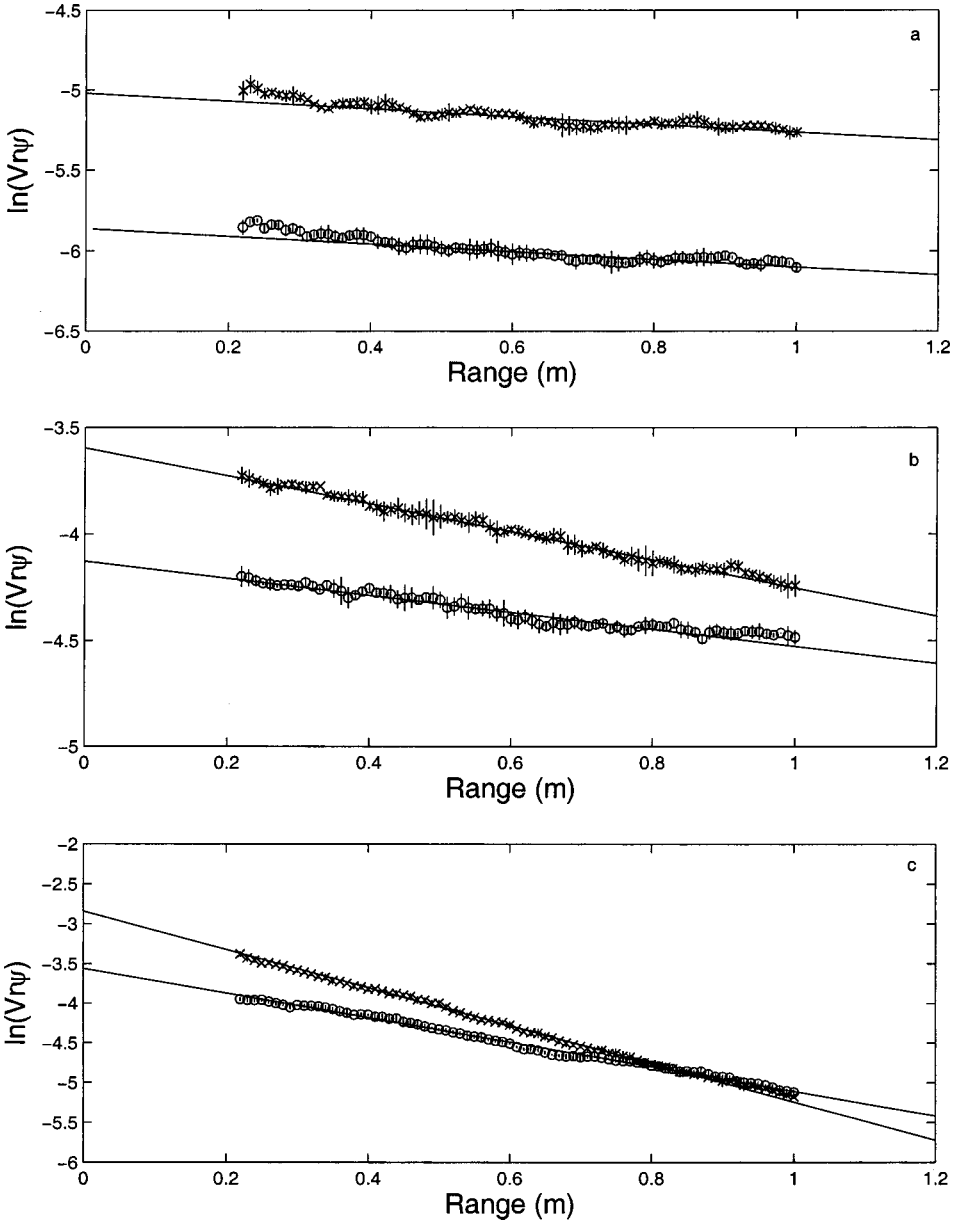

FIG. 6. Measurements of the variation of $\ln(Vr\psi)$ with range, r, from the transducer at (a) 1.0 MHz, (b) 2.0 MHz, and (c) 4.0 MHz, for sand suspensions with $\langle a_s \rangle = 57.75\ \mu$m (○) and $\langle a_s \rangle = 137.5\ \mu$m (×).

leaved with different particle sizes and repeat sizes. This procedure provided checks on the stability of the system over time and yielded error bars for the final results. The number of experiments conducted on each sediment and particle size is given in Table I.

To obtain the scattering properties of the sand suspensions required the system constant, K_t, to be known. One method is a full electronic and acoustic calibration of the system.[8,22] The electronic calibration requires measuring the voltage transfer function of the system, T_v. This includes measuring transmit signal levels, receiving amplification, and the form of the time varying gain if applied. The acoustic calibration requires measurements of the source level, $P_o r_o$, (Pa V^{-1} ref 1 m), and the receive sensitivity, $\mathfrak{R}$ (V Pa^{-1}), of the transducer. Also, to establish a_t generally requires the transducer beam pattern to be measured. This absolute calibration is a relatively time consuming process; however, given the sediment tower developed for the present study, most of the calibration can be circumvented by measuring the backscattered signal from suspensions with known scattering characteristics.

The calibration approach used was to rearrange Eq. (1) and have K_t on the lhs of the equation. This gives

$$K_t = \frac{Vr\psi}{K_s M^{1/2}} e^{2r\alpha}. \tag{6}$$

Conducting observations in the sediment tower on a homogeneous suspension, at a measured concentration, with a known scattering description, provided the value for the system calibration constant. Glass spheres were used for the suspension, since they were readily available in the required size range, and the scattering characteristics of glass spheres can be accurately predicted. If the electronic gain of the system is constant (this was the case for the present system), K_t has a single value; if time varying gain is applied to the system, K_t will be a function of range.

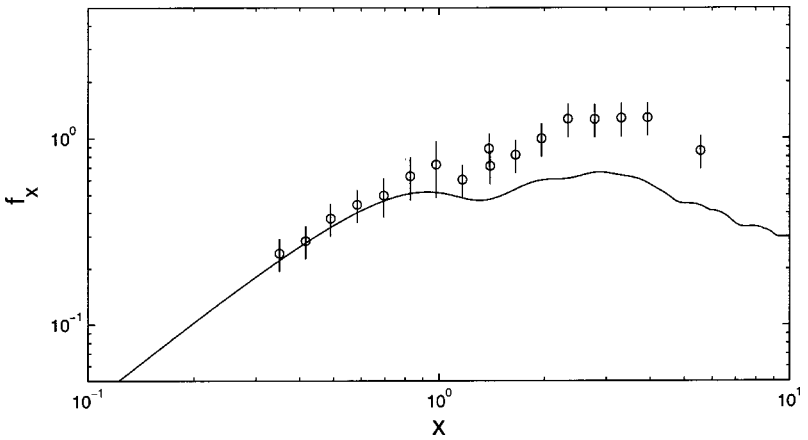

FIG. 7. Measurements of f_x (○) and calculated f_s (———) with $\gamma=1$, versus x.

An example of the measurement for K_t is given in Fig. 4. The data shown were from experiments on suspensions of glass spheres having mean radii of 98, 115, 137, and 195 μm. The plot shows the value of K_t with range for the four particle sizes. It can be seen that K_t was nominally constant with range, and the relatively small variations between the different suspensions sizes show consistent values of K_t could be obtained. The ostensibly uniform value of K_t with range further supports the homogeneity of the suspension in the tower. However, it is acknowledged that there were fluctuations in the suspension homogeneity during a run and from run to run, and this was overcome by repeating measurements and building up error statistics for the data collected.

Measurements of K_t were collected over a 3-year period interleaved with the sand suspension measurements. Carrying out glass sphere measurements at regular intervals throughout the measurement program provided an assessment of the system performance over time. To illustrate the quality of the measurements obtained in the sediment tower, the form function was calculated for the glass sphere experiments using the system constant for each frequency. The results are presented in Fig. 5. The dashed line represents the form function for a suspension having a uniform particle size; the solid line was calculated on the basis of a size distribution in suspension arising from the $\frac{1}{4}\,\phi$ sieves used to sieve the sediments. As can be seen in Fig. 5, the measured and predicted form functions show good agreement over $x=0.19-6.5$ which spans the region from the Rayleigh regime through to approximately the geometric. The error bars on the individual data are of the order of 10%–15%. It does not seem unreasonable, given the general agreement between the observations and the predictions for the glass spheres and the error bars measured, that the glass sphere observations provide an indication of the accuracy of the form function and total scattering cross section measurements for suspensions of sand grains.

VI. MEASUREMENTS ON SAND SUSPENSIONS

To obtain the form function and total scattering cross section, the expressions in Eq. (4) were employed. Examples of the data collected are shown in Fig. 6. The data show the variation of $\ln(Vr\psi)$ with range, r, from the transducer. The data were taken from two experiments carried out with sand suspensions having $\langle a_s\rangle=57.75\,\mu$m and $\langle a_s\rangle=137.5\,\mu$m. For each experiment the data have been averaged over the runs to form a mean and standard deviation. The variability observed in the data is due both to fluctuation in the suspended concentration and configuration noise. As shown in the figure, a regression line was calculated for each data set and the slope, κ, and the intercept with the ordinate, η, was measured. The first 0.2 m from the transducer were not used in the analysis to avoid the period of transmitter–receiver interference following transmission (crosstalk) and to circumvent inaccuracies in the calculation of ψ due to any imprecision in the value of a_t. Also the range was restricted to approximately 1 m to reduce signal to noise problems at the longer ranges. Using the measured value for η and κ the rhs of Eq. (4) was evaluated. It should be noted that for small values of x, nominally $x\leqslant 1$, the value for χ_x had a high degree of uncertainty due to $\kappa\approx 2\alpha_w$, therefore data analysis

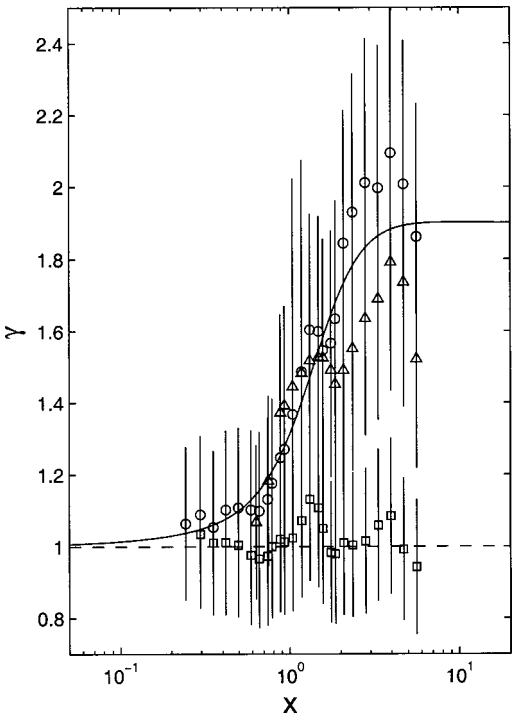

FIG. 8. Measurements for sand of the ratios f_x/f_s (○) and χ_x/χ_s (△) versus x, and Eq. (7) (———) with $\beta=1.9$. The equivalent calculation for the glass sphere results are given by (□).

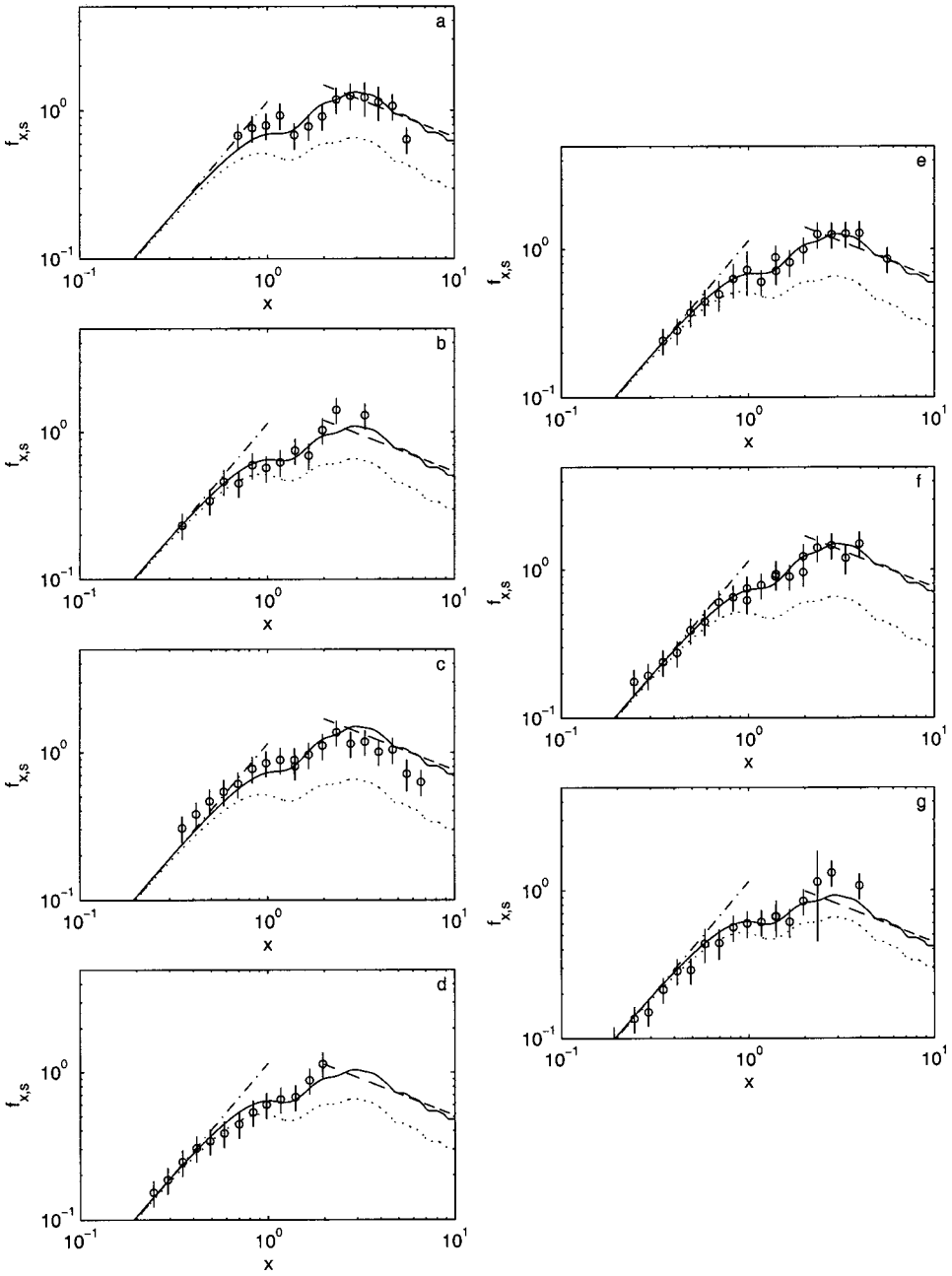

FIG. 9. Comparison of f_x (○) and f_s (———) for all of the sand suspensions, (···) $\gamma=1$ in Eq. (5a), (-·-) Rayleigh scattering and (--) geometric scattering. In the present figure and the following, plots $f_{x,s}$ represent f_x, f_s.

of the total scattering cross section was restricted to values above $x \approx 0.5$. Such a constraint did not apply to f_x.

An example of the measurements of f_x is shown in Fig. 7. The data show a steady increase in magnitude of f_x with x, with peak values in the region $x=2-3$. The solid line, f_s, was calculated using Eq. (5a) with $\gamma=1$. The measurements show that for $x \ll 1$, the Rayleigh region, the predictions based on sphere scattering are in close agreement with the observation. However, as x increases and geometric scattering is approached, there is an increased divergence between the measured value for f_x and the calculated value for f_s. Therefore, as alluded to in the Introduction, there is a functional dependence of γ on x.

To ascertain this dependence, the ratios f_x/f_s, and χ_x/χ_s, with $\gamma=1$, were calculated for all the glass sphere and sand suspension data, the outcome of which is shown in Fig. 8. Although there is scatter in the data and relatively large error bars, associated with measuring the ratios of the observed and predicted values, there is a clear trend of increasing divergence between the observations and the sphere based model with $\gamma=1$ for the sand data; however, as would be expected, no such trend is observed in the glass sphere data. To represent the difference the following simple expression was used.

$$\gamma = \frac{\beta x^3 + 0.5x + 3.5}{x^3 + 3.5}. \tag{7}$$

This had the required form, reducing to unity in the Rayleigh regime, increasing over the intermediate values for x, remaining constant for geometric scattering and with β accounting for the enhance scattering in the geometric regime. The structure of this curve is shown in Fig. 8 with $\beta=1.9$. β is the free parameter; it is independent of x and represents the

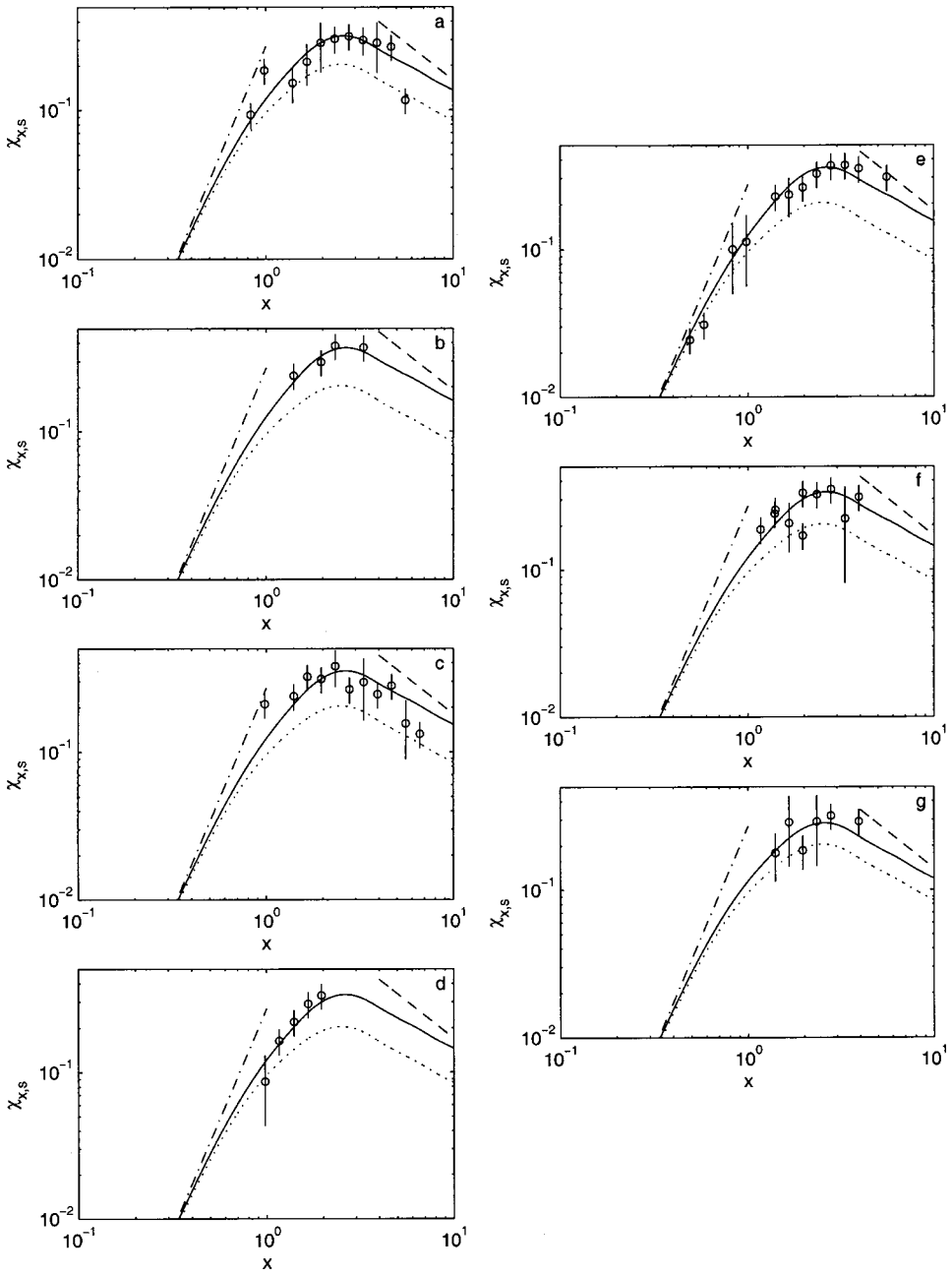

FIG. 10. Comparison of χ_x (○) and χ_s (———) for all of the sand suspensions, (···) $\gamma=1$ in Eq. (5b), (-·-) Rayleigh scattering and (--) geometric scattering. In the present figure and the following, plots $\chi_{x,s}$ represents χ_x, χ_s.

upper limit of γ. Equation (7) can be seen to compare reasonably well the data and, to first order, represents the enhanced scattering for irregularly shaped particles, from the Rayleigh regime through to the geometric scattering regime.

For comparison of the sphere model with the individual sediments used in the study, the value for β was allowed to vary and no constraint was placed on using the same value of β for calculating f_s and χ_s. To obtain the optimum value for β a routine was used which minimized $|\Gamma_x-\Gamma_s|/\Gamma_s$, where Γ was f or χ, as β was varied between 0.5 and 2.5 in step intervals of 0.1. The resulting values of β with calculated standard deviations are given in Table I. The results for the backscattering cross section measurements are shown in Fig. 9. The plots show the measured values for f_x, the low pass sphere calculations f_s using γ with β values from Table I, f_s with $\gamma=1$ and Rayleigh and geometric scattering. In general it can be seen that the enhanced sphere model reproduces the general features of the data. There is initially an increase in f_x and f_s with a $x^{3/2}$ dependency in the low x region. This is followed by a reduction in the increase of f_x and f_s, with a maximum value at $x\approx 3$. At higher values of x, as the geometric region is approached, there is a reduction of f_x and f_s which approaches a $x^{-1/2}$ dependency on x. There are minor divergences from these trends and there is some scatter in the data, both of which are probably associated with the detailed mineralogy, particle shape, and experimental uncertainty. However, as can be seen, the expression for γ does provide a reasonably accurate correction factor to the sphere scattering model. Figure 10 compares χ_x and χ_s. The measurement region is limited to $x>0.5$ for reasons previously outlined and the data is somewhat more variable than the measurement of the backscattering cross section. Within the limitation of the data set collected, the observation of χ_x and the calculated values for χ_s are in broad agreement.

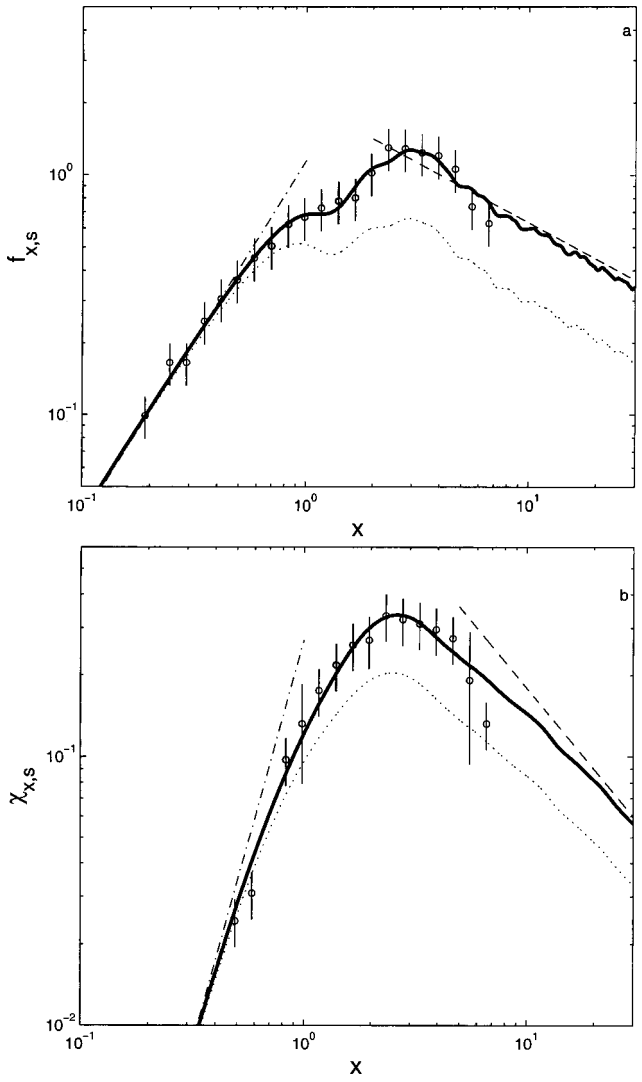

FIG. 11. (a) The variation in f_x (○) obtained by combining all the measurement on sand suspensions. (———) f_s with $\beta=1.9$, (···) f_s with $\gamma=1$. (b) The variation in χ_x (○) obtained by combining all the measurement on sand suspensions. (———) χ_s with $\beta=1.7$, (···) χ_s with $\gamma=1$. (-·-) is Rayleigh scattering and (--) is geometric scattering.

There is a reduction in χ_x and χ_s for low values of x, although only limited reliable observations could be obtained in the Rayleigh region to assess the x^3 dependency, the peak in the observations and calculation is around $x\approx 2.6$, and there is a reduction in χ_x and χ_s with x above this value, though it is difficult to fully validate the geometric x^{-1} dependency due to the upper limit of x in the data set.

In Fig. 11 all the sand suspension data have been combined to give representative values for f_x and χ_x. Figure 11(a) shows the variation of f_x and it can be seen the data follow the Rayleigh dependency for $x \ll 1$ and approach the geometric value for $x \gg 1$, though the data are marginally lower at the highest values of x measured. However, it is difficult to assess if this lower trend is genuine because of the upper limit of x measured. The form of f_s with $\beta=1.9$, given by the broad line, is in good agreement with the data and represents reasonably well the observations. The dotted line represents the sphere calculation with $\gamma=1$. Figure 11(b) shows the measurement for χ_x. Averaging the data over the seven different sand suspensions helps to clarify the tend in the measurements. Comparison of χ_s with $\beta=1.7$, shown by the broad line, shows acceptable agreement with the data over the limited range of x for which reliable values of χ_x could be measured. Again the dotted line shows the result when $\gamma=1$.

The data in Figs. 9–11 broadly support the low pass sphere, γ enhanced, description based on a single variable β. To further assess the general applicability of the γ term, previously reported data sets were examined. The first of these to be assessed was measurements[5] of the total scattering cross section collected on suspensions of sands. The data set complements the present study, in that a broad frequency range, nominally 1–100 MHz, was used on a limited number of sediment sizes, as opposed to the present work where a relatively narrow frequency band, 1–4 MHz, was used with a broad range of sediments and sediment sizes. In the analysis presented in Ref. 5 the data was fitted to a movable rigid sphere model, formulated using a two-parameter approach, to rescale χ_x on the ordinate and x on the abscissa. Inspection of the data, before rescaling, shows very similar trends to those of the present data; with low x values having approximately Rayleigh scattering, followed by increased enhanced scattering relative to a sphere as x increased, remaining at an almost constant difference in the geometric region. It was therefore considered interesting to compare how well the γ term of Eq. (7) accounted for the difference in the low pass sphere model and sediment scattering in this data set. Figure 12 shows a comparison of the γ enhance sphere scattering model, Eq. (5b), with the data. For the comparison, the value used for $\langle a_s \rangle$ was obtained from the sieved sizes given in the paper and not the optical diffraction size used by the authors in their analysis. The sieved size was chosen to be consistent with the present study. Therefore the abscissa was rescaled for x values based on the sieved size. For the quartz sediment no sieve size was available and therefore the optical diffraction size was scaled to a sieve size based on the other sediments where both measurements had been obtained. Table II lists the sediments and the values for $\langle a_s \rangle$. It can readily be seen in the plots that the application of the γ term does bring the low pass sphere model into close agreement with the measurements and accounts for most of the difference between the sphere and sediment scattering. The range of β, presented in Table II, between 1.2 and 2.2 is comparable with the values given in Table I. It is seen from Table II that β_χ increases with decreasing particle size. As noted in Ref. 5, this is considered to be associated with greater irregularity in the particle shape with reducing size. This increases the surface area relative to a sphere of nominally the same size and hence increases the geometric scattering cross section leading to higher values of β_χ. The results from the present study and those of Fig. 12 are therefore essentially equivalent in terms of the physical interpretation of the enhanced scattering with x.

The final comparison conducted is with the original data of Hay[2] which provided the first measurements of the form function for suspensions of sand grains. A relatively complicated jetting system was used to generate the suspension and measurements were conducted at 1, 2.25, and 5 MHz. The

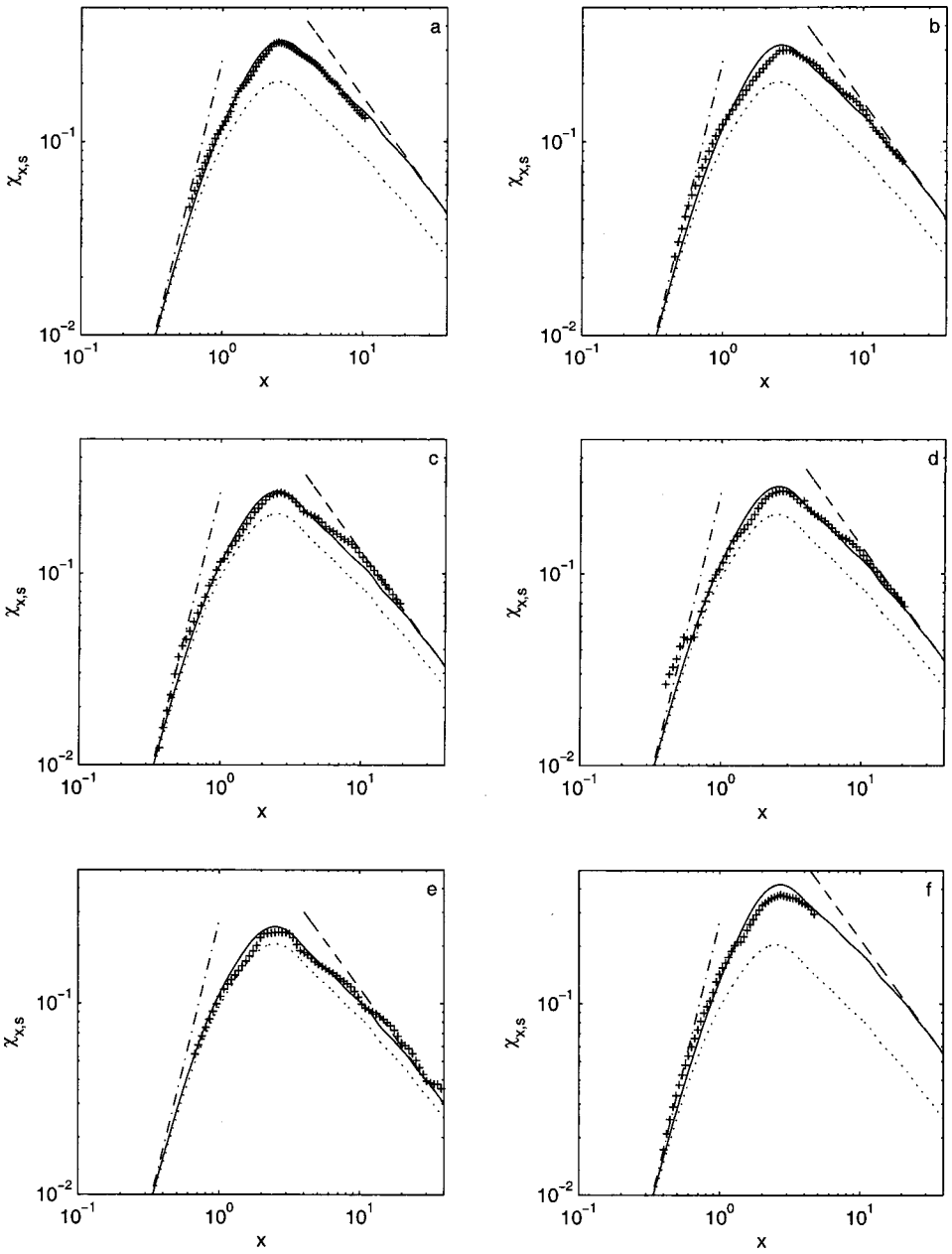

FIG. 12. Comparison of χ_x (+) and χ_s (———) for the sand suspensions of Ref. 5, (···) $\gamma=1$ in Eq. (5b), (-·-) Rayleigh scattering and (--) geometric scattering. (a) Assen sand 1, (b) Assen sand 2, (c) Ottawa sand, (d) Twente sand, (e) dune sand and (f) quartz particles.

results are presented in Fig. 13. Relative to the sphere scattering curve with $\gamma=1$, there is enhanced scattering. There is Rayleigh type behavior at low values of x, although the values appear somewhat elevated, between $x=1$ and 3 there is increasing divergence from the sphere scattering model with $\gamma=1$, while above $x=3$, the degree of elevation is variable. Applying the γ term does improve agreement with the data, although due to the small value of β_f, $\beta_f=1.2$, the effect is not as notable as in Fig. 9. Although this value is below the values observed in the present study, there is variability in β_f and this may simply be associated with this. Otherwise, at present, the difference in β_f between the present data set in Fig. 9, and Ref. 2 in Fig. 13, is not readily explainable.

TABLE II. The sediments used in Ref. 5. The second row gives the value for $\langle a_s \rangle$ in micrometers obtained from sieving, apart from the quartz particle which was estimated (see text). The third row gives the values of β_χ used in Eq. (7).

Assen 1	Assen 2	Ottawa	Twente	Dune	Quartz
24.5	49	49	49	98	11.5
1.7±0.1	1.6±0.1	1.3±0.1	1.4±0.1	1.2±0.1	2.2±0.2

VII. DISCUSSIONS AND CONCLUSIONS

The present study focused on examining the scattering properties of suspensions of marine sands. The work is part of on-going studies into the application of acoustics to the measurement of sediment processes. To obtain particle size and concentration, from the signal backscattered from a suspension of sediments, requires knowledge of the scattering properties of the sediments, which are used in an inversion algorithm to obtain sediment parameters. Here we have presented a series of measurements on different sands, broadly covering the Rayleigh, intermediate, and geometric scattering regimes. The model used to examine the data was that of

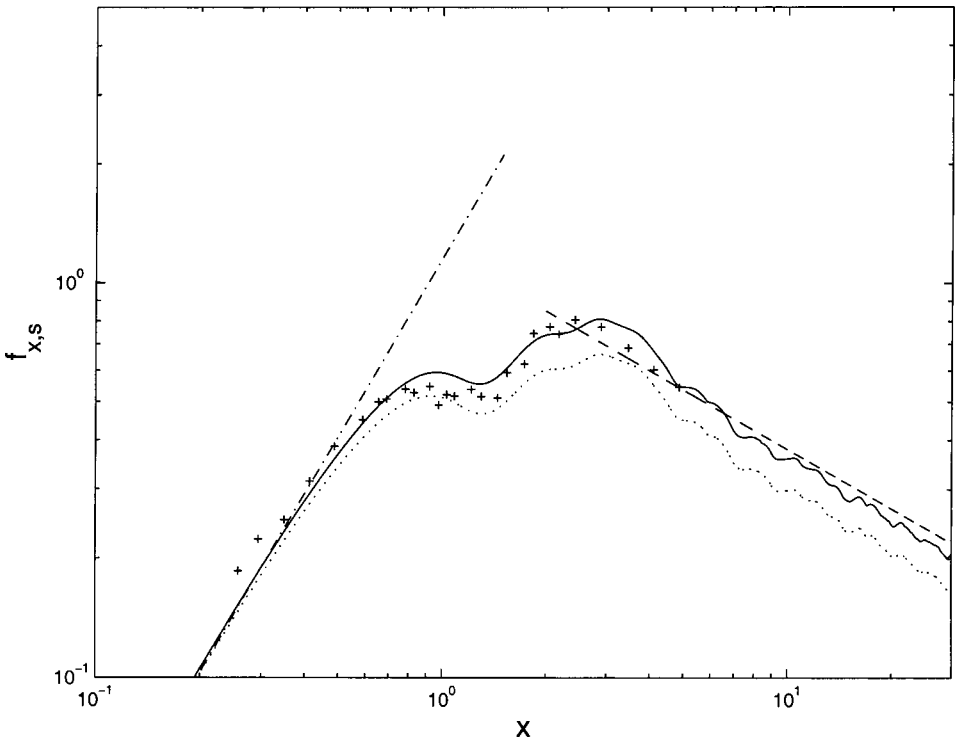

FIG. 13. Comparison of f_x (+) and f_s (———) for the sand suspensions of Ref. 2, (···) $\gamma=1$ in Eq. (5a), (-·-) Rayleigh scattering and (--) geometric scattering.

an elastic sphere modified using a smoothing function to remove the rapid oscillation normally observed in the form function for a sphere. The comparison showed that at low values of x, within the Rayleigh scattering regime, the scattering of sand grains is comparable with that of a sphere of similar size as measured by standard sieving. Above the Rayleigh region, there is a divergence between the sphere model and the observed scattering characteristics of sand, and this divergence is enhanced with increasing x up to $x\approx 3$. At higher values of x, as the geometric scattering region is approached, the difference in the sand and sphere scattering remains constant. The latter has been interpreted in terms of a theorem which states that the geometric cross section of a convex particle, averaged over all orientations, is equal to a quarter of the surface area of the particle. At high frequencies it is the geometric cross section which is measured and hence elevated scattering relative to a sphere would be expected. To account for the difference between the sphere model and the sediment scattering characteristics an enhancement factor, the γ term, was introduced. This term accounted for most of the differences between sphere model and the data collected for the present study. Application of the approach to other data sets gave similar improved agreement. Therefore, to first order, the γ term appears to have general applicability for sand suspensions. It has only one free parameter, β, which primarily rescales the γ term in the geometric region and thereby provides a simple relationship between the sphere model and the measured scattering characteristics of suspensions of sand.

In Ref. 5 a qualitative attempt was made to related particle shape irregularity, obtained from visual inspection of scanning electron micrographs, to their rescaling parameters. Although the approach was subjective, there did appear to be some correlation between particle size, estimated irregularity, and their rescaling parameters. In the present study the collected data was replotted, with $\langle a_s \rangle$ as the abscissa variable, to examine if there was any relationship between particle size and β; however, none was observed. Also visual inspection of the particle shapes in the scanning electron micrographs in Fig. 1, does not show an obvious relationship with the β values give in Table I. For each sediment examined, a number of sieved size fractions were used to obtain a range of $k\langle a_s \rangle$, and it may be that these had somewhat different shapes, which might have weakened any simple obvious relationship between the micrograph images for a particular sediment and the value of β. It may also be the case that simple visual inspection of scanning electron micrographs is not a sufficient parametrization of the particles and a more quantitative approach is required.

The reasons for conducting the present work are both ones of interest in the scattering problem and of making a contribution to the application of acoustics to sediment transport processes. For the sedimentologist their requirement is to use acoustics as a tool. It is clear from this study and that of Ref. 5 that individual sediments have somewhat different scattering characteristic depending on precise shape and composition. Unfortunately, this variability is not insignificant, and needs to be accounted for when extracting suspended sediment parameters from backscatter data. Although Ref. 5 showed increasing β_χ with reducing particle size, due to shape, the present data show β_f and β_χ for the larger particle sizes having comparable values to the smaller particles analyzed in Ref. 5. Therefore one could consider consolidating all the measurements of β reported here. Doing so gave $\beta_f=1.8\pm0.4$ and $\beta_\chi=1.6\pm0.3$. Further, since the mean values for β_f and β_χ are not significantly different when account is taken of the standard deviations, the data for β_f and β_χ could be combined to give $\beta=1.7\pm0.3$. Since, to first order, the γ term provides a generic description of the enhanced sand scattering relative to a sphere, this can be

utilized for inverting acoustic backscatter data to sediment concentration and particle size. There is one free parameter β, which is variable for different sediments and account needs to be taken of this variability, to provide error estimates for the sediment parameters extracted from the acoustic inversion.

ACKNOWLEDGMENTS

The authors would like to thank James Ellis, Judith Wong, Mairead Butler, and Kyle Betteridge for their contributions to the collection of the data. This paper was begun during a visit by PDT to the Marine Physical Laboratory at Scripps USA in March–April of 2003. PDT would like to thank Professor Michael J Buckingham for the invitation to work at Scripps and for the stimulating and interesting time he had. The work was funded by NERC, UK and ONR under its mine burial program.

[1] P. D. Thorne and D. M. Hanes, ''A review of acoustic measurement of small-scale sediment processes,'' Cont. Shelf Res. **22**, 603–632 (2002).
[2] A. E. Hay, ''Sound scattering from a particle-laden turbulent jet,'' J. Acoust. Soc. Am. **90**, 2055–2074 (1991).
[3] H. Cheng and A. E. Hay, ''Broadband measurements of the acoustic backscatter cross section of sand particles in suspension,'' J. Acoust. Soc. Am. **94**, 2247–2254 (1993).
[4] P. D. Thorne, K. R. Waters, and T. J. Brudner, ''Acoustic measurements of scattering by objects of irregular shape,'' J. Acoust. Soc. Am. **97**, 242–251 (1995).
[5] A. S. Schaafsma and A. E. Hay, ''Attenuation in suspensions of irregularly shaped sediment particles: A two-parameter equivalent spherical scatterer model,'' J. Acoust. Soc. Am. **102**, 1485–1502 (1997).
[6] J. Sheng and A. E. Hay, ''An examination of the spherical scatterer approximation in aqueous suspensions of sand,'' J. Acoust. Soc. Am. **83**, 598–610 (1988).
[7] G. H. Flammers, ''Ultrasonic measurements of suspended sediments,'' Geo. Survey Bull. No. 1141-A. (US GPO, Washington, DC, 1962).
[8] P. D. Thorne, P. J. Hardcastle, and R. L. Soulsby, ''Analysis of acoustic measurements of suspended sediments,'' J. Geophys. Res. **98(C1)**, 899–910 (1993).
[9] T. K. Stanton, D. Chu, P. H. Wiebe, and C. S. Clay, ''Average echoes from randomly orientated random-length finite cylinders: Zooplankton models,'' J. Acoust. Soc. Am. **94**, 3463–3472 (1993).
[10] T. K. Stanton, D. Chu, and P. H. Wiebe, ''Sound scattering by several sound zooplankton groups. II. Scattering models,'' J. Acoust. Soc. Am. **103**, 236–253 (1998).
[11] T. K. Stanton and D. Chu, ''Review and recommendations for modeling of acoustic scattering of fluid-like elongated zooplankton: Euphausiids and copepods,'' ICES J. Mar. Sci. **57**, 793–807 (2000).
[12] J. W. S. Rayleigh, *The Theory of Sound* (Dover, New York, 1945), Vol. II, p. 504.
[13] D. R. Palmer, ''Rayleigh scattering from nonspherical particles,'' J. Acoust. Soc. Am. **99**, 1901–1912 (1996).
[14] H. C. van de Hulst, *Light Scattering by Small Particles* (Dover, New York, 1981), p. 470.
[15] P. A. Chinnery, V. F. Humphrey, and J. Zhang, ''Low-frequency acoustic scattering by a cube. Experimental measurements and theoretical predictions,'' J. Acoust. Soc. Am. **101**, 2571–2582 (1997).
[16] A. Downing, P. D. Thorne, and C. E. Vincent, ''Backscattering from a suspension in the nearfield of a piston transducer,'' J. Acoust. Soc. Am. **97**, 1614–1620 (1995).
[17] G. C. Gaunaurd and H. Uberall, ''RST analysis of monostatic and bistatic acoustic echoes from an elastic sphere,'' J. Acoust. Soc. Am. **73**, 1–12 (1983).
[18] P. D. Thorne and S. C. Campbell, ''Backscattering by a suspension of spheres,'' J. Acoust. Soc. Am. **92**, 978–986 (1992).
[19] P. D. Thorne, L. Hayhurst, and V. F. Humphery, ''Scattering by nonmetallic spheres,'' Ultrasonics **30**, 15–20 (1992).
[20] G. W. C. Kaye and T. H. Laby, *Tables of Physical and Chemical Constants* (Longman, New York, 1973), p. 477.
[21] C. Libicki, K. W. Bedford, and J. F. Lynch, ''The interpretation and evaluation of a 3-MHz acoustic backscatter device for measuring benthic boundary layer sediment dynamics,'' J. Acoust. Soc. Am. , 1501–1511 (1989).
[22] P. D. Thorne and P. J. Hardcastle, ''Acoustic measurements of suspended sediments in turbulent currents and comparison with *in situ* samples,'' J. Acoust. Soc. Am. **101**, 2603–2614 (1997).

Environmental inversion and matched-field tracking with a surface ship and an L-shaped receiver array

Michael Nicholas, John S. Perkins, Gregory J. Orris, and Laurie T. Fialkowski
Naval Research Laboratory, Washington, DC 20375

Garry J. Heard
Defence R&D Canada-Atlantic, Dartmouth, NS, Canada B2Y 3Z7

(Received 27 October 2003; revised 10 August 2004; accepted 12 August 2004)

Acoustic data from the natural broadband signature of a quiet surface ship, recorded on the vertical leg of an L-shaped array, is used to invert for the local geo-acoustic parameters and the resulting effective environment is used for subsequent tracking of the surface ship using a matched-field tracking technique applied to the full array. The matched-field analysis includes a comparison of the incoherent product of the processed data from the horizontal and vertical subapertures with coherent processing of the data from the full L-shaped array. Subaperture processing is of interest since there is a (loose) requirement that the number of data snapshots be greater than or equal to the number of array elements. This presents averaging difficulties for large arrays when the source being observed is moving. Analyzing each array leg separately allows the use of a smaller number of snapshots from which averaged quantities are constructed. Taken separately, the vertical leg of the array provides range-depth information, while the horizontal leg provides bearing information. The incoherent product of each leg is compared to processing the full array coherently illustrating that the incoherent product generally worked as well, or better than, processing the full array, producing compact maxima at the ship location, and producing fewer false source locations. [DOI: 10.1121/1.1802755]

PACS numbers: 43.30.Wi, 43.30.Bp, 43.30.Gv, 43.30.Pc [WLS] Pages: 2891–2901

I. INTRODUCTION

Matched-field processing (MFP) is a generalization of plane wave beamforming where measured hydrophone data are correlated with simulated acoustic fields (replicas) which correspond to trial source locations.[1–3] Just as plane-wave beamforming determines the direction of acoustic sources by correlating with the phase delays associated with different arrival directions, MFP determines the locations of acoustic sources by correlation with simulated multipath structure arising from different source positions. Principally MFP has been applied to information on vertical arrays, although this is not a limitation of the method. Some of the more recent work has used long horizontal arrays,[4,5] tilted arrays,[6,7] and multiple vertical line arrays.[8] More recently, in the case where the source location is known (at least approximately), MFP has been extended to the task of inverting measured acoustic data for environmental parameters.[9–11] The focus of this paper is to perform environmental inversion followed by localization and tracking of a surface ship using an L-shaped receiver array comprised of one vertical segment and one horizontal segment, each with 32 elements. The matched-field analysis includes a comparison of the incoherent product of the processed data from the horizontal and vertical subapertures with coherent processing of the data from the full L-shaped array.

One problem that must be addressed in any MFP application is the possibility of a moving source. Generally speaking, for a stationary source, any averaging process performed on the data will increase the signal-to-noise ratio on the receiving array as a monotonically increasing function of the length of time used. The cross-spectral density (CSD) matrix is formed from such an averaging process, and its signal to noise information content is affected accordingly. Matched-field processing as implemented in this paper has at its heart the CSD matrix, an N by N data covariance matrix (as described in the next section). However, if a source is moving, then the amount of time that can be averaged over without violating the no motion assumption is limited. Song[12] has researched this very issue extensively and provided general rules for limits on averaging time. Tran and Hodgkiss[13] found that sources moving at low speeds do not significantly degrade results using standard MFP techniques. In the case of high speed sources, many methods have been suggested to overcome this difficulty, ranging from more sophisticated replica generation[3,12,14] to more sophisticated matched-field processors.[15,16] The particular matched-field processor employed in this work is referred to as eigenvalue or singular value decomposition. (See pages 407 and 408 of Ref. 1.) In our specific implementation all eigenvalues greater than zero (to machine precision) and their associated eigenvectors were used in the processing. All remaining components of the eigenvectors were neglected. In the past these methods have proved effective in reducing the influence of noise by separating the eigenvalue spectrum of the CSD matrix into two subspaces, one representing the desired signal and the other representing a combination of the underlying processes generally referred to as noise. Because a better description of the signal across the receiving array is usually found by including a larger percentage of the signal subspace, the best results are obtained for nonsingular CSD matrices. The general ''rule of thumb'' in forming a nonsingular CSD matrix

from data is to average over a number of time periods (snapshots) at least as large as the number of elements in the receiving array. Violations of this rule generally will result in rank-deficient matrices, requiring singular value decomposition methods. This creates an additional unusable subspace, reducing the performance of the matched-field processing algorithm. If CSD matrices for subapertures of a multidimensional array can be formed in such a way as to capture nonredundant information, then the averaging time period associated with the smaller subaperture will reduce many of the difficulties with the moving source. However, this might be at the expense of a decrease in spatial resolution.

In Sec. II we discuss environmental inversion using the radiated acoustic energy from a surface ship, used to validate and expand upon the archival environmental data. Section III contains a brief description of the experimental data set processed. In Sec. IV, results from the analysis of this experimental data are presented. In Sec. V, results are summarized.

II. MATCHED-FIELD INVERSION: FOCALIZATION ALONG A TRACK

In conventional MFP at a single frequency, a replica vector $[\mathbf{w}(\mathbf{x})]$ is created from a set of replica fields at each receiver. Although the replica fields are sometimes provided by a database of measured data,[17] they are more commonly provided by a numerical simulation model. The replica fields used to analyze the data from these experiments were generated by a range-dependent adiabatic mode propagation model.[18] Such models are appropriate when the environmental parameters are slowly varying. As will be seen in Sec. III, these conditions were satisfied. Their main advantage in this context is the speed in numerically calculating linear matched-field processors, as shown in Ref. 18. The replica vector is matched to a single frequency time-averaged data covariance matrix. In general, the output of a matched-field processor, called an ambiguity surface, is a function of three spatial coordinates, but this parameter space is often reduced to two by either assuming the target maintains a constant depth, or a constant azimuth. For the environmental inversions presented in this paper, the source track was assumed to be at a constant azimuth to the receiver arrays, along an iso-bathymetric line.

All of the work presented here is based on the Bartlett matched-field processor. For data collected during the time interval t_n it is defined by

$$B_{t_n}(\mathbf{x}) = \mathbf{w}^{\dagger}(\mathbf{x}) \cdot \mathbf{K}_{t_n} \cdot \mathbf{w}(\mathbf{x}), \tag{1}$$

where $\mathbf{w}(\mathbf{x})$ is the acoustic replica vector with components equal to the modeled complex acoustic pressure at the radial frequency ω for the ith receiver of the M distinct receivers in the array. The quantity $\mathbf{w}^{\dagger}(\mathbf{x})$ is the transpose conjugate of $\mathbf{w}(\mathbf{x})$. Each replica vector is scaled to have unit norm and depends on the source location at a range r and a depth z. In Eq. (1), $\mathbf{K}_{t_n}$ is a data covariance matrix with elements

$$K_{t_n,ij} = \frac{1}{N_p} \langle \tilde{p}_i \tilde{p}_j^* \rangle_{\Delta t_n}, \tag{2}$$

where $\tilde{p}^*$ is the complex conjugate of $\tilde{p}$, the angular brackets indicate an average over time, and N_p is a normalization constant defined as the trace of $\mathbf{K}$. The Δt_n used in our data analysis was 30 s, from which 15 2 s segments were used to create $\mathbf{K}_{t_n}$. Singular value decomposition was used to determine the eigenvectors $(\mathbf{v}_i)$ and associated eigenvalues (λ_i), allowing $\mathbf{K}_{t_n}$ to be written as[1]

$$\mathbf{K}_{t_n} = \mathbf{V} \cdot \Lambda \cdot \mathbf{V}^{\dagger},$$

where $\mathbf{V}$ is the matrix of eigenvectors with nonzero eigenvalues, $\mathbf{\Lambda}$ is the matrix of eigenvalues. If N_s is the number of nonzero eigenvalues, B_{t_n} can be written as

$$B_{t_n} = \sum_{i=1}^{N_s} \lambda_i |\mathbf{v}_i^{\dagger} \cdot \mathbf{w}|^2.$$

B_{t_n} is normalized in such a way that a perfect match between data and replica produces a maximum value of 1. Ambiguity surfaces are typically analyzed as $\log_{10}(B_{t_n})$, with a perfect match being 0 dB, and negative values being the degradation of the processor.

When the assumptions of no motion are valid, the average in Eq. (2) could be made arbitrarily long to achieve the desired signal-to-noise ratio. However, the source tracked in this work was, for a substantial portion of the time, moving too quickly to be considered stationary, limiting the averaging time. An alternative method to increase the signal-to-noise ratio is to use a longer fast Fourier transform (FFT). This approach was not used since the excessive speed of the source also manifests itself in the acoustic data by the introduction of a Doppler shift. The best results were obtained using a (rather large) 1/2 Hz bin width in the FFTs which kept the frequencies used for processing from significantly leaking to neighboring bins and thereby reducing the signal-to-noise ratio.

The environmental inversion method used was a variant of the method called ''focalization'' described in Collins and Kuperman.[19] This method uses a global optimization procedure to search simultaneously for environmental parameters as well as the physical position of the source. As the name implies, the algorithm ''focuses'' the environment and ''localizes'' the sources simultaneously. To invert for environmental parameters it is best if the source and receiver positions are known precisely. However, in practice this is often difficult to do, mainly because of platform motion. Thus many researchers have found that it is critical in inversion problems to allow the source and receiver positions to vary, otherwise the parameter values are skewed as the optimization procedure compensates for errors in the assumed source and receiver positions. In our particular case, since we knew the source and receiver positions reasonably well, those parameters were constrained to a relatively small interval. Similarly, the array depth and tilt parameters were also implemented within our inversion analysis. However, all results obtained found the vertical array with nearly zero tilt and positioned correctly in depth as measured during the array deployment. Thus these parameters could be considered fixed.

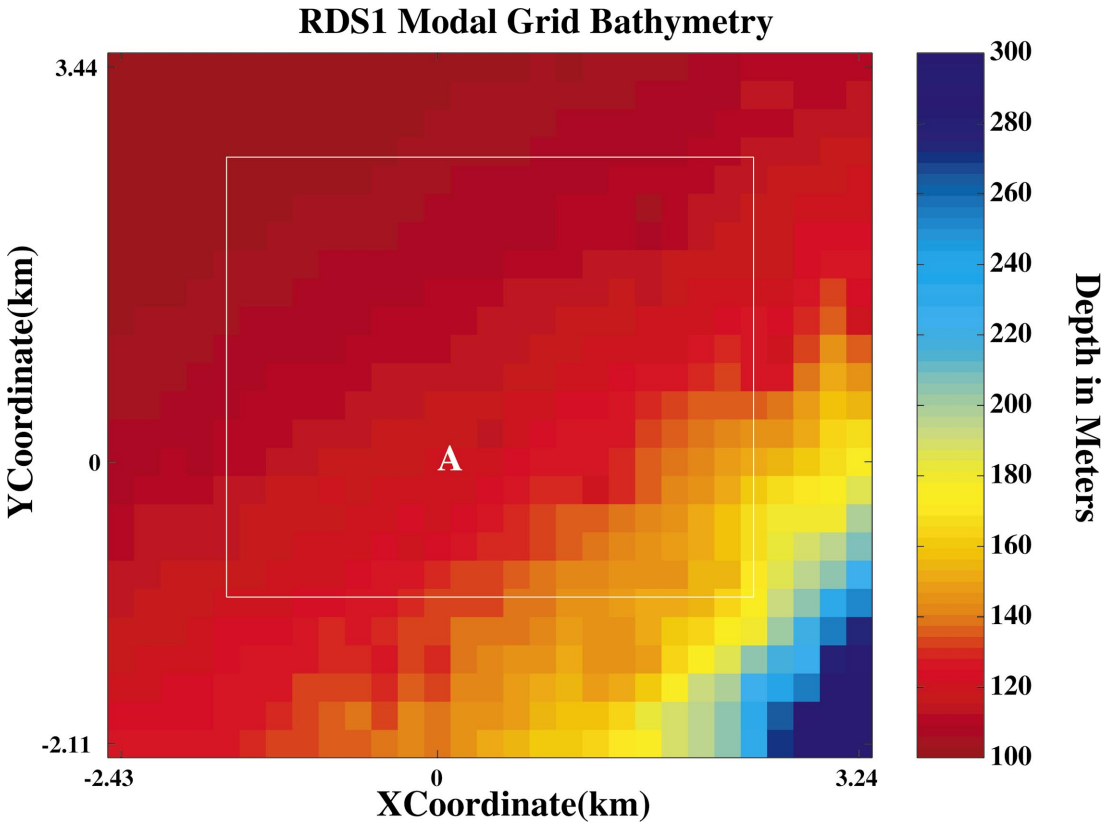

FIG. 1. Bathymetry (depths given in meters) for the RDS-1 experiment, roughly 100 miles southeast of Halifax, Nova Scotia. Our L-shaped acoustic receiver array was deployed close to the shelf break, in roughly 100 m of water. (The symbol "A" marks the position of the NRL L-shaped receiver array.) The MFP modes were computed on a grid of 29 pixels by 25 pixels, which spanned an area of 5.67 km (in latitude) by 5.55 km (in longitude). The white rectangular box delimits the area where replicas were computed on a much finer grid of 224 pixels by 267 pixels, giving a resolution of roughly 12.5 m both in latitude and longitude.

As previously discussed, the normal procedure in focalization is to use a global optimization procedure to simultaneously search for the environmental parameters and the spatial coordinates for the source position that maximizes $B_{t_n}(r,z)$. For each iteration of the simulated annealing, the replicas $\mathbf{w}(r,z)$ are computed for the estimated set of environmental and geometric parameters, and these replicas are matched to the source track data (which is a set of CSD matrices, $\{\mathbf{K}_{t_n}\}_{n=1}^{N}$ computed at times $\{t_n\}_{n=1}^{N}$) using the Bartlett matched-field processor. Since the source was moving, we have generalized this idea by maximizing $B_{t_n}(r,z)$ for a sequence of N covariance matrices corresponding to the times $\{t_n\}_{n=1}^{N}$ for the different covariance matrices. As a consequence of this maximization algorithm, we also obtain estimates of the ship position in range and depth for each of these covariance matrices. Although it is not an explicit requirement of the cost function (as defined below) that these ranges be in sequence, the focalization results do produce sequential ranges.

The details of the simulated annealing optimization algorithm we used can be found in the appendix of Collins and Kuperman.[9] However, for each iteration we perturb all parameters simultaneously, instead of one at a time. In an optimization procedure we normally think in terms of minimizing an error/cost function that depends on the search parameters. In simulated annealing this function is often referred to as an energy function. Thus we define our energy function for a sequence of N source positions as

$$E=\frac{1}{N}\sum_{n=1}^{N} E_{t_n},$$

where

$$E_{t_n}=1.0-B_{t_n,\max}, \quad \text{and}$$
$$B_{t_n,\max}=\max_{z_{\min}<z<z_{\max}}^{r_{\min}<r<r_{\max}}[B_{t_n}(r,z)]. \tag{3}$$

Here, the replicas $\mathbf{w}(r,z)$ were computed using the current estimate for the environmental parameters. At the beginning of each iteration of the simulated annealing algorithm, all parameters are perturbed along a predetermined optimally rotated coordinate system.[20] This rotated coordinate system also provides valuable information concerning the parameter hierarchy and parameter coupling.[21]

III. EXPERIMENTAL DATA SET

The first rapidly deployable systems experiment (RDS-1) used an L-shaped array with one vertical and one horizontal leg. RDS-1 was an international effort between scientists from the United States, Canada, the United Kingdom, and Australia. The experiment was conducted in the North Atlantic Ocean, about 100 miles South-East of Nova Scotia, Canada, during the Fall of 1997. A variety of receiver

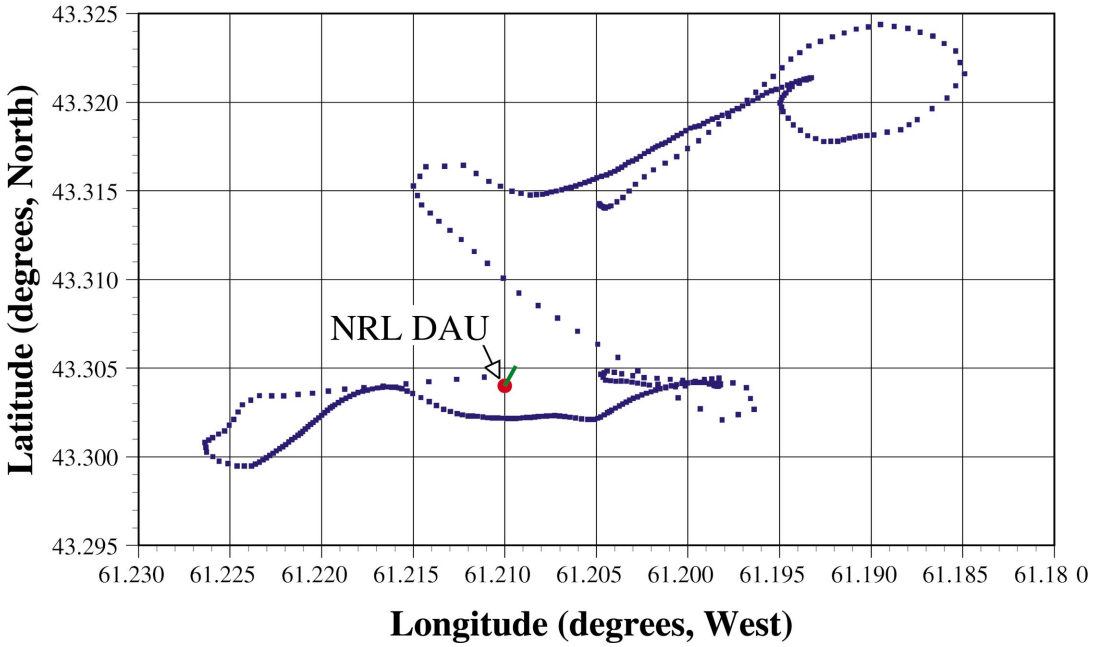

FIG. 2. Roughly 3 h of ship track for the Endeavour. The track begins at roughly 61.205°W 43.314°N and ends close to the position of the NRL DAU (Data Acquisition Unit). The data are taken from the onboard GPS navigation system. Each point is separated by 1 min of time. The horizontal leg of the receiver array is oriented at a 30° heading.

arrays and sources were part of this experiment, but only two are of concern in this current work. The sound source was ship generated noise from the Canadian vessel CFAV Endeavour, and the receive arrays were part of an autonomous satellite-linked system from the United States Naval Research Laboratory. We wish to stress that the source used was the Endeavour itself and not an acoustic transducer. To this end, the nominal source depth was taken to be 5 m. In fact, there was no reliable noise analysis data for the Endeavour, so we had no way of knowing *a priori* how it radiated as a source or what the spectral content of that sound might look like. Furthermore, there is the obvious fact that the vessel is certainly not a point source, and thus the 5 m source depth is somewhat arbitrary.

All results presented are from data received on the 64 element L-shaped array located in approximately 100 m of water at latitude 43° 18.24′ North (43.304°N) and longitude 61° 12.6′ West (61.210°W). The hydrophone spacing on the horizontal leg was 5 m, while the hydrophone spacing for the vertical leg was 2.5 m, with the first element positioned 5 m above the sea floor. The horizontal leg extended in a northeasterly direction (roughly 30° bearing) away from the point where it adjoins the vertical leg. Figure 1 shows the bathymetry around this location. The bathymetry data used in our calculations came from two sources. We began with archival data, but this was substantially augmented during the course of RDS-1 by logging the information from the Endeavour depth sounder. For this augmentation, a grid of ship tracks was laid out that was designed to fill in the areas where the archival data were sparse. The result was a fairly comprehensive data set. The computational grid for the mode functions used in the MFP is the full region shown in Fig. 1. This 29-by-25 grid covered a region that measured 5.67 km (in latitude) by 5.55 km (in longitude), which was sufficient for our calculations. Modes are calculated at the center of each

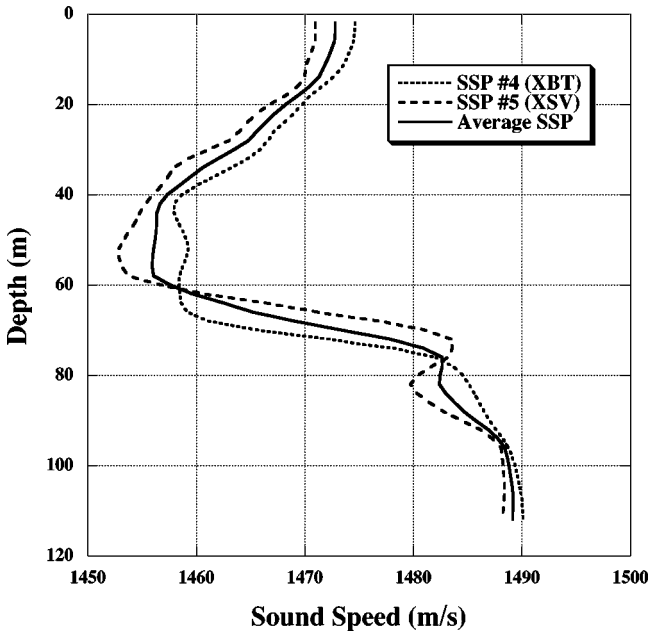

FIG. 3. Two measured sound speed profiles [one from an expendable bathythermograph (XBT), the other from an expendable sound velocity probe (XSV)] were averaged and smoothed to give the profile that was used in all our MFP. These two raw data sets were chosen because they were collected close in time to when our acoustic data were recorded, and were also spatially close to the Endeavour track.

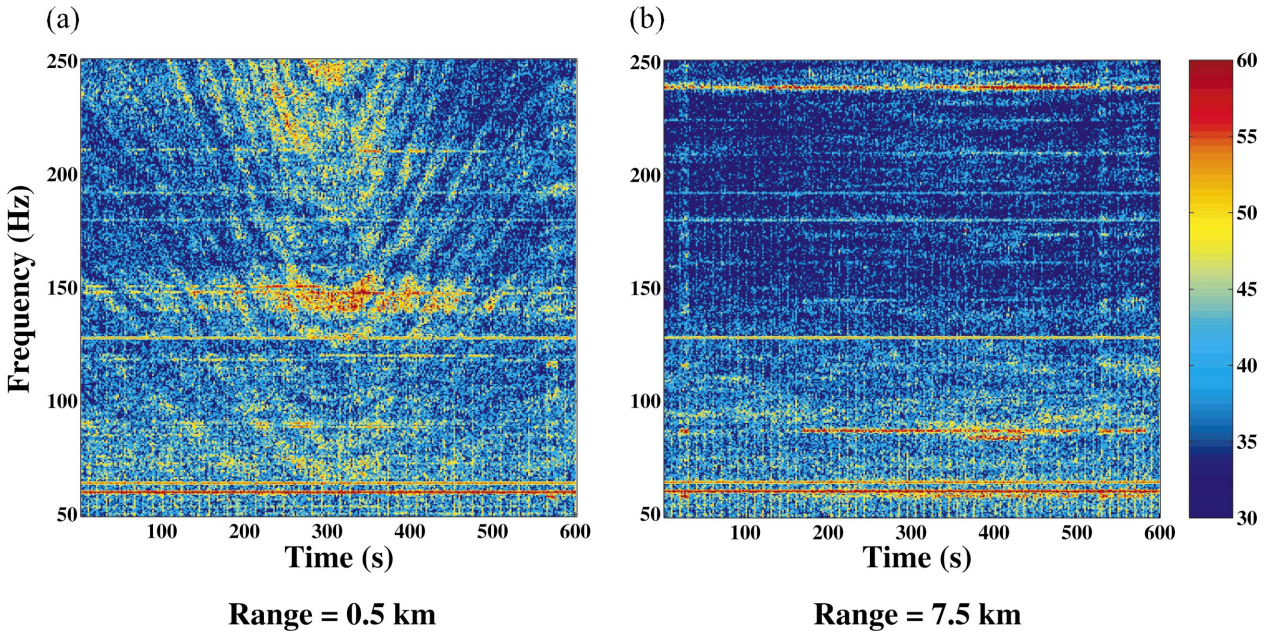

FIG. 4. Two spectrograms taken during RDS-1. In (a) the Endeavour passed within 0.5 km of our receiver array, producing a classic washtub pattern from the low-level broadband emissions spanning 50 Hz up to over 250 Hz. Many of the strong lines in the acoustic spectra persisted even when the Endeavour moved out to a range of 7.5 km, as shown in (b). Only the weak lines at frequencies of 118.5, 121, and 148 Hz were attributable to the Endeavour. Data for hydrophone number 48 was chosen because this was located half way along the vertical leg of the receiver array, putting it close to the middle of the water column. The scale given is in relative dB.

square pixel within which the depth is taken to be constant. Within this computational grid is the actual region of interest (shown by the box in Fig. 1) where the MFP and tracking were performed. Here the field was calculated on a much finer grid of 224 pixels horizontally by 267 pixels vertically, giving us a resolution (both in latitude and longitude) of roughly 12.5 m.

The ship speed (Endeavour) was usually about 2.6 m/s. This speed was taken into account when determining the appropriate amount of averaging necessary to achieve a stable cross-spectral density (CSD) matrix of the data without violating the no motion assumption. This led to our choice of a 30 s averaging time since the ship generally moved substantially less than one wavelength during this time interval. However, there were occasions when the ship was moving substantially faster, which introduced additional difficulties into the data analysis that we will discuss later. Figure 2 shows the vessel position as recorded by the onboard global positioning system (GPS)-linked navigation system, in which adjacent data points are separated in time by 60 s.

Both XBTs and XSVs were used to measure the sound speed profiles throughout RDS-1, and were spatially distributed throughout the main area of interest. Figure 3 shows two profiles collected close to the receiver arrays, at times just before and just after the acquisition of the acoustic data. The average of these two profiles (after some smoothing) was used in all the MFP in this paper.

IV. RESULTS

A. RDS-1 inversion for geophysical parameters

Since we had no *a priori* knowledge of the acoustic emissions from the Endeavour, one immediate problem was deciding at which frequency (or frequencies) to begin the processing. Figure 4(a) shows a spectrogram taken over a

TABLE I. RDS-1 geophysical parameters obtained from Benson, Chapman, and Antonion (see Ref. 22) (Archival) and obtained by inversion. The inverted set exhibits a much thinner sediment and different basement values, particularly for attenuation. We have also allowed for a sound speed gradient within the sediment.

	Parameter	Search range [min, max]	Archival value	Inverted value
1	Sound speed, top of sediment (m/s)	[1550, 1800]	1697	1784
2	Sediment sound speed gradient (m/s/m)	[0, 15]	0[a]	14.02
3	Sediment thickness (m)	[5, 40]	24	12.91
4	Sediment density (g/cm^3)	[1.1, 2.2]	1.72	2.14
5	Sediment attenuation (dB/λ)	[0.005, 0.250]	0.1	0.02
6	Basement sound speed offset (m/s)[b]	[0, 400]	279	38
7	Basement density offset (gm/cm^3)[b]	[0, 1]	0.41	0.36
8	Basement attenuation (dB/λ)	[0.005, 0.250]	0.1	0.02

[a]The archival data assumed no gradient in the sediment.
[b]Basement offset values are relative to the bottom of the sediment layer.

TABLE II. Comparing the performance of the inverted parameter set and those from Benson, Chapman, and Antonion (see Ref. 22) (Archival). The new environment yields significantly lower MFP degradations (indicating a closer match between the measured field on the receiver array and the computed field) and tracks the position of the surface vessel (Endeavour) at long range more closely than the archival environment. The range estimates are also monotonic for the new environment.

	Archival environment	Inverted environment	GPS navigation data
Short-range average degradation (dB)	3.5	1.4	
Long-range average degradation (dB)	4.6	2.1	
Range interval—short range (m)	1340–1500	1340–1440	1320–1430
Range interval—long range (m)	1860–1950	1780–1850	1720–1810

period of time when the Endeavour was moving past the L-shaped receive array. The classic washtub pattern, symmetrical about the point of closest approach (0.5 km), is a consequence of the Lloyd's mirror pattern as a function of frequency from the wideband signature of the ship. The Endeavour is generating broadband noise from around 50 Hz to at least 250 Hz, and these levels are quite low. Also clearly visible in Fig. 4(a) are a number of strong lines, many of which still persist even when the Endeavour moves out to a range of 7.5 km, as in Fig. 4(b). Unfortunately, all of these strong lines are attributable to passing cargo vessels, other research vessels, other acoustic signals being broadcast into the water, or artifacts of our acquisition system. Of the weaker ''lines'' present in Fig. 4 (all of which were often buried in the background noise), preliminary MFP analysis using the archival geophysical parameters revealed that only those at frequencies of 118.5, 121, and 148 Hz could be attributed to the Endeavour. Since there was no reason to favor any one of the three, we chose the first of these frequencies (118.5 Hz) for our environmental inversion. It was felt that these frequencies did not provide enough diversity to give any impact on a multifrequency inversion. However, in the MFP, incoherent averaging between 118.5 and 148 Hz does produce some sidelobe reduction. The inclusion of 121 Hz did not improve the results because it is somewhat redundant, being so close in frequency to the 118.5 Hz information.

The environmental inversion relied on data from a time period when the Endeavour was northeast of the receiving arrays and moving slowly toward the arrays from a range of roughly 1.4 km to a range of roughly 1.3 km. In addition to the fact that the ship was moving slowly, these data were used because the bathymetry between the receiver and the ship was nearly range independent. Eight CSD matrices were computed from a spectral domain average of 15 consecutive time periods, each of which used 2 s of the time series to calculate the FFT. (Each CSD matrix therefore contains information from 30 s of time.) The spatial search window [see Eq. (3)] was $r_{\min}=1.3$ km, $r_{\max}=1.5$ km, $z_{\min}=1$ m, and $z_{\max}=8$ m.

The results of the geophysical parameter inversion are shown in Table I, together with values for this region obtained from Benson, Chapman, and Antonion.[22] It should be noted that Benson and co-workers[22] did not permit a gradient in the sediment layer. The search windows for each parameter are also included in the table. Comparing these two sets of geophysical parameters, the inverted parameters exhibit a thinner sediment layer with a faster sound speed, as well as differences in the basement parameters. To give some indication of how well the inverted environment performs relative to the archival values, the degradations of the matched-

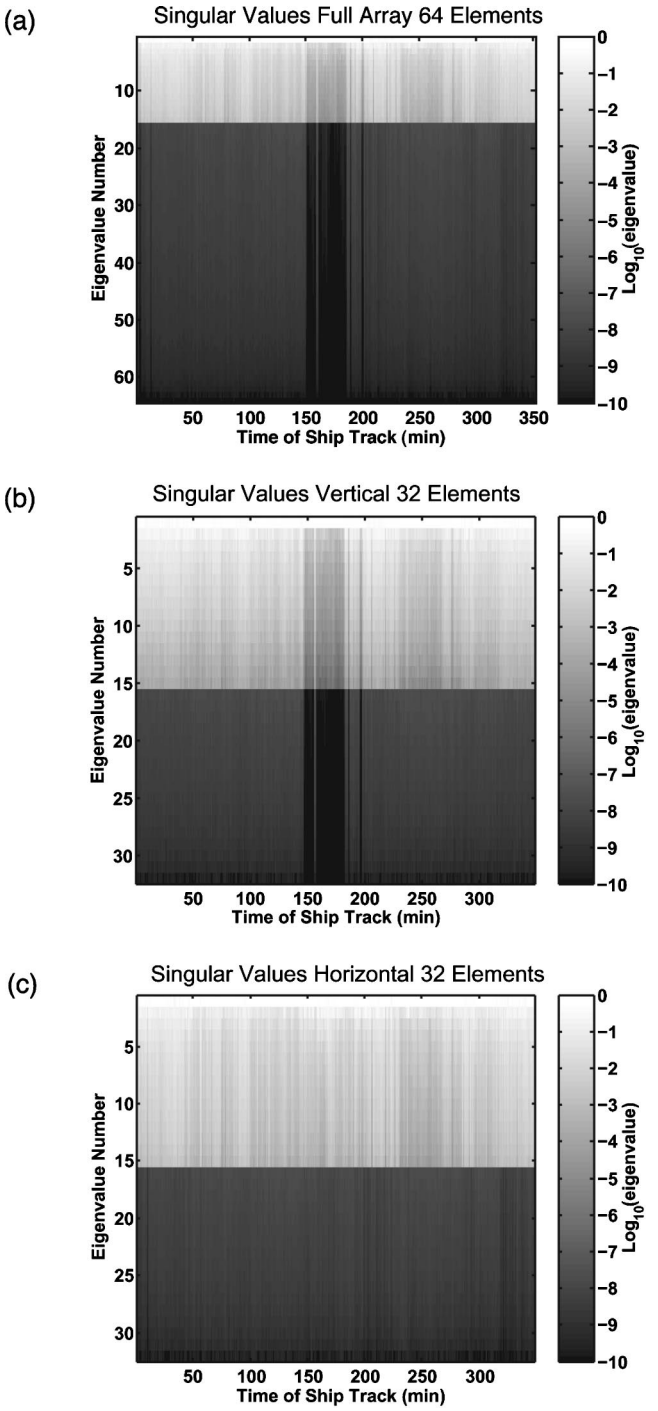

FIG. 5. Distribution of singular values of the CSD matrix as a function of time: all 64 channels (a), vertical 32 channels (b), horizontal 32 channels (c). Due to the time-limited nature of the processing, the CSD matrices are rank deficient with the number of nonzero values equal to the number of snapshots.

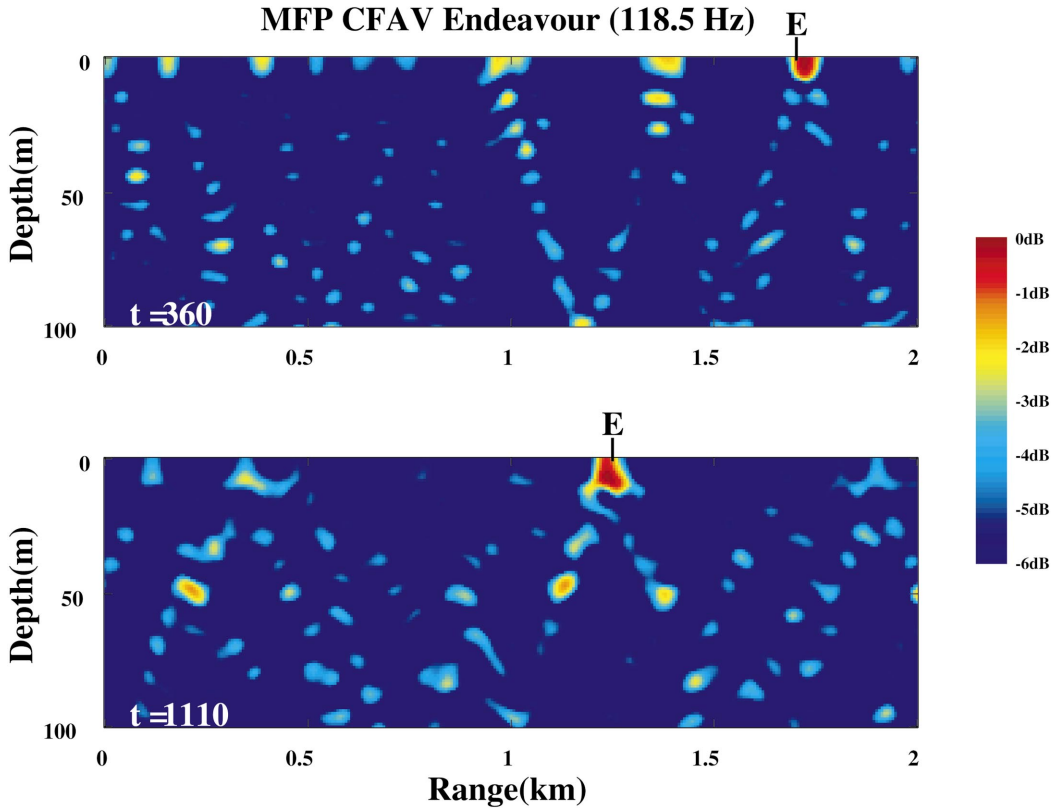

FIG. 6. Two results (taken from a sequence of many such results) of the MFP in the range-depth plane, at two locations along a range-independent track. This track was chosen to invert for the geophysical parameters. The source was a surface ship (Endeavour) that was arbitrarily chosen to be a point source at a depth of 5 m. In spite of these limitations the MFP is clearly able to track the (relatively quiet) surface ship using the inverted geophysical parameter set.

field processor are compared in Table II. The inverted parameter set yields significantly smaller degradations, indicating a greatly improved match of the replica field to the measured data. Additionally, the source range predictions for the two parameter sets are compared in Table II for two source tracks at different ranges. The inverted parameter set gives much better range predictions in both cases, and the predicted ranges are monotonic, in keeping with the data; this is not the case for the archival parameter set. It should be noted, however, that the coordinate rotation technique indicates that the sediment sound speed, the sediment sound speed gradient, and the sediment thickness are all coupled and are the most important parameters in their effect on the cost function. Therefore many combinations of these three parameters would give similar cost function values.

The time-limited averaging of the data created rank deficient CSD matrices. The singular value decomposition of these matrices produced only 15 usable eigenvalues, as seen in Fig. 5. Because of this relatively modest fraction of the full space, the usual eigenvalue approach of separating the signal and noise subspaces proved unreliable and thus the entire nonsingular portion of the CSD matrices were used in calculating B_{t_n}. Figure 6 shows two typical outputs of the matched-field processor in the range-depth plane using a range-independent environment, with replicas created using the inverted geophysical parameter set. In spite of the limitations imposed by assuming that the Endeavour was a point source, the inverted parameter set was seen to be adequate for providing MFP results that successfully locate the surface source. The position of the Endeavour is marked by the symbol ''E'' at the top edge of each plot.

To gain more information about the acoustic emissions from the Endeavour, we used MFP to probe the noise ema-

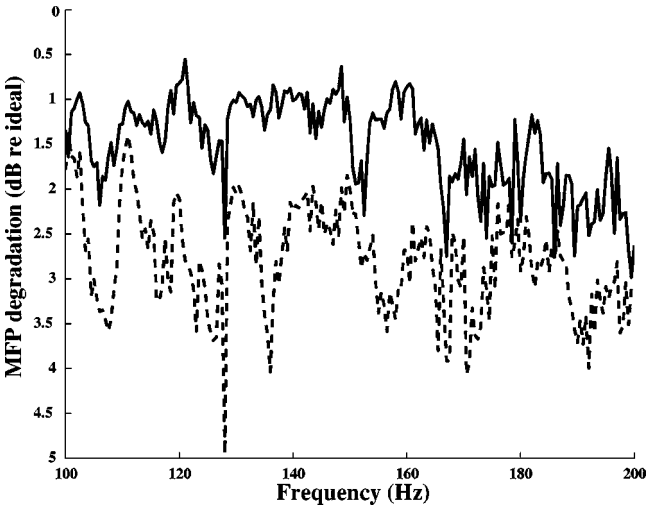

FIG. 7. Degradation from the MFP using information from the vertical leg of the receiver array, using the inverted parameter set. A small portion of the time series (30 s) was processed in 1 Hz increments from 100 up to 200 Hz. Any relatively strong noise output from the surface vessel will generate a low degradation in the MFP. Clearly the Endeavour generates fairly low-level broadband noise at the low speeds realized in our RDS-1 data set. The two curves are included to show the variability, and were produced from data taken 6 min apart. For the dashed curve, the Endeavour was slightly further away from the receiver array.

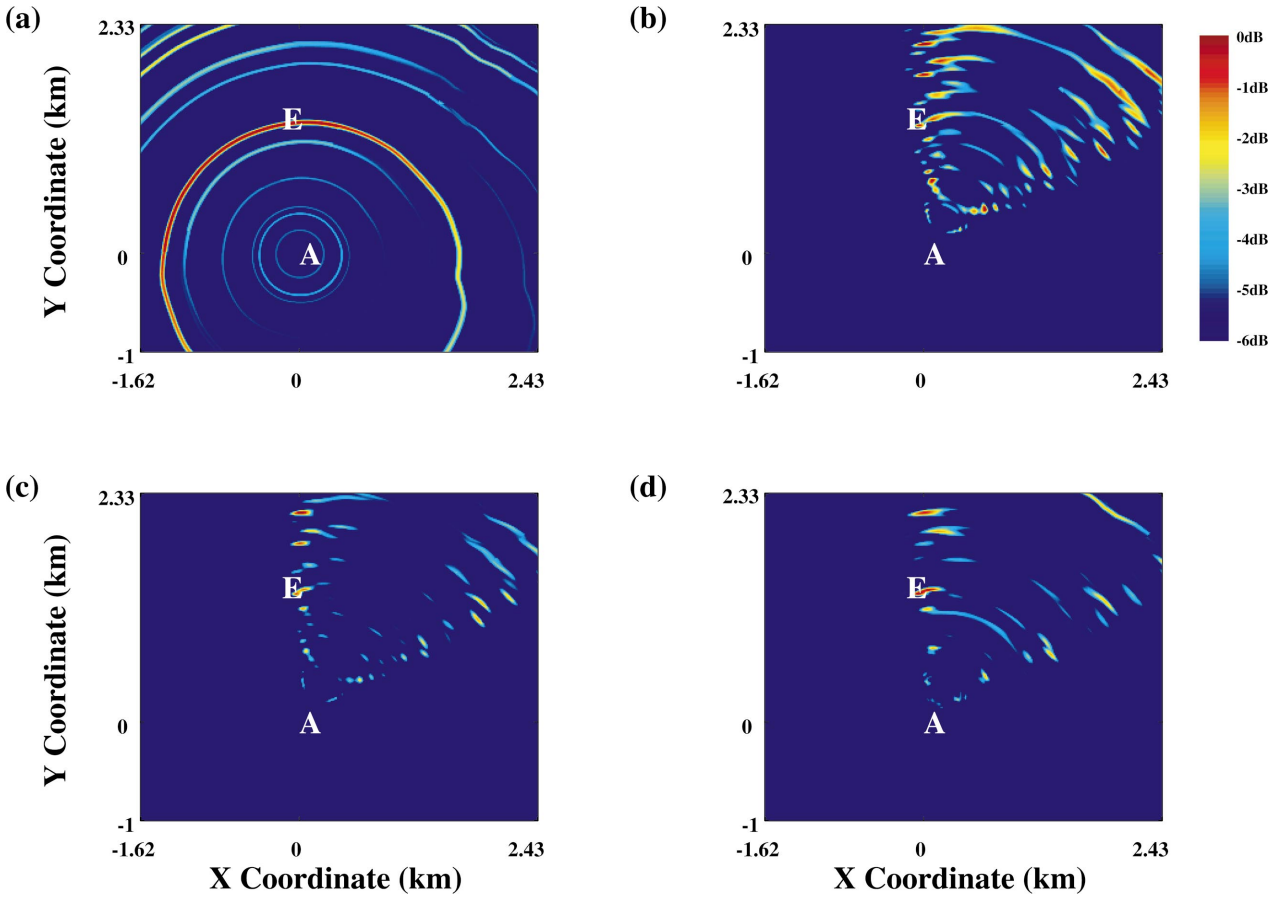

FIG. 8. Typical MFP results using the Endeavour as a surface sound source, taken from many such results for a 3 h period of time. These ambiguity surfaces are generated by processing the same portion of the time series using four different methods. (a) is the MFP result using the vertical leg only, (b) is for the horizontal leg only, (c) is for the coherent processing of all 64 elements of both array legs, and (d) is the incoherent product of the vertical and horizontal legs. These plots cover 6 dB of dynamic range. The Endeavour (symbol ''E'') is located north of the NRL L-shaped array (symbol ''A'').

nating from the particular spatial location of this vessel only. From the time series information on the vertical leg of the receive array (taken over a short period of time when the Endeavour was close), we used the inverted environmental parameters and processed the data in 1 Hz increments from 100 up to 200 Hz. The resulting degradations are shown in Fig. 7. The frequencies at which the degradations are smallest will be those that correspond to noise generated from the Endeavour. Clearly there are no strong lines, as we suspected from the spectra in Fig. 4. The two highest features are a broad peak centered around ~120 Hz, and a narrower one at 148 Hz. Other features in Fig. 7 turned out to be unrelated to the Endeavour upon further examination.

B. RDS-1 matched-field processing

Using the inversion results for the environmental parameters (described earlier), replicas at 118.5 Hz were computed for the environmental/modal grid described previously. As with the geophysical parameter inversion, the CSD matrices used 15 consecutive data segments, each of which used 2 s of the time series for the calculation of the FFT.

For a 3 h period of time 360 ambiguity surfaces were computed, and compared to the position of the Endeavour from the GPS logs. Figure 8 shows a plot of typical MFP ambiguity functions from near the beginning of this sequence, when the Endeavour was north of the receiver array: (a) results using the vertical leg only, (b) results for the horizontal leg only, (c) is for the coherent processing of all 64 elements of both array legs, and (d) is the incoherent product of the vertical and horizontal legs. At a later time the Endeavour had moved to the east of the receiver arrays. Typical MFP results at this later time are shown in Fig. 9.

Figures 8(a) and 9(a) show that processing only the vertical leg of the receiver arrays yields good range information as expected. There is some symmetry breaking resulting from variations in the bathymetry, but clearly there is very little bearing information to be had from processing data from this array only. The converse result is obtained when processing data received only for the horizontal leg, which yields good bearing information but does not reveal much about the range of the sound source. Figures 8(b) and 9(b) exhibit many strong maxima in the ambiguity surface, positioned along two fairly well defined radials. One of these radials extends through the bearing of the Endeavour, while the other is a result of the left-right ambiguity always present when processing information from horizontal arrays. The horizontal array has a heading of roughly 30°.

Processing all 64 elements coherently (from both array legs) combines the performance of each individual leg. The L-shaped configuration can provide information about both range and bearing, resulting in ambiguity surfaces with fewer

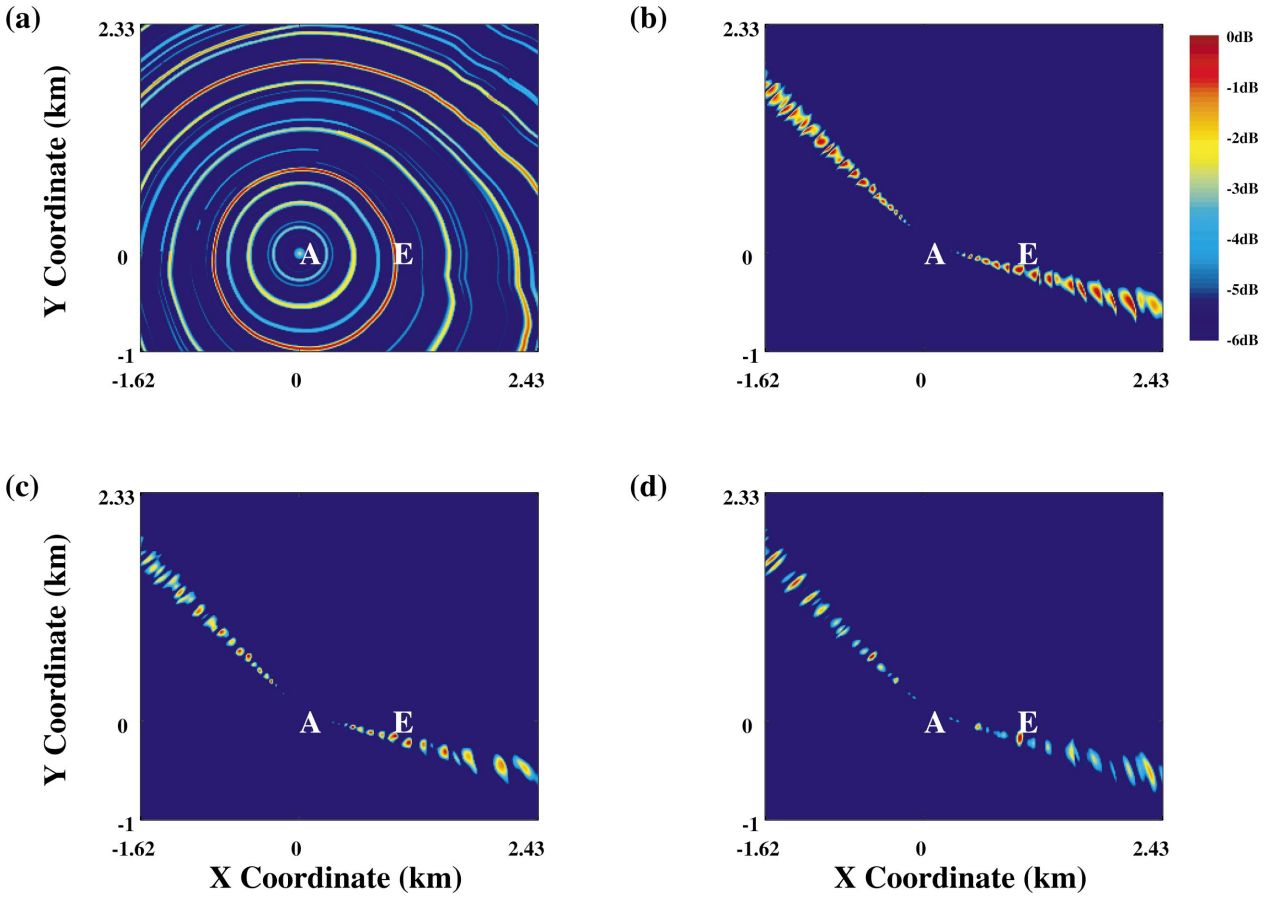

FIG. 9. Another example of using MFP to track a quiet surface ship (see Fig. 8). These four plots were for a later period of time, with the Endeavour located east of the receiver array. As with Fig. 8, (a) is the MFP result using the vertical leg only, (b) is for the horizontal leg only, (c) is for the coherent processing of all 64 elements of both array legs, and (d) is the incoherent product of the vertical and horizontal legs. These plots also have 6 dB of dynamic range.

and more compact maxima. As with the horizontal and vertical array, typical results are shown in Figs. 8(c) and 9(c). Some left-right ambiguity still exists, and there are still some false source positions at the wrong range. At those times when the source is moving quickly it is difficult to obtain a stable CSD matrix for an array of 64 hydrophones, since the time length averaging requirements compete with the fact that the source has moved on to another position during the time taken to acquire these snapshots. However, processing each 32-element leg separately helps in this regard, and one can then take an incoherent product to combine the individual advantages of the vertical array leg (good range information) and horizontal array leg (good bearing information). When combined, the environmental symmetry breaking from processing the vertical leg only (described earlier), while merely giving crude bearing information, is often enough to break the left-right ambiguity from processing the horizontal leg only. Figures 8(d) and 9(d) show that this method applied to information from an L-shaped array suppresses many of the false source positions. Combining all 360 ambiguity surfaces into a sequence of images covering a 3 h period shows the ambiguous source positions are not persistent.

Figure 10 shows the degradations for the 118.5 Hz data over the entire 3 h period of the Endeavour track analyzed. As one might expect, the best matches occurred at those instances where the ship was close to the receiver arrays and moving slowly. There is a brief period of time (~4500–

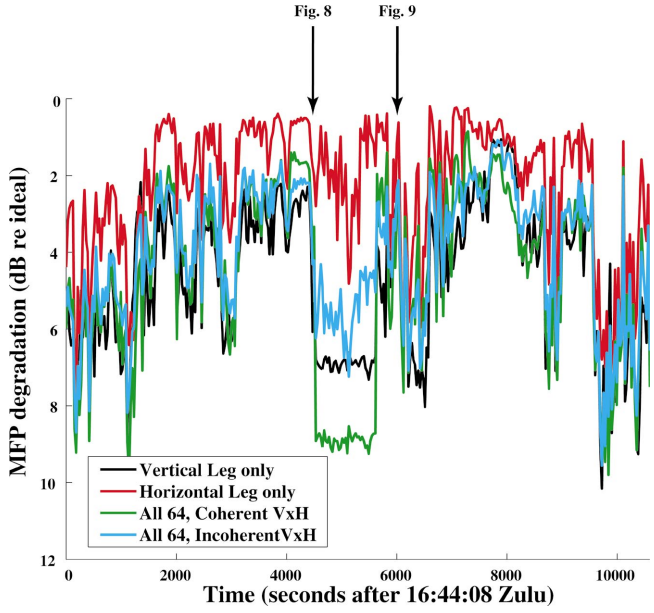

FIG. 10. MFP degradations of the 3 h time period studied from RDS-1. The best results (lowest degradations) were for those times when the Endeavour was moving slowly, and was closer in to the receiver array. The sudden drop in values from ~4500 to ~5600 s was the period when the Endeavour passed across the northeast endfire of the horizontal array. The curve labeled VxH is the incoherent average for the vertical and horizontal legs of the receiver array. We did not divide by the number of hydrophones when these values were computed. The points in time for which the results in Figs. 8 and 9 were calculated are also indicated.

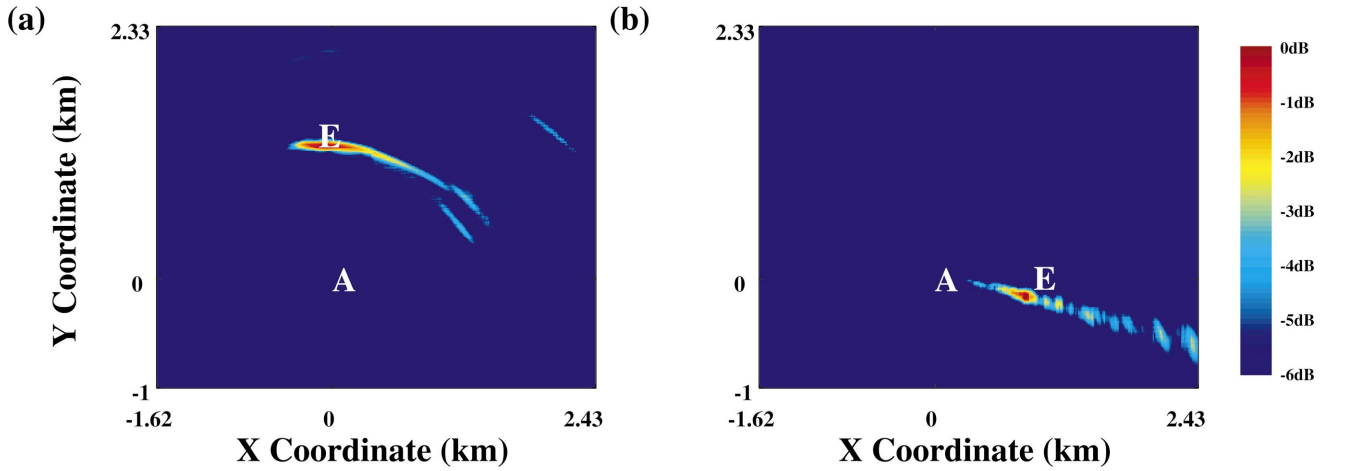

FIG. 11. Output from the source tracking algorithm of Fialkowski *et al.* (see Ref. 23). These are two typical examples taken from a sequence of hundreds of such plots that span the time period when we were tracking the Endeavour. Since the false source positions do not persist in time from snapshot to snapshot, the algorithm suppresses them relative to the (more persistent) true source position.

~5600 s) where there is a marked increase in the degradation amplitude. During this period the Endeavour's speed increased substantially as it moved across the northeast endfire of the horizontal array. MFP is based on the assumption that the acoustic propagation from the source does not change appreciably over the time interval of the data being processed. Clearly this assumption is violated over that time interval, during which the relative bearing from the receiver arrays to the Endeavour changes by more then 90°, and the ship has moved from waters that are slightly shallower to some that are slightly deeper. It is important to note in this figure that we have not normalized the degradations by the number of hydrophones in the receiver array, as is sometimes done. Since the degradations on the horizontal leg are so low, the degradations for VxH (the incoherent average) are somewhat better than for the vertical leg degradations alone.

As described in Sec. II, a sequence (in time) of MFP ambiguity surfaces can be used for source tracking by using a process called matched-field tracking (MFT).[23] Processing over long sequences of surfaces performs poorly when the sound source is making rapid heading changes or rapid speed variations, while taking too short a sequence does not provide good rejection of the spurious false source positions. Consequently, we typically search for possible tracks over eight consecutive MFP ambiguity surfaces. Figure 11 shows the results for the two Endeavour positions (North and East of the receiver arrays) that were used in several of the earlier figures. Comparing MFP results (Figs. 8 and 9) to MFT results (Fig. 11) illustrates how the tracking algorithm can remove the false source positions that do not persist from snapshot to snapshot in time.

V. SUMMARY

For a moving source, we inverted for the geophysical parameters using a sequence of data samples. The environment we obtained from this inversion enabled the successful MFP localization and tracking of a surface ship. The surface ship used as a sound source (Endeavour) radiated weak, broadband noise from 50 up to 250 Hz, with no prominent, sharp lines. We identified weak and variable (intensity) lines at 118.5, 121, and 148 Hz that were attributable to the Endeavour, and we were able to track the vessel for a full 3 h period. Signal-to-noise ratios were very low throughout this period, and the ship speed and heading were variable.

In processing the data, the vertical array gave good range information, with some symmetry breaking from the bathymetry. The horizontal array gave good bearing information. Treating all 64 elements (both arrays) coherently performs well in locating the Endeavour, while taking the incoherent product from the vertical and horizontal arrays generally performed as well or better. In this case, the processing of the orthogonal subapertures was a benefit in reducing the number of data snapshots needed for stable CSD matrices, which in principle could allow one to track faster targets. In our experience multidimensional arrays consisting of several subapertures arranged in similar physical orientations capture essentially redundant information.[13,24] The matched-field processor from each array produces a similar ambiguity surface to the others which, when incoherently summed, had no effect other than to make the ambiguities slightly larger. On the other hand, coherent processing of the data from the full pentagonal array takes advantage of the horizontal spatial extent of the array and serves to better localize the source position while suppressing false ambiguities.

ACKNOWLEDGMENTS

This work was supported by the Office of Naval Research. Thanks also to Defence R&D Canada-Atlantic who hosted the experimental component of this work on their vessel, RV Endeavour.

[1] A. B. Baggeroer, W. A. Kuperman, and P. N. Mikhalevsky, "An overview of matched field methods in ocean acoustics," IEEE J. Ocean. Eng. **18**, 401–424 (1993).
[2] H. P. Bucker, "Use of calculated sound fields and matched field detection to locate sound sources in shallow water," J. Acoust. Soc. Am. **59**, 368–373 (1976).
[3] A. Tolstoy, *Matched Field Processing for Underwater Acoustics* (World Scientific, Singapore, 1993).
[4] D. P. Knobles and S. K. Mitchell, "Broadband localization by matched

fields in range and bearing in shallow water,'' J. Acoust. Soc. Am. **96**, 1813–1820 (1994).
[5] *Experimental Inversion Methods for Exploration of the Shallow Water Environment*, edited by J.-P. Hermand, M. B. Porter, S. M. Jesus, and A. Caiti (Kluwer, Dordrecht, 2000).
[6] N. O. Booth, A. T. Abawi, P. W. Schey, and W. S. Hodgkiss, ''Detectability of low-level broad-band signals using adaptive matched-field processing with vertical aperture arrays,'' IEEE J. Ocean. Eng. **25**, 296–313 (2000).
[7] A. T. Abawi, N. O. Booth, and P. Schey, ''The effects of source motion on the performance of matched field processors,'' J. Acoust. Soc. Am. **107**, 2889–2890 (2000).
[8] B. Tracey, N. Lee, L. Zurk, and J. Ward, ''Array design and motion effects for matched field processing,'' J. Acoust. Soc. Am. **108**, 2645 (2000).
[9] M. D. Collins, W. A. Kuperman, and H. Schmidt, ''Nonlinear inversion for ocean-bottom properties,'' J. Acoust. Soc. Am. **92**, 2770–2783 (1992).
[10] *Full Field Inversion Methods in Ocean and Seismo-Acoustics*, edited by O. Diachok, A. Caiti, P. Gerstoft, and H. Schmidt (Kluwer, Dordrecht, 1995).
[11] ''Special issue on geoacoustic inversion in range-dependent shallow-water environments,'' IEEE J. Ocean. Eng. **28** (2003).
[12] H. C. Song, ''Performance bounds on the passive localization of a moving source for ocean acoustics,'' Ph.D. thesis, MIT, 1990.
[13] J.-M. Q. D. Tran and W. S. Hodgkiss, ''Matched-field processing of 200-Hz continuous wave (cw) signals,'' J. Acoust. Soc. Am. **89**, 745–755 (1991).
[14] C. A. Zala and J. M. Ozard, ''Matched-field processing for a moving source,'' J. Acoust. Soc. Am. **92**, 403–417 (1992).
[15] L. M. Zurk, N. Lee, and J. Ward, ''Source motion mitigation for adaptive matched field processing,'' J. Acoust. Soc. Am. **113**, 2719–2731 (2003).
[16] J. R. Daugherty and J. F. Lynch, ''Surface wave, internal wave, and source motion effects on matched field processing in a shallow water waveguide,'' J. Acoust. Soc. Am. **87**, 2503–2526 (1990).
[17] L. T. Fialkowski, M. D. Collins, W. A. Kuperman, J. S. Perkins, L. J. Kelly, A. Larsson, J. A. Fawcett, and L. H. Hall, ''Matched-field processing using measured replica fields,'' J. Acoust. Soc. Am. **107**, 739–746 (2000).
[18] W. A. Kuperman, M. B. Porter, J. S. Perkins, and R. B. Evans, ''Rapid computation of acoustic fields in three-dimensional ocean environments,'' J. Acoust. Soc. Am. **89**, 125–133 (1991).
[19] M. D. Collins and W. A. Kuperman, ''Focalization: Environmental focusing and source localization,'' J. Acoust. Soc. Am. **90**, 1410–1422 (1991).
[20] M. D. Collins and L. Fishman, ''Efficient navigation of parameter landscapes,'' J. Acoust. Soc. Am. **98**, 1637–1644 (1995).
[21] L. T. Fialkowski, J. F. Lingevitch, J. S. Perkins, D. K. Dacol, and M. D. Collins, ''Geoacoustic inversion using a rotated coordinate system and simulated annealing,'' IEEE J. Ocean. Eng. **28**, 370–379 (2003).
[22] J. Benson, N. R. Chapman, and A. Antonion, ''Geoacoustic model inversion using artifical neural networks,'' Inverse Probl. **16**, 1627–1639 (2002).
[23] L. T. Fialkowski, J. S. Perkins, M. D. Collins, M. Nicholas, J. A. Fawcett, and W. A. Kuperman, ''Matched-field source tracking by ambiguity surface averaging,'' J. Acoust. Soc. Am. **110**, 739–746 (2001).
[24] ''Santa Barbara Channel Experiment (SBCX) Test Plan,'' SPAWAR Systems Center San Diego internal publication (April 1, 1998).

Guided wave propagation in three-layer pavement structures

Nils Ryden[a)]
Department of Engineering Geology, Lund Institute of Technology, Lund University, Box 118, S-221 00, Sweden

Michael J. S. Lowe
Department of Mechanical Engineering, Imperial College, London SW7 2AZ, United Kingdom

(Received 10 March 2004; revised 25 August 2004; accepted 26 August 2004)

A study on guided waves in a layered half-space with large velocity contrasts and a decreasing velocity with depth is presented. Multiple mode dispersion curves are calculated in the complex wave number domain, taking into consideration the attenuation caused by leakage into the underlying half-space. The excitability of the modes by a vertical point force on the surface is also calculated. Results show that the measurable wave field at the surface of a pavement structure is dominated by leaky quasi-Lamb waves in the top and second layers. The fundamental antisymmetric mode of vibration is the dominating mode generated in the stiff top layer. This mode drives the complete system and continuity across the boundaries generates higher order modes in the embedded second layer. The interaction of leaky Lamb waves in the first two layers results in large variations in the excitability and the attenuation, so that only the waves corresponding to certain portions of the dispersion curves are measurable remote from the source at the pavement surface. It is concluded that these portions of dispersion curves can be individually resolved in practice, by using multichannel processing techniques. This holds the potential for a refined nondestructive testing technique for pavements.
[DOI: 10.1121/1.1808223]

PACS numbers: 43.35.Pt, 43.35.Cg, 43.40.Le [YHB] Pages: 2902–2913

I. INTRODUCTION

Guided waves are used in a broad range of applications ranging from global seismology to acoustic microscopy. These waves are formed by the interaction of longitudinal (α) and shear (β) bulk waves and the geometry of the medium. Consequently guided waves carry information on the structural properties (thickness, bonding, and elastic constants) of the medium. New applications using guided waves are continuously being developed and often each new application calls for a detailed analysis on the nature of wave propagation in each specific case (Lowe and Cawley, 1995a; b; Long *et al.*, 2003; Lefeuvre *et al.*, 1998).

The theoretical basis of wave propagation in a layered elastic half-space using matrix methods was introduced by Thomson (1950) and Haskell (1953). Since then a large number of studies on wave propagation in layered systems have been presented; see for example (Lowe, 1995). However, there are only a limited number of studies on guided waves in a multi-layered medium with large velocity contrasts and a decreasing velocity with depth (Picket, 1945; Jones, 1962; Vidale, 1964; Zhang and Lu, 2003). This case is of specific interest in acoustic nondestructive testing of pavements and is the motivation and focus for the work presented here. Another application that falls into this category is ultrasonic testing of some types of coated materials (Shuvalov and Every, 2002) and sandwich structures (Lefeuvre *et al.*, 2000), and it is possible that the generic findings here may also be useful in those fields.

Related studies have dealt with the case of one stiff (fast) layer on a lower velocity half-space (Press and Dobrin, 1956; Jones, 1962; Lefeuvre *et al.*, 1998; Cheng *et al.*, 2001; Ryden and Park, 2004). Yapura and Kinra (1995) investigated dispersion curves and mode shapes for a fluid–solid bilayer. Guided waves trapped in an embedded lower velocity layer have been studied by Parra and Xu (1994), and the opposite case with one embedded higher velocity layer by Lowe and Cawley (1995a, b). Dispersion curves of a bilayered plate were investigated by Jones and Thrower (1965), Laperre and Thys (1993), Lee and Cheng (2001), and Simonetti (2004). Similar studies on multilayered plates have been presented by Cheng *et al.* (2001) and Shull *et al.* (1994). To the author's knowledge, there are no studies on a three-layered half-space with large velocity contrasts and decreasing velocity with depth, where multiple modes of guided waves have been studied in the complex wave number domain.

It is the main purpose of this paper to study guided waves in this specific layer setting. Results should be applicable to any such layered system, but here the main emphasis is towards nondestructive testing of pavements. The present three-layer system represents an extension to a more realistic pavement structure from the two-layer system investigated by Ryden and Park (2004). Some background on surface wave testing of pavements is first presented. In the subsequent sections dispersion curves traced in the complex wave number domain along with leakage, excitability, and mode shapes are studied. A numerical example with two layers on a half-space is used to explain these characteristics. Practical

a)Electronic mail: nils.ryden@tg.lth.se

consequences from these results related to the application to nondestructive testing of pavements are also discussed.

II. BACKGROUND ON SURFACE WAVE TESTING OF PAVEMENTS

Nondestructive testing of civil engineering structures is useful in maintenance planning of old constructions and verification of material properties in new constructions. The determination of thickness and stiffness of each layer in a pavement construction are typical objectives. Surface wave methods in civil engineering applications are based on the dispersive nature of surface waves in a layered medium. This is used to estimate a shear wave velocity, i.e., stiffness-profile of the test site. The traditional testing procedure can be divided into three basic steps: (1) generation and measurement of stress waves in the field; (2) data processing and extraction of a measured dispersion curve; and (3) inversion of the measured dispersion curve to obtain an estimated shear wave velocity with depth profile.

The same basic principles of surface wave propagation are often assumed, regardless of the investigated medium. It is usually assumed that Rayleigh waves are the prevailing type of wave measured, with a depth penetration from the surface related to the wavelength (λ). In surface wave testing of pavements the measured dispersion curve is usually calculated directly from the wrapped phase difference between two receivers on the surface (Heisey *et al.*, 1982; Nazarian, 1984; Stokoe *et al.*, 1994). This apparently continuous dispersion curve ($\sim$30–30 000 Hz) is then used for the evaluation of layer properties through an iterative inversion procedure (Ganji *et al.*, 1998; Hunaidi, 1998; Xia *et al.*, 1999; Gucunski *et al.*, 2000; Wu *et al.*, 2002). This technique has proved to be most effective for the evaluation of the shear wave velocity in the top (asphalt) and bottom (subgrade) layer (Roesset *et al.*, 1990; Aouad, 1993). The properties of the embedded (base) layer have been more difficult to resolve (Aouad, 1993; Foinquinos *et al.*, 1995). However, the potential of evaluating deeper embedded layers in a nondestructive manner has always been one of the main motivations for surface wave testing of pavements. It is mainly the inclusion of higher modes that has been assumed to be the main source of the experienced difficulties (Aouad, 1993; Foinquinos *et al.*, 1995; Roesset *et al.*, 1990).

To resolve multiple modes of propagation, multichannel measurements and two-dimensional wave field transformation techniques have been introduced in near surface site characterization (Gabriels *et al.*, 1987; Park *et al.*, 1999; Foti, 2000; Forbriger, 2003; O'Neill, 2003; Beaty and Smith, 2003). These methods require more data to be collected in the field but are capable of resolving different modes of propagation in the typical soil site frequency range of 5 to 80 Hz. In an attempt to collect higher frequency multichannel equivalent data on a pavement structure, Ryden *et al.* (2001) proposed to use a synthetic array with only one accelerometer and a small hammer. The measured wave field spectrum obtained from this approach came out to be more complicated than expected (Ryden *et al.*, 2002). Abraham *et al.* (2000) and Inazaki and Xinglin (2003) presented similar data and also concluded that the observed dispersion curves in the phase velocity spectrum could not be readily evaluated.

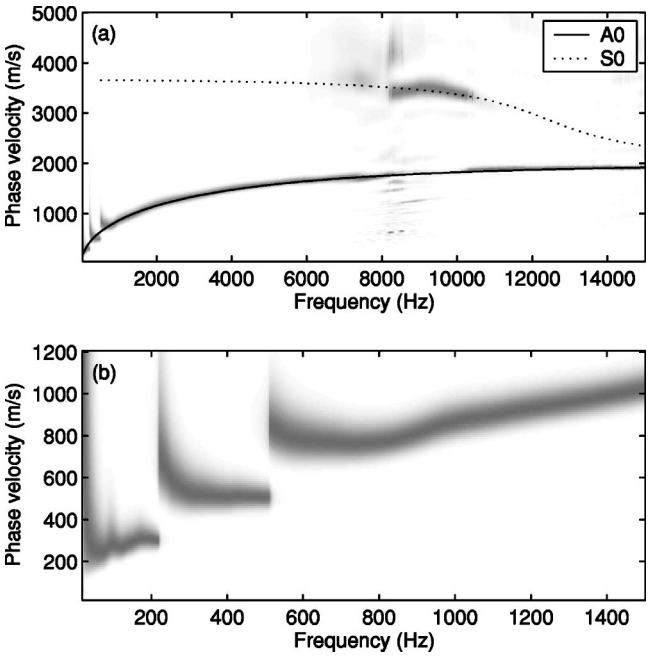

FIG. 1. (a) Gray shading corresponds to the measured phase velocity spectrum from a three-layer pavement construction. Predicted Lamb wave dispersion curves from the top layer as a free plate are superposed as solid (A0) and dotted (S0) lines. (b) The same measured data set displayed in a lower frequency and phase velocity range showing branches of dispersion curves.

Figures 1(a) and (b) shows such a typical measured phase velocity spectrum obtained from the wave field transformation technique presented by Park *et al.* (1998; 1999). The data set was collected over a three-layer pavement structure with 100 equally spaced stations from 0.05 to 5.00 m. The main trend of the data in Fig. 1(a) matches with the dispersion curve of the fundamental antisymmetric (A0) Lamb wave mode (Lamb, 1917) which would be predicted to propagate in the top layer only if it was detached from the others. In other words, the stiff top layer behaves quite independently of the layers beneath it. This characteristic trend was observed already in the early work on surface wave testing of pavements (Jones, 1955, 1962; Vidale, 1964; Jones and Thrower, 1965) and provides a practical technique to estimate both the shear wave velocity (β) and the thickness (d) of the stiff top layer. However, this approach has only been utilized in a few recent studies on surface wave testing of pavements (Akhlaghi and Cogill, 1994; Martincek, 1994). In Ryden *et al.* (2004) the free plate approach for the top layer was extended to include the symmetric (S0) mode since a portion of this mode can be observed in the measured phase velocity spectrum, for example between 8 and 10 kHz in Fig. 1(a). Martincek (1994) concluded from experimental results on pavements that the Lamb wave approximation was valid for all wavelengths smaller than five times the thickness of the stiff top layer. From a theoretical study on the influence of a lower velocity half-space Ryden and Park (2004) quantified the theoretical deviation involved in the free plate approximation to be less than 10%. This approximate approach holds as long as β in the top layer is higher

than α in the underlying medium (Jones and Thrower, 1965), i.e., for a large stiffness contrast. In the other case where β in the top layer is not higher than α in the lower velocity half-space (but still higher than β in the half-space) the cutoff frequency of the second mode occurs at a higher frequency (Zinin *et al.*, 1997). All the studies above made an implicit conclusion that the wave field generated from a vertical point source at the surface of a pavement system is dominated by Lamb type of waves in the stiff top layer.

In Fig. 1(b) the measured phase velocity spectrum is plotted in a lower frequency and phase velocity range. Several branches of dispersion curves are visible, limited by cutoff frequencies and abruptly changing phase velocities. A similar pattern was observed by Gucunski and Woods (1992) and Tokimatsu *et al.* (1992) in numerical modeling of surface wave measurements over a layer model with an embedded low velocity layer. They concluded that the observed discontinuities were created by mode jumping between successively higher modes. This phenomenon was later emphasized by other researchers too (Foti *et al.*, 2003; O'Neill, 2003; Zhang and Lu, 2003), but no studies have focused on the explanation of this behavior. Furthermore, in all these studies, the velocity of the bottom half-space was always set to be the highest velocity of the system in order to avoid tracing dispersion curves in the complex wave number domain.

III. WAVE PROPAGATION MODEL

The global matrix method proposed by Knopoff (1964) and implemented as described by Lowe (1995) is used to predict theoretical dispersion curves in this study. The wave propagation model can handle leaky waves (complex wave numbers) without modification and remains stable for high frequencies and large thickness values (Lowe, 1995). A system matrix (**S**) is assembled from all layer interface matrices ($\mathbf{D}_i$) describing the displacement and stress fields associated with harmonic wave propagation along the multilayered structure. In each layer interface matrix, stresses (σ) and displacements (u) are expressed as a function of the material properties; α, β, d, bulk density (ρ) of the layer, circular frequency (ω), and wave number (k). Each point on a dispersion curve represents a solution to **S** where all boundary conditions are satisfied simultaneously. The dispersion equation or characteristic equation then becomes

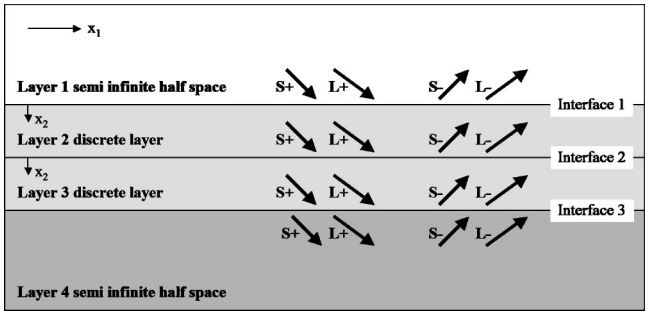

FIG. 2. Schematic illustration of the layered model used in the global matrix approach, after Lowe (1995).

$$f(\omega,k)=\det[\mathbf{S}]=0. \tag{1}$$

More details on the wave propagation model can be found in Knopoff (1964), Randall (1967), or Lowe (1995). Here only the final matrix equations as given by Lowe (1995) are presented. Each layer is represented with one matrix for the top interface ($\mathbf{D}_t$) and one matrix for the bottom interface ($\mathbf{D}_b$). The interface matrix describes the displacements and stresses at the interface as a function of the partial wave amplitudes (A) from above (index t) or below (index b) the interface. The thickness (d) in the x_2 direction of each layer is entered as x_2 into the equations for dispersion curve calculations and is zero for the half-space matrices. The partial waves A are divided into longitudinal waves (L) and shear waves (S). The $(+)$ and $(-)$ indices denote partial waves traveling down $(+)$ and up $(-)$ from the interface (see Fig. 2). The interface matrices are

$$\begin{Bmatrix} u_1 \\ u_2 \\ \sigma_{22} \\ \sigma_{12} \end{Bmatrix} = [\mathbf{D}_i] * \begin{Bmatrix} A_{(L+)} \\ A_{(L-)} \\ A_{(S+)} \\ A_{(S-)} \end{Bmatrix}, \tag{2}$$

where

$$[\mathbf{D}_{it}] = \begin{bmatrix} k_1 & k_1 g_\alpha & C_\beta & -C_\beta g_\beta \\ C_\alpha & -C_\alpha g_\alpha & -k_1 & -k_1 g_\beta \\ i\rho B & i\rho B g_\alpha & -2i\rho k_1 \beta^2 C_\beta & 2i\rho k_1 \beta^2 C_\beta g_\beta \\ 2i\rho k_1 \beta^2 C_\alpha & -2i\rho k_1 \beta^2 C_\alpha g_\alpha & i\rho B & i\rho B g_\beta \end{bmatrix}, \tag{3}$$

$$[\mathbf{D}_{ib}] = \begin{bmatrix} k_1 g_\alpha & k_1 & C_\beta g_\beta & -C_\beta \\ C_\alpha g_\alpha & -C_\alpha & -k_1 g_\beta & -k_1 \\ i\rho B g_\alpha & i\rho B & -2i\rho k_1 \beta^2 C_\beta g_\beta & 2i\rho k_1 \beta^2 C_\beta \\ 2i\rho k_1 \beta^2 C_\alpha g_\alpha & -2i\rho k_1 \beta^2 C_\alpha & i\rho B g_\beta & i\rho B \end{bmatrix} \tag{4}$$

and

$$g_\alpha = e^{iC_\alpha x_2}, \quad g_\beta = e^{iC_\beta x_2}, \tag{5}$$

$$C_\alpha = (\omega^2/\alpha^2 - k_1^2)^{1/2}, \quad C_\beta = (\omega^2/\beta^2 - k_1^2)^{1/2}, \tag{6}$$

$$B = \omega^2 - 2\beta^2 k_1^2. \tag{7}$$

When the four-by-four $\mathbf{D}_{ib}$ and $\mathbf{D}_{it}$, $(i=1,...,n)$ matrices have been calculated for each layer they are assembled to obtain the global **S** matrix so that stresses and displacements become continuous over the interfaces. For a layer model with four layers as in Fig. 2 the system matrix then becomes

$$\mathbf{S} = \begin{bmatrix} \mathbf{D}_{1b}^{-} & -\mathbf{D}_{2t} & & \\ & \mathbf{D}_{2b} & \mathbf{D}_{3t} & \\ & & \mathbf{D}_{3b} & -\mathbf{D}_{4t}^{+} \end{bmatrix}. \tag{8}$$

The $(-)$ index on $\mathbf{D}_{1b}$ above represents the outgoing (up) waves in the top half-space (columns two and four in $\mathbf{D}_b$) and the $(+)$ index on $\mathbf{D}_{4t}$ represents outgoing (down) waves in the bottom half-space (columns one and three in $\mathbf{D}_t$). These half-space matrices are only four-by-two matrices given that the incoming waves in the half-spaces are zero for unforced modal solutions. A free surface can be modeled by some modifications to the **D** matrix. However, exactly the same result can be obtained much more easily simply by setting the bulk wave velocities α and β in the top layer to arbitrary nonzero values and the bulk density to zero (Lowe, 1995). In this way the same matrices can be used for both vacuum and solid half-spaces.

A. Dispersion curves in the complex wave number domain

The dispersion curves are found by numerical searches for the ω-k pairs that make the value of the determinant of **S** vanish in Eq. (1). These modal solutions must be searched in the complex wave number domain in any part of the solution space where the phase velocity (corresponding to the real part of the wave number) becomes greater than the shear wave velocity in the lower half-space. Thus the numerical solution is in three variables: ω, k_{real} and $k_{\text{imaginary}}$. For such complex solutions the particle motion does not decrease exponentially with depth. Instead energy radiates down into the lower half-space, resulting in attenuation of the wave along the surface in the x_1 direction (Vidale, 1964), even though all materials are purely elastic. In this study the dispersion curve software ''Disperse'' developed at Imperial College (Pavlakovic *et al.*, 1997; Disperse, 2001) has been used to trace the dispersion curves in the complex wave number domain.

B. Excitability and leakage

The solution of the matrix equations gives dispersion curves representing any type of guided wave which may exist with particle motion in the x_1 and x_2 directions; these include modes such as interface waves and plate waves which may not always be measurable at the surface. Therefore it is useful to calculate some more information to help the interpretation of the waves which are actually detected in the measurements. The key information here is the excitability (E) at the surface and the leakage (κ) along the x_1 direction. The excitability indicates the extent to which each mode is excited when the surface force is applied; the leakage indicates how quickly the amplitude of the signal attenuates with the distance from the source. Both of these quantities differ for the different modes and also for different locations along each dispersion curve.

TABLE I. Reference layer model representing a flexible pavement construction.

Layer	β (m/s)	α (m/s)	ρ (kg/m^3)	Thickness (m)
1	1400	2914	2000	0.20
2	500	1041	2000	0.60
3	100	208	2000	∞

The excitability (E) of a particular mode at a particular frequency is defined as the ratio of displacement of that mode to the applied force when both quantities are measured at the same location and direction (Wilcox *et al.*, 2004). A harmonic vertical point force at the surface with a certain frequency will excite different modes along the surface to various degrees. The vertical displacement (u_2) from a vertical unit amplitude load at the surface is used to calculate the excitability as

$$E \propto u^2 f. \tag{9}$$

The attenuation due to the leakage of modes is calculated from the ratio between the imaginary part (k_i) and the real part (k_r) of the wave number. This is nonzero when the phase velocity exceeds the shear wave velocity in the lower half-space. Points on a dispersion curve with a large imaginary part of the wave number have large attenuation and are therefore not likely to appear in measured surface wave data. The attenuation coefficient (κ) is defined as

$$\kappa = \frac{2\pi k_i}{k_r}, \tag{10}$$

where κ is in nepers per wavelength, so that a wave of unit amplitude is reduced to an amplitude of $e^{-\kappa}$ after traveling one wavelength.

IV. ANALYSIS OF A THREE-LAYER REFERENCE MODEL

The same reference model, representing a flexible pavement construction with a relative stiff and thick base layer, is used throughout this study. The bulk wave velocities decrease with depth. All parameters are defined as elastic, homogenous, and isotropic. The thickness and elastic constants of each layer are given in Table I. Material attenuation is not included in the model. However, the dominating mechanism for loss of energy, leakage, is included. Thus the model correctly accounts for the effect of attenuation on experimental measurements, though a little underestimated.

A. Dispersion curves over a broad frequency range

The dispersion curves for all modes are first presented in the full frequency range that is normally utilized in pavement testing (Fig. 3). Within this frequency range there are more than 100 possible modes of propagation. The curves are

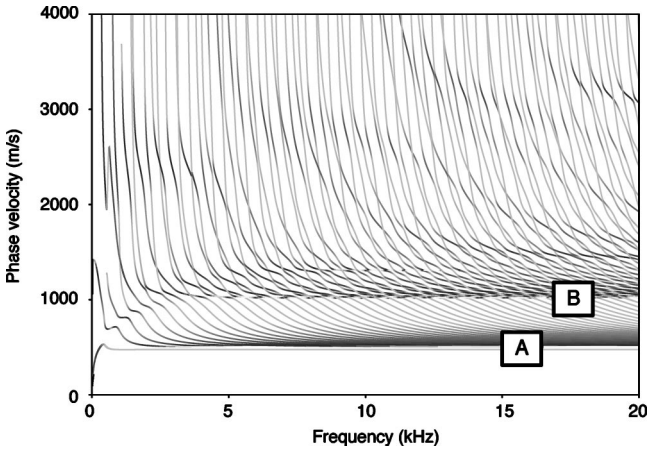

FIG. 3. Predicted dispersion curves from the three-layer reference model (Table I). Dark portions correspond to low attenuation due to leakage.

gray-scale coded with respect to the amount of attenuation due to leakage (from 0 to 0.55 np/m). Black points on each dispersion curve correspond to portions with low leakage in the x_1 direction. It is immediately evident from this figure that the full spectrum of modes is considerably more complex than the measured phase velocity spectrum presented in Fig. 1(a) and than what is normally presented from surface wave testing of pavements.

In order to explain the main trends of all the dispersion curves in Fig. 3, a two-layer model is first used for comparison purposes. The embedded second layer in the reference model (Table I) is excluded, so that the model consists only of the stiff surface layer on the half-space. The resulting dispersion curves are plotted in Fig. 4. For this reduced system there are only nine possible modes of propagation within the same frequency range as in Fig. 3. It should be noted how the overall trend of the black portions in Fig. 3 matches with the individual dispersion curves in Fig. 4. This comparison bears for all but the two lowest phase velocity trends (labeled A and B in Fig. 3), which are related to interface waves in the three-layer model (Stoneley, 1924). The overall trend of the first three modes in Fig. 4 (labeled 1–3) also matches fairly well with the measured phase velocity spectrum in Fig. 1(a). The second mode in Fig. 4 is closely linked

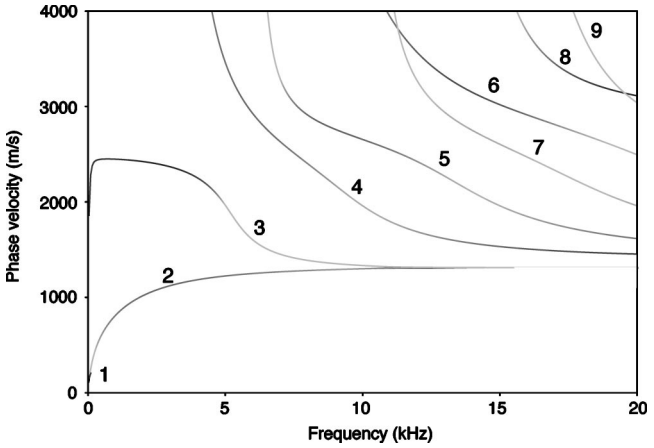

FIG. 4. Predicted dispersion curves from a two-layer model where the second layer from the reference model (Table I) has been excluded.

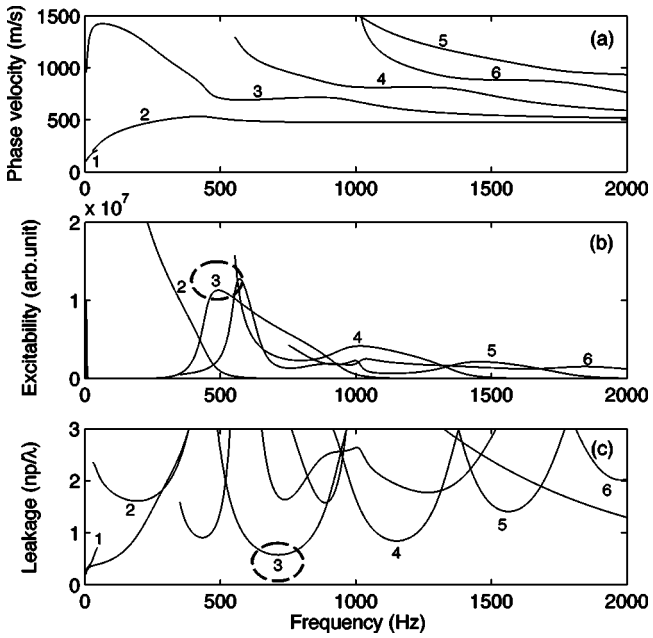

FIG. 5. (a) The first six modes from Fig. 3 with corresponding (b) excitability and (c) leakage.

to the antisymmetric Lamb wave mode (A0) in a free plate and is the dominating mode over most of the frequency range in this type of two-layer system (Ryden and Park, 2004).

Let us consider the trend of this mode (mode 2 in Fig. 4) in comparison to all the modes in Fig. 3 more closely. By following the individual higher modes in Fig. 3 from low to high frequencies it can be observed that all modes exhibit a terracelike portion close to phase velocities of the second mode in the two-layer system. At these terracelike portions the mode is less dispersive (straighter horizontally aligned dispersion curve) and less leaky (darker gray). This kind of terracelike behavior has been observed in other studies on bilayered plates (Yapura and Kinra, 1995; Simonetti, 2004). The general trend of the dispersion curves of the dominating layer seems to break up into small branches of dispersion curves in the three-layer model. At higher frequencies (>2 kHz) all individual modes of the three-layer system merge together and form the overall trend of the dispersion curves of the two-layer system. This indicates that the general trend of the observed wave field spectrum in Fig. 1(a) is mainly formed by the properties of the top and the bottom layer. However, at low frequencies (<2 kHz) branches of dispersion curves are more separated, revealing the presence of the embedded second layer in the three-layer model. This indicates that the observed branches of dispersion curves in Fig. 1(b) are the key features that can be used to estimate the properties of the complete three-layer pavement system. Therefore the following sections will be focused on these measurable branches at lower frequencies.

B. Branches of dispersion curves at lower frequencies

The first six modes from Fig. 3 are plotted in Fig. 5(a) in a smaller frequency range. The excitability of these modes is

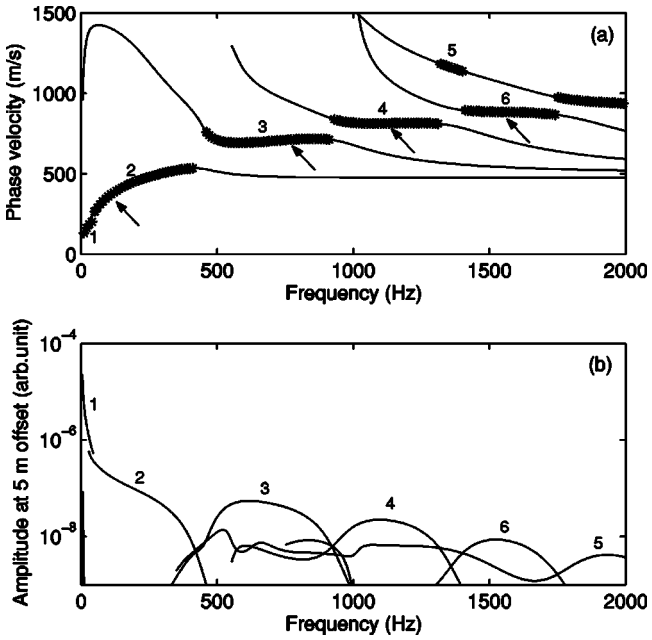

FIG. 6. (a) The first six modes from the reference model with dominating surface displacements at 5 m offset from the source marked with crosses. The arrows correspond to the locations of the mode shapes in Fig. 7. (b) The relative magnitude of surface displacements of each mode at 5-m offset from the source.

plotted in Fig. 5(b), showing that each mode will be excited with larger displacements at the surface within certain frequency bands. Figure 5(c) shows a similar behavior for the minima in leakage. However, frequencies with maximum excitability and minimum leakage are not fully correlated for each mode. For example, the third mode shows a maximum excitability at 495 Hz and a minimum leakage at 715 Hz, marked with circles in Figs. 5(b) and (c). This indicates that the dominating mode of propagation at a point on the surface at a chosen distance from the source will be dependent on a combination of the excitability and the amount of leakage, hence also the distance (x) from the source. Geometric spreading and intrinsic material attenuation will also reduce the amplitude as a function of distance from the source. Nevertheless, these latter two factors should remain constant for each frequency, so we can determine which mode is dominating surface displacements at a certain distance from the source and frequency from E and κ by using

$$U(x,\omega) = E^* e^{-(\kappa x/\lambda)}, \tag{11}$$

where U is the relative amount of surface displacement at a certain distance from the source. In Fig. 6(a) the dispersion curves with maximum U for each frequency at 5 m distance from the source are marked with crosses. Figure 6(b) shows the amount of displacement of each mode at this point on the surface; the actual amplitudes of the displacement shown here are arbitrary, what is significant is the relative values when comparing different modes and different frequencies. The pattern of the crosses reveals the same phenomenon as was experienced in the measured phase velocity spectrum [Fig. 1(b)]. It seems therefore that the existence of the observed branches of dispersion curves can be theoretically explained from the excitability and leakage of each mode.

C. Mode shapes

To further clarify the generation mechanism of the branches of dispersion curves predicted for the three-layer reference model, mode shapes are studied next. The mode shapes show how displacements or stresses vary as a function of depth (x_2) and can be used to study which layer or layers are affected by a particular mode and frequency. The mode shape is also calculated for a few wavelengths in the direction of propagation (x_1) to further illustrate the type of wave motion, although the distribution is known to be sinusoidal (modulated by an exponential decay in the cases of attenuating waves). In Figs. 7(a)–(d) mode shapes corresponding to the second, third, fourth, and sixth mode branches in Fig. 6(a) are plotted. Note that the grid form of display is used simply to show the shape; the sizes of the grid elements have no significance. Also, the plots only show an arbitrarily limited depth of the half-space.

The top layer shows the typical antisymmetric type of particle motion in all four figures. This agrees well with the earlier findings that the dominating type of wave propagation in this system is closely related with the A0 Lamb wave in a free plate [Fig. 1(a)]. The second layer also shows a mode shape similar to the mode shape of Lamb waves in a free plate (Graff, 1975) in all four cases. At the lowest branch the mode shape [Fig. 7(a)] can be identified as a fundamental mode which has a quasi-antisymmetric mode shape; since the layer is not free it is strictly not a Lamb wave mode shape but it is very similar. At the next higher branch [Fig. 7(b)] the second layer shows a fundamental mode which has a quasi-symmetric mode shape. In the next branch [Fig. 7(c)] the mode shape is quasi-antisymmetric. Finally, at the fourth branch (mode number 6) the mode shape [Fig. 7(d)] is back to symmetric and shows the particle motion of the first higher mode. Consequently, the branches correspond to successive higher modes of quasi-Lamb waves in the second layer. Since all phase velocities are higher than the shear wave velocity of the lower half-space, energy is leaking down into the lower velocity half-space in all four cases. This can be seen quite clearly by the mode shapes in the half-space which are in the form of radiating wavefronts.

The observed behavior can be explained from a physical examination of the continuity of both stresses and displacements along the layer boundaries. The stiff top layer, with its high bulk wave velocity material, carries most energy and propagates with a mode shape close to the A0 Lamb wave. Continuity across the layer boundaries forces the second layer to share the same frequency and wave number as the top layer. Since this second layer has a lower bulk wave velocity than the top layer, higher modes are generated to match the mode shape of the faster top layer. Hence, the generation mechanism of the observed branches at lower frequencies can be explained as a superposition of quasi-Lamb waves in the top and second layer. This can be seen in Fig. 8, which shows Lamb waves corresponding to the top (subscript 1) and second (subscript 2) layers as free plates, together with the crosses from Fig. 6. The free plate Lamb wave dispersion curves of the top and second layers intersect close to the corresponding mode shapes of each branch (exemplified with one circle in Fig. 8), e.g., the antisymmetric

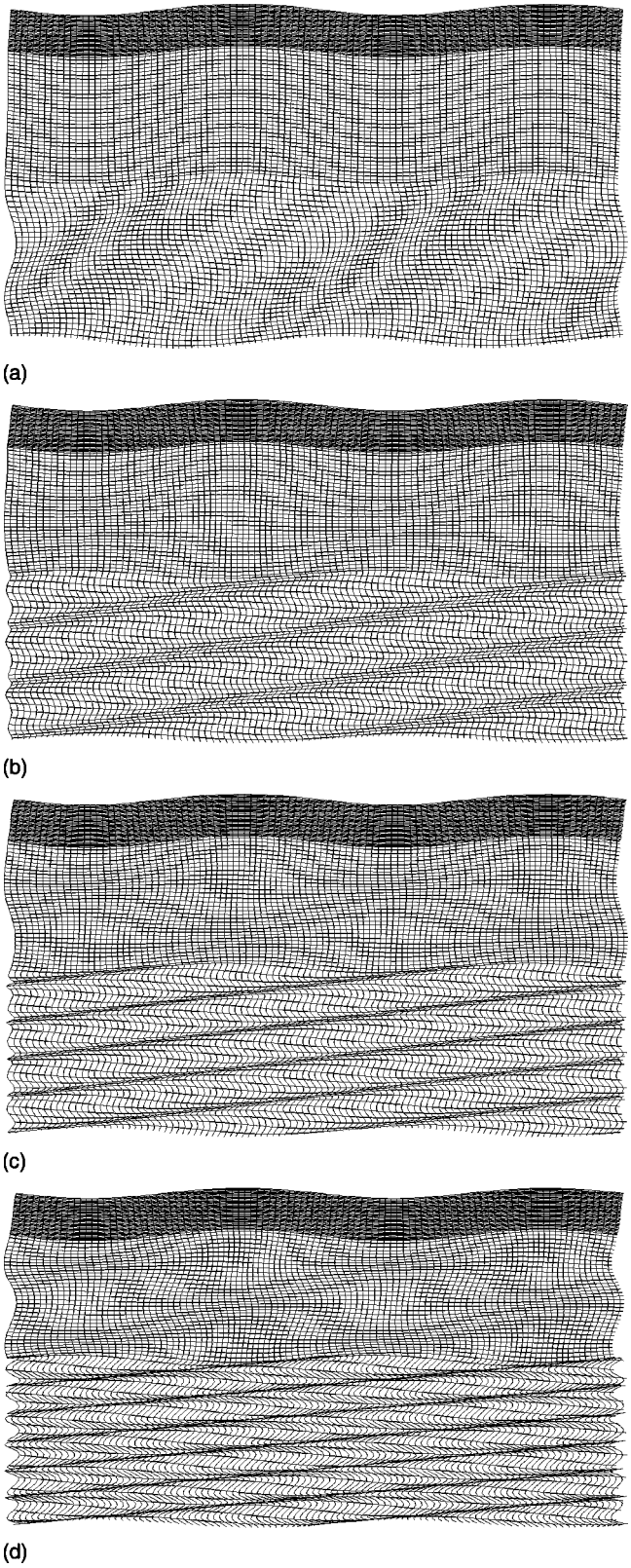

FIG. 7. Representative mode shapes of the four first branches marked with arrows in Fig. 6(a).

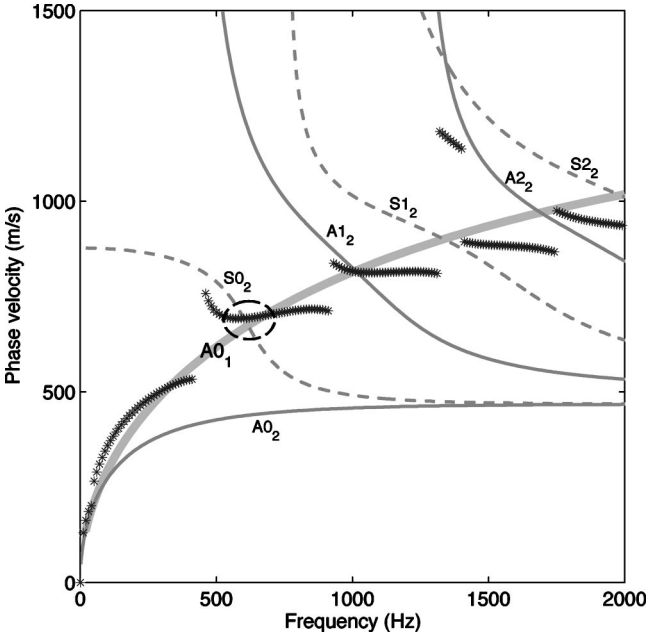

FIG. 8. Superposition of Lamb waves calculated from the (1) first and (2) second layer as free plates. (*) crosses mark the branches with dominating surface displacements at 5 m offset.

mode of the top layer $A0_1$ intersects with the symmetric mode of the second layer $S0_2$ within the second branch whose mode shape is illustrated in Fig. 7(b).

It should be noted that the mode shape is not constant but varies with frequency and phase velocity along each dispersion curve. By studying the change in mode shape along each dispersion curve it can be found that at frequencies when there is maximum surface displacements [Fig. 6(a)], there are large and smoothly varying normal (x_2) displacements over the interface between the first and second layers. At these peaks in surface displacement [Fig. 6(a)], the mode shapes in the first and second layers match, effectively resulting in dominating surface displacements. At higher and lower frequencies along the dispersion curve the mode shape shows a more abrupt change over the layer interface. This can be seen in Fig. 9 where the normal displacement is plotted as a function of depth at different frequencies along the fourth mode. The frequency is varied from 1000 to 2000 Hz in 200-Hz increments. At 1000 Hz the normal displacement varies smoothly over the interface between the first and second layers. At higher frequencies a more abrupt change develops. At phase velocities where higher mode dispersion curves drop below the main trend of the A0 mode in the corresponding free top layer, displacements at the layer interface between the first and second layers approach zero and the normal stress over the layer interface increases. At this stage there is no longer any possible harmonic wave motion in the top layer. Wave motion within the second layer then approaches the asymptotic solution of a clamped-free plate (Simonetti, 2004).

D. Parametric study

So far all the dispersion curves have been calculated from the properties of the fixed reference layer model (Table I). It could be debated that some of the results above are only valid for this specific layer model. Also, it is of practical interest to study how the measurable branches are related to

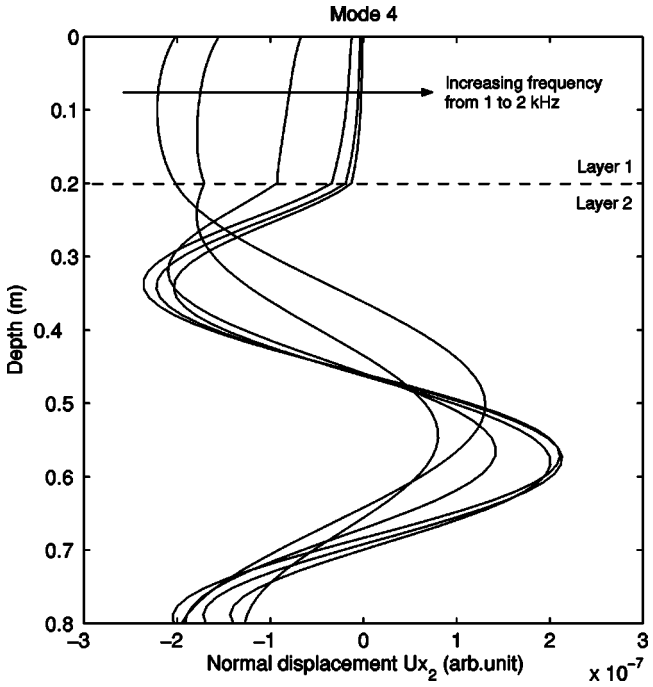

FIG. 9. Normal displacement (x_2) at different freqeuncies along the fourth mode of the reference model (Fig. 5).

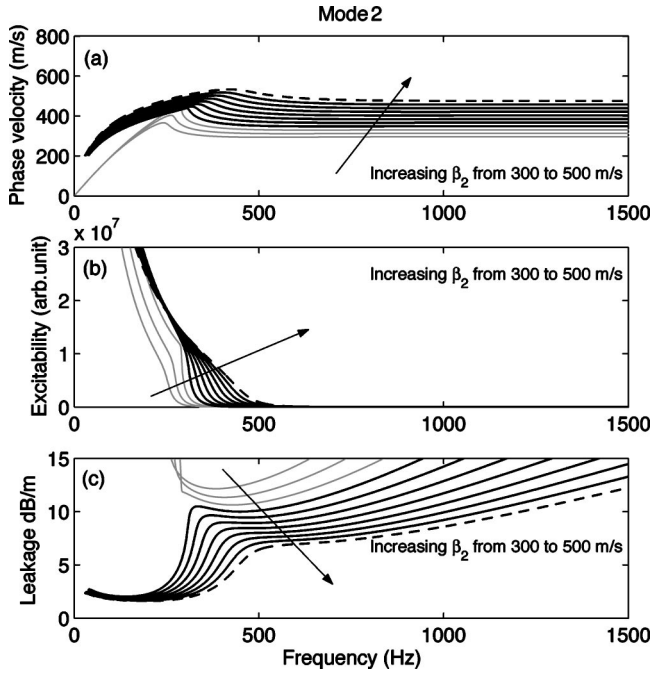

FIG. 10. Parametric study on the second mode when the shear wave velocity of the second layer is varied from 300 to 500 m/s in 20-m/s increments. The dotted line represents the reference case and gray dispersion curves mark the anomalous behavior of these modes.

different properties of the three-layer model. This motivates a parametric study on the low-frequency modes studied above.

The fundamental mode [labeled 1 in Fig. 5(a)] is very similar to the fundamental mode of the two-layer system. It has been concluded in previous studies on a two-layer model with one stiff (fast) layer on a lower velocity half-space that this mode is limited by the Rayleigh wave and the longitudinal or shear wave velocity of the lower velocity half-space depending on the velocity contrast (Vidale, 1964; Jones and Thrower, 1965; Zinin *et al.*, 1997). This cutoff behavior can be explained from the coupling between the high velocity layer and the half-space; the half-space will not support any modes propagating faster than the bulk wave velocities of the half-space (Nayfeh and Chimenti, 1984). Therefore we start with the second mode in this parametric study, which is unique for this three-layer system.

1. The second mode

The shear wave velocity of the second layer has been varied from 300 to 500 m/s in 20-m/s increments, keeping all other layer properties fixed. The resulting dispersion curves are plotted in Fig. 10. Note that the 500 m/s reference case corresponds to the results already shown (dotted line). Dispersion curves corresponding to the three lowest shear wave velocities (300–340 m/s) are colored gray since they deviate from the main trend of all the other curves. As expected the phase velocity increases with increasing shear wave velocity of the second layer [Fig. 10(a)]. However, the phase velocity of the gray dispersion curves is very much lower than the reference case in the low-frequency range where this mode was previously shown to dominate the surface displacements [Fig. 6(a)]. The excitability in Fig. 10(b) is also drastically reduced for these curves, but the main difference can be observed in the amount of leakage [Fig. 10(c)]. The gray dispersion curves all show a very large amount of attenuation due to leakage. Thus Figs. 10(b) and (c) indicate that this mode may not be measurable when the shear wave velocity of the second layer drops below 360 m/s.

2. The third mode

Figure 11 shows a similar parametric study on the third mode. This figure also reveals a deviation in the dispersion curves corresponding to the lowest shear wave velocities of the second layer (gray curves). Here the three gray dispersion curves seem to follow the pattern of the deviating gray dispersion curves from Fig. 10, indicating that this third mode actually covers both the second and the third branch observed for the reference layer model (Fig. 6). A similar mode jumping or mode coupling phenomenon was discovered by Yapura and Kinra (1995) in a bilayered plate.

3. The fourth mode

In Fig. 12 dispersion curves of the fourth mode are plotted for different shear wave velocities of both the first (β_1) [Fig. 12(a)] and the second (β_2) layer [Fig. 12(b)]. The fourth mode is clearly more sensitive to β_2 compared to β_1. But here it is interesting to see that a change in β_1 shifts the profile of the dispersion curve in one direction indicated with an arrow in Fig. 12(a), while a change in β_2 shifts it in another direction [Fig. 12(b)]. This indicates that both parameters may be detectable even at these relatively low frequencies if the shape of the measurable branch corresponding to this mode can be accurately detected.

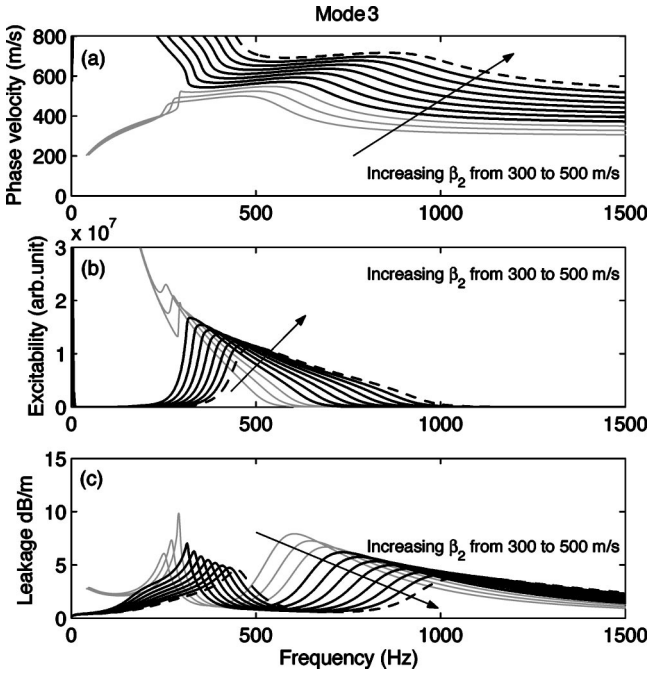

FIG. 11. Parametric study on the third mode when the shear wave velocity of the second layer is varied from 300 to 500 m/s in 20-m/s increments. The dotted line represents the reference case and gray dispersion curves mark the anomalous behavior of these modes.

E. Longitudinal waves in the top layer

In all sections above the focus has been on the individual branches of dispersion curves following the main trend of the A0 mode of the top layer as a free plate [Fig. 1(a)]. But in Fig. 1(a) there is a also a visible dispersion curve at about 3800 m/s matching the S0 Lamb wave mode of the top layer as a free plate. The limited frequency range of the visible portion of this mode [Fig. 1(a)] can be explained from the difference in excitability between the second and third modes in Fig. 4 (Ryden and Park, 2004). A closer study on the individual dispersion curves in Fig. 3, dominating surface displacements, and mode shapes, reveals a similar phenomenon as the findings along the A0 trend.

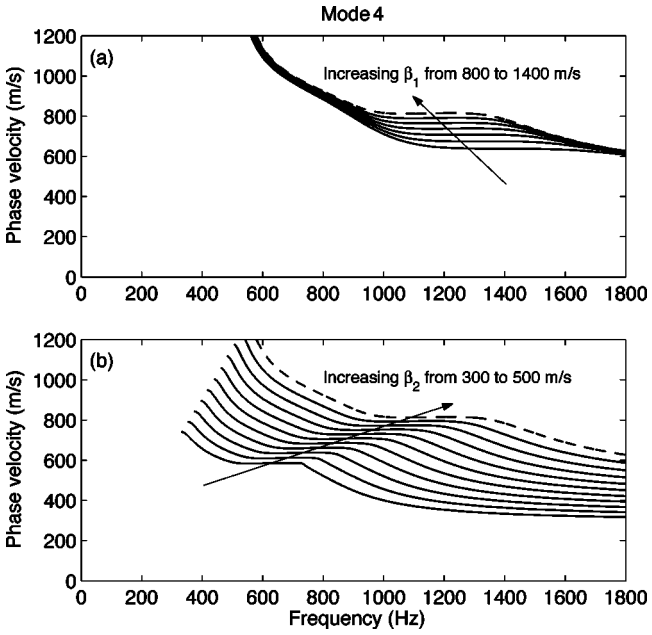

FIG. 12. Parametric study on the fourth mode when the shear wave velocity of the (a) second layer is varied from 300 to 500 m/s in 20-m/s increments, and the (b) first layer is varied from 800 to 1400 m/s in 100-m/s increments. Dotted line shows the reference case from Table I.

V. PRACTICAL CONSEQUENCIES IN APPLICATIONS TO PAVEMENTS

It is usually stated that the measured surface waves on a pavement profile are dominated by Rayleigh type of waves. But in this study it has been shown that wave propagation in this type of layered half-space is related to more general characteristics of guided waves in plates, and the Rayleigh type of waves can only be found at the asymptotes of very high (here >20 kHz) or very low (here <10 Hz) frequencies. These findings can possibly explain some of the reported difficulties and lack of sensitivity with the conventional approach of surface wave testing of pavements. In this section we examine some such observations.

A. Field testing

In the conventional field setup the wrapped phase difference between two receivers located a known distance (D) apart is measured. Spatial aliasing occurs when the phase difference exceeds half a wavelength (180°), resulting in a 360° cycle in the wrapped phase difference spectrum. The wrapped phase spectrum must be correctly unwrapped before a measured dispersion curve is calculated by using

$$c(f) = \frac{D 2\pi f}{\Delta\phi}, \tag{12}$$

where $\Delta\phi$ is the unwrapped phase difference in radians. Several researchers have reported on difficulties associated with the phase unwrapping process. Al-Hunaidi (1992) found that the wrapped phase difference spectrum measured over a pavement surface contained a spurious cycle that could not be explained. However, he observed that the most realistic measurement of phase velocity is obtained if this cycle is not unwrapped. This phenomenon may be explained from the branches of the dispersion curves studied in this paper. Let us consider the first jump at 220 Hz from the first to the second branch in Fig. 1(b). The phase velocity changes abruptly from 300 to 700 m/s. By rearranging Eq. (12) the corresponding wrapped phase spectrum from the dispersion curves in Fig. 1(b) can be obtained [Fig. 13(a)]. Here a typical receiver spacing of 2.0 m is chosen to sample these wavelengths (Heisey *et al.*, 1982). It is interesting to see that the abrupt jump in phase velocity almost creates an additional 360° cycle in the wrapped phase spectrum [marked as number 2 in Fig. 13(a)]. A longer receiver spacing or a greater phase velocity difference should actually produce a phase difference jump of more than 360°. If this additional cycle is included in the phase unwrapping process, the resulting dispersion curve will be erroneous, continuous, and smooth as indicated by the dotted line in Fig. 13(b). This indicates that the measured wrapped phase difference between two receivers is not a feasible approach to obtain a measured dispersion curve in this case.

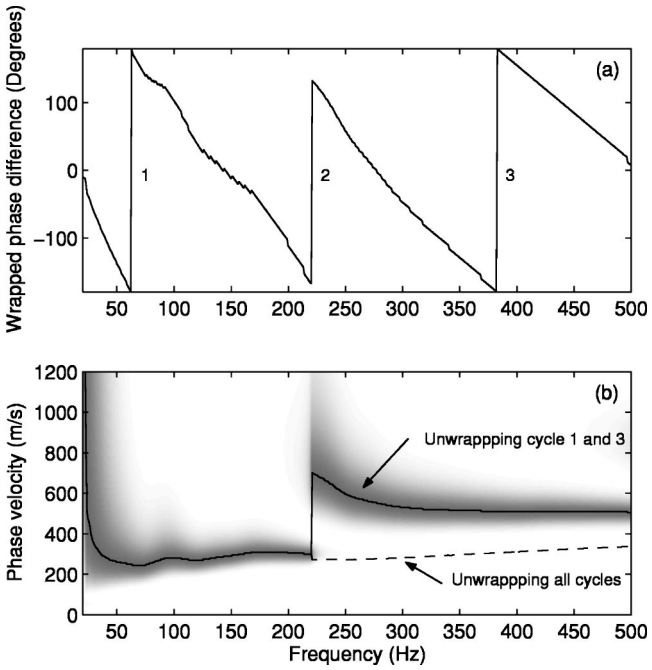

FIG. 13. (a) Wrapped phase spectrum calculated from the original data used for Fig. 1 with 2.0-m receiver spacing. The second cycle should not be unwrapped since it is created by the jump between the first and second branches at 220 Hz. (b) The effect on the dispersion curve if the second cycle is unwrapped before the dispersion curve is calculated.

Fluctuations in the measured dispersion curve have often been assumed to originate from reflections of body waves from the bottom of the asphalt layer or from horizontal boundaries and possible cracks in the pavement (Sheu *et al.*, 1988; Roesset *et al.*, 1990). However, since there are so many modes of propagation in this type of layered structure (Fig. 3), fluctuations caused by mode jumping should reasonably be expected.

B. Inversion of layer properties

Another issue is the Rayleigh wave assumption of wave propagation. Since in practice the measured dispersion curve is often analyzed from the Rayleigh wave perspective, some aspects of this procedure may be questioned. For example many sublayers (~10) are often used for the evaluation of a layer profile from the measured dispersion curve. From the Rayleigh wave perspective this resolution may be justified since the data contains measured phase velocities at many different wavelengths sampling different depths from the surface. But the analysis of the reference layer model used in this study gives another picture of the wavelength-depth relation. In the reference model, all higher modes starting from the first cutoff frequency of the fundamental mode (50 Hz or 4 m wavelength) correspond to leaky guided waves trapped in the first and second layers. Consequently all wavelengths from about 0.2 m (thickness of the top layer) to about 4.0 m sample the same depth but with different modes of propagation. This explains why the wavelength cannot be directly related to the depth in this kind of layer system. This also implies that it may not be possible to evaluate more layers than the main layers of the construction, i.e., three or four layers.

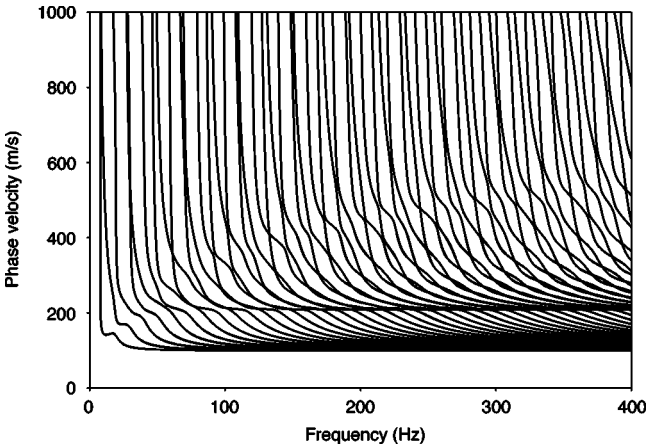

FIG. 14. Influence from a high velocity half-space at 5 m depth from the second layer in the reference layer model.

Another assumption that may have to be reconsidered is the use of a high velocity half-space to avoid tracing dispersion curves in the complex wave number domain. From the Rayleigh wave theory this may seem like a reasonable approximation, i.e., deep layers should only affect low frequencies. However, modal solutions correspond to standing waves in the thickness direction and, since no material damping is included, a high velocity half-space at deeper depths will influence modal solutions at higher frequencies, too. This is exemplified here (Fig. 14) by adding one more layer to the reference model (Table I), resulting in a new half-space with the same properties as the top layer. The thickness of the third layer, which was previously defined as a half-space, is now set to 5 m. Dispersion curves of this system are plotted in Fig. 14. Over the frequency range from 0 to 400 Hz, where the original reference model only showed three possible modes [Figs. 3 and 5(a)], there are now almost 100 modes.

As stated in the background on surface wave testing of pavements (Sec. II), many difficulties with the conventional approach have been assumed to originate from the influence of higher modes of propagation. In the light of Figs. 3 and 14 this seems quite realistic and it may be questioned if this kind of layered system can be represented with only one continuous dispersion curve. For example, it has been widely reported that results from surface wave testing of pavements are not very sensitivity to the properties of the embedded second layer (Aouad, 1993; Roesset *et al.*, 1990). This problem can be explained from the branches of dispersion curves that are difficult to resolve with the conventional method. If only one continuous dispersion curve without branches is used, this ''apparent'' dispersion curve will only be sensitive to the top and bottom layers. Figure 12 can explain more details on this topic. If the fourth mode is not resolved as a discrete branch, a change in shear wave velocity of the second layer will not be noticeable since the profiles of dispersion curves of this individual mode move in the same direction as the A0 mode of the top layer as a free plate. This direction is indicated with an arrow in Fig. 12(a). However, in Fig. 12(b) the arrow points in the direction normal to the A0 dispersion curve of the top layer as a free plate. So even

if a change in shear wave velocity of the second layer shows a higher relative sensitivity on the fourth mode, this change will be masked by the main trend of the A0 dispersion curve if this branch is not individually resolved in the measurements. The same holds for all the other higher modes following the trend of the A0 mode of the equivalent free top layer.

On the other hand, if the branches at lower frequencies are resolved, there is a potential for improved sensitivity to the embedded second layer. The instabilities which have been experienced with the partial derivatives approach for the inversion, when the apparent dispersion curve jumps between modes (Foti *et al.*, 2003), may actually be the promise for an improved surface wave method. Since a change in cutoff frequencies of the branches of the dispersion curves may hold more information on the structural properties than just the change in phase velocities, this information should preferably be included for the evaluation of the pavement layer properties. This could be done by using the complete phase velocity spectrum for the inversion of layer properties. Alternatively, the presented correlation between branches of dispersion curves and Lamb waves in the equivalent free layers may form the framework of a new simplified technique for the evaluation of pavement layer properties. Since the branches are sensitive to both the shear wave velocity of the top and second layers (Fig. 12) this implies that a lower frequency range than normally utilized in surface wave testing of pavements may be used. A lower frequency range has two major practical advantages: the measurement equipment could be simplified and the evaluated properties of materials (viscoelastic properties of the asphalt layer) should be closer to the frequency range of interest in pavement design, i.e., traffic loading.

VI. CONCLUSIONS

Wave propagation in a three-layered half-space with large velocity contrasts and decreasing velocity with depth has been investigated. Results show that it is only at the very high and very low frequency limits where wave propagation can be related to Rayleigh type of waves. Instead leaky guided waves dominate most of the frequency range that is suitable for nondestructive characterization of material properties.

A point source on the surface will generate a dominating quasi-antisymmetric Lamb wave in the high velocity top layer. This mode drives the complete system, and continuity across the boundaries generates higher modes in the embedded second layer. The interaction of leaky Lamb waves in the first two layers creates branches (portions) of dispersion curves measurable at the surface. In the lower frequency range these branches of dispersion curves can be individually resolved in practice, by using multichannel processing techniques. At higher frequencies there are theoretically substantially more modes than previously anticipated. All high-frequency branches merge together to form the dispersion curves corresponding to a stiff plate on a lower velocity half-space.

Several reported difficulties associated with surface wave testing of pavements can be explained from the presented theory. Abrupt jumps in phase velocity between branches of dispersion curves can create abrupt jumps in the measured wrapped phase spectrum also. These jumps can explain the reported difficulties in the phase unwrapping of the measured data and the cause of fluctuations in the measured dispersion curve.

It is concluded that future inversion techniques should be based on the complete phase velocity spectrum. With this approach not only phase velocities but also the overall pattern of branches of dispersion curves can be utilized. This holds the potential for a refined nondestructive testing technique for pavements.

ACKNOWLEDGMENTS

We would like to give our sincere thanks to Peab Sverige AB, VINNOVA, and the Swedish National Road Administration for financing this project. We also thank Dr. Choon B. Park, Kansas Geological Survey, and Dr. Peter Ulriksen, Lund University, for many helpful discussions.

Abraham, O., Pedersen, H., Hevin, G., Kergadallan, X., and Cote, Ph. (**2000**). ''The use of surface waves for non-destructive testing of concrete structures,'' Insight **42**(7), 444–446.

Akhlaghi, B. T., and Cogill, W. H. (**1994**). ''Application of the free plate analogy to a single-layered pavement system,'' Insight **36**, 514–518.

Al-Hunaidi, M. O. (**1992**). ''Difficulties with phase spectrum unwrapping in spectral analysis of surface waves nondestructive testing of pavements,'' Can. Geotech. J. **29**, 506–511.

Aouad, M. F. (**1993**). ''Evaluation of flexible pavements and subgrades using the spectral-analysis-of-surface-waves (SASW) method,'' Ph.D. thesis, Univ. of Texas at Austin, Texas.

Beaty, K. S., and Schmitt, D. R. (**2003**). ''Repeatability of multimode Rayleigh-wave dispersion studies,'' Geophysics **68**(3), 782–790.

Cheng, A., Murray, T. W., and Achenbach, J. D. (**2001**). ''Simulation of laser-generated ultrasonic waves in layered plates,'' J. Acoust. Soc. Am. **110**(2), 848–855.

Disperse (**2001**). ''A system for generating dispersion curves,'' User's manual version 2.0.11. Software version 2.0.15e. www.ndt.imperial.ac.uk.

Foinquinos, R., Roesset, J. M., and Stokoe, K. H. (**1995**). ''Response of pavement systems to dynamic loads imposed by nondestructive tests,'' Transp. Res. Rec. **1504**, 57–67.

Forbriger, T. (**2003**). ''Inversion of shallow-seismic wavefields part 1: Wavefield transformation,'' Geophys. J. Int. **153**, 719–734.

Foti, S. (**2000**). ''Multistation methods for geotechnical characterization using surface waves,'' Ph.D. thesis, Politecnico di Torino, Italy.

Foti, S., Sambuelli, L., Socco, V. L., and Strobbia, C. (**2003**). ''Experiments of joint acquisition of seismic refraction and surface wave data,'' Near Surface Geophys. **1**, 119–129.

Gabriels, P., Snider, R., and Nolet, G. (**1987**). ''In situ measurements of shear-wave velocity in sediments with higher-mode Rayleigh waves,'' Geophys. Prospect. **35**, 187–196.

Ganji, V., Gucunski, N., and Nazarian, S. (**1998**). ''Automated inversion procedure for spectral analysis of surface waves,'' J. Geotech. Geoenviron. Eng. **124**, 757–770.

Graff, K. E. (**1975**). *Wave Motion in Elastic Solids* (Oxford U.P., London).

Gucunski, N., and Woods, R. D. (**1992**). ''Numerical simulation of the SASW test,'' Soil Dyn. Earthquake Eng. **11**, 213–227.

Gucunski, N., Abdallah, I. N., and Nazarian, S. (**2000**). ''ANN backcalculation of pavement profiles from the SASW test,'' in Geotechnical Special Publication (ASCE) No. 98, *Pavement subgrade unbound materials, and nondestructive testing*, pp. 31–50.

Haskell, N. A. (**1953**). ''The dispersion of surface waves on multilayered media,'' Bull. Seismol. Soc. Am. **43**, 17–34.

Heisey, J. S., Stokoe, K. H., and Meyer, A. H. (**1982**). ''Moduli of pavement systems from spectral analysis of surface waves,'' Transp. Res. Rec. **852**, 22–31.

Hunaidi, O. (**1998**). ''Evolution-based genetic algorithms for analysis of non-destructive surface wave tests on pavements,'' NDT&E Int. **31**, 273–280.

Inazaki, T., and Xinglin, L. (**2003**). ''High-frequency seismic measurements using a piezoelectric type accelerometer array,'' in Proceedings of the Symposium on the Application of Geophysics to Engineering and Environmental Problems (SAGEEP 2003), San Antonio, TX, 6–10 April, CD-Rom, seis04.

Jones, R. (**1955**). ''A vibration method for measuring the thickness of concrete road slabs in situ,'' Mag. Concrete Res. **7**(20), 97–102.

Jones, R. (**1962**). ''Surface wave technique for measuring the elastic properties and thickness of roads: Theoretical development,'' Br. J. Appl. Phys. **13**, 21–29.

Jones, R., and Thrower, E. N. (**1965**). ''An analysis of waves in a two-layer composite plate and its application to surface wave propagation experiments on roads,'' J. Sound Vib. **2**(3), 328–335.

Knopoff, L. (**1964**). ''A matrix method for elastic wave problems,'' Bull. Seismol. Soc. Am. **54**, 431–438.

Lamb, H. (**1917**). ''On waves in an elastic plate,'' Proc. R. Soc. **93**, 114–128.

Laperre, J., and Thys, W. (**1993**). ''Experimental and theoretical study of Lamb wave dispersion in aluminium/polymer bilayers,'' J. Acoust. Soc. Am. **94**, 268–278.

Lee, Y. C., and Cheng, S. W. (**2001**). ''Measuring Lamb wave dispersion curves of a bilayered plate and its application on material characterization of coating,'' IEEE Trans. Ultrason. Ferroelectr. Freq. Control **48**(3), 830–837.

Lefeuvre, O., Zinin, P., and Briggs, G. A. D. (**1998**). ''Leaky surface waves propagating on a fast on slow system and the implications for material characterization,'' Ultrasonics **36**, 229–232.

Lefeuvre, O., Kolosov, O. V., Every, A. G., Briggs, G. A. D., and Tsukahara, Y. (**2000**). ''Elastic measurements of layered nanocomposite materials by Brillouin spectroscopy,'' Ultrasonics **38**, 459–465.

Long, R., Cawley, P., and Lowe, M. (**2003**). ''Acoustic wave propagation in buried iron water pipes,'' Proc. R. Soc. London, Ser. A **459**, 2749–2770.

Lowe, M. J. S. (**1995**). ''Matrix techniques for modeling ultrasonic waves in multilayered media,'' IEEE Trans. Ultrason. Ferroelectr. Freq. Control **42**, 525–542.

Lowe, M. J. S., and Cawley, P. (**1995a**). ''Comparison of the modal properties of a stiff layer embedded in a solid medium with the minima of the plane-wave reflection coefficient,'' J. Acoust. Soc. Am. **97**, 1625–1637.

Lowe, M. J. S., and Cawley, P. (**1995b**). ''The influence of the modal properties of a stiff layer embedded in a solid medium on the field generated in the layer by a finite-sized transducer,'' J. Acoust. Soc. Am. **97**, 1638–1649.

Martincek, G. (**1994**). *Dynamics of Pavement Structures* (E&FN Spon and Ister Science, London).

Nayfeh, A. H., and Chimenti, D. E. (**1984**). ''Reflection of finite acoustic beams from loaded and stiffened half-spaces,'' J. Acoust. Soc. Am. **75**, 1360–1368.

Nazarian, S. (**1984**). ''In situ determination of soil deposits and pavement systems by spectral analysis of surface waves method,'' Ph.D. thesis, Univ. of Texas at Austin, Texas.

O'Neill, A. (**2003**). ''Full-waveform reflectivety for modelling, inversion and appraisal of seismic surface wave dispersion in shallow site investigation,'' Ph.D. thesis, Univ. of Western Australia, Australia.

Park, C. B., Miller, R. D., and Xia, J. (**1998**). ''Imaging dispersion curves of surface waves on multi-channel records,'' Technical Program with Biographies, SEG, 68th Annual Meeting, New Orleans, Louisiana, pp. 1377–1380.

Park, C. B., Miller, R. D., and Xia, J. (**1999**). ''Multichannel analysis of surface waves,'' Geophysics **64**, 800–808.

Parra, J. O., and Xu, P. (**1994**). ''Dispersion and attenuation of acoustic guided waves in layered fluid-filled porous media,'' J. Acoust. Soc. Am. **95**, 91–98.

Pavlakovic, B., Lowe, M., Alleyne, D., and Cawley, P. (**1997**). ''Disperse a general purpose program for creating dispersion curves,'' Rev. Prog. Quant. Nondestr. Eval. **16**, 185–192.

Picket, G. (**1945**). ''Dynamic testing of pavements,'' J. Am. Concr. Inst. **16**(5), 473–489.

Press, F., and Dobrin, M. B. (**1956**). ''Seismic wave studies over a high-speed surface layer,'' Geophysics **XXI**(2), 285–298.

Randall, M. J. (**1967**). ''Fast programs for layered half-space problems,'' Bull. Seismol. Soc. Am. **57**, 1299–1315.

Roesset, J. M., Chang, D. W., Stokoe, K. H., and Auoad, M. (**1990**). ''Modulus and thickness of the pavement surface layer from SASW tests,'' Transp. Res. Rec. **1260**, 53–63.

Ryden, N., and Park, C. B. (**2004**). ''Surface waves in inversely dispersive media,'' Near Surface Geophysics, **2**(4), 187–197.

Ryden, N., Park, C. B., Ulriksen, P., and Miller R. D. (**2002**). ''Branching of dispersion curve in surface wave testing of pavements,'' in Proceedings of the Symposium on the Application of Geophysics to Engineering and Environmental Problems (SAGEEP 2002), Las Vegas, NV, 10–14 February, 12SE17.

Ryden, N., Park, C. B., Ulriksen, P., and Miller, R. D. (**2004**). ''A multimodal approach to seismic pavement testing,'' J. Geotech. Geoenviron. Eng. **130**, 636–645.

Ryden, N., Ulriksen, P., Park, C. B., Miller, R. D., Xia, J., and Ivanov, J. (**2001**). ''High frequency MASW for non-destructive testing of pavements-accelerometer approach,'' in Proceedings of the Symposium on the Application of Geophysics to Engineering and Environmental Problems (SAGEEP 2001), Denver, CO, RBA-5.

Sheu, J. C., Stokoe, K. H., and Roesset, J. M. (**1988**). ''Effect of reflected waves in SASW testing of pavements,'' Transp. Res. Rec. **1196**, 51–56.

Shull, P. J., Chimenti, D. E., and Datta, S. K. (**1994**). ''Elastic guided waves and the Floquet concept in periodically layered plates,'' J. Acoust. Soc. Am. **95**, 99–108.

Shuvalov, A. L., and Every, A. G. (**2002**). ''Characteristic features of the velocity dispersion of surface acoustic waves in anistropic coated solids,'' Ultrasonics **40**, 939–942.

Simonetti, F. (**2004**). ''Lamb wave propagation in elastic plates coated with viscoelastic materials,'' submitted to J. Acoust. Soc. Am.

Stokoe, K. H., Wright, G. W., James, A. B., and Jose, M. R. (**1994**). ''Characterization of geotechnical sites by SASW method,'' in *Geophysical Characterization of Sites*, ISSMFE Technical Committee #10, edited by R. D. Woods (Oxford, New Delhi).

Stoneley, R. (**1924**). ''Elastic waves at the surface of separation of two solids,'' Proc. R. Soc. **106**, 416–428.

Thomson, W. T. (**1950**). ''Transmission of elastic waves through a stratified solid medium,'' J. Appl. Phys. **21**, 89–93.

Tokimatsu, K., Tamura, S., and Kojima, H. (**1992**). ''Effects of multiple modes on Rayleigh wave dispersion characteristics,'' J. Geotech. Eng. **118**, 1529–1543.

Vidale, R. F. (**1964**). ''The dispersion of stress waves in layered media overlaying a half space of lesser acoustic rigidity,'' Ph.D. thesis, Univ. of Wisconsin.

Wilcox, P. (**2004**). ''Modeling the excitation of Lamb and SH waves by point and line sources,'' Review of Progress in Quantitative NDE, edited by D. O. Thompson and D. E. Chimenti (American Institute of Physics, New York), Vol. 23, 206–213

Wu, H., Wang, S., Abdallah, I., and Nazarian, S. (**2002**). ''A rapid approach to interpretation of SASW results,'' in Proceedings of the BCRA 2002, Lissabon, Portugal, pp. 761–770.

Xia, J., Miller, R. D., and Park, C. B. (**1999**). ''Estimation of near-surface shear-wave velocity by inversion of Rayleigh wave,'' Geophysics **64**, 691–700.

Yapura, C. L., and Kinra, V. K. (**1995**). ''Guided waves in a fluid-solid bilayer,'' Wave Motion **21**, 35–46.

Zhang, B., and Lu, L. (**2003**). ''Rayleigh wave detection of low-velocity layers in a stratified half-space,'' Acoust. Phys. **49**(5), 516–528.

Zinin, P., Lefeuvre, O., Briggs, G. A. D., Zeller, B. D., Cawley, P., Kinloch, A. J., and Thompson, G. E. (**1997**). ''Anomalous behaviour of leaky surface waves for stiffening layer near cutoff,'' J. Appl. Phys. **82**(3), 1031–1035.

Line source representation for laser-generated ultrasound in an elastic transversely isotropic half-space

David H. Hurley
Physics Group, Idaho National Engineering and Environmental Laboratory, Idaho Falls, Idaho 83415-2209

James B. Spicer
Department of Materials Science and Engineering, The Johns Hopkins University, Baltimore, Maryland 21218

(Received 14 February 2004; revised 16 July 2004; accepted 18 July 2004)

Theoretical and experimental results are presented for a laser line source in an elastic, transversely isotropic half-space. The thermoelastic source (laser source) is represented as an appropriately weighted shear stress dipole applied at the sample surface. The plane of isotropy coincides with the half-space boundary. Analytical expressions representing the out-of-plane displacements for the surface wave and for the epicentral cases are given for all crystal classes that exhibit elastic transverse isotropy. In addition, quasianalytical results are given for observation points off the epicentral axis. Theoretical wave forms for all of the source/observation geometries considered are compared with experimental wave forms generated in single crystal zinc samples. The close comparison between experiment and theory confirms, for this particular line source orientation and crystal symmetry, that a laser line source is accurately modeled using an equivalent boundary stress.
 [DOI: 10.1121/1.1791721]

PACS numbers: 43.35-Sx, 43.20.Bi, 43.35.Zc [YHB] Pages: 2914–2922

I. INTRODUCTION

Since the early 1980s, laser generated ultrasound has been used to determine material properties and to characterize material defects[1–3] To a large extent, the success of laser ultrasonics has been the researcher's ability to correctly predict the temporal evolution of the displacement wave form resulting from pulsed laser irradiation. Theories that assume isotropic elastic properties work well for crystalline materials that have randomly oriented grains which are small compared to the wavelength of the interrogating ultrasonic wave.[4] However, for single crystals, the anisotropic nature of the material must be considered.[5]

Stoneley,[6] studied the propagation of Rayleigh surface waves in certain single crystal systems. In particular, Stoneley analyzed three specific cases, surface waves propagating in the (0 0 1) plane of cubic crystals along the [1 0 0] and [1 1 0] directions, and in the basal plane of hexagonal crystals. Royer and Dieulesaint[7] extended the work of Stoneley to include the analysis of Rayleigh wave propagation in orthorhombic and tetragonal systems. The analysis by Stoneley[6] and Royer and Dieulesaint[7] considered the disturbance to have a planer phase front.

To gain a better understanding of the underlying physics, the finite extent of the source must also be considered. Kraut[8] extended the work of Lamb[9] by considering a transversely isotropic elastic half-space subjected to a source of finite extent. Kraut used the method of Cagniard-de Hoop[10,11] to study the resulting displacements in single crystal Beryl. Other researchers[12–15] have extended the work by Kraut.[8] For instance, Mourad *et al.*[14] used the Cagniard-de Hoop method to numerically obtain the solutions to Lamb's problem in an anisotropic half-space. In their paper, Mourad *et al.* assumed that the laser source could be modeled as a shear stress dipole[16–18] applied at the bounding surface. Of particular interest to this paper is the work by Payton[19] who has treated a general class of problems for crystals that exhibit transverse isotropy. Payton furnished a detailed analysis of the solution and the solution technique for a variety of transient problems in bounded and unbounded solids. In addition, Payton gave an explicit set of conditions, related to the elastic parameters of the material, that predict the existence of inflection points on the slowness curve. It is well known[5,8,19,20] that these inflection points lead to behavior in anisotropic materials that is markedly different from that in isotropic materials. Thus, while transverse isotropy is perhaps the simplest case to treat, it nonetheless exemplifies the peculiar behavior found in elastically anisotropic materials.

In this paper, the homogeneous equations of motion for a transversely isotropic material are solved subjected to a set of stress boundary conditions which has been shown to be equivalent to a thermoelastic line source in the limit of strong optical absorption.[18] The plane of isotropy coincides with the boundary plane and the epicentral direction coincides with the crystal symmetry axis and the x_3 axis, Fig. 1. For this problem geometry/crystal symmetry, the source specification and the solution are independent of the line source orientation.[18] However, for convenience the line source is taken to coincide with the x_1 axis. Expressions representing the out-of-plane displacements for wave propagation along (1) the free surface, (2) epicentral axis, and (3) off the epicentral axis are given. In all cases the solutions are sought using the method of Cagniard-de Hoop. The first two cases lend themselves to analytic solutions which in turn affords a detailed analysis of the solution procedure. The last case is solved using a quasianalytical approach in which the integration contour must be defined numerically. It is shown that for the epicentral and off epicentral cases, the form of the solution depends strongly on the nature of the material anisotropy. For the sake of comparison with experimental

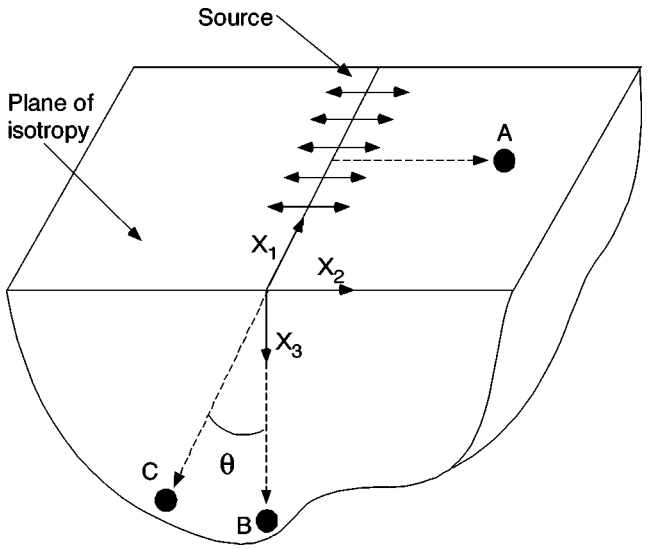

FIG. 1. Problem geometry with source location and observation points (A,B,C). The line source is parallel to the x_1 axis and the sample normal is parallel with the x_3 axis and the crystal symmetry axis.

results, particular attention will be paid to zinc. Theoretical results are compared with experimental wave forms in a sample of single crystal zinc. Owing to the transversely isotropic nature of the problem, the development of a line source solution closely parallels the development of the more general point source solution of Hurley and Spicer.[21,22]

II. THEORY

Before embarking on a solution procedure, it is convenient to classify transversely isotropic crystals according to the behavior of the displacements of these crystals along the symmetry axis. Borrowing notation from Payton,[19] these categories are

$$\begin{aligned}&\text{(i)}\quad (\alpha+\beta)<\gamma<(1+\alpha\beta),\\ &\text{(ii)}\quad (\beta+1)<\gamma<(\alpha+\beta)\quad\text{and}\quad (\gamma^2-4\alpha\beta)<0,\\ &\text{(iii)}\quad \gamma<(\beta+1)\quad\text{and}\quad (\gamma^2-4\alpha\beta)<0\ \text{ also }\ \beta>\alpha,\end{aligned} \tag{1}$$

where the ratios of the elastic stiffness components, α, β, γ and κ are defined as

$$\alpha=\frac{c_{33}}{c_{44}},\quad \beta=\frac{c_{11}}{c_{44}},\quad \kappa=(1+\alpha\beta-\gamma)^{1/2},$$
$$\gamma=1+\alpha\beta-\left(\frac{c_{13}}{c_{44}}+1\right)^2. \tag{2}$$

For crystals belonging to the first category in Eq. (1), the roots of the slowness equation are purely imaginary. In addition, there are no cusps in the wave-front curves that intersect the symmetry axis for class (i) crystals. The crystals belonging to categories (ii) and (iii) have complex roots. For class (iii) crystals, the triangular portion of the wave-front (lacuna) is centered on the symmetry axis. It will be shown that for class (i) crystals, the solutions along the free surface and along the epicentral direction behave in a similar manner to isotropic materials. However, the solution for class (ii) and (iii) crystals along the symmetry axis and off the symmetry axis differs profoundly from their isotropic counterpart.

For transversely isotropic materials with the plane of isotropy coinciding with the bounding plane, the equivalent stress boundary conditions are independent of line source orientation[18] and are given as

$$\begin{aligned}&(\sigma_{23})|_{x_3=0}=\tilde{F}\delta'(x_2)H(\tau),\quad (\sigma_{33})|_{x_3=0}=0,\\ &\tilde{F}=(F_3(1-\kappa)+F_2\alpha),\quad F_2=\frac{B_{22}T_0}{\alpha},\quad F_3=\frac{B_{33}T_0}{\alpha},\end{aligned} \tag{3}$$

where $T_0=q_0/\rho C$ (Refs. 17, 23, and 24) is the instantaneous temperature rise and B_{ij} are the thermal pressure coefficients. The time coordinate, $\tau=\sqrt{(C_{44}/\rho)}t$, which has dimensions of length, was introduced so that the current analysis is consistent with that of Payton.[19] The transformed homogenous equations of motion appropriate for a line source applied along a plane of transverse isotropy are given by

$$\begin{aligned}&-\beta\eta^2\overline{u_2}+\overline{u}_{2,33}-s^2\overline{u_2}+i\kappa\eta\overline{u}_{3,3}=0,\\ &i\eta\kappa\overline{u}_{2,3}-\eta^2\overline{u_3}+\alpha\overline{u}_{3,33}-s^2u_3=0.\end{aligned} \tag{4}$$

where s and η are the transform parameters for t and x_2, respectively.[25] Solutions to the above system of equations are of the form

$$\begin{aligned}&\overline{u_2}(\eta,x_3,s)=A_1e^{-k_1x_3}+A_2e^{-k_3x_3},\\ &\overline{u_3}(\eta,x_3,s)=A_3e^{-k_1x_3}+A_4e^{-k_3x_3},\end{aligned} \tag{5}$$

where $k_{1/3}$ are the physical roots to the slowness curve. Next, the following substitution will be made so as to facilitate the Cagniard inversion technique:

$$k=s\zeta,\quad \eta=s\omega. \tag{6}$$

The denominator of the secular equation can be rewritten using the above substitutions as

$$\alpha\zeta^4-\zeta^2((\alpha+1)+\gamma\omega^2)+(\beta\omega^4+(\beta+1)\omega^2+1)=0. \tag{7}$$

The four roots to Eq. (7) may be written as

$$\begin{aligned}&\zeta_1(\omega)=\frac{[(\alpha+1)+\gamma\omega^2+\sqrt{\phi(\omega)}]^{1/2}}{\sqrt{2\alpha}},\\ &\zeta_2(\omega)=-\zeta_1(\omega),\\ &\zeta_3(\omega)=\frac{[(\alpha+1)+\gamma\omega^2-\sqrt{\phi(\omega)}]^{1/2}}{\sqrt{2\alpha}},\\ &\zeta_4(\omega)=-\zeta_3(\omega),\\ &\phi(\omega)=[\gamma\omega^2+(\alpha+1)]^2-4\alpha[\beta\omega^4+(\beta+1)\omega^2+1].\end{aligned} \tag{8}$$

The coefficients A_3 and A_4 are related to A_1 and A_2 by the fact that the above displacements must solve the equations of motion. By substituting both solutions into the transformed equations of motion, it can be shown that

$$A_1=A_3\left[\frac{\alpha\zeta_1^2-\omega^2-1}{i\kappa\omega\zeta_1}\right], \tag{9}$$

$$A_2 = A_4\left[\frac{\alpha\zeta_3^2 - \omega^2 - 1}{i\kappa\omega\zeta_3}\right].$$

The coefficients $A_{3/4}$ are found by requiring the displacements in Eq. (5) satisfy the boundary conditions in Eq. (3),

$$A_3 = \frac{\tilde{F}\zeta_1\omega^2}{sC_{44}(\zeta_1 - \zeta_3)D}[\alpha\zeta_3^2 + (\kappa-1)\omega^2 + (\kappa-1)],$$

$$A_4 = \frac{-\tilde{F}\zeta_3\omega^2}{sC_{44}(\zeta_1 - \zeta_3)D}[\alpha\zeta_1^2 + (\kappa-1)\omega^2 + (\kappa-1)], \quad (10)$$

$$D = [2(1-\kappa)(\omega^4 + \omega^2) - (\gamma\omega^2 + \alpha)(\omega^2 + 1) - \alpha\zeta_1\zeta_3],$$

where D is the Rayleigh denominator.

A. Solutions along the bounding surface

For displacements along the bounding plane ($x_3 = 0$), the Cagniard integration path is along the imaginary ω axis. Operating on the u_3 displacement with the inverse Fourier operator as follows, and noting that u_3 is even in ω, gives

$$\overline{u_3}(x_2,0,s) = \mathrm{Re}\frac{1}{\pi}\int_0^\infty \tilde{u}_3(s,\omega)d\omega,$$

$$\tilde{u}_3(s,\omega) = \frac{-\tilde{F}\omega^2}{C_{44}D}[\alpha\zeta_1\zeta_3 + (1-\kappa)(\omega^2+1)]e^{is\omega|x_2|}, \quad (11)$$

$$\text{Cagniard Path} \rightarrow i\omega|x_2| = \tau = \text{real}.$$

Before the Cagniard inversion can be performed, the branch points and singularities associated with $\overline{u_3}$ must be identified. Branch points for $\xi(\omega)$ may arise in two distinct ways:

$$\text{(i)} \quad \phi(\omega) = 0,$$
$$\text{(ii)} \quad \gamma\omega^2 + (\alpha+1) \pm \sqrt{\phi(\omega)} = 0. \quad (12)$$

Presently, only the inversion of u_3 is being considered. Since u_3 is an even function of $\sqrt{\phi(\omega)}$, branch points arising from (i) in Eq. (12) need not be considered. The singularities in the function $D(\omega)$ will now be discussed. Since the branch points for this function have been discussed above, only pole singularities in $D(\omega)$ need to be considered. After squaring and simplifying, the equation for the Rayleigh denominator yields

$$a^6\omega^2 + a(a+2\alpha)\omega^4 + \alpha(2a+\alpha-\beta)\omega^2 + \alpha(\alpha-1) = 0,$$
$$a = 2\kappa - 2 + \gamma. \quad (13)$$

The roots of interest will lie on the positive imaginary axis. The remaining roots will lie on the nonphysical sheets of the Riemann surface. The (Rayleigh) pole of Eq. (13) will be denoted by $D(i\omega_r) = 0$. Now the integration contour and the subsequent inversion of the integral in Eq. (11) may be performed. Figure 2 shows the complex ω plane along with the integration contour. The real axis coincides with the Fourier inversion path and the imaginary axis coincides with the Cagniard inversion path. The inverted solution may be written formally as

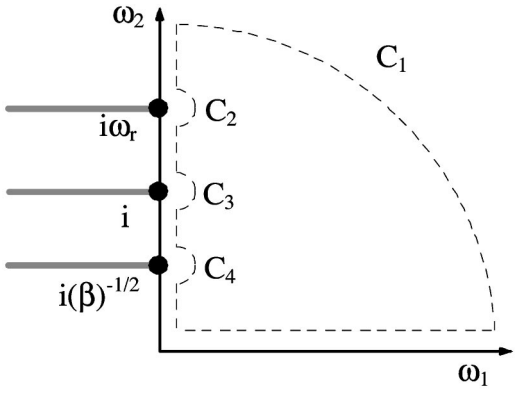

FIG. 2. Integration contour for the vertical displacement, u_3, at the bounding surface.

$$u_3(x_2,0,\tau) = L^{-1}\left[\frac{1}{\pi}\mathrm{Re}\left\{\int_{C_1} + P\int_\infty^1 \tilde{u}_3(s,i\omega_2)i\,d\omega + \{i\pi\,\text{residue@}\,\omega = i\omega_r\} + \int_{C_3} + \int_1^{1/\sqrt{\beta}} \tilde{u}_3(s,i\omega_2)i\,d\omega + \int_{C_4} + \int_{1/\sqrt{\beta}}^0 \tilde{u}_3(s,i\omega_2)i\,d\omega\right\}\right], \quad (14)$$

where L^{-1} is the inverse Laplace operator and the P in front of the second integral denotes the Cauchy principle value. A typical displacement wave form generated using Eq. (14) is shown in the inset of Fig. 3. The initial disturbance, referred to as the surface-skimming bulk wave, arrives at the longitudinal velocity and vanishes at the shear wave velocity. The later arriving Rayleigh wave travels as a Dirac delta function. The characteristics of the wave form for class (i), class (ii),

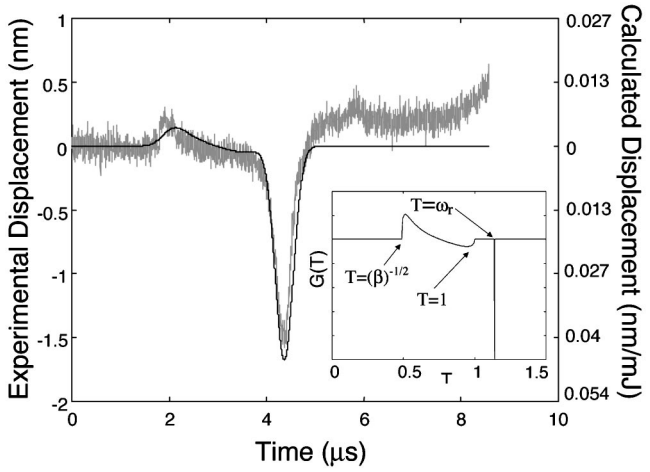

FIG. 3. Comparison between experiment and theory for the surface wave case. The sample is single crystal zinc with the c axis perpendicular to the free surface. The nonzero experimental displacement corresponding to the interval between the end of the surface skimming bulk wave and the arrival of the Rayleigh pulse is a result of pulse broadening. Inset: Theoretical displacement, u_3, for surface waves generated with a line source in zinc as a function of $T = \tau/x_2$. A delta function is represented by vertical line at $T = 1.13$.

and class (iii) materials are similar. The similarity is due to the fact that the contribution from the branch point corresponding to (i) in Eq. (12) does not affect the solution for the vertical displacement. However, this is not the case for the in-plane displacement components.

B. Solutions along the symmetry axis

Another class of solutions that can be inverted easily using the Cagniard technique corresponds to solutions along the epicentral axis, or for this particular experimental geometry, along the symmetry axis [see observation point (B) in Fig. 1]. The location of the Cagniard path in the complex plane depends on the category of crystal being investigated. For materials belonging to category (i), the Cagniard path is along the real ω axis. For class (ii) and (iii) materials, the Cagniard path is off the real ω axis. The formal solution for the out-of-plane displacement along the epicentral axis is given as

$$\begin{aligned}&\overline{u_3}(0,x_3,s)=\frac{1}{2\pi}\int_{-\infty}^{\infty}\tilde{u}_3(\eta,x_3,s)s\,d\omega,\\&\tilde{u}_3(\eta,x_3,s)=A_3e^{-\zeta_1x_3s}+A_4e^{-\zeta_3x_3s},\end{aligned}\tag{15}$$

where A_3 and A_4 are defined in Eq. (10). Also note that since the roots to the slowness equations, ζ_1 and ζ_3, are even functions of ω, $\tilde{u}_3(\eta,x_3,s)$ is also even, allowing the integration limit to be changed to the positive ω axis. For convenience the following substitutions are made:

$$\begin{aligned}&\varpi=\omega^2,\\&\overline{u_3}(0,x_3,s)=\frac{1}{\pi}\mathrm{Re}\{I_1+I_3\},\\&I_1=\int_0^{\infty}\overline{A}_3e^{-\zeta_1x_3s}\,d\varpi,\quad I_3=\int_0^{\infty}\overline{A}_4e^{-\zeta_3x_3s}\,d\varpi,\\&\overline{A}_{3/4}=\frac{A_{3/4}s}{2\sqrt{\varpi}}.\end{aligned}\tag{16}$$

This substitution consolidates the branch cuts along the real and imaginary axes so they both lie on the real axis. The Cagniard path for the integrals in Eq. (16) is defined by

$$\begin{aligned}&\zeta_{1/3}(\varpi)x_3=\tau,\\&\tau\ \text{is real and positive.}\end{aligned}\tag{17}$$

1. Solution for class (i) materials

For class (i) materials, the above condition on τ is met for real ϖ, giving the positive real ϖ axis as the Cagniard contour. Solving Eq. (8) for ϖ in terms of τ gives

$$\begin{aligned}&\varpi_{1/3}=\frac{-B\pm\sqrt{B^2-4AC}}{2A},\\&A=\beta,\\&B=\beta+1-\gamma(T)^2,\\&C=1-(\alpha+1)(T)^2+\alpha(T)^4,\end{aligned}\tag{18}$$

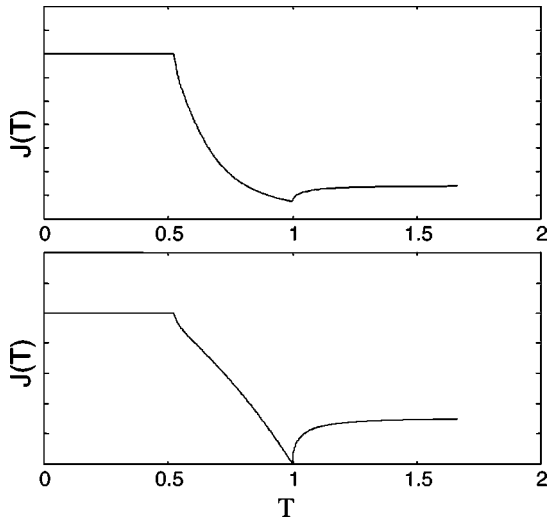

FIG. 4. Top: Theoretical displacement, u_3, for the epicentral wave generated with a line source in Beryl as a function of T. Bottom: Theoretical displacement, u_3, for the epicentral wave generated with a line source in an isotropic material (polycrystalline aluminum).

$$T=\frac{\tau}{x_3}.$$

Note that the definition for T has been redefined for the epicentral case (see Fig. 3 caption). Changing variables from ϖ to τ and operating on the expression for the vertical displacement, given in Eq. (16), with the inverse Laplace operator gives

$$\begin{aligned}&u_3(0,x_3,T)=\tilde{F}J(T),\\&J(T)=\frac{1}{\pi\tilde{F}}\mathrm{Re}\left\{\overline{A}_3\frac{\partial\varpi_1}{\partial\tau}H(T-1)\right.\\&\qquad\left.+\overline{A}_4\frac{\partial\varpi_3}{\partial\tau}H(T-1/\sqrt{\alpha})\right\}.\end{aligned}\tag{19}$$

A typical wave form generated from Eq. (19) using the material constants of Beryl is shown in Fig. 4. The displacement wave form for Beryl has characteristics similar to the displacement wave form for an isotropic material, also shown in Fig. 4. Both wave forms show the presence of two distinct wave arrivals.

2. Solution for class (ii) and (iii) materials

For class (ii) and (iii) materials, the Cagniard path no longer lies on the real ϖ axis. Before embarking on the solution for these materials, first the location of the branch points must be investigated. As was the case for solutions along $x_3=0$, branch points associated with $\zeta(\omega)$ may occur in two ways. In contrast to the surface wave case, the expression for $\overline{u_3}$ for the epicentral case is an odd function of $\sqrt{\phi(\varpi)}$, and as a consequence, the branch points arising from (i) need to be considered in addition to the branch points arising from (ii) [see Eq. (12)]. The expression for $\sqrt{\phi(\varpi)}$ may be rewritten as

$$\sqrt{\phi(\varpi)}=\sqrt{(\gamma^2-4\alpha\beta)(\varpi-\varpi_+)(\varpi-\varpi_-)},$$
$$\varpi_\pm=\frac{-[\gamma(\alpha+1)-2\alpha(\beta+1)]\mp\sqrt{4[\alpha(\alpha+\beta-\gamma)(1+\alpha\beta-\gamma)]}}{(\gamma^2-4\alpha\beta)}. \tag{20}$$

Taking zinc as an example, ζ_1 will have branch points at $\varpi=\varpi_-$ and $\varpi=\varpi_+$ while ζ_3 will have branch points at $\varpi=\varpi_-$, $\varpi=\varpi_+$, $\varpi=-1$, and $\varpi=-1/\beta$. The Cagniard path for the first integral is again defined by Eq. (17), but ϖ is now a complex variable given by

$$\varpi=\varpi_1+i\varpi_2. \tag{21}$$

Substituting Eq. (21) into Eq. (17), and equating the real and imaginary part of the equation gives

$$\gamma T^2\varpi_1+(\alpha+1)T^2-\alpha T^4=\beta(\varpi_1^2-\varpi_2^2)+(\beta+1)\varpi_1+1,$$
$$\gamma T^2\varpi_2=2\beta\varpi_1\varpi_2+(\beta+1)\varpi_2. \tag{22}$$

The second equation of Eqs. (22) is satisfied if $\varpi_2=0$. Since the branch points for class (ii) and (iii) materials lie on the real axis, the first equation in Eqs. (22) imposes the additional constraints

$$\varpi_-\leqslant\varpi_1\leqslant\varpi_+ \quad \text{for} \quad \zeta_1(\varpi),$$
$$-1/\beta\leqslant\varpi_1\leqslant\varpi_+ \quad \text{for} \quad \zeta_3(\varpi). \tag{23}$$

If $\varpi_2\neq 0$, then ϖ_2 and ϖ_1 can be expressed in terms of the parameter $T=\tau/x_3$ as follows:

$$\varpi_1(T)=\frac{\gamma T^2-(\beta+1)}{2\beta}, \quad \varpi_2(T)=\frac{[\sqrt{4\alpha\beta-\gamma^2}(T^2-T_-^2)(T^2-T_+^2)]}{2\beta}, \tag{24}$$
$$T_\pm^2=\frac{-[\gamma(\beta+1)-2\beta(\alpha+1)]\pm\sqrt{4\beta(\alpha+\beta-\gamma)(1+\alpha\beta-\gamma)}}{(4\alpha\beta-\gamma^2)}.$$

Using zinc as an example, the Cagniard paths for ζ_1 and ζ_2 are shown in Fig. 5. The expression for the out-of-plane displacement in Eq. (16) may be rewritten as

$$\overline{u_3}(0,x_3,\tau)=L^{-1}\left[\frac{1}{\pi}\mathrm{Re}\left\{\int_{\tau_0}^{\tau_+}I_{11}+\int_{\Gamma_1}I_{11}+\int_{\Gamma_2}I_{11}+\int_{\tau_0}^{\tau_e}I_{33}+\oint_{\varpi_+}I_{33}+\int_{\tau_e}^{\tau_0}I_{33}\int_{\tau_0}^{\tau_+}I_{33}+\int_{\Gamma_3}I_{33}+\int_{\Gamma_4}I_{33}\right\}\right],$$
$$I_{11}=\overline{A}_3e^{-s\tau}\frac{\partial\varpi}{\partial\tau}d\tau, \quad I_{33}=\overline{A}_4e^{-s\tau}\frac{\partial\varpi}{\partial\tau}d\tau,$$
$$\tau_0=T_0x_3=\sqrt{\frac{(\alpha+1)-\sqrt{(\alpha+1)^2-4\alpha}}{2}},$$
$$\tau_e=T_ex_3=\sqrt{\frac{-B+\sqrt{B^2-4\alpha C}}{2\alpha}}, \tag{25}$$
$$B=-(\varpi_+\gamma+\alpha+1),$$
$$C=\varpi_+^2\beta+\varpi_+(\beta+1)+1.$$

A plot of the theoretical displacement along the epicentral axis for zinc is given in the inset of Fig. 6. The character of the epicentral wave form for zinc is considerably different than its isotropic counterpart, shown in Fig. 4. The arrivals of the various wave fronts in Fig. 6 is best understood by referencing the portion of the wave front curve that pierces the symmetry axis, Fig. 5 inset. The first wave arrival corresponds to the longitudinal branch of the wave front curve. The solution gives zero for the portion of the wave that corresponds to the interior of the cuspidal triangle. This zone behind the leading wave front is referred to as a lacuna. The solution has a singularity at $T=T_+$ corresponding to the conical point on the wave front.

C. Observation points off the symmetry axis

Consider the inverse of Eq. (5) for observation points that are neither along the symmetry axis nor on the bounding surface. The geometry of the problem is shown in Fig. 1 where now the point of observation is point C. The source is a surface line source. The observation angle, θ, is defined as the angle between the symmetry axis and a line joining the source and observation point. Formally, the inverse of Eq. (5) is written as

$$\overline{u_3}(x_2,x_3,\tau)=L^{-1}\left[\frac{1}{\pi}\mathrm{Re}\int_0^\infty(A_3e^{-\zeta_1x_3s}+A_4e^{-\zeta_3x_3s})e^{is\omega|x_2|}s\,d\omega\right]. \tag{26}$$

The Cagniard path for Eq. (26) is defined by

(a) $\zeta_1x_3-i\omega|x_2|=\tau$,

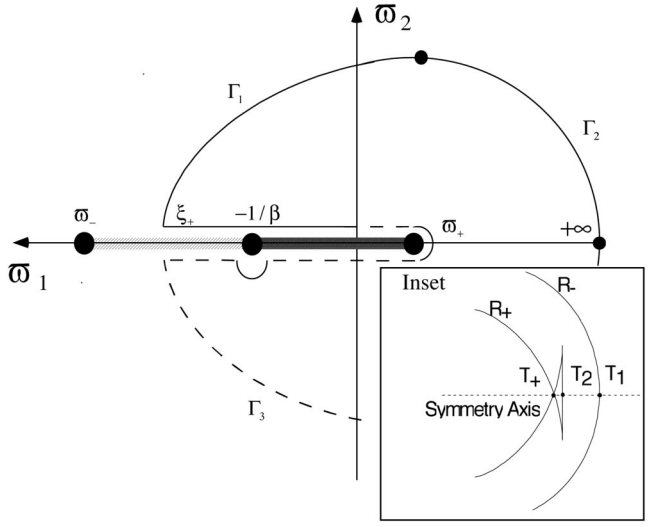

FIG. 5. Cargniard contour for zinc for observation points along the symmetry axis. Solid line represents contour corresponding to ζ_1 and the dashed line represents the contour corresponding to ζ_3. Inset: Enlargement of wave front near symmetry axis.

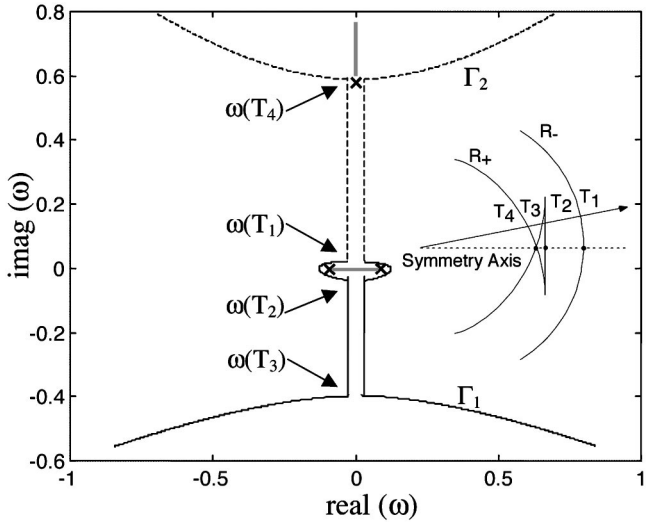

FIG. 7. Cargniard contour for zinc for observation points off the symmetry axis (θ=10°). Solid line represents contour corresponding to Eq. (27a) and the dashed line represents the contour corresponding to Eq. (27b). Inset: Enlargement of wave front near symmetry axis.

$$\text{(b)} \quad \zeta_3 x_3 - i\omega|x_2| = \tau, \tag{27}$$

τ is real and positve.

The parametric equations representing the Cagniard path are obtained by substituting Eqs. (8) into Eqs. (27) and squaring twice to eliminate the radicals. This procedure yields a fourth order equation for ω of the form

$$A(\theta)\omega^4 + B(\theta,T)\omega^3 + C(\theta,T)\omega^2 + D(\theta,T)\omega + E(\theta,T) = 0,$$

$$A(\theta) = F(\theta) + 4\alpha\beta - \gamma^2,$$

$$B(\theta,T) = \frac{8i\alpha T \sin(\theta) F(\theta)}{\cos^2(\theta)},$$

$$C(\theta,T) = 2F(\theta)G(\theta,T) - 16\frac{\alpha^2 T^2 \sin^2(\theta)}{\cos^4(\theta)} - 2(\alpha+1)\gamma + 4\alpha(\beta+1),$$

$$D(\theta,T) = \frac{8i\alpha T \sin(\theta) G(\theta,T)}{\cos^2(\theta)}, \tag{28}$$

$$E(\theta,T) = G(\theta,T) - (\alpha+1)^2 + 4\alpha,$$

$$F(\theta) = -\left(\frac{2\alpha \sin^2(\theta) + \gamma\cos^2(\theta)}{\cos^2(\theta)}\right)^2,$$

$$G(\theta,T) = \frac{2\alpha T^2 - (1+\alpha)\cos^2(\theta)}{\cos^2(\theta)}.$$

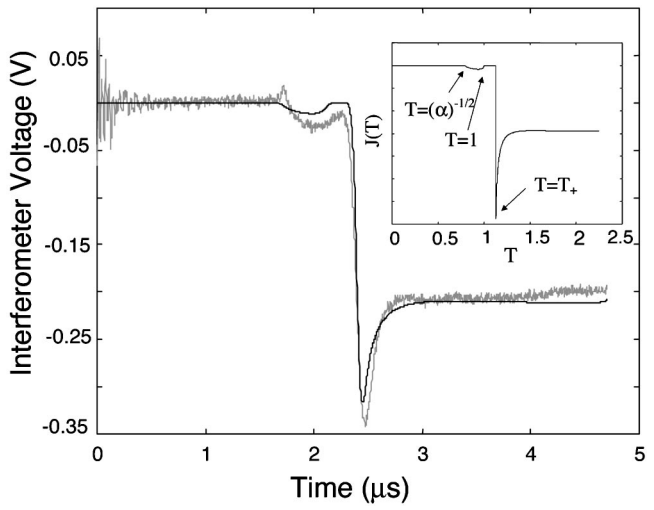

FIG. 6. Comparison between experiment and theory for the epicentral case. The sample is single crystal zinc with the *c* axis perpendicular to the free surface. The nonzero experimental displacement corresponding to the interior of the cuspidal triangle is a result of pulse broadening. Inset: Theoretical displacement, u_3, for the epicentral wave generated with a line source in zinc as a function of *T*.

Equation (28) has four complex roots, Θ_1, Θ_2, Θ_3, and Θ_4, which occur in complex conjugate pairs. The roots labeled Θ_1 and Θ_3 correspond to the physical sheets of the Riemann surface. For the special case of an isotropic solid, $\alpha=\beta=\gamma/2$, Eq. (28) can be factored into two second order equations that can be solved analytically. For the present problem of transverse isotropy, the roots must be found numerically.

The character of the Cagniard paths is dictated by the location of the lacunas relative to the observation direction. Thus, all crystal classes will have Cagniard paths with similar characteristics. As a representative example, the Cagniard path for zinc will be discussed in detail. The wave front for zinc is shown in the inset of Fig. 7. The lacunas in the R_+ branch are centered along the symmetry axis and along the bounding surface. Figure 7 shows the Cagniard path for an observation angle, θ=10°, that intersects the lacuna. With the Cagniard path numerically defined, the inversion of the transformed displacements, Eq. (26), may be performed. The off epicentral vertical displacement in zinc for a detection angle of 10° is shown in the inset of Fig. 8. The characteris-

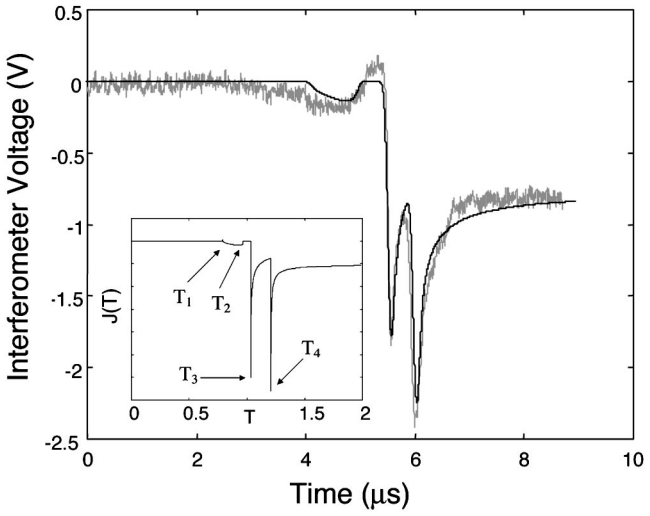

FIG. 8. Comparison between experiment and theory for an observation point off the symmetry axis. The sample is single crystal zinc with the *c* axis perpendicular to the free surface (θ=10°). Inset: Theoretical out-of-plane displacement due to line-source excitation in zinc as a function of *T*.

tics of the wave form shown in Fig. 8 are similar to the epicentral wave form shown in Fig. 6. The primary difference is the splitting of the wave resulting corresponding to the conical portion of the wave front.

III. EXPERIMENT

The experimental setup used to generate and detect ultrasound is shown in Fig. 9. The generation of the ultrasonic disturbance was accomplished by irradiating the sample with a pulsed Nd:YAG operating at 1.064 μm.[26–28] The transverse spatial profile was Gaussian and the temporal pulse length was approximately 10 ns. The energy per pulse was typically 20 mJ. The ultrasonic disturbance was detected with a skew-stabilized Michelson interferometer operating at 632.8 nm. The upper limit of the bandwidth was determined to a large extent by the frequency response of the photodetectors in the interferometer. The photodetectors were manufactured by EG&G (product designation FFD-040) and have a specified upper bandwidth limit of 150 MHz into a 50 Ω load. The lower limit of the bandwidth, estimated at 1 kHz, was dictated by the characteristics of the stabilization circuit. If the interferometer signal voltage is much smaller that the interferometer peak-to-peak voltage, then the signal voltage and the surface displacement are related as follows:

$$D_s = V_i\left(\frac{632.8\ \text{nm}}{2\pi}\right), \tag{29}$$

where D_s represents the surface displacement and V_i represents the ratio of the interferometer signal voltage to the peak to peak voltage.

For same side detection, care had to be taken so as not to saturate the photodiodes in the interferometer with light from the Nd:YAG laser that had scattered off the sample surface. A beam stop was used to collect the specular component of the scattered light while a 1.064 μm band reject filter was used to block the remaining scattered light from reaching the photodiodes. In order to approximate an infinite line source, a convex/concave lens combination was used as a telescope to expand the beam while a cylindrical lens was used to focus the generation beam to a line. This technique of generating a laser line source was exploited by Aindow *et al.*[29] to produce high amplitude surface acoustic waves. The approximate line dimensions, as measured from a piece of laser profiling paper, were 20 mm×0.2 mm.

The single crystal zinc specimens were cleaved along basal planes and then polished using Buehler Carbimet paper to produce a mirrorlike surface. The crystal orientation was determined using x-ray diffraction. The polished surface was perpendicular to the x-ray beam resulting in a diffraction pattern that had sixfold symmetry, confirming that the polished surface coincided with the basal plane. The cylindrical zinc sample used for same side detection had a radius of 15 mm and a length of 60 mm. The sample used for detection of epicentral waves had a radius of 15 mm and a length of 5 mm. The voltage signals from the interferometer were recorded using a LeCroy 9354m digital oscilloscope operating at 500 M samples/s.

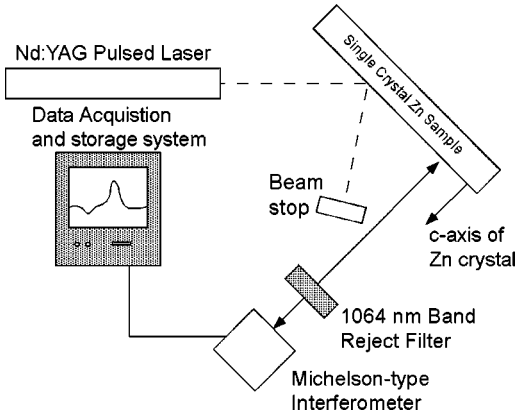

FIG. 9. Experimental setup. A Nd:YAG laser is used to generate the ultrasonic disturbance and a Michelson-type interferometer is used to detect the ultrasound.

IV. RESULTS AND DISCUSSION

A comparison between theory and experiment for same side detection is presented for single crystal zinc (*c* axis perpendicular to the surface) in Fig. 3. The experimental curve is single shot data and the source/receiver separation was 9.1 mm. The theoretical result, inset Fig. 3, is convolved with a Gaussian function (full width at half-maximum=300 ns) in order to mimic broadening effects. Pulse broadening for same-side detection is mainly caused by the finite transit time of the acoustic signal across the detection/generation spot. The first disturbance turns on and off at times corresponding to the arrival of the longitudinal wave and shear wave, respectively. The largest disturbance corresponds to the Rayleigh pole and is in the form of a traveling delta function. The amplitude of the Rayleigh wave for the theoretical curve was scaled to match the experimental amplitude. Since the data was single shot, comparison of theoretical and experimental amplitudes allows an estimate of the optical reflection coefficient. The theoretical amplitude, given in Eq. (18), is expressed by

$$A_{\text{Rayleigh}} = \bar{F}\psi_r q_0 \left(\frac{1}{\bar{N}\sqrt{\pi}} \right) \sqrt{C_{44}/\rho},$$
$$\bar{F} = \frac{1}{\rho C}\left[\frac{B_{33}}{C_{44}}(1-\kappa) + \frac{B_{22}}{C_{44}}\alpha \right], \tag{30}$$

where q_0 represents the absorbed laser energy and $\bar{N}$ represents the Gaussian pulse width. The data shown in Fig. 3 was produced by a 37 mJ pulse distributed over 1 cm. Scaling the theoretical amplitude of the Rayleigh wave to match the experimental data, the reflectivity at the sample surface was estimated to be 90%, which is comparable to published values for zinc. It should be noted that the accuracy of these results decreases as the aspect ratio, the ratio between the line source length and the source receiver distance, decreases.

Before comparing experiment and theory for the epicentral and off-epicentral cases, the effect of ultrasonic reflections from the back surface of the sample must be considered. Each time the wave reflects off the sample surface, the amplitude and temporal character of the wave are modified. The modification to the wave is described by reflection coefficients, which are a function of observation angle. For the isotropic case, Rose[17] shows that along the epicentral direction, reflection primarily alters the amplitude of the reflected wave. It is assumed that a similar result holds for anisotropic materials and for small angles off axis. Since the emphasis in this paper is to compare the temporal character between experiment and theory, the effect of reflection off the back surface will not be taken into account.

Figure 6 compares theory and experiment for displacement along the epicentral axis for a sample of single crystal zinc (c axis perpendicular to the free surface). The source/receiver distance was 5 mm and the signal was averaged 25 times to improve the signal-to-noise ratio. Again, the theoretical result was convolved with a Gaussian (FWHM=20 ns). Pulse broadening for detection along the epicentral direction is primarily due to the finite temporal pulse width of the generation laser. Zinc is a class (iii) crystal and, as a result, the displacement character differs markedly from its isotropic counterpart, Fig. 4. In a fashion similar to that of the surface wave case, the first disturbance turns on and off at times corresponding to the arrival of the longitudinal wave, T_1, and shear wave, T_2, respectively. After T_2, the displacement is identically zero until the arrival of the majority of the acoustic energy at T_+. A comparison between experiment and theory for an observation point off the symmetry axis, $\theta=10°$, is shown in Fig. 8. Similar to the analysis presented in Fig. 6, the data was averaged 25 times and convolved with a Gaussian ($\bar{N}=20$ ns). Figure 8 clearly shows the splitting of the wave caused by the conical portion of the wave front.

V. CONCLUSION

It was found that for a transversely isotropic half-space, the laser source could be modeled as a shear stress dipole applied at the free surface. A formal solution of the problem was found using double (Fourier–Laplace) transforms. The Cagniard–de Hoop technique was used to analytically invert the transformed solution for the epicentral case as well as for the surface wave case. A quasianalytical approach, where the Cagniard path was defined numerically, was used to invert the transformed solution for observation points off the symmetry axis.

Experimental validation of the theory was performed using single crystal zinc samples. The zinc samples were cut to have the free surface coincide with a plane of isotropy. Theoretical and experimental results for zinc agreed well for all the source/observation geometries considered.

ACKNOWLEDGMENTS

The authors gratefully acknowledge Dr. Robert E. Green for helpful suggestions regarding the experimental procedure and for supplying single crystal zinc samples. This work was sponsored by the U.S. Department of Energy, Office of Science-BES, Materials and Engineering Physics program under DOE Idaho Operations Office Contract No. DE-AC07-99ID13727.

[1] C. Scruby, R. Dewhurst, D. Hutchins, and S. Palmer, "Laser generation of ultrasound in metals," *Research Techniques in Nondestructive Testing* (Academic, New York, 1982), Vol. 5, pp. 281–327.
[2] C. Scruby, R. Smith, and B. Moss, "Microstructural monitoring by laser-ultrasound attenuation and forward scattering," NDT Int. **19**, 307–313 (1986).
[3] K. Telschow, "Microstructural characterization with a pulsed laser ultrasonic source," *Review of Progress in Quantitative Nondestructive Evaluation* (Plenum, New York, 1988), Vol. 7b, pp. 1211–1218.
[4] E. P. Papadakis, "Scattering in polycrystalline media," Methods Exp. Phys. **19**, 237–298 (1981).
[5] M. J. P. Musgrave, *Crystal Acoustics* (Holden-Day, Inc., San Francisco, 1970).
[6] R. Stoneley, Proc. R. Soc. London, Ser. A **232**, 447–458 (1955).
[7] D. Royer and E. Dieulesaint, "Rayleigh wave velocity and displacement in orthorhombic, tetragonal, hexagonal, and cubic crystals," J. Acoust. Soc. Am. **76**, 1438–1444 (1984).
[8] E. A. Kraut, Rev. Geophys. **1**, 401 (1963).
[9] H. Lamb, Philos. Trans. R. Soc. London, Ser. A **203**, 1 (1904).
[10] L. Cagniard, *Reflection and Refraction of Progressive Seismic Waves* (McGraw-Hill, New York, 1962).
[11] A. T. de Hoop, Appl. Sci. Res., Sect. B **8**, 349 (1960).
[12] R. Burridge, "Lamb's problem for an anisotropic half-space," Q. J. Mech. Appl. Math. **24**, 81–98 (1970).
[13] J. R. Willis and R. J. Bedding, "Arrivals associated with a class of self-similar problems in elastodynamics," Math. Proc. Cambridge Philos. Soc. **77**, 591–607 (1975).
[14] A. Mourad, M. Deschamps, and B. Castangnède, "Acoustic waves generated by a transient line source in an anisotropic half-space," Acust. Acta Acust. **82**, 839–851 (1996).
[15] R. L. Weaver, W. Sachse, and K. Y. Kim, "Transient elastic waves in a transversely isotropic plate," J. Appl. Mech. **63**, 337–346 (1996).
[16] C. B. Scruby, R. J. Dewhurst, D. A. Hutchins, and S. B. Palmer, "Quantitative studies of thermally generated elastic waves in laser-irradiated metals," J. Appl. Phys. **51**, 6210–6216 (1980).
[17] L. R. F. Rose, "Point source representation for laser generated ultrasound," J. Acoust. Soc. Am. **75**, 723–732 (1984).
[18] D. H. Hurley, "Laser-generated thermoelastic sources in anisotropic materials," J. Acoust. Soc. Am. **115**, 2054–2058 (2004).
[19] R. G. Payton, *Elastic Wave Propagation in Transversely Isotropic Media* (Martinus Nijhoff, The Hague, 1983).
[20] E. A. Kraut, Ph.D. thesis, University of California, Los Angeles, 1962.
[21] D. H. Hurley and J. B. Spicer, "Point-source representation for laser-generated ultrasound in an elastic, transversely isotropic half space," J. Appl. Phys. **86**, 3423–3427 (1999).
[22] In Ref. 21 it was shown that the vertical displacement along the epicentral

direction for a point source can be obtained by taking a temporal and spatial derivative of the line source solution.

[23] The effect of heat diffusion has been neglected and q_0 represents the laser energy absorbed by the sample. Rose (Ref. 17), states that a point-source representation for the radiation from a localized source is adequate for $\lambda \gg h$ where λ is the ultrasonic wavelength and h is the largest characteristic length relating to the source region. Ready (Ref. 24) has shown that the source is effectively localized within a region, $0 \leqslant h \leqslant \omega + (4kt)^{1/2}$, where ω is the laser beam radius and t is the time interval of interest. Considering laser generation in zinc, it can be shown that for a spot size of 10 μm, it is reasonable to neglect the effects of thermal diffusion for frequencies below 100 MHz.

[24] J. F. Ready, *Effects of High-Powered Laser Radiation* (Academic, New York, 1971).

[25] The solution procedure involves applying a Fourier/Laplace transform to remove dependence on the spatial and temporal variables: $F(\eta,s) = \int_{-\infty}^{\infty}\int_{0}^{\infty} f(x_2,t)e^{-(i\eta x_2 + s\tau)}\, d\tau\, dx_2$.

[26] S. J. Davies, C. Edwards, G. S. Taylor, and S. B. Palmer, "Laser-generated ultrasound: Its properties, mechanisms and multifarious applications," J. Phys. D **26**, 329–348 (1982).

[27] R. J. Dewhurst, C. Edwards, A. D. W. Mckie, and S. B. Palmer, "Comparative study of wide-band ultrasonic transducers," Ultrasonics **25**, 315–321 (1987).

[28] D. A. Hutchins, "Mechanisms of pulsed photoacoustic generation," Can. J. Phys. **64**, 1247–1264 (1986).

[29] A. M. Aindow, R. J. Dewhurst, and S. B. Palmer, "Laser-generation of directional surface acoustic waves pulses in metals," Opt. Commun. **42**, 116–120 (1982).

A resonant, self-pumped, circulating thermoacoustic heat exchanger

G. W. Swift[a] and S. Backhaus
Condensed Matter and Thermal Physics Group, Los Alamos National Laboratory, Los Alamos, New Mexico 87545

(Received 22 May 2004; revised 13 August 2004; accepted 16 August 2004)

An asymmetrical constriction in a pipe functions as an imperfect gas diode for acoustic oscillations in the pipe. One or more gas diodes in a loop of pipe create substantial mean flow, approximately proportional to the amplitude of the oscillations. Measurements of wave shape, time-averaged pressure distribution, mass flow, and acoustic power dissipation are presented for a two-diode loop. Analysis of the phenomena is complicated because both the mean flow and the acoustic flow are turbulent and each affects the other significantly. The quasi-steady approximation yields results in rough agreement with the measurements. Acoustically driven heat-transfer loops based on these phenomena may provide useful heat transfer external to thermoacoustic and Stirling engines and refrigerators. © *2004 Acoustical Society of America.* [DOI: 10.1121/1.1804634]

PACS numbers: 43.35.Ud, 43.25.Nm, 43.25.Qp [RR] Pages: 2923–2938

I. INTRODUCTION

Stirling's hot-air engine[1,2] of the early 19th century was one of the first heat engines to use oscillating thermodynamics of a gas in a sealed system. Since then, a variety of related engines and refrigerators has been developed, including Stirling refrigerators,[1,3] Ericsson engines,[4] orifice pulse-tube refrigerators,[5] standing-wave thermoacoustic engines and refrigerators,[6] free-piston Stirling engines and refrigerators,[7] and thermoacoustic-Stirling hybrid engines and refrigerators (also known as traveling-wave systems).[8–11] Combinations thereof, such as the Vuilleumier refrigerator[12] and the thermoacoustically driven orifice pulse-tube refrigerator,[13] have provided heat-driven refrigeration. Today, the efficient, mature members of this family of engines and refrigerators are in use in several niche markets, ranging from small cryocoolers with cooling powers below 10 W to large engines (e.g., for submarine propulsion) with powers near 100 kW.

Much of the recent evolution of this family of oscillating-gas thermodynamic technologies has been driven by the search for simplicity, reliability, and low fabrication costs through the elimination of moving parts, especially elimination of moving parts at temperatures other than ambient temperature, without seriously compromising efficiency. For example, the orifice pulse-tube refrigerator lacks the cold piston of previous cryogenic Stirling refrigerators; the free-piston Stirling engine lacks the crankshafts and connecting rods present in previous Stirling engines; and the thermoacoustic-Stirling hybrid engine eliminates pistons previously needed.

Heat exchangers may offer a second opportunity for dramatic improvement in simplicity, reliability, and low fabrication cost, particularly in engines and refrigerators of high power. All engines and refrigerators must reject waste heat to ambient temperature, and the ambient heat sink is often available as a flowing air stream or water stream. Engines must also accept heat from a heat source at a higher temperature, e.g., a stream of combustion products from a burner. Refrigerators must withdraw heat from a load at lower temperature, which is sometimes in the form of a flowing stream; examples include a stream of indoor air to be cooled and dehumidified and a stream of oxygen to be cooled and cryogenically liquefied. Hence, the typical heat exchanger in these engines and refrigerators must transfer heat between a steadily flowing ''process fluid'' stream such as these and the oscillating thermodynamic ''working gas'' (often pressurized helium).

In large, high-power engines and refrigerators, the thermal conductivity of solids is insufficient to carry the required heats without significant temperature differences, so geometrically complicated heat exchangers must usually be used to interweave the process fluid and the working gas, bringing them into intimate thermal contact. A shell-and-tube heat exchanger[14] is typical. In the orientation of Fig. 1(a), the working gas oscillates vertically through the insides of the many tubes, while the process fluid flows horizontally around and between the outsides of the tubes. Features specific to oscillating-gas engines and refrigerators impose unfortunate constraints on such heat exchangers as they are scaled up to higher power. Higher power demands more heat-transfer surface area, lest the efficiency suffer. However, tube lengths cannot be increased, because having such tube lengths greater than the oscillatory stroke of the working gas does not effectively transfer more heat. Hence, the obvious approach to scaleup is to increase the number of tubes in proportion to the power, keeping the length and diameter of each tube constant. Such heat exchangers can have hundreds or thousands of tubes, causing expense (because many parts must be handled, assembled, and joined) and unreliability (because many joints must be leak tight). Thermally induced stress poses an additional challenge to reliability when such a geometrically complex heat exchanger is at an extreme tem-

[a]Electronic mail: swift@lanl.gov; URL: www.lanl.gov/thermoacoustics/

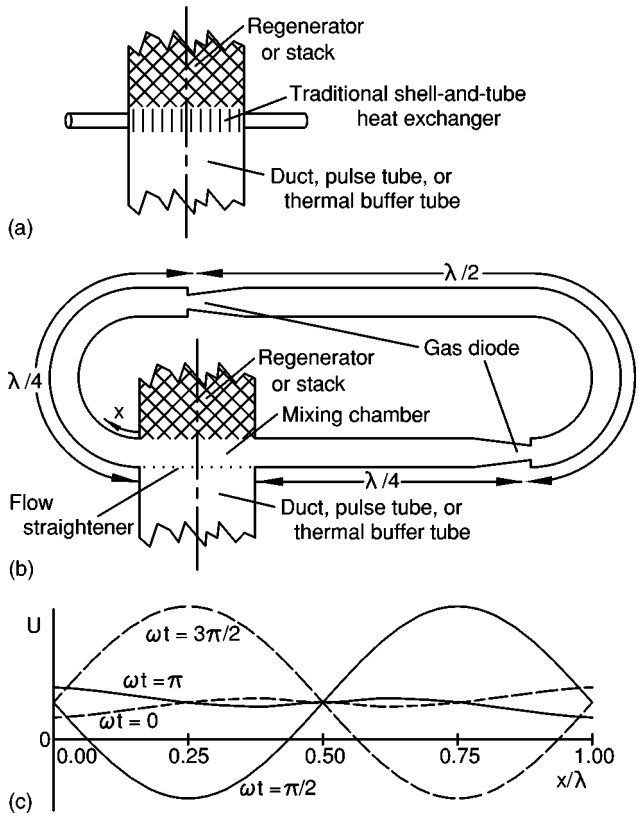

FIG. 1. (a) A portion of an oscillating-gas engine or refrigerator, containing a shell-and-tube heat exchanger or other traditional cross-flow heat exchanger. The heat exchanger is below a stack or regenerator, and is above a pulse tube, thermal buffer tube, or open duct. The oscillating flow of the working gas (e.g., pressurized helium) is vertical throughout. The steady flow of the process fluid (e.g., water) is horizontal through the heat exchanger. (b) A portion of an oscillating-gas engine or refrigerator, in which the traditional heat exchanger has been replaced by a single external pipe one wavelength long. Gas diodes at the velocity maxima create mean flow, which steadily transfers heat between the process fluid outside the pipe and the engine or refrigerator to which the pipe ends are attached. (c) Qualitative plot of volume velocity U as a function of location x in the pipe, at four equally spaced times t during a cycle of the wave. The zero of time phase is when the pressure in the mixing chamber is a maximum.

perature, i.e., a red-hot temperature for an engine or a cryogenic temperature for a refrigerator.

Another shortcoming of the heat exchangers of oscillating-gas engines and refrigerators is that they often must be located close to one another, simply because each heat exchanger must be adjacent to one end or the other of the nearest stack, regenerator, pulse tube, or thermal buffer tube, and these components themselves are typically short. The practical importance of this shortcoming is easily appreciated by considering the food refrigerator in the typical American kitchen. Its ''vapor compression'' cooling technology allows complete flexibility in the geometrical separation of the cold heat exchanger, where heat is absorbed from the inside of the cold box, and the ambient heat exchanger, where waste heat is rejected to the air in the kitchen, typically behind or under the refrigerator cabinet. With vapor-compression technology, not only can these heat exchangers be located freely, but their shapes can be chosen as needed for their circumstances, e.g., to accommodate fan-driven or natural convection, and to fit in and around the desired shape of the cold box or cabinet. In contrast, when one tries to adapt an oscillating-gas refrigerator to this application, the cold heat exchanger and ambient heat exchanger must be very close together, separated only by the regenerator or stack, whose length is typically only several centimeters. Hence, intermediate heat transfer equipment, such as heat pipes or pumped-fluid heat-transfer loops, must typically be used. These add complexity and expense.

To explore a new way to circumvent these shortcomings, we have begun to investigate the alternative heat-exchanger scheme illustrated in Fig. 1(b). This resonant, self-pumped, circulating thermoacoustic heat exchanger is a single pipe (or a few in parallel), which could be bent or coiled compactly, with a length equal to one wavelength of sound in the working gas in the pipe at the frequency of the engine's or refrigerator's oscillation. Both ends of the pipe are attached as ''branches'' to the ''trunk'' where a traditional heat exchanger would be expected. Oscillations of the gas in the pipe are caused by those in the trunk. Two gas diodes are in the pipe, each located a quarter wavelength from one end of the pipe. These create nonzero mean flow, so the motion of the working gas in the circulating heat exchanger is a superposition of oscillating flow and steady flow. Most of the extensive outside surface area of the pipe is available for thermal contact with the process fluid, which can flow either parallel or perpendicular to the pipe. The mean flow in the loop carries heat between this surface area and the mixing chamber in the trunk.

The gas diodes are the key to the heat-transfer circulation in Fig. 1(b). These are nonlinear flow elements having different flow resistances for flow in different directions. Gas diodes are typically much less perfect than electronic diodes, often with a ratio of backward and forward flow impedances less than a factor of 10. Gas diodes include the vortex diodes described by Mitchell,[15] the valvular conduit described by Tesla,[16] and the conical and tapered structures called jet pumps in some recent publications.[10,17]

The fact that the length of the pipe in Fig. 1(b) is one wavelength of sound leads to beneficial features, illustrated in Fig. 1(c). The gas diodes are located where the oscillating volume velocity[18] is a maximum, so they can create a large time-averaged pressure difference and a large mean flow, as explained more fully below. Meanwhile, the ends of the pipe are locations of minimal oscillating volume velocity, so that connecting the pipe to the trunk perturbs the oscillations in the trunk minimally. Figure 1(c) illustrates such minimal perturbation with the pipe ends presenting a real impedance to the trunk, but a slightly shorter pipe would add a positive imaginary part to that impedance, which could be useful for canceling unwanted compliance in the trunk. Estimates indicate that the mean flow can be many times larger than the oscillating flow amplitude where the pipe joins the trunk; Fig. 1(c) illustrates it as 2.4 times larger.

A nonresonant but otherwise similar concept was described by Mitchell[15] for a particular case: the heat exchanger at the ambient end of the pulse tube of an orifice pulse-tube refrigerator. Mitchell replaced this particular heat exchanger and the orifice by a heat-transfer loop containing one or more gas diodes to convert some of the oscillatory

power in the wave into mean flow of the working gas around the loop. The dissipation in the gas diode(s) and other acoustic dissipation in the loop serve the dissipative function of the original orifice, and the surface area along the entire path length of the loop serves the function of the original heat exchanger.

We undertook the work described here to investigate the main issues that are involved with using the resonant self-pumped loop for heat transfer. The insulated, electrically heated or water-cooled resonant loop described below was attached at both ends to a mixing chamber, where the sound wave was generated by a motor-driven piston and where heat from the electrically heated loop was rejected to water-cooled heat exchangers. Thermocouples monitored the temperature rise as the gas circulated through the insulated, heated loop; pressure transducers detected the oscillatory pressure associated with the wave and the time-averaged pressures associated with the mean flow. Most features of the experimental results are explained qualitatively by treating the oscillatory and mean flows as independently superimposed except at the gas diodes. The use of the quasi-steady approximation to analyze interactions of the oscillatory and mean flows throughout the loop, occurring through the Doppler effect and the nonlinearity of turbulent flow resistance, provides a better, reasonably quantitative interpretation of the measurements. An appendix summarizes the most tedious aspects of the application of the quasi-steady approximation to this situation.

II. APPARATUS AND PRELIMINARY MEASUREMENTS

From among the low-cost gases, we chose argon at a mean pressure $p_m = 2.4$ MPa for this investigation, because its high density gives it a low sound speed and small viscous and thermal penetration depths, which helped to keep the size of the apparatus and the thermal and acoustic powers small enough for easy experimentation. We chose ~ 50 Hz for the operating frequency and ~ 2 cm for the inside diameter of the pipe, for compatibility with a linear motor and piston (described below) that were available in our lab.

The apparatus is illustrated in Fig. 2. The one-wavelength loop shown in Fig. 2(a) had a total length of 6.33 m and was made mostly of seamless stainless-steel pipe with an inside diameter $D_{\text{pipe}} = 2.21$ cm. Long-radius elbows and fittings[19] smoothly matched this pipe's inside diameter. A valve at the velocity node halfway around the loop, at the top of Fig. 2(a), could be used to stop and start the mean flow while leaving the acoustics mostly undisturbed. Two geometrically identical sets of piping—one with thermocouples, heaters, and thermal insulation, the other cooled by flowing water—could be easily interchanged as desired for different types of measurements. For example, equilibration of the temperature profile around the loop required hours with the insulated pipes, but steady state could be reached in a few minutes with the water-jacketed pipes.

Gas diodes were located 1/4 and 3/4 of the way around the loop. Each was a machined brass cylinder with fittings brazed onto the ends, as shown in Fig. 2(b). The inside surface was a smooth cone 13.3 cm long, tapering from the 2.21 cm diameter of the loop piping at its large end to $D_{\text{gd}} = 1.4$ cm diameter at its small end, so the angle between the cone wall and the centerline was 1.75°. The inner edge at the small end was rounded with a radius of 2.3 mm. These dimensions were chosen to minimize acoustic power dissipa-

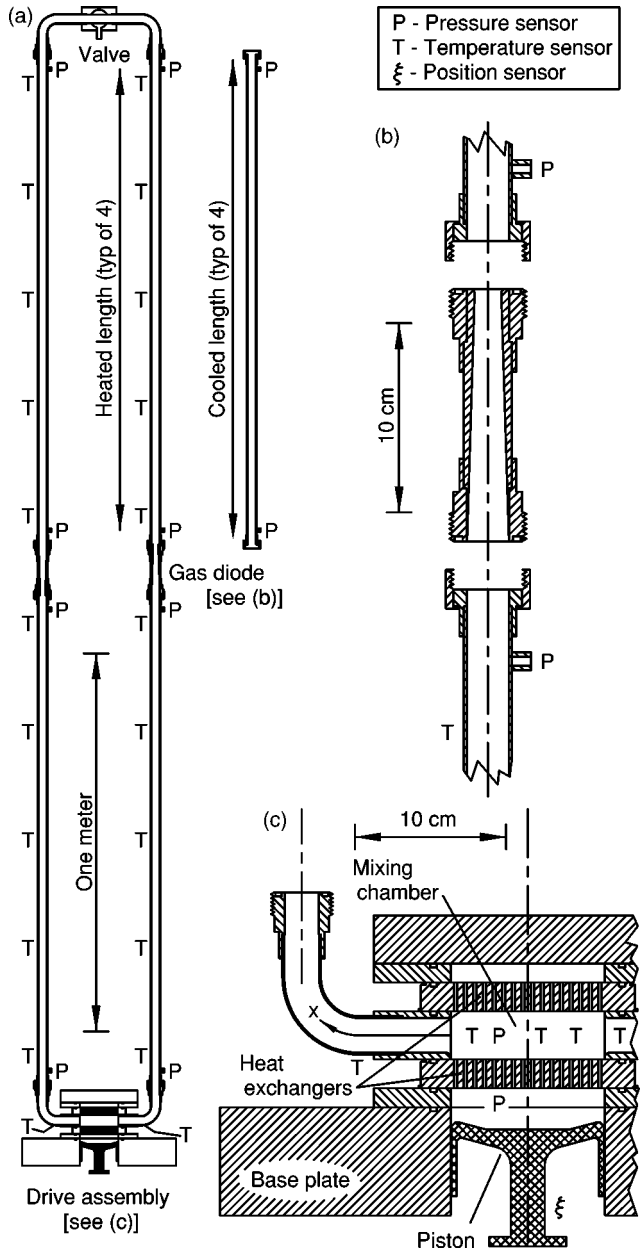

FIG. 2. Scale drawings of the apparatus. (a) Overview of the entire apparatus, except for the linear motor and its pressure housing below the bottom. The gas diodes were located 1/4 and 3/4 of the way around the loop of piping, and the valve was halfway around. The locations of most of the thermocouples (''T'') and pressure sensors (''P'') in the apparatus are shown in this view. The four long, straight runs of pipe (each having five thermocouples) were wrapped with heating blankets. The entire loop was then wrapped with thermal insulation. However, for some measurements, four alternative straight runs of pipe were used, each having a water jacket instead of the thermocouples, heater blanket, and insulation. The spatial extent of the heating blankets and water jackets is shown in the upper right. (b) Detailed view of one of the gas diodes, also showing how the fittings come apart. (c) Detailed view of the drive assembly. The piston, driven by a linear motor, insonified the apparatus. The two optional heat exchangers rejected heat to flowing water at ambient temperature. Temperature and pressure sensors not shown in (a) are shown here. Bolts holding the drive assembly together are not shown.

tion and to minimize the flow resistance into the small end while simultaneously generating a large time-averaged pressure difference, according to the analysis presented in Sec. III A.

Eight piezoresistive pressure transducers[20] were arrayed along the loop as shown in Fig. 2(a), and two more were located in the drive assembly as shown in Fig. 2(c). A lock-in amplifier[21] was used to measure their oscillating voltage amplitudes and phases to obtain the complex pressure amplitude p_1 at each location, and a five-digit voltmeter was used to measure their average voltages for calibration checks and to obtain the second-order, time-averaged pressures $p_{2,0}$ associated in part with the mean flow around the loop.[22] The reference side of the pressure transducer near the piston in Fig. 2(c) was always at atmospheric pressure, while the reference sides of the other nine transducers were held at 2.4 MPa so that the temperature dependence of the transducers' gains did not interfere with the measurements of $p_{2,0}$—otherwise, a small drift in temperature would have caused a large drift in average voltage, masking the small voltage changes due to time-averaged pressure. The four transducers closest to the two gas diodes were connected to the loop through thin-walled stainless-steel capillaries 4 cm long and 0.6 mm i.d. so that their temperatures were minimally affected by the wave in the pipe; this feature is discussed in more detail in Sec. III B. Simple modeling of the acoustics of these capillaries and the volumes associated with the transducers indicated that the amplitude drop along the capillary was only 0.1% and the phase shift was only 0.2°.

Figure 3(a) shows measurements of p_1 for a typical wave with the loop valve closed to prevent mean flow. The corresponding calculated curves in Figs. 3(a) and 3(b) were generated straightforwardly by integrating the acoustic momentum and continuity equations with DeltaE,[23] using ''cone'' for each gas diode's tapered portion and ''duct'' for the rest of the loop. (DeltaE's wall roughness factor for turbulence was set at 5×10^{-4}. Under the conditions of Fig. 3, turbulence is expected in the gas-diodes' cones and near the maxima in volume velocity $|U_1|$ in the 2.21-cm-i.d. pipe, where the gas displacement amplitude over viscous penetration depth is $|\xi_1|/\delta_\nu = 830$ and the Reynolds-number amplitude $|N_{R,1}| = |U_1| D_{\text{pipe}} \rho_m / S_{\text{pipe}} \mu = 580\ 000$, where D is diameter, ρ_m is mean density, S is cross-sectional area, and μ is viscosity.) An ''impedance'' at the small end of the cone accounted for the extra dissipation caused by the abrupt area change there, calculated as described near Eq. (19) in Sec. III A. To produce the calculated curves in Fig. 3, the mean pressure, temperature, frequency, and the pressure oscillation amplitude in the mixing chamber were fixed at the experimental values. The agreement between the measured and calculated pressure waves in Fig. 3(a) is excellent, inspiring confidence that the calculated wave of volume velocity U_1 is accurate, too. The left-right symmetry in Figs. 3(a) and 3(b) is nearly perfect: The asymmetry of the two gas diodes' orientations has a very small effect on the wave when the valve is closed.

Obtaining meaningful measurements of time-averaged pressure required a multi-step procedure. First, the time-averaged voltages from the pressure transducers were recorded while the apparatus was running in steady state. Next, the power to the drive piston was shut off and a valve was opened to equalize the pressures above and below the piston more quickly than would otherwise have occurred through the leakage around the piston. Time-averaged voltages were again recorded from each transducer, and these were subtracted from the earlier measurements. This subtraction accounted for different transducers having different offset voltages. These voltage differences were multiplied by the calibration constants of the transducers to yield $p'_{2,0}$ for each transducer. However, these values of $p'_{2,0}$ included a large common-mode effect of no interest to us, due mostly to the front-to-back time-averaged pressure difference across the moving piston, generated in part by nonlinear leakage past the piston. Hence, the common-mode part of $p'_{2,0}$ was eliminated by subtracting $p'_{2,0}$ in the mixing chamber from its value at each of the transducers, yielding $p_{2,0}$. Figure 3(c) shows a typical set of such results, with $p_{2,0} \equiv 0$ in the mixing chamber (at $x=0$ and $x=6.33$ m) a consequence of this procedural definition of $p_{2,0}$.

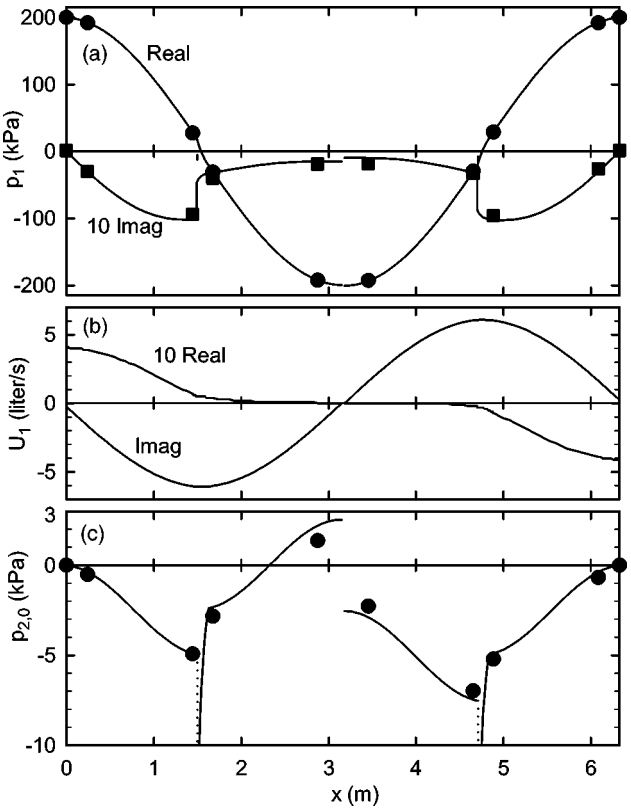

FIG. 3. A typical wave, with 2.4-MPa argon at 48.4 Hz, using the water-cooled loop and with the valve closed to enforce zero mean flow, as a function of position around the loop, with $x=0$ and $x=6.33$ m where the loop meets the mixing chamber. Both gas diodes were oriented to encourage flow in the positive-x direction, with their small ends toward smaller x. (a) Real and imaginary parts of the pressure wave. Points are measured values and lines are calculations. (b) Calculated real and imaginary parts of the volume-velocity wave. In (a) and (b), the standing-wave components are so much larger than the out-of-phase components that the latter have been multiplied by 10 for clarity. The zero of time phase is chosen so that the pressure oscillations in the mixing chamber are real. (c) The time-averaged pressure as a function of position, relative to its value in the mixing chamber. Points are measured values and lines are calculations. The two vertical dotted lines are at the small-x, small-diameter ends of the gas diodes. The vertical discontinuity is at the valve.

The calculated curve $p_{2,0}(x)$ shown in Fig. 3(c) includes both reversible nonlinear effects and irreversible nonlinear effects. The reversible effects arise from what can be loosely described as the acoustic version of Bernoulli's equation, with low time-averaged pressure at locations of high time-averaged velocity. The well-known lossless expression[24,25] obtained by properly time averaging lossless equations of fluid mechanics

$$p_{2,0}(x) = \frac{|p_1(x)|^2}{4\rho_m a^2} - \frac{\rho_m |U_1(x)|^2}{4[S(x)]^2} + C, \tag{1}$$

where a is the sound speed, with p_1 and U_1 from Figs. 3(a) and 3(b), was used to compute the smoothly varying portions of the curve of Fig. 3(c). The two steep portions of the solid curve in Fig. 3(c), extending below the bottom of the graph, indicate the contribution of $S(x)$ in the conical tapers of the gas diodes to Eq. (1).

The three abrupt steps in the curve of Fig. 3(c), two (dotted lines) at the small ends of the gas diodes and the third (no line) at the valve, mark changes in the constant C in Eq. (1) from region to region in the apparatus. The small end of each gas diode generates its step in $p_{2,0}$ from a combination of the effect of the step in area in Eq. (1) and the irreversible "minor loss."[26] The algorithm used to calculate the magnitude of the minor-loss contribution is described in Sec. III A. The steps in $p_{2,0}$ located at and caused by the gas diodes impose their sum across the valve at $x=3.2$ m, where the pressure difference of 4 kPa represents the effect that encourages nonzero mean flow as soon as the valve is opened. The experimental values of these irreversible steps shown in Fig. 3(c) are about 10% smaller than the calculated values. Other than this discrepancy, which is examined in more detail in Sec. III B, the agreement between the experimental and calculated values in Fig. 3(c) is excellent.

The insulated pipes included type K thermocouples and electric-resistance heaters with locations as shown in Fig. 2. The 22 thermocouples on the loop itself were spot welded to the outside of the pipe and were approximately equally spaced, except for a larger gap across the valve at the top. Wrapped around the outside of the straight sections of the loop were flexible heaters,[27] with power delivered by a variable autotransformer and measured with an electronic power meter.[28] Surrounding the heaters and all the unheated parts of the loop was a layer of flexible foam insulation, 2 cm thick, of the type often used to insulate residential hot water pipes. Measurements with the heaters and thermocouples and with no acoustics showed that the thermal conductance through this insulation was 2 W/°C, about twice the value estimated from the dimensions and the nominal insulating value "R5," the excess presumably due to imperfections associated with the valve, fittings, pressure transducers, elbows, etc., and the fact that the heaters covered only the convenient long parts of the loop. To reduce this heat leak, an additional layer of rigid fiberglass insulation (of the type often used to cover industrial steam pipes) was added to the straight portions, bringing their total diameter to 11.4 cm, and 3–5 cm of soft fiberglass was added around the elbows and valve (including the valve handle). This reduced the measured thermal conductance through the insulation to 1.15 W/°C. Figure 4 shows measurements of the temperature distribution $T(x)$ for three simple circumstances, giving some indication of the variability in local temperatures resulting from spatial nonuniformity in coverage by the electric heaters, acoustic power dissipation, and thermoacoustic heat pumping. With electric heat and no acoustic oscillations, the thermocouples closest to the unheated portions (the gas diodes and the valve) are the coolest. With the most intense acoustic oscillations, the thermocouples near the gas diodes, where dissipation of acoustic power is highest, are the warmest.

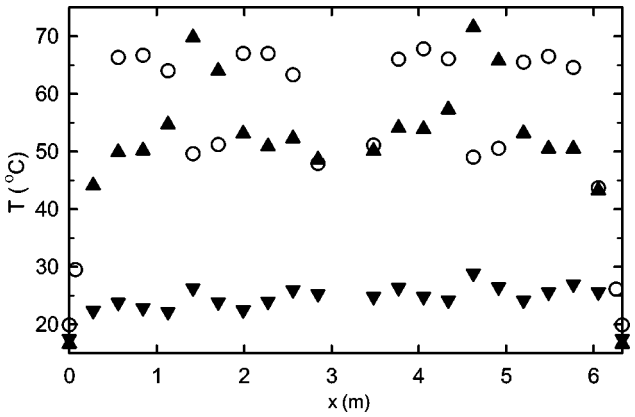

FIG. 4. Temperature T as a function of position x around the loop for three base line circumstances with the valve closed. Open circles: no acoustic power, 41 W applied with electric heaters, 1.15 W/°C insulation. Inverted triangles: No electric heat, 53 W of acoustic power applied with piston ($|p_1|=152$ kPa in the mixing chamber), 2 W/°C insulation. Erect triangles: No electric heat, 124 W of acoustic power applied with piston ($|p_1|=207$ kPa in the mixing chamber), 2 W/°C insulation. The points at $x=0$ and $x=6.33$ m are temperatures inside the mixing chamber; other points are temperatures on the wall of the loop.

Connecting both ends of the loop to the driving system, at the bottom of Fig. 2(a) and shown in more detail in Fig. 2(c), was the "mixing chamber." The mixing chamber was an open cylindrical space 10.2 cm in diameter and 3.18 cm tall, with the loop connections at diametrically opposite locations. In addition to the pressure transducer mounted in its side wall, the mixing chamber contained five thermocouples, extending into the gas itself, axially centered and at various radial and azimuthal positions. A sixth thermocouple extended into the loop 5 cm, on the "hot" side, i.e., the side delivering mean flow from the loop to the mixing chamber.

Water-cooled heat exchangers above and below the mixing chamber, shown in Fig. 2(c), were included when needed to remove heat from the system. Each heat exchanger was a cross-drilled brass block, with 404 holes of 2.26 mm diameter and 20.6 mm length through which the argon oscillated vertically, and 51 perpendicular holes of the same diameter and various lengths up to 10.2 cm through which ambient-temperature water flowed horizontally.

The oscillations in the system were driven by an oscillating piston of 10.16 cm diameter, below the lower heat exchanger. The piston was driven in turn by a linear motor, not shown in Fig. 2. The base plate, piston, and motor came as a complete package from the motor manufacturer,[29] with the motor housing sharing the same gas and mean pressure as the experimental system, so that perfect piston sealing was

unnecessary and the gas exerted no significant time-averaged force on the piston.

A mutual-inductance-based linear variable displacement transducer[30] (LVDT) was mounted on the motor to indicate the piston's mean position ξ_m and its complex displacement oscillation amplitude ξ_1. The LVDT was electrically excited at 10 kHz and monitored by a lock-in amplifier[21] operating at that frequency. With the lock-in time constant at 3 s, this LVDT–lock-in combination was calibrated *in situ* by driving the motor with enough dc current (first of one sign, then of the other) so that an opaque edge moving with the piston half blocked the light path of either of two light-emitting diode (LED)-photodiode sets. The known distance between the two LED-photodiode sets and the lock-in readings at the two positions yielded the calibration of the LVDT–lock-in combination. For measurements of ξ_m, this lock-in's time constant was kept at 3 s. For measurements of ξ_1, this lock-in's time constant was set at 10 μs, and its output was fed to the input of the lock-in used to measure p_1. With the piston moving at 50 Hz at just the right amplitude, comparison of the LVDT signal with the signals from the photodiodes showed that these measurements of ξ_1 are accurate to 1% in amplitude and 1° in phase.

To establish more confidence in the measurement of ξ_1, we temporarily replaced the loop, mixing chamber, and heat exchangers with the shortest possible 10-cm-diam cylinder and a dummy load, i.e., a valve functioning as a variable resistance in series with a tank of known volume V. The powers dissipated in the load[31] and delivered by the piston are given by

$$\dot{E}_{\text{load}} \cong \frac{\omega V}{2\gamma p_m} \text{Im}[p_{1,\text{pist}}\ \tilde{p}_{1,\text{tank}}], \tag{2}$$

$$\dot{E}_{\text{pist}} = -\frac{\omega S_{\text{pist}}}{2} \text{Im}[p_{1,\text{pist}}\ \tilde{\xi}_1], \tag{3}$$

where $\omega = 2\pi f$, f is the drive frequency, γ is the ratio of isobaric to isochoric specific heats, and the tilde denotes complex conjugation. Figure 5 shows a comparison of these powers for two different pressure amplitudes as the variable resistance was changed. The fact that the observed slopes on this plot are close to unity confirms the accuracy of the measurements of $\dot{E}_{\text{pist}}$ and, hence, of $|\xi_1|$ and the phase between ξ_1 and p_1.

The vertical offsets of the two sets of measurements in Fig. 5 depended on pressure amplitude and were larger than could be accounted for simply by thermal-hysteresis losses on the surface of the short 10-cm-diam cylinder. We assume that the excess is due to oscillatory leakage past the piston. Measurements of this excess power dissipation as a function of amplitude are fit well by

$$\dot{E}_{\text{leak}} = (0.000\,14\ \text{W/kPa}^{2.25})|p_1|^{2.25}. \tag{4}$$

Some aspects of this leakage dissipation (e.g., the dependence of $\dot{E}_{\text{leak}}$ on $|\xi_1|$ and ξ_m) were not fully explored at the detailed level of a few watts. Greater care was not justified, because other dissipative effects in the mixing chamber, such as the effect of amplitude-dependent turbulence on the thermal-hysteresis losses on the surfaces of the heat exchangers, are not understood at that level of detail. Overall, we estimate that the measurements of the acoustic power delivered to the mixing chamber by the piston have an uncertainty of about 2% due to sensor-calibration uncertainties plus a few watts due to this leakage dissipation.

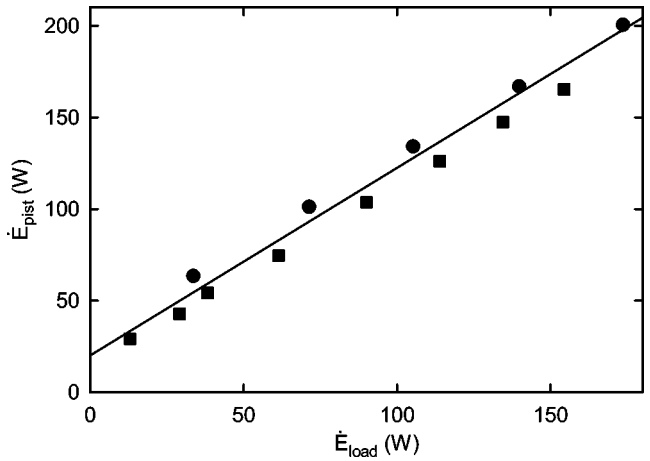

FIG. 5. Acoustic power delivered by the piston, $\dot{E}_{\text{pist}}$, as a function of acoustic power delivered to the dummy load, $\dot{E}_{\text{load}}$. Circles, $|p_1| = 240$ kPa in the mixing chamber. Squares, $|p_1| = 170$ kPa in the mixing chamber. The straight line, a guide to the eye, has a slope of unity and an arbitrary vertical offset.

During the course of the measurements, with temperature often a significant function of location x around the loop and with mean flow often nonzero, an easy experimental definition of loop resonance was needed so that the drive frequency could be chosen without having to map out the entire wave as shown in Fig. 3(a). We decided to use the condition

$$\text{Re}[\xi_1/p_{1,\text{pist}}] = 20\ \mu\text{m/kPa} \tag{5}$$

to define resonance, where $p_{1,\text{pist}}$ is the complex pressure oscillation amplitude above the piston and the numerical value of 20 μm/kPa is obtained from the calculated compliance of the mixing chamber, heat exchangers, and adjacent 10-cm-diam spaces in the driver assembly. The numerical value varied slightly with amplitude, because ξ_m varied slightly. For left-right symmetry in the loop, Eq. (5) implies that the impedances of both branches from the mixing chamber to the loop are real, an unambiguous definition of loop resonance frequency. For more general, asymmetrical conditions, Eq. (5) implies that the sum of the imaginary parts of the inverse impedances of the two branches is zero, so that if one end of the loop looks inertial the other must look compliant. Before recording any other data, measurements of ξ_1 and $p_{1,\text{pist}}$ were obtained, $\text{Re}[\xi_1/p_{1,\text{pist}}]$ was computed, f was adjusted, and the process was repeated until Eq. (5) was satisfied. This typically took only 1 min to reach a resonance frequency precise to ± 0.01 Hz. However, the accuracy of the resonance frequency determined in this way was in doubt ± 0.5 Hz. The numerical value used in Eq. (5) was uncertain because of uncertainty in how much of the calculated compliance volume, which included the heat-exchanger passages, should be regarded as isothermal instead of adiabatic. The more accurately known value of 17.4 μm/kPa was used

for measurements when the heat exchangers were omitted.

With the water-cooled pipes in use, the experimental resonance frequency defined in this way decreased when the valve was opened at fixed acoustic amplitude. The decrease varied from 0.5% at low amplitude to 0.7% at high amplitude. Most of this change can be attributed to the 0.4% increase in length of the loop as the passage inside the ''ball'' of the valve became part of the acoustic path. The experimental resonance frequency increased quadratically with acoustic amplitude, by 0.6% from low amplitude to $|p_1| = 240$ kPa when the valve was closed and by 0.8% when the valve was open. How much of this rise is attributable to temperature rise in the gas is unknown. Note that about a third of the acoustic power dissipation in the loop occurs in the gas diodes, which are at velocity maxima of the wave where a change in temperature has the largest effect on the resonance frequency.

In the calculations plotted in Fig. 3 and throughout the rest of the paper, the experimental frequency was used in the calculations. Forcing the calculations to mimic the experimentally defined resonance (i.e., to zero the sum of the calculated imaginary parts of the impedances of the two ends of the loop at the mixing chamber) could be accomplished either by setting the calculation's frequency 1% above the experimental resonance frequency or by reducing the calculation's temperature by 2% to reduce the sound speed by 1%. However, this alternative calculation scheme made little difference in other calculated results.

III. CIRCULATING MEAN FLOW

A. Theory

In Fig. 3(c), the step in $p_{2,0}$ across the valve shows that the loop is ready to deliver nonzero time-averaged mass flow $\dot{M}$ in the positive-x direction as soon as the valve is opened.[22] In this subsection, analysis directed toward understanding such time-averaged effects is presented. This analysis is based on simple assumptions, but nonetheless captures many of the experimental features described below. The quasi-steady approximation is central: We proceed as if the results of steady-flow analysis can be applied at each instant of time without memory of recent past history.

The irreversible part of the turbulent-flow pressure difference δp across any lumped element, including minor-loss components such as gas diodes, is conventionally[32] expressed using the minor-loss coefficient K

$$\delta p = K \rho u^2/2, \tag{6}$$

where ρ is the gas's density and u is its velocity at a reference location in the lumped element. Hence, for superimposed steady and oscillatory flows, the irreversible part of the time-averaged pressure difference developed across each component due to the time-dependent flow through it can be estimated using

$$\delta p = \frac{\omega}{2\pi} \oint_0^{2\pi/\omega} \delta p(t)\, dt \tag{7}$$

$$= \frac{\omega}{2\pi S^2}\left[\int_{t_0}^{\pi/\omega - t_0} K_+ \frac{1}{2}\rho(|U_1|\sin\omega t + \dot{M}/\rho)^2 dt \right.$$

$$\left. - \int_{\pi/\omega - t_0}^{2\pi/\omega + t_0} K_- \frac{1}{2}\rho(|U_1|\sin\omega t + \dot{M}/\rho)^2 dt \right], \tag{8}$$

where K_+ and K_- are the minor-loss coefficients for the two directions of flow through the component, S is the area on which the K's are based (conventionally, the smallest cross-sectional area of the component), t is time, and t_0 is the time at which the volume velocity crosses zero, i.e., t_0 satisfies $|U_1|\sin\omega t_0 + \dot{M}/\rho = 0$. (If $|\dot{M}/\rho| > |U_1|$, no solution for t_0 exists, and either the K_+ or K_- integral is carried out from 0 to $2\pi/\omega$. Otherwise, the zero crossing with $-\pi/2 < \omega t_0 < 0$ is chosen.) Equation (8) is a straightforward extension of the discussion near Eq. (7.76) in Ref. 33.

Our choice of notation for the steady flow calls for some explanation, because no choice seems completely satisfactory. Results below show that $\dot{M}$ is approximately proportional to the first power of the amplitude of the wave and is comparable in size to $\rho_m|U_1|$, but a subscript ''1'' would be misleading because it would improperly suggest that $\dot{M}$ is complex or oscillatory. A subscript ''m'' would inappropriately suggest that this steady flow exists in the absence of the sound wave (just as p_m and ρ_m exist in the absence of the wave). We have chosen to use $\dot{M}$, without subscripts, because it is simple and because the most reliable measurements described below detect mass flow, not volume flow. The mass flow $\dot{M}$ in this paper should not be confused with the much smaller, second-order time-averaged mass flow $\dot{M}_2 = \frac{1}{2}\mathrm{Re}[\rho_1 \tilde{U}_1] + \rho_m U_{2,0}$ in previous work.[10,11,33]

Assuming that all variables except t itself are independent of time, performing the integrals in Eq. (8) yields the irreversible second-order time-averaged pressure difference

$$\delta p_{2,0} = -K_-(\dot{M}^2/2\rho_m S^2 + \rho_m|U_1|^2/4S^2) \quad \text{for } \varepsilon \leqslant -1 \tag{9}$$

$$= \frac{\rho_m|U_1|^2}{8S^2}(K_+ - K_-)\left\{ 1 + 2\varepsilon^2 + \frac{K_+ + K_-}{K_+ - K_-}\frac{2}{\pi} \right.$$

$$\left. \times[(1+2\varepsilon^2)\sin^{-1}\varepsilon + 3\varepsilon\sqrt{1-\varepsilon^2}] \right\} \quad \text{for } |\varepsilon| \leqslant 1 \tag{10}$$

$$= K_+(\dot{M}^2/2\rho_m S^2 + \rho_m|U_1|^2/4S^2) \quad \text{for } \varepsilon \geqslant 1, \tag{11}$$

where the flow-rate ratio $\varepsilon = \dot{M}/\rho_m|U_1|$. Our gas diodes operate with $|\varepsilon| < 1$, so that the flow passes through zero twice during each cycle. When $|\varepsilon| > 1$, the flow is unidirectional. Signs have been chosen so that positive δp discourages positive $\dot{M}$ and K_+ corresponds to flow in the $+x$ direction.

To obtain $\delta p_{2,0}^{\mathrm{gd}}$ for our gas diodes' geometry from Eq. (10), we use the well-established Borda–Carnot expression[34]

$$K_- = (1 - S_{\mathrm{gd}}/S_{\mathrm{pipe}})^2 \tag{12}$$

for minor-loss flow through the abrupt expansion from S_{gd} to S_{pipe} to obtain $K_- = 0.364$. We combine equations and a

chart from Ref. 32, for an abrupt contraction with a rounded edge plus a term accounting for radial nonuniformity in a short conical expander, to obtain $K_+ = 0.04$. These quasi-steady estimates and the entire quasi-steady approach introduced in Eq. (8) should be accurate for oscillatory flow if the Reynolds number is sufficiently high and if the gas displacement is sufficiently large. For the conditions of Fig. 3, $|N_{R,1,\mathrm{gd}}| = |U_1| D_{\mathrm{gd}} \rho / S_{\mathrm{gd}} \mu = 920\ 000$, but $|\xi_1|/D_{\mathrm{gd}}$ is only 9, the latter condition perhaps not extreme enough for complete confidence in the quasi-steady approximation.[35,36]

Equations (9)–(11) with $K_+ = K_-$ still depend on ε, so apparently the oscillatory flow affects the time-averaged pressure drop across *symmetrical* turbulent components as well as across the asymmetrical gas diodes. Setting $K_+ = K_- \equiv K$ in Eqs. (9)–(11) yields

$$|\delta p_{2,0}| = K \frac{\rho_m}{2} \left(\frac{\dot{M}/\rho_m}{S_{\mathrm{pipe}}} \right)^2 \left(1 + \frac{1}{2\varepsilon^2} \right) \quad \text{for } |\varepsilon| \geqslant 1 \tag{13}$$

$$= K \frac{\rho_m}{2} \left(\frac{\dot{M}/\rho_m}{S_{\mathrm{pipe}}} \right)^2 \frac{[(1+2\varepsilon^2)\sin^{-1}|\varepsilon| + 3|\varepsilon|\sqrt{1-\varepsilon^2}]}{\pi \varepsilon^2} \quad \text{for } |\varepsilon| \leqslant 1. \tag{14}$$

This multiplicative enhancement of the steady-flow pressure drop across a symmetrical turbulent component grows from near unity at small $|U_1|$ though 3/2 at $|U_1| = \dot{M}/\rho_m$ toward a linear asymptote of $4\rho_m |U_1|/\pi \dot{M}$ at large $|U_1|$. The origin of this increase is the fundamentally nonlinear nature of turbulent flow resistance: If the flow is described by $\delta p(t) = R[U(t)]^n$ with $n \neq 1$, then the extra pressure difference caused by an increment of mass flow above the average value $\dot{M}$ is not canceled when an equal decrement below the average occurs half a cycle later.

In the loop under investigation here, opposing the pressure differences of Eq. (10) that are generated at the two gas diodes is the time-averaged pressure gradient throughout the rest of the loop due to $\dot{M}$ flowing around the loop. To estimate this pressure gradient, one might expect[37] that standard equations of fluid mechanics, such as

$$\frac{dp}{dx} = -f_M \frac{\rho_m}{2D_{\mathrm{pipe}}} \left(\frac{\dot{M}/\rho_m}{S_{\mathrm{pipe}}} \right)^2, \tag{15}$$

could be used for the mean flow through the uniform-area parts of the loop, where D_{pipe} is the pipe diameter and f_M is the Moody friction factor, which is given in most fluid mechanics textbooks (e.g., Ref. 26). Some of the calculated curves presented below rely on this simple treatment of the mean flow in the loop. However, Eq. (15) describes nonlinear, turbulent flow, so the arguments presented in the previous paragraph suggest that Eq. (15) could significantly underestimate the mean-flow resistance when oscillatory flow is superimposed. Furthermore, the Moody friction factor f_M depends on velocity, so the constant-K analysis leading to Eqs. (13) and (14) is not suitable. The appendix presents a derivation of expressions similar to Eqs. (13) and (14) taking the velocity dependence of f_M into account; the result is Eqs. (A9) and (A10).

To Eq. (15) or Eqs. (A9) and (A10) for the time-averaged pressure gradient along the uniform-diameter portions of the pipe are added two pressure drops due to drag on the mean flow by the conical surfaces of the two gas diodes,[32,38] four pressure drops due to steady-flow minor loss corrections in the four 90° elbows,[34] and one pressure drop due to steady-flow minor loss at the exit from the pipe to the mixing chamber; all of these may also be increased by nonzero $|U_1|$ according to the multiplicative enhancement of Eqs. (13) and (14). These seven pressure drops typically summed to about 50% of that of the uniform-diameter portions.

Setting the sum of the forcing pressures of the two gas diodes equal to the sum of all these opposing steady-flow pressure drops allows one to find $\dot{M}$. This must be done numerically because of the complicated nature of the equations. Qualitatively, Eq. (10) shows that $\delta p_{2,0}^{\mathrm{gd}}$ is proportional to the square of the wave amplitude and Eq. (15) shows that the opposing pressure gradient in the loop is nearly proportional to the square of the mean flow, so one can expect that the mean flow is roughly proportional to the wave amplitude.

Again using the quasi-steady approximation, the acoustic power consumed by a turbulent lumped element such as a gas diode due to the oscillatory component of the flow through it can be estimated using[39]

$$\Delta \dot{E} = \frac{\omega}{2\pi} \oint_0^{2\pi/\omega} \delta p(t) |U_1| \sin \omega t \, dt \tag{16}$$

$$= \frac{\omega}{2\pi S^2} \left[\int_{t_0}^{\pi/\omega - t_0} K_+ \frac{1}{2} \rho (|U_1| \sin \omega t + \dot{M}/\rho)^2 \times |U_1| \sin \omega t \, dt - \int_{\pi/\omega - t_0}^{2\pi/\omega + t_0} K_- \frac{1}{2} \rho (|U_1| \sin \omega t + \dot{M}/\rho)^2 \times |U_1| \sin \omega t \, dt \right]. \tag{17}$$

This is a straightforward extension of the discussion near Eq. (7.77) in Ref. 33. Again assuming that variables other than t itself are independent of time, performing the integrals yields[39]

$$\Delta \dot{E} = -\varepsilon K_- \frac{\rho_m |U_1|^3}{2S^2} \quad \text{for } \varepsilon \leqslant -1 \tag{18}$$

$$= \frac{\rho_m |U_1|^3}{3\pi S^2} (K_- + K_+) \left[\left(1 + \frac{\varepsilon^2}{2} \right) \sqrt{1-\varepsilon^2} + \frac{3}{2} \varepsilon \sin^{-1} \varepsilon - \frac{K_- - K_+}{K_- + K_+} \frac{3\pi\varepsilon}{4} \right] \quad \text{for } |\varepsilon| \leqslant 1 \tag{19}$$

$$= \varepsilon K_+ \frac{\rho_m |U_1|^3}{2S^2} \quad \text{for } \varepsilon \geqslant 1. \tag{20}$$

We then use $\delta p_1 = 2\Delta \dot{E}/|U_1|$ as an estimate of the first-order pressure difference caused by irreversible processes in such components.

As in Eqs. (9) and (10), note the nontrivial ε dependence in Eqs. (18)–(20), even if $K_+ = K_-$, indicating that acoustic-

power dissipation in a *symmetrical* turbulent component is increased by superimposed steady flow. This increase is given by a multiplicative factor

$$\left(1+\frac{\varepsilon^2}{2}\right)\sqrt{1-\varepsilon^2}+\frac{3}{2}\varepsilon\sin^{-1}\varepsilon \quad \text{for } |\varepsilon|\leqslant 1, \tag{21}$$

$$\frac{3\pi}{4}|\varepsilon| \quad \text{for } |\varepsilon|\geqslant 1 \tag{22}$$

if the component's K is independent of velocity. The Moody friction factor f_M depends on velocity, so a more complicated analysis must be used to estimate the dissipation of acoustic power in the straight portions of the pipe in the presence of superimposed steady flow. The appendix presents a derivation of expressions similar to Eqs. (18)–(20) taking the velocity dependence of f_M into account; the result is Eqs. (A11) and (A12).

B. Experiments with nonzero mean flow

To quantitatively test for $\dot{M}\neq 0$ as predicted in the previous subsection, we operated the loop with the valve open. The effect of the mean flow on wave shape and $p_{2,0}$ provided indirect measurements of $\dot{M}$, and the heat carried by $\dot{M}$ provided a nearly direct measure. The water-cooled pipes were most convenient for measurements of wave shape and $p_{2,0}$, because rapid equilibration to steady state enabled rapid data taking and because the spatial uniformity of temperature yielded more confidence in calculations of the wave. Measurements with the heated and insulated pipes were used to detect heat carried by $\dot{M}$.

With the valve open, the loop has the topology of a constricted annular resonator driven at one point, whose complicated behavior has been described by Muehleisen and Atchley.[40] Without constrictions or dissipation, the modes of such a resonator are degenerate: With the length of the loop equal to one wavelength, standing waves of any spatial phase and traveling waves of either direction satisfy the wave equation and share a single resonance frequency. Reference 40 shows that an area constriction eliminates the degeneracy, splitting the resonance into a ''high'' standing-wave mode and a ''low'' standing-wave mode. In the low mode, a velocity antinode is centered on the constriction, so the resonance frequency is reduced because of the increased inertance of the constriction. In the high mode, a pressure antinode is centered on the constriction, so the resonance frequency is increased by the reduced compliance of the constriction. In the present experiment, the gas diodes are constrictions, and the low mode is desired. The resonance condition described near Eq. (5) selects the low mode. Only 2 Hz higher in frequency, a weak local maximum in $|p_1|$ at the gas diodes suggests the presence of the high mode.

The steps at the gas diodes in the calculated curves for $\mathrm{Im}[p_1]$ and $p_{2,0}$ in Figs. 3(a) and 3(c) are based on Eqs. (19) and (10), respectively, with $S=S_{\mathrm{gd}}$ and $\dot{M}=0$. These steps, and all other features of the curves, are in qualitative agreement with the measured pressures. Figure 6 shows corresponding measurements and calculations for $\dot{M}\neq 0$, with the valve open at the top of the loop. The overall character of the wave is still that of a standing wave, as indicated by the cosine shape of $\mathrm{Re}[p_1]$ in Fig. 6(a), for which measured and calculated values are in good agreement. However, $\mathrm{Im}[p_1]$ changed dramatically when the valve was opened.

The solid lines in Figs. 6(a) and 6(b) represent the results of calculations using DeltaE, as described near the beginning of Sec. II and with the steady-flow phenomena calculated assuming that the mean and oscillatory components of the velocity are independent except at the gas diodes where they are linked through Eqs. (10) and (19). The dramatic disagreement between the experimental $\mathrm{Im}[p_1]$ and this calculation motivated us instead to model the Doppler effects (for which DeltaE cannot yet account) of opposite signs in the nearly equal counterpropagating traveling-wave components of the standing wave. In the Doppler model, implemented in a spreadsheet, we used

$$p_1=Ae^{-ik_+x}+Be^{ik_-x}, \tag{23}$$

$$U_1=\frac{iS}{\omega\rho_m}\left(1+im\frac{2\delta_\nu}{D}\right)(-ik_+Ae^{-ik_+x}+ik_-Be^{ik_-x}), \tag{24}$$

$$k_\pm=\frac{\omega}{a\pm\dot{M}/\rho S}\left(1-im\frac{[\delta_\nu+(\gamma-1)\delta_\kappa]}{D}\right), \tag{25}$$

where $k_\pm$ are the wave vectors for waves traveling with and against[41] the mean flow, A and B are the pressure amplitudes of those waves, δ_κ is the thermal penetration depth, and $i=\sqrt{-1}$. With $[\delta_\nu+(\gamma-1)\delta_\kappa]/D_{\mathrm{pipe}}=0.005$, the boundary-layer approximation used in Eqs. (23)–(25) is well justified. In the spreadsheet, the turbulence correction factor m is calculated according to the algorithm used in DeltaE[23] and described near Eq. (7.26) in Ref. 33, but with an additional correction due to the superimposed steady flow given in Eqs. (A15) and (A16). For laminar flow, $m=1$; for turbulent flow, $m>1$. In the Doppler-model spreadsheet, each of the four long runs of pipe was subdivided into eight pieces, and each gas-diode cone into two pieces; further subdivision did not change the results. Equations (23) and (24) were used for wave propagation in each such piece, with continuity of p_1 and U_1 joining solutions between pieces. As in the DeltaE calculation, Eq. (19) was used for the minor-loss contribution to δp_1 across the gas diodes and Eqs. (10), (A10), and the discussion in the paragraph following Eq. (15) were used to obtain $\dot{M}$. Complex U_1 at $x=0$ was used as an adjustable parameter to ensure that complex $p_1(0)=p_1(6.33\ \mathrm{m})$. The calculation's gas temperature, which was constant along the pipe, could also be adjusted slightly above the experimental value to enforce $\mathrm{Im}[U_1(0)]=\mathrm{Im}[U_1(6.33\ \mathrm{m})]$, corresponding to our operational definition of resonance, but this adjustment had a negligible effect. The result, shown as the dashed lines in Figs. 6(a) and 6(b), displays $\mathrm{Re}[p_1]$ and $\mathrm{Im}[p_1]$ in agreement with the experimental values. The agreement between this calculation and the measurements strongly suggests that the Doppler effect is primarily responsible for the large values of $\mathrm{Im}[p_1]$.

To consider this effect in more detail, notice that the measured $\mathrm{Im}[p_1]$ in Fig. 6(a) is not left-right antisymmetric; the depth of the minimum near $x=4.8$ m exceeds the height

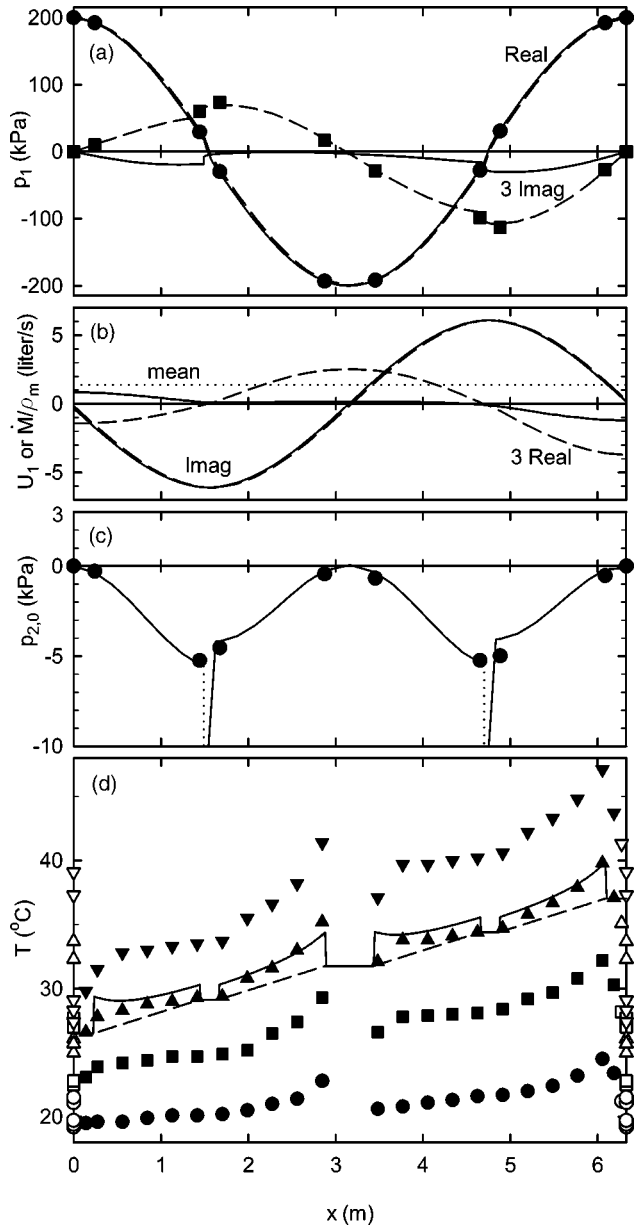

FIG. 6. (a)–(c) A typical wave, with 2.4-MPa argon at 48.1 Hz, using the water-cooled pipes and with the valve open to allow $\dot{M}\neq 0$. The two gas diodes were oriented to encourage flow in the positive-x direction, with their small ends toward smaller x. (a) Real and imaginary parts of the pressure wave as a function of position around the loop. Points are measured values and lines are calculations. (b) Calculated real, imaginary, and mean parts of the volume velocity. In (a) and (b), the standing-wave components are so much larger than the out-of-phase components that the latter have been multiplied by 3 for clarity. The zero of phase is chosen so that the pressure oscillations in the mixing chamber are real. (c) The time-averaged pressure as a function of position, relative to its value in the mixing chamber. Points are measured values and lines are calculations. The two vertical dotted lines are at the small-x, small-diameter ends of the gas diodes. (d) Temperature as a function of position around the loop, with the insulated pipes and the 2 W/°C insulation, under conditions similar to that of (a)–(c). Filled symbols are temperatures measured on the metal surface of the loop and open symbols are temperatures measured in the gas. Gas temperatures at $x=0$ and $x=6.33$ m are those at five locations in the mixing chamber. Circles, no electric heat. Squares, 79 W electric heat. Erect triangles, 167 W electric heat. Inverted triangles, 252 W electric heat. The curves represent calculated estimates corresponding to the erect triangles.

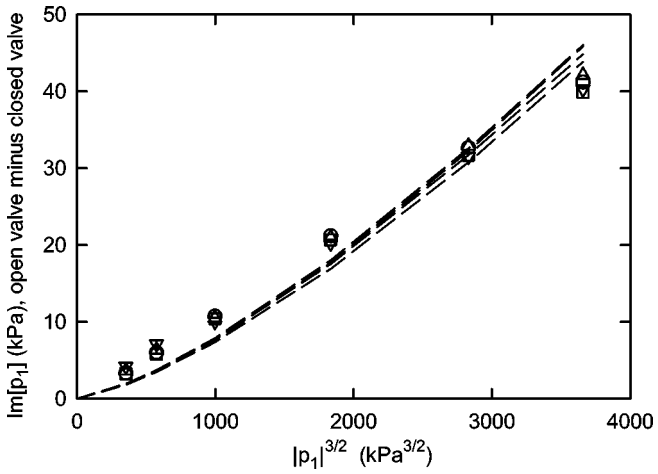

FIG. 7. The part of Im$[p_1]$ near the gas diodes that is associated with $\dot{M}\neq 0$, as a function of the amplitude of the wave. The horizontal axis is the amplitude of the pressure oscillation in the mixing chamber, raised to the 3/2 power. The four sets of symbols (measurements) and the four curves (calculations) correspond to the four pressure transducers closest to the two gas diodes. The measurements were taken with the water-cooled pipes.

of the maximum near $x=1.6$ m. This downward shift resembles that of the $\dot{M}=0$ data in Fig. 3(a), where Im$[p_1]$ <0 is associated with the flow of acoustic power into the loop from both ends. To more clearly distinguish the effect of $\dot{M}\neq 0$ from that of the acoustic power flow, in Fig. 7 we display the difference between $\dot{M}\neq 0$ and $\dot{M}=0$ measurements of Im$[p_1]$ at the four pressure transducers closest to the two gas diodes, at five different pressure amplitudes. The subtraction brings the results at the four transducers into agreement with one another, and plotting these against the 3/2 power of the wave amplitude yields a reasonably straight line. We do not understand why $\dot{M}\neq 0$ should contribute to Im$[p_1]$ in proportion to the 3/2 power of the wave amplitude.

Our spreadsheet-based Doppler calculations, also displayed in Fig. 7, show the difference between Im$[p_1]$ when $\dot{M}\neq 0$ and $\dot{M}=0$ more nearly proportional to the square of the wave amplitude. The difference between calculated and measured Im$[p_1]$ in Fig. 7 might simply be due to $\dot{M}$ depending on physics that we do not understand. However, one other candidate is apparent: Both the calculations and the measurements for $\dot{M}\neq 0$ displayed a remarkably strong dependence of Im$[p_1]$ on frequency as frequency was changed away from resonance. Both rose with frequency; measured values rose about 30% per Hz and calculated values about 40% per Hz. Hence, some of the difference between calculations and measurements in Fig. 7 could be a small amplitude-dependent error or ambiguity about what really constitutes resonance frequency or what gas temperature should be used in the calculations.

With such an imperfect understanding of Im$[p_1]$, we cannot be confident in the accuracy of Re$[U_1]$ in Fig. 6(b). However, Re$[p_1]$ appears to be well understood, and hence we should have confidence in the calculation of Im$[U_1]$ $\propto d\,\mathrm{Re}[p_1]/dx$, which is the dominant part of the volume-velocity wave. The time-averaged pressure difference across the gas diodes and the resulting mean flow are due to $|U_1|^2$

TABLE I. Contributions to $p_{2,0}$ in Fig. 6.

	Each	×mult=	net
Reversible:			
Pipe, Eq. (1)	±5.0 kPa	×2=	0.00 kPa
Cones, Eq. (1)	±10.0 kPa	×2=	0.00 kPa
Irreversible:			
Gas diodes	+1.68 kPa	×2=	+3.36 kPa
Pipe			−2.30 kPa
Cones	−0.28 kPa	×2=	−0.56 kPa
Elbows	−0.085 kPa	×4=	−0.34 kPa
Exit to mix. ch.			−0.16 kPa
Total:			0.00 kPa

at the gas diodes, where $\mathrm{Re}[U_1]$ is negligible.

Hence, uncertainty about $\mathrm{Im}[p_1]$ in Fig. 6(a) has a negligible effect on the calculated curve for $p_{2,0}$ in Fig. 6(c). The measured and calculated values of $p_{2,0}$ are in reasonable agreement. Table I shows the magnitudes of various contributions to the calculated curve. As in Fig. 3(c), the largest contributor is the reversible effect expressed by Eq. (1), so the agreement between measurements and calculations in that aspect of Fig. 6(c) strengthens confidence in our knowledge of $|U_1|$. The steps in $p_{2,0}$ at the gas diodes are smaller than they were in Fig. 3(c), reflecting the ε dependence in Eq. (10). The measured steps at the gas diodes appear significantly smaller than the calculations.

Closer examination of the time-averaged pressure difference across the gas diodes was challenging. Initially, the transducers closest to the gas diodes were simply installed in the pipes with their tips retracted slightly from the pipe inner surface, as suggested in Ref. 42. The most linear transducers were selected from our inventory, so that time-averaged voltage would have no significant contribution from oscillating pressure interacting with transducer nonlinearity;[42] we estimate that this effect is less than 10 Pa for any conditions encountered in these measurements. Nevertheless, following the measurement procedure described just above Eq. (1) and swapping transducers from place to place showed systematic errors as large as 0.7 kPa. We suspected that the temperature dependence of the transducers' offset voltages might be responsible, because the sensing element of the transducer might be at one temperature when the sound was on and another when it was off. Hence, we separated the transducers from the pipe by the 4 cm capillaries described in Sec. II. (The end-to-end time-averaged pressure difference in each capillary, due to nonlinear acoustics in the capillary and minor losses at its ends,[42] is estimated to be <5 Pa.) We also reduced the transducer bias voltage to 2.5 V instead of the manufacturer's recommended 10 V in a further attempt to keep the transducers near room temperature whether the sound wave was on or off. From among our most linear transducers, we also selected two with the lowest offset-voltage temperature dependence and used them for all measurements. Despite these efforts, swapping transducers from place to place and repeating experimental conditions suggests that a systematic error of ~0.2 kPa remains. (Random uncertainty associated with reading the voltmeter is ~0.1 kPa.)

With all these instrumental precautions, measurements of the time-averaged pressure differences across the gas diodes are shown in Fig. 8 as a function of the square of the wave amplitude. Filled symbols represent measurements with the valve closed; open symbols, the valve open. Pairs of data with the same symbols indicate a top-to-bottom interchange of the transducers, all other conditions being equal, displaying a lower bound of ~0.2 kPa on the remaining systematic uncertainty in the measurements.

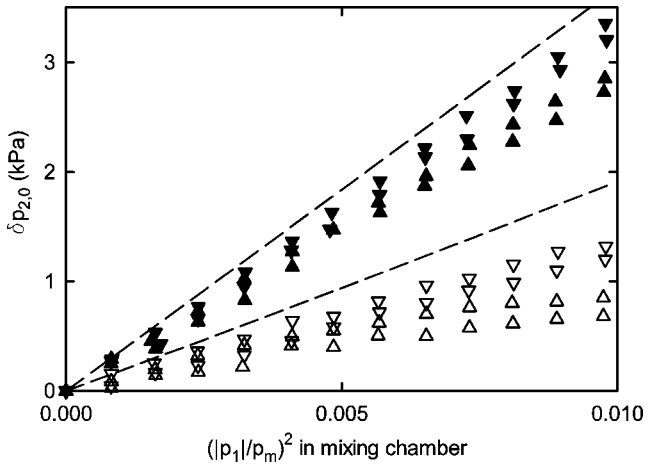

FIG. 8. Time-averaged pressure difference across the gas diodes as a function of the normalized square of the amplitude of the oscillating pressure in the mixing chamber. Filled symbols, valve closed. Open symbols, valve open. Erect triangles, gas diode near $x=1.6$ m. Inverted triangles, gas diode near $x=4.8$ m. Lines, corresponding calculations using Eq. (10) (plus, for the lower line, the small calculated steady-flow pressure difference across the cone and pipe segments between the pressure transducers).

The line in Fig. 8 corresponding to the $\dot{M}=0$ measurements was calculated using Eq. (10). The line corresponding to the $\dot{M}\neq 0$ measurements is the calculated value of $\delta p_{2,0}$ between the pressure transducers nearest to the gas diode, which is mostly due to Eq. (10) but with a typically 20% contribution from the impedance of the cone to steady flow. The quadratic dependence of $\delta p_{2,0}$ on $|p_1|$ in Fig. 8 corresponds to the quadratic dependence of $\delta p_{2,0}$ on $|U_1|$ in Eq. (10). However, the experimental magnitudes are significantly less than those predicted by Eq. (10) with the values for K_- and K_+ given below Eq. (11). Distracted for weeks by systematic errors arising from transducer imperfections, we did not at first recognize that this significant disagreement probably arises from an important hydrodynamic phenomenon. The time-averaged pressure change across the small end of each diode, indicated by the dotted vertical line segments in Figs. 3(c) and 6(c), is not sharply localized at the end of the diode. The pressure transducer 4.8 cm from the small end of the diode is actually located within the pressure-change zone. Subsequent measurements with the transducer 1.3 cm from the small end of the diode yielded measured $\delta p_{2,0}$ almost twice as large, and moving the transducer to 8.3 cm away from the end of the diode reduced the measured $\delta p_{2,0}$ significantly. This entire range of locations is probably within the zone of vortex formation, lateral spatial nonuniformity, and pressure recovery when the gas flows out of the small end of the diode, because these locations are within the gas stroke lengths $2|U_1|/\omega S_{\mathrm{gd}}=25$ cm and $2|U_1|/\omega S_{\mathrm{pipe}}=10$ cm.

Tentative conclusions can be drawn from Fig. 8 despite these uncertainties. The time-averaged pressure difference across the gas diodes is smaller with the valve open than with the valve closed, corresponding to the calculated reduction arising from $\varepsilon \neq 0$ in Eq. (10). The measured and calculated closed-open differences are in quantitative agreement, suggesting that the measured closed-open pressure difference might be a useful, quantitative measure of $\dot{M} \neq 0$ via the ε dependence in Eq. (10). However, the gas diode near $x = 4.8$ m was always stronger than the diode near $x = 1.6$ m. Swapping diodes, pipes, and/or transducers indicated that this phenomenon was not an artifact of hardware imperfections; it was associated with the diodes' locations and orientations in the acoustic wave. This is evidence of behavior beyond the quasi-steady approximation.

While Figs. 7 and 8 show indirect, pressure-based evidence of nonzero mass flow around the loop when the valve is open, temperature-based measurements such as shown in Fig. 6(d) provide direct evidence. Figure 6(d) shows typical appearances of measurements of temperature as a function of position around the loop with $\dot{M} \neq 0$. The temperature rises as the gas moves around the loop in the positive-x direction, receiving more and more heat from the electric heaters and from dissipation of acoustic power. For the erect triangles, two curves roughly illustrate the physics that we believe is most important for the appearance of the data. The dashed curve shows a rough estimate of the gas temperature as a function of x. Its slope is nonzero in the four electrically heated regions of the loop and is zero in the unheated regions near the ends of the loop, the valve, and the gas diodes. However, the measurements of temperature were made on the metal pipe, not in the gas; the difference between the pipe and gas temperatures must be proportional to the local rate of heat transfer from pipe to gas and inversely proportional to the local pipe-to-gas heat-transfer coefficient. The solid curve in Fig. 6(d) shows a rough estimate of the pipe temperature, calculated using a Nusselt number[14] of $0.02[N_R(x)]^{0.8}$, with the Reynolds number N_R based on the square root of the sum of the squares of the mean velocity and the x-dependent rms oscillatory velocity. This rough estimate seems to capture the main qualititative features of the data, presumably because the heat-transfer coefficient is highest near the gas diodes where the oscillatory velocity is highest.

The symbols in Fig. 9 represent steady flows inferred from data such as those in Fig. 6(d), independent of the details of the pipe-to-gas heat-transfer model. These mass flows are obtained from $\dot{Q} = \dot{M} c_p \Delta T$, where $c_p = 520$ J/kg °C is the isobaric specific heat of argon and $\dot{Q}$ and ΔT are the heat input and temperature rise obtained from measurements. $\dot{Q}$ is the electric power applied to the loop, minus an estimate of the heat leak through the insulation, plus an estimate of the acoustic power dissipated in the loop. The heat-leak correction varied from 8% to 20% for most of the data, but was 25% and 38% for the points at 50 and 25 kPa, respectively. The acoustic-power correction varied from 1% at the lowest amplitude through 10%–20% in the middle amplitudes to 30% and 60% for the measurements at 227 and 238 kPa,

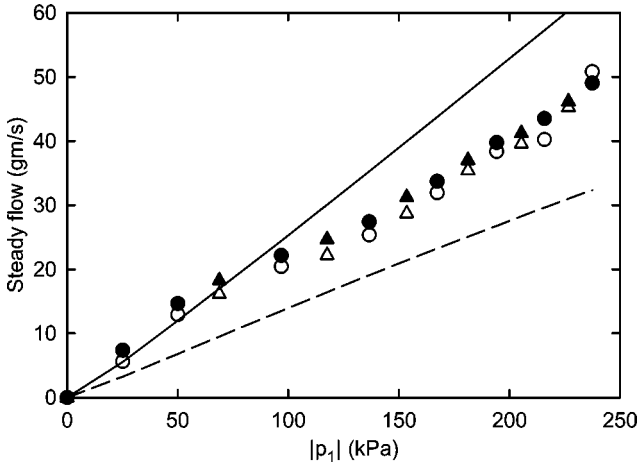

FIG. 9. Mass flow around the loop as a function of pressure amplitude in the mixing chamber. Symbols are based on measured electric heat and temperature rise, with the insulated pipes and the 1.15 W/°C insulation. Lines represent calculations, based on two different sets of assumptions.

respectively. This correction used the measured piston power, with an estimate of the small dissipation due to blowby and heat-exchanger impedance subtracted. The circles in Fig. 9 represent measurements with the loop average temperature in the range 43–47 °C and the temperature rise around the loop in the range 13–17 °C. The triangles represent measurements with higher heats and temperatures, with the loop average temperature in the range 57–60 °C and the temperature rise around the loop in the range 20–24 °C. Hence, the acoustic-power correction was a much larger fraction of the total power for the circles than for the triangles, and the fact that these two sets of measurements are well aligned in Fig. 9 indicates that the acoustic-power correction is not unreasonable. The open symbols in Fig. 9 are based on the full power as described above and the full temperature rise around the loop from $x = 0.14$ m to $x = 6.19$ m, using thermocouples that were not on the electrically heated portions of the loop. The filled symbols are based on half of the power and a temperature rise equal to the difference between the average temperature of thermocouples in the range 3.5 m$\leqslant x \leqslant$6.1 m and those in the range 0.3 m$\leqslant x \leqslant$2.8 m. The highest measured mass flow is 50 gm/s. The total mass of argon in the loop is only 95 gm, so the mean flow clears the entire loop every 2 s at the highest acoustic amplitude.

The two lines in Fig. 9 are two attempts to model the mass flow as a function of amplitude. The solid line represents the results of calculations assuming that the mean flow and the acoustic oscillations are independent, except at the gas diodes where Eq. (10) couples them. The resistance of the loop to mean flow is calculated using Eq. (15), a similar expression for the cone resistance, and small additions for the elbows and the mixing-chamber entrance. Thus, the solid line corresponds to the solid curves in Fig. 6. This calculation overestimates the mean flow, so it must overestimate the strength of the diodes or underestimate the mean-flow resistance of the rest of the loop. The dashed curve represents calculations also using Eq. (10) for the gas diodes but taking more complicated interactions between the steady and oscil-

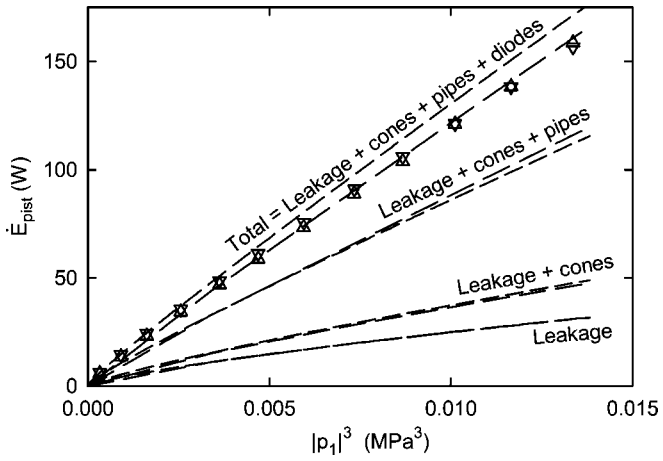

FIG. 10. Acoustic power as a function of the cube of the pressure amplitude in the mixing chamber. Symbols are measured acoustic power delivered by the piston. Experimental uncertainties are about 2%. Erect triangles, valve open; inverted triangles, valve closed. Lines are calculated acoustic power dissipation due to several sources. Short dashed lines, valve closed; long dashed lines, valve open.

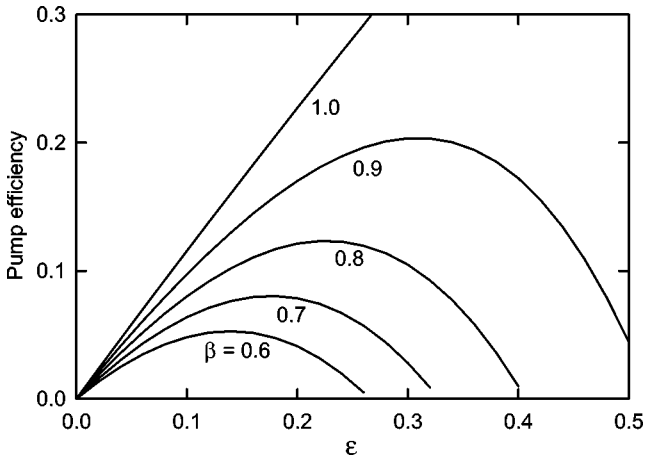

FIG. 11. The calculated energy efficiency of the gas-diode pump as a function of $\varepsilon = \dot{M}/\rho_m|U_1|$ and $\beta = (K_- - K_+)/(K_- + K_+)$.

lating flows into account elsewhere, including the Doppler effect of the mean flow on the oscillations and the enhancement of the mean-flow resistance by the oscillations as described in the appendix. This calculation underestimates the mean flow, so it is likely that the derivation in the appendix overestimates the effect of the oscillations on the mean-flow resistance.

C. Acoustic power consumption

Measurements of the acoustic power delivered by the piston, $\dot{E}_{\text{pist}}$, are shown in Fig. 10. The data are plotted as a function of the cube of the pressure amplitude, because Eq. (19) indicates that the acoustic power consumed by the diodes is proportional to the cube of the volume-velocity amplitude and the turbulent dissipation of acoustic power in the pipes, as in Eqs. (A11) and (A12), would be proportional to the cube of the volume-velocity amplitude if f_M were independent of velocity. The data fall on a curve that is slightly concave downwards, indicating a dependence on amplitude slightly weaker than the cubic. Measured piston power with $\dot{M}=0$ is indicated by the inverted triangles, and $\dot{M}\neq 0$ is indicated by the erect triangles.

Two sets of curves in Fig. 10 represent the results of calculations using the Doppler mathematics with Eq. (19) for the dissipation of acoustic power by the diodes and Eqs. (A11) and (A12) for the dissipation of acoustic power in the pipes. Although the total calculated power is in reasonable agreement with the measured power, the calculations show a significant difference in piston power between $\dot{M}=0$ and $\dot{M}\neq 0$ that was not observed. The difference in the calculated values arises from the dependence of Eq. (19) on $\dot{M}$; the diode should require less acoustic power when $\dot{M}\neq 0$. We do not understand why this difference does not appear in the measurements.

It is natural to consider the efficiency of an isolated gas diode as a pump. The power that it delivers to the mean flow is $\delta p_{2,0}^{\text{gd}}\dot{M}/\rho_m$, while the power it consumes is $\Delta\dot{E}_{\text{gd}}$. The ratio of these, obtained from Eqs. (10) and (19), is the efficiency of the pump itself, shown in Fig. 11. (The efficiency of the entire circulating system, where the heat-transfer surface area necessarily consumes additional acoustic power, is lower.) Equations (10) and (19) show that the pump efficiency is a function only of ε and of $\beta=(K_- - K_+)/(K_- + K_+)$. For the experiments described here, $\varepsilon\sim 0.2$ and $\beta = 0.80$, so the efficiency is only about 10%. It seems likely that gas diodes with β as high as about 0.90 are possible, yielding efficiencies as high as 20%.

Figure 11 indicates the importance of working near the optimal ε. For a given, desired $\dot{M}$ and a given $|p_1|$ at the trunk, this specifies the pipe area. Minimizing mean-flow and acoustic losses then suggests a single pipe with circular cross section. If the pipe area is large, the gas diode itself can consist of a plate with many conical holes in parallel, so that their taper angle can remain narrow while their length is short. Considerations of heat-transfer surface area and acoustic techniques to minimize dissipation[43] may call for x-dependent cross-sectional area along the pipe and for subdivision of parts of the loop into several parallel pipes.

IV. CONCLUSIONS

Gas diodes properly located in a resonant loop of piping can cause a substantial mean flow, which in turn can carry substantial heat. For example, near $\dot{M}=50$ gm/s this loop carried 400 W of heat from the electric heaters to the mixing chamber, the gas temperature rising only 25 °C along the circumference of the loop. Helium is more commonly used than argon in thermoacoustic and Stirling engines and refrigerators. Straightforward similitude scaling[44] of the 50 gm/s operating point to a 3 MPa, 80 Hz helium loop with total length 12.6 m and pipe diameter 4.4 cm shows that with the same temperature profile it would carry 6 kW, an order of magnitude that is of interest for many potential applications.

Whether this concept will find use in such applications will depend in part on economic trade-offs between the low fabrication costs and high reliability of this design and the lower acoustic power consumption of traditional heat ex-

changers. However, engineering design based on the ideas presented here is already showing ways to reduce the acoustic power consumption without compromising simplicity.[45]

The steady flow created by gas diodes in a resonant loop can be detected by its effect on the acoustic wave and on time-average pressure, as well as by the heat that it carries. The quasi-steady approximation yields results in rough agreement with such measurements. However, many interesting fundamental questions and areas for further research remain. The mutual influence of turbulent mean and oscillatory flows is a theoretical and experimental challenge; the quasi-steady approximation used here is clearly inadequate. Near the diodes, dense arrays of better pressure transducers will illuminate interesting physics of vortex rollup, dissipation, and pressure recovery at the small end of the diode and will answer very basic questions such as what angle suffices to prevent separation in the cone for flow out of the large end of the diode. Also, details of the three-dimensional mean and oscillatory velocity fields in the mixing chamber, and the associated dependence of temperature on position and time, promise to be very interesting to explore and to understand in a way that leads to uniform heat transfer to or from the face of a stack or regenerator.

ACKNOWLEDGMENTS

This work was supported by OBES/DMS in the U.S. Department of Energy's Office of Science. We thank Barton Smith and Konstantin Matveev for helpful conversations and David Gardner for practical contributions.

APPENDIX: QUASI-STEADY APPROXIMATION WITH REYNOLDS-DEPENDENT FRICTION FACTOR

To account for superimposed turbulent steady flow and turbulent oscillatory flow in a pipe of diameter D and cross-sectional area S in the quasi-steady approximation, the dependence of the Moody friction factor f_M on velocity should be taken into account.

If the volume flow rate U and hence the Reynolds number N_R vary sinusoidally in time, without an additive constant, then the instantaneous friction factor $f_M(t)$ has a complicated time dependence, which has been approximated[23,33] by using a Taylor-series expansion around the peak Reynolds number $|N_{R,1}|$

$$f_M(t) \simeq f_M + \frac{df_M}{dN_R}|N_{R,1}|(|\sin\omega t| - 1), \tag{A1}$$

where df_M/dN_R and f_M on the right side are evaluated at the peak Reynolds number. Integrating the instantaneous power dissipation over a full cycle yields the time-averaged dissipation of acoustic power per unit length arising from $\frac{1}{2}\mathrm{Re}[(dp_1/dx)\tilde{U}_1]$

$$\frac{d\dot{E}}{dx} = -\frac{2\rho_m|U_1|^3}{3\pi DS^2}\left[f_M - \left(1 - \frac{9\pi}{32}\right)|N_{R,1}|\frac{df_M}{dN_R}\right], \tag{A2}$$

where f_M and df_M/dN_R are evaluated at the peak Reynolds number $|N_{R,1}|$. (Note that df_M/dN_R is negative.)

It is straightforward to extend this approach to the present case of superimposed steady and oscillatory flow, for which

$$U(t) = \dot{M}/\rho_m + |U_1|\sin\omega t. \tag{A3}$$

The time-dependent friction factor is written as

$$f_M(t) \simeq f_{M,\max} + \frac{df_M}{dN_R}N_{R,\max}\left(\frac{|\dot{M}/\rho_m + |U_1|\sin\omega t|}{|\dot{M}/\rho_m| + |U_1|} - 1\right), \tag{A4}$$

where $f_{M,\max}$ and df_M/dN_R are evaluated at the maximum Reynolds number

$$N_{R,\max} = \frac{(|\dot{M}/\rho_m| + |U_1|)D\rho_m}{S\mu}. \tag{A5}$$

Then the instantaneous pressure gradient is taken to be

$$\frac{dp}{dx} = \pm f_M(t)\frac{\rho_m}{2D}\frac{[U(t)]^2}{S^2} \tag{A6}$$

with the sign chosen so that the pressure gradient opposes the flow at that instant. The time-averaged pressure gradient is obtained by evaluating

$$\frac{dp_{2,0}}{dx} = \frac{\omega}{2\pi}\int_0^{2\pi/\omega}\frac{dp}{dx}dt \tag{A7}$$

and the dissipation of acoustic power per unit length is obtained by evaluating

$$\frac{d\dot{E}}{dx} = \frac{\omega}{2\pi}\int_0^{2\pi/\omega}\frac{dp}{dx}|U_1|\sin\omega t\, dt. \tag{A8}$$

The integrations are performed piecewise between the zero crossings of $U(t)$ if they exist, as in Eqs. (8) and (17). With $\varepsilon = \dot{M}/\rho_m|U_1|$, the results are

$$\frac{dp_{2,0}}{dx} = -\mathrm{sign}(\varepsilon)\frac{\dot{M}^2}{2\rho_m DS^2}\left[\left(1 + \frac{1}{2\varepsilon^2}\right)f_{M,\max} - \frac{2\varepsilon^2 - 2|\varepsilon| + 1}{2\varepsilon^2(1+|\varepsilon|)}\frac{df_M}{dN_R}N_{R,\max}\right], \quad |\varepsilon| \geqslant 1 \tag{A9}$$

$$= -\mathrm{sign}(\varepsilon)\frac{\dot{M}^2}{2\rho_m DS^2}\left[\frac{(1+2\varepsilon^2)\sin^{-1}|\varepsilon| + 3|\varepsilon|\sqrt{1-\varepsilon^2}}{\pi\varepsilon^2}f_{M,\max} + \frac{\pi|\varepsilon|(3/2+\varepsilon^2) - 3|\varepsilon|(1+|\varepsilon|)\sqrt{1-\varepsilon^2} - (1+|\varepsilon|)(1+2\varepsilon^2)\sin^{-1}|\varepsilon|}{\pi\varepsilon^2(1+|\varepsilon|)}\frac{df_M}{dN_R}N_{R,\max}\right], \quad |\varepsilon| \leqslant 1 \tag{A10}$$

and

$$\frac{d\dot{E}}{dx} = -\frac{\rho_m |U_1|^3}{2DS^2}\left[|\varepsilon| f_{M,\max} + \frac{(3-2|\varepsilon|)(1-2|\varepsilon|)}{8(1+|\varepsilon|)} \frac{df_M}{dN_R} N_{R,\max}\right], \quad |\varepsilon| \geqslant 1 \tag{A11}$$

$$= -\frac{2\rho_m |U_1|^3}{3\pi DS^2}\left\{\left[\left(1+\frac{\varepsilon^2}{2}\right)\sqrt{1-\varepsilon^2} + \frac{3}{2}\varepsilon \sin^{-1}\varepsilon\right] f_{M,\max} - \left[\left(1+\frac{\varepsilon^2}{2}\right)\sqrt{1-\varepsilon^2} + \frac{3}{2}\varepsilon \sin^{-1}\varepsilon - \frac{9\pi}{32}\frac{1+4\varepsilon^2}{1+|\varepsilon|}\right] \times \frac{df_M}{dN_R} N_{R,\max}\right\}, \quad |\varepsilon| \leqslant 1. \tag{A12}$$

Equations (A9)–(A12) reduce to Eqs. (13), (14) and (18)–(20) for $df_M/dN_R = 0$ if $f_M\, dx/D$ is associated with K. Equation (A12) reduces to Eq. (A2) if $\varepsilon = 0$.

Viscous power dissipation can be written as $d\dot{E}/dx = -r_\nu |U_1|^2/2$, where r_ν is the resistance per unit length, suggesting that Eqs. (A11)–(A12) should be expressed as

$$r_{\nu,\mathrm{turb}} = \frac{\rho_m |U_1|}{DS^2}\left[|\varepsilon| f_{M,\max} + \frac{(3-2|\varepsilon|)(1-2|\varepsilon|)}{8(1+|\varepsilon|)} \frac{df_M}{dN_R} N_{R,\max}\right], \quad |\varepsilon| \geqslant 1 \tag{A13}$$

$$= \frac{4\rho_m |U_1|}{3\pi DS^2}\left\{\left[\left(1+\frac{\varepsilon^2}{2}\right)\sqrt{1-\varepsilon^2} + \frac{3}{2}\varepsilon \sin^{-1}\varepsilon\right] f_{M,\max} - \left[\left(1+\frac{\varepsilon^2}{2}\right)\sqrt{1-\varepsilon^2} + \frac{3}{2}\varepsilon \sin^{-1}\varepsilon - \frac{9\pi}{32}\frac{1+4\varepsilon^2}{1+|\varepsilon|}\right] \times \frac{df_M}{dN_R} N_{R,\max}\right\}, \quad |\varepsilon| \leqslant 1. \tag{A14}$$

When this is compared to the equivalent result for laminar flow in the boundary-layer approximation,[33] it is apparent that this model of turbulence multiplies the power dissipation $d\dot{E}/dx$ and the resistance per unit length by a factor

$$m = \frac{\delta_\nu N_{R,\max}}{4D}\left[|\varepsilon| f_{M,\max} + \frac{(3-2|\varepsilon|)(1-2|\varepsilon|)}{8(1+|\varepsilon|)} \frac{df_M}{dN_R} N_{R,\max}\right], \quad |\varepsilon| \geqslant 1 \tag{A15}$$

$$= \frac{\delta_\nu N_{R,\max}}{3\pi D}\left\{\left[\left(1+\frac{\varepsilon^2}{2}\right)\sqrt{1-\varepsilon^2} + \frac{3}{2}\varepsilon \sin^{-1}\varepsilon\right] f_{M,\max} - \left[\left(1+\frac{\varepsilon^2}{2}\right)\sqrt{1-\varepsilon^2} + \frac{3}{2}\varepsilon \sin^{-1}\varepsilon - \frac{9\pi}{32}\frac{1+4\varepsilon^2}{1+|\varepsilon|}\right] \times \frac{df_M}{dN_R} N_{R,\max}\right\}, \quad |\varepsilon| \leqslant 1. \tag{A16}$$

At low enough velocities, $m \to 1$; at lower velocities the flow is laminar. The $m = 1$ boundary between the laminar and turbulent zones occurs roughly at

$$|N_{R,\max}| \simeq 2000 \quad \text{for } D/\delta_\nu < 4, \tag{A17}$$

$$\frac{|N_{R,\max}|}{D/\delta_\nu} \simeq 500 \quad \text{for } D/\delta_\nu > 4. \tag{A18}$$

[1] G. Walker, *Stirling Engines* (Clarendon, Oxford, 1960).
[2] J. R. Senft, *Ringbom Stirling Engines* (Oxford University Press, Oxford, 1993).
[3] G. Walker, *Cryocoolers* (Plenum, New York, 1983).
[4] Ivo Kolin, *The Evolution of the Heat Engine* (Longman, London, 1972).
[5] R. Radebaugh, "A review of pulse tube refrigeration," Adv. Cryog. Eng. **35**, 1191–1205 (1990).
[6] G. W. Swift, "Thermoacoustic engines," J. Acoust. Soc. Am. **84**, 1145–1180 (1988).
[7] I. Urieli and D. M. Berchowitz, *Stirling Cycle Engine Analysis* (Hilger, Bristol, UK, 1984).
[8] C. M. de Blok, "Thermoacoustic system," Dutch Patent: International Application No. PCT/NL98/00515. US Patent No. 6,314,740 (13 November 2001).
[9] T. Yazaki, A. Iwata, T. Maekawa, and A. Tominaga, "Traveling wave thermoacoustic engine in a looped tube," Phys. Rev. Lett. **81**, 3128–3131 (1998).
[10] S. Backhaus and G. W. Swift, "A thermoacoustic-Stirling heat engine: Detailed study," J. Acoust. Soc. Am. **107**, 3148–3166 (2000).
[11] G. W. Swift, D. L. Gardner, and S. Backhaus, "Acoustic recovery of lost power in pulse tube refrigerators," J. Acoust. Soc. Am. **105**, 711–724 (1999).
[12] J. Wurm, J. Kinast, T. Roose, and W. Staats, *Stirling and Vuilleumier Heat Pumps* (McGraw–Hill, New York, 1991).
[13] K. M. Godshalk, C. Jin, Y. K. Kwong, E. L. Hershberg, G. W. Swift, and R. Radebaugh, "Characterization of 350 Hz thermoacoustic driven orifice pulse tube refrigerator with measurements of the phase of the mass flow and pressure," Adv. Cryog. Eng. **41**, 1411–1418 (1996).
[14] F. P. Incropera and D. P. DeWitt, *Introduction to Heat Transfer*, 2nd ed. (Wiley, New York, 1990).
[15] M. P. Mitchell, "Pulse tube refrigerator," US Patent No. 5,966,942, 19 October 1999; continuation in part 6,109,041, 29 August 2000.
[16] N. Tesla, "Valvular conduit," US Patent No. 1,329,559 (3 February 1920).
[17] A. Petculescu and L. A. Wilen, "Oscillatory flow in jet pumps: Nonlinear effects and minor losses," J. Acoust. Soc. Am. **113**, 1282–1292 (2003).
[18] What acousticians call the volume velocity is known as the volume flow rate in fluid mechanics. Its dimensions are volume per unit time.
[19] Size 16 (1 in.) VCO Couplings, Swagelok Company, Solon OH, www.swagelok.com.
[20] Endevco, San Juan Capistrano, CA.
[21] Model SR830, Stanford Research Systems, Sunnyvale CA, www.srsys.com.
[22] Consistent with Ref. 33, this article uses notation such as $p(t) = p_m + \mathrm{Re}[p_1 e^{i\omega t}] + p_{2,0} + \mathrm{Re}[p_{2,2} e^{i2\omega t}] + \ldots$ for time-dependent variables. The subscript "m" indicates a mean value that exists independent of the wave. The subscript "2,0" indicates a second-order, time-averaged correction to the mean value, caused by the wave.
[23] W. C. Ward and G. W. Swift, "Design environment for low amplitude thermoacoustic engines (DeltaE)," J. Acoust. Soc. Am. **95**, 3671–3672 (1994). Software and user's guide available either from the Los Alamos thermoacoustics web site at www.lanl.gov/thermoacoustics/ or from the Energy Science and Technology Software Center, U.S. Department of Energy, Oak Ridge, TN.
[24] T. G. Wang and C. P. Lee, "Radiation pressure and acoustic levitation," in *Nonlinear Acoustics*, edited by M. F. Hamilton and D. T. Blackstock (Academic, New York, 1998), pp. 177–205.
[25] L. D. Landau and E. M. Lifshitz, *Fluid Mechanics* (Pergamon, New York, 1982), Sec. 64.
[26] R. W. Fox and A. T. McDonald, *Introduction to Fluid Mechanics* (Wiley, New York, 1985).
[27] Model SRFG-348/5 rectangular silicone rubbber heaters, Omega Engineering, Stamford, CT, www.omega.com.
[28] Ohio Semitronics, Hilliard, OH.
[29] Model C2, Clever Fellows Innovation Consortium, Inc., Troy, NY, www.cficinc.com.
[30] Schaevitz Model 500 HR, Measurement Specialties, Inc., Fairfield, NJ, www.schaevitz.com.

[31] A. M. Fusco, W. C. Ward, and G. W. Swift, ''Two-sensor power measurements in lossy ducts,'' J. Acoust. Soc. Am. **91**, 2229–2235 (1992).
[32] I. E. Idelchik, *Handbook of Hydraulic Resistance*, 3rd ed. (Begell House, New York, 1994).
[33] G. W. Swift, *Thermoacoustics: A Unifying Perspective for some Engines and Refrigerators* (Acoustical Society of America, Sewickley, PA, 2002).
[34] V. L. Streeter, *Handbook of Fluid Dynamics* (McGraw–Hill, New York, 1961).
[35] B. L. Smith and A. Glezer, ''The formation and evolution of synthetic jets,'' Phys. Fluids **10**, 2281–2297 (1998).
[36] B. L. Smith and G. W. Swift, ''Power dissipation and time-averaged pressure in oscillating flow through a sudden area change,'' J. Acoust. Soc. Am. **113**, 2455–2463 (2003).
[37] Indeed, we *did* originally expect this, until experimental results induced us to consider the question more carefully.
[38] Equation (19), with the choices for K_+ and K_- described below Eq. (11), account for minor-loss effects at the small ends of the gas diodes, but not for the surface-induced friction factor in the conical portions.
[39] In US Patent No. 6,637,211, 28 October 2003, ''Circulating heat exchangers for oscillating wave engines and refrigerators,'' by G. W. Swift and S. N. Backhaus, Eqs. (4) and (5) are incorrect. Equations (16) and (17) here give the correct definition of acoustic power for a volume velocity equal to the sum of a time-independent term and a sinusoidal term.
[40] R. T. Muehleisen and A. A. Atchley, ''Fundamental azimuthal modes of a constricted annular resonator: Theory and measurement,'' J. Acoust. Soc. Am. **109**, 480–487 (2001).
[41] P. M. Morse and K. U. Ingard, *Theoretical Acoustics* (McGraw–Hill, New York, 1968).
[42] B. L. Smith and G. W. Swift, ''Measuring second-order time-average pressure,'' J. Acoust. Soc. Am. **110**, 717–723 (2001).
[43] T. J. Hofler, ''Thermoacoustic refrigerator design and performance,'' Ph.D. thesis, Physics department, University of California, San Diego, 1986.
[44] J. R. Olson and G. W. Swift, ''Similitude in thermoacoustics,'' J. Acoust. Soc. Am. **95**, 1405–1412 (1994).
[45] The thermoacoustic-Stirling engine described in Ref. 10 is now operating with a half-wavelength, one-diode hot heat transfer loop in place of its original internal electric-resistance hot heat exchanger. The performance of this hardware is described in ''A self-circulating heat exchanger for use in Stirling and thermoacoustic-Stirling engines,'' S. Backhaus and R. S. Reid, in preparation for the Space Technology International Forum 2005.

Modeling of viscous damping of perforated planar microstructures. Applications in acoustics

Dorel Homentcovschi[a] and Ronald N. Miles
Department of Mechanical Engineering, SUNY Binghamton, New York 13902-6000

(Received 12 February 2004; revised 14 July 2004; accepted 19 July 2004)

The paper contains an analysis of the viscous damping in perforated planar microstructures that often serve as backplates or protecting surfaces in capacitive microsensors. The focus of this work is on planar surfaces containing an offset system of periodic oval holes or its limit cases: a system of circular holes or of slits. The viscous damping is calculated as the sum of squeeze film and the holes' resistances. The optimum number of holes is determined which minimizes the total viscous damping for a given percentage of open area. Graphs and formulas are provided for designing these devices. In the case the open area is higher than 15% the numerical results show that the influence of the holes' geometry (circular or oval) has a slight influence on viscous damping. As the planar structures containing oval holes assure a better protection against dust particles and water drops, they should be preferred in designing protective surfaces for microphones working in a natural environment. The obtained results also can be applied in designing other MEMS devices that use capacitive sensing such as accelerometers, micromechanical switches, resonators, and tunable microoptical interferometers. © *2004 Acoustical Society of America.* [DOI: 10.1121/1.1798331]

PACS numbers: 43.38.Bs, 43.38.Ks [AJZ] Pages: 2939–2947

I. INTRODUCTION

The work of electrostatic transducers is based on the capacitive detection principle. Hence, two important parts of such a device are the diaphragm, in the case of microphones, or the proof mass in the case of accelerometers, and the backplate electrode. The small space between these elements is filled with fluid (air). This system of plates with the associated air layer between them will be referred to as a planar microstructure. On the other hand, in order to protect the diaphragm from external damages a certain perforated planar microstructure (for example, some gratings) may be placed in the front of the microphone at small distance from the diaphragm. In some design solutions a single perforated planar microstructure is used for both functions.

The gas flow between the closed parallel plates causes viscous and inertial forces. These forces decrease the microphone performance due to the noise associated with them, and their simulation is important in predicting the device behavior. The aim of such a simulation is to design a planar microstructure which maximizes the capacitance and penetration of sound waves and minimizes the parasitic fluid action (the viscous damping). In the case of membrane damping of the electrostatic transducer (sensor, microphone), the number of holes must determine the optimal required damping due to viscous losses in the air gap needed to obtain a flat frequency response.

The fluid dynamics can be described in terms of classical Navier–Stokes equations for an incompressible fluid. The special geometry of the problem, namely the small space between the plates (squeeze-film flow), yields some simplifications of the equations similar to the lubrication approximation in classical hydrodynamics. Thus, the effect of the inertial terms, other than the time derivative of velocities, is negligible. The basic equation resulting from this analysis is a Poisson equation; the source term contains a factor characterizing the frequency dependence, another one depending upon geometry, and also the normal velocity of the diaphragm.

This analysis provides first the squeeze-film damping of the microstructure. In order to decrease the viscous damping we consider a repetitive pattern of holes on the backplate, each of them having its own domain of influence (also called a ''cell''). In most applications the holes are considered circular.[1] The simulation in this case is simpler and in certain applications it gives the desirable data to be used for design purpose. An approximate formula for squeeze-film damping, for this situation, was obtained by means of some hydraulic considerations by Škvor.[2] Our studies revealed that other geometrical shapes of the holes can be used, such as ellipses and ovals. It is shown that the use of noncircular shapes of the holes can provide a reduction in damping for the same percent open area. As the elongated ovals (and the slits as a limit case) are more likely to be obtained technologically and can be used also for protecting purposes, in this paper we shall focus on the study of the viscous damping in this type of geometry of the planar microstructures. (In fact, a planar structure involving slits was used previously in[3] designing accelerometers.)

When the squeezing film and plate thicknesses are comparable, as is the case of the surface-micromachined planar microstructures, introduction of each new hole is associated with a ''*hole resistance*'' which is added to the squeeze-film damping.[4] The calculation of the hole resistance is obtained by modeling the flow in a hole as a Poiseuille flow in a pipe, described again by a Poisson equation for velocity. As the two components of the total viscous damping have opposite

[a]Permanent address: Institute of Mathematical Statistics and Applied Mathematics of Romanian Academy, Calea13 Septembrie #13, RO-76100, Bucharest, Romania. Electronic mail: homentco@binghamton.edu

variations with respect to the increase of number of holes, there is an optimum number of holes which assures an equilibrium between squeeze-film damping and holes resistance which provides a minimum to the viscous damping coefficient.

The developed method is applied, first, to the case of circular holes. The case of microplanar structures containing slits is considered in Sec. IV. In both cases there are analytical asymptotic formulas for squeeze-film damping, the holes resistance, and the optimum number of holes, assuring a minimum viscous damping for the microstructure. In Sec. V the case of planar microstructures having a repetitive pattern of oval holes is considered. The formulas for squeeze-film damping and the holes resistance involve two coefficients which have to be determined numerically by solving two boundary-value problems for Poisson's equations. By an optimization technique, formulas are obtained giving the optimum number of oval holes and the associated minimum value of the total damping coefficient. These formulas contain two numerical coefficients, N^* and B^*, depending only upon the holes' geometry. The numerical results show that while for small values of the ratio of the open area to the total area, AR, all geometrical parameters of the assigned oval pattern are important in determining the coefficient, B^*, entering in minimum viscous damping, in the case AR$>$0.15 this coefficient depends mainly upon the area ratio of the pattern. The coefficient, N^*, entering into the expression for optimum number of holes, is sensitive also to the other geometrical parameters. Hence, it is possible that in the case of elongated holes the geometrical parameters other than AR may be used for optimizing the structure based on other criteria such as the number of holes, mechanical resistance, and penetration of sound waves. Particularly, in the case of microphones working in a natural environment, it is likely that a microplanar structure having oval holes will work better as a protecting surface against dust particles and water drops than a planar surface having circular holes.

The analysis of this paper is directed mainly to the acoustical domain. The results also can be used for designing purposes of MEMS in other applications such as accelerometers,[3,5–7] micromechanical switches,[8] various resonators,[9] and tunable microoptical interferometers.[10]

II. SQUEEZE-FILM DAMPING

In order to study the viscous squeeze-film damping on a microphone, we model the air in the gap between the diaphragm and backplate (or between the diaphragm and the protecting structure) as an incompressible viscous gas. We refer the motion of the fluid at a Cartesian system whose origin is halfway between the plates average position and the xOy plane is parallel to the backplate surface.

A. Equations of the fluid dynamics

The complete system of equations for describing the motion of an incompressible viscous fluid consists of the continuity equation and the Navier–Stokes equations

$$\nabla\cdot\mathbf{v}=0, \tag{1}$$

$$\rho\left(\frac{\partial\mathbf{v}}{\partial t}+(\mathbf{v}\cdot\nabla)\mathbf{v}\right)=\rho\mathbf{g}-\nabla p+\mu\nabla^2\mathbf{v}, \tag{2}$$

where ρ is the density, μ is viscosity, p the pressure, $\mathbf{v}$ denotes the velocity field, and $\mathbf{g}$ is the gravity acceleration.

In the case of simple harmonic oscillations (of ω-angular frequency), we have

$$p=p_\omega e^{-i\omega t},\quad \mathbf{v}=\mathbf{v}_\omega e^{-i\omega t},\quad \frac{\partial p}{\partial t}=-i\omega p.$$

The system of equations (1) (2) becomes

$$\nabla\cdot\mathbf{v}_\omega=0, \tag{3}$$

$$-i\omega\rho\mathbf{v}_\omega+\rho(\mathbf{v}\cdot\nabla)\mathbf{v}_\omega=\rho\mathbf{g}\exp(i\omega t)-\nabla p_\omega+\mu\nabla^2\mathbf{v}_\omega. \tag{4}$$

We consider now dimensionless variables. As the domain in our case is the narrow air gap between the diaphragm and backplate, we will use different scales on the x, y, and z directions

$$x=L_0x',\quad y=L_0y',\quad z=d_0z',$$

$$v_{\omega x}=V_0v_x',\quad v_{\omega y}=V_0v_y',\quad v_{\omega z}=\epsilon V_0v_z',$$

$$p_\omega-p_ae^{i\omega t}=P_0p',$$

d_0 being the distance between the plates at equilibrium, L_0 a characteristic length of the plane domain, V_0 a reference velocity, and $\epsilon=d_0/L_0$ a small parameter. We drop the primes and try to remember that we are now working in dimensionless variables. To the lower order in ϵ we obtain the equations corresponding to the lubrication approximation[12]

$$\frac{\partial v_x}{\partial x}+\frac{\partial v_y}{\partial y}+\frac{\partial v_z}{\partial z}=0, \tag{5}$$

$$\frac{\partial^2 v_x}{\partial z^2}+iK^2v_x=\frac{\partial p}{\partial x}, \tag{6}$$

$$\frac{\partial^2 v_y}{\partial z^2}+iK^2v_y=\frac{\partial p}{\partial y}, \tag{7}$$

$$\frac{\partial p}{\partial z}=0. \tag{8}$$

We have denoted

$$P_0=\frac{\mu V_0L_0}{d_0^2},\quad K=d_0\sqrt{\frac{\rho_0\omega}{\mu}}. \tag{9}$$

B. The boundary conditions for the velocity

Since we consider the gas as a viscous fluid, the appropriate boundary condition is the sticking of fluid particles to the solid walls. Hence, in dimensionless variables the boundary conditions on the solid walls (the membrane and the backplate) have the form

$$v_x(x,y,\pm\tfrac{1}{2})=0,\quad v_y(x,y,\pm\tfrac{1}{2})=0, \tag{10}$$

$$v_z(x,y,-\tfrac{1}{2})=0,\quad v_z(x,y,\tfrac{1}{2})=w. \tag{11}$$

By w we denote the Oz component of the velocity of the diaphragm, assumed a known quantity.

C. The representation of the velocity field

Equation (8) shows that within the lubrication approximation the pressure is constant across the gap depending only on x and y. Therefore, Eqs. (6) and (7) can be integrated and the integration constants can be determined by using the boundary conditions (10). There results

$$v_x(x,y,z)=\left(\frac{\cos\left(\frac{(1+i)}{\sqrt{2}}Kz\right)}{\cos\left(\frac{1+i}{2\sqrt{2}}K\right)}-1\right)\frac{i}{K^2}\frac{\partial p}{\partial x}, \tag{12}$$

$$v_y(x,y,z)=\left(\frac{\cos\left(\frac{(1+i)}{\sqrt{2}}Kz\right)}{\cos\left(\frac{1+i}{2\sqrt{2}}K\right)}-1\right)\frac{i}{K^2}\frac{\partial p}{\partial y}. \tag{13}$$

Equation (5) becomes

$$\frac{\partial v_z}{\partial z}=\left(1-\frac{\cos\left(\frac{(1+i)}{\sqrt{2}}Kz\right)}{\cos\left(\frac{1+i}{2\sqrt{2}}K\right)}\right)\frac{i}{K^2}\left(\frac{\partial^2 p}{\partial x^2}+\frac{\partial^2 p}{\partial y^2}\right).$$

The component v_z results by integrating this equation and using the first condition (11)

$$v_z=\left(z+\frac{1}{2}-\frac{\sin\left(\frac{(1+i)}{\sqrt{2}}Kz\right)}{\left(\frac{(1+i)}{\sqrt{2}}K\right)\cos\left(\frac{1+i}{2\sqrt{2}}K\right)}-\frac{\tan\left(\frac{(1+i)}{2\sqrt{2}}K\right)}{\left(\frac{(1+i)}{\sqrt{2}}K\right)}\right)\frac{i}{K^2}\left(\frac{\partial^2 p}{\partial x^2}+\frac{\partial^2 p}{\partial y^2}\right). \tag{14}$$

Thus, we succeed in obtaining a representation of the velocity field of the air in the gap by means of the pressure function, which is the main unknown function of the problem.

D. The pressure equation

From the second of Eqs. (11), on the upper plate, $z=1/2$, the velocity component v_z equals the value w defined by the motion of the diaphragm. Thus, the relationship (14) yields the equation for the pressure field in the form

$$\frac{\partial^2 p}{\partial x^2}+\frac{\partial^2 p}{\partial y^2}=12Mw, \tag{15}$$

where we have denoted

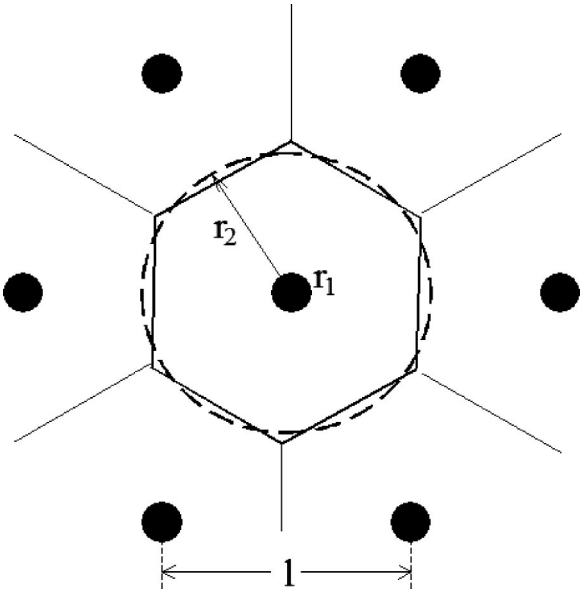

FIG. 1. The cell corresponding to a regular web of circular holes and its equivalent circular cell.

$$M=\frac{i}{12}K^2\left(\frac{\tan\left(\frac{(1+i)}{2\sqrt{2}}K\right)}{\frac{(1+i)}{2\sqrt{2}}K}-1\right)^{-1}.$$

Equation (15) is a Poisson-type equation. The frequency enters only in the right-side term by means of the parameter M. This will give the same dependence upon frequency for the pressure and also for the forces resulting by pressure integration.

In the case of small values of K, a series expansion yields

$$M=1-\frac{id_0^2\rho_0\omega}{10\mu}+O\left(\frac{K^4}{100}\right).$$

A simple dimensional analysis reveals that for the case of air and frequencies between 100 Hz and 20 kHz the value $M=1$ is a very good approximation.

E. Boundary conditions for the pressure

We suppose that on the backplate there is a periodic system of holes, as shown in Fig. 1, and define a cell $\mathcal{C}$ as the space occupied by a hole and its surrounding web space (the plane region where the hole is collecting the flow). By $\mathcal{D}^h$ we denote the domain of the hole and by $\mathcal{D}$ the domain of the cell corresponding to the plate region ($\mathcal{D}=\mathcal{C}-\mathcal{D}^h$), and, finally, $\mathcal{D}'$ is the domain resulting from $\mathcal{D}$ by similarity transformation given by the scaling relationship.

On the holes we have the atmospheric pressure. This gives the condition

$$p=0, \tag{16}$$

on the rim C_D of the holes. In the case we consider also the holes resistance—the pressure on the rim of the hole equals a constant (unknown) value p_1.

In order to avoid considering a boundary-value problem for the plane domain external to the infinite number of holes, we will take advantage of the condition on the symmetry lines. Also, on the all symmetry lines for the pressure C_N in the xOy plane we have the condition

$$\frac{\partial p}{\partial n}=0. \tag{17}$$

F. Example: Squeeze-film damping for the circular cells

We consider, for the beginning, the case where the domain D is an annulus of $r_1<r_2$ radii. We take $L_0=r_2$ and denote $r_0=r_1/r_2$. Equation (15) becomes, in polar coordinates

$$\frac{1}{r}\frac{\partial}{\partial r}\left(r\frac{\partial p}{\partial r}\right)=12Mw, \quad \text{for } r_0<r<1, \tag{18}$$

and the associated boundary conditions can be written as

$$p(r_0)=0, \quad \frac{\partial p}{\partial r}(1)=0. \tag{19}$$

The solution of Eq. (18) satisfying the conditions (19) can be written as

$$p(r)=12Mw\left(\frac{r^2}{4}-\frac{r_0^2}{4}-\ln\sqrt{\frac{r}{r_0}}\right).$$

We have also

$$\int\int_{\mathcal{D}'} p\,dxdy=12\pi Mw\left(\frac{3}{8}-\frac{r_0^2}{2}+\frac{r_0^4}{8}+\frac{1}{2}\ln r_0\right).$$

Finally, the force on the basic domain D can be written as

$$F^c=12\frac{\pi\mu r_2^4}{d_0^3}M\left(\frac{1}{2}\left(\frac{r_1}{r_2}\right)^2-\frac{1}{8}\left(\frac{r_1}{r_2}\right)^4-\frac{1}{2}\ln\frac{r_1}{r_2}-\frac{3}{8}\right)w^{\text{phys}}. \tag{20}$$

In the case of small values of K in Eq. (9) (this means in fact for not very high frequencies), the resulting expression coincides with the formula given by Skvor in Ref. 2

$$F^S=\frac{12\pi\mu r_2^4}{d_0^3}\left(\frac{1}{2}\left(\frac{r_1}{r_2}\right)^2-\frac{1}{8}\left(\frac{r_1}{r_2}\right)^4-\frac{1}{2}\ln\frac{r_1}{r_2}-\frac{3}{8}\right)w^{\text{phys}} \tag{21}$$

1. Remark

The obtained formulas for an annulus do not directly represent the array of holes typically used in designing a backplate. It is still possible to consider the external circle as an approximation of a regular hexagon (of the same area) and as a result, formula (21) can be used in the case of circular holes uniformly located in the corners of some squares or regular triangles for approximate calculation of the force F^S over an elementary cell.

III. THE HOLES' RESISTANCE

Some differences have been reported between the theoretically determined values of the viscous damping and the experimentally measured values.[11] One source of the errors is considered as being the zero-pressure condition on the rim of the holes. In the case where the thickness h of the backplate is comparable to the gap thickness d_0, the resistance of the holes becomes an important component of the total viscous damping.

A. The general case

In order to determine the ''holes' resistance'' we assume a constant pressure p_1 along the upper edge of the hole and model the motion in the hole as a Poiseuille flow in a pipe driven by the pressure gradient

$$\frac{\partial p}{\partial z}=-\frac{p_1}{h}.$$

In this case the only nonvanishing component of velocity is v_z,[12] and we can write the equation

$$\Delta v_z=\frac{p_1}{\mu h} \quad \text{in } \mathcal{D}^h, \tag{22}$$

with the *Dirichlet-type* boundary condition

$$v_z=0, \quad \text{along } C_D. \tag{23}$$

The rate of flow in the domain $\mathcal{D}^h$ can be written as

$$Q\equiv\int\int_{\mathcal{D}^h} v_z(x,y)dxdy=\frac{p_1}{\mu h}\mathcal{A}^hQ^0,$$

where $\mathcal{A}^h$ is the area of the domain $\mathcal{D}^h$, and Q^0 being a coefficient determined only by the geometry of the hole.

By equating this rate of flow with the air leaving the space between the diaphragm and backplate $Q^s=\mathcal{A}w^{\text{phys}}$ (by $\mathcal{A}$ we have denoted the area of the domain $\mathcal{D}$), there results the value of the pressure p_1 as

$$p_1=\frac{\mu h\mathcal{A}}{\mathcal{A}^hQ^0}w^{\text{phys}}.$$

Now, the supplementary force F^h for the cell $\mathcal{C}$, due to hole resistance, can be written as

$$F^h=\frac{\mu h\mathcal{A}^2}{\mathcal{A}^hQ^0}w^{\text{phys}}. \tag{24}$$

B. Example: The case of circular holes

In the case of a circular hole of r_1—radius, Eq. (22) becomes

$$\frac{1}{r}\frac{d}{dr}\left(r\frac{dv_z}{dr}\right)=\frac{p_1}{\mu h}, \quad \text{for } 0\leqslant r<r_1.$$

The solution satisfying the condition (23) is

$$v_z(r)=\frac{p_1}{4\mu h}(r^2-r_1^2),$$

and, correspondingly, the rate of flow can be written as

$$Q=\frac{\pi p_1}{8\mu h}r_1^4.$$

In this case there results $Q^0=r_1^2/8$ and, correspondingly, the supplementary force for a cell is

$$F^h=8\pi\mu h\frac{r_2^4}{r_1^4}w^{\text{phys}}. \tag{25}$$

C. The optimum number of circular holes

Let us denote by N the number of circular holes of a unit of area u^2. Then, we have

$$\pi r_2^2 N=u^2, \quad r_1^2/r_2^2=\text{AR}.$$

By considering the formulas (21) and (25) for the squeeze-film damping over a cell and the hole resistance, we can determine[13] an optimum number of holes for a given value of AR, which assures an equilibrium between squeeze film and holes resistance

$$N_{\text{opt}}=\sqrt{\frac{3}{2hd_0^3}}\frac{(\text{AR})}{\pi}\left[\frac{1}{2}(\text{AR})-\frac{1}{8}(\text{AR})^2-\frac{1}{4}\ln(\text{AR})-\frac{3}{8}\right]^{1/2}u^2,$$

and the associated minimum value of the total damping coefficient $B=F/w^{\text{phys}}$ as

$$B_{\min}=\frac{8\sqrt{6}\mu}{(\text{AR})}\sqrt{\frac{h}{d_0^3}}\left[\frac{1}{2}(\text{AR})-\frac{1}{8}(\text{AR})^2-\frac{1}{4}\ln(\text{AR})-\frac{3}{8}\right]^{1/2}u^2.$$

In the next sections we shall extend these results for two different geometries of the holes: the case of the slits between solid strips and the case of oval holes.

IV. THE CASE OF PLANAR MICROSTRUCTURES CONTAINING SLITS

In some cases for protection of microphones planar microstructures containing periodic slits can be used, i.e., the limit case of holes as long gaps between rectilinear strips. This type of structure can also be used as the second electrode in the case of condenser microphones. In fact, planar microstructures containing parallel slits have been used for fabricating micromachined capacitive accelerometers.[3]

We consider the geometry in Fig. 2 containing a periodic structure of $2L_0$—width strips separated by $2r$—wide slits.

A. The squeeze-film damping

In the case where the domain $\mathcal{D}$ is a strip parallel to $Ox-$axis, $0<y<L_0$, we take L_0 as the reference length. Equation (15) becomes

$$\frac{d^2p}{dy^2}=12Mw, \quad 0<y<1. \tag{26}$$

The boundary conditions become

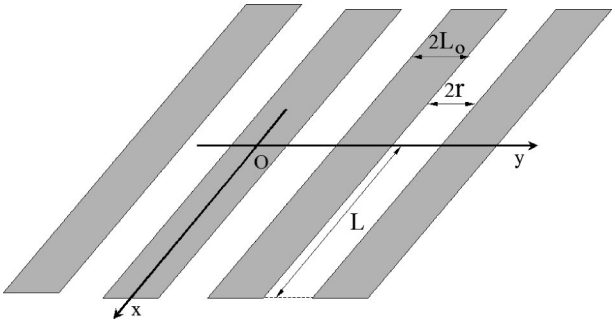

FIG. 2. A microstructure containing slits.

$$p(1)=0, \tag{27}$$

$$\frac{dp}{dy}(0)=0. \tag{28}$$

The solution of Eq. (26) satisfying the boundary conditions (27), (28) is

$$p(x)=6M(y^2-1)w.$$

The force on a rectangle of L—length of the strip can be obtained by integration in the form

$$F^s=8M\mu L\frac{L_0^3}{d_0^3}w^{\text{phys}}. \tag{29}$$

B. The slit's resistance

Equation (22) becomes in this case

$$\frac{d^2v_z}{dy^2}=\frac{p_1}{\mu h}, \quad L_0<y<L_0+2r, \tag{30}$$

with the boundary conditions on the slit sides

$$v_z(L_0)=0, \quad v_z(L_0+2r)=0. \tag{31}$$

Then, the solution of Eq. (30) satisfying the conditions (31) can be written as

$$v_z(x)=\frac{p_1}{2\mu h}(y-L_0)(y-L_0-2r).$$

The rate of flow corresponding to this velocity on a section of length L of the slit is

$$Q=\frac{2p_1r^3}{3\mu h}L.$$

There results $Q^0=r^2/3$ and formula (24) yields the hole (slit) resistance as

$$F^h=\frac{6\mu h(L_0+r)^2}{r^3}Lw^{\text{phys}}. \tag{32}$$

C. Optimal strip thickness and designing relationships

The total mechanical resistance on a backplate strip (of L width) due to viscosity can be obtained by adding the resistance due to sqeezing film (29) with the slit resistance given by formula (32)

$$R=\left(\frac{8L_0^3}{d_0^3}+6(L_0+r)^2\frac{h}{r^3}\right)\mu L. \tag{33}$$

We denote now by N the number of the slits on a unit length u and by AR the area ratio of the plate. Therefore

$$L_0+r=\frac{u}{2N}, \tag{34}$$

$$r=u\frac{(\mathrm{AR})}{2N}. \tag{35}$$

Formula (33) gives the damping coefficient $\mathcal{B}$ on L—width of the backplate, as

$$\mathcal{B}\equiv NR=\mu L\left(\frac{(1-(\mathrm{AR}))^3}{d_0^3}\frac{u^3}{N^2}+\frac{12h}{(\mathrm{AR})^3}\frac{N^2}{u}\right).$$

This expression has a minimum value

$$\mathcal{B}_{\min}=4\sqrt{3}\mu\left(\frac{1-(\mathrm{AR})}{(\mathrm{AR}}\right)^{3/2}\sqrt{\frac{h}{d_0^3}}Lu,$$

corresponding to the value of N

$$N_{\mathrm{opt}}=\frac{[(\mathrm{AR})(1-(\mathrm{AR}))]^{3/4}}{\sqrt[4]{12hd_0^3}}u. \tag{36}$$

The relationship (36) determines the optimum number of parallel slits in terms of the area ratio AR, backplate thickness h, and average distance d_0 between backplate and diaphragm. Once N_{opt} is determined the relationships (34) and (35) provide the optimum strip and slit widths

$$L_{\mathrm{opt}}=\frac{1-(\mathrm{AR})}{2N_{\mathrm{opt}}}u$$

$$r_o=\frac{(\mathrm{AR})}{2N_{\mathrm{opt}}}u.$$

1. Example

Let us consider as an example: $u=1$ mm, AR=0.2, $d_0=0.005$ mm, $h=0.004$ mm. *There results*

$$N_{\mathrm{opt}}=29/\mathrm{mm},\quad L_{\mathrm{opt}}=0.014\ \mathrm{mm},$$

$$r_{\mathrm{opt}}=0.0035\ \mathrm{mm},\quad L=1\ \mathrm{mm},$$

$$\mathcal{B}^0_{\min}=0.1785\times10^{-3}\ \mathrm{Ns/m}.$$

V. NUMERICAL SIMULATION OF VISCOUS DAMPING: THE CASE OF OVAL HOLES

A. The squeeze-film damping in the case of periodic oval holes

We consider the backplate structure in Fig. 3(a). It consists of a periodic pattern of offset oval holes. (By oval we mean the geometrical form of a rectangle with two half-circles of r radius added to smaller sides.) The basic domain, D, we are using to determine the pressure is also shown in Fig. 3(a) and the corresponding canonical domain D' resulting from D by similarity transformation given by the scaling relationship, is also drawn in Fig. 3(b).

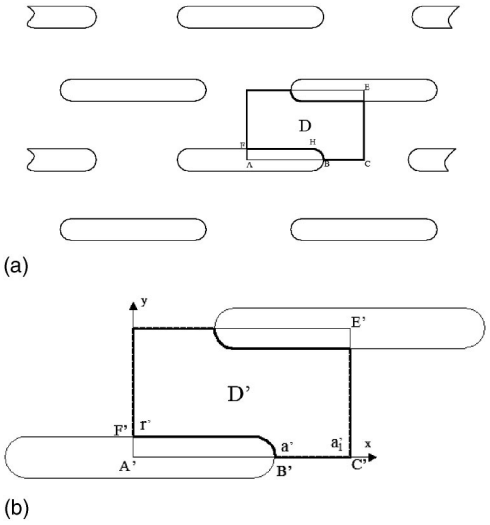

FIG. 3. (a) An uniform offset system of oval holes. (b) The basic domain corresponding to the planar microstructure in (a).

We take as the scaling length the distance L_0 between two neighbor rows of holes. Consequently, we have in the domain D', $C'E'=1$, and denote: $A'C'=a'_1$, $A'B'=a'$, $A'F'=r'$, $r'L_0=r$. We denote again by AR the area ratio of the plate (the fraction of the hole area to the cell area), and hence

$$4r(a-r)+\pi r^2=(\mathrm{AR})\mathcal{A}.$$

The physical pressure in domain D can be obtained by considering the physical variables in Sec. II A and equation in Sec. II D

$$p^{\mathrm{phys}}(x,y)=-12\frac{\mu L_0^2}{d_0^3}\hat{p}\left(\frac{x}{L_0},\frac{y}{L_0}\right)w^{\mathrm{phys}}.$$

$\hat{p}(x,y)$ denotes the solution of the boundary-value problem

$$\Delta\hat{p}(x,y)=1,\quad \text{in } D', \tag{37}$$

$$\hat{p}(x,y)=0\quad \text{on } C'_D,$$
$$\frac{\partial\hat{p}(x,y)}{\partial n}=0\quad \text{on } C'_N. \tag{38}$$

Here, C'_D is the part of the boundary of the domain D' where the pressure is known (the rim of the holes) and C'_N the part of the boundary-containing segment of symmetry lines.

The viscous force on a cell given by the squeezing-film damping can be expressed as

$$F^S_{\mathrm{cell}}=24\mu\frac{L_0^4}{d_0^3}Ma'_1C_pw^{\mathrm{phys}}, \tag{39}$$

where the pressure coefficient C_p has the expression

$$C_p=-\int\int_{D'}\hat{p}(x',y')dx'dy'\Big/\int\int_{D'}dx'dy'. \tag{40}$$

Thus, the determination of the squeezing-film damping on a cell requires the solving of the boundary-value problem (37) and (38) and calculation of the pressure coefficient C_p by using formula (40).

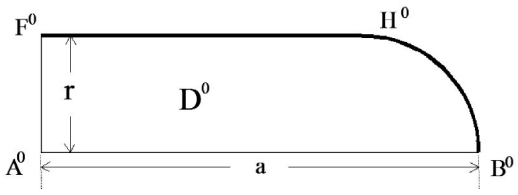

FIG. 4. The domain D^0 considered in determination of the resistance of the oval holes.

B. The resistance of oval holes

In order to determine the oval holes' resistance we consider the domain D^0 in Fig. 4 corresponding to a quarter fraction of hole, scaled by the width r. In this case the rate of flow through the hole can be obtained as

$$Q=\int\int_{\mathcal{D}^h} v_z(x,y)dx\,dy=\frac{p_1}{\mu h}r^2\mathcal{A}^hQ^0\left(\frac{a}{r}\right), \tag{41}$$

where $\mathcal{A}^h$ is the area of an oval hole and Q^0 is

$$Q^0\left(\frac{a}{r}\right)=-\int\int_{D^{h0}}\hat{v}_z(x',y')dx'dy'\Big/\int\int_{D^{h0}}dx'dy'. \tag{42}$$

The function $\hat{v}_z(x,y)$ is the solution of the Poisson equation

$$\Delta\hat{v}_z(x,y)=1,\quad \text{in } D^{h0}, \tag{43}$$

satisfying the boundary conditions

$$\begin{aligned}&\hat{v}_z(x,y)=0,\quad \text{along } F^0H^0B^0,\\ &\frac{\partial\hat{v}_z}{\partial x}=0,\quad \text{along } F^0A^0,\\ &\frac{\partial\hat{v}_z}{\partial y}=0,\quad \text{along } A^0B^0.\end{aligned} \tag{44}$$

Now, the supplementary force due to the oval hole resistance F^h can be written as

$$F^h=\frac{\mu h\mathcal{A}^2}{r^2Q^0(a/r)\mathcal{A}^h}w^{\text{phys}}. \tag{45}$$

The function Q^0 has been determined numerically. We preferred a finite element approach in an effort to use programs familiar to the solid mechanics researchers. In order to model the Poisson's equation we used ANSYS 2D steady heat-transfer elements. Thus, by solving numerically the boundary-value problem (43), (44), and computing the integral in (42), there results the function plotted in Fig. 5. The two limit cases have definite physical meanings: for $a=r$ we have the case of circular holes in which case $Q^0=1/8$, while for $a\to\infty$ we obtain the slit case where $Q^0=1/3$ as in Secs. III B and IV B.

C. The optimal number of oval holes for a planar microstructure

Adding the squeeze-film damping with the oval hole resistance results in the total viscous force on a cell in the form

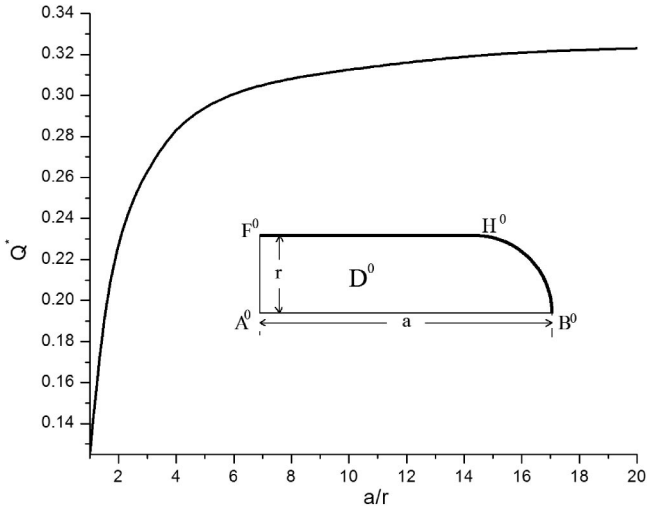

FIG. 5. The function Q^0 for determining the viscous resistance of the oval holes.

$$F^T_{\text{cell}}=\left(\frac{24\mu L_0^4Ma_1'}{d_0^3}C_p+\frac{\mu h\mathcal{A}^2}{r^2\mathcal{A}^h}\frac{1}{Q^0(a/r)}\right)w^{\text{phys}}.$$

Let us now denote by N the number of holes of a unit of area u^2. Then we have

$$\mathcal{A}=\frac{u^2}{N},\quad \mathcal{A}^h=(\text{AR})\cdot\mathcal{A},\quad \mathcal{A}=2a_1'L_0^2$$

$$\frac{1}{r^2}=\frac{2a'^2}{a_1'(\text{AR})^2u^2}R^2N,\quad k\equiv\frac{a'}{a_1'},$$

$$R\equiv 1+\sqrt{1-\frac{4-\pi}{2}\frac{a_1'}{a'^2}(\text{AR})}.$$

The total force on u^2 area results in the form

$$F^T=\left(\frac{6MC_p}{a_1'd_0^3}\frac{u^4}{N}+\frac{2ha'^2}{a_1'}\frac{R^2}{(\text{AR})^3Q^0(a/r)}N\right)\mu w^{\text{phys}}.$$

The total viscous damping force has a minimum value for $N=N_{\text{opt}}$

$$N_{\text{opt}}=\frac{10^{-4}\sqrt{M}u^2}{\sqrt{hd_0^3}}N^*. \tag{46}$$

The corresponding damping coefficient $\mathcal{B}_{\min}=F^T_{\min}/w^{\text{phys}}$ can be written as

$$\mathcal{B}_{\min}=\sqrt{\frac{48hM}{d_0^3}}\mu u^2B^*. \tag{47}$$

The numerical coefficients N^* and B^* depend only on the geometry of the oval holes

$$N^*=\frac{\sqrt{3C_p(\text{AR})^3Q^0(a/r)}}{a'R}10^4, \tag{48}$$

$$B^*=\frac{a'}{a_1'}\sqrt{\frac{C_p}{(\text{AR})^3Q^0(a/r)}}R. \tag{49}$$

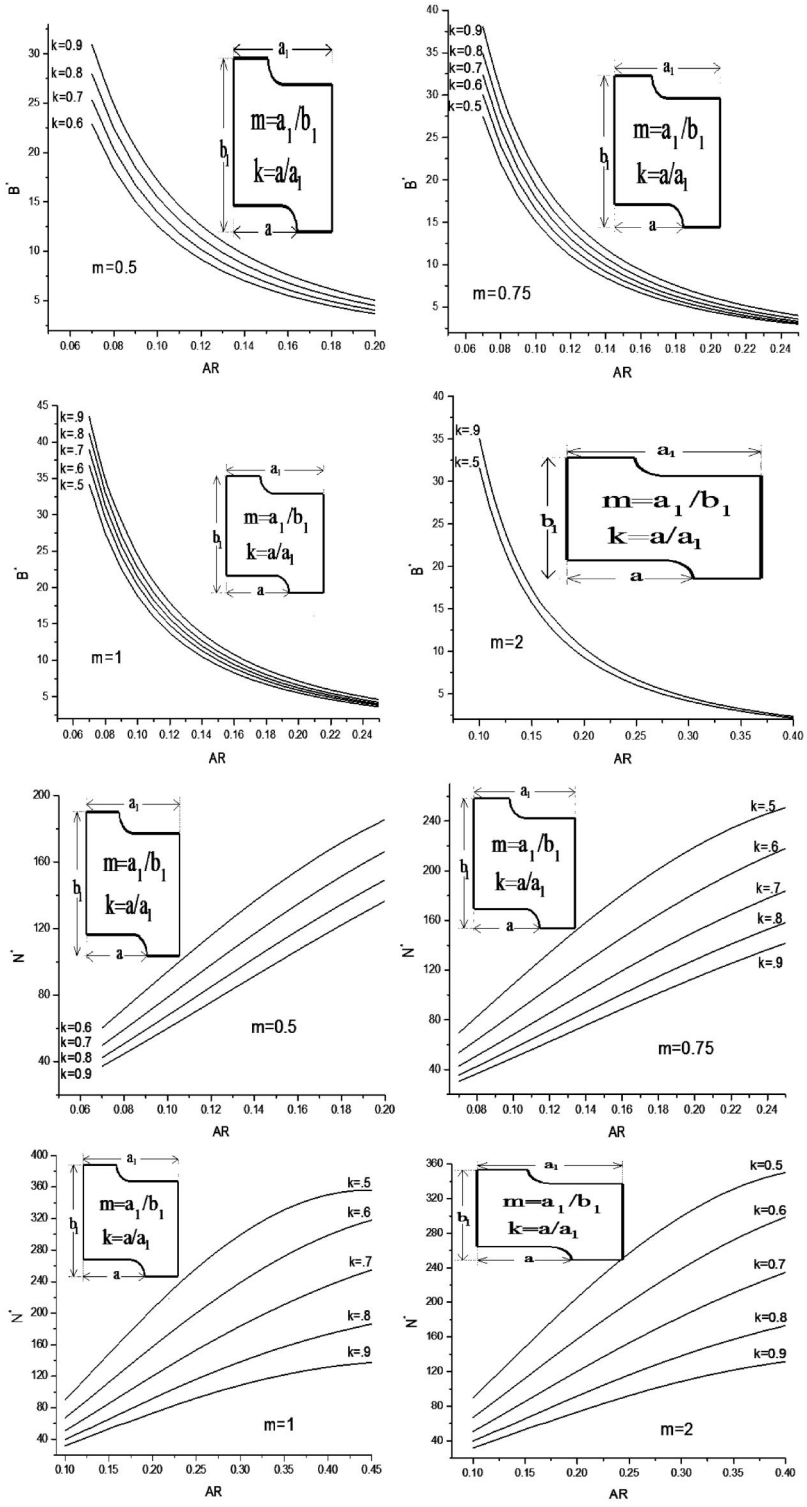

FIG. 6. (a) The numerical coefficient B^* for calculating the minimum damping coefficient for several dimensions of the basic domain (m) and holes (k). (b) The numerical coefficient N^* for determining the optimum number of holes for several dimensions of the basic domain (m) and holes (k).

D. Numerical results and designing relationships

The formulas (48) and (49) for determining the numerical coefficients N^* and B^* have been applied for certain hole geometries described by the dimensions of the domain D^*: $m \equiv a_1'$, $k \equiv a'/a_1'$, and for a sequence of values of area ratio AR between 0.08 and 0.4.

The boundary-value problem (37) and (38) has to be solved many times; this is why we preferred a more efficient complex variable boundary element method[14] which is doing all the computation only on the boundary curve.

The graphs of the coefficients B^* and N^* are presented in Figs. 6(a) and (b), respectively. It is evident that for small values of the area ratio all the geometrical parameters of the oval pattern are important in determining the minimum value of viscous damping coefficient. In the case AR$>$0.15 the variation of the coefficient B^* with k is very slow. Therefore, the value of this coefficient can be adjusted by choosing the proper value of hole area ratio AR. On the other hand, the coefficient N^* is very sensitive to values of k; thus, it is possible by choosing this parameter properly to obtain a per-

forated planar microstructure satisfying other designing demands.

The presented graphs involve only the geometrical parameters of the oval holes: AR, $m=a_1'$, $k=a'/a_1'$. Consequently, they can be used for calculating the damping coefficient and the optimum number of holes for different distances between plates, backplate thicknesses, frequencies, and viscosities.

Once the values of the parameters AR, a_1', and a' are decided (and implicitly the values of numerical coefficients B^* and N^*), the number of holes is given by the relationship (46) and the physical dimensions of the cell by formulas

$$b_{1o}=\frac{u}{\sqrt{2a_1'N_{\text{opt}}}},$$

$$a_{1o}=a_1'b_{1o}, \quad a_o=a'b_{1o},$$

$$r_o=\frac{2a_o}{4-\pi}\left(1-\sqrt{1-\frac{(2-\pi/2)(\text{AR})u}{a_oN_{\text{opt}}}}\right).$$

VI. CONCLUSIONS

In the case of small area ratio the optimal geometry of the holes of planar microstructures is determined by all the geometrical parameters of the structure.

For AR$>$0.15 the influence of the other geometrical parameters other than AR on the damping coefficient is very slight. Therefore, it is possible to adjust the holes pattern to fulfill other designing criteria as number of holes, structure resistance, penetration of sound waves, etc. For example, a protecting surface having oval holes rather than circular ones will be more appropriate for protecting a microphone diaphragm against dust particles and water drops.

The designing formulas in the case of oval holes contain the constants B^* and N^* depending only on the geometry of the holes. These coefficients can be computed by solving the Poisson's equation (with certain mixed boundary conditions) by using the appropriate software. Otherwise, the coefficients can be evaluated by using the graphs provided in the paper. Once B^* and N^* are determined, the total viscous damping and the optimum number of holes can be obtained for various backplate thicknesses, distances between plates, frequencies, and viscosities.

ACKNOWLEDGMENTS

The authors acknowledge the help in using the ANSYS software by Ph.D. students Matthew J. Aubrey and Weili Cui. This work has been supported through NIH Grant R01 DC05762-1A1, and DARPA Grant DAAD17-00-C-0149 to R.N.M.

[1] J. Bergquist, "Finite-element modeling and characterization of a silicon condenser microphone with a highly perforated backplate," Sens. Actuators, A **39**, 191–200 (1993).
[2] Z. Skvor, "On acoustical resistance due to viscous losses in the air gap of electrostatic transducers," Acustica **19**, 295–297 (1967–1968).
[3] U. E. Gerlach-Mayer, "Micromachined capacitive accelerometer," Sens. Actuators, A **25–27**, 555–558 (1991).
[4] M. Rossi, *Acoustics and Electroacoustics* (Artech House, Norwood, 1988).
[5] M. J. Novack, "Design and fabrication of thin film micromachined accelerometer," M.S. thesis (1992), Massachusetts Institute of Technology.
[6] Y.-J. Yang, "Squeeze-film damping for MEMS structures," M.S. thesis (1998), Massachusetts Institute of Technology.
[7] Y.-J. Yang and S. D. Senturia, "Numerical simulation of compressible squeezed-film damping," Solid-State Sensors and Actuators Workshop, Hilton Head, SC, June 1996.
[8] S. Pacheco, C. T.-C. Nguyen, and L. P. B. Katehi, "Micromechanical electrostatic K-band switches," Proceedings IEEE, MTT-S International Microwave Symposium, Baltimore, Maryland, 7–12 June, 1998, pp. 1569–1572.
[9] T. Mattila, P. Hakkinen, O. Jaakola, J. Kiihamaki, J. Kyynarainen, A. Oja, H. Seppa, P. Seppala, and T. Sillanpaa, "Air damping in resonant micromechanical capacitive sensors," in 14th European Conference on Solid-State Transducers, EUROSENSORS XIV (Copenhagen), pp. 221–224, Aug. 2000.
[10] M. S. Wu, E. C. Vail, G. S. Li, W. Yuen, and C. J. Chang-Hasnain, "Widely and continuously tunable micromachined resonant cavity detector with wavelength tracking," IEEE Photon Technol. Lett. **8**, 98–100 (1996).
[11] E.-S. Kim, Y.-H. Cho, and M.-U. Kim, "Effect of holes and edges on the squeeze film damping of perforated micromechanical structures," IEEE, Int. Conf. MEMS, 1999, Trans. Circuits and Systems II, TCAS 1999.
[12] F. M. White, *Viscous Fluid Flow* (McGraw-Hill, New York, 1992).
[13] D. Homentcovschi and R. Miles, "Viscous damping of perforated planar micromechanical structures," Sensors and Actuators A (in press).
[14] D. Homentcovschi, D. Cocora, and R. Magureanu, "Some developments of the CVBEM application to the mixed boundary value problems for the Laplace equation," Eng. Anal. **4**, 15–20 (1987).

Cross-talk phenomena in a 1-3 connectivity piezoelectric composite

Mikaël Wilm, Raphaël Armati, William Daniau, and Sylvain Ballandras
Département LPMO, Institut FEMTO–ST, CNRS UMR 6174, 32 avenue de l'Observatoire, Besançon, France

(Received 18 February 2004; revised 16 July 2004; accepted 18 August 2004)

Many works have been devoted to the estimation of cross-talk effects in one-dimensional ultrasound probes. The main aspect limiting the interest of these works concerns the lack of control of the electrical boundary conditions applied to the array which may dramatically affect the results of cross-talk measurements. In this paper the concept of mutual admittances is recalled. Computations based on a periodic finite-element analysis are performed, jointly to measurements of cross talks in the case of a 1-3 connectivity piezoelectric composite. Quantitative comparisons show the capability of the proposed approach to predict almost all the contributions experimentally observed in a large frequency range. © *2004 Acoustical Society of America.* [DOI: 10.1121/1.1804631]

PACS numbers: 43.38.Hz, 43.38.Fx [AJZ] Pages: 2948–2955

I. INTRODUCTION

Ultrasound devices for medical imaging applications and nondestructive evaluation are mainly based on multi-periodic transducer arrays like piezoelectric (PZT)-based composites.[1] Recently, micromachined ultrasound transducers[2] have appeared as a potential competitor and an alternative to the now-well-developed piezocomposite-based ultrasound probes.

Due to their periodicities, ultrasound probes can exhibit strong cross talks and parasitic modes, such as lateral modes due to Bragg diffraction in piezocomposites, which are particularly undesirable, especially in phased arrays.[3] Many works have been dealt with in order to estimate cross-talk effects and their influence on radiation patterns, and to reduce them by modifying the geometry of the array (for instance, by adding undercuts) or the materials of such complex transducers.[4–6] However, the electrical boundary conditions applied to the array, when measuring cross talks, may significantly change the measurement results, since the cells neighboring the excited one can be either short or open circuited. In the same way, no rigorous theory has been clearly addressed to calculate cross-talk levels in periodic transducers. Whatever the electrical boundary conditions adopted for cross-talk measurements, they must be reliable and simple enough to comply with an efficient theoretical description, so that cross-talk evaluation results can be rigorously analyzed and interpreted, with the help of the theory. Moreover, the model must be able to predict any contribution of the vibrating structure to the electrical response of the device. It means that it has to be used with no loss of generality.

In this paper we present a theoretical approach well known in the surface-acoustic-wave domain, that introduces the concept of harmonic and mutual admittances.[7] This approach is combined with a multi-periodic finite-element method to compute cross-talk levels in ultrasound transducers.[8] This approach is preferred to alternative methods based, for instance, on equivalent-homogenized-material derivation[9] for different reasons. First, the use of a periodic finite-element analysis (FEA) was found appropriate to accurately describe all the modes excited in the structure, and more particularly those specifically due to the periodic nature of the substrate. Second, the capability of deriving an operator relating all the voltages and the currents of the array to each other allows for handling almost any electrical boundary conditions, assuming the array is large enough to get rid of mechanical edge conditions. The FEA is also preferred to the plane-wave-expansion (PWE) method.[10] Even if the proposed work can be performed by the use of the PWE approach, since one computes the harmonic admittance of a piezocomposite, the use of the FEA formulation allows one to take into account complex geometries of real transducers, and also propagation media such as backing or matching layers surrounded by water.[11,12]

Although complete transducers can be studied with our approach, the proposed work only concerns a 1-3 connectivity piezoelectric composite vibrating in air in order to demonstrate the reliability of the method. In Sec. II, we generalize the concepts of harmonic and mutual admittances to bi-dimensional arrays and we show their interest for the study of real ultrasound probes. In Sec. III, we compute the harmonic admittance of a 1-3 piezocomposite and we describe modes guided by the structure. Measurements of mutual admittances are then performed according to the experimental setup described in Sec. IV, and compared to computation results in Sec. V.

II. BRIEF ELEMENTS OF THEORY

The concept of harmonic and mutual admittances was first introduced in the case of surface-acoustic-wave devices.[7]

Let us first consider the general case of an infinite bi-periodic transducer array where all electrodes are grounded except one, i.e.,

$$V_{n,q}=\begin{cases} V_{m,p}\neq 0 & \text{for } n=m \text{ and } q=p \\ 0 & \text{for } n\neq m \text{ or } q\neq p \end{cases}. \tag{1}$$

 0001-4966/2004/116(5)/2948/8/$20.00

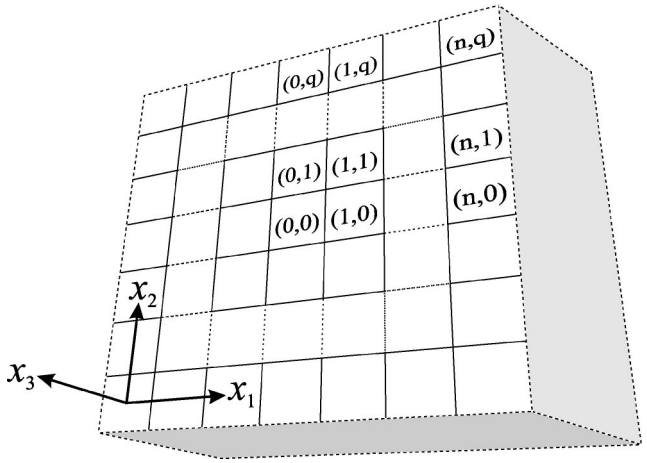

FIG. 1. Schematic diagram of a portion of an infinite bi-dimensional array.

Indexes m, n, p, and q represent the coordinates of the considered cell in the whole bi-dimensional array of elementary transducers, as represented in Fig. 1.

Figure 2 illustrates the simple case of a one-dimensional periodic array where the potential V_0 of the cell 0 is fixed to a nonzero value, whereas the other cells are grounded.

The mutual admittance between two electrodes, $y_{m-n,p-q}$, is defined by the ratio $I_{n,q}/V_{m,p}$, yielding

$$I_{n,q}=y_{m-n,p-q}V_{m,p}, \tag{2}$$

where $I_{n,q}$ is the electrical current flowing through the $(n,q)^{\text{th}}$ grounded cell of the array and $V_{m,p}$ is the potential applied to the $(m,p)^{\text{th}}$ cell according to Eq. (1). Due to the translation symmetry of the structure, $y_{m-n,p-q}$ only depends on the difference between m and n, and p and q, respectively. $y_{m-n,p-q}$ only depends on the distance between the two considered cells and does not depend on their respective positions.

In the case of any potential distribution, the superposition theorem leads to

$$I_{n,q}=\sum_{m,p=-\infty}^{+\infty} y_{m-n,p-q}V_{m,p}. \tag{3}$$

Let us consider now a specific potential distribution, also called harmonic excitation (in the space domain), where the phase varies linearly with m and p

$$V_{m,p}=V_0\exp(-j2\pi(m\gamma_1+p\gamma_2)), \tag{4}$$

where γ_1 and γ_2 are called excitation parameters; $2\pi\gamma_1$ and $2\pi\gamma_2$ are the phase differences applied between two neighboring rows along the first and the second direction of the array, respectively. As previously, one illustrates this specific excitation with the simple case of a one-dimensional array in Fig. 3.

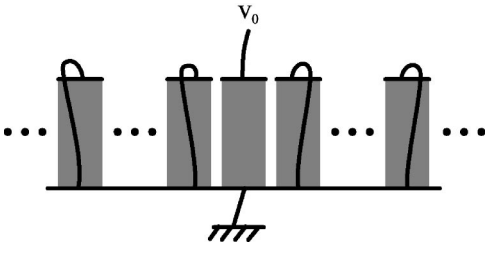

FIG. 2. Electrical boundary conditions of a one-dimensional array for which mutual admittances are defined.

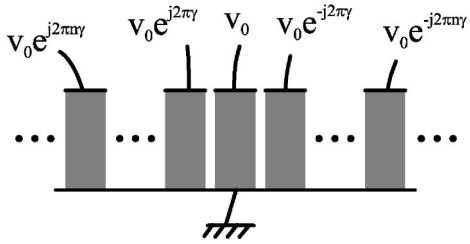

FIG. 3. Potential distribution for the simplified case of a one-dimensional array in the case of a spatially harmonic excitation.

It then can be derived

$$V_{m,p}=V_{n,q}\exp(-j2\pi((m-n)\gamma_1+(p-q)\gamma_2)). \tag{5}$$

The ratio between $I_{n,q}$ and $V_{n,q}$ defines the harmonic admittance $Y(\gamma_1,\gamma_2)$, referring to the harmonic excitation described in Eq. (4).

Equations (3) and (5) yield

$$Y(\gamma_1,\gamma_2)=\frac{I_{n,q}}{V_{n,q}}=\sum_{m,p=-\infty}^{+\infty} y_{m-n,p-q}\exp(-j2\pi((m-n)\gamma_1+(p-q)\gamma_2)), \tag{6}$$

which can be rewritten as

$$Y(\gamma_1,\gamma_2)=\sum_{m,p=-\infty}^{+\infty} y_{m,p}\exp(-j2\pi(m\gamma_1+p\gamma_2)), \tag{7}$$

where m and p now represent the distance from each cell to a reference cell, for instance, the cell (0,0). The terms $y_{m,p}$

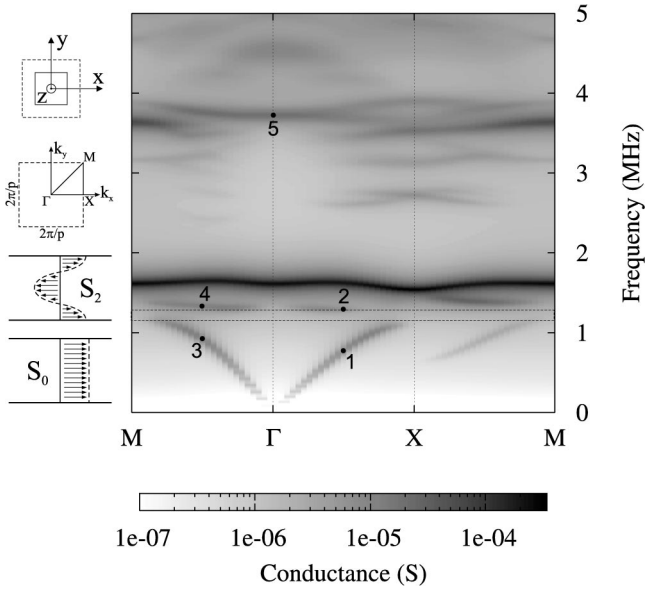

FIG. 4. Harmonic admittance considering the path $M-\Gamma-X-M$ corresponding to the first Brillouin zone. The dashed lines correspond to the band gap separating the S_0 and S_2 modes schemed on the left side of the plot. The unit cell and the first Brillouin zone are also represented. Numbers 1–5 indicate modes for which the displacement field is represented in Figs. 5 and 6.

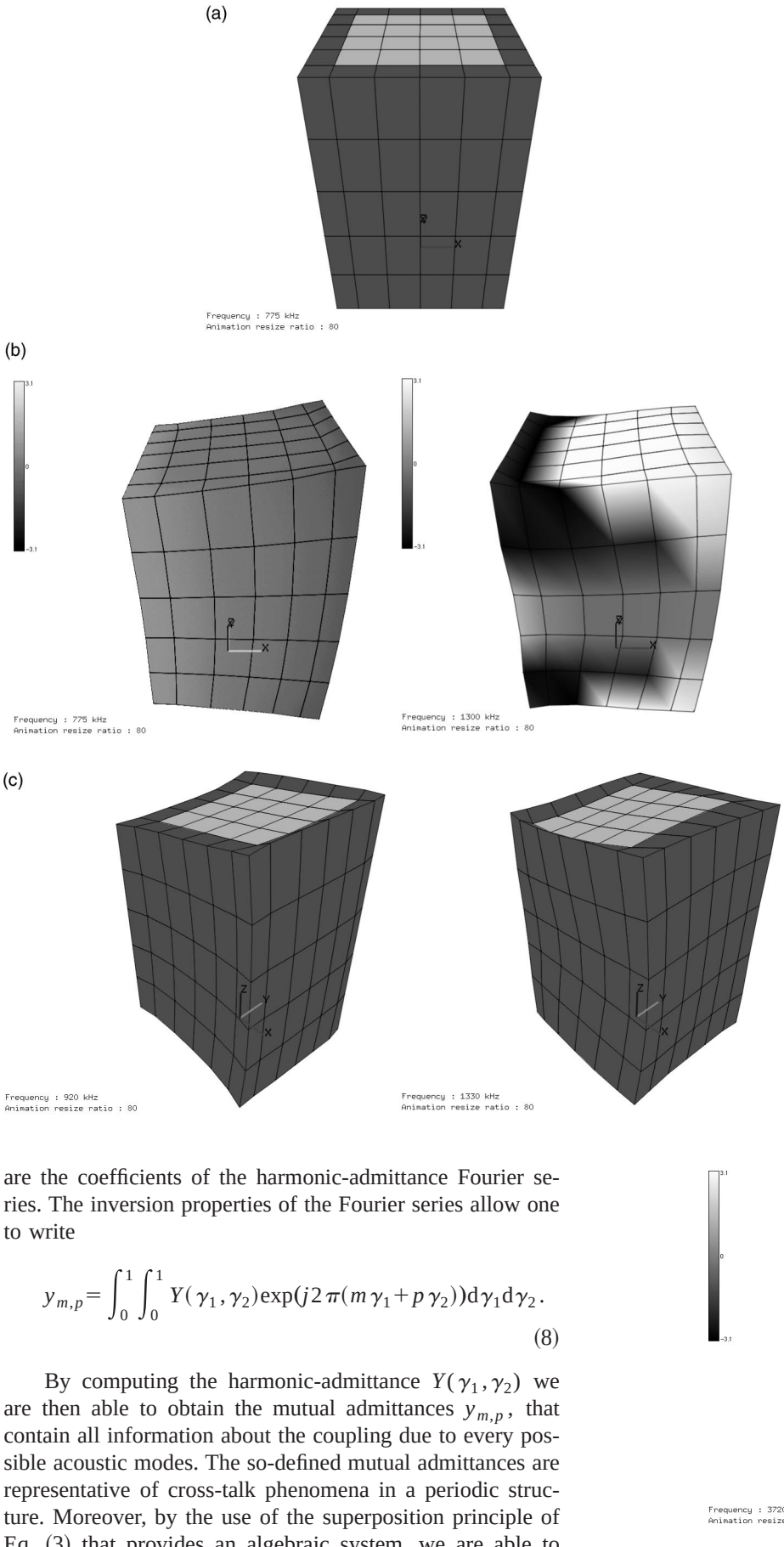

FIG. 5. (a) Mesh of the elementary cell and shapes of the S_0 and S_2 modes, (b) for $\gamma_1 = 0.25$ and $\gamma_2 = 0$ at, respectively, 775 kHz (1 in Fig. 4) and 1300 kHz (2 in Fig. 4), and then (c) for γ_1 and γ_2 equal to 0.25 at, respectively, 920 kHz (3 in Fig. 4) and 1330 kHz (4 in Fig. 4). The phase of the displacements along the x_1 axis is indicated in gray scale when computed.

are the coefficients of the harmonic-admittance Fourier series. The inversion properties of the Fourier series allow one to write

$$y_{m,p} = \int_0^1 \int_0^1 Y(\gamma_1, \gamma_2) \exp(j2\pi(m\gamma_1 + p\gamma_2)) \mathrm{d}\gamma_1 \mathrm{d}\gamma_2 . \tag{8}$$

By computing the harmonic-admittance $Y(\gamma_1, \gamma_2)$ we are then able to obtain the mutual admittances $y_{m,p}$, that contain all information about the coupling due to every possible acoustic modes. The so-defined mutual admittances are representative of cross-talk phenomena in a periodic structure. Moreover, by the use of the superposition principle of Eq. (3) that provides an algebraic system, we are able to estimate the response of a transducer array to any electrical excitation or load strategy, since nonactive elements of a

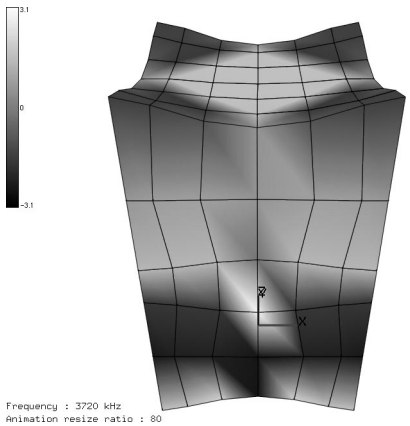

FIG. 6. Shape of the lateral mode arising at 3.7 MHz, for γ_1 and γ_2 equal to zero, corresponding to 5 in Fig. 4. The phase of the displacements along the z axis is indicated in gray scale.

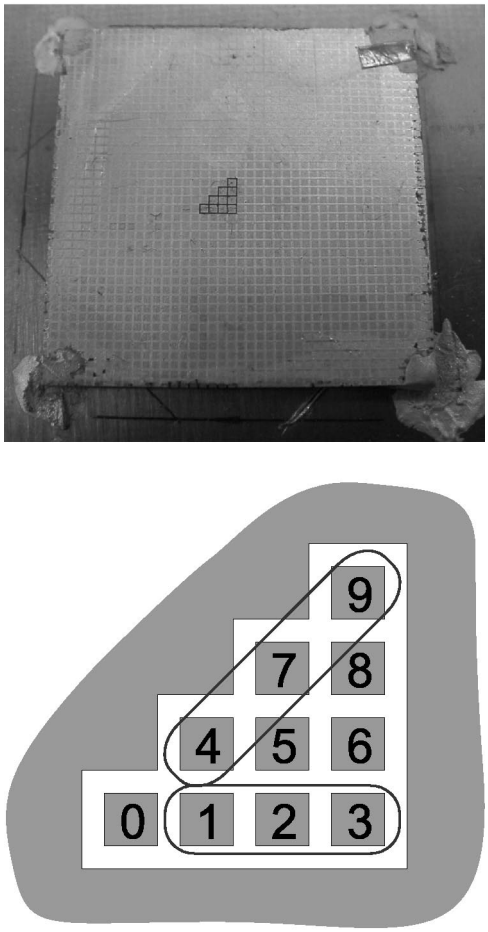

FIG. 7. Studied 1-3 piezo-composite and its electrode pattern on the top side.

transducer can be either short circuited, or open circuited, or even loaded with an impedance, depending on whether they are in emission or reception mode. One can consider a potential excitation where $V_{n,q}$ are fixed as desired, and subsequently the currents $I_{n,q}$ have to be estimated since they become the unknowns of the problem. Or one can consider a current excitation, and the potentials $V_{n,q}$ become the unknowns. Finally, one can impose an external electrical load to each of the elements—for instance, $Z_{\text{ext}}=50\ \Omega$—for which an extra relation ($V_{n,q}=Z_{\text{ext}}I_{n,q}$) allows one to solve the problem.

The concepts of mutual and harmonic admittances can be extended to any vibration field of the array, in particular to normal displacements of the front side of an actual transducer. By computing mutual normal displacements, one obtains the normal-displacement profile of the array when only one element is excited. The real radiation pattern can then be computed, which takes into account parasitic modes propagating in the array and radiating in the propagation medium. One can also compute the harmonic pressure and subsequently the mutual pressures generated by the transducer front side in the propagation medium. The frequency spectrum (in Pa/V) is then obtained with the mutual admittance of the excited cell, also called auto admittance, and one can see the effects of parasitic modes on the transducer bandwidth.

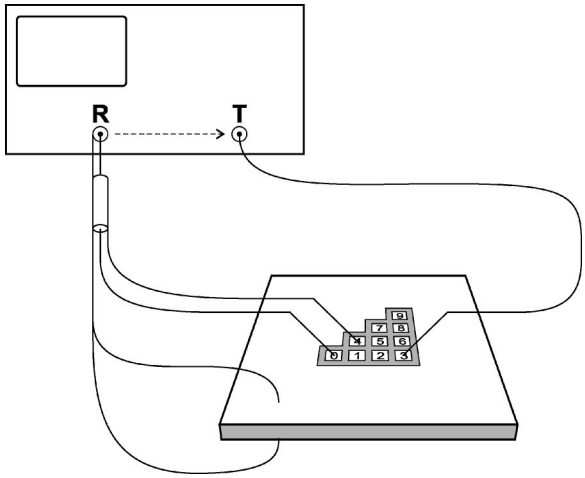

FIG. 8. Schematic diagram of the experimental setup for the measurement of the mutual admittances, by the use of a network analyzer. Only the grounding of cell 4 is represented knowing that all cells are grounded except the excited cell and the probed cell.

In order to obtain harmonic quantities, whether it is the admittance or displacements, we use a periodic finite-element method able to simulate any complex multi-periodic piezoelectric transducer, by meshing only one elementary cell. This approach is described in Ref. 8. The finite-element method allows one to take into account real complex geometries of complete transducers, consisting of the piezoelectric element, possible undercuts, and matching layers. Moreover, media where the transducer radiates such as backing or water can be taken into account thanks to a finite-element/boundary-element method[11,12] associated with the periodic-Green's-function formalism.[13–15] The use of a sparse-matrix solver[16] makes the time consumption not prohibitive in spite of the number of triplets $(\omega, \gamma_1, \gamma_2)$ for which the admittance is computed.

We apply the method to a 1-3 connectivity composite vibrating in air, in order to demonstrate the reliability of the approach by experimental assessment.

III. HARMONIC ADMITTANCE

Figure 4 shows the harmonic admittance computed in the first Brillouin zone[17] for a piezoelectric biperiodic composite, considering the properties of the one experimentally measured and described in the next section. This plot provides the evolution of the harmonic admittance versus the excitation figures and then can be considered as the dispersion curve of the piezoelectrically coupled modes of the composite. The interest of the first Brillouin zone is that, for such a geometry of the unit cell, all the absolute band gaps of the vibrating structure are exhibited in the dispersion diagram.

The point Γ corresponds to a synchronous excitation of the whole array, i.e., γ_1 and γ_2 are zero. At the point X, γ_2 is still equal to zero but γ_1 is equal to 0.5. It means that two adjacent rows along the x_1 axis are in opposite phase. Between Γ and X, a phase is introduced between two adjacent rows, which varies linearly from 0 to π.

One can first observe at about 1.6 MHz (for γ_1 and γ_2 equal to zero) the fundamental longitudinal mode also called

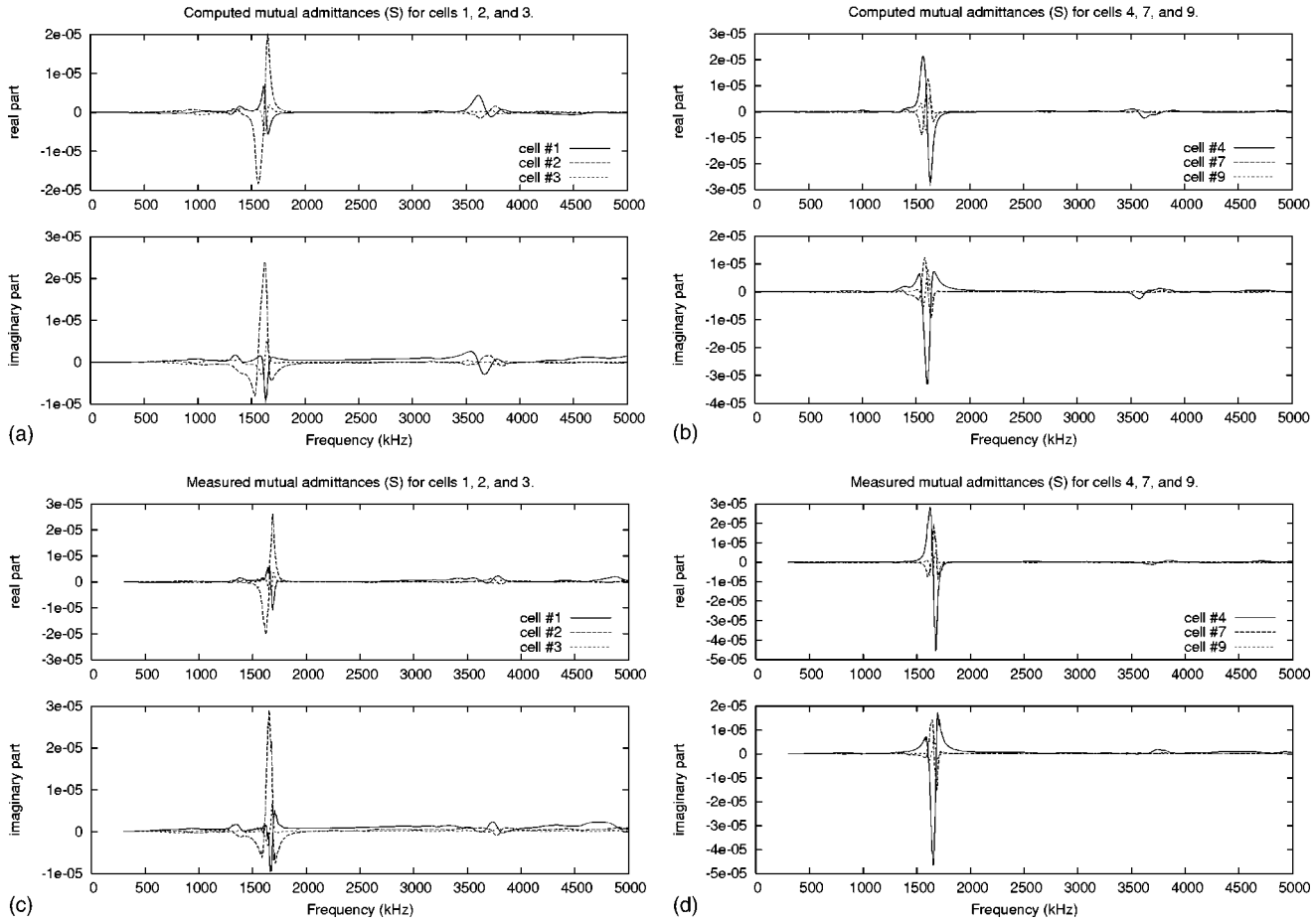

FIG. 9. Mutual admittances for (a) cells 1–3 and (b) cells 4, 7, and 9, calculated after computing the harmonic admittance; (c) and (d), corresponding measured mutual admittances.

thickness mode. At lower frequencies, two specific modes propagate in the structure when both γ_1 and γ_2 are not equal to 0 or 0.5. According to the notation of Ref. 18, these waves are identified, by viewing the displacement fields, as the first and third Lamb-like modes S_0 and S_2. Figure 5 shows the elementary-cell mesh and the S_0- and S_2-mode shapes for $\gamma_1 = 0.25$ and $\gamma_2 = 0$ at 775 kHz (for the S_0) and 1300 kHz (for the S_2), and for γ_1 and γ_2 equal to 0.25 at, respectively, 920 and 1330 kHz. In the case $\gamma_1 = 0.25$ and $\gamma_2 = 0$, the gray scale indicates for both modes the phase of the displacements along the x_1 axis, which conforms with the diagrams of the two modes reported in Fig. 4. The location of the plotted modes is indicated in Fig. 4 by numbers 1–4, respectively. Moreover, the difference of material properties is clearly visible since the epoxy matrix is less rigid than the PZT rods. When the composite vibrates according to the S_2 mode, if one considers the PZT rods only, it is as if they exhibit a vibration comparable to a flexural mode along their thickness, that generates the shear wave propagating in the plate. Note that a second-degree interpolation is used in the finite-element analysis and the inner nodes of the mesh elements are not plotted.

In Fig. 4, a gap is then observed between the thickness-mode frequency and 2.4 MHz. Above this latter frequency many modes appear that have to be related to the so-called lateral modes due to Bragg diffraction.[19] Because of the composite nature of the material, a lot of lateral modes arise as well as their harmonics, more or less piezoelectrically coupled, and it can be difficult to distinguish one lateral mode from another, even by viewing their vibration shapes. The third harmonic of the thickness mode, classically observed for an homogeneous plate, does not exist any more in that composite case if one considers a pure mode, because of the energy conversion between the pure thickness mode, the first lateral mode, and then the successively arising lateral modes.

Figure 6 shows the vibration shape of the lateral mode that appears at 3.7 MHz, and identified by number 5 in Fig. 4. That latter corresponds to the third harmonic of the well-known first lateral mode where the corners of the unit cell vibrate in opposite phase with the PZT-rod center and, what is more, with a greater magnitude. One has to note that the fundamental first and second lateral modes are located between 2.4 and 3 MHz, but they are not piezoelectrically coupled enough to be visible in Fig. 4.

IV. EXPERIMENTAL SETUP

The studied transducer is a bi-periodic 1-3 connectivity piezoelectric composite, consisting of PZT square-section rods embedded in an epoxy matrix. The period is 600 μm in each direction. The PZT rods are 900 μm thick and 445 μm wide, yielding a thickness-over-width ratio equal to 2.02. The measured resonance frequency is about 1.6 MHz.

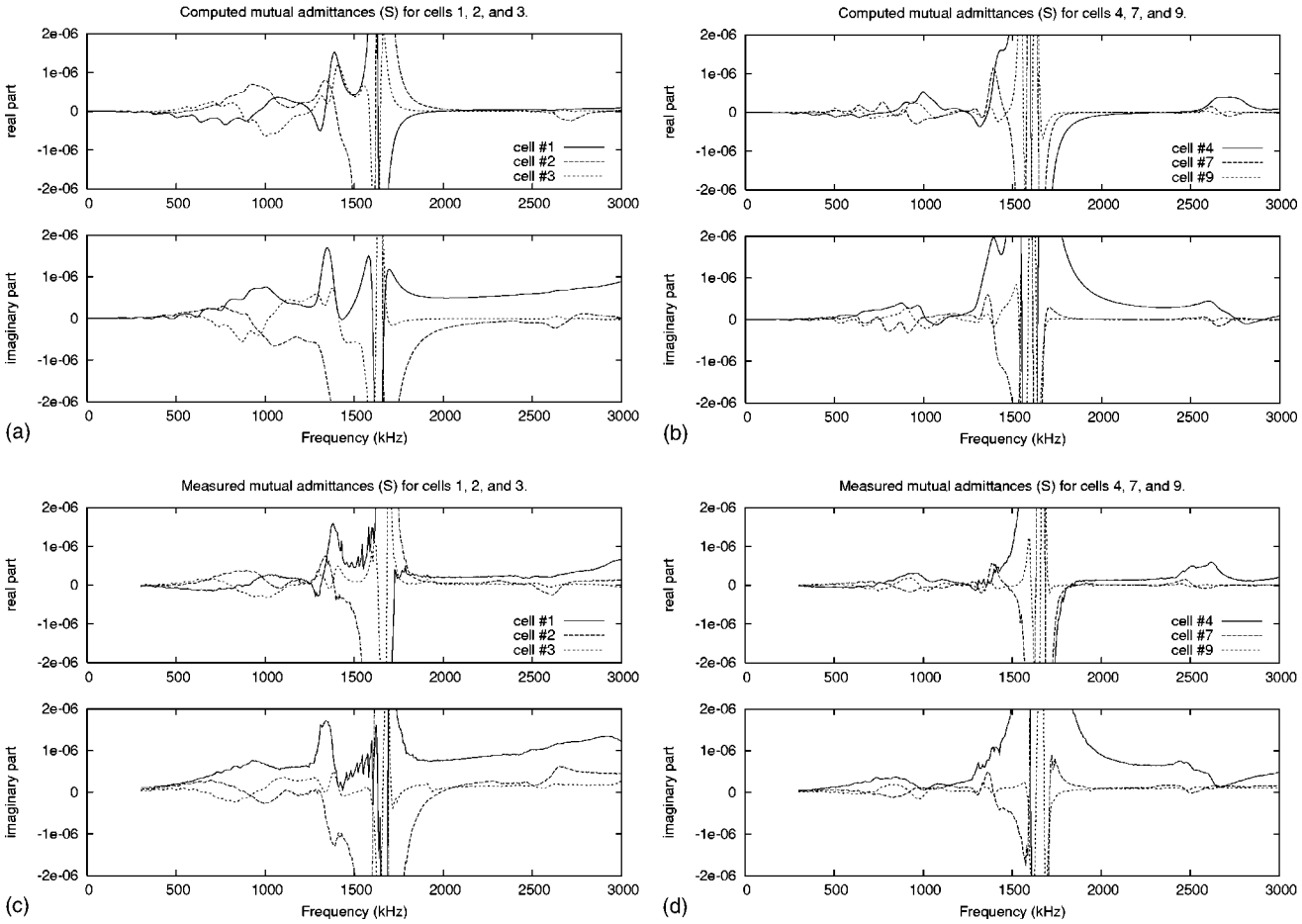

FIG. 10. Close-up of Fig. 9.

In order to measure the mutual admittances, according to the previous definition, we have patterned ten electrodes on the top side of the metallized composite, corresponding to ten elementary cells, as represented in Fig. 7.

The cell 0 is electrically excited by applying an harmonic potential, the others being connected to the ground, except the probed electrode. The remaining metallized surface of the top side is also connected to the ground, in order to comply with the mutual-admittance definition. As a consequence, the electrode pattern allows one to probe each of the ten unit cells. A network analyzer is then used to estimate the transmission parameter between the excited and the probed cell, as schematically represented in Fig. 8, providing the so-called mutual admittance. The electrical-port impedance of the network analyzer is 50 Ω. Since the electrode pattern is located in the middle of the top side and the composite is large enough, the edge effects are expected to be without influence.

V. RESULTS AND DISCUSSION

Figures 9(a) and 9(b) show the mutual admittances, deduced from the integration of the harmonic admittance [see Eq. (8)] computed for each value of the excitation parameters γ_1 and γ_2, and the angular frequency ω. Figures 10(a) and 10(b) are a close-up of the preceding curves between 0 and 3 MHz.

Figures 9(c) and 9(d) show the measured mutual admittances, according to the experimental setup described above, and to be compared with the computed ones. As for the computation results, Figs. 10(c) and 10(d) are a close-up of Figs. 9(c) and 9(d).

Finally, one plots in Fig. 11 the magnitude and the phase of the measured mutual admittances for the three first neighbors along the x_1 axis and along the diagonal.

Below 1.1 MHz, one can observe contributions that grow with frequency as a kind of continuum of modes. This can be related to the contribution of the S_0 mode. Since the mutual admittances integrate all the excitation figures [by definition, see Eq. (8)], the S_0 mode which exists from 0 to 1.1 MHz is responsible for these contributions. It appears more coupled as frequency grows up, until it enters its Bragg conditions, then much weaker contributions are noted. Furthermore, this continuum of modes exhibits periodic ripples. When propagating along the array, the S_0 mode is submitted to multiple partial reflections at the interfaces PZT resin, and constructive or destructive interferences occur. A stronger contribution is then observed at 1.35 MHz which corresponds to the S_2 mode. One can note that, between the S_0 and S_2 modes, there is a gap in which almost no mode arises and that can be identified on the mutual admittances. The S_2 mode is much localized in terms of frequency than the S_0 mode, yielding larger responses on the mutual admittances than the S_0 does. The S_0 and S_2 contributions are evidenced

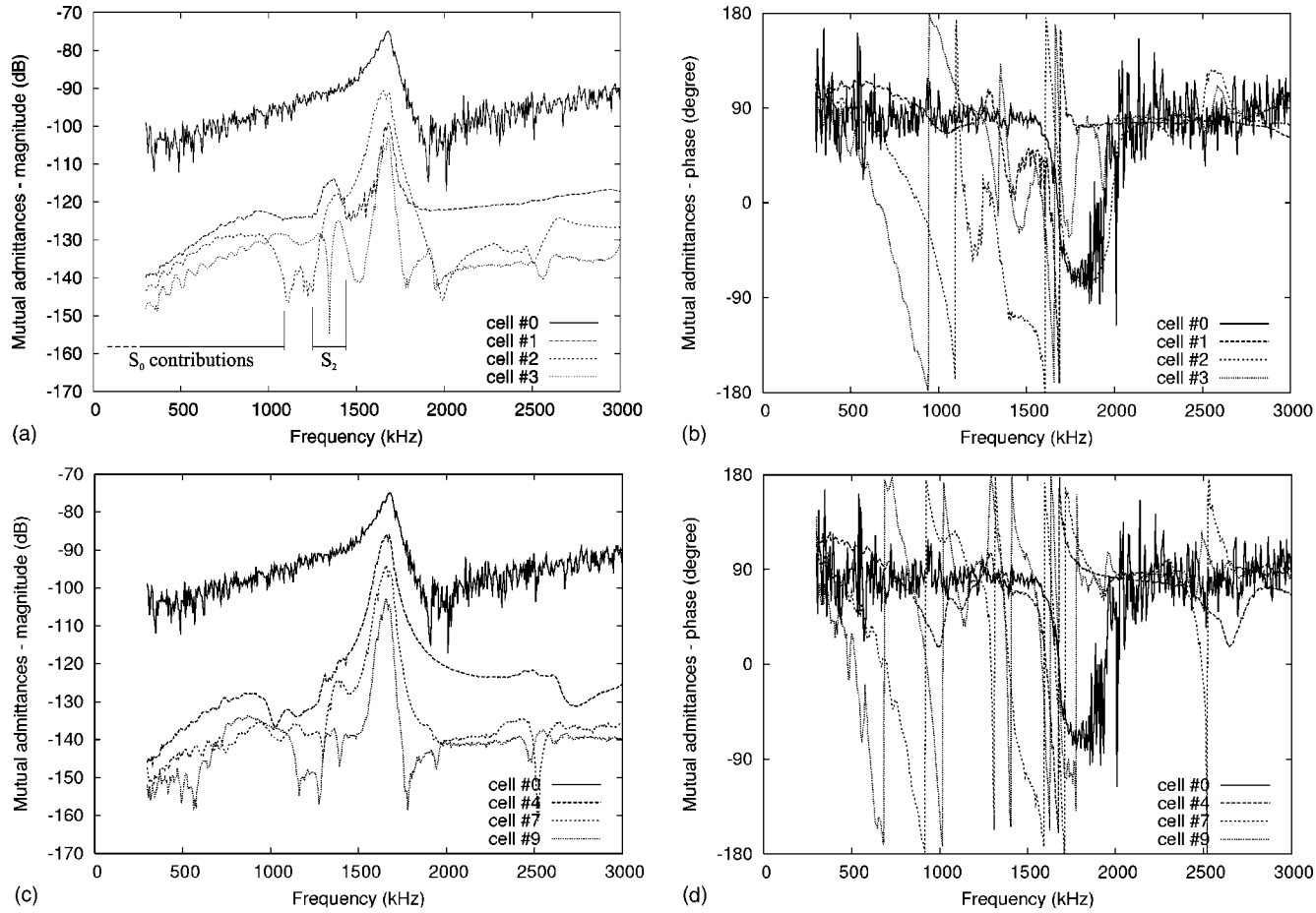

FIG. 11. Measured mutual admittances in magnitude and phase for (a)-(b) cells 1–3 and (c)-(d) cells 4, 7, and 9, compared with the auto admittance of the excited cell.

in Fig. 11(a). A large variation of the mutual admittances is then observed, related to the fundamental longitudinal mode (thickness mode), and truncated in Fig. 10. At frequencies above that modes, large contributions are observed from 3.5 MHz. Weaker contributions are found near 2.6 MHz. All these contributions have to be related to the lateral modes, especially the first and second ones for the 2.6 MHz contributions. Lateral modes are due to Bragg diffraction when the in-plane wavelength $\lambda_{\parallel}$ becomes equal or smaller than the period of the array. Because of the number of the lateral modes and their harmonics and the fact that they superpose themselves, one cannot deduce their contributions to mutual admittances as easily as for the S_0 and S_2 Lamb-like modes.

Comparing computation and measurement results, one obtains below 3 MHz a very good agreement between computations and experiments. Above this frequency, the agreement is not so significant, although computations give qualitatively good results. Many reasons can be invoked. First we certainly have to refine the mesh to accurately simulate the numerous lateral modes and their harmonics which take place at frequencies above 2.4 MHz. Next, the material constants of the PZT and the epoxy-based matrix are not easily estimated with accuracy, and their losses are still more complicated to investigate. Nevertheless, cross-talk levels are well predicted qualitatively and quantitatively, especially concerning the thickness mode and the Lamb-like modes propagating in the array.

Finally, if one considers the thickness-mode frequency, along the diagonal, the admittance magnitude decreases regularly with a 10 dB loss between each cell. More unexpected is the variation of the magnitude for the cells 1–3. The decrease is indeed not regular since the admittance of cell 2 is greater than that of cells 1 and 3. Between the excited cell and the neighboring cells 1 and 3, we have, respectively, 25 and 30 dB, whereas the second cell is only 15 dB lower. This behavior is to be related to the frequency nearness of the thickness mode and of the S_2 Lamb-like mode. When exciting one cell, this cell and the second neighbor have principally a longitudinal vibration, whereas the first and third neighbors exhibit a shear-wave behavior according to the S_2-mode shape, as represented in Fig. 12. This

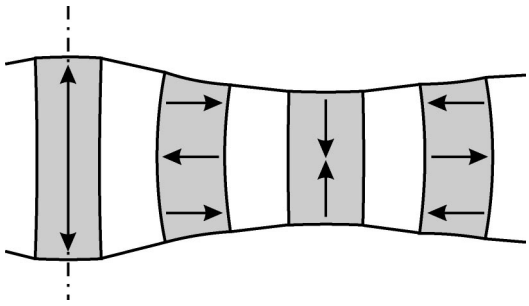

FIG. 12. Schematic diagram of the coupling between the thickness mode and the S_2 mode.

kind of behavior is strongly dependent on the materials and the dimensions of the array and does not systematically appear.

VI. CONCLUSION

We have adapted a one-dimensional approach, well known in the surface-acoustic-wave domain, by introducing the concept of harmonic and mutual admittances for a two-dimensional periodic transducer. Comparison between experiments and theoretical computations demonstrates the efficiency of the proposed approach.

We have computed the harmonic admittance and the mutual admittances of a 1-3 connectivity piezoelectric composite and estimated the contributions of modes propagating in the structure to cross talks. Two Lamb-like modes propagate at frequencies lower than that of the fundamental longitudinal mode. Their influence on the mutual admittances is well described by the model. Particularly, taking into account the periodic nature of the array allows one for accessing subtile properties of such a device, like band-gap behavior and other particular spectral contributions. At higher frequencies, many lateral modes due to Bragg diffraction propagate in the composite. A reliable representation of such contributions requires refined computations and a good knowledge of material properties (particularly shear velocities and losses). Finally, according to the theoretical approach, we have measured the mutual admittances for the composite and shown the reliability of the method.

This work tends to demonstrate that the computation of mutual quantities provides a reliable tool for the description and furthermore the optimization of cross-talk effects in piezocomposite transducers and more generally in ultrasound probes.

ACKNOWLEDGMENTS

The authors want to thank the Technical Center of Framatome-ANP in Saint-Marcel (France), and Parallel Design SAS in Sophia-Antipolis (France), for their support during this study.

[1] W. A. Smith, ''The role of piezocomposites in ultrasonic transducers,'' in Proceedings of the IEEE Ultrasonics Symposium, Montreal, Quebec, Canada, October 3–6, IEEE #89CH279-2, 755–766 (1989).
[2] Ö. Oralkan, A. Sanli Ergun, J. A. Johnson, M. Karaman, U. Demirci, K. Kaviani, Th. H. Lee, and B. T. Khuri-Yakub, ''Capacitive micromachined ultrasonic transducers: Next-generation arrays for acoustic imaging?,'' IEEE Trans. Ultrason. Ferroelectr. Freq. Control **49**, 1596–1610 (2002).
[3] D. Certon, N. Felix, E. Lacaze, F. Teston, and F. Patat, ''Investigation of cross-coupling in 1-3 piezocomposite arrays,'' IEEE Trans. Ultrason. Ferroelectr. Freq. Control **48**, 85–92 (2001).
[4] G. S. Kino and R. Baer, ''Theory for cross-coupling,'' in Proceedings of the IEEE Ultrasonics Symposium, Atlanta, Georgia, October 31, November 1, 2, IEEE #83CH1947-1, 1013–1019 (1983).
[5] C. Negreira, H. Gomez, N. Perez, I. Nuñez, and J. Eiras, ''Lateral modes and diffracted field behaviour in non-periodical 1-3 piezocomposite transducers,'' in Proceedings of the IEEE Ultrasonics Symposium, Sendai, Miyagi, Japan, October 5–8, IEEE #98CH36102, 641–644 (1998).
[6] N. Lamberti, P. Gori, G. Caliano, A. Iula, R. Carotenuto, and M. Pappalardo, ''Radiation pattern distortion caused by the interelement coupling in linear array transducers,'' in Proceedings of the IEEE, Nevada, October 17–20, IEEE #99CH37027, 1071–1075 (1999).
[7] Y. Zhang, J. Desbois, and L. Boyer, ''Characteristic parameters of surface acoustic waves in a periodic metal grating on a piezoelectric substrate,'' IEEE Trans. Ultrason. Ferroelectr. Freq. Control **40**, 183–192 (1993).
[8] S. Ballandras, M. Wilm, P.-F. Edoa, A. Soufyane, and V. Laude, ''Finite-element analysis of periodic piezoelectric transducers,'' J. Appl. Phys. **93**, 702–711 (2003).
[9] J. Guyonvarch, D. Certon, L. Ratsimandresi, F. Patat, and M. Lethiecq, ''Application of normal mode theory to modeling of cross-coupling in 1D piezocomposite arrays,'' in Proceedings of the IEEE Ultrasonics Symposium, Atlanta, Georgia, October 7–10, IEEE #01CH37263, 973–976 (2001).
[10] M. Wilm, S. Ballandras, V. Laude, and Th. Pastureaud, ''A full 3D plane-wave-expansion model for 1-3 piezoelectric composite structures,'' J. Acoust. Soc. Am. **112**, 943–952 (2002).
[11] S. Ballandras, V. Laude, Th. Pastureaud, M. Wilm, W. Daniau, A. Reinhardt, W. Steichen, and R. Lardat, ''A FEA/BEM approach to simulate complex electrode structures devoted to guided elastic wave periodic transducers,'' in Proceedings of the IEEE Ultrasonics Symposium, Munich, Germany, October 8–11, IEEE #02CH37388C, 309–312 (2002).
[12] M. Wilm, S. Ballandras, A. Reinhardt, V. Laude, R. Lardat, R. Armati, W. Daniau, F. Lantéri, J.-F. Gelly, and O. Burat, ''A 3-D mixed finite-element/boundary-element model for the simulation of periodic ultrasound transducers radiating in layered media,'' in Proceedings of the IEEE Ultrasonics Symposium, Honolulu, Hawaii, October 5–8, IEEE #03CH37476C, 1654–1657 (2003).
[13] V. P. Plessky and Th. Thorvaldsson, ''Periodic green's functions analysis of SAW and leaky SAW propagation in a periodic system of electrodes on a piezoelectric crystal,'' IEEE Trans. Ultrason. Ferroelectr. Freq. Control **42**, 280–293 (1995).
[14] P. Ventura, J.-M. Hodé, and M. Solal, ''A new efficient combined FEM and periodic green's function formalism for the analysis of periodic saw structures,'' in Proceedings of the IEEE Ultrasonics Symposium, Seattle, Washington, November 7–10, IEEE #95CH35844, 263–268 (1995).
[15] A. Reinhardt, Th. Pastureaud, S. Ballandras, and V. Laude, ''Scattering matrix method for modeling acoustic waves in piezoelectric, fluid, and metallic multilayers,'' J. Appl. Phys. **94**, 6923–6931 (2003).
[16] T. A. Davis and I. S. Duff, ''An unsymmetric-pattern multifrontal method for sparse LU factorization,'' SIAM J. Matrix Anal. Appl. **18**, 140–158 (1997).
[17] L. Brillouin, *Wave Propagation in Periodic Structures* (Dover, New York, 1953).
[18] D. Royer and E. Dieulesaint, *Elastic Waves in Solids 1* (Springer, Berlin, 2000).
[19] D. Certon, F. Patat, F. Levassort, G. Feuillard, and B. Karlsson, ''Lateral resonances in 1-3 piezoelectric periodic composite: Modeling and experimental results,'' J. Acoust. Soc. Am. **101**, 2043–2051 (1997).

Analytical-numerical matching for fluid-loaded structures with discontinuities

Christopher D. Park
General Dynamics, 14700 Lee Road, Chantilly, VA 20151

Linda P. Franzoni and Donald B. Bliss
Department of Mechanical Engineering, Duke University, Durham, North Carolina 27708-0300

(Received 27 August 2003; revised 9 June 2004; accepted 2 August 2004)

The method of analytical-numerical matching (ANM) is applied to several example problems involving the radiation and vibration of a fluid-loaded cylindrical shell with structural discontinuities. These problems are used to verify the accuracy of the method compared to a purely numerical approach, and to demonstrate the usefulness of ANM for solving problems involving nonaxisymmetric forcing and constraints on structures that are otherwise axisymmetric. The principal advantage of the ANM method for this application is its ability to employ a spectral method (modal decomposition in azimuth) in the solution of a problem that is nonaxisymmetric. ANM divides the original problem into local and global subproblems that are solved separately. The discontinuity is handled using a high-resolution local finite-element model. Smooth forces are derived from solving an analytical matching problem on the local domain, and these smooth forces are then applied to a low-resolution numerical global problem. The superposition of solutions to the subproblems is equivalent to the solution of the original problem. For fluid loading, the local high-resolution model is solved *in vacuo*, and the effects of fluid loading are included completely by the low-resolution global problem.
[DOI: 10.1121/1.1798272]

PACS numbers: 43.40.Ey, 43.40.Rj [ANN] Pages: 2956–2968

I. INTRODUCTION

The calculation of radiation and scattering from a fluid-loaded shell with discontinuities such as ribs and/or attachments is challenging, both in terms of accuracy and computational effort. Incident external waves or internal forcing set the structure in motion, which excites an acoustic field in the surrounding fluid. Typically, for submerged structures, the heavy fluid loading has a strong effect on the structural motion, and the structure–fluid system must be solved in a fully coupled manner. Even when the fully coupled system is solved, some modes of motion radiate efficiently, whereas others are nonradiating. One effect of structural discontinuities is to couple radiating and nonradiating modes through interactions at discontinuities.

For a smooth fluid-loaded shell, the numerical resolution is set by the need to resolve the shortest structural waves on the shell. However, when structural discontinuities are introduced much finer resolution is required to resolve the detailed shape. An example of a shell with structural discontinuities is shown in the sketch of Fig. 1 labeled ''original.'' The shell may be subject to vibrating motion of the constraint, or may be excited by an incident acoustic field. It has been shown that it is necessary to resolve discontinuities with high accuracy.[1–3] Whenever the constraint condition at a discontinuity involves displacement or velocity, which it does in almost all cases, failure to accurately converge the motion at structural discontinuities produces convergence errors over the entire structure. Scattering problems for complex structures are often difficult to converge for this reason. Typically, a very large numerical problem involving many disparate scales must be solved to high resolution. This paper describes the successful application of a method to reformulate such problems into local and global parts to obtain high accuracy with rapid convergence.

Many engineering problems involve systems with disparate length scales, and a number of methods utilizing scale separation have been developed. In an analytical framework, the method of matched asymptotic expansions (MAE) is a prime example. In a purely numerical framework, adaptive meshing schemes for finite-element analysis (FEA) are widely used. Between these approaches are various hybrid schemes that combine an analytical treatment with a numerical scheme, or at least use analytical insight to join two numerical schemes. For instance, the work of Barbone patches a near-field numerical scheme to a far-field analytical solution.[4] Recent work with numerical hybrid schemes include a spectral super-element method to handle wave propagation in structures with local nonuniformities,[5] and a method to couple independently modeled domains through an application of Lagrange multipliers.[6]

The ANM approach differs from other methods in at least two ways. First, it is a matching scheme (not a patch) in which solutions are overlapped, and thus draws its inspiration from MAE. Second, and different from all other methods, ANM separates local and global regions by the introduction of canceling smooth forces with special properties. As such, it relies less on the properties of the governing equations themselves to decompose a problem into constituent parts. The approach, which is explained in more detail in the next section, allows regions of rapid change to be solved in

isolation, leaving only a dynamically equivalent smooth forcing to act on the large-scale problem.

This paper considers a fluid-loaded cylindrical shell driven by a localized discontinuity. There are several other approaches available to solve this problem. A direct approach is a three-dimensional FEA treatment of the shell and perhaps some region of the surrounding fluid. The region around the discontinuity must be resolved to very high accuracy, and this would be done with a scheme incorporating variable mesh density. The fluid loading could also be handled by finite elements enveloping the body with a transition to infinite elements on an outer surface; alternatively, the fluid loading can be handled by boundary elements. The problem with this direct approach is the high computational cost associated with solving this very large problem.

For axisymmetric structures, the fully 3D direct approach is inefficient in comparison to a spectral method that decomposes the azimuthal dependence in modes. Because the structure is axisymmetric except for the constraint, the approach described in this paper can be used to treat the constraint efficiently within the context of a spectral method. Since many problems of practical importance involve structures that are largely axisymmetric but have various important attachments, other approaches have been considered in the literature. In particular, Farhat[7,8] has developed a fictitious domain decomposition method that reduces the problem to a series of two-dimensional problems coupled by Lagrange multipliers. However, although the method is much faster than the direct 3D method, the azimuthal discontinuities cause slower convergence. One application of the present work is to illustrate how a matching method can be used to replace azimuthal discontinuities with equivalent smooth forces and greatly accelerate convergence of a spectral method, while isolating the discontinuity in a well-defined subproblem.

II. DESCRIPTION OF ANALYTICAL-NUMERICAL MATCHING

The ANM method is a hybrid analytical and numerical technique. A low-resolution numerical solution (global) and a high-resolution (local) analytical (or numerical) solution are formally matched to form a composite solution that is valid over the entire spatial and frequency range. In the overall problem, discrete forces are replaced by smooth distributed forces. A matching solution on a local domain accounts for the difference between the original discrete force and the smooth distributed force. Figure 1 shows a schematic of the ANM decomposition as applied to an elastic cylindrical shell with a rigid constraint.

To the original problem, consisting of an elastic cylindrical shell with a rigid constraint, a smooth distributed force is added and subtracted (leaving the original problem unchanged). The principle of superposition is applied in order to separate the problem into subproblems. The original structure without a constraint, but with a smooth force, becomes the global problem. The remainder consists of the opposite sign smooth force, the constraint, and the structure. If the combination of the smooth forces and the forces due to the constraint combine to bring the structure to rest outside the region over which the smooth force is applied, then the remaining problem becomes local (confined to the smooth-force region) and can be subdivided again.

Since the region outside the smoothing region is at rest, there is no displacement, and there are no higher derivatives of displacement beyond the boundaries of the smoothing region. Therefore, the smoothing region can be thought of as having a fixed–fixed boundary. Further subdivision leads to a problem with the constraint (that will be driven by a force or torque) on a fixed–fixed domain, and a problem with an opposite sign smooth force on the same local spatial domain; see Fig. 1.

The ANM method was originally developed by Bliss[9,10] for the analysis of free-vortex wakes in rotorcraft aerodynamics. ANM increased the efficiency of this computationally intensive problem by orders of magnitude. More recently, fluid-mechanical applications of ANM include the analysis and solution of wing aerodynamics for compressible unsteady flow and the development of an acoustic boundary element method.[11–13]

ANM was applied to wave propagation problems by Loftman and Bliss, who calculated acoustic radiation from fluid-loaded membranes and curved shells with structural discontinuities.[1–3] For these applications, the numerical subproblems were solved using modal methods. Franzoni and Park[14] used finite-element analysis with ANM for predicting the response of a thick beam with discontinuities.

III. ANM FOR A CYLINDRICAL SHELL WITH A DISCONTINUITY

The structural vibration problem posed in Fig. 1 is an elastic shell with a rigid attachment on its inner wall. The ANM subproblems consist of the constraint surrounded by a small portion of shell (the local problem), a smooth distributed force acting on the same portion of shell (the matching problem), and the same distributed force acting in the opposite direction at the appropriate location on the full shell (the global problem). The individual subproblems including the choice of local region and the determination of the smooth distributed force are discussed in the following subsections. A more detailed derivation of ANM applied to this problem is found in the thesis by Park.[15]

A. The local problem

A region around the discontinuity is chosen as the domain for the local problem. The outer boundary of this piece of shell is held fixed, as shown in the ''local'' sketch of Fig. 1. The choice of a circular patch rather than some other geometrical shape allows for the smoothest possible set of forces for the subsequent matching and global problems. Geometrical shapes with corners introduce new discontinuities into the problem, and are therefore avoided. The size of the circular patch (otherwise known as the smoothing region) is not unique and is chosen based on two considerations. The patch is ''circular'' in the sense of a curvilinear mapping onto the curved shell surface; if unwrapped (not projected) to be flat, it would form a standard polar coordinate system. The radius of the circular patch must be large enough so that any through-the-thickness effects due to the discontinuity are no

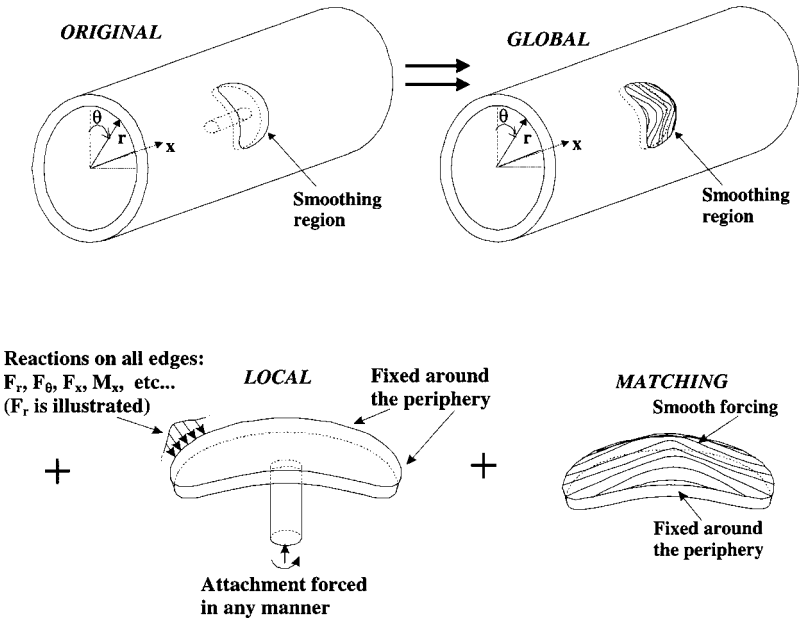

FIG. 1. The ANM process applied to a cylindrical shell with an attachment. Original problem contains a discontinuity attached at the inner surface.

longer significant at the boundary. However, it is also desirable for the smoothing region to be somewhat small, to avoid complicated wave behavior in this region, to assure relatively simple behavior around the region boundaries, and to limit the size of the computational subproblem.

A high-resolution finite-element analysis is performed on the local problem, where the constraint is forced separately in all of its degrees of freedom and the boundary is held fixed. Special attention is given to ensure accurate numerical resolution in the region around the discontinuity where rapid variations are expected. Transfer functions between the forcing of the constraint and the response, including the reaction forces and moments on the boundary, are calculated and stored.

B. The matching problem

The matching problem consists of a set of smooth distributed forces acting over the same local domain as the previous high-resolution local problem. In order to determine the set of smooth forces, the circular patch of shell is modeled analytically using shell theory. It is also possible, although not necessarily as computationally efficient, to solve the matching problem numerically; high resolution is not required, since there is no discontinuity in the domain. The smooth distributed forces are represented as a series of smoothly varying independent functions with unknown coefficients. These coefficients are determined by a set of constraint equations that arise from the following: the geometric boundary conditions on displacement and slope; the desire that the forces have a certain level of smoothness (i.e., go to zero at the boundaries and have no slope there); and the requirement that the reactions be identical in magnitude and of opposite sign relative to those of the previous high-resolution local problem. The purpose of this last constraint is to ensure that when the local and matching subproblems are added together, they do not transfer any edge forces or moments to the rest of the shell.

1. Governing equations for a thin elastic shell

To formulate the matching problem, an appropriate set of governing equations must first be identified. For a thin shell ($h \ll a$), the Love–Timoshenko (L–T) governing equations (including dynamic terms) can be adapted to the present coordinate system [Fig. 2(a)] and expressed in dimensionless form, as given in Eq. (1).

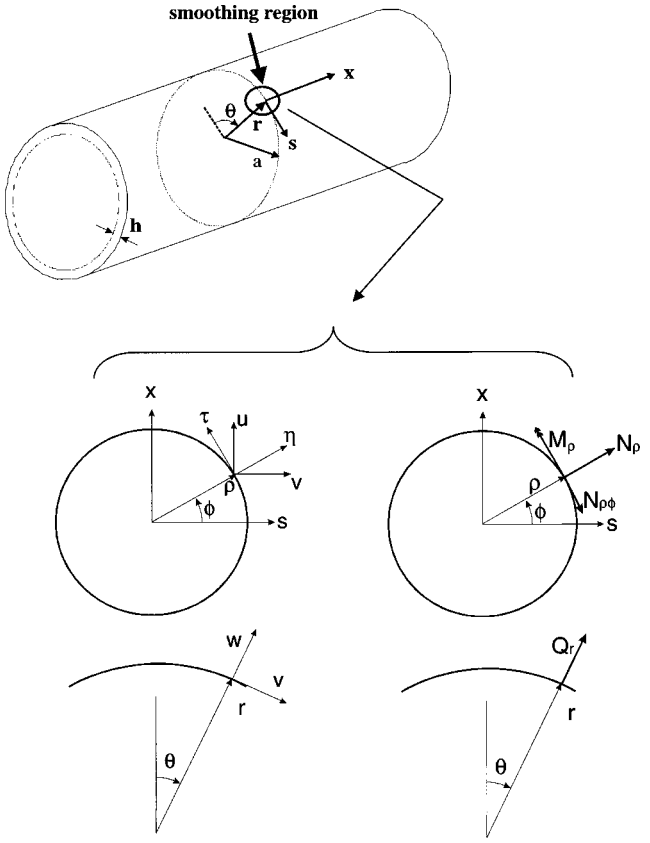

FIG. 2. (a) Generalized shell geometry and coordinate system. (b) Displacements and reactions for local and matching problems, in local polar coordinates.

$$\begin{bmatrix} \frac{\partial^2}{\partial x^2}+\frac{(1-\nu)}{2}\frac{\partial^2}{\partial s^2}+K_p^2 & \frac{(1-\nu)}{2}\frac{\partial^2}{\partial x\partial s} & \nu\frac{\partial}{\partial x} \\ \frac{(1+\nu)}{2}\frac{\partial^2}{\partial x\partial s} & \frac{(1-\nu)}{2}\frac{\partial^2}{\partial x^2}+\frac{\partial^2}{\partial s^2}+\beta^2\left((1-\nu)\frac{\partial^2}{\partial x^2}+\frac{\partial^2}{\partial s^2}\right)+K_p^2 & \frac{\partial}{\partial s}-\beta^2\left(\frac{\partial^3}{\partial x^2\partial s}+\frac{\partial^3}{\partial s^3}\right) \\ \nu\frac{\partial}{\partial x} & \frac{\partial}{\partial s}+\beta^2\left((2-\nu)\frac{\partial^3}{\partial x^2\partial s}+\frac{\partial^3}{\partial s^3}\right) & 1+\beta^2\left(\frac{\partial^2}{\partial x^2}+\frac{\partial^2}{\partial s^2}\right)^2+K_p^2 \end{bmatrix} \begin{Bmatrix} u \\ v \\ w \end{Bmatrix} = \begin{Bmatrix} -p_x \\ -p_s \\ -p_r \end{Bmatrix}, \tag{1}$$

The variables u, v, and w are the normalized axial, azimuthal, and radial displacements in the x, s, and r directions, respectively.[16] All displacements and coordinate directions are normalized by the shell radius, a. The nondimensional pressure, p_r, and tractions, p_s and p_x, are normalized by the factor $Eh/[a(1-\nu^2)]$. E is the Young's modulus of elasticity of the shell material and ν is the Poisson's ratio. Note that the nondimensional arc length, s, is equivalent to θ in Fig. 2(a). Additionally, the factor $\beta^2=(1/12)(h^2/a^2)$ and the inertial terms have been expressed in Helmholtz form, with the definition $K_p\equiv\omega a/c_p$, where ω is the frequency of harmonic vibration (rad/s), and c_p is the longitudinal wave speed for the shell.

Because ANM is a hybrid method, it is important that the numerical and analytical components of the solution have a consistent level of accuracy. To replace a discontinuity with an equivalent set of smooth pressures and tractions, the response in all three of the cylindrical coordinate directions must be determined accurately. The Love–Timoshenko governing equations, which are used in this work, have been verified to be accurate in all three coordinate directions when in-plane tractions and out-of-plane pressures are applied. It is noted that the Love–Timoshenko shell equations are much more accurate than the more approximate Donnell–Mushtari set of equations.[17] In fact, it can be shown that the Donnell–Mushtari equations do not solve static equilibrium, rendering them inappropriate for most analyses that include strong in-plane coupling.

2. Edge reactions for a thin elastic shell

Expressions for the edge reactions for the Love–Timoshenko formulation are defined by Ugural.[16] Following Ugural's nomenclature taken from the figure in Ref. 16, p. 440, the in-plane reaction components (N_x,N_θ,$N_{x\theta}$), moment components (M_x,M_θ,$M_{x\theta}$), and transverse shear edge reaction components (Q_x,Q_θ) are written in terms of derivatives of displacements u, v, and w. Note, however, that the radial coordinate and displacement differ in sign from that given in Ref. 16, where relative to the present notation $y=s$ and $z=a-r$.

The matching problem is defined over a circular geometry that is not directly compatible with the global cylindrical coordinate system [Fig. 2(a)]. Therefore, the governing equations and reaction expressions are transformed to a more appropriate local polar coordinate system as shown in Fig. 2(b). This transformation is also discussed fully in Ugural.[16]

A matching solution is formulated by computing the displacements and therefore, the smooth applied force that will cause edge reactions that exactly oppose those produced by the local problem. In local polar form, there are four reaction types to be matched as illustrated in Fig. 2(b): the out-of-plane shear, Q_r; the bending moment, M_ρ; the in-plane shear, $N_{\rho\phi}$; and the in-plane tension, N_ρ.

3. Formulating the matching solution

The matching solution for the 3D shell is solved by first defining a set of displacements with unknown coefficients. From these functions for displacements, the reaction components are then written in terms of the unknown coefficients. Boundary conditions are then applied, where the edge reaction components of the local problem are set equal and opposite to the edge reaction components of the matching problem. In addition, smoothing conditions (on lower derivatives) are applied at the boundary, as was explained in Ref. 14 and other previous ANM work. Imposing boundary conditions and smoothing conditions gives a system of equations for the unknown coefficients. Solving the system for the coefficients determines the displacements, and by substitution into the governing equation also determines the smooth forcing. The implication is that this smooth forcing produces the reaction force and moment components that will exactly cancel the reactions of the local subproblem.

As an example, consider the case where the mth local polar cosine mode of transverse shear is to be canceled in the matching problem. The matching problem transverse displacement, w, must be a valid solution of the governing equation and satisfy the geometric boundary conditions (fixed end conditions). Bessel functions of the first kind, with appropriate arguments, are chosen for convenience since their form leads to simplifications upon substitution into the structural operator. The transverse displacement is written as a series of the form

$$w=\sum_{n=1}^{N} C_n J_m(k_{nm}\rho)\cos(m\phi), \tag{2}$$

where C_n are yet-to-be-determined coefficients and N is the number of constraint conditions (thus, the number of terms) required to define the displacement field, and the constants k_{nm} are the first through Nth zeros (roots) of the Bessel function; thus at the smoothing boundary, $J_m(k_{nm}\rho)|_{\rho=1}=0$ for each n and therefore $w|_{\rho=1}=0$.

Since the transverse shear reaction case can be formulated from transverse displacement only, the in-plane displacements u and v are prescribed to be zero. This fact greatly simplifies the governing equations and reaction expressions, so that the radial pressure is given by

$$p_r = \sum_{n=1}^{N} C_n(\beta^2 k_{nm}^4 - K_p^2) J_m(k_{nm}\rho)\cos(m\phi). \tag{3}$$

For this choice of w, the geometric boundary condition on displacement is automatically satisfied. The second built-in geometric boundary condition, namely that slope equal zero, $\partial w/\partial\rho|_{\rho=1}=0$, yields the first constraint equation used to solve the Bessel function coefficients, C_n, in Eq. (2). Constraining additional derivatives of w at the boundary satisfies the natural boundary condition criteria. Note that $\partial^n w/\partial\phi^n|_{\rho=1}=0$ for all n since all the Bessel functions in Eq. (2) vanish when $\rho=1$. Also recall that the in-plane displacements u and v are defined to be zero in this example.

Due to the imposed conditions on displacements and derivatives of displacement from the aforementioned constraints, all in-plane reactions (N_ϕ or N_ρ) are identically zero. The remaining nonzero edge-reaction components can be reduced, normalized, and expressed in local polar coordinates as

$$M_r = -\beta^2 \left.\frac{\partial^2 w}{\partial\rho^2}\right|_{\rho=1} \qquad Q_r = -\beta^2 \left.\left(\frac{\partial^3 w}{\partial\rho^3} + \frac{1}{\rho}\frac{\partial^2 w}{\partial\rho^2}\right)\right|_{\rho=1}. \tag{4}$$

Prescribing zero moment at the boundary places a condition on the second radial derivative, leaving only the third radial derivative term in the transverse shear equation. The constraints placed on transverse shear and moment become the second and third equations used in solving for the coefficients C_n.

Displacement smoothness is satisfied, in part, by virtue of the natural smoothness of the Bessel functions. Additionally, it is observed that the zeroth through third radial derivatives of w have either vanished or have been prescribed at the boundaries. The fourth and fifth radial derivatives of w are directly coupled to the applied pressure, p_r, through the governing equations. Note that the radial component of pressure is zero around the periphery, due to the conditions on w.

To ensure the smoothness of the applied pressure, it is desired that $\partial p_r/\partial\rho|_{\rho=1}=0$. This condition becomes the fourth and final constraint equation used to solve for C_n.

Once the first N roots (k_{nm}) are defined for a given mode, m (found easily in tabulated form), w is written as

$$w = C_1 J_m(k_{1m}\rho)\cos(m\phi) + C_2 J_m(k_{2m}\rho)\cos(m\phi) + C_3 J_m(k_{3m}\rho)\cos(m\phi) + C_4 J_m(k_{4m}\rho)\cos(m\phi). \tag{5}$$

Using the constraint equations described, the linear system of equations for the unknown constants C_n is defined. The resulting displacement produces unit transverse shear Q_r with a local modal dependence of $\cos(m\phi)$. Substituting the displacement coefficients C_n into Eq. (3) gives the applied pressure (or smooth force). A similar method is used to produce a matching solution for each mode of the in-plane reactions. Note that a unique set of coefficients C_n can always be found as long as an independent set of basis functions (in this case the Bessel functions) is used in Eq. (2). In previous work polynomials with unknown coefficients were used to represent displacement. The constraint equations form a linearly independent set of equations; therefore, the resulting system should never be ill-conditioned or singular.

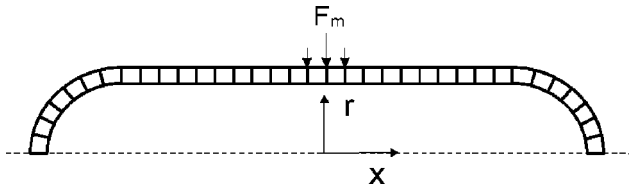

FIG. 3. Modal/FEA solution method for the example problem The problem is reduced to a separate 2D FEA model for each mode, m.

C. The global problem

The global solution is found by applying the negative of the pressures and tractions from the matching solution to the full (original) structure minus the discontinuity. The global problem is smooth in the structural sense, containing no regions of rapid variation; therefore, it is modeled using low-order numerics (in some problems, the global solution may also be found analytically). For the example problems in this paper, the computer code SONAX has been used to solve the global problem.

SONAX is a structural-acoustic computer program, developed by researchers at the U.S. Naval Research Lab (NRL), which can be used to predict radiation and scattering from structural bodies of revolution. A typical configuration for analysis would be a cylindrical shell with hemispherical endcaps. In some cases the shell might have circumferential ribs, which still allow the body to be axisymmetric. The full equations of elasticity are solved for the structure and the acoustic wave equation is solved for the fluid. Harmonic time dependence is assumed. The governing equations, which are separable, are Fourier decomposed around the azimuth. An approach based on structural finite elements and acoustic boundary elements is then used to solve the problem posed in radial and axial coordinates (r,x) for each azimuthal mode; see Fig. 3.

Because SONAX uses a Fourier decomposition around azimuth, any forcing applied to the shell must be decomposed into azimuthal harmonics; then, the problem is solved for each harmonic and the overall result reassembled. Therefore, the applied forcing is decomposed in global azimuth such that

$$\xi(r,\theta,x) = \sum_{m=0}^{\infty} A_m(r,x)\cos(m\theta) + B_m(r,x)\sin(m\theta), \tag{6}$$

where ξ represents any of the three applied pressures or tractions. For the radial line force example, the forcing and corresponding radial and axial response are even functions in global azimuth. The global problem displacements are subsequently solved in the same form as Eq. (6).

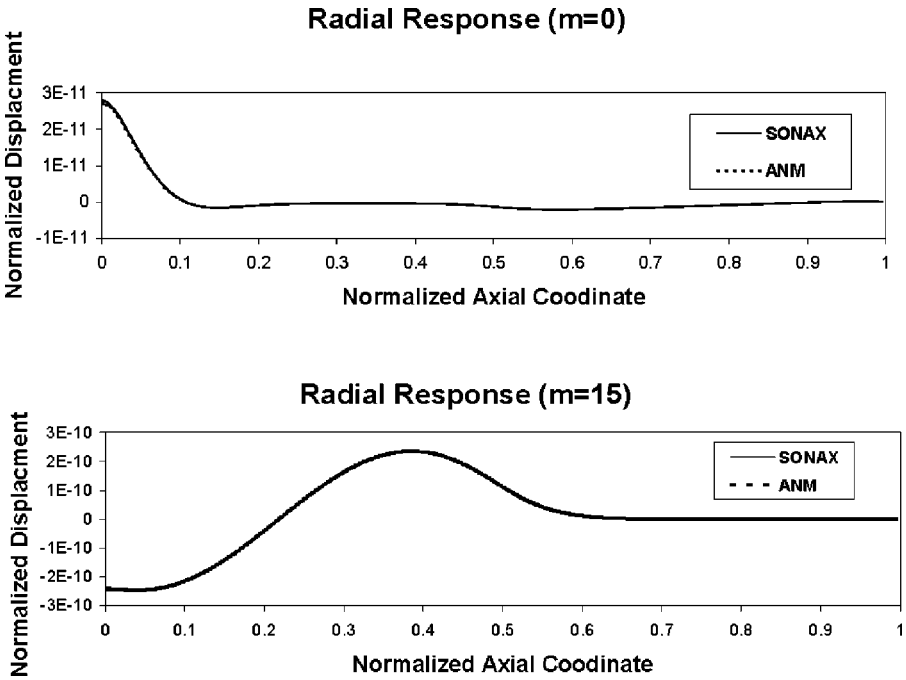

FIG. 4. Radial response of outer shell surface, SONAX vs ANM, radial "hat" forcing case.

IV. EXAMPLE PROBLEMS

Three example problems are now presented, each one having a different purpose. The first example problem is used to verify the ANM method. For this task, a problem was chosen that could be solved using an axisymmetric numerical code (i.e., SONAX). There is no computational advantage to using ANM for this problem, but it serves to demonstrate accuracy of the method. The second and subsequent example problems cannot be solved by the axisymmetric code without the use of ANM. For these problems the constraint is forced in a motion tangential to the shell, or rocked in an antisymmetric motion. These problems are chosen to illustrate certain features of the ANM method. After these problems are described, the extension of ANM to include fluid loading is developed in Sec. V. All example problems use the same basic shell.

A. Verification problem

For verification purposes, ANM is used to compute the structural vibration of a shell excited by a harmonic line force applied in the radial direction, and this result is compared to that of SONAX. The radial line force is used for the verification model since it is a forcing function that a modal/FEA method (i.e., SONAX) can analyze accurately on a mode-by-mode basis.

A 3D elastic cylindrical shell with hemispherical endcaps *in vacuo* is harmonically excited by a linearly varying radial line force, F, that is aligned with the global axis, as shown in Fig. 3. The line force is applied over a short axial span of 1.5% of the total length ($2L$) of the shell (the scale is exaggerated in the figure). The radial force profile is that of a triangular "hat" function, varying nondimensionally from 0 to 1 to 0, symmetric with respect to the axial dimension (x) of the shell. It is a Dirac delta function in global azimuth, θ, and is applied harmonically at a frequency of 750 rad/s. The thickness of the shell, $h=0.05$ m, is 1% of the radius, $a=5.0$ m. The overall shell length ($2L=20$ m) is 4 times the shell radius. The material properties are $E=1.95\times10^{11}$ Pa, $\nu=0.28$, $\rho=7700$ kg/m^3, and $c_p=5242$ m/s, corresponding to a steel shell. The solution for the transverse response of the inner and outer surfaces of the shell is desired.

The ANM solution is found by assembling the local, matching, and global surface displacement solutions. The assembled ANM solution is considered with respect to global azimuth, θ, in Eq. (6) and is compared with the traditional modal/FEA (SONAX) solution on a mode-by-mode basis. The SONAX solution is found in a straightforward manner by applying the modal decomposition of the radial hat function to the shell. While it is expected that the ANM and SONAX solutions may exhibit some differences in convergence in the force application region, it is also expected that globally, the two solutions will exhibit excellent agreement.

When using the ANM method, the local and matching solutions are not solved modally. However, for comparison with SONAX, these solutions are decomposed so that an equivalent mode-by-mode comparison can be made between the ANM and SONAX solutions. Figure 4 shows the nondimensional radial displacement response comparison for the outer-shell surface along the shell axis for the global azimuthal modes 0 and 15. The displacement response (normalized by the shell radius, a) is plotted as a continuous function along the normalized axial coordinate (0 to 1.0, where the shell half-length, L, is normalized to 1.0). It is noted that the displacement response is in the form of Eq. (6). The modal response from Fig. 4 is actually a distributed array of the modal coefficients A_m. The response is an even function in global azimuth. The results show excellent agreement in both the global and local regions for a wide range of global azimuthal wave number.

Figure 5 shows the actual (not modal) radial response that is calculated using the first 50 modes of the SONAX so-

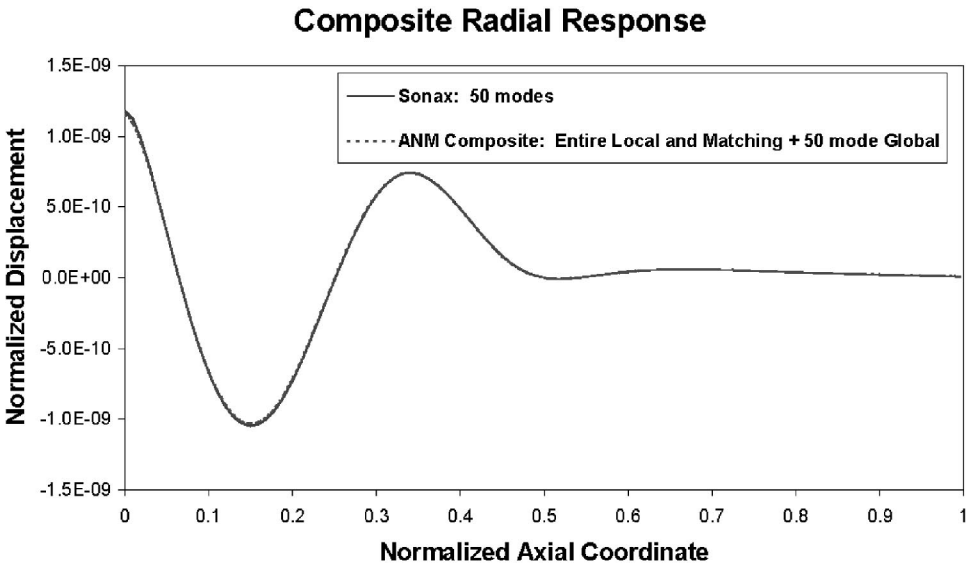

FIG. 5. Radial response of SONAX and ANM solutions, where the SONAX and global ANM solutions contain the first 50 modes, radial hat forcing case.

lution compared with an ANM solution using the actual local and matching subproblem solutions and the first 50 modes of the ANM global subproblem solution. The mode-by-mode (Fig. 4) and modally composed (Fig. 5) solutions for the ANM method show near-perfect agreement with the traditional modal/FEA SONAX solution, thus verifying the accuracy of the ANM method.

B. Cylindrical shell driven by tangential motion of a rigid attachment

A 3D cylindrical shell (identical to that from the previous example) is harmonically driven by a prescribed tangential in-plane motion of a rigid circular attachment to the inner surface of the shell (as in Fig. 1, but with different motion). The diameter of the cylindrical support ($2s$) is equal to the shell thickness, h, or 1% of the shell radius, a. Since the support is defined as being rigid, the in-plane motion is modeled as a prescribed tangential displacement (of magnitude D) distributed over the small circular patch of the support attachment interface on the inner surface of the shell. This problem is not amenable to solution by the previously described traditional modal/FEA method, SONAX. In this example problem, where the constraint is forced in a motion that is tangential to the shell, the ANM solution is shown to be independent of smoothing region size.

The modal/FEA method cannot easily handle the nonaxisymmetric distributed displacement condition (i.e., the displacement is prescribed for a finite region of the shell surface). To model this distributed displacement constraint condition, a modal/FEA method would require multiple linearly independent solutions that would be weighted through an influence matrix to satisfy the prescribed distributed displacement condition over the full interface region. This method is generally considered prohibitively complex and computationally expensive. However, ANM may be used to preprocess the prescribed surface displacement so that the global ANM subproblem is driven by a set of distributed pressures and tractions that can be solved using the standard modal/FEA method. Thus, this example demonstrates a new capability made possible by supplementing modal/FEA methods with ANM.

The ANM solution to this problem is found using a process identical to that presented in the previous example. The local reaction information is used to produce a corresponding matching solution. The matching solution uses the same formulations developed for the previous example. The library of matching solutions for each individual reaction type/mode is weighted to cancel the local solution reactions of the present example. The negative of the resultant smooth pressures and tractions is then decomposed in global azimuthal modes and applied to the modal/FEA global model. The global problem is solved using SONAX.

For verification purposes, the ANM process was repeated using three choices for the local/matching region radius, l_s (0.85 m, 1.30 m, and 1.95 m). Recall that the same problem may be solved using any choice for l_s that satisfies the criteria discussed regarding the absence of through-the-thickness effects at the boundary. Since all of the forces pass through the local/matching region, if an identical solution is produced when the original problem is solved using several independent (different smoothings) ANM solutions, then the solution and the corresponding ANM model must be accurate.

As expected, the actual solution is shown to be independent of the ANM smoothing region used. Figure 6 plots the radial modal displacement response of the shell for global azimuthal mode $m=10$. Global solutions for the three different smoothing sizes are plotted. It is clear that these solutions converge sequentially in the region outside of their respective smoothing regions. Additionally, the composite ANM solution (local+matching+global) is plotted. It is verified that the composite ANM solution for each of the three independently solved problems is identical. The fact that the global solutions overlay each other outside the smoothing regions and that the overall composite ANM solutions for the three cases are identical confirm the accuracy of the method.

As an aside, it is interesting to observe in Fig. 6 that the global radial solution for the largest smoothing length (smoothing region 3) exhibits a different waveform inside

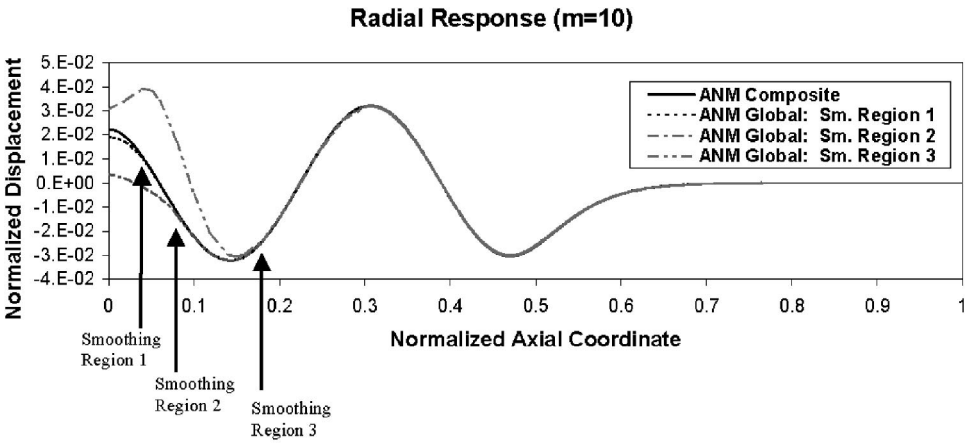

FIG. 6. Global and composite ANM solutions for the radial response of the shell subjected to tangential motion of the constraint.

the local/matching region as compared to the other global solutions or the composite ANM solution. This result indicates that as the local/matching smoothing region radius, l_s, is increased to the largest size (smoothing region 3), and the driving frequency, ω, remains constant, the local and matching subproblems pass through a resonance for the transverse (radial) response; yet in the end the result is the same as for the smaller smoothing region cases.

C. Cylindrical shell driven by rotation of a rigid attachment

In the third example problem the rigid constraint is rocked in an antisymmetric motion in a plane of constant axial position. A convergence study is performed for this case, and the modal content of the ANM subparts is discussed. The local subproblem contains the high modal content, but is not solved modally in ANM. This example problem is also used to discuss numerical resolution and convergence issues with respect to the type of forcing (displacement-driven or force-driven) applied.

The same 3D cylindrical shell with hemispherical endcaps *in vacuo* is driven by the harmonic rocking motion of a rigid support attached to the inner surface of the shell, as shown in Fig. 1. First, a prescribed moment drives the rotation of the support; second, the problem is driven by a prescribed rotation. Except for the scaling and the interpretation of the constraint condition, the two problem solutions are really the same. However, as will be shown, the two cases exhibit very different convergence rates when the problem is solved using a modal solution method.

The excitation is depicted in an axial view of the shell cross section in Fig. 7. Solutions for the transverse response of the inner and outer surfaces of the shell are desired. The modal convergence rates between the ANM and modal/FEA SONAX solutions are compared for both forcing types. This problem is analyzed *in vacuo*; however, the fluid-loaded version is a direct extension of the *in vacuo* case and will be presented later.

These types of problems exhibit significant localized deformation at the attachment interface, and are therefore extremely difficult to converge when typical numerical methods are employed. It is also expected that this type of excitation will yield significant out-of-plane surface displacements, which are particularly important when acoustic scattering or radiation is considered.

Figure 8(a) shows the normalized displacement around the azimuth at the axial location $x=0$ for the composite ANM solution and for the global component of ANM. In Fig. 8(b), the scale is expanded around the discontinuity and the separate components (local, matching, and global) are shown along with the ANM composite solution. Note, both the global and matching solutions are smooth, and it is the local component that captures the rapid variation.

1. Convergence study

For the purpose of quantifying error and studying convergence, the spatial average of the mean-square surface displacement was used

$$\text{mean-square displacement} = \frac{1}{S}\int_S \int |w_\infty|^2 dS, \tag{7}$$

where w_∞ is the converged radial displacement at the inner surface of the cylinder. Similarly, the spatial average of the mean-square surface displacement error is defined by

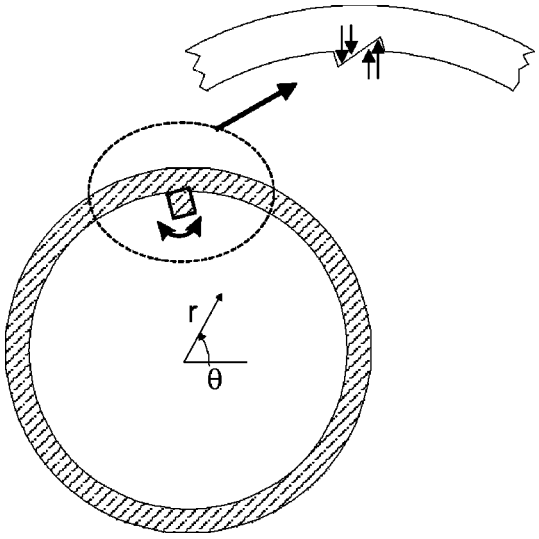

FIG. 7. Rocking motion of attachment to inside of cylindrical shell.

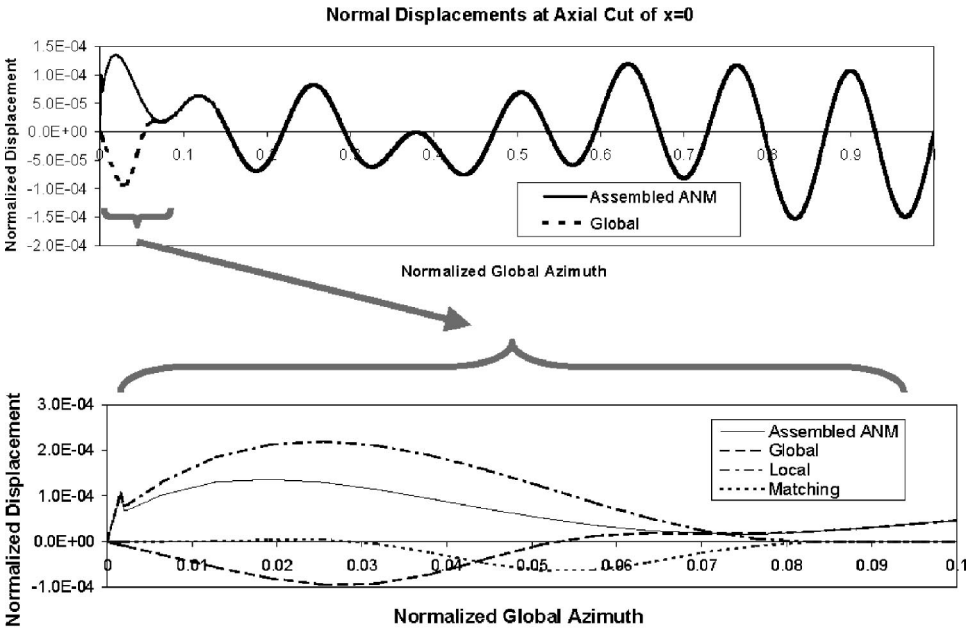

FIG. 8. (a) Global problem and assembled ANM displacements, taken at a cross section over the $x-0$ plane. (b) All of the ANM subproblem solutions and the composite ANM solution plotted over the local/matching region. Rocking motion case.

$$\text{mean-square error} = \frac{1}{S}\int\int_{S} |w_M - w_\infty|^2 dS, \tag{8}$$

where w_M is the approximate surface displacement obtained for a certain degree of numerical resolution. Then, the percent rms error is given by

$$\text{percent error} = \sqrt{\frac{\text{mean-square error}}{\text{mean-square displacement}}} \times 100. \tag{9}$$

For the rocking motion problem, the radial displacement can be written as a Fourier sine series in azimuth at the ith axial location

$$w_M(a,\theta,x_i) = \sum_{m=1}^{M} B_{m,i} \sin m\theta. \tag{10}$$

The exact solution $w_\infty(a,\theta,x_i)$ is obtained when $M \to \infty$. For equally spaced nodes in the axial direction, the approximate mean-square displacement (due to truncation of the sine series) becomes

$$\text{mean-square displacement}(M) = \frac{1}{N_{\text{nodes}}} \sum_{i=1}^{N_{\text{nodes}}} \sum_{m=1}^{M} \frac{|B_{m,i}|^2}{2}. \tag{11}$$

In Eq. (11) the surface integral of Eq. (7) is evaluated by integration in the azimuthal direction and a summation in the axial direction, and the exact mean-square displacement is obtained when $M \to \infty$. Then, the mean-square error can be shown to be

$$\text{mean-square error}(M) = \frac{1}{N_{\text{nodes}}} \sum_{i=1}^{N_{\text{nodes}}} \sum_{m=M+1}^{\infty} \frac{|B_{m,i}|^2}{2}. \tag{12}$$

Equations (11) and (12) are used in Eq. (9) to calculate the error due to modal truncation. This error is shown in Fig. 9(a) for the case of a prescribed moment applied to the constraint and in Fig. 9(b) for the case of a prescribed rotation. Two curves are labeled on each figure. The dashed curve corresponds to the case where the entire problem must be resolved modally, as if the problem had been done using SONAX or another modal/FEA approach. The solid curve corresponds to the error associated with ANM where only the global part of the solution must be resolved using a modal approach.

Recall that the ANM composite solution is the superposition of the local, matching, and global solutions. The local and matching solutions are solved separately by other means, and therefore do not contribute to the modal truncation error. Since the global solution is smooth, it converges relatively rapidly. For convergence with a moment constraint when only a few modes are retained, the error from both methods is similar, as shown in Fig. 9(a). As more modes are added, the ANM method begins to show superior performance, with

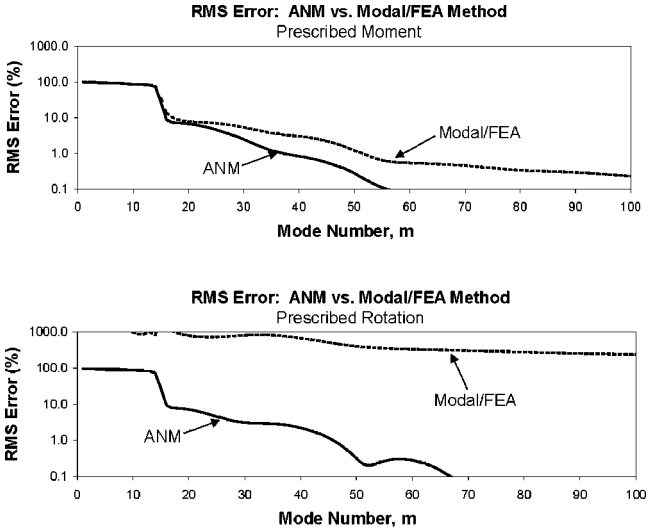

FIG. 9. Convergence comparisons of solutions for (a) moment-driven constraint, and (b) rotation-driven constraint.

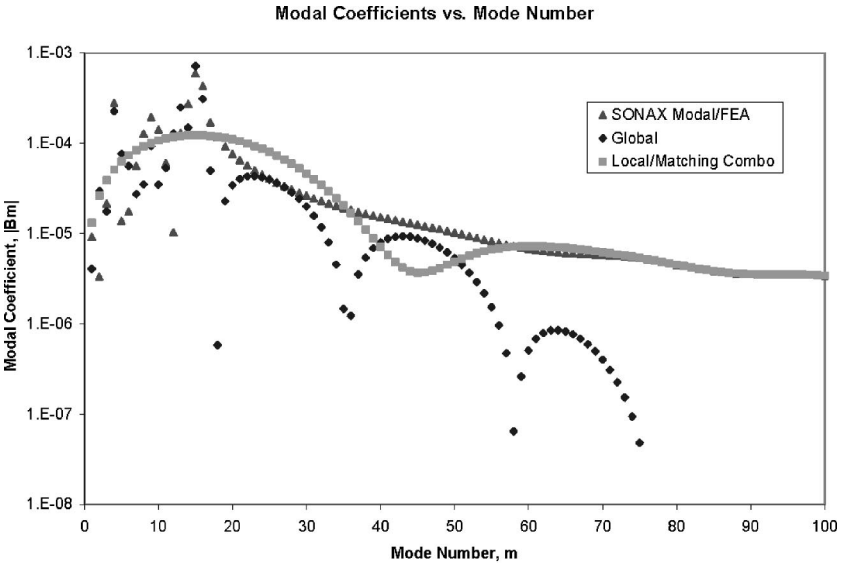

FIG. 10. Modal content of ANM component problems and of SONAX-type solution.

the error being almost an order of magnitude smaller for a given number of modes.

In Fig. 9(b), where the rotation is prescribed at the drive point, the difference between the modal/FEA method and the ANM method is very large, regardless of how many modes are used. For a fully converged solution, using Eq. (10) the angular displacement at the drive point is given by

$$\left.\frac{dw_\infty}{d\theta}\right|_{(a,0,0)} = \sum_{m=1}^{\infty} mB_{m,0} \equiv D, \tag{13}$$

where D is the prescribed angular rotation that satisfies the constraint. However, if a finite number of modes are summed then the displacement at the constraint is not D, namely

$$\left.\frac{dw_\infty}{d\theta}\right|_{(a,0,0)} = \sum_{m=1}^{M} mB_{m,0} \equiv D_M, \tag{14}$$

where M is the number of modes retained. Since D_M does not equal the desired angular rotation at the constraint, the coefficients $B_{m,j}$ must be scaled to match the desired rotation. This outcome is equivalent to applying a different moment on the constraint. Therefore, for the case of constrained displacement the surface displacement is given by

$$w_M(a,\theta,x_i) = (D/D_M)\sum_{m=1}^{M} B_{m,i}\sin m\theta. \tag{15}$$

Similar to the previous derivation, the spatially averaged mean-square error is found by subtracting w_M in Eq. (15) from w_∞ calculated from Eq. (10), and averaging this quantity over the area (integrating in azimuth and summing in the axial direction), namely:

$$\text{mean-square error}(M) = \frac{1}{N_{\text{nodes}}}\sum_{i=1}^{N_{\text{nodes}}}\sum_{m=M+1}^{\infty}\frac{|((D/D_m)\gamma_{mM}-1)B_{m,i}|^2}{2}, \tag{16}$$

where $\gamma_{mM} = \{\begin{smallmatrix} 1 & m \le M \\ 0 & m > M \end{smallmatrix}\}$.

The percent error associated with Eq. (16) is calculated using Eq. (9). Because of the presence of the scaling factor, this error for the angular displacement constraint case is much larger than for the moment constraint case. The outstanding performance by the ANM method in Fig. 9(b) is due to the fact that the large local deformations around the constraint are accurately captured in the ANM local solution. Physically, the lack of resolution at the drive point propagates error throughout the entire shell structure. Whereas, when the drive point is not accurately resolved in the moment constraint case, the error is fairly localized around the drive point, and that error is not transferred to the rest of the shell.

2. Modal content

Even though the ANM local and matching solutions are not obtained by modal methods, it is insightful to modally decompose these solutions to observe their contribution to the overall solution. Furthermore, understanding the modal contributions of the local and matching solutions helps to explain the convergence behavior shown in Fig. 9. The overall modal content of the solution and the modal content of the constituent parts are shown in Fig. 10. In this comparison, the modal content of the local and matching solutions is combined. Note that the global solution contains mostly low mode numbers and that the amplitudes of the higher modes fall rapidly with increasing mode number. In addition, at high mode numbers the local and matching solutions continue to be important, and comprise almost the entire content of the overall solution. At low mode numbers, both the global and the local and matching solutions all contribute to the overall content in a complicated way. The dominant behavior of the local and matching solutions at high mode number explains the excellent performance of the ANM method in the previous convergence study.

V. ANM WITH FLUID LOADING

The extension of the previously described approach to include fluid loading is surprisingly straightforward. The principal problem for ANM when adding a surrounding fluid is that the fluid provides an additional medium in which waves can propagate, and this appears to complicate the con-

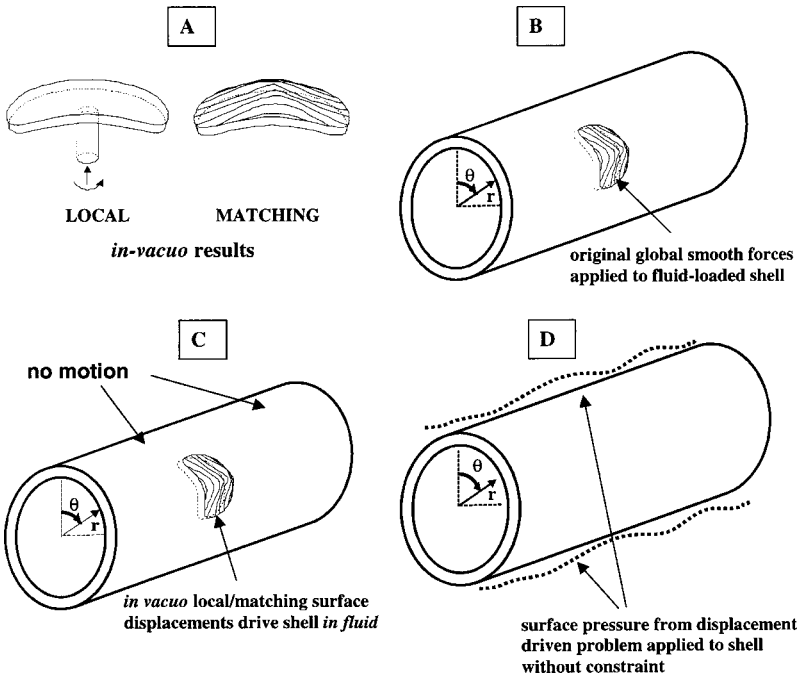

FIG. 11. ANM process for fluid loading, using *in vacuo* local and matching results to obtain the solution to the original fluid-loaded problem.

cept of local, matching, and global regions. It turns out that the local and matching problems can still be solved as dry structures, exactly as before, using the basic approach developed by Loftman and Bliss.[1–3]

Since these problems really must be solved in the presence of the fluid, additional distributed smooth forces are introduced that exactly cancel the fluid forces on the local and matching problems, and also cancel the fluid forces on the surrounding shell which must remain at rest. These additional smooth forces are equal and opposite the fluid pressures on the shell that are due to the *in vacuo* displacements of the local and matching regions. It should be noted that although the local problem may have rapid spatial variations, the associated fluid pressures are typically smoother and more slowly varying. Note that an additional smooth force is also applied to the global problem. This smooth force is just the fluid surface pressure produced by the *in vacuo* local and matching problem motions with the rest of the shell held at rest.

The above approach to fluid loading is outlined in Fig. 11. First, as indicated in Fig. 11(a), the local and matching ANM problems are solved *in vacuo*. Second, the smooth forces that are derived from the matching problem are applied to the fluid-loaded global structure, as in Fig. 11(b). Note if the global structure were not fluid loaded, the ANM solution would be the superposition of these three subproblems. However, in the fluid-loaded case, the problem is not complete because the fluid-loaded effects of the local and matching displacements have not been included, both in the local smoothing region and on the remainder of the shell. To account for this effect, a calculation is performed with the surface of the fluid-loaded shell held at rest, except in the smoothing region where the local and matching displacements are applied, as shown in Fig. 11(c). This calculation gives fluid pressures over the surface of the entire shell, which are interpreted as an additional smooth force. Finally, these pressures are then applied to the fluid-loaded shell to obtain a correction to the global problem, as shown in Fig. 11(d). The displacements given by the composite ANM solution are comprised of the *in vacuo* local and matching displacements [Fig. 11(a)] plus those from the fluid-loaded global problem [Fig. 11(b)] and the displacements from the global problem correction for fluid loading [Fig. 11(d)]. The surface pressures are obtained by superposition of the results for surface pressure from the subproblems described by Figs. 11(b) and (c).

In Figs. 12 and 13, results are shown for a *fluid-loaded* steel cylindrical shell in water. The shell was excited by rotating a constraint, as illustrated in Fig. 1. The same shell *in vacuo* was used in the convergence study with the same excitation. The problem was solved using ANM, but with different size smoothing regions (indicated by L_s). The fact that the solutions coincide on a mode-by-mode basis confirms both the accuracy of the method, and the property that solutions are independent of smoothing region size.

Figure 12 shows the magnitude of surface velocity modal coefficients of the composite ANM solution versus the axial location measured from the drive point. Recall that the global problem is solved using a finite-element analysis for each mode after modally decomposing in azimuth. The results shown in Fig. 12 are for azimuthal mode numbers 1 and 4. Similar results were obtained for all the azimuthal modes, and excellent agreement was found in all cases. However, it should be noted that it was necessary to use the fluid-loading correction to the global solution, as illustrated in Fig. 11, in order to obtain such accurate results.

In Fig. 13, a similar plot is shown for the modal amplitudes of far-field pressure. The angle of radiation is measured from the shell axis, with 90 deg being directly above the constraint and perpendicular to the axis of the shell (i.e., ''beam aspect''). Again, results for two different size smoothing regions are shown on the same plot. The fact that these curves overlay each other so well confirms that the method works, and that the solution is independent of the

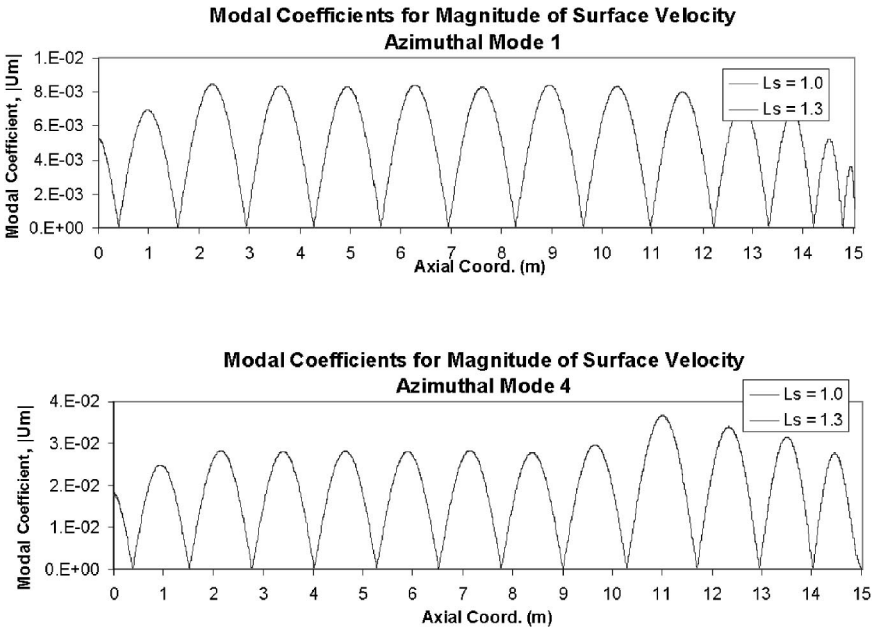

FIG. 12. Amplitude of modal coefficients for modes 1 and 4 for two smoothing regions (complete overlap of solutions)—surface velocity.

smoothing radius. These results are typical of all of the problems that have been studied thus far using ANM.

VI. CONCLUSIONS

This paper has illustrated the successful application of analytical-numerical matching to complicated problems in structural acoustics. When used in combination with a modal/FEA computer analysis such as SONAX, this method has allowed high-accuracy results to be obtained efficiently. Because ANM isolates regions of rapid change around structural discontinuities and solves them separately to a high resolution, computational methods like SONAX can be used much more effectively. In realistic terms, a new computational capability to handle azimuthally localized constraints with a computer code developed for axisymmetric structures has been achieved.

In addition to this new capability, there are other important contributions of this paper in terms of convergence and fluid loading. A convergence study was performed that demonstrated the sensitivity to the type of constraint (force-driven versus displacement-driven). It was shown that a displacement-driven problem is much slower to converge, since the error at the drive point is transferred to the entire structure. If a modal method is used, a high number of modes must be retained in order to properly resolve the constraint (i.e., modal wavelengths must be smaller than the constraint size). For displacement-driven problems, it must be stressed that the lowest modes are incorrect unless there is high resolution around the drive point. With inadequate resolution, errors in radiated or scattered sound fields will be large because the lower modes dominate the radiated field. In the case of a force-driven problem, the error around the drive point remains local, and does not have as significant an effect on the overall results.

For realistic problems involving scattering, both displacement- and force-driven constraint problems must be solved, so resolution around constraints will always be an

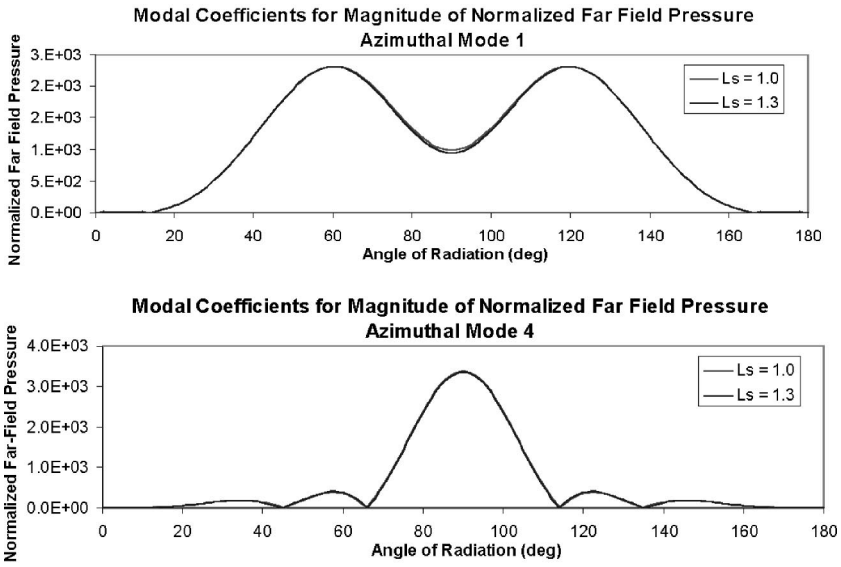

FIG. 13. Amplitude of modal coefficients for modes 1 and 4 for two smoothing regions—far-field pressure.

issue. ANM provides a means by which the fluid-loaded shell with structural discontinuities can be solved at low resolution. The region containing rapid variations is isolated and solved dry. This leads to a more computationally efficient method for handling fluid-loaded problems of this type.

A characteristic of the ANM approach is that different analysis methods can be used for each aspect of the problem. In the present work, the global problem was solved by a modal-FEA code specialized for radiation and scattering from axisymmetric fluid-loaded shells; the local problem was solved with a traditional, commercially available FEA code; and the matching problem was done analytically using shell equations. Note, that similar methods could have been used for any two, or all three of the subproblems. Nevertheless, from the standpoint of desiring one unified approach embodied in a single code, the use of different analysis methods can be viewed as a disadvantage. However, especially in large-scale computation, there can be efficiency and accuracy advantages to addressing each of these problems in the manner that is most individually appropriate. For instance, there can be enormous gains in efficiency using a modal-FEA code, rather than a full 3D FEA code for an axisymmetric body; conversely, a full 3D code would be the preferred way to model a dynamically complex constraint. As a practical matter, many specialized codes exist in industry and research settings, and ANM provides a way for these codes to be utilized in concert, in a way that is not specific to any one code or class of numerical procedures. Although ANM may not be the best approach for all problems, the flexibility to couple different analysis methods is certainly an advantage in many situations.

ACKNOWLEDGMENTS

This research was supported by the Office of Naval Research Grant N00014-98-0746; Dr. Luise Couchman was the ONR grant monitor. The authors would also like to thank Dr. Terry Bazow of Metron, Inc., for performing the SONAX computations and exchanging data files with us; and Dr. Rickard Loftman for developing an early set of matching solutions.

[1] R. C. Loftman and D. B. Bliss, ''The application of analytical/numerical matching to structural discontinuities in structural/acoustic problems,'' J. Acoust. Soc. Am. **101**, 925–932 (1997).
[2] R. C. Loftman and D. B. Bliss, ''Scattering from fluid-loaded cylindrical shells with periodic circumferential constraints using analytical/numerical matching,'' J. Acoust. Soc. Am. **106**, 1271–1283 (1999).
[3] R. C. Loftman and D. B. Bliss, ''The application of analytical/numerical matching to structural discontinuities in structural/acoustic problems,'' J. Acoust. Soc. Am. **101**, 925–932 (1997).
[4] J. Montgomery and P. Barbone, ''Diffraction from simple shapes by a hybrid asymptotic-finite element method,'' J. Acoust. Soc. Am. **104**, 1964–1972 (1998).
[5] S. Gopalakrishnan and J. F. Doyle, ''Spectral superelements for wave propagation in structures with local nonuniformities,'' Comput. Methods Appl. Mech. Eng. **121**, 77–90 (1995).
[6] P. J. Halliday and K. Grosh, ''Dynamic response of complex structural intersections using hybrid methods,'' J. Appl. Mech. **66**, 653–659 (1999).
[7] C. Farhat and U. Hetmaniuk, ''A fictitious domain decomposition method for the solution of partially axisymmetric acoustic scattering problems. I. Dirichlet boundary conditions,'' Int. J. Numer. Methods Eng. **54**, 1309–1332 (2001).
[8] U. Hetmaniuk and C. Farhat, ''A fictitious domain decomposition method for the solution of partially axisymmetric acoustic scattering problems. II. Neumann boundary conditions,'' Int. J. Numer. Methods Eng. **58**, 63–81 (2002).
[9] D. B. Bliss and R. J. Epstein, ''Free vortex problems using analytical/numerical matching with solution pyramiding,'' AIAA J. **33**, 894–903 (1995).
[10] D. B. Bliss and W. O. Miller, ''Efficient free wake calculations using analytical/numerical matching,'' J. Am. Helicopter Soc. **38**(2), 43–52 (1993).
[11] R. J. Epstein and D. B. Bliss, ''Aeroacoustic boundary element method using analytical/numerical matching,'' AIAA J. **35**, 244–254 (1997).
[12] D. B. Bliss and R. J. Epstein, ''Novel approach to aerodynamic analysis using analytical/numerical matching,'' AIAA J. **34**, 2225–2232 (1996).
[13] R. J. Epstein and D. B. Bliss, ''An acoustic boundary element using analytical/numerical matching,'' J. Acoust. Soc. Am. **101**, 92–106 (1997).
[14] L. P. Franzoni and C. D. Park, ''An illustration of analytical numerical matching with finite element analysis for structural vibration problems,'' J. Acoust. Soc. Am. **108**, 2856–2864 (2000).
[15] C. Park, ''An efficient method for solving the structural dynamics of finite elastic structures containing discontinuities using analytical/numerical matching with finite element analysis,'' Ph.D. thesis, Duke University, 2001.
[16] A. C. Ugural, *Stresses In Plates and Shells*, 2nd ed. (McGraw-Hill, New York, 1999).
[17] A. Leissa, *Vibration of Shells* (American Institute of Physics, Columbus, OH, 1993).

Sound field modeling in a street canyon with partially diffusely reflecting boundaries by the transport theory

Thierry Le Pollès,[a] Judicaël Picaut,[b] and Michel Bérengier
Laboratoire Central des Ponts et Chaussées, Section Acoustique Routière et Urbaine, Route de Bouaye, B.P. 4129, 44341 Bouguenais cedex, France

Claude Bardos
Laboratoire Jacques-Louis Lions, Université Pierre et Marie Curie, Boîte courrier 187, 75252 Paris Cedex 05, France

(Received 23 February 2004; revised 16 July 2004; accepted 21 July 2004)

The transport theory, applied to the concept of sound particles, seems to be well adapted to predict the sound propagation in urban areas, including most complex effects, like diffuse scattering by building facades, atmospheric attenuation, scattering by urban objects in streets, etc. In this paper, the transport theory is then applied to the sound field modeling in an empty street canyon with partially diffusely building facades. In this case, the temporal and spatial distribution of sound energy in a street is the solution of a transport equation, with mixed specular-diffuse boundary conditions. Using an asymptotic approach, the transport equation may be reduced to a diffusion equation for the sound energy, where the diffusion coefficient depends only on the building facades properties. Comparisons with experiments show that the diffusion model gives consistent results with experimental data, both for the sound attenuation level and the reverberation time. © *2004 Acoustical Society of America.* [DOI: 10.1121/1.1791720]

PACS numbers: 43.50.Vt, 43.20.Fn, 43.28.Fp, 43.50.Lj [DKW] Pages: 2969–2983

I. INTRODUCTION

Noise propagation in urban areas is a problem of major importance for people living in modern large cities and has attracted considerable attention in recent years. Consequently, many mathematical and numerical models have been derived to predict the sound propagation and reverberation time in streets, using, for example, image-source methods, modal approaches, the classical theory of reverberation, or statistical descriptions.[1] Most of mathematical models, as well as commercial software, have been developed, assuming building facades as perfectly reflecting planes, without protrusions. There are only a few models including both specular and diffuse reflections.[2,3] However, the multiple scattering of sound by surface irregularities has a large influence on the sound field energy distribution.[4,5] Moreover, most of the time, models are applied only to specific urban configurations, like suburban areas with separated buildings, street canyons, streets with intersections, etc., but cannot be generalized to all urban areas and particularly to city centers where the architectural morphology is very complex and buildings are very numerous. According to these limitations, the purpose of the present paper is to propose a general mathematical formalism, to predict the temporal and the spatial distribution of the sound field energy in urban areas, including diffuse reflections by building facades and latter, the scattering by urban objects in streets, atmospheric attenuation, wind effects.

The model is based on an application of the classical theory of particle transport applied to the concept of sound particles. The analytical approach is presented in the first part of this paper and allows describing the sound energy distribution in urban areas by a transport equation. Boundary equations are also introduced in order to take into account the diffuse reflections on building facades. In the second part, an application to a street canyon is proposed. An asymptotic approach is then presented in order to replace the transport equation with the associated boundary conditions, by a diffusion equation. All facade effects are then included in a single term, the diffusion coefficient. Moreover, in order to take into account the absorption by the openings, the pavement and the building facades, boundary conditions, consistent with the transport model, are proposed for the diffusion equation. The solution of the diffusion equation is then presented for partially diffusely reflecting boundaries according to Lambert's law and compared with measurements in a street, with good agreement, both in terms of reverberation times and sound level attenuation along the street.

II. TRANSPORT THEORY

A. Sound particle concept

By assumption, the acoustic field is split in two parts, the direct field and the reverberant field. Our study is devoted to the last one, which is the result of a large energy mixing, due to multiple specular reflections, diffraction, and scattering on boundaries and in the street. In the wide range of frequencies usually met in architectural acoustics, the effects of phase cancellation and addition are averaged, in such a way that the sound sources may be considered as noncorrelated. Consequently, a street can be characterized by its capacity to distribute and to attenuate sound energy. Thus, de-

[a]Current address: Laboratoire Ondes et Acoustique, ESPCI, 10 rue Vauquelin, 75231 Paris Cedex 05, France.
[b]Corresponding author. Electronic mail: Judicael.Picaut@lcpc.fr; URL: http://www.lcpc.fr

spite neglecting the undulatory nature of the sound field, energetic models may provide satisfactory and sufficient data such as echogram, reverberation time, and sound attenuation. According to the geometrical acoustics assumptions, the sound propagation may be represented by a ray beam that represents the path of an infinitesimal entity or energy packet, named sound particle or phonon.[6–8] In this way, as mentioned by Joyce,[6] geometrical acoustics is a special case of the classical-particle dynamic. A sound particle is then defined as a classical point particle by its elementary energy e, its position $\mathbf{x}$, and its velocity $\mathbf{v}$, the norm of which is equal to the sound velocity c. Interactions and collisions between particles are neglected. The phonon obeys classical mechanics laws based on Hamilton stationary action principle and, in this case, undergoes a straight line until its impact with obstacles or building facades. During a collision with a scattering object or with a surface, the velocity direction is deflected instantaneously. This approach makes it possible to view the reverberant field as a gas of sound particles and to link the sound energy distribution to the evolution of the sound particle density. The classical formalism of gas theory can then be applied to acoustics problems: The energetic approach may be seen as an application, for acousticians, of the transport theory commonly used in statistical mechanics.

B. Single particle distribution function

A particular state of a system with N particles is described by $3N$ coordinates of positions $(\mathbf{x}_1,\mathbf{x}_2\ldots\mathbf{x}_N)$ and $3N$ coordinates of velocities $(\mathbf{v}_1,\mathbf{v}_2\ldots\mathbf{v}_N)$. This state is represented by a point in a $6N$-dimension phase space $\mathbb{G}$. If, at a given time t, it was possible to know each particle position and velocity, it would have been then possible to predict their position and velocity at time $t+dt$. However, the number of sound particles being very large, the practical implementation is very difficult. As a consequence, the problem must be approached in a probabilistic way. By assumption, urban areas are considered as ergodic. Hence, the description of the N particles system can be reduced to the knowledge of an artificial single particle system.[9] The phase space $\mathbb{G}$ is then reduced to a six-dimensional phase space Γ involving the three usual space and velocity coordinates $(\mathbf{x}_1,\mathbf{v}_1)$ noted afterwards $(\mathbf{x},\mathbf{v})$. Moreover, mutual particle interaction is not taken into account. The statistical behavior of a sound particle is here obtained from statistical mechanics. A probability density, named single particle distribution function $f(\mathbf{x},\mathbf{v},t)$ (SPDF), encountered in physical domains as neutron transport theory, plasma physics, and chemistry[10] is introduced.[9] It is defined as $f(\mathbf{x},\mathbf{v},t)d\mathbf{x}d\mathbf{v}$. It represents the amount of particles, at time t, with velocity $\mathbf{v}$ to within about $d\mathbf{v}$, in an elementary volume $d\mathbf{x}$ located at $\mathbf{x}$. It must satisfy the normalization condition

$$\int\int f(\mathbf{x},\mathbf{v},t)d\mathbf{x}d\mathbf{v}=1. \tag{1}$$

The local density $n(\mathbf{x},t)$ of sound particles is then defined by the integration of the SPDF over the velocity space

$$w(\mathbf{x},t)=en(\mathbf{x},t)=e\int_V f(\mathbf{x},\mathbf{v},t)d\mathbf{v} \quad \text{for } \mathbf{x}\in X, \quad \text{and } \mathbf{v}\in V. \tag{2}$$

The local flow of sound particles can be expressed by

$$\mathbf{J}(\mathbf{x},t)=\int_V \mathbf{v}f(\mathbf{x},\mathbf{v},t)d\mathbf{v} \quad \text{for } \mathbf{x}\in X, \text{ and } \mathbf{v}\in V, \tag{3}$$

which represents the number of particles crossing an area per unit of time and surface. The energy flow can also be defined by a similar way, to give

$$\mathbf{E}(\mathbf{x},t)=e\mathbf{J}(\mathbf{x},t)=e\int_V \mathbf{v}f(\mathbf{x},\mathbf{v},t)d\mathbf{v} \quad \text{for } \mathbf{x}\in X, \quad \text{and } \mathbf{v}\in V. \tag{4}$$

C. Transport equation

In this paper, scattering by urban objects in the street is neglected. Since collisions of phonons only take place on the boundaries, the evolution of the sound particle density in urban areas is similar to the evolution of the molecular density in a rarefied gas or Knudsen gas. The main equation of the model, can be derived from transport theory[9] to give directly

$$\frac{\partial f}{\partial t}+\mathbf{v}\cdot\nabla_{\mathbf{x}}f=0 \quad \text{for } \mathbf{x}\in X, \text{ and } \mathbf{v}\in V, \tag{5}$$

where $\nabla_{\mathbf{x}}f$ represents the spatial derivation. This is the transport equation of the free molecular flow also called the Liouville equation. It describes the spatial and temporal evolution of the sound particle density and consequently of the sound field energy. This equation expresses the variation of the particle density during dt according to a transport phenomenon.

It can be noted that Eq. (5) could be generalized[9] to take into account much more phenomena, like the atmospheric attenuation, the wind effect, and the scattering by urban objects, by introducing, respectively, an absorption term σ, a strength of transport $\mathbf{F}$ and a scattering term, such as

$$\frac{\partial f}{\partial t}+\mathbf{v}\cdot\nabla_{\mathbf{x}}f-\sigma f+\mathbf{F}\cdot\nabla_{\mathbf{v}}f = \left.\frac{\partial f}{\partial t}\right|_{\text{scattering}} \quad \text{for } \mathbf{x}\in X, \quad \text{and } \mathbf{v}\in V. \tag{6}$$

However, the present study is restricted to the simple case of empty streets, without atmospheric attenuation and without wind effects.

D. Boundary conditions

Typically, surfaces are made up of many irregularities due to window recesses, decorative structures, etc. According to the size of facade irregularities and frequency, reflections may be specular or not. Most of the time, the wide frequency range encountered implies a mix of these two kinds of reflections. First of all, it is convenient to introduce the outward unit normal $\mathbf{n}$ on the boundary. $\Gamma^{\pm}$ represents the points $(\mathbf{x}, \mathbf{v})$ in the phase space Γ, which satisfy the relation

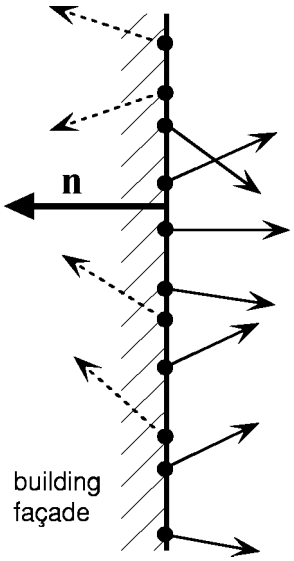

FIG. 1. Incident and reflected sound particles on a building facade. Γ^+ and Γ^- represent the incident (arrow with a dashed line) and reflected (arrow with a continuous line) sound particles on a building facade with the normal **n**.

$$\Gamma=\Gamma^+\cup\Gamma^- \quad \text{with} \quad \Gamma^\pm=\{(\mathbf{x},\mathbf{v})/\mathbf{x}\in\partial X,\mathbf{v}\in\mathbb{R}^3,0<\pm\mathbf{n}\cdot\mathbf{v}\}. \tag{7}$$

The restriction of the SPDF to the set Γ^+ (Γ^-, respectively) is noted below f^+ (f^-, respectively). Γ^+ and Γ^- represent the incident and reflected sound particles on the building facades [Fig. 1]. When $\mathbf{n}\cdot\mathbf{v}>0$, the particle velocity is in the same direction as the normal to the wall: particles are incident. Inversely, when $\mathbf{n}\cdot\mathbf{v}<0$, particles are reflected.

1. Facade absorption

In the present approach, the wall absorption is expressed in a probabilistic way by considering the probability $\alpha(\mathbf{x})$ for $\mathbf{x}\in\partial X$, that a sound particle hitting a facade at the position **x** is absorbed. In this part of the paper, the facade absorption is a function of boundary coordinates and is supposed to be independent of the incident angle, although it would be possible to take it into account. Nevertheless, it would imply an increase in the complexity of the model. This facade absorption is defined in the range [0, 1].

2. Specular and nonspecular reflections

The part of nonspecular and specular reflection is expressed by the accommodation coefficient $d(\mathbf{x})$ for $\mathbf{x}\in\partial X$, from 0, for nonspecular reflection, to 1 for perfect specular reflection. This accommodation coefficient can be in relation to the diffuse-reflection coefficient[11] $\delta=1-d$, used for example, in computer modeling based on geometrical acoustics. The use of d instead of δ is more consistent with the transport theory. This parameter is representative of the boundary morphology. However, it may be noted that several works have ever been done to find its values in some practical cases of room acoustics,[11] but results are not relevant for building facades yet.

According to the definition of d, the sound reflection may be specular or not. Figure 2 shows some examples of

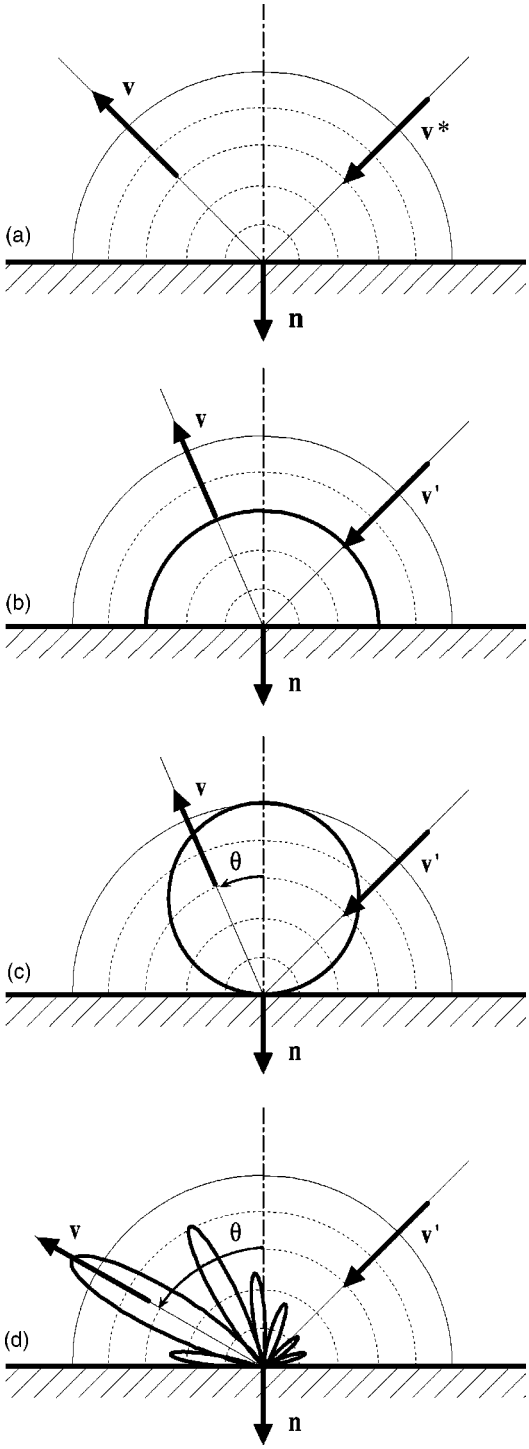

FIG. 2. Schematic representation of different reflection laws on a building facade: (a) specular reflection, (b) uniform reflection, (c) Lambert's Law ($\cos\theta$), (d) generic form $\mathcal{R}(\mathbf{x},\mathbf{v},\mathbf{v}')$. **v** is the reflected velocity. $\mathbf{v}'$ is a random incident velocity. $\mathbf{v}^*$ is the incident velocity leading to a specular reflection in the direction of **v**.

reflection laws, where **v** is the reflected velocity, $\mathbf{v}'$ is a random incident velocity, and $\mathbf{v}^*$ is the incident velocity leading to a specular reflection in the direction of **v**. In the first case [Fig. 2a], the reflection can be considered in a deterministic way. Indeed, the knowledge of the incidence velocity $\mathbf{v}^*$ on the building facade determines the velocity **v** of the particle, after reflection, by the relation

$$\mathbf{v}=\mathbf{v}^*-2(\mathbf{n}\cdot\mathbf{v}^*)\mathbf{n}. \tag{8}$$

In the second case, surface reflection laws can be introduced in the model, in order to characterize the angular dependence of the scattered field during the reflection process. Hence, the effects of surface morphology are included in the analytical boundary conditions. As an example, the uniform reflection law [Fig. 2(b)] distributes in an equal way the energy whereas the Lambert's law favors the normal direction [Fig. 2(c)]. In a general way [Fig. 2(d)], the nonspecular reflection can be taken into account by considering a probabilistic approach. Thus, a positive, integrable, and smooth function $\mathcal{R}(\mathbf{x},\mathbf{v},\mathbf{v}')$, defined on $\Gamma^{\pm}$ is introduced. This reflection law represents the probability that an incident sound particle with a velocity $\mathbf{v}'$ leaves the boundary, at position $\mathbf{x}$ after reflection, with a velocity $\mathbf{v}$. The reflection law is normalized according to the following relation:

$$\int_{\Gamma^+}\mathcal{R}(\mathbf{x},\mathbf{v},\mathbf{v}')d\mathbf{v}'=1 \quad \text{for } \mathbf{x}\in\partial X, \text{ and } \mathbf{v}\in V, \tag{9}$$

and must satisfy the reciprocity relation which expresses the conservation of the number of particles on the boundaries[12]

$$\int_{\Gamma^-}\mathcal{R}(\mathbf{x},\mathbf{v},\mathbf{v}')d\mathbf{v}=1 \quad \text{for } \mathbf{x}\in\partial X \text{ and } \mathbf{v}\in V. \tag{10}$$

3. Boundary equation

The boundary conditions express the flow of reflected particles as a function of the incident particle flow. By considering the part of specularly and nonspecularly reflected sound particles, the flow conservation is written

$$\begin{aligned}|\mathbf{n}\cdot\mathbf{v}|f^-(\mathbf{x},\mathbf{v},t)=(1-\alpha(\mathbf{x}))\Big[&d(\mathbf{x})|\mathbf{n}\cdot\mathbf{v}^*|f^+(\mathbf{x},\mathbf{v}^*,t)\\&+(1-d(\mathbf{x}))\int_{\Gamma^+}\mathcal{R}(\mathbf{x},\mathbf{v},\mathbf{v}')|\mathbf{n}\cdot\mathbf{v}'|\\&\times f^+(\mathbf{x},\mathbf{v}',t)d\mathbf{v}'\Big] \quad \text{for } \mathbf{x}\in\partial X, \text{ and } \mathbf{v}\in\Gamma^-,\end{aligned} \tag{11}$$

where the left member of this expression represents the reflected flow. The right member term weighted by the reflection coefficient $[1-\alpha(\mathbf{x})]$, expresses the specular flow (first term) and the nonspecular flow (second term). This approach makes it possible to take into account, in a general way, the whole physical phenomena occurring on building facades.

The sound frequency is not introduced in Eq. (11). In this model, as already discussed before, interferences are neglected. However, it can be remarked that absorption coefficients, accommodation coefficients, and reflection laws can be frequency dependent. In a practical point of view, a boundary Eq. (11), with a specific absorption, accommodation and reflection law, for each frequency band of interest can be considered. Moreover, it is also interesting to note that this general approach can also be applied in room acoustics.

Whereas the absorption coefficient may be easily measured for building facades, the choice of the accommodation coefficient and the reflection law is a more complicated problem. Although such problems have been investigated in room acoustics, for the determination of the scattering and diffusion coefficient of diffuse reflectors,[13,14] only a few studies have been carried out for building facades. Consequently, there is no available result at the present time. In a practical point of view, the choice of the accommodation coefficient is not really a problem since any values between 0 and 1 can be used. For the moment, Lambert's law can be considered for the reflection law. This already gave excellent results in the sound field modeling in room acoustics[15,16] as well in urban acoustics.[17,18] Moreover, the use of Lambert's law makes it possible to solve easily the transport equation with the above boundary conditions, for a street canyon. This is presented in the next section.

III. SOUND PROPAGATION IN A STREET CANYON WITH LAMBERT'S REFLECTION LAW

As an example, the model is applied to the sound propagation in an empty street canyon with partially diffusely reflecting surfaces characterized by Lambert's Law. In this case, the problem is completely defined by the transport Eq. (5) with the boundary conditions (11). However, nowadays, there is no exact analytical solution for such a system of equations. Although the problem could be simulated by numerical Monte Carlo algorithm, the choice was done to find an asymptotic solution.

Let us consider a street canyon, where the width is much smaller than the length and height. For mathematical reasons and in order to find an asymptotic solution, the sound absorption due to the pavement and the building facades, is neglected during this step. However, in Sec. III B 2, the absorption will be introduced by a simple way. If the sound source is located on the ground [Fig. 3(a)], the sound propagation in a street canyon is then similar to the propagation between two parallel planes [Fig. 3(b)]. If the reflection law is symmetrical with respect to the normal to the facades and does not produce grazing reflection (as Lambert's law for example), then, the problem can be solved by an asymptotic approach derived by Börgers *et al.*[19] The aim of this approach is to show that the transport equation with the appropriate boundary conditions (see Sec. III A 1) may be reduced to a diffusion equation. This result can be proved using extensive mathematical developments that are detailed in the next section. In the first step of this mathematical derivation (see Sec. III A 2), the distribution function $f(\mathbf{x},\mathbf{v},t)=f(x,y,z,v,w,t)$ is expressed as a product of two functions $q(x,y,t)$ and $\phi(z,u,v,w)$. By considering Lambert's law at the building facade, the last function $\phi(z,u,v,w)$ can be easily calculated, leading to a constant for every z. It suggests that the sound energy is uniform in the street section. Afterward, the main problem is to determine the function $q(x,y,t)$, expressing the distribution of sound particles in a parallel plane between the building facades. That is carried out in the second step of the mathematical derivation (see Sec. III A 3). By considering the probabilistic path of a sound particle between the two planes, it makes it possible to determine the probability density function of the displacement of the sound particles, which is simply equal to $q(x,y,t)$.

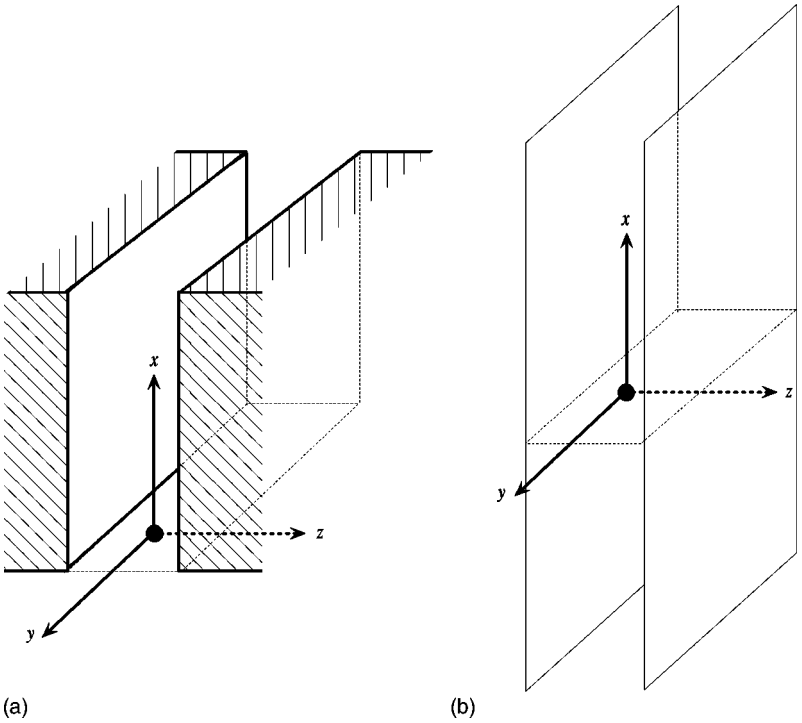

FIG. 3. Schematic representation of a street canyon with a sound source located on the pavement (a), as two parallel and infinite planes (b).

Function $q(x,y,t)$ is then solution of a diffusion equation, where the diffusion coefficient may be written as a function of the accommodation coefficient and the street width.

A. Asymptotic model

1. Geometry

Mathematically, the propagation space Y is defined by the spaces X and Z such as $Y=X\times Z$, where $X\in\mathbb{R}^2$ and $Z\in]0,h[$. The path of a sound particle in Y is defined by its position $\mathbf{x}$ and its velocity $\mathbf{v}$ normalized to the speed of sound c

$$\begin{cases} \mathbf{x}=(x,y,z) \text{ with } (x,y)\in X,\ z\in Z, \\ \mathbf{v}=(u,v,w) \text{ with } (u,v,w)\in[-c,c]\times[-c,c] \\ \quad \times[-c,c] \text{ and } u^2+v^2+w^2=c^2. \end{cases} \tag{12}$$

The boundary domain ∂Y of the space propagation Y, is simply equal to $\partial Z\times X$, where ∂Z is a surface of planes $z=0$ and $z=h$. Without sound absorption, the boundary conditions are only expressed in terms of specular and Lambert's reflections, defined, in the last case, by the equation

$$\mathcal{R}(\mathbf{v},\mathbf{v}')=\mathcal{A}|w|, \tag{13}$$

or, in spherical coordinates

$$\begin{cases} u=c\sin\theta\cos\varphi, \\ v=c\sin\theta\sin\varphi, \\ w=c\cos\theta, \\ du\,dv\,dw=c^2\sin\theta\,d\theta\,d\varphi, \end{cases} \tag{14}$$

by

$$\mathcal{R}(\theta,\theta')=\mathcal{A}c|\cos\theta|, \tag{15}$$

where $\mathcal{A}$ is found by considering the normalization condition (10). θ is defined between 0 and $\pi/2$ for $z=0$ and between $\pi/2$ and π for $z=h$. φ is varying from 0 to 2π. This normalization condition implies

$$\int_0^{\pi/2}\int_0^{2\pi}\mathcal{A}c^3\cos\theta\sin\theta\,d\varphi\,d\theta=\mathcal{A}\pi c^3=1, \tag{16}$$

leading to

$$\mathcal{A}=\frac{1}{\pi c^3}. \tag{17}$$

Substituting Eq. (17) in Eq. (13) yields

$$\mathcal{R}(\mathbf{v},\mathbf{v}')=\frac{|w|}{\pi c^3}, \tag{18}$$

or, in spherical coordinates,

$$\mathcal{R}(\theta,\theta')=\frac{|\cos\theta|}{\pi c^2}. \tag{19}$$

According to the Eq. (11) the boundary condition is simply given by

$$f^-(\mathbf{x},\mathbf{v},t)=df^+(\mathbf{x},\mathbf{v}^*,t)+\frac{1-d}{\pi c^3}\int_{\Gamma^+}|w'|f^+(\mathbf{x},\mathbf{v}',t)dv', \quad \text{for } \mathbf{x}\in\partial Y,\ \mathbf{v}\in\Gamma^-. \tag{20}$$

2. Asymptotic form of the distribution function

Two changes in the transport Eq. (5) are necessary to reach a diffusion approximation. First, the time t is rescaled to t/ε. Physically, this change means that long time is needed to observe a mixture of the sound particles between the planes. Second, the variable z is replaced by εz. That means that the two planes are brought closer one to the other, in order to have more changes of the sound particle velocity direction, by increasing the frequency collision on the planes. Finally, according to these changes, the aim of this

approach is to study the limit of the distribution function $f(x,y,\varepsilon z,u,v,w,t/\varepsilon)$, noted $f_\varepsilon(x,y,z,u,v,w,t)$ in the following developments, as ε tending to zero and which is solution of the transport equation

$$\frac{\partial f_\varepsilon}{\partial t}+\frac{1}{\varepsilon}u\frac{\partial f_\varepsilon}{\partial x}+\frac{1}{\varepsilon}v\frac{\partial f_\varepsilon}{\partial y}+\frac{w}{\varepsilon^2}\frac{\partial f_\varepsilon}{\partial z}=0. \tag{21}$$

By construction, the boundary conditions of $f_\varepsilon(x,y,z,u,v,w,t)$ are the same as for the distribution function $f(x,y,z,u,v,w,t)$ given at Eq. (20), since they are only applied on the particle velocity variable (u,v,w). According to Eq. (21), one can have

$$w\frac{\partial f_\varepsilon}{\partial z}=-\varepsilon\left[\varepsilon\frac{\partial f_\varepsilon}{\partial t}+u\frac{\partial f_\varepsilon}{\partial x}+v\frac{\partial f_\varepsilon}{\partial y}\right]. \tag{22}$$

The limit of Eq. (22) when ε tends to zero, leads to

$$\lim_{\varepsilon\to 0} w\frac{\partial f_\varepsilon}{\partial z}=\lim_{\varepsilon\to 0}-\varepsilon\left[\varepsilon\frac{\partial f_\varepsilon}{\partial t}+u\frac{\partial f_\varepsilon}{\partial x}+v\frac{\partial f_\varepsilon}{\partial y}\right]=0. \tag{23}$$

In this relation, variables x, y, and t appear just as parameters. To the limit, the distribution fonction $f_\varepsilon(x,y,z,u,v,w,t)$ tends to a distribution function $f(x,y,z,u,v,w,t)$, which can be expressed as the product of two functions $q(x,y,t)$ and $\phi(z,u,v,w)$, such as

$$f(x,y,z,v,w,t)=q(x,y,t)\times\phi(z,u,v,w), \tag{24}$$

where $\phi(z,u,v,w)$ is a positive function, normalized to unity

$$\int \phi(z,u,v,w)dzdudvdw=1, \tag{25}$$

and which verifies, from Eq. (23),

$$w\frac{\partial}{\partial z}\phi(z,u,v,w)=0. \tag{26}$$

The last result means that the distribution function is constant between the planes. By extension, it suggests that the sound energy in a street canyon is uniform on a street section. It may be noted that this assumption has been already used by several authors.[17,20,21] Following this asymptotic approach, an expression of $\phi(z,u,v,w)$ for Lambert's law can also be given. The introduction of Eq. (24) in the boundary Eq. (20) yields

$$\begin{aligned}|w|\phi^-(z,\mathbf{v})q(x,y,t)&=d|w|\phi^+(z,\mathbf{v}^*)q(x,y,t)+(1-d)\int_{\Gamma^+}\mathcal{R}(\mathbf{v},\mathbf{v}')|w'|\\&\quad\times\phi^+(z,\mathbf{v}')q(x,y,t)d\mathbf{v}',\quad \mathbf{v}\in\Gamma^-,\end{aligned} \tag{27}$$

where the notations ϕ^+ and ϕ^- are introduced to restrict the function ϕ to the sets Γ^+ Γ^-, corresponding to the incident and reflected particles at the boundary. This equation can be simplified by eliminating $q(x,y,t)$. Considering Lambert's law (18) at $z=0$ and $z=h$, Eq. (27) gives the two following boundary equations [Fig. 4]:

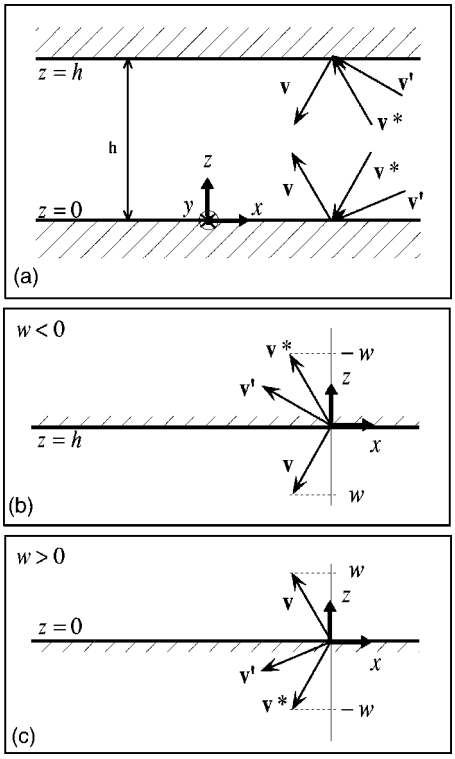

FIG. 4. Schematic representation of the reflection of a sound particle on boundaries (a). Vector projection on the z-axis for $w<0$ (b) and for $w>0$ (c). $\mathbf{v}'$, $\mathbf{v}^*$, and $\mathbf{v}$ are respectively the incident velocity, the specific velocity leading to specular reflection along $\mathbf{v}$, and the reflected velocity. w is the projection of $\mathbf{v}$ on the z-axis.

$$\begin{aligned}\phi(h,u,v,w)&=d\,\phi(h,u,v,-w)+(1-d)\frac{1}{\pi c^3}\\&\quad\times\int|w'|\phi(h,\mathbf{v}')d\mathbf{v}'\quad\text{for } w<0,\end{aligned} \tag{28}$$

$$\begin{aligned}\phi(0,u,v,w)&=d\,\phi(0,u,v,-w)+(1-d)\frac{1}{\pi c^3}\\&\quad\times\int|w'|\phi(0,\mathbf{v}')d\mathbf{v}'\quad\text{for } w>0.\end{aligned} \tag{29}$$

In addition, according to Eq. (26), the function $\phi(z,u,v,w)$ does not depend on z. Then, the following boundary conditions can be considered

$$\phi(h,u,v,-w)|_{w<0}=\phi(0,u,v,w)|_{w>0}, \tag{30}$$

$$\phi(0,u,v,-w)|_{w>0}=\phi(h,u,v,w)|_{w<0}. \tag{31}$$

The substitution of Eqs. (30) and (31) into the boundary Eqs. (28) and (29), gives

$$\begin{aligned}\phi(h,u,v,w)&=d\left[d\,\phi(0,u,v,-w)+(1-d)\frac{1}{\pi c^3}\right.\\&\quad\left.\times\int|w'|\phi(0,\mathbf{v}')d\mathbf{v}'\right]+(1-d)\frac{1}{\pi c^3}\\&\quad\times\int|w'|\phi(h,\mathbf{v}')d\mathbf{v}'\quad\text{for } w<0,\end{aligned} \tag{32}$$

and

$$\phi(0,u,v,w)=d\Bigg[d\,\phi(h,u,v,-w)+(1-d)\frac{1}{\pi c^3}\times\int|w'|\phi(h,\mathbf{v}')d\mathbf{v}'\Bigg]+(1-d)\frac{1}{\pi c^3}\times\int|w'|\phi(0,\mathbf{v}')d\mathbf{v}'\quad\text{for } w>0. \tag{33}$$

In Eqs. (32) and (33), the calculation of each integral gives a constant. Consequently, the last two equations may be written more simply

$$\phi(h,u,v,w)=d^2\phi(0,u,v,-w)+A\quad\text{for } w<0, \tag{34}$$

and

$$\phi(0,u,v,w)=d^2\phi(h,u,v,-w)+B\quad\text{for } w>0, \tag{35}$$

where A and B are two constants. Introducing Eq. (34) in Eq. (35), according to the sign of w, it gives

$$\phi(0,u,v,w)=d^2[\phi(0,u,v,w)+A]+B\quad\text{for } w>0, \tag{36}$$

that leads to

$$\phi(0,u,v,w)=\frac{Ad^2+B}{1-d^2}=a_-\quad\text{for } w<0, \tag{37}$$

where a_- is a constant. A similar approach can be applied at $z=h$, leading to

$$\phi(h,u,v,w)=\frac{Bd^2+A}{1-d^2}=a_+\quad\text{for } w>0, \tag{38}$$

where a_+ is also constant. In order to define a_+ and a_-, Eqs. (38) and (37) can be introduced in Eqs. (28) and (29), giving

$$a_-=da_++a_+(1-d)\frac{1}{\pi c^3}\int|w'|d\mathbf{v}'\quad\text{for } w<0, \tag{39}$$

$$a_+=da_-+a_-(1-d)\frac{1}{\pi c^3}\int|w'|d\mathbf{v}'\quad\text{for } w>0. \tag{40}$$

It can be noticed that this system of linear equations has only one solution, given by $a_+=a_-$. Finally, the constant a_+ is found by applying the condition of normalization given by Eq. (25)

$$\int\phi(z,u,v,w)dz\,du\,dv\,dw=a_+\int_0^h dz\int du\,dv\,dw=a_+4\pi hc^2=1, \tag{41}$$

that gives

$$\phi(z,u,v,w)=a_+=\frac{1}{4\pi hc^2}. \tag{42}$$

As expected, $\phi(z,u,v,w)$ only depends on the street width h. The distribution of the sound energy is inversely proportional to h.

The last work is to find $q(x,y,t)$ expressing the spatial and temporal distribution of sound particles in a plane (xOy) between the planes $z=0$ or $z=h$. Since the sound particle distribution is uniform between planes, the problem may be considered in any planes. In the next sections, an expression of the function $q(x,y,t)$ is derived by probabilistic considerations on the horizontal displacement [i.e., parallel to the (x,y) plane] of a sound particle between the two main planes. The main idea is to break up the trajectory of a particle between the planes (Fig. 5), in two types of elementary path: one corresponding to two successive Lambert's collisions with the plane (path AB in Fig. 5 for example) and a second corresponding to two Lambert's collisions including n specular reflections (paths BG and GI in Fig. 5, with 4 and 1 specular reflections, respectively). All the sound particles trajectories can be described by a succession of elementary paths, each one defined by the distribution of distance of propagation, and by the flight time between two Lambert's reflections, without and with specular reflections. Then, by applying the central limit theorem, the distribution of distance of propagation for any sound particle trajectory between the planes [i.e., $q(x,y,t)$] may be determined. This development is detailed in the next sections.

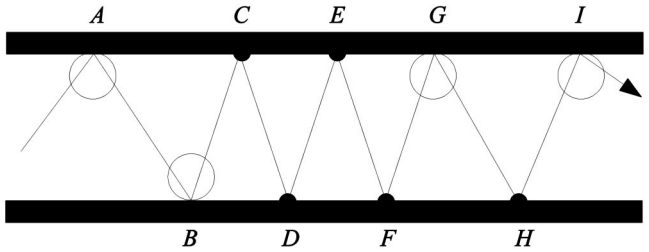

FIG. 5. Two-dimensional path of a sound particle between two planes, with Lambert's reflections (○) and specular reflections (●).

3. Path of a sound particle between two successive Lambert's reflections

a. Distribution of the horizontal distance of propagation. Let us assume that the initial reflection of a sound particle at $(x,y)=(0,0)$ is defined by a Lambert's reflection. The sound velocity, after reflection, is then distributed over the half-space $\mathbb{R}^2\times\mathbb{R}^+$, at $z=0$, or over the half-space $\mathbb{R}^2\times\mathbb{R}^-$, at $z=h$, according to Lambert's Law, by the density probability (18). After this first reflection, the sound particle is propagating along a straight line, between the two planes. The distance of propagation is then depending on the sound velocity w [Fig. 6]. Mathematically, the projection in the

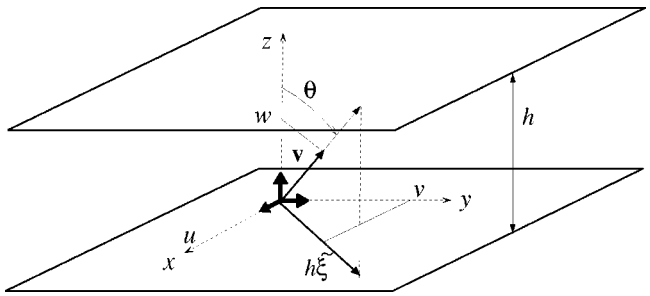

FIG. 6. Sound particle displacement from the plane $z=0$ to the plane $z=h$. The projection of the distance of propagation, in the (xOy) plane, is noted $h\tilde{\xi}$. $\mathbf{v}=(u,v,w)$ is the reflected velocity.

plane (xOy) of the propagation distance between the facades, can be written as $h\tilde{\xi}$, where $\tilde{\xi}$ is a random variable, given by

$$\tilde{\xi}=\frac{\sqrt{u^2+v^2}}{|w|}=\frac{\sqrt{c^2-w^2}}{|w|}. \tag{43}$$

According to the probability theory,[22] the associated repartition function for $\tilde{\xi}$ is given by

$$P(|h\tilde{\xi}|\leqslant hr)=P(|\tilde{\xi}|\leqslant r)$$
$$=\int_{\sqrt{c^2-w^2}/r}^{+\infty}\int_{-\infty}^{+\infty}\int_{-\infty}^{+\infty}\mathcal{R}(\mathbf{v},\mathbf{v}')du\,dv\,dw, \tag{44}$$

for $r>0$, which can be easily calculated in spherical coordinates:

$$P(|\tilde{\xi}|\leqslant r)=\frac{1}{\pi}\int_0^{2\pi}\left[\int_0^{\arctan(r)}\cos\theta\sin\theta\,d\theta\right]d\varphi$$
$$=\frac{r^2}{1+r^2}. \tag{45}$$

By definition, the probability density is found by deriving the repartition function. Derivation of Eq. (45) leads to

$$\tilde{G}(r)=\frac{2r}{(1+r^2)^2}. \tag{46}$$

Thus, the distribution of the horizontal distance of propagation after a Lambert's reflection, is given by

$$h\tilde{G}(r)=h\frac{2r}{(1+r^2)^2}. \tag{47}$$

b. Flight time of propagation between two collisions. Following the same method, the fight time of propagation between two collisions (after a Lambert's reflection) can be easily calculated. Considering a sound particle leaving, for example, the plane at $z=0$, with a sound velocity $\mathbf{v}=(u,v,w)$, it will takes a time

$$h\tilde{\tau}=\frac{h}{|w|}, \tag{48}$$

for hitting the opposite plane, where $\tilde{\tau}$ is a random variable. The flight time of propagation between two collisions is found by calculating the first moment of $h\tilde{\tau}$, noted $\mathbb{E}(h\tilde{\tau})$, given by, for Lambert's Law

$$\mathbb{E}(h\tilde{\tau})=h\mathbb{E}(\tilde{\tau})=\int_0^{+\infty}\int_{-\infty}^{+\infty}\int_{-\infty}^{+\infty}\frac{h}{|w|}\mathcal{R}(\mathbf{v},\mathbf{v}')du\,dv\,dw. \tag{49}$$

In spherical coordinates, Eq. (49) leads to

$$h\mathbb{E}(\tilde{\tau})=\frac{h}{\pi c}\int_0^{\pi/2}\tan\theta\,d\theta\int_0^{2\pi}d\varphi=\frac{2h}{c}. \tag{50}$$

4. Path of a sound particle between two Lambert's reflections, including n specular reflections

a. Distribution of the distance of propagation. Let us consider a sound particle, submitted to n specular reflections between two Lambert's reflections. According to the specular reflection properties, the reflection angle and the incident angle are equal after each specular reflection. The distribution of the distance of propagation between n successive specular reflections is then defined by the probability (46), corresponding to the propagation after the first Lambert's reflection.

Using the definition of the accommodation coefficient d, the probability $P(n=k)$ that $n=k$ specular reflections occur between two successive Lambert's reflections, is equal to the probability d^k (corresponding to k specular reflections) times the probability $(1-d)$ that the last reflection is a Lambert's reflection

$$P(n=k)=(1-d)d^k. \tag{51}$$

As suggested above, the distance between two successive reflections is equal to the first distance of propagation. Then, the total distance of propagation, corresponding to n specular reflections between two Lambert's reflections is equal to $h\xi=h(1+n)\tilde{\xi}$, where ξ is a random variable. The probability that $|h\xi|<hr$ is then given by

$$P(|\xi|<r)=P[(1+n)|\tilde{\xi}|\leqslant r]. \tag{52}$$

The two random variables $\tilde{\xi}$ and n being independent, this last relation can be simplified as follows:

$$P(|\xi|<r)=\sum_{k=1}^{+\infty}P[(1+n)=k,k|\tilde{\xi}|\leqslant r],$$
$$=\sum_{k=1}^{+\infty}P[(1+n)=k]\times P(k|\tilde{\xi}|\leqslant r),$$
$$=\sum_{k=1}^{+\infty}P[(1+n)=k]\times P(|\tilde{\xi}|\leqslant r/k),$$
$$=\sum_{k=1}^{+\infty}(1-d)d^{k-1}\int_0^{r/k}\tilde{G}(s)ds. \tag{53}$$

The probability density associated to the horizontal distribution of propagation, and corresponding to n specular reflections between two Lambert's reflections is then equal to

$$G(r)=\sum_{k=1}^{+\infty}(1-d)d^{k-1}\frac{1}{k}\tilde{G}\left(\frac{r}{k}\right). \tag{54}$$

b. Flight time of propagation. By definition, the flight time corresponding to n specular reflections between two Lambert's reflections, is equal to the first moment of $h\tau=h(1+n)\tilde{\tau}$ (see Sec. III A 3 *b*), then by

$$\mathbb{E}(h\tau)=h\mathbb{E}[(1+n)\tilde{\tau}]. \tag{55}$$

The two random variables τ and n being independent, this last relation can be simplified to give

$$\mathbb{E}(h\tau)=\mathbb{E}(1+n)\times h\mathbb{E}(\tilde{\tau}). \tag{56}$$

The last term of the right member of this equation is given at Eq. (50). The first term is simply the first moment of the probability density (51), which can be easily calculated. Finally, the corresponding flight time is given by

$$\mathbb{E}(h\tau)=\frac{1}{1-d}\times\frac{2h}{c}. \tag{57}$$

5. Application of the central limit theorem

With the knowledge of the probability distributions of the horizontal displacements between Lambert's reflections (including 0, 1 or more specular reflections), the objective of this last part is to determine the distribution of the sum of these random variables, corresponding to the propagation of a sound particle including multiple successive Lambert's reflections, with and without specular reflections.

Let us denote S_k the sum of realizations ξ_i of the independent random variables ξ, by

$$S_k=\sum_{i=1}^{k}\xi_i. \tag{58}$$

With this definition, a sound particle leaving one of the two planes at $(x,y)=(0,0)$, and which will realize k Lambert's reflections, will travel a horizontal distance hS_k. If the second moments of ξ were finite, then the central limit theorem for random variables of finite variance would imply that hS_k converges, in distribution, to a normal distribution. In order to evaluate this convergence, the method consists in finding an asymptotic expansion of the characteristic function $\varphi(h\lambda)$ of the random variable hS_k

$$\varphi(h\lambda)=\mathbb{E}[\exp(i\lambda hS_k)]. \tag{59}$$

- The first step is to investigate the characteristic function $\tilde{\phi}(\lambda)$ of $\tilde{\xi}$, which is given (by definition) by

$$\tilde{\phi}(h\lambda)=\mathbb{E}[\exp(i\lambda\tilde{\xi})]=\frac{1}{2\pi}\int_0^{\infty}\int_0^{2\pi}\tilde{G}(r)\exp[i|\lambda|r\cos\theta]d\theta\,dr. \tag{60}$$

  Then, the asymptotic approach detailed by Börgers *et al.*[19] gives

$$\tilde{\phi}(\lambda)=1+\frac{|\lambda|^2}{2}\log|\lambda|+O(|\lambda|^2). \tag{61}$$

- The second step is to find an appropriate expansion for the characteristic function $\phi(\lambda)$ of ξ. Using Eq. (61), $\phi(\lambda)$ is given by

$$\begin{aligned}\phi(\lambda)&=\frac{1}{2\pi}\int_0^{\infty}\int_0^{2\pi}G(r)\exp[i|\lambda|r\cos\theta]d\theta\,dr,\\&=\frac{1}{2\pi}\int_0^{\infty}\int_0^{2\pi}\sum_{k=1}^{+\infty}(1-d)d^{k-1}\frac{1}{k}\tilde{G}\left(\frac{r}{k}\right)\\&\quad\times\exp[i|\lambda|r\cos\theta]d\theta\,dr,\\&=\sum_{k=1}^{+\infty}(1-d)d^{k-1}\tilde{\phi}(\lambda),\\&=1+\frac{1+d}{2(1-d)^2}|\lambda|^2\log|\lambda|+O(|\lambda|^2).\end{aligned} \tag{62}$$

- The last step is to write the characteristic function $\varphi(h\lambda)$ of the random variable hS_k. The independence of the random variable ξ_i, leads to

$$\begin{aligned}\varphi(h\lambda)&=\mathbb{E}[\exp(i\lambda hS_k)],\\&=\{\mathbb{E}[\exp(i\lambda h\xi)]\}^k,\\&=[\phi(h\lambda)]^k,\\&=\left[1+\frac{1+d}{2(1-d)^2}|\lambda|^2h^2\log|\lambda|h+O(h^2)\right]^k.\end{aligned} \tag{63}$$

According to the central limit theorem,[19] k should be about $O(1/h^2\log h^{-1})$ in order for the hS_k to converge to a normal distribution. A timescale can now be deduced in such a way that the number of flight segments over the appropriate scaled time interval is of this order in h. For real $t>0$, let us define

$$m_h(t)=\left[\frac{t}{h\mathbb{E}(\tau)}\right]=\left[\frac{(1-d)c}{2h}t\right], \tag{64}$$

where $[a]$ denotes the largest integer less than or equal to a. Let us define, for a time $t>0$

$$t=\frac{t_h}{h\log(1/h)}. \tag{65}$$

Substituting t by Eq. (65) in Eq. (64), one can remark that $k=m_h(t_h)$ is about $O(1/h^2\log h^{-1})$. Finally, according to the central limit theorem, to the limit of h tending to 0, hS_k converges to a normal distribution, such as

$$\varphi(h\lambda)=[\phi(h\lambda)]^{m_h(t_h)}\rightarrow\exp\left(-\sigma^2t\frac{|\lambda|^2}{2}\right), \tag{66}$$

with

$$\sigma^2=\frac{(1+d)}{(1-d)}\frac{c}{2}. \tag{67}$$

This last equation expresses that the limit of the $\varphi(h\lambda)$ is the characteristic function of a two-dimensional, normally distributed, random variable with covariance $t\sigma^2$ and whose probability density function $G(x,y,t)$ is defined by

$$G(x,y,t)=\frac{1}{2\pi t\sigma^2}\exp\left[-\frac{x^2+y^2}{2t\sigma^2}\right]. \tag{68}$$

The probability density G describes the spatial and temporal distribution of sound particles in the horizontal plane $z=0$, and is equal, by construction, to the function $q(x,y,t)$. Moreover, by definition, Eq. (68) is solution of the following diffusion equation:

$$\frac{\partial}{\partial t}q(x,y,t)-\mathcal{K}\frac{\partial^2}{\partial x^2}q(x,y,t)-\mathcal{K}\frac{\partial^2}{\partial y^2}q(x,y,t)=0, \tag{69}$$

where $\mathcal{K}$ is defined as the diffusion coefficient, by

$$\mathcal{K}=h\frac{\sigma^2}{2}=\frac{(1+d)}{(1-d)}\frac{hc}{4}. \tag{70}$$

This result shows that the sound particles displacement between the planes may be approached by a diffusion process. By analogy, it means that the sound field between the planes is also a solution of a diffusion equation defined by only one parameter, the diffusion coefficient. This coefficient expresses the diffuse behavior of the boundaries by including

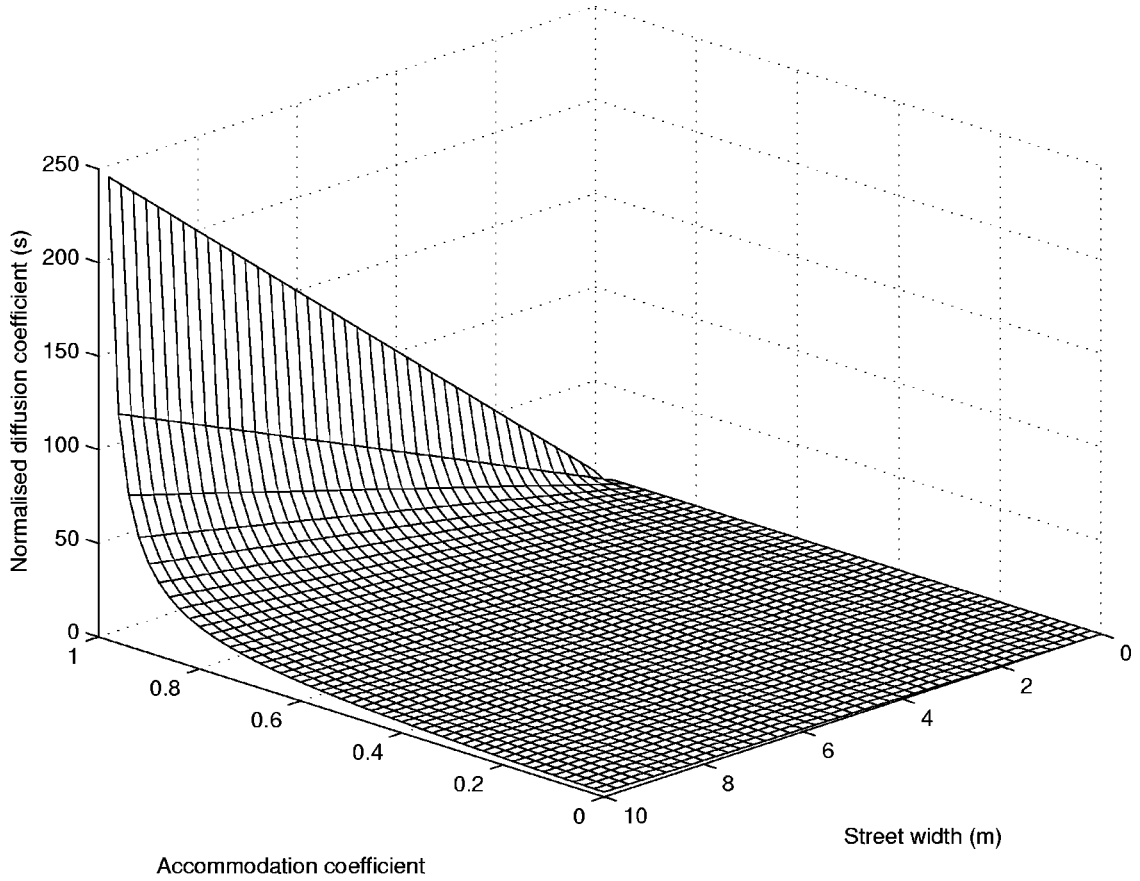

FIG. 7. Variation of the normalized diffusion coefficient $\mathcal{K}/c$ with the street width and the accommodation coefficient.

the part of diffuse and specular reflections through the accommodation coefficient d. According to Eq. (70), the diffusion coefficient $\mathcal{K}$ decreases with d, which means that the energy of the sound field will need more time to spread between the planes [Fig. 7]. On the other hand, when d increases, the reflection becomes more specular, and the sound energy spreads very quickly. Moreover, as expected, the distance between the planes (i.e., the street width) is also introduced in the expression of the diffusion coefficient. When the planes are closer, the sound energy remains for a long time at the same place, while, for larger distances between planes, the sound energy will be distributed very quickly.

In addition, this result gives a mathematical justification of a previous work,[23] where the solution of a diffusion equation was already used to model the sound propagation in urban areas. However, at that time, the diffusion coefficient was found by simple hypothesis, and through a fitting on experimental data. Within the framework of the experimentation given in Ref. 23, the diffusion coefficient along the main axis of a street canyon of length 96 m and width 8 m, was estimated at 3360 m^2/s. This value is quite in agreement with Eq. (70), by assuming Lambert's reflections and in condition of taking $d=0.66$. It means that the boundaries were more specular than diffuse in this street.

B. Sound energy in the street

Although it should be possible to consider a street canyon as two infinite and perfectly reflecting planes, the choice was done now to consider a more realistic geometry. Let us consider a three-dimensional street of length L, width h, and height H, with a sound source located in the middle of a street section at (x_0,y_0) in the street [Fig. 8]. According to

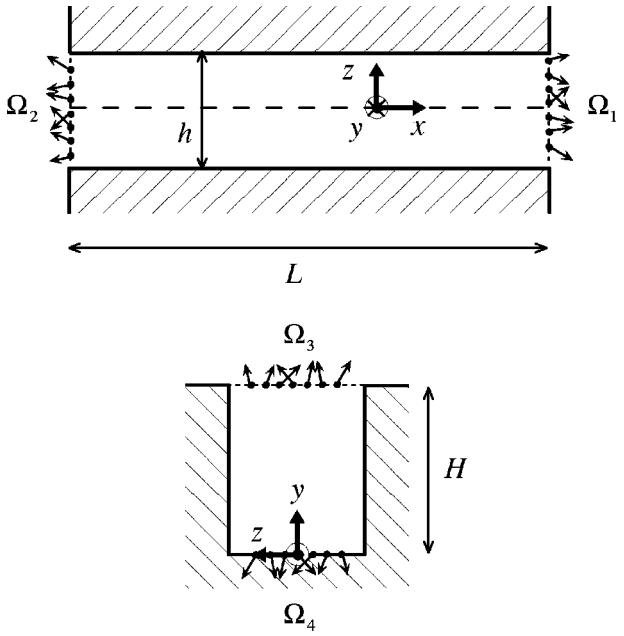

FIG. 8. Geometry of the street and representation of the boundary conditions: Ω_1, Ω_2, and Ω_3 represent the incident sound particles at the openings at $x=L$, $x=0$ and $z=H$, respectively. Ω_4 represents the incident sound particles on the pavement.

the previous result, the sound distribution in the (xOy) direction follows a diffusion process, in such a way that the sound energy density in the street is the solution of the diffusion Eq. (69). In order to have a more realistic solution of the temporal and spatial distribution of sound energy in the street, the sound absorption by the openings, the pavement and the building facades must be introduced in the diffusion model. However, these boundary conditions have to be consistent with the transport theory.

1. Absorption by the openings

Absorption at the openings can be taken into account by introducing an exchange coefficient η_{open} in the conventional boundary conditions of the diffusion equation, at both extremities and at the opened top, respectively, by

$$-\mathcal{K}\frac{\partial q(x,y,t)}{\partial x}=\eta_{\text{open}}q(x,y,t) \quad \text{at } x=L, \quad \forall z\in[0,h], \quad \forall y\in[O,H], \tag{71}$$

$$\mathcal{K}\frac{\partial q(x,y,t)}{\partial x}=\eta_{\text{open}}q(x,y,t) \quad \text{at } x=0, \forall z\in[0,h], \quad \forall y\in[O,H], \tag{72}$$

and

$$-\mathcal{K}\frac{\partial q(x,y,t)}{\partial y}=\eta_{\text{open}}q(x,y,t) \quad \text{at } y=H, \quad \forall x\in[O,L], \quad \forall z\in[0,h]. \tag{73}$$

From Eq. (24), the distribution function may be written as the product of two functions $q(x,y,t)$ and $\phi(z,u,v,w)$. For example, the total flow of sound energy at the extremity $x=L$ should be written

$$J_1(L,y,z,t)=-\mathcal{K}\left.\frac{\partial q(x,y,t)}{\partial x}\right|_{x=L} \times\int_{\Omega_1}\phi(z,u,v,w)du\,dv\,dw, \tag{74}$$

$$=\eta_{\text{open}}q(L,y,t) \times\int_{\Omega_1}\phi(z,u,v,w)du\,dv\,dw, \tag{75}$$

where Ω_1 [Fig. 8] is defined by

$$\Omega_1=\{[\mathbf{x}=(L,y,z);\mathbf{v}]/\mathbf{v}\in\mathbb{R}^3,0<\mathbf{n}\cdot\mathbf{v}\}, \tag{76}$$

and where $\mathbf{n}$ is the outgoing normal to the opening. Ω_1 expressed the sound particles whose velocity are oriented along the normal to the opening. In an equivalent way, Ω_2 and Ω_3 can also be defined for the opening at $x=0$ and $y=H$. From Eq. (3), the outgoing sound particle flow at the openings, can also be expressed by

$$J(x,y,z,t)=\int|\mathbf{v}\cdot\mathbf{n}|f(x,y,z,u,v,w,t)du\,dv\,dw, \tag{77}$$

which gives, at $x=L$

$$J_1'(L,y,z,t)=q(L,y,t)\int_{\Omega_1}u\,\phi(z,u,v,w)du\,dv\,dw. \tag{78}$$

By construction, Eqs. (78) and (75) are equal. Since $\phi(z,u,v,w)$ is constant for Lambert's Law, the exchange coefficient η_{open} must verify

$$\eta_{\text{open}}\int_{\Omega_1}du\,dv\,dw=\int_{\Omega_1}u\,du\,dv\,dw. \tag{79}$$

The last two integrations can easily be performed using the spherical coordinates (14), leading to (at $x=L$)

$$\eta_{\text{open}}=\frac{c}{2}. \tag{80}$$

A similar approach may be used for the absorption at $x=0$ and at the opened top $y=H$, using the boundary conditions (72) and (73), respectively, giving the same expression for the exchange coefficient. As expected, the exchange coefficient at the opening only depends on the reflection law and the speed of sound c, but not on the street size.

2. Sound absorption by the pavement and the building facades

The same procedure can also be used for the sound absorption by the pavement and the building facades. Let us consider the exchange coefficient η_p of the street pavement. The standard boundary condition for the street pavement can be written

$$\mathcal{K}\frac{\partial q(x,y,t)}{\partial y}=\eta_p q(x,y,t) \quad \text{at } y=0 \quad \forall x\in[O,L], \quad \forall z\in[0,h]. \tag{81}$$

According to the definition of the distribution function, the total energy flow which is absorbed by the pavement, at $y=0$, is written

$$J_4(x,0,z,t)=q(x,0,t)\int_{\Omega_4}v\,\phi(z,u,v,w)du\,dv\,dw, \tag{82}$$

where Ω_4 [Fig. 8] is defined by

$$\Omega_4=\{[\mathbf{x}=(x,0,z);\mathbf{v}]/\mathbf{v}\in\mathbb{R}^3,0<\mathbf{n}\cdot\mathbf{v}\}. \tag{83}$$

The total energy flow of sound particles through the pavement can also be found using Eq. (24). The sound energy absorbed by the pavement is the product between the total energy flow through the pavement and the absorption coefficient α_p of the pavement

$$J_4'(x,0,z,t)=\alpha_p\int_{\Omega_4}|v|f(x,0,z,u,v,w,t)du\,dv\,dw. \tag{84}$$

By construction, Eqs. (82) and (84) are equal, that implies

$$\eta_p\int_{\Upsilon}du\,dv\,dw=\alpha_p\int_{\Omega_4}v\,du\,dv\,dw, \tag{85}$$

leading to the exchange coefficient of the pavement

$$\eta_p = \alpha_p \frac{c}{2}. \tag{86}$$

As expected, the exchange coefficient of the pavement is equivalent to the product of the exchange coefficient of the open top with the absorption coefficient of the pavement. It may be noted that this procedure cannot be applied to the building facades at $z=0$ and $z=h$, since the diffusion process (i.e., the diffusion equation) is only valid in the x and y directions. However, the sound absorption by building facades may have a major part in the sound decay in the street, and then, cannot be neglected. In order to take it into account in the model, a simple way is to introduce the absorption coefficient of the building facades in the exchange coefficient of the pavement. Let us consider the total equivalent absorption area of the street (without the openings)

$$A = \alpha_p hL + 2\alpha_f HL, \tag{87}$$

$$= hL\left(\alpha_p + 2\frac{H}{h}\alpha_f\right), \tag{88}$$

$$= hL\alpha_p', \tag{89}$$

where α_p' is the equivalent absorption coefficient of the pavement, including the absorption by the building facades. With this definition, the exchange coefficient of the pavement, including the facade effects, is

$$\eta_p' = \alpha_p' \frac{c}{2} = \left[\alpha_p + 2\frac{H}{h}\alpha_f\right]\frac{c}{2}. \tag{90}$$

3. Solution of the diffusion equation

The sound energy in the street is the solution of the diffusion Eq. (69), in accordance with the boundary conditions (71)–(73) at the openings, and Eq. (81) (with η_p' instead of η_p) at the pavement. A similar solution was already proposed in Ref. 24 and can be written

$$q(x,y,t) = \sum_{n=1}^{\infty}\sum_{m=1}^{\infty}\frac{a_n}{u_n}\frac{b_m}{v_m}\left[u_n\cos\left(\frac{u_n x}{L}\right) + B_{\text{open}}\sin\left(\frac{u_n x}{L}\right)\right]\left[v_m\cos\left(\frac{v_m y}{H}\right) + B_p\sin\left(\frac{v_m y}{H}\right)\right]\exp\left[-\left(\frac{u_n^2}{L^2}+\frac{v_m^2}{H^2}\right)\mathcal{K}t\right], \tag{91}$$

where the a_n, b_m, u_n, and v_m coefficients verify

$$(u_n^2 - B_{\text{open}}^2)\tan u_n = 2B_{\text{open}}u_n, \tag{92}$$

and

$$(v_m^2 - B_p B_{\text{open}})\tan v_m = (B_p + B_{\text{open}})v_m, \tag{93}$$

where $B_{\text{open}} = \eta_{\text{open}}L/\mathcal{K}$ and $B_p = \eta_p' H/\mathcal{K}$. The ratio a_n/u_n and b_m/v_m are given by the initial conditions. For a point source at (x_0, y_0), they are expressed by

$$\frac{a_n}{u_n} = \frac{2}{L}\frac{u_n\cos(u_n x_0/L) + B_{\text{open}}\sin(u_n x_0/L)}{u_n^2 + B_{\text{open}}^2 + 2B_{\text{open}}}, \tag{94}$$

and

$$\frac{b_m}{v_m} = \frac{2}{H}\frac{v_m\cos(v_m y_0/H) + B_p\sin(v_m y_0/H)}{v_m^2 + B_p^2 + 2B_p + \cos^2 v_m (v_m^2 + B_p^2)(B_{\text{open}} - B_p)/(v_m^2 - B_p B_{\text{open}})}. \tag{95}$$

The reverberation time, at position (x,y) in the parallel plane to the building facades, can be determined by estimating the slope of the decay given by Eq. (91). The sound level in the stationary state, at position (x,y), is found by integrating Eq. (91) over the time t.

In order to validate the transport approach and the diffusion model, Eq. (91) has been compared with experimental results obtained in a street canyon. This is described in the next section.

IV. EXPERIMENTAL VALIDATION

A. Measurements in a street

A recent experiment[25] was realized in a pedestrian street of 210 m long, 18 m high, and 7.90 m wide [Fig. 9]. The morphology of the building facades was uniform all along the street and was composed by a periodic arrangement of windows. The facades was mainly constituted by stone, glass, and woodworks with a low absorption coefficient α_f around 0.05. This absorption coefficient is slightly smaller than some values suggested in Ref. 26, for example, but seems more suitable for the Kervegan street. The pavement made of cobblestones was considered as a perfectly reflecting surface ($\alpha_p = 0$).

The sound source (a pistol shot) was located 0.52 m above the pavement at 50 m from the west end of the street [Fig. 9]. An array of nine microphones was moved from 6 to 50 m from the sound source, step by step every 2 m. A reference microphone was also located 2 m from the sound source, to activate the data acquisition. Acoustic measurements were performed with AVM MI17 ICP microphones, Brüel and Kjær microphones type 4135, 4165, and GRAS microphones type 40AF, fixed on Brüel and Kjær preamplifier type 2619 and 2639. Measurements (i.e., impulse responses) were recorded on an integrated digital recorder TEAC GX-1 with AR-GXMC and AR-GXPA input amp cards, connected to a PC notebook. The sample frequency and the recording time were, respectively, 20 480 Hz and 3 s. A 10 kHz low pass filter was applied on each acquisition channel. A meteorological data acquisition system was also set up in the street for the measurement of the temperature, atmospheric pressure, humidity, and wind speed. To avoid the small fluctuations of the sound source between two con-

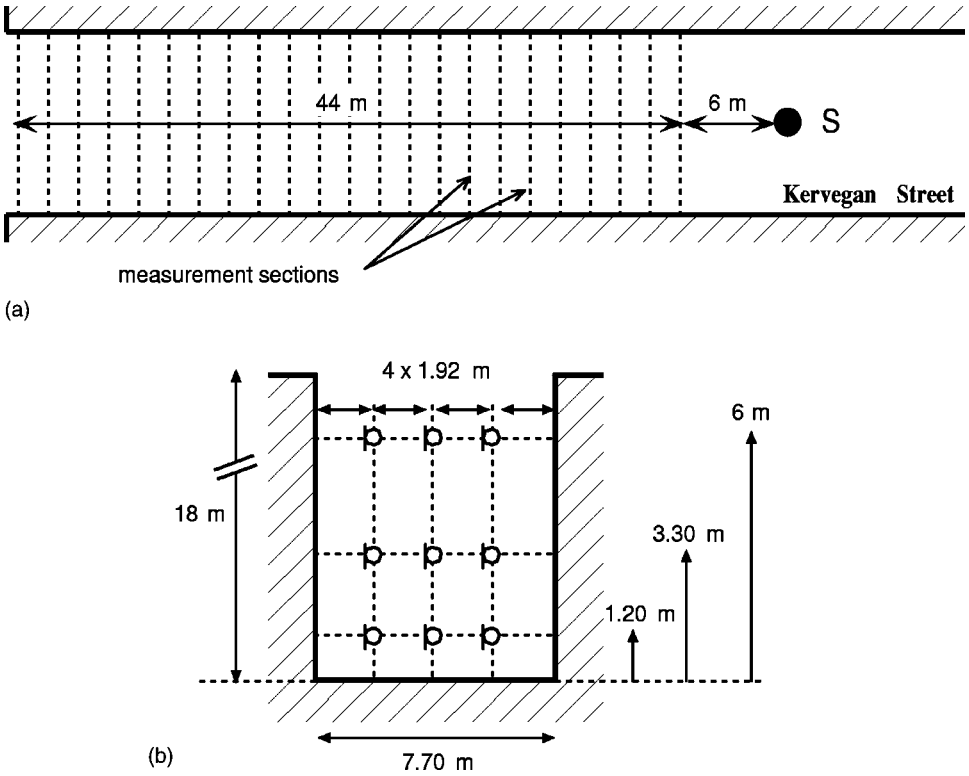

FIG. 9. Measurements in the Kervegan street (Nantes, France). Location of the microphones array along the street (a) and in the street section (b).

secutive shots, five measurements (i.e., five pistol shots) were recorded for each location of the array of microphones.

In order to consider only the effect of the street morphology on the sound propagation in the street, the atmospheric attenuation was compensated on each impulse response.[27] Sound levels and reverberation times $RT30$ were calculated for each 1/3 octave bands between 500 and 5000 Hz and for each impulse response. Then, values were averaged over the five measurements for each position along the street and for each microphone.

B. Model validation

As presented in Ref. 25, the measurements show that reverberation times and sound pressure levels are quite uniform inside a street section, even very close to the sound source, for all 1/3 octave bands between 500 and 5000 Hz. The model is then in agreement with the experimental results. It suggests that it is reasonable to assume a uniform sound field in a street section.

Since the reverberation time and the sound level may be assumed constant along the width, the data are averaged in order to give a mean value for each measurement section and for each 1/3 octave band. Moreover, as presented in Ref. 25, the shape of the sound attenuation in the street are almost similar for each 1/3 octave band. The sound attenuation are also averaged over the frequency range between 500 and 5000 Hz, to give a single reference curve for the sound attenuation in the street. The direct field is compensated to consider the reverberant field only.

Inversely, it was shown[25] that the sound decay for each measurement section is frequency dependent (the $RT30$ decreases with the frequency). Thus, the upper and the lower limits of the measured reverberation times along the street, compose the reference curve for the sound decay in the street.

Since no information is available for the accommodation coefficient of the building facades, the solution of the diffusion equation is calculated for several values of d between 0 (perfectly diffuse) and 1 (perfectly specular), and compared to the references curves.

Figure 10 shows the comparison for the reverberation times along the street, with the solution of the diffusion equation for $d=0.2$ to 0.9. It can be observed that the model is in agreement with experimental data if d is contained between 0.4 and 0.7. At low frequency, the best agreement is obtained with lower accommodation coefficient. In contrary, for high frequencies, d must be larger. Figure 10 also shows that the reverberation time is very sensitive to the choice of the accommodation coefficient. A small change in d produces large variations of the reverberation time.

Figure 11 presents the mean sound attenuation measured along the street, compared to the diffusion model for d between 0 and 0.9. When regarding near the sound source, it seems that all accommodation coefficients are consistent with the experimental results. However, when the source-receiver distance increases, the diffusion model fails for lower accommodation coefficient. The best agreement is obtained for d between 0.8 and 0.5, which is more or less in agreement with the conclusion relative to the reverberation time. The Kervegan street is an ancient street with highly modulated facades, which explains why the accommodation coefficient should be smaller (i.e., the building facades are very diffuse). For streets with modern buildings, the accommodation coefficient should be larger (i.e., reflections should be more specular).

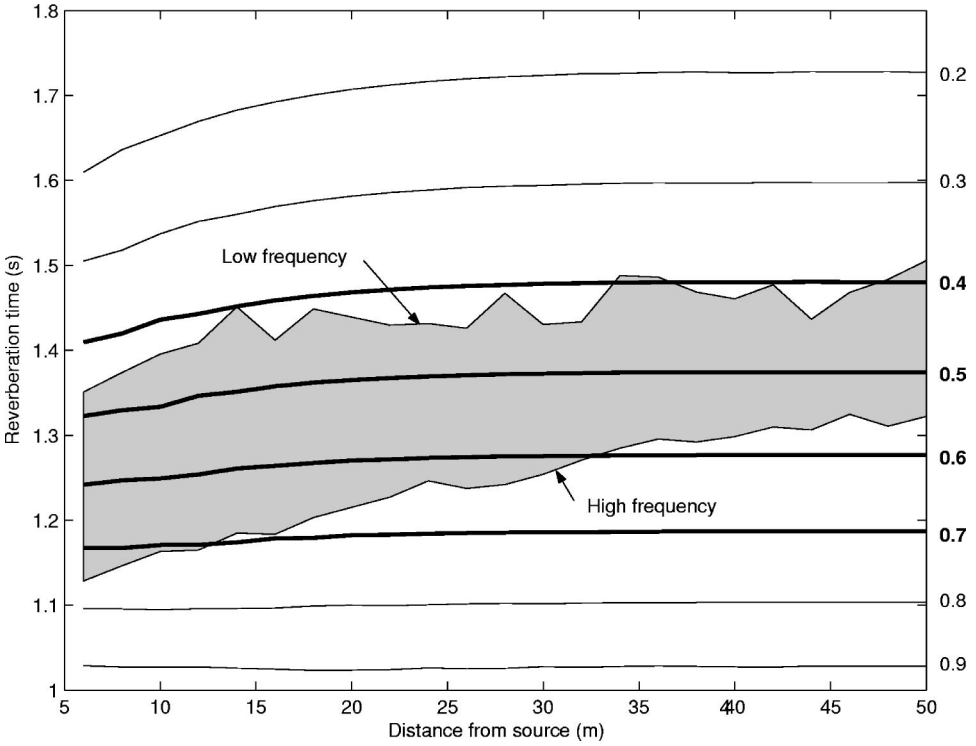

FIG. 10. Reverberation times calculated by the diffusion model for $d=0.2,0.3,\ldots,0.9$ compared with the experimental data measured in the Kervegan Street. Experimental data are symbolized by the domain defined by the upper and the lower limits (filled in gray). Analytical solutions are represented by continuous lines, and noted on the right of the figure. Solutions with $d=4$ to $d=0.7$ (thick lines) are consistent with experimental data.

It can also be noted also that the diffusion model is very sensitive to the choice of the absorption coefficient for the determination of the reverberation time, while, for the sound attenuation along the street, a small variation of the absorption does not fundamentally change the shape of the curves. Overall, considering the uncertainties on the absorption coefficients and the reflection law principally, the diffusion model gives consistent results with experimental data.

V. CONCLUSION

A general approach, based on the transport theory of sound particles, has been investigated for the sound field modeling in architectural acoustics. Using simple considerations, it is shown that the sound energy in a diffusely reflecting enclosure could be the solution of transport equation. For street canyons, using Lambert's reflection law, the transport equation may be reduced to a diffusion equation for the sound energy. The whole process is then characterized by the diffusion coefficient, which takes into account the street width and the accommodation coefficient. In order to solve the diffusion equation, exchange coefficients are introduced in the boundary conditions to predict the absorption by the openings, the pavement, and the building facades of the

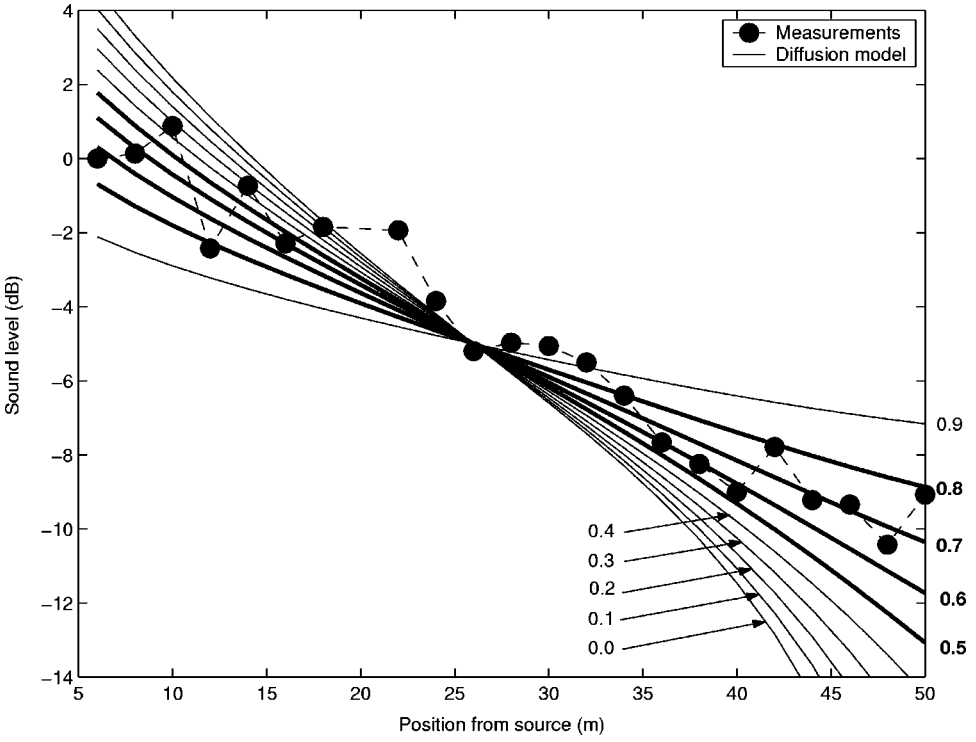

FIG. 11. Calculated sound level for $d=0.0,0.1,\ldots,0.9$, compared with experimental data. Solutions with $d=0.5$ to $d=0.8$ (thick lines) are consistent with measurements.

street. The solution of the diffusion equation is given and compared to experimental data, with a nice agreement both for the reverberation time and the sound attenuation.

In spite of the complexity of the scattering of sound by building facade, only one parameter, the diffusion coefficient, has to be introduced in the model. This is the main result. In the present paper, the expression of the diffusion equation is given for Lambert's law, but similar developments could be also investigated for any reflection law having a symmetry around the normal to the wall, and without grazing reflection. For more complicated laws, other asymptotic approaches should be envisaged. In a practical point of view, it will be interesting to consider real reflection laws (instead of Lambert's law) and appropriate accommodation coefficients for the building facades, in order to validate and apply the model in all types of urban areas. That is also needed to estimate or measure these two parameters, as already done in room acoustics. In addition, it can also be noted, that, in practice, building facades may be different on both sides of the street, for the absorption or the diffusion. It should also be necessary to include this into the model. In addition, instead of including the sound absorption by building facades in the boundary conditions of the diffusion equation, it could be more accurate to include absorption in the transport approach directly, when developing the asymptotic solution. At last, it would also be interesting to investigate the generalized transport Eq. (6) in order to have a more accurate model of the sound field description in urban areas.

[1] J. Picaut, J. Hardy, and L. Simon, "Prediction of background noise in a built-up area: A periodic disposition of buildings," Phys. Rev. E **60**, 4851–4859 (1999).

[2] M. Ismail and D. Oldham, "The effect of the scattering of sound from building façades on urban noise propagation," 10th International Congress on Sound and Vibration, Stockholm, Sweden (International Institute of Acoustics and Vibration (IIAW), Royal Insitute of Technology (KIT)-Sweden, Scandinavia Vibration Society (SVIB)-Sweden, International Insitute of Acoustics and Vibration, 2003).

[3] K. Heutschi, "A simple method to evaluate the increase of traffic noise emission level due to buildings, for a long straight street," Appl. Acoust. **44**, 259–274 (1995).

[4] R. H. Lyon, "Role of multiple reflections and reverberation in urban noise propagation," J. Acoust. Soc. Am. **55**, 493–503 (1974).

[5] J. Kang, "Sound propagation in street canyons: Comparisons between diffusely and geometrically reflecting boundaries," J. Acoust. Soc. Am. **107**, 1394–1404 (2000).

[6] W. B. Joyce, "Sabine's reverberation time and ergodic auditorium," J. Acoust. Soc. Am. **58**, 643–655 (1975).

[7] M. Vorländer, "Simulation of the transient and steady-state sound propagation in rooms using a new combined ray-tracing/image-source algorithm," J. Acoust. Soc. Am. **86**, 172–178 (1989).

[8] J. L. B. Coelho, "Room acoustics design by a sound energy transition approach," Acust. Acta Acust. **86**, 903–910 (2000).

[9] M. M. R. Williams, *Mathematical Methods in Particle Transport Theory* (Butterworths London, 1971).

[10] A. M. Weinberg and E. P. Wigner, *The Physical Theory of Neutron Chain Reactors* (University of Chicago, Chicago, 1958).

[11] M. Hodgson, "Evidence of diffuse surface reflections in rooms," J. Acoust. Soc. Am. **89**, 765–771 (1991).

[12] W. B. Joyce, "Exact effect of surface roughness on the reverberation time of a uniformly absorbing spherical enclosure," J. Acoust. Soc. Am. **64**, 1429–1436 (1978).

[13] J. J. Embrechts, D. Archambeau, and G. Stan, "Determination of the scattering coefficient of random rough diffusing surfaces for room acoustics applications," Acust. Acta Acust. **87**, 482–494 (2001).

[14] M. Vorländer and E. Mommertz, "Definition and measurement of random-incidence scattering coefficients," Appl. Acoust. **60**, 187–199 (2000).

[15] J. Kang, *Acoustics of Long Spaces* (Thomas Telford, London, 2002).

[16] H. Kuttruff, *Room Acoustics*, 4th ed. (Spon Press, London, 2000).

[17] J. Kang, "Reverberation in rectangular long enclosures with diffusely reflecting boundaries," Acust. Acta Acust. **88**, 77–87 (2002).

[18] S. Wu and E. Kittinger, "On the relevance of sound scattering to the prediction of traffic noise in urban streets," Acustica **81**, 36–42 (1995).

[19] C. Börgers, C. Greengard, and E. Thomann, "The diffusion limit of free molecular flow in thin plane channel," SIAM (Soc. Ind. Appl. Math.) J. Appl. Math. **52**, 1057–1075 (1992).

[20] C. H. Chew, "Prediction of traffic noise from expressways—Part II: Buildings flanking both sides of expressways," Appl. Acoust. **32**, 61–72 (1991).

[21] H. G. Davies, "Multiple-reflection diffuse-scattering model for noise propagation in streets," J. Acoust. Soc. Am. **64**, 517–521 (1978).

[22] D. Foata and A. Fuchs, *Calcul Des Probabilités, Cours, Exercices et Problèmes Corrigés* (Dunod, Paris, 1998).

[23] J. Picaut, J. Hardy, and L. Simon, "Sound field modeling in streets with a diffusion equation," J. Acoust. Soc. Am. **106**, 2638–2645 (1999).

[24] J. Picaut, L. Simon, and J.-D. Polack, "Sound field in long rooms with diffusely reflecting boundaries," Appl. Acoust. **56**, 217–240 (1999).

[25] J. Picaut, T. Le Pollès, P. L'Hermite, and V. Gary, "Experimental study of sound propagation in a street," Appl. Acoust. (to be published).

[26] D. J. Oldham and M. M. Radwan, "Sound propagation in city streets," Building Acoustics **1**, 65–88 (1994).

[27] J. Picaut and L. Simon, "A scale model experiment for the study of sound propagation in urban areas," Appl. Acoust. **62**, 327–340 (2001).

Development of a time-frequency representation for acoustic detection of buried objects

Vincent Valeau,[a] James Sabatier,[b] R. Daniel Costley,[c] and Ning Xiang[d]
National Center for Physical Acoustics, Coliseum Drive, The University of Mississippi, University, Mississippi 38677

(Received 13 September 2002; revised 6 August 2004; accepted 6 August 2004)

A recently developed apparatus permits the detection of buried objects, such as landmines, by remotely sensing the variations of ground vibration that occur over the buried object with a laser Doppler vibrometer (LDV), when the ground is insonified by means of acoustic-to-seismic coupling. As it is currently implemented, the LDV scans individual points on the ground. The technique shows much promise, but it is slow when compared to some other techniques. This work demonstrates that mines can be detected as the LDV beam moves continuously across the ground, by using an optimal time-frequency representation of the LDV signals. This improvement has the potential to significantly increase scanning speeds. The vibrometer output signal is analyzed by means of time-frequency representations, which exhibit characteristic acoustic ''signatures'' when scanning over buried objects. The most efficient representation appears to be the smoothed spectrogram weighted by the time-frequency coherence function. It detects the searched signal energy enhancements while filtering out most features due to speckle noise. Detection is then efficiently achieved by searching simultaneous extrema of the marginals and moments of this representation. Experiments show that scanning speeds up to 3.6 km/h can be achieved for successful detection of buried landmines in outdoor ground. [DOI: 10.1121/1.1806824]

PACS numbers: 43.60.Qv, 43.60.Gk, 43.60.Rw [JCB] Pages: 2984–2995

I. INTRODUCTION

Over the last few years, a new acoustic technique to detect buried objects has been developed.[1] Its first application is the detection of landmines,[2–4] as landmines have proliferated in many of the world's conflicts. Current conventional detectors rely on detecting the metallic parts of landmines, causing many manufacturers to focus their efforts in building nonmetallic landmines. Therefore, there is a need for new techniques aimed at detecting nonmetallic objects. Among those, this new acoustic technique appears to be very successful in terms of detection probability and false alarm rate.[5]

This technique relies on the *acoustic-to-seismic* (A/S) coupling phenomenon. The physics of airborne sound penetrating into the ground has been well described.[6–10] Outdoor ground is a particulate material containing air-filled pores. It permits the coupling of energy from an airborne acoustic wave into waves propagating through both its frame and through the fluid contained in its pores. A buried object (sometimes referred to as ''target'' in this study) presents a different acoustic impedance to waves traveling through the ground because it lacks porosity. Recently, Donskoy[11] has shown that the acoustic compliance of a mine is much greater than that of the soil media. As a result, the buried object scatters the incident acoustic energy. This yields a local enhancement of the A/S coupled motion in the soil over a buried object that can be detected by measuring the ground surface vibration.

The first successful experiments using a laser Doppler vibrometer (LDV) to detect A/S coupled ground motion[12] led to the development of the actual landmine detector prototype, which has been proven efficient over the past several years.[2–4] Additionally, modeling[13–17] has shown the influence of buried objects on the A/S coupled surface vibration. In its current configuration, the landmine detection technique consists of first insonifying the ground by means of A/S coupling. A LDV remotely measures the ground vibration at discrete points along a virtual grid projected on the ground, with the laser beam going from one point to the next one. A map of ground vibration is constructed from the LDV measurements made over this grid and makes possible the detection of local variations of the vibration induced by buried objects. Because outdoor measurements are often conducted under hostile experimental conditions and because the roughness of natural ground causes the LDV signals to be corrupted with speckle noise, time averages have to be performed for each LDV measurement. Consequently, the time required for data acquisition can be incompatible with real applications.

To overcome this problem, the present study proposes to assess the feasibility of detecting buried objects by sweeping the laser beam across the ground. Spatial variations of ground vibrations along a straight line are then detected by

[a]Present address: LEPTAB, Pôle Sciences et Technologies, Av. M. Crépeau, La Rochelle Cedex 17042, France. Electronic mail: vvaleau@univ-lr.fr
[b]Electronic mail: sabatier@olemiss.edu
[c]Present address: Miltec Research & Technology, Inc., Oxford Enterprise Center, 9 Industrial Park, Oxford, MS 38655. Electronic mail: dcostley@miltecresearch.com
[d]Present address: School of Architecture and Department of Electrical, Computer, and System Engineering, Rensselaer Polytechnic Institute, Troy, NY 12180. Electronic mail: xiangn@rpi.edu

means of a single continuously scanning LDV measurement similar to the method used by Khan *et al.*[18] The first advantage of this technique is an important decrease in scan-time since the laser beam does not have to stop at each grid point. Moreover, the landmine detector can be mounted on a moving vehicle, for use in road demining missions. A system that scans continuously is better suited for such applications.

Performing suitable and efficient processing of the LDV signal is then compulsory, and the main contribution of this paper concerns this problem. The signal to be analyzed is a superposition of sine waves with time-varying amplitudes and phases, corrupted by many optical noise artifacts. Its representation in the time-frequency plane exhibits characteristic features accounting for energy increases when scanning above a target, referred to in the following as a ''mine signature.'' A mine signature can thus be detected by using time-frequency representations.[19] Time-frequency is a ''natural'' approach to this problem as the time variable is immediately interpretable as a spatial position and frequency contains the clues for target presence. Adaptations of the classical spectrograms[20] are then achieved in order to detect the typical changes of signal spectral content that are associated with the presence of a target. In the case of high scanning speed, the rarely used notion of time-frequency coherence appears to be of great practical interest to filter out nonacoustic contributions in this application.

Section II presents the acoustic detection technique. The proposed sweeping LDV scanning is then described in Sec. III. Section IV discusses the signal processing tools needed to process the LDV signals; it starts from the well-known spectrogram and presents how an efficient tool can be developed from it, given the physical phenomena that must be detected. Section V is a synthesis of the results and system performances achieved in this study in terms of scanning speed, target depth, and ground nature.

II. ACOUSTIC DETECTION OF BURIED OBJECTS

A. Physical background

When airborne sound is present on the surface of a soil, air contained within the connected pores in the soil is caused to oscillate in and out of the pores. In this way, the energy from the vibrating air above the soil surface couples with the air in the soil pores. This process is both dependent on the frequency of the sound waves and on the properties of the soil. Hence, the penetration of the sound waves is strong if the air permeability is high; conversely, low air permeability leads to weak coupling between vibrations of air above the surface and air in the pores.[8] Through momentum transfer at the air–soil boundary and viscous friction at the pore walls, some energy is also transferred to the soil frame. This transfer of energy can be successfully described by Biot's model.[7,9]

The Biot equations of motion include two compressional wave solutions that propagate simultaneously in both fluid and solid and have different propagation constants.[6] The waves are referred to as the waves of the first and second kind, or simply as ''fast'' and ''slow'' waves. The fast wave is relatively unattenuated, nondispersive, and most of the wave's energy is contained in the matrix displacement. Conversely, the slow wave is highly attenuated with depth and very dispersive and most of the energy is in the fluid. The key aspect of the physics of air-filled solids as used in the acoustic technology for mine detection is that air-borne sound is preferentially coupled into the soil through the slow wave, as was shown experimentally in Ref. 10. Although most of the energy of the slow wave is contained in the fluid displacement, it can be observed by sensing the matrix displacement or velocity. This can be achieved, for example, by measuring the vibrational velocity of the surface.

The speed of this slow wave is much slower than the sound speed in air, so the slow wave is refracted towards the normal. It seems then highly plausible that it scatters from targets buried in soils (or even from inhomogeneities of soil properties) and reflects back to the surface, which locally increases the vibrational velocity of the surface. Kargl[21] modeled the scattering of the slow wave with sea mines buried in sediment. Recent works[13,14] aim at modeling the physics of scattering from buried objects in air-filled porous materials, but it is clearly observed experimentally by sensing the surface velocity of a soil acoustically excited by A/S coupling.[1]

B. Experimental setup

Soil is acoustically excited with two loudspeakers generating airborne sound waves directed towards the ground at sound pressure levels of about 100 dB, C-weighted. The resulting A/S-coupled vibration is remotely estimated by using a LDV (PSV 200 manufactured Polytec P I, Inc.). The LDV emits a laser beam onto the vibrating surface of the ground area under test. The surface vibration causes a Doppler shift of the reflected light, which is sensed by a photo detector. The output of the photo detector is a frequency-modulated signal whose modulating signal is the vibrating surface velocity. After demodulation, the obtained signal is a voltage proportional to the instantaneous velocity of the point where the laser beam strikes the ground.

A set of LDV measurements is carried out at discrete points of a virtual grid projected onto the surface. Typically, the grid contains 16×16 points, evenly spaced over a square meter. In such an arrangement, the spatial resolution is approximately 6 cm. This spatial resolution can be adjusted as a function of the expected size of the buried object. In the usual configuration, the excitation signal is a pseudo-random noise covering a frequency range between 80 and 300 Hz. Experience has shown that this band contains frequencies for which buried objects present are most visible. The measured vibrational velocity is collected, Fourier-transformed, and averaged in the complex frequency domain. More details about the detection and the associated processing may be found in Ref. 1 or 3. An image is constructed showing the mean ground velocity amplitude within a given frequency band. The presence of a mine is indicated by an area of local velocity enhancement in this frequency band. Figure 1, taken from Ref. 2, shows an example: a VS 2.2 plastic mine is buried at a depth of 7.5 cm. In Fig. 1(a) the color dots show the 16×16 LDV measurement locations with integrated velocity values in the frequency band between 130 and 160 Hz

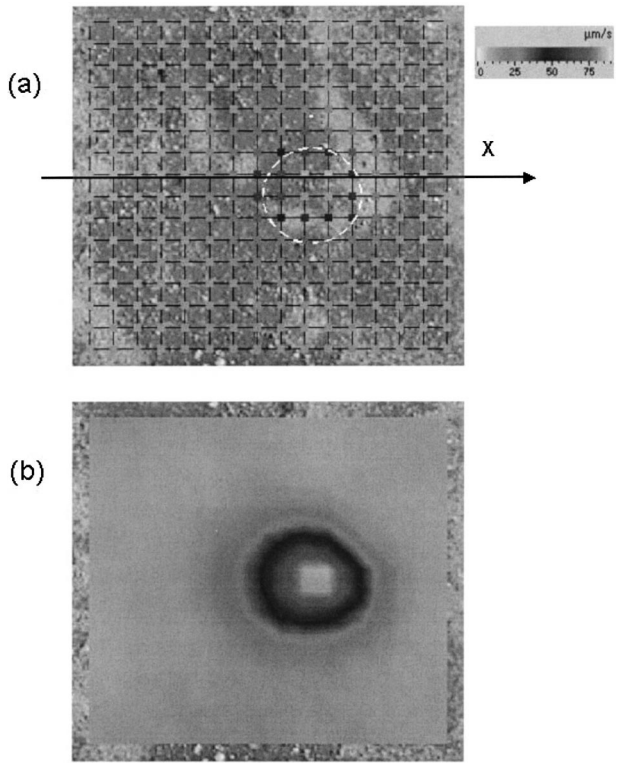

FIG. 1. Ground velocity measurement for a VS 2.2 plastic mine buried at 7-cm depth (from Ref. 1). Velocity is integrated in the frequency band [130,160] Hz. (a) Color dots showing the LDV measurement locations (color scale is provided). (b) Color map after interpolation and spatial filtering.

(color scale is given). In Fig. 1(b) a color map is derived from Fig. 1(a) after interpolation and spatial filtering. The presence of the buried mine is clearly visible in this example. The grid covers an area of one square meter.

As mentioned in Sec. I, outdoor conditions and natural ground roughness greatly increase the noise level. It is then that the processing of LDV signals with bad signal-to-noise ratios can be critical. A single-point measurement requires the laser beam to be kept still as the signals are collected so that averages can be computed and the velocity spectrum estimated. The required time for the laser beam to be kept at the same point strongly depends on experimental conditions such as ground surface, wind, etc. After completion the laser beam is moved to the next point. Scanning along a 1-m-long line can take from about 20 s to more than a minute, and scanning a whole square meter can take up to 20 min. This procedure gives excellent results in terms of detection probability and false alarm rate,[1] but its main drawback is that it is time-consuming and the time required for data acquisition is not compatible with real applications.

III. CONTINUOUSLY SCANNING LDV

A. Principle

In order to reduce the time required for detection, the possibility of using a continuously scanning LDV has been investigated. This is achieved by sweeping the laser beam over the ground with a constant velocity. In other words, the ground velocity variations are measured by means of a single ''sweeping'' measurement along a straight line parallel to an axis $\vec{x}$, as plotted in Fig. 1(a). For this last example (see Sec. II), the velocity map of a square meter can then be obtained by sweeping the laser beam along 16 parallel lines instead of 16×16 measurements with the grid method. This new procedure is a good candidate to be integrated in future configurations, as the whole apparatus will be mounted on a vehicle moving at a steady speed. Hence, the applicability of this continuous LDV scan and the subsequent signal processing are of great importance for the integration of this landmine detection technique in real applications.

The experiment, which was performed in order to assess the feasibility of such an approach, is sketched in Fig. 2. A mirror, whose position is controlled with a function generator, drives the laser beam position. Hence, it is assumed that the position of the impact of the laser beam on the ground is proportional to the control signal. In this study, LDV scans are carried out along 1-m-long lines. A buried object is located under the trajectory of the beam. In order to repeat the experience several times, the laser beam is swept back and forth over the mine; the beam position is thus controlled by a

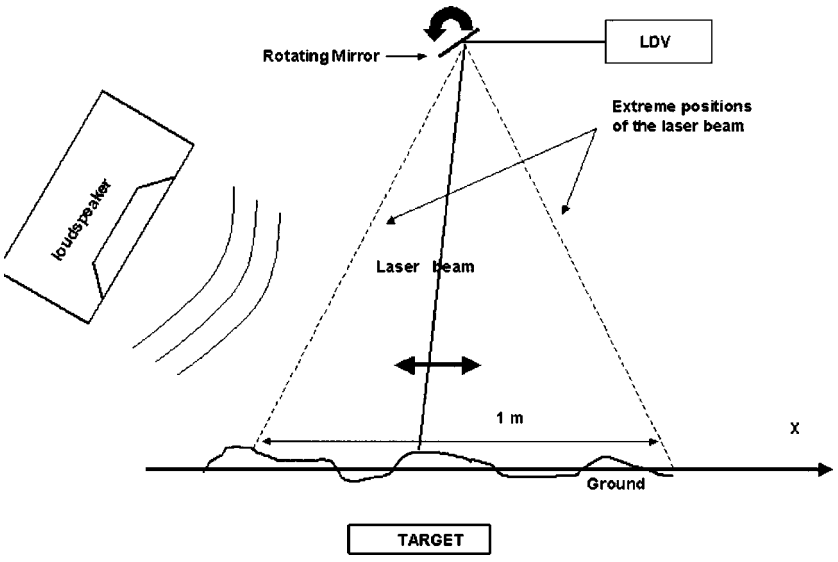

FIG. 2. Sketch of the sweeping LDV scan experiment.

saw-tooth signal, whose frequency will be referred to as the ''sweep rate.'' This back-and-forth sweeping scan gives some indication about the repeatability of the detection. The sweep rate is proportional to the velocity of the laser beam position on the ground: as the swept distance in one period is usually 2 m, a sweep rate of 0.1 Hz corresponds to a laser beam speed (or ''scanning speed'') of 0.2 m/s, or 720 m/h.

The airborne acoustic waves which couple into the ground are generated by loud speakers: the sound pressure level is 100 dBC in the vicinity of the scanned area. The acoustic excitation is a superposition of single frequency sine waves, whose number is usually four in the presented results. These frequencies are located in the low-frequency range 80–300 Hz, which is the range for which scattering of sound waves by buried objects is most visible. Former experiments showed that this frequency range is mostly dependent upon the resonance of the target free air acoustical admittance (i.e., the ratio of the velocity of the target top plate over the incident acoustic pressure). It seems to be independent of the target size and mostly controlled by the mechanical properties that contribute to the target's acoustical compliance.

Because of A/S coupling, the measured ground vibration is a superimposition of the generated airborne sine waves. Above a target, the measurement signal exhibits not only an increase in amplitude at these frequencies, but also phase changes. Therefore, changes in signal energy and phase at these frequencies as the laser beam sweeps the ground indicates the presence of a buried object. Some nonlinearities such as those observed by Donskoy[11] have also been observed, but their levels are generally 40 dB below the linear frequency components. Hence the nonlinear components levels are much nearer to the velocity noise floor of current LDV devices and are not expected to influence the measurements presented in this study.

In all the experiments reported here, the buried object was a cylindrical anti-tank (AT) mine with a diameter of about 30 cm. Experiments to determine whether smaller objects can be detected with this technique, such as antipersonal mines (with diameters smaller than 10 cm), are presently in progress. All experiments have been implemented outdoors in dirt roads, gravel roads, and natural ground (i.e., a lane of natural loess soil). All of the mines were buried at least one year before these measurements were made. The signal processing methods will be evaluated for different situations, and the influence of the following parameters is studied: most importantly the speed of the laser beam, but also the type of ground and its surface, and the object depth.

B. Measurement noise

In recent studies, spatially continuous LDV scans have been used in different applications for analyzing vibrating structures in order to detect damage[18] or to measure vibrational mode shapes.[22] The detection of temporal changes in signal characteristics was not of interest, as in this study. Moreover, the context of the present study is very different as measurements are performed outdoors on ''real'' grounds,

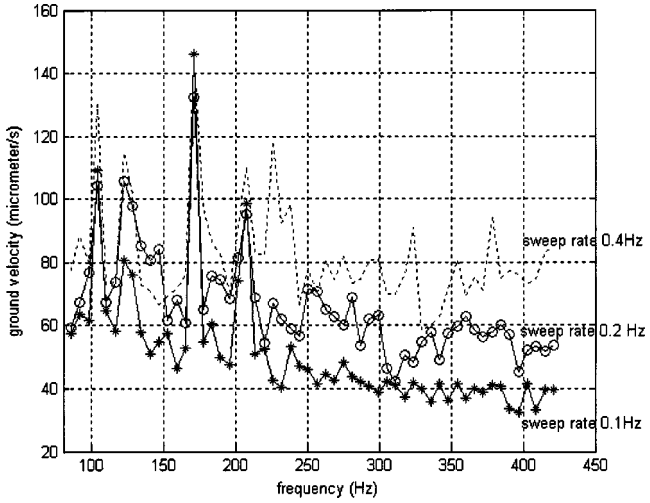

FIG. 3. Power density spectrum of the measured vibrational velocity over a buried object (landmine) for different sweep rates: 0.1 Hz (plain line with stars), 0.2 Hz (plain line with circles), and 0.4 Hz (dotted line). Excitation frequencies are 105, 125, 170, and 205 Hz.

away from the well-controlled environment of a laboratory. These uncompromising conditions imply that noise will be an important limiting factor.

Indeed, the type of optical noise, known as ''speckle noise,''[23] is critical in this study. Light back-scattered from the ground is composed of a population of wavelets with random relative phases called ''speckles.'' When the ground surface is rough the population of speckles contributing to the reflected light changes with time, causing random phase changes, or speckle noise, in the photo detector output. Rougher ground corresponds to higher speckle noise levels. The problems increase when the laser beam is swept over the surface: when the speed of the beam over the ground increases, the speckle population changes faster, and the speckle noise level increases. Because of speckle noise, there is a limit in the sweep rate (or scanning speed) above which detection is impossible because the noise level is too high. Other sources of noise are photo detector shot-noise and vibrations of the LDV platform (due to wind, for instance). Platform vibrations will result in an apparent velocity not related to the ground motion, introducing spurious information. However, these noise sources are likely to be minor compared to speckle noise. In this study all noise sources are assumed to be additive components of the photo detector output (i.e., the measured vibrational velocity).

LDV measurement noise can be clearly observed by considering Fig. 3. The laser beam has been swept back and forth over a mine buried at 5-cm depth in the loess soil which has been acoustically excited via A/S coupling. The excitation frequencies were 105, 125, 170, and 205 Hz. The resulting ground velocity amplitude at these frequencies is of the order of a hundred μm/s, which is similar to other measurements.[2] The power density spectrum (PDS) of the output velocity has been computed for sweep rates of 0.1, 0.2, and 0.4 Hz, and 200 estimates of the PDS have been frequency averaged to achieve this measurement. The four single frequencies are fairly visible for all sweep rates, but the noise floor level increases substantially with the scanning

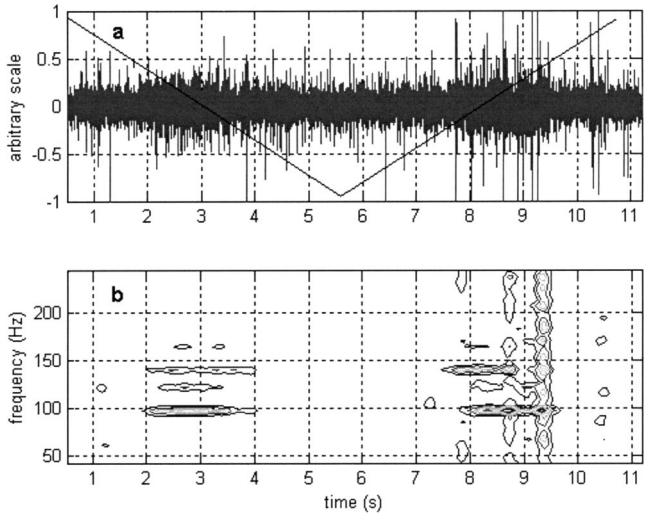

FIG. 4. LDV output signal for scanning over a SIM30 type mine buried in a dirt road (5 cm depth) at scanning speed 0.2 m/s. (a) Temporal signal in which 1 m was scanned in 5 s. (b) Contour plot of smoothed spectrogram. The mine signature appears around $t=3$ and 8.5 s.

speed, which characterizes speckle noise. For a sweep rate of 0.8 Hz, the single tones are not discernable anymore; the output signal consists mainly of speckle noise.

An example of the temporal representation of an output signal is represented in Fig. 4(a), in which a laser beam is scanned over a SIM30 type mine (diameter 30 cm) buried at about 5-cm depth in a dirt road. The signal is plotted over one return trip of the laser beam above the mine. The signal driving the position of the laser is also plotted. The associated sweep rate is 0.1 Hz (scanning speed 0.2 m/s); hence, a 1-m distance is scanned in 5 s. An increase of the vibration amplitude is observed for each pass of the laser beam over the mine (about $t=3$ and 8.5 s). Many bursts are also noticeable and their presence is recurrent in collected data. These bursts will be referred to in the following as burst noise. They are the consequences of sudden occurrence of speckle dropout.[23]

IV. DEVELOPMENT OF A TIME-FREQUENCY REPRESENTATION

A. Need for time-frequency analysis

The acoustic excitation is a superposition of single-frequency sine waves (see Sec. III A) whose frequencies are noted as f_i. Hence the instantaneous velocity of the ground surface is a sum of four sine waves. In order to detect the presence of a target, it is intended to estimate the variation of the spectral density of this velocity along a straight line (axis $\vec{x}$, see Fig. 1). $v(x,t)$ is the two-variable function describing the ground velocity at position x and time t:

$$v(x,t)=\sum_{q=1}^{N} A_q(x)\cos(2\pi f_q t+\varphi_q(x)). \tag{1}$$

$A_q(x)$ and $\varphi_q(x)$ are respectively the amplitude and phase of the vibrational velocity at position x and frequency f_q. The spatial variations $A_q(x)$ along the x-axis permit the detection of the presence of buried objects. These functions can have many forms, but it is generally observed that a buried object induces a local maximum of $A_q(x)$, which permits its detection.[1] The aim is to estimate the functions $A_q(x)$ in a single sweeping LDV measurement along the axis x. The sweeping velocity in m/s of the laser is noted as λ. At time t, the laser beam is scanning the ground at velocity $v(x=\lambda t,t)$. Hence, by sweeping the laser beam over the ground, a signal $s(t)$ is obtained which is, after demodulation,

$$s(t)=\sum_{q=1}^{N} A_q(t)\cos(2\pi f_q t+\varphi_q(t))+b(t),$$
$$\text{with } t=x/\lambda. \tag{2}$$

Noise $b(t)$ is an additive noise (see Sec. III B). The spatial velocity variations $A_q(x)$ can be simply retrieved from the amplitude modulations functions $A_q(t)$ by the rescaling operation $x=\lambda t$.

$\hat{s}(t)$ is now constructed from the real-valued $s(t)$ and its Hilbert transform[20] as the imaginary part to obtain the so-called analytic function. We assume that $A_q(x=\lambda t)$ is a slowly varying function compared to $\cos(2\pi f_q t+\varphi_q(x=\lambda t))$, which is achieved, for objects of the size of AT mines, for sweeping velocities λ of less than 20 m/s. This corresponds to a maximum sweep rate of 10 Hz. Under this condition, the frequency content of the amplitude modulation functions $A_q(t)$ are located at sufficiently low frequencies so as not to spill over the domain containing the frequencies f_q. If this is achieved, the Hilbert transform $H[s(t)]$ gives exactly the imaginary part of the analytical signal $\hat{s}(t)$ of $s(t)$,[24] which yields

$$\hat{s}(t)=s(t)+jH[s(t)]=\sum_{q=1}^{N} A_q(t)e^{j\varphi_q(t)}e^{j2\pi f_q t}+\hat{b}(t), \tag{3}$$

where $\hat{b}(t)$ represents the complex version of noise $b(t)$. The term $A_q(t)e^{j\varphi_q(t)}$ is the time-varying complex envelope for the component at frequency f_q for the deterministic part of signal $\hat{s}(t)$. $A_q(t)$ is called the instantaneous amplitude of the single tone f_q component. It is exactly the amplitude of the vibrational velocity component at frequency f_q and at position $x=\lambda t$. The signal $\hat{s}(t)$ is strongly nonstationary due to amplitude modulation and violent noise fluctuations, due essentially to burst noise. Time-frequency analysis techniques are signal-processing tools, which are widely used to analyze nonstationary signals. Hence, in order to estimate the ''time-varying'' spectrum of the signal $\hat{s}(t)$, we wish to have a complex time-frequency representation $S(t,f)$ which would be ideally a

$$S(t,f)=\sum_{q=1}^{4} A_q(t)e^{j\varphi_q(t)}\delta(f-f_q)+B(t,f), \tag{4}$$

with $B(t,f)$ being a time-frequency representation of the noise measurement $b(t)$. Ultimately, the idea is to retrieve, for the excitation frequency f_q, the spatial variations $A_q(x)$ and $\varphi_q(x)$ of the velocity amplitude and phase, respectively, from the modulus and phase angle of $S(t,f_q)$ in the exposed time-frequency representations.

The next part deals with how to generate efficient time-frequency representations for detecting the spatial variations

$A_q(x)$. The question of detecting and using optimally local phase variations $\varphi_q(t)$ is addressed in Secs. IV C and IV D. Section IV E provides tools for a simple automation of the detection from the signal time-frequency representation.

B. Use of smoothed spectrograms

The most popular estimator of ''time-varying'' spectrum is the short-time Fourier transform (STFT). Let us first define the STFT of signal $s(t)$ in the discrete time domain[20,25]

$$\mathrm{STFT}_N^s(t_i,f_i)=\frac{1}{\sqrt{2N+1}}\sum_{\tau=-N}^{N}\hat{s}(\tau)h_N(\tau-t_i)e^{-j2\pi f_i\tau}, \tag{5}$$

in which t_i and f_i are discrete time and frequency, τ is a discrete lag variable, and h_N is the short-time window, whose length is $(2N+1)$. This relation describes the discrete Fourier transform of a portion of signal $\hat{s}$, centered on instant t_i. The window length $(2N+1)$ has to be short enough so that local properties of signal $\hat{s}(t)$ do not change ''too much'' within this duration. It means that the variations of the complex envelope $A_q(t)e^{j\varphi_q(t)}$ have to remain stationary enough along the window length. Meanwhile, the frequency spread of each peak, linked to the time-frequency spread obtainable with the STFT in terms of uncertainty,[20] must remain small enough so that each frequency peak stays distinct from the other peaks in the time-frequency plane. The spectrogram is defined as the squared modulus of the STFT:

$$\mathrm{SP}_N^s(t_i,f_i)=|\mathrm{STFT}_N^s(t_i,f_i)|^2. \tag{6}$$

For analyzing noisy signals, the spectrogram can give high variance estimates of the time-varying spectrum. In order to improve variance estimates, averages may be used. For this purpose, $(2M+1)$ calculations of $\mathrm{SP}_N^s(t_i+\eta\times K,f_i)$, taken at instants $(t_i+\eta\times\mathrm{K})$ around instant t_i, are used to perform an averaged estimation of $\mathrm{SP}_N^s(t_i,f_i)$. The subsequent ''locally averaged'' version of the spectrogram is called the smoothed spectrogram. The smoothed spectrogram used in this study is adapted from the one proposed by Martin and Flandrin[25] and can be written

$$\mathrm{SP}_{N,M}^s(t_i,f_i)=\sum_{\eta=-\infty}^{\infty}g_M(\eta)\mathrm{SP}_N^s(t_i+\eta\times\mathrm{K},f_i). \tag{7}$$

This estimator of the time-varying spectrum is used in this study to get an estimation of the variation of the ground surface velocity amplitude. As an example, a contour plot of the smoothed spectrogram of the signal presented in Fig. 4(a) (see Sec. III B, a SIM30 mine buried in a dirt road) is presented in Fig. 4(b). Time is on the horizontal axis and frequency is on the vertical axis. The ground is acoustically excited at frequencies 95, 120, 145, and 170 Hz. The energy at those frequencies is clearly enhanced when the scanning beam passes above the mine, as the scattering of the acoustic wave by the target locally leads to an increase of the ground surface velocity. This set of horizontal features associated with the passage of the laser beam over a mine is the ''mine signature'' allowing its detection. It is also noticed that during the second passage of the beam over the mine, some vertical features appear. These features are the time-frequency representations of burst noise: they are wide-band and usually have a short duration. Burst noise is troublesome because it can mask the mine signature or, for some longer bursts, can be interpreted as an ambiguous signature. It is also interesting to notice that the occurrence of burst noise is not repeatable; the laser beam passes twice over the mine, but burst noise occurs only once.

When using smoothed spectrograms, a proper adjusting of the windows h_N and g_M and of the increment K is necessary and crucial. The window h_N is 4096 points long ($N=4096$), which, at a sampling frequency of 25 kHz, allows a frequency resolution of 6 Hz. Window g_M smoothes the data in the frequency domain. Both windows h_N and g_M are rectangular windows in the presented results. For calculating the smoothed spectrogram at time t_i, 20 averages are performed (i.e., $M=20$). The critical parameter is the increment K, which determines the amount of smoothing: it sets up the time length over which the smoothing is achieved (i.e., $2MK$), a duration that will be referred as the smoothing length in the following. Introducing the parameter K allows for an adjustment of the smoothing length while keeping constant the computational load (M constant). An equivalent spatial smoothing length is also defined, and is equal to $(2MK\lambda/f_s)$, where λ is the speed of the scanning beam and f_s is the sampling frequency (25 kHz in this paper).

Figure 5 illustrates the influence of the smoothing length. A VS-1.6 mine (diameter 24 cm) is buried at 5-cm depth in the loess soil. The soil is excited at frequencies of 105, 125, 170, and 205 Hz. The laser beam scans above the mine about instant $t=6.2$ s, and moves at scanning speed 0.4 m/s (sweep rate 0.2 Hz). The spatial smoothing length is set to 1 cm (top, $K=15$), 16 cm (middle, $K=250$), and 64 cm (bottom, $K=1000$). On the right, the contour plots of the smoothed spectrograms (the equivalent spatial scale is on the top of the graphs) are depicted, and for a better visualization of the smoothing effect, the corresponding three-dimensional representation is plotted on the left. The mine signature appears about instant $t=6$ s, and the equivalent size of the signature is about 20 cm, which reasonably approaches the mine size. An additional feature appears around instant $t=7$ s at the higher frequencies, and is supposedly due to local variations of the soil acoustical properties. This kind of event is referred as ''clutter,'' and can be mixed with a mine signature, although here its apparent size (about 10 mm) is much less than the size of the searched object.

It is noticed that a smoothing length of 16 cm (middle) gives better results than a 1 cm length (top), as noise is substantially filtered out. In more hostile cases (i.e., for higher scanning speeds), a smoothing length of the order of a few cm does not allow the mine to be detected, while the mine is detected for smoothing lengths between 15 and 25 cm. On the other hand, a smoothing length that is too large (bottom) results in a loss of resolution power of the ground velocity variations: here the effect is the loss of the mine signature, as it mixes with clutter. Therefore, a tradeoff is necessary between variance reduction and the detection of refined velocity variations. Practically, a smoothing length ranging from $D/2$ and D gives best results, D being the equivalent diameter of the searched object.

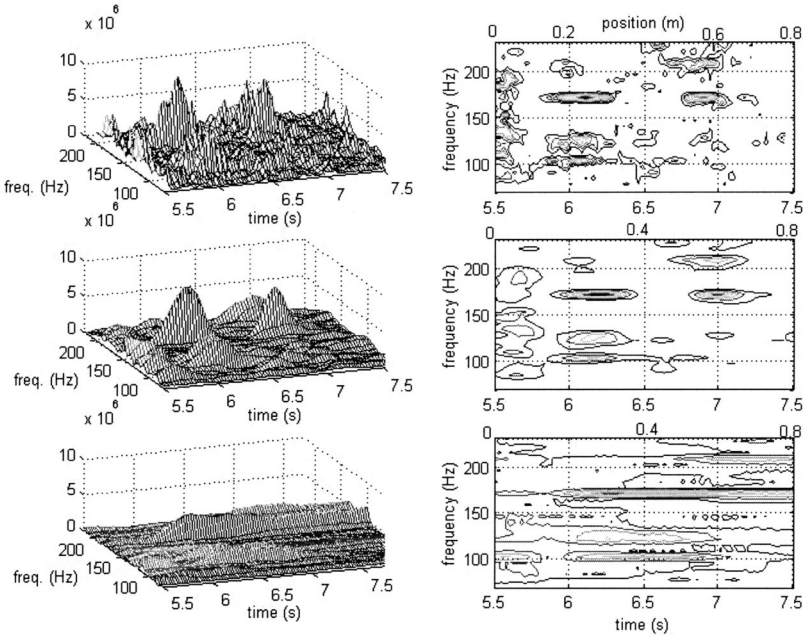

FIG. 5. Scan of a mine of diameter 24 cm buried at 5-cm depth in loess soil (scanning speed 0.4 m/s). Smoothed spectrograms are represented in three dimensions (left) and in contour plots (right). For contour plots, spatial position (m) is on the top horizontal scale and time (s) on the bottom horizontal scale. Influence of the smoothing length on the spectrogram: 1 cm (top), 16 cm (middle), and 64 cm (bottom).

Let us emphasize here that in the results presented, the spatial resolution has been set to about 2.5 cm. This spatial resolution is set by the choice of the increment $[t_{i+1}-t_i]=\Delta_t$ and corresponds to $\lambda\Delta_t$: it is the distance between two consecutive estimation points. The resolution power for the estimation of the spatial velocity variations is a function of both the spatial resolution and the smoothing length.

C. Use of phase information: The time-frequency coherence

As proposed in Eq. (4), we wish to find a complex representation of the signal, which would estimate both variations of amplitude $A_q(x)$ and phase $\varphi_q(x)$ of the ground acoustic velocity. The estimation of $A_q(x)$ was the concern of the last section. For obtaining the phase, a reference signal is required. In this study, the reference signal $r(t)$ is the excitation signal sent to the loudspeakers: this signal provides the phase reference, being the sum of single-tones with constant amplitudes and phases. Conversely, the analyzed signal $s(t)$ is a sum of single tones with time-varying amplitudes and phases. In order to obtain the evolution of the phase $\varphi_q(t)$, one has to evaluate the complex cross-spectrum between $r(t)$ and $s(t)$. In fact, due to the nonstationary nature of $s(t)$, this cross-spectrum is a time-varying cross-spectrum. Hence, the following estimator is proposed to obtain a time-frequency representation of this time-varying cross-spectrum, noted $CSP^{s,r}_{N,M}(t_i,f_i)$:

$$\mathrm{CSP}^{s,r}_{N,M}(t_i,f_i)=\sum_{\eta=-\infty}^{\infty} g_M(\eta)\mathrm{STFT}^{s}_{N}(t_i+\eta\times\mathrm{K},f_i)^* \times \mathrm{STFT}^{r}_{N}(t_i+\eta\times\mathrm{K},f_i), \quad (8)$$

where * denotes the complex conjugate. This estimator is a direct extension to the cross-spectrum of the estimator of the smoothed spectrogram written in Eq. (7). The phase variations $\varphi_q(t_i)$ at discrete time t_i and acoustic excitation frequency f_q are estimated directly from the phase of this time-varying cross-spectrum estimator:

$$\varphi_q(t_i)=\mathrm{Arg}[\mathrm{CSP}^{s,r}_{N,M}(t_i,f_q)], \quad (9)$$

where function Arg[...] denotes the phase angle of a complex quantity. From Eq. (8), it is also possible to propose an estimator of the time-varying coherence (or ''time-frequency coherence'') that we may write as

$$C^{s,r}_{N,M}(t_i,f_i)=\frac{|\mathrm{CSP}^{s,r}_{N,M}(t_i,f_i)|^2}{\mathrm{SP}^{s}_{N,M}(t_i,f_i)\mathrm{SP}^{r}_{N,M}(t_i,f_i)} \quad (10)$$

A theoretical approach to the notions of time-frequency cross-spectrum and time-frequency coherence may be found in Ref. 26. Although those quantities were mathematically derived and justified, very few practical applications[27] have been carried out with the time-frequency coherence so far. In practice the calculation of this coherence function requires the simultaneous acquisition of both the input signal of the sound source $r(t)$ and the LDV output signal $s(t)$.

In order to estimate the spatial variations of the ground velocity phase, the phase angle of the time-varying cross-spectrum is calculated. It is then possible to observe, for a given excitation frequency f_q, the temporal (or equivalently spatial) evolution of the ground velocity phase as the beam scans over a buried object. An example is shown in Fig. 6. It considers the same signal as in Fig. 4 resulting from the detection of a mine buried in a dirt road. At the lowest acoustic excitation frequency $f_1=95$ Hz, the squared amplitude estimate $A_1(t)^2$ (i.e., smoothed spectrogram at frequency f_1), phase estimate $\varphi_1(t)$ (from the phase angle of the cross-spectrum at f_1), and coherence time-variations $C^{s,r}_{N,M}(t_i,f_1)$ are considered. They are respectively depicted in Figs. 6(a)–(c). In Fig. 6(a), the two ''bumps'' of the velocity amplitude around instant 3 and 8.5 s are the consequence of scanning over the target. In Fig. 6(b), we notice that those local enhancements of the velocity energy $A_1(t)^2$ coincide with a local stabilization of the corresponding phase $\varphi_1(t)$. In other

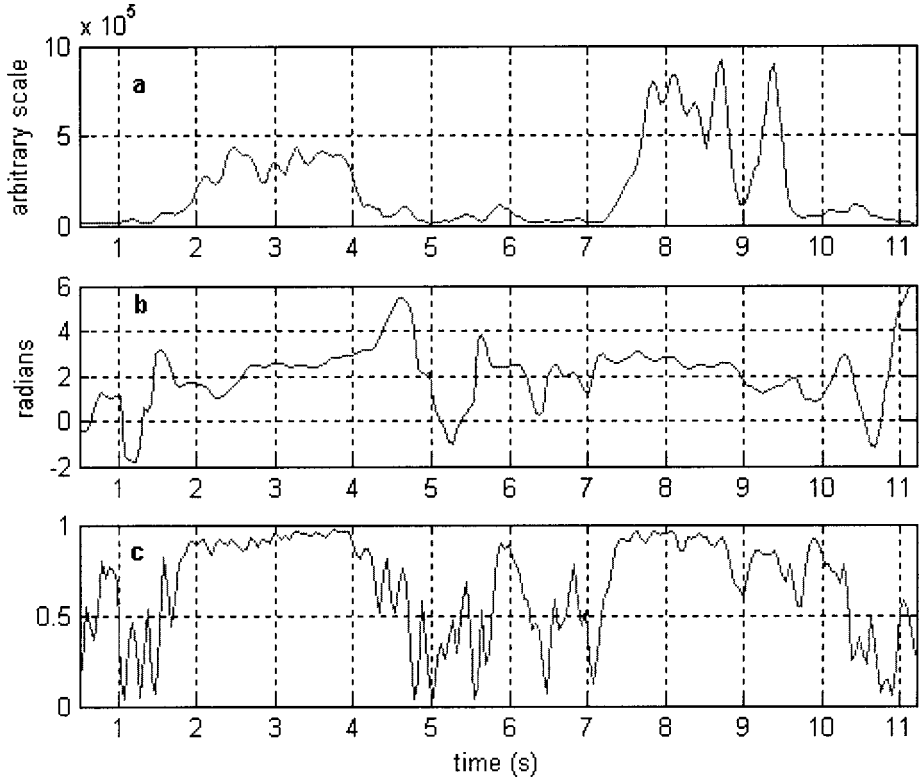

FIG. 6. Same scan as Fig. 4. (a) Smoothed spectrogram represented at frequency $f_1 = 95$ Hz. (b) Angle phase of the time varying cross-spectrum at frequency f_1. (c) Time-frequency coherence represented at frequency f_1.

words, when the beam scans off-target locations, the estimated velocity phase varies rapidly with time (or position), but this phase remains quite steady over the buried objects. This phenomenon is very characteristic, and the spatial stability of phase is a good clue for detecting the presence of a mine. Now, the coherence is a good indicator of the stability in time of the phase of a single tone, and this justifies its use, as demonstrated in Fig. 6(c). Coherence at frequency f_1 is close to one when scanning over the mine and drops down when scanning off-mine.

D. Coherence-weighted spectrogram

Another characteristic example can be found in Fig. 7. A scan (sweep rate 0.1 Hz, scanning speed 0.2 m/s) is made over a mine buried in the loess soil at 5 cm depth, and the smoothed spectrogram is represented in Fig. 7(a). Some wide-band features appear also, for example, around instants 9.3 and 10.5 s, and are the consequence of burst noise. As in Fig. 6, the quantities $A_3(t)^2$, $\varphi_3(t)$, and $C^{s,r}_{N,M}(t_i, f_3)$ are plotted for frequency $f_3 = 145$ Hz in Figs. 7(b), (c), and (d), respectively. In Fig. 7(b), it can be seen that noise burst enhances the estimated velocity more than the mine itself: a burst of noise could then be mixed with a mine if considering only the spectrogram at one frequency and not in the whole time-frequency plane, where mine signature has a very characteristic shape. Now, as noticed in the former example, the mine locally stabilizes the velocity phase, as anywhere else, and, especially when burst noise occurs, the phase varies randomly [Fig. 7(c)]. This results in a very low coherence when scanning outside of the mine vicinity [Fig. 7(d)]. As burst noise results in bumps of the estimated velocity energy but also in a low coherence, it is suggested that an efficient time-frequency representation of the signal may be the coherence-weighted spectrogram that may be defined as

$$\mathrm{CWSP}^{s,r}_{N,M}(t_i, f_i) = \mathrm{SP}^{s}_{N,M}(t_i, f_i) \times C^{s,r}_{N,M}(t_i, f_i). \qquad (11)$$

This coherence-weighted spectrogram is plotted in Fig. 7(e). As a result, the mine signature appears with an enhanced contrast, but the artifacts due to burst noise are mostly removed.

Another example may be found in Fig. 8. The same scan as Fig. 4 (dirt road) is repeated at a higher sweep rate of 0.3 Hz (scanning speed around 2.2 km/h). In 10 s, the laser beam comes back and forth three times over the target. The smoothed spectrogram, time-frequency coherence, and coherence-weighted spectrogram are plotted respectively in Figs. 8(a)–(c). Mine signatures hardly appear in the spectrogram, as speckle noise causes a bad signal-to-noise ratio. The time-frequency coherence does not show the mine signature, because the contrast of coherence between off- and on-target locations is weak. On the other hand, the coherence-weighted spectrogram allows for detection each time the beam passes over the mine, and appears as a successful tool for analyzing the data. Interestingly, about time 2.3 s, the mine signature occurs at the same time as a violent burst noise, which results in masking the signature. One could think that such portions of the signal, corresponding to violent burst noise, consist essentially in noise and do not carry any acoustic information, but this is probably wrong as the mine signature is reconstituted after coherence-weighting. The coherence-weighting is basically a sort of filtering which acts at all frequencies. It removes contributions that are of an optical nature, more especially burst noise, and leaves in the spectrogram most of the energy which is induced from acoustic effect.

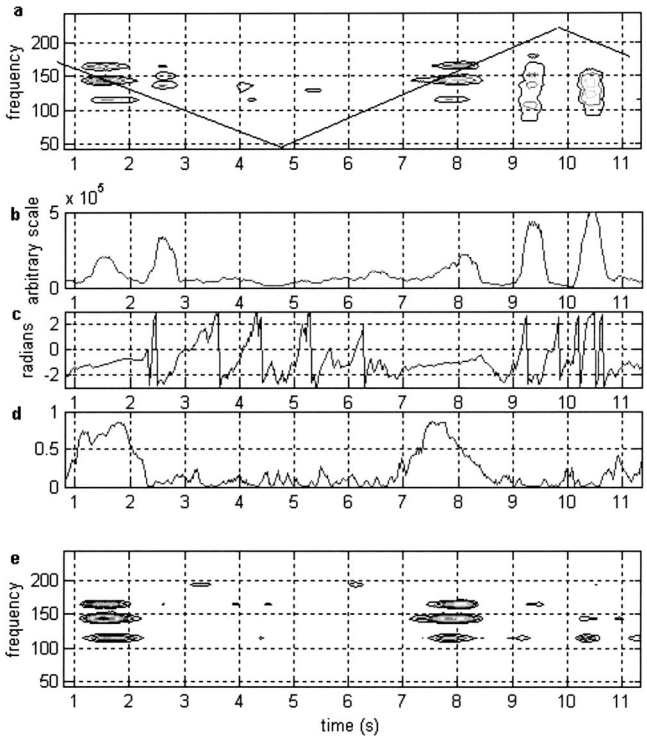

FIG. 7. Scan of a mine buried at 5 cm depth in loess soil (scanning speed 0.2 m/s). (a) Contour plot of smoothed spectrogram. (b) Smoothed spectrogram represented at frequency $f_3 = 145$ Hz. (c) Angle phase of the time varying cross-spectrum at frequency f_3. (d) Time-frequency coherence represented at frequency f_3. (e) Contour plot of coherence-weighted spectrogram.

One can conclude that the spectrogram takes exclusively into account variations of instantaneous amplitude of each single tone. Time-frequency coherence is mostly governed by phase stability but is less sensitive to an increase of energy; hence it does not appear as a representation with enough contrast of the signal to deliver "good" mine signatures. As for the coherence-weighted spectrogram, it combines both advantages of spectrogram and coherence, as it allows, in a single representation, to take into account both

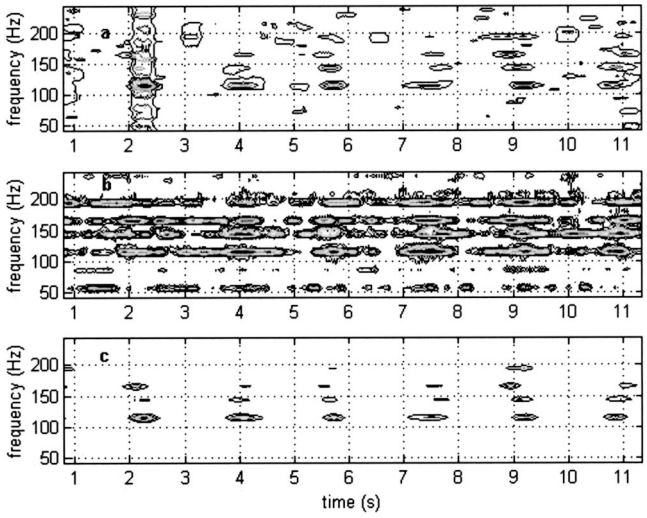

FIG. 8. Same scan as Fig. 5 but scanning speed 0.6 m/s (about 2.2 km/h). Contour plots of (a) smoothed spectrogram, (b) time-frequency coherence, and (c) Coherence-weighted spectrogram.

local increase of velocity amplitude and local stability of velocity phase. So far, the coherence-weighted spectrogram is the time-frequency representation that reconstitutes the mine signatures with the best quality in terms of shape and contrast.

It can be seen that an event in the time-frequency plane has to be considered under shape-based criteria to be validated as a mine signature. Now, in order to make an easier automation of mine detection, one can consider the marginal and moments of the representation: they provide one-variable functions (time functions) that can be more manageable than the time-frequency representation itself.

E. Use of marginal and moments

Let $D^s(t,f)$ be a real and positive time-frequency representation of the signal $s(t)$. The time marginal of this distribution is obtained by integrating the distribution over frequency for a given time:

$$P(t) = \int D^s(t,f) 2\pi \, df. \tag{12}$$

The quantity $P(t)$ provides an estimation of the instantaneous energy of the signal, i.e., $\Sigma_{q=1}^{N} A_q^2(t)$, although it does not give an exact estimate if the distribution is a spectogram.[20] The instantaneous energy estimate is of great practical interest as it provides, for position $x = \lambda t$, an estimation of the amount of energy contained in the ground surface velocity. This quantity should be at the maximum when the beam scans over a buried object.

The local frequency $\langle f \rangle_t$ is the average frequency of the distribution for a given time *t*, or first conditional moment of the distribution:

$$\langle f \rangle_t = \frac{1}{P(t)} \int f D^s(t,f) df. \tag{13}$$

This quantity is often called instantaneous frequency signal. In this case, as the signal is a sum of several single tones components, this notion is not of straightforward physical interpretation, but the first conditional moment is used in the calculation of the function

$$\sigma^2(t) = \frac{1}{P(t)} \int (f - \langle f \rangle_t)^2 D^s(t,f) df. \tag{14}$$

This quantity provides an estimation of the instantaneous bandwidth: it represents the local spread in frequency for a given time *t*, and it will be seen in the following that this quantity, coupled with the instantaneous energy estimate, provides a robust clue for detecting the presence of a buried object. In this study, these two quantities are calculated from the coherence-weighted spectrogram.

Figure 9 provides an example of the use of the estimates of instantaneous energy and bandwidth. The same buried mine as in Fig. 4 is scanned again, but at a sweep rate of 0.48 Hz (about 3.6 km/h scanning speed). The vertical bold solid lines indicate the approximate instants for the passages of the beam over the target (about every second). The spectrogram and coherence-weighted spectrograms are plotted in Figs. 9(a) and (b). As expected, most of noncoherent signal struc-

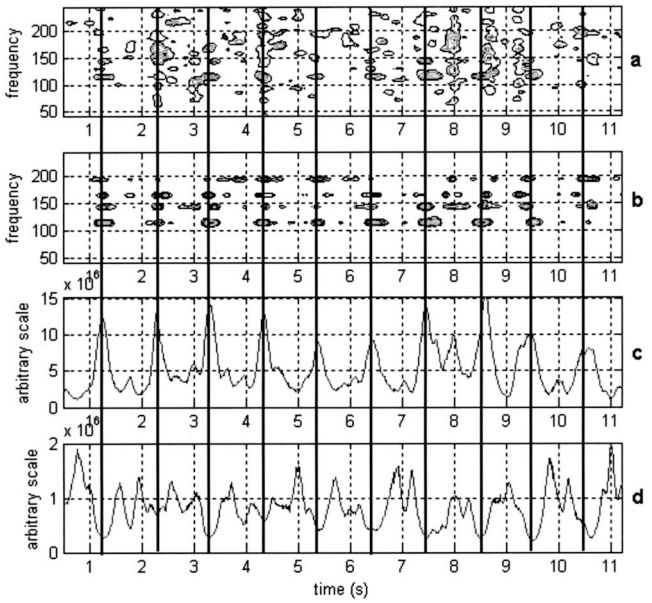

FIG. 9. Same scan as Fig. 4 but scanning speed about 1 m/s (3.6 km/h). Vertical bold lines show the approximate times for passages over buried mine. (a) Contour plot of smoothed spectrogram. (b) Contour plot of coherence-weighted spectrogram. (c) Time marginal of the coherence-weighted spectrogram. (d) First conditional moment of the coherence-weighted spectrogram.

tures are removed by coherence-weighting the spectrogram. Although the mine signature appears clearly most of the time, some signatures are somewhat ambiguous. The time marginal (or instantaneous energy estimate) and first conditional moment (or instantaneous bandwidth estimate) are plotted respectively in Figs. 9(c) and (d). The instantaneous energy very clearly increases each time the laser beam passes over the target, and successfully detects the local increase of velocity energy above the target. It is also very noticeable that those maxima of energy are associated with minima of the instantaneous bandwidth. The instantaneous bandwidth is difficult to interpret in the case of multi-component signals; however, it is noticed most of the time that the surface velocity bandwidth is lower on-target than off-target. This might be explained by the fact that the energy is mostly contained in the excitation frequency band when on-target, as off-target the signal is a more wide-band because the part of energy contained by wide-band noise is relatively more important. Hence, the simultaneous occurrence of energy maxima and bandwidth minima is able to validate the mine signature as the ambiguous features around $t=10.5$ s. Another example is the representation content in the time interval (7–9 s), which is somewhat ''messy.'' The criteria based on energy and bandwidth permits the validation of mine signatures as the features around time $t=7.5$ s and $t=8.5$ s, and an artifact around $t=8$ s, which is locally more wide-band (no bandwidth minimum), that shall be rejected. On the other hand, the frequency bandwidth minimum does not appear clearly when the beam scans above the target about $t=2.5$ and 4.5 s. The characteristic shape of the time-frequency signature is then useful to identify a mine signature.

In conclusion, a simple method for automatic recognition of the mine signature is the detection of the simultaneous occurrence of time marginal maxima and first conditional moment minima of the coherence-weighted spectrogram. For ambiguous cases, a more complicated shape-based criteria aiming at recognizing a signature in the time-frequency plane may lead to a final decision about mine presence.

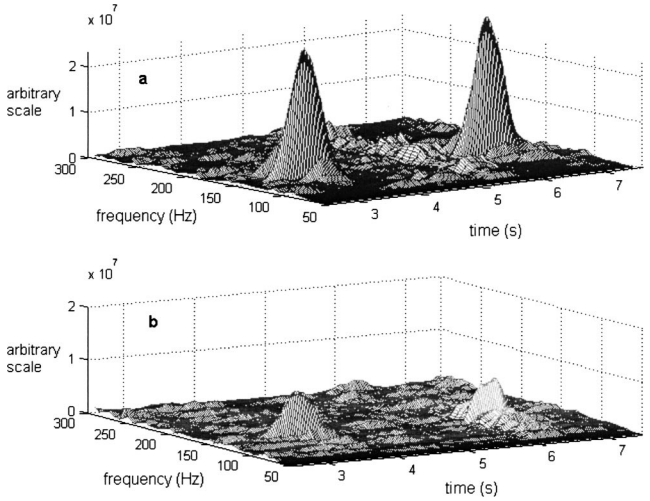

FIG. 10. Three-dimensional plots of the smoothed spectrogram for scan over M19 mine buried in a gravel road. Influence of depth: (a) 5 cm and (b) 12.5 cm.

V. PERFORMANCES AND LIMITATIONS OF THE METHOD

In order to assess the performance of the sweeping scan procedure for acoustic detection of landmines, measurements have been carried out on different types of grounds: a dirt road, a gravel road, and a lane of natural loess soil. Mines were buried at 5-cm depth, except for a set of experiments where the depth was 12.5 cm. The mine was always detected with sweep rates of 0.2 Hz and lower, which corresponds to a scanning speed of 1.4 km/h. Detection depends on the ground nature, the mine depth, and the ground surface nature.

Detection is easier in roads than in loess soil, as the acoustical properties of the soil are more variable in natural ground. Those variations can accompany zones of higher vibrational velocity, or so-called clutter, and can be interpreted as a buried object when scanning the ground only in one dimension (see Sec. IV B). This clutter can be recognized by constructing a two-dimensional image of the ground velocity, which can be achieved by scanning the ground with several parallel beams. When scanning grounds such as gravel or dirt roads, mines were detected with sweep rates up to 0.4 Hz (2.8 km/h) for mines buried at 5-cm depth. Detection can be achieved at even higher speeds in more favorable conditions (see Fig. 9 with a detection at 3.6 km/h scanning speed). For measurements over a deep mine (12.5 cm), the detection was not regularly achieved for speeds higher than 1.4 km/h. Indeed, the scattering of acoustic waves by buried objects gets weaker when the buried object is deeper. Hence, the contrast of velocity amplitude between off and on-target locations is weaker for deep mines than shallow mines. This is very clearly shown in Fig. 10. Two mines of the same type (M19)

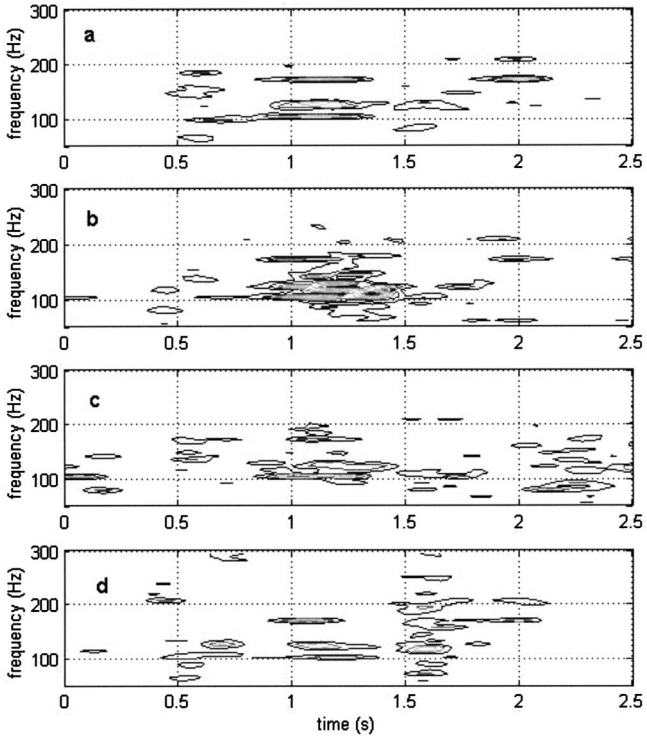

FIG. 11. Smoothed spectrogram for VS1.6 mine buried at 5-cm depth in loess soil (2.8 km/h scanning speed). Influence of objects on the laser path: (a) none, (b) thick patch of grass above the mine, (c) thin layer of grass scattered all along the path, and (d) 5-cm-diam stone beside the mine.

were buried in the same gravel road, at depths of 5 and 12.5 cm. The laser beam moved back and forth over the location of the mine, and the spectrogram of the signal is given for the shallow (a) and deep (b) mines, for a scanning speed of 2.8 km/h. The peak energy is higher for the shallow mine than for the deep mine, which confirms that the contrast between on- and off-target locations is diminished when the depth is increased, making the detection more difficult.

The detection technique has been tested on various types of surfaces, including gravel roads, dirt roads, and natural soil. Even for a very rough surface such as a gravel road, mines can be reliably detected. This is remarkable as rough surfaces provide strong speckle noise at high scanning speeds (see, for example, Fig. 10 showing a scanning over a gravel road at 2.8 km/h scanning speed). A set of measurements investigating the influence of diverse elements on the surface has been carried out over a mine (VS16 type) buried at 5 cm depth in loess soil. Those elements were a thick and a thin layer of loose grass; a patch of grass just above the mine; and some pebbles or a big stone placed on the laser path. Figure 11 represents the smoothed spectrograms of the measured signals prior to coherence-filtering, in order to observe the effects of those objects placed on the laser beam path. Figure 11(a) shows the mine's acoustic signature at 2.8 km/h scanning speed. Figure 11(b) shows the spectrogram obtained after a thick patch of grass (dimension are about a fourth of the object size) was placed above the mine; the components of the mine signature do not appear distinctly because of a broadband speckle noise burst due to the grass. In Fig. 11(c), a thin layer of grass is scattered all along the laser path. In Fig. 11(d), a big stone (about 5 cm in diameter) was placed about 10 cm beside the mine (about $t = 1.6$ s for spectrogram). The stone produced a burst of speckle noise in the spectrogram. In all cases, after applying some coherence-filtering to the spectrograms of Fig. 11, the mine signature is reconstituted and most speckle artifacts are removed. In these experiments, only a thick layer of loose grass was able to prevent the detection.

VI. CONCLUSIONS

The study presented in this paper is concerned with the processing of the signal coming from a recently developed acoustic detector. This apparatus detects buried objects, such as landmines, by remotely sensing the variations of ground vibration that occur over a buried object with a LDV, when the ground is insonified by means of acoustic-to-seismic coupling. It is demonstrated in this paper that it is possible, with suitable signal processing, to detect landmines buried outdoors by using a continuous LDV scan. This step is vital in the development of the detector, for future integration to a moving vehicle, and for reaching scanning speeds compatible with real applications.

Time-frequency representations of collected signals deliver the characteristic ''signatures'' that permit the detection of temporal changes of energy and phase occurring when the laser beam scans over a buried object. Indeed, the spectrum temporal variations contain the clues for detection, and time is directly interpretable in terms of spatial position. Energy enhancements are detected using smoothed spectrograms with adequate smoothing length. Experimental data show that vibration phase is relatively stable over buried objects and unsteady elsewhere. Thus time-frequency coherence exhibits maxima when scanning over objects; it also filters out efficiently most speckle noise contributions. Finally, the coherence-weighted spectrogram appears to deliver the most contrasted signature by fusing together the searched clues in terms of energy and phase variations. Moreover, the time marginal and first conditional moment of this representation provides one-variable functions whose extrema indicate efficiently the presence of a mine, and thus make possible a quite simple automation of the detection process.

In the tests performed in this study, detection is systematically achieved in natural ground and roads for mines buried at 5-cm depth at 2.8 km/h scanning speeds. This speed can reach 3.6 km/h in favorable conditions, and has to be decreased to 1.4 km/h for deep mines (12.5 cm depth).

At this time, a new detector is being developed consisting of multiple parallel LDV beams that scan simultaneously. A two-dimensional vibration map, similar to that in Fig. 1, will then be constructed from a single sweeping measurement, by using the signal processing method presented in this paper.

ACKNOWLEDGMENTS

This work is supported by the U.S. Army Communications-Electronics Command, Night Vision and Electronics Sensors Directorate. The authors thank Ronald Craig for his dedication and expertise in collecting the data for this paper. Any opinions, findings and conclusions, or

recommendations expressed in this paper are those of the authors and do not necessarily reflect the views of U.S. Army Communications-Electronics Command.

[1] J. M. Sabatier and K. E. Gilbert, ''Method for detecting buried object by measuring seismic vibrations induced by acoustical coupling with a remote source of sound,'' U.S. patent, No. 6,081,481 (2000).

[2] J. Sabatier and N. Xiang, ''An investigation of acoustic-to-seismic coupling to detect buried anti-tank landmines,'' IEEE Trans. Geosci. Remote Sens. **39**, 1146–1154 (2001).

[3] J. Sabatier and N. Xiang, ''Laser-Doppler based acoustic-to-seismic detection of buried mines,'' Proc. SPIE **3710**, 215–222 (1999).

[4] N. Xiang and J. Sabatier, ''An experimental study on anti-personnel landmines detection using acoustic-to-seismic coupling,'' J. Acoust. Soc. Am. **113**, 1333–1341 (2003).

[5] E. M. Rosen, K. D. Sherbondy, and J. M. Sabatier, ''Performance assessment of a blind test using the University of Mississippi's acoustic/seismic laser Doppler vibrometer (LDV) Mine Detection Apparatus at A. P. Hill,'' in Proc. SPIE Conference on *Detection and Remediation Technologies for Mines and Minelike Targets V*, edited by A. C. Dubey *et al.* (2000), pp. 656–666.

[6] M. A. Biot, ''Theory of propagation of elastic waves in a fluid saturated porous solid. II. Higher frequency range,'' J. Acoust. Soc. Am. **28**, 179–191 (1956).

[7] J. M. Sabatier, H. E. Bass, L. N. Bolen, K. Attenborough, and V. V. S. S. Sastry, ''The interaction of airborne sound with the porous ground. The theoretical formulation,'' J. Acoust. Soc. Am. **79**, 1345–1352 (1986).

[8] K. Attenborough, J. M. Sabatier, H. E. Bass, and L. N. Bolen, ''The acoustic transfer function at the surface of a layered poroelastic soil,'' J. Acoust. Soc. Am. **79**, 1353–1358 (1986).

[9] J. M. Sabatier, H. E. Bass, L. N. Bolen, and K. Attenborough, ''Acoustically induced seismic waves,'' J. Acoust. Soc. Am. **80**, 646–649 (1986).

[10] C. J. Hickey and J. M. Sabatier, ''Measurements of two types of dilatational waves in an air-filled unconsolidated sand,'' J. Acoust. Soc. Am. **102**, 128–136 (1997).

[11] D. Donskoy, A. Ekimov, N. Sedunov, and M. Tsionskiy, ''Nonlinear seismo-acoustic land mine detection and discrimination,'' J. Acoust. Soc. Am. **111**, 2705–2714 (2002).

[12] W. P. Arnott and J. Sabatier, ''Laser-Doppler vibrometer measurements of acoustic to seismic coupling,'' Appl. Acoust. **30**, 279–291 (1990).

[13] S. Taherzadeh, ''A hybrid numerical model to predict the effect of buried objects on the acoustic-to-seismic coupling on ground surfaces,'' J. Acoust. Soc. Am. **109**, 2287 (2001).

[14] D. Velea, R. Waxler, J. M. Sabatier, and C. J. Hickey, ''Acoustic scattering by a buried object with a compliant top in a rigid porous material,'' J. Acoust. Soc. Am. **109**, 2287 (2001).

[15] D. L. Berry, S. N. Chandler-Wilde, and K. Attenborough, ''Acoustic scattering by a near surface obstacle in a rigid porous medium,'' J. Sound Vib. **170**, 161–179 (1994).

[16] J. M. Sabatier, D. Velea, N. Xiang, and R. Waxler, ''Resonant frequency response and surface particle velocity profiles for buried land mines: Theory and Experiment,'' J. Acoust. Soc. Am. **111**, 2419 (2002).

[17] D. Velea, R. Waxler, and J. M. Sabatier, ''A fast effective fluid model for the scattering of normally incident sound off of a buried landmine,'' J. Acoust. Soc. Am. **111**, 2420 (2002).

[18] A. Z. Khan, A. B. Stanbridge, and D. J. Ewins, ''Detecting damage in vibrating structures with a scanning LDV,'' Opt. Lasers Eng. **32(6)**, 583–592 (1999).

[19] V. Valeau, J. Sabatier, and N. Xiang, ''Application of time-frequency analysis to landmine detection using a laser Dopper vibrometer,'' J. Acoust. Soc. Am. **107**, 2829 (2000).

[20] L. Cohen, *Time-frequency Analysis* (Prentice-Hall, Englewoods Cliffs, NJ, 1995).

[21] S. G. Kargl and R. Lim, ''A transition-matrix formulation of scattering in homogeneous, saturated, porous media,'' J. Acoust. Soc. Am. **94**, 1527–1550 (1993).

[22] A. B. Stanbridge and D. J. Ewins, ''Modal testing using impact excitation and a scanning laser Doppler vibrometer,'' Shock Vib. **7(2)**, 91–100 (2000).

[23] C. B. Scruby and L. E. Drain, *Laser Ultrasonics: Techniques and Applications* (Hilger, Bristol, 1990), Chap. 3.

[24] B. Boashash, ''Estimating and interpreting the instantaneous frequency of a signal-Part 1: Fundamentals,'' Proc. SPIE **80(4)**, 520–538 (1992).

[25] W. Martin and P. Flandrin, ''Wigner-Ville spectral analysis of nonstationary processes,'' IEEE Trans. Acoust., Speech, Signal Process. **33(6)**, 1461–1470 (1985).

[26] L. B. White and B. Boashash, ''Cross-spectral analysis of nonstationary processes,'' IEEE Trans. Inf. Theory **36(2)**, 830–835 (1990).

[27] E. G. Lovett and K. M. Ropella, ''Time-frequency coherence analysis of atrial fibrillation termination during procainamide administration,'' Ann. Biomed. Eng. **25(6)**, 975–984 (1997).

Constructing a cochlear transducer function from the summating potential using a low-frequency bias tone

Chul-Hee Choi[a)]
Bobby R. Alford Department of Otorhinolaryngology and Communicative Sciences, Baylor College of Medicine, Houston, Texas 77030

Mark E. Chertoff and Lin Bian
Department of Hearing and Speech, University of Kansas Medical Center, Kansas City, Kansas 66160

David Lerner
Department of Mathematics, University of Kansas, Lawrence, Kansas 66045

(Received 14 April 2004; revised 19 July 2004; accepted 19 July 2004)

A new method is developed to construct a cochlear transducer function using modulation of the summating potential (SP), a dc component of the electrical response of the cochlea to a sinusoid. It is mathematically shown that the magnitude of the SP is determined by the even-order terms of the power series representing a nonlinear function. The relationship between the SP magnitudes and the second derivative of the transducer function was determined by using a low-frequency bias tone to position a high-frequency probe tone at different places along the cochlear transducer function. Two probe tones (6 kHz and 12 kHz) ranging from 70 to 90 dB SPL and a 25-Hz bias tone at 130 dB SPL were simultaneously presented. Electric responses from the cochlea were recorded by an electrode placed at the round window to obtain the SP magnitudes. The experimental results from eight animals demonstrated that the SP magnitudes as a function of bias levels are essentially proportional to the second derivative of a sigmoidal Boltzmann function. This suggests that the low-frequency modulated SP amplitude can be used to construct a cochlear transducer function. © *2004 Acoustical Society of America.* [DOI: 10.1121/1.1791722]

PACS numbers: 43.64.Bt, 43.64.Ld, 43.64.Nf, 43.64.Ri [BLM] Pages: 2996–3007

I. INTRODUCTION

Hair cells are the sites where mechano-electric transduction (MET) takes place in the cochlea. MET is a nonlinear process in which acoustic signals are converted into electrical signals through deflection of hair-cell stereocilia Howard and Hudspeth, 1988; Hudspeth, 1982). Deflection of the stereocilia towards the tallest stereocilia opens hair-cell transducer channels allowing K^+ ions to enter the cell, resulting in depolarization. Deflection in the opposite direction closes transducer channels decreasing the hair-cell receptor potentials and leads to hyperpolarization. Cochlear MET shows an asymmetrical sigmoidal curve that has been described by several mathematical functions such as a second-order Boltzmann function relating transducer conductance to hair bundle displacement (Crawford *et al.*, 1989) and a hyperbolic-tangent function relating hair-cell receptor potential to angular displacement of stereocilia (Weiss and Leong, 1985).

The characteristics of cochlear MET *in vivo* can be obtained from the cochlear microphonic (CM), a far-field potential produced primarily by the spatial summation of outer hair-cell (OHC) receptor currents, recorded at the round window (RW) in response to Gaussian noise (Choi *et al.*, 2002; Bian and Chertoff, 2001, 1998; Chertoff *et al.*, 1997, 1996), pure tones (Patuzzi *et al.*, 1989; Patuzzi, 1987; Dallos, 1985; Dallos *et al.*, 1972), or tones biased by a low-frequency tone (Nieder and Nieder, 1971, 1968a, 1968b). Recently, a cochlear transducer function (f_{Tr}) was derived from distortion product otoacoustic emissions (DPOAEs) originating from the nonlinear transduction processes in the OHCs (Bian *et al.*, 2002, 2004).

Another possible way to construct a cochlear f_{Tr} is to use the summating potential (SP), a dc component in the electrical response of the cochlea generated from both IHCs (inner hair cells) and OHCs (Durrant *et al.*, 1998; Harvey and Steel, 1992; Cody and Russell, 1985; Russell and Sellick, 1983; Johnstone and Johnstone, 1966; Davis *et al.*, 1958). This possibility was described first by Cheatham and Dallos (1997), who suggested that dc changes of the cochlear response are related to the second derivative of the f_{Tr}. If this relationship is true, the SP can be used to estimate the cochlear transducer function. Deriving a cochlear f_{Tr} from the SP may be useful in evaluating cochlear function under certain pathologic conditions because the SP is less sensitive to vector summation than the CM (Whitfield and Ross, 1965) and still present even with hearing loss, unlike DPOAEs (Klis and Smoorenburg, 1988, 1985). Moreover, because the SP may be dominated by IHC receptor currents, it may reflect the IHC transducer (Durrant *et al.*, 1998), whereas other physiologic signals used to construct a cochlear transducer function (i.e., CM and DPOAE) are generated from the OHCs. Therefore, the first goal of this study was to develop a theory for constructing a cochlear transducer function from the SP. The second goal was to construct a cochlear transducer function from the SP data obtained from physiological

a)Electronic mail: cchoi@bcm.tmc.edu

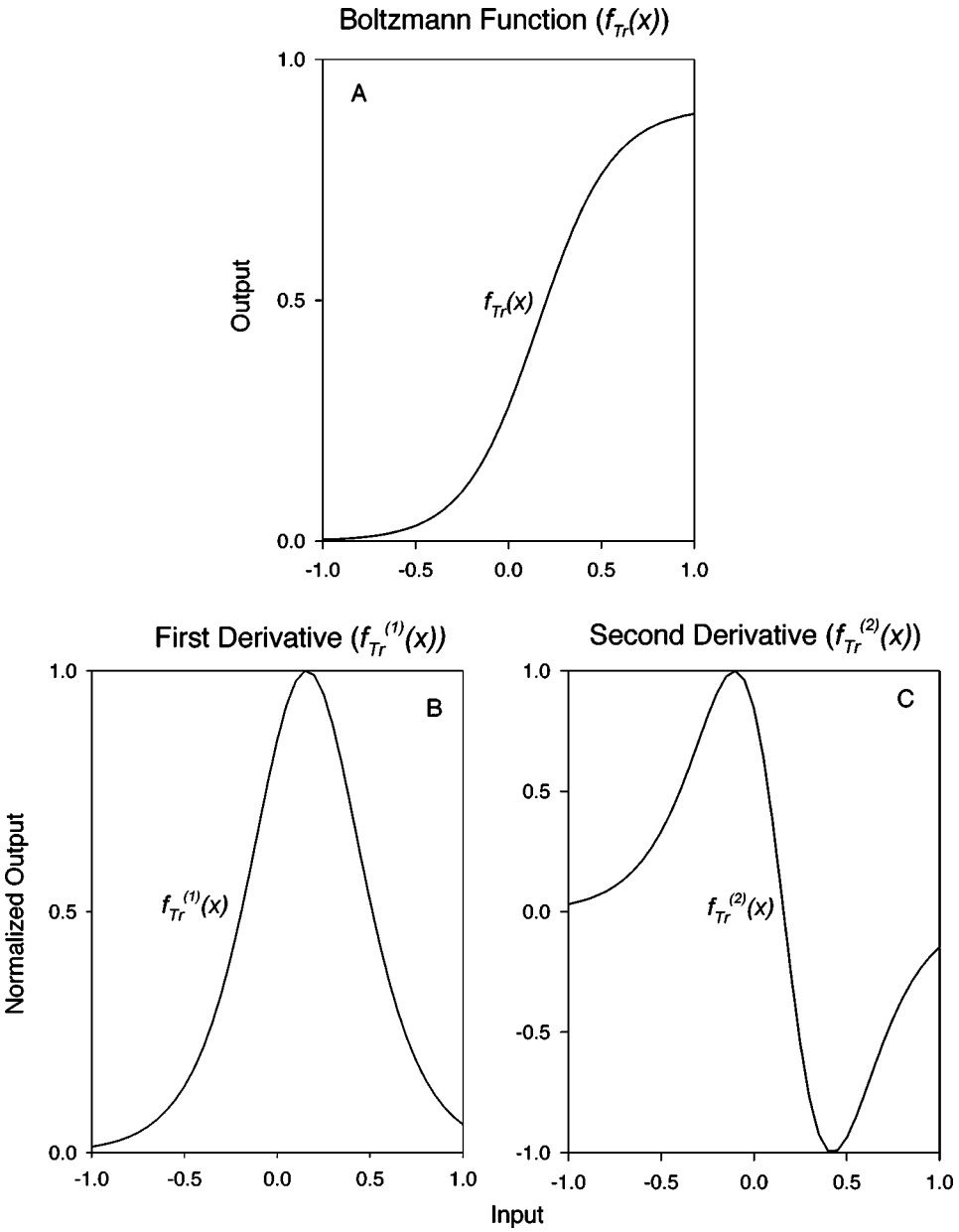

FIG. 1. A second-order Boltzmann function [panel (A)] representing a cochlear transducer function [f_{Tr}] and its first and second derivatives [panels (B) and (C)]. The parameter values used to calculate the Boltzmann function is 0.88 for A, -5 for b, -0.8 for c, 0.07 for d, and 8 for e.

experiments and examine the effects of signal manipulation.

A. Theory for deriving a cochlear transducer function

The cochlear f_{Tr} is assumed to be represented by a second-order Boltzmann function of the general form (Hudspeth, 1982)

$$f_{\mathrm{Tr}}(x)=\frac{A}{1+e^{(bx-c)}[1+e^{(dx-e)}]}, \tag{1}$$

where $f_{\mathrm{Tr}}(x)$ is the hair-cell receptor current, x is the displacement of the stereocilia, A is the maximal conductance, the constants b and d are related to the slope of f_{Tr} or the sensitivity of the transduction process, and c and e are constants related to the resting position of the stereocilia. Panels (A), (B), and (C) of Fig. 1 illustrate such a function and its first two derivatives. Our purpose in this section is to show how the dc component of the response from the f_{Tr} is related to the second derivative of the unknown transducer function using a probe tone of low amplitude at high frequency and a low-frequency bias tone.

We first expand the transducer function in a Taylor series about an arbitrary point x_0

$$f_{\mathrm{Tr}}(x)=\sum_{n=0}^{\infty} a_n(x_0)(x-x_0)^n, \tag{2}$$

where $a_n(x_0)=f_{\mathrm{Tr}}^{(n)}(x_0)/n!$ and $f_{\mathrm{Tr}}^{(n)}$ is the nth derivative of f_{Tr} at x_0. We regard x_0 as an operating point and consider the effect of placing a probe tone $x_p=L\cos(\theta)$ at x_0. For clarity of exposition, we have suppressed the sinusoidal time dependence of both x_0 and x_p. Thus, the total input has the form $x=x_0+x_p$, and

$$f_{\mathrm{Tr}}(x)=f_{\mathrm{Tr}}(x_0)+\sum_{n=1}^{\infty} a_n(x_0)L^n\cos^n(\theta). \tag{3}$$

This can now be expanded in a Fourier series to obtain

$$f_{\mathrm{Tr}}(x) = f_{\mathrm{Tr}}(x_0) + B_0(x_0) + \sum_{n=1}^{\infty} B_n(x_0) L^n \cos(n\theta), \quad (4)$$

where

$$B_0(x_0) = \sum_{n=1}^{\infty} \frac{a_{2n}(x_0)}{2^{2n}} \binom{2n}{n} L^{2n} \quad (5)$$

involves only the even multiples of θ, where $\binom{2n}{n}$ are binomial coefficients.

To obtain the summating potential, the response to the bitonal stimuli can be low-pass filtered to remove all the harmonics of x_p, leaving the dc component $f_{\mathrm{Tr}}(x_0) + B_0(x_0)$. Since $f_{\mathrm{Tr}}(x_0)$ is just the response of the transducer to the bias tone, subtracting it yields the SP at x_0 in response to the probe tone

$$SP(x_0) = B_0(x_0) = \frac{1}{2} \frac{f_{\mathrm{Tr}}^{(2)}(x_0)}{2!} L^2 + \frac{3}{8} \frac{f_{\mathrm{Tr}}^{(4)}(x_0)}{4!} L^4 + \frac{5}{16} \frac{f_{\mathrm{Tr}}^{(6)}(x_0)}{6!} L^6 \ldots . \quad (6)$$

For small amplitudes L of the probe tone ($0 < L \leqslant 1$), only the first term of this series is significant, i.e.,

$$SP(x_0) \approx \frac{L^2}{4} \cdot f_{\mathrm{Tr}}^{(2)}(x_0). \quad (7)$$

In particular, the summating potential at x_0 is proportional to the second derivative of the transducer function at x_0.

This relation is illustrated by using Eq. (6) in a computer simulation to compare the contribution of the second derivative term to the SP relative to a total contribution of the first 20 terms of the series as L is varied from 70 dB SPL (0.06 Pa) to 120 dB SPL (20 Pa). As shown in Fig. 2 for higher probe tone levels ($L > 1.0$ Pa), the higher-order terms contribute more to the SP, while the contribution of the second-order term drastically decreases. However, at low probe tone levels, the magnitude of SP is essentially determined by the second-order term of the power series [Eqs. (5) and (6)].

B. Simulation

A computer simulation was done to explore the theoretical relationship between SP and $f_{\mathrm{Tr}}^{(2)}(x)$ and a practical method to construct the $f_{\mathrm{Tr}}(x)$ from the SP waveform obtained using one bias signal.

In this simulation, a bitonal stimulus consisting of a low-frequency bias tone (25 Hz) and a higher frequency probe tone (6000 Hz) was used. The level of the bias tone was -1 to $+1$ to represent the cochlear transducer functions within an operating range of ± 1 Pa (Dallos, 1986; Russell *et al.*, 1986). The level of the probe tone ranged from 0 to $+1$ in 16 steps. The bitonal stimulus and the bias tone alone were sent to the Boltzmann function of Eq. (1), respectively, and the corresponding results are shown in panels (A) and (B) of Fig. 3. The response of the bias tone alone was subtracted from that of the bitonal stimulus [panel (C) of Fig. 3] to eliminate the response to the bias tone in the bitonal case. The subtracted result was low-pass filtered at 500 Hz to preserve the modulated SP due to the variation of bias tone amplitude.

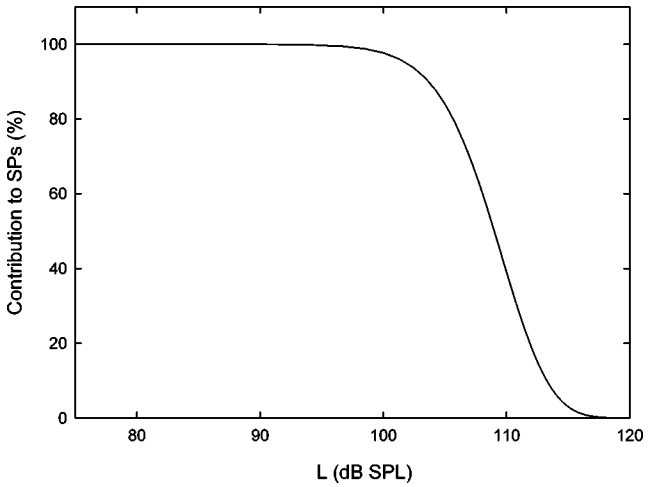

FIG. 2. Simulation: the contribution of the second derivative to the magnitude of the SP at different probe tone level ranging from 70 dB SPL (0.06 Pa) to 120 dB SPL (20 Pa). For probe tone level below 100 dB SPL (2 Pa), the second derivative is responsible for 100% of the magnitude of the SP computed from a total of 20 even-order terms. However, the contribution of the second derivative drastically decreases when the probe tone levels are above 100 dB SPL.

The SP waveform is indicated as solid line in panel (D) of Fig. 3. SPa and SPb of panel (D) correspond to SPa and SPb of panel (B), illustrating the SP during the positive and negative slope during one cycle of the bias tone. SPb [panel (D)] was flipped to overlap with SPa and averaged. The SP waveform was fitted to the actual $f_{\mathrm{Tr}}^{(2)}(x)$ using a curve-fitting method (SIGMAPLOT, version 8.0). The accuracy of the fitting was determined by the correlation coefficient (r^2) between SP and $f_{\mathrm{Tr}}^{(2)}(x)$. The r^2 between the SP and $f_{\mathrm{Tr}}^{(2)}(x)$ was approximately 1.0, suggesting that the SP magnitude was well matched in shape to the second derivative of the $f_{\mathrm{Tr}}(x)$. This means that the SP magnitude is essentially proportional to $f_{\mathrm{Tr}}^{(2)}(x)$.

The effect of the probe level on the accuracy of the fitting is investigated to test the approximation that as L approaches zero, the SP is proportional to $f_{\mathrm{Tr}}^{(2)}(x)$. Figure 4 indicates the correlation (r^2) between SP and $f_{\mathrm{Tr}}^{(2)}(x)$ as a function of the probe tone level. When the probe level decreased from 1 to 0.1, the r^2 increased asymptotically. At probe level below 0.3 Pa (84 dB SPL), the r^2 reaches nearly 1.0. The result of this simulation suggests that a cochlear transducer curve can be obtained from the SP.

II. METHODS

A. Animal preparation

Ten Mongolian gerbils weighing from 49 to 67 grams were used as experimental subjects. The experiment followed the guidelines of the Institutional Animal Care and Use Committee at the University of Kansas Medical Center.

The gerbils were initially anesthetized with pentobarbital (64 mg/kg) and subsequently maintained with 1/2 of the initial dose given every hour. The rectal temperature was monitored and maintained constant at 37 °C with a heating pad (Harvard). With the removal of the right pinna and the surrounding skin and muscle, the postauricular part of the

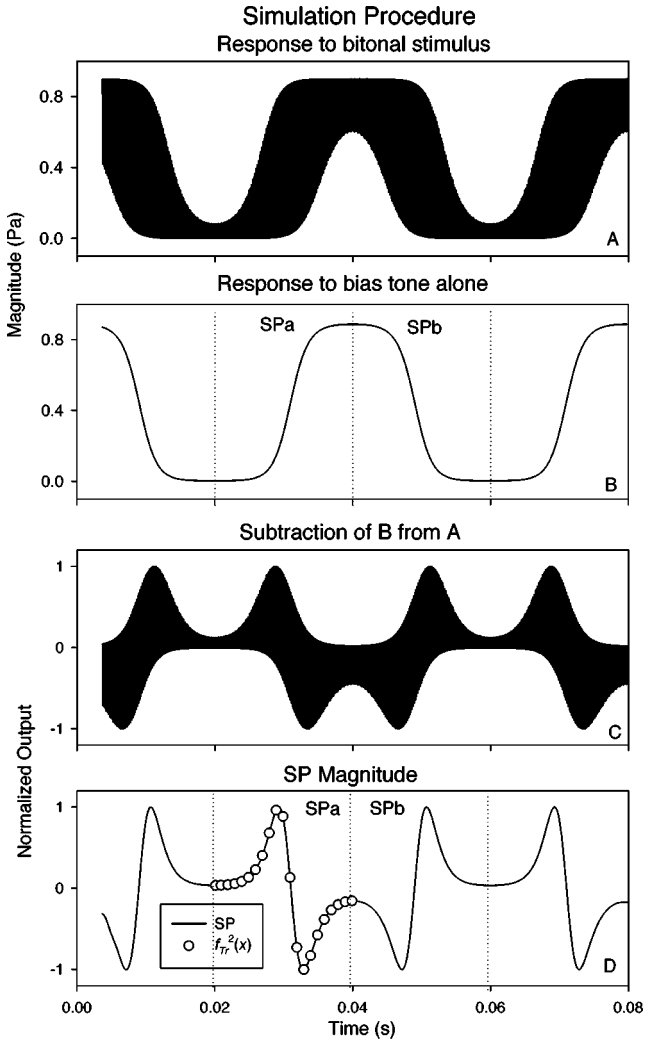

FIG. 3. Simulation procedure: the responses of combination tone and bias tone sent to the Boltzmann function are shown in panels (A) and (B). The response of the bias tone is subtracted from the combination tone [panel (C)] and low-pass filtered at 500 Hz [panel (D)]. The responses are normalized to unity. In panel (D), the SPa waveform (solid line) was fitted to the second derivative (opened circles). The correlation coefficient is 1, indicating that the SP waveform is essentially proportional to the second derivative.

bulla was opened by a dental drill (Volvere GX) and kept opened during the entire experiment. A plastic tube was used to seal the bony ear canal. At the end of the tube, a calibrated probe microphone (Etymotic ER-7C) was positioned about 5 mm from the umbo of the tympanic membrane to monitor and record the acoustic signals. A ball-tip silver wire electrode insulated by #31 polymide tubing [Micro ML (College Point, NY)] was placed on the round window and glued to the bulla opening. The fluid that condensed at the RW niche was absorbed with a cotton wick.

B. Experimental procedures

At the beginning of the experiment, compound action potential (CAP) thresholds elicited by tone bursts were estimated at frequencies of 1, 2, 4, 8, and 16 kHz by visually inspecting N_1 on a digital storage oscilloscope (Hitachi VC-6045A). Two out of ten animals were excluded in the data analysis because of hearing thresholds above 30 dB SPL across the whole frequency range.

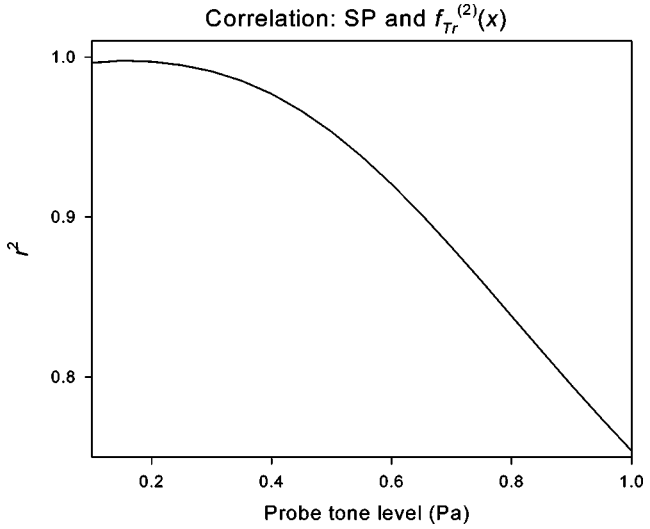

FIG. 4. Effect of the probe tone level on the accuracy of the curve fitting. The correlation coefficient (r^2) between SP and $f_{\mathrm{Tr}}^{(2)}(x)$ changes as the probe tone levels changes. As the probe level decreases, the r^2 increases, asymptotically approaching 1.0 below the probe level of 0.3 Pa.

Prior to each recording session, the CM magnitude was inspected to monitor the physiologic status of animals throughout the experiment with a 2000-Hz tone at 90 dB SPL. There were six recordings based on the two different probe frequencies and three different probe levels. Prior to the actual recording with the probe tone, one recording was conducted with only the bias tone with various amplitudes. The whole recording lasted about 1.5 h.

C. Stimuli and signal delivery

A probe tone was presented at frequencies of 6000 and 12 000 Hz with amplitudes ranging from 70 to 90 dB SPL in 10-dB steps. The bias tone was presented at 25 Hz and its amplitude was systematically decreased from 70 (about 130 dB SPL) to 0 Pa in 21 steps. Only data from the 70 Pa bias level were considered in this paper because lower levels show limited saturation of the transducer function. The bias tone lasted for 250 ms. Figure 5 shows an example of the acoustic signal recorded from the ear canal when the probe tone (6000 Hz) was presented with the bias tone (25 Hz and 97 dB SPL) at the same time. The maximum level (130 dB SPL) of the bias tone for one animal was calibrated in the tube sealed to the bony ear canal with a sound-level meter (Quest 1800).

Acoustic input signals consisting of a probe tone and a bias tone were produced from an array processor (Tucker-Davis Technology, TDT, AP2) and sampled at 65 536 Hz in a 16-bit digital-to-analog converter (TDT, DA3-4). The probe tone was sent to a headphone buffer (TDT, HB6) which connected to a headphone (Etymotic ER-3A). The probe tube of the headphone was coupled to a speculum attached to the ear canal. An ER-7C was attached to the speculum to monitor and record the acoustic signal. The bias tone was amplified and sent to a subwoofer (Paradigm Servo-15). An aluminum acoustic funnel covering the subwoofer was used to guide the bias tone to the bony ear canal via a silicon tube.

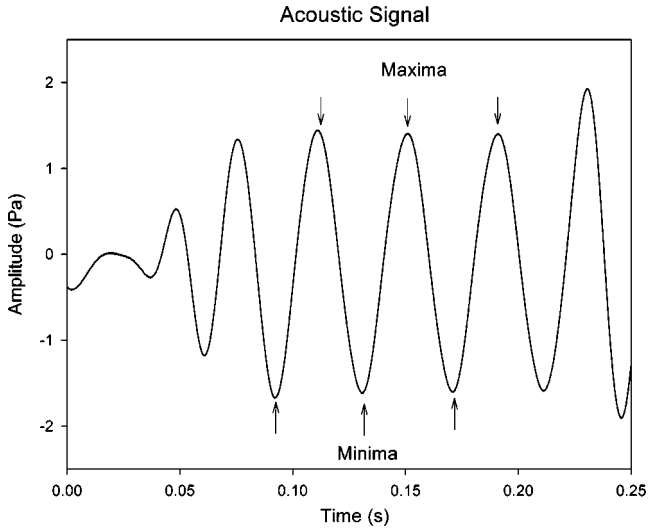

FIG. 5. An example of the acoustic signal (probe tone+bias tone). The peak amplitude of the bias tone is 97 dB SPL and the probe tone level is 70 dB SPL. Three segments (arrows) at the peaks and troughs of the bias tone were used to obtain the SP.

D. Data acquisition and analysis

The acoustic signals from the ER-7C were low-pass filtered at 16 kHz, amplified 10 times, and sampled at 65 536 Hz (TDT, AD2). Electric responses from the cochlea were recorded from the electrode placed at the round window, and a needle electrode inserted into the neck muscles served as ground. The responses were band-pass filtered between 0.03 Hz–30 kHz and amplified 500 times through a preamplifier (Stanford SR560), low-pass filtered at 16 kHz (54 dB/octave), and amplified 10 times (Stewart VBF 10M), and finally sampled at 65 536 Hz (TDT, AD2).

The data were analyzed with MATLAB (6.1 MathWorks). The SP waveform was obtained with a method similar to that used in the simulation. The cochlear transducer function was constructed from the SP waveform obtained at the highest bias level (70 Pa). The cochlear responses from bias tone in the bitonal stimulus and bias tone alone were compared and scaled to each other in order to reduce possible experimental errors which might occur at different recording times during the experiment. Then, the scaled responses to the bias tone alone were subtracted from that of the bitonal case and low-pass filtered at 500 Hz to filter out the cochlear response to the probe tone.

Generally, the cochlear f_{Tr} can be derived from integrating the SP function in response to the bias level two times. However, because the constants of integration were not available in our data, a curve-fitting method was used to construct the cochlear transducer function from the SP. The accuracy of the curve-fitting method was evaluated by the correlation between the SP magnitude and the second derivative. By curve fitting the SP data to the formula of $f_{\mathrm{Tr}}^{(2)}(x)$ (Bian *et al.*, 2002), the parameters of $f_{\mathrm{Tr}}(x)$ were obtained and a cochlear f_{Tr} was constructed. Finally, significant differences between these parameters were statistically tested by a repeated measure analysis of variance (SPSS 11.0). Statistical significance was determined by a probability of less than 0.05.

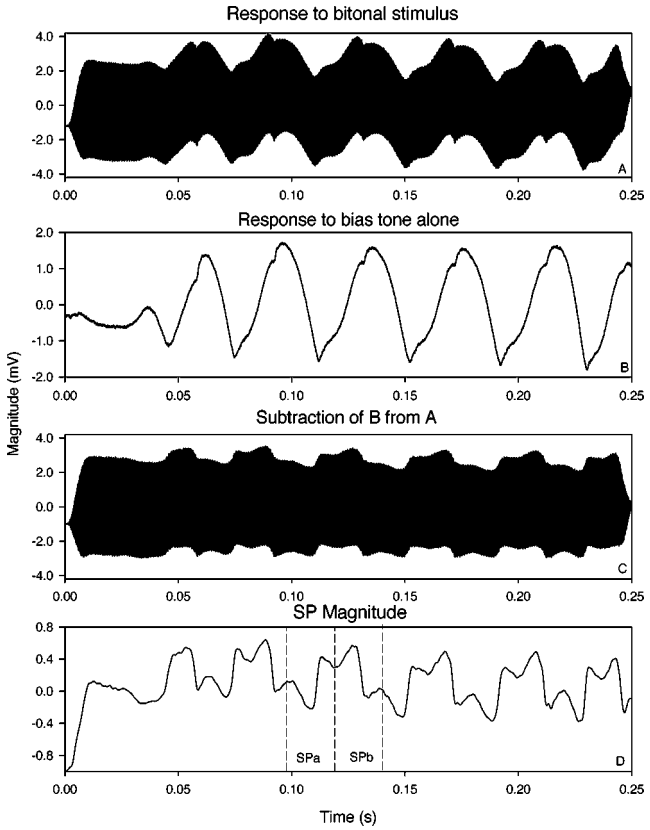

FIG. 6. The waveforms of the cochlear responses. Panel (A) and (B) show the waveforms obtained from the combination tone and the bias tone alone, respectively. Panel (C) illustrates the subtracted waveform of the bias tone from the combination tone while panel (D) is the low-pass filtered waveform, which is called the SP-bias function when plotted as a function of the bias level. SPa and SPb represent a descending and ascending side of a cycle of the bias tone response, respectively.

III. RESULTS

A. SP magnitudes

Figure 6 illustrates the cochlear responses obtained from one animal to the bitonal stimulus [panel (A)] and only the bias tone [panel (B)], respectively. Panel (C) shows the subtracted waveform of the response of the bias tone from that of the bitonal stimulus. Panel (D) represents the SP waveform obtained by low-pass filtering the waveform in panel C.

The SP-bias functions were plotted using the bias tone levels as input and the SP magnitude as output signal. Individual SP-bias functions obtained from eight animals for probe levels of 90, 80, and 70 dB SPL and frequencies of 6 and 12 kHz are shown in Fig. 7. Around the bias level of 0 Pa (± 5 Pa), the SP-bias function shows a very steep slope. However, beyond this level, there is a noticeable difference in the shape of the SP-bias functions across levels, suggesting the shape of the SP-bias function is probe level dependent. For example, at the probe level of 90 dB SPL [panel (A) of Fig. 7], the size of the SP decreased more slowly for positive bias levels than it did at 80 dB SPL. The size of the SP at 90 dB SPL was similar to that at 80 dB SPL. Furthermore, the absolute value of SP was larger for positive bias levels than negative bias levels. These results were similar to those at 12 kHz for the two highest signal levels. At the probe level of 70 dB SPL [panel (C)], however, the SP mag-

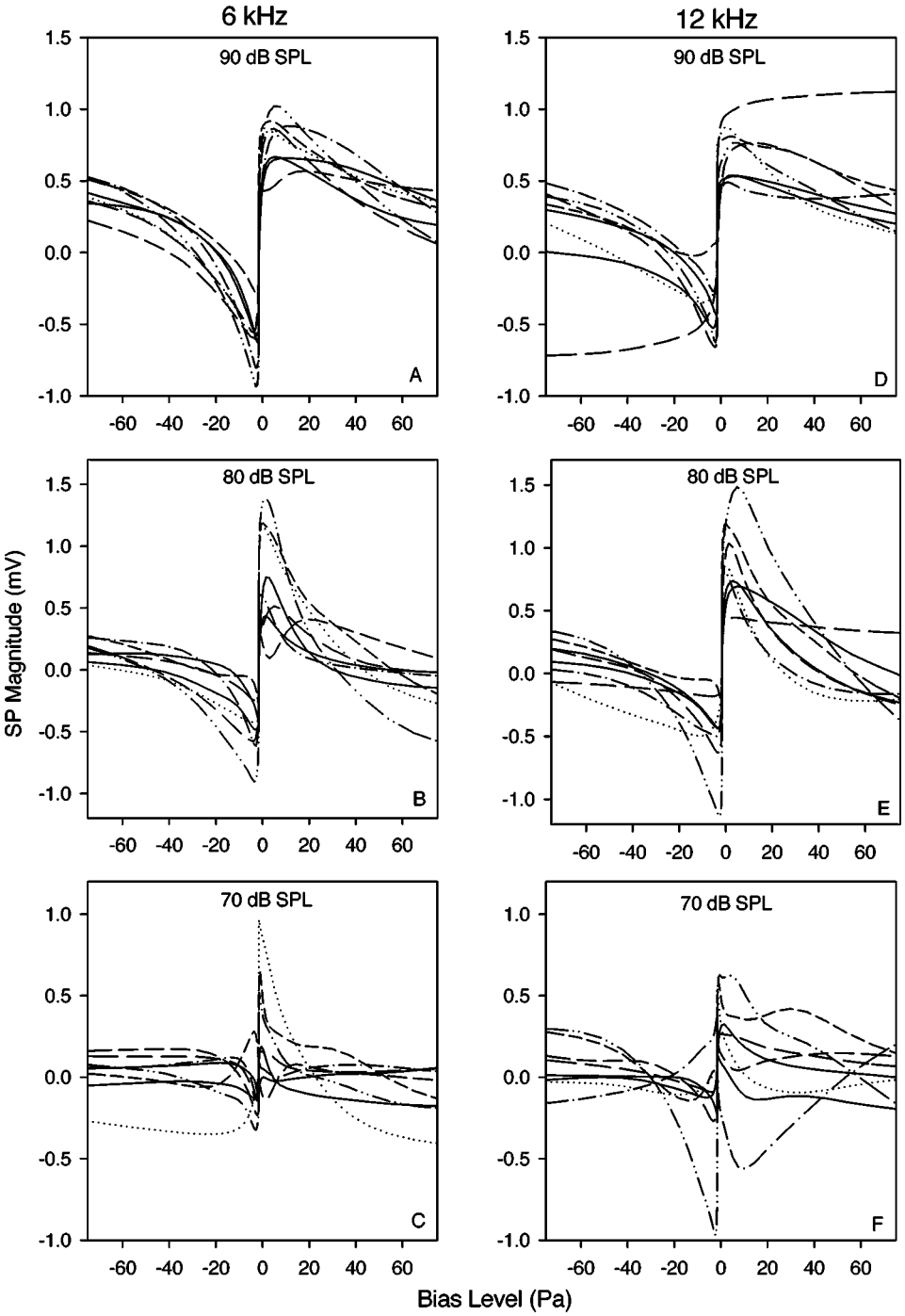

FIG. 7. Individual SP-bias functions obtained from eight animals in response to 90, 80, and 70 dB SPL of both 6 and 12 kHz. For each animal, the SP-bias functions represent the average obtained from three cycles.

nitude was smaller and variable, making it difficult to observe these trends.

B. Constructing a Boltzmann function from SP

The SP-bias function for each animal was fit to the second derivative of $f_{\mathrm{Tr}}(x)$ by a curve-fitting method in SIGMAPLOT (version 8.0). In the curve-fitting method, the values of the parameters were continually changed until the maximal fit between the SP-bias function and the second derivative was obtained. The set of parameters showing the highest r^2 between the SP data and $f_{\mathrm{Tr}}^{(2)}(x)$ was selected to derive the cochlear transducer function because it indicated the least error between the data and $f_{\mathrm{Tr}}^{(2)}(x)$. Figure 8 illustrates r^2 between the SP data (solid line) averaged across all the animals and the $f_{\mathrm{Tr}}^{(2)}(x)$ [dotted line] for different probe frequencies and levels. The mean and standard deviation of r^2 are also displayed in Table I. The r^2 is about 0.94 at 90 and 80 dB SPL, indicating the SP is essentially proportional to the second derivative of the Boltzmann function. At 70 dB SPL, the average r^2 across all animals is smaller and more variable than the higher signal levels.

Table I shows the mean and standard deviation (s.d.) of the parameters of $f_{\mathrm{Tr}}(x)$ across the animals for the probe level and frequency. Although there is considerable variability in the parameters, some consistencies among the parameters can be observed among the probe level and frequency. For the slope parameters b and d, the values of d are much greater than those of b. The value of the b/d ratio is very

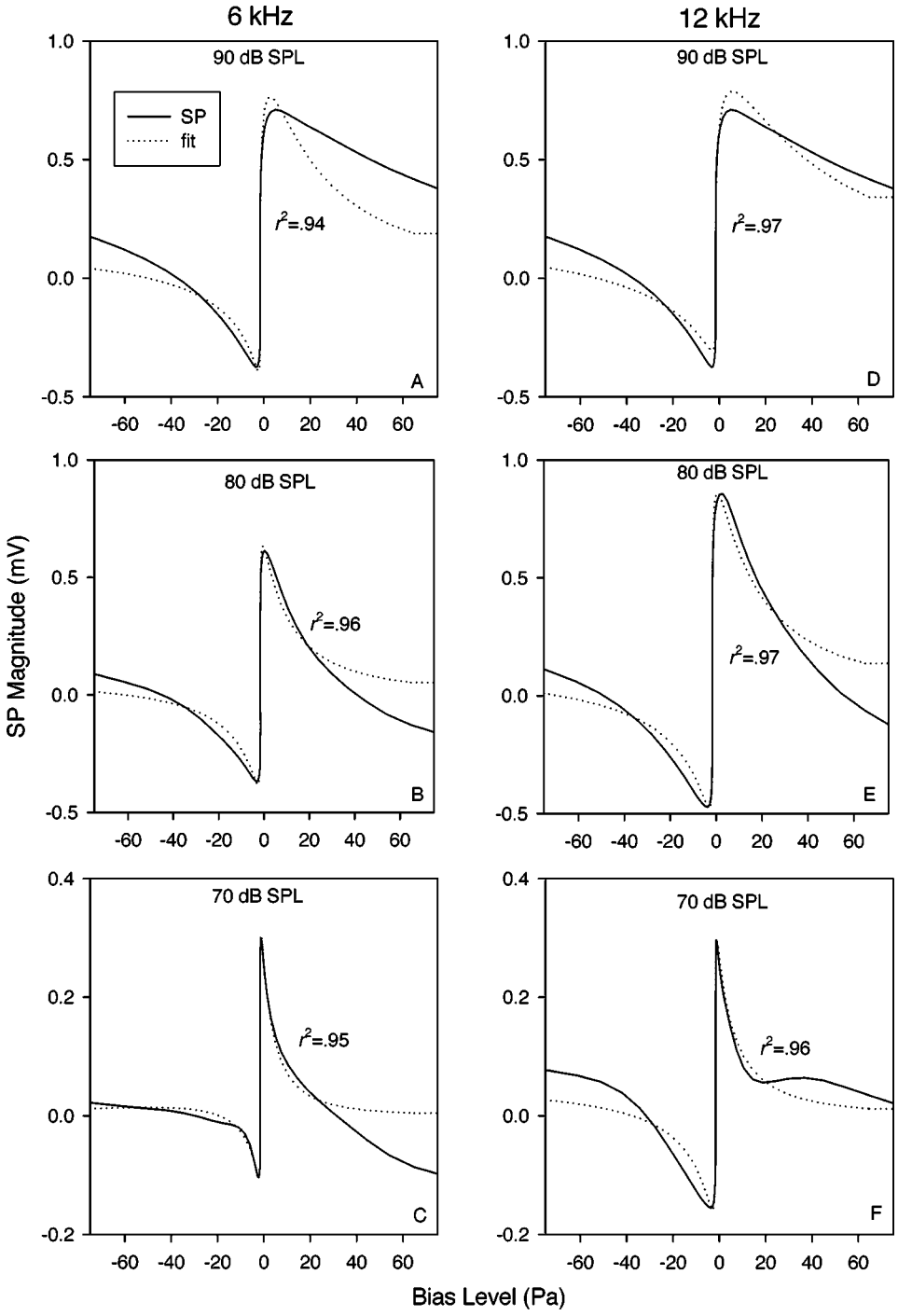

FIG. 8. Mean SP-bias functions and their curve-fitting results at 90, 80, and 70 dB SPL of both 6 kHz and 12 kHz. The correlation coefficients (r^2) between SP and $f_{\mathrm{Tr}}^{(2)}(x)$ were very high, indicating that the SP are well fitted to $f_{\mathrm{Tr}}^{(2)}(x)$.

TABLE I. Curve-fitting results: the mean and standard deviation (s.d.) of the parameters of $f_{\mathrm{Tr}}(x)$ across the animals when the second derivative of $f_{\mathrm{Tr}}(x)$ was fit to the SP data and the correlation coefficient (r^2) between the second derivative and the SP data.

Hz	dB SPL	A	b	c	d	e	r^2
6 kHz	90	0.127±0.071	0.40±0.13	−5.34±0.44	3.82±0.34	0.68±0.20	0.92±0.02
	80	0.009±0.007	0.33±0.73	−3.11±1.23	4.81±0.67	0.14±0.58	0.93±0.02
	70	−0.003±0.026	0.07±3.57	−3.45±2.10	7.03±3.46	0.10±1.64	0.79±0.18
12 kHz	90	0.148±0.046	0.41±0.17	−5.41±0.52	3.35±0.81	0.58±0.31	0.94±0.06
	80	0.017±0.007	0.42±0.13	−3.46±0.69	4.06±0.72	0.23±0.32	0.94±0.03
	70	0.023±0.027	−0.01±1.31	−4.93±1.71	3.95±3.72	11.59±33.36	0.74±0.33

Mean±s.d.

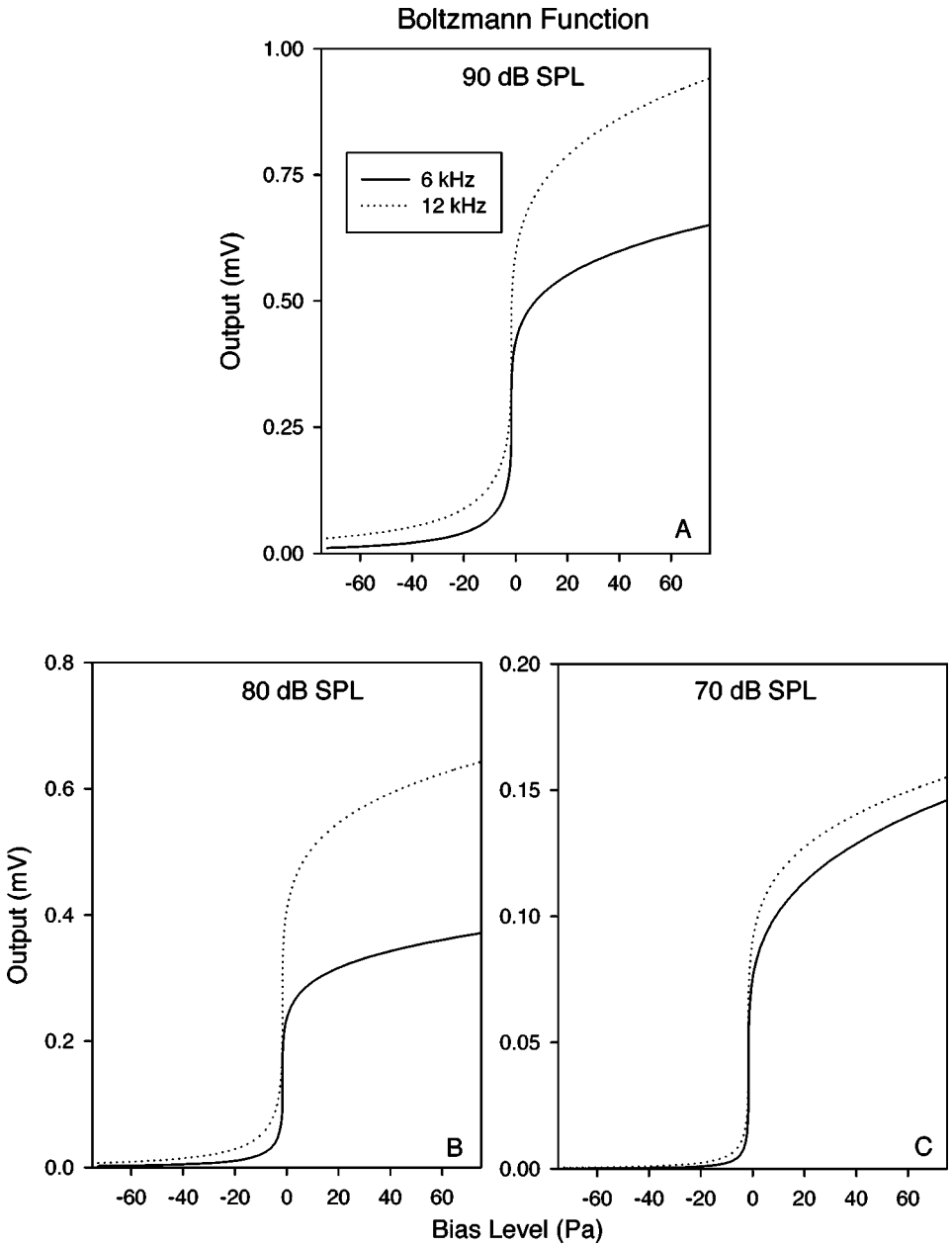

FIG. 9. Second-order Boltzmann functions obtained from the parameters of the fitted second derivative at 90, 80, and 70 dB SPL of both 6 and 12 kHz.

small, indicating an asymmetrical sigmoidal curve for $f_{\mathrm{Tr}}(x)$. For the parameters c and e, c is negative but e is positive. Although the c and e parameters are highly variable, the absolute value of c is much greater than e.

Figure 9 illustrates the averaged Boltzmann functions plotted from the parameters of the $f_{\mathrm{Tr}}(x)$ fit to the averaged SP data across the animals. The Boltzmann functions show a drastic large slope around 0 Pa (± 5 Pa) and a smaller slope as the bias level increases. In addition, they are asymmetric between the positive and negative bias levels. For example, the slope of the Boltzmann function is bigger at the positive bias level than that of the negative level. The maximal outputs of the Boltzmann function are level dependent, indicating that it increases as the probe level increases. The maximal outputs at a high probe frequency are also bigger than that of low the frequency. Finally, the slope changes for the positive bias level at high probe frequency are much bigger than that of low probe frequency, while there are no significant slope changes for the negative bias level between high and low probe frequencies.

IV. DISCUSSION

A. Modulation of SP magnitude by bias tone

The results show that the dc component of the cochlear response is modulated by the presence of a bias tone. The variation in dc magnitude occurs because the bias tone drives the probe tone into different positions along the curve with the different slope. When the probe tone is placed where the slope of the curve is largest or where the curve saturates, the dc magnitude is close to zero. However, when the probe tone is located between these regions, the dc magnitude is largest.

Based on its definition as the dc component of the cochlear potential, we identify the modulated dc component obtained here with the summating potential. The low-frequency bias tone was used to vary the position of the

basilar membrane (BM) and place the probe tone at different locations along the hair-cell transducer curve. The SP magnitude is small at the zero crossings of the acoustic bias tone, positive for the positive directions of the bias tone, and negative for the negative directions of the bias tone. The zero magnitude of the SP is involved with the resting position of the BM, while the positive and negative magnitudes of the SP are associated with the BM displacement towards ST and SV, respectively (Cheatham and Dallos, 1994, 1997). The modulation of the SP magnitude is consistent with the findings of Durrant and Dallos (1974), who recorded the SP using an electrode placed in scala vestibuli (SV) and in scala tympani (ST) in guinea pigs. Their study showed that the SP was reversibly enhanced or depressed at low bias levels and generally depressed at high bias levels.

B. Effects of signal level

1. Bias tone level

The experimental results demonstrate that the SP magnitude reaches a maximum or minimum at ± 5 Pa (107 dB SPL) and then decreases. The maximal bias level used in our study was 70 Pa (130 dB SPL). This is larger than the bias levels adopted in low-frequency bias tone experiments by others, for example, 107 dB SPL (Patuzzi and Sellick, 1984), 105 dB SPL (Klis and Smoorenburg, 1985), 100 dB SPL (Durrant and Dallos, 1972, 1974), and 95 dB SPL (Cheatham and Dallos, 1994; Klis and Smoorenburg, 1988). Although there is a difference in the maximal bias level used in each study, a rollover in the SP-bias function, particularly shown by Durrant and Dallos (1974), is similar to the modulation patterns in our present study.

At first appearance, the large bias level and associated domain of the transducer function seem beyond everyday listening levels. However, it is not so large when considering the mechanical tuning curve of the BM across frequency. It is generally agreed that there is a 40–60-dB difference between the tip and tail regions of the mechanical tuning curve of the BM (Robles *et al.*, 1986; Ruggero *et al.*, 1997). The BM response to the bias tone of 25 Hz is 40 to 60 dB lower than the BM response measured at the characteristic location of the high-frequency probe tone. Therefore, the maximal bias level at the BM location for the probe tone where the SP is produced could be 70 to 90 dB SPL. This range is within the saturation level of the dc receptor potential of the IHC and the ac receptor potential of the OHC (Russell *et al.*, 1986; Dallos, 1986). Therefore, the range (± 130 dB SPL) of the bias level used in our study matches to a ± 90-dB SPL input range and may properly represent the operating range of a cochlear transducer function that can be derived from the SP.

Another concern about the high level bias tone is that the maximal bias level (130 dB SPL) in our study is beyond the signal level (within 120 dB SPL) at which the middle-ear response is linear. At this signal level, the annular ligament may modify the propagation of the acoustic wave through the middle-ear, causing the middle-ear transfer function to be nonlinear (Pascal *et al.*, 1998). If the nonlinearity created a dc response in the stapes velocity, it might influence the SP response of the cochlea recorded at the round window. However, we assume that this dc component of the middle-ear would be similar in the bias tone alone and combination tone conditions. Therefore, subtracting the cochlear response of the bias tone from the combination tone response in our study should exclude the intervention of the middle-ear by eliminating the effect of the bias tone. In a separate experiment on three gerbils, the middle-ear transfer function obtained by measuring stapes velocity with a laser Doppler vibrometer (LDV, Polytec HLV 1000) showed linearity with no distortion or dc shift (Bian *et al.*, 2004).

2. Probe tone level

There was a significant difference in the shape of the SP-bias function for different probe levels. This is similar to the results of Durrant and Dallos (1974), who demonstrated significant effects of probe level on the SP magnitude for different probe levels (50, 70, 90 dB SPL) with the differential electrode technique. In their study, the SP continued to increase even at the highest bias level for a probe tone level of 90 dB SPL. For the lower probe levels of 70 and 50 dB SPL, the SP reached the maximum at 90 and 70 dB SPLs of bias level, respectively and then decreased. However, this phenomenon was not exhibited in the works of Durrant and Dallos (1972) and Durrant and Gans (1975), who observed no systematic level-dependent effects on the SP with electrical biasing of the cochlear partition. The inconsistent results with the Durrant studies may be due to the method of biasing the BM. The one study used acoustic biasing and placed the probe tone at different phases of the bias tone, whereas the other two studies used techniques of electrically biasing the cochlear partition by placing electrodes in fine holes in the bony cochlear wall over SV, SM, and ST. It is possible that opening the cochlea altered the physiology and eliminated the probe level effect.

The total SP modulation depth (maximum SP $-$ minimum SP) changed as a function of the probe level. When the probe level increased, this modulation depth increased. These results agree with the work of Klis and Smoorenburg (1985, 1988), who compared the normalized SP modulation depths relative to different probe levels representing the dynamic range of the cochlear transducer curve. The results of our study are also consistent with the finding of Bian and Chertoff (1998), indicating that the dynamic range of the cochlear transducer curve at higher signal level is greater than that of the lower level.

It is interesting to note that at the probe levels of 80 and 90 dB SPL, the SP magnitude was greatly modulated and the shape of the SP-bias function was visually closer to that of $f_{\mathrm{Tr}}^{(2)}(x)$ used in the simulation. In theory, the lowest probe level (70 dB SPL) should be the best condition. However, at this level the response amplitude was smaller and more variable, making an accurate estimation of SP difficult. Another explanation is that a cochlear transducer function could change with probe level. That is, the cochlear transducer function may be not a static nonlinear function but a dynamic one. Therefore, it may be necessary for future research to use a wide range of probe levels to estimate the transducer curve more accurately.

C. Cochlear transducer function

1. Parameter estimates and transducer characteristics

The cochlear transducer functions were constructed from the parameters of the Boltzmann function obtained by curve fitting the SP-bias data to the second derivative of the Boltzmann function. The experimental results indicated that the parameters of the Boltzmann function were affected by probe tone level and frequency. The maximal conductance parameter, A, and the slope parameter, d, varied depending on level while the resting position parameters, c and e, were affected by level and frequency. The increase in A parameter at high levels as shown in Table I represents an increase in the dynamic range (DR) of the cochlear transducer function reported by other studies. This is similar to the finding of Bian *et al.* (2002) who derived a sigmoidal curve representing cochlear transduction from DPOAE and others using the cochlear microphonic (Bian and Chertoff, 1998; Patuzzi and Moleirinho, 1998).

Comparing the Boltzmann parameters between the two probe frequencies, the A parameter at 12 kHz was greater than that at 6 kHz. This is not compatible with the observations of other studies (Bian and Chertoff, 2001) which showed that the dynamic range (DR) of the MET transfer function in the high-frequency region is reduced compared with that in the low-frequency region. The difference may be due to the different potentials recorded in studies. Bian and Chertoff (2001) recorded the CM, whereas the present study used the SP. The CM recorded from the round window for high frequencies is susceptible to vector summation canceling or reducing CM amplitude. In contrast, this may not occur for the SP (Whitfield and Ross, 1965).

2. Source: OHC or IHC transducer?

Although many studies have been conducted on the SP for several decades, the source of the SP still remains an unsolved problem. In other words, it is not clear which type of hair cell contributes to the cochlear transducer function obtained from the SP in our study.

Most previous studies (Davis *et al.*, 1958; Johnstone and Johnstone, 1966; Dallos, 1973; Dallos and Cheatham, 1991) have concluded that the SP production is essentially dominated by the OHCs. Particularly, Dallos (1973) found that the SP magnitude is strongly associated with OHC damage, whereas it is weakly related to IHC damage. This domination of the OHCs on the SP also exists at the apex of the guinea pig cochlea. The Dallos model was supported by other authors (McMullen and Mountain, 1985; Geisler *et al.*, 1990). However, the OHC contribution to SP production was not observed at the base of the cochlea when presenting high-frequency stimuli at low and moderate levels (Russell *et al.*, 1986; Cody and Russell, 1987). This discrepancy between the two studies can result from the different location of the electrode used in each experiment and possible differences between physiological or electrochemical properties of hair cells at the base and apex of the cochlea (Zheng *et al.*, 1997).

On the other hand, relatively recent studies (Durrant *et al.*, 1998; van Emst *et al.*, 1995, 1996, 1997; Zheng *et al.*, 1997) have focused on the role of the IHCs in the SP production. Although they used different species as experimental subjects, their results may provide an implication for the origin of the SP. After investigating the relationship between IHC and OHC damage using different doses of carboplatin and the SP recorded from the round window of chinchillas, Durrant *et al.* (1998) reported that the contribution of IHCs varies with input signal levels. The relative contribution of IHCs on the SP generation increased from about 50% to at least 70% as the signal level decreased from high signal levels to low and moderate signal levels. van Emst *et al.* (1995, 1996) investigated the role of basolateral voltage-dependent K^+ channels on SP production by perfusing the guinea pig's cochlea with two different K^+ channel blockers [tetraethylammonium (TEA) and 4-aminopyridine (4-AP)]. When these drugs blocked K^+ channels in the basolateral membrane of the IHC, the SP magnitude was significantly decreased. In addition, van Emst *et al.* (1998), using a computational model, showed that the K^+ channels of the IHC are directly involved in the production of the dc receptor potential at low frequencies and modify the size of the dc response at high frequencies. With either acute chemical deafferentation or surgical deafferentation, Zheng *et al.* (1997) revealed evidence that IHCs are the major source of the SP recorded from the round window in chinchillas at low to moderate signal levels. This observation is consistent with the results that the OHCs generate little SP at the base of the cochlea in response to the high-frequency stimuli at low and moderate levels (Russell *et al.*, 1986; Cody and Russell, 1987).

Considering the recent studies emphasizing the role of the IHCs in SP generation, it is tempting to conclude that the cochlear transducer function obtained from the SP in our study is mainly dominated by IHC responses. However, there is no direct evidence to support this view in the present study. A possible way to determine the source of the SP is to compare the cochlear transducer function derived from the SP to that obtained from the CM which is mainly generated by the OHCs. It was shown that the modulation envelope of the measured CM using a low-frequency bias tone is very similar to the first derivative of the cochlear transduction curve (Nieder and Nieder, 1971). If there is a difference between the cochlear transducer functions obtained from SP and CM, the difference may reflect the difference between IHCs and OHCs. Morever, using the carboplatin approach by Durrant *et al.* (1998) to eliminate IHCs, one can investigate whether the transducer function obtained in our study represents IHC or OHC properties.

D. Technical issues

The SP was obtained from the subtraction of the cochlear responses to the bias tone alone from those from the bitonal stimulus. This assumes that the SP response to the bias alone and the SP response to the bitonal stimulus are the same. Therefore, the subtraction would yield the SP due to the probe tone alone. If they are not the same size, the SP produced by the probe tone may be inaccurate. This could occur if the physiologic state of the animal changed during the recording of the bias alone and the bitonal stimulus. One solution to this problem is to build one stimulus composed of

the bias tone, the probe tone, and the bitonal stimulus in sequence. Using the same stimulus may increase the accuracy of measuring the SP.

With the curve-fitting method relating $f_{\mathrm{Tr}}^{(2)}(x)$ to the SP data, the derived parameters of the Boltzmann function could be different using different initial conditions, although the r^2 was the same indicating an equally good fit to the data. As one solution to this problem, Bian *et al.* (2002) proposed to normalize the data by comparing the SP magnitudes at the peaks of the bias tone with the tail portion without biasing and fit the data with a first-order $f_{\mathrm{Tr}}(x)$ instead of the second-order $f_{\mathrm{Tr}}(x)$. However, because the first-order $f_{\mathrm{Tr}}(x)$ is a symmetric function, it may not truly reflect the asymmetry of the cochlear transducer function obtained in our study.

V. SUMMARY AND CONCLUSIONS

The present study investigated the relationship between SP and the cochlear transducer function characterizing mechano-electric transduction (MET). Mathematical exploration showed that the dc component representing SP is produced from the even-order terms of a Taylor series. Furthermore, it suggested that the dc component is essentially proportional to the second derivative of the nonlinear function for a low-level signal. A computer simulation using a low-frequency bias tone with various amplitudes showed that the dc magnitudes were modulated by the low-frequency bias tone. The modulation pattern of the dc magnitude was very similar to the shape of the second derivative of the sigmoidal Boltzmann function.

A physiologic experiment using gerbils as subjects and signals similar to the simulation was completed to estimate a cochlear transducer function. The experimental results were similar to the theory that at low signal levels the SP magnitude is essentially proportional to the second derivative of the cochlear transducer function. However, the SP-bias functions were level dependent. Although there was considerable variability in the parameters of the derived $f_{\mathrm{Tr}}(x)$, the parameters also showed a level dependence. The present study suggests that the cochlear transducer function can be constructed from the SP data.

ACKNOWLEDGMENT

This study was supported in part by the National Institute on Deafness and Other Communication Disorders of the National Institute of Health, Grant Nos. R01 DC02117 and R03 DC006165.

Bian, L., and Chertoff, M. E. (**1998**). ''Differentiation of cochlear pathophysiology in ears damaged by salicylate or a pure tone using a nonlinear systems identification technique,'' J. Acoust. Soc. Am. **104**, 2261–2271.

Bian, L., and Chertoff, M. E. (**2001**). ''Distinguishing cochlear pathophysiology in 4-aminopyridine and furosemide treated ears using a nonlinear systems identification technique,'' J. Acoust. Soc. Am. **109**, 671–685.

Bian, L., Chertoff, M. E., and Miller, E. (**2002**). ''Deriving a cochlear transduction function from low-frequency modulation of distortion product otoacoustic emissions,'' J. Acoust. Soc. Am. **112**, 198–210.

Bian, L., Linhardt, E. E., and Chertoff, M. E. (**2004**). ''Cochlear hysteresis: Observation with low-frequency modulated distortion product otoacoustic emissions,'' J. Acoust. Soc. Am. **115**, 2159–2172.

Cheatham, M. A., and Dallos, P. (**1994**). ''Stimulus biasing: A comparison between cochlear hair cell and organ of Corti response patterns,'' Hear. Res. **75**, 103–113.

Cheatham, M. A., and Dallos, P. (**1997**). ''Low-frequency modulation of inner hair cell and organ of Corti responses in the guinea pig cochlea,'' Hear. Res. **108**, 192–212.

Chertoff, M. E., Steele, T. C., Ator, G. A., and Bian, L. (**1996**). ''Characterizing cochlear mechano-electric transduction using a nonlinear systems identification procedure,'' J. Acoust. Soc. Am. **100**, 3741–3753.

Chertoff, M. E., Steele, T. C., and Bian, L. (**1997**). ''Characterizing cochlear mechano-electric transduction in ears damaged with pure tones,'' J. Acoust. Soc. Am. **102**, 441–450.

Choi, C.-H., Chertoff, M. E., and Yi, X. (**2002**). ''Characterizing cochlear mechano-electric transduction with a nonlinear system identification technique: The influence of the middle ear,'' J. Acoust. Soc. Am. **112**, 2898–2909.

Cody, A. R., and Russell, I. J. (**1985**). ''Outer hair cells in the mammalian cochlea and noise-induced hearing loss,'' Nature (London) **315**, 662–665.

Cody, A. R., and Russell, I. J. (**1987**). ''The responses of hair cells in the basal turn of the guinea-pig cochlear to tone,'' J. Physiol. (London) **383**, 551–569.

Crawford, A. C., Evans, M. G., and R. Fettiplace, (**1989**). ''Activation and adaptation of transducer currents in turtle hair cells,'' J. Physiol. (London) **419**, 405–434.

Dallos, P. (**1973**). *The Auditory Periphery: Biophysics and Physiology* (Academic, New York).

Dallos, P. (**1985**). ''Response characteristics of mammalian cochlear hair cells,'' J. Neurosci. **5**, 1591–1608.

Dallos, P. (**1986**). ''Neurobiology of cochlear inner and outer hair cells: Intracellular recordings,'' Hear. Res. **22**, 185–198.

Dallos, P., and Cheatham, M. A. (**1991**). ''Cochlear hair cell function reflected in intracellular recordings in vivo,'' in *Sensory Transduction*, edited by D. P. Corey and S. D. Roper (The Rockefeller University Press, New York), pp. 371–393.

Dallos, P., Schoeny, Z. G., and Cheatham, M. A. (**1972**). ''Cochlear summating potentials: Descriptive aspects,'' Acta Oto-Laryngol., Suppl. **302**, 1–46.

Davis, H., Deatherage, B. H., Eldredge, D. H., and Smith, C. A. (**1958**). ''Summating potentials of the cochlea,'' Am. J. Physiol. **195**, 251–261.

Durrant, J. D., and Dallos, P. (**1972**). ''Influence of direct-current polarization of the cochlear partition on the summating potentials,'' J. Acoust. Soc. Am. **52**, 542–552.

Durrant, J. D., and Dallos, P. (**1974**). ''Modification of DIF summating potential components by stimulus biasing,'' J. Acoust. Soc. Am. **56**, 562–570.

Durrant, J. D., and Gans, D. (**1975**). ''Biasing of the summating potentials,'' Acta Oto-Laryngol. **80**, 13–18.

Durrant, J. D., Wang, J., Ding, D. L., and Salvi, R. J. (**1998**). ''Are inner or outer hair cells the source of summating potentials recorded from the round window?'' J. Acoust. Soc. Am. **104**, 370–377.

Geisler, C. D., Yates, G. K., Patuzzi, R. B., and Johnstone, B. M. (**1990**). ''Saturation of outer hair cell repeptor currents causes two-tone suppression,'' Hear. Res. **44**, 241–256.

Harvey, D., and Steel, K. P. (**1992**). ''The development and interpretation of the summating potential response,'' Hear. Res. **61**, 137–146.

Holton, T., and Hudspeth, A. J. (**1986**). ''The transduction channel of hair cells from the bullfrog characterized by noise analysis,'' J. Physiol. (London) **375**, 195–227.

Howard, J., and Hudspeth, A. J. (**1988**). ''Compliance of the hair bundle associated with gating of mechnoelectrical transduction channels in the bullfrog's saccular hair cell,'' Neuron **1**, 189–199.

Hudspeth, A. J. (**1982**). ''Extracellular current flow and the site of transduction by vertebrate hair cells,'' J. Neurosci. **2**, 1–10.

Hudspeth, A. J., and Corey, D. P. (**1977**). ''Sensitivity, polarity, and conductance change in the response of vertebrate hair cells to controlled mechanical stimuli,'' Proc. Natl. Acad. Sci. U.S.A. **76**, 2407–2411.

Johnstone, J. R., and Johnstone, B. M. (**1966**). ''Origin of summating potential,'' J. Acoust. Soc. Am. **40**, 1405–1413.

Klis, J. F. L., and Smoorenburg, G. F. (**1985**). ''Modulation at the guinea pig round window of summating potentials and compound action potentials by low-frequency sound,'' Hear. Res. **20**, 15–23.

Klis, J. F. L., and Smoorenburg, G. F. (**1988**). ''Cochlear potentials and their modulation by low-frequency sound in early endolymphatic hydrops,'' Hear. Res. **32**, 175–184.

Lukashkin, A. N., and Russell, I. J. (**1998**). ''A descriptive model of the receptor potential nonlinearities generated by the hair cell mechanoelectrical transducer,'' J. Acoust. Soc. Am. **103**, 973–980.
McMullen, T. A., and Mountain, D. C., (**1985**). ''Model of d.c. potentials in the cochlea: Effects of voltage-dependent cilia stiffness,'' Hear. Res. **17**, 127–141.
Neely, S. T., and Kim, D. O. (**1983**). ''An active cochlear model showing sharp tuning and high sensitivity,'' Hear. Res. **9**, 123–130.
Nieder, P., and Nieder, I. (**1968a**). ''Some effects of tonal interactions as seen in the cochlear microphone,'' J. Acoust. Soc. Am. **43**, 1092–1106.
Nieder, P., and Nieder, I. (**1968b**). ''Studies of two-tone interaction as seen in the guinea pig microphone,'' J. Acoust. Soc. Am. **44**, 1409–1422.
Nieder, P., and Nieder, I. (**1971**). ''Determination of microphonic generator transfer characteristic from modulation data,'' J. Acoust. Soc. Am. **49**, 478–492.
Pascal, J., Bourgeade, A., Lagier, M., and Legros, C. (**1998**). ''Linear and nonlinear model of the human middle ear,'' J. Acoust. Soc. Am. **104**, 1509–1516.
Patuzzi, R. B. (**1987**). ''A model of the generation of the cochlear microphonic with nonlinear hair cell transduction and nonlinear basilar-membrane mechanics,'' Hear. Res. **30**, 73–82.
Patuzzi, R. B. (**1998**). ''The Godman–Hodgkin–Katz equation and graphical 'load-line' analysis of ionic flow through outer hair cells,'' Hear. Res. **125**, 71–97.
Patuzzi, R. B., and Moleirinho, A. (**1998**). ''Automatic monitoring of mechano-electrical transduction in the guinea pig cochlea,'' Hear. Res. **125**, 1–16.
Patuzzi, R. B., and Sellick, P. M. (**1984**). ''The modulation of the sensitivity of the mammalian cochlea by low frequency tones. II. Inner ear cell receptor potentials,'' Hear. Res. **13**, 9–18.
Patuzzi, R. B., Yates, G. K., and Johnstone, B. M. (**1989**). ''Outer hair cell current and sensorineural hearing loss,'' Hear. Res. **42**, 47–72.
Robles, L., Ruggero, M. A., and Rich, N. C. (**1986**). ''Basilar-membrane mechanics at the base of the chinchilla cochlea. I. Input–output functions, tuning curves, and phase responses,'' J. Acoust. Soc. Am. **80**, 1364–1374.
Ruggero, M. A., Rich, N. C., Recio, A., Narayan, S. S., and Robles, L. (**1997**). ''Basilar-membrane responses to tones at the base of the chinchilla cochlea,'' J. Acoust. Soc. Am. **101**, 2151–2163.
Russell, I. J., Cody, A. R., and Richardson, G. P. (**1986**). ''The responses of inner and outer hair cells in the basal turn of the guinea-pig cochlea and in the mouse cochlea grown *in vitro*,'' Hear. Res. **22**, 199–216.
Russell, I. J., and Sellick, P. M. (**1983**). ''Intracellular studies of hair cells in the mammalian cochlea,'' J. Physiol. (London) **284**, 261–290.
Santos-Sacchi, J. (**1989**). ''Asymmetry in voltage-dependent movements of isolated outer hair cells from the organ of Corti,'' J. Neurosci. **9**, 2954–2962.
Santos-Sacchi, J. (**1993**). ''Harmonics of outer hair cell motility,'' Biophys. J. **65**, 2217–2227.
van Emst, M. G., Giguère, C., and Smoorenburg, G. F. (**1998**). ''The generation of dc potentials in a computational model of the organ of Corti: Effects of voltage-dependent K^+ channels in the basolateral membrane of the inner hair cell,'' Hear. Res. **115**, 184–196.
van Emst, M. G., Klis, S. F. L., and Smoorenburg, G. F. (**1996**). ''4-aminopyridine effects on summating potentials in the guinea pig,'' Hear. Res. **102**, 70–80.
van Emst, M. G., Klis, S. F. L., and Smoorenburg, G. F. (**1997**). ''Identification of the nonlinearity governing even-order distortion products in cochlear potentials,'' Hear. Res. **114**, 93–101.
van Emst, M. G., Klis, S. F. L., and Smoorenburg, G. F. (**1995**). ''Tetraethylammonium effects on cochlear potentials in the guinea pig,'' Hear. Res. **88**, 27–35.
Weiss, T. F., and Leong, R. (**1985**). ''A model for signal transmission in an ear having hair cells with free-standing stereocilia. IV. Mechanoelectric transduction stage,'' Hear. Res. **20**, 175–195.
Whitfield, I. C., and Ross, H. F. (**1965**). ''Cochlear-microphonic and summating potentials and the outputs of individual hair-cell generators,'' J. Acoust. Soc. Am. **38**, 126–131.
Zheng, X-Y., Ding, D-L., McFadden, S. L., and Henderson, D. (**1997**). ''Evidence that inner hair cells are the major source of cochlear summating potentials,'' Hear. Res. **113**, 76–88.

Response of the cat eardrum to static pressures: Mobile versus immobile malleus

Hanif M. Ladak[a)]
Department of BioMedical Engineering, McGill University, Montréal H3A 2B4, Canada

Willem F. Decraemer and Joris J. J. Dirckx
Laboratory of BioMedical Physics, University of Antwerp, Antwerpen B-2020, Belgium

W. Robert J. Funnell[b)]
Departments of BioMedical Engineering and Otolaryngology, McGill University, Montréal H3A 2B4, Canada

(Received 18 February 2004; revised 9 August 2004; accepted 12 August 2004)

A phase-shift shadow moiré interferometer was used to measure the shape of the cat eardrum with a normal mobile malleus and with an immobile malleus as it was cyclically loaded with static middle-ear pressures up to ± 2.2 kPa. The shape was monitored throughout the loading and unloading phases, and three complete cycles were observed. The mobile-manubrium measurements were made in five ears. In three ears, the malleus was then immobilized with a drop of glue placed on the head of the malleus. Eardrum displacements were calculated by subtracting shape images pixel by pixel. The measurements are presented in the form of gray-level full-field shape and displacement images, of displacement profiles, and of pressure-displacement curves for selected points. Displacement patterns with a mobile malleus show that pars-tensa displacements are larger than manubrial displacements, with the maximum pars-tensa displacement occurring in the posterior region in all cats except one. Displacements vary from cycle to cycle and display hysteresis. For both the mobile-malleus and immobile-malleus cases, the eardrum response is nonlinear. The response is asymmetric, with lateral displacements being larger than medial displacements. With a mobile malleus, manubrial displacements exhibit more pronounced asymmetry than do pars-tensa displacements. [DOI: 10.1121/1.1802673]

PACS numbers: 43.64.Ha [BLM] Pages: 3008–3021

I. INTRODUCTION

Static pressure differences across the eardrum occur in everyday life. They can, for example, be caused by atmospheric pressure changes felt in an elevator or airplane before the Eustachian tube opens to equilibrate the middle ear to ambient pressure. It is a common experience that, when the Eustachian tube function is impaired (e.g., due to a cold), these pressure differences increase the hearing threshold by decreasing the transmission of sound energy across the middle ear. Since the eardrum is a significant determinant of the transmission characteristics of the middle ear, it is important to understand its response to large static pressures.

Most experimental work on the mechanical behavior of the eardrum concentrates on its dynamic response. In contrast, very little work has focused on its static response, although because of technological limitations early investigators tried to elucidate the acoustical transmission characteristics of the eardrum using static pressures (e.g., Kessel, 1874; Dahmann, 1930). The first full-field quantitative measurements of static eardrum displacement patterns (Dirckx, 1990; Dirckx and Decraemer, 1991; Decraemer *et al.*, 1991) were done using a phase-shift shadow moiré interferometer. With this noncontacting optical device, the shape of a human cadaver eardrum was measured in response to a sequence of positive and negative static middle-ear pressures. Since then, moiré interferometry has also been used to measure the static mechanical response of the cat eardrum (Decraemer and Dirckx, 1991; Stoffels, 1993; Funnell and Decraemer, 1996) and of the gerbil eardrum (von Unge *et al.*, 1993, 1999; Dirckx *et al.*, 1998; Dirckx and Decraemer, 2001). Parnes *et al.* (1996) used electronic speckle-pattern interferometry to measure the response of the eardrum to static pressures, and Vorwerk *et al.* (1998) recorded the motion of the human eardrum in response to quasistatic pressures using an endoscope and a video-recording system.

All of the above experiments were performed with an intact middle ear; however, for purposes of modeling static eardrum response, it is also useful to study its mechanical response in isolation from middle-ear structures such as the ossicles and ligaments, by immobilizing the ossicles. Quantitative data on static eardrum displacement patterns with an immobile malleus would simplify refinement of existing computer models of the eardrum. In many such models (e.g., Funnell and Laszlo, 1978), assumptions are made about the material properties of the eardrum. For instance, the Young's modulus, or stiffness, of the eardrum is assumed to be constant over its surface. With the availability of experimental data, one could use numerical optimization techniques to determine distributions of material properties over the entire

[a)]Present address: Department of Medical Biophysics, Medical Sciences Building, The University of Western Ontario, London N6A 5C1, Canada. Electronic mail: hladak@uwo.ca
[b)]Electronic mail: robert.funnell@mcgill.ca

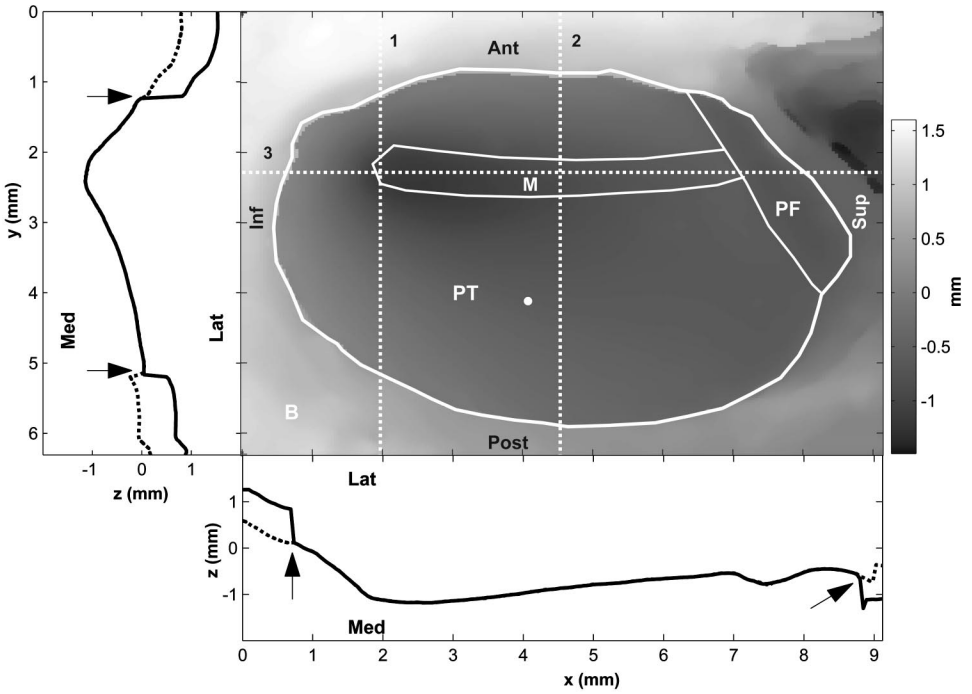

FIG. 1. Gray-level image of resting shape of eardrum of cat MY1216L. The thick white line encloses the visible portion of the eardrum. The pars tensa (PT), manubrium (M), and pars flaccida (PF) are outlined, and the surrounding bony tissue is indicated (B). The dot indicates a point on the pars tensa for which pressure-displacement curves are later plotted. The anterior (Ant), posterior (Post), inferior (Inf), and superior (Sup) directions are also indicated. These anatomical directions are approximate. The cat eardrum is actually tilted, so the pars flaccida is both posterior and superior (dorsal) and the manubrium runs in the antero-inferior to postero-superior direction. The bottom panel shows a horizontal profile through the umbo, and the leftmost panel shows a vertical profile through the umbo. The locations of the profiles are shown on the image by dotted lines 1 and 3; line 2 is referred to later in the text. The umbo is located at the intersection of lines 1 and 3. The medial (Med) and lateral (Lat) directions are indicated for the profiles. Solid profiles are after phase unwrapping with the coarse grating to determine the height of true jumps (see Sec. II E), whereas dotted profiles are after phase unwrapping but without using the coarse grating. The arrows indicate the locations of true jumps caused by overhanging ear-canal tissue.

surface of the eardrum. This would involve systematically adjusting the material properties until predicted displacement patterns match measured ones. Immobilizing the malleus would allow one to perform the optimization without having to take into account the additional complexity of the mechanical loading effects of the ossicular chain on the eardrum. Indeed, computer simulations of the eardrum with an immobile malleus have previously been used to study the effects of individual eardrum shape differences on the eardrum mechanical response (Funnell and Decraemer, 1996). The dynamic response of the eardrum has been studied experimentally under this condition in order to understand the effects of otosclerosis (Margolis *et al.*, 1978; Naito, 1990; von Unge *et al.*, 1991), but no such experiments have been reported for the static response.

The objective of this work was to measure the response of the cat eardrum to a sequence of static pressures before and after immobilizing the malleus. Complete loading/unloading cycles were measured repeatedly under both conditions.

II. METHODS

A. Apparatus

The shape of the eardrum is measured using phase-shift shadow moiré interferometry. In the moiré method, the shadow of a grating consisting of parallel lines is cast onto the surface to be measured. The shadow is a set of deformed lines and forms a moiré interference pattern when viewed through the original grating. The moiré interference images are recorded using a CCD camera and frame store. Four phase-shifted images are obtained by translating the object being measured away from the grating. The four images are combined mathematically, pixel by pixel, to form a single shape image in which the value of each pixel is proportional to the z coordinate of a point, and the column and row numbers of the pixel are proportional to the x and y coordinates, respectively. Mathematical details of the method can be found elsewhere (Dirckx *et al.*, 1988). The phase-shift moiré apparatus used in this work has been described previously (Dirckx and Decraemer, 1989). The depth-measuring resolution of the interferometer is 20 μm, and the spacings between pixels along the x and y axes are 46 and 32 μm, respectively.

As an example, Fig. 1 shows a gray-level image representing the ''resting shape'' of the eardrum of cat MY1216L. The resting shape is defined as the shape measured at the very start of a set of measurements with no pressure being applied. The gray levels in this image vary from black (points furthest from the reader) to white (points closest to the reader). The darker central region enclosed by the thick white line is the eardrum, whereas the lighter region surrounding it (B) represents the bony part of the ear canal. The areas of the eardrum corresponding to the pars tensa (PT), pars flaccida (PF), and manubrium (M) are roughly outlined by white lines. The large black area to the right of the pars

flaccida is a region of bone that is far from the reference plane of the moiré interferometer, and therefore not imaged correctly. A vertical profile through the umbo is shown to the left of the image, and a horizontal profile through the manubrium is shown at the bottom. The locations of the profiles are shown on the image by dotted lines 1 and 3. The umbo is located at the intersection of these two lines.

Note that there is no specific relationship between the columns and rows in the image and the anatomy. However, in all of the images acquired in this work, the manubrium was generally oriented to be approximately parallel to the *x* axis, i.e., it was parallel to the rows in the image.

B. Specimen preparation

Measurements were made on five fresh temporal bones obtained from adult cats (MY0923R, MY1216L, MY1630L, MY1721L, MY2626L), which had been used for purposes unrelated to the auditory system. The cats were sacrificed with an intracardiac injection of pentobarbital Na solution (60 mg/kg body weight). The temporal bones were removed from the cats approximately 15–30 min *post mortem*. When the temporal bones were removed, the auditory and facial nerves were cut. The bulla and petrous bones were intact. No holes were introduced into the middle ear, as evidenced by the ability to maintain a constant pressure in the middle-ear space during the measurement procedure, which is described in the next section.

In order to provide a good view of the eardrum, the ear canal is resected to within 1 mm of the eardrum. Since the moiré technique requires a diffusely reflecting surface, the lateral surface of the eardrum is coated with a thin uniform layer of drawing ink (Pelican Drawing Ink A, 18 White). This ink does not significantly affect the mechanical response of the eardrum (Dirckx and Decraemer, 1997). In order to apply pressures to the middle-ear cavities, a small hole is drilled in the middle-ear wall, and a plastic tube for applying pressures is glued to the hole using Loctite 406 cyanoacrylate, which provides an airtight connection. The specimen is then placed in the moiré apparatus. Total preparation time is about 2.5 to 3 h for a single specimen.

C. Measurement procedure

Three cycles of pressure are applied to the eardrum. Each cycle starts from rest (i.e., zero pressure in the middle-ear cavities) and involves loading the eardrum by applying positive middle-ear pressures in the order 0.1, 0.2, 0.4, 0.7, 1.1, 1.6, and 2.2 kPa, then unloading back to 0 Pa in the reverse order. The eardrum is then loaded by applying negative middle-ear pressures in the same order and unloaded in the reverse order. The pressure values used in this experiment cover the pressure range normally encountered in everyday life. We shall see that the displacement of the eardrum levels off at the extreme applied pressures, so that the entire displacement range is covered.

At each step in a cycle, the pressure is maintained at a constant value, and eardrum shape is measured using the moiré apparatus with a grating having a pitch of 4 lines/mm. A single shape measurement, including time to save the image to a hard disk, takes 45 s. A shape measurement is made 5 s after the pressure is adjusted to a new level. This ensures that both pressure and eardrum shape have stabilized. Once the eardrum shape is measured at a given level, the pressure is immediately changed to the next level. All three cycles are measured in immediate succession with no pauses in between. Once all three cycles have been measured, the grating is replaced by a coarser one having a pitch of 0.8 lines/mm, and a single unpressurized shape measurement is made. As explained in Sec. II E, the last measurement with the coarse grating is used as a guide for ''phase unwrapping.'' The time required to measure all three cycles and the shape with the coarser grating is about 1.25 h. A total of 86 shape measurements is made: 85 using the fine grating, and one using the coarse grating.

D. Mallear fixation

For three of the five specimens, after measurements had been made with a mobile malleus, the specimen was removed from the apparatus and the malleus was fixed to the middle-ear wall. (In one of the five cats, the malleus could not be fixed, and one other was used to investigate the effects of measurement time as discussed below.) A small hole is drilled in the middle-ear wall superior to the pars flaccida. In this region, the mallear neck and head are separated from the adjacent middle-ear wall by a small gap. Once the malleus is exposed, a small drop of glue (Loctite 406 cyanoacrylate) is placed on its head to fix the malleus to the intact portion of the middle-ear wall. The glue is placed on the mallear head when it is somewhat viscous so that it does not run onto the eardrum. This particular glue cures within seconds, which is much less than the time required to place the specimen back in the moiré interferometer. Once the glue is completely dry, the hole is sealed airtight with dental cement. When the middle ear is exposed to air, as in this procedure for fixing the malleus, the mucosal lining can dry out (Tonndorf and Khanna, 1972). To prevent desiccation of the lining while the malleus is being fixed, the above manipulations are done in the mist of a humidifier (Defensor 505). The mist was used to keep the outer surface of the bone moist and did not enter the middle-ear cavity. At the output of the humidifier, the mist formed a cloud with a diameter of approximately 30 cm, and the temporal bone was held in the middle of this cloud with the eardrum facing away from the output of the humidifier.

Once the malleus is fixed, the specimen is remounted in the moiré apparatus, and its response to static pressures is measured again as outlined in the previous section. The total time to fix the malleus and remount the specimen is 1.5 to 2 h. No leaks were detected around the sealed hole during subsequent pressurized shape measurements.

In one of the five specimens (MY1721L), the malleus was not fixed. Instead, after the first set of shape measurements was made, the specimen was left in the apparatus for 2 h, and shape measurements were then repeated. This specimen served as a control to assess changes in specimen shape and response with time.

E. Phase unwrapping

The z values at each pixel in a moiré shape image are computed as phase angles derived from the four phase-shifted moiré interference images, and the result is therefore ''wrapped'' into the range 0 to λ, where λ is the size of the ambiguities that must be unwrapped. The value of λ is obtained by calibration of the moiré interferometer (Dirckx and Decraemer, 1990). The z coordinates in the wrapped shape image must be ''unwrapped'' to produce a shape image such as the one in Fig. 1. The unwrapping is done by adding multiples of λ where required. For the measurements reported here with the fine grating of 4 lines/mm, $\lambda = 0.74$ mm. A two-step procedure is used to unwrap the wrapped images measured with the fine grating. First each wrapped image is unwrapped using an automatic method (Dirckx *et al.*, 1988; Dirckx, 1990; Funnell and Decraemer, 1996). The procedure involves first unwrapping the central column of the image; profile 2 in Fig. 1 indicates the location of the central column. The column is scanned pixel by pixel from its center to the top and then from the center to the bottom. During each scan, a running offset is added to each pixel. The offset is incremented or decremented by λ whenever the difference between two successive pixels exceeds a threshold value of $\pm\lambda/2$. Once the central column is unwrapped, each row is unwrapped in turn using the same procedure: each row is scanned first from the center to the left, then from the center to the right, and a running offset is added.

The above algorithm works well for smooth surfaces, but problems arise when there are true abrupt jumps in the z coordinates, as are present in the eardrum-shape images where the bony ear-canal tissue overhangs the periphery of the eardrum. The height of each jump is wrapped into the range 0 to λ It is not clear from examining the data how many multiples of λ need to be added to correctly reconstruct a jump. Although interest here is focused on the eardrum itself and not on the bony region surrounding it, it is necessary to reconstruct the height of this region properly for better visualization and, more importantly, for correct registration, which is described in the following section. Therefore, the second step in the unwrapping procedure involves correcting the heights of true jumps in unwrapped images measured using the fine grating. Abrupt height variations can be measured correctly if a larger value of λ is used so that all surface-height variations remain within the range 0 to λ (Zhao *et al.*, 1994). Since λ is proportional to the period of the grating, a coarser grating will result in a larger value of λ, denoted by λ_c. A grating with 0.8 lines/mm is therefore used to obtain a supplementary eardrum shape image at zero pressure (corresponding to the 86th measurement). For this grating, λ_c is 3.7 mm. Since all points on the eardrum are less than 3.5 mm away from the grating, images measured with this grating need not be unwrapped; moreover, the heights of true jumps are correctly determined since they are all less than λ_c. Given that the resolution obtained with the coarse grating is poorer than that obtained with the fine grating, the coarse grating cannot be used to make all shape measurements, especially in response to pressures where the induced shape changes—calculated as differences between shape images—are subtle. The measurement with the coarse grating simply serves as a guide for correcting unwrapped images measured with the fine grating. The image measured with the coarse grating is used to correct the first image measured with the fine grating by pairwise matching of the images: image 1 is compared with the one measured with the coarse grating pixel by pixel and integer multiples of λ are added to the former image to minimize the differences between the two images. Once image 1 is corrected, it is used to correct image 2. Once image 2 is corrected, it is used to correct image 3, and so on until all 85 images measured with the fine grating have been corrected. The images are corrected in this order since the z-coordinate difference between two images with different pressures may well be greater than λ unless the pressures are close together.

The dotted curves in Fig. 1 are vertical and horizontal profiles, after automatic unwrapping but before correction using the supplementary coarse image; the arrows indicate places where there are true jumps in the data that are not unwrapped properly. The solid curve is the same profile after pairwise matching with the image measured using the coarse grating: the heights of the jumps are unwrapped properly.

F. Data registration

As explained above, after the eardrum response is measured with a mobile malleus, the specimen is removed from the apparatus, the malleus is fixed, and the specimen is placed back in the apparatus for further measurements. When the specimen is replaced, its orientation with respect to the interferometer grating is usually not quite the same as before it was removed. The change in orientation involves a small rigid-body translation and rotation of the specimen with respect to the grating. To compare shape measurements made after mallear fixation with those made with a mobile malleus, the measured surfaces must be aligned or ''registered'' with respect to one another.

To register the data, a rigid-body transformation must be found which aligns the two data sets. While the eardrum may change shape, the bony region surrounding the eardrum does not change shape with pressure or time and can be used to find the transformation. The Iterative Closest Point (ICP) algorithm by Besl and McKay (1992) is used to calculate the transformation. Given an initial estimate of the rigid-body transformation, the algorithm iteratively refines it until points on one surface (here, the bony region in the fixed-malleus data set) are aligned with their closest counterparts on a reference surface (the bony region in the data set with a mobile malleus). The iterations stop when the mean-square distance between corresponding points on the two surfaces does not change significantly between iterations. The advantage of the ICP algorithm is that it does not require one to identify corresponding landmarks on both surfaces, which is difficult to do very accurately; however, it is necessary to provide an initial estimate of the transformation.

A simple technique is used to find an initial transformation. Features are roughly identified on the bone in the shape image with a mobile malleus, and corresponding features are identified in the image with a fixed malleus. The bone surrounding the eardrum contains some features (e.g., sharp cor-

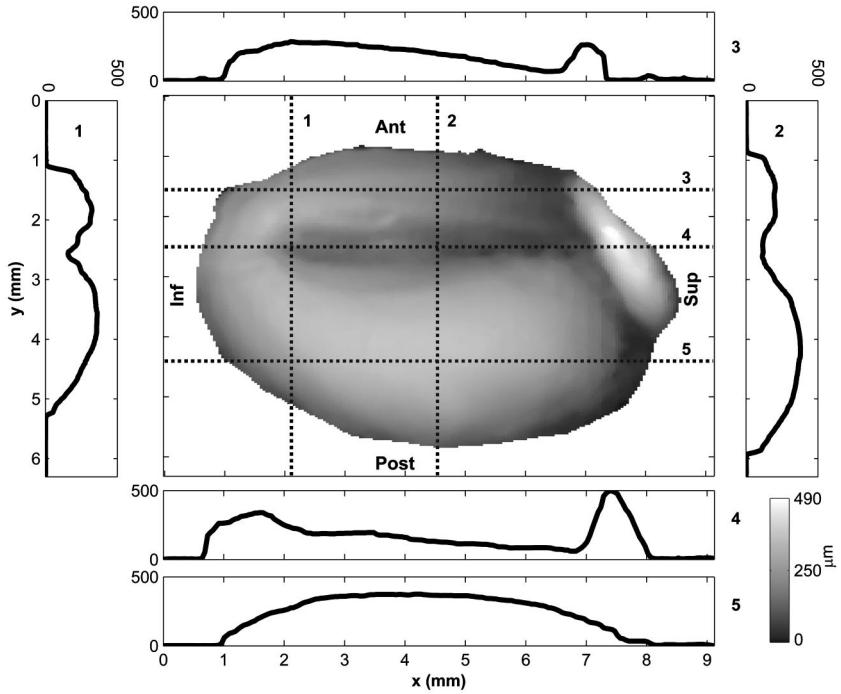

FIG. 2. Gray-level displacement image and profiles for cat MY1216L measured at a pressure of +2.2 kPa during the first cycle. The gray levels in the image are proportional to displacement magnitude with white corresponding to the largest displacement (490 μm, occurring in the pars flaccida) and black to the smallest (0 μm). Dotted lines indicate where the profiles are extracted from. Profile 1 was taken through the umbo; 2 was extracted halfway along the manubrium and perpendicular to it; 3 was taken midway in the anterior pars tensa; 4 passes through the length of the manubrium; and 5 passes through the point of maximal pars-tensa displacement. Displacements indicated on the profiles are in μm.

ners formed by the resection process) that can be identified in both images. The features do not represent the same anatomical landmark from one cat to the next, but they are points that are easy to identify in two different shape images of the same eardrum. The correspondences are not exact, but are good enough for an initial estimate. Generally about 10–15 points are used. Once the points are identified, the rigid-body transformation that maps points in the fixed-malleus image to points in the mobile-malleus image is estimated by minimizing the mean-square distance between the two sets of points. The minimization technique described by Horn (1987) is used because it is efficient, requiring no iterations. Since the correspondences are not exact, the transformation is not very good and needs to be refined using the ICP algorithm described above.

The root-mean-square difference in z coordinates of the bony region, after registration of the fixed-malleus data to the mobile-malleus data, was within 30 μm, indicating good registration.

III. RESULTS

A. Mobile malleus

1. Full-field displacement patterns

Changes in eardrum shape produced by the application of pressure are subtle and difficult to see in gray-level representations of the pressurized shape data. To emphasize these changes, full-field displacement patterns are presented in this section, and profiles through the shape data are presented in the next section. The displacement field for a pressure p, denoted as $\Delta z_p(x,y)$, is defined as $\Delta z_p(x,y) = z_p(x,y) - z_0(x,y)$, where $z_p(x,y)$ is the shape measured at pressure p and $z_0(x,y)$ is the resting shape measured at the very start of the experiment.

Figure 2 shows a gray-level image of the displacement field for cat MY1216L for the largest positive pressure used in this study (+2.2 kPa) during the first cycle of pressurization. The gray levels in the image are proportional to displacement magnitude, with white corresponding to the largest displacement (490 μm, occurring in the pars flaccida) and black to the smallest (0 μm). Also shown are profiles through the displacement field; the locations of the profiles are shown on the image by dotted lines. Displacements of the pars tensa, both anterior and posterior, are larger than manubrial displacements; this is best seen in profiles 1 and 2. The posterior pars tensa displaces more than the anterior pars tensa. As seen in profile 5, a broad maximum occurs in the posterior pars tensa. The largest pars-tensa displacement is 380 μm. The manubrium appears to be rigid, with manubrial displacements (profile 4) increasing approximately linearly from the superior end to the inferior end. The displacement of the umbo is 250 μm. As indicated by profiles 3 and 4, the pars flaccida bulges considerably, having a maximum displacement of 490 μm. The ends of some of the profiles stop abruptly as the periphery of the eardrum is obscured by overhanging tissue.

Figure 3 shows iso-amplitude displacement contours at +2.2 kPa for all five cats. The difference in amplitude between adjacent contours is 50 μm. As a guide, some of the contours are labeled. The thick black line represents the outline of the visible portion of the eardrum. Patterns for the other cats are qualitatively similar to that for cat MY1216L, but there are some differences, especially in displacement magnitudes. For cats MY1630L, MY2626L, and MY1721L, pars-flaccida displacements are not as large as pars-tensa displacements. In cat MY0923R, the largest pars-tensa displacement occurs in the anterior region, as opposed to the posterior region as in the other cats. Visual inspection of this specimen did not reveal any pathology which could have resulted in localized differences in compliance.

Displacement patterns for other pressures and cycles are qualitatively similar. For extreme negative pressures, how-

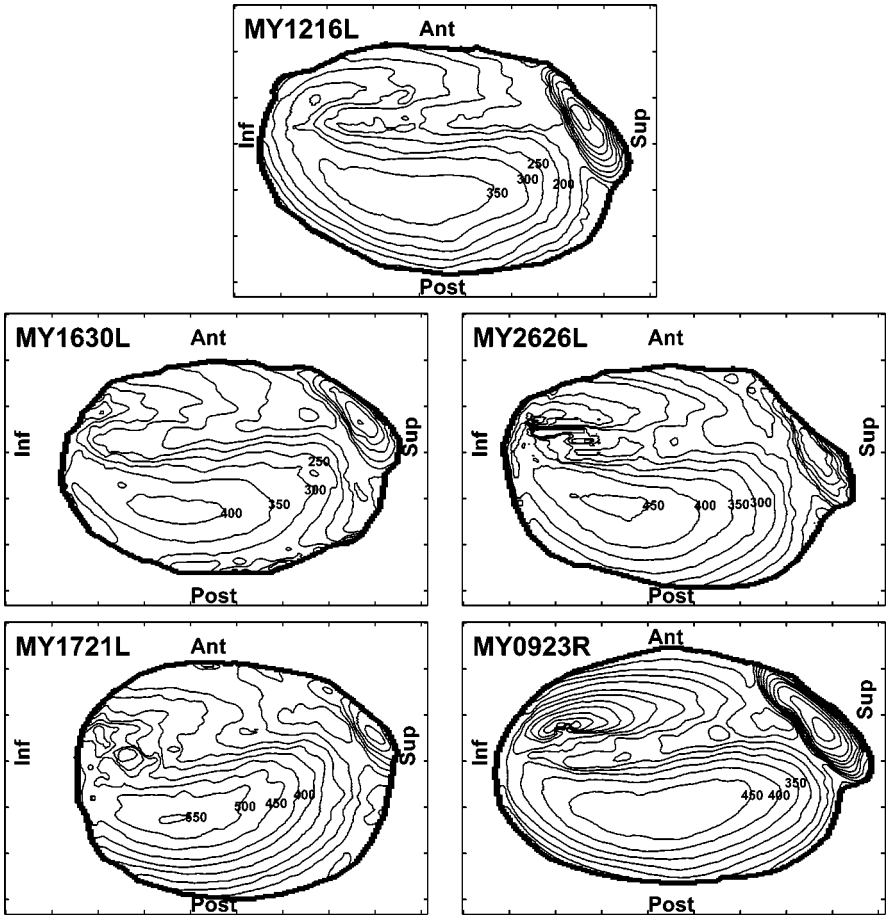

FIG. 3. Iso-amplitude displacement contours for all cats used in this study, measured at a pressure of +2.2 kPa during the first cycle. Displacements are in μm, and adjacent contours are 50 μm apart. Note that in cat MY0923R measurements were made on the right ear instead of the left ear as in the other cats. To facilitate comparison of MY0923R with the other cats, the image of the eardrum was mirrored to look like the others.

ever, the location of the maximum pars-tensa displacement is slightly inferior to that for positive pressures.

2. Pressurized shape profiles

Changes in eardrum curvature are best shown by plotting profiles through the pressurized shape data. Figure 4 shows vertical profiles through the pressurized shape data for cat MY1216L. The profiles are taken at the same location as profile 2 in Fig. 1. Panel (a) shows the response to positive pressures during loading (i.e., while the pressure is increased from 0 Pa to +2.2 kPa), whereas panel (b) shows the response to negative pressures, also during loading (i.e., the

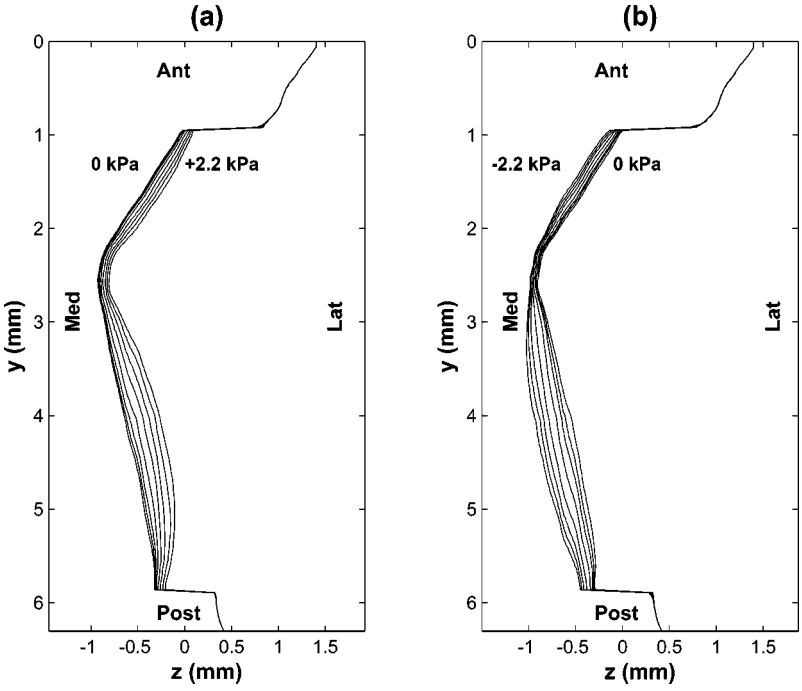

FIG. 4. Vertical profiles through pressurized shape data for cat MY1216L, where z is the height of each point on the eardrum relative to the tympanic ring. The profiles are taken through a point halfway along the manubrium and perpendicular to it. (a) For first cycle while sequentially loading from 0 kPa (leftmost profile) to +0.1, +0.2, +0.4, +0.7, +1.1, +1.6, and finally +2.2 kPa. (b) For first cycle while loading from 0 kPa (rightmost profile) to −0.1, −0.2, −0.4, −0.7, −1.1, −1.6, and −2.2 kPa.

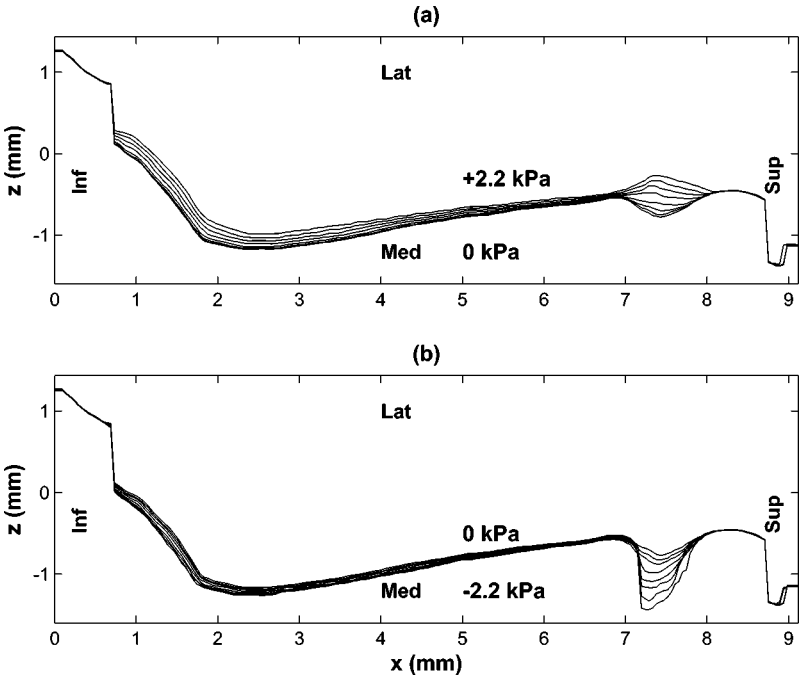

FIG. 5. Horizontal profiles through pressurized shape data for cat MY1216L. The profiles are taken through the manubrium. (a) For first cycle while loading from 0 to +2.2 kPa. (b) For first cycle while loading from 0 to −2.2 kPa.

pressure is changed from 0 Pa to −2.2 kPa). The displacements do not reach zero at the anterior and posterior ends because the periphery of the eardrum is hidden beneath overhanging tissue.

The description of eardrum convexity and concavity in this paragraph refers to the sections of the eardrum shape profile anterior and posterior to the manubrium in Fig. 4. In the rest position [0 kPa, panel (a)], both sections of the eardrum are almost straight in their paths from the manubrium to the tympanic ring. Positive middle-ear pressures make both sections convex outward. When the pressure is returned to zero [panel (b)], the unpressurized shapes of both sections are now slightly convex outward and are somewhat different from the resting shapes measured at the beginning of the experiment. Small negative pressures straighten both sections, and extreme negative pressures make them concave. When the pressure is returned to zero after the negative excursion, both sections of the shape profile (not shown) are slightly concave and are again different from profiles previously measured at zero pressure. Similar patterns are seen in profiles for the other cats: anterior and posterior sections of the eardrum become increasingly convex outward with larger positive middle-ear pressures, but become straighter and finally concave with negative middle-ear pressure.

Displacements of the manubrium and pars tensa are asymmetric with respect to the sign of the applied pressure, with the lateral displacements caused by positive middle-ear pressures being larger than the medial displacements caused by negative pressures. The asymmetry appears to be more pronounced for the manubrium than for the pars tensa.

Figure 5 shows horizontal profiles through the manubrium of cat MY1216L, at the same location as profile 3 in Fig. 1. Panel (a) shows the response to positive middle-ear pressures during loading, whereas panel (b) shows the response to negative pressures. As mentioned above, the manubrium appears to be rigid and has smaller displacements superiorly. The portion of the pars tensa inferior to the umbo in these profiles is convex outward in its resting position, and becomes even more curved when positive pressures are applied. Negative pressures reduce the curvature of this portion, but do not make the pars tensa concave or even straight in this area.

The pars flaccida, located superior to the manubrium, bulges considerably. In its initial state it is concave, but it becomes convex outward with positive pressures. The pars flaccida is sucked further into the middle-ear cavity when negative pressures are applied.

3. Pressure-displacement curves

Figure 6 shows how displacements for a typical point on the pars tensa vary with pressure and cycle for cat MY1216L. The point is located in the posterior pars tensa, and is indicated by the dot in Fig. 1. Eardrum response is nonlinear, with displacements growing less than in proportion to applied pressure, as seen by the S shape of the pressure-displacement curves. For instance, the maximal displacement is 258 μm at a pressure of +1.1 kPA during the first cycle while loading, whereas it is only 380 μm at a pressure of +2.2 kPA during the same cycle. Although the pressure was doubled, the maximal displacement increased by a factor of only 1.38. As noted above, the response of the eardrum is asymmetric with respect to the sign of the applied pressure: lateral displacements caused by positive middle-ear pressures are larger than medial displacements caused by negative pressures. This is particularly noticeable at the extreme pressures. For example, the displacement magnitude is 380 μm at a pressure of +2.2 kPa during the first cycle, whereas it is only 314 μm at −2.2 kPa for the first cycle. The curves exhibit hysteresis, with displacements measured during unloading being larger than those measured during loading. The hysteresis seen here was also found by Dirckx

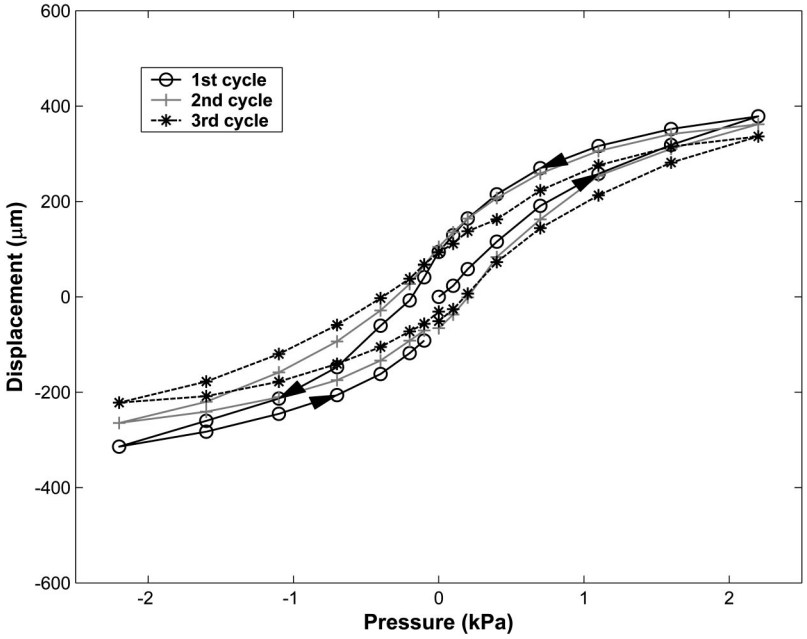

FIG. 6. Pressure-displacement curves for cat MY1216L taken through a point in the posterior pars tensa, for three cycles labeled with different symbols. The arrows indicate the temporal order of the measurements. Lateral displacements are positive, whereas medial displacements are negative.

and Decraemer (2001) in the gerbil. Displacement magnitudes also vary from cycle to cycle, generally decreasing from the first cycle to the last. In general, the behavior of soft tissue such as the eardrum depends upon its history, and the shape of the hysteretic force-displacement loop may change from one cycle to the next. If the material is taken through the same load cycle repeatedly, the force-displacement curve will normally converge to a stable shape; the material is said to have been ''preconditioned'' (Fung, 1993). Preconditioning has been observed in tympanometry (Gaihede, 1996). It is not clear whether the variations from cycle to cycle in the current study are due to gradual *post-mortem* changes or to the lack of a sufficient number of preconditioning cycles, or to a combination of both.

Pressure-displacement curves for the other cats are similar except for differences in displacement magnitudes and in the degree of hysteresis. In cat MY1630L, displacements for negative pressures during unloading are, for the most part, smaller than during loading; the opposite is true in the other cats. In cat MY1721L, there is very little variation from one cycle to the next.

B. Immobile malleus

1. Full-field displacement patterns

Figure 7 is a gray-level displacement image for cat MY1216L for a pressure of $+2.2$ kPa for the first cycle of loading, with the malleus immobilized. Displacement images for other positive pressures are similar. (The displacement image is computed after registration.) With a fixed malleus,

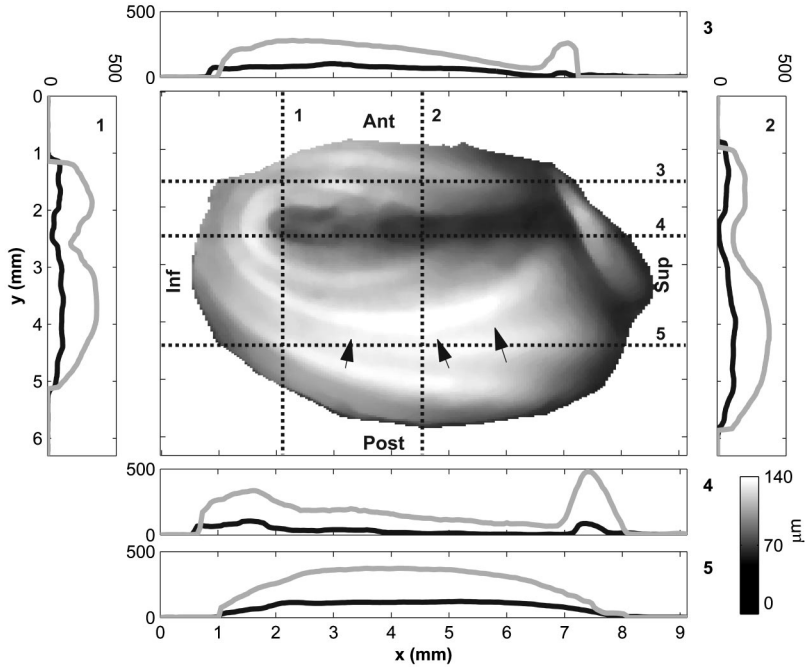

FIG. 7. Gray-level displacement image and profiles for cat MY1216L measured at a pressure of $+2.2$ kPa during the first cycle after immobilizing the malleus. Dotted lines indicate where the profiles are extracted from, with black profiles corresponding to the fixed-malleus data and gray profiles corresponding to the mobile-malleus data. Displacements indicated on the profiles are in μm. The arrows indicate artifacts that show up as dark bands in bright regions of the displacement image; the arrows outline the path of one such band.

TABLE I. Displacement of the pars flaccida before and after mallear fixation measured at a pressure of +2.2 kPa during the first cycle of pressurization.

	Displacement		
	Fixed (μm)	Mobile (μm)	Fixed/mobile
MY1216L	100	490	20%
MY1630L	320	380	84%
MY0923R	415	630	66%

artifactual bands resembling iso-depth contours are visible, and show up as dips and peaks in the displacement profiles. The bands are the dark streaks in areas where the displacement image should be white. As an example, one of the bands is shown by arrows in Fig. 7. The bands are caused by very small systematic errors associated with the shape-reconstruction algorithm used with the moiré apparatus (Ladak *et al.*, 2000). Although the errors are small and completely masked for the large displacements observed with a mobile malleus at high pressures, they are not completely masked for small displacements. The black profiles are for the fixed-malleus data, and the gray ones are for the mobile-malleus data. Profile 4 shows that the manubrium is immobile, or almost so, along most of its length. Profile 2 further illustrates that the manubrium is practically immobile superiorly, whereas profile 1 shows that the manubrium displaces slightly near the umbo.

For this cat, with a fixed malleus there is a broad displacement maximum in the posterior pars tensa with a magnitude of 140 μm; this value is about 37% of the corresponding maximum value for the mobile-malleus case. For cats MY1630L and MY0923R, the maximum pars-tensa displacements with fixed mallei were 52% and 46% of the mobile-malleus values, respectively.

The maximum pars-flaccida displacement for cat MY1216L is 100 μm, which is only about 20% of the value for the mobile case. This is a surprisingly large decrease. For cats MY1630L and MY0923R, the maximum pars-flaccida displacements with fixed mallei were 84% and 66% of the mobile-malleus values, respectively. Table I lists maximal pars-flaccida displacements before and after mallear fixation, as well as the ratio of displacement after fixation to displacement in the mobile-malleus case.

Figure 8 shows fixed-malleus iso-amplitude displacement contours for all three cats. The difference in amplitude between adjacent contours is 25 μm. The patterns are somewhat distorted by the systematic errors discussed above. The patterns are qualitatively similar, although the pattern for cat MY0923R exhibits a strong maximum in the anterior pars tensa as well as in the posterior pars tensa. In cats MY1630L and MY0923R, the manubrium displaces more than in cat MY1216L. Examination of the specimens after the experiments indicated that the head of the malleus in each of these cats was indeed fixed to the middle-ear wall. However, it is possible for the manubrium to bend. The displacement of the umbo and of the superior end of the manubrium are tabulated in Table II for all three cats in which the malleus could be fixed. Ideally, if the manubrium is perfectly fixed, displacements along its length should be zero. For comparison, the displacement with a normal mobile malleus is also listed. The ratio of fixed/mobile displacement is a measure of the degree of manubrial fixation, with values closer to zero indicating more fixation relative to the mobile case. Results are reported for a pressure of +2.2 kPa because this represents an extreme case for which manubrial displacement would be largest. As can be seen, with a mobile malleus, the manubrium of cat MY0923R displaces more than that of cat MY1630L, and the manubrium of cat MY1630L displaces more than that of cat MY1216L except near the superior end. The same trend is observed in manubrial displacements after mallear fixation, with the manubrium of MY0923R displac-

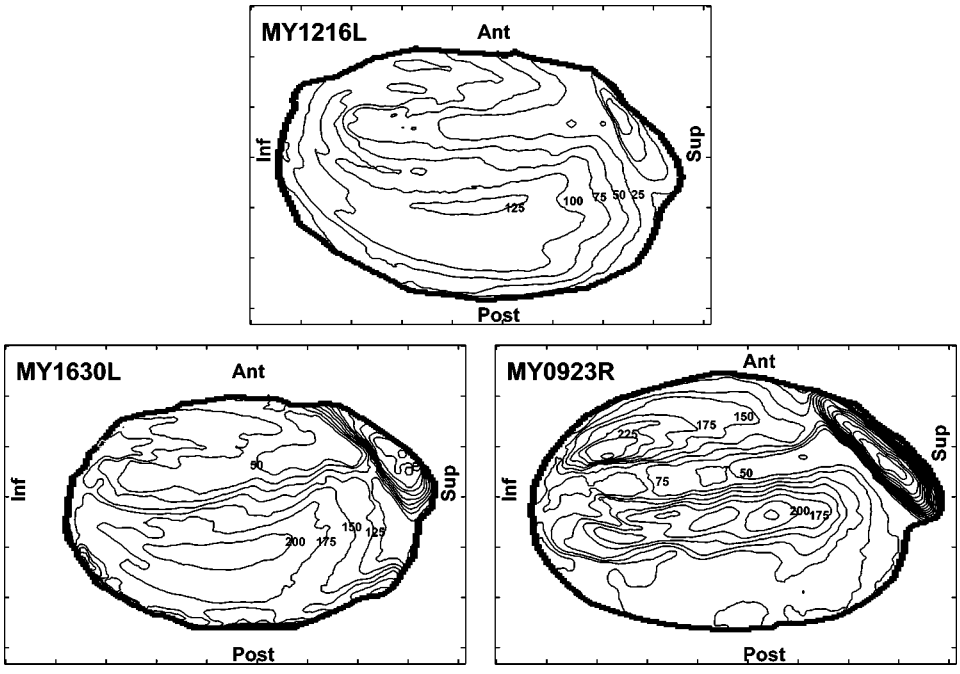

FIG. 8. Iso-amplitude displacement contours for all cats in which the malleus was immobilized. The data are for a pressure of +2.2 kPa during the first cycle. Displacements are in μm, and adjacent contours are 25 μm apart. Note that in cat MY0923R measurements were made on the right ear instead of the left ear as in the other cats. To facilitate comparison of MY0923R with the other cats, the image of the eardrum was mirrored to look like the others.

TABLE II. Displacements of the umbo and superior end of manubrium before and after mallear fixation measured at a pressure of +2.2 kPa during the first cycle of pressurization.

	Displacement at umbo			Displacement at superior end of manubrium		
	Fixed (μm)	Mobile (μm)	Fixed/mobile	Fixed (μm)	Mobile (μm)	Fixed/mobile
MY1216L	32	156	21%	5	70	7%
MY1630L	54	181	30%	10	60	17%
MY0923R	68	226	31%	20	90	22%

ing more than that of MY1630L, which displaces more than that of MY1216L. The fixed/mobile ratio indicates that the manubrium of cat MY1216L is better fixed than that of cats MY1630L and MY0923R. Furthermore, the degree of manubrial fixation in cat MY1630L is greater than that in cat MY0923R at the superior end of the manubrium. Manubrial displacements with a fixed malleus are small and remain small during pressurization.

Displacement patterns for negative pressures in all cats except MY0923R are similar to those for positive pressures, but the location of the pars-tensa maximum is pushed slightly in the postero-inferior direction. In cat MY0923R, the displacement pattern becomes considerably simpler than that for positive pressures, and the location of maximum displacement occurs in the posterior pars tensa as opposed to the anterior pars tensa as it does for positive pressures in this cat.

2. Pressurized shape profiles

Figure 9 shows vertical profiles through the pressurized shape data for cat MY1216L after mallear fixation and registration to the mobile-malleus data. The profiles are taken at the same location as profile 2 in Fig. 1. For clarity, only profiles for pressures of 0 (very first measurement), ±1.1 and ±2.2 kPa are shown; the fixed-malleus profiles are in black. Superimposed in gray are corresponding profiles for pressures of ±2.2 kPa for the mobile-malleus case. The sections of the pars tensa both anterior and posterior to the manubrium in these profiles are convex outward at rest and the curvature increases with positive middle-ear pressures. Negative pressures straighten both sections, but in the fixed-malleus case do not make them concave in this particular cat. In the other cats, extreme negative pressures do make both sections of the pars tensa slightly concave in vertical profiles extracted at the same location, but the change in shape is not as dramatic as with a mobile malleus.

3. Pressure-displacement curves

With a fixed malleus, the pressure-displacement curves that were obtained vary considerably from cat to cat, and are described individually here. Figure 10(a) is a pressure-displacement curve for cat MY1216L; the curve is for the same point as that shown in Fig. 1 by the dot. The curves show the same general features as those for the mobile-malleus data. During the first cycle, displacements increase less than in proportion to the applied pressure. For example, when the pressure is doubled from +1.1 to +2.2 kPa, the displacement increases by only 1.6 times. Nonlinearity is more pronounced for the unloading branch than for the loading branch. Displacements for the next two cycles are smaller than for the first cycle, and the loading branches appear to be almost linear.

Figure 10(b) shows pressure-displacement curves for cat MY1630L. Nonlinearity is more pronounced in this cat. Displacement magnitudes for the first two cycles and the positive part of the third cycle are similar, but for the negative part of the third cycle the displacement magnitudes are much smaller than for the other cycles. It is not clear why the third cycle is so different; there was no leakage in the pressurization apparatus.

Figure 10(c) shows the same curves for cat MY0923R. In this cat, displacements vary considerably from cycle to cycle. The first cycle is very different from the second and third, which are quite similar. During the first cycle, medial

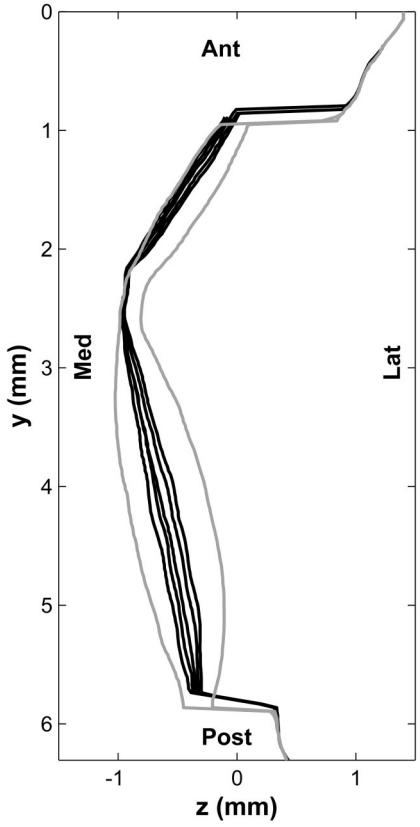

FIG. 9. Vertical profiles through pressurized shape data for cat MY1216L. Fixed-malleus (black) and mobile-malleus (gray) data are shown after registration. The profiles are taken through a point halfway up the manubrium.

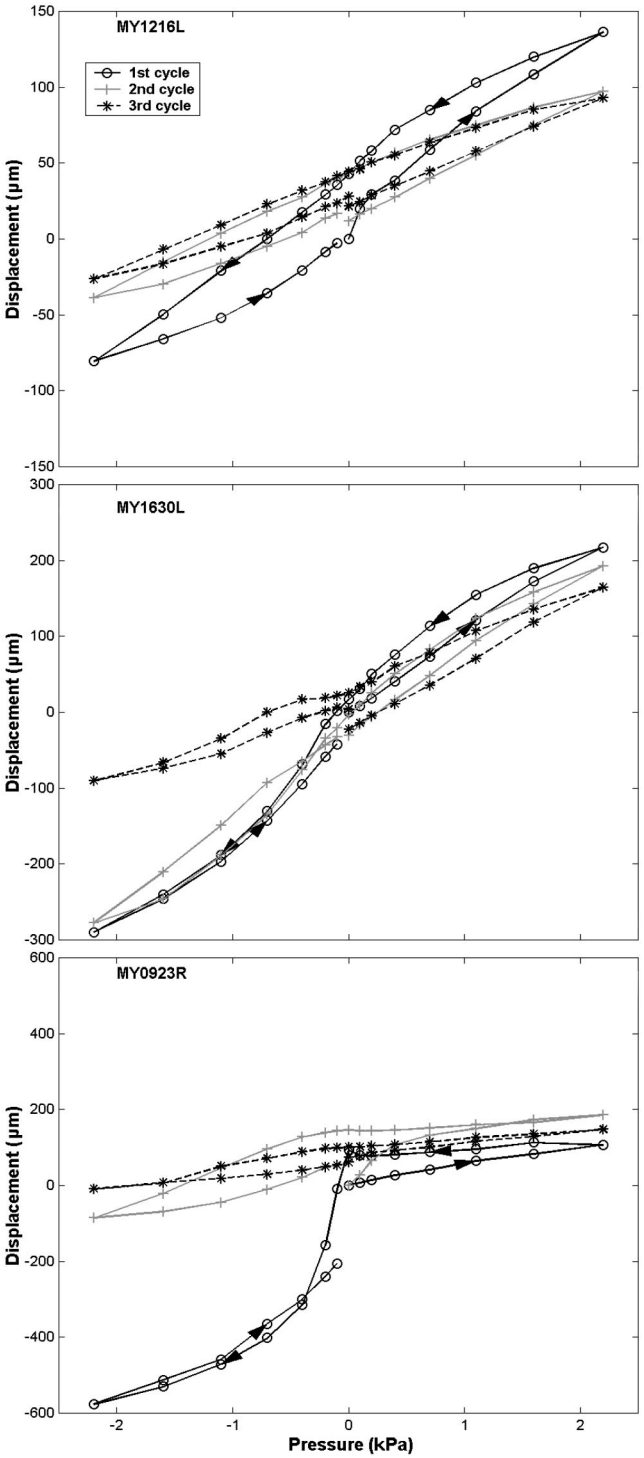

FIG. 10. Pressure-displacement curves for cats MY1216L, MY1630L, and MY0923R after mallear fixation for a point in the posterior pars tensa. The arrows indicate the temporal order of the measurements. Lateral displacements are positive, whereas medial displacements are negative.

displacements in response to negative middle-ear pressures are much larger than lateral displacements due to positive pressures. After the negative excursion, the eardrum does not return to its original shape, and the unpressurized shape measured at the beginning of the second cycle is considerably different from that measured at the beginning of the experiment.

4. Effects of measurement time

In cat MY1721L, the malleus was not fixed. Instead, the response to a sequence of three cycles was first measured and then, after a wait of 2 h (which was the longest time required to fix the malleus in the other specimens), the response to another three cycles was measured. This specimen serves as a control to test what effects, if any, measurement time and mallear-fixation time have on the response. Figure 11 shows pressure-displacement curves for a typical point on the pars tensa; the black curve is for the first set of three measurements, whereas the gray one is for the second set. As the responses were similar from one cycle to the next in any one set of measurements for this cat, all three cycles for one set of measurements were averaged in order to simplify the graph. Displacements measured during the second sequence of loading are generally smaller than those measured during the first sequence. The largest difference in displacement magnitude over the entire surface of the pars tensa is less than 50 μm and occurs at the highest pressures. This value is much smaller than the difference seen after malleus fixation, implying that measurement and fixation times have only a small effect on eardrum behavior. For comparison, the largest difference in pars-tensa displacement after mallear fixation and at a pressure of $+2.2$ kPa (first cycle) was 240 μm for cat MY1216L, 225 μm for cat MY1630L, and 325 μm for cat MY0923R.

IV. DISCUSSION

The displacement patterns previously measured in response to large static pressures in cats (Stoffels, 1993), humans (Dirckx and Decraemer, 1991), and gerbils (von Unge *et al.*, 1993; Dirckx and Decraemer, 2001), with a normal mobile malleus, are similar in that the pars-tensa displacements are always larger than manubrial displacements, with the largest pars-tensa displacements generally occurring in the posterior region rather than in the anterior region. With the exception of one cat (MY0923R), the displacement patterns measured in this work are similar to those measured previously. Modeling studies indicate that eardrum response is sensitive to variations in shape, stiffness, and thickness (e.g., Funnell and Laszlo, 1978), each of which may vary not only among cats but also spatially across the surface of the eardrum in any particular cat. Finite-element calculations utilizing subject-specific shape information for cat MY0923R indicated that local variations in shape do not alone account for all of the differences between displacement patterns for cat MY0923R and the other cats (Ladak, 1998). Furthermore, there were no visible localized differences in thickness. It is quite plausible that the local stiffness of the anterior pars tensa in this cat was lower than that of the posterior pars tensa, resulting in larger displacements in the anterior region.

This is the first time that complete loading and unloading cycles have been measured in cats. The observed pressure-displacement curves indicate that eardrum response is not elastic, i.e., the original shape of the eardrum is not restored when loads are removed. The eardrum, like many other tissues, is viscoelastic (Decraemer *et al.*, 1980). The

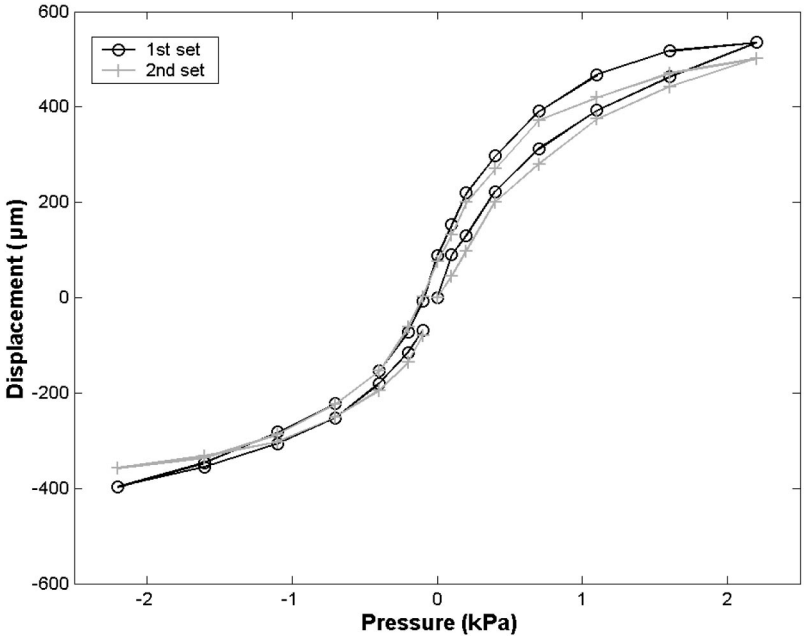

FIG. 11. Averaged pressure-displacement curves for cat MY1721L taken through a point in the posterior pars tensa. The second set was taken 2 h after the first set. Each set consists of three cycles averaged together. Lateral displacements are positive, whereas medial displacements are negative.

multiple loading/unloading cycles measured in each eardrum in this work are more repeatable than those measured previously in cats (Stoffels, 1993) because a stricter schedule and protocol were followed for the measurements reported here. The response of soft tissues generally depends on their loading/unloading histories. Indeed, in clinical tympanometry differences in measurement protocol do result in pronounced differences in tympanometric data (Osguthorpe and Lam, 1981).

With a mobile malleus, eardrum response is complicated by the mechanical load exerted on it by the rest of the middle ear. For instance, at high pressure levels, ossicular response in humans is known to be asymmetric and nonlinear (Hüttenbrink, 1989), which in turn affects eardrum response. Asymmetry in ossicular displacements at high pressures has been said to arise from slippage in the joints between the malleus and the incus and between the incus and the stapes (Guinan and Peake, 1967; Cancura, 1980; Hüttenbrink, 1989; Decraemer *et al.*, 2003)—the joints are easily stretched by large positive middle-ear pressures but are only slightly compressed by negative pressures. Another source of nonlinearity in the ossicular response may be the annular ligament connecting the stapes to the oval window, which limits the displacement of the stapes (Price, 1974; Price and Kalb, 1986; Pascal *et al.*, 1998); indeed, Price and Kalb (1991) feel that this is the main source of nonlinearity in middle-ear response at high pressures.

In order to characterize the behavior of the eardrum independently of the ossicular chain, experiments with an immobile malleus were conducted. This permits comparison with a finite-element model of the eardrum, for example, without the complication of a complete middle-ear model. With an immobile malleus, pars-tensa displacements decrease because of the decreased mobility of the manubrium. Even with an immobile malleus, the eardrum response is seen to exhibit features such as nonlinearity, asymmetry and hysteresis, although the degree of nonlinearity is somewhat reduced. There are considerable differences in pressure-displacement curves measured among the three cats, which could reflect interindividual differences in shape, stiffness, and thickness. The eardrum displacements reported here for large static pressures after mallear fixation are several times larger than the thickness of the eardrum; this suggests that, at the very least, geometric nonlinearities must be taken into account in constructing finite-element models of the eardrum that are valid at high pressures (Ladak and Funnell, 1995). It may also be necessary to consider nonlinearities of material properties. In any case, it appears that eardrum nonlinearity cannot be completely ignored in comparison with nonlinearities arising from other middle-ear structures, as has been assumed by previous investigators (Price and Kalb, 1991; Wada and Kobayashi, 1990).

With reference to Figs. 7 and 8 and Table II, it is clear that the technique used to render the malleus immobile does not result in every point on the manubrium having exactly zero displacement. Although the point on the mallear head that is glued to the middle-ear wall remains fixed, the manubrium appears to bend. The apparent bending of the manubrium observed here may be consistent with the manubrial bending discussed by Funnell *et al.* (1992) and Decraemer *et al.* (1994), although it is difficult to quantitatively compare that bending, in the linear regime at frequencies of 2 kHz and higher, with the present relatively low-resolution static measurements in the nonlinear regime. The 1992 and 1994 results suggested that there is likely to be less bending at lower frequencies, which is consistent with the fact that pronounced bending is not seen in the present measurements.

Displacement patterns for the pars flaccida are qualitatively similar before and after mallear fixation and between individuals. However, there is considerable interindividual variability in the size of the displacements both before and after mallear fixation. In all cases, displacement magnitude decreases after mallear fixation, but the degree of decrease as indicated by the fixed/mobile ratio in Table I exhibits interindividual differences. Variability in this decrease may be related to individual differences in the properties of the pars

flaccida or to the degree of manubrial fixation. One might expect that the greater the degree of manubrial fixation is, the greater the decrease in pars-flaccida displacement will be after fixation. Note that in cat MY1216L the decrease in pars-flaccida displacement is dramatic, as is the decrease in manubrial displacements, particularly at the superior end. In cats MY1630L and MY0923R, the degree of decrease in manubrial displacement is not as large as in cat MY1216L, and neither is the degree of decrease in pars-flaccida displacements. However, the relationship between degree of mallear fixation and pars-flaccida mobility is not clear from these data since in cat MY1630L the malleus is less mobile after fixation than in cat MY0923R, while the degree of decrease of pars-flaccida displacement in cat MY1630L is lower than that of cat MY0923R. Experiments in the same animal in which the degree of manubrial fixation is varied would certainly help address whether the variability in the degree of decrease in pars-flaccida displacement is related to the degree of manubrial fixation.

V. CONCLUSION

In this study, the shape of the cat eardrum was measured with a normal mobile malleus and an immobile malleus during cyclical loading with static middle-ear pressures up to ± 2.2 kPa. The shape was monitored throughout the loading and unloading phases, and three complete cycles were observed. The use of a coarse grating, to complement the fine grating used for most of the measurements, was shown to permit resolution of the phase ambiguities of the moiré technique at locations where the bony ear canal overhangs the eardrum.

Displacement patterns with a mobile malleus show that pars-tensa displacements are larger than manubrial displacements, as expected, with the maximum pars-tensa displacement occurring in the posterior region in all cats except one. For both the mobile-malleus and immobile-malleus cases, the eardrum response is nonlinear with displacements growing less than in proportion to applied pressure. Moreover, the response is asymmetric, with lateral displacements (caused by positive middle-ear pressures) being larger than medial displacements. With a mobile malleus, manubrial displacements exhibit more pronounced asymmetry than pars-tensa displacements. In both cases, displacement magnitudes vary from cycle to cycle.

Considerable variability was observed in the responses to negative pressures. The eardrum shape may change from being convex outward to being concave. The erratic results for negative pressures might be due to a mechanical instability such as snap-through buckling of the eardrum. This is a form of instability in which a sudden jump from one equilibrium configuration to a very different equilibrium configuration occurs at a specific pressure, and is observed as a local reversal in curvature. As mentioned previously, eardrum mechanical response is sensitive to shape changes, and the sudden shape changes associated with snap-through buckling could produce a drastically different displacement when the pressure is changed than would be expected if snap-through did not occur.

Although the results presented here (e.g., Fig. 11) indicate that the underlying mechanical properties of the eardrum did not necessarily change much during the course of the experiment, more work is required to clarify the roles of variability, preconditioning, and *post-mortem* effects.

This work provides a basis for constructing and validating models of the nonlinear response of the eardrum in response to large static pressures. Beyond that, it will contribute to the interpretation of measurements of the response of the entire middle ear to large static pressures (Decraemer *et al.*, 2003) and ultimately to the detailed modeling of the mechanics and acoustics of tympanometry. Once nonlinear models such as that proposed by Ladak and Funnell (1995) are validated using the data measured in this work, such models can, in principle, be used to simulate any loading pattern, including static pressure applied to the lateral side of the eardrum as in tympanometry. Furthermore, by including inertial and damping effects in such models, it would be possible to simulate the response to sinusoidal tones superimposed on static pressures as in tympanometry.

ACKNOWLEDGMENTS

Funding for this work was provided through an operating grant from the Canadian Institutes of Health Research (W.R.J.F.), and through fellowships from the Natural Sciences and Engineering Research Council of Canada (H.M.L.) and the Québec-Belgium Exchange Program (H.M.L.). We thank J. Lauzière for editing the manuscript.

DEDICATION

This paper is dedicated in memory of Amina Ladak, Maurice B. Decraemer and L. Grace Funnell.

Besl, P. J., and McKay, N. D. (**1992**). ''A method for registration of 3-D shapes,'' IEEE Trans. Pattern Anal. Mach. Intell. **14**, 239–256.

Cancura, W. (**1980**). ''On the statics of malleus and incus and on the function of the malleus-incus joint,'' Acta Oto-Laryngol. **89**, 342–344.

Dahmann, H. (**1930**). ''On the physiology of hearing: Experimental studies on the mechanics of the ossicular chain, as well as on the behaviours of tones and air pressure II–IV,'' Zeitschr. f. Hals. Nas. Ohrenheilkd. **27**, 329–368.

Decraemer, W. F., and Dirckx J. J. J. (**1991**). ''Moiré-shift interferometer measurements of the shape of human and cat tympanic membrane,'' Proc. SPIE Vol. 1429, Holography, Interferometry, and Optical Pattern Recognition in Biomedicine, 26–33.

Decraemer, W. F., Maes, M. A., Vanhuyse, V. J., and Vanpeperstraete, P. (**1980**). ''A non-linear viscoelastic constitutive equation for soft biological tissues based upon a structural model,'' J. Biomech. **13**, 559–564.

Decraemer, W. F., Dirckx, J. J. J., and Funnell, W. R. J. (**1991**). ''Shape and derived geometrical parameters of the adult, human tympanic membrane measured with a phase-shift moiré interferometer,'' Hear. Res. **51**, 107–122.

Decraemer, W. F., Khanna, S. M., and Funnell, W. R. J. (**1994**). ''Bending of the manubrium in cat under normal sound stimulation,'' SPIE Proc. **2329**, 74–84.

Decraemer, W. F., Gea, S. L. R., and Dirckx, J. J. J. (**2003**). ''Three-dimensional displacement of the gerbil ossicular chain under static pressure changes,'' 26th Midwinter Research Meeting of the Association for Research in Otolaryngology, Abstract #975 (ARO Web site).

Dirckx, J. J. J., Decraemer, W. F., and Dielis, G. (**1988**). ''Phase shift method based on object translation for full field automatic 3-D surface reconstruction from moiré topograms,'' Appl. Opt. **27**, 1164–1169.

Dirckx, J. J. J., and Decraemer, W. F. (**1989**). ''Phase shift moiré apparatus for automatic 3-D surface measurement,'' Rev. Sci. Instrum. **60**, 3698–3701.

Dirckx, J. J. J. (**1990**). ''Automated moiré topography and its applications for shape and deformation measurements of the tympanic membrane,'' Ph.D. thesis, University of Antwerp, UIA, November 1990.
Dirckx, J. J. J., and Decraemer, W. F. (**1990**). ''Automatic calibration method for phase shift shadow moiré interferometry,'' Appl. Opt. **29**, 1474–1476.
Dirckx, J. J. J., and Decraemer, W. F. (**1991**). ''Human tympanic membrane deformation under static pressure,'' Hear. Res. **51**, 93–105.
Dirckx, J. J. J., and Decraemer, W. F. (**1997**). ''Coating techniques in optical metrology,'' Appl. Opt. **36**, 2776–2782.
Dirckx, J. J. J., Decraemer, W. F., von Unge, M., and Larsson, Ch. (**1998**). ''Volume displacement of the gerbil eardrum pars flaccida as a function of middle ear pressure,'' Hear. Res. **118**, 35–45.
Dirckx, J. J. J., and Decraemer, W. F. (**2001**). ''Effect of middle ear components on eardrum quasi-static deformation,'' Hear. Res. **157**, 124–137.
Fung, Y. C. (**1993**). *Biomechanics: Mechanical Properties of Living Tissues*, 2nd ed. (Springer, New York).
Funnell, W. R. J., and Decraemer, W. F. (**1996**). ''On the incorporation of moiré shape measurements in finite-element models of the cat eardrum,'' J. Acoust. Soc. Am. **100**, 925–932.
Funnell, W. R. J., and Laszlo, C. A. (**1978**). ''Modeling of the cat eardrum as a thin shell using the finite-element method,'' J. Acoust. Soc. Am. **63**, 1461–1467.
Funnell, W. R. J., Khanna, S. M., and Decraemer, W. F. (**1992**). ''On the degree of rigidity of the manubrium in a finite-element model of the cat eardrum,'' J. Acoust. Soc. Am. **91**, 2082–2090.
Gaihede, M. (**1996**). ''Tympanometric preconditioning of the tympanic membrane,'' Hear. Res. **102**, 28–34.
Guinan, Jr., J. J., and Peake, W. T. (**1967**). ''Middle-ear characteristics of anesthetized cats,'' J. Acoust. Soc. Am. **41**, 1237–1261.
Horn, B. K. P. (**1987**). ''Closed-form solution of absolute orientation using unit quaternions,'' J. Opt. Soc. Am. A **4**, 629–642.
Hüttenbrink, K. N. (**1989**). ''The mechanics of the middle ear at static air pressures,'' Acta Otolaryngol. (Stockh.) Suppl. **451**, 1–35.
Kessel, J. (**1874**). ''On the influence of the middle-ear muscles on the displacements and vibrations of the eardrum in the cadaver ear,'' Arch. Ohrenheilkd. **8**, 80–92 (in German).
Ladak, H. M. (**1998**). ''Finite-element and experimental analyses of the response of the cat eardrum to large static pressures,'' Ph.D. thesis, McGill University, Montréal.
Ladak, H. M., and Funnell, W. R. J. (**1995**). ''On the effects of geometric nonlinearities in a finite-element model of the cat eardrum,'' Proc. IEEE Engineering in Medicine & Biology Society 17th Annual Conference and 21st Canadian Medical & Biological Engineering Conference, Montreal, QC, pp. 1439–1440.
Ladak, H. M., Decraemer, W. F., Dirckx, J. J. J., and Funnell, W. R. J. (**2000**). ''Systematic errors in small deformations measured using shadow-moiré topography,'' Appl. Opt. **39**, 3266–3275.
Margolis, R. H., Osguthorpe, J. D., and Popelka, G. R. (**1978**). ''The effects of experimentally-produced middle ear lesions on tympanometry in cats,'' Acta Oto-Laryngol. **86**, 428–436.
Naito, Y. (**1990**). ''Holographic observation of the tympanic membrane vibration after stapes fixation,'' Nippon Jibi Inkoka Gakkai Kaiho **93**, 2021–2027.
Osguthorpe, J. D., and Lam, C. (**1981**). ''Methodologic aspects of tympanometry in cats,'' Otolaryngol.-Head Neck Surg. **89**, 1037–1040.
Parnes, S. M., Cacace, A. T., Castracane, J., Conerty, M., and Gardner, G. M. (**1996**). ''Advances in the development of the interferometric otoscope,'' Laryngoscope **106**, 263–267.
Pascal, J., Bourgeade, A., Lagier, M., and Legros, C. (**1998**). ''Linear and nonlinear model of the human middle ear,'' J. Acoust. Soc. Am. **104**, 1509–1516.
Price, G. R. (**1974**). ''Upper limit to stapes displacement: Implications for hearing loss,'' J. Acoust. Soc. Am. **56**, 195–197.
Price, G. R., and Kalb, J. T. (**1986**). ''Mathematical model of the effect of limited stapes displacement on hazard from intense sounds,'' J. Acoust. Soc. Am. Suppl. 1 **80**, S122.
Price, G. R., and Kalb, J. T. (**1991**). ''Insights into hazards from intense impulses from a mathematical model of the ear,'' J. Acoust. Soc. Am. **90**, 219–227.
Stoffels, E. J. A. J. (**1993**). ''Geautomatiseerde moiré topografie, en zijn toepassing voor vorm-, vervormings- en diktemetingen aan het kattetrommelvlies'' (Automated moiré topography and its application to shape, deformation and thickness measurements of the cat eardrum), Unpublished report of a period of practical training, Hogeschool Eindhoven, Faculty of Technics, Technical Physics (in Dutch).
Tonndorf, J., and Khanna, S. M. (**1972**). ''Tumpanic-membrane vibrations in human cadaver ears studied by time-averaged holography,'' J. Acoust. Soc. Am. **52**, 1221–1233.
von Unge, M., Borg, E., and Bagger-Sjöbäck, D. (**1991**). ''Mechanoacoustic properties of the tympanic membrane: A study on isolated Mongolian gerbil temporal bones,'' Am. J. Otol. **12**, 407–419.
von Unge, M., Decraemer, W. F., Bagger-Sjöbäck, D., and Dirckx, J. J. J. (**1993**). ''Displacement of the gerbil tympanic membrane under static pressure variations measured with a real-time differential moiré interferometer,'' Hear. Res. **70**, 229–242.
von Unge, M., Decraemer, W. F., Dirckx, J. J. J., and Bagger-Sjöback, D. (**1999**). ''Tympanic membrane displacement patterns in experimental cholesteatoma,'' Hear. Res. **128**, 1–15.
Vorwerk, U., Steinicke, G., and Begall, K. (**1999**). ''Observation of eardrum movements during quasi-static pressure changes by high-speed digital imaging,'' Audiol. Neuro-Otol. **4**, 150–155.
Wada, H., and Kobayashi, T. (**1990**). ''Dynamical behaviour of middle ear: Theoretical study corresponding to measurement results obtained by a newly developed measuring apparatus,'' J. Acoust. Soc. Am. **87**, 237–245.
Zhao, H., Chen, W., and Tan, Y. (**1994**). ''Phase-unwrapping algorithm for the measurement of three-dimensional object shapes,'' Appl. Opt. **33**, 4497–4500.

Analytic treatment of the compound action potential: Estimating the summed post-stimulus time histogram and unit response

Mark E. Chertoff[a)]
Department of Hearing and Speech, University of Kansas Medical Center, Kansas City, Kansas 66103-0001

(Received 11 June 2004; revised 21 July 2004; accepted 23 July 2004)

The convolution of an equation representing a summed post-stimulus time histogram computed across auditory nerve fibers $[P(t)]$ with an equation representing a single-unit wave form $[U(t)]$, resulted in an analytic expression for the compound action potential (CAP). The solution was fit to CAPs recorded to low and high frequency stimuli at various signal levels. The correlation between the CAP and the analytic expression was generally greater than 0.90. At high levels the width of $P(t)$ was broader for low frequency stimuli than for high frequency signals, but delays were comparable. This indicates that at high signal levels there is an overlap in the population of auditory nerve fibers contributing to the CAP for both low and high frequency stimuli but low frequencies include contributions from more apical regions. At low signal levels the width of $P(t)$ decreased for most frequencies and delays increased. The frequency of oscillation of $U(t)$ was largest for high frequency stimuli and decreased for low frequency stimuli. The decay of $U(t)$ was largest at 8 kHz and smallest at 1 kHz. These results indicate that the hair cell or neural mechanisms involved in the generation of action potentials may differ along the cochlear partition. © *2004 Acoustical Society of America.* [DOI: 10.1121/1.1791911]

PACS numbers: 43.64.Pg, 43.64.Nf, 43.64.Rj [BLM] Pages: 3022–3030

I. INTRODUCTION

The long-term goal of this research is to develop clinical measures that describe and distinguish the underlying pathophysiology resulting in sensorineural hearing loss. Previously, cochlear function was estimated via a cochlear transducer function derived from cochlea microphonic (Chertoff *et al.*, 1996) and distortion product ototacoustic emission (Bian *et al.*, 2002) data. The results indicated that the transducer function was both sensitive and specific to different ototoxic agents (Bian and Chertoff, 1998; 2001). The cochlear microphonic and distortion product otoacoustic emission mainly assess outer hair cell function. However, in patients with hearing loss, hair cell deterioration as well as neuronal degeneration can occur (Schuknecht, 1964) and techniques to assess neuronal survival are lacking. The CAP and its physiologic components may be useful for developing an approach to assess neuronal integrity. For example, Hall (1990) showed that the maximum amplitude and the slope of the growth functions of the electrically evoked CAP could be used to estimate neuronal survival in cochlear implant patients.

The compound action potential (CAP) recorded with an electrode placed on the round window represents the summed electrical activity from the discharges of auditory eighth nerve fibers. Goldstein and Kiang in 1958, proposed that the relation between the single-unit response and the CAP could be described as a convolution integral given as

$$\mathrm{CAP}(t) = A \cdot \int_{-\infty}^{t} P(t)U(t-\tau)\,d\tau, \tag{1}$$

where $P(t)$ is the probability density function taken over the population of nerve fibers (i.e., the sum of the post-stimulus time histograms obtained from individual fibers), $U(t)$ is the unit response wave form, and A is the number of units in the population.

The principle assumptions for the relation expressed by Eq. (1) are that $U(t)$ is identical across fibers of different characteristic frequencies (CFs) and spontaneous rates (SRs) and the discharges of individual fibers are mutually independent. The first assumption was verified by Prijs (1986) who used the spike-triggered averaging technique to obtain $U(t)$ from single units with different CFs. Prijs showed that $U(t)$ was a biphasic wave form with characteristics that did not differ across CF. The second assumption was addressed by Johnson and Kiang (1976) by simultaneously recording discharge patterns from pairs of auditory nerve fibers. The authors concluded that the cross-correlation between pairs of fiber discharges for tone-evoked activity was consistent with two independent sequences. Thus Eq. (1) seems to be a valid description for the relation between single-unit auditory nerve fibers and the CAP.

Understanding the relation between single-unit discharges and the CAP has led to the development of many models of the CAP (de Boer, 1975; Elberling, 1976a; Dolan *et al.*, 1983; Teas *et al.*, 1962; Versnel *et al.*, 1992a; McMahon and Patuzzi 2002). Some approaches have used a theoretically derived $U(t)$ (de Boer, 1975; McMahon and Patuzzi 2002) whereas others have derived $U(t)$ from masking procedures (Elberling, 1976b) or the spike-triggered averaging technique (Kiang *et al.*, 1976; Versnel *et al.*, 1992a; Wang, 1979). $P(t)$ has been theoretically derived using a probabilistic pulse generator (de Boer, 1975) or empirically by summing post-stimulus time histograms obtained from single-unit recordings of auditory nerve fibers (Kiang *et al.*, 1976;

a)Author to whom correspondence should be addressed. Electronic mail: mchertof@kumc.edu

Versnel *et al.*, 1992a; Wang, 1979). In general, the results show that the models based on convolving $P(t)$ with $U(t)$ are quite successful in replicating the morphology of the CAP wave form and some of the changes in CAP latency and amplitude as a function of signal level.

Another use of Eq. (1) is to use a recorded CAP, an assumed $U(t)$, and derive $P(t)$ through deconvolution (Elberling, 1976b; de Sauvage, 1985). Elberling (1976b) used this approach with a logarithmic transformation of the derived $P(t)$ to obtain "response areas" of the cochlea that contribute to the CAP in normal and hearing impaired individuals. In his work Elberling assumed a particular form of $U(t)$ that was derived from masking studies of the CAP and assumed that $U(t)$ was the same for each subject. In the present paper, a different method is used to obtain $P(t)$ and $U(t)$. The approach is to assume functional forms for $P(t)$ and $U(t)$, derive an analytic solution to Eq. (1) and fit the solution to recorded CAPs. An advantage of this approach is that there is no assumption that $U(t)$ is similar across individuals. This is an important consideration given that some evidence suggests that $U(t)$ may differ between normal and pathologic cochleas (Prijs, 1986, Versnel *et al.*, 1992b). The purpose of this paper is to derive an analytic solution to Eq. (1) and describe the influence of signal frequency and level on the components $P(t)$ and $U(t)$ that make up the CAP. Subsequent research will address the influence of hair cell damage and neural degeneration on $P(t)$ and $U(t)$.

Theoretical treatment: The analytic solution of Eq. (1) requires functional forms for $P(t)$ and $U(t)$. Assume that in response to a short duration signal such as a tone burst, $P(t)$ can be expressed as a gamma function given as

$$P(t)=\left(\frac{t-\alpha}{\beta}\right)^{\gamma-1}\cdot e^{(-t-\alpha)/\beta} \quad \text{for } t\geqslant\alpha,$$
$$0 \quad \text{otherwise.} \tag{2}$$

The parameters t and α represent time and time delay from stimulus onset, respectively. β influences the width of $P(t)$ with larger values leading to a broader $P(t)$ and γ influences the slope. Equation (2) is similar to the function used by Versnel *et al.* (1992a) to model the envelope of single-unit post-stimulus time histograms in response to click stimuli. However, unlike Versnel *et al.* (1992a) who fit γ to individual PSTs, in this study γ was considered a constant equal to 2 for simplicity of calculations.

The unit wave form is given as

$$U(t)=e^{-kt}\sin(\omega t), \tag{3}$$

i.e., a damped sinusoidal function where k is a decay constant, $\omega=2\pi f$ and f is frequency. This function was chosen because with large damping it resembles a single-unit wave form and McMahon and Patuzzi (2002) used a similar function and successfully modeled the CAP.

In the Laplace domain, Eq. (1) can be expressed as

$$\mathrm{CAP}(s)=A\cdot P(s)U(s), \tag{4}$$

where

$$P(s)=\frac{e^{-s\alpha}\left(\frac{1}{\beta}\right)^{\gamma-1}\Gamma(\gamma)}{\left(s+\frac{1}{\beta}\right)^{\gamma}} \tag{5}$$

and

$$U(s)=\frac{\omega}{(s+k)^2+\omega^2}. \tag{6}$$

Setting $\gamma=2$, substituting Eqs. (5) and (6) into (4), and converting Eq. (4) to the time domain via the inverse Laplace transform (Maple 7.0) yields

$$\begin{aligned}\mathrm{CAP}(t)=&-\frac{A\beta H(t-\alpha)}{c^2}\\ &\times\{\omega e^{(-t+\alpha)/\beta}[c(t-\alpha)-2\beta(\beta k-1)]\\ &+e^{k(-t+\alpha)}[a\sin(\omega(\alpha-t))-b\cos(\omega(\alpha-t))]\},\end{aligned} \tag{7}$$

where

$$a=\beta\omega^2-(\beta k-1)^2,$$
$$b=2\beta\omega(1-\beta k),$$
$$c=\beta^2\omega^2+(\beta k-1)^2,$$

and $H=$ the Heaviside function which$=0$ for $t\leqslant\alpha$ and 1 for $t>\alpha$. Equation (7) represents an analytic solution of the CAP in the time domain and the negative sign in front of A is to plot the CAP with N_1 (Fig. 1) downwards.

II. METHODS

A. Subjects, animal preparation, and data acquisition

The CAPs used in this study were data previously recorded from seven normal animals in Chertoff *et al.* (2003) and the remaining four normal animals were from pilot experiments ongoing in the laboratory. A total of 11 Mongolian gerbils (*Meriones unguiculatus*) weighing between 40 and 60 grams with normal hearing were used as subjects. Normal hearing was defined as CAP thresholds at or below 30 dB SPL for 1, 2, 4, 8, and 16 kHz.

As a majority of the data in this study comes from surgical and data acquisition procedures previously reported (Chertoff *et al.*, 2003) only a brief report is presented. Animals were sedated with Nembutal (64 mg/kg), the right pinna removed, and the bulla opened with a surgical drill. A silver ball electrode was placed in the round-window niche and a needle electrode placed in the neck served as ground. A cotton wick in the niche kept the bulla dry throughout the experiment.

Two millisecond tone bursts were created in an array processor (Tucker-Davis Technology, TDT AP2) and downloaded to a 16-bit D/A converter (TDT, DA1) sampling at 65.536 kHz. The output of the D/A was routed to an attenuator (TDT PA4), headphone buffer (TDT HB6), and subsequently to a probe-tube headphone (Etymotic ER-2) attached

to a speculum sealed to the animal's bony external ear canal. A probe microphone (Etymotic ER-7C) placed in the speculum monitored signal level.

CAPs were elicited by 1-, 2-, 4-, 8-, and 16-kHz tone bursts at levels ranging from 100 dB SPL to 15 dB SPL in 5-dB increments. Signals were delivered with alternating polarity to reduce contamination from the cochlear microphonic. The electrophysiologic signal recorded by the round-window electrode was sent to two amplifiers in series for a total amplification of 5000 (Stanford SR560, Steward VBF 10), band-pass filtered (0.03–25 kHz), and digitized at 65.536 kHz (TDT, AD2). The CAP was monitored on a computer screen by two investigators and when the CAP was clearly visible, the signal was stored on disk. At most, 500 stimulus presentations were required to obtain a CAP.

B. CAP wave form and statistical analysis

Compound action potential wave forms from each animal and signal level were loaded into MATLAB (The MathWorks) and fit with Eq. (7) using a nonlinear least squares fitting routine (NLINFIT, MATLAB). Initial conditions to the fitting routine were modified until the best fit could be obtained for each wave form. Next, the residuals of the fit and the original CAP data were used to obtain 95% confidence intervals for each of the parameters (NLPARCI, MATLAB). If the confidence interval for a parameter included zero, the parameter was not statistically significant and deemed unreliable. In these cases, the parameter was not included in any further statistical analysis.

A hierarchical linear model was used to determine if the parameters of Eq. (7) varied as a function of frequency and signal level. A hierarchical analysis was used instead of the more common repeated measures analysis of variance because it does not require the assumption of compound symmetry and is not influenced by missing data (Wu, 1996). One question of interest was to determine if a given parameter changed with signal level and if so, did the change differ between frequencies. This was addressed first by examining the frequency-by-level interaction. If significant the hierarchical analysis determined the significance of the slope of the parameter-level function for each frequency. Next, Bonferonni *t*-tests were used to test the slopes among frequencies. If a frequency main effect was significant, the mean parameter value (computed across level) was compared between

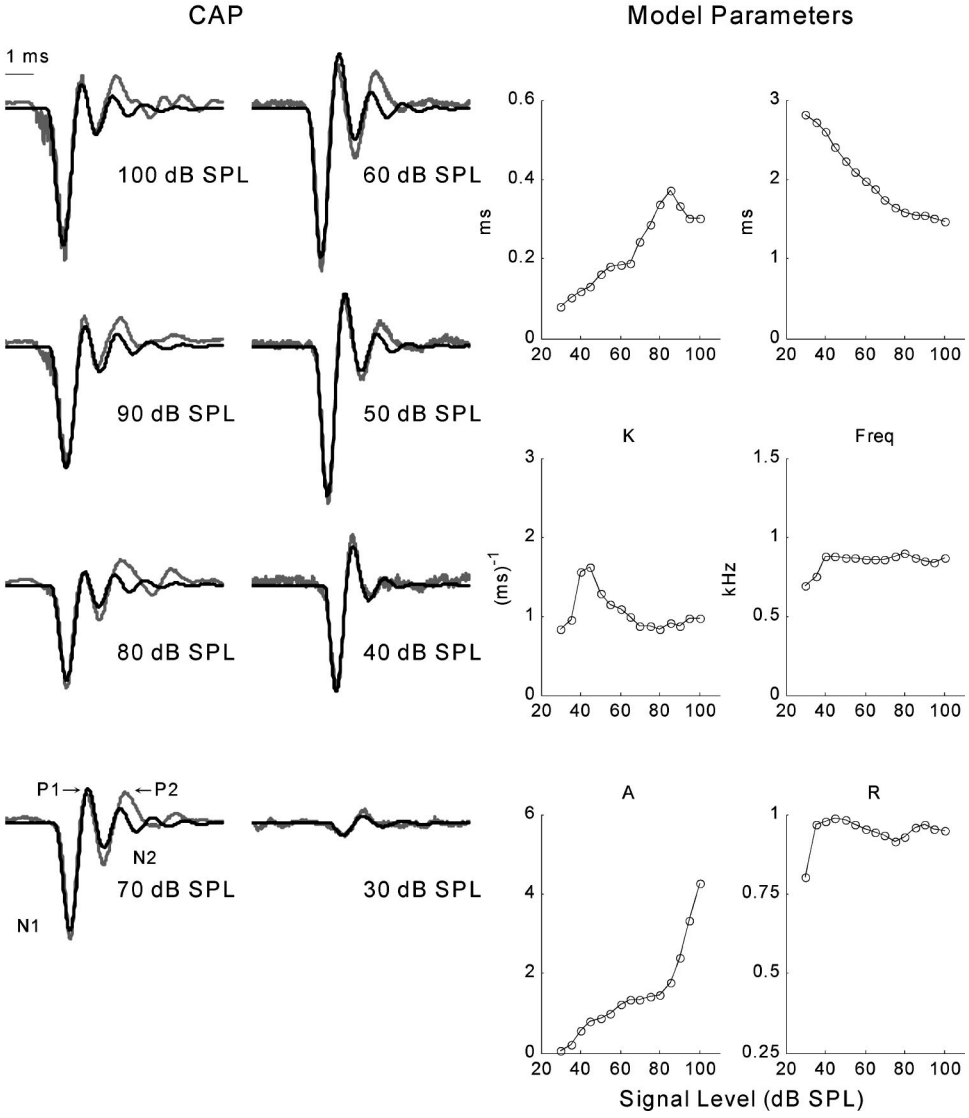

FIG. 1. Wave forms represent the CAP (grey) and fit of Eq. (7) (black) to a 4 kHz tone burst for one animal. The influence of signal level (5 dB increments) on the model parameters is illustrated in the right panel.

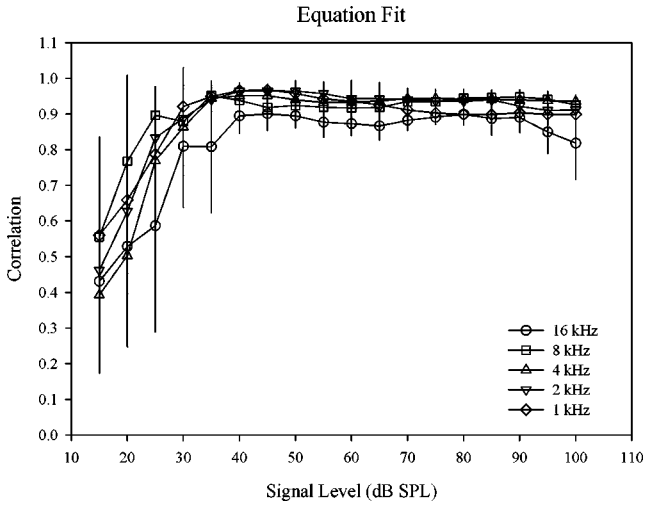

FIG. 2. Mean correlation, computed across all animals, between CAP recordings and Eq. (7) as a function of stimulus frequency and level. Symbols represent the different stimulus frequencies and the error bars are ±1 standard deviation.

frequencies using Bonferonni *t*-tests. An alpha of 0.05 was used to determine significant interaction and main effects. To control for a Type 1 error for the multiple (10) post-hoc comparisons, a $p \leqslant 0.005$ was considered a significant difference.

III. RESULTS

A. Model fit and reliability

An example of the CAPs to 4 kHz tone bursts, the fit of Eq. (7), and the corresponding parameters for one representative animal is illustrated in Fig. 1. On the left are the recorded CAPs (grey) and the predicted CAPs (black) for signal levels ranging from 100 dB SPL to 30 dB SPL in 10 dB increments. Equation (7) modeled the N_1 and the P_1 components of the CAP quite accurately whereas the fit was somewhat poorer for the N_2 and the P_2 components. On the right, the parameters of Eq. (7) for each signal level (5 dB increments) are illustrated. The size of β and A tend to increase with signal level whereas α (or delay) decreases. The decay constant (k) of $U(t)$ shows some variation around 40 dB SPL, but is stable at other signal levels. Similarly, the frequency of the unit wave form oscillation is stable around 1 kHz. The fit, or correlation coefficient, (R) of Eq. (7) to the CAP remains high at most signal levels, ranging from a low of 0.80 at 30 dB SPL to 0.99 at 45 dB SPL.

The mean (±1 standard deviation) correlation coefficient between Eq. (7) and the CAP for each frequency is shown in Fig. 2. At 40 dB SPL and above, Eq. (7) fits the CAP quite well for each frequency with limited variation among animals. Below approximately 40 dB SPL the predicted CAP does not fit well because its small amplitude close to threshold leads to a poor signal-to-noise ratio. For this reason, subsequent analyses were performed only on data for signal levels $\geqslant$40 dB SPL.

Table I shows the percentage of responses at which the coefficients were statistically significant. Percentage is defined as the number of times a coefficient was statistically significant divided by the total number of recordings. For frequencies below 16 kHz the number of recordings was 143. For 16 kHz, the total number of recordings was 135 because not all animals received the 100 dB SPL or 95 dB SPL stimulus level. At 16 kHz, β and A were least reliable, only occurring for approximately 65% of the wave forms, whereas the remaining parameters occurred about 87% of the time. In contrast, for stimuli below 16 kHz, the coefficients were more reliable. For example, at 2 kHz and 4 kHz, the coefficients were significant for all of the animals at all signal levels.

TABLE I. Number of reliable responses (%) obtained for each parameter and signal frequency.

	Frequency (Hz)				
Coefficient	16 000[a]	8000[b]	4000	2000	1000
β	63.70	85.31	100.00	100.00	94.41
A	65.93	86.71	100.00	100.00	94.41
α	86.67	97.20	100.00	100.00	99.30
f	86.67	97.20	100.00	100.00	99.30
K	86.67	97.20	100.00	100.00	99.30

[a]Total number of possible responses = 135 because some animals did not receive the 100 or 90 dBSPL stimulus conditions at 16 kHz.
[b]Total number of possible responses = $n \times l$ where $n = 11$ subjects, $l = 13$ signal levels for a total of 143.

B. $P(t)$ parameters

Figure 3 illustrates the influence of signal level and frequency on the parameters that characterize $P(t)$. The magnitude of the β coefficient (left panel), which governs $P(t)$ width, increased significantly with increasing signal level for 2, 4, 8, and 16 kHz. The rate of increase was similar for 4, 8, and 16 kHz whereas for 2 kHz, the slope was less than that at 4 and 8 kHz. In contrast to the increase in β with signal level, the β coefficient for the 1 kHz stimulus showed a slight, but significant, decrease with signal level. Overall the size of β differed with frequency. β for 1 kHz was largest followed by 2, 4, and 8 kHz and the size of β did not differ between 8 and 16 kHz.

The scaling coefficient of Eq. (7), A, also varied with level and frequency (middle panel). As signal level increased, A increased significantly for each stimulus frequency. The rate of increase was largest for 8 kHz and the slopes of the A-level functions did not differ among 1, 2, 4, and 16 kHz. Collapsed across signal level, the A coefficient was significantly larger for 8 kHz than any other frequency. The A coefficient for 2 and 4 kHz was larger than 1 kHz.

The influence of signal level and frequency on the delay parameter, α, is shown in the right panel. As signal level increased α decreased for each of the frequencies. The slope of the delay-level function varied among the frequencies. For 1 kHz, α changed more rapidly than α for 4, 8, and 16 kHz. The slope for the 2 and 4 kHz stimuli were similar but steeper than 8 and 16 kHz. Finally, the slope of the delay-level function was steeper for 16 kHz than 8 kHz. A significant frequency effect occurred showing that the overall latency at 1 kHz was greater than 16 kHz, 2 kHz was greater than 8 kHz, and 4 kHz was greater than 16 kHz.

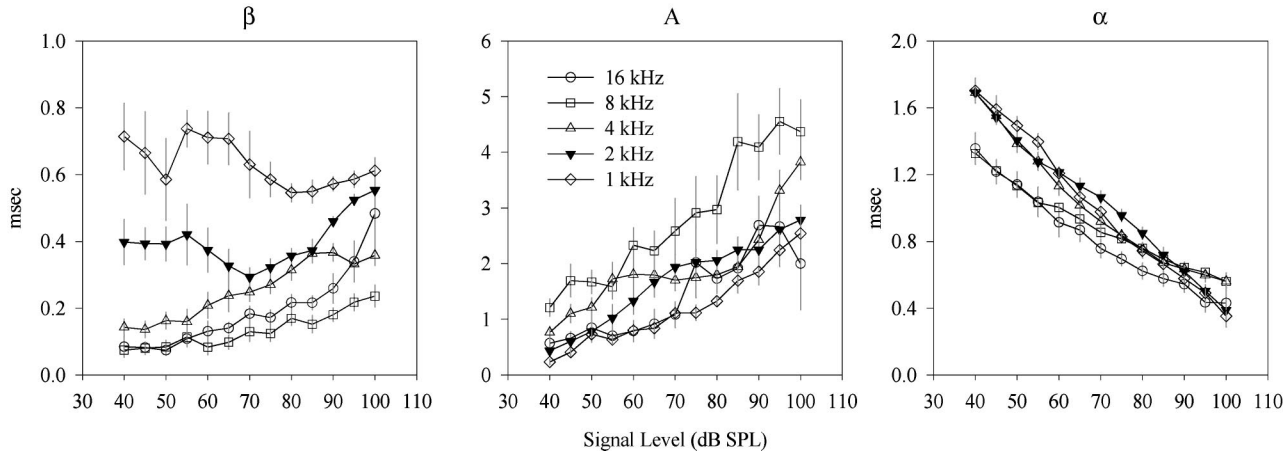

FIG. 3. Influence of signal frequency and level on the parameters β (left panel), A (middle panel), and α (right panel) that characterize $P(t)$. Symbols represent different stimulus frequencies and error bars are ± 1 standard error of the mean. The filled symbol is to ease the visualization of the influence of signal level on β at 2 kHz.

C. $U(t)$ parameters

The frequency coefficient for $U(t)$ varied as a function of stimulus frequency [Fig. 4, panel (A)]. The frequency of $U(t)$ did not differ between 2 kHz and 4 kHz but both were significantly smaller than 8 and 16 kHz. The $U(t)$ frequency for 8 kHz did not differ from that of 16 kHz. The frequency for the 1 kHz stimulus was smaller than any other frequency and it varied with signal level [panel (B)]. Frequency increased from ~500 Hz at 40 dB SPL to ~900 Hz at 60 dB SPL where it saturated at a value similar to that of the 2 and 4 kHz stimuli.

The influence of signal frequency on the decay constant, k, of the unit wave form is illustrated in Fig. 5 [panel (A)]. At 8 kHz, k was significantly larger than any other frequency whereas k for 1 kHz was the smallest. There was no significant difference between 2, 4, and 16 kHz. Panel (B) illustrates that k varied significantly as a function of signal level for two frequencies. At 8 kHz, k increased with an increase in signal level until 100 dB SPL where it declined. In contrast, k decreased in increasing signal level for the 4 kHz stimulus.

IV. DISCUSSION

A. Model fit

The research in this paper is an initial step for developing a method using the CAP and its underlying components to estimate neuronal survival in hearing impaired individuals. The convolution of a functional representation of a summed post-stimulus time histogram from auditory nerve fibers with a functional representation of a unit response provided an analytic expression for the CAP [Eq. (7)]. The expression fit well to recorded CAP wave forms for signal levels at and above 40 dB SPL. This suggests that the model first proposed by Goldstein and Kiang (1958) is an accurate representation of the contribution of single-unit auditory nerve fibers to the CAP.

A closer observation of Fig. 1 shows that Eq. (7) more accurately estimates the amplitudes of N_1 and P_1, especially at the lower signal levels. At high signal levels, the amplitude of N_2 and P_2 were usually underestimated. This was a common observation across many animals and stimulus frequencies. One reason is that the functional representations of

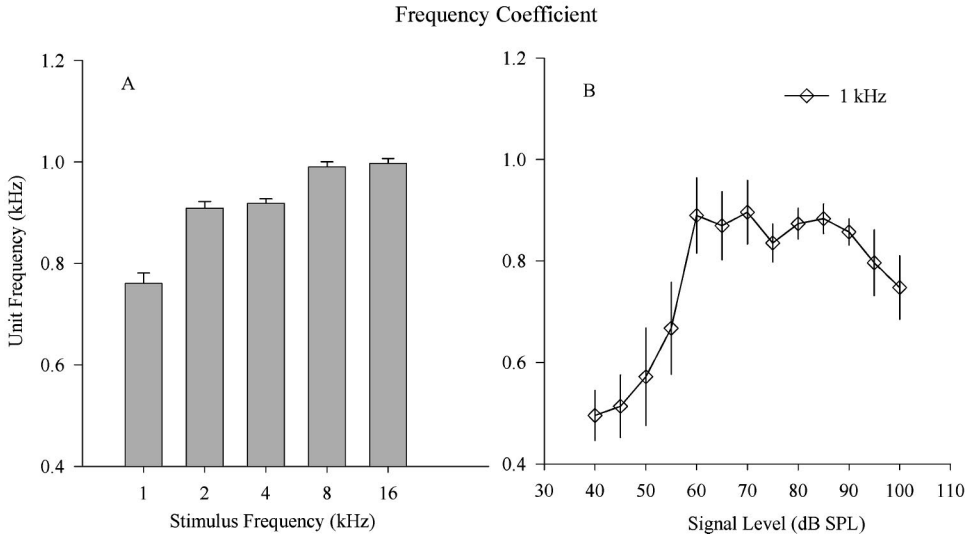

FIG. 4. Panel (A) illustrates the average frequency coefficient of $U(t)$ for the different stimulus frequencies. Panel (B) shows the influence of signal level on the frequency coefficient for $U(t)$ in response to the 1 kHz tone burst. Error bars in both panels are ± 1 standard error of the mean.

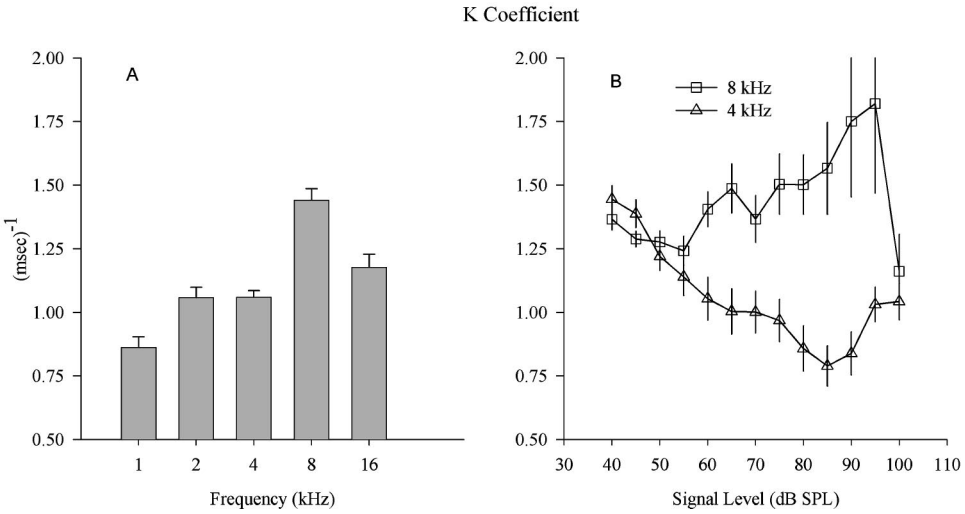

FIG. 5. The average decay constant k of $U(t)$ as a function of stimulus frequency [panel (A)]. Panel (B) demonstrates the influence of signal level on k for the 4 and 8 kHz stimuli. Error bars in both panels are ± 1 standard error of the mean.

$P(t)$ and/or $U(t)$ [Eqs. (2) and (3)] were too simplistic. For example, a function with multiple peaks could be a better approximation of $P(t)$ (Versnel *et al.*, 1992a) and its convolution with $U(t)$ would provide the additional amplitude of N_2 and P_2. Another possibility is that N_2 and P_2 reflect the contribution of sources other than from primary auditory nerve fibers. Although there is general agreement that N_1 comes from the firing of auditory nerve fibers (Dallos, 1973) the source of the additional peaks is less clear. The cochlear nucleus has been proposed as the source for the later peaks (Møller, 2000), with the anteroventral cochlear nucleus being the source for P_1 (Sellick *et al.*, 2003). However, recent work by McMahon *et al.* (2004) suggests that the peaks after N_1 are from a resonance in the auditory nerve fibers due to the activation kinetics of the voltage-gated sodium channels and the lack of potassium channels at the peripheral dendrites. Understanding the source of these latter peaks will be important for further development of Eq. (7). Terms may need to be added to account for contributions from cochlear nucleus neurons or perhaps modifications of $U(t)$ may be necessary to account for the single-unit response.

A reliable estimate of the parameters describing $P(t)$ and $U(t)$ was very high for stimuli below 16 kHz. At 16 kHz, however, β and A occurred less frequently than at other frequencies. It is possible that this reflects the fit of Eq. (7) to the CAP for 16 kHz. Often, the CAPs in response to 16 kHz started with a positive summating potential that did not occur, generally, for lower frequency stimuli. This led to slightly poorer fits of Eq. (7) to the data and may have lead to a decrease in the accuracy of these coefficients.

B. $P(t)$ parameters

The influence of signal level and frequency on the delay and width of $P(t)$ is summarized in Fig. 6. In the top panel, Eq. (2) was solved using the mean α and β coefficients from the 8 kHz and the 1 kHz stimuli conditions. The maximum of the $P(t)$ for each frequency has been normalized to one to emphasize the change in $P(t)$ delay and width. At 100 dB SPL, the delay at 8 kHz is slightly longer to that at 1 kHz whereas at 40 dB SPL, the reverse is true, indicating that the slope of the delay-level function was less steep for the 8 kHz (-0.0123 ms/dB) than for the 1 kHz (-0.0227 ms/dB) stimulus. These results are similar to Burkard *et al.* (1993) who showed, in gerbil, that the slope of the CAP delay-level function ranged from -0.0117 for 8 kHz to -0.0298 ms/dB for 1 kHz. The variation in the absolute delay and difference in the delay-level functions for 1 kHz and 8 kHz stimuli indicates that the populations of auditory nerve fibers contributing to the CAP are level and frequency dependent. At high signal levels, the population of auditory nerve fibers producing the CAP come from basal cochlear regions and is similar for both low and high frequency stimuli. In contrast, at low signal levels the populations separate and fibers contributing to the CAP come from fibers whose characteristic frequencies (CFs) are similar to the stimulus frequency.

In addition to the delay of $P(t)$ varying as a function of frequency and level, the width of $P(t)$ varied with frequency and level. Low frequencies yielded β values consistently larger than values obtained with high frequency stimulation indicating the width of $P(t)$ was broader for low frequency stimuli than for high frequency stimuli (Fig. 6). One explanation may be that small populations of fibers contribute more than one discharge at different times during the stimulus, thereby broadening the width of $P(t)$. However, this is unlikely given that stimulus duration was only 2 ms and the neurons may be in their refractory state. A more likely explanation for the low and high frequency discrepancy is due to the response area and latency dispersion of auditory nerve fibers. At high sound pressures, the response area for single auditory nerve fibers is broad and a fiber will respond to frequencies at and below its CF (Rose *et al.*, 1971). Thus, a low frequency tone burst presented at high signal levels will excite many nerve fibers with a wide range of CFs. Assuming that traveling wave delay is $\sim 1/\mathrm{CF}$ (Eggermont, 1976) then the latency of these fibers will be different, i.e., high CF fibers and low CF fibers will not discharge at the same time. Therefore, in theory, summing PST histograms across the population of these nerve fibers would result in a broad $P(t)$. In response to a high-level high frequency tone burst, however, only high frequency nerve fibers are stimulated. The delays among these fibers are similar and produce a narrow $P(t)$.

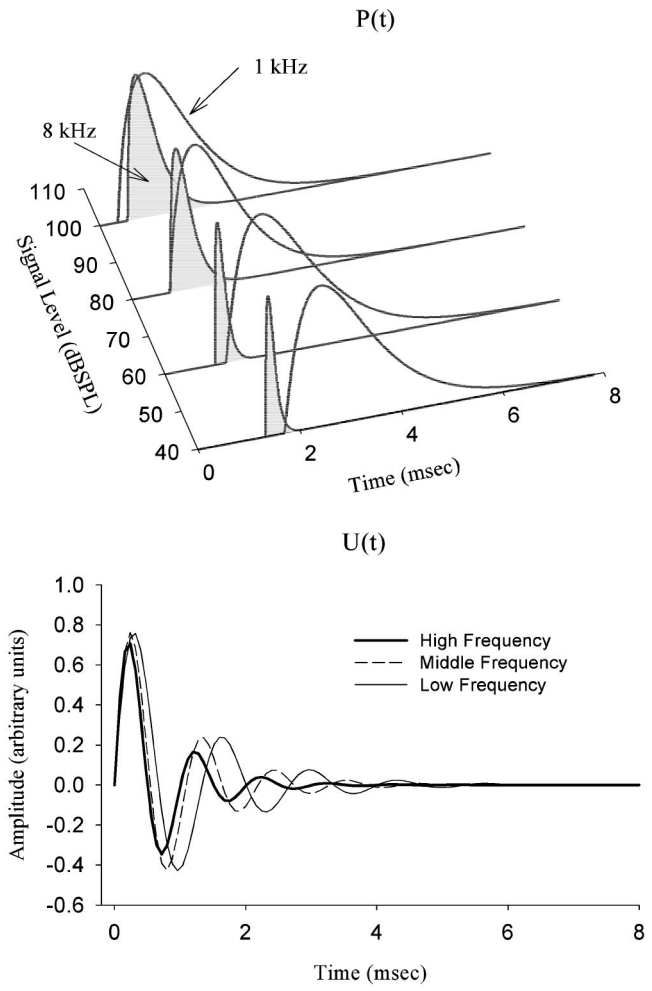

FIG. 6. The top panel summarizes the influence of signal frequency and level on $P(t)$. Mean values for β and α at 8 kHz (gray) and at 1 kHz (white) were computed across all animals for each of the signal levels illustrated. The amplitude was normalized to 1. The bottom panel illustrates the change in $U(t)$ for low (1 kHz), middle (2 kHz), and high (8 kHz) frequency tone bursts presented at 100 dB SPL. The decay constant k (ms^{-1}) was 0.86, 1.06, and 1.44, and the frequency of oscillation was 0.748, 0.914, and 0.994 kHz for 1, 2, and 8 kHz, respectively.

For frequencies greater than 1 kHz, β decreased with a decrease in signal level indicating a decrease in the width of $P(t)$ (represented by 8 kHz in Fig. 6). This result is consistent with the estimated summed PST obtained through deconvolution by Elberling (1976b, Fig. 3) and the computer simulations by Bappert *et al.* (1980). Similar to the frequency effect, a narrowing of $P(t)$ reflects a change in the response area of auditory nerve fibers and the synchrony of discharge among fibers. At a low signal level the response area of a single auditory nerve fiber is limited to frequencies similar to the fiber's CF, or, in terms of a population of fibers, only a small group of fibers will respond to the stimulus. Given that these fibers will be from similar regions of the cochlear partition, their response delays will be similar. Similar delays among the nerve fibers will allow for synchronous discharges and result in a narrow $P(t)$.

Assuming that the size of $U(t)$ did not change with signal level, then A can be interpreted as an index of the number of single units contributing to $P(t)$. Therefore the decrease in A with signal level indicates fewer auditory nerve fibers are contributing to $P(t)$, thereby reducing the amplitude of the CAP. Interestingly, the results showed that A was biggest for the 8 kHz stimulus. This may reflect a variation in the distribution of densities of auditory nerve fibers as a function of CF. Larger A values for the 8 kHz stimulus could indicate a larger density of auditory nerve fibers at the 8 kHz CF region than other frequencies. Spoendlin (1972) showed that the density of auditory nerve fibers measured in the osseous spiral lamina varied along the length of the cochlea and was greatest in the upper basal turn in cat. A greater density of nerve fibers with synchronous discharges would lead to a larger amplitude of the CAP compared to the CAP obtained from fewer fibers.

C. $U(t)$ parameters

The parameters of the unit wave form, $U(t)$, derived from fitting Eq. (7) to CAP data revealed a damped sinusoidal wave form with a frequency of approximately 1 kHz (Fig. 6, bottom panel). Other techniques such as spike-triggered averaging (Kiang *et al.*, 1976; Wang, 1979; Versnel *et al.*, 1992a; Prijs, 1986), or masking procedures (Elberling, 1976a) have yielded similar results.

A more detailed comparison of $U(t)$ obtained in this study with $U(t)$ obtained from other methods can be made by comparing the amplitude and width of the $U(t)$ peaks among studies. In this study, the location of the positive and negative peaks of $U(t)$ occur at $t+nT$ and $t+(2n+1)(T/2)$ respectively, where t is defined at the time where $d(U(t))/dt=0$, T is the period of oscillation and $n \geqslant 0$ ($n=0$ for the first positive and negative peak). Because the $U(t)$ in our study was dimensionless, comparison to peak amplitudes of other studies could be made by examining a peak amplitude ratio. Substituting the time for the first positive peak and first negative peak into Eq. (3) and taking the absolute value of the ratio of the solutions gives the relative amplitude of the two peaks. Using mean values for k and for f with high (8 kHz), middle (2 kHz), and low (1 kHz) frequencies used to plot $U(t)$ in Fig. 6, yields 2.06, 1.78, and 1.78 respectively. These results are comparable to those obtained by Versnel *et al.* (1992a) in guinea pig. From their tables 1 and 2, the mean amplitude of the first peak of $U(t)$ was 0.13 μV and the second peak was 0.07 μV, resulting in a ratio of 1.86.

A similar comparison can be made between the widths of the peaks of the $U(t)$ from Versnel *et al.* (1992a) and from the widths of the peaks of the $U(t)$ obtained in the present study. Versnel and colleagues proposed that $U(t)$ could be fit by $U(t)=c(t-t_0)\cdot e^{[-(t-t_0)^2/2\sigma^2]}$ whose parameters differ for both the negative and the positive phase of $U(t)$. Substituting mean values from their control animals (their tables 1 and 2), and solving this equation (Maple, 7.0) for t at 50% of the peak amplitude, yields the bandwidth of a peak. Similarly, the 50% bandwidth for the first two peaks of $U(t)$ from the present study can be obtained by solving for t in Eq. (3) using the parameters in Fig. 6. The width of the first peak of Versnel *et al.* (1992a) was 0.24 ms whereas in the present study the width of the first peak was larger, 0.33 ms. The second peak in both studies was similar being 0.30 and 0.33

ms for each study, respectively. The narrower width of the first peak relative to the second peak is also consistent with the visual observation of $U(t)$ from Wang (1979).

Overall, the $U(t)$ found in the present study is similar to investigations using spike-triggered averaging. The consistent difference is the width of the first peak. This reflects a limitation of the function used to describe the unit wave form [Eq. (3)]. Equation (3) oscillates at one frequency and perhaps by choosing a different function may allow for variation in peak widths. Presently, however, the simplicity of Eq. (3) for computation and interpretation, and the high correlation coefficients of the model to physiologic data may warrant its continued use.

The physiologic significance of $U(t)$ lies in its relation to a single-unit action potential. Recorded from the round window, $U(t)$ is a description of the extracellular potential generated from a single auditory nerve fiber. The extracelluar potential is the second derivative of an intracellular recorded action potential (Clark and Plosney, 1968). As such, the peaks of $U(t)$ represent the physiology underlying the generation of an action potential. Therefore, the first positive peak of $U(t)$ reflects sodium entry into the nerve fiber due to an increase in sodium conductance (Hodgkin and Huxley, 1952). Then the potassium conductance increases allowing potassium to leave the nerve fiber, and creates the first negative peak of $U(t)$. Finally, the second positive $U(t)$ peak reflects the repolarization of the fiber. It is interesting to note that the frequency of oscillation of $U(t)$ varied as a function of stimulus frequency. High frequency stimuli had higher frequency oscillations of $U(t)$ than low frequency stimuli. If $U(t)$ reflects ion channel properties inherent in the action potential, this suggests that these properties may vary along the cochlear partition. It is also possible, however, that the frequency effect reflects properties of the extracellular medium. Capacitance of the extracellular fluid and/or associated tissue could produce a frequency dependent alteration in $U(t)$.

V. CONCLUSIONS

The analytic function of the CAP developed by the convolution of a functional form of a summed post-stimulus time histogram $[P(t)]$ with a function representing a unit response $[U(t)]$ fit well to physiologic recordings of the CAP. The parameters that describe $P(t)$ and $U(t)$ changed as a function of signal level and frequency. The change in the $P(t)$ parameters indicate a variation in the number and location of auditory nerve fibers that contribute to the CAP. Alterations in $U(t)$ may reflect underlying changes in the ion channel properties associated with eighth nerve fibers or hair cells along the length of the cochlear partition. Overall, the high correlations between Eq. (7) and the recorded CAPs, and the physiologic interpretation of the CAP components are encouraging for future research examining the CAP as an index of neuronal integrity in hearing impaired individuals.

ACKNOWLEDGMENTS

The author thanks Lin Bian, Jeff Lichtenhan, and Xing Yi for their help with data collection, scientific discussion, and reviewing earlier versions of this paper. David Lerner's critique of the mathematical treatment and Byron Gajewski's help with the statistical analysis are greatly appreciated. This study was supported by Grant No. R01 DC02117 from the National Institute on Deafness and other Communication Disorders of NIH, and USPHS Grant No. HD02528 to the Smith Mental Retardation and Human Development Research Center at the University of Kansas Medical Center.

Bappert, E., Hoke, M., Lütkenhöner, B., and Niestroj, B. (**1980**). ''Intensity dependence of the compound action potential and the deconvolution technique,'' Scand. Audiol. Suppl. **11**, 46–57.

Bian, L., and Chertoff, M. E. (**1998**). ''Differentiation of cochlear pathophysiology in ears damaged by salicylate or a pure tone using a nonlinear systems identification procedure,'' J. Acoust. Soc. Am. **104**, 2261–2271.

Bian, L., and Chertoff, M. E. (**2001**). ''Distinguishing cochlear pathophysiology in 4-aminopyridine and furosemide treated ears using a nonlinear systems identification technique,'' J. Acoust. Soc. Am. **109**, 671–685.

Bian, L., Chertoff, M. E., and Miller, E. (**2002**). ''Deriving a cochlear transducer function from low-frequency modulation of distortion product otoacoustic emissions,'' J. Acoust. Soc. Am. **112**, 198–210.

Burkard, R., Voigt, H. F., and Smith, R. L. (**1993**). ''A comparison of N1 of the whole nerve action potential and wave i of the brain-stem auditory evoked response in Mongolian gerbil,'' J. Acoust. Soc. Am. **93**, 2069–2076.

Chertoff, M. E., Steele, T. C., Ator, G. A., and Bian, L. (**1996**). ''Characterizing cochlear mechano-electric transduction using a nonlinear system identification procedure,'' J. Acoust. Soc. Am. **100**, 3741–3753.

Chertoff, M. E., Yi, X., and Lichtenhan, J. T. (**2003**). ''Influence of hearing sensitivity on mechano-electric transduction,'' J. Acoust. Soc. Am. **114**, 3251–3263.

Clark, J., and Plonsey, R. (**1968**). ''The extracellular potential field of the single active nerve fiber in a volume conductor,'' Biophys. J. **8**, 842–864.

de Boer, E. (**1975**). ''Synthetic whole-nerve action potentials for the cat,'' J. Acoust. Soc. Am. **58**, 1030–1045.

de Sauvage, R. C. (**1985**). ''Origins of eighth nerve unit response pattern in round window cap recordings,'' Hear. Res. **18**, 121–125.

Dallos, P. (**1973**). ''Cochlear potentials,'' in *The Auditory Periphery, Biophysics and Physiology*, edited by P. Dallos, (Academic, New York), pp. 328–353.

Dolan, D. F., Teas, D. C., and Walton, J. P. (**1983**). ''Relation between discharges in auditory nerve fibers and whole-nerve response shown by forward masking: An empirical model for the AP,'' J. Acoust. Soc. Am. **73**, 580–591.

Eggermont, J. J. (**1976**). ''Analysis of compound action potential responses to tone bursts in the human and guinea pig cochlea,'' J. Acoust. Soc. Am. **60**, 1132–1139.

Elberling, C. (**1976a**). ''Simulation of cochlear action potentials recorded from the ear canal in man,'' in Electrocochleography, edited by R. Rubin, C. Elberling, and G. Salomon (University Park Press, Baltimore), pp. 151–168.

Elberling, C. (**1976b**). ''Deconvolution of action potentials recorded from the ear canal in man,'' in Disorders of Auditory Function, edited by S. D. G. Stevens (Academic, London), Vol. II, pp. 109–117.

Goldstein, M. H., and Kiang, N. Y. S. (**1958**). ''Synchrony of neural activity in electric responses evoked by transient acoustic stimuli,'' J. Acoust. Soc. Am. **30**, 107–114.

Hall, R. D. (**1990**). ''Estimation of surviving spiral ganglion cells in the deaf rat using the electrically evoked auditory brainstem response,'' Hear. Res. **45**, 123–136.

Hodgkin, A. L., and Huxley, A. F. (**1952**). ''A quantitative description of membrane current and its application to conduction and excitation in nerve,'' J. Physiol. (London) **117**, 500–544.

Johnson, D. H., and Kiang, N. Y. S. (**1976**). ''Analysis of discharges recorded simultaneously from pairs of auditory nerve fibers,'' Biophys. J. **16**, 719–734.

Kiang, N. Y. S., Moxon, E. C., and Kahn, A. R. (**1976**). ''The relationship of gross potentials recorded from the cochlea to single unit activity in the auditory nerve,'' in *Electrocochleography*, edited by R. Rubin, C. Elberling, and G. Salomon (University Park Press, Baltimore), pp. 95–115.

McMahon, C. M., and Patuzzi, R. B. (**2002**). ''The origin of the 900 Hz

spectral peak in spontaneous and sound-evoked round-window electrical activity,'' Hear. Res. **173**, 134–142.
McMahon, C. M., Brown, D. J., and Patuzzi, R. B. (**2004**). ''Transient focal cooling at the round window and cochlear nucleus shows round window CAP originates from cochlear neurons alone,'' Hear. Res. **190**, 75–86.
Møller, A. R. (**2000**). ''Electrical potentials in the cochlea,'' Hearing (Academic, California), pp. 95–122.
Prijs, V. F. (**1986**). ''Single-unit response at the round window of the guinea pig,'' Hear. Res. **21**, 127–133.
Rose, J. E., Hind, J. E., Anderson, D. J., and Brugger, J. F. (**1971**). ''Some effects of stimulus intensity on response of auditory nerve fibers in squirrel monkey,'' J. Neurophysiol. **34**, 685–699.
Schuknecht, H. F. (**1964**). ''Further observations on the pathology of presbycusis,'' Arch. Otolaryngol. **80**, 369–382.
Sellick, P., Patuzzi, R., and Robertson, D. (**2003**). ''Primary afferent and cochlear nucleus contributions to extracellular potentials during tone-bursts,'' Hear. Res. **176**, 42–58.
Spoendlin, H. (**1972**). ''Innervation densities of the cochlea,'' Acta Oto-Laryngol. **73**, 235–248.
Teas, D. C., Eldredge, D. H., and Davis, H. (**1962**). ''Cochlear responses to acoustic transients: An interpretation of whole-nerve action potentials,'' J. Acoust. Soc. Am. **34**, 1438–1459.
Versnel, H., Schoonhoven, R., and Prijs, V. F. (**1992a**). ''Single-fibre and whole-nerve responses to clicks as a function of sound intensity in the guinea pig,'' Hear. Res. **59**, 138–156.
Versnel, H., Schoonhoven, R., and Prijs, V. F. (**1992b**). ''Round-window recorded potential of single-fibre discharge (unit response) in normal and noise-damaged cochleas,'' Hear. Res. **59**, 157–170.
Wang, B. (**1979**). ''The relation between the compound action potential and unit discharges of the auditory nerve,'' Doctoral dissertation, Dept. of Electrical Engineering and Computer Science, M.I.T., Cambridge, MA.
Wu, Y. B. (**1996**). ''An application of hierarchical linear models to longitudinal studies,'' Res. Nurs. Health **19**, 75–82.

Estimation of the level and phase of the simple distortion tone in the modulation domain

Aleksander Sek
Institute of Acoustics, Adam Mickiewicz University, 85 Umultowska, 61-614 Poznan, Poland

Brian C. J. Moore[a)]
Department of Experimental Psychology, University of Cambridge, Downing Street, Cambridge CB2 3EB, England

(Received 15 October 2003; revised 26 July 2004; accepted 27 July 2004)

These experiments were designed to test the idea that nonlinearities in the auditory system can introduce a distortion component into the internal representation of the envelope of a sound, and to estimate the phase of the hypothetical distortion component. In experiment 1, a two-alternative forced-choice (2AFC) task with feedback was used to measure psychometric functions for detecting 5-Hz probe modulation of a 4-kHz sinusoidal carrier in the presence of a masker modulator with components at 50 and 55 Hz ($m=0.3$ for each component). Performance was measured as a function of the relative phase, $\Delta\varphi$, of the probe relative to the ''venelope'' (envelope of the envelope) of the masker. Performance was poorest for $\Delta\varphi=135°$. In experiment 2, $\Delta\varphi$ was fixed at 135°, m was set to 0.48 for each masker component, and psychometric functions for detecting probe modulation were measured using a 2AFC task without feedback. For small probe modulation depths ($m\approx0.03$), the detectability index, d', was consistently negative, consistent with the existence of a weak distortion product which can ''cancel'' the probe modulation. The distortion component for the conditions of the experiment was estimated to have a phase of about $-25°$ relative to the venelope. [DOI: 10.1121/1.1795331]

PACS numbers: 43.66.Dc, 43.66.Mk, 43.66.Nm, 43.66.Ba [NFV] Pages: 3031–3037

I. INTRODUCTION

Several recent models for the perception of amplitude modulation (AM) in sounds are based on the idea that the envelopes of the outputs of the (peripheral) auditory filters are fed to a second array of overlapping bandpass filters tuned to different envelope modulation rates (Kay, 1982; Dau *et al.*, 1997a; 1997b; Ewert and Dau, 2000; Ewert *et al.*, 2002; Verhey *et al.*, 2003). This set of filters is usually called a ''modulation filter bank'' (MFB). Psychoacoustical evidence consistent with the concept of an MFB has come from experiments involving detection of ''probe'' modulation in the presence of masker modulation; these experiments appear to show frequency selectivity in the modulation domain (Bacon and Grantham, 1989; Houtgast, 1989).

Dau *et al.* (1997a) conducted an experiment to assess whether modulation masking could be explained in terms of the temporal similarity of the envelopes of the signal and masker, rather than in terms of the MFB. They amplitude modulated a 5-kHz sinusoidal carrier with a masker that consisted of the third to seventh harmonics of a 30-Hz fundamental frequency; the phases of the components were random. The task was to detect sinusoidal probe modulation in the range 20 to 120 Hz. The amount of modulation masking increased progressively as the probe frequency was increased from 20 to about 100 Hz. There was no maximum in the masking function at 30 Hz, even though the temporal envelope pattern of the masker and signal was similar at this frequency. The results were consistent with the idea that the auditory system performs a spectral analysis of the envelope. However, Verhey *et al.* (2003) later suggested that the failure of Dau *et al.* (1997a) to find a peak in the modulation masking pattern at the frequency corresponding to the ''missing fundamental'' resulted from the modulation masker impairing detection of the signal modulation on some trials and enhancing it on others, depending on the specific choice of (random) masker component phases.

Moore *et al.* (1999) examined modulation masking for cases where the probe modulation was at a frequency remote from any spectral frequency in the masker modulation, but there was nevertheless a similarity between the temporal pattern of the masker modulation and the probe modulation. This was achieved by using a two-component modulator. The ''beats'' between these two components had a rate that was equal to or close to the probe frequency. A similar method had been used earlier by Sheft and Yost (1997) to examine modulation detection interference (MDI). Moore *et al.* found that the threshold for detecting 5-Hz probe modulation was affected by the presence of a pair of masker modulators beating at a 5-Hz rate (40 and 45 Hz, 50 and 55 Hz, or 60 and 65 Hz). The threshold was dependent on the phase of the probe modulation relative to the beat cycle of the masker modulators; the threshold elevation was greatest when the peak amplitude of the probe modulation coincided with a peak in the beat cycle. The maximum threshold elevation of the 5-Hz probe produced by the beating masker modulators was 7–12 dB greater than that produced by the individual components of the masker modulators. These results cannot be explained in terms of the spectra of the envelopes of the stimuli, as the beating masker modulators did

a)Electronic mail: bcjm@cam.ac.uk

not produce a 5-Hz component in the spectra of the envelopes. Moore *et al.* (1999) proposed an explanation for their results based on the idea that nonlinearities within the auditory system, such as basilar-membrane compression, introduce distortion in the internal representation of the envelopes of the stimuli. This notion was initially suggested by Shofner *et al.* (1996) on the basis of an electrophysiological study using two-component modulators. In the case of two-component beating modulators, a weak component, corresponding to the simple difference component, would be introduced at the beat rate.

Verhey *et al.* (2003) conducted experiments similar to those of Moore *et al.* (1999), but included conditions using both two-component and three-component masker modulators. Following Ewert *et al.* (2002), they used the term ''venelope'' to refer to the (ac-coupled) envelope of the envelope. Like Moore *et al.*, Verhey *et al.* found that, for a probe modulation frequency equal to the masker venelope periodicity, the probe modulation depth at threshold varied with the phase of the probe relative to the venelope. However, unlike Moore *et al.*, Verhey *et al.* found that thresholds were lower for the in-phase condition, where maxima in the probe coincided with maxima in the venelope, than for the antiphase condition. In comparable experiments, described later, Füllgrabe *et al.* (2004) found large individual differences in the relative probe phase leading to the poorest detectability of the probe modulation.

Verhey *et al.* argued that basilar-membrane compression could not explain their results, as it leads to the prediction of a phase effect opposite to that found by them. They proposed that the auditory system extracts the venelope prior to the MFB, and in a separate pathway, as suggested earlier by Ewert *et al.* (2002). The concept of venelope extraction may be regarded as a functional way of creating an internal representation that contains both the envelope and the venelope. Several researchers have also noted that venelope or ''beat'' cues may be present at the outputs of modulation filters tuned to the first-order or ''carrier'' rates (Ewert *et al.*, 2002; Fullgrabe and Lorenzi, 2003; Millman *et al.*, 2003; Verhey *et al.*, 2003); such cues might be used for the detection of the envelope beats (Millman *et al.*, 2003).

The present paper is particularly concerned with two issues. First, we wished to establish more clearly how the detectability of probe modulation depends on the relative phase of the probe and the venelope of a two-component masker modulator beating at the same rate as the probe. Second, we wished to establish whether the effect produced by the two-component masker modulator could be explained in terms of the introduction by the auditory system of a distortion component at the venelope rate. In experiment 1 we measured psychometric functions for the detection of probe modulation for eight different relative phases of the probe and venelope. We measured psychometric functions rather than estimating thresholds using an adaptive procedure, since it was not obvious that the psychometric functions would always be monotonic (or that d' would always be positive), as explained below. Also, we wished to assess whether the form of the psychometric functions could be explained using the assumption of a distortion component. In experiment 2 we measured psychometric functions for the detection of probe modulation in the presence of a two-component masker modulator using the relative phase that had been found in experiment 1 to lead to the poorest performance. A two-alternative forced-choice task without feedback was used. We anticipated that if a distortion component at the venelope rate was present, and was out of phase with the probe modulation, it might lead to negative d' values for some probe modulation depths, i.e., the probe would be consistently identified in the wrong interval. The results showed that this was indeed the case.

II. EXPERIMENT 1: PSYCHOMETRIC FUNCTIONS FOR DIFFERENT PROBE AND VENELOPE PHASES

A. Stimuli

The carrier was a 4-kHz sinusoid with a level of 70 dB SPL. This relatively high carrier frequency was chosen so that the spectral sidebands produced by the modulation would not be resolved. The probe modulation frequency was 5 Hz. The masker modulator was composed of two sinusoids with frequencies of 50 and 55 Hz. The modulation index, m, for each masker modulator component was 0.3. Each modulator started in sine phase. The equation describing the masker *envelope*, $E(t)$, is

$$E(t) = 1 + 0.3\sin(2\pi 55t) + 0.3\sin(2\pi 50t), \quad (1)$$

where t is time. Although the individual modulator components had zero amplitude at time zero, the venelope had its maximum value (0.6) at time zero. The venelope of the masker modulator repeated at a 5-Hz rate, but there was no 5-Hz component in the modulation spectrum of the masker. The phase of the probe modulation relative to the venelope is defined in terms of $\Delta\varphi$, where $\Delta\varphi$ is zero when the peak in the amplitude of the probe modulation coincides with the peak in the venelope. This meant that, for $\Delta\varphi = 0$, the signal starting phase was advanced by 90° ($\pi/2$ radians) relative to sine phase. Values of $\Delta\varphi$ were 0, 45, 90, 135, 180, 225, 270, and 315°.

On each trial, the carrier was presented in two bursts separated by a silent interval of 300 ms. Each burst had 20-ms raised-cosine rise and fall ramps, and an overall duration (including rise/fall times) of 1000 ms. The modulation was applied during the whole of the carrier, and the starting phase of the modulation is defined relative to the start of the carrier.

Stimuli were generated using a Tucker-Davis Technologies array processor (TDT-AP2) in a host PC, and a 16-bit digital to analog converter (TDT-DD1) operating at a 50-kHz sampling rate. The stimuli were attenuated (TDT-PA4) and sent through an output amplifier (TDT-HB6) to a Sennheiser HD580 earphone. Only one ear was tested for each subject. Subjects were seated in a double-walled sound-attenuating chamber.

B. Procedure

Psychometric functions were measured using a two-interval forced-choice procedure. The masker modulation

was present in both intervals of a trial, and the probe modulation was presented in either the first or the second interval, selected at random. The task of the subject was to indicate, by pressing one of two buttons, the interval containing the probe modulation. Feedback was provided by lights following each response. For each subject and each value of $\Delta\varphi$, five different values were used for the modulation depth of the probe, m_p. The values were chosen individually for each subject and each value of $\Delta\varphi$ on the basis of pilot trials, so as to give values for the detectability index, d', ranging from just above zero to about 2–3. A run started with five trials using the largest value of m_p. Then, in successive trials, stimuli with each value of m_p were presented once, in descending order. This sequence was repeated ten times to give a total of 55 trials per run. With this procedure, subjects receive an easily detected stimulus once every five trials, which helps them to ''remember'' what aspect of the stimulus they should be listening to. Without such a reminder, subjects may ''lose'' the most effective detection cue, leading to unduly poor performance for low probe modulation depths (Taylor *et al.*, 1983; Moore and Sek, 1992). Results from the first five trials of each run were discarded. Each run was repeated at least 20 times, so that at least 200 judgments were obtained for each value of m_p.

C. Subjects

Three subjects were tested. One was author AS. The other two subjects were paid for their services. All subjects had absolute thresholds less than 20 dB HL at all audiometric frequencies and had no history of hearing disorders. All had previous experience in psychoacoustic tasks, including tasks similar to the one used here. They received extensive practice during the pilot trials used to determine appropriate values of m_p to be used in the main experiment.

D. Results

The percent-correct scores were converted to d' values using standard tables (Hacker and Ratcliff, 1979). The pattern of results was similar across subjects. Psychometric functions for a representative subject (AW) are shown by the open squares in Fig. 1; d' is plotted as a function of $20\log(m_p)$ (the solid squares connected by dashed lines show predictions which are explained later). Performance varied markedly with $\Delta\varphi$. Poorest performance was found for $\Delta\varphi = 135°$ and 180°. Best performance was found for $\Delta\varphi = 0°$ and 315°. This pattern of results was found for all three subjects and is similar to that found by Verhey *et al.* (2003), but differs from that found by Moore *et al.* (1999). There were some cases of negative d' values in the results. However, none of the d' values was significantly below 0, based on confidence intervals for d' calculated as described by Miller (1996).

To estimate threshold values of m_p giving a d' value of 1, the data were fitted with functions of the form

$$\log_{10}(d') = a + b\log_{10}(m_p), \tag{2}$$

where a and b are fitting constants. Since the d' values were sometimes negative for the two smallest values of m_p, the fitting was done using only the data for the three largest values of m_p. The resulting threshold estimates are shown in Table I. The pattern of results is similar across subjects, all three showing the highest thresholds for $\Delta\varphi = 135°$. A within-subjects analysis of variance on the threshold values with factor phase showed a highly significant effect of phase: $F(7,14) = 15.598$, $p < 0.001$. The threshold values are somewhat lower than those estimated by Verhey *et al.* (2003) in their most similar condition (5-kHz carrier, masker modula-

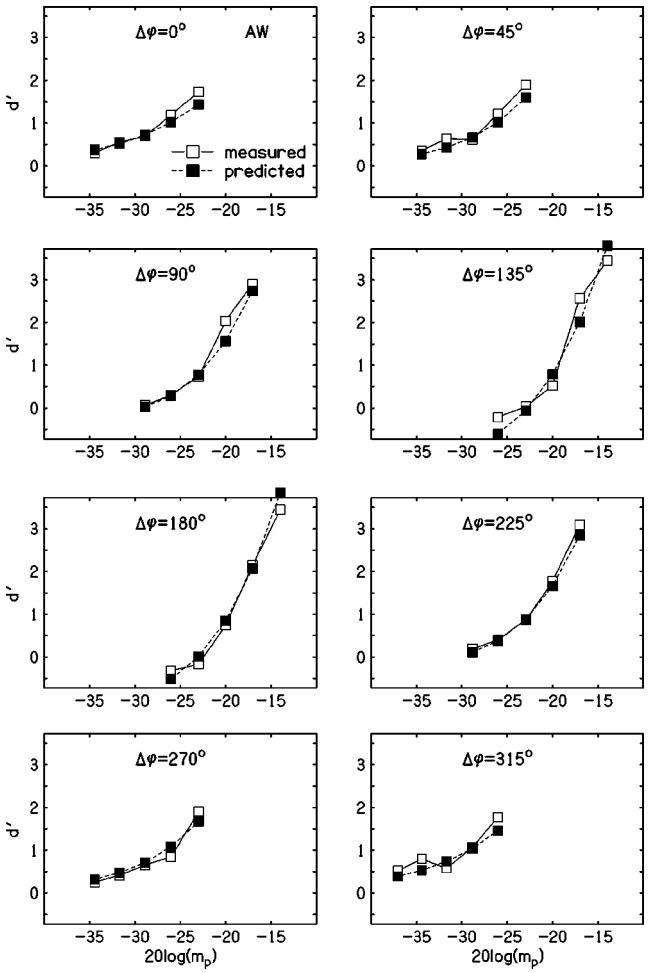

FIG. 1. Open squares show results of experiment 1 for subject AW. The detectability index, d', for detecting 5-Hz probe modulation is plotted as a function of $20\log(m_p)$, where m_p is the modulation depth of the probe. Each panel shows results for one relative phase of the probe modulation relative to the beat cycle (the venelope) of the masker modulator; the relative phase is denoted $\Delta\varphi$. Filled squares connected by dashed lines show predictions derived as described in the text.

TABLE I. Thresholds ($d' = 1$) estimated from the functions relating $\log(d')$ to $\log(m_p)$.

Phase, degrees	JL	AW	AS	Mean
0	−28.4	−26.8	−26.0	−27.1
45	−26.6	−26.6	−23.0	−25.4
90	−23.7	−22.1	−19.5	−21.8
135	−18.3	−18.6	−18.4	−18.4
180	−19.0	−19.2	−21.6	−19.9
225	−20.6	−22.4	−22.4	−21.8
270	−24.1	−26.1	−26.5	−25.6
315	−26.4	−29.0	−27.3	−27.6

tors at 40 and 45 Hz), perhaps because the signal duration used here was longer (1000 ms versus 600 ms).

Two methods were used to estimate the value of $\Delta\varphi$ giving poorest performance. Both methods are based on the assumption that the function relating the threshold to the value of $\Delta\varphi$ is symmetrical about the value of $\Delta\varphi$ giving the highest threshold. In the first method, the mean thresholds were fitted with a function of the following form:

$$\text{slope} = \max - A(\Delta\varphi - \varphi_{\text{offset}})^2, \tag{3}$$

where max is the maximum value of the function, A is a constant, and φ_{offset} is the value of $\Delta\varphi$ at the maximum of the function. The best-fitting value of φ_{offset} was 155°. In the second method, the data were fitted with a single cycle of a sine function, where the amplitude, the dc-offset, and the phase were free parameters. The best-fitting function had a maximum for $\Delta\varphi = 155°$. The two methods are consistent in indicating that the poorest performance was obtained for $\Delta\varphi = 155°$.

The results are consistent with the idea that a nonlinearity in the auditory system introduced a weak distortion component into the internal representation of the envelope with a phase of $-25°$ relative to the venelope. We denote the effective modulation depth of the hypothetical distortion component by m_d. The pattern of results can be understood in the following way. The probe modulation was probably detected as a change in the depth of 5-Hz modulation; for comparable effects of phase using noise carriers, see Bacon and Grantham (1989) and Strickland and Viemeister (1996). Regardless of the value of $\Delta\varphi$, subjects had to distinguish the 5-Hz modulation of depth m_d in the nonsignal interval from the 5-Hz modulation in the signal interval resulting from the vector sum of the distortion component and the probe modulation, which is denoted m_{sum}. For some values of $\Delta\varphi$ (135° and 180°), the distortion component and probe modulation tend to cancel, leading to a small value of m_{sum} and to poor performance. For other values of $\Delta\varphi$ (0° and 315°), the distortion component and probe modulation are almost in phase, leading to a large value of m_{sum} and to good performance. However, the value of d' should be monotonically related to $m_{\text{sum}} - m_d$ (the difference in modulation depth in the two intervals), and the relationship should be the same for all values of $\Delta\varphi$.

To test this prediction, for each subject a starting value was assumed for m_d. Assuming that the distortion component had a phase relative to the venelope of $-25°$, the value of m_{sum} was calculated for each value of m_p. The correlation of the d' values with the values of $m_{\text{sum}} - m_d$ was then determined, and the value of m_d was systematically varied to determine the value giving the highest correlation. The resulting values of m_d, expressed as $20\log(m_d)$, were -29.1, -28.3, and -30.2 for JL, AW, and AS, respectively, and the corresponding correlations were 0.97, 0.97, and 0.94. These values for $20\log(m_d)$ suggest that the effective magnitude of the hypothetical distortion component is very low, corresponding to a barely detectable amount of modulation for a sinusoidal carrier (Zwicker, 1952; Sek and Moore, 1994; Dau *et al.*, 1997a; Kohlrausch *et al.*, 2000; Moore and Glasberg, 2001). Increasing the assumed value of m_d by, for example, 6 dB resulted in substantial decreases in the correlation of the d' values with the values of $m_{\text{sum}} - m_d$. Averaging across subjects, the correlation decreased from 0.96 to 0.75. Decreasing the assumed value of m_d by 6 dB resulted in somewhat smaller decreases in the correlation, to a mean value of 0.91. Thus, the magnitude of the distortion component is unlikely to be much bigger than estimated above, but it could be somewhat smaller.

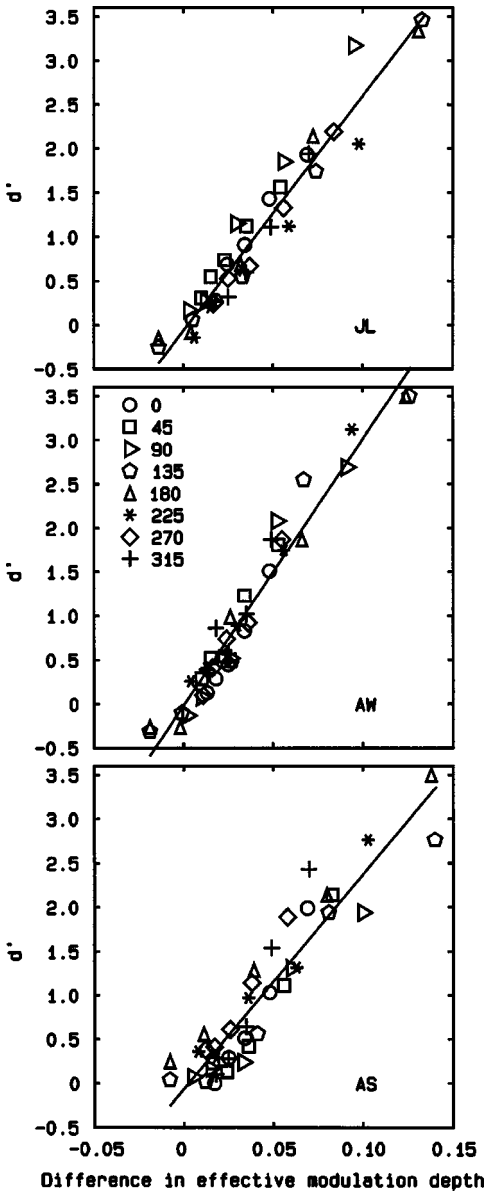

FIG. 2. Scatter plots of the values of d' against the values of $m_{\text{sum}} - m_d$ (see the text), denoted here "difference in effective modulation depth." Each panel shows results for one subject. Each symbol shows results for one value of $\Delta\varphi$, as indicated in the key. Linear regression lines are also shown.

Figure 2 shows scatter plots of the values of d' against the values of $m_{\text{sum}} - m_d$. It is clear that the data for the different values of $\Delta\varphi$ all lie along the same function for each subject and that d' is almost linearly related to $m_{\text{sum}} - m_d$. The scatter plots in Fig. 2 were fitted with linear regression lines, which are shown in the figure, and these lines were used to generate predicted values of d' for each value of $\Delta\varphi$ and m_p. The predictions for AW are shown as filled squares and dashed lines in Fig. 1. There is no evidence

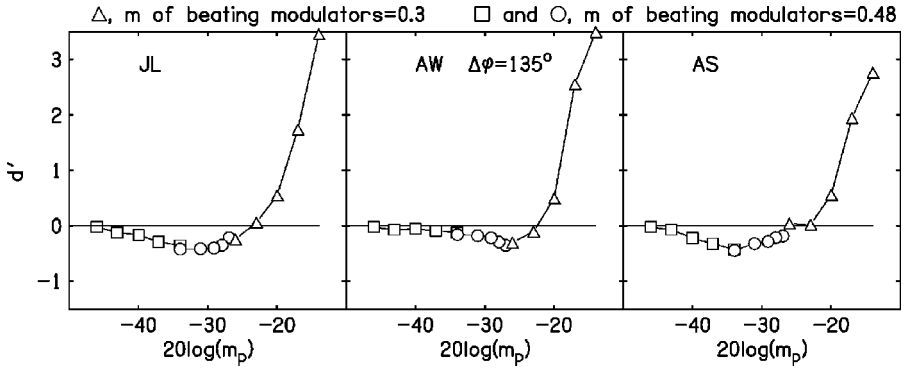

FIG. 3. The squares and circles show results of experiment 2, in which no feedback was given and each component of the masker had a modulation depth of 0.48. The triangles reproduce results from experiment 1 in which feedback was given and each component of the masker had a modulation depth of 0.3. The value of $\Delta\varphi$ was fixed at 135°. Each panel shows results for one subject.

for any systematic discrepancy between the predicted and obtained values. This was also true for the results of the other subjects.

In summary, the results are consistent with the idea that the masking of the 5-Hz probe modulation by the two-component masker modulator was caused by a low-level 5-Hz distortion component in the internal representation of the masker envelope. This distortion component appears to have a phase of about −25° relative to the venelope of the masker.

III. EXPERIMENT 2: PSYCHOMETRIC FUNCTIONS DETERMINED WITHOUT FEEDBACK USING VERY LOW PROBE MODULATION DEPTHS

A. Rationale

In experiment 2, we sought further evidence for the hypothetical envelope distortion product.

The experiment was similar to experiment 1, but was modified in the following ways.

(1) Only a single value of $\Delta\varphi$ was used, namely 135°. This was the value that led to the poorest performance in experiment 1. For this value of $\Delta\varphi$, the envelope distortion product should have been almost opposite in phase to the probe modulation.
(2) No feedback was given. This meant that subjects could not use the feedback to modify their strategy, and made it more likely that they would always pick the interval in which the modulation depth sounded greater.
(3) The modulation depth of the two-component masker modulator was increased. The value of m for each component of the masker was set to 0.48. This was done since it seemed likely that the magnitude of the hypothetical distortion product would increase with increasing modulation depth of the masker (Moore and Sek, 2000; Sek and Moore, 2003). One possible problem here is that the phase of the hypothetical distortion product might change with the modulation depth of the masker. Thus, the value of $\Delta\varphi$ of 135° might not be optimal for producing cancellation of the probe modulation. The maximum amplitude of the masker modulator, given that the two modulator components started in sine phase, was 0.9573. To avoid overmodulation, the modulation depth of the probe was not allowed to exceed 0.0447. Given that $\Delta\varphi$ was 135°, the maximum amplitude of the masker and probe modulators combined was 0.9839.
(4) The probe modulation depths were chosen to be small, so that they were likely to be comparable with the modulation depth of the hypothetical distortion product, as estimated in experiment 1. This was done to increase the likelihood of finding cancellation effects.
(5) Several closely spaced values of m_p were used, to avoid the possibility of missing the range of values of m_p over which d' was negative.

B. Method

The subjects were the same as for experiment 1. The stimuli and method were also almost the same as for experiment 1, except that no feedback was provided. Two sets of runs were conducted, covering different ranges of the probe modulation depth, m_p. In one set, the values were 0.005, 0.007, 0.01, 0.014, and 0.02. In a second set, the values were 0.02, 0.028, 0.035, 0.04, and 0.045. Each run was repeated at least 40 times, so that at least 400 judgments were obtained for each value of m_p.

C. Results

The results for each subject are shown in Fig. 3. The results for the two sets of values of m_p used in experiment 2 are shown by squares and circles. The triangles show results from experiment 1 for $\Delta\varphi$=135°; note, however, that the masker modulation depth was greater in experiment 2 than in experiment 1. The results for small values of m_p show that there is a range over which d' is consistently negative. The minimum value of d' occurs for $20\log(m_p)\approx-30$, although the value varies across subjects from −34 to −27. At the minimum, the value of d' is about −0.43. Confidence intervals for d' were calculated as described by Miller (1996). For 400 forced-choice trials and for $d'\approx0.4$, the 95%-confidence interval is about ±0.2. Thus, d' values in the vicinity of the minimum differ significantly from zero ($p<0.05$).

The results support the idea that the auditory system generates a weak envelope distortion component at the venelope rate (5 Hz). When the probe modulation depth is comparable to the effective modulation depth of the distortion component, and when $\Delta\varphi$=135°, the probe and distortion component modulation nearly cancel, leading subjects to select the "wrong" interval as containing the probe modulation. It seems reasonable to assume that the probe and distortion component are nearly equal in effective modulation

depth when d' is at its most negative value. As noted above, the minimum value of d' occurred for $20\log(m_p) \approx -30$. Thus, the results suggest that the distortion component in the internal representation of the envelope has a magnitude approximately equal to that produced by an input modulation depth of 0.032.

The estimated values of m_d for individual subjects are similar to those estimated from the data of experiment 1, and are in the same rank order; the value is highest for AW and lowest for AS. It is curious that the estimated values were not higher for experiment 2 than for experiment 1, as the masker modulation depth was greater in experiment 2. Possibly, the relative phase of the distortion component varies with the masker modulation depth, and the value of $\Delta\varphi$ chosen for experiment 2 was not optimal for producing cancellation of the distortion component and probe modulation.

The effective level of the distortion component estimated from experiments 1 and 2 is comparable to that estimated by Moore *et al.* (1999). For a two-component modulator with $m=0.3$ for each component, the distortion product was estimated to have an effective modulation index of 0.027 ($20\log m=-33.7$). In their model, Ewert *et al.* (2002) and Verhey *et al.* (2003) assumed that the effective magnitude of the venelope component was scaled by a factor of 0.3 relative to the envelope. For example, for a two-component modulator with $m=0.3$ for each component, the venelope amplitude fluctuates between 0 and 0.6, so the scaled venelope would have a peak-to-valley ratio of 0.2. Due to the fact that the two-component modulator does not produce a sinusoidal venelope, the venelope component at the difference frequency would have a value of m of about 0.076 ($20\log m=-22.4$). This is somewhat larger than estimated from experiments 1 and 2. The difference across studies may simply reflect individual differences.

IV. DISCUSSION

There are various ways in which nonlinearities in the auditory system might introduce a distortion component at the venelope rate into the internal representation of the envelope. Basilar-membrane compression is probably not involved, since that nonlinearity would introduce a distortion component that was 180° out of phase with the venelope. In any case, the detection of AM of a sinusoidal carrier probably depends strongly on the use of information from the high-frequency side of the excitation pattern evoked by the carrier (Zwicker, 1956; Moore and Sek, 1994; Kohlrausch *et al.*, 2000). This part of the excitation pattern appears to be processed almost linearly on the basilar membrane, at least for medium to high frequencies (Rhode and Robles, 1974; Sellick *et al.*, 1982), so a distortion component at the venelope rate would not be introduced. Basilar-membrane nonlinearity might play a greater role if subjects were forced to attend to the outputs of auditory filters tuned close to the carrier frequency (which is not the case for most previous studies, or the current one).

In experiments similar to the present ones, Füllgrabe *et al.* (2004) measured the detectability of 5-Hz probe modulation of a 5-kHz carrier in the presence of a ''second-order'' modulator (Lorenzi *et al.*, 2001a; 2001b), as a function of the relative phase, $\Delta\varphi$, between the probe modulation and the venelope of the second-order modulation. They included conditions with a notched noise centered at 5 kHz, which was intended to restrict off-frequency listening. In the absence of the notched noise, the value of $\Delta\varphi$ leading to poorest detectability of 5-Hz second-order modulation varied with the first-order modulation rate, suggesting that at least one component of the nonlinearity that generates the envelope distortion product is time varying; an instantaneous nonlinearity would lead to an envelope distortion component with a relative phase that was independent of the first-order rate. In the presence of the notched noise, the value of $\Delta\varphi$ giving poorest detectability hardly varied with first-order modulation rate, but it did vary across subjects, from about 45° to 135°. These results suggest that more than one mechanism may contribute to the nonlinearity.

Possible nonlinearities contributing to distortion in the internal representation of the envelope occur in peripheral transduction processes (Yates, 1990), and peripheral adaptation effects (Smith, 1977). The model of Dau and co-workers (Dau *et al.*, 1997a; 1997b) incorporates ''adaptation loops'' to simulate adaptation processes, which introduce strong nonlinearity, but only for very low modulation rates (below about 2 Hz). Verhey *et al.* (2003) considered several models for generating a distortion component at the venelope rate. These included a ''threshold'' model, which effectively produced half-wave rectification of the ac-coupled envelope, and a model in which the venelope was explicitly extracted. They concluded that the venelope model gave the best fit to their data. However, for this model, the best performance is predicted to occur when $\Delta\varphi$ is *exactly* equal to 0° and the worst performance is predicted when $\Delta\varphi$ is *exactly* 180°. In our experiment 1, performance was poorest for $\Delta\varphi=135$ and 180°, and the form of the data suggested a threshold maximum centered at about 155°. In the study of Füllgrabe *et al.* (2004), described above, the value of $\Delta\varphi$ leading to poorest performance was often below 180° when no notched noise was used, and was consistently below 180° when a notched-noise was used. Thus, it seems clear that the envelope distortion component is not always exactly in phase with the venelope, and that the distortion component phase may vary from one subject to another. This casts some doubt upon the idea that the envelope distortion component results from explicit extraction of the venelope at some stage in the auditory system.

V. CONCLUSIONS

The following conclusions can be drawn from this study.

(1) Experiment 1 showed that, in the presence of a pair of masker modulators beating at a 5-Hz rate (50 and 55 Hz), the detectability of 5-Hz probe modulation was dependent on the phase of the probe modulation relative to the beat cycle of the masker modulators. The relative phase, $\Delta\varphi$, is defined as zero when the peak amplitude of the probe modulation coincides with a peak in the beat cycle (the peak in the venelope of the masker). The best

performance occurred when $\Delta\varphi$ was 0° or 315°. The poorest performance occurred when $\Delta\varphi$ was 135° or 180°.

(2) The pattern of the results for experiment 1 could be fitted well based on the assumption that the auditory system introduced a weak distortion component in the modulation spectrum at a 5-Hz rate. Performance appears to be based on the difference between the modulation depth of the distortion component (in the nonsignal interval) and of the vector sum of the distortion component and the probe modulation (in the signal interval). The value of d' is linearly related to this difference.

(3) Experiment 2 used a fixed value of $\Delta\varphi$ of 135°; this was the value that led to the poorest performance in experiment 1. In contrast to experiment 1, no feedback was given. The results showed that d' values were consistently negative over a range of probe modulation depths, m_p; in other words, over this range of m_p subjects consistently identified the probe modulation as being in the wrong interval of the two-alternative forced-choice task. The value of m_p leading to the most negative value of d' was about 0.032 [$20\log(m_p) = -30$].

(4) The results are consistent with the idea that nonlinearities within the auditory system can introduce a weak distortion component in the internal representation of the envelopes of the stimuli, although a compressive nonlinearity does not account for the results. In the case of two-component beating modulators, a weak component is introduced at the beat rate. Even for large modulation depths of the two-component modulator, the effective modulation depth of the distortion component appears to be only about 0.03.

(5) For the conditions of our experiment, the envelope distortion component appears to have a phase between 0° and −45° relative to the venelope; the best estimate of the relative phase was −25°. However, the relative phase may vary across conditions (e.g., with the frequencies of the masker modulator components) and across subjects.

ACKNOWLEDGMENTS

This work was supported by the Wellcome Trust and the Medical Research Council (UK). We thank Neal Viemeister, Torsten Dau, Christian Lorenzi, and one anonymous reviewer for helpful comments on an earlier version of this paper.

Bacon, S. P., and Grantham, D. W. (**1989**). "Modulation masking: Effects of modulation frequency, depth, and phase," J. Acoust. Soc. Am. **85**, 2575–2580.

Dau, T., Kollmeier, B., and Kohlrausch, A. (**1997a**). "Modeling auditory processing of amplitude modulation. I. Detection and masking with narrow-band carriers," J. Acoust. Soc. Am. **102**, 2892–2905.

Dau, T., Kollmeier, B., and Kohlrausch, A. (**1997b**). "Modeling auditory processing of amplitude modulation. II. Spectral and temporal integration," J. Acoust. Soc. Am. **102**, 2906–2919.

Ewert, S. D., and Dau, T. (**2000**). "Characterizing frequency selectivity for envelope fluctuations," J. Acoust. Soc. Am. **108**, 1181–1196.

Ewert, S. D., Verhey, J. L., and Dau, T. (**2002**). "Spectro-temporal processing in the envelope-frequency domain," J. Acoust. Soc. Am. **112**, 2921–2931.

Füllgrabe, C., and Lorenzi, C. (**2003**). "The role of envelope beat cues in the detection and discrimination of second-order amplitude modulation," J. Acoust. Soc. Am. **113**, 49–52.

Füllgrabe, C., Moore, B. C. J., Demany, L., Ewert, S., Sheft, S., and Lorenzi, C. (**2004**). "Modulation masking produced by 2nd-order modulators," J. Acoust. Soc. Am. (submitted).

Hacker, M. J., and Ratcliff, R. (**1979**). "A revised table of d' for M-alternative forced choice," Percept. Psychophys. **26**, 168–170.

Houtgast, T. (**1989**). "Frequency selectivity in amplitude-modulation detection," J. Acoust. Soc. Am. **85**, 1676–1680.

Kay, R. H. (**1982**). "Hearing of modulation in sounds," Physiol. Rev. **62**, 894–975.

Kohlrausch, A., Fassel, R., and Dau, T. (**2000**). "The influence of carrier level and frequency on modulation and beat-detection thresholds for sinusoidal carriers," J. Acoust. Soc. Am. **108**, 723–734.

Lorenzi, C., Soares, C., and Vonner, T. (**2001a**). "Second-order temporal modulation transfer functions," J. Acoust. Soc. Am. **110**, 1030–1038.

Lorenzi, C., Simpson, M. I., Millman, R. E., Griffiths, T. D., Woods, W. P., Rees, A. *et al.* (**2001b**). "Second-order modulation detection thresholds for pure-tone and narrow-band noise carriers," J. Acoust. Soc. Am. **110**, 2470–2478.

Miller, J. (**1996**). "The sampling distribution of d'," Percept. Psychophys. **58**, 65–72.

Millman, R. E., Green, G. G., Lorenzi, C., and Rees, A. (**2003**). "Effect of a noise modulation masker on the detection of second-order amplitude modulation," Hear. Res. **178**, 1–11.

Moore, B. C. J., and Glasberg, B. R. (**2001**). "Temporal modulation transfer functions obtained using sinusoidal carriers with normally hearing and hearing-impaired listeners," J. Acoust. Soc. Am. **110**, 1067–1073.

Moore, B. C. J., and Sek, A. (**1992**). "Detection of combined frequency and amplitude modulation," J. Acoust. Soc. Am. **92**, 3119–3131.

Moore, B. C. J., and Sek, A. (**1994**). "Effects of carrier frequency and background noise on the detection of mixed modulation," J. Acoust. Soc. Am. **96**, 741–751.

Moore, B. C. J., and Sek, A. (**2000**). "Effects of relative phase and frequency spacing on the detection of three-component amplitude modulation," J. Acoust. Soc. Am. **108**, 2337–2344.

Moore, B. C. J., Sek, A., and Glasberg, B. R. (**1999**). "Modulation masking produced by beating modulators," J. Acoust. Soc. Am. **106**, 908–918.

Rhode, W. S., and Robles, L. (**1974**). "Evidence from Mössbauer experiments for nonlinear vibration in the cochlea," J. Acoust. Soc. Am. **55**, 588–596.

Sek, A., and Moore, B. C. J. (**1994**). "The critical modulation frequency and its relationship to auditory filtering at low frequencies," J. Acoust. Soc. Am. **95**, 2606–2615.

Sek, A., and Moore, B. C. J. (**2003**). "Testing the concept of a modulation filter bank: The audibility of component modulation and detection of phase change in three-component modulators," J. Acoust. Soc. Am. **113**, 2801–2811.

Sellick, P. M., Patuzzi, R., and Johnstone, B. M. (**1982**). "Measurement of basilar membrane motion in the guinea pig using the Mössbauer technique," J. Acoust. Soc. Am. **72**, 131–141.

Sheft, S., and Yost, W. A. (**1997**). "Modulation detection interference with two-component masker modulators," J. Acoust. Soc. Am. **102**, 1106–1112.

Shofner, S., Sheft, S., and Guzman, S. J. (**1996**). "Responses of ventral cochlear nucleus units in the chinchilla to amplitude modulation by low-frequency, two-tone complexes," J. Acoust. Soc. Am. **99**, 3592–3605.

Smith, R. L. (**1977**). "Short-term adaptation in single auditory-nerve fibers: Some poststimulatory effects," J. Neurophysiol. **49**, 1098–1112.

Strickland, E. A., and Viemeister, N. F. (**1996**). "Cues for discrimination of envelopes," J. Acoust. Soc. Am. **99**, 3638–3646.

Taylor, M. M., Forbes, S. M., and Creelman, C. D. (**1983**). "PEST reduces bias in forced-choice psychophysics," J. Acoust. Soc. Am. **74**, 1367–1374.

Verhey, J. L., Ewert, S., and Dau, T. (**2003**). "Modulation masking produced by complex tone modulators," J. Acoust. Soc. Am. **114**, 2135–2146.

Yates, G. K. (**1990**). "Basilar membrane nonlinearity and its influence on auditory nerve rate-intensity functions," Hear. Res. **50**, 145–162.

Zwicker, E. (**1952**). "Die Grenzen der Hörbarkeit der Amplitudenmodulation und der Frequenzmodulation eines Tones (The limits of audibility of amplitude modulation and frequency modulation of a pure tone)," Acustica **2**, 125–133.

Zwicker, E. (**1956**). "Die elementaren Grundlagen zur Bestimmung der Informationskapazität des Gehörs (The foundations for determining the information capacity of the auditory system)," Acustica **6**, 356–381.

Sequential F0 comparisons between resolved and unresolved harmonics: No evidence for translation noise between two pitch mechanisms[a)]

Christophe Micheyl[b)] and Andrew J. Oxenham[c)]
Research Laboratory of Electronics, Massachusetts Institute of Technology, Cambridge, Massachusetts 02139-4307

(Received 29 May 2003; revised 24 June 2004; accepted 13 August 2004)

Carlyon and Shackleton [J. Acoust. Soc. Am. **95**, 3541–3554 (1994)] suggested that fundamental-frequency (F0) discrimination performance between resolved and unresolved harmonics is limited by an internal ''translation'' noise between the outputs of two distinct F0 encoding mechanisms, in addition to the encoding noise associated with each mechanism. To test this hypothesis further, F0 difference limens (DLF0s) were measured in six normal-hearing listeners using sequentially presented groups of harmonics. The two groups of harmonics presented on each trial were bandpass filtered into the same or different spectral regions, in such a way that both groups contained mainly resolved harmonics, both groups contained only unresolved harmonics, or one group contained mainly resolved and the other only unresolved harmonics. Three spectral regions (low: 600–1150 Hz, mid: 1400–2500 Hz, or high: 3000–5250 Hz) and two nominal F0s (100 and 200 Hz) were used. The DLF0s measured in across-region conditions were well accounted for by a model assuming only two sources of internal noise: the encoding noise estimated on the basis of the within-region results plus a constant noise associated with F0 comparisons across different spectral regions, independent of resolvability. No evidence for an across-pitch-mechanism translation noise was found. A reexamination of previous evidence for the existence of such noise suggests that the present negative outcome is unlikely to be explained by insufficient measurement sensitivity or an unusually large across-region comparison noise in the present study. While the results do not rule out the possibility of two separate pitch mechanisms, they indicate that the F0s of sequentially presented resolved and unresolved harmonics can be compared internally at no or negligible extra cost. [DOI: 10.1121/1.1806825]

PACS numbers: 43.66.Hg, 46.66.Fe [NFV] Pages: 3038–3050

I. INTRODUCTION

Harmonic complex tones generally evoke a sensation of pitch corresponding to their fundamental frequency (F0). This sensation, which is elicited even when the F0 component itself is absent from the physical spectrum, is generally referred to as complex pitch, fundamental pitch, residue pitch, or periodicity pitch. Although the mechanisms mediating periodicity pitch have been studied experimentally for over a century, they remain uncertain. One important open question is whether F0 perception is mediated by a single mechanism in all circumstances (e.g., Meddis and O'Mard, 1997), or whether different mechanisms operate, depending on whether the harmonics are resolved or not in the auditory periphery (e.g., Carlyon and Shackleton, 1994). Resolved harmonics are thought to be represented individually in the auditory periphery, and can be individually ''heard out,'' whereas unresolved harmonics combine within the periphery to produce complex waveforms with a repetition rate corresponding to the F0.

One of the seemingly strongest arguments in favor of the ''two pitch mechanisms'' hypothesis was put forward by Carlyon and Shackleton (1994). They showed that performance in a task where listeners had to compare the F0s of two harmonic complexes presented simultaneously in different spectral regions was significantly worse than predicted in conditions where one group of harmonics was resolved and the other was unresolved, but not when both groups were resolved. They argued that this was consistent with the existence of an extra source of internal noise associated with the ''translation'' between the outputs of the two F0-encoding mechanisms, in addition to the encoding noise associated with each mechanism. Carlyon and Shackleton further noted that existing implementations of a single, autocorrelation-based model of F0 encoding did not account for the finding of better F0 discrimination performance between two resolved complexes than between one resolved and one unresolved complex irrespective of spectral region (see also Carlyon, 1998).

More recently, Carlyon *et al.* (2000) found that thresholds for detecting mistuning between two simultaneous F0-modulated complexes filtered into different spectral regions were larger when the two complexes were of a different resolvability status than when they were of the same resolvability status (at least for modulation rates below 10 Hz). These authors also proposed a model for predicting the

[a)]Portions of this work were presented at the 145th meeting of the Acoustical Society of America, Nashville, Tennessee, 28 April–2 May 2003 [J. Acoust. Soc. Am. **113**, 2225 (2003)] and at the International Symposium on Hearing, Dourdan, France, 24–28 August 2003.

[b)]Electronic mail: cmicheyl@mit.edu
[c)]Electronic mail: oxenham@mit.edu

thresholds in simultaneous across-region conditions from those measured in within-region conditions, but they did not test specifically for translation noise between the outputs of two distinct mechanisms for the pitch of resolved and unresolved harmonics in that study. Similarly, an earlier study by Carlyon *et al.* (1992) looked at F0 comparisons between simultaneous F0-modulated complexes, using both resolved and unresolved harmonics, but did not test specifically for translation noise. Thus, the currently available empirical evidence for translation noise remains limited to a single study (Carlyon and Shackleton, 1994).

The present study provides a further test of the existence of translation noise in comparisons between F0 estimates derived from resolved and unresolved harmonics. Thresholds for F0 comparisons between *sequential* harmonic complexes filtered into the same or different spectral regions were measured in six normal-hearing listeners. The nominal F0s and spectral regions were chosen in such a way that the stimuli contained either mostly resolved or only unresolved harmonics. In one set of conditions, the two tones being compared on each trial were filtered into the same spectral region (within-region comparisons). In this situation, the harmonics of both complexes had the same resolvability status. In another set of conditions, the two complexes were filtered into different spectral regions (across-region comparisons). In this situation, depending on which particular combination of spectral regions and nominal F0 was used, the harmonics of the two complexes had either the same or a different resolvability status. By comparing thresholds in these different conditions, we could estimate the size of the encoding noise, the (across-region) comparison noise, and the (across-mechanism) translation noise, and determine the significance of their respective influences.

II. METHODS

A. Listeners

Overall, six subjects (one female, five male, ages between 26 and 46 years) took part in the experiment. All had pure-tone hearing thresholds not exceeding 20 dB HL at octave frequencies between 250 and 8000 Hz. All listeners received substantial training in F0 discrimination using the same stimuli and conditions as used in this study. The listeners were initially trained with stimuli filtered into the same frequency region, so that they could grasp the pitch discrimination task without being confused by timbre differences. Following this initial training phase, the listeners were trained in F0 discrimination with complexes filtered into different spectral regions, until stable thresholds were obtained. Overall, the listeners had received at least 35 h of training before data collection began.

B. Stimuli

The stimulus design was inspired by Shackleton and Carlyon (1994). These authors used a combination of three spectral regions and two F0s in order to tease apart the influence of resolvability from that of F0 or spectral region alone. Our selection of spectral regions was based on a convergence of evidence, suggesting that for F0s between about 100 and 200 Hz, harmonics above about the 10th are unresolved (Hoekstra, 1979; Houtsma and Smurzynski, 1990; Bernstein and Oxenham, 2003). Accordingly, in the ''unresolved'' conditions of the present study, only harmonics above the 10th were contained in the passbands of the spectral regions. We tried to improve on Shackleton and Carlyon's design by choosing spectral regions whose 3-dB passbands always contained at least three harmonics, yet never contained the F0 component itself, and had roughly equal widths on a Cam or ERB_N scale (Glasberg and Moore, 1990; Moore, 2003). In addition, consecutive spectral regions were separated by a roughly equal number of Cams.

TABLE I. Summary of the resolvability conditions produced by combining one of two different nominal F0s with one of three different spectral regions. Entries with the letter R indicate conditions involving essentially resolved harmonics. Entries with the letter U indicate conditions involving only unresolved harmonics.

F0 (Hz)	Low 600–1150 Hz	Mid 1400–2500 Hz	High 3000–5250 Hz
100	R	U	U
200	R	R	U

The stimuli consisted of harmonic complexes filtered into one of three different spectral regions defined by the following corner frequencies: 600–1150 Hz (low), 1400–2500 Hz (mid), or 3000–5250 Hz (high), with spectral slopes on the two sides of 48 dB/oct. Depending on the condition being tested, the two complexes presented successively in each trial were filtered into the same or different spectral regions. Three conditions involved within-region comparisons (low-low, mid-mid, and high-high) and three involved across-region comparisons (low-mid, low-high, mid-high). The nominal F0 of the complexes was either 100 or 200 Hz, leading to 12 combinations of F0 and spectral region. The actual F0s of the complexes presented during the experiment were positioned symmetrically on a logarithmic scale around a reference frequency, which was randomized across trials over a 1-semitone (roughly $\pm 3\%$) range around the nominal F0 (100 or 200 Hz). The spectral regions and F0s were chosen such that the passbands would contain (a) resolved harmonics at both nominal F0s in the low region, (b) only unresolved harmonics at both F0s in the high region, and (c) only unresolved harmonics at the lower F0 but resolved harmonics at the higher F0 in the mid region; this is summarized in Table I.

A background noise was used to mask combination tones. As in Bernstein and Oxenham's (2003) study, the background noise was designed to produce roughly equal pure-tone masked thresholds over a wide frequency range. It was characterized by a flat spectral envelope below 600 Hz, and a spectral slope of -2 dB/oct above that frequency. The noise was low-pass filtered at a cutoff of 16 kHz. It started 500 ms before the first interval and ended 500 ms after the second interval, for a total duration of 2500 ms, including 100-ms raised-cosine ramps. The tones had an overall duration of 500 ms, including 20-ms raised-cosine ramps. The spectrum level of the noise in its flat spectral portion (below 600 Hz) was set 30 dB below the level of the individual

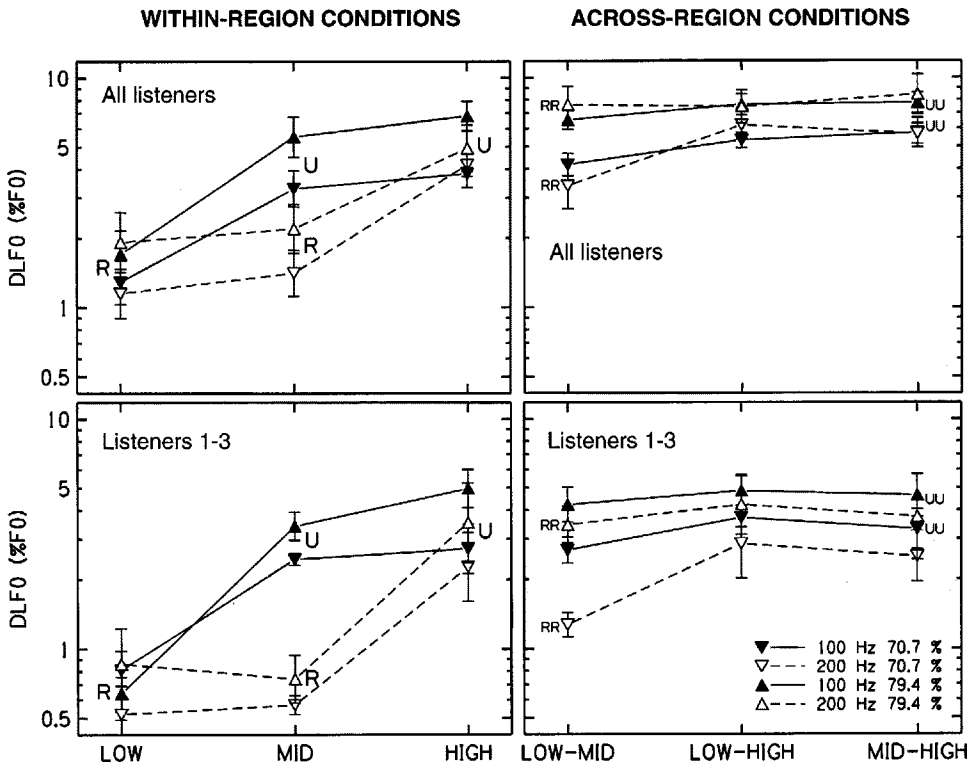

FIG. 1. Mean DLF0s in within-region and across-region conditions. The left-hand panels show within-region data; the right-hand panels show across-region data. The upper panels show averages across all six listeners; the lower panels show averages across listeners 1–3. The different spectral regions used to produce the different conditions are indicated on the abscissa. DLF0s measured using the 100-Hz nominal F0 are indicated by filled symbols connected by solid lines, those measured using the 200-Hz nominal F0 by open symbols connected by dashed lines. For within-region conditions (left-hand panels), DLF0s measured in conditions involving resolved harmonics are indicated by the letter R, and DLF0s measured in conditions involving only unresolved harmonics are indicated by the letter U, next to the corresponding symbols. In across-region conditions (right-hand panels), DLF0s measured in conditions involving two resolved groups are indicated by the letters RR, and DLF0s measured in conditions involving two unresolved groups are indicated by the letters UU, next to the corresponding symbol. (The symbols corresponding to conditions involving one resolved and one unresolved group are not associated to letters in order to avoid cluttering.) Note that while the letters R and U in the within-region panels are associated with more than one symbol, the letters RR and UU in the across-region panels correspond to the single nearest symbol. The 70.7%-correct DLF0s are represented by downward-pointing triangles; the 79.4%-correct DLF0s are represented by upward-pointing triangles. The error bars represent the standard error of the geometric mean across listeners, after removing any overall differences in performance between listeners (i.e., after subtracting their average from the log-transformed DLF0s in each listener).

harmonics within the complexes. The harmonics were added in sine phase and presented at a level of 45 dB SPL per component in the passband.

C. Procedure

DLF0s were measured using an adaptive two-interval, two-alternative forced-choice (2I-2AFC) procedure with either a two-down, one-up or a three-down, one-up rule, tracking the 70.7% and 79.4% correct points, respectively. On each trial, listeners were presented with two successive complex tones differing in F0 by $\Delta F0$. Their task was to judge which of the two intervals contained the complex with the higher F0. The two observation intervals were marked visually, and visual feedback was provided after each trial.

At the beginning of a run, $\Delta F0$ was set to 40%. Depending on the convergence point used (70.7% or 79.4%), $\Delta F0$ was reduced after two or three consecutive correct responses; in all cases, it was increased following an incorrect response. The factor of variation of $\Delta F0$, which was initially 4, was reduced to 2 the first time that $\Delta F0$ went from decreasing to increasing, and to $\sqrt{2}$ the second time (which corresponded to the third overall reversal, a reversal being defined as a change in the direction of variation of $\Delta F0$, either from increasing to decreasing, or from decreasing to increasing). Thresholds were estimated based on the last 12 reversals at the last step size, out of a total of 16 reversals in each track (see below).

Within each run, two independent tracks were randomly interleaved, with each track assigning the higher F0 to a different spectral region. For instance, in the low-mid condition, one track had the higher F0 assigned to the low region and the other track had the higher F0 assigned to the mid region. This allowed us to control for (and calculate) any response biases, or pitch shifts, due to differences in spectral region. Response biases could arise if listeners responded on the basis of spectral region or timbre, rather than periodicity pitch, thus selecting the observation interval that contained the complex filtered in the higher region, not that with the higher F0. Pitch shifts could arise due to a genuine influence of spectral region on pitch (Walliser, 1969; Ohgushi, 1978; Moore and Moore, 2003a,b). Although no such response biases or pitch shifts could occur in within-region conditions (as both tracks were identical), these conditions were run in the same way for consistency. Based on the differences between the raw DLF0s measured in each interleaved pair of tracks, we could estimate the amount of spectral-region bias

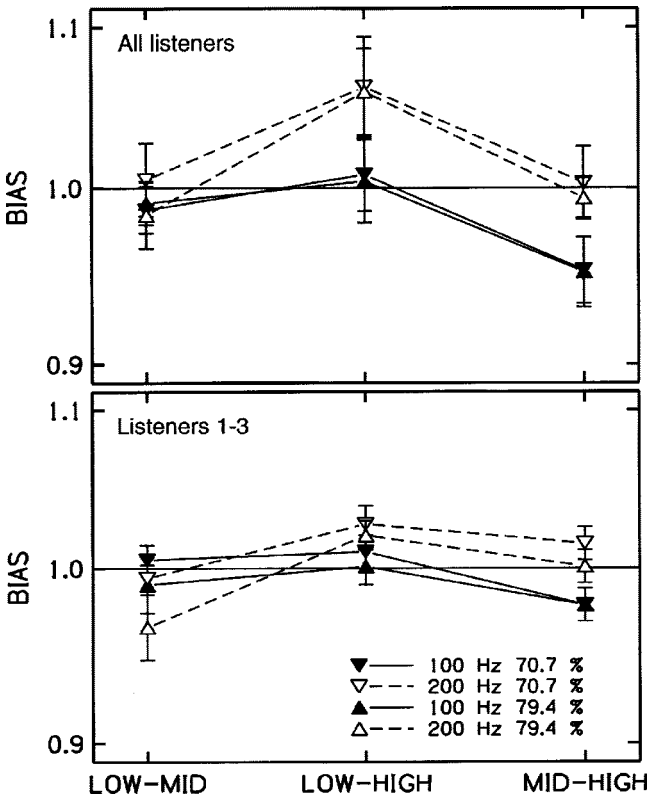

FIG. 2. Spectral-region bias in across-region conditions. The upper panel shows averages across all six listeners; the lower panel shows averages across listeners 1–3. The different spectral regions used to produce the different conditions are indicated on the abscissa. The amount of bias is represented on the ordinate as a multiplicative factor. Values around one indicate no spectral region bias. Values below one indicate a tendency to report the stimulus in the higher spectral region as having the lower F0; values above 1 indicate a tendency to hear the stimulus in the higher spectral region as having the higher F0. Data obtained using a 100-Hz nominal F0 are indicated by filled symbols connected by solid lines; those obtained using a 200-Hz nominal F0 are indicated by open symbols connected by dashed lines. The downward-pointing triangles correspond to 70.7%-correct points, the upward-pointing triangles to 79.4%-correct points. The error bars represent the standard error of the geometric mean across listeners, after removing any overall differences in performance between listeners.

in each condition, and determine the ''true'' DLF0s (after removing the spectral-region bias) in the corresponding condition, as described in Appendix A. Only the ''true'' DLF0s, computed as described in Appendix A, were used in the figures, statistical analyses, and model predictions presented in this article. For clarity, these ''true'' DLF0s are simply referred to as ''DLF0s'' throughout the paper, the expression ''raw DLF0s'' being reserved for the original DLF0s measured in each interleaved track of the adaptive procedure. Three ''true'' DLF0s were obtained in each condition. Pooling across runs and listeners always involved geometric, rather than arithmetic, averages.

D. Apparatus

The stimuli were generated digitally and played out via a soundcard (LynxStudio LynxOne) with 24-bit resolution and a sampling frequency of 32 kHz. The stimuli were then passed to a headphone buffer (TDT HB6) before being presented to the subject via the left earpiece of Sennheiser HD 580 headphones. Subjects were seated in a double-walled sound-attenuating chamber. Intervals were marked by ''lights'' on a virtual response box, displayed on a computer screen, and subjects responded via a computer keyboard.

III. RESULTS

A. DLF0s

Figure 1 shows the DLF0s measured in the within-region conditions (left) and the across-region conditions (right). The upper two panels show mean results obtained by averaging across all six listeners. The lower two panels show the mean results averaged across only three of the above six listeners. The data of these three listeners were isolated because they showed the lowest thresholds and the clearest dissociation, in the within-region conditions, between conditions that involved resolved harmonics and conditions that did not. Selecting these listeners for illustration will be important when examining the evidence for translation noise in mixed-resolvability conditions. This is because those listeners with the lowest levels of encoding noise (i.e., lower thresholds) are perhaps the most likely to exhibit the effects of any additional noise sources. Accordingly, we ran two sets of analyses in parallel: one on the data of all six listeners and one on the data of listeners 1–3 only.

Consider first the within-region data shown in the left-hand panels. As expected, the 79.4%-correct thresholds were generally higher than the 70.7%-correct thresholds [$F(1,5) = 28.95$, $p < 0.005$].[1] Also as expected, conditions involving resolved harmonics (which are indicated by the letter R next to the corresponding symbols in Fig. 1) produced lower thresholds than conditions with unresolved harmonics (which are indicated by the letter U). The average DLF0s in the three selected listeners (lower left panel) are in good agreement with those obtained in earlier studies involving comparable stimuli (Hoekstra, 1979; Shackleton and Carlyon, 1994). Most importantly, the difference between resolved- and unresolved-harmonic conditions observed in these three listeners is at least as large as that observed in these earlier studies.

The right-hand panels in Fig. 1 show the DLF0s measured in across-region conditions. When the whole study group was considered (upper right panel), no significant difference was observed between the DLF0s measured in conditions involving one resolved and one unresolved group, and those measured using both resolved or both unresolved groups (which are marked as ''RR'' and ''UU,'' respectively, in Fig. 1) [$F(1,5) = 0.26$; $p = 0.630$]. Furthermore, the DLF0s measured using two resolved groups (i.e., in the low-mid condition with the 200-Hz nominal F0, which is marked as ''RR'' in Fig. 1) did not differ significantly from those measured using two unresolved groups (i.e., in the mid-high condition with the 100-Hz nominal F0, which is marked as ''UU'' in Fig. 1) [$F(1,5) = 1.77$, $p = 0.241$]. In the subset of listeners (listeners 1–3) whose within-region data showed the clearest dissociation between resolved and unresolved conditions, the DLF0s measured using two groups of resolved harmonics were smaller than those measured using two unresolved groups. This difference was marginally significant [$F(1,2) = 18.48$, $p = 0.050$].

As in the within-region conditions, a significant difference was found between the 70.7%- and the 79.4%-correct DLF0s [$F(1,5)=47.97$, $p=0.001$ for all six listeners; $F(1,2)=52.84$, $p=0.018$ for the three selected listeners]. The increase in DLF0s between the 70.7%- and 79.4%-correct points, although somewhat variable across conditions, did not differ significantly across conditions and was around 50% on average. Assuming unbiased responding, 70.7% and 79.4% correct in a 2AFC task correspond to d' values of about 0.77 and 1.16, respectively—also an increase of about 50%. This finding of similar proportional increases in DLF0 and d' is consistent with earlier results (Plack and Carlyon, 1995).

B. Spectral-region bias

Figure 2 shows the estimated amount of spectral-region bias in the across-region conditions, calculated as described in Appendix A. The amount of bias is expressed as a multiplicative factor: a value of 1 indicates no bias; values below 1 indicate a tendency to respond that the stimulus in the higher spectral region has the lower pitch; values above 1 indicate a tendency to respond that the stimulus in the higher spectral region has the higher pitch. Although a seemingly large bias was apparent in some conditions (see low-high 200 Hz and mid-high 100-Hz conditions, in which the average bias corresponded to about a semitone), a *post-hoc* statistical analysis, with Bonferroni correction, of the whole-group data failed to reveal any significant biases ($p>0.05$ in all cases). The data from the subset of listeners 1–3, whose within-region DLF0s were the lowest, showed even less departure from no bias.

C. Comparisons with model predictions

As mentioned in the Introduction, Carlyon and Shackleton (1994) proposed that performance in tasks involving F0 comparisons between harmonic complexes filtered into different spectral regions may be limited by three sources of internal noise: encoding noise, across-region comparison noise, and, when the complexes are processed via different mechanisms, across-mechanism translation noise. The size of these different internal noises can be estimated based on the DLF0s measured in different conditions. For instance, the size of the encoding noise for a specific nominal F0 and frequency region can be estimated directly from the DLF0s measured with complexes filtered into the same region, since in that situation only encoding noise should be present. Based on Green and Swets (1966), for a 2AFC task,

$$d'_{2AFC}=\frac{2\Delta}{\sqrt{2\sigma_e^2}}, \tag{1}$$

where Δ is the distance along the relevant internal decision axis between the means of the two distributions of activity (probability densities) evoked by the two stimuli to be compared. The two distributions are assumed to be Gaussian, with common variance σ_e^2. The $_{2AFC}$ subscript after d' is here to avoid confusion with the d' that would be obtained in a yes/no task; given the same Δ and σ_e^2, d'_{2AFC} is $\sqrt{2}$ times d'. Based on the present findings and the earlier results by

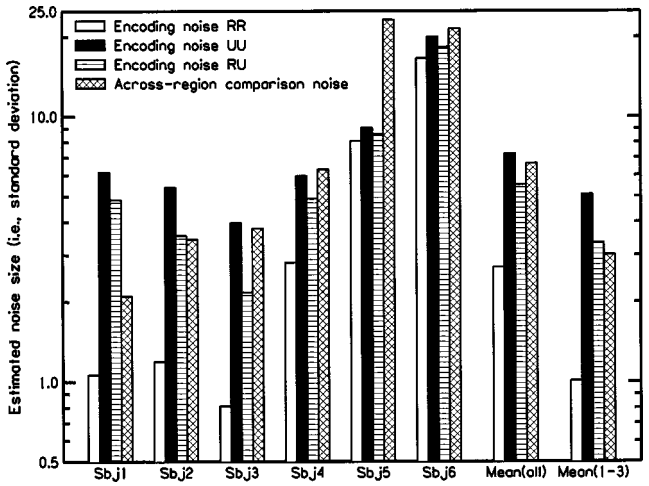

FIG. 3. Estimated sizes (i.e., standard deviations) of the encoding noise associated with comparisons between two resolved groups (empty bars), two unresolved groups (black bars), or one resolved and one unresolved group (horizontal-strip bars), and of the across-region comparison noise (crossed bars). The first six groups of bars correspond to individual data; the remaining two groups of bars show averages across all six listeners and across the three selected listeners. (See text for details.)

Plack and Carlyon (1995), showing that in frequency or F0 discrimination tasks d' is proportional to the F0 difference ($\Delta F0$) in Hz between the two stimuli being compared, and assuming for simplicity that the factor relating d'_{2AFC} to $\Delta F0$ expressed in percent of the F0 is constant and equal to unity, the size of the encoding noise[2] can be estimated as

$$\sigma_e=\sqrt{2}\frac{\mathrm{DLF0}}{d'_{2AFC}}, \tag{2}$$

where DLF0 is the measured $\Delta F0$ at threshold (in % of F0), and d'_{2AFC} is calculated as two times the z-score (computed using the inverse of the standard cumulative normal function) of the input probability corresponding to the targeted percent correct in the 2AFC task (Green and Swets, 1966).

When the two complexes within a trial are filtered into different spectral regions, the encoding noises in the two observation intervals may differ and across-region comparison noise must be added. In that situation, provided the two complexes being compared both contain either resolved or unresolved harmonics (so that no translation noise is present), one has

$$d'_{2AFC}=\frac{2\mathrm{DLF0}}{\sqrt{\sigma_{e1}^2+\sigma_{e2}^2+\sigma_c^2}}, \tag{3}$$

where DLF0 is the ΔF0 at threshold measured in the considered across-region condition (say, low-mid) at the considered nominal F0 (say, 200 Hz), σ_{e1}^2 and σ_{e2}^2 are the variances of the encoding noises associated with the two considered spectral regions (in this example, low and mid) for the same nominal F0, and σ_c^2 is the variance of the across-region comparison noise in the considered condition (low-mid, 200 Hz F0).

Rearranging the terms in Eq. (3), one obtains

$$\mathrm{DLF0}=\tfrac{1}{2}d'_{2AFC}\sqrt{\sigma_{e1}^2+\sigma_{e2}^2+\sigma_c^2}. \tag{4}$$

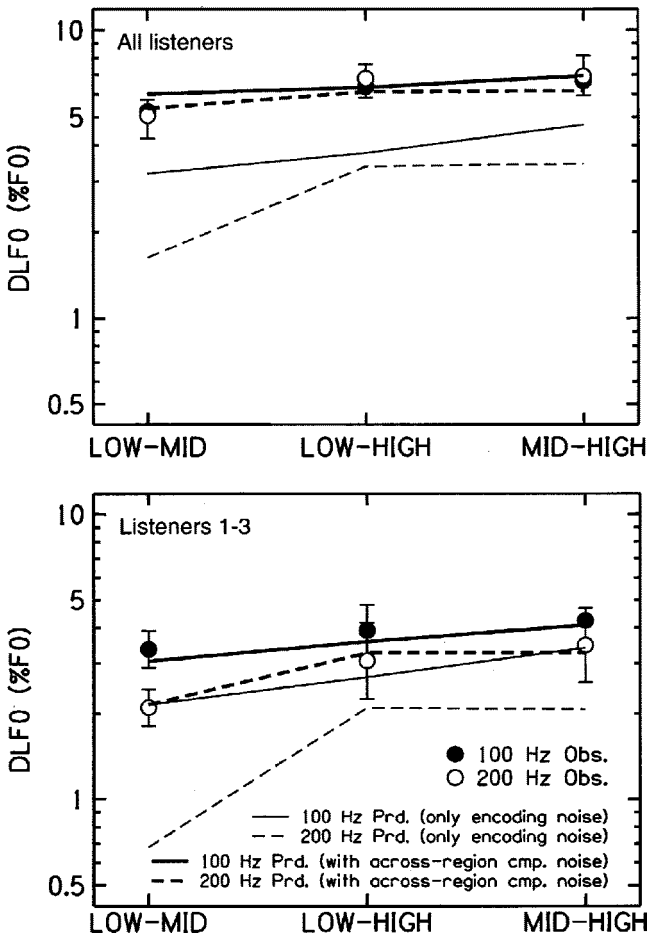

FIG. 4. Comparison between the observed and the predicted DLF0s in the across-region conditions. The upper panel shows averages across all six listeners; the lower panel shows averages across listeners 1–3. The symbols show the geometric mean of the 70.7%- and 79.4%-correct DLF0s measured in each condition. As for Fig. 2, DLF0s obtained using the 100-Hz nominal F0 are indicated by filled symbols and DLF0s measured using the 200-Hz nominal F0 are indicated by open symbols. The error bars represent the standard error of the geometric mean across listeners, after removing any overall differences in performance between listeners. The lines represent predictions. The solid lines correspond to predictions for the 100-Hz nominal F0, the dashed lines to predictions for the 200-Hz nominal F0. The thin lines correspond to predictions using only encoding noise. The thick lines correspond to predictions assuming encoding and across-region comparison noise. (See text for details.)

The variances σ_{e1}^2 and σ_{e2}^2 can be derived directly from the DLF0s measured in within-region conditions (in the above example, low 200 Hz and mid 200 Hz) using Eq. (2). The variance σ_c^2 can then be estimated as the value minimizing the root-mean-square (rms) difference between the mean log-transformed DLF0s predicted using Eq. (4) and the measured (i.e., observed) ones, over all across-region conditions in which the two groups of harmonics are either both resolved or both unresolved.

The best-fitting estimate of the across-region comparison noise size, measured as its standard deviation, σ_c, is shown in Fig. 3 for each of the six listeners. The (geometric) mean noise sizes across all six listeners or just the three selected listeners are shown on the right. The size of the combined encoding noises ($\sqrt{\sigma_{e1}^2+\sigma_{e2}^2}$) associated with F0 comparisons between two groups of resolved harmonics (RR), two groups of unresolved harmonics (UU), and one resolved versus one unresolved group are plotted for comparison. As expected from the DLF0s measured in within-region conditions, the total amount of encoding noise was generally smaller for resolved than for unresolved harmonics. On average, the across-region comparison noise was of roughly the same size as the total amount of encoding noise associated with comparisons between one resolved and one unresolved group.

Before trying to estimate the size of the across-mechanism translation noise, it is worth examining first how well the observed DLF0s in conditions involving one resolved and one unresolved complex can be predicted using only encoding and across-region comparison noise. Figure 4 shows the 75%-correct across-region DLF0s predicted using Eq. (4) with the across-region comparison noise set to zero (thin lines) or to its best-fitting value, held constant across conditions (thick lines). The thin lines show predictions assuming that the DLF0s in across-region conditions were, like those measured in within-region conditions, limited only by encoding noise. ''Observed'' DLF0s corresponding to roughly 75% correct, which were calculated as the geometric mean of the 70.7%- and 79.4%-correct DLF0s measured in across-region conditions (shown in Fig. 1), are plotted here as symbols. As can be seen, the predictions obtained with the across-region comparison noise set to zero generally resulted in substantial underestimates of the actual DLF0s. On the other hand, the predictions derived with a constant (nonzero) across-region comparison noise, derived through optimal fitting of the DLF0s only in across-region conditions involving two groups of resolved or two groups of unresolved harmonics, provided a good fit to the whole set of across-region DLF0s, including those measured using one resolved and one unresolved group. The observed and predicted (log-transformed) DLF0s were compared using an ANOVA for repeated measures. Only the four combinations of nominal F0 and spectral region that involved across-region comparisons between one resolved and one unresolved group were included in this analysis. No significant difference was found between the predicted and the observed thresholds [$F(1,5)=0.00$, $p=0.973$ for the whole study group; $F(1,2)=0.06$, $p=0.831$ for the subset of three listeners]. This indicates that the present results can be accounted for with a model assuming only two additive sources of internal noise: one source of F0 encoding noise, the size of which varies across conditions, depending primarily on whether the harmonics are resolved or not; and another source of noise, associated with across-region comparisons, the size of which is constant across conditions. No other source of internal noise is needed to explain the present results. Furthermore, adding an extra source of noise in conditions involving comparisons between one resolved and one unresolved group of harmonics would not improve the accuracy of fit because, as can be seen in Fig. 4, the predictions do not systematically underestimate the thresholds observed in these conditions. In other words, the present results provide no evidence for the existence of an across-pitch-mechanism translation noise.

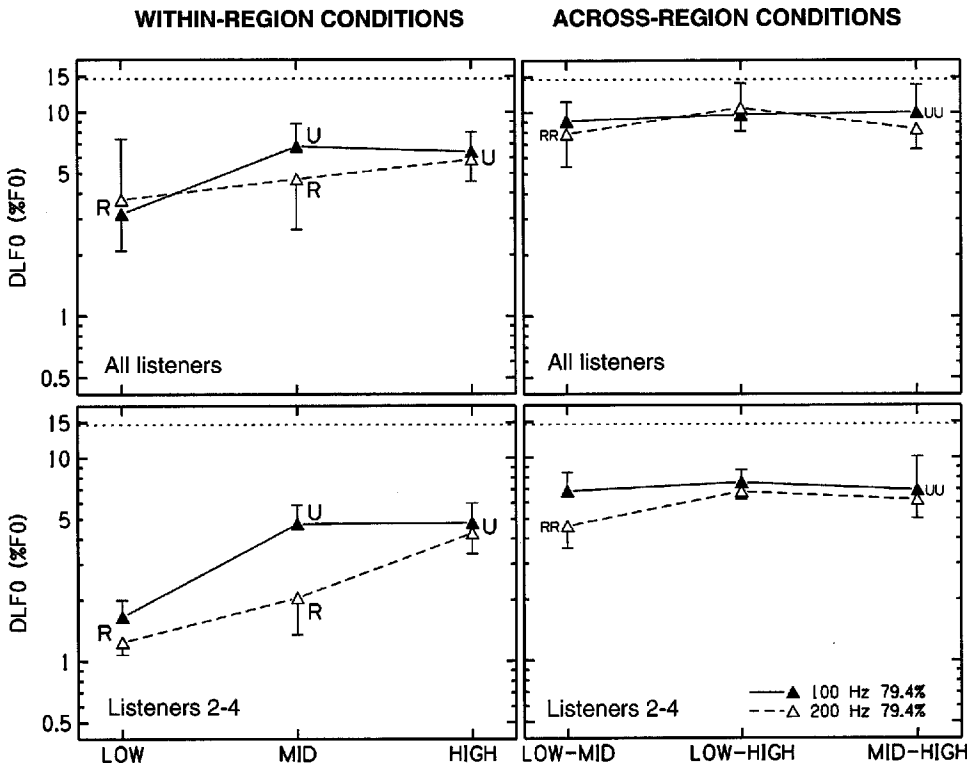

FIG. 5. Mean DLF0s measured in within-region and across-region conditions using a 4-semitone randomization range for the nominal-F0. The general format is the same as for Fig. 1. The only differences are that the upper panels show averages across five listeners (listeners 2–6) and the lower panels show averages across listeners 2–4, and that only 79.4%-correct DLF0s were measured.

IV. EFFECTS OF INCREASING THE F0 RANDOMIZATION RANGE

A. Rationale

One possible reason why no evidence for an across-pitch-mechanism translation noise was found in the preceding experiment is that listeners avoided comparing the F0s of the two complexes presented in the two observation intervals when one of these complexes was resolved and the other was unresolved. Indeed, listeners could in theory do the task as if it were a one-interval task, ignoring one of the two observation intervals and simply comparing the F0 in the other observation interval to an internal criterion corresponding to the nominal F0. If the F0 in the chosen observation interval were higher than the criterion, the listener would designate that interval as the one containing the higher-F0 complex. Listeners may have been led to use this ''one interval'' strategy in conditions involving one resolved and one unresolved group because, in those conditions, direct comparisons between the F0s of the two stimuli were perhaps strongly limited by translation noise.

In order to test whether the DLF0s measured in conditions involving one resolved and one unresolved group in experiment I could be accounted for by this type of explanation, we calculated the smallest F0 difference (ΔF0) required to achieve a given percentage of correct responses (70.7% or 79.4%) with this ''one-interval'' strategy. In order to obtain a conservative test, it was assumed that both the internal criterion and the F0 derived from the selected observation interval were completely noise-free (i.e., perfect coding was assumed). Thus, the ΔF0s indicated below must be regarded as an absolute lower bound on the DLF0s: observed DLF0s smaller than these values cannot be explained in terms of the above-described ''one-interval'' strategy; DLF0s larger than these values may be explained in terms of this strategy, provided the amount of coding noise is sufficiently small. Naturally, if perfect coding is assumed *and* the nominal F0 of the stimuli is not roved across trials, listeners can achieve 100% correct. If the nominal F0 is roved across trials over a range R (in semitones), then the F0 difference, ΔF0, required to obtain a certain proportion of correct responses, Pc, is simply equal to $2R(Pc-0.5)$ semitones. In experiment I, the nominal F0 of the stimuli was roved over a 1-semitone range (roughly $\pm 3\%$). With this roving range, the formula predicts that 70.7% of correct responses can be achieved with a ΔF0 of only 2.4%, and that 79.4% correct can be achieved with a ΔF0 of 3.5%. Since these lower bounds are smaller than the DLF0s measured in conditions involving one resolved and one unresolved group (see Fig. 1), the possibility that listeners used the ''one interval'' strategy in these conditions cannot be ruled out. Thus, it is possible in theory that the lack of evidence for translation noise in experiment I was due to the fact that listeners never directly compared the F0s of resolved and unresolved complexes.

One way of encouraging listeners to compare the F0 of the two stimuli presented within each trial is to increase the randomization range of the nominal F0. Accordingly, we retested five out of the six listeners who had taken part in experiment I using the same F0 and region conditions, but this time with an F0 randomization range of 4 semitones instead of just 1 semitone. Using the above formula, it can be

shown that with such a randomization range, listeners would need a ΔF0 of at least 14.6% to perform at 79.4% correct. If the DLF0s measured in the second experiment are below this predicted value, one could conclude that listeners were comparing the F0s of the resolved and unresolved stimuli. On the other hand, if the DLF0s are larger than the predicted values above, this would support the view that listeners were relying on an internal reference rather than comparing the two observation intervals. Furthermore, if it turned out that the measured thresholds are significantly larger than the predicted ones specifically in conditions involving one resolved and one unresolved group of harmonics, this would be consistent with the existence of translation noise.

B. Methods

The stimuli and procedure were the same as in the first experiment. The only differences were in the size of the F0 roving range, which was now 4 semitones (i.e., ±2 semitones around the nominal F0), and in the targeting of only one percent-correct value (79.4%) instead of two. The six listeners who had taken part in experiment I also took part in experiment II. However, one listener (listener 1) became unavailable before the end of that second experiment. Thus, only the data from listeners 2–6 could be retained in the final analyses. As in experiment I, two sets of analyses were run in parallel: one on the data of all five listeners, the other on the data of a subset of three listeners who showed the lowest thresholds and whose within-region data showed the largest difference between conditions that involved resolved harmonics and those that did not. As listener 1 was no longer available, these were now listeners 2–4.

C. Results and discussion

The results of experiment II are shown in Fig. 5. In the across-region conditions, the measured DLF0s were significantly lower on average than the prediction of the internal-reference model (14.6%), even in the whole study group (Fig. 5, left panel) [$t(71)=2.50$, $p<0.01$]. This indicates that listeners were not simply basing their responses on comparisons with a constant internal reference F0.

Furthermore, although a visual comparison between Figs. 1 and 5 suggests that increasing the roving range produced some increase in the DLF0s, statistical comparisons between the 79.4%-correct thresholds measured in the 1- and 4-semitone roving-range conditions in the five listeners who took part in both experiments showed no significant difference. The same analysis, when run on the data of the three selected listeners (listeners 2–4), led to the same outcome. This lack of a significant effect of the roving range is consistent with the notion that listeners were not relying on a fixed internal reference in either experiment I or II.

As with experiment I, the DLF0s measured in within-region conditions were used to estimate the amount of internal noise present in these conditions. These internal noise estimates were then used to predict the DLF0s measured in across-region conditions assuming only across-region (no across-pitch-mechanism translation) noise. Once again, no significant difference was found between the observed and predicted DLF0s in conditions involving comparisons between one resolved and one unresolved group, independent of whether the analysis was carried out on the data of all five listeners [$F(1,4)=0.22$, $p=0.664$] or of the three selected listeners [$F(1,2)=1.82$, $p=0.310$].

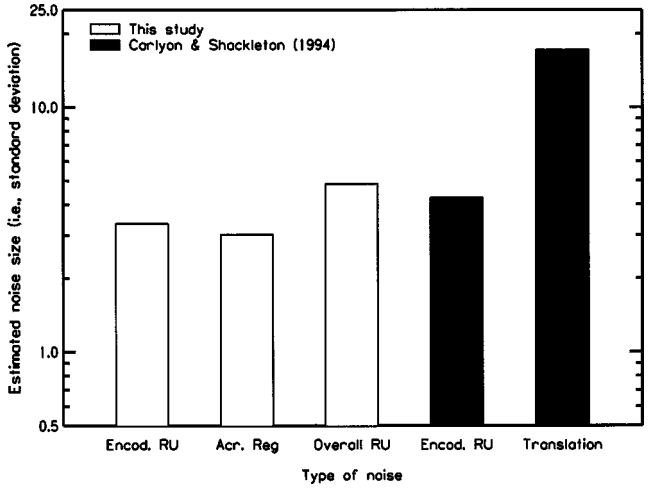

FIG. 6. Estimated size (i.e., standard deviations) of the encoding noise, the across-region comparison noise, the across-pitch-mechanism translation noise, and/or the total noises involved in comparisons between one resolved and one unresolved group in the present study (empty bars) and in the study of Carlyon and Shackleton (1994) (solid bars). (See text for details.)

In summary, the apparent lack of translation noise in experiments I and II is not likely to be due to listeners using an internal reference F0 and failing to actually compare F0s across spectral regions. This leaves us with other interpretations to consider in the general discussion: either there is no across-pitch-mechanism translation noise in the auditory system or, at least, the size of this noise is small in comparison to that of the other sources of observer- or measurement-related noise present in this study.

V. GENERAL DISCUSSION

A. Was the across-mechanism translation noise swamped by the across-region comparison noise?

A possible reason why the observed and predicted DLF0s in resolved–unresolved conditions differed very little is that translation noise was swamped by the other sources of internal noise present in the across-region conditions, namely, the encoding and across-region comparison noises. Since both of these sources of internal noise are present whenever listeners compare the F0s of harmonics in different frequency regions, one might argue that if the translation noise is not large enough to have an effect in the presence of these other sources of internal noise, its influence will never be observed, except perhaps under conditions involving comparisons between resolved and unresolved harmonics filtered into the same spectral region (and, consequently, no across-region-comparison noise). However, it is possible that some experimental situations yield less across-region comparison noise than others. For instance, Carlyon and Shackleton (1994) found no significant across-region noise in F0 comparisons between simultaneously presented groups of harmonics (we discuss this finding in more detail below).

Furthermore, as the detrimental influence of differences in spectral region or timbre on DLF0s appears to vary substantially across listeners, it is also conceivable that in some listeners (possibly those with extensive musical training), the size of the across-region comparison noise is so reduced that it becomes negligible. Although some of our listeners had some musical training and all were trained in both the within- and across-region conditions prior to data collection, we cannot rule out the possibility that other listeners might exhibit smaller amounts of across-region comparison noise.

In order to test whether the lack of evidence for translation noise in the present study could be due to the presence of unusually large encoding and/or across-region comparison noise, we compared the size (standard deviation) of the total amount of noise in our across-resolvability conditions to the size of the encoding noise associated with comparisons between one resolved and one unresolved complex in Carlyon and Shackleton's (1994) study. Details on how these estimates were obtained from the data plotted in Carlyon and Shackleton's article are provided in Appendix B. Three important considerations are worth mentioning here: (a) Because Carlyon and Shackleton found no significant across-region comparison noise, the only significant source of internal noise in their simultaneous experiment besides translation noise was encoding noise. (b) Since the performance in simultaneous comparisons between two unresolved complexes in Carlyon and Shackleton's study was enhanced by the detection of pitch pulse asynchronies, the encoding noise for unresolved complexes could only be predicted from the sequential comparisons. (c) While Carlyon and Shackleton's experiment testing for across-region comparisons involved four groups of harmonics on each trial (two in each observation interval), ours involved only two, and in both experiments translation noise was thought to compete with the encoding noise associated with two complexes, not four. These three considerations indicate that the relevant comparison is between the *total* amount of (encoding and across-region) noise associated with across-region comparisons involving one resolved and one unresolved complexes in the present study, and the amount of *encoding* noise associated with corresponding comparisons in Carlyon and Shackleton (1994), as predicted from the sequential-comparison data in that study.

Figure 6 compares the sizes (or standard deviations) of the internal noises computed in the present study (for the three listeners of experiment I) with those estimated from the data plotted in Carlyon and Shackleton's (1994) article (Figs. 6, 7, and 9 in that article). It can be seen that the amount of encoding noise associated with comparisons between one group of resolved and one group of unresolved harmonics in the three selected listeners of the present study is similar to that measured in three listeners by Carlyon and Shackleton (1994). Nevertheless, because of the additional across-region comparison noise found in this study, the total noise potentially competing with translation noise was slightly larger in the present study than in Carlyon and Shackleton (1994) (compare ''overall RU M&O'' with ''encoding RU C&S'' in Fig. 6). In theory, this could have limited the ability of the present study to find evidence for translation noise. However, the reanalysis of Carlyon and Shackleton's data also reveals that the size (standard deviation) of the putative translation noise in their study was about four times larger than the overall size of the other sources of internal noise associated with comparisons between one resolved and one unresolved complex (compare the last two histogram bars in Fig. 6).

If a translation noise of the size found by Carlyon and Shackleton had been present in our study, would it have been detected? More generally speaking, how large should the translation noise have been in order for its influence on the DLF0s to be detectable in the present study? In order to answer this question, we gradually increased the previously estimated size of the internal noise added to the encoding noise in conditions involving comparisons between one resolved and one unresolved group in experiment I, recomputed the DLF0 predictions with the artificially increased internal noise size, and compared the newly predicted thresholds with the observed ones. Repeating this procedure until the ANOVA yielded a significant outcome ($p<0.05$), we found that increasing the size (standard deviation) of the noise added to the total amount of encoding noise in resolved–unresolved comparisons by 75% was sufficient to produce a statistically significant deviation between the predicted and observed thresholds [$F(1,5)=6.74$, $p=0.049$]. A 75% increase in the size (standard deviation) of the across-region comparison noise was found to correspond roughly to a 50% increase in the total amount of (encoding plus across-region comparison) noise measured in the considered conditions. To yield this 50% increase in total noise size, the added (''translation'') noise should have a size slightly (i.e., about 12%) larger than that of the total amount of encoding plus across-region comparison noise already present in the resolved-vs.-unresolved conditions.[3] The size of the translation noise estimated from Carlyon and Shackleton's (1994) data was about four times the total amount of (encoding) noise that was associated with resolved–unresolved comparisons in that study, and it is between 2 and 3.5 times the total amount of (encoding plus across-region comparison) noise measured in the present study (depending on whether one considers the data of all six listeners or only those of the three selected listeners, respectively). All of these ratios are substantially larger than the 12% difference needed to produce a statistical increase in DLF0s here. Thus, had an additional noise with the same relative size as that observed in Carlyon and Shackleton's (1994) study been present here, its influence would have been detected. To check this conclusion, we also tried adding to the total amount of internal noise measured in resolved–unresolved conditions here, another noise with the same absolute (rather than relative) size as the translation noise in Carlyon and Shackleton (1994). As expected, this resulted in a statistically significant difference between the predicted and observed DLF0s in the considered conditions [$F(1,5)=14.51$, $p=0.013$]. These observations indicate that the discrepancy between the present results and those of Carlyon and Shackleton (1994) cannot be explained simply by insufficient statistical power or the presence of unusually large encoding and/or across-region comparison noise in present study.

B. Reevaluating past claims for translation noise

How can the apparent discrepancy between the results of Carlyon and Shackleton (1994), suggesting the existence of a large across-pitch mechanism translation noise, and the present ones, showing no evidence for such noise, be resolved? Carlyon and Shackleton's (1994) evidence for translation noise, just like the present lack thereof, rests entirely on comparisons between observations and predictions. However, in their study, the predictions were derived from performance measures obtained in conditions that differed markedly from the ones in which the predictions were applied. Specifically, performance measures in F0 discrimination between *sequential* groups of harmonics filtered into the *same* spectral region were used to predict performance in F0 comparisons between *simultaneous* groups of harmonics filtered into *different* spectral regions. Because these two types of experimental situations may involve very different internal processes, the interpretation of the differences between predictions and observations in Carlyon and Shackleton's study is uncertain. The evidence for translation noise in that study is further limited by the fact that the authors had to exclude comparisons between observations and predictions in conditions that involved two groups of unresolved harmonics because, as they pointed out, performance in those conditions was probably mediated by the detection of pitch pulse asynchronies between the two complexes. The results obtained in conditions involving comparisons between two unresolved groups being ruled out, the evidence for translation noise in Carlyon and Shackleton (1994) rests entirely on the worse-than-predicted performance in F0 comparisons between one resolved and one unresolved group. However, this finding may be explained by reasons other than translation noise. For instance, when both resolved and unresolved contiguous harmonics are presented simultaneously, resolved harmonics have been shown to dominate the pitch percept (e.g., Plomp, 1967). Possibly, this makes it harder to detect differences in F0 across spectral regions due to some form of masking of the less salient pitch evoked by the unresolved harmonics, or some other form of interference. Recent results by Gockel *et al.* (2004) indicate that such interference effects do exist. These authors showed that F0 discrimination performance between two sequential complexes consisting of unresolved harmonics was impaired by the simultaneous presentation of another complex, filtered in a lower spectral region and containing resolved harmonics. Gockel *et al.* argued that this interference effect might explain the finding of lower-than-predicted performance in Carlyon and Shackleton's conditions involving simultaneous comparisons between a resolved and an unresolved complex.

C. One or two pitch mechanisms?

In view of the above analysis, it appears that the evidence currently available to support the hypothesis that F0 comparisons between resolved and unresolved harmonics are significantly affected by translation noise is, at best, limited. However, it is important to stress that rejecting the hypothesis of the existence of translation noise between the outputs of two different F0-encoding mechanisms for resolved and unresolved harmonics is not tantamount to rejecting the hypothesis that these two F0-encoding mechanisms exist. It is quite possible that the F0 estimates derived from resolved and unresolved harmonics by two distinct F0-encoding mechanisms are already reconciled into a common code before they are compared, or that these F0 estimates, although they are derived through different mechanisms, are expressed in the same form.

There remain some results in the literature that have been interpreted as suggesting the existence of different pitch encoding mechanisms for resolved and unresolved harmonics. Plack and Carlyon (1995) and White and Plack (1998) have shown qualitatively different effects of duration on DLF0s for resolved and unresolved harmonics, which may be construed as an indication that different underlying mechanisms are operating. More recently, Grimault *et al.* (2002) have obtained results that were interpreted as indicating the involvement of different mechanisms in the learning of F0 discrimination with resolved and unresolved harmonics, which also would be hard to reconcile with the assumption that the same mechanism mediates F0-discrimination performance in both cases.

D. A note on across-region comparison noise in F0 discrimination

Our finding of significant across-region comparison noise is consistent with a number of earlier studies that have found poorer F0 discrimination when the two stimuli consist of different harmonics than when they contain identical harmonics (e.g., Ritsma, 1963; Faulkner, 1985; Moore and Glasberg, 1990). Moore and Glasberg (1990) showed that DLF0s could be increased when the complexes occupied roughly the same spectral region and even shared many common harmonics. This suggests that even subtle differences in timbre can interfere with the processing of differences in F0. The interference may be due to distraction of the listener's attention away from the relevant sensory dimension (i.e., pitch) by irrelevant variations along another dimension (i.e., timbre). Thus, the expression "across-region comparison noise," which we borrowed from Carlyon and Shackleton (1994), should not be taken too literally, as it may not relate specifically to across-region comparisons, but may instead or also reflect a general distracting effect of timbre differences on F0 comparisons. Whatever mechanism is at the origin of the increase in thresholds from within- to across-region conditions, our quantitative predictions demonstrate that the influence of this mechanism can be modeled successfully as a simple additive source of noise. Indeed, adding a constant amount of noise to the estimated amount of encoding noise associated with each combination of F0 and spectral region condition was sufficient to produce predicted thresholds very close to the observed ones in all the across-region conditions. A model assuming a constant multiplicative across-region-comparison noise, which would predict a proportional upward shift in thresholds from within- to across-region conditions, would clearly not be adequate. It would, for example, predict a larger than observed difference in thresholds be-

tween the all-resolved, low-mid 200-Hz condition and the unresolved-resolved, mid-high or low-high 200-Hz conditions.

E. Influence of spectral region on pitch perception

Another result of the present study, which deserves mention in relation to the question of across-region comparison noise, concerns the question of across-region bias. In this study, no significant spectral-region bias was found. This may seem surprising given that the changes in timbre between the two observation intervals were very salient. Previous studies indicate that for harmonic complexes differing in spectral composition, equal F0s do not necessarily produce exactly equal pitches (e.g., van den Brink, 1977; Chuang and Wang, 1978; Singh and Hirsh, 1992). Such influences of spectral region on perceived pitch should have shown up as bias in our study. However, several factors can explain the apparent lack of influence of timbre on pitch in most of the conditions tested in this study. First, our listeners were provided extensive training in the F0-discrimination task; even though they may have been initially tempted to rely more on timbre than on pitch, such an extensive training with trial-by-trial feedback may have eliminated most of this initial inclination. Second, it has been shown that when faced with conflicting pitch and timbre cues (e.g., increasing F0 but decreasing spectral region), most listeners follow periodicity pitch rather than timbre, provided the complexes contain more than two components (Smoorenburg, 1970; Laguitton *et al.*, 1998); our harmonic complexes generally contained more than two components. Finally, various results in the literature indicate that timbre can be varied without affecting pitch (Plomp, 1967; Hafter and Richards, 1988; Demany and Semal, 1993; for consistent results in cochlear-implant listeners, see McKay *et al.*, 2000). These prior results and the present ones, showing little spectral bias, are generally consistent with the idea that, in trained listeners, periodicity pitch is little (or not) influenced by timbre, although it remains possible that our listeners learned to ''recalibrate'' their pitch judgments depending on spectral region.

VI. CONCLUSIONS

The results obtained in this study are consistent with previous studies in showing that (1) DLF0s for harmonic complexes filtered into the same spectral region are significantly worse for unresolved than for resolved harmonics, and that (2) DLF0s for sequential harmonic complexes filtered into different spectral regions are generally worse than DLF0s for sequential complexes filtered into the same spectral region. They reveal that, whatever effect is responsible for worse performance in the across-region conditions, this effect may be modeled simply and adequately as an additive source of internal noise whose size is constant across all conditions tested here. The results provide no evidence for the hypothesis that sequential F0 comparisons between two sequentially presented groups of harmonics, one resolved and the other unresolved, are significantly limited by ''translation'' noise between the internal F0 estimates derived from these two groups. We have shown that the discrepancy between Carlyon and Shackleton's (1994) results and the present ones could not be explained simply by insufficient statistical power or an unusually large across-region comparison noise in the present study: if an additional noise with a size similar to the translation noise in Carlyon and Shackleton's study had been present here, its influence would have been detected. While the present results do not definitely rule out the possible existence of an across-pitch-mechanism translation noise in the auditory system (disproving the existence of something that can be arbitrarily small is a difficult task), at the very least, they show that even if such a noise does exist, its influence on the F0 discrimination thresholds of typical listeners is negligible. Finally, we stress that even if the existence of translation noise could be conclusively ruled out, this would not necessarily rule out the possibility that the F0s of resolved and unresolved harmonics are encoded via different mechanisms in the auditory system. However, if these different mechanisms do exist, it appears that the F0s derived from resolved and unresolved harmonics are already expressed in a similar code at the stage at which F0 comparisons between sequential tone complexes are made.

ACKNOWLEDGMENTS

This work was supported by the National Institutes of Health (NIDCD Grant R01 DC 05216). We thank Hedwig Gockel, Robert Carlyon, Nathaniel Durlach, and an anonymous reviewer for helpful comments on an earlier version of this manuscript. Brian Moore and Christopher Plack are also acknowledged for interesting comments on some of the results at the ISH 2003 Conference, which helped to improve the manuscript.

APPENDIX A: FORMULAS FOR ESTIMATING BIAS AND "TRUE" THRESHOLDS IN ACROSS-REGION CONDITIONS

In across-region conditions, DLF0s were measured using two interleaved tracks. In one track, the stimulus with the higher F0 was filtered into the higher spectral region. In the other track, the stimulus with the higher F0 was filtered in the lower spectral region. If the listeners' decisions are influenced by the spectral region in which the tones are filtered, an effect we refer to here as ''spectral region bias,'' the raw thresholds measured on the two tracks should be different. Spectral region bias might result from a genuine influence of spectral region on perceived F0, so that, for example, tones filtered in a higher spectral region are perceived as having a higher F0 than tones of the same F0 filtered in a lower spectral region. Alternatively, it might result from listeners inadvertently discriminating signals along the ''wrong'' dimension, i.e., timbre instead of periodicity pitch, on some of the trials.

In order to estimate the size and direction of the spectral region bias and determine the ''true'' DLF0s after accounting for this bias, we used an approach based on that described in the Appendix of Oxenham and Buus (2000). The general idea behind this approach, as applied to the present case, is that the influence of spectral region can be modeled as a shift

in the value of the perceived F0. A positive shift is taken to indicate that filtering a tone into a higher spectral region increases its perceived F0 relative to some ''true'' internal value. A negative shift indicates that filtering the tone into a higher spectral region decreases its perceived F0 relative to some ''true'' internal value. Oxenham and Buus (2000) considered an additive shift on a logarithmic (dB) scale. Here, we use an equivalent approach, consistent with our use of a multiplicative rule for step-size changes in the DLF0-measurement procedure, by considering a multiplicative shift on a linear (Hz) scale. Accordingly, at threshold, the F0 of the higher-F0 tone in each track can be expressed as a function of the F0 of the lower-F0 tone, as follows:

$$\mathrm{F0}_{hi1} = \mathrm{F0}_{lo1} \cdot \Delta \cdot k, \tag{A1}$$

$$\mathrm{F0}_{hi2} = \frac{\mathrm{F0}_{lo2}}{k} \Delta, \tag{A2}$$

where $F0_{hi1}$ and $F0_{lo1}$ are the F0s of the two stimuli in the track in which the higher-F0 stimulus is presented in the higher spectral region, $F0_{hi2}$ and $F0_{lo2}$ are the F0s of the two stimuli in the track in which the higher-F0 stimulus is presented in the lower spectral region, k is the spectral region bias expressed as a factor, and Δ is the proportional difference between the two F0s corresponding to the ''true'' threshold, also expressed as a factor.

The raw DLF0s for each track are, in percents,

$$\mathrm{DLF0}_1 = 100\left(\frac{\mathrm{F0}_{hi1}}{\mathrm{F0}_{lo1}} - 1\right), \tag{A3}$$

$$\mathrm{DLF0}_2 = 100\left(\frac{\mathrm{F0}_{hi2}}{\mathrm{F0}_{lo2}} - 1\right). \tag{A4}$$

The ''true'' DLF0s, Δ, are then computed as the geometric mean of the raw DLF0s expressed as factors rather than percentages (for simplicity):

$$\Delta = \sqrt{\frac{\mathrm{F0}_{hi1}}{\mathrm{F0}_{lo1}} \cdot \frac{\mathrm{F0}_{hi2}}{\mathrm{F0}_{lo2}}}. \tag{A5}$$

The bias, k, is computed as the square root of the ratio of the raw DLF0s (expressed as factors):

$$k = \sqrt{\frac{\mathrm{F0}_{hi1}}{\mathrm{F0}_{lo1}} / \frac{\mathrm{F0}_{hi2}}{\mathrm{F0}_{lo2}}}. \tag{A6}$$

APPENDIX B: THE SIZE OF THE INTERNAL NOISES IN CARLYON AND SHACKLETON (1994)

The size of the encoding and translation noises associated with across-region comparisons between one resolved and one unresolved group of harmonics in Carlyon and Shackleton (1994) was estimated using the data shown in their Figs. 6 and 9. First, the d' values for sequential comparisons shown in Fig. 6 were used to derive the size of the encoding noise, σ_e, associated with each complex. It is important to note that the d' values in that figure and all the other figures in Carlyon and Shackleton (1994)'s article were computed as $\sqrt{2}$ times the z-score of the measured percent correct in the 2AFC task, so that they correspond to yes/no-task-equivalent d' values—not to be confused with d'_{2AFC}. Accordingly, we have

$$\sigma_e = \frac{\Delta \mathrm{F0}}{d'_{seq}}, \tag{B1}$$

where ΔF0 is the F0 difference between the two stimuli (Carlyon and Shackleton tested 3.5% and 7.1%), and d'_{seq} is the mean across all three listeners of the observed d' values in the considered condition, read from Fig. 6 in Carlyon and Shackleton (1994). Technically, all the variables in this and the following equations should have subscripts indicating to which condition they correspond. These subscripts are not shown here to avoid cluttering.

The total amount of encoding noise, σ_{etot}, associated with F0 comparisons between two complexes filtered into different spectral regions was then calculated as

$$\sigma_{\mathrm{etot}} = \sqrt{\sigma_{e1}^2 + \sigma_{e2}^2}, \tag{B2}$$

where σ_{e1}^2 and σ_{e2}^2 are the variances of the encoding noises associated with the two considered spectral regions. A summary measure of the total amount of encoding noise associated specifically with comparisons between one resolved and one unresolved complex was obtained by averaging the squared values of σ_{etot} obtained in the different conditions that involved one resolved and one unresolved group.

The size of the translation noise, σ_t, was derived by comparing the above-predicted amount of encoding noise (σ_{etot}) and the total amount of noise estimated using the d' values observed in the simultaneous-comparison conditions involving both resolved and unresolved complexes (Fig. 7 in Carlyon and Shackleton's article). Specifically, the translation noise was calculated as

$$\sigma_t = \sqrt{\left(\frac{\Delta F0}{d'_{sim}}\right)^2 - \sigma_{\mathrm{etot}}^2}. \tag{B3}$$

Equation (B3) can be understood more easily as a rearrangement of the equation below, which gives the predicted performance in the task used by Carlyon and Shackleton (1994) to measure DLF0s between simultaneously presented complexes:

$$d'_{sim} = \frac{\Delta F0}{\sqrt{\sigma_{\mathrm{etot}}^2 + \sigma_t^2}}, \tag{B4}$$

[1]This and all the other statistical analyses in this article were applied to the log-transformed, rather than the untransformed, DLF0s.

[2]The expression ''encoding noise'' is used here for consistency with Carlyon and Shackleton (1994). Admittedly, the amount of internal noise derived using Eq. (2) may incorporate contributions from other sources of internal noise than those associated specifically with the encoding *per se* of the stimulus F0. For instance, it may include memory-related noise associated with the comparison of the F0 of the complex in the second observation interval with the memory trace of the F0 of the complex in the first interval (see Durlach and Braida, 1969). The derived amount of encoding noise subsumes the contributions from all the internal sources of noise involved even when the F0 comparisons are made within the same spectral region.

[3]If σ_{EAT} represents the standard deviation of the combined encoding plus across-region-comparison plus translation noise, σ_{EA} represents the standard deviation of the combined encoding plus across-region-comparison

noise, and σ_T represents the standard deviation of the sole translation noise, we have $\sigma_{EAT}=\sqrt{\sigma_{EA}^2+\sigma_T^2}$. Knowing that $\sigma_{EAT}/\sigma_{EA}=1.5$, it follows that $\sigma_T/\sigma_{EA}=\sqrt{1.5^2-1}$. The right term in the preceding equation is approximately equal to 1.12, indicating that the translation noise must be roughly 12% larger than the combined encoding plus across-region noise to which it is added in order to cause a 50% increase in the size (standard deviation) of the total amount of noise.

Bernstein, J. G., and Oxenham, A. J. (**2003**). ''Pitch discrimination of diotic and dichotic tone complexes: Harmonic resolvability or harmonic number?'' J. Acoust. Soc. Am. **113**, 3323–3334.

Carlyon, R. P. (**1998**). ''Comments on ''A unitary model of pitch perception'' [J. Acoust. Soc. Am. **102**, 1811–1820 (1997)],'' J. Acoust. Soc. Am. **104**, 1118–1121.

Carlyon, R. P., and Shackleton, T. M. (**1994**). ''Comparing the fundamental frequencies of resolved and unresolved harmonics: Evidence for two pitch mechanisms,'' J. Acoust. Soc. Am. **95**, 3541–3554.

Carlyon, R. P., Demany, L., and Semal, C. (**1992**). ''Detection of across-frequency differences in fundamental frequency,'' J. Acoust. Soc. Am. **91**, 279–292.

Carlyon, R. P., Moore, B. C. J., and Micheyl, C. (**2000**). ''The effect of modulation rate on the detection of frequency modulation and mistuning of complex tones,'' J. Acoust. Soc. Am. **108**, 304–315.

Chuang, C. K., and Wang, W. S. (**1978**). ''Psychophysical pitch biases related to vowel quality, intensity difference, and sequential order,'' J. Acoust. Soc. Am. **64**, 1004–1014.

Demany, L., and Semal, C. (**1993**). ''Pitch versus brightness of timbre: Detecting combined shifts in fundamental and formant frequency,'' Music Percept. **11**, 1–14.

Durlach, N. I., and Braida, L. D. (**1969**). ''Intensity perception. I. Preliminary theory of intensity resolution,'' J. Acoust. Soc. Am. **46**, 372–383.

Faulkner, A. (**1985**). ''Pitch discrimination of harmonic complex signals: Residue pitch of multiple component discrimination?'' J. Acoust. Soc. Am. **78**, 1993–2004.

Glasberg, B. R., and Moore, B. C. J. (**1990**). ''Derivation of auditory filter shapes from notch noise data,'' Hear. Res. **47**, 103–138.

Gockel, H., Carlyon, R. P., and Plack, C. J. (**2004**). ''Across frequency interference effects in fundamental frequency discrimination: Questioning evidence for two pitch mechanism,'' J. Acoust. Soc. Am. (in press).

Green, D. M., and Swets, D. A. (**1966**). *Signal Detection Theory and Psychophysics* (Wiley, New York).

Grimault, N., Micheyl, C., Carlyon, R. P., and Collet, L. (**2002**). ''Evidence for two pitch encoding mechanisms using a selective auditory training paradigm,'' Percept. Psychophys. **64**, 189–197.

Hafter, E. R., and Richards, V. M. (**1988**). ''Discrimination of the rate of filtered impulses,'' Percept. Psychophys. **43**, 405–414.

Hoekstra, A. (**1979**). ''Frequency discrimination and frequency analysis in hearing,'' Ph.D. dissertation, Institute of Audiology, University Hospital, Groningen, Netherlands.

Houtsma, A. J. M., and Smurzynski, J. (**1990**). ''Pitch identification and discrimination for complex tones with many harmonics,'' J. Acoust. Soc. Am. **87**, 304–310.

Laguitton, V., Demany, L., Semal, C., and Liegeois-Chauvel, C. (**1998**). ''Pitch perception: a difference between right- and left-handed listeners,'' Neuropsychologia **36**, 201–207.

McKay, C. M., McDermott, H. J., and Carlyon, R. P. (**2000**). ''Place and temporal cues in pitch perception: Are they truly independent?'' ARLO **1**, 25–30.

Meddis, R., and O'Mard, L. (**1997**). ''A unitary model of pitch perception,'' J. Acoust. Soc. Am. **102**, 1811–1820.

Moore, B. C. J. (**2003**). *An Introduction to the Psychology of Hearing* (Elsevier Science, Amsterdam).

Moore, B. C. J., and Glasberg, B. R. (**1990**). ''Frequency discrimination of complex tone with overlapping and non-overlapping harmonics,'' J. Acoust. Soc. Am. **87**, 2163–2177.

Moore, G. A., and Moore, B. C. J. (**2003a**). ''Perception of the low pitch of frequency-shifted complexes by normal-hearing listeners,'' J. Acoust. Soc. Am. **113**, 977–985.

Moore, B. C. J., and Moore, G. A. (**2003b**). ''Discrimination of the fundamental frequency of complex tones with fixed and shifting spectral envelopes by normally hearing and hearing-impaired subjects,'' Hear. Res. **182**, 153–163.

Ohgushi, K. (**1978**). ''On the role of spatial and temporal cues in the perception of the pitch of complex tones,'' J. Acoust. Soc. Am. **64**, 764–771.

Oxenham, A. J., and Buus, S. (**2000**). ''Level discrimination of sinusoids as a function of duration and level for fixed-level, roving-level, and across-frequency conditions,'' J. Acoust. Soc. Am. **107**, 1605–1614.

Plack, C. J., and Carlyon, R. P. (**1995**). ''Differences in frequency modulation detection and fundamental frequency discrimination between complex tones consisting of resolved and unresolved harmonics,'' J. Acoust. Soc. Am. **98**, 1355–1364.

Plomp, R. (**1967**). ''Pitch of complex tones,'' J. Acoust. Soc. Am. **41**, 1526–1533.

Ritsma, R. J. (**1963**). ''On pitch discrimination of residue tones,'' Int. Audiol. **2**, 34–47.

Shackleton, T. M., and Carlyon, R. P. (**1994**). ''The role of resolved and unresolved harmonics in pitch perception and frequency modulation discrimination,'' J. Acoust. Soc. Am. **95**, 3529–3540.

Singh, P. G., and Hirsh, I. J. (**1992**). ''Influence of spectral locus and F0 changes on the pitch and timbre of complex tones,'' J. Acoust. Soc. Am. **92**, 2650–2661.

Smoorenburg, G. F. (**1970**). ''Pitch perception of two-frequency stimuli,'' J. Acoust. Soc. Am. **48**, 924–941.

Walliser, K. (**1969**). ''Zusammenhänge zwischen dem Schallreiz und der Periodentonhöhe,'' Acustica **21**, 319–328.

White, L. J., and Plack, C. J. (**1998**). ''Temporal processing of the pitch of complex tones,'' J. Acoust. Soc. Am. **103**, 2051–2063.

Sample discrimination of frequency differences with distracters[a)]

Donna L. Neff[b)] and Eric C. Odgaard[c)]
Boys Town National Research Hospital, 555 North 30th Street, Omaha, Nebraska 68131

(Received 3 September 2003; revised 3 August 2004; accepted 11 August 2004)

This study examined the effect of the type and frequency range of remote frequency distracters on sample discrimination of frequency differences (SD-F). For baseline SD-F conditions, normal-hearing listeners judged frequency differences between pairs of target tones drawn from Gaussian frequency distributions near 2000 Hz. In experiment 1, the distracters were pairs of random-frequency tones, fixed-frequency tones, or noise bands, with one distracter above and one below the target region. Three frequency separations of targets and distracters were tested, none overlapping the target region. Effects of fixed-frequency or noise-band distracters were small compared to that of random-frequency distracters, which drove performance to near chance. In experiment 2, dominance of the low-frequency distracter was supported by the effects of changing distracter level, by presenting only the higher- or lower-frequency distracter, and by the pattern of weights derived from trial-by-trial responses. Performance recovered only when the lower-frequency distracter was attenuated 40–50 dB relative to the targets. In experiment 3, all stimulus distributions were shifted 2 octaves higher in frequency; the stronger influence of the distracter frequency below the target remained. The results demonstrate the importance of both stimulus variability and frequency relationships in the interaction of targets and distracters for SD-F.
 [DOI: 10.1121/1.1802571]

PACS numbers: 43.66.Lj, 43.66.Fe [GDK] Pages: 3051–3061

I. INTRODUCTION

The peripheral auditory system provides listeners with the ability to ''filter'' incoming acoustic stimuli to optimize detection of narrow-band targets in the presence of broadband or remote-frequency maskers (e.g., Glasberg and Moore, 1990; Patterson *et al.*, 1982). Such filtering should remove irrelevant, remote-frequency energy from the decision process. When stimulus properties are unpredictable, however, numerous studies have shown that frequency selectivity appears to break down and detection or discrimination tasks can become very difficult. Normal-hearing listeners often perform poorly even when the target stimuli are isolated in time or frequency from the distracter or masker stimuli. (e.g., Watson *et al.*, 1975; Kidd and Watson, 1992; Kidd *et al.*, 1994, 2002; Leek *et al.*, 1991; Neff and Green, 1987; Oh and Lutfi, 1998; Richards *et al.*, 2002). Across tasks with uncertain stimuli, both large individual differences and effects of training are observed, suggesting the influence of more central processes. This paper describes the first of a series of studies that investigated the interaction of target and distracter stimuli in ''sample-discrimination'' (SD) tasks (e.g., Berg and Robinson, 1987; Lutfi, 1989). As discussed in more detail below, SD tasks offer several advantages, including: (1) a theoretical framework to quantify the degree of stimulus variation and compare performance to that of an ideal listener; (2) a straightforward approach to obtaining weights for individual stimuli to discern listeners' decision strategies; and (3) ease of manipulating task difficulty to obtain desired levels of performance in the baseline (no-distracter) conditions. The present study focused on effects of frequency variability on SD, given the large detrimental effects of frequency uncertainty in informational-masking studies using random-frequency maskers and fixed-frequency signals.

Many studies have used SD, with and without extraneous tones, to examine the ability of listeners to internalize properties of randomly varying stimuli (e.g., Berg and Robinson, 1987; Doherty and Lutfi, 1999; Stellmack *et al.*, 1997; Lutfi, 1989, 1990, 1992, 1994; Weber, 1995). Typically, the task uses two overlapping, Gaussian distributions on a particular stimulus dimension (e.g., frequency). Tones are drawn from a randomly selected distribution, and listeners indicate which of the two distributions was sampled. In the two-interval, forced-choice (2IFC) version of the task, both distributions are sampled on every trial in random order. Feedback is provided, and listeners are instructed to use the properties of the stimulus distributions as the basis of their responses. Task difficulty can be controlled by adjusting the separation between the means (Δ) and the standard deviations (σ) of the distributions, for distributions with equal or unequal σ's. Performance of human listeners can be related to that of an ideal observer for the baseline (no distracter) condition, using Eq. (1) (Green and Swets, 1966)

$$d' \text{ ideal} = n^{1/2}\Delta/\sigma, \tag{1}$$

where n is the number of tones sampled from each distribution. Previous studies (Lutfi, 1989, 1990, 1992; Weber, 1995) showed listeners approximate ideal performance only for one or two tones for SD tasks. As n was increased, ideal

[a)]Portions of this research were presented at the 143rd meeting of the Acoustical Society of America, Pittsburgh, PA, June 2002.
[b)]Electronic mail: neff@boystown.org
[c)]Current affiliation: University of South Florida, St. Petersburg, FL 33701.

performance improved as the square root of n, whereas human performance grew more nearly as the cube root of n, regardless of the physical dimension varied. The present study therefore used two target tones per listening interval, which allowed performance in the baseline conditions to be well predicted by ideal, but assured that both baseline and distracter conditions used tonal complexes rather than single tones.

A number of studies have examined the use of trial-by-trial information on stimuli and listeners' responses to calculate ''weights'' for individual stimulus components and thus infer listeners' decision processes (e.g., Berg, 1989, 1990, 2004; Lutfi, 1995; Richards and Zhu, 1994). These weights can contribute useful information about the strategies of individual listeners beyond that revealed by overall performance (e.g., Stellmack *et al.*, 1997; Willihnganz *et al.*, 1997). Weights can be influenced by changing instructions to the subject about which components in a multicomponent stimulus are the targets (e.g., Southworth and Berg, 1995; Stellmack *et al.*, 1997). In the present study, both overall performance and weights are used to examine listening strategies for SD of frequency differences (SD-F) with distracter stimuli. The stimuli are simple enough to directly compare interpretations based on weights with effects of removing certain components. The correlation approach is used to estimate weights, based on the frequency (or level variation in some cases) of each stimulus component, as summarized in Eq. (2) (Lutfi, 1995)

$$W_i = r_{R(\Delta Fi)}\sigma_R / \sigma_{\Delta Fi}, \tag{2}$$

where W_i is the listener's weight for the ith component, $r_{R(\Delta Fi)}$ is the point biserial correlation of the listener's binary response (interval selected for 2IFC) with the difference in frequency (or level) across intervals for the ith component, σ_R is the standard deviation of the listener's binary response, and $\sigma_{\Delta Fi}$ is the standard deviation of the distribution of frequency (or level) changes across the intervals for the ith component. As described in detail in other papers (e.g., Stellmack *et al.*, 1997; Lutfi, 1995), the decision variable is assumed to be a weighted sum of the stimulus differences between intervals of the components. To better convey absolute magnitudes, weights were not normalized to sum to 1.0.

Relatively few studies have examined SD-F, focusing instead on discrimination of level differences. In a study most similar to this one, Lutfi (1992) examined SD-F with variable-frequency distracter tones. The frequency distribution for the distracters was midway between the two target distributions (e.g., target means of 1975 and 2025 Hz; distracter mean of 2000 Hz). The stimuli were 10-tone sequences, similar to those used by Watson (e.g., Watson *et al.*, 1975). The ratio of σ's for the target and distracter distributions was varied from half to double to assess the interaction of target and distracter variability. For all four listeners, Lutfi observed a systematic deterioration in performance from near ideal to chance as the variability of the distracter increased relative to that of the target. For conditions with equal target and distracter variability, performance was generally poor ($d' = 0.5–1.0$, whereas ideal $= 2.0$), but improved somewhat with increasing stimulus variability. In another study, Lutfi (1994) examined the ability of listeners to process stimulus variability in different frequency regions, specifically, their ability to make use of within- versus across-channel cues for detecting intensity changes in tone sequences presented simultaneously across five frequency regions. Each sequence had five tones, and the level, frequency, and duration of each tone was varied with each presentation by sampling from Gaussian distributions for each stimulus parameter. The statistical relationships across the five sequences were manipulated by using the same or different standard deviations for the Gaussian stimulus distributions, across the three dimensions (i.e., frequency, level, duration) or the five frequency regions. The target was an intensity increment to all tones for the sequence centered at 1000 Hz. Lutfi found little evidence that listeners could make use of cross-dimensional correlations. They did appear to use cross-frequency correlates to improve performance, but only when the properties of the target sequence differed from that of the distracter sequences. This suggests that listeners have some ability to judge properties of distributions across frequency regions, albeit limited.

In the present study, across-channel interference is examined for much simpler stimuli—simultaneous pairs of target tones presented alone or combined with several types of distracters. Given the large, detrimental effects produced by random-frequency, multicomponent maskers on the detection of a fixed-frequency signal, it was expected that random-frequency distracter tones would degrade performance more than fixed-frequency tones or noise bands. Perhaps distracter-frequency variation would have less effect in the present study than in informational masking studies, however, because both signal and distracter have essentially equal frequency variation and the use of only one or two distracter tones. In the first experiment, the target-tone distributions were near 2000 Hz. The distracter stimuli were from three different frequency regions increasing in distance from the target. The distracters were pairs of random-frequency tones, fixed-frequency tones, or noise bands, with one distracter above and one below the target region. The results revealed large detrimental effects of the random-frequency distracters, and an unexpected dominance of the lower-frequency distracter. Gaussian level variation was also added to some conditions, but it had such a small influence compared to frequency variation that level effects are only briefly summarized. In experiment 2, only random-frequency distracters from the distributions farthest from the target were used. Relative levels of the target versus distracter tones were manipulated to further test the influence of distracter frequency. Again, the results indicated dominance of the lower-frequency distracter. In the final experiment, the frequency distributions of targets and random-frequency distracters were shifted higher to determine if absolute frequency region would influence performance. The stronger influence of the distracter below the target frequency remained. Both performance (d') and weights were used to assess the effects of the distracters on SD-F.

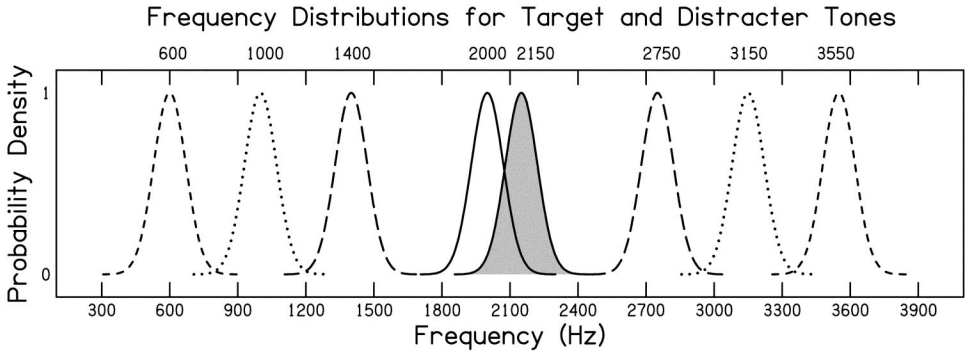

FIG. 1. Schematic of the Gaussian stimuli distributions used for the targets (solid lines) and random-frequency distracters (broken lines). Mean frequencies are indicated above the distributions. Pairs of distracter tones flanked the target region at three distances from the target region. Pairs of distracter distributions are differentiated by line type. Fixed-frequency distracters were the mean frequencies of these distributions. Noise-band distracters had the same bandwidth as the distributions. See the text for further detail.

II. GENERAL METHOD

A. Listeners

Four college-student volunteers (two female, two male) received an hourly payment for their participation. None had previous experience with SD tasks. All had normal hearing, defined as thresholds of 5 dB HL or less at octave frequencies from 500 to 4000 Hz (ANSI, 1989). Listeners completed 400 trials of practice in the SD task without distracters before data collection began, and had full knowledge of all stimulus conditions. To assure the task was understood, practice conditions began with nonoverlapping target distributions widely spaced in frequency. Performance was required to be perfect before proceeding. The frequency distance between distributions was then decreased over consecutive blocks of trials to the degree of overlap in the baseline conditions. Listeners were tested in individual soundproof rooms for 2-h sessions (with frequent breaks) several days a week.

B. Stimuli

The target stimuli were pairs of sinusoids (two tones per observation interval), drawn at random from frequency distributions that were Gaussian on a linear scale in hertz. As illustrated in Fig. 1 (solid lines), the target distributions for all but the last experiment had mean frequencies of 2000 and 2150 Hz (Δ of 150 Hz). The d' ideal for target-alone conditions is thus 2.1 [Eq. (1)]. In the first experiment, the distracters were two random-frequency tones, fixed-frequency tones, or bands of noise, with one distracter above and one below the target region. Distributions for the random-frequency distracters had the same σ (100 Hz) and total range (600 Hz for $\pm 3\ \sigma$) as the target distributions. Center frequencies for the distracter distributions were $\pm$600, 1000, or 1400 Hz from the mean of the nearest target distribution. In Fig. 1, different line types indicate the pairs of distracter distributions for the three distances. Fixed-frequency distracters were the mean frequencies of these distributions. Noise-band distracters were 600 Hz wide to match the range of the random-frequency distracters. Unless specified, each target tone, distracter tone, or noise band (total power) was 67 dB SPL. The conditions of experiment 1 were also tested with random level ''jitter'' added to each of the tonal components (i.e., target tones, fixed- or random-frequency distracters). For each 2IFC interval, the level of each component was drawn from a Gaussian distribution (mean of 67 dB, σ of ± 3 dB). No level variation was added to the noise-band distracters. Experiment 2 used only random-frequency distracters farthest from the target to test the effect of changing overall level of the distracters. First, overall level of the two distracters was changed together (i.e., both set to 50 dB compared to 70-dB targets), and then the level of one distracter was set equal to the targets while the level of the other distracter was decreased across blocks of trials (fixed within block). Experiment 3 also used only random-frequency distracters, but shifted all stimulus distributions higher in frequency. The target distributions had means of 3850 and 4000 Hz and the distracter distributions had means of 2450 and 5400 Hz (a distance of $\pm$1400 Hz). In all experiments, stimuli were 100 ms with 5-ms, cosine-squared ramps, and targets and distracters were presented simultaneously.

For fixed- or random-frequency sinusoidal stimuli, waveform files were generated using 16-bit DACs at 20 kHz and low-pass filtered at 8 kHz. Separate DACs were used for target and distracter waveforms. For noise bands, analog broadband noise was bandpass filtered (KEMO, 96 dB/oct) and gated via a voltage-controlled amplifier, using digitally generated, 5-ms, cosine-squared ramps. Gating waveforms were generated at a rate of 10 kHz and low-pass filtered at 4 kHz. Stimuli were then passed through a circuit of passive attenuators, mixers, and amplifiers, and presented diotically over TDH-39 earphones with circumaural (001) cushions to listeners seated in individual soundproof booths. Stimulus presentation and data collection were computer controlled.

C. Procedure

On every trial of the nonadaptive 2IFC procedure, a pair of target tones was drawn from each of the two target distributions and presented in the first or second interval with equal probability. Distracters, when present, were in both intervals of each trial. For example, for random-frequency distracters, one tone each was drawn from the lower- and higher-frequency distracter distributions (four tones total per interval—two targets and two distracters). Listeners were instructed to select the interval with the higher-frequency pair of *target* tones (this was emphasized), and correct-answer

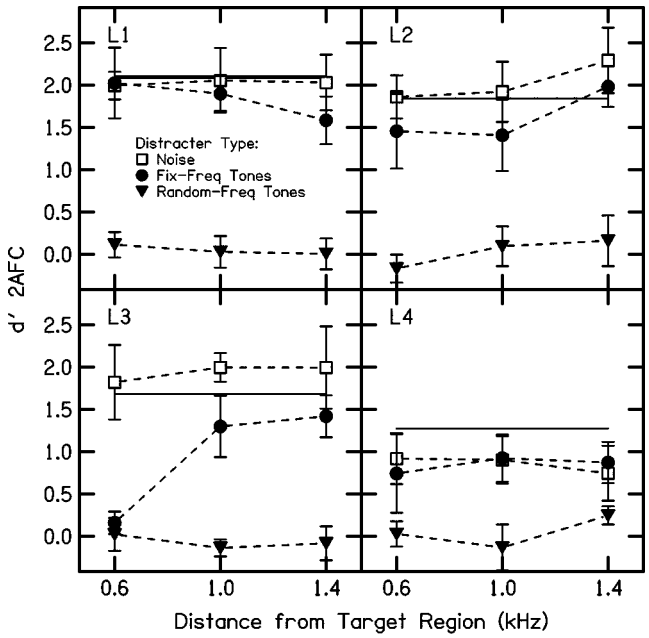

FIG. 2. Performance as a function of the distance of the distracters from the target region (kHz), with listeners plotted across panels. Solid horizontal lines indicate performance in the no-distracter condition. In each panel, data for the three distracter conditions have different symbols as indicated in the legend.

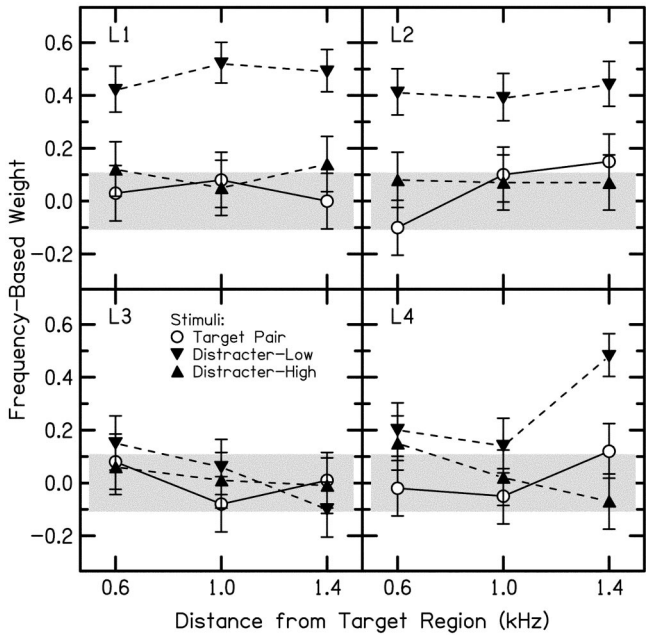

FIG. 3. Frequency-based weights for the random-frequency distracter condition as a function of the distance of the distracter tones from the target region (kHz). Error bars indicate confidence interval ($p=0.99$). Listeners are plotted across panels; shaded areas in each panel indicate weights that are not significantly different from 0.0 ($p>0.01$). Weights for the target-tone pair and the low- and high-frequency distracter tones have different symbols as indicated in the legend.

feedback was provided. Intervals were separated by 400 ms and marked by lights on a response box. Percentage correct for each block of 100 trials was converted to d' values taking into account the 2IFC procedure used. Six complete replications of all conditions were completed for each experiment. For each replication, listeners began with the target-alone condition, and then were tested on the conditions with distracters in random order. Data presented for each listener's performance are mean d' values across replications; the error bars indicate 99%-confidence intervals. To calculate weights, the 600 trials available for each listener and condition were pooled. Weights were calculated as in Eq. (2) (see Willihnganz *et al.*, 1997 for further detail). For tonal distracters, the weight includes the correlation of each listener's response with the difference in distracter frequency across intervals (or level, for conditions with level variation) for the 2IFC trials. For target-tone pairs, frequencies for the pair of target tones in each interval were first averaged, and then weights were calculated.

III. EXPERIMENT 1: EFFECT OF DISTRACTER TYPE AND LEVEL VARIATION

A. Results for conditions without level variation

Figure 2 presents performance (d') for individual listeners as a function of the frequency distance of distracters from the target region, for conditions without added level variation. Solid horizontal lines indicate performance for targets alone. The remaining functions show performance with the three types of distracters: noise bands (squares), fixed-frequency tones (circles), and random-frequency tones (triangles). Listeners are ordered by performance in the baseline conditions, with L1 near ideal, L2 and L3 somewhat lower ($d'=1.8$ and 1.7, respectively), and L4 as the lowest ($d'=1.3$). For L4, noise-band or fixed-frequency distracters produce essentially a constant decrement in performance of 0.5 d' units regardless of distracter distance from the target region. L4 was the only listener to show any detrimental effect of noise. Noise bands had little effect on performance for L1, but actually aided performance a small amount for L2 and L3 for bands remote from the target region. Fixed-frequency distracters closest to the target region produced the largest range of performance across listeners (e.g., near ideal for L1 compared to chance for L3). For most conditions, however, fixed-frequency tonal distracters produced small reductions of d' of 0.5 units or less. The most consistent and largest effects are for random-frequency distracters, with performance for all listeners at or near chance across conditions. Anecdotally, listeners reported clear perceptual awareness of the fixed-frequency distracter tones or noise, which they were able to rapidly learn to ignore within the first few trials. For random-frequency distracters, however, listeners reported difficulty achieving any segregation of targets and distracters and wanted assurance that the signal had not been "unplugged."

In Fig. 3, frequency-based weights for the target-tone pair (open circles), and the lower- and higher-frequency distracters (downward- and upward-pointing triangles, respectively) are presented for the random-frequency distracter condition. Shaded areas indicate weights that are not significantly different from 0.0 ($p<0.01$). For three out of four listeners (not L3), the low-frequency distracter tone appeared to dominate performance, with highly significant weights. These weights indicate that listeners were following instruc-

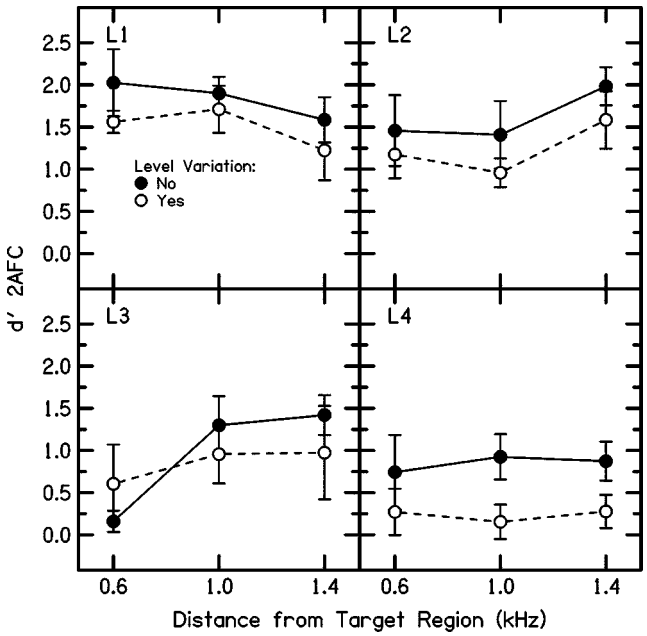

FIG. 4. Comparison of performance for the fixed-frequency distracter condition with and without level variation, as a function of distance of the distracters from the target region. Listeners are plotted across panels.

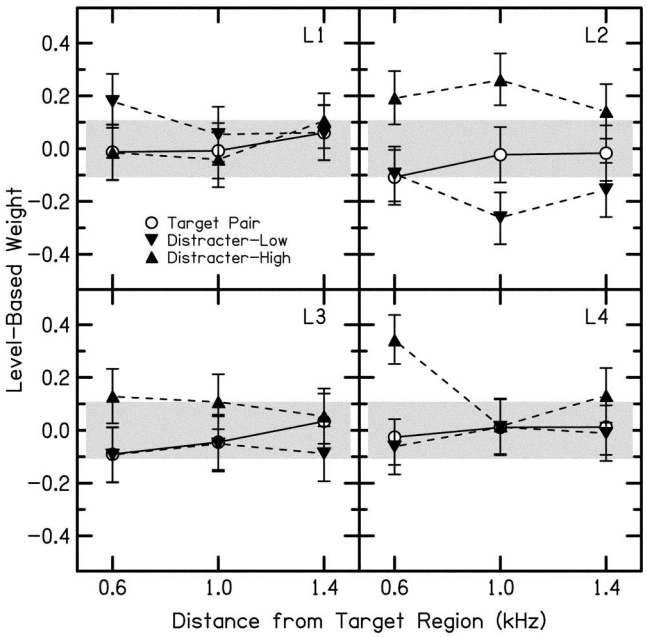

FIG. 5. Level-based weights for the fixed-frequency distracter conditions with level variation; same format as Fig. 3. There are no corresponding frequency-based weights.

tions to select the interval with the tone(s) that were higher in frequency, but often based their votes on the low-frequency distracter. This is consistent with overall performance near chance for these conditions. Distance of the distracter tone from the target frequency region seemed of little consequence. For the low-frequency distracter, only L4 showed a large increase in the weight at the most remote position. For high-frequency distracters, the weights were significant only for L3 and L4 and then only for the nearest distance.

B. Results for conditions with level variation

As described earlier, experiment 1 also included conditions with level variation added to all tonal stimuli. Performance did not change from the pattern shown in Fig. 2 for the noise-band distracters, given level variation added only to the target tones. For random-frequency distracters, performance also was nearly identical to that shown in Fig. 2. It remained near chance, with little range for further decrement. Level variation affected performance only for the fixed-frequency distracters. A comparison of results for fixed-frequency conditions with (open symbols) and without (closed symbols, replotted from Fig. 2) level variation is shown in Fig. 4. With the exception of the atypical crossover for L3 at the closest target-distracter distance, level variation produced a constant and similar decrement in performance (mean of 0.4 d' units) for all listeners, despite differences in performance across listeners without level variation. Thus, level variation alone degraded performance by a small and consistent amount, whereas frequency variation alone typically reduced performance to near chance. Frequency-based weights for conditions with level variation for random-frequency distracters are not shown, as they are nearly identical for all listeners to weights without level variation (Fig. 3). Thus, the addition of level variation had little influence on either performance or frequency-based weights, perhaps due to the randomized testing order of conditions. The results indicate the stability of the frequency-based weights across conditions and little influence of level variation on listener strategy.

Weights based on *level* changes across intervals of a trial were calculated for the random-and fixed-frequency distracter conditions. Note that judgments of target frequency remained the basis of the SD-F task. Level-based weights for random-frequency distracters are not shown, as nearly all were nonsignificant. Figure 5 shows level-based weights for the fixed-frequency distracter conditions, using the same format as Fig. 3 (except for the *Y*-axis range). L2 showed the largest influence of level variation, with significant negative weights for the low-frequency distracter and positive weights for the high-frequency distracter. Although her overall SD-F performance remained high, these weights suggest a tendency to avoid intervals with higher-level, lower-frequency distracters and select intervals with higher-level, higher-frequency distracters. L4 also shows one large positive weight for the high-frequency distracter closest to the target. All other weights are small or nonsignificant. Overall, the level-based weights suggest insensitivity to this degree of Gaussian level variation (18-dB total range) in the presence of frequency variation. Whereas this experiment examined the effects of level ''jitter'' within trials, the next experiment examined the effect of manipulating the overall level of targets versus distracters. The expectation was that listeners would be able to use constant differences in level across stimuli to aid separation of target and distracter tones.

IV. EXPERIMENT 2: EFFECT OF OVERALL VS RELATIVE DISTRACTER LEVEL

The results of experiment 1 for random-frequency distracter tones showed performance at or near chance, indepen-

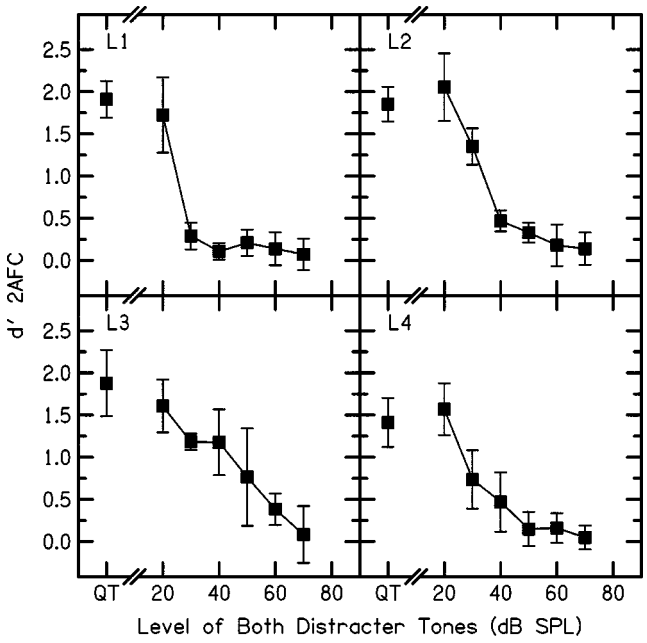

FIG. 6. Performance as a function of the level of both distracter tones (dB SPL) for random-frequency distracters placed farthest from the target region. Level was changed in 10-dB steps, increasing to equal the level of the target-tone components. Listeners are plotted across panels.

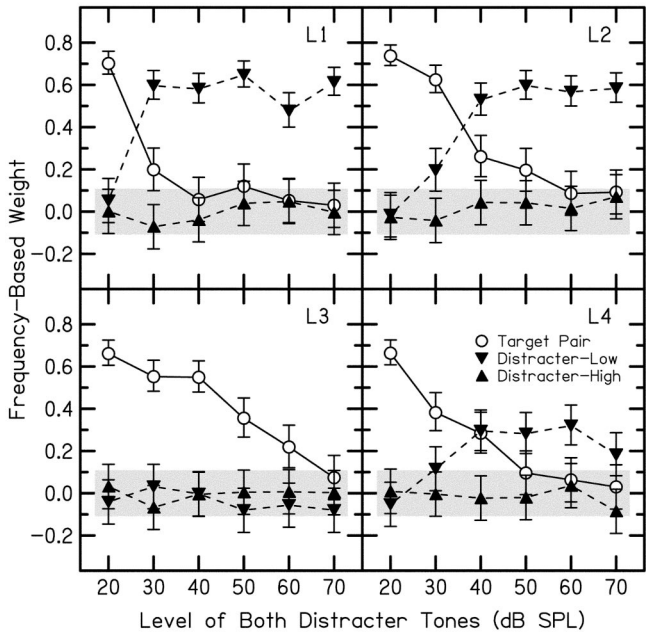

FIG. 7. Frequency-based weights for the target-tone pair and the low- and high-frequency distracter tones as a function of the level of both distracter tones (dB SPL); same format as in previous plots of weights.

dent of the distance of the distracter from the target region. This experiment tested the effect of varying the overall level of random-frequency distracters. Only distracters at the farthest distance from the target region (±1400 Hz) were used. In one set of conditions, both distracter tones of the pair were decreased by the same amount in 10-dB steps from levels equal to the target (70 dB SPL per pair, or 67 dB per component) to levels near the threshold of audibility for the distracters (20 dB SPL per pair, or 17 dB per component). In a second set of conditions, one distracter tone of the pair (high or low frequency relative to the target) was fixed in level equal to the target tones (67 dB SPL), while the other was decreased in 10-dB steps from 67 to 17 dB SPL. In both sets of conditions, a baseline condition without distracters was included, and the conditions were tested in random order.

A. Results for varying level of the pair of distracter tones

Performance (d') as a function of increasing distracter level is shown in Fig. 6 for conditions in which both random-frequency distracter tones were varied in level together. The results for the QT condition (no distracters) were in good agreement with corresponding values from experiment 1 (horizontal lines, Fig. 2). Results for the 70-dB condition (equal-level distracter and target tones) also replicated the results of experiment 1, with performance for all listeners near chance. The degree of difficulty listeners had using large differences in level to aid target detection was unexpected. Performance equal to the no-distracter condition was attained only for the lowest distracter level tested, which was 50 dB lower than the target pair. For L1 and L2, large error bars for that condition indicate performance was not yet stable for recovery to baseline performance. L3 showed the most systematic effects, with performance decreasing about 0.5 d' unit for each 10-dB increase in distracter level. For the other listeners, performance dropped rapidly and remained poor for distracters that were 40 dB less intense than the target tones and at frequencies remote from the target region.

The frequency-based weights for these conditions are presented in Fig. 7 as a function of the level of both distracter tones, using the same format as Fig. 3. The pattern of weights across stimuli was consistent with experiment 1, in that there were no significant weights for the higher-frequency distracter tone regardless of distracter level. There were, however, large weights for three of the four listeners (not L3) for the lower-frequency distracter. Just as in experiment 1, L3 differed from the other listeners in showing no significant weights for either distracter frequency, but steadily decreasing weights (and poorer performance) for the target-tone pair with increasing distracter level. Thus, her ability to detect the target tones was affected by the distracters, but she was not responding to the distracters *per se*. Weights for the other listeners indicated that they were responding to the frequency changes of the lower-frequency distracter as if it were the target. For all listeners, changes in target-pair weights accurately reflected changes in performance across conditions in Fig. 6, with larger target weights corresponding to higher d' values.

B. Results for independent changes in level for each distracter

These conditions tested the effect of holding the level of one of the distracter tones constant as the level of the other distracter was varied. Across conditions, either the high- or the low-frequency distracter was fixed at the maximum level (67 dB SPL, equal to the target tones), and the level of the other distracter was fixed (within blocks) at ''0'' (not

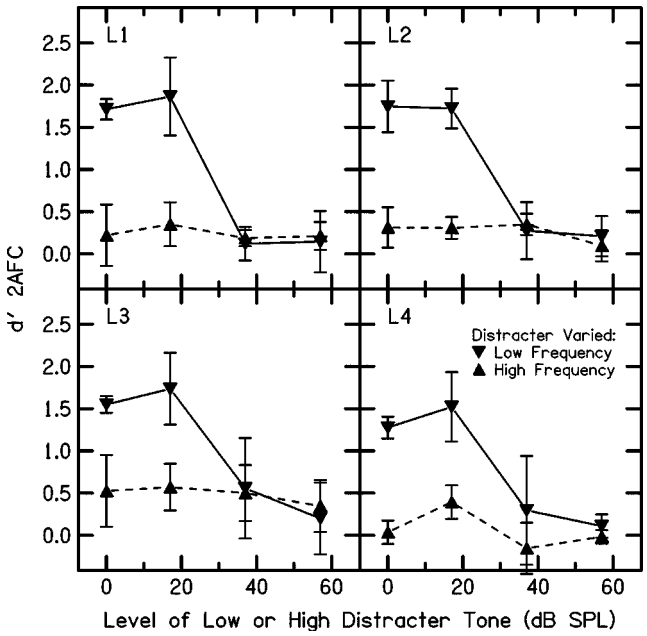

FIG. 8. Performance as a function of the level of the low- or high-frequency distracter (dB SPL) for random-frequency distracters placed farthest from the target region. For the two functions, the symbol legend indicates which distracter was varied in level while the other was held constant.

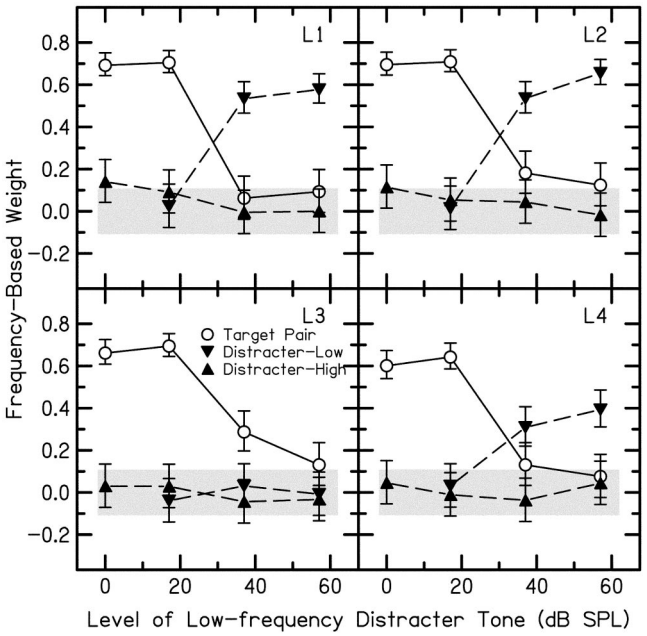

FIG. 9. Frequency-based weights for conditions in which the low-frequency distracter was varied in level, using the same format as previous plots of weights. Weights correspond to performance shown in Fig. 8 by downward-pointing triangles.

present), 17, 37, or 57 dB SPL. Performance (d') is shown in Fig. 8, with downward-pointing triangles for conditions in which the lower-frequency distracter tone was varied in level while the higher-frequency distracter remained constant at 67 dB SPL, and upward-pointing triangles for the reverse (varied high distracter level, fixed low distracter level). The results again confirmed the dominance of the lower-frequency distracter. Performance hovered near chance when the lower-frequency distracter was equal in level to the target-tone components, with little influence of the higher-frequency distracter regardless of level. Similarly, when the higher-frequency distracter tone was fixed at target-tone level, good performance was sustained only until the lower-frequency distracter tone increased to 37 dB SPL and then fell to near chance. Performance for the "0-dB" conditions (one distracter absent, the other at maximum level) clearly indicated the relative influence of the two distracters, with large detrimental effects for the low-frequency distracter alone but little effect of the high-frequency distracter alone.

Figures 9 and 10, respectively, present the frequency-based weights for conditions in which the low- or high-frequency distracter was varied in level (with the other distracter constant). The distracter that is varied is indicated in the abscissa label, and the format and symbols are the same as in previous figures for weights. Again, note that the 0-dB condition on the abscissa indicates that the featured distracter was absent, but the other distracter was at maximum level (e.g., for Fig. 9, only the high-frequency distracter). The pattern of results in Figs. 9 and 10 was consistent with previous results in that listeners appeared to base their responses on the lower-frequency distracter. In Fig. 9, the weights for the maximum-level, higher-frequency distracter were mostly nonsignificant for all listeners. L3 again differed from the others in that she also had no significant weights for the low-frequency distracter. However, L3's large weights for the target pair decreased monotonically as the level of the low-frequency distracter increased. For the other three listeners, weights for the low-frequency distracter increased as the weights for the target decreased.

Weights in Fig. 10 for varying the level of the high-frequency distracter (low-frequency distracter fixed at maximum) also showed the dominant influence of the low-frequency distracter, but the patterns differed more across

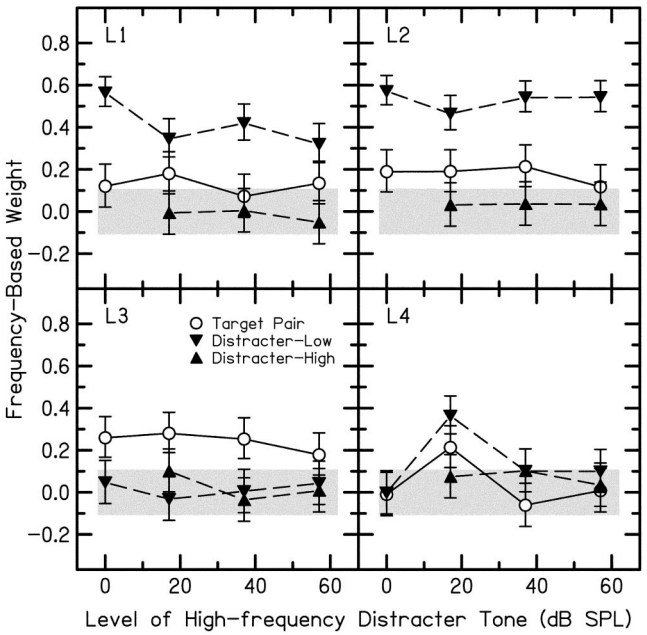

FIG. 10. Frequency-based weights for conditions in which the high-frequency distracter was varied in level, using the same format as Fig. 9. Weights correspond to performance shown in Fig. 8 by upward-pointing triangles.

listeners. The pattern for L1 and L2 is most straightforward, showing no significant weights as a function of increasing level for the high-frequency distracter, but consistent large positive weights for the low-frequency distracter. Weights for the target pair were significant and positive, but much smaller than for the low-frequency distracter. Consistent with Fig. 9, L3 again showed no significant weights to either distracter tone, but only relatively small weights to the target. We infer that she was basing her responses on the target pair, but the task was made very difficult by distracter tones, particularly the low-frequency distracter tone. For L4, the lack of significant weights for most stimuli and conditions, combined with corresponding performance at chance for these conditions (see Fig. 8) suggests that this listener was simply responding at random. Because L4 in Fig. 9 had large positive weights to the target when the low-frequency distracter was absent or low level, again the results suggest an overwhelming influence of the low-frequency distracter for this listener. Overall, varying the level of the distracters together or independently added further evidence for the comparatively greater influence of the lower-frequency distracter. Because the weights were derived from frequency variation, and frequency variation was the variable on which listeners were to base their responses, the weights clearly revealed the stimulus components used by listeners for their decisions.

V. EXPERIMENT 3: EFFECT OF MOVING STIMULI TO HIGHER FREQUENCIES

This experiment tested whether shifting the frequency regions of the targets and distracters would change the basic pattern of the results, particularly the dominance of the lower-frequency distracter tone. Distribution means for the pairs of target tones were shifted to 3850 and 4000 Hz. The baseline (no distracters), fixed-frequency, and random-frequency distracter conditions were tested for the largest frequency separation used before of ± 1400 Hz, which corresponds to a mean frequency of 2450 Hz for the low-frequency distracter distribution and 5400 Hz for the high-frequency distracter. Thus, the lower distracter was now well above the former target region. Three of the four listeners (L1–L3) participated; all other aspects of the stimuli and procedure remained the same.

Performance (d') for the "high-target" conditions for the three listeners and mean across listeners are presented in Fig. 11 (closed symbols) for the baseline and two distracter conditions. The open symbols, replotted from Fig. 2, indicate corresponding performance with the 2100-Hz target region. For the no-distracter condition, performance was either similar (L1 and L2) or degraded (L3) for the high-target conditions. For the random-frequency distracters, performance remained near chance. For the fixed-frequency distracters, however, all listeners clearly had more difficulty with the higher-frequency stimuli. This is particularly clear for L1 and L2, because their performance did not change for the target-alone conditions at higher frequencies. Weights were not available for these fixed-frequency conditions, but listeners reported that the lower-frequency distracter continued to be the stimulus they believed made the task difficult. There is support for these anecdotal comments in the weights for the

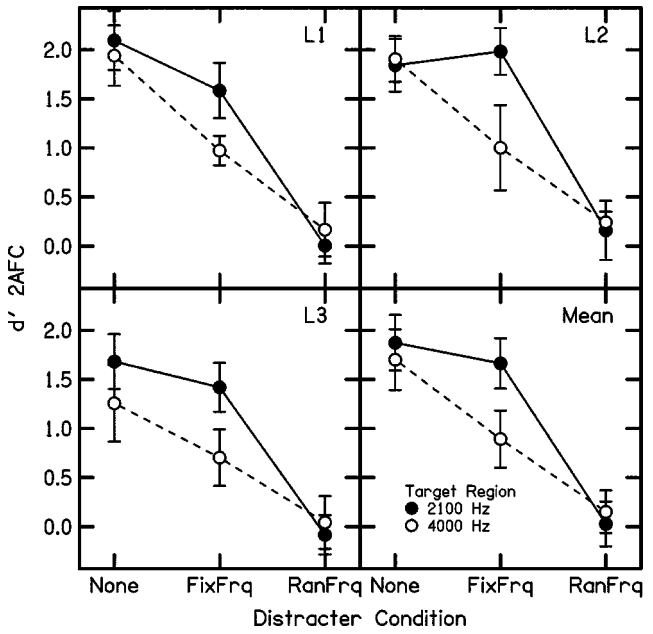

FIG. 11. Performance for stimuli shifted to higher-frequency regions, with target distributions at 3850 and 4000 Hz and distracter distributions at 2450 and 5400 Hz (solid circles). The labels on the abscissa indicate conditions with no-distracter (None), fixed-frequency distracters (FixFrq), and random-frequency distracters (RanFrq). Lines connecting points simply aid comparisons across conditions. Performance using lower-frequency stimuli is replotted from Fig. 2.

random-frequency distracters, which are shown in Fig. 12. All three listeners had large positive weights for the lower-frequency distracter, with nonsignificant weights for the target pair and the higher-frequency distracter. For L3, this was a large increase in the weight for the lower-frequency distracter compared to the previous conditions with targets near 2000 Hz, so her pattern now matches that of the other listen-

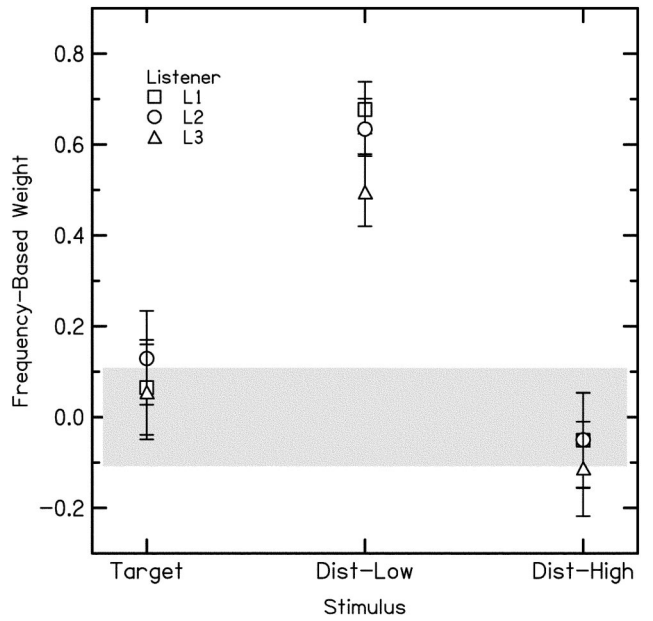

FIG. 12. Frequency-based weights for the target-tone pair, and the low- and high-frequency distracter tones for stimuli shifted to higher frequencies. The weights correspond to overall performance in Fig. 11. Shaded areas indicate weights not significantly different from 0.0 ($p > 0.01$).

ers. The weights suggest all listeners tended to select the intervals in which the low-frequency distracter tone had the higher frequency. Thus, shifting the stimuli to a higher frequency region appeared to make the fixed-frequency distracters more effective, but the random-frequency distracters retained or increased their large effects, including the dominance of the lower-frequency distracter.

VI. DISCUSSION

Overall, the results demonstrated that listeners have great difficulty with a frequency-based SD task with distracters that also vary in frequency. Performance that was near ideal in the baseline conditions dropped to near chance for conditions with one or two random-frequency distracter tones. Moving the distracters farther away from the target region did little to aid performance. Fixed-frequency tones or noise bands in the same frequency regions as the random-frequency distracters, however, produced much smaller or no detrimental effects (with noise improving performance a small amount for some listeners and conditions). Thus, it was not the presence of energy *per se* in particular frequency regions that governed performance with the distracters, but rather the frequency variability and bandwidth of the distracters. The large detrimental effects of the random-frequency distracters are consistent with the results of studies of informational masking, in which random-frequency maskers with small numbers of components can greatly degrade the ability to detect a fixed-frequency signal (e.g., Kidd *et al.*, 1994; Neff and Dethlefs, 1995; Oh and Lutfi, 1998). Similar to the present results, these maskers can produce large decrements in performance despite masker components falling in frequency regions remote from the signal frequency. The SD-F task differs from informational-masking tasks in several ways, most notably in the frequency discrimination versus detection decision required of the listeners and the introduction of frequency variability for both target and distracter stimuli. To perform well on either task, however, subjects must either perceptually separate target/signal tones from the distracter/masker tones or discover consistent perceptual cues associated with adding the target/signal tones to the stimulus complex. The two tasks are also similar in that frequency variability in the irrelevant tones (maskers or distracters) apparently hinders the use of peripheral auditory frequency selectivity to distinguish relevant from irrelevant stimuli. Further, reducing the degree of frequency randomization for the irrelevant stimuli by fixing masker or distracter frequencies across trials reduces the detrimental effect of the interfering stimuli. Although performance can differ greatly across individuals for fixed-frequency distracters/maskers, the effects are always much smaller than the corresponding effect of random-frequency distracters/maskers for a given listener.

With random-frequency distracters, a potentially important and unexpected result was the apparent dominance of the distracter tone below the target frequency, which was observed in independent stimulus sets throughout the present study. Perhaps the randomization of testing order within sets of conditions and the participation of the same set of subjects throughout accounts for some of the stability in weights over time. Both the differential pattern of weights across stimulus components and the effects of level manipulations of target and distracters on overall performance, however, were so robust and consistent across listeners that it will be important to pursue the generality and source of this effect. Recall that the distracter tones always flanked the target region in frequency, with one above and one below. Performance is often at or near chance for these conditions based on *target*-tone judgments. The weights suggest that listeners were following instructions to pick the interval with the higher-frequency tone(s), but often responded to the lower-frequency distracter instead of the targets. Listeners' descriptions of their percepts also support the relative importance of the lower-frequency distracter tone. For the random-frequency distracters, listeners spontaneously asked whether the target stimuli had been removed from the stimuli to confound them. All listeners also reported variability in the percepts across trials, rather like the visual ''Necker cube'' effect, as the target and distracter tones apparently vied for perceptual dominance. Listeners reported that they could clearly ''hear out'' the target tones in some trials, albeit with great effort, but then they would ''lose it'' for large numbers of trials. With fixed-frequency distracters, listeners reported that the lower-frequency distracter tone still attracted their attention, but it could be easily ignored after the first few trials. The authors, who have extensive experience listening to these stimuli, concur with these reports. Future research comparing responses of listeners to reports of the percept from trial to trial might reveal whether measurable changes in performance are associated with these changes in percepts.

Another important aspect of the present data is the relative insensitivity to the distance between the target and distracter frequency region. The most remote random-frequency distracters degraded performance as much as those at the closest distance, although target and random-frequency distracter distributions never overlapped. For noise-band distracters with bandwidths equal to the Gaussian distracter distributions, performance either remained the same as baseline or improved with increasing distance from the target region. The effects, however, were not large. For fixed-frequency distracters, some listeners showed changes in performance with distance, but these changes were not consistent across listeners. For example, L3's performance was poorest for the 0.6-kHz distance, whereas L1's performance was the best for that condition (see Fig. 2). The relative distance between target and distracters seemed of little consequence for random-frequency distracters, which supports interpretation of the data as reflecting nonperipheral processes such as selective attention.

The effect of level variation for the distracters and targets was not explored extensively. For the degree of variation tested (18-dB range for the Gaussian distribution), the fixed-frequency distracters showed a fairly constant decrement in performance for all conditions, and the magnitude of the decrement was similar across listeners. Note that these manipulations are not the same as a multidimensional SD task in which both frequency and level variation are present and used as the basis of listener judgments (e.g., Lutfi, 1990). Further, because listeners were instructed to judge the target-

tone frequency variation, level variation never provided information for identifying the correct interval. More extensive conditions are needed to clarify the role of level variation for the fixed-frequency distracter. However, for random-frequency distracters, the effect of varying *overall* level of targets versus distracter tones was clear. Listeners were remarkably insensitive to the relative level of the random-frequency distracter tones. Our expectation was that the smallest level change (of 10 dB) to both distracters would be sufficient for listeners to perceptually differentiate targets from distracters, particularly given that these level differences were fixed across the entire block of trials, and listeners were fully informed of the difference in stimulus levels before each condition was tested. The results, however, showed that 30–50-dB differences were required to significantly improve performance (e.g., Fig. 6). Further, when the relative level of each distracter was varied independently, the results confirmed the earlier evidence from weights that the low-frequency distracter was primarily responsible for the poor performance. Weights for conditions in which the level of each distracter was varied independently showed an apparent trading relation in listeners' strategies for responding to target tones versus the lower-frequency distracter, with little effect of the higher-frequency distracter. Shifting the stimuli to a higher-frequency region did not diminish the influence of the lower-frequency distracter. It is not clear from the present conditions why the lower-frequency distracter tone had such a large effect. Consistent with much of the earlier work with SD of frequency differences (e.g., Lutfi, 1990, 1992, 1994), the distributions used here were based in linear frequency scales. Thus, the distribution of lower frequency distracter tones would be larger relative to the width of the auditory filter than that of the targets or higher-frequency distracter. Given the apparent insensitivity of listeners to the distance of the frequency region from the target, however, it seems unlikely that the change in frequency variation for linear versus logarithmic scales will account for the effect. Similarly, loudness differences for low- and high-frequency distracters cannot be an important factor, given the continued interference of the low-frequency tone even when presented at much lower levels than the other stimuli.

As noted earlier, most studies that have examined interactions of distracter and target frequency have used level differences for complexes or brief sequences of fixed-frequency tones (e.g., Dai and Berg, 1992; Doherty and Lutfi, 1999; Lutfi, 1992, 1994; Stellmack *et al.*, 1997; Willihnganz *et al.*, 1997). The latter two studies are of particular interest, in that weighting functions were obtained for children and adults in SD of level differences with three-component complexes (250, 1000, 4000 Hz). Listeners were instructed to focus on one component as the target (''analytical'' listening) or focus on all three as targets (''synthetic'' listening). For synthetic listening conditions and stimuli with equal mean levels for all components (Willihnganz *et al.*), the children had large individual differences in weighting functions, with no clear dominance of any frequency component. For adults, however, weights increased (on average) with component frequency. For corresponding analytical listening conditions (Stellmack *et al.*), the children had roughly equal weights for all three components. Adults, in contrast, had the largest weights for the target. Weights for both low- and high-frequency distracters were small and essentially equal. In both studies, the weights predicted a substantial percentage of the listener's responses even when performance in terms of percent correct approached chance. In our SD-F conditions, level-based weights showed no dominance of any component (targets or distracters). For frequency-based weights, however, the low-frequency distracter was clearly more heavily weighted. In many conditions with the random-frequency distracter, overall performance was near chance, as defined by responses to the target tones. The weights contributed valuable information, in that they suggested this occurred because listeners were often responding to the lower-frequency distracter tone instead of the targets.

Lutfi (1992) included conditions in which SD-F was examined with distracter tones that also varied in frequency. The ratio of target to distracter standard deviations was manipulated across conditions to test the effect of the relative stimulus variability. The stimuli were ten-tone sequences in which the sixth tone was the target. The center frequency of the distracter distribution was at 2000 Hz, with the two target distributions at various distances above and below that region. The frequency configuration of targets and distracter, therefore, was quite different from the present study. Consistent with the present results, however, overall performance for equal-variance targets and distracters was very poor. The relative variability of stimuli has been clearly established as an important factor in studies of auditory selective attention, as formalized by Lutfi in his CoRE (Component Relative Entropy) model (cf., Lutfi, 1993; Lutfi and Doherty, 1994). SD-F data from the present study suggest that factors other than stimulus variance also have a strong influence on auditory selective attention. Specifically, stimulus frequency appears to be important. Recent work by Alexander and Lutfi (2003), using procedures and stimuli very different from the present study, provides further support for listening strategies that emphasize frequencies below the target. They examined informational masking with random-frequency maskers and sinusoidal signals at 0.8, 2.0, or 5.0 kHz, with no components near the signal frequency. Potential masker components were spaced at 1/3-octave intervals from 522 to 8346 Hz. Masker uncertainty was produced by randomly and independently playing components at each frequency with a probability of 0.5 or 1.0 on each trial. Informational masking, defined as the difference in performance between the two probability conditions, increased with the number of masker components *below* the signal frequency for both the normal-hearing and hearing-impaired adult listeners. Both groups also had similar weights, with masker frequencies below the signal weighted more heavily. Further research is needed to determine the generality of these frequency effects in uncertain listening conditions and assess whether such effects reflect basic properties of auditory selective attention.

ACKNOWLEDGMENTS

This work was supported in part by a grant from the NIDCD (R01 DC00925). We are grateful to Tom Creutz for software development, Christina Kessler for collecting pilot data, and Walt Jesteadt and two anonymous reviewers for their help in improving this paper.

Alexander, J. M., and Lutfi, R. A. (**2003**). ''Upward spread of informational masking in normal-hearing and hearing-impaired listeners,'' J. Acoust. Soc. Am. **113**, 2287.

ANSI (**1989**). ANSI S3.9-1989, ''American National Standards specification for audiometers'' (American National Standards Institute, New York).

Berg, B. G. (**1989**). ''Analysis of weights in multiple observation tasks,'' J. Acoust. Soc. Am. **86**, 1743–1746.

Berg, B. G. (**1990**). ''Observer efficiency and weights in a multiple observation task,'' J. Acoust. Soc. Am. **88**, 149–158.

Berg, B. G. (**2004**). ''A molecular description of profile analysis: Decision weights and internal noise,'' J. Acoust. Soc. Am. **115**, 822–829.

Berg, B. G., and Robinson, D. E. (**1987**). ''Multiple observations and internal noise,'' J. Acoust. Soc. Am. Suppl. 1 **81**, S33.

Dai, H., and Berg, B. G. (**1992**). ''Spectral and temporal weights in spectral-shape discrimination,'' J. Acoust. Soc. Am. **92**, 1346–1355.

Doherty, K. A., and Lutfi, R. A. (**1999**). ''Level discrimination of single tones in a multitone complex by normal-hearing and hearing-impaired listeners,'' J. Acoust. Soc. Am. **105**, 1831–1840.

Glasberg, B. R., and Moore, B. C. J. (**1990**). ''Derivation of auditory filter shapes from notched-noise data,'' Hear. Res. **47**, 103–138.

Green, D. M., and Swets, J. A. (**1966**). *Signal Detection Theory and Psychophysics* (Krieger, Huntington, NY).

Kidd, Jr., G., Mason, C. R., and Arbogast, T. L. (**2002**). ''Similarity, uncertainty, and masking in the identification of nonspeech auditory patterns,'' J. Acoust. Soc. Am. **111**, 1367–1376.

Kidd, Jr., G., Mason, C. R., Deliwala, P. S., Woods, W. S., and Colburn, H. S. (**1994**). ''Reducing information masking by sound segregation,'' J. Acoust. Soc. Am. **95**, 3475–3480.

Kidd, G. R., and Watson, C. S. (**1992**). ''The 'proportion-of-the-total-duration rule' for the discrimination of auditory patterns,'' J. Acoust. Soc. Am. **92**, 3109–3118.

Leek, M. R., Brown, M. E., and Dorman, M. F. (**1991**). ''Informational masking and auditory attention,'' Percept. Psychophys. **50**, 205–214.

Lutfi, R. A. (**1989**). ''Informational processing of complex sound. I. Intensity discrimination,'' J. Acoust. Soc. Am. **86**, 934–944.

Lutfi, R. A. (**1990**). ''Informational processing of complex sound. II. Cross-dimensional analysis,'' J. Acoust. Soc. Am. **87**, 2141–2148.

Lutfi, R. A. (**1992**). ''Informational processing of complex sound. III. Interference,'' J. Acoust. Soc. Am. **91**, 3391–3401.

Lutfi, R. A. (**1993**). ''A model of auditory pattern analysis based on component-relative-entropy,'' J. Acoust. Soc. Am. **94**, 748–758.

Lutfi, R. A. (**1994**). ''Discrimination of random, time-varying spectra with statistical constraints,'' J. Acoust. Soc. Am. **95**, 1490–1500.

Lutfi, R. A. (**1995**). ''Correlation coefficients and correlation ratios as estimates of observer weights in multiple-observation tasks,'' J. Acoust. Soc. Am. **97**, 1333–1334.

Lutfi, R. A., and Doherty, K. A. (**1994**). ''Effect of component-relative-entropy on the discrimination of simultaneous tone complexes,'' J. Acoust. Soc. Am. **96**, 3443–3450.

Neff, D. L., and Dethlefs, T. M. (**1995**). ''Individual differences in simultaneous masking with random-frequency, multicomponent maskers,'' J. Acoust. Soc. Am. **98**, 125–134.

Neff, D. L., and Green, D. M. (**1987**). ''Masking produced by spectral uncertainty with multicomponent maskers,'' Percept. Psychophys. **41**, 409–415.

Oh, E. L., and Lutfi, R. A. (**1998**). ''Nonmonotonicity of informational masking,'' J. Acoust. Soc. Am. **104**, 3489–3499.

Patterson, R. D., Nimmo-Smith, I., Weber, D. L., and Milroy, R. (**1982**). ''The deterioration of hearing with age: Frequency selectivity, the critical ratio, the audiogram and speech threshold,'' J. Acoust. Soc. Am. **72**, 1788–1803.

Richards, V. M., and Zhu, S. (**1994**). ''Relative estimates of combination weights, decision criteria, and internal noise based on correlation coefficients,'' J. Acoust. Soc. Am. **95**, 423–434.

Richards, V. M., Tang, Z., and Kidd, Jr., G. (**2002**). ''Informational masking with small set sizes,'' J. Acoust. Soc. Am. **111**, 1359–1366.

Southworth, C., and Berg, B. G. (**1995**). ''Multiple cues for the discrimination of narrow-band sounds,'' J. Acoust. Soc. Am. **98**, 2486–2492.

Stellmack, M. A., Willihnganz, M. S., Wightman, F. L., and Lutfi, R. A. (**1997**). ''Spectral weights in level discrimination by preschool children: Analytic listening conditions,'' J. Acoust. Soc. Am. **101**, 2811–2821.

Watson, C. S., Wroton, H. W., Kelly, W. J., and Benbassat, C. A. (**1975**). ''Factors in the discrimination of tonal patterns. I. Component frequency, temporal position, and silent intervals,'' J. Acoust. Soc. Am. **57**, 1175–1185.

Weber, D. L. (**1995**). ''Information integration of pooled versus paired samples,'' J. Acoust. Soc. Am. **98**, 1903–1908.

Willihnganz, M. S., Stellmack, M. A., Lutfi, R. A., and Wightman, F. L. (**1997**). ''Spectral weighting in level discrimination by preschool children: Synthetic listening conditions,'' J. Acoust. Soc. Am. **101**, 2803–2810.

The apparent immunity of high-frequency "transposed" stimuli to low-frequency binaural interference

Leslie R. Bernstein and Constantine Trahiotis
Department of Neuroscience and Department of Surgery (Otolaryngology), University of Connecticut Health Center, Farmington, Connecticut 06030

(Received 10 March 2004; revised 20 July 2004; accepted 21 July 2004)

Discrimination of interaural temporal disparities (ITDs) was measured with either conventional or transposed ''targets'' centered at 4 kHz. The targets were presented either in the presence or absence of a simultaneously gated diotic noise centered at 500 Hz, the interferer. As expected, the presence of the low-frequency interferer resulted in substantially elevated threshold-ITDs for the conventional high-frequency stimuli. In contrast, these interference effects were absent for ITDs conveyed by the high-frequency transposed targets. The binaural interference effects observed with the conventional high-frequency stimuli were well accounted for, quantitatively, by the model described by Heller and Trahiotis [L. M. Heller and C. Trahiotis, J. Acoust. Soc. Am. **99**, 3632–3637 (1996)]. The lack of binaural interference effects observed with the high-frequency transposed stimuli was not predicted by that model. It is suggested that transposed stimuli may be one of a class of stimuli that do not foster an obligatory combination of binaural information between low- and high-frequency regions. Under those conditions that do foster such an obligatory combination, one could still consider models of binaural interference, such as the one described in Heller and Trahiotis, to be valid descriptors of binaural processing.
[DOI: 10.1121/1.1791892]

PACS numbers: 43.66.Pn, 43.66.Ba [AK] Pages: 3062–3069

I. INTRODUCTION

It has recently been shown that the processing of ongoing interaural temporal disparities (ITDs) at high frequencies can be enhanced by using ''transposed stimuli'' similar to those first employed by van de Par and Kohlrausch (1997). The purpose of using transposed stimuli is to provide high-frequency auditory channels with envelope-based information that mimics waveform-based information normally available in only low-frequency channels. Specifically, the use of high-frequency transposed stimuli yielded both smaller threshold-ITDs (Bernstein and Trahiotis, 2002) and larger extents of laterality (Bernstein and Trahiotis, 2003) than did the use of ''conventional'' high-frequency stimuli such as narrow bands of Gaussian noise and sinusoidally amplitude-modulated (SAM) tones. Furthermore, with several of the high-frequency transposed stimuli, threshold-ITDs were as small, and extents of laterality were as large, as those measured with low-frequency pure tones and bands of noise having low center-frequencies.

Such findings may be interpreted to mean that the high-frequency channels of the auditory system are not, in and of themselves, less sensitive to ITDs than are the low-frequency channels. It occurred to us that transposed stimuli could be useful in evaluating current accounts and/or explanations of what has been termed ''binaural interference.'' In order to understand why this is so, it is necessary to consider what is generally known empirically about binaural interference and the nature of the theoretical explanations that have been offered to account for it.

Examples of binaural interference can be found in several experiments demonstrating that sensitivity to ITDs conveyed by a ''target'' presented within one spectral region can be degraded by the presence of a second, simultaneously gated stimulus, the ''interferer.'' An important characteristic of binaural interference is that the interferer occupies a spectral region remote from that of the target (e.g., McFadden and Pasanen, 1976; Davis, 1985; Zurek, 1985; Dye, 1990; Trahiotis and Bernstein, 1990; Bernstein, 1991; Buell and Hafter; 1991; Woods and Colburn, 1992; Buell and Trahiotis, 1993; Stellmack and Dye, 1993; Bernstein and Trahiotis, 1992a; 1995; Heller and Trahiotis, 1995). Another important characteristic of binaural interference is that it is asymmetric in that low-frequency stimulation adversely affects the processing of ITDs conveyed by high-frequency targets but high-frequency stimulation does not adversely affect the processing of ITDs conveyed by low-frequency targets.

The general theoretical framework used to account for binaural interference was first described by Buell and Hafter (1991) and incorporates a form of ''non-optimal'' processing wherein binaural interference arises from an obligatory combination of ITD-information conveyed by the target and the interferer, respectively. According to this model, the ITD-information conveyed within the target frequency channel and within the interferer frequency channel receive differential weights. The weights for the target and interferer, respectively, are inversely proportional to the magnitude of the threshold-ITD measured when each is presented in isolation. As a result, the stimulus having the lowest threshold-ITD, be it target or interferer, contributes most to the decision.

Recently, Heller and Trahiotis (1996) showed that predictions of binaural interference measured in an ITD-detection task could be markedly improved if the Buell and Hafter (1991) weights were augmented to include a factor representing the relative slopes of functions relating extent of

laterality to ITD for targets and interferers presented in isolation. Based on Heller and Trahiotis' model, one would predict that less binaural interference would be observed for high-frequency transposed targets than for conventional high-frequency stimuli. This is so because high-frequency transposed stimuli, unlike their conventional high-frequency counterparts, yield threshold-ITDs and extents of laterality that are similar to those obtained with low-frequency stimuli. Therefore, within the model, high-frequency transposed stimuli would receive greater weighting *vis-a-vis* the weighting applied to low-frequency interferers than would their conventional high-frequency counterparts. The Buell and Hafter (1991) model would also predict less interference for transposed targets but would do so based only on their relatively smaller threshold-ITDs.

In light of these issues, the purposes of this investigation were (1) to measure and to compare binaural interference effects obtained with either transposed or conventional high-frequency targets in an ITD-discrimination task and (2) to determine whether either of the quantitative models of binaural interference discussed above could account for the data. It will be seen that high-frequency transposed targets appear to be ''immune'' to binaural interference from low-frequency stimulation. In addition, it appears that neither of the models can account for the lack of interference obtained with transposed stimuli. The empirical and theoretical results, taken together, suggest that high-frequency transposed stimuli are, in some sense, ''special'' in that they appear to allow listeners effectively to disregard the presence of concurrent low-frequency stimulation and behave in a more ''optimal'' fashion.

II. EXPERIMENT 1

A. Stimuli

Five high-frequency stimuli served as targets: (1) a 4-kHz tone sinusoidally amplitude-modulated (SAM) at 128 Hz; (2) a 200-Hz-wide band of Gaussian noise centered at 4 kHz; (3) a 128-Hz tone transposed to 4 kHz; (4) a 50-Hz-wide band of Gaussian noise centered at 128 Hz that was transposed to 4 kHz; (5) a 100-Hz-wide band of Gaussian noise centered at 128 Hz that was transposed to 4 kHz. The transposed stimuli were generated in the manner described in detail by Bernstein and Trahiotis (2002; 2003). Briefly, the time-domain representation of a low-frequency tone or a narrow band of low-frequency Gaussian noise was (linearly) half-wave rectified by setting all negative values to zero. Rectified waveforms were then transformed to the frequency domain and the spectral components above 2 kHz were filtered out by setting their magnitudes to zero (see pp. 1027–1028 of Bernstein and Trahiotis, 2002 for a justification of the choice of this type of rectification and filtering). Rectified and filtered waveforms were then transformed back to the time domain and multiplied by a 4-kHz sinusoidal ''carrier.'' The product was a transposed stimulus having an envelope whose time signature mimicked that of the rectified and filtered low-frequency tone or low-frequency narrow band of noise.

Examples of each type of high-frequency target are depicted in Fig. 1. The left-hand panels show randomly chosen 50-ms epochs of each type of target; the right-hand panels show the (long-term) power spectrum of each target calculated over several tens of seconds. Beginning with the left-hand panels, note that there are six or seven envelope maxima for each type of target during the 50-ms epochs depicted. This reflects the fact that, by construction, the expected number of envelope maxima per second for each type of target is 128. For the SAM and transposed targets, this is more or less intuitively appreciated given that the basic waveforms that served as the ''modulators'' of the 4-kHz carriers were, as indicated in the figure, all centered on 128 Hz. For the 200-Hz-wide Gaussian noise target, some explanation seems in order. As shown by Rice (1954), the expected number of envelope maxima per second for a Gaussian noise is equal to 0.6411 times its bandwidth in Hz. Therefore, the bandwidth of the Gaussian noise target was chosen to be 200 Hz so that its rate of envelope fluctuation would be approximately 128 Hz, thereby matching the rate of envelope fluctuation of the other four types of targets.

There were three primary reasons for choosing a rate of envelope fluctuation of 128 Hz. First, transposed stimuli having a rate of envelope fluctuation of 128 Hz or so have been shown to produce the greatest enhancements of ITD-processing at high frequencies (e.g., van de Par and Kohlrausch, 1997; Bernstein and Trahiotis, 2002; 2003). Second, 128 Hz is well within the range of rates of envelope fluctuation that yield the smallest threshold-ITDs for conventional high-frequency stimuli such as SAM tones, two-tone complexes, and bands of Gaussian noise (see Henning, 1974; McFadden and Pasanen, 1976; Nuetzel and Hafter, 1981; Bernstein and Trahiotis, 1994). Third, the choice of this rate causes the vast majority of the energy to occur between 3750 Hz and 4250 Hz for all five types of targets (see right-hand panels of Fig. 1). This ensured that the energy within each type of target would fall almost entirely within the approximately 500-Hz-wide auditory filter centered at 4 kHz (see Moore, 1997). This was deemed necessary to help maximize the validity of comparisons of data obtained with the various targets and, perhaps, to simplify interpretations of the results. Also note that one of the two types of conventional targets (the SAM tone) was deterministic and had a discrete spectrum while the other one (the band of Gaussian noise) was stochastic and had a continuous spectrum. In somewhat parallel fashion, one of the transposed targets (the 128-Hz tone transposed to 4 kHz) was deterministic and had a discrete spectrum, while the other two transposed targets (the 50-Hz-wide and 100-Hz-wide bands of noise centered at 128 Hz which were each transposed to 4 kHz) were stochastic and had continuous spectra. These differences notwithstanding, the relative amounts of power within corresponding ''sidebands'' composing each of the three types of transposed stimuli was equal. For example, consider the sidebands centered on 3872 Hz. The level of that sideband within the spectrum of the target generated by transposing a 50-Hz-wide noise (fourth row) is 17 dB below the level of the corresponding sideband in the spectrum of the target generated by transposing a tone (third row). That difference results from the fact that the power of that sideband for the transposed

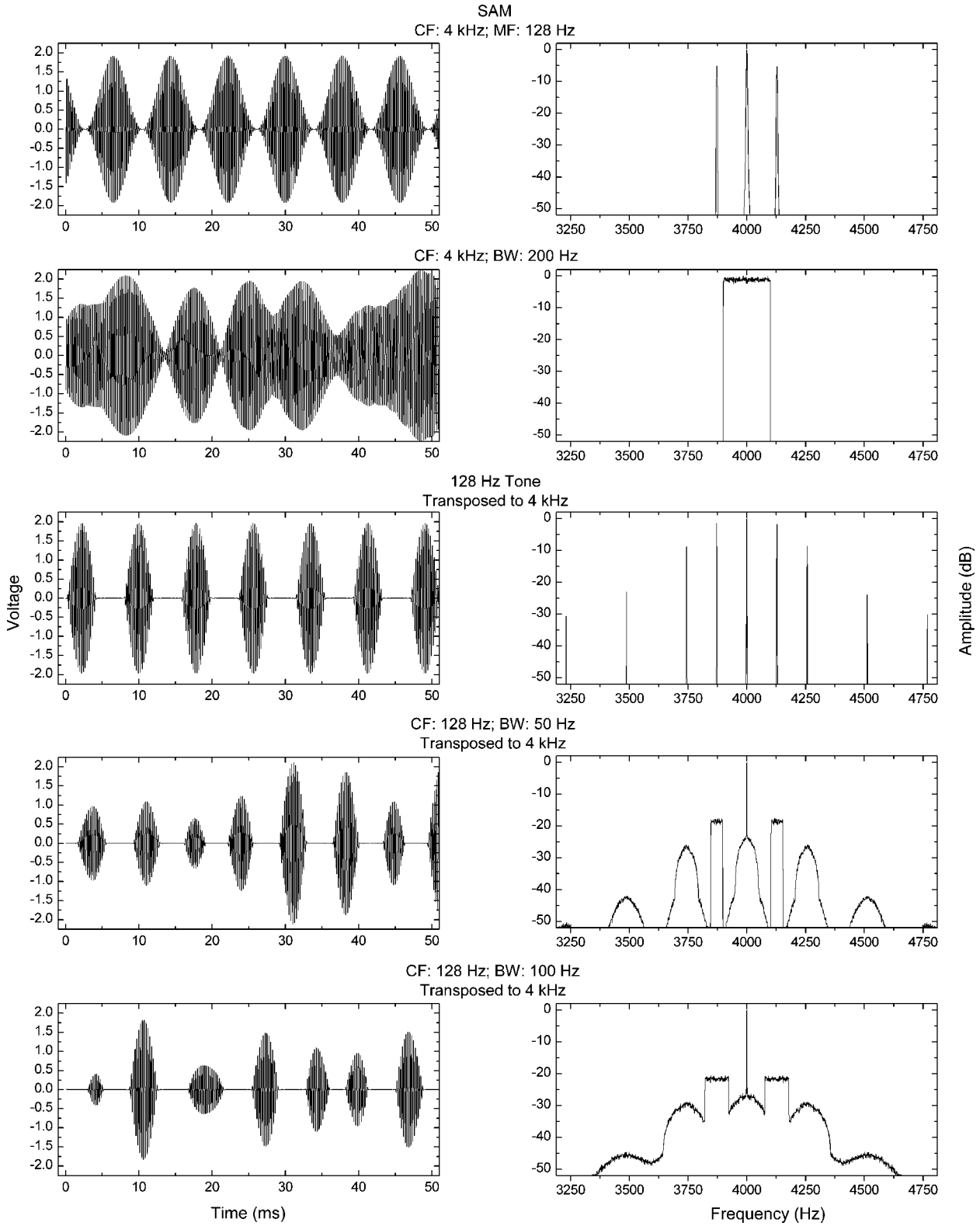

FIG. 1. Left-hand panels: Randomly chosen 50-ms epochs of the five types of targets employed in the main experiment. Right-hand panels: The long-term power spectra of each of the five types of targets.

noise is spread across a 50-Hz-wide band of frequencies, rather than being concentrated at a single spectral frequency. Consistent with this, the level of the 3872-Hz sideband within the spectrum of the target generated by transposing a 100-Hz-wide noise (fifth row) is another 3 dB below the level of the corresponding sideband in the spectrum of the target generated by transposing a 50-Hz-wide band of noise. These comparisons ignore the negligible additional power contributed to the 3872-Hz sidebands that results from ''overlap'' with neighboring sidebands.

The stimulus that served as the interferer was a 400-Hz-wide band of Gaussian noise centered at 500 Hz. Such a

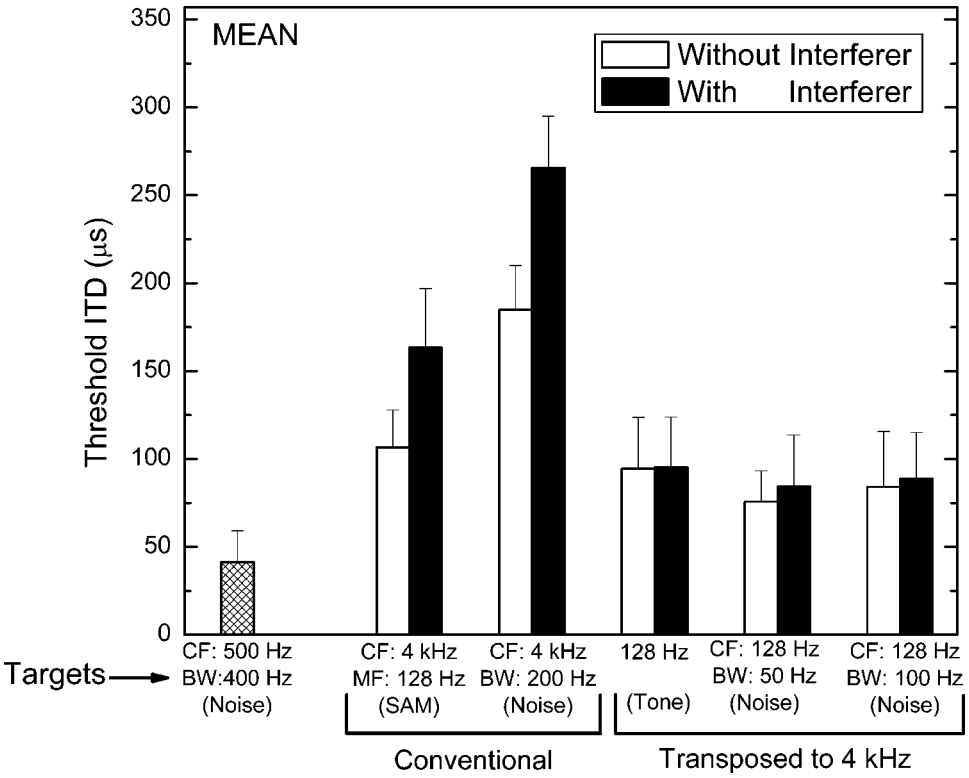

FIG. 2. Mean threshold-ITDs obtained in the main experiment. The types of target stimuli are indicated along the abscissa. Unfilled bars indicate threshold-ITDs for targets presented in the absence of the interferer; filled bars indicate threshold-ITDs obtained in the presence of the interferer. The cross-hatched bar at the left of the figure indicates the mean threshold-ITD obtained when the 400-Hz-wide band of noise centered at 500 Hz that served as the interferer was presented in isolation.

stimulus was found by Bernstein and Trahiotis (1995) to produce substantial amounts of binaural interference for the resolution of ITDs conveyed by target bands of noise centered at 4 kHz. Thus, overall, the types of targets used in the experiment were chosen to optimize sensitivity to ITD in high-frequency channels while the interferer was chosen to maximize the possibility of observing binaural interference effects, should they occur.

All targets and interferers were generated digitally as 8192-point buffers using a sampling rate of 20 kHz (TDT AP2). Each stimulus used in the experiment was 300 ms long including 20-ms $\cos^2$ rise-decay ramps and was extracted from the appropriate longer buffer. The stimuli were low-pass filtered at 8.5 kHz (TDT FLT2), and each was presented via Etymotic ER-2 insert earphones at a level matching 70 dB SPL as produced by TDH-39 earphones in a 6-cc coupler.[1] Interfering stimuli were presented diotically and were gated on and off synchronously and identically with the target stimuli.

B. Procedures

Threshold-ITDs were determined using a four-interval, two-cue, two-alternative, temporal forced choice, adaptive task. Each trial consisted of a warning interval (500 ms) and four 300-ms observation intervals separated by 400 ms. Each interval was marked visually by a computer monitor. Feedback was provided for approximately 400 ms after the listener responded. The stimuli in the first and fourth intervals were diotic. The listener's task was to detect the presence of an ITD (left-ear leading) that was presented with equal *a priori* probability in either the second or the third interval. The remaining interval, like the first and fourth intervals, contained diotic stimuli.

The starting phases of the components that composed each stimulus (prior to the imposition of an ITD) were chosen randomly for each observation interval within and across trials. All of the conventional waveforms required for a given trial were computed immediately prior to that trial. Because of the time required to generate the high-frequency transposed stimuli, it was necessary to calculate the transposed waveforms prior to each adaptive run. Twenty independently calculated tokens of the desired type of transposed stimulus were stored and one of them was chosen randomly (with replacement) for each of the four observation intervals defining a trial. Twenty tokens were employed so that the behavioral data were not dependent upon the occurrence of any particular stimulus. This set-size was considered to be sufficiently large based on Siegel and Colburn's (1989) findings that only 10 independently generated tokens of noise yielded essentially equivalent performance to that measured with "running" noise in a binaural discrimination task.

Ongoing ITDs were imposed by applying linear phase-shifts to the representation of the signals in the frequency domain and then gating the signals destined for the left and right ears coincidentally, after transformation to the time domain. The ITD for a particular trial was determined adaptively in order to estimate 70.7% correct (Levitt, 1971). The initial step-size for the adaptive track corresponded to a factor of 1.584 (equivalent to a 2-dB change of ITD, assuming ITD to be a "10 log" quantity) and was reduced to a factor of 1.122 (equivalent to a 0.5-dB change of ITD, assuming ITD to be a "10 log" quantity) after two reversals. A run was terminated after 12 reversals and threshold was defined as the geometric mean of the ITD across the last 10 reversals.

Four normal-hearing adults served as listeners and three consecutive estimates of threshold-ITD were first obtained

from each listener for each of the stimuli presented in isolation. Those stimuli were tested in random order. Then, three more estimates were obtained after revisiting the same stimulus conditions in reverse order. Estimates of threshold for targets presented in the presence of the interferer were obtained in the same manner after the estimates of threshold were obtained with targets presented in isolation. The same ordering of conditions was used for all listeners and all listeners received substantial practice before formal collection of data began. For each listener and stimulus condition, final estimates of thresholds were calculated by averaging the individual thresholds obtained from the six adaptive runs.

C. Results and discussion

Figure 2 contains the means of the threshold-ITDs (taken across the four listeners) obtained in each of the experimental conditions. The types of target stimuli are indicated along the abscissa. Unfilled bars indicate threshold-ITDs obtained without the interferer; filled bars indicate threshold-ITDs in the presence of the interferer. The cross-hatched bar at the far left of the figure indicates the mean threshold-ITD obtained when the 400-Hz-wide band of noise centered on 500 Hz that served as the interferer was presented in isolation. The error bars represent the standard errors of each mean threshold-ITD.

Visual comparisons among the data reveal two important trends. First, threshold-ITDs obtained with the high-frequency transposed targets are, on the average, smaller than those obtained with the conventional high-frequency targets. This general outcome replicates our earlier findings (Bernstein and Trahiotis, 2002). Second, sensitivity to ITD was degraded in the presence of the interferer for conventional targets, but not for transposed targets. That is, it appears that high-frequency transposed targets are effectively immune to binaural interference. This general outcome confirms the results of our preliminary or ''pilot'' studies (Bernstein and Trahiotis, 2001).

The data in Fig. 2 were subjected to a three-factor ([conventional vs transposed targets]×[no interference vs interference]×[stochastic vs deterministic targets]), within-subjects analysis of variance. In order to perform a ''balanced'' analysis of variance, the data obtained when the targets were either 50-Hz-wide or 100-Hz-wide bands of noise centered at 125 Hz and transposed to 4 kHz were averaged, respectively, within interference and no-interference conditions.[2] The error terms for the main effects and for the interactions were the interaction of the particular main effect (or the particular interaction) with the subject ''factor'' (Keppel, 1973). In addition to testing for significant effects, the proportions of variance accounted for (ω^2) were determined for each significant main effect and interaction (Hays, 1973).

Consistent with visual inspection of the data, the main effect of conventional vs transposed targets was highly significant (assuming a criterion of $\alpha<0.05$) [$F(1,3)=137.80$, $p=0.001$] and accounted for 35% of the variability of the data. This reflects the fact that, on average, listeners were more sensitive to ITDs conveyed by transposed targets as compared to their conventional counterparts. The main effect of interference vs no interference was also significant [$F(1,3)=57.17$, $p=0.005$] and accounted for 6% of the variability in the data. This reflects the fact that, on average, threshold-ITDs were elevated in the presence of the interferer. More importantly, for our purposes, the interaction of [conventional vs transposed targets]×[interference vs no interference] conditions was also significant [$F(1,3)=33.31$, $p=0.01$] and accounted for 4% of the variability. This outcome reinforces the general conclusion stated above that only the conventional targets, and not the transposed targets, were subject to binaural interference.

The third main effect, deterministic vs stochastic targets, was also significant [$F(1,3)=17.33$, $p=0.025$] and accounted for 7% of the variability in the data. This reflects the fact that, on average, threshold-ITDs obtained with the deterministic targets were smaller than those obtained with the stochastic targets. It is also the case that the interaction of [conventional vs transposed targets]×[deterministic vs stochastic targets] was also significant [$F(1,3)=65.72$, $p=0.004$], accounting for 11% of the variability. This reflects the observation that threshold-ITDs for the transposed targets were essentially identical whether the stimuli were deterministic or stochastic while threshold-ITDs measured with the conventional SAM stimuli were smaller than those measured with the narrow-band Gaussian noise. The latter outcome replicates findings previously reported in an earlier, independent investigation that also included those two particular SAM and noise stimuli (Bernstein and Trahiotis, 1994).

Finally, neither the interaction of [interference vs no interference]×[deterministic vs stochastic targets], nor the triple interaction among all three factors reached statistical significance (for both types of interactions, $p>0.25$). This means that the double interactions found to be statistically significant do not have to be qualified by reference to levels of a third factor. In total, the within-subjects main effects and interactions accounted for 62% of the total variance in the data. Said differently, the properties of the stimuli accounted for the majority of the total variability in the data. Considering that only four listeners participated in the study, the large amount of variability accounted for attests to the robustness of the changes in threshold-ITD brought about by the specific properties of the stimuli.

III. TESTING THE HELLER/TRAHIOTIS QUANTITATIVE MODEL OF BINAURAL INTERFERENCE

In 1996, Heller and Trahiotis described an extension of the Buell and Hafter (1991) ''weighted combination'' model that was successful in accounting for binaural interference in an experiment measuring threshold-ITDs. A fundamental underlying assumption of that model and of the Buell and Hafter model is that interference arises from an obligatory, across-frequency-channel, combination of binaural cues. That is, the processing of the targets and interferers is assumed to be ''non-optimal'' in that low-frequency diotic interferers, which convey no information useful for detecting ITDs within high-frequency targets, are not ignored. Said differently, the ITD value of zero conveyed by the low-frequency interferer is included in the decision variable and serves to ''dilute'' the value of the ITD conveyed by the high-frequency target. As a result, in the presence of the

low-frequency interferer, ITDs imposed on the high-frequency target must be increased in order to reach threshold.

The reader is referred to the appendix of Heller and Trahiotis (1996) for a detailed explication of their model and its relation to the model of Buell and Hafter (1991). In what follows, a brief summary of the material in that appendix is presented so that the manner in which the predictions for this study were derived can be understood.

In mathematical terms, the Heller and Trahiotis (1996) model can be represented by

$$d'_{t+i}=\frac{a\Delta x_t+b\Delta x_i}{\sqrt{a^2\sigma_t^2+b^2\sigma_i^2}}, \tag{1}$$

where d'_{t+i} represents the listener's sensitivity to changes in target-ITD in the presence of the interferer. The term Δx_t represents the change in lateral position resulting from the imposition of an ITD on the target when it is presented in isolation. In parallel fashion, Δx_i represents the change in lateral position resulting from the imposition of an ITD on the interferer, presented in isolation. Estimates of changes in lateral position (Δx_t and Δx_i), as a function of ITD, are obtained by using an acoustic pointing task to determine the slope, *s*, of the linear portion (between values of ITD of 0 and 600 μs) relating the IID of the pointer to the ITD of the target or interferer when each is presented in isolation. Within this rubric,

$$\Delta x_t=s_t\Delta\mathrm{ITD}_t, \tag{2}$$

$$\Delta x_i=s_i\Delta\mathrm{ITD}_i. \tag{3}$$

Note that the changes in lateral position, (Δx_t and Δx_i) are quantified by the IID of the pointer in dB.

Returning to Eq. (1), the terms σ_t and σ_i represent the square-roots of the variances associated with the auditory processing that results in changes in the lateral position of the target and interferer, respectively. The values σ_t and σ_i are in units of dB. They are estimated by equating $\Delta\mathrm{ITD}_t$ and $\Delta\mathrm{ITD}_i$ in Eqs. (2) and (3), respectively, with the (threshold) values of ITD required to yield $d'=1$. When that is done

$$d'_t=s_t\mathrm{threshITD}_t/\sigma_t=1, \tag{4}$$

$$d'_i=s_i\mathrm{threshITD}_i/\sigma_i=1. \tag{5}$$

It follows that

$$\sigma_t=s_t\mathrm{threshITD}_t, \tag{6}$$

$$\sigma_i=s_i\mathrm{threshITD}_i. \tag{7}$$

Within Eq. (1), the weights *a* and *b*, applied to the target and interferer ''channels,'' respectively, are taken to be inversely proportional to σ_t^2 and σ_i^2, respectively.

When the interferer is diotic and, therefore, $\Delta\mathrm{ITD}_i=0$, making appropriate substitutions and rearrangements among the relations given above (see Heller and Trahiotis, 1996, p. 3637) yields an equation that can be used to make predictions of target-threshold-ITDs in the presence of an interferer:

$$\mathrm{threshITD}_{t+i}=\mathrm{threshITD}_t\sqrt{1+\left[\frac{s_t\mathrm{threshITD}_t}{s_i\mathrm{threshITD}_i}\right]^2}. \tag{8}$$

Note that, as emphasized by Heller and Trahiotis (1996), the predicted threshold-ITDs under conditions of interference are determined completely by quantities (i.e., threshold-ITDs and slopes of lateralization) obtained when targets and interferers are each presented in isolation. It is also the case that setting the slopes, s_t and s_i to 1 in Eq. (8), yields the formulation used by Buell and Hafter (1991) to predict interference effects. The fundamental difference between the two models is that the Heller and Trahiotis model derives predictions directly in terms of changes in laterality while the Buell and Hafter model derives predictions directly in terms of changes in stimulus-ITD.

In order to derive predictions of threshold-ITDs for targets presented simultaneously with the interferer in the current experiment, an acoustic pointing task was used to determine the slope of the linear function relating the IID of the pointer to values of ITD from 0 to 600 μs for each of the five types of target and for the interferer utilized in the main experiment. The acoustic pointing task was the one employed successfully in several previous investigations. Briefly, the listener was required to adjust the interaural intensitive disparity (IID) of a 200-Hz-wide noise centered at 500 Hz until its intracranial position matched that of the stimulus that conveyed the ITD (see, Bernstein and Trahiotis, 1985, 2003; Heller and Trahiotis, 1996).

Three of the four listeners who participated in the main experiment were available to participate in the acoustic pointing task. For each listener and type of stimulus (target or interferer), the slope relating the IID of the pointer to ITD was computed via linear regression. Because those slopes were highly similar across listeners, we computed the average slope, taken across the three listeners, separately for each of the six stimuli (five types of target and the interferer). Those mean slopes and the mean threshold-ITDs obtained in the main experiment were entered into Eq. (8) to derive predictions of ITD-thresholds for each type of target in the presence of the interferer. For archival purposes, those slopes and threshold-ITDs are provided in Table I.

Figure 3 contains the data obtained in the main experiment replotted from Fig. 2 along with the predictions of threshold-ITD in the presence of the interferer. The crosses represent predictions obtained with the Buell and Hafter (1991) model; the asterisks represent predictions obtained with the Heller and Trahiotis (1996) model. Beginning with the conventional targets, note that the predictions derived with the Heller and Trahiotis model are very accurate, being well within the standard error of the measurement of the data themselves (see Fig. 2). The Buell and Hafter model, however, overestimates the effects of interference. These two general outcomes replicate the findings of Heller and Trahiotis.

In contrast, and of great import for the purposes of this study, note that *both* models, which assume an obligatory, non-optimal combination of information in the low- and high-frequency channels, fail to predict the absence of interference effects that was found with the transposed stimuli. Given the success of the Heller and Trahiotis (1996) model in accounting for interference effects with conventional high-frequency targets, its inability to account for data obtained

TABLE I. Mean threshold-ITDs and mean lateralization slopes for the five types of targets and the interferer when each was presented in isolation. The values were entered into Eq. (8) in order to derive predicted threshold-ITDs for targets in the presence of the interferer.

Stimulus	Mean Threshold-ITD (μs)	Mean Lateralization Slope (dB/μs)
Interferer		
Noise (CF: 500 Hz; Bw: 400 Hz) [Interferer]	41.2	0.038
Targets		
Conventional		
SAM (CF: 4 kHz; MF: 128 Hz)	106.5	0.020
Noise (CF: 4 kHz; BW: 200 Hz)	184.9	0.009
Transposed to 4 kHz		
Tone (128 Hz)	94.4	0.029
Noise (CF: 128 Hz; BW: 50 Hz)	75.8	0.028
Noise (CF: 128 Hz; BW: 100 Hz)	84.2	0.028

with transposed stimuli does not appear to be attributable to some kind of ''experimental error'' or shortcoming in the experiment, per se. The model's failure is consistent with the notion that listeners were somehow able to ''ignore'' the non-information-bearing diotic low-frequency interferer and base their decisions solely on changes in ITDs conveyed by the high-frequency transposed targets. At this time, it is unclear to us what factor(s) render the transposed stimuli employed in this experiment effectively immune to binaural interference. Perhaps future experiments using a wide variety of transposed and conventional targets and interferers will provide information concerning which stimulus conditions are necessary for binaural interference effects to occur and help clarify why binaural interference effects appear to be asymmetric with respect to frequency. At this time it is not clear whether such asymmetric binaural interference effects stem from properties of the binaural system per se, or instead reflect ''floor effects'' resulting from the overall greater sensitivity to ITDs conveyed by low-frequency conventional stimuli, as compared to their conventional high-frequency counterparts.

IV. SUMMARY AND CONCLUSIONS

Threshold-ITDs were measured with a variety of conventional and transposed ''targets'' centered at 4 kHz. The targets were presented either in the presence or absence of a simultaneously gated diotic noise centered at 500 Hz, the interferer. As expected, the presence of the low-frequency interferer resulted in substantially elevated threshold-ITDs

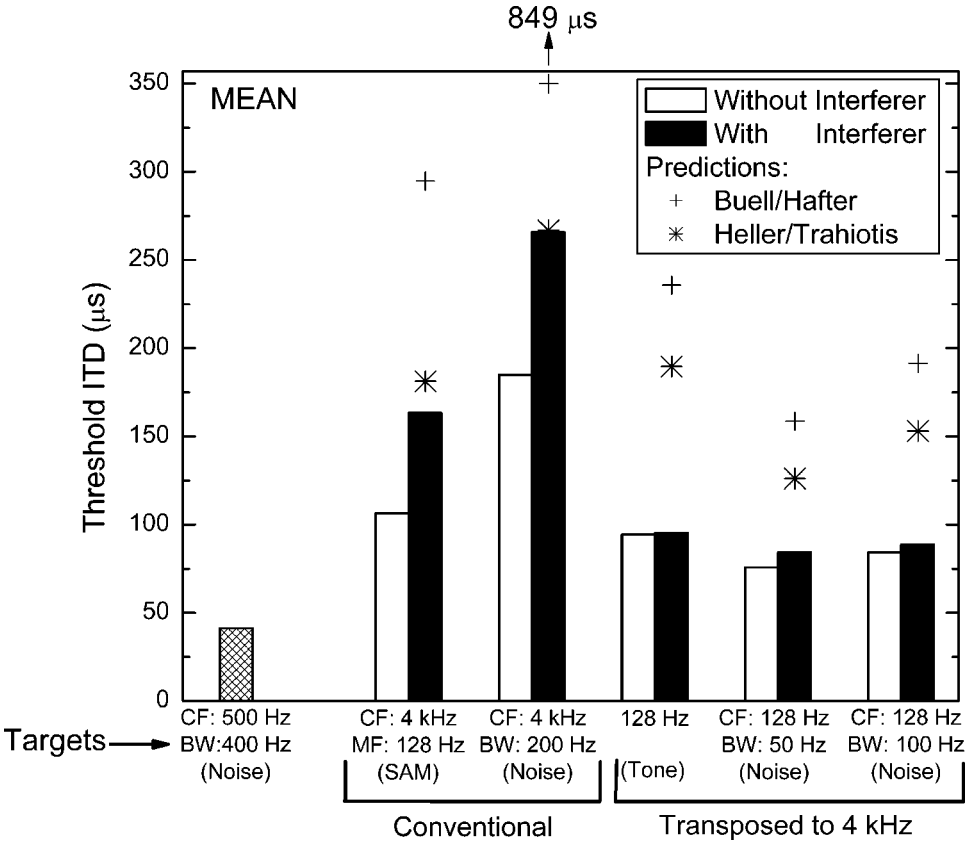

FIG. 3. Data replotted from Fig. 2 accompanied by predictions of threshold-ITD for targets in the presence of the interferer. Crosses represent predictions obtained with the Buell and Hafter (1991) model; asterisks represent predictions obtained with the Heller and Trahiotis (1996) model.

for the conventional high-frequency stimuli. In contrast, these interference effects were either greatly attenuated or absent for ITDs conveyed by the high-frequency transposed targets. The binaural interference effects observed with the conventional high-frequency stimuli were well accounted for, quantitatively, by the model described by Heller and Trahiotis (1996). The lack of binaural interference effects observed with the high-frequency transposed stimuli was not predicted by that model. It is suggested that transposed stimuli may be one of a class of stimuli that do not foster an obligatory combination of binaural information between low- and high-frequency regions. If this were the case, then one could still consider models of binaural interference, such as the one described in Heller and Trahiotis to be valid descriptors of binaural processing under those conditions that do foster such an obligatory combination.

ACKNOWLEDGMENTS

The authors thank Dr. Thomas N. Buell, Dr. Richard L. Freyman, and Dr. Armin Kohlrausch. Their insightful comments served to strengthen the presentation. This research was supported by research grants NIH DC-04147, DC-04073, and DC-00234 from the National Institute on Deafness and Other Communication Disorders, National Institutes of Health.

[1]Stimulus levels produced according to the calibration supplied with the Etymotic ER-2 earphones sounded less loud than stimuli presented at nominally the same level via TDH-39 earphones, according to their calibration. Dr. Mead Killion, of Etymotic Research, validated our listening experience and agreed with us that the two respective methods of calibration would be expected to produce levels of stimulation differing by about 10 dB. We chose to ''calibrate'' the outputs of the Etymotic earphones to the nominal levels produced by the TDH-39s so that listeners in this study would receive levels of stimulation directly comparable to those utilized by us and others in prior psychophysical experiments employing TDH-39s. We verified that the levels from the Etymotic earphones were appropriate by presenting a high-frequency, stimulus to one ear via an Etymotic ER-2 earphone and simultaneously to the other ear via a TDH-39 earphone. We then adjusted the relative levels between the two ears to produce a ''centered'' intracranial image, as is produced by diotic stimuli in normal-hearing listeners. In order to produce a centered image, it was necessary to impose a 10-dB larger voltage on the Etymotic ER-2 than would be expected on the basis of its calibration. Incidentally, the same type of ear-to-ear comparison allows one to compare and to cross-calibrate any earphone to any other one, notwithstanding local variations in the frequency response of the earphones.

[2]This was determined to be justified on two separate grounds. First, as the data in Fig. 2 show, threshold-ITDs obtained with those two targets were virtually identical within interference and no-interference conditions. Second, two additional, separate, analyses of variance were performed while including only the data obtained with the 50-Hz-wide noise or only the 100-Hz-wide noise (rather than their mean). All three sets of analyses of variance resulted in the same factors and interactions either reaching or failing to reach statistical significance. Therefore, our averaging of the data across those two targets neither distorted nor compromised the meaning (and meaningfulness) of the statistical analysis.

Bernstein, L. R. (**1991**). ''Spectral interference in a binaural detection task,'' J. Acoust. Soc. Am. **89**, 1306–1313.

Bernstein, L. R., and Trahiotis, C. (**1985**). ''Lateralization of low-frequency, complex waveforms: The use of envelope-based temporal disparities,'' J. Acoust. Soc. Am. **77**, 1868–1880.

Bernstein, L. R., and Trahiotis, C. (**1992**). ''Spectral interference in a binaural detection task: Effects of temporal fringe and masking bandwidth,'' J. Acoust. Soc. Am. **94**, 735–742.

Bernstein, L. R., and Trahiotis, C. (**1994**). ''Detection of interaural delay in high-frequency SAM tones, two-tone complexes, and bands of noise,'' J. Acoust. Soc. Am. **95**, 3561–3567.

Bernstein, L. R., and Trahiotis, C. (**1995**). ''Binaural interference effects measured with masking-level difference and with ITD- and IID-discrimination paradigms,'' J. Acoust. Soc. Am. **98**, 155–163.

Bernstein, L. R., and Trahiotis, C. (**2001**). ''Using transposed stimuli to reveal similar underlying sensitivity to interaural timing information at high and low frequencies: Support for the Colburn-Esquissaud hypothesis,'' in *Physiological and Psychophysical Bases of Auditory Function: Proceedings of the 12th International Symposium on Hearing*, edited by D. J. Breebaart, A. J. M. Houtsma, A. Kohlrausch, V. F. Prijs, and R. Schoonhoven (Shaker Publishing, The Netherlands), pp. 137–144.

Bernstein, L. R., and Trahiotis, C. (**2002**). ''Enhancing sensitivity to interaural delays at high frequencies by using 'transposed stimuli','' J. Acoust. Soc. Am. **112**, 1026–1036.

Bernstein, L. R., and Trahiotis, C. (**2003**). ''Enhancing interaural-delay-based extents of laterality at high frequencies by using 'transposed stimuli','' J. Acoust. Soc. Am. **113**, 3335–3347.

Buell, T. N., and Hafter, E. R. (**1991**). ''Combination of binaural information across frequency bands,'' J. Acoust. Soc. Am. **90**, 1894–1900.

Buell, T. N., and Trahiotis, C. (**1993**). ''Interaural temporal discrimination using two sinusoidally amplitude-modulated, high-frequency tones: Conditions of summation and interference,'' J. Acoust. Soc. Am. **93**, 480–487.

Davis, J. B. (**1985**). ''Remote frequency masking: Differential effects in binaural versus monaural detection,'' Thesis, Boston University, Boston, MA.

Dye, Jr., R. H. (**1990**). ''The combination of interaural information across frequencies: Lateralization on the basis of interaural delay,'' J. Acoust. Soc. Am. **88**, 2159–2170.

Hays, W. L. (**1973**). *Statistics for the Social Sciences* (Holt, Rinehart, and Winston, New York).

Heller, L. M., and Trahiotis, C. (**1995**). ''Interference in detection of interaural delay in a SAM tone produced by a second, spectrally remote SAM tone,'' J. Acoust. Soc. Am. **97**, 1808–1816.

Heller, L. M., and Trahiotis, C. (**1996**). ''Extents of laterality and binaural interference effects,'' J. Acoust. Soc. Am. **99**, 3632–3637.

Henning, G. B. (**1974**). ''Detectability of interaural delay in high-frequency complex waveforms,'' J. Acoust. Soc. Am. **55**, 84–90.

Keppel, G. (**1973**). *Design and Analysis: A Researchers Handbook* (Prentice-Hall, Englewood Cliffs, NJ).

Levitt, H. (**1971**). ''Transformed up-down methods in psychoacoustics,'' J. Acoust. Soc. Am. **49**, 467–477.

McFadden, D., and Pasanen, E. G. (**1976**). ''Lateralization at high frequencies based on interaural time differences,'' J. Acoust. Soc. Am. **59**, 634–639.

Moore, B. C. J. (**1997**). ''Frequency analysis and pitch perception,'' *Handbook of Acoustics*, edited by Malcome Crocker (Wiley, New York), Vol. III, pp. 1447–1460.

Nuetzel, J. M., and Hafter, E. R. (**1981**). ''Discrimination of interaural delays in complex waveforms: Spectral effects,'' J. Acoust. Soc. Am. **69**, 1112–1118.

Rice, S. O. (**1954**). ''Mathematical analysis of random noise,'' in *Selected Papers on Noise and Stochastic Processes*, edited by N. Wax (Dover, New York), pp. 133–294.

Siegel, R. A., and Colburn, H. S. (**1989**). ''Binaural processing of noisy stimuli: Internal/external noise ratios for diotic and dichotic stimuli,'' J. Acoust. Soc. Am. **86**, 2122–2128.

Stellmack, M. A., and Dye, R. H. (**1993**). ''The combination of interaural information across frequencies: The effects of number and spacing of components, onset asynchrony, and harmonicity,'' J. Acoust. Soc. Am. **93**, 2933–2947.

Trahiotis, C., and Bernstein, L. R. (**1990**). ''Detectability of interaural delays over select spectral regions: Effects of flanking noise,'' J. Acoust. Soc. Am. **87**, 810–813.

van de Par, S., and Kohlrausch, A. (**1997**). ''A new approach to comparing binaural masking level differences at low and high frequencies,'' J. Acoust. Soc. Am. **101**, 1671–1680.

Woods, W. S., and Colburn, H. S. (**1992**). ''Test of a model of auditory object formation using intensity and ITD discrimination,'' J. Acoust. Soc. Am. **91**, 2894–2902.

Zurek, P. M. (**1985**). ''Spectral dominance in sensitivity to interaural delay for broadband stimuli,'' J. Acoust. Soc. Am. Suppl. 1 **78**, S18.

Cats exhibit the Franssen Effect illusion

Micheal L. Dent,[a] Daniel J. Tollin, and Tom C. T. Yin
Department of Physiology, University of Wisconsin, Madison, Wisconsin 53706

(Received 11 June 2004; revised 26 August 2004; accepted 1 September 2004)

The Franssen Effect (FE) is a striking auditory illusion previously demonstrated only in humans. To elicit the FE, subjects are presented with two spatially-separated sounds; one a transient tone with an abrupt onset and immediate ramped offset and the other a sustained tone of the same frequency with a ramped onset which remains on for several hundred ms. The FE illusion occurs when listeners localize the tones at the location of the transient signal, even though that sound has ended and the sustained one is still present. The FE illusion occurs most readily in reverberant environments and with pure tones of ~1–2.5 kHz in humans, conditions where sound localization is difficult in humans. Here, we demonstrate this illusion in domestic cats using, for the first time, localization procedures. Previous studies in humans employed discrimination procedures, making it difficult to link the FE to sound localization mechanisms. The frequencies for eliciting the FE in cats were higher than in humans, corresponding to frequencies where cats have difficulty localizing pure tones. These findings strengthen the hypothesis that difficulty in accurately localizing sounds is the basis for the FE. © *2004 Acoustical Society of America.* [DOI: 10.1121/1.1810136]

PACS numbers: 43.66.Qp, 43.66.Gf, 43.80.Lb [AK] Pages: 3070–3074

I. INTRODUCTION

Experiments on the localization of acoustic stimuli have revealed a number of important features of sounds that increase localization accuracy, including broad bandwidths (Butler, 1986), rapid onsets (Rakerd and Hartmann, 1986), and anechoic environments (Hartmann, 1983). The Franssen Effect (FE) is an auditory illusion that emerges when listening conditions are less than ideal, and may be related to the well-studied precedence effect (Wallach *et al.*, 1949). The FE can be demonstrated by turning on a transient tone to one speaker with a sudden onset and slowly decaying offset while simultaneously turning on a second long-duration tone with a slowly rising onset to another speaker at a different location. In the FE, listeners are unable to discriminate these paired tones, located on either side of the listener's midline, from a single sustained tone with an abrupt onset presented from the location where the transient signal was presented (Franssen, 1962). The subjects apparently perceive the Franssen stimuli as only one fused stimulus coming from the location of the transient tone even though that tone is no longer physically present. The illusion occurs only for narrowband sounds (Yost *et al.*, 1997) in reverberant environments (Hartmann and Rakerd, 1989), but for sounds lasting indefinitely (Berkley, 1983).

The FE is thought to occur because listeners have difficulty localizing tones with no transient onset information (i.e., the sustained tone) in reverberant rooms, and because the signals are within a frequency range (~1.5–3.0 kHz) where neither the interaural time or level difference cue is adequate for accurate localization (Hartmann and Rakerd, 1989; Stevens and Newman, 1936; Yost *et al.*, 1997). Listeners can localize the transient with its sudden onset, while localization of the later steady-state sound poses more difficulty, especially in reverberant environments. In one hypothesis for the FE, when reflections are present they tend to corrupt localization cues from the sustained tone, resulting in cues that are ''implausible'' because they do not correspond to the frequency-specific interaural cues experienced naturally (Hartmann and Rakerd, 1989). Accurate localization is nearly impossible in this condition, particularly for frequencies where the cues are not reliable. Listeners apparently resolve this implausible situation by continuing to locate the sustained tone at the location of the transient.

The FE has never been demonstrated in any nonhuman animal, and human experiments have employed discrimination procedures rather than sound localization tasks. Hence, one of the hypothesized bases for the FE (negative relationship between absolute sound localization accuracy and the FE) has not been tested directly. The correlation between the frequency dependency of the FE and localization would be strengthened if similar effects were found in another species whose localization abilities differ from humans. We therefore tested cats, whose localization deficit occurs at a higher frequency than in humans. As in humans, localization in cats is good at low and high frequencies, but gradually worsens to the poorest performance at around 4 kHz instead of 1.5 kHz (Casseday and Neff, 1973; Martin and Webster, 1987; Populin and Yin, 1998). If the frequencies where the FE is effective are due to the inability to localize sounds, then the frequencies where the FE illusion succeeds in cats should be found at higher frequencies than in humans.

II. METHODS

A. Subjects and materials

Three adult female cats were outfitted with head holders, eye coils, and coil connectors (Populin and Yin, 1998). All

[a]Electronic mail: mdent@buffalo.edu. Current address: Department of Psychology, 361 Park Hall, University at Buffalo-SUNY, Buffalo, New York 14260.

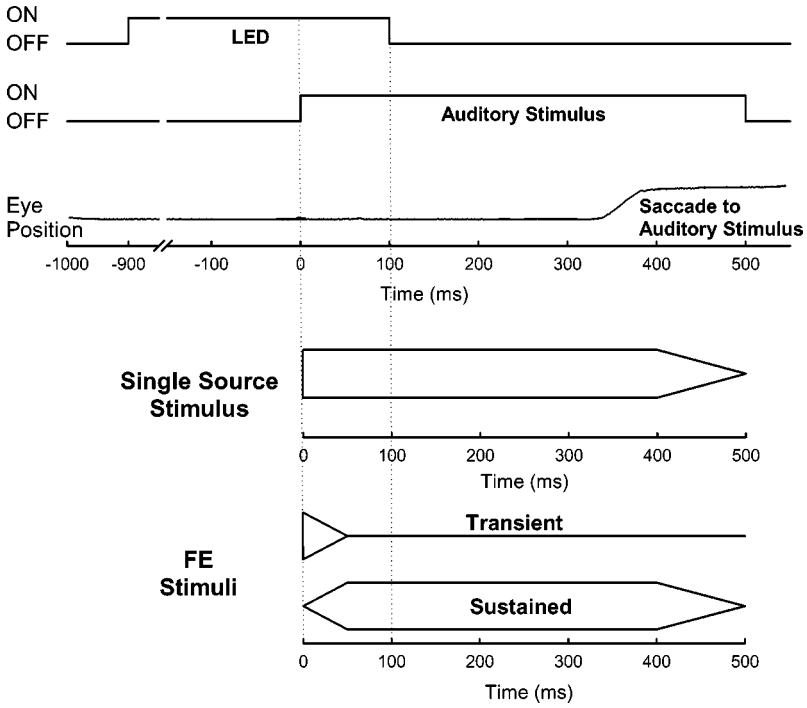

FIG. 1. Schematics of FE and SS stimulus conditions. Cats were required to fixate on an LED until its offset, after which a gaze shift was required to either a SS stimulus presented to one location ($\pm 30°$) or the paired Franssen stimuli presented to both locations. In the Franssen condition, a transient tone burst with an immediate offset ramp is presented to one side while the same tone is presented simultaneously to the other side with a slow onset ramp (50 ms) and long sustained duration. The stimuli began 100 ms before the fixation LED was terminated so that the cue to make a saccade came only after the stimuli had been on for 100 ms and the transient stimulus was already OFF for 50 ms.

procedures were approved by the University of Wisconsin Animal Care and Use Committee and complied with NIH guidelines for animal use.

During experimental sessions, cats were placed in the center of a dark sound-attenuating chamber whose walls and major pieces of equipment were covered with sound-absorbent foam (10.2 cm Sonex; Illbruck Co.). The cats were placed in a restraint bag with their heads free and faced a bank of 15 frequency-response matched loudspeakers (Morel Acoustics, Model MDT20). For this experiment, only two of the speakers at $\pm 30°$ azimuth ($0°$ elevation) were used to test for the FE though the other speakers were used for training and standard trials. The speakers were arranged horizontally and vertically along arcs 90 cm from the center of the head ranging from $\pm 80°$. Speakers were hidden from view by a black translucent cloth. A 2.0-mm-diameter red LED was suspended over the center of each speaker. The gaze position (i.e., the position of the eyes in space resulting from combined head movement and eye saccades) was recorded using the scleral search coil technique.

Cats were tested under these echo-reduced conditions as well as under echoic conditions where the walls, ceilings, and floors of the testing booth were lined with heavy-duty plastic panels. The inner dimensions of the acoustic chamber were $2.2 \times 2.5 \times 2.5$ m. We used the method described by Yost *et al.* (1997) to demonstrate that these two conditions differed in their reverberation characteristics. For each room condition, the response to 50 presentations of a 100-μs click was obtained, averaged, and then bandpass filtered between 500–12000 Hz. The microphone was placed where the center of the cat's head was during the experiments and the speaker was placed at $(0°,0°)$. The rms level of the averaged response for the first 5 ms of the recording, which contains the direct signal from the source (the acoustic delay from the speaker to the microphone was not included in the 5-ms window) was compared to the rms level of the recording for the next 25 ms, which contains the acoustic reflections. Following Yost *et al.* (1997), we took the $20 \log_{10}$ of the ratio of these two levels to determine how much lower the reflections were compared to the initial click. For the echo-reduced chamber, the last 25 ms was down 24.9 dB from the initial 5 ms, and for the echoic condition the ratio was lowered by only 18.4 dB. Hence there was a 6.5 dB difference in room conditions, which was smaller than the 13.2 dB difference obtained in the Yost *et al.* (1997) study. The differences between our echoic and echo-reduced rooms were also evident in the magnitude spectrum of the averaged click recordings. The additional reflections in our echoic room would be expected to introduce prominent peaks and valleys into the spectrum due to comb-filtering effects. To quantify this, we computed the standard deviation of the spectrum (from 500–12000 Hz), which was 7.8 dB for the echo-reduced room and increased to 10.3 dB for the echoic room. In summary, our treatment of the echo-reduced room with plastic panels changed the characteristics of the listening condition at the position of the cat's head, albeit not as much as that described by Yost *et al.* (1997).

B. Stimuli and procedures

On each day of testing, the cats were presented with a wide range of different auditory and visual stimuli from all possible locations. Schematics of the stimuli of interest for these experiments are depicted in Fig. 1. The stimuli were either broadband noises or pure tones from 250 to 9000 Hz and were presented from either $+30°$ or $-30°$ on the horizontal plane. The single source (SS) stimuli had a total duration of 500 ms, which was comprised of an immediate onset, a 400-ms sustained portion, and a 100-ms linear ramp offset. The FE stimuli consisted of two signals presented simultaneously, one to the $-30°$ and one to the $+30°$ locations, or *vice versa*. The transient signal had an immediate

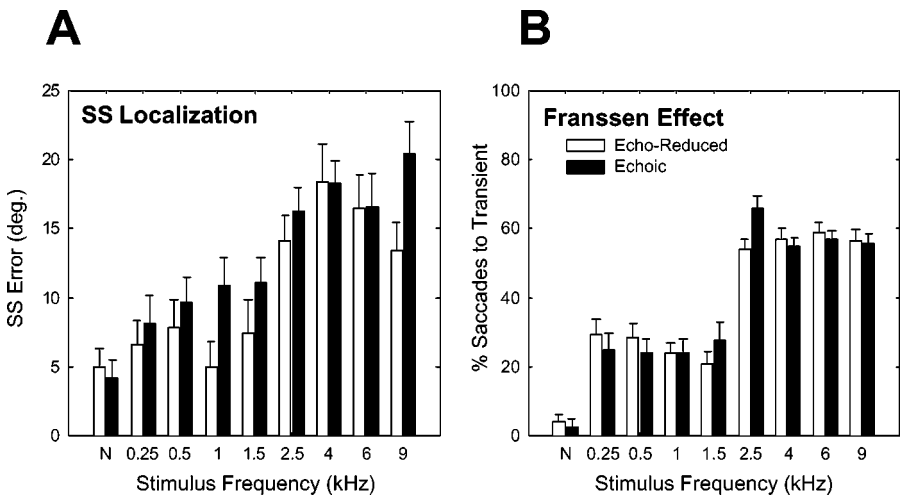

FIG. 2. Mean horizontal error in localizing SS stimuli as a function of stimulus frequency (a) and mean percent saccades to transient stimulus location during Franssen stimuli (b) as a function of stimulus frequency for three cats. For both graphs, echo-reduced conditions are the white bars and echoic conditions are the black bars. Data are averaged across the left and right stimulus conditions. Error bars represent between-subject standard errors.

onset, followed by a 50-ms linear ramp offset, for a total duration of 50 ms. The sustained signal had a 50-ms linear ramp onset, a 350-ms sustained portion, and a 100-ms linear ramp offset, for a total duration of 500 ms. The stimuli were presented such that the maximum amplitudes of their envelopes were the same as the maximum amplitude of the corresponding sustained stimulus that produced a level of 60 dB SPL. The stimuli were roved by ± 10 dB across trials.

The cats were trained using operant conditioning to indicate via gaze shifts the apparent two-dimensional location of various auditory and visual targets. During testing, FE trials were interspersed within experimental sessions of standard trials at a 10–15% rate. A delayed saccade paradigm was used to measure responses to these stimuli (as well as for the SS stimuli). Here, the cats fixate (within $\pm 4°$) a LED at the midline (0°,0°) for a variable time period ($\sim$1000 ms) and then make gaze shifts to the sound source upon termination of the LED. In these trials, the acoustic stimuli began 100 ms before termination of the LED, but cats were required to maintain fixation until the LED was gated off. The delayed saccade task was purposely used so that, for the FE stimuli, the transient signal had been terminated for 50 ms while the sustained signal remained on when the trigger (LED offset) was given to make the saccade. When the FE is experienced, the cats will look towards the location of the transient and not towards the location of the ongoing sustained sound. If the FE is not operating, the cats will look towards the sustained sound's location because at the time of LED offset it is the only sound on.

Responses to the SS stimuli were required to be within an electronic acceptance window centered on the target (± 8 to 15°) for $\sim$750 ms for a food reward of a puree of cat food. The reward contingency for the FE stimuli differed from our usual criteria; since these stimuli are illusory and have no ''correct'' response, the cats were rewarded on all trials in which they attempted this task.

C. Data analysis

The dependent variable in these experiments was the final two-dimensional gaze position after the gaze shift to the apparent location of the acoustic target. We used a velocity criterion (Populin and Yin, 1998) to determine when the eye movements began and ended by determining the time when the magnitude of the velocity of the eye movement exceeded 2 SD of the mean velocity computed during the fixation of the initial LED. All trials were used in the analysis of the data even if the cat had not been rewarded, ensuring that the accuracy of the responses reported here was not confounded by the size of the acceptance window. Each data point for each cat in the SS conditions was based on at least 40 trials while data points in the FE conditions were based on at least 20 trials. Horizontal errors in localizing the stimuli were reported as a function of stimulus frequency. Errors were computed separately for each trial as the difference in degrees between the actual stimulus source and the final eye position of the cat. For the FE stimuli, the trials in which the cats made gaze shifts greater than 5° away from the midline towards the side of the transient signal location were considered to exhibit the FE.

III. RESULTS

Three domestic cats were trained on a delayed saccade task using operant conditioning procedures with a food reward to make gaze shifts to either a stimulus presented from a single source location (SS) or from pairs of locations (FE), schematics of which are shown in Fig. 1. For the FE trials, the fixation LED was on during the transient signal and remained on for at least 50 ms after it was turned off. When the LED turned off (the signal to make the gaze shift to the target), the sustained signal continued. The mean saccade latency was 230 ms (S.D.$=$97 ms) for the FE stimuli so that by the time of the gaze shift, the transient signal had been off for 280 ms, on average. In this experiment, a gaze shift to the transient signal location during presentation of the FE stimuli is indicative that the FE was elicited. That is, the cats were looking towards an illusory signal location after that signal had been turned off for almost 300 ms despite the presence of the sustained signal at the other speaker.

Mean results from three cats are shown in Fig. 2. Errors for localizing the SS stimuli (A) were low (5–10°) for broadband noises and pure tones from 0.25 to 1.5 kHz. For tone frequencies of 2.5 to 9 kHz errors were much higher (15–20°). These results are similar to previous studies on the localization of pure tones by cats (Casseday and Neff,

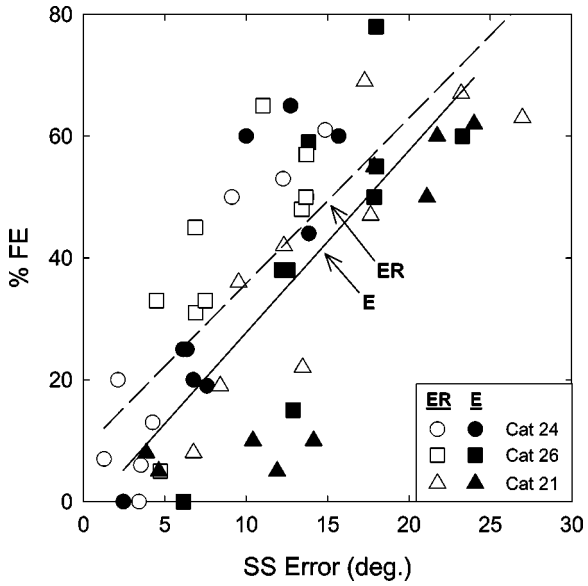

FIG. 3. Percent of trials where the FE is elicited as a function of error in localizing SS stimuli across all frequencies tested. Data are shown separately for each cat (symbol type) and room condition (E=echoic, black symbols; ER=echo-reduced, white symbols). Mean regression lines are also shown for all three cats in the ER (dashed line) and E conditions (solid line).

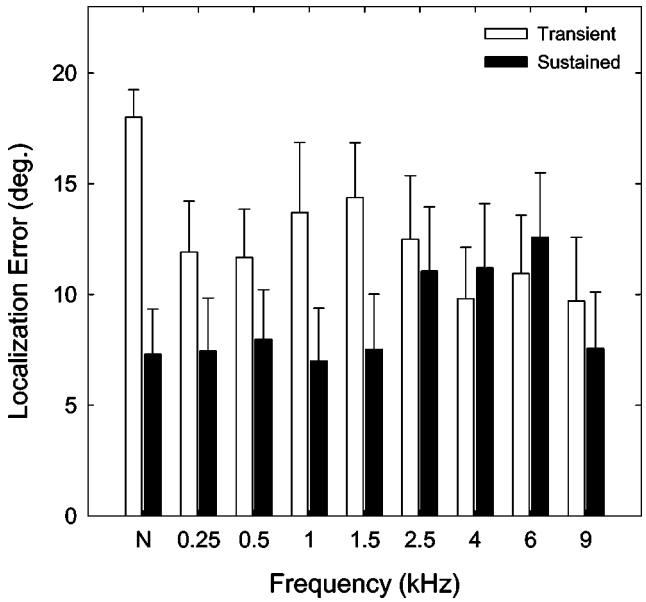

FIG. 4. The mean horizontal error in localizing the transient (white bars) and sustained (black bars) FE stimuli as a function of stimulus frequency for three cats. Data are averaged across the left and right stimulus conditions and across the echo-reduced and echoic room conditions. Error bars represent between-subject standard errors.

1973; Martin and Webster, 1987; Populin and Yin, 1998). In Fig. 2(b), the incidence of the FE illusion is depicted as the percent of responses towards the transients. When the stimuli were broadband noises, the cats rarely ($<5\%$ of all trials) made saccades to the transient, choosing to almost exclusively look towards the sustained sound. When the stimuli were pure tones ranging from 0.25 to 1.5 kHz, the cats looked at the transient on a higher proportion ($\sim 25\%$) of trials, and in the remainder of the trials looked towards the sustained sound. At higher frequencies, the cats very often ($>50\%$) looked towards the transient signal location rather than to the sustained sound. Both the localization of SS stimuli and the occurrence of the FE illusion were equally prevalent in the echo-reduced and echoic conditions. These results suggest that for pure tones, especially at higher frequencies, the cats are experiencing a phantom sound located at the transient signal's location even though that sound had been extinguished for some time, similar to the FE illusion found in humans.

To test the hypothesis that the FE is experienced most readily for stimuli that are difficult to localize on their own, Fig. 3 shows the percentage of trials where the FE was elicited against the mean error in localizing SS stimuli across all frequencies. Supporting this hypothesis, for all cat correlations [r-values ranged from $+0.76$ to $+0.93$ across cats, mean echo-reduced (ER) $r=0.79$, mean echoic (E) $r=0.75$] and slopes (mean ER=2.72; mean E=2.99) were high. Thus, the correlation between sound localization difficulty and the incidence of the FE illusion is high for cats, in agreement with the data from humans (Yost *et al.*, 1997). Furthermore, consistent with expectations, the FE in cats was not elicited at the same frequencies as in humans, but rather was more pronounced at higher frequencies where SS localization is difficult for cats.

Since we used localization procedures, we also calculated mean errors for localizing FE stimuli when the cats indicated the transient or sustained FE stimuli (Fig. 4). Localization errors for the transients were high for broadband noise and slightly higher for low-frequency pure tones than for high-frequency tones. Errors were fairly constant for the sustained signals across all frequencies, increasing slightly at higher frequencies, mirroring the same trend for SS trials (Fig. 2). Thus, at the lowest frequencies where the FE is operating on only a small percentage of the trials, the illusion is not only not as prevalent, but it is also not as robust since the cats are not looking accurately at the transient's location.

IV. DISCUSSION

These experiments demonstrate, for the first time, that a nonhuman animal experiences the auditory Franssen Effect illusion. Although there is always some uncertainty in determining whether an animal is experiencing an illusion such as the FE in the same way a human does, our methodology of first training cats to look to the apparent locations of simple stimuli that can be accurately localized (e.g., broadband noise) for a food reward and then interspersing, on a small percentage of trials, stimuli expected to elicit the illusion (and for which we do not define a ''correct'' response) is one way to determine objectively how cats perceive complex illusory stimuli. We have also used this technique successfully to demonstrate that cats experience the precedence effect (Populin and Yin, 1998; Tollin and Yin, 2003).

In our experiments, cats localize FE stimuli towards the location of the transient, ignoring the much longer steady-state sound, predominantly at high frequencies. The fact that this happens at the high frequencies where cats have trouble localizing single source stimuli and not at low frequencies or with broadband noise stimuli, which cats localize more accurately, supports the hypothesis that cats experience this

auditory illusion. An alternative explanation for the findings, that the cats simply look towards the first stimulus (i.e., the transient), is not supported by our data since there were many stimulus conditions where the cats almost never looked towards the transient (e.g., broadband noise).

Although our localization methodology differed significantly from the discrimination methods used in previous studies of the FE in humans, the correlations between poor sound localization ability for SS tones and the incidence of the FE were quite similar across species. There were differences, however, in the prevalence of the FE between cats and humans. In Yost *et al.* (1997), when humans were asked to discriminate the paired FE signals from the SS signal at the transient's location, the FE was evoked on ~2% of trials for broadband noises, similar to the cats. However, the FE reached a maximum of only ~35% of trials for 1.5 kHz tones. Our cats showed a more pervasive FE, indicating the auditory image at the transient's location in 44–78% of all trials for all frequencies above 2.5 kHz. This difference is likely seen because the cats were actively localizing the sounds while the human observers only had to discriminate a difference between SS and FE stimuli, a difference which need not be based on apparent location. Until similar localization experiments are completed on humans, a direct comparison of the prevalence of the FE in cats and humans cannot be made.

Another difference between our results and those from humans was that we found little dependence on room conditions. The cats exhibited errors in localizing SS stimuli and also showed the FE equally under echo-reduced and echoic room conditions (see regression lines in Fig. 3). This difference might be due to either excessive acoustic reflections from the equipment necessary to conduct these experiments under our echo-reduced conditions, or from the less-reflective echoic conditions presented to our cats compared to the humans. Our acoustic measurements of the testing chamber under echoic and echo-reduced conditions suggest the latter explanation, but since the previous experiments on the FE illusion in humans used discrimination rather than localization procedures, we do not know whether the higher incidence and independence of the acoustic environment of the FE in cats are due to species differences or differences in methodology.

The FE is thought to be related to the precedence effect (PE), another auditory illusion where the initial acoustic stimulus location dominates over any later occurring stimulus locations (Wallach *et al.*, 1949). Although the PE illusion has been demonstrated in a number of animal species (Dent and Dooling, 2003; Keller and Takahashi, 1996; Kelly, 1974; Tollin and Yin, 2003), this is the first demonstration of the Franssen illusion in nonhumans and the first to show it using a localization, rather than a discrimination, task. Mechanisms for the PE, which occur for time periods $<\sim 100$ ms, are likely to be different from those involved in this illusion because of the long-lasting nature of the suppression of the directional information from the sustained stimulus, which has been shown to last indefinitely in humans (Berkley, 1983). Now that the illusion has been demonstrated in cats, we can seek its underlying neural correlates.

ACKNOWLEDGMENTS

We thank Elizabeth McClaine and Janet Ruhland for experimental assistance. This work was supported by NIDCD Grants No. DC006124 to MLD and No. DC00116 and No. DC02840.

Berkley, D. A. (**1983**). ''Room acoustics and listening,'' J. Acoust. Soc. Am. **73**, S17.

Butler, R. A. (**1986**). ''The bandwidth effect on monaural and binaural localization,'' Hear. Res. **21**, 67–73.

Casseday, J. H., and Neff, W. D. (**1973**). ''Localization of pure tones,'' J. Acoust. Soc. Am. **54**, 365–372.

Dent, M. L., and Dooling, R. J. (**2003**). ''Investigations of the precedence effect in budgerigars: effects of stimulus type, intensity, duration, and location,'' J. Acoust. Soc. Am. **113**, 2146–2158.

Franssen, N. V. (**1962**). *Stereophony* (Phillips Technical Library, Einhoven, The Netherlands); English translation (1964).

Hartmann, W. M. (**1983**). ''Localization of sound in rooms,'' J. Acoust. Soc. Am. **74**, 1380–1391.

Hartmann, W. M., and Rakerd, B. (**1989**). ''Localization of sound in rooms IV. The Franssen effect,'' J. Acoust. Soc. Am. **86**, 1366–1373.

Keller, C. H., and Takahashi, T. T. (**1996**). ''Responses to simulated echoes by neurons in the barn owl's auditory space map,'' J. Comp. Physiol., A **178**, 499–512.

Kelly, J. B. (**1974**). ''Localization of paired sound sources in the rat: small time differences,'' J. Acoust. Soc. Am. **55**, 1277–1284.

Martin, R. L., and Webster, W. R. (**1987**). ''The auditory spatial acuity of the domestic cat in the interaural horizontal and median vertical planes,'' Hear. Res. **30**, 239–252.

Populin, L. C., and Yin, T. C. T. (**1998**). ''Behavioral studies of sound localization in the cat,'' J. Neurosci. **18**, 2147–2160.

Rakerd, B., and Hartmann, W. M., (**1986**). ''Localization of sound in rooms, II: the effects of single reflecting surface,'' J. Acoust. Soc. Am. **80**, 1695–1706.

Stevens, S. S., and Newman, E. B. (**1936**). ''The localization of actual sources of sound,'' Am. J. Psychol. **48**, 297–306.

Tollin, D. J., and Yin, T. C. T. (**2003**). ''Psychophysical investigation of an auditory spatial illusion in cats: the precedence effect,'' J. Neurophysiol. **90**, 2149–2162.

Wallach, H., Newman, E. B., and Rosenzweig, M. R. (**1949**). ''The precedence effect in sound localization,'' Am. J. Psychol. **52**, 315–336.

Yost, W. A., Mapes-Riordan, D., and Guzman, S. J. (**1997**). ''The relationship between localization and the Franssen Effect,'' J. Acoust. Soc. Am. **101**, 2994–2997.

Source localization in complex listening situations: Selection of binaural cues based on interaural coherence

Christof Faller[a)]
Mobile Terminals Division, Agere Systems, Allentown, Pennsylvania

Juha Merimaa[b)]
Institut für Kommunikationsakustik, Ruhr-Universität Bochum, Germany

(Received 27 January 2004; revised 19 July 2004; accepted 19 July 2004)

In everyday complex listening situations, sound emanating from several different sources arrives at the ears of a listener both directly from the sources and as reflections from arbitrary directions. For localization of the active sources, the auditory system needs to determine the direction of each source, while ignoring the reflections and superposition effects of concurrently arriving sound. A modeling mechanism with these desired properties is proposed. Interaural time difference (ITD) and interaural level difference (ILD) cues are only considered at time instants when only the direct sound of a single source has non-negligible energy in the critical band and, thus, when the evoked ITD and ILD represent the direction of that source. It is shown how to identify such time instants as a function of the interaural coherence (IC). The source directions suggested by the selected ITD and ILD cues are shown to imply the results of a number of published psychophysical studies related to source localization in the presence of distracters, as well as in precedence effect conditions. [DOI: 10.1121/1.1791872]

PACS numbers: 43.66.Qp, 43.66.Pn, 43.66.Ba [AK] Pages: 3075–3089

I. INTRODUCTION

In most listening situations, the perceived directions of auditory events coincide with the directions of the corresponding physical sound sources. In everyday complex listening scenarios, sound from multiple sources, as well as reflections from the surfaces of the physical surroundings, arrive concurrently from different directions at the ears of a listener. The auditory system does not only need to be able to independently localize the concurrently active sources, but it also needs to be able to suppress the effect of the reflections. In this paper, a modeling mechanism is proposed to explain both of these features. Before describing this modeling mechanism in more detail, related psychophysical localization experiments and psychoacoustic models are reviewed.

Localization accuracy in the presence of concurrent sounds from different directions has been investigated by several authors. A detailed review is given by Blauert (1997). The effect of independent distracters on the localization of a target sound has been recently studied by Good and Gilkey (1996), Good *et al.* (1997), Lorenzi *et al.* (1999), Hawley *et al.* (1999), Drullman and Bronkhorst (2000), Langendijk *et al.* (2001), Braasch and Hartung (2002), and Braasch (2002). The results of these studies generally imply that the localization of the target is either not affected or only slightly degraded by introducing one or two simultaneous distracters at the same overall level as the target. When the number of distracters is increased or the target-to-distracter ratio (T/D) is reduced, the localization performance begins to degrade. However, for most configurations of a target and a single distracter in the frontal horizontal plane, the accuracy stays very good down to a target level only a few dB above the threshold of detection (Good and Gilkey 1996, Good *et al.* 1997, Lorenzi *et al.* 1999). An exception to these results is the outcome of the experiment of Braasch (2002), where two incoherent noises with exactly the same envelope were most of the time not individually localizable.

In order to understand the localization of a source in the presence of reflections from different directions, the precedence effect needs to be considered. Extensive reviews have been given by Zurek (1987), Blauert (1997), and Litovsky *et al.* (1999). The operation of the precedence effect manifests itself in a number of perceptual phenomena: fusion of subsequent sound events into a single perceived entity, suppression of directional discrimination of the later events, as well as localization dominance by the first event. The directional perception of a pair of stimuli with an interstimulus delay shorter than 1 ms is called summing localization. The weight of the lagging stimulus reduces with increasing delay up to approximately 1 ms, and for delays greater than that the leading sound dominates the localization judgment, although the lag might never be completely ignored. Echo threshold refers to the delay where the fusion breaks apart. Depending on stimulus properties and individual listeners, thresholds between 2–50 ms have been reported in the literature (Litovsky *et al.*, 1999).

Localization accuracy within rooms has been studied by Hartmann (1983), Rakerd and Hartmann (1985, 1986), and Hartmann and Rakerd (1989) (see also a review by Hartmann, 1997). Overall, in these experiments the localization performance was slightly degraded by the presence of reflections. Interestingly, using slow-onset sinusoidal tones and a single reflecting surface, Rakerd and Hartmann (1985) found

[a)]Current address: Guetrain 1, CH-8274 Tägerwilen, Switzerland; Electronic mail: cfaller@agere.com
[b)]Also at Laboratory of Acoustics and Audio Signal Processing, Helsinki University of Technology.

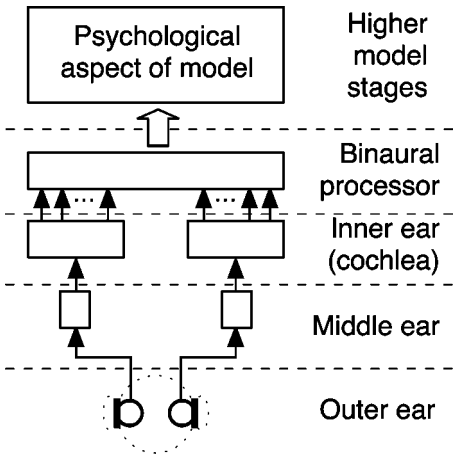

FIG. 1. A model of spatial hearing covering the physical, physiological, and psychological aspects of the auditory system.

that the precedence effect sometimes failed completely. In a follow-up study, the relative contribution of the direct sound and the steady state interaural cues to the localization judgment was found to depend on the onset rate of the tones (Rakerd and Hartmann, 1986). Nevertheless, absence of an attack transient did not prevent the correct localization of a broadband noise stimulus (Hartmann, 1983). Giguère and Abel (1993) reported similar findings for noise with the bandwidth reduced to one-third octave. Rise/decay time had little effect on localization performance except for the lowest center frequency (500 Hz), while increasing the reverberation time decreased the localization accuracy. Braasch *et al.* (2003) investigated the bandwidth dependence further, finding that the precedence effect started to fail when the bandwidth of noise centered at 500 Hz was reduced to 100 Hz.

The auditory system features a number of physical, physiological, and psychological processing stages for accomplishing the task of source direction discrimination and ultimately the formation of the auditory spatial image. The structure of a generic model for spatial hearing is illustrated in Fig. 1. There is little doubt about the first stages of the auditory system, i.e., the physical and physiological functioning of the outer, middle, and inner ear are known and understood to a high degree. However, already the stage of the binaural processor is less well known. Different models have used different approaches to explain various aspects of binaural perception. The majority of proposed localization models are based on an analysis of *interaural time difference* (ITD) cues using a coincidence structure (Jeffress, 1948), or a cross-correlation implementation that can be seen as a special case of the coincidence structure. Evidence for cross-correlation-like neural processing has also been found in physiological studies (Yin and Chan, 1990). However, such excitation-excitation (EE) type cells are but one kind of neural units potentially useful for obtaining binaural information (see, e.g., the introduction and references of Breebaart *et al.*, 2001). With current knowledge, the interaction between the binaural processor and higher level cognitive processes can only be addressed through indirect psychophysical evidence.

For a single source in free field, sound from only one direction arrives at the ears of a listener and thus causally determines the ITD and *interaural level difference* (ILD) cues (Gaik, 1993), which appear in the auditory system as a result of reflections, diffraction, and resonance effects caused by the head, torso, and the external ears of the listener. However, in complex listening situations, i.e., in the presence of several sound sources and/or room reflections, it often occurs that sound from several different directions concurrently reaches the position of the listener. Furthermore, the superposition of sound emanating from several directions results in instantaneous ITD and ILD cues that most of the time do not correspond to any of the source directions. Nevertheless, humans have a remarkable ability to resolve such complex composites of sound into separate localizable auditory events at directions corresponding to the sound sources.

Few binaural models have specifically considered localization in complex listening situations. To begin with, Blauert and Cobben (1978) investigated a model with the essential features of most current models, including a simulation of the auditory periphery and cross-correlation analysis. In a precedence effect experiment they concluded that the correct cross-correlation peaks were available but the model could not explain how to identify them. Later, Lindemann (1986a) extended the model with contralateral and temporal inhibition, combining the analysis of both ITD and ILD cues within a single structure that was shown to be able to simulate several precedence effect phenomena (Lindemann, 1986b). The model of Lindemann was further extended by Gaik (1993) to take into account naturally occurring combinations of ITD and ILD cues in free field. A different phenomenological model, using localization inhibition controlled by an onset detector, was proposed by Zurek (1987), and developed into a cross-correlation implementation by Martin (1997). Hartung and Trahiotis (2001) were able to simulate the precedence effect for pairs of clicks without any inhibition, just taking into account the properties of the peripheral hearing. However, this model was not able to predict the localization of continuous narrow-band noises in a comparison of several models by Braasch and Blauert (2003). The best results were achieved with a combined analysis of ITD cues with the model of Lindemann (1986a) and ILD cues using a modified excitation-inhibition (EI) model (Breebaart *et al.*, 2001) extended with temporal inhibition. For independent localization of concurrent sources with nonsimultaneous onsets, Braasch (2002) has proposed a cross-correlation difference model.

In this paper, we propose a single modeling mechanism to explain various aspects of source localization in complex listening situations. The basic approach is very straightforward: only ITD and ILD cues occurring at time instants when they represent the direction of one of the sources are selected, while other cues are ignored. It will be shown that the *interaural coherence* (IC) can be used as an indicator for these time instants. More specifically, by selecting ITD and ILD cues coinciding with IC cues larger than a certain threshold, one can in many cases obtain a subset of ITD and ILD cues similar to the corresponding cues of each source presented separately in free field. The proposed cue selection method is implemented in the framework of a model that considers a physically and physiologically motivated periph-

eral stage, whereas the remaining parts are analytically motivated. Fairly standard binaural analysis is used to calculate the instantaneous ITD, ILD, and IC cues. The presented simulation results reflect psychophysical data from a number of localization experiments cited earlier, involving independent distracters and precedence effect conditions.

The paper is organized as follows. The binaural model, including the proposed cue selection mechanism, is described in Sec. II. The simulation results are presented in Sec. III with a short discussion of each case related to similar psychophysical studies. Section IV includes a general discussion of the model and results, followed by conclusions in Sec. V.

II. MODEL DESCRIPTION

The model can be divided into three parts: auditory periphery, binaural processor, and higher model stages. In this section, each of the model stages is described in detail, followed by a discussion of the features of the model.

A. Auditory periphery

Transduction of sound from a source to the ears of a listener is realized by filtering the source signals either with head-related transfer functions (HRTFs) or with measured binaural room impulse responses (BRIRs). HRTF filtering simulates the direction dependent influence of the head and outer ears on the ear input signals. BRIRs additionally include the effect of room reflections in an enclosed space. In multisource scenarios, each source signal is first filtered with a pair of HRTFs or BRIRs corresponding to the simulated location of the source, and the resulting ear input signals are summed before the next processing stage.

The effect of the middle ear is typically described as a bandpass filter. However, since this paper is only considering simulations at single critical bands, the frequency weighting effect of the middle ear has been discarded in the model. The frequency analysis of the basilar membrane is simulated by passing the left and right ear signals through a gammatone filterbank (Patterson *et al.* 1995). Each resulting critical band signal is processed using a model of neural transduction as proposed by Bernstein *et al.* (1999). The envelopes of the signals are first compressed by raising them to the power of 0.23. The compressed signals are subjected to half-wave rectification followed by squaring and a fourth order low-pass filtering with a cutoff frequency of 425 Hz. The resulting nerve firing densities at the corresponding left and right ear critical bands are denoted x_1 and x_2. These parts of the model are implemented using the freely available Matlab toolboxes from Slaney (1998) and Akeroyd (2001).

Internal noise is introduced into the model in order to describe the limited accuracy of the auditory system. For this purpose independent Gaussian noise, filtered with the same gammatone filters as the considered critical band signals, is added to each critical band signal before applying the model of neural transduction. The noise is statistically independent for each critical band, as well as for the left and right ears. For the critical band centered at 2 kHz, a sound pressure level (SPL) of 9.4 dB has been chosen according to Breebaart *et al.* (2001) who fitted the level of the noise to describe detection performance near the threshold of hearing. For other critical bands the level is scaled according to the hearing threshold curves (ISO 389, 1975). For the 500 Hz band, an SPL of 14.2 dB is used.

B. Binaural processor

As mentioned in Sec. I, the present study does not make a specific physiological assumption about the binaural processor. The only assumption is that its output signals (e.g., binaural activity patterns) yield information which can be used by the upper stages of the auditory system for discriminating ITD, ILD, and IC. Given this assumption, the proposed model computes the ITD, ILD, and IC directly. Note that here ITD, ILD, and IC are defined with respect to critical band signals after applying the neural transduction.

The ITD and IC are estimated from the normalized cross-correlation function. Given x_1 and x_2 for a specific center frequency f_c, at the index of each sample n, a running normalized cross-correlation function is computed according to

$$\gamma(n,m)=\frac{a_{12}(n,m)}{\sqrt{a_{11}(n,m)a_{22}(n,m)}}, \tag{1}$$

where

$$\begin{aligned}
a_{12}(n,m)&=\alpha x_1(n-\max\{m,0\})x_2(n-\max\{-m,0\})\\
&\quad+(1-\alpha)a_{12}(n-1,m),\\
a_{11}(n,m)&=\alpha x_1(n-\max\{m,0\})x_1(n-\max\{m,0\})\\
&\quad+(1-\alpha)a_{11}(n-1,m),\\
a_{22}(n,m)&=\alpha x_2(n-\max\{-m,0\})x_2(n-\max\{-m,0\})\\
&\quad+(1-\alpha)a_{22}(n-1,m),
\end{aligned}$$

and $\alpha\in[0,1]$ determines the time constant of the exponentially decaying estimation window

$$T=\frac{1}{\alpha f_s}, \tag{2}$$

where f_s denotes the sampling frequency. $\gamma(n,m)$ is evaluated over time lags in the range of $[-1,1]$ ms, i.e., $m/f_s\in[-1,1]$ ms. The ITD (in samples) is estimated as the lag of the maximum of the normalized cross-correlation function,

$$\tau(n)=\arg\max_m \gamma(n,m). \tag{3}$$

Note that the time resolution of the computed ITD is limited by the sampling interval.

The normalization of the cross-correlation function is introduced in order to get an estimate of the IC, defined as the maximum value of the instantaneous normalized cross-correlation function,

$$c_{12}(n)=\max_m \gamma(n,m). \tag{4}$$

This estimate describes the coherence of the left and right ear input signals. In principle, it has a range of [0,1], where 1 occurs for perfectly coherent x_1 and x_2. However, due to the DC offset of the halfwave rectified signals, the values of c_{12}

are typically higher than 0 even for independent (nonzero) x_1 and x_2. Thus, the effective range of the interaural coherence c_{12} is compressed from [0,1] to [a,1] by the neural transduction. The compression is more pronounced (larger a) at high frequencies, where the low pass filtering of the half-wave rectified critical band signals yields signal envelopes with a higher DC offset than in the signal wave forms (Bernstein and Trahiotis, 1996).

The ILD is computed as

$$\Delta L(n) = 10 \log_{10}\left(\frac{L_2(n,\tau(n))}{L_1(n,\tau(n))}\right), \tag{5}$$

where

$$L_1(n,m) = \alpha x_1^2(n-\max\{m,0\}) + (1-\alpha)L_1(n-1,m),$$

$$L_2(n,m) = \alpha x_2^2(n-\max\{-m,0\}) + (1-\alpha)L_2(n-1,m).$$

Note that due to the envelope compression the resulting ILD estimates will be smaller than the level differences between the ear input signals. For coherent ear input signals with a constant level difference, the estimated ILD (in dB) will be 0.23 times that of the physical signals.

The sum of the signal power of x_1 and x_2 that contributes to the estimated ITD, ILD, and IC cues at time index n is

$$p(n) = L_1(n,\tau(n)) + L_2(n,\tau(n)). \tag{6}$$

Choosing the time constant T is a difficult task. Studies of binaural detection actually suggest that the auditory system integrates binaural data using a double-sided window with time constants of both sides in the order of 20–40 ms (e.g., Kollmeier and Gilkey, 1990). However, a double sided window with this large time constant will not be able to simulate the precedence effect, where the localization of a lead sound should not be influenced by a lagging sound after only a few milliseconds. The difference could be explained by assuming that the auditory system responsible for binaural detection further integrates the binaural data originally derived with a better time resolution. In this paper we have chosen to use a single-sided exponential time window with a time constant of 10 ms, in accordance with the time constant of the temporal inhibition of the model of Lindemann (1986a).

C. Higher model stages

A vast amount of information is available to the upper stages of the auditory system through the signals from the auditory periphery. The focus of this study lies only in the analysis of the three interchannel properties between left and right critical band signals that were defined in the preceding section: ITD, ILD, and IC. It is assumed that at each time instant n the information about the values of these three signal properties, $\{\Delta L(n), \tau(n), c_{12}(n)\}$, is available for further processing in the upper stages of the auditory system.

Consider the simple case of a single source in free field. Whenever there is sufficient signal power, the source direction determines the nearly constant ITD and ILD which appear between each left and right critical band signal with the same center frequency. The (average) ITDs and ILDs occurring in this scenario are denoted "free-field cues" in the following. The free-field cues of a source with an azimuthal angle ϕ are denoted τ_ϕ and ΔL_ϕ. It is assumed that this kind of a one source free-field scenario is the reference for the auditory system. That is, in order for the auditory system to perceive auditory events at the directions of the sources, it must obtain ITD and/or ILD cues similar to the free-field cues corresponding to each source that is being discriminated. The most straightforward way to achieve this is to select the ITD and ILD cues at time instants when they are similar to the free-field cues. In the following it is shown how this can be done with the help of the IC.

When several independent sources are concurrently active in free field, the resulting cue triplets $\{\Delta L(n), \tau(n), c_{12}(n)\}$ can be classified into two groups: (1) Cues arising at time instants when only one of the sources has power in that critical band. These cues are similar to the free-field cues [direction is represented in $\{\Delta L(n), \tau(n)\}$, and $c_{12}(n) \approx 1$]. (2) Cues arising when multiple sources have non-negligible power in a critical band. In such a case, the pair $\{\Delta L(n), \tau(n)\}$ does not represent the direction of any single source, unless the superposition of the source signals at the ears of the listener incidentally produces similar cues. Furthermore, when the two sources are assumed to be independent, the cues are fluctuating and $c_{12}(n) < 1$. These considerations motivate the following method for selecting ITD and ILD cues. Given the set of all cue pairs, $\{\Delta L(n), \tau(n)\}$, only the subset of pairs is considered which occurs simultaneously with an IC larger than a certain threshold, $c_{12}(n) > c_0$. This subset is denoted

$$\{\Delta L(n), \tau(n) | c_{12}(n) > c_0\}. \tag{7}$$

The same cue selection method is applicable for deriving the direction of a source while suppressing the directions of one or more reflections. When the "first wave front" arrives at the ears of a listener, the evoked ITD and ILD cues are similar to the free-field cues of the source, and $c_{12}(n) \approx 1$. As soon as the first reflection from a different direction arrives, the superposition of the source signal and the reflection results in cues that do not resemble the free-field cues of either the source or the reflection. At the same time IC reduces to $c_{12}(n) < 1$, since the direct sound and the reflection superimpose as two signal pairs with different ITD and ILD. Thus, IC can be used as an indicator for whether ITD and ILD cues are similar to free-field cues of sources or not, while ignoring cues related to reflections.

For a given c_0 there are several factors determining how frequently $c_{12}(n) > c_0$. In addition to the number, strengths, and directions of the sound sources and room reflections, $c_{12}(n)$ depends on the specific source signals and on the critical band being analyzed. In many cases, the larger the c_0 the more similar the selected cues are to the free-field cues. However, there is a strong motivation to choose c_0 as small as possible while still getting accurate enough ITD and/or ILD cues, because this will lead to the cues being selected more often, and consequently to a larger proportion of the ear input signals contributing to the localization.

It is assumed that the auditory system adapts c_0 for each specific listening situation, i.e., for each scenario with a con-

stant number of active sources at specific locations in a constant acoustical environment. Since the listening situations do not usually change very quickly, it is assumed that c_0 is adapted relatively slowly in time. In Sec. III B 1, it is also argued that such an adaptive process may be related to the buildup of the precedence effect. All simulations reported in this paper consider only one specific listening situation at a time. Therefore, for each simulation a single constant c_0 is used.

D. Discussion

The physiological feasibility of the cue selection depends on the human sensitivity to changes in interaural correlation. The topic has been investigated by Pollack and Trittipoe (1959a, 1959b), Gabriel and Colburn (1981), Grantham (1982), Koehnke *et al.* (1986), Jain *et al.* (1991), Culling *et al.* (2001), and Boehnke *et al.* (2002). These investigations agree in that the sensitivity is highest for changes from full correlation, whereas the estimates of the corresponding just noticeable differences (JNDs) have a very large variance. For narrow band noise stimuli centered at 500 Hz, the reported JNDs range from 0.0007 (Jain *et al.*, 1991, fringed condition) to 0.13 (Culling *et al.*, 2001) for different listeners and different stimulus conditions. The sensitivity has been generally found to be lower at higher frequencies. However, all the cited studies have measured sensitivity to correlation of the ear input wave forms instead of correlation computed after applying a model of neural transduction. As discussed in Sec. II B, the model of Bernstein *et al.* (1999) reduces the range of IC, indicating overall lower JNDs of IC as defined in this paper. Furthermore, the model has been specifically fitted to yield constant thresholds at different critical bands when applied to prediction of binaural detection based on changes in IC (Bernstein and Trahiotis, 1996). With these considerations it can be concluded that at least the JNDs reported by Gabriel and Colburn (1981), Koehnke *et al.* (1986), and Jain *et al.* (1991) are within the range of precision needed for the simulations in Sec. III.

The auditory system may not actually use a hard IC threshold for selecting or discarding binaural cues. Instead of pure selection, similar processing could be implemented as an IC based weighting of ITD and ILD cues with a slightly smoother transition. However, the simple selection criterion suffices to illustrate the potential of the proposed method, as will be shown in Sec. III. Interestingly, van de Par *et al.* (2001) have argued that the precision needed for normalization of the cross-correlation function is so high that it is unlikely that the auditory system is performing the normalization *per se*. Since normalized cross correlation, nevertheless, describes the perception of IC well, it will be utilized in this paper.

The cue selection can also be seen as a multiple looks approach for localization. Multiple looks have been previously proposed to explain monaural detection and discrimination performance with increasing signal duration (Viemeister and Wakefield, 1991). The idea is that the auditory system has a short term memory of ''looks'' at the signal, which can be accessed and processed selectively. In the case of localization, the looks would consist of momentary ITD, ILD, and IC cues. With an overview of a set of recent cues, ITDs and ILDs corresponding to high IC values could be adaptively selected.

III. SIMULATION RESULTS

As mentioned earlier, it is assumed that in order to perceive an auditory event at a certain direction, the auditory system needs to obtain cues similar to the free-field cues corresponding to a source at that direction. In the following, the proposed cue selection is applied to several stimuli that have been used in previously published psychophysical studies. In all cases both the selected cues as well as all cues prior to the selection are illustrated, and the implied directions are discussed in relation to the literature.

The effectiveness of the proposed cue selection is assessed using a number of statistical measures. The biases of the ITD and ILD cues with respect to the free-field cues τ_ϕ and ΔL_ϕ are defined as

$$\begin{aligned} b_\tau &= |E\{\tau(n)\} - \tau_\phi|, \\ b_{\Delta L} &= |E\{\Delta L(n)\} - \Delta L_\phi|, \end{aligned} \tag{8}$$

respectively, and the corresponding standard deviations are given by

$$\begin{aligned} \sigma_\tau &= \sqrt{E\{(\tau(n) - E\{\tau(n)\})^2\}}, \\ \sigma_{\Delta L} &= \sqrt{E\{(\Delta L(n) - E\{\Delta L(n)\})^2\}}. \end{aligned} \tag{9}$$

The biases and standard deviations are computed considering only the selected cues [Eq. (7)]. When there is more than one source to be discriminated, these measures are estimated separately for each source by grouping the selected cues at each time instant with the source known to have free-field cues closest to their current values.

For many cases, the larger the cue selection threshold c_0, the smaller the bias and standard deviation. The choice of c_0 is a compromise between the similarity of the selected cues to the free-field cues and the proportion of the ear input signals contributing to the resulting localization. The proportion of the signals contributing to the localization is characterized with the fraction of power represented by the selected parts of the signals, given by

$$p_0 = \frac{E\{p(n)w(n)\}}{E\{p(n)\}}, \tag{10}$$

where $p(n)$ is defined in Eq. (6) and the weighting function $w(n)$ is

$$w(n) = \begin{cases} 1, & \text{if } c_{12}(n) > c_0, \\ 0, & \text{otherwise.} \end{cases} \tag{11}$$

In this paper, the cue selection is only considered independently at single critical bands. Except for different values of c_0, the typical behavior appears to be fairly similar at critical bands with different center frequencies. For most simulations, we have chosen to use the critical bands centered at 500 Hz and/or 2 kHz. At 500 Hz the binaural processor operates on the input wave forms, whereas at 2 kHz the model of auditory periphery extracts the envelopes of the input signals and feeds them to the binaural processor. Where

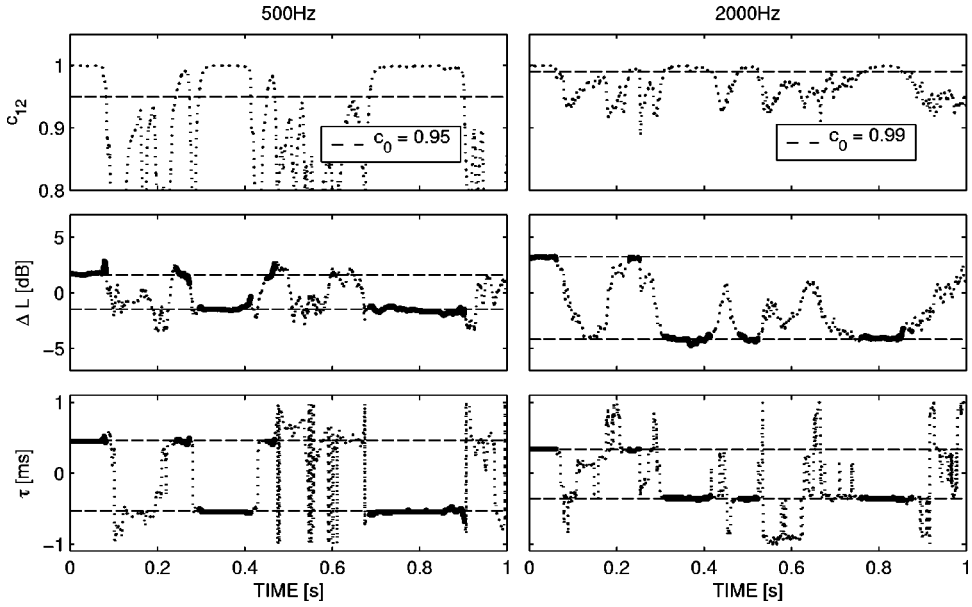

FIG. 2. IC, ILD, and ITD as a function of time for two independent speech sources at ±40° azimuth. Left column, 500 Hz; and right column, 2 kHz critical band. The cue selection thresholds (top row) and the free-field cues of the sources (middle and bottom rows) are indicated with dashed lines. Selected cues are marked with bold solid lines.

appropriate, results for other critical bands are also shown or briefly discussed. However, considering the way the auditory system eventually combines information from different critical bands is beyond the scope of this paper. As mentioned earlier, the simulations are carried out with a single constant cue selection threshold c_0 for each case. It is assumed that the auditory system has already adapted c_0 to be effective for the specific listening situation. Unless otherwise noted, the specific c_0 was chosen such that a visual inspection of the simulation results implies an effective cue selection.

Two kinds of plots are used to illustrate the cue selection. In some cases the instantaneous ITD and ILD values are plotted as a function of time, marking the values which are selected. For other examples, the effect of the cue selection is visualized by plotting short-time estimates of *probability density functions* (PDFs) of the selected ITD and ILD cues. Unless otherwise noted, the PDFs are estimated by computing histograms of ITD and ILD cues for a time span of 1.6 s. The height of the maximum peak is normalized to one in all PDFs. In both types of plots, free-field cues resulting from simulations of the same source signals without concurrent sound sources or reflections, are also indicated (the Matlab code used for these simulations is available at http://www.acoustics.hut.fi/software/cueselection/).

Listening situations in free field are simulated using HRTFs measured with the KEMAR dummy head with large pinnae, taken from the CIPIC HRTF Database (Algazi *et al.*, 2001). All simulated sound sources are located in the frontal horizontal plane, and, unless otherwise noted, all the stimuli are aligned to 60 dB SPL averaged over the whole stimulus length.

A. Independent sources in free-field

In this section, the cue selection method is applied to independent stimuli in an anechoic environment. As the first example, the operation of the selection procedure is illustrated in detail for the case of independent speech sources at different directions. Subsequently, simulation results of the effect of target-to-distracter ratio (T/D) on localization of the target stimulus are presented.

1. Concurrent speech

Localization of a speech target in the presence of one or more competing speech sources has been investigated by Hawley *et al.* (1999) and Drullman and Bronkhorst (2000). Drullman and Bronkhorst (2000) utilized an anechoic virtual environment using both individualized and nonindividualized HRTFs for binaural reproduction of the stimuli. They reported slight but statistically significant degradation in localization performance when the number of competing talkers was increased beyond 2. The experiment of Hawley *et al.* (1999), on the other hand, was conducted in a ''sound-field room'' (reverberation time of approximately 200 ms), as well as using headphone reproduction of the stimuli recorded binaurally in the same room. While not strictly anechoic, their results are also useful for evaluating our anechoic simulation results. Hawley *et al.* (1999) found that apart from occasional confusions between the target and the distracters, increasing the number of competitors from 1 to 3 had no significant effect on localization accuracy. As discussed in Sec. I, room reflections generally make the localization task more difficult, so a similar or a better result would be expected to occur in an anechoic situation. Note that the overall localization performance reported by Drullman and Bronkhorst (2000) was fairly poor, and the results may have been affected by a relatively complex task requiring listeners to recognize the target talker prior to judging its location.

Based on the previous discussion, the cue selection has to yield ITD and ILD cues similar to the free-field cues of each of the speech sources in order to correctly predict the directions of the perceived auditory events. Three simulations were carried out with 2, 3, and 5 concurrent speech sources. The signal of each source consisted of a different phonetically balanced sentence from the Harvard IEEE list (IEEE, 1969) recorded by the same male speaker. As the first

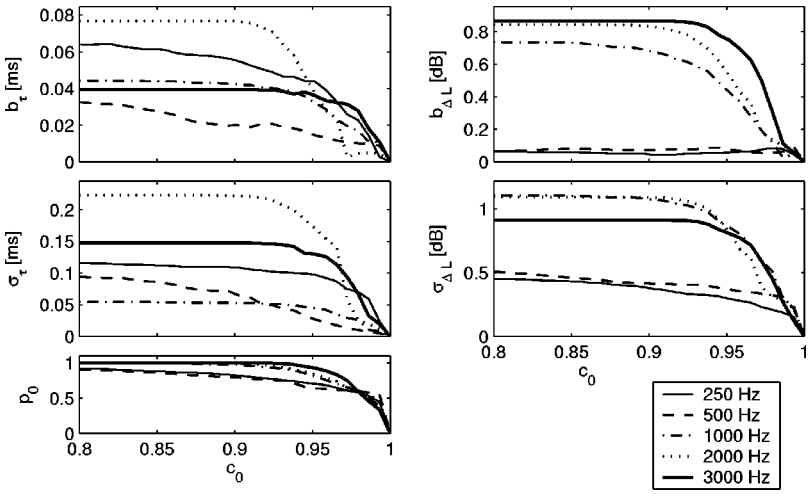

FIG. 3. ITD and ILD bias (top panels), standard deviation (middle panels), and relative power (bottom left panel) of the selected signal portions as a function of the cue selection threshold c_0 for two independent speech sources. Data are shown for the 250, 500, 1000, 2000, and 3000 Hz critical bands.

case, 2 speech sources were simulated at azimuthal angles of $\pm 40°$. Figure 2 shows the IC, ILD, and ITD as a function of time for the critical bands with center frequencies of 500 Hz and 2 kHz. The free-field cues which would occur with a separate simulation of the sources at the same angles are indicated with the dashed lines. The selected ITD and ILD cues [Eq. (7)] are marked with bold solid lines. Thresholds of $c_0 = 0.95$ and $c_0 = 0.99$ were used for the 500 Hz and 2 kHz critical bands, respectively, resulting in 65% and 54% selected signal power [Eq. (10)]. The selected cues are always close to the free-field cues, implying perception of two auditory events located at the directions of the sources, as reported in the literature. As expected, due to the neural transduction IC has a smaller range at the 2 kHz critical band than at the 500 Hz critical band. Consequently, a larger c_0 is required.

The performance of the cue selection was assessed as a function of c_0 for the same two speech sources and the critical bands with center frequencies of 250, 500, 1000, 2000, and 3000 Hz. Figure 3 shows the ITD and ILD biases [Eq. (8)] and standard deviations [Eq. (9)], as well as the fraction of signal power corresponding to the selected cues [Eq. (10)] as a function of c_0. The biases and standard deviations were computed for both sources separately, as described earlier, and then averaged over 1.6 s of the signals. The graphs indicate that both the biases and the standard deviations decrease with increasing c_0. Thus, the larger the c_0, the closer the obtained cues are to the reference free-field values. Furthermore, the selected signal power decreases gradually until fairly high values of c_0. The general trend of having higher absolute ILD errors at high frequencies is related to the overall larger range of ILDs occuring at high frequencies due to more efficient head shadowing.

The simulation with three independent talkers was performed with speech sources at 0° and $\pm 30°$ azimuth, and the simulation of five talkers with two additional sources at $\pm 80°$ azimuth. In both cases the results were fairly similar at different critical bands, so the data are only shown for the 500 Hz band. Panels (A) and (B) of Fig. 4 show PDFs of ITD and ILD without the cue selection for the three and five

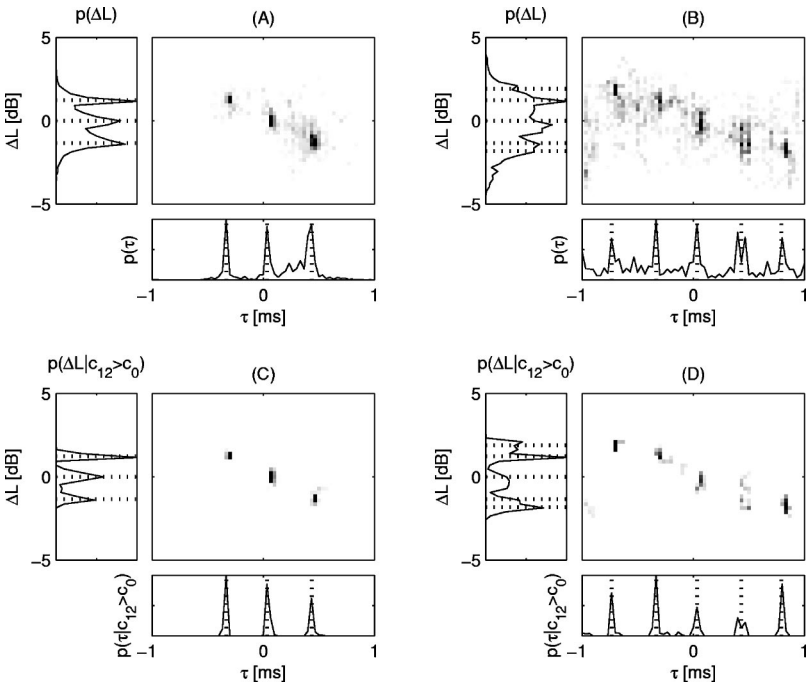

FIG. 4. PDFs of ITD and ILD for three (A) and five (B) independent speech sources and corresponding PDFs when cue selection is applied [(C) and (D)]. The values of the free-field cues for each source are indicated with dotted lines. Data are shown for the 500 Hz critical band.

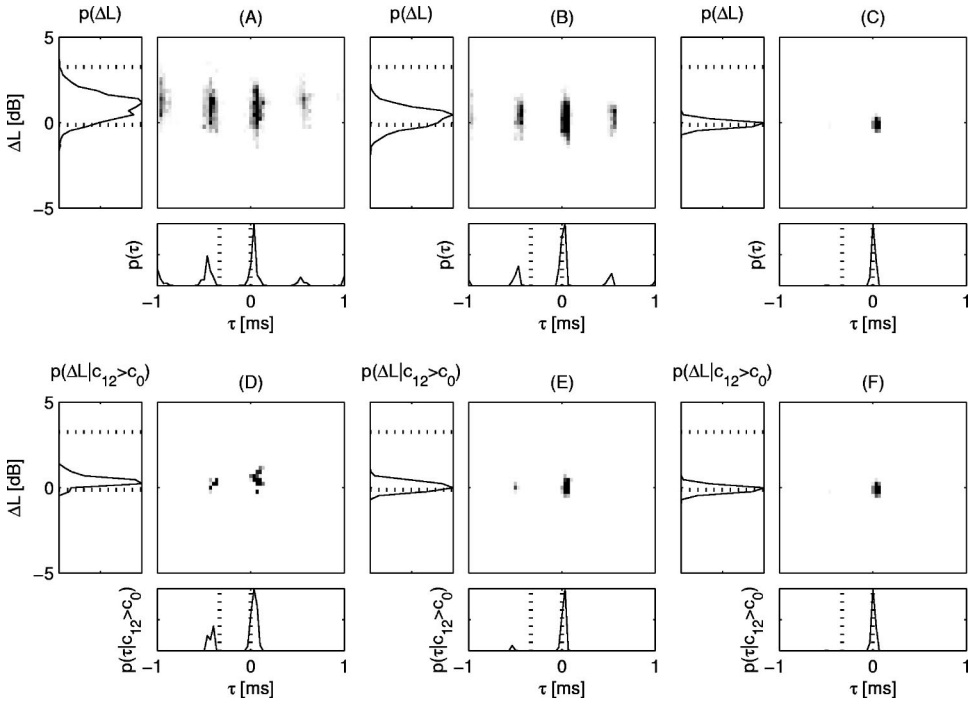

FIG. 5. PDFs of ITD and ILD for a click-train and white Gaussian noise at different T/D ratios: −3, −9, −21 dB (A)–(C), and the corresponding PDFs when cue selection is applied (D)–(F). The values of the free-field cues are indicated with dotted lines. Data are shown for the 2 kHz critical band.

speech sources, respectively. Panels (C) and (D) of Fig. 4 show similar PDFs of the selected cues. The selection threshold was set at $c_0 = 0.99$ corresponding to 54% selected signal power for the three sources and 22% for the five sources. In both cases, even the PDFs considering all cues show ITD peaks at approximately correct locations, and the cue selection can be seen to enhance the peaks. With the cue selection, the widths of the peaks (i.e., the standard deviations of ITD and ILD) in the three source case are as narrow as in separate one source free-field simulations, which implies robust localization of three auditory events corresponding to the psychophysical results of Hawley *et al.* (1999) and Drullman and Bronkhorst (2000). In the case of five sources, the peaks get slightly broader. The ITD peaks are still narrow and correctly located but at the 500 Hz critical band, the range of ILD cues is insufficient for distinct peaks to appear along the ILD axis. This result is also in line with the classic duplex theory (Rayleigh, 1907) of sound localization, stating that at low frequencies ITD cues are more salient than ILD cues.

2. Click-train and noise

Good and Gilkey (1996) and Good *et al.* (1997) studied the localization of a click-train target in the presence of a simultaneous noise distracter. Using loudspeaker reproduction in an anechoic chamber, localization performance was shown to degrade monotonously with a decreasing target-to-distracter ratio (T/D). The investigated T/D ratios were defined relative to the individual detection threshold of each listener for the case when the target sound was presented from the same direction as the distracter. With a target level just a few dB above the detection threshold, localization performance in the left-right direction (e.g., frontal horizontal plane) was still found to be nearly as good as without the distracter. The degradation started earlier and was more severe for the up-down and front-back directions. The results for the left-right direction were later confirmed by Lorenzi *et al.* (1999), who conducted a similar experiment with sound sources in the frontal horizontal plane. However, the detection levels of Lorenzi *et al.* (1999) were slightly higher, maybe due to utilization of a sound-treated chamber instead of a strictly anechoic environment. Furthermore, Lorenzi *et al.* (1999) found a degradation in performance when the stimuli were low-pass filtered at 1.6 kHz, unlike when the stimuli were high pass filtered at the same frequency.

A simulation was carried out with a white noise distracter directly in front of the listener and a click-train target with a rate of 100 Hz located at 30° azimuth. Assuming a detection level of −11 dB (the highest value in Good *et al.* 1997), the chosen absolute T/D of −3, −9, and −21 dB correspond to the relative T/D of 8, 2, and −10 dB, respectively, as investigated by Good and Gilkey (1996). The PDFs for the critical band centered at 500 Hz did not yield a clear peak corresponding to the direction of the click train. Motivated by the fact that in this case higher frequencies are more important for directional discrimination (Lorenzi *et al.*, 1999), we investigated further the 2 kHz critical band. Panels (A)–(C) of Fig. 5 show PDFs of ITD and ILD without the cue selection for the selected T/D ratios. Corresponding PDFs obtained by the cue selection [Eq. (7)] are shown in panels (D)–(F). The thresholds for the panels (D)–(F) were $c_0 = 0.990$, $c_0 = 0.992$, and $c_0 = 0.992$, respectively, resulting in 3%, 9%, and 99% of the signal power being represented by the selected cues.

The PDFs in Fig. 5 imply that the target is localized as a separate auditory event for the T/D ratios of −3 dB and −9 dB. However, for the lowest T/D ratio the target click-train is no longer individually localizable, as also suggested by the results of Good and Gilkey (1996). In panels (A) and (B), ITD peaks are seen to rise at regular intervals due to the periodicity of the cross-correlation function, while the cue selection suppresses the periodical peaks as shown in panels

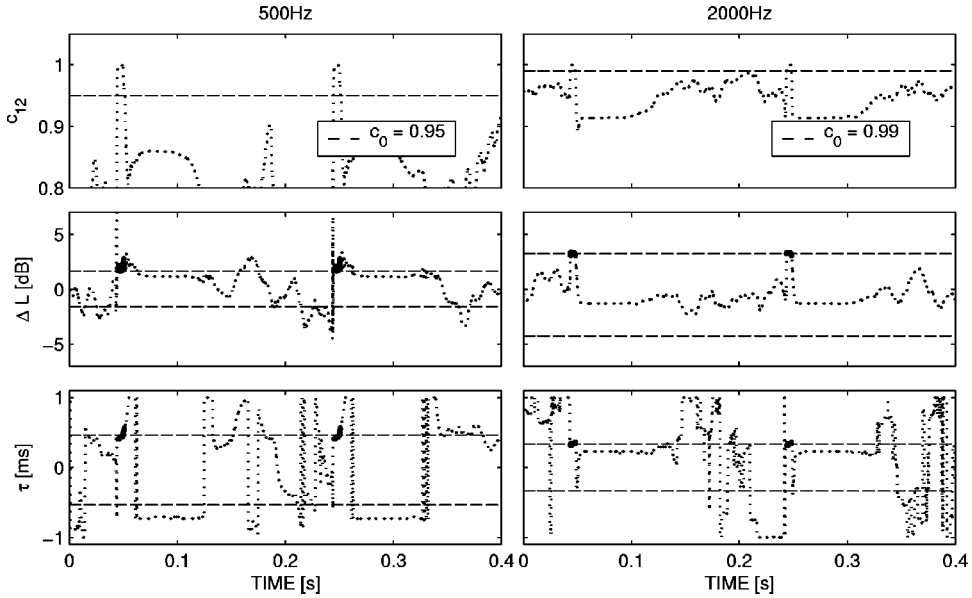

FIG. 6. IC, ILD, and ITD as a function of time for a lead/lag click-train with a rate of 5 Hz and an ICI of 5 ms. Left column, 500 Hz; and right column, 2 kHz critical band. The cue selection thresholds (top row) and the free-field cues of the sources (middle and bottom rows) are indicated with dashed lines. Selected cues are marked with bold solid lines.

(D) and (E). Note that when the click-train is individually localizable, only the recovered ITD cues are close to the free-field cues of both sources, whereas a single broad ILD peak appears. This is in line with the findings of Braasch (2003) that in the presence of a distracter, ILDs are less reliable cues for localization, and that ITDs also gain more importance in the subjective localization judgment. The ITD peaks corresponding to the click-train are also shifted away from the distracter. Such a pushing effect caused by a distracter in front of the listener was observed for one listener in a similar experiment (Lorenzi *et al.*, 1999) and for most listeners when the target was an independent noise signal (Braasch and Hartung 2002). On the contrary, Good and Gilkey (1996) reported a pulling effect, which was also the case for two listeners in the experiment of Lorenzi *et al.* (1999).

B. Precedence effect

This section illustrates the cue selection within the context of the precedence effect. Pairs of clicks are used to demonstrate the results for wide band signals (in this case a signal with at least the width of a critical band). Sinusoidal tones are simulated with different onset rates and the cues obtained during the onset are shown to agree with results reported in the literature.

1. Pairs of clicks

In a classical precedence effect experiment, a lead/lag pair of clicks is presented to the listener (Blauert, 1997; Litovsky *et al.*, 1999). The leading click is first emitted from one direction, followed by another identical click from another direction after an *interclick interval* (ICI) of a few milliseconds. As discussed in Sec. I, the directional perception changes depending on ICI.

Figure 6 shows IC, ILD, and ITD as a function of time for a click train with a rate of 5 Hz analyzed at the critical bands centered at 500 Hz and 2 kHz. The lead source is simulated at 40° and the lag at −40° azimuth with an ICI of 5 ms. As expected based on earlier discussion, IC is close to one whenever only the lead sound is within the analysis time window. As soon as the lag reaches the ears of the listener, the superposition of the two clicks reduces the IC. The cues obtained by the selection with $c_0=0.95$ for the 500 Hz and $c_0=0.985$ for the 2 kHz critical band are shown in the figure, and the free-field cues of both sources are indicated with dashed lines. The selected cues are close to the free-field cues of the leading source and the cues related to the lag are ignored, as is known to happen based on psychophysical studies (Litovsky *et al.* 1999). The fluctuation in the cues before each new click pair is due to the internal noise of the model.

The performance of the cue selection was again assessed as a function of c_0 for the critical bands with center frequencies of 250, 500, 1000, 2000, and 3000 Hz. The statistical measures were calculated from a 1.6 s signal segment. Figure 7 shows ITD and ILD biases [Eq. (8)] and standard deviations [Eq. (9)], as well as the power of the selected cues [Eq. (10)] as a function of c_0. The biases and standard deviations were computed related to the free-field cues of the leading source, since localization of the lag should be suppressed if the selection works correctly. Both the biases and standard deviations decrease as c_0 increases. Thus the larger the cue selection threshold c_0, the more similar the selected cues are to the free-field cues of the leading source.

At a single critical band, the energy of the clicks is spread over time due to the gammatone filtering and the model of neural transduction. Therefore, with an ICI of 5 ms, a large proportion of the critical band signals related to the clicks of a pair is overlapping, and only a small part of the energy of the lead click appears in the critical band signals before the lag. Consequently, the relative signal power corresponding to the selected cues is fairly low when requiring small bias and standard deviation, as can be seen in the left bottom panel of Fig. 7.

Localization as a function of ICI: The previous experiment was repeated for ICIs in the range of 0–20 ms using the 500 Hz critical band. The chosen range of delays includes summing localization, localization suppression, and independent localization of both clicks without the precedence effect

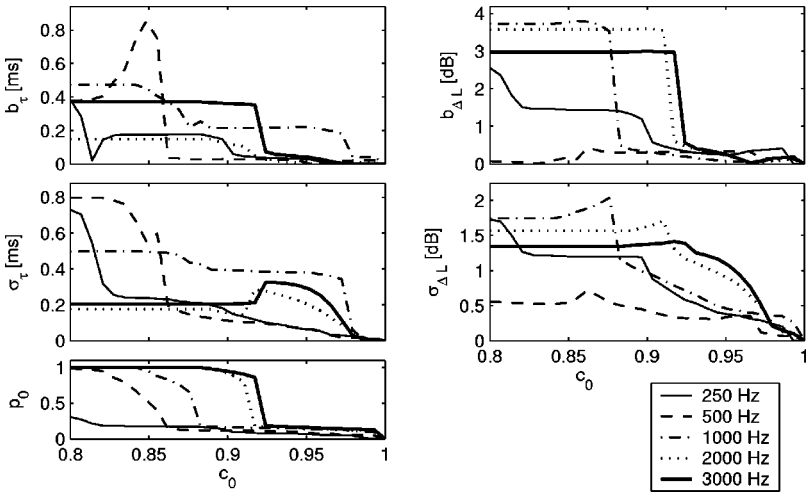

FIG. 7. ITD and ILD bias, standard deviation, and relative power of the selected signal portions as a function of the cue selection threshold c_0 for a lead/lag click-train. Data are shown for the 250, 500, 1000, 2000, and 3000 Hz critical bands.

(Litovsky *et al.*, 1999). For all previous simulations, a suitable c_0 was chosen as a compromise between similarity of the cues to free-field cues and how frequently cues are selected. Here, each ICI corresponds to a different listening situation, since the different delays of the lag imply different acoustical environments. It is thus expected that the most effective c_0 may also differ depending on ICI.

Several different criteria for determining c_0 were assessed. Indeed, using the same c_0 for all ICIs did not yield the desired results. The criterion of adapting c_0 such that the relative power of the selected cues [Eq. (10)] had the same value for each simulation did not yield good results either. Thus, a third criterion was adopted. The cue selection threshold c_0 was determined numerically for each simulation such that σ_τ (the narrowness of the peaks in the PDFs of ITD) was equal to 15 μs. This could be explained with a hypothetical auditory mechanism adapting c_0 in time with the aim of making ITD and/or ILD standard deviation sufficiently small. Small standard deviations indicate small fluctuations of the selected cues in time and thus non-time-varying localization of auditory events. The resulting PDFs of ITD and ILD as a function of ICI with and without the cue selection are shown in Fig. 8.

The PDFs without the cue selection (rows 1 and 2 in Fig. 8) indicate two independently localized auditory events for most ICIs above 1 ms. Furthermore, the predicted directions depend strongly on the delay. On the contrary, the PDFs with the cue selection show that the selected cues correctly predict all the three phases of the precedence effect (summing localization, localization suppression, and independent localization). At delays less than approximately 1 ms the ITD peak moves to the side as the delay increases, as desired, but the ILD cues do not indicate the same direction as the ITD cues. However, this is also in line with existing psychophysical literature. Anomalies of the precedence effect have been observed in listening tests with band pass filtered clicks

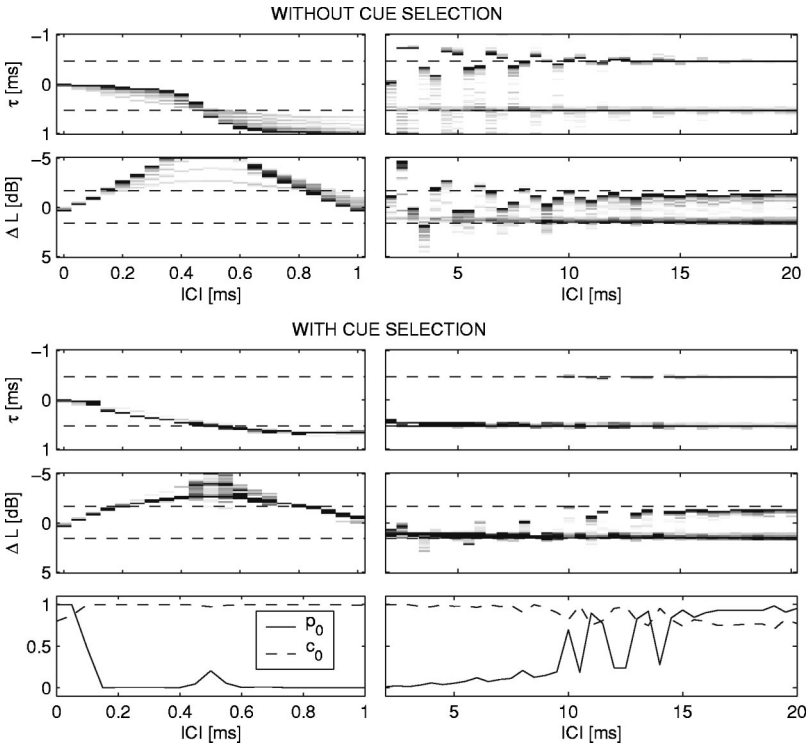

FIG. 8. PDFs of ITD and ILD as a function of the interclick interval (ICI) for a click-train: without cue selection (rows 1 and 2) and with cue selection (rows 3 and 4). Cue selection threshold c_0 and relative power p_0 of the selected signal portion (bottom row).

(Blauert and Cobben, 1978), suggesting a contribution of the extracted misleading ILDs to the localization judgment. For delays within the range of approximately 1–10 ms there is only one significant peak in the PDFs, indicating localization in the direction of the lead. For larger delays two peaks appear, suggesting two independently localized auditory events. Note that the fusion of two clicks has been found to sometimes break down earlier, but 10 ms is within the range of reported critical thresholds for localization dominance (Litovsky *et al.*, 1999; Litovsky and Shinn-Cunningham, 2001).

The bottom row of Fig. 8 shows the selection threshold c_0 and the relative power p_0 of the signal corresponding to the selected cues as a function of the ICI. For most ICIs up to approximately 8 ms, the relative power of the selected signal portion almost vanishes. However, there is one characteristic peak of p_0 at approximately 0.5 ms. The experiment was repeated for a number of critical bands in the range of 400 to 600 Hz with the observation that the location of this peak moves along the ICI axis as a function of the center frequency of the considered critical band. Furthermore, the general trends of the selected cues were very similar to those at the 500 Hz band in that they all strongly implied the three phases of the precedence effect. Thus, by considering a number of critical bands the three phases of the precedence effect can indeed be explained by the cue selection such that at each ICI a signal portion with nonvanishing power is selected.

Cue selection threshold and precedence buildup: For the previous experiment, it was hypothesized that the criterion for determining c_0 is the standard deviation of ITD and/or ILD. The computation of these quantities involves determining the number of peaks (i.e., the number of individually localized auditory events) adaptively in time, which might be related to the buildup of precedence. A buildup occurs when a lead/lag stimulus with ICI close to the echo threshold is repeated several times. During the first few stimulus pairs, the precedence effect is not active and two auditory events are independently perceived. After the buildup, the clicks merge to a single auditory event in the direction of the lead (Freyman *et al.*, 1991). An adaptive process determining c_0 would require a certain amount of stimulus activity and time until an effective c_0 is determined and it could thus explain the time-varying operation of the precedence effect.

The precedence effect literature also discusses a breakdown of precedence when, for instance, the directions of the lead and lag are suddenly swapped (Clifton, 1987; Blauert, 1997; Litovsky *et al.*, 1999). However, more recent results of Djelani and Blauert (2001, 2002) indicate that the buildup is direction specific, suggesting further that what has been earlier reported as breakdown of precedence is rather a consequence of precedence not being built up for a new lag direction. Djelani and Blauert (2002) also showed that without stimulus activity the effect of the buildup decays slowly by itself, which supports the idea of an adaptive c_0. In order to model the direction-specific buildup, c_0 would also need to be defined as a function of direction. However, testing and developing the corresponding adaptation method is beyond the scope of this paper and will be part of the future work.

2. Onset rate of a sinusoidal tone

Rakerd and Hartmann (1986) investigated the effect of the onset time of a 500 Hz sinusoidal tone on localization in the presence of a single reflection. In the case of a sinusoidal tone, the steady state ITD and ILD cues result from the coherent sum of the direct and reflected sound at the ears of a listener. Often these cues do not imply the direction of either the direct sound or the reflection. Rakerd and Hartmann (1986) found that the onset rate of the tone was a critical factor in determining how much the misleading steady state cues contributed to the localization judgment of human listeners. For fast onsets, localization was based on the correct onset cues, unlike when the level of the tone raised slowly. The cue selection cannot, as such, explain the discounting of the steady state cues, which always have IC close to one. However, considering just the onsets the following results reflect the psychophysical findings of Rakerd and Hartmann (1986).

Figure 9 shows IC, ILD, and ITD as a function of time for a 500 Hz tone with onset times of 0, 5, and 50 ms. The simulated case corresponds approximately to the ''WDB room'' and ''reflection source 6'' condition reported by Rakerd and Hartmann (1986). The direct sound is simulated in front of the listener, and the reflection arrives with a delay of 1.4 ms from an azimuthal angle of 30°. A linear onset ramp is used and the steady state level of the tone is set to 65 dB SPL. The ITD and ILD cues selected with a threshold of $c_0=0.93$ are marked with bold solid lines and the free-field cues of the direct sound and the reflection are indicated with dashed lines. Note that the direct sound reaches the ears of the listener at approximately 7 ms. For onset times of 0 and 5 ms, ITD and ILD cues are similar to the free-field cues at the time when IC reaches the threshold. However, with an onset time of 50 ms the ITD and ILD cues no longer correspond to the free-field cues, which is suggested by the degraded localization performance in the experiment of Rakerd and Hartmann (1986).

In order to predict the final localization judgment, another selection mechanism would be needed to only include the localization cues at the time instants when the cue selection becomes effective. The dependence on the onset rate can be explained by considering the input signals of the binaural processor. During the onset, the level of the reflected sound follows that of the direct sound with a delay of 1.4 ms. Thus, the slower the onset, the smaller the difference. The critical moment is when the level of the direct sound rises high enough above the level of the internal noise to yield IC above the selection threshold. If the reflection has nonnegligible power at that time, localization cues will be biased to the steady state direction already when the selection begins.

C. Independent sources in a reverberant environment

As a final test for the model, the localization of 1 and 2 speech sources was simulated in a reverberant environment. The utilized BRIRs were measured with a Neumann KU 80 dummy head in an empty lecture hall with reverberation times of 2.0 and 1.4 s at the octave bands centered at 500 and

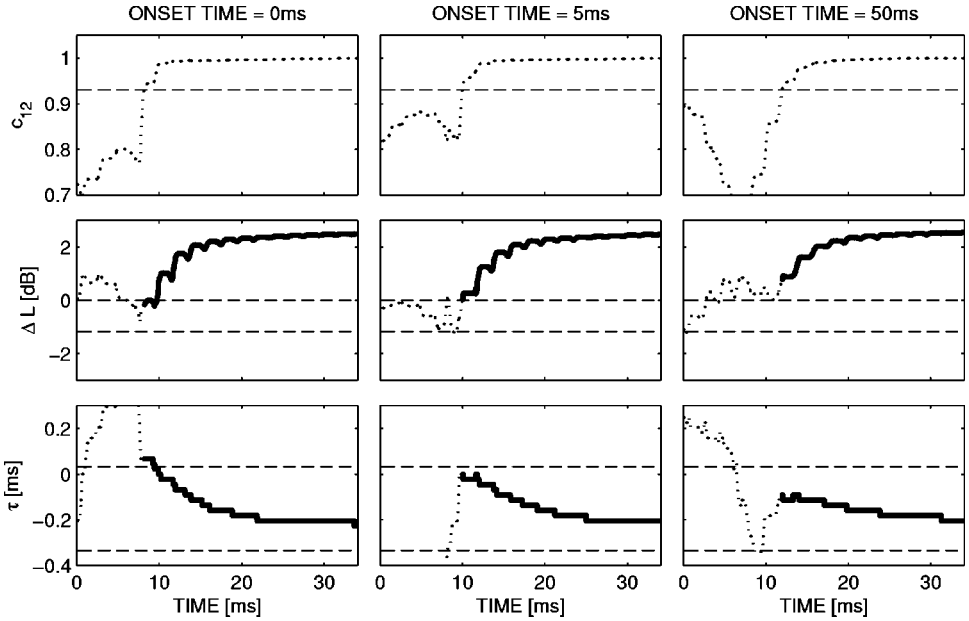

FIG. 9. IC, ILD, and ITD as a function of time for a 500 Hz sinusoidal tone and one reflection. The columns from left to right show results for onset times of 0 ms, 5 ms, and 50 ms. The cue selection threshold of $c_0 = 0.95$ (top row) and the free-field cues of the source and the reflection (middle and bottom rows) are indicated with dashed lines. Selected cues are marked with bold solid lines. Data are shown for the 500 Hz critical band.

2000 Hz, respectively. The same phonetically balanced speech samples as used in Sec. III A 1 were convolved with BRIRs simulating sources at 30° azimuth for the case of one source and ±30° for the two sources. The case of two talkers included again two different sentences uttered by the same male speaker. For computing the free-field cues, the BRIRs were truncated to 2.3 ms, such that the effect of the reflections was ignored.

The chosen hall is a very difficult case for localization due to lots of diffuse reflections from the tables and benches all around the simulated listening position. At the 500 Hz critical band, the ITD and ILD cues prior to the selection did not yield any meaningful data for localization. The cue selection resulted in high peaks close to the free-field cues, but it was not able to suppress all other peaks implying different directions. A subsequent investigation showed that these erroneous peaks appear at different locations at different critical bands. Thus, processing of localization information across critical bands should be able to further suppress them. At 2 kHz, the results for a single critical band were clearer and they will be illustrated here.

Panels (A) and (B) of Fig. 10 show PDFs of ITD and ILD without the cue selection, and panels (C) and (D) show the corresponding PDFs of the selected cues. Since the cue selection in this case samples the ITD and ILD relatively infrequently, the PDFs were computed considering 3 s of signal. Similar results are obtained when the PDFs are computed from different time intervals. The cue selection criterion for both the 1 and 2 source scenarios was $c_0 = 0.99$, resulting in 1% of the signal power corresponding to the selected cues. Without the cue selection, the PDFs do not yield much information for localization in either of the cases.

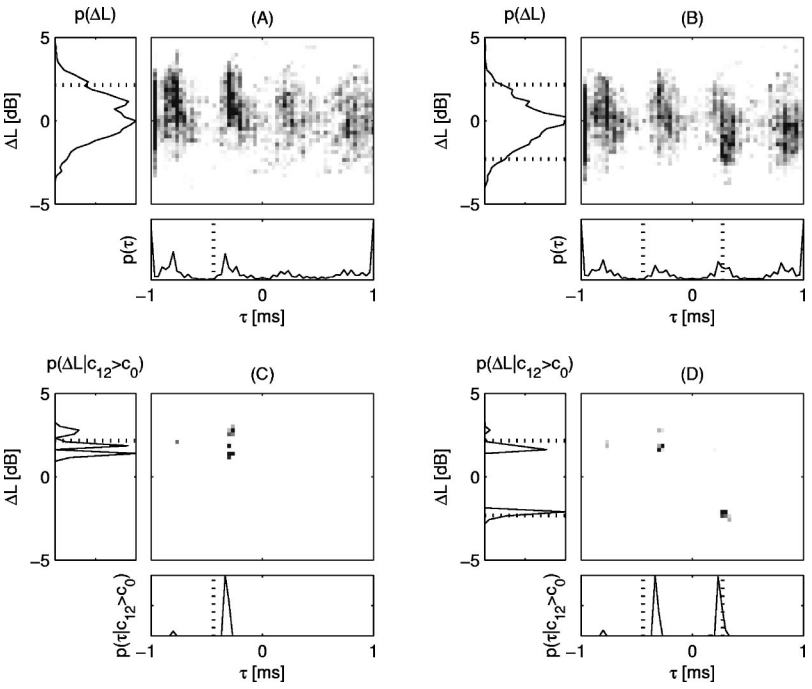

FIG. 10. PDFs of ITD and ILD for 1 (A) and 2 (B) speech sources in a reverberant hall and the corresponding PDFs when cue selection is applied (C) and (D). The values of the free-field cues for each source are indicated with dotted lines. Data are shown for the 2 kHz critical band.

Periodicity of the cross-correlation function is clearly visible and it is difficult to distinguish between the one and two source cases. However, with the cue selection sharp peaks arise relatively close to the free-field cues. In the two source case, the right source is practically correctly localized, whereas the ITD cues of the left source are slightly biased towards the center. Note that contrary to the results in Sec. III A 2, the localization is in this case shifted towards the competing sound source. As discussed, also this kind of a pulling effect has been reported in psychoacoustical studies (Good and Gilkey, 1996; Lorenzi *et al.*, 1999; Braasch and Hartung, 2002).

IV. GENERAL DISCUSSION

In the preceding sections, the selection of ITD and ILD cues based on IC was introduced into a localization model and applied to simulations of a number of complex listening scenarios. In comparison to several existing localization models, a significant difference in the proposed method is the way that the signal power at each time instant affects the localization judgment. In models not designed for complex listening situations, the localization cues and subsequently the final localization judgment are often derived from a time window including the whole stimulus, or of a time integration of a binaural activity pattern computed with running non-normalized cross correlation. In such cases, the contribution of each time instant to the final localization depends on the instantaneous power. In our approach, only the cues during the selected time instants contribute to localization. Thus the model can in many cases neglect localization information corresponding to time instants with high power, if the power is high due to concurrent activity of several sound sources (or concurrent activity of sources and reflections). The relative power of individual sources also affects how often ITD and ILD cues corresponding to each source are selected.

The proposed model also bears resemblance to earlier models of the precedence effect. The temporal inhibition of the model of Lindemann (1986a) tends to hold the highest peaks of the running cross-correlation function (calculated with the stationary inhibition that incorporates ILDs into the model). The higher a peak (i.e., the higher the IC at the corresponding time instant), the stronger the temporal inhibition. The cue selection achieves a somewhat similar effect without a need for an explicit temporal inhibition mechanism, since the localization suppression is directly related to the IC estimated with a similar time window. However, the effect can also be quite different in some scenarios. Whereas the model of Lindemann (1986a) only ''remembers'' the peaks corresponding to a high IC for a short time (time constant of 10 ms), the cue selection with a slowly varying c_0 has a much longer memory. The frequency of the time instants when the direct sound of only one source dominates within a critical band depends on the complexity of the listening situation. In complex cases (e.g., Sec. III C), only a small fraction of the ear input signals contribute to localization, and new localization information may be acquired relatively infrequently. We, nevertheless, assume that it is the cues at these instants of time that determine the source localization. During the time when no cues are selected, the localization of the corresponding auditory events is assumed to be determined by the previously selected cues, which is in principle possible. Localization of sinusoidal tones based only on their onsets (Rakerd and Hartmann 1985, 1986) and a related demonstration called the ''Franssen effect'' (Franssen, 1960; Hartmann and Rakerd, 1989) show that a derived localization judgment can persist for several seconds after the related localization cues have occurred. In precedence effect conditions (Sec. III B) the cue selection naturally derives most localization information from signal onsets, as is explicitly done in the model of Zurek (1987) (see also Martin, 1997). However, the cue selection is not limited to getting information from onsets only, and it does not necessarily include all onsets.

Throughout the paper, the resulting ITD and ILD cues were considered separately instead of deriving a combined localization judgment. The mutual role of ITDs and ILDs is often characterized with time-intensity trading ratios (Blauert, 1997) or in the form of the classic duplex theory (Rayleigh, 1907): ITD cues dominate localization at low frequencies and ILDs at high frequencies. However, in complex listening situations the relative weights of these cues may change. Wightman and Kistler (1992) have shown that in the presence of conflicting ITD and ILD cues, ITD cues will dominate the localization judgment of broadband noise as long as low frequency energy is present. Furthermore, Braasch (2003) has found that the presence of a distracting sound source even strengthens the weight of ITD cues. Nevertheless, the results of Rakerd and Hartmann (1986) suggest that steady-state ITDs can sometimes be completely neglected, unlike ILD cues. Considering the relative weights of ITD and ILD cues in more detail is beyond the scope of this paper. However, in future work it will be interesting to assess whether the proposed cue selection reflects the relative importance of ITD and ILD cues, i.e., whether the cue selection, for example, recovers more reliably ITD cues in cases where they are weighted more than ILD cues, and vice versa.

The cue selection mechanism could be seen to perform a function that Litovsky and Shinn-Cunningham (2001) have characterized as ''a general process that enables robust localization not only in the presence of echoes, but whenever any competing information from a second source arrives before the direction of a previous source has been computed.'' For the purposes of this paper, ITD and IC cues were analyzed using a cross-correlation model, whereas ILDs were computed independently. Similar cue selection could also be implemented in other localization models, such as the excitation-inhibition (EI) model of Breebaart *et al.* (2001) involving joint analysis of ITD and ILD cues within a physiologically motivated structure. In the EI model, full coherence is not represented by maximum activity but by zero activity. Thus, as opposed to specifying a lower bound of IC for the cue selection, an upper bound of activity would need to be determined.

As shown in Sec. III, the cue selection model was able to simulate most psychophysical results reviewed in the introduction by using a selection threshold adapted to each specific listening scenario. Although this paper is limited to

localization based on binaural cues, it should be mentioned that the precedence effect has also been observed in the median sagittal plane where the localization is based on spectral cues instead of interaural differences (Blauert, 1971; Litovsky *et al.,* 1997). Thus, the cue selection model does not fully describe the operation of the precedence effect. Furthermore, the model cannot as such explain the discounting of ITD and ILD cues occurring simultaneously with a high IC during the steady state sound in two scenarios: a sinusoidal tone presented in a room (Rakerd and Hartmann 1985, 1986; Hartmann and Rakerd, 1989) and two independent noise sources with the same envelopes presented from different directions (Braasch, 2002). The psychophysical results of Litovsky *et al.* (1997) show that the localization suppression is somewhat weaker in the median plane than in the horizontal plane, which could be interpreted as evidence for another suppression mechanism, possibly operating simultaneously with a binaural mechanism such as the proposed cue selection. Indeed, simulating all the results cited in this paragraph would appear to require some additional form of temporal inhibition.

V. CONCLUSIONS

A cue selection mechanism was presented for modeling source localization in complex listening scenarios. The cue selection can simulate both localization of several concurrently active independent sources and suppression of the localization of reflected sound by considering ITD and ILD cues only when IC at the corresponding critical band is larger than a certain threshold. It was shown that at time instants when this occurs, ITD and ILD are likely to represent the direction of one of the sources. Thus, by looking at the different ITD and ILD values during the selected time instants one can obtain information about the direction of each source.

The proposed cue selection mechanism was implemented in the framework of a binaural model considering the known periphery of the auditory system. The remaining parts of the model were analytically motivated for the sake of focus on the cue selection method without having to consider the specific properties and limitations of existing physiologically motivated models. Nevertheless, it was pointed out in the discussion that in principle the proposed cue selection method is physiologically feasible.

The binaural model with the proposed cue selection was verified with the results of a number of psychophysical studies from the literature. The simulation results suggest relatively reliable localization of concurrent speech sources both in anechoic and reverberant environments. The effect of target-to-distracter ratio corresponds qualitatively to published results of localization of a click-train in the presence of a noise distracter. Localization dominance is correctly reproduced for click pairs and for the onsets of sinusoidal tones. It was also hypothesized that the buildup of precedence may be related to the time the auditory system needs to find a cue selection threshold which is effective for the specific listening situation. As a final test, the model was applied for source localization in a reverberant hall with one and two speech sources. The results suggest that also in this most complex case the model is able to obtain cues corresponding to the directions of the sources.

ACKNOWLEDGMENTS

The authors gratefully acknowledge discussions with Frank Baumgarte, Jens Blauert, Toni Hirvonen, Aki Härmä, Matti Karjalainen, Kalle Palomäki, and John Worley. The work of Juha Merimaa has been supported by the research training network for Hearing Organization and Recognition of Speech in Europe (HOARSE, HPRN-CT-2002-00276) and the Finnish Graduate School in Electronics Telecommunications and Automation (GETA).

Akeroyd, M. A. (**2001**). ''A binaural cross-correlogram toolbox for MATLAB,'' http://www.biols.susx.ac.uk/home/Michael_Akeroyd/download2.html

Algazi, V. R., Duda, R. O., Thompson, D. M., and Avendano, C. (**2001**). The CIPIC HRTF Database, IEEE Workshop on Applications of Signal Processing to Audio and Acoustics, New Paltz, NY, pp. 99–102.

Bernstein, L. R., and Trahiotis, C. (**1996**). ''The normalized correlation: Accounting for binaural detection across center frequency,'' J. Acoust. Soc. Am. **100**, 3774–3784.

Bernstein, L. R., van de Par, S., and Trahiotis, C. (**1999**). ''The normalized interaural correlation: Accounting for NoSπ thresholds obtained with Gaussian and ''low-noise'' masking noise,'' J. Acoust. Soc. Am. **106**, 870–876.

Blauert, J. (**1971**). ''Localization and the law of the first wavefront in the median plane,'' Acustica **50**, 466–470.

Blauert, J. (**1997**). *Spatial Hearing: The Psychophysics of Human Sound Localization*, revised ed. (The MIT Press, Cambridge, MA).

Blauert, J., and Cobben, W. (**1978**). ''Some consideration of binaural cross correlation analysis,'' Acustica **39**, 96–104.

Boehnke, S. E., Hall, S. E., and Marquadt, T. (**2002**). ''Detection of static and dynamic changes in interaural correlation,'' J. Acoust. Soc. Am. **112**, 1617–1626.

Braasch, J. (**2002**). ''Localization in the presence of a distracter and reverberation in the frontal horizontal plane. II. Model algorithms,'' Acust. Acta Acust. **88**, 956–969.

Braasch, J. (**2003**). ''Localization in the presence of a distracter and reverberation in the frontal horizontal plane. III. The role of interaural level differences,'' Acust. Acta Acust. **89**, 674–692.

Braasch, J., and Blauert, J. (**2003**). ''The precedence effect for noise bursts of different bandwidths. II. Comparison of model algorithms,'' Acoust. Sci. Tech. **24**, 293–303.

Braasch, J., and Hartung, K. (**2002**). ''Localization in the presence of a distracter and reverberation in the frontal horizontal plane. I. Psychoacoustical data,'' Acust. Acta Acust. **88**, 942–955.

Braasch, J., Blauert, J., and Djelani, T. (**2003**). ''The precedence effect for noise bursts of different bandwidths. I. Psychoacoustical data,'' Acoust. Sci. Tech. **24**(5), 233–241.

Breebaart, J., van de Par, S., and Kohlrausch, A. (**2001**). ''Binaural processing model based on contralateral inhibition. I. Model structure,'' J. Acoust. Soc. Am. **110**, 1074–1088.

Clifton, R. K. (**1987**). ''Breakdown of echo suppression in the precedence effect,'' J. Acoust. Soc. Am. **82**, 1834–1835.

Culling, J. F., Colburn, H. S., and Spurchise, M. (**2001**). ''Interaural correlation sensitivity,'' J. Acoust. Soc. Am. **110**, 1020–1029.

Djelani, T., and Blauert, J. (**2001**). ''Investigations into the build-up and breakdown of the precedence effect,'' Acust. Acta Acust. **87**, 253–261.

Djelani, T., and Blauert, J. (**2002**). ''Modelling the direction-specific build-up of the precedence effect,'' Forum Acusticum, Sevilla, Spain.

Drullman, R., and Bronkhorst, A. W. (**2000**). ''Multichannel speech intelligibility and talker recognition using monaural, binaural, and three-dimensional auditory presentation,'' J. Acoust. Soc. Am. **107**, 2224–2235.

Franssen, N. V. (**1960**). Some considerations on the mechanism of directional hearing, Ph.D. thesis, Technische Hogeschool, Delft, The Netherlands.

Freyman, R. L., Clifton, R. K., and Litovsky, R. Y. (**1991**). ''Dynamic processes in the precedence effect,'' J. Acoust. Soc. Am. **90**, 874–884.

Gabriel, K. J., and Colburn, H. S. (**1981**). ''Interaural correlation discrimination: I. Bandwidth and level dependence,'' J. Acoust. Soc. Am. **69**, 1394–1401.
Gaik, W. (**1993**). ''Combined evaluation of interaural time and intensity differences: Psychoacoustic results and computer modeling,'' J. Acoust. Soc. Am. **94**, 98–110.
Giguère, C., and Abel, S. M. (**1993**). ''Sound localization: Effects of reverberation time, speaker array, stimulus frequence, and stimulus rise/decay,'' J. Acoust. Soc. Am. **94**, 769–776.
Good, M. D., and Gilkey, R. H. (**1996**). ''Sound localization in noise: The effect of signal to noise ratio,'' J. Acoust. Soc. Am. **99**, 1108–1117.
Good, M. D., Gilkey, R. H., and Ball, J. M. (**1997**). ''The relation between detection in noise and localization in noise in the free field,'' in *Binaural and Spatial Hearing in Real and Virtual Environments*, edited by R. H. Gilkey and T. R. Anderson (Lawrence Erlbaum Associates, Mahwah, NJ), pp. 349–376.
Grantham, D. W. (**1982**). ''Detectability of time-varying interaural correlation in narrow-band noise stimuli,'' J. Acoust. Soc. Am. **72**, 1178–1184.
Hartmann, W. M. (**1983**). ''Localization of sound in rooms,'' J. Acoust. Soc. Am. **74**, 1380–1391.
Hartmann, W. M. (**1997**). ''Listening in a room and the precedence effect,'' in *Binaural and Spatial Hearing in Real and Virtual Environments*, edited by R. H. Gilkey and T. R. Anderson (Lawrence Erlbaum Associates, Mahwah, NJ), pp. 349–376.
Hartmann, W. M., and Rakerd, B. (**1989**). ''Localization of sound in rooms, IV: The Franssen effect,'' J. Acoust. Soc. Am. **86**, 1366–1373.
Hartung, K., and Trahiotis, C. (**2001**). ''Peripheral auditory processing and investigations of the ''precedence effect'' which utilize successive transient stimuli,'' J. Acoust. Soc. Am. **110**, 1505–1513.
Hawley, M. L., Litovsky, R. Y., and Colburn, H. S. (**1999**). ''Speech intelligibility and localization in a multi-source environment,'' J. Acoust. Soc. Am. **105**, 3436–3448.
IEEE (**1969**). ''IEEE recommended practice for speech quality measurements,'' IEEE Trans. Audio Electroacoust. **17**, 137–148.
ISO 389 (**1975**). ''Acoustics—standard reference zero for the calibration of pure-tone audiometers.''
Jain, M., Gallagher, D. T., Koehnke, J., and Colburn, H. S. (**1991**). ''Fringed correlation discrimination and binaural detection,'' J. Acoust. Soc. Am. **90**, 1918–1926.
Jeffress, L. A. (**1948**). ''A place theory of sound localization,'' J. Comp. Physiol. Psychol. **61**, 468–486.
Koehnke, J., Colburn, H. S., and Durlach, N. I. (**1986**). ''Performance in several binaural-interaction experiments,'' J. Acoust. Soc. Am. **79**, 1558–1562.
Kollmeier, B., and Gilkey, R. H. (**1990**). ''Binaural forward and backward masking: Evidence for sluggishness in binaural detection,'' J. Acoust. Soc. Am. **87**, 1709–1719.
Langendijk, E. H. A., Kistler, D. J., and Wightman, F. L. (**2001**). ''Sound localization in the presence of one or two distracters,'' J. Acoust. Soc. Am. **109**, 2123–2134.
Lindemann, W. (**1986a**). ''Extension of a binaural cross-correlation model by means of contralateral inhibition. I. Simulation of lateralization of stationary signals,'' J. Acoust. Soc. Am. **80**, 1608–1622.
Lindemann, W. (**1986b**). ''Extension of a binaural cross-correlation model by means of contralateral inhibition. II. The law of the first wave front,'' J. Acoust. Soc. Am. **80**, 1623–1630.
Litovsky, R. Y., and Shinn-Cunningham, B. G. (**2001**). ''Investigation of the relationship among three common measures of precedence: Fusion, localization dominance, and discrimination suppression,'' J. Acoust. Soc. Am. **109**, 346–358.
Litovsky, R. Y., Colburn, H. S., Yost, W. A., and Guzman, S. J. (**1999**). ''The precedence effect,'' J. Acoust. Soc. Am. **106**, 1633–1654.
Litovsky, R. Y., Rakerd, B., Yin, T. C. T., and Hartmann, W. M. (**1997**). ''Psychophysical and physiological evidence for a precedence effect in the median sagittal plane,'' J. Neurophysiol. **77**, 2223–2226.
Lorenzi, C., Gatehouse, S., and Lever, C. (**1999**). ''Sound localization in noise in normal-hearing listeners,'' J. Acoust. Soc. Am. **105**, 1810–1820.
Martin, K. D. (**1997**). ''Echo suppression in a computational model of the precedence effect,'' IEEE ASSP Workshop on Applications of Signal Processes to Audio and Acoustics, New Paltz, NY.
Patterson, R. D., Allerhand, M. H., and Giguère, C. (**1995**). ''Time-domain modeling of peripheral auditory processing: A modular architecture and software platform,'' J. Acoust. Soc. Am. **98**, 1890–1894.
Pollack, I., and Trittipoe, W. (**1959a**). ''Binaural listening and interaural noise cross correlation,'' J. Acoust. Soc. Am. **31**, 1250–1252.
Pollack, I., and Trittipoe, W. (**1959b**). ''Interaural noise correlation: Examination of variables,'' J. Acoust. Soc. Am. **31**, 1616–1618.
Rakerd, B., and Hartmann, W. M. (**1985**). ''Localization of sound in rooms. II. The effects of a single reflecting surface,'' J. Acoust. Soc. Am. **78**, 524–533.
Rakerd, B., and Hartmann, W. M. (**1986**). ''Localization of sound in rooms. III. Onset and duration effects,'' J. Acoust. Soc. Am. **80**, 1695–1706.
Rayleigh, L. (**1907**). ''On our perception of sound direction,'' Philos. Mag. **13**, 214–232.
Slaney, M. (**1998**). ''Auditory toolbox: Version 2,'' Technical Report No. 1998-010, http://rvl4.ecn.purdue.edu/~malcolm/interval/1998-010/
van de Par, S., Trahiotis, C., and Bernstein, L. R. (**2001**). ''A consideration of the normalization that is typically included in correlation-based models of binaural detection,'' J. Acoust. Soc. Am. **109**, 830–833.
Viemeister, N. F., and Wakefield, G. H. (**1991**). ''Temporal integragion and multiple looks,'' J. Acoust. Soc. Am. **90**, 858–865.
Wightman, F. L., and Kistler, D. J. (**1992**). ''The dominant role of low-frequency interaural time differences in sound localization,'' J. Acoust. Soc. Am. **91**, 1648–1661.
Yin, T. C. T., and Chan, J. C. K. (**1990**). ''Interaural time sensitivity in medial superior olive of cat,'' J. Neurophysiol. **64**, 465–488.
Zurek, P. M. (**1987**). ''The precedence effect,'' in *Directional Hearing*, edited by W. A. Yost and G. Gourevitch (Springer-Verlag, New York), pp. 85–105.

Speech perception and talker segregation: Effects of level, pitch, and tactile support with multiple simultaneous talkers

Rob Drullman and Adelbert W. Bronkhorst
TNO Human Factors, Dept. of Perception, P.O. Box 23, 3769 ZG Soesterberg, The Netherlands

(Received 22 March 2004; revised 12 August 2004; accepted 13 August 2004)

Speech intelligibility was investigated by varying the number of interfering talkers, level, and mean pitch differences between target and interfering speech, and the presence of tactile support. In a first experiment the speech-reception threshold (SRT) for sentences was measured for a male talker against a background of one to eight interfering male talkers or speech noise. Speech was presented diotically and vibro-tactile support was given by presenting the low-pass-filtered signal (0–200 Hz) to the index finger. The benefit in the SRT resulting from tactile support ranged from 0 to 2.4 dB and was largest for one or two interfering talkers. A second experiment focused on masking effects of one interfering talker. The interference was the target talker's own voice with an increased mean pitch by 2, 4, 8, or 12 semitones. Level differences between target and interfering speech ranged from −16 to +4 dB. Results from measurements of correctly perceived words in sentences show an intelligibility increase of up to 27% due to tactile support. Performance gradually improves with increasing pitch difference. Louder target speech generally helps perception, but results for level differences are considerably dependent on pitch differences. Differences in performance between noise and speech maskers and between speech maskers with various mean pitches are explained by the effect of informational masking. [DOI: 10.1121/1.1802535]

PACS numbers: 43.66.Wv, 43.71.Es [AK] Pages: 3090–3098

I. INTRODUCTION

In a recent paper on the cocktail party phenomenon, Bronkhorst (2000) gives an extensive review of studies on the intelligibility of speech presented against a background of competing speech. Bronkhorst identifies a number of topics that merit further study. Two of these will be touched upon in this paper. First, we will consider the interference by competing talkers (particularly in diotic listening), their number, and the role of different voices. Second, there is the closely related issue of selective attention, in particular the situation where the listener concentrates on one particular talker, trying to minimize the distraction by other talkers. Apart from maximizing the difference between target and interference acoustically (level, spectrum, and pitch cues), another way to facilitate the focusing of attention is to provide information through a different modality. The type of support examined here is tactile (and in some case visual) information about the temporal fluctuations in the speech signal.

A. Multitalker environment

In an environment with many competing talkers, the target speech is embedded in a background of voice babble, with masking characteristics which come close to that of speech noise. That is, both have a similar long-term average spectrum, limited spectral and temporal fluctuations, and lack of linguistic content. Going to fewer competing talkers will increase the difference in masking, with a gradual shift from energetic to more informational masking. Energetic masking refers to the case when the interference (e.g., noise or speech) contains sufficient energy to make the target speech (partly) inaudible or at least unintelligible; informational masking occurs when (portions of) the speech interference is intelligible and so similar to the target speech that it becomes difficult for the listener to disentangle target and interfering speech. The effect of the similarity of target and masking voice(s) is most clearly demonstrated in studies with different-sex vs same-sex maskers (cf. Drullman and Bronkhorst, 2000). Recently, Brungart (2001) and Brungart *et al.* (2001) have conducted a series of experiments on energetic and informational masking using the Coordinate Response Measure (CRM) paradigm. In this paradigm, target and masker phrases are very similar. In a first study with a single interfering talker, Brungart (2001) investigated same-talker, same-sex, and different-sex target and masker voices. He found a clear dominance of informational masking over energetic masking, with least masking for different-sex talkers and most masking for same-talker conditions. The results were not monotonically related to the signal-to-noise ratio (SNR).[1] In a follow-up study, Brungart *et al.* (2001) used multiple simultaneous talkers and found essentially similar results. At negative SNRs, however, performance strongly depended on the number of interfering talkers: intelligibility was worse with two or three interfering talkers than with a single interfering talker.

Regarding the issue of voice (dis)similarity, in particular between male and female voices, an important role is attributed to differences in pitch when segregating simultaneous speech signals. The effect of pitch, defined on a segmental level, on the segregation of concurrent vowels has been the subject of several studies (e.g., Assmann and Summerfield, 1990; Culling and Darwin, 1993). For longer speech messages, Brokx and Nooteboom (1982) performed an interesting study using the same talker for target and interference

while manipulating the pitch difference. An experiment with LPC-resynthesized monotonous target speech showed a 20% increase in keyword recognition when going from same pitch to a 3-semitone difference. With a 12-semitone difference intelligibility decreased again, which the authors explain by the inseparability of the harmonics of target and interfering speech, yielding perceptual fusion of coinciding voiced portions. The results of a second experiment with natural speech and normal intonation did not show this decrease: keyword recognition was about 20% better when the target pitch was double that of the interference than when the pitches were the same. Brokx and Nooteboom (1982) related these findings to perceptual fusion, occurring when two simultaneous sounds have identical pitches, and to perceptual tracking when the pitches of target and interference cross each other, so that the listener may inadvertently switch his attention from target to interfering speech. In a recent study, Darwin *et al.* (2003) used PSOLA processing—pitch synchronous overlap add (Moulines and Charpentier, 1990), resulting in more naturally sounding manipulated speech compared to LPC resynthesis—with target and interfering speech from the same voice. Darwin *et al.* (2003) measured male and female talkers with the CRM paradigm, preserving the normal intonation of the sentences. They found no improvement when going from 0 to 1 semitone pitch difference, but a 12% increase in score when going to a difference of 2 semitones, averaged over SNRs of -6 to $+3$ dB. Stretching the difference to 12 semitones yielded a 24% increase.

B. Tactile support

Several methods of (vibro)tactile stimulation have been used in the past as an aid for speech perception by people with severe hearing impairment (Sherrick, 1984). The fact that experiments have shown (limited) benefits in speech perception shows that tactile information can indeed give some support. In several cases, multiple-channel tactile support was investigated; in this paper, however, we will restrict ourselves to single-channel tactile support. Normally, information is conveyed by presenting the amplitude fluctuations of the (filtered) speech signal to a tactile transducer, attached to the hand, wrist, or finger. Converting acoustic information in this manner appears to be appropriate, both in terms of sensitivity (with some amplification of modulation frequencies below 20 Hz, which are especially important for speech) and recognition of syllable rhythm and stress (Weisenberger, 1986; Weisenberger and Miller, 1987). A study by Summers *et al.* (1994) on the perception of time-varying pulse trains showed that information transfer for vibrotactile stimuli was highest when frequency and amplitude modulation were used together. This result was demonstrated explicitly for the perception of voice fundamental frequency and the identification of sentence stress. Although these and other studies in principle give ample evidence for the efficacy of tactile information transfer, the question still remains whether there is a natural or direct mapping of the acoustic events into the tactile domain—our fingers are simply not made to listen. Mahar *et al.* (1994) performed a number of cross-modal experiments to examine the similarity of auditory and tactile representations for speech(-like) stimuli. They concluded that comparisons between auditory and tactile stimuli are easier to perform than comparisons between auditory and visual, when it comes to word stress, amplitude variations, and temporally distributed information in general.

In this paper two experiments are described in which the effects of both acoustic factors and tactile support on speech intelligibility in multiple-talker conditions were studied. In the first experiment the speech-reception threshold (SRT) for sentences was measured against a background of one to eight interfering talkers or against speech noise. Vibro-tactile support was given by presenting the low-pass-filtered speech signal (0–200 Hz) simultaneously to the index finger. In order to obtain a clearer picture of the interaction between informational masking and the presence of tactile support, a second experiment was carried out, which focused on the effects of masking for one interfering talker, using different pitches and levels of the target and interfering voices. Again, speech intelligibility was determined both with and without tactile support.

II. EXPERIMENT 1: MULTIPLE COMPETING TALKERS

A. Stimuli, design

The target stimuli consisted of 13 lists of 13 meaningful Dutch sentences of 8 to 9 syllables pronounced by a male talker and representing conversational speech (Versfeld *et al.*, 2000). The interfering sound was either masking noise with the long-term average spectrum (and average rms level) of this talker or speech of other male talkers. A total of 60 sentences (15 sentences for each of 4 talkers) was used to create the speech interference. These meaningful sentences were taken from the original set of Plomp and Mimpen (1979), and were all different from the target sentences. The 15 sentences for each talker were concatenated and used either as a single interfering voice or mixed to produce 2, 4, or 8 interfering voices. The latter number was actually created by doubling the material for the 4-talker version; i.e., each talker occurred twice but with different initial sentences. All sentence and noise material was stored into WAV files with 44.1-kHz sampling rate and 16-bit resolution.

Because of the spectral shaping of the masking noise, it provides optimal (long-term) energetic masking of the target speech. In order to optimize the amount of energetic masking by the interfering talkers, their spectra were equalized with respect to the noise. Spectral shaping was done on each individual file with interfering speech (containing 1, 2, 4, or 8 talkers) in 8 octave bands from 63 Hz to 8 kHz, using a Behringer 8024 equalizer. Subsequently, the speech files were given the same A-weighted speech level as the noise (speech parts that were more than 14 dB below peak level were discarded, cf. Steeneken and Houtgast, 1986). The end result was that the overall long-term level of the speech masker was kept constant (equal to the noise masker), regardless of the number of interfering voices. However, it should be noted that equalizing the spectra is not enough to equalize energetic masking. Due to temporal modulations in the speech maskers, less masking will be produced than for a nonfluctuating masker (cf. Festen and Plomp, 1990). As the amount of fluctuations is reduced when more interfering

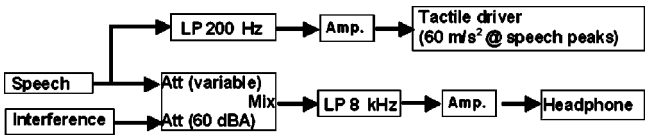

FIG. 1. Block diagram of the signal processing. Speech and interfering signal are mixed at a variable SNR and presented monaurally. Tactile information is derived from the low-pass filtered speech signal.

talkers are present, we may assume that the difference in energetic masking between speech and noise maskers will decrease with increasing number of interfering talkers. For the sake of clarity, the long-term rms values of the target sentences and of the speech or noise maskers were used to define the (global) SNR in the listening experiments.

There were ten conditions in which five types of interference were investigated in an experimental design with and without tactile support. Three extra conditions (with 1, 2, or 8 interfering talkers) were added in which the tactile support was replaced by visual support. This was done in order to determine whether stimulating a different modality with the same information would give the same results.

B. Signal processing

Figure 1 shows a block diagram of the signal processing for the presentation of auditory and tactile information. For the auditory pathway, target speech was mixed with the interference (noise or interfering speech) at a variable SNR and presented diotically over earphones. Tactile information consisted of the low-pass filtered target speech signal, presented through a vibrator. The cutoff frequency for the low-pass filter was set at 200 Hz. In this way the tactile stream contained all relevant information about the amplitude fluctuations (cf. Drullman *et al.*, 1994) and, moreover, conveyed the pitch variations of the target voice which might be used as an additional cue.

Signal processing was done in real time, using a standard PC equipped with an Aardvark Direct Pro 24/96 sound card. The auditory streams for target speech and interference were led through Tucker Davis PA4 attenuators and a SM3 mixer, a Krohn-Hite 3342 low-pass filter at 8 kHz (48 dB/oct), a Tucker Davis HB6 telephone amplifier, and presented over Sennheiser HD 250 headphones. The tactile stream was led through a Krohn-Hite 3342 low-pass filter (200 Hz, with 20-dB gain), a B&K 2706 amplifier to a B&K 4810 shaker. The setting of the amplifier and shaker was such that the maximum acceleration was 60 ms^{-2} at the speech peaks. This level was sufficient for the subjects to feel the tactile stimulation and not too high to be uncomfortable. For the visual support, the shaker was replaced by a small hand-held box with a red LED. The LED was controlled in the same way as the tactile driver, i.e., the brightness varied in accordance with the low-pass filtered speech amplitude.

C. Subjects

Subjects were 12 normal-hearing native Dutch students, mostly from Utrecht University, whose ages ranged from 19 to 26 years. All had pure-tone air-conduction thresholds less than 15 dB HL at octave frequencies from 125 Hz to 2 kHz and less than 25 dB HL up to 8 kHz. They were paid for their services.

D. Procedure

From the 13 lists of sentences, five were used for auditory presentation only, five for auditory presentation with tactile support, and three for auditory presentation with visual support. Lists were presented in a fixed order. Each list was used for one condition. Blocks of five auditory or auditory+tactile conditions were presented in a sequence. Half of the subjects started with the auditory-only conditions, the other half with the auditory+tactile conditions. The first condition in a block was the noise interference; the four interfering-talker conditions were balanced according to a 4×4 Latin square. The final three lists were used for the auditory+LED conditions (1, 2, or 8 interfering talkers), which were presented in random order.

In the SRT measurements, the level of the interference was fixed at 60 dBA for every condition; the level of the target sentences was changed according to an up–down adaptive procedure (Plomp and Mimpen, 1979). The first sentence in a list was presented at a level below the reception threshold. This sentence was repeated, each time at a 4-dB higher level, until the listener could reproduce it without a single error. The remaining 12 sentences were then presented only once, in a simple up–down procedure with a step size of 2 dB. A response was scored as correct only if all words were correctly reproduced by the subject. Subjects made verbal responses, which were not recorded. The average SNR for sentences 4–13 was adopted as the SRT for that particular condition. The interference was presented in a constant loop and was silenced in between the individual target sentences by muting the PA4 attenuator. On and offset of the interference was 500 ms before and after presentation of a target sentence.

Measurements were conducted for each subject individually in a sound-proof room. Subjects received written and oral instructions. During the conditions with tactile stimulation, they had their right arm on a special rest, so that they could feel the vibrations of the B&K shaker with their index finger, through a hole in the armrest.[2] An accelerometer which was mounted on the shaker merely functioned as the contact between shaker and figer. Prior to the actual tests, subjects were given a brief training (10–15 min), in order to get familiar with the target voice and with the procedure. Single words, short combinations of words (2–4 syllables), and entire sentences (different from the ones used in the tests) were presented, at a fixed SNR of −2 dB. While listening to target speech and interference, subjects received the tactile stimulation. They were explicitly told to note the correspondence between what they heard and felt. All subjects reported that they did indeed note this correspondence. There was no training for the visual support.

E. Results

The mean results of the SRT measurements as a function of type of interference and tactile/visual support are plotted

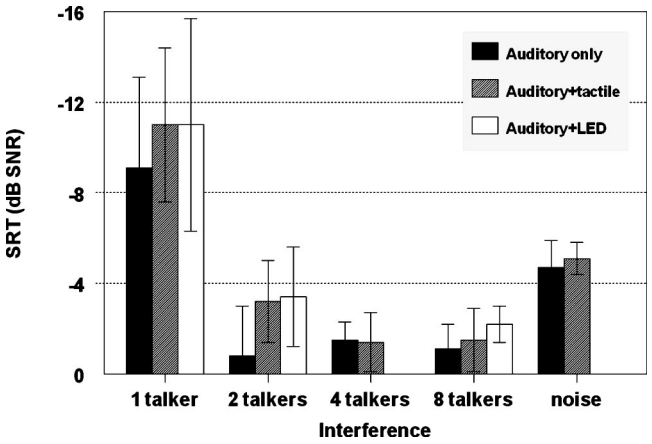

FIG. 2. Mean SRTs and standard deviations as a function of interference (1, 2, 4, or 8 interfering talkers, or noise). The more negative the SRT, the better the intelligibility.

in Fig. 2. Due to a technical error in the visual support for the first subject, results for the audio+LED conditions are based on 11 tests instead of 12. There appears to be a small overall effect of a lower SRT (i.e., higher intelligibility) when tactile or visual support is given. A two-way ANOVA with repeated measures revealed significant effects of tactile support ($p<0.05$) and type of interference ($p<0.001$), but no significant interaction. Overall, the mean SRT for auditory presentation is -3.4 dB and for auditory+tactile -4.4 dB. A separate analysis for the LED conditions showed that the overall change in SRT due to visual support is barely significant ($p=0.066$). Neither is there any significant interaction with the number of competing talkers. However, closer inspection of the data shows that the statistical analysis is strongly affected by the large variance in the conditions with only one interfering talker, as shown in Fig. 2. The standard deviations without and with tactile support are 4.0 and 3.4 dB, respectively, which is 2 to 4 times higher than the standard deviations for conditions with more interfering talkers or noise. We have therefore repeated the within-subjects ANOVA while excluding the single-interfering-talker conditions, and found a significant interaction between interference type and the presence of tactile or visual support ($p=0.028$). This confirms what is easily observed in Fig. 2, namely that the nonauditory support causes a relatively large (2.4-dB) release from masking when there are two interfering talkers, but that the effect vanishes when the number of interfering talkers is increased, or when noise is used as interference.

The conditions with only one interfering talker are nevertheless of interest because the mean SRTs are very low: -9.1 dB for auditory only and -11.0 dB with tactile support. Although the standard deviations are high, the SRTs scores are by far the best of all conditions. With only one interfering voice, it is probably possible to listen in the dips of the temporal envelope (momentary low-energy speech fragments) of the interference. This effect is apparently subject dependent and it is greatly reduced when more interfering voices are present.

III. EXPERIMENT 2: PITCH-VARYING SINGLE INTERFERING TALKER

The results of the above experiment indicate that the gain resulting from tactile or visual support is largest when there are only one or two interfering talkers, and disappears when the interference is babble or noise. Because informational masking has a similar dependency on the type of interference, this suggests that the gain is mainly a release from informational masking. However, it is not clear how much informational masking occurs in the particular speech material that we have used. As discussed in the Introduction, earlier research has indicated that informational masking depends on pitch differences between target and interfering speech (Brokx and Nooteboom, 1982; Darwin *et al.*, 2003). We therefore decided to carry out a second experiment in which the effect of tactile support was evaluated as a function of controlled pitch differences between target and interfering speech.

In a first approach, the same SRT paradigm as in experiment 1 was used. Results with 12 subjects showed no effects of tactile support and some effect of pitch difference. However, there was a large difference in performance between subjects. We concluded that for this type of experiment, with a single interfering voice that can be highly similar to the target voice, the SRT paradigm is not suitable. This is because the slope of the psychometric function can be very shallow or even obtain negative values (e.g., Brungart, 2001), so that there is a poor convergence of the adaptive procedure. To have a better differentiation between conditions, the percentage of correctly received words in a sentence list was used, as described in the following subsections.

A. Stimuli, design

A total of 420 sentences of a male target talker was taken from the same database as used in the first experiment (Versfeld *et al.*, 2000). Another 39 sentences from the same talker were used as interference. Both target sentences and (concatenated) interfering sentences were processed in such a way (see below) that the difference in average pitch would vary between conditions.

Sixty conditions for target speech and interference were investigated in an experimental design with five average pitch differences of 0, 2, 4, 8, and 12 semitones, six fixed SNRs of -16, -12, -8, -4, 0, and $+4$ dB, each with and without tactile support. The 420 target sentences were divided into 60 lists of 7 sentences, and instead of using an adaptive design as in the SRT, series of sentences were now presented at fixed SNRs. Intelligibility was measured by scoring the number of correctly received words per sentence (which contained on average 6.1 words).

B. Signal processing

Of all 420 target sentences the mean pitch per sentence was determined first. The algorithm used is based on an accurate autocorrelation method, with a frame duration of 10 ms (Boersma, 1993). The overall mean pitch of the 420 sentences was 105 Hz with a standard deviation of 15 Hz. In

TABLE I. Mean word scores (standard deviations) in percentages for the different conditions in experiment 2.

	Auditory only					Auditory+tactile				
	Δ pitch (semitones)					Δ pitch (semitones)				
SNR (dB)	0	2	4	8	12	0	2	4	8	12
−16	38(26)	38(17)	43(22)	51(21)	53(17)	40(28)	45(21)	49(23)	46(22)	65(17)
−12	64(19)	55(23)	60(27)	70(17)	79(12)	56(16)	71(17)	64(22)	82(11)	84(12)
−8	70(24)	72(22)	72(22)	82(13)	95 (6)	79(23)	79(15)	74(18)	87(11)	94 (7)
−4	56(21)	61(24)	69(23)	89(12)	96 (4)	65(16)	66(24)	73(15)	93 (7)	99 (2)
0	46(14)	49(26)	76(18)	97 (4)	99 (1)	73(21)	76(15)	90(13)	98 (3)	100 (1)
+4	76(29)	78(25)	92 (9)	100 (1)	100 (0)	87 (7)	91(12)	98 (3)	99 (2)	99 (1)

order to have control over the mean pitch differences between target and interfering sentences, all target sentences were resynthesized to have a mean pitch of 105 Hz. That is, the entire pitch contour of a sentence (voiced parts) was shifted up or down to get a mean of 105 Hz; the natural pitch contour was preserved. Signal processing was done by means of a PSOLA algorithm, implemented in the PRAAT software package (Boersma and Weenink, 1996). Subsequently, the interfering sentences were processed by making copies with mean pitches at 0, +2, +4, +8, and +12 semitones relative to 105 Hz.

Signal processing for the presentation of the auditory and tactile stimuli was identical as in the first experiment (see Fig. 1). In this second experiment there was no visual (LED) presentation.

C. Subjects

Subjects were ten normal-hearing native Dutch students, whose ages ranged from 19 to 25 years. They were different from the ones used in the first experiment. All had pure-tone air-conduction thresholds less than 15 dB HL at octave frequencies from 125 Hz to 2 kHz and less than 25 dB HL up to 8 kHz. They were paid for their services.

D. Procedure

From the 60 lists of 7 sentences, 30 were used for auditory only presentation and 30 for auditory+tactile presentation. Lists were presented in a fixed order, one list for one condition. The 30 auditory and 30 auditory+tactile conditions were presented consecutively. Half of the subjects started with the auditory conditions, the other half with the auditory+tactile conditions. Different mean pitches for interfering speech were balanced according to a 5×5 Latin square; the order of presentation of the SNRs was randomized. Conditions with the same pitch were presented in a block.

Measurements were performed for each subject individually in a sound-proof room. Subjects listened to the target speech and had to reproduce as many words of the target sentence as they could. Each target sentence was presented once, and word scores for sentence 2–7 were counted. The rest of the procedure was similar to the first experiment. Training was done prior to the real test, with +6 and +2 semitones pitch difference at a fixed SNR of −4 dB.

E. Results

Table I shows the results (means and standard deviations) for the different experimental conditions. Figures 3–5 display the results graphically, pooled over tactile conditions, pitch differences, and SNRs, respectively. As in the previous experiment, relatively high standard deviations are found. For the sake of clarity, the spread in the data is not displayed in Figs. 3–5, but is given only in Table I. The scores were

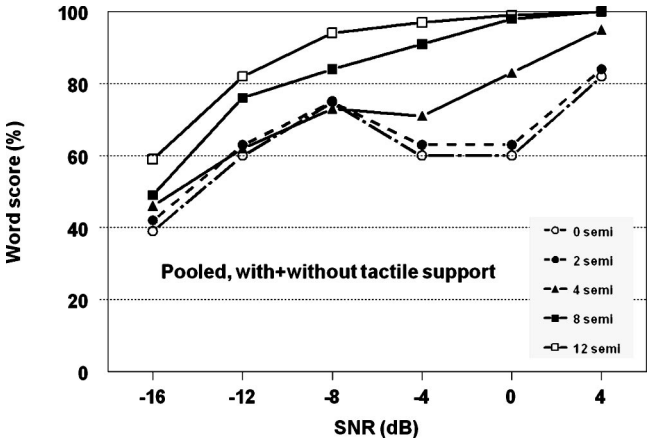

FIG. 3. Mean number of words correct as a function of SNR for target and interfering speech of the same talker. Data are pooled over auditory only and auditory+tactile support. Different curves correspond to mean pitch differences between target and interfering voice.

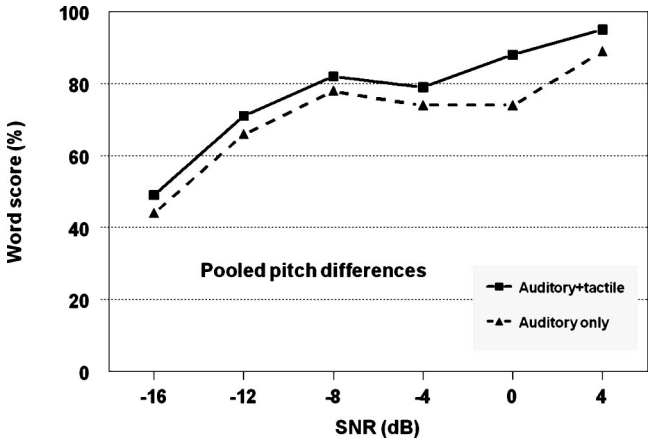

FIG. 4. Mean number of words correct as a function of SNR for target and interfering speech of the same talker. Data are pooled over a range of mean pitch differences between the voices (0 to 12 semitones). The two curves show the results with and without tactile support.

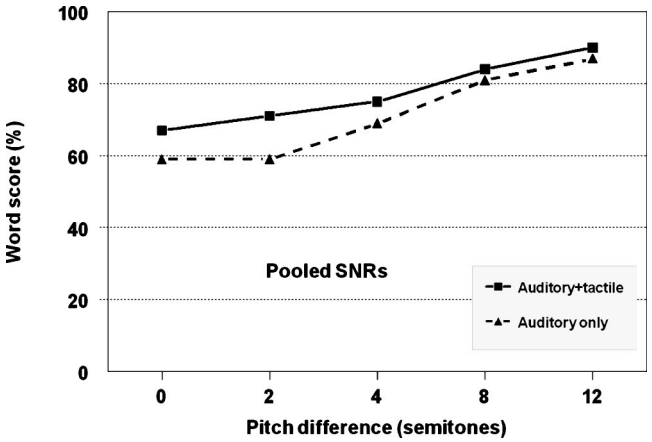

FIG. 5. Mean number of words correct as a function of mean pitch difference between target and interfering of the same talker. Data are pooled over a range of SNRs (−16 to +4 dB). The two curves show the results with and without tactile support.

analyzed by means of a repeated-measures ANOVA with three factors.[3] For the full experimental design, significant main effects are found for tactile support ($p<0.05$), pitch difference ($p<0.001$), and SNR ($p<0.001$). Of the four interactions, only the interaction between pitch difference and SNR is significant ($p<0.001$). The results of Figs. 4 and 5 indicate a small *overall* increase from 71% to 77% in word score due to tactile support. Performance improves with increasing pitch difference (Fig. 5), both with and without tactile support. A closer look at Fig. 3 shows a dip in the performance near 0-dB SNR when the mean pitch difference is 0 or 2 semitones. This is a situation where target and interference are most alike acoustically, and tactile support would presumably be most effective. Indeed, the data in Table I show a maximal increase of 27% for 0- and 2-semitone pitch differences at 0 dB SNR. For the entire range of SNRs, Fig. 6 displays the scores for the pooled 0- and 2-semitone conditions. A separate ANOVA on this subset reveals a significant interaction between tactile support and SNR ($p<0.02$). *Post hoc* comparisons (Tukey HSD) show a significant effect of tactile support at 0-dB SNR: from 48% words correct without to 75% words correct with tactile support.

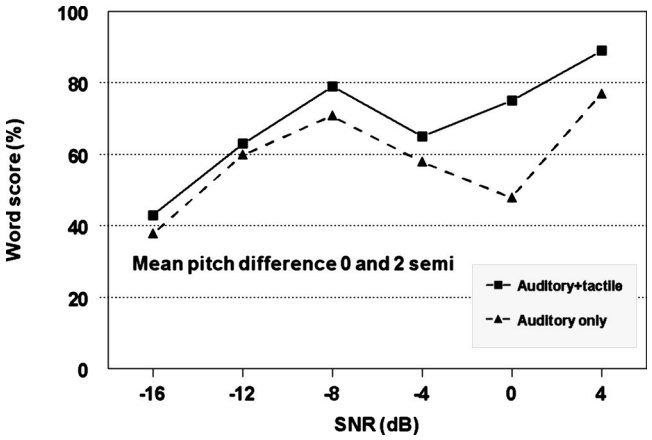

FIG. 6. As Fig. 4, but data pooled over mean pitch differences of 0 and 2 semitones only.

IV. GENERAL DISCUSSION

A. Tactile support

Both experiment 1 and 2 show evidence of a significant benefit of tactile support in sentence and word intelligibility. Due to the different measurement methods in the experiments, results are not directly comparable. We tried to employ the same SRT paradigm for experiment 2 as we did in experiment 1, but had to use a word-score paradigm because of the large differences in SRT performance between individual listeners.

In experiment 1 a tactile benefit of 0–2.4 dB in SRT (average 1 dB) is found. This gain does not, however, translate to a very high improvement in intelligibility such as found for sentences in steady-state noise, which show a steep slope of the psychometric function (about 15% per dB; see Versfeld *et al.*, 2000). In particular, when there is a single interfering talker, the steepness is reduced substantially. This cannot be derived from the data found in experiment 1,[4] but an indication is given by the results of experiment 2 (Fig. 4), where we see slopes of about 5%/dB around 50% intelligibility. Such shallow slopes for conditions with one interfering talker were also found by Brungart (2001) and Brungart *et al.* (2001). Thus, the 1-dB average gain in SRT found in experiment 1 seems to be roughly consistent with the average improvement in intelligibility of 6% in experiment 2.

All in all, we find evidence that presenting speech information through a different modality can indeed give some support in perception. This is true for vibrotactile support and—although investigated only in a limited set of conditions—also for visual support. It is most probably the focusing of attention that is responsible for the slight benefit: listeners are made aware of the moment the target talker is present, which can give them just a little advantage of ''listening in.'' The tactile or visual information itself does not contain any new or distinct elements that are not already present in the auditory signal. In this respect the visual cues given in our experiment are fundamentally different from the cues provided by lipreading.

B. Number of interfering talkers

The results of experiment 1 (Fig. 2) show a clear increase of the SRT when two or more interfering talkers are present. With the long-term interference levels being equal, this effect must be attributed to reduced ''dip listening.'' The presence of more talkers obstructs the advantage of listening to the target speech in case of low-energy fragments in the interfering speech. This effect is noted in many other studies on speech perception (e.g., Brungart *et al.*, 2001; Hawley *et al.*, 2004). Dip listening, however, is a very general psychoacoustical phenomenon (cf. Buus, 1985). In the present study, the advantage of dip listening vanishes already when going from one to two interfering talkers. Pooled over the tactile conditions, the SRT increases from −10 to −2 dB. The latter level remains approximately constant with four or eight interfering talkers.

Previous experiments with the same type of sentences showed an intelligibility score of only 36% for two simultaneous male voices presented at an SNR of 0 dB (Drullman

and Bronkhorst, 2000). These results were obtained from monaural listening, so they could be slightly better when presented diotically, like in the present experiment 1. Nevertheless, a score of 50% (definition of the SRT) at a SNR of −9.1 dB, as in experiment 1 (left-hand black bar in Fig. 2), would normally imply a (much) higher intelligibility at 0 dB. This discrepancy can probably be explained by the fact that level differences between target and masker act as a cue to the listeners (cf. Brungart, 2001). A low-level target voice can easily be discerned from a single high-level masking voice. The opposite it also true, and the result is that the psychometric function can have a local minimum around 0 dB SNR (see Fig. 3). Because the SRT paradigm starts at a low (negative) SNR, it normally converges also to a low SRT, except when it reaches SNRs around 0 dB: then, the outcome becomes unpredictable. This is—we think—the main reason why the SRT paradigm proved to be unsuccessful in our second experiment, and it probably also accounts for the very large standard deviations found for a single interfering talker in experiment 1.

Quantitative comparison between the present experiment 1 (without tactile support) and the study by Brungart *et al.* (2001) with multiple simultaneous talkers (one, two, or three interfering talkers) is difficult. The CRM paradigm they used is more a word intelligibility than a sentence intelligibility task. Moreover, target speech and interfering speech only differ in three keywords. The nature and timing of target and interfering speech is such that there is maximum masking of the keywords, so dip listening is less probable than with our speech material and paradigm. This is true even with a single interfering talker, because of temporal comodulation between target and interference. Despite the differences between the two studies, results from both our experiment 1 and from experiments by Brungart *et al.* (2001) show a substantial decrease in performance for more than one interfering talker. Our SRTs are always at (slightly) negative SNRs, and performance appears to fall into one of three categories: single interfering talker, many interfering talkers, or interfering noise. Surprisingly, the use of noise instead of speech makes it easier to understand the target talker, even compared to having as many as 8 interfering talkers: the SRT decreases from about −1.5 dB to about −5 dB for noise. This difference between speech and noise maskers is also clearly present in the results of Brungart *et al.* (2001) and can be best explained by the effect of informational masking (see also Sec. IV D below).

C. Pitch and level differences

The results of experiment 2 show that performance gradually improves when the difference in pitch between target and interfering voice increases (Fig. 5). However, the improvement is not monotonic, as can be seen in Fig. 3. When the difference is only 2 semitones, there is virtually no improvement compared to the condition with identical voices. These results are not exactly in agreement with results from the study by Darwin *et al.* (2003). As mentioned in the Introduction, they found increases of 12% up to 24% for pitch differences of 2 and 12 semitones, respectively, averaged over SNRs of −6 to +3 dB. In our experiment 2, averaged over −8- to +4-dB SNR, the increase for a 12-semitone pitch difference is 36%. This may be explained by the difference in sentence material and task, but it may also be caused by the particular talker. Darwin *et al.* (2003) show different results for four male talkers for which the performance of the listeners can vary significantly. The largest effect of the imposed pitch differences is found for talkers with a rather flat intonation. When a talker has a more expressive intonation, the effect is reduced, and it can even disappear. In another study, Bird and Darwin (1998) used monotone, natural male speech and PSOLA processing to present two sentences from the same talker with pitch differences from 0 to 12 semitones. With a limited number of interfering sentences, Bird and Darwin (1998) measured a maximum increase in word score of about 18% and 40% for pitch differences of 2 and 12 semitones, respectively.

In summary, our results show increases in performance for large pitch differences (12 semitones) that are generally in line with results from other studies. Differences must be attributed to talker characteristics, sentence material, and methodology. For small pitch differences (2 semitones), our experiment does not show any improvement in intelligibility, whereas other studies do find an improvement of over 10%.

We already mentioned that level differences in experiment 1 appear to act as a cue for separating two simultaneous voices. The results of experiment 2 indicate that a higher level for target speech generally helps perception, but that the results depend on pitch differences. An increase of the SNR causes a monotonic improvement of the intelligibility for conditions with large pitch differences of 8 and 12 semitones (Fig. 3). This monotonic relation starts to break down for a pitch difference of 4 semitones and disappears for differences of 2 and 0 semitones. In the latter cases, we see a clear decrease in the scores at SNRs of −4 and 0 dB. This leads to the conclusion that if a pitch difference is large, the cues for separating the two voices are strong enough to yield a high intelligibility score. If, on the other hand, the pitches are closer together, similar levels for target and interference make separation, and hence intelligibility, more difficult. These results are consistent with those of Brungart (2001), who reports large differences in performance between different-sex or same-sex (and same-talker) conditions. However, when manipulating only the pitch, as was done in the study by Darwin *et al.* (2003), the differences in performance are less clear than in the present study. Darwin *et al.* (2003) could only find a similar combined effect of pitch and level differences when they used both pitch and vocal-tract length changes, so in fact simulating two sex-related features of the voices. Results from the present study indicate that pitch manipulation alone may be sufficient to induce the level effect.

D. Energetic and informational masking

We did not record the responses of the subjects when they had to reproduce the target sentence. So, we cannot make a proper analysis of the errors that they made. From our observations during the experiments we conclude that intrusions were sometimes made, but more often subjects would reproduce only a few words or have complete blanks.

The subjects knew that the target and interfering sentences consisted of meaningful, everyday speech (syntactically and semantically correct), so intrusions are less likely to occur than in the CRM paradigm used by Brungart and colleagues. We think the fact that interfering noise and speech of many talkers yield different performances in the first experiment is sufficient evidence for informational masking.

As discussed in Sec. IV B, speech intelligibility decreases when the number of interfering talkers increases, and part of this effect can be attributed to dip listening. Momentary differences in energetic masking can, of course, occur during simultaneous presentation of target and interfering talker(s), as there is no fixed temporal alignment between them. It is also plausible that informational masking reduces as a function of the number of talkers because, when the interference sounds more like voice babble and separate words are not perceived clearly anymore, there is less chance that the target voice is confounded with one of the interfering voices.

The assumed reduction of informational masking with four and eight interfering talkers in experiment 1 implies that a value of the SRT is approached which must come close to the SRT in noise. Yet, there remains a gap of some 3.5 dB, in favor of the noise masker. We cannot explain this by differences in energetic masking. Speech babble and speech noise have very similar short- and long-term spectro-temporal characteristics. So, it must be assumed that there is still some form of informational masking. A possible explanation for this is provided by Hawley *et al.* (2004), who make a distinction between different levels of linguistic informational masking. In the case of one or two interfering talkers, when the interfering speech is still intelligible, grammatical and semantic information affect the ability of the listener to single out the target speech. With four or eight interfering talkers, the resulting babble can act as an informational masker at a lower linguistic level, by claiming phonetic and lexical processing resources even if this does not lead to any understanding of the interfering speech.

V. CONCLUSIONS

From the present experiments on multimodal speech perception, we can draw the following conclusions.

(1) Tactile support of diotically presented speech yields a moderate but significant increase of intelligibility in critical listening conditions. The observed benefit in intelligibility is between 0% and 27% (average 6%) and the shift in the SRT between 0 and 2.4 dB (average 1 dB). Although this was tested only in a limited number of conditions, it seems that a similar benefit occurs when temporal modulations are presented visually.

(2) The benefit due to tactile support depends on the type of interference. It is relatively large when there are one or two interfering talkers, but vanishes when the interference is steady-state noise or babble. In the case that the target and interfering voice are the same, and pitch differences are introduced, the maximum benefit is reached for a minimum pitch difference (0–2 semitones) and equal average speech levels.

(3) An increasing pitch difference between target and interfering speech causes a gradual increase of the intelligibility. The increase is up to 36%, averaged over SNRs from −8 to +4 dB.

(4) In conditions when target and interfering speech are highly similar (same voices with no or small pitch differences), the psychometric function becomes very shallow, and can even show a local minimum around 0-dB SNR.

[1]The generic term ''signal-to-noise ratio'' (SNR) is used throughout the paper. Noise can be either actual noise or interfering speech. ''Signal'' stands for target speech.

[2]The index finger was used as the most convenient means to convey tactile information and because there is a synchrony in the perception of the auditory and tactile stimuli (Hirsh and Sherrick, 1961).

[3]The statistical analyses presented here are based on the raw percentage scores. Analysis of the arcsine-transformed scores yields essentially the same results in terms of significance.

[4]Analogous to Versfeld *et al.* (2000) and Plomp and Mimpen (1979), we tried to derive psychometric functions of the SRT data for the conditions with one interfering talker in experiment 1. However, due to the limited number of data per SNR over 12 subjects, it was not possible to generate reliable slopes.

Assmann, P. F., and Summerfield, Q. (**1990**). ''Modeling the perception of concurrent vowels: Vowels with different fundamental frequencies,'' J. Acoust. Soc. Am. **88**, 680–697.

Bird, J., and Darwin, C. J. (**1998**). ''Effects of a difference in fundamental frequency in separating two sentences,'' in *Psychophysical and Physiological Advances in Hearing*, edited by A. R. Palmer, A. Rees, A. Q. Summerfield, and R. Meddis (Whurr, London, UK), pp. 263–269.

Boersma, P. (**1993**). ''Accurate short-term analysis of the fundamental frequency and the harmonics-to-noise ratio of a sampled sound,'' Proc. Institute of Phonetic Sciences University of Amsterdam **17**, 97–110.

Boersma, P., and Weenink, D. (**1996**). ''PRAAT. A system for doing phonetics by computer,'' Report 132, Institute of Phonetic Sciences, University of Amsterdam (http://www.fon.hum.uva.nl/praat).

Brokx, J. P. L., and Nooteboom, S. G. (**1982**). ''Intonation and the perceptual separation of simultaneous voices,'' J. Phonetics **10**, 23–36.

Bronkhorst, A. W. (**2000**). ''The cocktail party phenomenon: A review of research on speech intelligibility in multiple-talker conditions,'' Acust. Acta Acust. **86**, 117–128.

Brungart, D. S. (**2001**). ''Informational and energetic masking effects in the perception of two simultaneous talkers,'' J. Acoust. Soc. Am. **109**, 1101–1109.

Brungart, D. S., Simpson, B. D., Ericson, M. A., and Scott, K. R. (**2001**). ''Informational and energetic masking effects in the perception of multiple simultaneous talkers,'' J. Acoust. Soc. Am. **110**, 2527–2538.

Buus, S. (**1985**). ''Release from masking caused by envelope fluctuations,'' J. Acoust. Soc. Am. **78**, 1958–1965.

Culling, J. F., and Darwin, C. J. (**1993**). ''Perceptual separation of simultaneous vowels: Within and across-formant grouping by F_0,'' J. Acoust. Soc. Am. **93**, 3454–3467.

Darwin, C. J., Brungart, D. S., and Simpson, B. D. (**2003**). ''Effects of fundamental frequency and vocal-tract length changes on attention to one of two simultaneous talkers,'' J. Acoust. Soc. Am. **114**, 2913–2922.

Drullman, R., and Bronkhorst, A. W. (**2000**). ''Multichannel speech intelligibility and talker recognition using monaural, binaural, and three-dimensional auditory presentation,'' J. Acoust. Soc. Am. **107**, 2224–2235.

Drullman, R., Festen, J. M., and Plomp, R. (**1994**). ''Effect of temporal envelope smearing on speech reception,'' J. Acoust. Soc. Am. **95**, 1053–1064.

Festen, J. M., and Plomp, R. (**1990**). ''Effects of fluctuating noise and interfering speech on the speech-reception threshold for impaired and normal hearing,'' J. Acoust. Soc. Am. **88**, 1725–1736.

Hawley, M. L., Litovsky, R. L., and Culling, J. F. (**2004**). ''The benefit of binaural hearing in a cocktail party: Effect of location and type of interferer,'' J. Acoust. Soc. Am. **115**, 833–843.

Hirsh, I. J., and Sherrick, C. E. (**1961**). ''Perceived order in different sense modalities,'' J. Exp. Psychol. **62**, 423–432.

Mahar, D. M., Mackenzie, B., and McNicol, D. (**1994**). ''Modality-specific differences in the processing of spatially, temporally, and spatiotemporally distributed information,'' Perception **23**, 1369–1386.
Moulines, E., and Charpentier, F. (**1990**). ''Pitch synchronous waveform processing techniques for text-to-speech synthesis using diphones,'' Speech Commun. **9**, 453–467.
Plomp, R., and Mimpen, A. M. (**1979**). ''Improving the reliability of testing the speech reception threshold for sentences,'' Audiology **18**, 43–52.
Sherrick, C. E. (**1984**). ''Basic and applied research on tactile aids for deaf people: Progress and prospects,'' J. Acoust. Soc. Am. **75**, 1325–1342.
Steeneken, H. J. M., and Houtgast, T. (**1986**). ''Comparison of some methods for measuring speech levels,'' Report IZF 1986-20, TNO Institute for Perception, Soesterberg, The Netherlands.
Summers, I. R., Dixon, Ph. R., Cooper, Ph. G., Gratton, D. A., Brown, B. H., and Stevens, J. C. (**1994**). ''Vibrotactile and electrotactile perception of time-varying pulse trains,'' J. Acoust. Soc. Am. **95**, 1548–11558.
Versfeld, N. J., Daalder, L., Festen, J. M., and Festen, J. M. (**2000**). ''Method for the selection of sentence materials for efficient measurement of the speech reception threshold,'' J. Acoust. Soc. Am. **107**, 1671–1684.
Weisenberger, J. M. (**1986**). ''Sensitivity to amplitude-modulated vibrotactile signals,'' J. Acoust. Soc. Am. **80**, 1707–1715.
Weisenberger, J. M., and Miller, J. D. (**1987**). ''The role of tactile aids in providing information about acoustic stimuli,'' J. Acoust. Soc. Am. **82**, 906–916.

A comparison of vowel normalization procedures for language variation research

Patti Adank[a)]
Center for Language Studies, Radboud University Nijmegen, PO Box 9103, 6500 HD Nijmegen, The Netherlands

Roel Smits
Max Planck Institute for Psycholinguistics, PO Box 310, 6500 AH Nijmegen, The Netherlands

Roeland van Hout
Center for Language Studies, Radboud University Nijmegen, PO Box 9103, 6500 HD Nijmegen, The Netherlands

(Received 24 February 2004; revised 9 July 2004; accepted 26 July 2004)

An evaluation of vowel normalization procedures for the purpose of studying language variation is presented. The procedures were compared on how effectively they (a) preserve phonemic information, (b) preserve information about the talker's regional background (or sociolinguistic information), and (c) minimize anatomical/physiological variation in acoustic representations of vowels. Recordings were made for 80 female talkers and 80 male talkers of Dutch. These talkers were stratified according to their gender and regional background. The normalization procedures were applied to measurements of the fundamental frequency and the first three formant frequencies for a large set of vowel tokens. The normalization procedures were evaluated through statistical pattern analysis. The results show that normalization procedures that use information across multiple vowels (''vowel-extrinsic'' information) to normalize a single vowel token performed better than those that include only information contained in the vowel token itself (''vowel-intrinsic'' information). Furthermore, the results show that normalization procedures that operate on individual formants performed better than those that use information across multiple formants (e.g., ''formant-extrinsic'' $F2$-$F1$).
[DOI: 10.1121/1.1795335]

PACS numbers: 43.70.Jt, 43.71.Es, 43.70.Kv [AL] Pages: 3099–3107

I. INTRODUCTION

In their widely cited study on vowel perception, Ladefoged and Broadbent (1957) argue that three types of information are conveyed when a talker pronounces a vowel sound: (a) Phonemic information, i.e., the intended phonemic identity of the vowel sound; (b) anatomical/physiological information about the talker's vocal tract shape, gender, or physiology; and (c) sociolinguistic information, i.e., information about the talker's group characteristics, such as regional background or socioeconomic status. The first type of information is related to the linguistic message, whereas the second and the third types are talker-related. All three information types have been found to systematically affect formant frequencies (e.g., Peterson and Barney, 1952, for the first two information types and Hindle, 1978 and Labov, 2001, for the third type).

The influence of anatomical/physiological and sociolinguistic talker-related factors on formant frequencies has generally been treated as unwanted variation in research on vowel perception (Peterson and Barney, 1952; Pols *et al.*, 1973). Several studies aimed at eliminating the talker-related variation by designing procedures that can be subsumed under the heading of vowel, or talker, normalization (e.g., Gerstman, 1968; Lobanov, 1971; Nordström, 1976; Nearey, 1978; Syrdal and Gopal, 1986; Miller, 1989).

Traditionally, vowel normalization procedures are classified according to the type of information they employ. The procedures are defined as either vowel-intrinsic or vowel-extrinsic (Ainsworth, 1975; Nearey, 1989). Vowel-intrinsic procedures use only acoustic information contained within a single vowel token to normalize that vowel token. These procedures typically consist of a nonlinear transformation of the frequency scale (log, mel, bark), and/or a transformation based on a combination of formant frequencies (e.g., $F1$-$F10$). An example of an intrinsic procedure can be found in Syrdal and Gopal (1986). Vowel-extrinsic procedures, on the other hand, assume that information is required that is distributed across more than one vowel of a talker; e.g., the formant frequencies of the point vowels for that talker. Examples of extrinsic procedures can be found in Gerstman (1968), Lobanov (1971), Nordström (1976), and Nearey (1978). Generally speaking, vowel-intrinsic procedures were developed with the primary aim of modeling human vowel perception, while vowel-extrinsic procedures were developed with the purpose of obtaining higher percentages correctly classified vowel tokens for automatic speech recognition purposes.

In recent years, vowel normalization procedures have

[a)]Author to whom correspondence should be addressed. Electronic mail: p.adank@student.ru.nl

been applied in studies with a purpose other than modeling vowel perception or improving automatic vowel classification, i.e., in language variation studies describing the linguistic characteristics of vowel systems for specific languages or language varieties. These variation studies included vowel-intrinsic as well as vowel-extrinsic procedures. Labov (2001) used Nearey's (1978) logmean procedure for the description of the vowel system of Philadelphia. Most *et al.* (2000) used the procedure proposed by Syrdal and Gopal (1986) to describe the Hebrew vowel system. Watson *et al.* (2000) used Lobanov's (1971) procedure for their description of the vowels of New Zealand-English. Hagiwara (1997) transformed the formant values for the (Californian) American-English vowels to bark, as did Deterding (1997) for the vowels of Standard Southern British-English. Finally, Hillenbrand *et al.* (1995) transformed the vowels of American-English to $F1$-$F0$ and $F3$-$F2$ on a mel scale.[1]

However, using normalization procedures in language variation research is not without drawbacks. It has been reported that some normalization procedures introduce artificial variation patterns into the description when the vowel systems of the languages/dialects to be compared are not phonologically equivalent (Disner, 1980). Moreover, there are indications that applying normalization procedures reduces sociolinguistic variation in the acoustic representation along with the anatomical/physiological variation (Hindle, 1978). However, Labov (2001), evaluated the same two procedures as Hindle (1978), (i.e., Nearey, 1978 and Nordström, 1976) and stated that Hindle's conclusion was too strong and that most of the sociolinguistic variation was retained in the normalized data after normalization using Nearey's procedure.

The purpose of the present study is to establish to what extent vowel normalization procedures are suitable for use in language variation research and which (type of) procedure performs best. We attempted to extend earlier studies that compare vowel normalization procedures, such as Hindle (1978), Disner (1980), Syrdal and Gopal (1986), Nearey (1989), and Labov (2001) and to evaluate how well the procedures preserve sociolinguistic variation in normalized vowel data. Although the earlier studies can be said to have evaluated normalization procedures on how well they preserve sociolinguistic differences, they are limited in that a small number of talkers was used (Hindle, 1978; Labov, 2001), or in that the vowel systems that were compared were not phonologically equivalent (Disner, 1980).

We compared a set of eleven normalization procedures to a baseline condition (no normalization, i.e., formant frequencies in Hz) using measurements of the nine monophthongal vowels of Dutch, produced by 160 talkers of Dutch who were stratified for their gender and regional background. For each vowel token, the fundamental frequency and the frequencies of the first three formants were measured. Subsequently, we applied the procedures to the acoustic measurements, thus generating eleven normalized representations of the vowel data. These representations were compared on how well they preserved phonemic and sociolinguistic information and to what degree they succeeded in reducing anatomical/physiological information in each representation as compared to the other representations.

II. METHOD

A. Speech material

We used a database of measurements previously described in Adank *et al.* (2004) and in Adank (2003). These materials consist of recordings of 160 talkers of Dutch who were stratified for their regional background (speaking one of eight regional varieties of Standard Dutch) and their gender. The talkers can be regarded as professional language users, as they were all teachers of Dutch at secondary education institutes at the time the recordings were made. All 160 talkers produced two tokens of each of nine monophthongal vowels of Dutch, /ɑ a ɛ ɪ i ɔ u ʏ y/, in a neutral /sVs/ context.

Two speech communities were distinguished: The Netherlands and Flanders (Belgium). Two different varieties of Dutch can be identified: Northern Standard Dutch as spoken in the Netherlands, and Southern Standard Dutch as spoken in Flanders. The pronunciation of the two varieties has evolved differently from the time the Dutch area was split up in the 19th century. See Van de Velde *et al.* (1997) for a detailed overview. The 160 talkers were sampled across four regions per speech community: A central region, an intermediate region, and two peripheral regions. The central region is the economically and culturally dominant region in each speech community. For the Netherlands, the central region is the west, consisting of the provinces of North Holland, South Holland and Utrecht, also known as ''the Randstad.'' The cities Amsterdam, Rotterdam, Utrecht, and The Hague are part of the Randstad. In Flanders, the central region is ''Brabant.'' Brabant comprises the Belgian provinces Antwerpen and Flemish Brabant, with the cities of Antwerpen and Leuven, respectively. The intermediate region in the Netherlands encloses the southern part of the province Gelderland and part of the province Utrecht. The intermediate region in Flanders is the province East Flanders. In the Netherlands, the two peripheral regions are the province Limburg, in the south of the Netherlands, and the province Groningen, in the north of the Netherlands. The two peripheral regions for Flanders are the provinces (Belgian) Limburg and West Flanders. In each of the eight regions, recordings were made of twenty talkers, ten women and ten men.

The vowel tokens were recorded as a task in a so-called ''sociolinguistic interview'' in which vowels and consonants were elicited in a wide variety of tasks. All target vowels were produced in a carrier sentences task, which was repeated twice in the course of the interview. The vowels were available in three different consonantal contexts (CVC, CVCV, or V). The vowels in the CVC contexts (/sVs/) were selected for further processing. In total, 2880 vowel tokens were recorded: Two tokens of each of the nine monophthongal Dutch vowels, produced by 160 talkers.

Recording conditions were different for each of the talkers. Some were interviewed in an empty classroom and others were interviewed at their own home. Due to these differences in recording conditions, in rare cases, background

TABLE I. The selected procedures, divided according to whether they use vowel-intrinsic or vowel-extrinsic information.

	Vowel-intrinsic procedures
HZ	baseline condition, formant frequencies in Hz
LOG	log-transformation of the frequency scale
BARK	bark-transformation of the frequency scale
MEL	mel-transformation of the frequency scale
ERB	ERB-transformation of the frequency scale
S & G	Syrdal and Gopal's (1986) bark-distance model
	Vowel-extrinsic procedures
LOBANOV	Lobanov's (1971) z-score transformation
NEAREY1	Nearey's (1978) single logmean procedure
NEAREY2	Nearey's (1978) shared logmean procedure
GERSTMAN	Gerstman's (1968) range normalization
NORDSTRÖM	Nordström's (1976) vocal-tract scaling
MILLER	Miller's (1989) formant-ratio model

noises were audible. Whenever this was the case, the speech segment was excluded from further analysis.

$F0$, $F1$, $F2$, and $F3$ were extracted from each token's temporal mid point. $F0$ was extracted automatically with the speech-processing software program Praat using an autocorrelation-based procedure that was evaluated as the best option available in Praat (Boersma, 1993). The formant frequencies were obtained through a semiautomatic procedure developed by Nearey *et al.* (2002). For further details of the process through which the acoustic measurements were obtained, see Adank *et al.* (2004) and Adank (2003).

B. Selection of normalization procedures

Only normalization procedures that were described in previously published studies on acoustic vowel normalization were selected. A variety of studies evaluate the performance of procedures, either for use in language variation and change (Hindle, 1978; Disner, 1980), for a phonetic theory of vowel perception (Nearey, 1978, 1992; Syrdal, 1984; Nearey, 1978), or for automatic speech recognition (Deterding, 1990). We included all procedures described in these six studies that take formant frequencies as their input and that generate output in the form of normalized versions of those formant frequencies.[2] Table I lists the selected procedures.

Each procedure was implemented as follows. HZ, or the baseline condition, refers to the frequencies for the fundamental frequency $F0$ and formant frequencies $F1$ through $F3$. LOG refers to log-transformed $F0$ through $F3$ in Hz. BARK, the bark-transformation of the baseline, was implemented with Traunmüller's (1990) Eq. (1).[3] We decided to use this transformation, because Traunmüller (1990) shows that his equation fits Zwicker's (1961) table of critical bands better than Zwicker and Terhardt's (1980)

$$F_i^{\mathrm{B}} = 26.81 \times \left(\frac{F_i}{1960 + F_i} \right) - 0.53. \tag{1}$$

F_i in (1) is $F0$, $F1$, $F2$, or $F3$. The mel-transformed data, MEL, was obtained by transforming $F0$ through $F3$ using Stevens and Volkmann's (1940) equation as in (2)

$$F_i^{\mathrm{M}} = 2595 \times \ln\left(1 + \frac{F_i}{700} \right). \tag{2}$$

The ERB-transformation was implemented using Glasberg and Moore's (1990) Eq. (3).

$$F_i^{\mathrm{E}} = 21.4 \times \ln(0.004\,37 \times F_i + 1). \tag{3}$$

Syrdal and Gopal's bark-distance transformation (S & G) was implemented by first transforming $F0$ through $F3$ to bark using (1) and subsequently by applying Eqs. (4) and (5). Syrdal and Gopal (1986) originally used Zwicker and Terhardt's (1980) bark-transformation, while we used Traunmüller's (1990) for reasons stated above. We chose to use one type of bark-transformation in the present study; as a consequence Syrdal and Gopal's procedure was implemented with a bark-transformation different from the one they used in their 1986 paper.

$$F_1^{\mathrm{S\&G}} = F_1^{\mathrm{B}} - F_0^{\mathrm{B}}, \tag{4}$$

$$F_2^{\mathrm{S\&G}} = F_3^{\mathrm{B}} - F_2^{\mathrm{B}}. \tag{5}$$

Gerstman's (1968) normalization (GERSTMAN) was calculated for $F0$ through $F3$ as in (6)

$$F_{ti}^{\mathrm{Gerstman}} = 999 \times \frac{F_{ti} - F_{ti}^{\min}}{F_{ti}^{\max} - F_{ti}^{\min}}, \tag{6}$$

where $F_{ti}^{\min}$ is the minimum value of F_i for all nine vowels for talker t and $F_{ti}^{\max}$ is the maximum of F_i for the nine monophthongal vowels for that talker. Lobanov's (1971) z-score transformation was calculated for $F0$ through $F3$ as in Eq. (7)

$$F_{ti}^{\mathrm{Lobanov}} = \frac{F_{ti} - \mu_{ti}}{\delta_{ti}}, \tag{7}$$

where μ_{ti} is the average formant frequency across the nine monophthongal vowels for talker t and δ_{ti} refers to the standard deviation for average μ_{ti}. Nearey's (1978) single logmean (NEAREY1) was calculated for $F0$ through $F3$ as in Eq. (8)

$$F_{ti}^{\mathrm{Nearey1}} = F_{ti}^{\mathrm{L}} - \mu_{D_{ti}^{\mathrm{L}}}, \tag{8}$$

where F_{ti}^{L} is the log-transformed value of F_i for talker t and $\mu_{D_{ti}^{L}}$ is the average across the log-transformed formant frequencies across the nine vowels for that talker t. NEAREY1 uses a separate scale factor for each formant. Nearey's (1978) shared logmean (NEAREY2) uses a scale factor that is identical across formants. NEAREY2 was calculated for $F0$ through $F3$ as in (9).

$$F_{ti}^{\mathrm{Nearey2}} = F_{ti}^{\mathrm{L}} - (\mu_{D_{0t}^{\mathrm{L}}} + \mu_{D_{1t}^{\mathrm{L}}} + \mu_{D_{2t}^{\mathrm{L}}} + \mu_{D_{3t}^{\mathrm{L}}}). \tag{9}$$

The shared logmean $F_{ti}^{\mathrm{Nearey2}}$ is thus based on the four logmeans for $F0$, $F1$, $F2$, $F3$ ($\mu_{D_{0t}^{L}}$, $\mu_{D_{1t}^{L}}$, $\mu_{D_{2t}^{L}}$, and $\mu_{D_{3t}^{L}}$) in Eq. (9). Each log-transformed $F0$ or formant frequency is expressed as its distance to the shared logmean for a given talker t. Nordström's (1976) vocal-tract scaling, or NORDSTRÖM, was calculated as in (10) and (11)

$$F_i^{\mathrm{Nordström}} = kF_i^{\mathrm{female}}, \tag{10}$$

$$k = \frac{L^{\text{male}}}{L^{\text{female}}} = \frac{\mu_{F_3}^{\text{male}}}{\mu_{F_3}^{\text{female}}}, \tag{11}$$

where the scaling factor k in (11) expresses the ratio of the length L^{female} of the average female vocal tract to the length L^{male} of the average male vocal tract. k is calculated across all vowel tokens with an $F1$ greater than 600 Hz (across all 160 talkers), $\mu_{F_3}^{\text{male}}$ is the average $F3$ for all male talkers calculated across all vowel tokens with $F1 > 600$ Hz and $\mu_{F_3}^{\text{female}}$ is the average $F3$ for all female talkers calculated across all vowel tokens with $F1 > 600$ Hz. All values of $F0$ through $F3$ for the female talkers were subsequently transformed using (10). Finally, Miller's (1989) formant-ratio model was implemented using Eqs. (12)–(15).

$$F_{1t}^{\text{Miller}} = \left(\frac{F_{1t}^{\text{L}}}{SR} \right), \tag{12}$$

$$F_{2t}^{\text{Miller}} = \left(\frac{F_{2t}^{\text{L}}}{F_{1t}^{\text{L}}} \right), \tag{13}$$

$$F_{3t}^{\text{Miller}} = \left(\frac{F_{3t}^{\text{L}}}{F_{2t}^{\text{L}}} \right), \tag{14}$$

$$SR = k \left(\frac{\mu_{F_{0t}^{\text{L}}}}{k} \right)^{1/3}, \tag{15}$$

SR in (15) expresses Miller's talker-specific ''Sensory reference,'' which was calculated using the geometric average of all values of $F0$ for talker t, expressed by $\mu_{F_{0t}^{\text{L}}}$. The constant k reflects the geometric average of the overall average $F0$ across the 80 male (148 Hz) and 80 female talkers (234 Hz) and was set to 186 Hz for the present study.

III. RESULTS

A. Preserving phonemic variation

A series of discriminant analyses was carried out to establish how well the normalization procedures preserved information about the vowel token's intended phonemic identity in the normalized acoustic variables (two variables for S & G, three for MILLER, and four for all other methods). The acoustic variables served as predictors, while the intended vowel category, having nine possible values, was the dependent variable. A high percentage correctly classified vowel tokens indicates that the procedure succeeded at preserving phonemic variation.

Discriminant analysis (DA) is a standard pattern recognition technique that uses the pooled within-groups covariance matrix of the acoustic variables to classify cases. Linear discriminant analysis (LDA) assumes that the within-groups covariance matrices are equal across categories. If the data do not meet this assumption (which often holds for vowel formant frequencies), Quadratic discriminant analysis (QDA) is the appropriate analysis. However, although QDA theoretically models the individual vowel distributions more accurately, it has the drawback that it requires much larger numbers of parameters to be estimated than LDA, thus risking overfitting the data. Therefore, LDA as well as QDA were carried out. The results are presented in Table II.

TABLE II. Percentages correctly classified vowel tokens for LDA 1 and QDA 1 on the pooled data from 160 talkers. The dependent variable for each analysis is vowel category and $F0$ through $F3$ served as predictors. For LDA 1, all percentages higher than 81%, indicated by "$^{\uparrow}$," or lower than 77%, "$^{\downarrow}$," (all percentages are rounded off to the nearest whole number) are significantly different from the baseline condition (HZ). For QDA 1, this is 83% and 79%, respectively.

		LDA 1	QDA 1
	HZ	79	81
	LOG	80	81
Vowel-intrinsic	BARK	80	82
	ERB	80	82
	MEL	80	82
	S & G	$69^{\downarrow}$	70
	LOBANOV	$92^{\uparrow}$	$93^{\uparrow}$
	NEAREY1	90	$91^{\uparrow}$
Vowel-extrinsic	NEAREY2	$82^{\uparrow}$	83
	GERSTMAN	$84^{\uparrow}$	$86^{\uparrow}$
	NORDSTRÖM	$82^{\uparrow}$	$84^{\uparrow}$
	MILLER	$76^{\downarrow}$	77

Table II shows, first, that the percentages correctly classified vowel tokens for QDA 1 are only 1% to 2% higher than those for LDA 1. Given the parsimony of the LDA model relative to QDA, we decided to use LDA instead of QDA in the rest of this study. Second, it appears for LDA 1 that five procedures performed better than the baseline (HZ) and two procedure performed worse. LOBANOV (92%) and NEAREY1 (90%) preserved the phonemic variation in the data best of all procedures, followed by GERSTMAN (84%), NORDSTRÖM (82%), and NEAREY2 (82%), while MILLER (76%) and S & G (69%) performed poorest of all. No significant improvement over the baseline was found for the scale transformations LOG, BARK, ERB, and MEL.

Disner (1980) compared four procedures with raw data in Hz: Gerstman's range normalization (1968), Lobanov's z-transformation (1971), Nearey's logmean procedure (1978), and Harshman's (1970) PARAFAC model (not discussed in the present study). She applied these procedures to vowel data from six Germanic languages: English, Norwegian, Swedish, German, Danish, and Dutch. Disner calculated the percentage of scatter reduction of the formant frequencies per vowel in an $F1/F2$ plot per procedure. Her results show, although no specific procedure is the most effective for all the languages, that Nearey's procedure is generally the most effective (especially for Danish and Dutch). Lobanov's procedure is slightly less effective than Nearey's, followed by Gerstman's. Overall, our results seem compatible with Disner's.

Syrdal (1984) compared eight normalization procedures with raw data in Hz: The log-transformation, the bark-transformation, Syrdal's bark-difference model (1984), two versions of Miller (1980), two versions of Nearey's (1978) procedure, and Gerstman (1968). She applied them to Peterson and Barney's (1952) data set and calculated the percentage correctly classified vowel tokens from LDA. Overall, our results in Table II show a pattern similar to Syrdal's. Syrdal reports that Nearey's procedure (similar to NEAREY1) per-

TABLE III. Percentages correctly classified vowel tokens for LDA 2–4 on the pooled data from 160 talkers. The dependent variable for each analysis is gender (chance level 50%). For LDA 2, all percentages lower than 92% differ significantly from the baseline (HZ). For LDA 3, this is 87%, and for LDA 4, this is 78%. For all LDAs, percentages lower than 53% indicate performance at chance level (labeled with "*"). LDAs 3 and 4 were not carried out for S & G and MILLER; these procedures do not use $F0$, or $F1$-$F3$ in the same way as the other procedures [cf. Eqs. (4–5) and (12–15)].

	Predictor variables	LDA 2 $F0$, $F1$, $F2$, $F3$	LDA 3 $F0$	LDA 4 $F1$, $F2$, $F3$
	HZ	93	89	80
	LOG	93	89	80
Vowel-intrinsic	BARK	93	89	80
	ERB	93	89	80
	MEL	92	89	80
	S & G	53*	⋯	⋯
	LOBANOV	50*	51*	51*
	NEAREY1	50*	51*	49*
Vowel-extrinsic	NEAREY2	81	78	69
	GERSTMAN	53*	53*	51*
	NORDSTRÖM	83	82	52*
	MILLER	79	⋯	⋯

formed best, while we found that NEAREY1 performed second best, after LOBANOV (not evaluated by Syrdal). One major difference between Syrdal's results and our results is that Syrdal reports that the bark-difference procedure (nearly identical to S & G) performed better (85.9%) than her baseline condition (82.3%), while we found that S & G performed poorer than the baseline. This discrepancy may be partly attributed to differences in the implementation of the bark-transformation: Syrdal used Zwicker and Terhardt's (1980) and we used Traunmüller's (1990). Furthermore, we used talkers of Dutch and Syrdal's talkers spoke American English. Dutch may be one of the languages that cannot be described adequately by S & G's second dimension [cf. Eq. (5)]. Syrdal and Gopal (1986) stated that the critical distance for the front-back dimension [cf. Eq. (4)] is language-specific and that this distance is not a language-universal measure reflecting front-back vowel distinctions.

B. Reducing anatomical/physiological variation

Three LDAs were carried out (LDA 2–4) to establish to what extent anatomical/physiological gender-related variation was eliminated from the transformed data. LDA 2 evaluated whether information on the talker's gender was present in all four procedures' output. For LDA 2, the procedures' output variables served as predictors. LDA 3 and LDA 4 were carried out to investigate whether differences between the procedures found for LDA 2 could be attributed for the most part to gender-specific $F0$-differences, or to differences in the formant frequencies. In LDA 3, $F0$ served as the sole predictor, and $F1$, $F2$, and $F3$ served as predictors in LDA 4. For all three LDAs, it is assumed that a procedure is successful at eliminating gender-related anatomical/physiological variation when performing at chance level (50%).

Table III shows the results for LDA 2–4. For LDA 2, 93% of the vowel tokens were categorized correctly (i.e., as spoken by a male or female talker) for HZ, indicating that the raw measurements display considerable anatomical/physiological variation. Only LOBANOV, NEAREY1, and GERSTMAN performed at chance level for LDA 2, the other procedures did not eliminate all gender-specific variation. In particular, the scale transformations did not remove any gender-related variation. The results for LDA 3 show first that $F0$ displays a lot of gender-specific variation; for HZ 89% of the vowel tokens could be classified correctly when only $F0$ was entered as a predictor variable. The variation in $F0$ stems most likely from differences in the anatomy and physiology of the larynx of males and females. The pattern in the results for LDA 3 is similar to the pattern found for LDA 2: LOBANOV, NEAREY1, and GERSTMAN performed best (at chance level), while all the other procedures perform above chance level. Finally, $F1$, $F2$, and $F3$ display anatomical/physiological gender-related variation as well, although less than $F0$. This variation probably originates from differences in vocal-tract length between males and females. NORDSTRÖM, a procedure designed to account for vocal-tract length differences, eliminated gender-related variation completely. Recall that LDA 3 showed that NORDSTRÖM was not successful at eliminating the (larynx-related) anatomical/physiological variation in $F0$.

Syrdal (1984) carried out an LDA that classified the data as having been produced by a man, woman, or a child. The results in our Table III are compatible with the results in Syrdal's (1984) Table II. For the procedures that are common to our study and Syrdal's study, Syrdal found that Nearey's and Gerstman's procedures performed best (at chance level), while the other procedures performed above chance level.

C. Preserving sociolinguistic variation

The 160 talkers were stratified for regional background (eight regional varieties). LDA 5 served to establish to what extent regional (sociolinguistic) variation was preserved in the transformed acoustic representations of the vowel data. $F0$ through $F3$, transformed through each normalization procedure, were entered as predictors. Region served as the dependent variable, having eight levels. The analysis was repeated for each of the nine vowels, to eliminate the effect of the vowel token's category. If a certain procedure brought a classification level down from a value above chance level

TABLE IV. Results for LDA 5: Percentages of vowel tokens that were classified into the correct region, for each vowel category, for each normalization procedure. The number of cases per vowel category is 320. Percentages higher than 18% (rounded) are significantly higher than chance level (12.5%), percentages at chance level are indicated with ''*''.

		/ɑ/	/a/	/ɛ/	/ɪ/	/i/	/ɔ/	/u/	/ʏ/	/y/	Average
Vowel-intrinsic	HZ	27	23	36	35	29	29	33	38	26	31
	LOG	26	20	37	33	26	31	33	36	26	30
	BARK	27	22	35	34	26	29	33	37	27	30
	ERB	26	22	35	34	26	30	33	37	27	30
	MEL	27	22	35	33	26	29	33	37	25	30
	S & G	22	19	32	30	20	25	25	28	22	25
Vowel-extrinsic	LOBANOV	26	18	35	31	28	27	32	25	31	28
	NEAREY1	23	19	34	31	29	29	33	31	28	28
	NEAREY2	28	20	27	35	31	31	30	32	25	30
	GERSTMAN	25	22	36	34	19	26	25	31	26	27
	NORDSTRÖM	27	21	37	33	29	30	33	34	27	30
	MILLER	23	17*	35	31	31	25	29	32	23	27
	Average	26	20	35	33	26	28	31	33	26	29

(12.5%), it must be concluded that the procedure reduces systematic sociolinguistic variation related to the talker's regional background.

Table IV shows the results for LDA 5. It can first be observed, that the percentages correctly classified vowel tokens are generally above chance level across all procedures, indicating that none of the investigated procedures eliminated all sociolinguistic variation. Second, some differences between procedures can be observed: S & G eliminated more sociolinguistic variation than the other procedures, followed by GERSTMAN and MILLER, LOBANOV, and NEAREY1. Procedures that reduce anatomical/physiological variation most effectively show a larger reduction of the sociolinguistic variation. Furthermore, this reduction is not uniform across vowels for a given procedure (e.g., LOBANOV shows a large reduction for /a/ and a small reduction for /ɛ/). Table IV shows finally that /ɛ/, /ɪ/, and /ʏ/ display the most regional variation. The point vowels /a/ and /i/ show little regional variation, while /u/ shows slightly more variation.

D. Comparing the sources of variation

The LDA-based analyses presented in the previous section treat the normalization issue as a pattern recognition problem: How accurately can vowel identity, talker-gender, and regional background be recognized from the normalized acoustic data. The present analysis is based on the reverse approach: how much of the variation in the normalized data can be explained from the three factors vowel, talker-gender, and regional background. Several Multivariate Analyses of Variance (MANOVA) were carried out to reveal how the procedures deal with the variation in the acoustic measurements related to the three variation sources (phonemic, anatomical/physiological, and sociolinguistic). In each MANOVA, the talker's gender (''Gender''), the talker's regional background (''Region''), and the vowel token's category (''Vowel'') were used to predict the variation in the transformed acoustic variables. Only the baseline procedure HZ and the three procedures that were most successful at preserving phonemic variation and reducing anatomical/physiological variation, LOBANOV, NEAREY1, and GERSTMAN, were included. The MANOVAs were repeated three times, once with $F0$, $F1$, $F2$, $F3$ as dependent variables, once with $F1$, $F2$, $F3$, and once with only $F1$ and $F2$. This was done to evaluate the effect of eliminating $F0$, and $F0$ as well as $F3$, from the analysis. The multivariate measure of effect size for each set of factors and interaction terms was η^2, which reveals the proportion of the total variation in the dependent variable that is accounted for by the variation in the independent variable. The significance level was estimated using Pillai's trace.[4]

A high value for η^2 in Table V for the factor Vowel indicates that a lot of the phonemic variation in the dependent variables can be predicted by the vowel categories, indicating the preservation of phonemic variation in the acoustic variables. Subsequently, a low value of η^2 for the factor Gender indicates that there is relatively little anatomical/physiological gender-related variation present in the dependent variables. Finally, a high value for η^2 for the interaction between Vowel and Region indicates that sociolinguistic (regional) variation is preserved in the dependent variables. The interaction between Region and Vowel gives a better indication about the presence of regional variation in the data than the factor Region by itself. It seems likely that (large) effects for Region would only be found if the size and shape of the entire vowel systems differ across regions. This does not seem plausible, given the results in Table IV for the cardinal vowels /a/ and /i/, which were relatively stable across regions. Instead, a significant effect of η^2 for Vowel×Region indicates that some vowels show more regional variation than others, which seems plausible, given the relatively high percentages of /ɛ/, /ɪ/, and /ʏ/ in Table IV.

Table V shows that η^2 is highest for the factor Vowel across all procedures. Only for HZ, the largest variation in the dependent variables could be accounted for by the factor Gender (for $F0$ through $F3$, Gender shows a larger effect than Vowel). In contrast, there is no effect for Gender for LOBANOV and NEAREY1, and only a very small effect for GERSTMAN. This corroborates the earlier finding that these three procedures effectively removed all anatomical/physiological variation from the acoustic measurements. No significant effects were found for Region for LOBANOV and NEAREY1, and relatively small effects for HZ and

TABLE V. Results for the four multivariate analyses of variance: η^2 for each significant factor, for each of the four procedures ($p<0.001$). Values of η^2 not significantly different from 0 are not included. For each procedure, the analysis is repeated for three different sets of dependent variables. The number of tokens per analysis is 2880.

	HZ			LOBANOV			NEAREY1			GERSTMAN		
η^2	*F*0 *F*1 *F*2 *F*3	*F*1 *F*2 *F*3	*F*1 *F*2	*F*0 *F*1 *F*2 *F*3	*F*1 *F*2 *F*3	*F*1 *F*2	*F*0 *F*1 *F*2 *F*3	*F*1 *F*2 *F*3	*F*1 *F*2	*F*0 *F*1 *F*2 *F*3	*F*1 *F*2 *F*3	*F*1 *F*2
Vowel	0.527	0.695	0.893	0.579	0.760	0.932	0.556	0.731	0.914	0.568	0.743	0.917
Region	0.075	0.080	0.063	⋯	⋯	⋯	0.041	0.051	0.067	⋯	⋯	⋯
Gender	0.770	0.656	0.537	⋯	⋯	⋯	0.018	0.014	0.014	⋯	⋯	⋯
Vowel×Region	0.120	0.151	0.183	0.150	0.190	0.236	0.126	0.159	0.200	0.139	0.173	0.207
Vowel×Gender	0.064	0.079	0.108	0.014	0.017	0.019	0.011	0.014	0.016	0.019	0.024	0.025
Region×Gender	0.017	0.010	0.011	⋯	⋯	⋯	0.016	0.016	0.019	⋯	⋯	⋯
Vowel×Region×Gender	0.031	0.036	0.036	0.030	0.032	⋯	⋯	⋯	⋯	0.039	0.043	0.039
Vowel×Region×Gender	⋯	⋯	⋯	0.030	0.033	0.033	⋯	⋯	⋯	0.029	0.033	0.032

GERSTMAN. In the light of the discussion of the relevance of the effect for Region versus Vowel×Region, the small effects for HZ and GERSTMAN should not be overrated. Table V shows relatively large effects for all four procedures for Vowel×Region. The effects are largest for LOBANOV and GERSTMAN, indicating that a larger proportion of the sociolinguistic variation in the data can be accounted for after transforming data with these two procedures. Table V shows further that excluding *F*0 from the analysis leads to higher values for η^2 for all four MANOVAs for Vowel and Vowel×Region. Excluding *F*0 as well as *F*3 results in even higher values for η^2 for Vowel and Vowel×Region.[5] In summary, it appears from Table V that, after normalization with LOBANOV and GERSTMAN, the phonemic and the sociolinguistic variation are preserved best of all four procedures in the dependent variables, while the gender-related anatomical/physiological variation appears to be minimized.

IV. DISCUSSION

The aim of this study was to establish to what extent procedures for vowel normalization are suitable for use in language variation research. We carried out three evaluations using eleven normalization procedures that were applied to Dutch vowel data from talkers who were stratified for the factors region and gender.

The procedures were first evaluated on how well they preserved phonemic variation in the transformed vowel data, second on how well they reduced anatomical/physiological variation, and third on how well they preserved sociolinguistic (regional) variation. Given the results for these comparisons, it can be concluded that procedures for vowel normalization can be useful tools in dealing with (unwanted) anatomical/physiological talker-specific variation in studies investigating regional variation in vowel systems. However, this is only valid for a subset of the procedures evaluated: LOBANOV, or Lobanov's (1971) z-score transformation, NEAREY1, or Nearey's (1978) single logmean procedure, and GERSTMAN, or Gerstman's (1968) range transformation. These three procedures were found to preserve phonemic variation best, reduce anatomical/physiological variation most effectively, while at the same time preserving nearly all sociolinguistic variation in the acoustic measurements. After comparing the three sources of variation (vowel, region, and gender) by multivariate analysis, LOBANOV turned out to be the best procedure, although the difference with NEAREY1 is relatively small.

Although this paper does not aim to develop a theory of how listeners normalize vowels, below we discuss the results from a perceptual perspective. Our finding that the three most successful procedures are all vowel-extrinsic procedures and the least successful procedures are all vowel-intrinsic procedures is surprising, because it has been suggested that intrinsic procedures reflect or resemble processes involved in human speech perception better than extrinsic procedures (Syrdal and Gopal, 1986). Vowel-intrinsic models were considered to be more suitable as models for human vowel perception because they, in analogy with human listeners (e.g., Assmann *et al.*, 1982), can normalize a single vowel from a speaker without information about other vowels from that speaker (Nearey, 1989). Vowel-extrinsic procedures, on the other hand, generally require information across multiple vowels (if not all) per speaker to calculate the scale factors necessary for the normalization. Thus, to normalize one vowel from a speaker, the procedure first has to know all other vowel positions of that speaker. Nevertheless, it should not be overlooked that listeners have had years of exposure to different talkers' voices before being able to categorize vowel tokens effectively. Even if listeners are presented with a new speaker, they may use their experience of hearing other, perhaps similar, voices. Given our results for the three vowel-extrinsic procedures, we hypothesize that LOBANOV, NEAREY1, and GERSTMAN can account for the listeners' experience through the use of scaling factors that model the distribution of other vowels produced by the same talker.

But why did some of the vowel-intrinsic procedures perform so poorly? For instance, Syrdal and Gopal's (1986) S & G performed poorer than raw data in Hz at most tasks evaluated. Overall, the poor performance of this procedure can be attributed to the fact that it did not succeed in clustering the transformed vowel data as effectively as most vowel-extrinsic procedures. However, another explanation may be that it incorporates information across different formants (e.g., *F*3-*F*2) for a given vowel token. The overall results

TABLE VI. Classification of the normalization procedures according to whether they use vowel-intrinsic or vowel-extrinsic information, and whether they use formant-intrinsic or formant-extrinsic information.

Information	Vowel-intrinsic	Vowel-extrinsic
Formant-intrinsic	HZ, LOG, BARK, MEL, ERB	GERSTMAN, LOBANOV, NEAREY1
Formant-extrinsic	S & G	NORDSTRÖM, MILLER, NEAREY2

show that vowel-extrinsic procedures that incorporate information across formants (NEAREY2, NORDSTRÖM, and MILLER) perform poorer than those who include only information within formants (LOBANOV, NEAREY1, and GERSTMAN). This pattern is especially clear for NEAREY1 and NEAREY2, which differ only in that NEAREY2 includes information across formants, while NEAREY1 does not. Summarizing, we find that procedures using information across vowels performed better than procedures using only information within vowels and procedures using information within formants performed better than those using information across formants. Given this pattern in the results, we suggest to expand the traditional intrinsic/extrinsic division of procedures to the formants. This way, formant-intrinsic and formant-extrinsic categories are distinguished as well as vowel-intrinsic and vowel-extrinsic categories. The procedures that were evaluated in the present paper are classified according to this extended division in Table VI.

In conclusion, vowel-extrinsic, formant-intrinsic normalization procedures can be useful and accurate tools for research investigating language variation. Application of these normalization procedures to the measurements of the fundamental frequency. The frequencies of the first three formants produced by different talkers eliminates anatomical/physiological variation. The variation that remains in the data is either phonemic or sociolinguistic in nature. Normalization is especially useful when data from male and female talkers is to be compared, as the successful procedures eliminated all variation related to the talker's gender. An additional benefit for language variation research is that the most successful procedures are also the easiest to implement. Finally, Hindle's (1978) concern, applying normalization procedures may reduce sociolinguistic variation in the acoustic representation along with the anatomical/physiological variation, does not generally hold. Instead, it appears that our results for LOBANOV, NEAREY1, and GERSTMAN confirm results reported in Labov (2001): most sociolinguistic variation was retained in the normalized data.

ACKNOWLEDGMENTS

This research was supported by the Netherlands Organization for Research (NWO) through the Flemish Netherlands Committee (VNC) under project nr. 205-41-069 (PI Roeland van Hout).

[1]We considerer a scale transformation such as a transformation to a bark-scale, or to a mel-scale, to be a normalization procedure as well.

[2]The following procedures were not selected: Wakita (1977), Bladon and Lindblom (1981), Hermansky *et al.* (1985), and Pickering (1986), which were all four evaluated in Deterding (1990), and Harshman (1970), as described in Disner (1980).

[3]Traunmüller (1990) provides a low frequency correction as well as a high frequency correction. We decided not to use either for the following reasons. First, although the low frequency correction ensures that the transformed data resembles the rounded values of Zwicker's (1961) table more closely, Traunmüller (1990) states that the uncorrected form approximates the actual empirical data in Zwicker *et al.* (1957) more closely at low frequencies. Second, the high frequency correction aims to reduce inaccuracies above 20.1 Bark (around 8 kHz), but we were only interested in the frequency regions up to 4 kHz.

[4]One of the appropriate tests available in multivariate analysis of variance, used for reflecting the proportion of the variance in the dependent variable that can be accounted for, given the independent variable(s). See Stevens (1979).

[5]It may suffice to use only $F1$ and $F2$ to describe the data acoustically. To find further evidence for this idea, LDA 1 (cf. Table II) was repeated for the four procedures HZ, LOBANOV, NEAREY1 and GERSTMAN, this time using only (transformed) $F1$ and $F2$ as predictors. The results for HZ showed that 72% of the vowel tokens could be correctly classified when only $F1$ and $F2$ were entered as predictors, as opposed to 79% for LDA 1, for LOBANOV this was 91% as opposed to 92% for LDA 1, for NEAREY1 it was 87% as opposed to 90% for LDA 1, and for GERSTMAN a percentage of 83% was found as opposed to 84% for LDA 1. Overall, the scores for the analysis with $F1$ and $F2$ as predictors are 1–7 percent points lower than the analysis with $F0$, $F1$, $F2$, and $F3$ as predictors. The largest difference (7%) was found for the untransformed data, the percentages for the transformed data decreased only 1%–3%. It thus appears that Dutch may be described relatively effectively using only $F1$ and $F2$, after transformation through LOBANOV, NEAREY1, or GERSTMAN.

Adank, P. (**2003**). ''Vowel normalization: a perceptual-acoustic study of Dutch vowels,'' PhD thesis, University of Nijmegen.

Adank, P., van Hout, R., and Smits, R. (**2004**). ''An acoustic description of the vowels of Northern and Southern Standard Dutch,'' J. Acoust. Soc. Am. **116**, 1729–1738.

Ainsworth, W. A. (**1975**). ''Intrinsic and extrinsic factors in vowel judgements,'' in *Auditory Analysis and Perception of Speech*, edited by G. Fant and M. A. A. Tatham (Academic, London).

Assmann, P. F., Nearey, T. M., and Hogan, J. T. (**1982**). ''Vowel identification: Orthographic, perceptual, and acoustics aspects,'' J. Acoust. Soc. Am. **71**, 975–989.

Bladon, R. A., and Lindblom, B. (**1981**). ''Modeling the judgement of vowel quality differences,'' J. Acoust. Soc. Am. **69**, 1414–1422.

Boersma, P. (**1993**). ''Accurate short-term analysis of fundamental frequency and the harmonics-to-noise ratio of a sampled sound,'' in *Proceedings of the Institute of Phonetic Sciences of the University of Amsterdam*, **17**, pp. 97–110.

Deterding, D. (**1990**). ''Speaker normalization for automatic speech recognition,'' PhD thesis, University of Cambridge.

Deterding, D. (**1997**). ''The formants of monophthong vowels in Standard Southern British English Pronunciation,'' J. Int. Phon. Assoc. **27**, 47–55.

Disner, S. (**1980**). ''Evaluation of vowel normalization procedures,'' J. Acoust. Soc. Am. **67**, 253–261.

Gerstman, L. (**1968**). ''Classification of self-normalized vowels,'' IEEE Trans. Audio Electroacoust. **AU-16**, 78–80.

Glasberg, B. R., and Moore, B. C. J. (**1990**). ''Derivation of auditory filter shapes from notched noise data,'' Hear. Res. **47**, 103–138.

Hagiwara, R. (**1997**). ''Dialect variation and formant frequency: The American English vowels revisited,'' J. Acoust. Soc. Am. **102**, 655–658.

Harshman, T. (**1970**). ''Foundations of the PARAFAC procedure: Models and conditions for an ''explanatory'' multi-model factor analysis,'' In Working Papers in Phonetics, **16**, Phonetics Lab UCLA.

Hermansky, H., Hanson, B. A., and Wakita, H. (**1985**). ''Low-dimensional representation of vowels based on all-pole modeling in the physiological domain,'' Speech Commun. **10**, 509–512.

Hillenbrand, J., Getty, L. A., Clark, M. J., and Wheeler, K. (**1995**). ''Acous-

tic analysis of American English vowels,'' J. Acoust. Soc. Am. **97**, 3099–3111.
Hindle, D. (**1978**). ''Approaches to formant normalization in the study of natural speech,'' in *Linguistic Variation, Models and Methods*, edited by D. Sankoff (Academic, New York).
Labov, W. (**2001**). *Principles of Linguistic Change: Vol. II: Social factors* (Blackwell, Oxford).
Ladefoged, P., and Broadbent, D. E. (**1957**). ''Information conveyed by vowels,'' J. Acoust. Soc. Am. **29**, 88–104.
Lobanov, B. M. (**1971**). ''Classification of Russian vowels spoken by different speakers,'' J. Acoust. Soc. Am. **49**, 606–608.
Miller, J. D. (**1989**). ''Auditory-perceptual interpretation of the vowel,'' J. Acoust. Soc. Am. **85**, 2114–2134.
Most, T., Amir, O., and Tobin, Y. (**2000**). ''The Hebrew Vowel System: raw and normalized acoustic Data,'' Lang Speech **43**, 295–308.
Nearey, T. M. (**1978**). *Phonetic Feature Systems for Vowels* (Indiana University Linguistics Club, Indiana).
Nearey, T. M. (**1989**). ''Static, dynamic, and relational properties in speech perception,'' J. Acoust. Soc. Am. **85**, 2088–2113.
Nearey, T. M. (**1992**). ''Applications of generalized linear modeling to vowel data,'' in Proceedings of the 1992 International Conference on Spoken Language Processing, 583–587.
Nearey, T. M., Assmann, P., and Hillenbrand, J. (**2002**). ''Evaluation of a strategy for automatic formant tracking,'' J. Acoust. Soc. Am. **112**, 2323.
Nordström, P. E. (**1976**). ''Female and infant vocal tracts simulated from male area functions,'' J. Phonetics **5**, 81–92.
Peterson, G. E., and Barney, H. L. (**1952**). ''Control methods used in the study of the vowels,'' J. Acoust. Soc. Am. **24**, 175–184.
Pickering, J. B. (**1986**). ''Auditory vowel formant variation,'' PhD thesis, Oxford University.
Pols, L. C. W., Tromp, H. R. C., and Plomp, R. (**1973**). ''Frequency analysis of Dutch vowels from 50 male speakers,'' J. Acoust. Soc. Am. **53**, 1093–1101.
Stevens, J. P. (**1979**). ''Comments on Olson: Choosing a test statistic in multivariate analysis of variance,'' Psychol. Bull. **86**, 355–360.
Stevens, S. S., and Volkmann, J. (**1940**). ''The relation of pitch to frequency: A revised scale,'' Am. J. Psychol. **53**, 329–353.
Syrdal, A. K. (**1984**). ''Aspects of a model for the auditory representation of American English vowels,'' Speech Commun. **4**, 121–135.
Syrdal, A. K., and Gopal, H. S. (**1986**). ''A perceptual model of vowel recognition based on the auditory representation of American English vowels,'' J. Acoust. Soc. Am. **79**, 1086–1100.
Traunmüller, H. (**1990**). ''Analytical expressions for the tonotopic sensory scale,'' J. Acoust. Soc. Am. **88**, 97–100.
Van de Velde, H., van Hout, R., and Gerritsen, M. (**1997**). ''Watching Dutch change,'' J. Sociolinguistics **1**, 361–391.
Watson, C. I., Maclagan, M., and Harrington, J. (**2000**). ''Acoustic evidence for vowel change in New Zealand English,'' Language Variation and Change **12**, 51–68.
Wakita, H. (**1977**). ''Normalization of vowels by vocal tract length and its application to vowel identification,'' IEEE Trans. Acoust., Speech, Signal Process. **ASSP-25**, 183–192.
Zwicker, E. (**1961**). ''Subdivision of the audible frequency range into critical bands (Frequenzgruppen),'' J. Acoust. Soc. Am. **33**, 248.
Zwicker, E., Flottorp, G., and Stevens, S. S. (**1957**). ''Critical bandwidth in loudness summation,'' J. Acoust. Soc. Am. **29**, 548–557.
Zwicker, E., and Terhardt, E. (**1980**). ''Analytical expressions for critical-band rate and critical bandwidth as a function of frequency,'' J. Acoust. Soc. Am. **68**, 1523–1525.

Acoustic-phonetic correlates of talker intelligibility for adults and children[a)]

Valerie Hazan[b)] and Duncan Markham
Department of Phonetics and Linguistics, University College London, Gower Street, London WC1E 6BT, United Kingdom

(Received 3 January 2003; revised 19 July 2004; accepted 20 August 2004)

This study investigated acoustic-phonetic correlates of intelligibility for adult and child talkers, and whether the relative intelligibility of different talkers was dependent on listener characteristics. In experiment 1, word intelligibility was measured for 45 talkers (18 women, 15 men, 6 boys, 6 girls) from a homogeneous accent group. The material consisted of 124 words familiar to 7-year-olds that adequately covered all frequent consonant confusions; stimuli were presented to 135 adult and child listeners in low-level background noise. Seven-to-eight-year-old listeners made significantly more errors than 12-year-olds or adults, but the relative intelligibility of individual talkers was highly consistent across groups. In experiment 2, listener ratings on a number of voice dimensions were obtained for the adults talkers identified in experiment 1 as having the highest and lowest intelligibility. Intelligibility was significantly correlated with subjective dimensions reflecting articulation, voice dynamics, and general quality. Finally, in experiment 3, measures of fundamental frequency, long-term average spectrum, word duration, consonant–vowel intensity ratio, and vowel space size were obtained for all talkers. Overall, word intelligibility was significantly correlated with the total energy in the 1- to 3-kHz region and word duration; these measures predicted 61% of the variability in intelligibility. The fact that the relative intelligibility of individual talkers was remarkably consistent across listener age groups suggests that the acoustic-phonetic characteristics of a talker's utterance are the primary factor in determining talker intelligibility. Although some acoustic-phonetic correlates of intelligibility were identified, variability in the profiles of the ''best'' talkers suggests that high intelligibility can be achieved through a combination of different acoustic-phonetic characteristics.
[DOI: 10.1121/1.1806826]

PACS numbers: 43.71.Bp, 43.71.Es, 43.70.Gr [PFA] Pages: 3108–3118

I. INTRODUCTION

Many studies have sought to determine acoustic-phonetic correlates of speech intelligibility. The finding of robust and consistent acoustic-phonetic correlates would have implications for the development of speech enhancements that will potentially benefit listener populations with degraded intelligibility (e.g., individuals with impaired hearing, second language learners). The characterization of speaker clarity is also important for the selection of talkers used in standard speech audiometric materials and in speech technology applications.

Previous studies on the acoustic-phonetic correlates of talker intelligibility have involved relatively small numbers of talkers and listeners. Because a listener's experience with a talker's dialect is likely to affect talker intelligibility (e.g., Evans and Iverson, 2004), these studies have been carried out with listeners and talkers from a same dialect group. Some studies have assessed the intelligibility of a range of different talkers in order to find ''intrinsically clear'' talkers, i.e., talkers who are of relatively higher intelligibility for given speech materials than other talkers with a similar profile. Others have compared the intelligibility of ''casual'' and ''clear'' speaking styles for a same talker or group of talkers and have therefore focused on the acoustic-phonetic characteristics of ''deliberately clear'' speech. In a study of ''intrinsically clear'' speech with only five talkers, intelligibility was found to be related to word and vowel duration, size of vowel space and cues to consonantal contrasts (Bond and Moore, 1994), and it was claimed that ''intrinsically clear'' speech shared common characteristics with ''deliberately clear'' speech. Using intelligibility data obtained for ten male and ten female adult talkers of American English, Bradlow *et al.* (1996) found the intelligibility of key words in Harvard sentences (Fisher *et al.*, 1986) to be correlated with a number of global and fine-grained acoustic characteristics. These included fundamental frequency (F0) range, measures reflecting vowel space size (range in F1, vowel space dispersion, F2-F1 distance for /i/ and F2-F1 distance for /a/), and precision of articulation at the fine-grained acoustic-phonetic level. It was concluded that an ''intrinsically clear'' talker was likely to have the following profile: ''a woman who produces sentences with a relatively wide range in fundamental frequency, employs a relatively expanded vowel

[a)]Portions of this work were presented in Hazan, V. and Markham, D. (**2002**). ''The perception of speaker characteristics in adults and children,'' in *Phonetics and its Applications. Festschrift for Jens-Peter Koester on the Occasion of this 60th Birthday*, edited by A. Braun and H. R. Masthoff (Steiner, Stuttgart), pp. 118–126, and in Markham, D. and Hazan, V. (**2004**). ''The effect of talker- and listener-related factors on intelligibility for a real-word, open-set perception test,'' J. Speech, Hear. Lang. Res. **47**, 725–737.

[b)]Electronic mail: v.hazan@phon.ucl.ac.uk

space that covers a broad range in F1, precisely articulates her point vowels and has a high precision of intersegmental timing.''

Many more studies have searched for acoustic-phonetic measures that distinguish utterances in the ''casual'' and ''clear'' speaking styles produced by the same talker. A clear speaking style is considered to lead to greater intelligibility for normal-hearing and hearing-impaired listeners (e.g., Picheny *et al.*, 1985; Uchanski *et al.*, 1996) and language-impaired children (Bradlow *et al.*, 2003). It also benefits subjects listening to speech in a non-native language, although to a lesser extent than native listeners (Bradlow and Bent, 2002). ''Deliberately clear'' speech usually involves a reduction in speech rate and an increase in what might be termed articulatory precision (Picheny *et al.*, 1985, 1986). It also has other acoustic-phonetic characteristics that serve to increase the distinctiveness of different speech sounds. According to Krause and Braida (2004), who controlled for the effect of speaking rate by training talkers to produce clear speech at conversational speaking rates, these include increased energy in the 1000–3150-Hz frequency range and increased depth of low-frequency modulations of the intensity envelope. Ferguson and Kewley-Port (2002) focused on the effect of speaking style on a single phonetic class, vowels. They found that vowels produced in ''deliberately clear'' speech appeared to have higher F1 and more extreme values of F2. Vowel duration also varied significantly across speaking styles, with clear vowels being on average twice as long as conversational vowels.

Further information on acoustic-phonetic correlates of intelligibility comes from studies that evaluate the contribution of individual acoustic-phonetic measures to intelligibility. The effect of speaking rate on intelligibility is well attested with slower speaking rates facilitating successful perception (Cox *et al.*, 1987). There is also some evidence that faster talkers are less intelligible in single word presentations (Bond and Moore, 1994) and that fast speech by a set of talkers is less intelligible than the same words produced at medium and slow rates (Bradlow and Pisoni, 1999). However, manipulating segmental duration in itself has not yielded any consistent effect (Gordon-Salant, 1986; Montgomery and Edge, 1988; Uchanski *et al.*, 2002). The effect of speaking rate may therefore be related to greater articulatory precision in slower speech rather than to the effect of segmental duration; this view is supported by the fact that it is possible for trained talkers to produce clear speech at conversational speech rates (Krause and Braida, 2002, 2004). Consonant-to-vowel (CV) amplitude ratios have also been shown to affect intelligibility. Gordon-Salant (1986) and Hazan and Simpson (1998) both found that CV syllables with artificially enhanced CV amplitude ratios were more intelligible than syllables with smaller differences in amplitude between the consonant and vowel, as did Montgomery and Edge (1988) when testing hearing-impaired listeners. However, speech from different talkers has not typically been examined for the effects of naturally occurring CV amplitude differences on perception. In a small-scale study with only four talkers producing nonsense vowel–consonant–vowel (VCV) test materials, CV ratio was not correlated with consonant intelligibility (Simpson and Hazan, 1997).

It is acknowledged in many studies that individual talkers may vary greatly in the degree to which they achieve higher intelligibility via the modifications of their speech that occur as a result of a change in speaking style (Ferguson and Kewley-Port, 2002; Gagne *et al.*, 2002; Bradlow *et al.*, 2003). As individual acoustic-phonetic features found in clear speech have not necessarily led to increases in intelligibility when manipulated in isolation, it does appear that a combination of the right individual ''enhancements'' may be required in order for clear speech to be more intelligible (Bradlow *et al.*, 2003). It is possible, though, that the key acoustic enhancement has simply not yet been identified. Whether the acoustic-phonetic characteristics of ''intrinsically clear'' speech are the same as those of ''deliberately clear'' speech has not been firmly established. Although some acoustic-phonetic characteristics do seem to be common between these two types of clear speech, substantially fewer studies have been carried out on ''intrinsically clear'' speech.

In summary, the fact that talkers vary significantly in terms of their intrinsic intelligibility is well accepted, but the factors that determine talker intelligibility are not yet fully understood. Two key issues, that have not hitherto received much attention, need to be addressed in investigations of acoustic-phonetic correlates of talker intelligibility. First, it is important to evaluate whether given talkers are consistently clear across a range of listeners. Indeed, this would establish that the correlates of intelligibility are to be found in the acoustic-phonetic characteristics of the talkers, and not strongly influenced by the interrelation between listener and talker characteristics. Such a finding would have implications for models of speech perception, as these vary in the extent to which an effect of listener experience is predicted to affect talker intelligibility. For example, the exemplar model of spoken word perception (Goldinger, 1998; Palmeri *et al.*, 1993), claims that, in word recognition, tokens are classified according to their similarity to stored exemplars. The results of word recognition experiments with priming and stimulus tokens produced by the same or different talkers suggest that talker-specific properties of the tokens heard are retained within the representation of these exemplars in long-term memory (Goldinger, 1997). Further support for the view that fine-grained aspects of tokens are retained in memory comes from work with children aged 2 to 4 years, which showed that they produced fine-grained patterns of phonetic realization that were representative of the adult community in which they lived (Watt *et al.*, 2003). As there is evidence that the episodic memory of a particular voice may facilitate the perception of other voices with similar acoustic-phonetic characteristics (Goldinger, 1996), a listener's experience of different types of voices could partly determine the relative intelligibility of unknown talkers. It would therefore be expected that listener's previous language experience could affect the intelligibility of particular talkers and thus that there would not be a high degree of consistency across listeners, in the relative intelligibility of a range of talkers. A second issue is whether the same acoustic-phonetic characteristics are correlated with intelligibility across a

range of clear talkers, or whether there is evidence of substantial individual variability in the strategies used to achieve high intelligibility. To answer both these questions, it is essential to investigate talker intelligibility in a study involving a wide range of listeners and of talkers.

Our study was carried out in three phases. The aim of experiment 1 was to establish whether the intrinsic intelligibility of a talker was primarily dependent on the acoustic-phonetic characteristics of the talker's speech or whether it was dependent on a combination of talker and listener characteristics. We obtained intelligibility data from adult, 11–12-year-old and 7–8-year-old listeners for speech from 45 adult and child talkers, homogeneous for regional accent, in order to establish whether the relative intrinsic intelligibility of different talkers was consistent across listeners differing in age and gender. The aim of experiment 2 was to get listeners' subjective judgments of voice characteristics for a subgroup of ''good'' and ''poor'' talkers from experiment 1, in order to guide the choice of acoustic-phonetic measures to be made in experiment 3. To this end, a subjective listener ratings experiment was carried out on speech materials for a subgroup of 24 adult voices in our dataset with the highest and lowest intelligibility. Finally, in experiment 3, a range of acoustic-phonetic measurements was carried out for the full range of 45 talkers, in order to look for acoustic-phonetic correlates of intelligibility. Our choice of acoustic-phonetic measurements was guided both by the findings of experiment 2 and that of previous studies of deliberately and intrinsically clear speech.

In short, the aim of the study was to evaluate which acoustic-phonetic measures appeared to be most strongly correlated with intelligibility, and whether these varied with talker type. On the basis of previous studies, we expected that measures of speaking rate and of articulatory precision (as reflected by vowel space size) would prove to be most strongly correlated with intelligibility, but that these correlates might be less strong for child talkers than adult talkers due to increased within- and across-talker variability in some acoustic-phonetic characteristics of children's speech up to the age of 15 years (Lee *et al.*, 1999).

II. EXPERIMENT 1: INTELLIGIBILITY DATA

A. Speech materials

A monosyllabic-word test was developed for this study (Markham and Hazan, 2002). A set of 700 unique monosyllables from a listing of all legal CVC combinations in English (with the consonant being either a singleton or cluster) was assessed for familiarity for British 7-year-old children. A subset of words that were considered by at least six out of seven primary school teachers or literacy educators to be ''definitely'' familiar for this age group were chosen and examined further. From this list, a subset of 124 words that addressed all frequent consonant confusions attested to in the literature (e.g., Miller and Nicely, 1955; Redford and Diehl, 1999) and which contained a large spread of vowels was selected as the test material.

B. Talkers and listeners

Forty-five talkers of British English with a neutral or mild South-Eastern English accent were recruited for recordings (Markham and Hazan, 2002). These included 18 women (mean 33.11 years, s.d. 10.9), 15 men (mean 30.7 years; s.d. 10.5), six girls (mean 13.2 years; s.d. 0.5) and six boys whose voices had not yet broken (mean 13.2 years; s.d. 0.9). Children of this age were selected as they would still be expected to produce speech with greater within-talker variability than adults, at least in some acoustic-phonetic dimensions (Lee *et al.*, 1999), yet would be able to produce fluent read speech and cope with the recording conditions. Recordings were made in an anechoic chamber: speech was recorded to DAT at a sampling rate of 44.1 kHz and a simultaneous recording of laryngeal activity was made using an electrolaryngograph (Fourcin, 1974). The word materials were elicited by having each talker read from a computer screen short phrases in the form of a carrier phrase (e.g., ''the next three words are''), followed by three of the test-words and ending with the fourth word ''it.'' This structure was used so that similar intonation contours would be used on each of the three test-words with the final word ''it'' attracting the terminal fall in intonation. In this way, each test-word could be segmented and concatenated in different word combinations. Each of the 124 test-words was recorded twice. The recordings were transferred to PC using a digital DAT-PC interface at the original sampling rate and were then segmented into individual files for each test word. Each of the stimuli was levelled to a fixed rms level and 20-talker babble was added to produce a signal-to-noise ratio of +6 dB.[1] This relatively low level of background noise was added to avoid ceiling effects in the perceptual task.

In order to investigate the effect of listener-age on talker intelligibility, the listener cohort included 45 listeners from each of three different age groups: adults (mean age: 29.9 years, s.d. 7.10), 11–12-year olds (mean 11.11 years, s.d. 0.6) and 7–8-year olds (mean 7.11 years, s.d. 0.3). For children, the upper age limit was chosen in order to have a listener group close in age to the child talker group. The younger age limit of 7–8 years was chosen because there is evidence of poorer intelligibility for speech in noise (e.g., Fallon *et al.*, 2000) and degraded speech (Eisenberg *et al.*, 2000) in this age range but children have the concentration span and cognitive abilities to cope with the same test as adult listeners. Listeners were only included if they had pure tone audiometric thresholds of 25 dB HL or less at octave intervals between 0.5 and 8 kHz and if they completed the CELF Recalling Sentences screening test within criterion (Semel *et al.*, 1987).

C. Presentation conditions

In order to evaluate whether talker intelligibility would be improved when the listener was given the opportunity to ''tune in'' to the specific acoustic characteristics of a talker before hearing the test-words, listeners were tested in two conditions: triplet and single-word.[2] In the triplet condition, a set of three test-words by a given talker, each separated by a 200-ms gap, was preceded by a carrier phrase (''the next

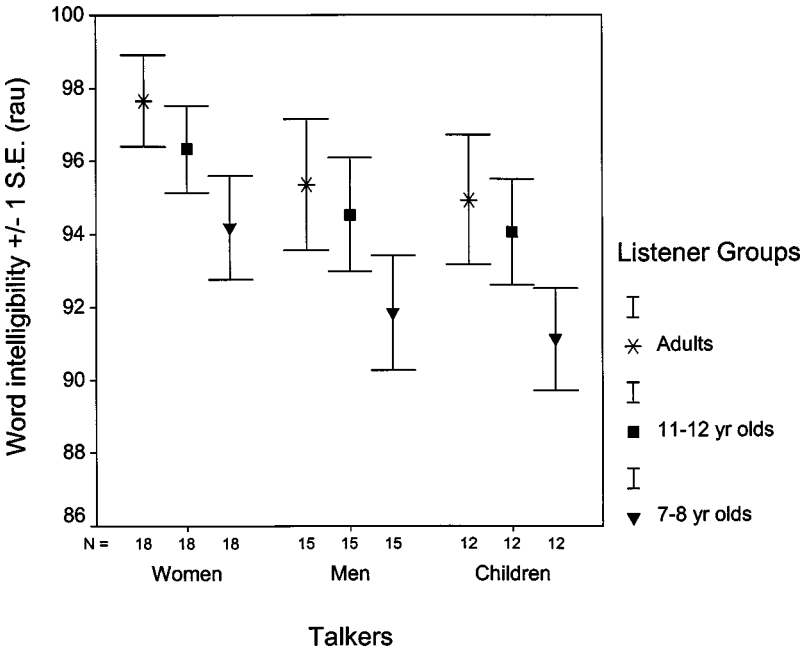

FIG. 1. Word intelligibility rates in rationalized arcsine units (rau) obtained for men, women, and 12–13-year-old talkers by listener groups of adults, older children (11–12 years) and younger children (7–8 years). The error bars represent one standard error above and below the mean.

three words are'' *or* ''and now please say'') by the same talker. In this condition, each listener heard 27 words (25 unique words plus two duplicates) from each of 15 talkers presented in a fully randomized fashion. The single-word condition involved the presentation of individual words without a carrier sentence; each listener heard a further 25 unique words from each of 15 talkers that had not been heard in the triplet condition, presented in a fully randomized fashion.

D. Test design

The design of the perceptual test was subject to a number of constraints dictated by the age and availability of child listeners. It was important that multiple listeners for each age group heard the same talkers, so as to minimize the contribution of individual listener differences to word recognition scores. At the same time, it was desirable that a listener should not become overly familiar with a talker's voice. It was judged that 25 tokens per talker would be an appropriate number of words, resulting in five sets of words to make up the total of 124 test-words (with one set of 24 words instead of 25). As the words were to be presented as triplets, the nearest multiple of three is 27 words. Thus, each listener would hear 24–25 unique words from a speaker, plus 2 or 3 duplicates. The number of talkers that could be presented to each listener was dictated by the amount of testing time appropriate for young children. It was calculated that a listener could hear 27 words from 15 talkers in each of two conditions within two testing sessions.

The 45 talkers were divided into three subgroups of 15 (six women, five men, two boys, and two girls), and 135 listeners were divided into three listener groups of 45 subjects (each containing 15 younger children, 15 older children, and 15 adults). Each listener group heard talkers from one talker subgroup. The listener group was divided into five subgroups of nine subjects. Each subgroup heard a different 27 words spoken by each talker in the talker block. Thus, each test-word produced by a particular talker was heard by nine different listeners, and the totality of test-words from each talker by 45 listeners. Each test-word was heard approximately three times by each listener.

E. Test methodology

Children and adults were tested in quiet rooms on school or university premises. Stimuli were presented using a laptop with Sennheiser HD433 headphones at a fixed comfortable listening level. Testing was completed over two sessions. At the first session, the audiometric screening was carried out and listeners heard approximately half of the randomized triplets (72 triplets) and 150 words from the single-word condition. The second session occurred after an interval of approximately one week, and subjects heard the remainder of the triplets (63 triplets) and single words (225 words) and completed the language screening test. Total testing time was approximately 60 min.

F. Results

A repeated-measures ANOVA showed that the effect of test condition (triplet versus single-word) was not significant, and there was no significant listener group by condition interaction. Data obtained for the triplet and single-word conditions was therefore aggregated, and a mean intelligibility score per talker was calculated for each listener group (adult, older children, younger children). The scores were converted to percent-correct scores, and then converted to rationalized arcsine transform units (rau) (Studebaker, 1985) to minimize the relation between mean score and variance and enable statistical comparisons across the entire scale. Mean intelligibility scores obtained for women, men, and child talkers by adult, 11–12-year-old and 7–8-year-old listeners are shown in Fig. 1.

For further statistical analysis of listener effects, a mean score (in rau) was obtained for each listener for each talker group: adult male (AM), adult female (AF), child male

(CM), and child female (CF). Analyses of variance for repeated measures were carried out to evaluate the within-subject factor of talker group and the between-subject factor of listener group (adults, older children, younger children). The main effect of talker group was significant [$F(3,396) = 15.35; p < 0.0001$]; pairwise comparisons with Bonferroni adjustments showed that women were more intelligible (96.04 rau) than the other groups of talkers (ranging from 93.2 to 93.6 rau). The partial eta squared showed that the factor of talker group by itself accounted for only 10% of the overall variance.

The between-subject effect of listener group was also significant [$F(2,132) = 14.11; p < 0.0001$]; Duncan's *post hoc* test showed that younger child listeners had lower intelligibility scores (91.97 rau) than older children (94.5 rau) and adults (95.54 rau). The partial eta squared showed that the effect of listener group by itself accounted for 20.2% of the overall variance. There was no significant talker group by listener group interaction.

Mean intelligibility rates obtained for individual talkers were strongly correlated across listener groups (Pearson's $r = 0.88–0.93$) with the strongest correlation obtained between adult and 11–12-year-old listeners ($r = 0.926$, $N = 45$, $p < 0.0001$) and between 7–8-year-old and 11–12-year-old listeners ($r = 0.923$, $N = 45$, $p < 0.0001$).[3]

In conclusion, slightly but significantly lower intelligibility scores were obtained for younger listeners (mean: 7.11 years) than older children (mean: 11.11 years) and adults, but older child listeners did not differ significantly from adults. These slight differences in intelligibility may be due to factors such as task difficulty, attention, and greater masking effects operating for younger children listening to speech in noise (e.g., Fallon *et al.*, 2000; Hall *et al.*, 2002). A striking fact, though, was that the relative intelligibility of individual talkers was remarkably consistent across listener age groups: a talker who was found to be clear for adult listeners was also clear for child listeners and vice versa.

As a group, women talkers were slightly but significantly more intelligible than men or children, but talker rankings based on intelligibility scores over all listener groups reveal that there were ''good'' and ''poor'' talkers in each group. Despite the greater variability in at least some acoustic-phonetic aspects of child speech attested to in studies such as Lee *et al.* (1999), child talkers aged 13 were overall no less intelligible than adult male talkers. The difference in intelligibility between men and girls may have been masked due to a ceiling effect (Markham and Hazan, 2004).

III. EXPERIMENT 2: SUBJECTIVE RATINGS OF TALKER INTELLIGIBILITY

In an attempt to obtain indications as to what physical measurements might prove most promising for the analysis of acoustic-phonetic correlates of intelligibility, an additional perceptual experiment was devised. Listeners' subjective judgments of talker voice characteristics were collected for a subset of adults talkers identified in experiment 1 as being the least and most intelligible.

A. Methodology

1. Materials

The six most intelligible and the six least intelligible men and women were selected. An identical set of eight triplet sentences from experiment 1 was prepared for each of the 24 talkers. In experiment 2, these were presented without the addition of background noise. Score sheets were devised, requiring listeners to provide judgments about ten voice dimensions and each talker's age and accent. The voice dimensions were modified versions of those used by Sulter (1996) in a study of listener characterization of various voice characteristics. They were chosen to tap different dimensions related to excitation characteristics, physiology, dynamics, and articulation. The final set of dimensions consisted of the following scales: *mumbly–precise, unpleasant–pleasant, muffled–clear, husky–not husky, creaky–not creaky, nasal–not nasal, high for a (fe)male-low for a (fe)male, thin–rich, weak–powerful*, and *harsh–smooth.*

2. Listeners

Twenty-three listeners (age range 18–30 years, mean 21.2, s.d. 2.10) were recruited from among university students who had training in phonetics, including voice quality terminology. The listeners had not participated in experiment 1. They were required to have no history of hearing deficit (self-reported) and to be from the same accent group as the talkers (South-Eastern British English). Listeners were paid for their participation in the experiment.

3. Test procedure

Testing was computer-controlled and conducted individually, in a small sound-treated room. Testing time was usually approximately 45 min. The same equipment was used as in experiment 1.

Listeners heard two triplets each time they pressed a key, and were then required to provide judgments on three scales. Most scales had seven points marked along them, with only the extreme points labeled. The scale for *age* had six points, with labels for each 10-year age span covered by that point. The section for *accent* required written comment. The orientation of the scales on the score sheets was varied, so that labels at the left or right of each scale were not consistently negative (e.g., *muffled, nasal*) or positive (e.g., *smooth, pleasant*) terms. Four pairs of triplets were heard in total, allowing scores for the ten dimensions described above, plus the judgments of age and accent. The order of dimensions for scoring was varied across talkers. Listeners heard all triplets from a single talker before moving on to the next talker, with men and women alternating.

B. Results

Multivariate analyses of variance carried out on the data for the ''good'' and ''poor'' talker groups showed significant differences between groups for the dimensions *mumbly–precise* ($p = 0.001$), *unpleasant–pleasant* ($p = 0.006$), *muffled–clear* ($p = 0.002$), and *weak–powerful* ($p = 0.006$) in the expected direction (see Table I and Fig. 2). To confirm the findings above, correlations were calculated between lis-

TABLE I. Mean and standard deviation measures for the listener ratings obtained for all dimensions for the group of "good" and "poor" talkers, as defined by intelligibility rates obtained in experiment 1. Ratings are on a scale of 1 to 7, with 7 representing the highest score on the positive attribute of the pair. The dimensions marked as** differed significantly between talker groups ($p<0.05$).

	"Good" talkers		"Poor" talkers	
Dimension	Mean	s.d.	Mean	s.d.
Mumbly/precise**	4.96	*0.84*	3.39	*1.06*
Unpleasant/pleasant**	4.28	*0.69*	3.48	*0.60*
Muffled/clear**	3.72	*0.85*	2.43	*0.96*
Weak/powerful**	3.29	*1.00*	2.22	*0.68*
Noncreaky/creaky	2.85	*0.87*	2.76	*0.93*
Harsh/smooth	3.15	*0.77*	3.39	*0.50*
Not husky/husky	2.77	*0.38*	2.98	*0.90*
High/low for a (fe)male**	4.33	*0.73*	4.42	*1.19*

tener ratings and the mean intelligibility rates per talker (rau units) averaged over all listener groups obtained in experiment 1. Five of the dimensions in experiment 2 were significantly correlated with intelligibility: *mumbly–precise* ($\rho=0.780$, $N=24$; $p=0.0001$), *unpleasant–pleasant* ($\rho=0.546$, $N=24$; $p=0.006$), *muffled–clear* ($\rho=0.738$; $N=24$; $p<0.0001$), *weak–powerful* ($\rho=0.481$; $N=24$; $p=0.017$), and *high/low for a (fe)male* ($\rho=0.413$; $N=24$; $p=0.045$). Cross-correlations across dimensions revealed that the *mumbly–precise* and *muffled–clear* dimensions appeared to have been used to rate similar voice characteristics ($\rho=-0.923$; $N=24$; $p=0.0001$).

C. Discussion

From this experiment, one might conclude that less intelligible talkers are judged as sounding *mumbly, unpleasant, muffled*, and *weak* relative to the more intelligible talkers. These key descriptors appear to relate to articulation (*mumbly–precise/muffled–clear*), voice dynamics (*weak–powerful*), and general quality (*unpleasant–pleasant*). None of the dimensions that related to the quality of voiced excitation (*harsh–smooth, creaky–non creaky, husky–not husky*) were significantly correlated with intelligibility.

IV. EXPERIMENT 3: PHYSICAL MEASUREMENTS

A number of acoustic-phonetic characteristics were measured for all 45 talkers in an attempt to establish the physical correlates of the differences in talker intelligibility established in experiment 1 and the differences in subjective impressions of voice characteristics established in experiment 2. Some measures were chosen on the basis of the dimensions that were found in experiment 2 to be correlated with intelligibility: measures of vowel formant spacing and consonant–vowel intensity ratio were chosen as they are indicative of articulatory precision, and measures of long-term average spectrum were chosen as reflecting voice dynamics. Fundamental frequency and word duration (i.e., speaking rate) measures were also included on the basis that they had been found to be correlated with intelligibility in a number of previous studies (e.g., Bond and Moore, 1994; Bradlow *et al.*, 1996).

A. Methodology

1. Long term average spectrum (LTAS) measures

A measure of long-term average spectrum (LTAS) for each talker was obtained for the 124 aggregated test-words used in the intelligibility testing, which had been normalized for level. Analyses used an FFT with a length of 2048 sample points, and windows overlapping by 1024 points, giving a value for the LTAS at multiples of 21.53 Hz. These spectra were then smoothed with a 2-oct-wide Hamming window over the frequency range of 50 Hz to 10 kHz.

2. Fundamental frequency measurements

Measures of fundamental frequency were obtained by analyzing the electrolaryngograph signal (Fourcin, 1974, 1982) obtained during the speech recording. Fundamental frequency statistics were obtained by analyzing the aggregated test-words and two instances of the precursor sentences. Three measures were examined: F0 range (in octaves), F0 median, and F0 irregularity. The frequency range of vocal fold vibration in the speech sample was obtained by first measuring individual vocal fold periods and then setting up a histogram with probability of occurrence plotted against larynx frequency, with the frequency scale divided into a numbers of "bins" on a logarithmic scale (Carlson and Miller, 1998). Here, a second-order histogram was used: these histograms are based on the period-by-period measurements of vocal fold excitation but exclude consecutive larynx excitation cycles that fall within different frequency bins in order to give a measure relating to regular voice production. The F0 range was based on the difference between the 10th and 90th centiles in fundamental frequency values. These values were converted to semitones (with a baseline of 50 Hz) so that a range in octaves could be calculated, in order to permit a comparison across talkers with very different fundamental frequencies. A measure of vocal fold irregularity (in percent) was also obtained. For this analysis, a scatterplot of F01 vs. F02 was constructed, where F01 is the frequency value of the first vocal fold cycle in any pair of cycles and F02 is the frequency value of the immediately following cycle of the pair. The irregularity measure uses deviation from ordinary intonation changes as the basis for the estimation of irregularity, with special reference to bin sizes that are directly based on perceptual difference limens.[4]

3. Word duration measurements

Total word duration (i.e., a comparative measure of speaking rate), consonant-to-vowel (CV) intensity ratio, and formant frequency measurements were made on a subset of 41 test-words from each of the 45 talkers ($n=1845$). This subset was chosen to contain sets of words from similar lexical neighborhoods (e.g., cheap, cheat, cheek) and to include variation in terms of consonant manner and place of articulation. These words were manually segmented and phonetically annotated by an experienced phonetician, using speech analysis software which provided displays of the wide-band spectrogram and waveform. Total duration was automatically

measured for each word from the word-start and word-end markers. For final plosives, the end marker was placed at the end of the aspiration segment.

4. CV intensity ratio measurements

First, the rms amplitude was calculated for each annotated segment by first calculating the amplitude in dB once a sample, using a rectangular window of size 1 ms, and then, from the values obtained, calculating the average intensity over the whole annotated segment. The CV ratio was then calculated for each token by deducting the average intensity for the vowel in dB from that of the consonant. CV ratios were then averaged over a particular class of test-words. For each talker, CV ratios for nasals were based on the measurements of 12 test-words (''meat, met, might, neat, net, night, pan, tan, can, them, then, sum, sun''); CV ratios for fricatives were based on the measurements of 12 test-words (''for, saw, sure, fort, sort, short, feet, seat, sheet'') and CV ratios for plosives were based on the measurement of 12 test-words in initial position (''pan, tan, can, pick, tick, kick, pop, top, cop''), and 14 test-words in word final position (cheap, cheat, cheek, shop, shot, shock, park, part, pop, top, cop, pick, tick, kick).

5. Vowel formant measurements

Words were selected that contained the vowel /ae/ (back, bad, bag, bat, cat, had, hat, pat), the vowel /i/ (feet, heat, seat, sheet, beat, cheat, cheap, cheek), and the vowel /u/ (boo, do, goo, too, zoo). Formant frequencies were measured manually, using speech analysis software that provided a simultaneous display of the speech waveform, wide-band spectrogram, and short-term spectral cross-section. Measurements were taken from the vowel with the cursor placed at the center of the relatively steady-state region. First and second formant frequencies were calculated from the spectrum of a single cycle in the target region using the spectrographic display to confirm estimates of formant location. All measurements were made by the same experimenter. Eight tokens of each vowel were measured for each of the 45 talkers (i.e., total of 360 measurements per vowel). The frequency measures obtained were transformed to an auditory frequency scale—the ERB (equivalent rectangular bandwidth) scale (Glasberg and Moore, 1990). A number of measures were derived from the formant frequency measures: the Euclidian distance between F1 and F2 in ERB-rate units for each vowel, and two measures which would reflect the vowel space size of the talker: the difference between the first formant frequencies for /i/ and /ae/ and the difference between the second formant frequencies for /i/ and /u/.

B. Results

1. Long-term average spectrum (LTAS) measures

Two measures of the long-term average spectrum were obtained for each talker: a measure of spectrum slope and the total energy in the 1- to 3-kHz region. The measure of spectrum slope was obtained by fitting a straight line using least squares to the smoothed spectrum on dB versus log frequency scales for frequencies between 0.5 and 4 kHz. The measure of total energy in 1- to 3-kHz frequency band was chosen as it was strongly correlated with intelligibility in Krause and Braida (2004); in our data, it correlates more strongly with the intelligibility data than total energy measures for other frequency regions (0.5–3 kHz, 1–2 kHz, 0.5–2 kHz). As the calculations were made on speech materials that had been normalized to a fixed level, the values obtained can be used for comparisons across talkers. LTAS slope varied from −7.86 to −13.3 dB/decade (mean: −10.3, s.d. 1.47). The total energy in the 1- to 3-kHz region (total energy 1–3 kHz) was −1.93 dB (s.d. 2.88) for adult female talkers ($n=18$), −3.36 dB (s.d. 2.72) for adult male talkers ($n=15$) and −1.40 dB (s.d. 1.81) for child talkers ($n=12$). An analysis of variance was applied to evaluate the effect of talker group and of talker gender on the two summary measures: both were found to be nonsignificant.

TABLE II. Correlation coefficients (Pearson's r) showing the relation between the measure of total energy between 1 and 3 kHz and intelligibility measures in rationalized arcsine units (rau) for three groups of listeners: adults, children aged 11–12 years (OC), and children aged 7–8 years (YC). Significant values ($p<0.05$) are starred as*, significant values ($p<0.001$) are starred as**.

Total energy 1–3 kHz	Word intelligibility (rau)			
	All	Adult listeners	OC listeners	YC listeners
All talkers $N=45$	0.640**	0.614**	0.605**	0.628**
Women $N=18$	0.715**	0.672*	0.645*	0.697**
Men $N=15$	0.779**	0.803**	0.746**	0.763**
Children $N=12$	0.377	0.332	0.415	0.364

There were weak or no significant correlations between word intelligibility and the measure of LTAS slope. However, relatively strong correlations were obtained between word intelligibility and the total energy (1–3 kHz) measure (see Table II) when carried out on the whole talker set ($n=45$). When correlations were carried out on separate talker groups, the strongest correlations were obtained for adult male talkers, and no significant correlation between word intelligibility and total energy (1–3 kHz) was obtained for child talkers.

2. Fundamental frequency measures

Means and standard deviations were obtained for each main talker group for the measures of F0 median, F0 range, and F0 irregularity.[5] Pearson's correlations were carried out to evaluate any correlation between the fundamental frequency and word intelligibility measures. The only significant, if weak, correlations were between the F0 irregularity measures and word intelligibility scores for adult listeners ($r=-0.39$, $N=38$; $p=0.014$) older child listeners ($r=-0.40$; $N=38$, $p=0.013$) and younger children listeners ($r=-0.367$; $N=38$, $p=0.024$).

3. Word duration

The total duration of each of 41 words per talker was measured and the mean word duration per talker was calcu-

TABLE III. Correlation coefficients (Pearson's r) showing relation between mean word duration and intelligibility measures in rationalized arcsine units (rau) for three groups of listeners: adults, children aged 11–12 years (OC), and children aged 7–8 years (YC). Significant values ($p<0.05$) are starred as*, significant values ($p<0.001$) are starred as**.

Mean word duration	Word intelligibility (rau)			
	All	Adult listeners	OC listeners	YC listeners
All talkers $N=45$	0.382*	0.364*	0.362*	0.368**
Women $N=18$	0.370	0.317	0.426	0.402
Men $N=15$	0.672*	0.676*	0.672*	0.668*
Children $N=12$	−0.066	0.044	−0.143	−0.138

lated to give some general measure of speaking rate. The mean word duration was 0.512 s (s.d. 0.05) for adult female talkers ($N=18$), 0.453 s (s.d. 0.04) for adult male talkers ($N=15$), and 0.503 s (s.d. 0.04) for child talkers ($N=12$). There was a significant effect of talker group on mean word duration [$F(2,42)=8.248$; $p=0.001$]. *Post hoc* analyses revealed that men had a significantly faster speaking rate than women and children, a finding in agreement with observations by Byrd (1994). The correlation between mean word duration (reflecting speaking rate) and intelligibility rate was significant but not particularly strong ($r=0.382$, $N=45$, $p=0.01$). Correlations were then calculated separately for each talker group. These were relatively strong for adult male talkers ($r=0.672$, $N=15$, $p=0.006$) but nonsignificant for women and child talkers (See Table III).

4. CV ratios

As there was no significant difference between the intensity ratios obtained for /m/ and /n/, the data for both nasals were aggregated. For the same reason, the data for the three stops /p/, /t/, and /k/ were aggregated across syllable positions (23 tokens×45 talkers). There were no significant correlations between word intelligibility rates and either CV ratio for nasals, CV ratio for fricatives, or CV ratios for stops.

5. Vowel formant measures

Mean values of F1 and F2 (expressed in ERB-rate units) and Euclidian distance between F1 and F2 were calculated for the three vowels /i/, /ae/, and /u/ for all talker groups. Here, separate means were calculated for girls and boys in order to evaluate any difference in formant values between these two groups.

Repeated-measures analyses of variance were carried out on mean Euclidian distance calculated per vowel and per talker to look at the within-subject effect of vowel and between-subject effect of talker group. The effect of vowel was significant [$F(2,82)=217.07$; $\eta_p^2=0.841$; $p=0.000$], as expected and this factor alone accounts for 84% of the overall variance. The effect of talker group was also significant [$F(3,41)=52.18$, $\eta_p^2=0.792$; $p=0.000$]: *posthoc* tests (Tukey's HSD) showed that formant values for men differed from the other groups of talkers, and that those for girls differed from women.

Pearson's correlations were calculated between mean word intelligibility (all groups) and a number of formant measures for the complete talker set: F1 and F2 values for /i/, /ae/, and /u/, Euclidean distances between F1 and F2 for the three vowels, difference in F1 values for /i/-/ae/, and difference in F2 values for /i/-/u/. The only significant correlation was between word intelligibility and the difference in F2 value between /i/ and /u/ ($r=0.401$; $N=45$; $p=0.006$).

6. Summary of correlations between acoustic-phonetic measures and word intelligibility

A multiple regression analysis was applied to the data using a forward stepwise method. The metrics that were correlated with intelligibility calculated over all listener groups (total energy in 1–3-kHz frequency band, word duration, difference in F2 between /i/ and /u/) were included in the analysis. The dependent variable was the word intelligibility rate (in rau) aggregated over all listener groups for all talkers. The final model included only two metrics: total energy 1–3 kHz and word duration. The R^2 for the model with these two metrics as predictors was 0.48 ($R^2=0.41$ for the energy 1–3 kHz measure alone). In order to evaluate whether the same acoustic-phonetic metrics correlated with intelligibility for adult and child listeners, the regression analysis was repeated for the word intelligibility rate obtained for each listener group. The model remained as above. In order to see whether talker gender affected this model, the regression analysis was carried out separately on intelligibility data for women and men. For women talkers, the model included the same metrics as for the complete talker database. For men, the model included total energy 1–3 kHz and difference in F2 between /i/ and /u/, with an R^2 of 0.61 for the long-term spectrum measure alone and a change in R^2 of 0.13 when the vowel space size metric was added.

7. Correlations between acoustic measures and subjective ratings

The results of subjective ratings with the 24 adult listeners tested in experiment 2 were correlated with the acoustic-phonetic measures obtained in experiment 3 (Spearman's rho). Correlations that are significant at the 0.01 level (two-tailed) are reported. The total energy 1–3 kHz measure correlated with the following rating scales: *clear–unclear, mumbly–precise, weak–powerful, pleasant–unpleasant*. The difference in F2 between the vowels /i/ and /u/, which is a broad measure of vowel space, correlated with the following scales: *mumbly–precise, unclear–clear*. Word duration correlated with the following scales: *mumbly–precise* and *unclear–clear*. The measures of fundamental frequency regularity, mean CV ratio (all consonants), and /i/-/a/ difference in F1 were not correlated with any of the subjective rating scales.

TABLE IV. Profiles of the five most and least intelligible talkers (af=adult female, am=adult male, cm=child male). Their ranking relative to the complete group of 45 talkers is given for the acoustic-phonetic dimensions and subjective ratings found to correlate with word intelligibility. ''='' indicates a tie in ranking. The subjective rating descriptors are derived from the seven-point numerical scale. No subjective ratings are given for talker cm-06 as only adult talkers were included in experiment 2.

	Rank (1–45)				Subjective ratings			
Talker	Word intelligibility (all)	LTAS 1–3 kHz	Word duration	Difference of F2/i/–/u/	Mumbly–precise	Unpleasant–pleasant	Clear–unclear	Powerful–weak
af-06	1	1=	3	6	Extremely precise	Pleasant	Very clear	Powerful
af-14	2=	19=	16	11	Very precise	Pleasant	Clear	Fairly weak
am-10	2=	9	17	40	Very precise	Pleasant	Clear	Powerful
am-08	4	27	25	18	Precise	Pleasant	Fairly unclear	Fairly weak
af-12	5	35	1	16	Precise	Fairly pleasant	Fairly unclear	Very weak
	.	.	.	.				
am-12	40	42	39	42	Mumbly	Unpleasant	Very unclear	Very weak
af-15	41	39	29	39	Fairly mumbly	Fairly unpleasant	Very unclear	weak
cm-06	42	19=	19	4	*	*	*	*
am-13	44	43=	40	44	Mumbly	Fairly pleasant	Very unclear	Fairly weak
am-14	45	39	44	45	Mumbly	Fairly pleasant	Unclear	weak

8. Profiles of "best" and "worst" talkers

The profiles of the ''best'' and ''poorest'' talkers, in terms of their ranking on the acoustic-phonetic measures and voice dimensions that were correlated with intelligibility, revealed great heterogeneity between talkers of similar intelligibility (see Table IV). For example, the ''best'' talker, af-06, did rank highly in terms of the key acoustic-phonetic measures and was rated as having a very clear, powerful and extremely precise voice. However, the second most intelligible talker received average ratings for both the key acoustic-phonetic measures and subjective rating scales. Somewhat greater consistency was obtained for the four adult talkers with lowest intelligibility.

V. DISCUSSION

This study, which involved a larger number of talkers and listeners than previous studies of this kind, enabled us to investigate whether the relative intelligibility of a range of talkers was consistent over groups of listeners differing in

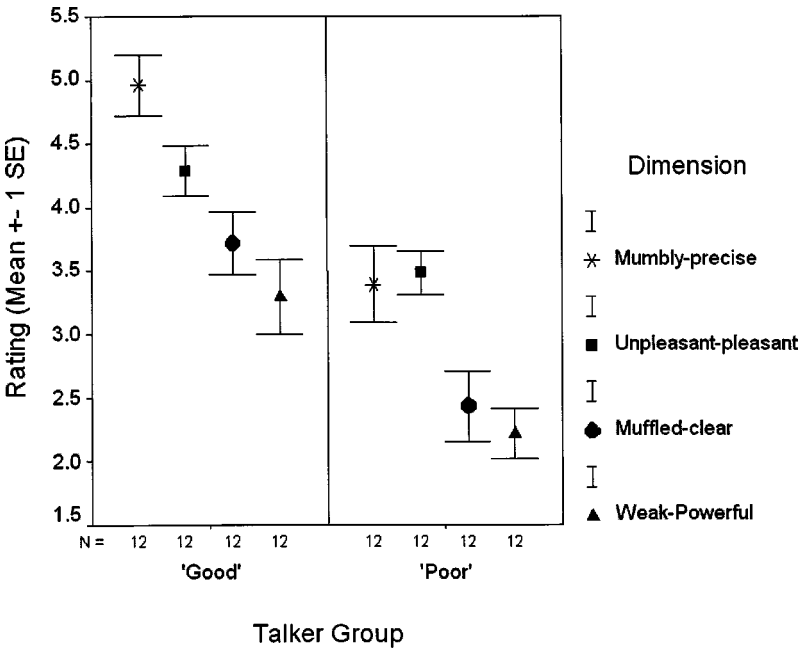

FIG. 2. Listener ratings for four voice dimensions that differed significantly between the ''good'' and ''poor'' talker groups. The error bars represent one standard error above and below the mean.

age and gender, and whether acoustic-phonetic correlates of intelligibility could be found. In experiment 1, it was found that talkers, chosen from a homogeneous regional-accent group, varied significantly in intelligibility for words presented in a low degree of background noise. Women were, as a group, more intelligible than men but the talker gender effect was much less clear-cut than in a previous study of talker intelligibility (Bradlow *et al.*, 1996). Talkers aged 12 to 13 years were, overall, no less intelligible than adult talkers, either for adult or child listeners.

The fact that the relative intelligibility of individual talkers was remarkably consistent across listener age groups strongly suggests that the acoustic-phonetic characteristics of a talker's utterance are the primary factor in determining talker intelligibility, at least when the talker and listener are from the same dialect group. This view is reinforced by the fact that the same acoustic-phonetic measures (total energy in the 1- to 3-kHz region of the long-term average spectrum and word duration) were important predictors of intelligibility for both adults and child listeners. Whether this finding is problematic for the exemplar model of word recognition depends on whether it is assumed that the intelligibility of words produced by novel talkers is more greatly affected by recently heard exemplars than exemplars long stored in memory. Indeed, the child listeners in our study had much greater recent exposure to other children's voices than our adult listeners who were university students, and presumably a less extensive exposure to adult voices than our adult listeners. However, their intelligibility rates for child talkers were not any higher than intelligibility rates for our adult listeners (university students).

Previous studies of intrinsically clear speech had highlighted a number of potential candidates in terms of acoustic-phonetic correlates of intelligibility, notably range in F1, vowel space dispersion, F2-F1 distance for /i/ and F2-F1 distance for /æ/, vowel and word duration, and precision of articulation. Our study failed to replicate many of these findings. Indeed, no significant correlation between intelligibility and fundamental frequency range were obtained. Our study also failed to show significant correlations between intelligibility and either F1 range, and F2-F1 Euclidian distance for /i/ or for /æ/, either for the whole talker group or for groups selected in terms of age and gender. Some measures that were not found to be significantly correlated with intelligibility in the Bradlow *et al.* (1996) study were significant in our study. These include speaking rate and F2 range (difference between F2 for /i/ and F2 for /u/). The amount of energy in the key frequency region between 1 and 3 kHz that was found to be a primary factor in our study was also significantly correlated with intelligibility in Krause and Braida's study of ''deliberately clear'' speech. It is noteworthy that CV ratio was not found to be correlated with word intelligibility either here or in a number of previous studies (Bradlow *et al.*, 1996; Krause and Braida, 2004) even though enhancements in CV ratio in highly controlled studies have been shown to lead to improvements in intelligibility.

Some of the differences in the acoustic-phonetic correlates of intelligibility highlighted in these studies may be due, to a certain extent, to differences in speech materials or in the methods used to elicit clear speech. For example, the lack of effect of fundamental frequency characteristics found in our study may be due to our use of single-word material, as opposed to sentence-length material as used in a number of previous studies.[6] However, these effects cannot fully explain the extent of the variability seen across studies. There is also evidence that high intelligibility can be achieved by different talkers through a combination of different acoustic-phonetic characteristics, and that there are no acoustic-phonetic characteristics that *consistently* lead to high intelligibility. Indeed, although a slower speaking rate and high intensity in the spectral region richest in phonetic feature information do appear to promote high intelligibility, these are neither necessary nor sufficient to produce ''intrinsically clear'' speech as some ''good'' talkers in our study did not rank highly on any of the spectral, intensity, or durational measures made. Similarly, great variability in acoustic-phonetic characteristics of clear speech was found for five talkers producing clear speech at conversational speaking rates (Krause and Braida, 2004). This was attributed to the use by talkers of different strategies to achieve clear speech at normal speaking rates, but may also be a more general characteristic of clear speech. The degree of internal consistency within a talker in the production of different speech sound categories may be an important factor as Newman *et al.* (2001) found an effect on perception of the extent of within-talker variability in production. Kinematic studies of speech production under different speaking styles also revealed a high degree of intersubject variability (Perkell *et al.*, 2002).

In conclusion, this study has shown that there is great consistency across listeners in terms of what is considered a highly intelligible talker. This has practical implications in terms of talker selection for speech technology or speech audiometry applications, as a selection based on intelligibility data obtained for adult listeners is likely to generalize to other listener populations. Although some acoustic-phonetic correlates of intelligibility were identified, there is significant individual variability in the characteristics of ''intrinsically clear'' speech across talkers. A fruitful approach, in a further study on the acoustic-phonetic correlates of clear speech, would be to evaluate talker intelligibility for different types of speech materials produced by a range of talkers in casual and deliberately clear speaking styles, in order to investigate the relation between deliberately clear and intrinsically clear speech and the robustness of the ''good'' and ''poor'' talker classification.

ACKNOWLEDGMENTS

This study was funded by the Wellcome Trust (055651/Z/98/ JRS/ JP/ JAT). We thank staff and pupils at City of London School for Boys, St Christopher's School, Notting Hill and Ealing Secondary School, Broomwood Hall, Newton Preparatory School, St Paul's Cathedral School, and Thomas' Preparatory School, Battersea. We also thank Stuart Rosen for carrying out the long-term spectrum analyses, and Andrew Faulkner and the two anonymous reviewers for their helpful comments on a previous version of the paper.

[1]The original babble file contains 20-talker babble. Due to some spectral variation across the recording, a time-shifted duplicate of the babble was mixed with the original file to generate a more constant level of noise.

[2]The rationale for this decision and data relating to talker normalization are described in more detail in a separate paper (Markham and Hazan, 2004) which focused on a detailed analysis of the perceptual data collected in this study.

[3]A more detailed analysis of word error rates and individual listener scores for this data set can be found in Markham and Hazan (2004).

[4]The following procedure is used to obtain the irregularity measure. The number of cycles in all frequency bins are summed (Total). The number of cycles in all bins that lie on the diagonal and all bins that lie immediately above and below the diagonal are then summed (DiagTotal). Irregularity % is calculated using the following formula: Irregularity=((Total−DiagTotal/Total)×100).

[5]Some F0 measures are missing for certain talkers due to the poor quality of the electrolaryngograph signal for these talkers.

[6]It must be noted, though, that sentence-length materials have limitations when making acoustic measurements because of the greater variability caused by contextual effects (Krause and Braida, 2004).

Bond, Z. S., and Moore, T. J. (**1994**). ''A note on the acoustic-phonetic characteristics of inadvertently clear speech,'' Speech Commun. **14**, 325–337.

Bradlow, A. R., and Bent, T. (**2002**). ''The clear speech effect for non-native listeners,'' J. Acoust. Soc. Am. **112**, 272–284.

Bradlow, A. R., Krause, N., and Hayes, E. (**2003**). ''Speaking clearly for children with learning disabilities: Sentence perception in noise,'' J. Speech Lang. Hear. Res. **46**, 80–97.

Bradlow, A. R., and Pisoni, D. B. (**1999**). ''Recognition of spoken words by native and non-native listeners: talker-, listener- and item-related factors,'' J. Acoust. Soc. Am. **106**, 2074–2085.

Bradlow, A. R., Torretta, G. M., and Pisoni, D. B. (**1996**). ''Intelligibility of normal speech. 1. Global and fine-grained acoustic-phonetic talker characteristics,'' Speech Commun. **20**, 255–272.

Byrd, D. (**1994**). ''Relations of sex and dialect to reduction,'' Speech Commun. **15**, 39–54.

Carlson, E., and Miller, D. (**1998**). ''Aspects of voice quality: display, measurement and therapy,'' Int. J. Lang Commun. Disord. **33**, 304–309.

Cox, R., Alexander, G., and Gilmore, C. (**1987**). ''Intelligibility of average talkers in typical listening environments,'' J. Acoust. Soc. Am. **81**, 1598–1608.

Eisenberg, L. S., Shannon, R. V., Schaefer Martinez, A., Wygonski, J., and Boothroyd, A. (**2000**). ''Speech recognition with reduced spectral cues as a function of age,'' J. Acoust. Soc. Am. **107**, 2704–2710.

Evans, B., and Iverson, P. (**2004**). ''Vowel normalization for accent: An investigation of best exemplar locations in northern and southern British English sentences,'' J. Acoust. Soc. Am. **115**, 352–361.

Fallon, M., Trehub, S. E., and Schneider, B. A. (**2000**). ''Children's perception of speech in multitalker babble,'' J. Acoust. Soc. Am. **108**, 3023–3029.

Ferguson, S. H., and Kewley-Port, D. (**2002**). ''Vowel intelligibility in clear and conversational speech for normal-hearing and hearing-impaired listeners,'' J. Acoust. Soc. Am. **112**, 259–271.

Fisher, W., Doddington, G., and Goudie-Marshall, K. (**1986**). ''The DARPA speech recognition research database: specifications and status,'' in *Proceedings of the DARPA workshop on speech recognition*, pp. 93–99.

Fourcin, A. (**1974**). ''Laryngographic examination of vocal fold vibration,'' in *Ventilatory and Phonatory Control Systems*, edited by B. Wyke (Oxford U. P., Oxford), pp. 315–333.

Fourcin, A. J. (**1982**). ''Electrolaryngographic assessment of vocal fold function,'' J. Phonetics **14**, 435–442.

Gagné, J. P., Rochette, A. J., and Charest, M. (**2002**). ''Auditory, visual and audiovisual clear speech,'' Speech Commun. **37**, 213–230.

Glasberg, B. R., and Moore, B. C. J. (**1990**). ''Derivation of auditory filter shapes from notched-noise data,'' Hear. Res. **47**, 103–138.

Goldinger, S. (**1996**). ''Words and voices: Episodic traces in spoken word identification and recognition memory,'' J. Exp. Psychol. Learn. **22**, 1166–1183.

Goldinger, S. (**1997**). ''Words and voices: perception and production in an episodic lexicon,'' in *Talker Variability in Speech Processing*, edited by K. Johnson and J. Mullennix (Academic, San Diego), pp. 33–66.

Goldinger, S. D. (**1998**). ''Echoes of echoes? An episodic theory of lexical access,'' Psychol. Rev. **105**, 251–279.

Gordon-Salant, S. (**1986**). ''Recognition of natural and time/intensity altered CVs by young and elderly subjects with normal hearing,'' J. Acoust. Soc. Am. **80**, 1599–1607.

Hall, J. W., Grose, J. H., Buss, E., and Dev, M. B. (**2002**). ''Spondee recognition in a two-talker masker and a speech-shaped noise masker in adults and children,'' Ear Hear. **23**, 159–165.

Hazan, V., and Simpson, A. (**1998**). ''The effect of cue-enhancement on the intelligibility of nonsense word and sentence materials presented in noise,'' Speech Commun. **24**, 211–226.

Krause, J. C., and Braida, L. D. (**2002**). ''Investigating alternative forms of clear speech: The effects of speaking rate and speaking mode on intelligibility,'' J. Acoust. Soc. Am. **112**, 2165–2172.

Krause, J. C., and Braida, L. D. (**2004**). ''Acoustic properties of naturally produced clear speech at normal speaking rates,'' J. Acoust. Soc. Am. **115**, 362–378.

Lee, S., Potamianos, A., and Narayanan, S. (**1999**). ''Acoustics of children's speech: developmental changes of temporal and spectral parameters,'' J. Acoust. Soc. Am. **105**, 1455–1468.

Markham, D., and Hazan, V. (**2002**). ''The UCL Talker Database,'' Speech, Hearing and Language: UCL work in progress **14**, 1–17.

Markham, D., and Hazan, V. (**2004**). ''The effect of talker- and listener-related factors on intelligibility for a real-word, open-set perception test,'' J. Speech Hear. Res. **47**, 725–737.

Miller, G. A., and Nicely, P. E. (**1955**). ''An analysis of perceptual confusions among some English consonants,'' J. Acoust. Soc. Am. **27**, 338–352.

Montgomery, A. A., and Edge, R. A. (**1988**). ''Evaluation of 2 speech enhancement techniques to improve intelligibility for hearing-impaired adults,'' J. Speech Hear. Res. **31**, 386–393.

Newman, R. S., Clouse, S. A., and Burnham, J. L. (**2001**). ''The perceptual consequences of within-talker variability in fricative production,'' J. Acoust. Soc. Am. **109**, 1181–1196.

Palmeri, T., Goldinger, S., and Pisoni, D. (**1993**). ''Episodic encoding of voice,'' J. Exp. Psychol. Learn. **19**, 309–328.

Perkell, J. S., Zandipour, M., Matthies, M. L., and Lane, H. (**2002**). ''Economy of effort in different speaking conditions. I. A preliminary study of intersubject differences and modeling issues,'' J. Acoust. Soc. Am. **112**, 1627–1641.

Picheny, M. A., Durlach, N. I., and Braida, L. D. (**1985**). ''Speaking clearly for the hard of hearing. 1. intelligibility differences between clear and conversational speech,'' J. Speech Hear. Res. **28**, 96–103.

Picheny, M. A., Durlach, N. I., and Braida, L. D. (**1986**). ''Speaking clearly for the hard-of-hearing. 2. acoustic characteristics of clear and conversational speech,'' J. Speech Hear. Res. **29**, 434–446.

Redford, M. A., and Diehl, R. L. (**1999**). ''The relative perceptual distinctiveness of initial and final consonants in CVC syllables,'' J. Acoust. Soc. Am. **106**, 1555–1565.

Semel, E., Wiig, E. H., and Secord, W. (**1987**). ''CELF-R: Clinical Evaluation of Language Fundamentals-Revised,'' The Psychological Corporation, San Antonio, TX.

Simpson, A., and Hazan, V. (**1997**). ''Enhancing the intelligibility of natural VCV stimuli: talker effects,'' Speech, Hearing and Language: UCL work in progress **10**, 79–90.

Studebaker, G. A. (**1985**). ''A rationalized arcsine transform,'' J. Speech Hear. Res. **28**, 455–462.

Sulter, A. M. (**1996**). ''Variation of voice quality features and aspects of voice training in males and females,'' doctoral dissertation, University of Groningen, 1996.

Uchanski, R. M., Choi, S. S., Braida, L. D. *et al.* (**1996**). ''Speaking clearly for the hard of hearing .4. further studies of the role of speaking rate,'' J. Speech Hear. Res. **39**, 494–509.

Uchanski, R. M., Geers, A. E., and Protopapas, A. (**2002**). ''Intelligibility of modified speech for young listeners with normal and impaired hearing,'' J. Speech Lang. Hear. Res. **45**, 1027–1038.

Watt, D., Docherty, G. J., and Foulkes, P. (**2003**). ''First accent acquisition: a study of phonetic variation in child directed speech,'' in Proceedings of 15th International Congress of Phonetic Sciences, Barcelona, pp. 1959–1962.

Formant discrimination in noise for isolated vowels[a)]

Chang Liu[b)] and Diane Kewley-Port[c)]
Department of Speech and Hearing Sciences, Indiana University, Bloomington, Indiana 47405

(Received 4 April 2004; revised 9 August 2004; accepted 9 August 2004)

Formant discrimination for isolated vowels presented in noise was investigated for normal-hearing listeners. Discrimination thresholds for $F1$ and $F2$, for the seven American English vowels /i, ɪ, ɛ, æ, ʌ, a, u/, were measured under two types of noise, long-term speech-shaped noise (LTSS) and multitalker babble, and also under quiet listening conditions. Signal-to-noise ratios (SNR) varied from −4 to +4 dB in steps of 2 dB. All three factors, formant frequency, signal-to-noise ratio, and noise type, had significant effects on vowel formant discrimination. Significant interactions among the three factors showed that threshold-frequency functions depended on SNR and noise type. The thresholds at the lowest levels of SNR were highly elevated by a factor of about 3 compared to those in quiet. The masking functions (threshold vs SNR) were well described by a negative exponential over $F1$ and $F2$ for both LTSS and babble noise. Speech-shaped noise was a slightly more effective masker than multitalker babble, presumably reflecting small benefits (1.5 dB) due to the temporal variation of the babble. [DOI: 10.1121/1.1802671]

PACS numbers: 43.71.Es, 43.66.Fe [RLD] Pages: 3119–3129

I. INTRODUCTION

As one of the world languages with a crowded vowel space, American English has vowels that typically show considerable spectral overlap in the two-dimensional $F1\times F2$ vowel formant space (Peterson and Barney, 1952; Hillenbrand *et al.*, 1995). Spectral overlap between vowels resulting from talker and context differences suggest that vowels with the same formant-frequency values ($F1$ and $F2$) appear to belong to different vowel categories. In spite of this ambiguity, formant frequencies, especially $F1$ and $F2$, are critical to vowel perception and categorization. Thus, a long-term goal of our research is to establish a model of vowel perception to represent listeners' abilities to discriminate changes of formant frequencies both within and between vowels. To date, most formant discrimination research has been conducted in quiet, and the purpose of this research is to examine formant discrimination in noise.

Formant discrimination has been investigated systematically in a variety of experimental conditions (Flanagan, 1955; Kewley-Port and Watson, 1994; Hawks, 1994; Kewley-Port, 1995; Kewley-Port and Zheng, 1999; Liu and Kewley-Port, 2004b). In these studies, either $F1$ or $F2$ was changed by different amounts and the smallest change in formant frequencies that could be detected, represented by ΔF, was defined as the threshold of vowel formant discrimination. The first study estimating discrimination thresholds for single-formant frequencies was conducted by Flanagan (1955), using synthetic, steady-state vowels. Thresholds for $F1$ at 300, 500, and 700 Hz and for $F2$ at 1000, 1500, and 2000 Hz were measured, with the finding that thresholds were approximately 3%–5% of the formant frequency, as expressed in terms of the Weber ratio, $\Delta F/F$.

Over the last decade, Kewley-Port and her colleagues have investigated vowel formant discrimination systematically from optimal to more ordinary listening conditions for both formant-synthesized and high-fidelity speech. Kewley-Port and Watson (1994), using formant-synthesized speech (Klatt, 1980), measured thresholds for formant discrimination under optimal listening conditions, in which isolated vowels were presented under minimal stimulus uncertainty in quiet to well-trained listeners. They found that thresholds were constant at 14 Hz for $F1<800$ Hz and increased with formant frequency at a rate of 10 Hz/1000 Hz for $F2$. The Weber ratio in the $F2$ region was approximately 1.5%. To investigate formant discrimination under other more ecologically representative conditions, several factors have been manipulated systematically such as fundamental frequency ($F0$), phonetic context, level of stimulus uncertainty, listener training, and the addition of a word identification task. For example, thresholds for vowel formant discrimination were measured in different phonetic contexts including syllables, phrases, and sentences (Kewley-Port, 1995; Kewley-Port and Zheng, 1999; Liu and Kewley-Port, 2004b). Kewley-Port (1995) investigated the effect of the phonetic context /CVC/ on formant discrimination for the /ɪ/ vowel and suggested that thresholds in a /CVC/ were significantly increased compared to thresholds for isolated vowels. When phonetic context increased further to phrases and sentences in formant-synthesized speech, performance for formant discrimination became even worse (Kewley-Port and Zheng, 1999). Thresholds for high-fidelity speech, which was synthesized in STRAIGHT (Kawahara *et al.*, 1999) and sounded more natural than formant-synthesized speech, showed similar effects for phonetic contexts (Liu and Kewley-Port, 2004b), although thresholds were elevated compared to format-synthesized speech. Besides phonetic context, the level of stimulus uncertainty and subject training were found to significantly affect formant frequency discrimination.

[a)]Portions of the data were presented at the 141st and 142nd meeting of the Acoustical Society of America [J. Acoust. Soc. Am. **109**(5), 2295 (Liu and Kewley-Port, 2001); J. Acoust. Soc. Am. **110**(5), 2658 (Liu and Kewley-Port, 2001)].

[b)]Electronic mail: chang.liu@wichita.edu
[c)]Electronic mail: kewley@indiana.edu

Compared to thresholds at minimal stimulus uncertainty (Kewley-Port and Watson, 1994), a medium level of stimulus uncertainty appeared to increase thresholds for isolated vowels by 130% (Kewley-Port and Zheng, 1999; Kewley-Port, 2001). In another condition, naive listeners in their first block of testing still showed much more difficulty in discriminating formant frequency than highly trained listeners with a reduction of 230% associated with training (Kewley-Port, 2001).

Since formant frequencies are represented on a nonlinear scale in the cochlea, Kewley-Port and Zheng (1999) and Liu and Kewley-Port (2004b) have described a straightforward method of summarizing formant thresholds data. That is, thresholds for vowel formant discrimination, ΔF, were transformed to an auditory scale (Kewley-Port and Zheng, 1999). Several auditory scales including log frequency, Moore's equivalent rectangular bandwidth (ERB rate) scale (Moore and Glasberg, 1987; Glasberg and Moore, 1990), and Zwicker's (1961) critical-band scale (z), were examined. Of the three auditory scales, the z scale showed the flattest functions and was the most effective in reducing effects of formant frequency and fundamental frequency. Applying the z transform to vowel formant discrimination in phrases and sentences under more ordinary listening conditions, thresholds were described as constant at 0.28 barks for formant-synthesized speech (Kewley-Port and Zheng, 1999). Recently, in a similar study (Liu and Kewley-Port, 2004b) using high-fidelity speech, reported thresholds were constant at 0.37 barks, which can be thought of as a norm for formant discrimination in modest length sentences.

Thus, effects of a number of factors, such as phonetic context, level of stimulus uncertainty, training, and an additional identification task, in vowel formant discrimination tasks have been systematically studied. These factors were investigated under the quiet listening condition. However, one challenge to perceiving speech in everyday conversation is the typically noisy environment. Background noise can mask the speech signal so that listeners have less acoustical information to perceive and identify the speech sounds. Thus, the purpose of this research is to investigate how noise affects formant discrimination.

Noise variables that influence speech perception are level, and the spectral and temporal properties of the noise. Speech reception thresholds (SRT) are constant at low noise levels but increase proportionally to the increase of noise level for middle and high noise levels in the presence of the steady noise (Plomp and Mimpen, 1979). Speech perception becomes more difficult as bandwidth increases such that noise reduces the audibility of larger portions of the speech spectrum (Dubno and Dirks, 1982; Stelmachowicz *et al.*, 1990). In addition, listeners are sensitive to the temporal fluctuation in noise, i.e., they take advantage of intermittent noise, modulated noise, and multitalker babble compared to a noise without modulation (Miller and Licklider, 1950; Kalikow *et al.*, 1977; Festen, 1993).

Although a number of investigations have been conducted on speech perception in noise, little research has been concerned with the effects of noise on vowel formant discrimination. The present study investigates the degree to which noise influences formant thresholds spectrally and temporally using two types of noise: long-term speech-shaped noise and multitalker babble in comparison to a quiet condition. Two noise factors were manipulated systematically in this study: the overall signal-to-noise ratio and noise type.

TABLE I. Formant frequency (Hz and bark) for $F1$ and $F2$ for seven female vowels.

$F1$ Vowel	i	u	ɪ	ɛ	æ	ʌ	a
Frequency (Hz)	270	280	430	580	678	700	818
Barks	2.7	2.8	4.3	5.6	6.3	6.5	7.4
$F2$ Vowel	u	a	ʌ	æ	ɛ	ɪ	i
Frequency (Hz)	1124	1281	1454	1960	2078	2132	2562
Barks	9.6	10.1	10.9	12.9	13.3	13.4	14.7

II. METHOD

A. Speech stimuli

Vowel formant discrimination was measured for seven American English vowels /i, ɪ, ɛ, æ, ʌ, a, u/. This selection of seven vowels provided a broad coverage of formant frequencies that range from 270 to 2562 Hz as shown in Table I. Vowels were recorded in the syllable context of /bVd/ from a female talker. Many sentences and phrases with each of the seven vowels were originally recorded from the female talker. Syllables (/bVd/) with similar neutral prosody were selected at the eighth position of one nine-word sentence to serve as the original stimuli for formant shifts and future resynthesis. All speech stimuli with and without formant shifts were resynthesized from these original syllables in a modified version of STRAIGHT (Kawahara *et al.*, 1999), which uses a pitch-adaptive method for speech analysis and synthesis. The resynthesized speech stimuli without any change of the acoustic parameters in STRAIGHT (the standard stimuli) sounded quite similar to original natural-speech stimuli and they were referred to the high-fidelity speech. Formant shifts, as described in Liu and Kewley-Port (2004a), were manipulated based on the standard stimulus as follows: a matrix in MATLAB representing the spectrogram (amplitude $\times$time$\times$frequency) of the standard syllable, was obtained by the analysis in STRAIGHT. Visually this spectrogram has very smooth formant peaks. To shift a formant peak, the temporal location of the formant across the syllable, including transitions, was visually identified. In each time frame (i.e., one spectrum), formant shift was manipulated for the portion between the valleys on either side of the formant peak. Amplitude in the low-frequency valley was adjusted to be a constant across the frequency range corresponding to the frequency shift, while the high-frequency valley was collapsed by replacing the original amplitude values with the shifted peak, such that the shift in the selected formant frequency resulted in no change in other formants (see Liu and Kewley-Port, 2004a). Detail in the formant peaks was preserved in this procedure, with the valleys only somewhat changed. This modified 2D matrix was reloaded into STRAIGHT and used with other unchanged acoustic param-

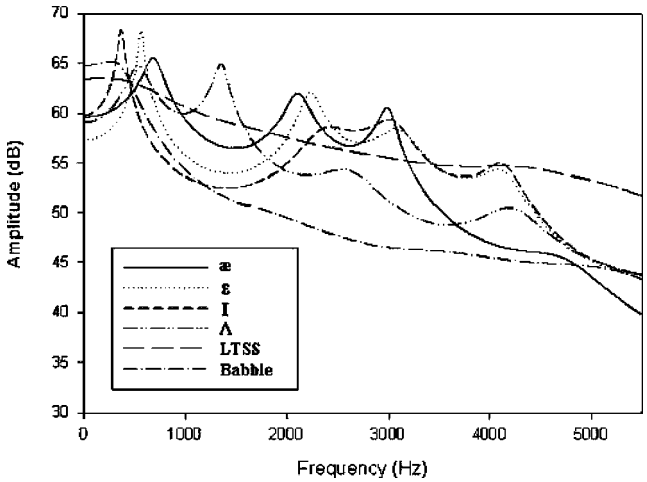

FIG. 1. LPC spectra of four vowels, LTSS noise, and multitalker babble for an overall vowel level of 70 dB SPL and an overall SNR of 0 dB.

eters such as $F0$ and amplitude contours for resynthesis [for more details, see Liu and Kewley-Port (2004a) and their Fig. 1]. Although formants at both formant transitions (onset and offset) as well as the steady state were adjusted in each /bVd/ syllable, only isolated vowels were selected as speech stimuli in the present study. These isolated vowels were edited by deleting the formant transition at the beginning and end of the syllable such that only the relatively steady-state vowel nucleus remained. The duration of isolated vowels varied from 107 to 206 ms as expected in natural speech.

Formant frequency shifts were manipulated in STRAIGHT in sets of 24 for each vowel. Selected formant frequencies, $F1$ and $F2$ of the seven vowels, were increased by 0.7% to 17% over 24 steps using a linear scale with a step size of 0.7%. For example, the $F1$ of the /ɛ/ vowel is 580 Hz, and the shifts of $F1$ ranged from 4.1 Hz (0.7%) to 98.6 Hz (17%). This procedure is the same as that of Liu and Kewley-Port's study (2004b).

B. Maskers

Two types of noise were selected as maskers in this study: long-term speech-shaped noise and multitalker babble (Kalikow *et al.*, 1977). Long-term speech-shaped noise (LTSS) is similar to white noise in that it does not fluctuate; however, it has more masking efficiency due to the similarity between the spectra of speech signals and LTSS. On the other hand, the multitalker babble is a time-varying masker in which occasional elements of speech signal may coincide with momentary minima in the level of the masker such that the multitalker babble has less masking efficiency than LTSS noise. In order to match the shape of the noise as well as possible to the speech of this talker, the LTSS noise was generated from uniform noise that was shaped by a filter with the average spectrum of long-term speech calculated over the 40 sentences and 9 phrases from the female talker. The babble selected is the 12-talker babble produced by Kalikow *et al.* (1977) that has been used frequently in the literature. The spectra of LTSS noise, multitalker babble, and four of the seven isolated vowels (/ɪ, ɛ, æ, ʌ/) with signal-to-noise ratio at 0 dB are shown in Fig. 1. As expected for the natural vowels, local signal-to-noise ratios are variable for $F1$ and $F2$ for these four vowels under either LTSS noise or babble. Spectra of the other three vowels (/a, i, u/) also showed the similar variability on local SNRs for $F1$ and $F2$ regions, with the exception of a relatively lower local SNR for $F2$ of the vowel /u/. The primary spectral difference between the two noises is that the babble has less high-frequency energy than the LTSS noise, and therefore local SNR for $F2$ is much higher (about 6 dB). Given the large variability in formant amplitude for these naturally produced vowels, it was not practical to experimentally control local SNR for each formant and noise. Instead, the overall signal-to-noise ratio was manipulated and the local SNR values were evaluated *post hoc*. Pilot data suggested that performance for vowel formant discrimination was mainly affected for SNRs between -4 and $+4$ dB, where vowels at -4-dB SNR were barely detectable. Thus, SNR was varied from -4 to $+4$ dB with a step size of 2 dB in the present study.

C. Listeners

Six American English native speakers, between 21 and 39 years old, participated in this study. All listeners had normal hearing with pure-tone thresholds of 15 dB HL or better at octave intervals from 250 to 8000 Hz and were paid for their participation.

D. Procedure

Speech stimuli were presented to the right ears of listeners, who were seated in a sound-treated, IAC booth, via calibrated TDH-39 earphones. Stimulus presentation was controlled by a series of TDT modules, including a 16-bit D/A converter (DA1), a programmable filter (PF1), and a headphone buffer (HB6), using a sample rate of 11 025 Hz. A low-pass filter with a cutoff frequency of 5000 Hz and a slope of 80 dB/octave, and an attenuation level set by the calibration procedure, was configured in the programmable filter and applied to the summed speech plus noise signal. The vowel /ɛ/, with a duration of 3 s, was used as the calibration sound. The sound-pressure level measured in the NBS-9A 6-c^3 coupler by a Larson-Davis sound-level meter (model 2800) with the linear weighting band was set at 70 dB SPL for the vowel stimuli.

The LTSS noise was generated by the TDT waveform generator (WG2), then filtered (PF1) and attenuated (PA4), and finally added to the vowel stimuli via the weighted summer (SM3). A FIR filter was designed to match the long-term speech spectrum of the female talker. The babble masker was generated by randomly selecting a segment of multitalker babble of an appropriate length from a 30-s sample of the babble (Kalikow *et al.*, 1977). This selected babble segment was then presented with the vowel stimuli through the dual channels of the converter (DA1) separately. After being attenuated (PA4), the babble was summed with the vowel stimuli via the weighted summer (SM3). The level of LTSS noise and multitalker babble was attenuated so as to achieve the overall signal-to-noise ratio at -4, -2, 0, $+2$, and $+4$ dB or turned off for the quiet condition.

Test procedures were similar to those of Kewley-Port and Zheng (1999). Formant thresholds were measured using a modified three-interval, two-alternative forced-choice (2AFC) procedure with a two-down, one-up tracking algorithm, estimating the frequency increment required for 71%-correct responses (Levitt, 1971). In each trial, the standard was presented in the first interval, followed by two intervals, in one of which was the incremented-formant vowel and in the other was the standard vowel. The listener's task was to indicate which interval contained the stimulus that differed from the standard. Sixty trials were run in each block for the quiet only condition and 90 trials each for the LTSS noise and babble conditions. Only one formant was tested in each block, varying SNR and quiet.

There were three experiments in this study. In the first experiment, formant thresholds were measured in quiet for all seven vowels. In the second experiment, thresholds were measured in LTSS noise with interleaved trials of the quiet condition. In each block, vowels with only one shifted formant were presented. The SNR values were randomly varied trial by trial with quiet with the range from -4 to $+4$ dB. Thus, six conditions (five SNR levels in noise plus quiet) with only one formant and one vowel were presented in each block. Seven vowels were presented to the listeners in a quasirandom order such that the sequence of vowel presentations was different among listeners. Only one vowel was presented in one session (per day) and $F1$ and $F2$ were alternated in successive blocks for threshold measurements. In the third experiment, thresholds were measured in the multitalker babble (Kalikow *et al.*, 1977) using the same procedures as the second experiment, again with interleaved quiet-condition trials. In each masking trial of the second and third experiment, the maskers began 1 s before the standard vowel and continued for 1 s after the three vowel intervals. The intervals between vowel presentations, within each trial, were 400 ms in duration.

Prior to the collection of experimental data, listeners had extensive training in each of the conditions. The duration of each block was approximately 4 min for the quiet condition and 7–8 min for the noise conditions. Every session was composed of six or seven blocks. At the beginning of each experiment (quiet only, LTSS noise, and multitalker babble), listeners were given one training session in which $F1$ and $F2$ of vowel /ɛ/ were presented so that listeners became familiar with the procedures. After the training session, the test sessions were begun. A mean value of ΔF for each listener was averaged over the ΔF values for the last four blocks in which performance was stable by visual inspection. Group means, i.e., ΔF for each formant, were calculated as the average of the ΔF thresholds across the six listeners.

III. RESULTS

A. Thresholds for formant discrimination in quiet

Average thresholds of ΔF as a function of formant frequency for $F1$ and $F2$ for the seven vowels tested in quiet are shown in Fig. 2. Comparisons for the quiet conditions presented in each of the three experiments (quiet only and quiet trials interleaved with masking trials in experiment 2 and 3) were made with a two-way (listening condition X, formant frequency) repeated-measure analysis of variance (ANOVA). Results showed that there was no significant effect of listening conditions on formant discrimination in the quiet [$F(2,10)=2.75$, $p=0.112$], whereas higher formant frequency significantly increased thresholds [$F(13,65)=18.31, p<0.001$]. In addition, the interaction between the formant frequency and listening conditions was not significant [$F(26,130)=0.971$, $p=0.511$]. The Tukey *post hoc* test suggested that there was no significant difference for the thresholds between any two of the three quiet listening conditions. Not surprisingly, effects of formant frequency were similar to those obtained in a previous study (Kewley-Port and Watson, 1994), that is, thresholds (ΔF) were reasonably constant in the $F1$ region (<800 Hz), and elevated with increases of formant frequency in the $F2$ region.

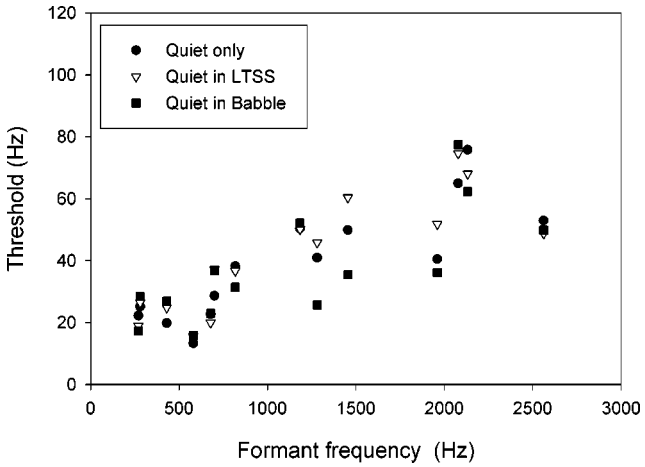

FIG. 2. Thresholds of vowel formant discrimination (ΔF) in Hz as a function of formant frequency in quiet conditions for three procedures: quiet only, quiet trials interleaved with LTSS noise trials, and quiet trials interleaved with babble trials.

The thresholds in Hz were converted to thresholds in an auditory scale in bark (Z), using Traunmüller's equation (1990). As expected, the transformation produced thresholds (ΔZ) that were relatively flat across $F1$ and $F2$ values of formant frequency (see Fig. 3). Linear regression on all three quiet conditions showed that there was no significant linear relationship between thresholds (ΔZ) and formant frequency (barks), suggesting flat patterns for all three quiet conditions [quiet only, $F(1,12)=0.607$, $p=0.451$; quiet with LTSS, $F(1,12)=0.382$, $p=0.548$; quiet with babble, $F(1,12)=2.103$, $p=0.173$]. However, a two-way (listening condition X, formant frequency) ANOVA again suggested that listening condition had no significant effect on ΔZ [$F(2,10)=2.542$, $p=0.128$], whereas formant frequency did have a significant effect on ΔZ [$F(13,65)=8.707, p<0.001$]. The significant effect of formant frequency on ΔZ might be due to the patterns of variability seen for some thresholds across the formant frequency in the three quiet conditions (ranging from 0.108 to 0.294 barks). Altogether, the three quiet conditions showed similar average thresholds (about 0.20 barks) and similar variability over formants (standard deviation of 0.05–0.06 barks for the three quiet conditions).

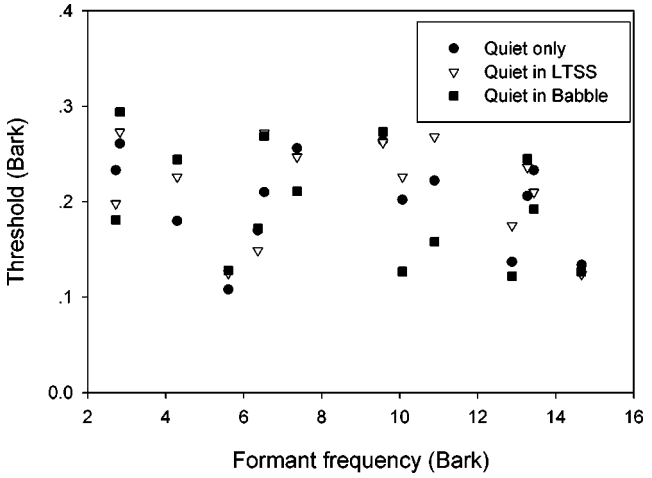

FIG. 3. Thresholds of vowel formant discrimination (ΔZ) in bark as a function of formant frequency in quiet conditions for three procedures: quiet only, quiet trials interleaved with LTSS noise trials, and quiet trials interleaved with babble trials.

B. Thresholds for formant discrimination in LTSS noise

Because statistical analyses showed similar results for thresholds in ΔF and ΔZ, only thresholds in ΔZ are reported here. Thresholds in barks for only the LTSS noise and the interleaved quiet condition are shown in Fig. 4. The lines connecting the thresholds are only intended to help compare visually the different SNR conditions. Thresholds in ΔZ were analyzed by a two-way (formant frequency X, SNR) repeated-measure ANOVA. The analysis showed that formant frequency $[F(13,65)=9.331, p<0.001]$, SNR $[F(5,25)=133.5, p<0.001]$ and the interaction between formant frequency and SNR $[F(65,325)=7.341, p<0.001]$ all showed significant effects. The Tukey *post hoc* tests of threshold-frequency (ΔZ) functions across the SNRs indicated four different patterns: (1) quiet condition; (2) SNR=+4 dB; (3) SNR=+2 and 0 dB; and (4) SNR=−2 and −4 dB.

Simple main effects analyses revealed that formant frequency was a significant effect for every SNR and the quiet condition ($p<0.01$). Under the quiet listening condition and noise conditions at high SNRs, thresholds in ΔZ showed relatively flat patterns over formant frequencies. However, thresholds increased markedly in the $F2$ regions under noise conditions at low SNRs, such as −2 and −4 dB, suggesting more effects of noise on the $F2$ regions than the $F1$ regions (see Fig. 4). In order to measure whether thresholds at $F1$ region are different from thresholds at $F2$ region, planned comparisons between thresholds for $F1$ and $F2$ regions under each SNR condition, including the quiet condition, were completed. Results suggested that thresholds in the $F1$ region were significantly lower than thresholds in the $F2$ regions for only noise conditions with SNR at −2 $[F(1,5)=83.928, p<0.001]$ and −4 dB $[F(1,5)=125.184, p<0.001]$. There was no significant difference for thresholds (ΔZ) between $F1$ and $F2$ regions at +4 dB, +2 dB, 0 dB, or for the quiet condition ($p>0.08$). Thus, masking elevates thresholds in the $F2$ region compared to $F1$ at low SNRs.

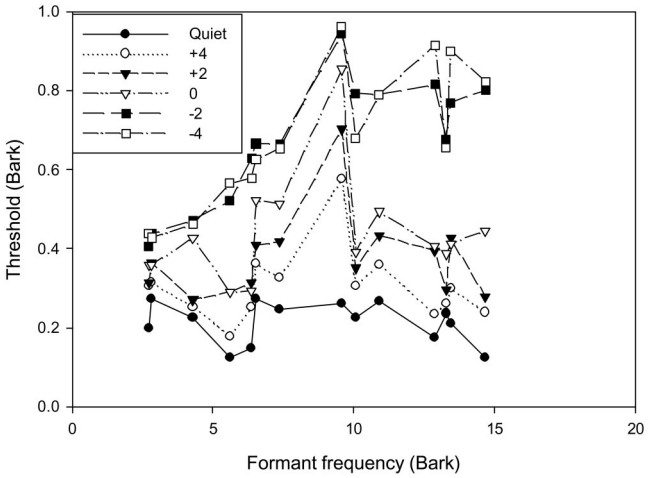

FIG. 4. Thresholds of vowel formant discrimination (ΔZ) in bark as a function of formant frequency in quiet and in LTSS noise conditions with SNR at −4, −2, 0, +2, and +4 dB.

TABLE II. Local SNR in the frequency region of each formant of the seven vowels for $F1$ (top) and $F2$ (bottom) for LTSS noise in dB.

$F1$ Overall SNR	i	u	ɪ	ɛ	æ	ʌ	a
4	12.6	12.2	9.6	11.7	9.7	8.3	10.4
2	10.6	10.2	7.6	9.7	7.7	6.3	8.4
0	8.6	8.2	5.6	7.7	5.7	4.3	6.4
−2	6.6	6.2	3.6	5.7	3.7	2.3	4.4
−4	4.6	4.2	1.6	3.7	1.7	0.3	2.4
$F2$ Overall SNR	u	a	ʌ	ɛ	æ	ɪ	i
4	−2.9	8.9	7.7	6.6	8.5	4.3	2.0
2	−4.9	6.9	5.7	4.6	6.5	2.3	0
0	−6.9	4.9	3.7	2.6	4.5	0.3	−2.0
−2	−8.9	2.9	1.7	0.6	2.5	−1.7	−4.0
−4	−10.9	0.9	−0.3	−1.4	0.5	−3.7	−6.0

Another perspective on the results is provided by masking functions, which demonstrate more clearly how thresholds change with decreasing local SNRs. Local SNRs are the measured signal-to-noise ratios for each individual formant. The local SNRs in the frequency region of each formant was obtained by measuring the 1/3-octave levels centered around the formants relative to the noise level using a Larson-Davis sound-level meter (2800 model), as shown in Table II.

In Fig. 5, it appears that thresholds in bark as a function of local SNR improve for $F1$ and $F2$ for the seven vowels as SNR increases. An exponential decay function and a linear function were fit to the masking function. Because the threshold in noise will eventually reach the threshold in quiet, the quiet threshold was used as a reference to normalize thresholds in noise. The normalized thresholds were calculated by subtracting the quiet threshold (0.201 barks) from each threshold in Fig. 5 and then used for the exponential decay regression function. Analysis of the nonlinear regression suggested that the exponential decay function fit well to the masking function ($r=-0.779$). The function, $\Delta Z = 0.201 + 0.378 * e^{(-0.083 * \mathrm{SNR})}$, shown in Fig. 5, suggests that thresholds improved exponentially with the increase in local

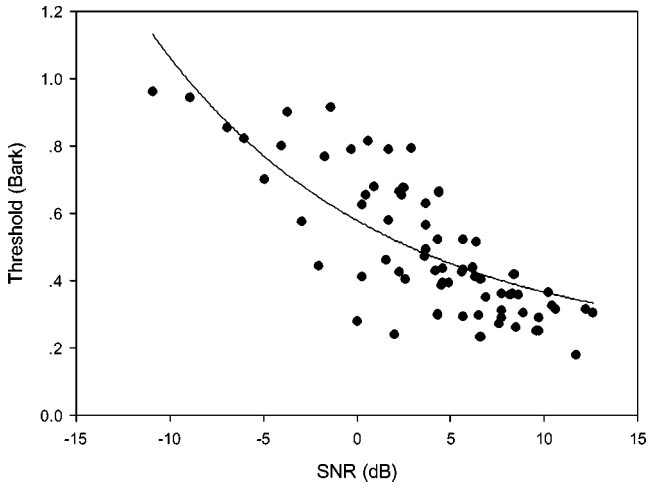

FIG. 5. The masking effects of LTSS noise (ΔZ) on vowel formant thresholds as a function of local SNR are displayed along with the nonlinear (exponential decay) regression function.

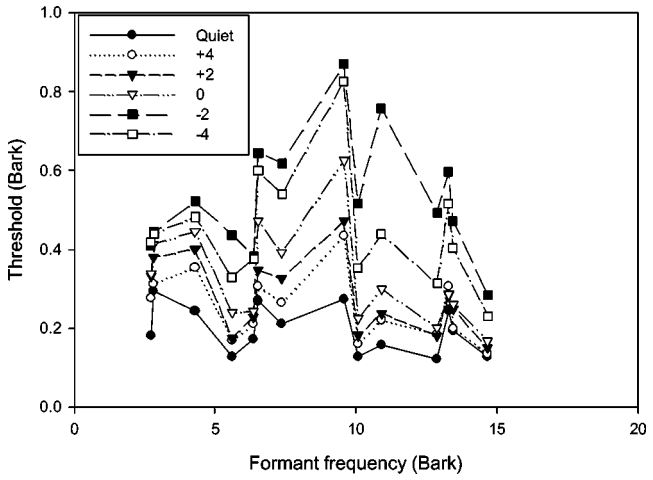

FIG. 6. Thresholds of vowel formant discrimination (ΔZ) in bark as a function of formant frequency in quiet and in multitalker babble conditions with SNR at −4, −2, 0, +2, and +4 dB.

SNR and approached the threshold in quiet (0.201 barks) when SNR was above 30 dB. The linear regression was also completed, yielding a strong relationship between thresholds in ΔZ and SNRs ($r=-0.812$). However, because the masking function shows an asymptotic pattern and it is reasonable to predict that the threshold will approach the threshold in quiet as SNR reaches a high level, nonlinear regression was considered a more principled description of the masking function.

C. Thresholds for formant discrimination in multitalker babble

Similar to the LTSS noise condition, thresholds in multitalker babble were analyzed in Hz (ΔF) and barks (ΔZ). Again results for the two statistical analyses were quite similar and only thresholds in barks (ΔZ) are reported here. As expected, results of a two-factor (formant frequency X, SNR) repeated-measure ANOVA on ΔZ suggested that effects of formant frequency [$F(13,65)=7.176, p<0.001$], SNR [$F(5,25)=88.214, p<0.001$], and the interaction between formant frequencies and SNR [$F(65,325)=2.400, p<0.001$] were significant. As seen in Fig. 6, frequency functions in ΔZ were dependent on overall SNRs. Based on the Tukey *post hoc* tests across the SNRs, patterns of threshold-frequency functions were categorized into four groups: (1) quiet, +4 and +2 dB; (2) 0 dB; (3) −2 dB; and (4) −4 dB. Examining functions for the quiet condition and high-level SNRs, ΔZ was relatively constant across the formants of $F1$ and $F2$ regions, whereas at low SNRs, particularly −2 and −4 dB, variability of ΔZ increased, especially for the mid-frequency formants (i.e., $F1$ of /a/ and $F2$ of /u/). Simple main effects analysis suggested that there was significant effect of the formant frequency under each listening condtion ($p<0.01$). However, different from in the LTSS noise, planned comparisons in the babble suggested that there was no significant difference between thresholds for $F1$ and $F2$ regions under each SNR and the quiet condition ($p>0.07$). These patterns of ΔZ frequency under different SNRs in multitalker babble are different from those patterns in LTSS noise, primarily in the $F2$ region as expected, given the differences in the noise spectra (Fig. 1).

Similar to the LTSS noise condition, the local SNRs for each formant were obtained by measuring the 1/3-octave levels of vowels and babble (long-term average) with a Larson-Davis sound-level meter (2800 model) (Table III). As shown in Fig. 1 and Table III, in $F2$ region, the level of vowel formants is much higher than the masking level of multitalker babble. The masking function for ΔZ over $F1$ and $F2$ for the seven vowels is shown in Fig. 7 along with a negative exponential function that was fit by nonlinear regression ($r=-0.622$). The nonlinear regression function, represented as $\Delta Z=0.201+0.340*e^{(-0.094*\mathrm{SNR})}$, suggested that thresholds in ΔZ decrease exponentially with increasing SNRs and approach the threshold for the quiet condition (0.201 barks) for SNR above 30 dB.

D. Comparison between LTSS noise and multitalker babble

Having considered the thresholds for each noise type separately, another analysis was completed to compare them

TABLE III. Local SNR for the frequency region at each formant of the seven vowels for $F1$ (top) and $F2$ (bottom) for multitalker babble in dB.

$F1$ Overall SNR	i	u	ɪ	ɛ	æ	ʌ	a
4	8.3	8.2	7.7	11.6	10.9	10.7	11.3
2	6.3	6.2	5.7	9.6	8.9	8.7	9.3
0	4.3	4.2	3.7	7.6	6.9	6.7	7.3
−2	2.3	2.2	1.7	5.6	4.9	4.7	5.3
−4	0.3	0.2	−0.3	3.6	2.9	2.7	3.3
$F2$ Overall SNR	u	a	ʌ	ɛ	æ	ɪ	i
4	4.9	14.1	15.7	15.1	22.3	21.3	22.4
2	2.9	12.1	13.7	13.1	20.3	19.3	20.4
0	0.9	10.1	11.7	11.1	18.3	17.3	18.4
−2	−1.1	8.1	9.7	9.1	16.3	15.3	16.4
−4	−3.1	6.1	7.7	7.1	14.3	13.3	14.4

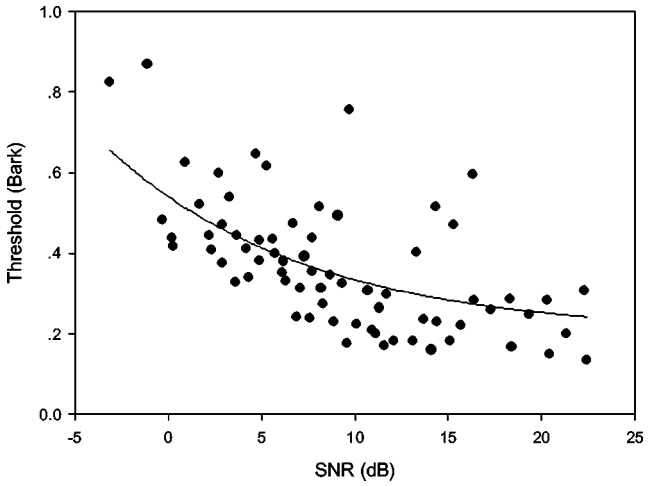

FIG. 7. The nonlinear (exponential decay) regression function for the masking effects of multitalker babble on vowel formant discrimination.

directly. Average thresholds for LTSS noise across formant frequencies compared to average thresholds for multitalker babble for each SNR experimental condition are shown in Fig. 8. A three-way (noise type X, formant frequency X, SNR) ANOVA on ΔZ showed significant main effects for all three factors [noise type: $F(1,5)=77.994$, $p<0.001$; SNR: $F(5,25)=223.992$, $p<0.001$; formant: $F(13,65)=9.410$, $p<0.001$]. In addition, all interactions between the three factors were also significant [noise type X SNR: $F(5,25)=13.783$, $p<0.001$; noise types X formant: $F(13,65)=4.648$, $p<0.001$; SNR X formant: $F(65,325)=4.253$, $p<0.001$; noise type X SNR X formant: $F(65,325)=2.100$, $p<0.001$]. Thus, the overall performance for vowel formant discrimination on ΔZ was better for multitalker babble listening condition than that for LTSS noise across formant frequency and overall SNRs. Simple main effect analyses suggested that thresholds for babble were always significantly lower than LTSS noise for the same SNR ($p<0.05$). Differences in thresholds between LTSS noise and babble increased as the masking level increased (i.e., SNR decreased). It can be seen, however, that performance improves

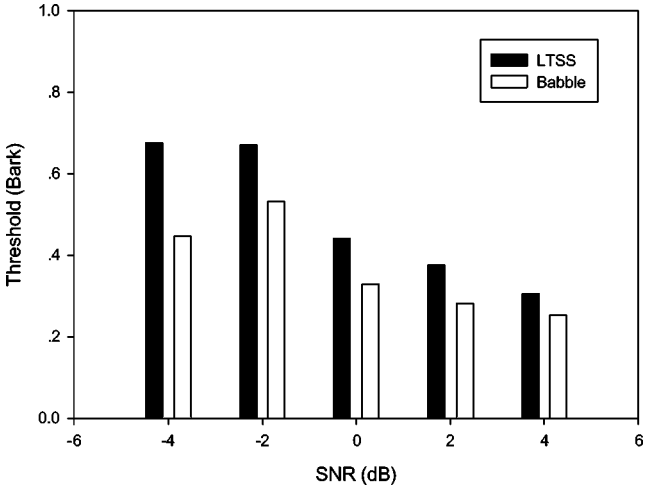

FIG. 8. Comparison of average thresholds of formant discrimination (ΔZ) in barks between LTSS noise and babble, for different SNR conditions at -4, -2, 0, $+2$, and $+4$ dB.

under multitalker babble by approximately 4 dB compared to that under LTSS noise. For example, average thresholds for formant discrimination in the presence of babble with SNR$=-4$ dB are comparable to thresholds in LTSS noise at 0 dB, A more detailed analysis of the difference between the efficiency of the two maskers is presented in the discussion.

In summary, several factors significantly influenced vowel formant discrimination, including formant frequency, signal-to-noise ratio, and noise type. Formant discrimination improved exponentially as SNR was increased, and finally approached the threshold in the quiet listening condition. In addition, each of these three factors did not affect the formant discrimination independently. Instead, the three factors interacted with each other, producing different patterns of formant discrimination.

IV. DISCUSSION

A. Vowel formant discrimination for high-fidelity speech in quiet

Kewley-Port and her colleagues (Kewley-Port and Watson, 1994; Liu and Kewley-Port, 2004b) have determined that thresholds of formant-frequency discrimination as a function of formant frequency in Hz are described by a piecewise-linear model for both formant-synthesized isolated vowels and high-fidelity vowels in syllables. To test whether this piecewise-linear model would be a good fit to the present high-fidelity isolated vowels in quiet (Fig. 2), two linear regressions were calculated, one in the low-frequency region (frequencies$<$800 Hz) and the other in the high-frequency region (frequencies $>$800 Hz). Because there was no significant difference in thresholds between the three quiet conditions, ΔF averages over three quiet conditions were used in the linear regression analysis. Results suggested that ΔF thresholds for formant-frequency discrimination for $F1(<800\,\text{Hz})$ were relatively constant at about 23.5 Hz and the regression was not significant as expected [$F(1,16)=0.662$, $p=0.428$; $r=0.199$]. However, for formants greater than 800 Hz, a modest correlation between ΔF and formant frequency ($r=0.540$) and a significant linear regression [$F(1,22)=9.048$,$p<0.01$] were obtained. The $F2$ linear regression function indicated that thresholds increase with increasing formant frequency at a rate of 14 Hz/1000 Hz for formant frequencies above 800 Hz. Thus, the piecewise model accounted well for the present data for high-fidelity vowels, consistent with the earlier data for formant-synthesized vowels (Kewley-Port and Watson, 1994).

Comparison of the thresholds for isolated vowels reported by Kewley-Port and Watson (1994) and those from the present study shows that thresholds for formant-synthesized isolated vowels were significantly lower than those for high-fidelity isolated vowels in this study (two-tailed t-test, $p<0.001$). The increased thresholds for high-fidelity vowels may be due to the greater acoustic variability overall in the high-fidelity speech, such as higher $F0$ variability and more variability in spectral patterns, than the formant-synthesized speech. Previously, Liu and Kewley-Port (2004b) reported that formant discrimination was slightly better for formant-synthesized speech than for high-

fidelity speech for both syllables and sentences. Those results, together with this study, suggest that formant discrimination thresholds are somewhat higher for high-fidelity speech than for formant-synthesized speech when similar conditions are compared. When an auditory scale transform of ΔF to barks (ΔZ) was applied, relatively constant threshold-frequency functions (Fig. 3) were obtained similar to formant-sythesized speech. However, higher average thresholds were obtained for high-fidelity vowels ($m=0.20$ barks) compared to the formant-synthesized isolated vowels ($m=0.12$ barks, averaged over the same seven vowel categories but with different formant frequencies). Thus, the result of the ΔZ transformation flattens the effect of formant frequency for vowels in quiet. The remaining discussion will refer to results in barks to allow us to focus on the effects of the other experimental manipulations.

B. Vowel formant discrimination in LTSS noise and multitalker babble

1. Effects of the noise level

Performance for vowel formant discrimination was significantly affected by SNR, as shown in threshold-frequency functions (see Figs. 4 and 6) as well as in masking functions (Figs. 5 and 7). As noise levels increased, thresholds elevated, particularly for SNR at -2 and -4 dB. As shown in Figs. 5 and 7, the negative exponential of the fitted masking functions for LTSS noise and babble showed that thresholds decreased to an asymptotic level of performance, approaching thresholds in the quiet condition. These results suggest that the underlying pattern of the masking functions for both noises is well-described by negative exponential functions.

An unexpected result in the present data was that thresholds for -2-dB SNR were higher than thresholds for -4-dB SNR for many formants in LTSS noise and babble, although the level of the masker was lower. This could be due to different strategies that listeners used for vowel formant discrimination at these two high-level noise conditions. In quiet, formant discrimination presumably depends on the comparisons of changes in the spectral shape. The systematic increase in thresholds with noise up to -2-dB SNR suggests that spectral comparison was also used in the presence of noise. However, at -4-dB SNR the standard vowel was mostly masked by noise, but as a consequence of the increment in the formant, the vowel with the formant shift became more detectable than the standard vowel. Thus, listeners might use a ''nondetectable and detectable'' decision rule in the -4-dB SNR formant discrimination condition. The ''nondetectable and detectable'' strategy used at -4-dB SNR might make the discrimination task easier than the spectral strategy used in -2-dB SNR, thus accounting for the lower thresholds obtained at -4-dB SNR.

2. Effects of the formant frequency

When vowels were presented in the quiet condition and in the noise conditions at the high SNR condictions, thresholds as ΔZ suggested a relatively flat pattern over formant frequency. However, when vowels were presented at low SNRs (-2 and -4 dB) for LTSS noise, thresholds, in ΔZ, were significantly higher in the $F2$ region than thresholds in the $F1$ region. These differences are the result of the local SNRs for those formants. As shown in Table II, the local SNRs for $F2$ were lower than those for $F1$, resulting in more masking in the $F2$ region for LTSS noise. For a given overall SNR, especially at -2 and -4 dB, local SNRs for most of the $F2$ values were below 0 dB, such that a larger formant shift was needed for the vowel discrimination in the $F2$ regions than in the $F1$ region for LTSS noise (see Table II). On the other hand, for multitalker babble with a different spectral shape, local SNRs for $F2$ were higher than local SNRs for $F1$ (see Table III) and there was no significant difference in thresholds as ΔZ across frequency, even at low SNR conditions (-2 and -4 dB).

3. Effects of the noise type

Two types of noise were used in this study, LTSS noise and multitalker babble with both spectral and temporal differences. Comparisons of average thresholds for the overall SNR conditions (Fig. 8) suggested that performance of vowel formant discrimination was better for multitalker babble than that for LTSS noise, consistent with other studies of speech perception in noise (Festen and Plomp, 1990; Peters *et al.*, 1998). Festen and Plomp (1990) investigated speech-reception thresholds (SRTs) under steady-state noise and multitalker babble with matched spectral shapes. They found a benefit of 7 dB for babble background containing the temporal fluctuations compared to a steady-state noise. Another study by Peters *et al.* (1998) suggested that SRTs for sentences from the HINT test (Nilsson *et al.*, 1994) were improved by 8 dB for noise with speech modulation compared to the steady-state noise. These results suggested that temporal dips provided usable acoustic cues for speech perception. The amount that listeners can benefit from the temporal variation of background noise levels is dependent upon the modulation index of background noise, and the spectra of noise and speech signals.

To compare these earlier masking studies to the present data, a more detailed comparison of the performance for vowel formant discrimination for the two types of noise in relation to the local SNRs was made. The regression functions, $\Delta Z=0.201+0.378*e^{(-0.083*\mathrm{SNR})}$ for LTSS noise and $\Delta Z=0.201+0.340*e^{(-0.094*\mathrm{SNR})}$ for babble, are displayed in Fig. 9. Because ranges of the local SNRs for the LTSS noise and babble were different (-10.9 to 12.6 dB for LTSS noise and -3.1 to 22.4 dB for babble; see Figs. 5 and 7), only the overlapping SNR range (-5 to 15 dB) was shown in Fig. 9.

The comparison of these exponential masking functions for the LTSS noise and babble (Fig. 9) indicates that thresholds for formant discrimination improved with SNRs for both maskers. They both approach the thresholds in the quiet condition, estimated at 0.2 barks, while there was about 1.5-dB benefit for babble at the overlapping SNR regions. These results suggest that, in a noisy environment, listeners may benefit from amplitude variation over time in the masker such that temporal dips in the masker provide extra looks at spectral cues. Comodulation masking release (CMR) is another possible mechanism (Festen, 1993). The masker

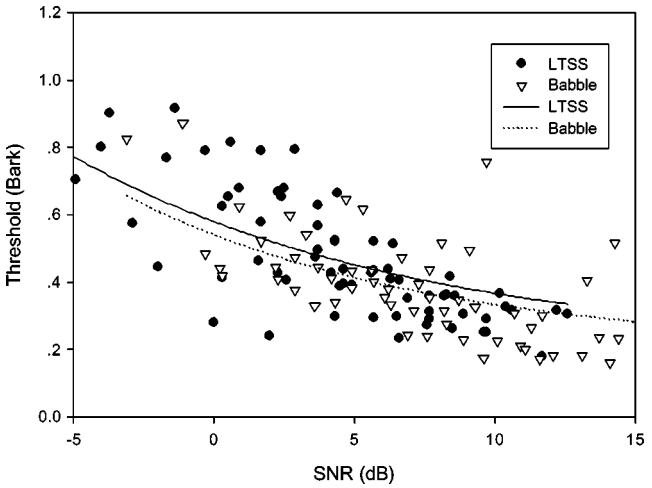

FIG. 9. Nonlinear (exponential decay) regression functions for LTSS noise and babble, shown for the overlapping region between −5- and +15-dB local SNR.

comodulation allows the comparison of information across critical bands such that the auditory system may be able to better distinguish masker from signal. Thus, a masking release is obtained. However, for these vowel stimuli, the benefit of 1.5 dB from the temporal variation in the masker is smaller than the 7–8 dB for recognition of words and sentences (Festen and Plomp, 1990; Peters *et al.*, 1998). The reason for this difference is not clear. First, isolated vowels have little temporal variation, compared to that of the words and sentences previously investigated. Thus, for vowels, the interaction between the noise types and the speech signals is quantitatively different because temporal dips in the babble do not reveal as much information for vowels as for words and sentences. Second, the above comparison between LTSS noise and babble in terms of local SNRs removed level difference between the noises in order to estimate the effect of temporal structure of the masker on formant discrimination; however, as shown in Fig. 1, the long-term spectrum of the babble is different from that of the LTSS noise such that the difference between the two masking functions may still be related to spectral differences between the two maskers such that the benefit of babble may be underestimated. For example, one possibility could be greater upward spread of masking because the babble has greater low-frequency energy than the LTSS noise. Overall, the comparison of the two noises in this study is limited because their long-term spectra were not matched.

C. Range of formant discrimination abilities

Everyday communication commonly occurs in noisy conditions. To represent more ordinary listening conditions, listeners in this study were tested in background noise. As noted earlier, ΔZ for quiet conditions over all the formants, 0.20 barks, is the baseline for formant discrimination under optimal listening conditions for high-fidelity speech. Listeners had difficulty in discriminating vowels in the adverse listening conditions, in particular when noise was present at high levels with overall SNRs of −2 and −4 dB. The range of average thresholds for all noise conditions (five SNRs) was from 0.305 to 0.677 barks for LTSS noise and from 0.252 to 0.531 barks for multitalker babble. At the highest levels of LTSS noise, −2- and −4-dB SNR, thresholds for formant discrimination increased by 3.3 and 3.4 times, respectively. The corresponding values for multitalker babble were 2.6 and 2.2. Performance was degraded even in the high-SNR noise condition. Thresholds were increased by 1.5 and 1.2 times, respectively, for LTSS noise and babble for the highest SNR condition (+4 dB).

A previous study on formant discrimination in more ordinary listening conditions for high-fidelity speech (Liu and Kewley-Port, 2004b) suggested that thresholds for formant discrimination were 0.301, 0.342, and 0.365 barks for high-fidelity syllables, phrases, and sentences, respectively. Using the baseline of 0.20 barks for optimal listening conditions, target vowels embedded in a longer phonetic context degraded the formant discrimination ability by 1.5, 1.7, and 1.8 times in high-fidelity speech for syllables, phrases, and sentences, respectively. Thus, high levels of noise (−2- and −4-dB overall SNR) had a much more detrimental effect on thresholds (poorer by 2–3 times) than did longer phonetic context. Summarizing, both phonetic context and background noise have significant detrimental effects on vowel formant discrimination. The extent of the effects depends on the length of phonetic context and the characteristics of the background noise such as noise level, spectrum of the noise, and temporal properties of the noise.

D. Formant discrimination and distance in vowel space

Vowel distribution in the $F1\times F2$ space depends on the language (Bradlow, 1993). English has a crowded vowel space in $F1\times F2$ with overlapping vowel areas (Peterson and Barney, 1952; Hillenbrand *et al.*, 1995). There is overlap of vowel categories even for a single talker due to the consonantal contexts (Broad and Fertig, 1970). Given this overlap of the important acoustical properties $F1$ and $F2$, several mechanisms that specify how vowels are identified accurately and rapidly have been investigated. Some approaches apply a normalization scheme (Syrdal and Gopal, 1986; Miller, 1989). Others have suggested that vowel identification depends on dynamic transitions and vowel duration, as well as other characteristics of vowel spectra (Nearey and Assmann, 1986; Strange, 1989).

The identification of vowels logically depends, in part, on the ability to discriminate differences in the vowel spectra. When background noise is present, listeners need greater spectral distance to discriminate between formants than the baseline of 0.2 barks for isolated vowels. For example, for the most challenging condition ($F2$ of /u/ vowel), listeners needed almost 1-bark distance to detect the changes in formants. Given the wide range of formant frequency thresholds observed here, from 0.2 to 1.0 barks depending on listening conditions, let us consider whether the distance between vowel categories relates discrimination to identification. Several studies have measured vowels formants produced by different talkers for steady-state vowels. Calculating the Euclidean distance between all pairs of English vowels in the $F1\times F2$ vowel space in barks, Kewley-Port and Zheng (1999)

reported that 0.56 barks was the average of formant distances between the closest vowel pairs produced by 16 speakers with different American English dialects. Clearly, under optimal listening conditions, vowels in the American English vowel space are far enough apart for listeners to discriminate formant differences (threshold about 0.2 barks). However, under very adverse listening conditions, for example an overall SNR of −4 dB for LTSS noise, listeners needed an average distance of 0.677 barks to discriminate differences in formant frequency, which was larger than the average formant distance (0.56 barks) between the close vowel pairs. This comparison between distances among vowel categories and thresholds of vowel discrimination may explain why listeners find many vowels confusing in noisy environments, especially vowels that are close to each other. Given that vowel formant thresholds are 0.305 and 0.252 barks for the SNR level at +4 dB for LTSS noise and babble, respectively, and that typical home environments have SNRs better than +5 dB (Pearson, Bennett, and Fidell, 1977), this level of background noise should not interfere significantly in vowel perception. Specific research comparing vowel discrimination and identification in noise will clarify under what noise level vowel perception becomes compromised.

V. SUMMARY

The goal of this study was to investigate formant discrimination for high-fidelity isolated vowels in quiet and under noisy conditions by manipulating several factors including formant frequency, signal-to-noise ratio, and noise type. Results suggested that formant discrimination was significantly influenced by all three factors. Masking noise significantly degraded formant discrimination, especially when the overall level of noise was greater than that of the vowels. Compared to thresholds in quiet (0.2 barks), thresholds were elevated by about a factor of 3 for SNRs lower than 0 dB. In the noise condition, when the local signal-to-noise ratio was equated, formant discrimination was better by 1.5 dB for multitalker babble than for LTSS noise, suggesting that listeners may have been able to take advantage of the temporal variability of the masking in multitalker babble. The masking functions were well-described by negative exponentials across $F1$ and $F2$, which converged on the threshold for vowels in quiet, for both LTSS noise and multitalker babble.

ACKNOWLEDGMENTS

This research was supported by the National Institute of Health Grant No. DC-02229 to Indiana University. This research was part of the first author's doctoral dissertation at Indiana University. Dr. Charles Watson, Dr. Larry Humes, and Dr. Danial Maki are gratefully acknowledged for their suggestions and comments on the study. The authors are also appreciative of comments made by Dr. Randy Diehl, and two anonymous reviewers on an earlier version of the manuscript.

Bacon, S. P., Opie, J. M., and Montoya, D. Y. (**1998**). "The effects of hearing loss and noise masking on the masking release for speech in temporally complex backgrounds," J. Speech Lang. Hear. Res. **41**, 549–563.

Bradlow, A. R. (**1993**). "Language-specific and universal aspects of vowel production and perception: A cross-linguistic study of vowel inventories," Unpublished Ph.D. dissertation, Cornell University, Ithaca, NY.

Broad, D. J., and Fertig, R. H. (**1970**). "Formant-frequency trajectories in selected CVC-syllable nuclei," J. Acoust. Soc. Am. **47**, 1572–1582.

Dubno, J. R., and Dirks, D. D. (**1982**). "Evaluation of hearing-impaired listeners using a Nonsense Syllable Test. I. Test reliability," J. Speech Hear. Res. **25**, 141–148.

Festen, J. M. (**1993**). "Contributions of comodulation masking release and temporal resolution to the speech-reception threshold masked by an interfering voice," J. Acoust. Soc. Am. **94**, 1295–1300.

Festen, J. M., and Plomp, R. (**1990**). "Effects of fluctuating noise and interfering speech on the speech-reception threshold for impaired and normal hearing," J. Acoust. Soc. Am. **88**, 1725–1736.

Flanagan, J. L. (**1955**). "A difference limen for formant frequency," J. Acoust. Soc. Am. **27**, 613–617.

Glasberg, B. R., and Moore, B. C. J. (**1990**). "Derivation of auditory filter shapes from notched-noise data," Hear. Res. **47**, 103–138.

Hawks, J. W. (**1994**). "Difference limens for formant patterns of vowel sounds," J. Acoust. Soc. Am. **95**, 1074–1084.

Hillenbrand, J., Getty, L. J., Clark, M. J., and Weeler, K. (**1995**). "Acoustic characteristics of American English Vowels," J. Acoust. Soc. Am. **97**, 3099–3111.

Kalikow, D. N., Stevens, K. M., and Elliott, L. L. (**1977**). "Development of a test of speech intelligibility in noise using sentence materials with controlled word predictability," J. Acoust. Soc. Am. **61**, 1337–1351.

Kawahara, H., Masuda-Kastuse, I., and Cheveigne, A. (**1999**). "Restructuring speech representations using a pitch-adaptive time-frequency smoothing and an instantaneous-frequency-based $F0$ extraction: Possible role of a repetitive structure in sounds," Speech Commun. **27**, 187–207.

Kewley-Port, D. (**1995**). "Thresholds for formant-frequency discrimination of vowels in consonantal context," J. Acoust. Soc. Am. **97**, 3139–3146.

Kewley-Port, D. (**2001**). "Vowel formant discrimination: Effects of stimulus uncertainty, consonantal context, and training," J. Acoust. Soc. Am. **110**, 2141–2155.

Kewley-Port, D., and Watson, C. S. (**1994**). "Formant-frequency discrimination for isolated English vowels," J. Acoust. Soc. Am. **95**, 485–496.

Kewley-Port, D., and Zheng, Y. (**1999**). "Vowel formant discrimination: Towards more ordinary listening conditions," J. Acoust. Soc. Am. **106**, 2945–2958.

Klatt, D. H. (**1980**). "Software for cascade/parallel formant synthesizer," J. Acoust. Soc. Am. **67**, 971–995.

Levitt, H. (**1971**). "Transformed up–down methods in psychoacoustics," J. Acoust. Soc. Am. **49**, 467–477.

Liu, C., and Kewley-Port, D. (**2004a**). "STRAIGHT: A new speech synthesizer for vowel formant discrimination," ARLO **5(2)**, 31–36.

Liu, C., and Kewley-Port, D. (**2004b**). "Vowel formant discrimination in high-fidelity speech," J. Acoust. Soc. Am. **116**, 1224–1233.

Miller, G. A., and Licklider, J. C. R. (**1950**). "The intelligibility of interrupted speech," J. Acoust. Soc. Am. **22**, 167–173.

Miller, J. D. (**1989**). "Auditory-perceptual interpretation of the vowel," J. Acoust. Soc. Am. **85**, 2114–2134.

Moore, B. C. J., and Glasberg, B. R. (**1987**). "Formulae describing frequency selectivity as a function of frequency and level, and their use in calculating excitation patterns," Hear. Res. **28**, 209–225.

Nearey, T. M., and Assmann, P. F. (**1986**). "Modeling the role of inherent spectral change in vowel identification," J. Acoust. Soc. Am. **80**, 1297–1308.

Nilsson, M., Soli, S. D., and Sullivan, J. A. (**1994**). "Development of the Hearing in Noise Test for the measurement of speech reception thresholds in quiet and in noise," J. Acoust. Soc. Am. **95**, 1085–1099.

Pearsons, K. S., Bennett, R. L., and Fidell, S. (**1977**). "Speech levels in various noise environments (EAP-600/1-77/025)," US Environmental Protection Agency, Washington, DC.

Peters, R. W., Moore, B. C. J., and Baer, T. (**1998**). "Speech reception thresholds in noise with and without spectral and temporal dips for hearing-impaired and normally hearing people," J. Acoust. Soc. Am. **103**, 577–587.

Peterson, G. E., and Barney, H. L. (**1952**). "Control method used in a study of the vowels," J. Acoust. Soc. Am. **24**, 175–184.

Plomp, R., and Mimpen, A. M. (**1979**). "Speech-reception threshold for sentences as a function of age and noise level," J. Acoust. Soc. Am. **66**, 1333–1342.

Stelmachowicz, P. G., Lewis, D. E., Kelly, W. J., and Jesteadt, W. (**1990**). ''Speech perception in low-pass filtered noise for normal and hearing-impaired listeners,'' J. Speech Hear. Res. **33**, 290–297.
Strange, W. (**1989**). ''Evolving theories of vowel perception,'' J. Acoust. Soc. Am. **85**, 2081–2087.
Syrdal, A. K., and Gopal, H. S. (**1986**). ''A perceptual model of vowel recognition based on the auditory representation of American English vowels,'' J. Acoust. Soc. Am. **79**, 1086–1100.
Traunmüller, H. (**1990**). ''Analytical expressions for the tonotopic sensory scale,'' J. Acoust. Soc. Am. **88**, 97–100.
Zwicker, E. (**1961**). ''Subdivision of the audible frequency range into critical bands (*Frequenzgruppen*),'' J. Acoust. Soc. Am. **33**, 248.

Frequency-place compression and expansion in cochlear implant listeners

Deniz Başkent[a)]
Department of Biomedical Engineering, University of Southern California, Los Angeles, California 90089 and Department of Auditory Implants and Perception, House Ear Institute, 2100 W. Third Street, Los Angeles, California 90057

Robert V. Shannon
Department of Biomedical Engineering, University of Southern California, Los Angeles, California 90089 and Department of Auditory Implants and Perception, House Ear Institute, 2100 W. Third Street, Los Angeles, California 90057

(Received 28 September 2003; revised 18 August 2004; accepted 19 August 2004)

In multichannel cochlear implants, low frequency information is delivered to apical cochlear locations while high frequency information is delivered to more basal locations, mimicking the normal acoustic tonotopic organization of the auditory nerves. In clinical practice, little attention has been paid to the distribution of acoustic input across the electrodes of an individual patient that might vary in terms of spacing and absolute tonotopic location. In normal-hearing listeners, Başkent and Shannon (J. Acoust. Soc. Am. **113**, 2003) simulated implant signal processing conditions in which the frequency range assigned to the array was systematically made wider or narrower than the simulated stimulation range in the cochlea, resulting in frequency-place compression or expansion, respectively. In general, the best speech recognition was obtained when the input acoustic information was delivered to the matching tonotopic place in the cochlea with least frequency-place distortion. The present study measured phoneme and sentence recognition scores with similar frequency-place manipulations in six Med-El Combi 40+ implant subjects. Stimulation locations were estimated using the Greenwood mapping function based on the estimated electrode insertion depth. Results from frequency-place compression and expansion with implants were similar to simulation results, especially for postlingually deafened subjects, despite the uncertainty in the actual stimulation sites of the auditory nerves. The present study shows that frequency-place mapping is an important factor in implant performance and an individual implant patient's map could be optimized with functional tests using frequency-place manipulations. [DOI: 10.1121/1.1804627]

PACS numbers: 43.71.Es, 43.71.Pc, 43.66.Ts [PFA] Pages: 3130–3140

I. INTRODUCTION

Cochlear implants (CI) partially restore hearing to deaf people by electrical stimulation of the auditory nerves. The electrodes are organized in an array to deliver the spectral information roughly consistent with the tonotopic organization of the cochlea, with lower frequency information delivered in the apical region and higher frequency information delivered in the basal region. However, little attention has been paid during the standard fitting process to the spacing or absolute tonotopic location of the electrodes.

The implant processor controls how the spectral content of the acoustic input is assigned onto the electrodes. Despite the uncertainty in the current spread and the stimulation location in nerves, the tonotopic range of stimulation in the cochlea is primarily determined by the active length of the electrode array and its insertion depth. When the array is fully inserted, the most apical contact is usually 20–30 mm from the round window depending on electrode type. The active stimulation range of the electrode array is typically 13.5 or 16.5 mm in length for Clarion I and Clarion II, 16.5 mm for Nucleus 22 and Nucleus 24, and 26.4 mm for Med-El Combi 40+. Greenwood's frequency-place function (1990) describes the characteristic frequency along the organ of Corti as a function of cochlear place. Assuming an average length of 35 mm for human cochlea, an array of 16 mm would stimulate a cochlear region that corresponds to an acoustic frequency range of 1–12 kHz for a 20-mm-insertion depth, and an acoustic frequency range of 500–6000 Hz for a 25-mm-insertion depth. Similarly, a 26-mm-long array inserted to a depth of 30 mm would cover a tonotopic range of 185–11 800 Hz. While the electrode array position may vary from patient to patient, many of the present cochlear implant clinical fitting programs offer only a limited choice for the overall spectral range of analysis filters as well as partitioning of individual bandwidths; common ranges are 350–6800 Hz for Clarion II, 150 Hz–10 kHz (SPEAK strategy Table 9) for Nucleus 22, and from 200–300 to 5500–8000 Hz for Med-El Combi 40+. As a result, the acoustic frequency range assigned to the stimulation region in the cochlea can be wider or narrower than the acoustic characteristic frequency range of that region, resulting in compression or expansion of the frequency-to-place mapping, respectively. Often there is also a tonotopic shift due to the discrepancy

a)Electronic mail: dbaskent@hei.org

between the actual electrode location and the acoustic information assigned. In some cases such a shift might be the result of an electrode that is not fully inserted, while in other cases the shift may be due to the assignment of the default signal processing parameters.

Başkent and Shannon (2003) measured the effects of compression and expansion in frequency-place mapping on speech recognition by normal-hearing (NH) subjects. Implant electrode arrays with different insertion depths and different number of electrodes were simulated using a noise-band vocoder (e.g., Shannon *et al.*, 1995). In the vocoder the cochlear tonotopic range of stimulation was represented by noise carrier bands while the input acoustic frequency range was determined by the frequency range of the analysis bands. The stimulation range was held constant by employing the same noise carrier bands for each condition while the analysis frequency range was made wider (compressed map) or narrower (expanded map) relative to the carrier frequency range. Speech recognition was generally better when the analysis range matched the carrier range than for any frequency-place expansion and compression condition, even when the matched condition eliminated a considerable amount of acoustic information. This result suggests that speech recognition, at least without training, is dependent on the mapping of acoustic frequency information onto the appropriate cochlear place. Fu and Shannon (1999) found a similar result with frequency-place shift. Vowel recognition by NH subjects was significantly reduced if the frequency information was presented to a simulated cochlear location more than 3 mm from its normal tonotopic location. They also observed a similar drop in performance with implant users when the input frequency range was shifted prior to implant processing. Whitford *et al.* (1993) attempted to modify the processor maps of implant users by matching the acoustic input range to the characteristic frequency of the stimulation range and observed some improvement in the open-set sentence recognition scores in low levels of noise.

A theoretical issue addressed by the present study is the flexibility of perceptual pattern recognition for altered speech tonotopic patterns. When NH subjects were tested with frequency-place maps different than the normal acoustic map, such as shifted (Fu and Shannon, 1999), compressed, or expanded maps (Başkent and Shannon, 2003), there was a reduction in phoneme and sentence recognition performance. Prior to the experiments NH subjects had experience with only the normal acoustic frequency-place map, which is perceptually ''burned in'' over a lifetime of hearing. In contrast, CI users had experience with two frequency-place maps: the normal acoustic map (from the previous history of normal acoustic hearing), and the frequency-place map of the implant processor, which is likely to be different than the acoustic map. It is not clear whether or how speech pattern recognition would be able to adapt to the new implant frequency-place map. The present study does not address the time course of such long-term adaptation, but rather looks at the instantaneous effects of spectral distortions in the mapping. If CI users are affected by spectral alterations in a manner similar to NH subjects, fitting the frequency-place map for an individual implant user would be beneficial. A map optimized from the beginning might make the overall adaptation faster and the final asymptotic performance higher.

In cochlear implants there are several factors that affect the frequency-place mapping, but cannot be estimated with certainty. These factors include physical quantities such as the exact insertion depth of the electrode array, the proximity of the electrodes to the spiral ganglia where the actual stimulation occurs, and the actual length of the cochlea, physiological factors such as nerve survival pattern and the temporal and spatial pattern of stimulation in the auditory nerves, and anatomical factors such as possible structural abnormalities of the cochlea. It may be possible to obtain more detailed information about the position of the implanted electrodes using sophisticated images from radiographs (Marsh *et al.*, 1993; Cohen *et al.*, 1996) or CT scans (Ketten *et al.*, 1998; Skinner *et al.*, 2003). However, even if the relative insertion depth can be determined in individual implant patients the medial-lateral location of the electrode in the scala tympani might still not be accurately determined. Moreover, because many factors affecting the current flow cannot be imaged, it would still not be possible to know the absolute location and characteristic frequency of the neurons activated by each electrode. Because of these uncertainties, the best assessment of electrode location and frequency-place matching might be accomplished functionally rather than by imaging.

In the present study we used the nominal value for insertion depth as reported by Med-El for fully inserted electrode arrays. All participating subjects had full insertions. In reality, however, there is probably a large variation in the actual electrode locations across subjects due to individual differences in cochlear length, medial lateral electrode location, and nerve survival. One purpose of the study was to assess whether an optimum map could be obtained despite the unknown factors by starting with a map based on estimated values and fine-tuning it with behavioral tests.

In Experiment 1, we used the fact that implant users are sensitive to spectral shifts in frequency-place maps (Fu and Shannon, 1999) to find an estimate for the electrode insertion depth behaviorally. The array location producing the best performance (12–24 mm, with electrodes 4–9) was used in Experiments 2 and 3.

A typical value used in applying the Greenwood mapping function for the average cochlear length of human is 35 mm. However, measurements by Ulehlova *et al.* (1987) showed a range from 28 to 40 mm, with an average length of 34.2 mm for 28 men. When Ketten *et al.* (1998) estimated cochlear lengths of implant subjects from CT scans, they found an average length of 33 mm for 20 subjects (range 29–37.5 mm). In Experiment 2 we varied the assumed cochlear length used in the calculations of the frequency map and explored the effects on speech recognition. Subjects had peak performance at different values, but performance did not change significantly over a range of a few mm. Therefore we used the typical value of 35 mm for the average cochlear length for all subjects in Experiments 3 and 4.

The behaviorally measured parameter values for electrode array location and cochlear length from Experiments 1

TABLE I. Information about subjects, all users of Med-El Combi 40+. Reasonable scores for sentence recognition with subjects S5 and S6 (as shown with asterisks) could be obtained with simpler sentences (HINT) only, where the subjects were also allowed to listen to each sentence as many times as needed. Baseline scores were collected using subject's clinical map.

Subject	Age	Duration of profound deafness (years)-etiology	Experience with CI (years)	Baseline vowel score (corrected for chance)	Baseline consonant score (corrected for chance)	Baseline sentence score (IEEE or *HINT)	Overall acoustic input frequency range of the original map
S1	39	30-high fever	2.5	60.00	55.26	38.22	300–5500 Hz, 6 or 12 electrodes later: 200–8500 Hz, 10, 11, or 12 electrodes
S2	62	12-noise exposure	1	68.18	70.18	92.81	300–5500 Hz, all 12 electrodes
S3	46	26-unknown	2	82.50	86.67	93.94	Map 1 and 2: 300–5500 Hz Map 3: 300–7000 Hz 9 electrodes
S4	25	from birth-unknown	5	70.00	85.91	84.52	300–7000 Hz, 9 or 12 electrodes
S5	36	from birth-pregnancy rubella	3 total, 1 year with replacement	42.73	30.71	17.5* (HINT)	300–5500 Hz, all 12 electrodes
S6	40	from birth-unknown	4.5	44.55	52.63	12.8* (HINT)	300–7000 Hz, Map 1 and 2: 6 electrodes Map 3: all 12 electrodes

and 2 were used as baseline estimates for Experiments 3 and 4. From these baseline values, frequency-place compression and expansion conditions were produced with a 6-electrode processor in Experiment 3, and expansion conditions with a 12-electrode processor in Experiment 4.

II. EXPERIMENTAL METHOD

A. Subjects

Six Med-El Combi 40+ users (S1–S6), aged 25–62, participated in experiments. All were reported to have full electrode insertions at surgery. Detailed information about subjects is summarized in Table I. Center frequencies are shown in Table II for the analysis bands assigned to electrodes in the clinical maps of subjects.

Three subjects (S1, S2, and S3) were postlingually, and three (S4, S5, and S6) were prelingually deafened. All subjects were born into hearing families and therefore have used oral communication as their main communication mode, and some had been provided with speech correction therapies for long periods of time.

The baseline sentence scores given in Table I are for IEEE sentences, which were too difficult for subjects S5 and S6. They were retested with simpler HINT sentences and were allowed to listen to each sentence as many times as needed. Even with the simpler materials their open-set scores were too low to fully observe the effects of spectral manipulations. These subjects participated in Experiment 3 only. Due to time constraints S4 did not participate in Experiments 1 and 2, and S3 did not participate in Experiment 4.

TABLE II. Center frequencies of clinical maps used by the subjects.

	Band-pass filter center frequencies for 12 electrodes (Hz)											
Subject	1	2	3	4	5	6	7	8	9	10	11	12
S1, S2, S5	338	430	549	701	894	1137	1444	1845	2349	2987	3889	4918
S3	352	487	off	672	930	off	1273	1771	off	2420	3456	4544
S4	358	507	off	722	1017	off	1445	2057	off	2890	4225	6013
S6	390	off	658	off	1114	off	1867	off	3147	off	5319	off

B. Speech stimuli

Vowel stimuli (selected from recordings by Hillenbrand *et al.*, 1995) consisted of ten presentations (five male and five female talkers) of twelve medial vowels in CVC syllables, including ten monophthongs and two diphthongs, presented in a /h/-vowel-/d/context (heed, hid, head, had, hod, hawed, hood, who'd, hud, heard, hayed, hoed). Chance level on this test was 8.33% correct, and the single-tailed 95% confidence level was 12.48% correct based on a binomial distribution.

Consonants (selected from recordings by Shannon *et al.*, 1999) consisted of six presentations (three male and three female talkers) of 20 medial consonants (b, tʃ, d, ð, f, g, ʒ, k, l, m, n, p, r, s, ʃ, t, v, w, j, z) in CVC syllables, presented in an /a/-consonant-/a/ context. Chance performance level for this test was 5% correct, and the single-tailed 95% confidence level was 8.27% correct based on a binomial distribution.

Two different sets of stimuli were used for sentence recognition tests: IEEE sentences (IEEE, 1969) spoken by a single male talker and HINT sentences (Nilsson *et al.*, 1994) spoken by multiple talkers. IEEE sentences are phonetically balanced across lists and the predictability of the words is relatively low. Subjects S1 and S2 were also retested with HINT sentences. HINT sentences are contextually easier, have fewer key words, and are more similar to natural speech in daily life compared to IEEE sentences. Subjects had not heard any of the test sentences prior to the study. Each list consisted of ten sentences and two lists were presented for each condition. The presentation order of lists was randomized across subjects and conditions.

C. Procedures

Speech stimuli were presented via a loudspeaker in a sound field at 70 dB on an A-weighted scale in a sound-treated room. In the vowel and consonant identification tests, subjects were asked to choose the phoneme they heard from a menu displayed on the computer screen. All stimuli were presented in random order via custom software (Robert, 1998). In the sentence recognition test, they were asked to repeat or type the words they heard in sentences, again presented in random order via custom software (Tiger Speech Recognition System developed by Qian-Jie Fu). The map in the experimental processor was changed before every test. The conditions of a specific experiment were presented in random order to minimize learning effects.

D. Med-El Combi 40+ implant system

The electrode array of the Combi 40+ consists of 12 electrodes spaced 2.4 mm apart covering a total length of 26.4 mm in cochlea. The electrodes are numbered 1–12 from apex to base. The array is designed for insertions as deep as 31 mm inside the round window. Stimuli were delivered to the implant via a research TEMPO+processor, which is worn behind-the-ear (BTE) and can process acoustic frequencies from 200 Hz to 8.5 kHz.

E. Device parameters

For every subject, thresholds and maximum loudness levels were determined using the standard clinical method to customize the experimental processor for an individual subject. The input dynamic range was automatically adjusted by the processor. The TEMPO+processor uses the CIS strategy and the electrodes are stimulated in the monopolar mode.

F. Experimental conditions

In Experiments 1–3 we used a set of six electrodes that had a narrower stimulation range than the default 12 electrodes of the device. A narrower stimulation range was selected to facilitate flexibility in manipulating the spectral content of speech over a range of electrode array configurations. In the ''matched'' condition the input acoustic range was equal to the range of characteristic frequencies of the array, calculated by Greenwood equation. If an insertion depth of 31 mm is assumed, the six middle electrodes of the implant cover a range of 12 mm, from 12 to 24 mm from the round window. With the additional assumption of 35 mm for an average cochlear length, the normal acoustic frequencies corresponding to this range would be between 611 Hz and 3.82 kHz.

In Experiment 1, the speech was processed with an analysis frequency range of 611 Hz–3.82 kHz in each condition. A spectral shift was created by activating a different set of six electrodes in each condition, located at different distances from the round window, as shown schematically at the top of Fig. 1 and summarized in Table III. As a result, from condition 1 to 7 the cochlear location of the array of six electrodes was shifted basally by 2.4 mm per condition.

Experiment 2 simulated the effects of variation in individual cochlear length on the frequency-place mapping, by changing the assumed cochlear length used in the Greenwood equation from 31 to 39 mm in 1 mm steps. The set of six middle electrodes (4–9), which gave the peak performance in Experiment 1, were activated in all conditions. The assumed location of the most apical electrode was fixed at a constant insertion angle (~470°), equivalent to 24 mm insertion for a cochlea of 35 mm. As a result, the acoustic frequency corresponding to the apical electrode location was constant for all experimental conditions, since the Greenwood function scales the frequency-to-place map with cochlear length. As the assumed cochlear length increased the proportion of the cochlea occupied by the electrode array decreased, resulting in smaller analysis frequency range for longer cochleae, as shown in the top portion of Fig. 2. The conditions are summarized in Table IV.

In Experiment 3, frequency-place compression conditions were generated with the same set of six electrodes as the previous experiment (4–9). The acoustic input range in mm was made wider than the stimulation range (assumed to be from 12 to 24 mm from the round window) at each end by +1 mm, +2 mm, +3 mm, and +4 mm. The frequency range of the acoustic input was calculated by converting the range in mm with the Greenwood equation. Similarly, for expansion conditions the acoustic input range was made narrower than the stimulation range at each end by −1 mm, −2 mm,

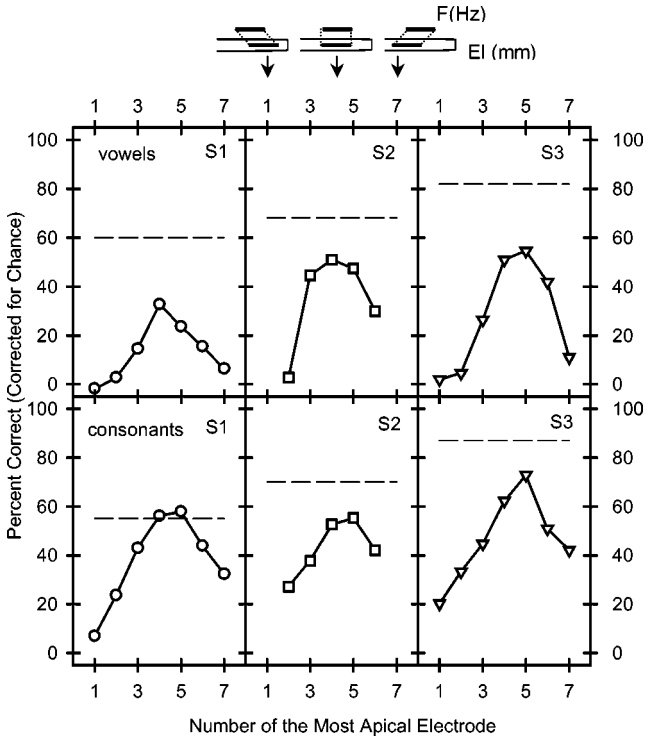

FIG. 1. Individual percent correct scores of subjects S1, S2, and S3 from Experiment 1 as a function of the shifted electrode array position. The top and bottom rows show the vowel and consonant recognition scores, corrected for chance, respectively. The dashed lines show the scores with the processor map that the patient uses in daily life. The experimental maps are schematically shown above the figure and linked to corresponding conditions in the figure with arrows. The open-ended tube represents the cochlea where the open end shows the base and the closed end shows the apex. The line in the cochlea shows the assumed position of the electrode array and the line above the cochlea shows the estimated location of the acoustic input range calculated from Greenwood's (1990) function. Different sets of electrodes from 1–6 to 7–12 were activated while the same center frequency range of 611–3.82 k Hz was assigned to electrodes in every condition.

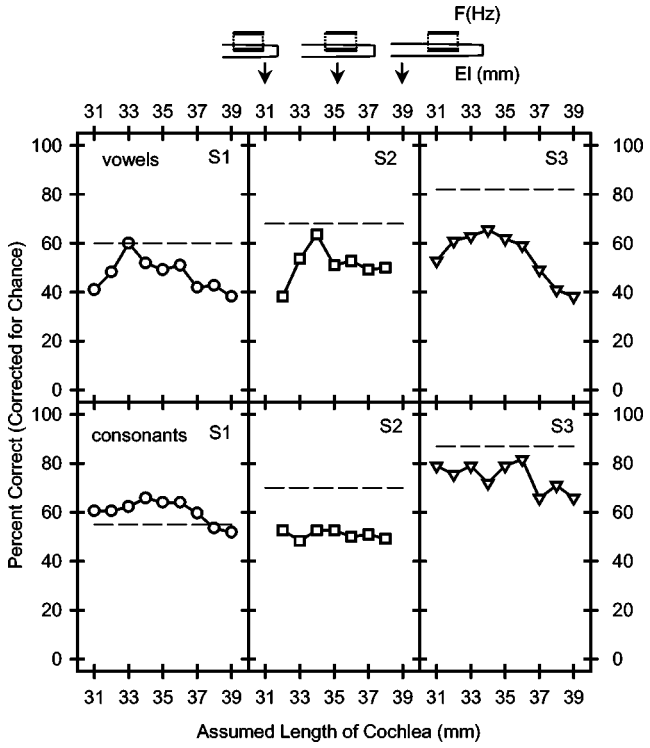

FIG. 2. Individual percent correct scores of subjects S1, S2, and S3 from Experiment 2 as a function of assumed cochlear length. The assumed cochlear length was used in the Greenwood equation to calculate the frequency range matching the stimulation range. The top and bottom rows show the vowel and consonant recognition scores, corrected for chance, respectively. Similar to Fig. 1 dashed lines show patient's performance with the processor map and the conditions are schematized above the figure. In all conditions electrodes 4–9 were activated with an array length of 12 mm and the most apical electrode was fixed at the same insertion angle of 470°. As a result, even though the array length and the insertion depth are the same, the proportion of the cochlear range covered by the array becomes wider or narrower relative to the cochlear length.

−3 mm, and −4 mm. This manipulation also resulted in narrower frequency bands that were assigned to each electrode. The compression and expansion conditions are schematically shown on top of Fig. 3 and more details can be found in Başkent and Shannon (2003), where similar conditions were simulated. The corresponding frequencies for these conditions are given in Table V.

Based on an assumed insertion depth of 31 mm, the whole array of 12 electrodes lies between 5 and 31 mm from the round window. The widest range of frequencies that Tempo+ can process is 200 Hz–8.5 kHz. When this range is translated into cochlear distance with the Greenwood equation, the corresponding range in mm is narrower than the stimulation range of 26.4 mm, the overall length of 12 electrodes. Thus, the normal map used in the implant processors may result in frequency-place expansion. Experiment 4 produced similar expansion conditions to Experiment 3. The analysis range was made narrower than the stimulation range by −3 mm, −4 mm, −5 mm, −6 mm, −7 mm, and −8 mm on each end. The experimental conditions are summarized in Table VI.

III. RESULTS

A. Experiment 1: Shifted electrode array

Subjects S1, S2, and S3 participated in Experiment 1. The individual percent correct scores from vowel and consonant recognition tests as a function of the shift condition are

TABLE III. Basal shift conditions for Experiment 1, shown as a function of the most apical electrode number in the array of six electrodes activated.

Shift condition (most apical electrode)	1	2	3	4	5	6	7
Activated electrodes in the electrode array	1–6	2–7	3–8	4–9	5–10	6–11	7–12
Center frequency range (Hz)	611–3.82 k	611–3.82 k	611–3.82 k	611–3.82 k	611–3.82 k	611–3.82 k	611–3.82 k

TABLE IV. Center frequency ranges of the analysis bands in Experiment 2, calculated with Greenwood equation using the assumed cochlear length. Electrodes 4–9 were activated in all conditions. The most apical electrode of the array (4) was at the same insertion angle (470°) for all conditions.

Assumed cochlear length (mm)	31	32	33	34	35	36	37	38	39
Modified electrode array location (mm)	9.3–21.3	9.9–21.9	10.6–22.6	11.3–23.3	12.0–24.0	12.7–24.7	13.4–25.4	14.1–26.1	14.7–26.7
Center frequency range (Hz)	611–4.77 k	611–4.49 k	611–4.24 k	611–4.02 k	611–3.82 k	611–3.64 k	611–3.48 k	611–3.35 k	611–3.20 k

shown in Fig. 1. The scores are corrected for chance. Vowel recognition scores are presented in the top row while the consonant recognition scores are presented in the bottom row. Different symbols show scores from different subjects. The same symbol is used for the same subject in all following figures to facilitate comparison of the results across experiments. The dashed lines show the performance of subjects listening to the same stimuli with a map they use in daily life. Generally, experimental conditions resulted in lower performance levels compared to the processor map. This difference may be due to variations in experience as well as to the fact that the experimental maps only used six electrodes, and had much narrower stimulation and acoustic input ranges.

Figure 1 shows that subjects had peak performance around conditions 4 and 5, with electrodes 4–9 and 5–10 activated, respectively. Electrodes 4–9 were selected to be used for all subjects in Experiments 2 and 3.

B. Experiment 2: Effect of assumed individual cochlear length

Figure 2 shows vowel and consonant recognition scores, corrected for chance, for the same subjects as in Experiment 1 (S1, S2, and S3) as a function of varying assumed values for cochlear length. The peaks in vowel recognition scores of S1 and S3 suggest that these subjects might have cochleae that are only 33–34 mm long. However, generally there was only a small effect on vowel recognition over a wide range of assumed cochlear lengths, and an even smaller effect on consonants. These results show that an inaccuracy in the estimate for cochlear length does not change the results significantly. Therefore an assumed length of 35 mm, which has typically been used in Greenwood mapping calculations, was selected for use in Experiments 3 and 4.

TABLE V. Frequency-place mismatch conditions of Experiment 3. Six electrodes (4–9, assumed to be located from 12 to 24 mm from the round window) were activated. For each condition the table lists the acoustic input range in cochlear distance, center frequencies of bandpass filters, and the overall frequency range of analysis bands in Hz.

Frequency-place mismatch condition	Range of acoustic input (mm)	Band-pass filter center frequencies for six channels (Hz)						Overall frequency range of analysis bands (Hz)
−4 mm (expansion)	20–16	1168	1322	1493	1684	1899	2137	1025–2367
−3 mm (expansion)	21–15	998	1200	1443	1735	2075	2475	887–2762
−2 mm (expansion)	22–14	850	1096	1404	1788	2266	2863	752–3196
−1 mm (expansion)	23–13	721	997	1361	1841	2475	3309	611–3847
0 mm (matching)	24–12	611	906	1320	1896	2700	3820	493–4522
+1 mm (compression)	25–11	509	821	1279	1953	2945	4407	394–5467
+2 mm (compression)	26–10	423	743	1239	2011	3212	5082	314–6305
+3 mm (compression)	27–9	348	670	1200	2070	3502	5855	247–7482
+4 mm (compression)	28–8	281	604	1162	2131	3816	6744	207–8082

TABLE VI. Frequency-place mismatch conditions of Experiment 4. All 12 electrodes (1–12, assumed to be located from 5 to 31 mm from the round window) were activated. For each condition the table lists the acoustic input range in cochlear distance, center frequencies of bandpass filters, and the overall frequency range of analysis bands in Hz.

Frequency-place mismatch condition	Range of acoustic input (mm)	Band-pass filter center frequency range (Hz)	Overall frequency range of analysis bands (Hz)
−8 mm (expansion)	23.2–12.8	699–3407	645–3647
−7 mm (expansion)	24.2–11.8	590–3933	535–4264
−6 mm (expansion)	25.2–10.8	495–4538	440–4981
−5 mm (expansion)	26.2–9.8	412–5231	358–5815
−4 mm (expansion)	27.2–8.8	340–6028	287–6784
−3 mm (expansion)	28.2–7.8	278–6943	227–7911

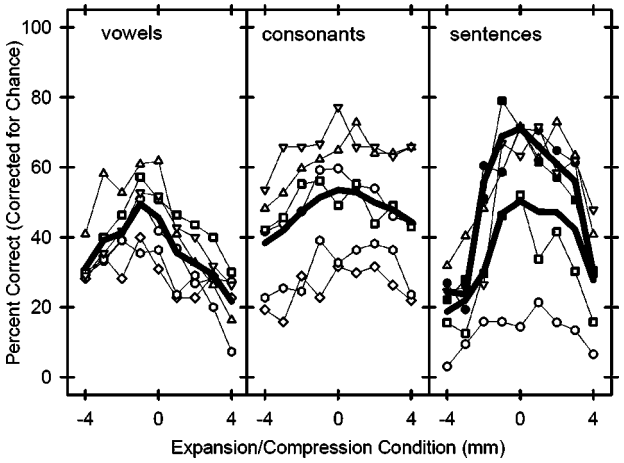

FIG. 4. Average percent correct scores of all subjects, shown with thick lines, superimposed on the individual scores from Fig. 3, shown with open symbols. In sentence recognition scores, the upper thick line shows the average scores of S1 and S2 with HINT sentences, and the lower thick line shows the average scores of subjects S1, S2, S3, and S4 with IEEE sentences.

C. Experiment 3: Frequency-place compression and expansion with six electrodes

Figure 3 shows the individual percent correct scores of all subjects as a function of compression and expansion with six middle electrodes (4–9). Vowel and consonant recognition scores, corrected for chance, are plotted in the top and middle rows, respectively. S1 was tested twice with vowels and consonants. Both curves are presented here (shown with open circles in the left top and left middle panels) to demonstrate the test–retest reliability. The scores of S5 and S6, who were both prelingually deaf, were very low, almost at the level of a single-channel processor performance for consonants. Percent correct scores for sentences are shown in the bottom row. S1 and S2 were tested with IEEE sentences (open symbols) as well as HINT sentences (filled symbols). Even with simpler sentences (HINT) S5 and S6 could not achieve significant sentence recognition.

The average scores from all subjects (thick lines) are presented in Fig. 4 superimposed on the individual scores

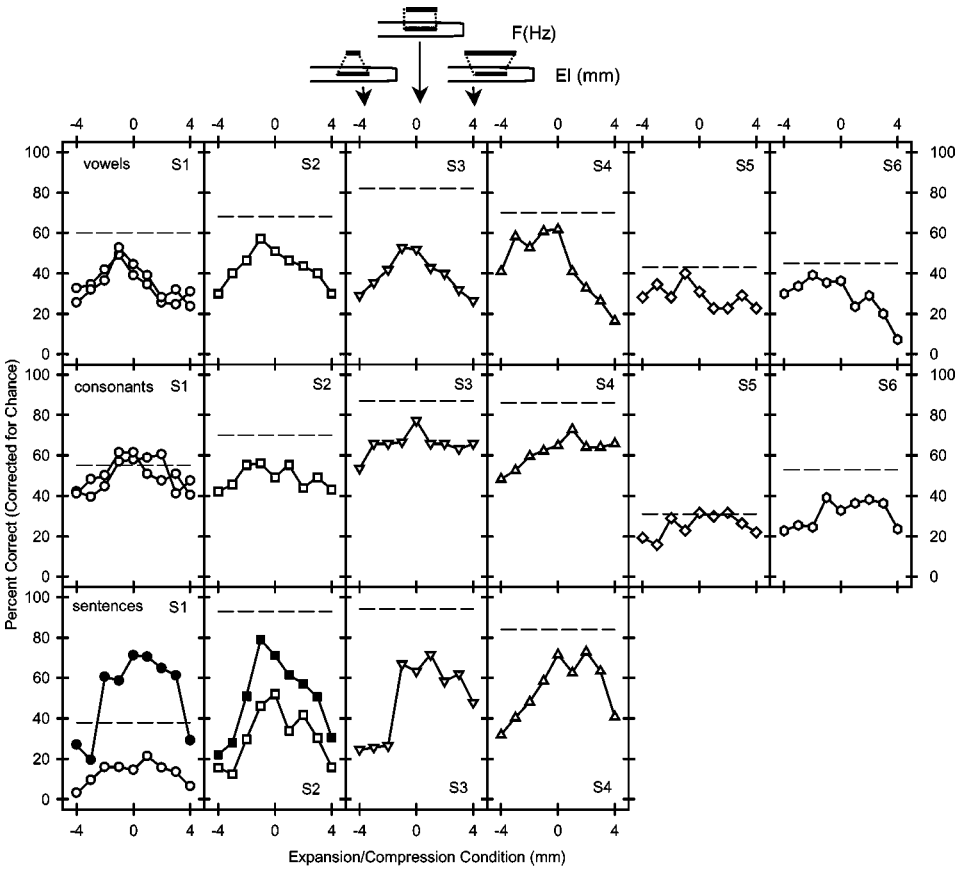

FIG. 3. Individual percent correct scores of all subjects from Experiment 3 as a function of compression and expansion in frequency-place mapping. The top and middle rows show the vowel and consonant recognition scores, corrected for chance, respectively, and the bottom row shows the sentence recognition scores. S1 was tested twice with vowels and consonants to show the test reliability. S1 and S2 were tested with both IEEE (open symbols) and HINT sentences (filled symbols). Similar to Fig. 1 dashed lines show patient's performance with the processor map and the experimental maps are schematically shown above the figure. In all conditions electrodes 4–9 were activated with an array length of 12 mm while the frequency range assigned to the electrodes was made narrower or wider than the stimulation range of the electrode array.

TABLE VII. F and p values calculated with one-way repeated-measures ANOVA for expansion and compression conditions of Experiment 3. Due to the small number of subjects HINT sentences were not included.

Expansion	F	p	Compression	F	p
Vowels, $n=6$ $F(4,20)$	13.65	<0.001	Vowels $n=6$ $F(4,20)$	13.41	<0.001
Consonants $n=6$ $F(4,20)$	15.89	<0.001	Consonants $n=6$ $F(4,20)$	5.11	<0.01
IEEE sentences $n=4$ $F(4,12)$	10.63	<0.001	IEEE sentences $n=4$ $F(4,12)$	7.61	<0.01

(symbols connected with thin lines). The left and middle panels show the average scores from vowel and consonant recognition tests, respectively. The lower thick line in the right panel shows the average score from subjects S1, S2, S3, and S4 with IEEE sentences, and the upper thick line shows the average score from subjects S1 and S2 with HINT sentences.

A one-way repeated-measures ANOVA showed that there was a significant effect of compression and expansion on performance for all stimuli (see Table VII for corresponding F and p values). In general, performance was best for the matched condition (0 mm) and poorer for both frequency-place expansion and compression. For vowels, a post hoc Tukey test revealed that -3 mm, -2 mm, and -1 mm expansion scores were not significantly different than the 0 mm condition (where input frequency theoretically matched the stimulation range). In simulations, frequency-place expansion produced a larger effect on vowel recognition than compression (Başkent and Shannon, 2003), whereas with implant users a larger performance drop was observed with compression than with expansion. As in the simulations, the effects of both expansion and compression were smaller on consonants, which are generally more robust to spectral distortions compared to vowels (Shannon *et al.*, 1998; Friesen *et al.*, 2001). A Tukey test showed no significant difference in results from -2 mm expansion to $+3$ mm compression with consonants, which is a much wider range than observed for vowels. Similar to simulations, consonant recognition scores of Cl subjects dropped significantly only with high degrees of compression ($+4$ mm) and expansion (-3 mm). With IEEE sentences, the best performance was obtained around 0 mm matching condition with a tolerance of a few mm of compression; a Tukey test showed that scores from -1 mm expansion to $+3$ mm compression were not significantly different. The performance dropped significantly with further mismatch. HINT sentences display a sharper peak around the 0 mm matched condition with a larger drop compared to IEEE sentences with increasing mismatch. The number of subjects who listened to HINT sentences (two) was not sufficient to run a statistical test.

1. Similarity of the experimental map to implant processor map

One key question in the study is whether each subject's ''reference map'' was determined by the normal acoustic tonotopic map or the map implemented in the clinical speech processor. Postlingually deafened patients had extensive experience with normal acoustic mapping prior to deafness, whereas prelingually deafened patients had little to no experience with the normal acoustic map, so their reference map might be determined by the implant map of the everyday processor. Başkent (2003, Fig. 4.20) showed that the reduction of speech recognition under conditions of compression and expansion could be modeled by the sum of squared differences in band center frequencies between the acoustic and experimental maps. This result was observed in implant simulations with normal-hearing listeners, and might also apply to implant users, especially if postlingually deafened.

To assess the potential influence of the normal acoustic tonotopic map and the implant processor map on the results of Experiment 3 a similarity metric was calculated:

$$\text{similarity\_factor} = \frac{1}{\text{error\_rms}}, \tag{1}$$

with error_rms defined as

$$\text{error\_rms} = 10\sqrt{\Sigma_{i=1}^{N} \log_{10}^2(f_{c\_\exp}(i)/f_c(i))/N}, \tag{2}$$

where N=number of electrodes, $f_{c\_\exp}$=center frequencies of the experimental map, and f_c=center frequencies of the comparison map (i.e., either the normal acoustic map or the implant processor map). The similarity factor quantifies the similarity between two maps by comparing center frequencies of the analysis bands between experimental processors and either the normal tonotopic map or the implant processor map. The value of the index ranges from one to an asymptotic zero: When the maps that are compared are identical the index is unity and as the maps differ the index decreases. The values of similarity factors for the experimen-

TABLE VIII. Similarity of experimental conditions to normal acoustic map (0 mm, tonotopically matched map) and implant processor maps (shown in Table II for each subject).

Compression/ expansion conditions		exp -4 mm	exp -3 mm	exp -2 mm	exp -1 mm	normal map (0 mm)	comp $+1$ mm	comp $+2$ mm	comp $+3$ mm	comp $+4$ mm
Similarity to normal acoustic map		0.66	0.73	0.81	0.90	1.00	0.90	0.80	0.72	0.64
Similarity to implant processor map	S1, S2, S5	0.75	0.79	0.81	0.79	0.75	0.69	0.63	0.57	0.51
	S3	0.70	0.75	0.78	0.78	0.75	0.69	0.64	0.57	0.51
	S4	0.75	0.82	0.86	0.86	0.81	0.74	0.66	0.59	0.52
	S6	0.78	0.86	0.94	0.93	0.85	0.77	0.69	0.63	0.57

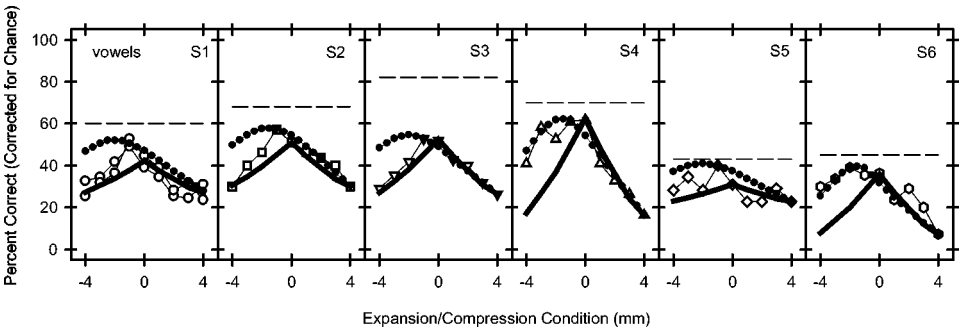

FIG. 5. Vowel recognition percent scores from Experiment 3, reproduced from Fig. 3. The solid line shows the performance predicted from the similarity of the experimental map to patient's implant processor map while the dotted line shows the prediction from the similarity of the experimental map to the normal acoustic map.

tal maps are given in Table VIII when compared to normal acoustic and implant processor maps.

Figure 5 duplicates vowel recognition scores from Fig. 3 with two similarity indices added. The similarity index function for the implant processor map (dotted line) was scaled to fit the data at the lowest and highest values. The similarity function for the acoustic tonotopic map (thick solid line) was scaled to fit the lowest point and the value at 0 mm (matching map). Figure 5 shows that the vowel recognition results of the postlingually deafened subjects S1, S2, and S3 were similar to the pattern predicted by the similarity to the normal acoustic map. The pattern of performance of the prelingually deafened subjects S4, S5, and S6 was similar to that predicted by the similarity to their implant processor map. Postlingually deaf subjects' speech recognition appears to be sensitive to the spectral mismatch relative to the normal acoustic map, similar to NH listeners. Prelingually deafened subjects, however, might not have had sufficient acoustic input during the critical period that normally establishes the acoustic tonotopic map, and so their performance appears to be determined more by similarity to the processor map.

D. Experiment 4: Expansion with all 12 electrodes

Experiments 1–3 used six electrodes covering 12 mm in the cochlea. The subjects' experience with their implant, which was as long as 5 years, was with the full stimulation range of the default 12-electrode array (26.4 mm). To confirm that similar effects occur with the entire array, we repeated the expansion conditions using all 12 electrodes of the device.

S1, S2, and S4 participated in this experiment. Figure 6 shows individual (small open symbols) and average scores (thick line) with the 12-electrode processor expansion conditions combined with average scores of the same subjects with six-electrode processor from Experiment 3 (dotted line).

The 12-electrode processor has better spectral resolution, covers a much wider stimulation range and acoustic input range, and employs additional apical electrodes, compared to the six-electrode processor. For example, for the same −3 mm expansion condition, the 12-electrode processor has a stimulation range of 26.4 mm and an analysis range of 20.4 mm, while the six-electrode processor has a stimulation range of 12 mm and an analysis range of 6 mm. As a result scores were higher with the 12-electrode processor compared to the six-electrode processor for the same expansion conditions. Yet, similar to the six-electrode processor, performance decreased as the expansion increased. The performance around −3 mm expansion resulted in performance similar to that of the clinical processor. It is not clear, however, if higher performance levels could be achieved with a better matched condition because device limitations did not allow such mapping.

Figure 7 shows a comparison of the similarity metric functions to the individual vowel recognition scores of the subjects with 12-channel processor (open symbols). As a reference, vowel recognition scores with the six-channel processor are also included (filled symbols). Similar to Fig. 5, the prediction referenced to the similarity to the normal acoustic map is shown by the thick solid line and the prediction by the similarity to the subjects' processor map is shown by the dotted line. The dashed lines show subject performance with the everyday processor map. The dotted lines imply that the −4 mm and −5 mm expansion conditions with 12 electrodes are most similar to the mapping used in subjects' implant processors, except that the analysis bands of the experimental maps were partitioned in equal cochlear distances instead of logarithmic steps. Similar to Experiment 3, the performance by S1 and S2, who were postlingually deafened, followed the prediction based on similarity to the

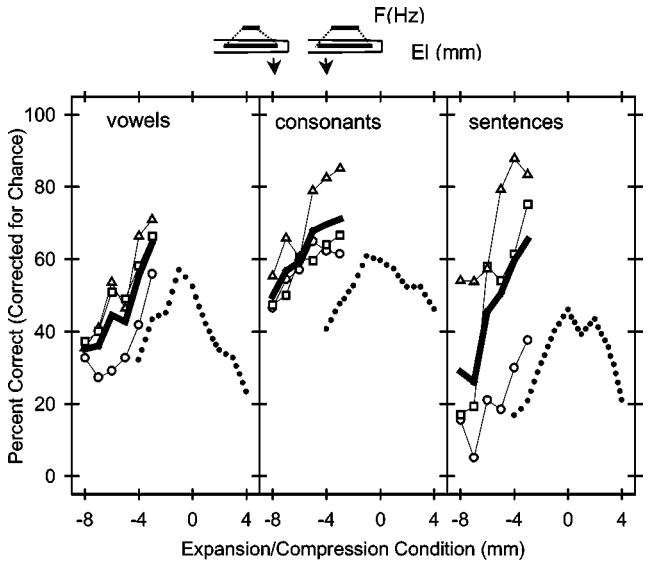

FIG. 6. Percent correct scores of subjects S1, S2, and S4 from Experiment 4. The open symbols show the individual scores for 12-electrode expansion conditions. The superimposed thick lines are the average scores of subjects with 12 electrodes. The dotted lines are the average scores of the same subjects from expansion and compression conditions with six middle electrodes, taken from Experiment 3. The expansion conditions are schematically shown above the figure.

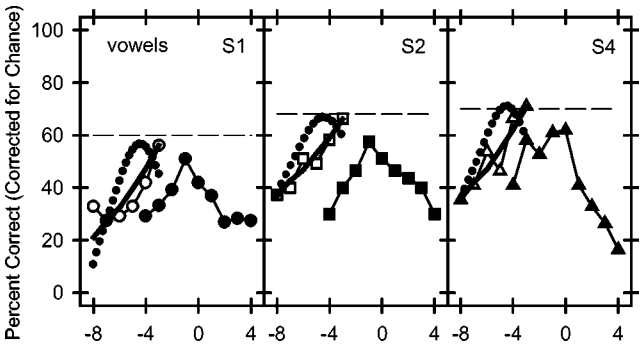

FIG. 7. Individual vowel recognition percent scores with 12-electrode processor from Experiment 4, shown by open symbols, and scores with six-electrode processor from Experiment 3, shown by filled symbols. The solid line shows the performance predicted from the similarity of the experimental map to patient's implant processor map while the dotted line shows the prediction from the similarity of the experimental map to the normal acoustic map. The dashed lines show the performance of subjects with the implant processor map.

normal acoustic map. Prelingually deafened subject S4 also showed a pattern similar to that predicted by the normal acoustic map, although the two predicted patterns were not sufficiently different to make a clear distinction, given the variability in the data in this case.

IV. DISCUSSION AND CONCLUSIONS

Speech recognition in cochlear implant listeners was significantly affected by alterations in the frequency-to-electrode mapping. Previous work in both acoustic simulations and in implant listeners had shown that speech recognition decreases with spectral distortions in the mapping, including apical-basal shift (Fu and Shannon, 1999; Dorman *et al.*, 1997), nonlinear warping (Shannon *et al.*, 1998), or compression–expansion (Başkent and Shannon, 2003). The present study expands the general pattern of frequency-place mismatch results to include frequency-place compression and expansion in cochlear implant listeners. The results have theoretical value as they quantify how speech pattern recognition is affected by alterations in the cochlear representation of speech. In addition, the present results have practical value, as they show the inherent tradeoffs between electrode array insertion depth, number of active electrodes, and input frequency range, to provide basic guidelines for optimal fitting of implant patients.

The implant subjects displayed a similar pattern of results despite the large variation in their speech recognition skills. Consistent with the acoustic simulations by Başkent and Shannon (2003) best speech recognition was obtained with frequency-place maps with the least spectral distortion. Both compression and expansion reduced recognition, especially with vowels, which are more sensitive to spectral manipulations. Yet, there was a significant difference between NH and implant subjects in their exposure to frequency-place maps, and the implant results showed two distinct patterns that might be determined by the individual subject's reference map. A simple model of frequency-place distortion fit the data from NH subjects (Başkent, 2003) and postlingually deafened subjects by weighting frequency-place mismatch relative to the normal acoustic tonotopic map. The same model fit the data from prelingually deafened subjects based on the similarity of the experimental map to the map in their individual processor. In Experiment 4, where the expansion conditions were applied with all 12 electrodes, the performance by the postlingually deafened subjects was again closer to the prediction by the similarity of the experimental condition to the normal acoustic map.

The changes in performance observed in the present study are acute effects observed immediately after the subject was given a new map, without any time to adapt to the new processor. It is not clear how much implant patients would be able to adapt to such compressed or expanded maps over time. The results of this study show that the choice of the frequency-place map has a significant effect on speech perception and choosing a better fitting map might instantly increase the performance of an implant patient. If a patient is initially given the best-fit map, any further adaptation could then start from this high performance level. Complementary to the findings of the present study with fully inserted arrays, Başkent and Shannon (2004) showed that it is particularly important to fit patients with partial insertions, who generally do not perform as well as patients with full insertions, with an optimum map. Although studies have shown improved performance with experience over the first few months of implant use (Tyler *et al.*, 1997; Fu *et al.*, 2002; and Fu and Galvin, 2003) it has not been demonstrated that such learning has a differential effect for different processor parameters. It seems likely that experience will increase performance for any processor setting, so it may be important to start with the setting that produces the best speech recognition to optimize long-term as well as short term outcomes.

One potential difficulty in such experiments with cochlear implants is the uncertainty inherent in several key parameters such as cochlear length, electrode array insertion depth, and its lateral distance from modiolus, and the best frequencies of the nerves actually stimulated by each electrode. The experiments in the present study demonstrated that, even though the physical values of these key parameters cannot be known with certainty, optimal values for a frequency-to-electrode map can be functionally estimated starting with approximate initial values. Phoneme recognition in Experiments 1–4 was always a simple function of the underlying manipulation, showing peak performance at a certain parameter value and a drop in performance as the value of that parameter was increased or decreased. Vowels and sentences were the speech materials most sensitive to the manipulations. Given the simplicity of these functions, a clinical procedure could be developed to rapidly converge on the optimal set of parameters controlling the frequency-to-electrode mapping for an individual patient. A subset of vowels could be selected that are most sensitive to frequency-place distortion. A simple optimizing algorithm could be developed to converge on the frequency-place mapping that maximizes vowel recognition for that reduced set in each individual patient, without the costs and risks of x rays and CT scans.

ACKNOWLEDGMENTS

The authors would like to thank Med-El Corp., especially Amy Barco, for providing the equipment and software, help recruiting subjects and their travel expenses, Peter Nopp, for valuable suggestions, Rachel Cruz, Dawna Mills, Pam Fiebig, and Michelle Colburn, for help recruiting subjects, and the subjects for their valuable efforts. Also the comments by Peter Assmann, two anonymous reviewers, and Anastasios Sarampalis are greatly appreciated. Funding for the study was provided in part by NIDCD Grant No. R01-DC-01526 and Contract No. N01-DC-92100.

Başkent, D. (**2003**). ''Speech recognition under conditions of frequency-place compression and expansion,'' Ph.D thesis, University of Southern California, CA.

Başkent, D., and Shannon, R. V. (**2003**). ''Speech recognition under conditions of frequency-place compression and expansion,'' J. Acoust. Soc. Am. **113**, 2064–2076.

Başkent, D., and Shannon, R. V. (**2004**). ''Interactions between cochlear implant electrode insertion depth and frequency-place mapping,'' J. Acoust. Soc. Am. (accepted for publication).

Cohen, L. T., Xu, J., Xu, S. A., and Clark, G. M. (**1996**). ''Improved and simplified methods for specifying positions of the electrode bands of a cochlear implant array,'' Am. J. Otol. **17**, 859–865.

Dorman, M. F., Loizou, P. C., and Rainey, D. (**1997**). ''Simulating the effect of cochlear-implant electrode insertion depth on speech understanding,'' J. Acoust. Soc. Am. **102**, 2993–2996.

Friesen, L., Shannon, R. V., Başkent, D., and Wang, X. (**2001**). ''Speech recognition in noise as a function of the number of spectral channels: Comparison of acoustic hearing and cochlear implants,'' J. Acoust. Soc. Am. **110**, 1150–1163.

Fu, Q.-J., and Shannon, R. V. (**1999**). ''Recognition of spectrally degraded and frequency-shifted vowels in acoustic and electric hearing,'' J. Acoust. Soc. Am. **105**, 1889–1900.

Fu, Q.-J., Shannon, R. V., and Galvin, J. (**2002**). ''Perceptual learning following changes in the frequency-to-electrode assignment with the Nucleus-22 cochlear implant,'' J. Acoust. Soc. Am. **112**, 1664–1674.

Fu, Q.-J., and Galvin, J. (**2003**). ''The effects of short-term training for spectrally mismatched noise-band speech,'' J. Acoust. Soc. Am. **113**, 1065–1072.

Greenwood, D. D. (**1990**). ''A cochlear frequency-position function for several species: 29 years later,'' J. Acoust. Soc. Am. **87**, 2592–2605.

Hillenbrand, J., Getty, L., Clark, M., and Wheeler, K. (**1995**). ''Acoustic characteristics of American English vowels,'' J. Acoust. Soc. Am. **97**, 3099–3111.

Institute of Electrical and Electronics Engineers (**1969**). IEEE recommended practice for speech quality measurements.

Ketten, D. R., Skinner, M. W., Wang, G., Vannier, M. W., Gates, G. A., and Neely, J. G. (**1998**). ''*In vivo* measures of cochlear length and insertion depth of Nucleus cochlear implant electrode arrays,'' Ann. Otol. Rhinol. Laryngol. Suppl. **175**, 1–16.

Marsh, M. A., Xu, J., Blamey, P. J., Whitford, L. A., Xu, S. A., Silverman, J. M., and Clark, G. M. (**1993**). ''Radiologic evaluation of multichannel intracochlear implant insertion depth,'' Am. J. Otol. **14**, 386–391.

Nilsson, M., Soli, S., and Sullivan, J. (**1994**). ''Development of the Hearing in Noise Test for the measurement of speech reception thresholds in quiet and noise,'' J. Acoust. Soc. Am. **95**, 1085–1099.

Robert, M. E. (**1998**). CONDOR: Documentation for Identification Test Program. Los Angeles. House Ear Institute, CA.

Shannon, R. V., Zeng, F.-G., Kamath, V., Wygonski, J., and Ekelid, M. (**1995**). ''Speech recognition with primarily temporal cues,'' Science **270**, 303–304.

Shannon, R. V., Zeng, F.-G., and Wygonski, J. (**1998**). ''Speech recognition with altered spectral distribution of envelope cues,'' J. Acoust. Soc. Am. **104**, 2467–2476.

Shannon, R. V., Jensvold, A., Padilla, M., Robert, M. E., and Wang, X. (**1999**). ''Consonant recordings for speech testing,'' J. Acoust. Soc. Am. **106**, L71–L74.

Skinner, M. W., Ketten, D. R., Holden, L. K., Harding, G. W., Smith, P. G., Gates, G. A., Neely, J. G., Kletzker, G. R., Brunsden, B., and Blocker, B. (**2003**). ''CT-Derived estimation of cochlear morphology and electrode array position in relation to word recognition in Nucleus 22 recipients,'' J. Assoc. Res. Otolaryngol. **3**, 332–350.

Tyler, R. S., Parkinson, A. J., Woodworth, G. G., Lowder, M. W., and Gantz, B. J. (**1997**). ''Performance over time of adult patients using the Ineraid or nucleus cochlear implant,'' J. Acoust. Soc. Am. **102**, 508–522.

Ulehlova, L., Voldrich, L., and Janisch, R. (**1987**). ''Correlative study of sensory cell density and cochlear length in humans,'' Hear. Res. **28**, 149–151.

Van Tasell, D. J., Soli, S. D., Kirby, V. M., and Widin, G. P. (**1987**). ''Speech waveform envelope cues for consonant recognition,'' J. Acoust. Soc. Am. **82**, 1152–1161.

Whitford, L. A., Seligman, P. M., Blamey, P. J., McDermott, H. J., and Patrick, J. F. (**1993**). ''Comparison of current speech coding strategies,'' Adv. Oto-Rhino-Laryngol. **48**, 85–90.

The effect of overlap-masking on binaural reverberant word intelligibility[a)]

Brad Libbey[b)] and Peter H. Rogers
Georgia Institute of Technology, Atlanta, Georgia 30332-0405

(Received 23 September 2002; accepted for publication 24 March 2004)

Reverberation interferes with the ability to understand speech in rooms. Overlap-masking explains this degradation by assuming reverberant phonemes endure in time and mask subsequent reverberant phonemes. Most listeners benefit from binaural listening when reverberation exists, indicating that the listener's binaural system processes the two channels to reduce the reverberation. This paper investigates the hypothesis that the binaural word intelligibility advantage found in reverberation is a result of binaural overlap-masking release with the reverberation acting as masking noise. The tests utilize phonetically balanced word lists (ANSI-S3.2 1989), that are presented diotically and binaurally with recorded reverberation and reverberation-like noise. A small room, 62 m^3, reverberates the words. These are recorded using two microphones without additional noise sources. The reverberation-like noise is a modified form of these recordings and has a similar spectral content. It does not contain binaural localization cues due to a phase randomization procedure. Listening to the reverberant words binaurally improves the intelligibility by 6.0% over diotic listening. The binaural intelligibility advantage for reverberation-like noise is only 2.6%. This indicates that binaural overlap-masking release is insufficient to explain the entire binaural word intelligibility advantage in reverberation. © *2004 Acoustical Society of America.*
[DOI: 10.1121/1.1781621]

PACS numbers: 43.71.Gv, 43.66.Dc, 43.66.Pn, 43.55.Hy [DOS] Pages: 3141–3151

I. INTRODUCTION

Reverberation is the summation of attenuated, time-delayed echoes of an acoustic signal. It would be convenient to assume that reverberation solely reduces intelligibility (Steinberg, 1929), but this assumption is incorrect. Acoustic architects often consider early echoes desirable since they increase the amplitude of the signal reaching a listener. This increase in amplitude due to reverberation can increase speech intelligibility if it raises the level above ambient noise levels (Hodgson and Nosal, 2002). Lochner and Burger's (1958) work demonstrates this effect for single echoes, and more recently, Watkins and Holt (2000) demonstrate the fusion of complex early reflections for vowel sounds. Early echoes do not benefit intelligibility when the sound pressure level is equal in anechoic and reverberant recordings. The present work is concerned with this constant amplitude condition, where the early echoes are detrimental to word intelligibility.

Later arriving echoes tend to reduce intelligibility more severely than the early echoes. Reverberation is highly dependent on the physical properties of the enclosed space as well as the location of the source and the listener within the space, so the division between early and late echoes is ambiguous (Soulodre *et al.*, 1989). The interference is especially pronounced for listeners with hearing impairments (Nábělek and Mason, 1981), or non-native speakers (Takata and Nábělek, 1990). The reason for this reduction is not entirely known. One probable cause is that the later echoes mask the speech that arrives directly from the source (Bolt and MacDonald, 1949). An alternative possibility is that the reverberation distorts phonetic transitions essential for identification (Nábělek *et al.*, 1996). In this alternate case the reverberation and direct speech are considered as one signal with characteristics that are quite different from the direct speech alone.

A. Overlap-masking

It is useful to understand how reverberation alters the attributes of speech and thereby reduces word intelligibility. Reverberation is well understood in terms of physical acoustics, but theories are incomplete on the specific alterations of speech characteristics that cause intelligibility reduction. Bolt and MacDonald (1949) and Nábělek *et al.* (1989) propose two contributing factors to the degradation of speech in reverberation: self-masking and overlap-masking. Self-masking refers to the time and frequency alterations of an individual phoneme. Reverberation slows onsets and decays of transient sounds. As such, it is not masking in the traditional sense. For example, the sound of an isolated /t/, which is essentially a transient noise burst, becomes less abrupt in the presence of reverberation. Reverberation also disrupts formant transitions between vowels by smearing temporal frequency changes. These and other disruptions reduce the phonetic information necessary for identification.

The present work focuses on overlap-masking as opposed to self-masking. Overlap-masking occurs when a preceding phoneme and its echoes mask a subsequent phoneme. In this interpretation, the phonemes might be thought of as

[a)]Portions of this work were presented in "Further investigations on binaural intelligibility of reverberant speech," J. Acoust. Soc. Am. **111**, 2430 (2002).
[b)]Electronic mail: libbey@mail.com

self-masked phoneme units. The unit is a masker when it occurs first and a maskee when it follows. An example of overlap-masking is two phonemes with similar frequency content occurring sequentially with a brief delay between them. The initial phoneme will endure because of reverberation and may overlap the second phoneme and its associated reverberation. The maskee in this case is the second phoneme's direct response as well as the second phoneme's echoes. This overlap-masking impoverishes the second phoneme. Arai *et al.* (2002) assume overlap-masking is occurring and exploit it in a processing scheme to improve word intelligibility. They reduce the energy of redundant portions of anechoic speech so that it is less likely to mask subsequent phonemes when broadcast in an auditorium. This is done by identifying steady state portions of speech with the ''mean square of the [cepstral] regression coefficients for each time trajectory of the logarithmic envelope of a subband.'' Hodoshima *et al.* (2004) find the intelligibility of words processed with this technique to be 5.4% greater than for unprocessed words when played in simulated rooms with 0.9–1.3 s of reverberation.

A listener's ability to detect and identify the second phoneme depends on energetic masking, suppression of remote frequencies, and informational masking. Energetic masking affects detection at the auditory periphery (Zwicker and Fastl, 1999), where energy spreads out due to the response of the basilar membrane. Suppression may occur due to energy in remote bands resulting in a second form of masking (Moore and Vickers, 1997). Informational masking occurs centrally and is associated with identification (Kidd *et al.*, 2002). In this third case, a phoneme may be detectable but not identified by central auditory processing. The intelligibility tests presented in the following do not distinguish between these masking types.

B. Binaural intelligibility advantage

The degradation caused by reverberation seems to go largely unnoticed by normal listeners in small reverberant rooms, and the binaural system's contributions to this perception are frequently observed. Many investigations explore the binaural perception of speech in reverberation, additive noise, and in the presence of interfering talkers. Bronkhorst (2000) tabulates the large binaural advantages in his review of the cocktail party phenomenon. However, Loven and Collins (1988) show that significant interactions exist between reverberation and noise. Therefore, research needs to address reverberation without noise to accurately assess binaural intelligibility.

Earlier work investigates intelligibility in noiseless conditions for a variety of room configurations. Moncur and Dirks (1967) compare near ear, far ear, and binaural listening for $T_{60}=0.9$, 1.6, and 2.3 s. Their data show a binaural advantage of 7.1%, 10.2%, and 9.5% word intelligibility, respectively, over the near ear alone. (Intelligibility advantages represent differences between intelligibility scores. They involve subtraction only and do not represent a percentage change in % correct.) Nábělek and Mason (1981) investigate this binaural advantage for hearing impaired listeners and find a binaural advantage of approximately 6.7% word intelligibility at $T_{60}=0.5$ s. Nábělek and Robinson (1982) perform the most comprehensive analysis in quiet on a variety of age groups for $T_{60}=0.4$, 0.8, and 1.2 s. For 27 year olds with normal hearing, they find an overall binaural intelligibility advantage of 1.8%, 4.2%, and 5.3%, respectively. The variation in these results illustrates the effect of different rooms and listening conditions on intelligibility scores (Nábělek and Robinette, 1978).

The present work focuses on the binaural system's ability to increase intelligibility in reverberation. Several binaural mechanisms may be responsible, including binaural overlap-masking release, source localization, or higher level speech processing. The first two receive much attention in terms of psychoacoustic and speech perceptual studies, the third is speculative.

Binaural masking release refers to the decrease in the threshold of detection of a signal in noise when both ears are used. The intelligibility tests presented here consider the possibility that the binaural system reduces the effect of reverberation and increases intelligibility in a manner similar to how it reduces the effect of noise in binaural detection tasks. Specifically, that the binaural system reduces overlap-masking in reverberation much as it reduces noise masking.

Mechanisms responsible for localization or the precedence effect (Wallach *et al.*, 1949) may also be responsible for the binaural advantage. In this case, binaural information might isolate the direct signal or remove some of the echoes prior to word identification. Colburn (1996) and Wittkop *et al.* (1997) illustrate several low level binaural processing models that might help to explain this based on source localization. It is difficult to understand how these mechanisms work in the presence of multiple echoes.

Binaural interactions are often not associated with high level speech processing, but the possibility cannot be ruled out. Dichotic experimentation provides evidence that phonetic integration occurs at higher levels (Jovicic, 1990; Miyata *et al.*, 1991). While localization mechanisms and higher level processing are probable causes for binaural advantages of speech, they are not segregated in the binaural experiments presented in the following.

We hypothesize that the binaural system cancels uncorrelated reverberation received at each ear. Reverberation is assumed to act as uncorrelated noise that masks subsequent reverberant phonemes. This reverberation is reduced similar to binaural masking release, familiar from psychoacoustic detection experiments (Koenig *et al.*, 1977). Further support comes from models that propose to improve signal quality based on the uncorrelated (Allen *et al.*, 1977) and the spatially incoherent (Flanagan and Lummis, 1970) character of reverberation at the ears. In casual listening tests, these algorithms reduce the perception of reverberation by reducing the reverberant tails and improving spectral content over the recorded reverberation. They are unsuccessful at increasing the recognition of consonants in CVC word tests (Bloom and Cain, 1982).

The present research tests this hypothesis by measuring the intelligibility of binaural and diotic words. Data from these tests show that binaural overlap-masking release accounts for only a portion of the binaural intelligibility advan-

tage and that localization mechanisms and higher level processing are acting as well.

II. METHOD

This work investigates binaural overlap-masking release in a pair of word intelligibility tests. These tests cannot disprove overlap-masking. Instead, they focus on the binaural system's ability to reduce reverberation in a manner similar to how it reduces masking noise. The first test compares the intelligibility of words with reverberation to words with reverberation-like noise for diotic presentations. It determines the signal to noise ratio (SNR) at which words masked by noise are as intelligible as words ''masked'' by reverberation. The second test looks again at reverberation and reverberation-like noise, but includes binaural presentations in addition to diotic. It examines the possibility that the binaural intelligibility advantage is actually a form of binaural masking release.

In the present work, intelligibility is measured directly for an experimental design with multiple factors at fixed levels. Traditionally, experiments addressing binaural noise cancellation measure detection. Koenig *et al.* (1977) investigate the detection of amplitude modulated sentences in reverberation alone. They conclude that the binaural system squelches reverberation as it does noise. The alternative to detection is to alter experimental factors such that a particular percentage of words are understood correctly, say 50% intelligible (Levitt and Rabiner, 1967a). This poses difficulties when multiple variables are to be included in an experimental design. The standard up–down methods used to adjust an experimental variable to achieve the desired level are not suitable for multiple factors (Levitt, 1971; Levitt and Rabiner, 1967b). Furthermore, many of the factors used in the designs are fixed and discreet. It is not possible to make continuous adjustments to achieve the desired intelligibility. Therefore, this research measures intelligibility differences as opposed to intelligibility level differences. An overview of the measurement process is presented in the following. Details for each individual test are given in Sec. III.

A. Anechoic recording of words

Phonetically balanced 50 word lists (ANSI, 1989) are chosen over consonant-vowel-consonant and rhyme tests because of their ability to discriminate the effects of reverberation. Kruger *et al.* (1991) find that a phonetically balanced word test is more sensitive to changes in reverberation time and has lower variance than the modified rhyme test or test sentences. Human speakers pronounce the phonetically balanced lists in a random order in an anechoic chamber. A carrier phrase is not included due to concerns that the phrase might interfere with the word, and since the phrase is not phonetically balanced this could bias the experiment. A recommendation for future tests is to have the speakers produce three phonetically balanced words in rapid succession. The second word being the target and the first and third words coming from lists not otherwise used during the test.

The anechoic recording technique places a human speaker in a chair approximately 100 cm away from a 36 cm computer monitor mounted on a pipe. The text is shown on the monitor and the person repeats the word they read. A 13 mm free field microphone (Larson Davis model 2540) is positioned approximately 15 cm from the speaker's mouth at an angle of 45°. Each anechoic word is digitally recorded at 44.1 kHz and 16 bits using a calibrated sound card (SB4171). The recorded words are not altered to compensate for any frequency response characteristics of the recording system since it has a relatively flat response. A 60 Hz high pass filter removes unwanted low frequency noise that is present in the anechoic chamber, and noise occurring before and after the word is manually truncated.

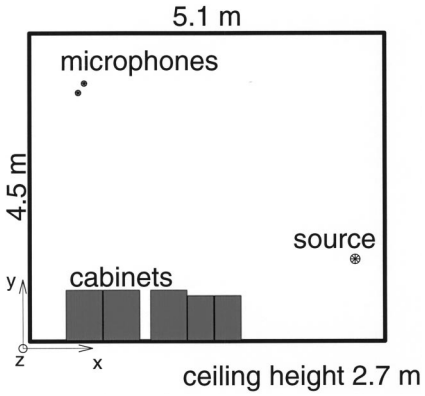

FIG. 1. Layout of the reverberant room illustrating the source, microphones, and other objects in the room.

The two tests use 14 unique lists from ANSI (1989), including lists number 1, 3, 4, 5, 6, 7, 8, 9, 10, 11, 12, 13, 15, and 16. Different speakers pronounce these lists, for the first test a speaker (S1) pronounces lists 3–10. The second test reuses six of these pronounced lists and adds three additional speakers pronouncing overlapping word lists. (S1, lists 3, 4, 5, 7, 8, 9; S2, lists 7, 8, 9, 11, 12, 13; S3, lists 1, 11, 12, 13, 15, 16; and S4, lists 1, 3, 4, 5, 15, 16.) This arrangement results in 26 speaker/list combinations, or a total of 1300 recorded words. Responses produced or recorded inaccurately are eliminated and the same word, produced by another speaker, replaces that response (18 out of 1300 anechoic words are substituted in this manner.)

B. Reverberant room

The reverberant room has dimensions of $5.1\times4.5\times2.7$ m, Fig. 1. The walls are painted drywall without windows, carpeting covers a concrete floor, and the ceiling is standard office, porous, pressed fiber. Five metal file cabinets occupy the room, they are 1.4 m tall occupying a total floor area of 1.7 m^2. The broadband reverberation time is 0.6 s. $T_{60}=0.8$ s for the 500 Hz octave band, $T_{60}=0.6$ s for the 1 kHz band, and $T_{60}=0.6$ s for the 2 kHz band.

A loudspeaker source is positioned in one corner of the room and the microphones in the opposite corner. The coordinate positions are (4.7,1.2,2.1) m and (0.7,3.7,1.2) m respectively, resulting in a separation distance of 4.8 m. This distance is greater than the calculated critical radius, $r_c=0.6$ m. A critical radius is the distance from a source to where the direct energy is equivalent to the diffuse energy. For a suspended omni-directional source,

$$r_c = k\sqrt{\frac{V}{T_{60}}}\ \text{m}, \tag{1}$$

where V is the volume of the room in m^3 and $k=0.06$ (Pierce, 1991, pages 267–269). The source and listener separation is also greater than the calculated perceptual critical distance of 2.0 m. Peutz (1971) defines the perceptual critical distance as the distance ''beyond which the intelligibility is constant,'' and sets $k=0.2$ in Eq. (1).

C. Intelligibility testing

The heart of the intelligibility test consists of presenting reverberant words to listeners and assessing their replies. The test administrator instructs the listeners before this testing occurs. They are asked to listen to each word, reply immediately with the word they think they heard, to guess on confusing words, and to reply with the comment ''don't know'' for words they cannot guess. The subjects are not given any additional information to aid their responses. The subjects are untrained and not familiar with the testing material, but are given 30 practice words before the real test begins. Feedback is not provided during either the practice or the test session. A computer monitor prompts listeners to click a button to advance through the words. The words are played to the subjects over headphones binaurally and diotically. Binaural implies that both ears receive information as if in a natural acoustic environment. In this case, the signals are generally different in each ear. Diotic conditions present only one signal to both ears. This eliminates the possibility of ear advantages and reduced loudness associated with monaural listening.

A single microphone (Larson Davis model 2560) at short range records the subjects responses digitally (22.05 kHz, 16 bits). The test administrator scores each response as correct or incorrect based on comparisons to the textual word and the anechoic recording (down sampled to 22.05 kHz). When no response is given the word is judged incorrect, and when the response is incompletely recorded, it is assessed on an individual basis. 5200 replies are recorded, of these 44 are blank and 52 are incomplete.

D. Recorded reverberation

Two loudspeaker units (Kenwood KFC-1058S, 9 cm) mounted face to face approximate a single omni-directional source. This is not an accurate model of a person speaking in a room since a real voice is directionally dependent. Yet, this configuration is thought to be more favorable than a baffled piston or dipole. The anechoic words are prefiltered to control the time, frequency, and amplitude characteristics of the loudspeaker system. The inverse filter for the loudspeaker system is created by a least-squares time inversion of the impulse response of the sound card, amplifier (Realistic MPA-95), and loudspeakers.

The recorded reverberant words include both the direct arrival and reverberation. A research assistant sitting in the room wore two microphones next to her ears to record the reverberant words. This was done to maintain interaural level and time differences, although spectral weighting is distorted. The two microphones, 13 mm random incidence (Larson Davis model 2560), are positioned with the gratings horizontal and level with the top of the ear canal entrance. They are mounted on a cap such that they apply a small amount of pressure to the upper pinna. The assistant faces the source and no word is recorded if the head is turned more than 6°. This angle is ensured by measuring the flight time from loudspeaker to each microphone. Ideally, a mannequin head would be used, but one was not available during this phase of testing.

The recorded reverberant words require filtering and scaling before being played over headphones, similar to the preparations for the loudspeaker system. The headphone presentation system consists of an Echo MIA sound card, Sony MDR-CD470 headphones, and the subjects' occluded ears. This system does not have a flat frequency response. Inverse filters help correct these discrepancies based on the system response of the headphones placed on a Head Acoustics mannequin (Russotti *et al.*, 1988). The headphones are replaced between each of eight measurements to account for minor variations due to positioning (Kulkarni and Colburn, 2000). The impulse responses of the left and right channels are independently averaged and inverted using a least-squares time domain solution. The measured system responses will not contain accurate pinna spectral weighting because of individual listener differences and placement variations. Prefiltering the prepared words flattens the frequency characteristics of the headphone response, and shortens the impulse response received at a listener's eardrums. All signals are scaled so that the average sound pressure level of the prepared words is 66 dB (ref 20 μPa) for all treatments. A 5 ms segment of a Hanning window fades the signal on and off in order to prevent clicks at the start and finish of a word.

E. Listeners

The listeners' ages range from 21 to 35 years with a mean age of 26 years. Each listener takes a threshold of hearing test using the same headphone system as the intelligibility test. This test is not based on a standardized testing procedure and results should be interpreted in the context of this work. The subjects' equivalent threshold level is 27 dB (ref 20 μPa) at 250 Hz with a standard error of 6 dB. The mean difference between subjects' left and right ear was 3 dB with a standard error of 4 dB and a maximum difference of 9 dB. Data also exist at 1 and 4 kHz, but is limited by the quietest sound that could be produced by the equipment. The subjects are capable of detecting 1 and 4 kHz pure tones quieter than 12 and 17 dB, respectively. The differences between the left and right ear are not available for the higher frequencies because of this equipment limitation.

F. Noise

Recording and playback systems carry with them the possibility of added noise, this is controlled through a variety of techniques. Noise was limited by choosing a room with limited external disturbances. The ventilation system is disconnected and recordings are made during the night. Equip-

TABLE I. The experimental design for the diotic test showing the word lists from ANSI (1989) in columns, the listeners across the top, and the SNR treatment along the left side. The final row is recorded reverberation and two word lists are assigned to this factor level for each listener.

	Listener			
SNR (dB)	L1	L2	L3	L4
−14	7	6	4	10
−12	8	5	3	9
−9	9	4	5	7
−6	10	3	6	8
−3	3	9	7	6
0	4	10	8	5
SRR=−12	5,6	7,8	9,10	3,4

ment noise adds a low frequency carrier to all the recorded signals. This is reduced by a finite impulse response filter with a cutoff of 60 Hz. The signal to ambient noise ratio in all the tests is approximately 30 dB, based on analysis of the prepared word lists used in the tests. This ratio is slightly better for octave bands from 0.5 to 4 kHz, and a bit worse out of this region.

III. WORD INTELLIGIBILITY TESTS

A. Diotic test

The diotic test compares the intelligibility of recorded reverberant words to anechoic words with reverberation-like additive noise, details of this reverberation-like noise follow in sec. III A 2. The purpose of this comparison is to equate diotic word intelligibility in reverberation to that in reverberation-like noise, so that a subsequent test can compare binaural advantages accurately. By equating the overall intelligibility level, binaural deviations from this base point will vary at essentially a constant rate relative to the independent variable and therefore be comparable.

1. Experimental design

The experimental design (Table I) includes three factors: SNR, listener, and word list. The principal factor, SNR, consists of seven levels, six of which represent various ratios of anechoic word energy to the energy of the reverberation-like noise. The SNRs for these six levels are −14, −12, −9, −6, −3, and 0 dB. The remaining factor level is recorded reverberation. For this level, no alterations are made to the signal to reverberation ratio (SRR) of the original recording. Therefore, the presentations include the direct arrival and the reverberation. The SRR is approximately −12 dB and is based on the energy of the direct path word divided by the energy in the reverberant echoes for the duration of the word. A simulated room is used to calculate these energies and is based on the method of images as proposed by Allen and Berkley (1979). The various levels of the SNR factor permit matching the intelligibility of words in reverberation-like noise to those with normal reverberation.

Four listeners participate, one female and three males all with normal hearing, aged 21 to 31 with a mean age of 26 years. None of the listeners could be considered trained, but two of the listeners had taken similar word intelligibility tests previously. Each listener hears eight unique word lists (ANSI (1989) lists: 3–10) spoken by one male American English speaker. Six of the eight lists are assigned to the six SNR levels and the recorded reverberation condition is assigned the remaining two lists. The assignments are different for each listener and distributed to balance the design as much as possible. Presentation order is completely randomized with respect to word list and SNR.

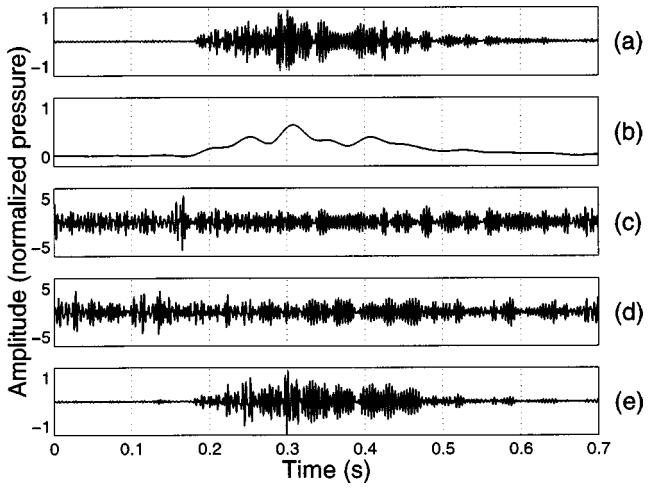

FIG. 2. The generation of reverberation-like noise by showing a single octave band (centered at 244 Hz) of the reverberation without the direct arrival for the word "sick" is exemplified. (a) Time history, (b) envelope 0–22.5 Hz, (c) wave form fine structure, (d) fine structure with randomized phase, (e) time history reconstructed from (b) and (d).

2. Reverberation-like noise

If reverberation masks the direct signal as hypothesized, then an additive noise signal should be able to imitate the reverberation and produce the same effects. However, the spectral and temporal characteristics of the reverberation are notably different from randomly distributed noise. Gelfand and Silman (1979) suggest that multiple echoes act as speech shaped noise. Therefore, the reverberation, not including the direct signal, is manipulated to produce noise that has slowly varying spectral properties similar to reverberation, but differs in that the relative phase between frequency components is randomized.

This noise signal is generated by isolating the reverberation from the direct signal by subtracting the anechoic word from the recorded reverberation. This is possible because the arrival delay of the direct signal is known. The isolated reverberation is then divided into octave bands, Fig. 2. From each of these bands a modulation envelope is determined by taking the absolute value of the time domain octave signal and low pass filtering it at 22.5 Hz. Drullman *et al.* (1994) show that this cutoff frequency will not substantially reduce intelligibility. Dividing the original octave band by its envelope gives the wave form fine structure, the high frequency carrier of the modulation. Without other alterations, the wave form fine structure can be recombined with the envelope to reconstruct the reverberation without loss of information, in other words, the output would exactly match the recorded reverberation.

Instead, the phase of the wave form fine structure is randomized independently within each band to convert the

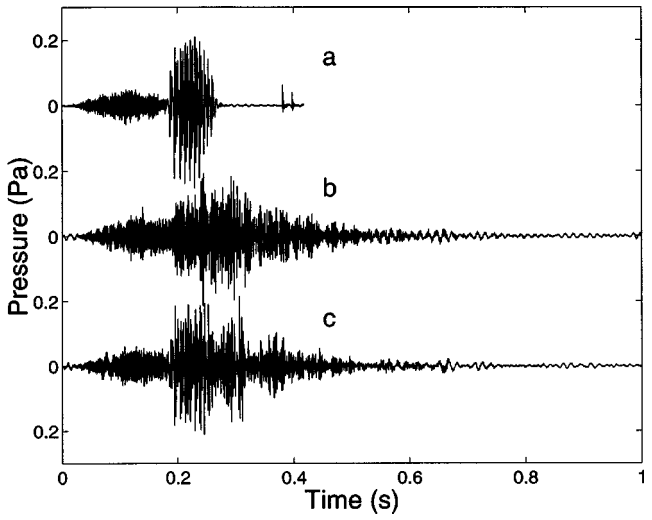

FIG. 3. Broad band, time domain version of the word "sick." (a) Anechoic, (b) recorded reverberation (direct+reverberation $T_{60}=0.6$ s), (c) anechoic +reverberation-like noise.

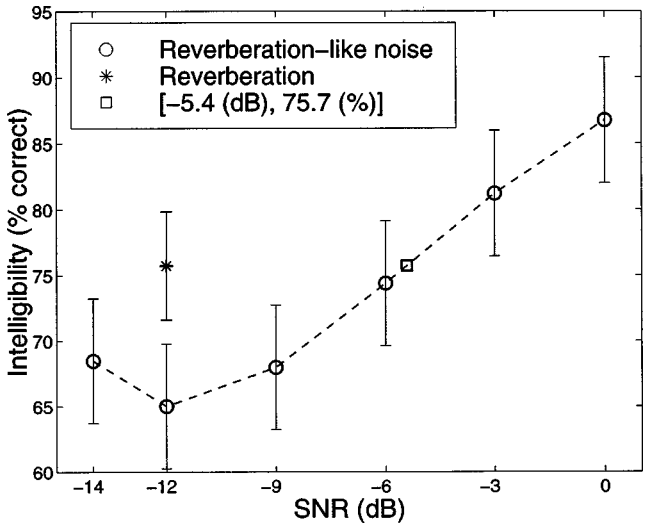

FIG. 4. The diotic intelligibility data for the SNR treatment ($Y_{\cdots k\cdot}=\mu\ldots+\gamma_k$), as fit by the analysis of variance model, Eq. (2). Error bars are the 90% confidence intervals for the family of all pairwise comparisons between the fitted means shown. The box shows the SNR that matches intelligibility of words in reverberation-like noise to the intelligibility of recorded reverberation.

reverberation into noise. This is done by windowing 93 ms segments of the fine structure with 65 ms of overlap using a rectangular window. A fast Fourier transform of each of these windows is produced. The phase of each frequency component is randomly selected from a flat distribution between 0 and 2π and the negative frequency components are assigned the appropriate complex conjugate value. After the inverse transform, the wave form fine structure maintains the same frequency content as the original, but with a randomized phase. The short segments are then windowed with a Blackman window and added back together. The Blackman window has the desirable property that for overlaps greater than 65% of the window length summing the windows produces temporal fluctuations of less than 0.3%. The new wave form fine structure is multiplied by the modulation envelope and octave bands are recombined to produce the reverberation-like noise.

The reverberation-like noise is added to the scaled anechoic word to produce the desired treatment, Fig. 3. The experimental design dictates the signal (anechoic word) to noise ratio. This ratio is implemented by varying the energy of each anechoic word relative to the energy in the noise. In both cases, the energy is averaged over the period during which the anechoic word exists. This technique provides the exact SNR for each individual word. The combined anechoic word and reverberation-like noise is finally scaled so that all treatments are presented at 66 dB.

3. Diotic test results

The analysis of variance for the diotic test used the following model:

$$Y_{ijkl}=\mu\ldots+\alpha_i+\beta_j+\gamma_k+\epsilon_{ijkl}, \tag{2}$$

where Y_{ijkl} is the intelligibility of a given listener for a specific treatment, $\mu...$ is the overall mean, α_i is the effect of the listening subject, β_j is the effect of word list, γ_k is the effect of SNR, ϵ_{ijkl} is the residual distributed as $N(0,\sigma^2)$ with the standard error $\sigma=4.5\%$ intelligibility. Two-factor interactions are not considered in the model because of the small test size. The results of this model pertain only to the factor levels included in the study, the data are normal with constant error variance across the SNR treatments.

Subject's mean performance ranges from 66.8% to 81.5% intelligibility, a statistically significant difference ($p=0.000\,03$). This large variation appears to be due to two subjects who had taken similar word intelligibility tests in the past. Differences in the word lists are also significant ($p=0.000\,06$) with the best list 13.5% more intelligible than the worst. Although the lists are designed to give equivalent results, this was not the case in this test, nonetheless, the effect is minimal on the factor of interest.

The recorded reverberation is 75.7% intelligible and serves as a base point to which the reverberation-like noise is compared, Fig. 4. A Tukey multiple comparison procedure facilitates pairwise comparisons of treatment means with not less than a 90% family confidence level ($\alpha\leqslant 0.1$). Under this test, the noise treatment is shown to be less intelligible than the reverberation when SNR=SRR=−12 dB. Interpolating between the reverberation-like noise fitted means yields a SNR of −5.4 dB, at which point a word in reverberation-like noise is as intelligible as a word in reverberation.

While this result is of primary importance, it is also interesting to examine the entire set of data. This suggests that the anechoic word is not being used for identification when its energy is low. Instead, word identification relies heavily on the information contained in the reverberation-like noise. The apparent dip at −12 dB as compared to −14, −9, and −6 dB is not statistically significant in a Tukey multiple comparison procedure. One should interpret all intelligibility levels $\leqslant -6$ dB as being equivalent. In this range, increasing the signal amplitude relative to the noise did not increase intelligibility. One would expect an intelligibility increase if the reverberation-like noise functioned solely as a masker. Intelligibility increases steadily at a rate of 2%/dB

TABLE II. The principal factors of the binaural test are shown as row and column labels. Entries are word intelligibility (% correct) as determined from Eq. (4) and the analysis of variance model, Eq. (3).

	Presentation style factor		
Interference factor	Diotic L or R	Binaural L&R	Diotic L/2+R/2
Recorded reverberation	$Y_{\ldots 11\cdot}=71.0$	$Y_{\ldots 12\cdot}=77.0$	$Y_{\ldots 13\cdot}=70.5$
Reverberation-like noise	$Y_{\ldots 21\cdot}=69.2$	$Y_{\ldots 22\cdot}=71.8$	$Y_{\ldots 23\cdot}=75.7$

beyond −6 dB SNR, indicating the anechoic signal is important for identification in this region.

Specifying SRR is ambiguous because the echoes are generally coherent with the signal. This does not mean that they will add constructively with the signal. Constructive interference with the signal depends on the arrival delay of the echo and spectral content of the signal. Nonetheless, Lochner and Burger (1964) suggest that some of the early echoes are useful. They measure the subjective integration of a single echo for a variety of time delays. Based on these data, they include a weighted portion of the first 95 ms of the reverberation with the signal energy when computing the SRR. This increases the signal energy relative to the interfering reverberation, and matches intelligibility of reverberant words to words with white noise. The SRR level specified for the diotic test does not integrate early echoes. If this is done, integrating 5 ms of the reverberant echoes into the signal matches the SRR and SNR levels at 75.7% intelligibility for reverberation and reverberation-like noise. Lochner's 95 ms integration time clearly differs from the 5 ms integration time determined here. This difference illustrates that an integration time is dependent on the characteristics of the reverberation (Janssen, 1957; Soulodre *et al.*, 1989), and the type of noise used for comparison.

B. Binaural test

This test examines the hypothesis that binaural overlap-masking release is responsible for the binaural intelligibility advantage of reverberant words. It does this by looking at various diotic and binaural presentations of two channel reverberant recordings and words with reverberation-like noise.

1. Experimental design

The principal factor of this test, interference, considers the intelligibility of words recorded in reverberation to words with reverberation-like additive noise (Table II). Binaural reverberation-like noise is generated with an algorithm similar to that used in the diotic test (Sec. III A 2). However, this algorithm processes the left and right ear independently with a unique phase randomization for each channel. Independent processing and the long window length used for phase randomization eliminate binaural cues about the location of individual echoes. Interaural time and spectral weighting differences that exist in reverberation do not exist in the reverberation-like noise. The longest delay between echoes is 2 ms while the phase randomization window is 93 ms. Since each channel's phase is randomized independently the relative phase of the left and right channels is lost over this interval. This guarantees that no individual echo's localization cues are preserved between channels. The envelopes do contain binaural information that is not eliminated, but their characteristic time is longer than 44 ms due to the lowpass filter at 22.5 Hz. The binaural envelope differences represent the room characteristics in general, but not the locations of individual echoes. Unlike the interfering signals, the direct word is the same in each ear for both reverberation and reverberation-like noise. The SNR of the anechoic words relative to the reverberation-like noise is −5.4 dB, as determined in the diotic test, compared to the SRR of −12 dB. This principal factor produces reverberation-like noise without binaural localization cues associated with normal reverberation.

The second factor, presentation style, determines the binaural advantage and provides information about the type of processing that causes the advantage. This factor includes three levels: a diotic level where either the left or the right channel (L or R) plays to both ears, a binaural level where the left and right channels (L&R) are directed to the appropriate ears, and a diotic level where the left and right channels are averaged (L/2+R/2). The diotic L or R is essentially a control treatment similar to the diotic experiment above. The binaural L&R references the diotic L or R to determine if a binaural advantage exists.

The diotic L/2+R/2 level is included to determine if two-channel noise averaging is enough to account for the binaural advantage. This is conceivable since the direct signal is always located at $0\pm6°$ azimuth and will average constructively. The reverberation and noise are uncorrelated[1] across channels and will be reduced in amplitude when averaged. Averaging reduces the level by 2.9 dB for reverberation and 3.0 dB for reverberation-like noise. This average is computed for all words used in this test over a period corresponding to the duration of the original anechoic word.

There are six normal hearing subjects who participate in this experiment, one female and five males, aged 22 to 35 with a mean age of 25 years. All of the listeners are untrained, but are given a practice period to acquaint them with the testing procedure. A third factor of the experimental design accounts for differences in these listeners. Each listener hears twelve word lists (ANSI (1989) lists: 1, 3, 4, 5, 7, 8, 9, 11, 12, 13, 15, and 16). These word lists make up a fourth factor of the experimental design. A total of four male American English speakers constitute the fifth and final factor of the experimental design. Each list is spoken by two of these speakers.

These five factors form an experimental design that is balanced for all two-factor interactions except the interaction of list and speaker (Table III). In this case, some speaker/list combinations are used more than others. Three-factor interactions involving the presentation style and the interference are balanced as well.

2. Binaural test results

The analysis of variance for the binaural test used the following model:

TABLE III. The experimental design of the binaural test. Presentation styles are described in the text. Recorded reverberation (including the direct signal) is designated "recorded." Reverberation-like noise (including the anechoic signal) is designated "noise." Word lists are from ANSI (1989).

Presentation	Interference	Listener	Speaker	Word list
L or R	Recorded	L1	S1	PB4
L or R	Recorded	L1	S2	PB8
L or R	Recorded	L2	S2	PB12
L or R	Recorded	L2	S3	PB16
L or R	Recorded	L3	S3	PB13
L or R	Recorded	L3	S4	PB1
L or R	Recorded	L4	S1	PB9
L or R	Recorded	L4	S4	PB5
L or R	Recorded	L5	S1	PB3
L or R	Recorded	L5	S3	PB11
L or R	Recorded	L6	S2	PB7
L or R	Recorded	L6	S4	PB15
L or R	Noise	L1	S3	PB13
L or R	Noise	L1	S4	PB1
L or R	Noise	L2	S1	PB9
L or R	Noise	L2	S4	PB5
L or R	Noise	L3	S1	PB3
L or R	Noise	L3	S2	PB7
L or R	Noise	L4	S2	PB11
L or R	Noise	L4	S3	PB15
L or R	Noise	L5	S2	PB12
L or R	Noise	L5	S4	PB4
L or R	Noise	L6	S1	PB8
L or R	Noise	L6	S3	PB16
L&R	Recorded	L1	S1	PB3
L&R	Recorded	L1	S2	PB7
L&R	Recorded	L2	S2	PB11
L&R	Recorded	L2	S3	PB15
L&R	Recorded	L3	S3	PB12
L&R	Recorded	L3	S4	PB16
L&R	Recorded	L4	S1	PB8
L&R	Recorded	L4	S4	PB4
L&R	Recorded	L5	S1	PB5
L&R	Recorded	L5	S3	PB13
L&R	Recorded	L6	S2	PB9
L&R	Recorded	L6	S4	PB1
L&R	Noise	L1	S3	PB12
L&R	Noise	L1	S4	PB16
L&R	Noise	L2	S1	PB8
L&R	Noise	L2	S4	PB4
L&R	Noise	L3	S1	PB5
L&R	Noise	L3	S2	PB9
L&R	Noise	L4	S2	PB13
L&R	Noise	L4	S3	PB1
L&R	Noise	L5	S2	PB7
L&R	Noise	L5	S4	PB15
L&R	Noise	L6	S1	PB3
L&R	Noise	L6	S3	PB11
L/2+R/2	Recorded	L1	S3	PB11
L/2+R/2	Recorded	L1	S4	PB15
L/2+R/2	Recorded	L2	S1	PB7
L/2+R/2	Recorded	L2	S4	PB3
L/2+R/2	Recorded	L3	S1	PB4
L/2+R/2	Recorded	L3	S2	PB8
L/2+R/2	Recorded	L4	S2	PB12
L/2+R/2	Recorded	L4	S3	PB16
L/2+R/2	Recorded	L5	S2	PB9
L/2+R/2	Recorded	L5	S4	PB1
L/2+R/2	Recorded	L6	S1	PB5
L/2+R/2	Recorded	L6	S3	PB13
L/2+R/2	Noise	L1	S1	PB5
L/2+R/2	Noise	L1	S2	PB9
L/2+R/2	Noise	L2	S2	PB13
L/2+R/2	Noise	L2	S3	PB1
L/2+R/2	Noise	L3	S3	PB11
L/2+R/2	Noise	L3	S4	PB15
L/2+R/2	Noise	L4	S1	PB7
L/2+R/2	Noise	L4	S4	PB3
L/2+R/2	Noise	L5	S1	PB8
L/2+R/2	Noise	L5	S3	PB16
L/2+R/2	Noise	L6	S2	PB12
L/2+R/2	Noise	L6	S4	PB4

$$Y_{ijklmn} = \mu\ldots + \alpha_i + \beta_j + \gamma_k + \delta_l + \varepsilon_m + \alpha\delta_{il} + \alpha\varepsilon_{im} + \delta\varepsilon_{lm} + \epsilon_{ijklmn}, \quad (3)$$

where Y_{ijklmn} is the intelligibility of a given listener for a specific treatment, $\mu\ldots$ is the overall mean, α_i is the effect of the listening subject, β_j is the effect of word list, γ_k is the effect of the speaker, δ_l distinguishes between reverberation and reverberation-like noise, ε_m contrasts diotic and binaural listening, $\alpha\delta_{il}$, $\alpha\varepsilon_{im}$, and $\delta\varepsilon_{lm}$ are two-factor interactions, ϵ_{ijklmn} is the residual distributed as $N(0,\sigma^2)$ with the standard error $\sigma = 6.1\%$ intelligibility. The results of this model pertain only to the factor levels included in the study, the data are normal with constant error variance across the principal treatments.

Subject's mean performance ranges from 65.8% to 78.0% intelligibility. Some listener scores are significantly different from others ($p = 0.001$), therefore this effect is kept in the model to remove individual listener bias. The listener/interference and listener/presentation style interactions are insignificant ($p = 0.18$ and $p = 0.83$, respectively). However one of the listeners appears to not utilize binaural information, she had a 1.1% monaural advantage for reverberation and a 4.5% monaural advantage for reverberation-like noise.[2] Differences in the word lists are also significant ($p = 0.02$) with the best list being 18.4% more intelligible than the worst. Individual speakers differ significantly ($p = 0.000\,02$) with the best speaker being 17.2% more intelligible than the worst.

Word intelligibility treatment means are computed from the factor level effects using Eq. (4) and are presented in Table II,

$$Y_{\ldots lm\cdot} = \mu\ldots + \delta_l + \varepsilon_m + \delta\epsilon_{lm}. \quad (4)$$

Comparisons between treatment means are of greater interest than the treatment means on their own. A Holm multiple comparison procedure tests the null hypothesis for a set of five pairwise comparisons between treatment means. This small set is sufficient to elucidate pertinent results. The pairwise comparisons' confidence intervals are plotted in Fig. 5,

$$\hat{D}_1 = Y_{\ldots 11\cdot} - Y_{\ldots 21\cdot} = \text{L or R reverb.} - \text{L or R noise},$$

$$\hat{D}_2 = Y_{\ldots 12\cdot} - Y_{\ldots 11\cdot} = \text{L\&R reverb.} - \text{L or R reverb},$$

$$\hat{D}_3 = Y_{\ldots 22\cdot} - Y_{\ldots 21\cdot} = \text{L\&R noise} - \text{L or R noise},$$

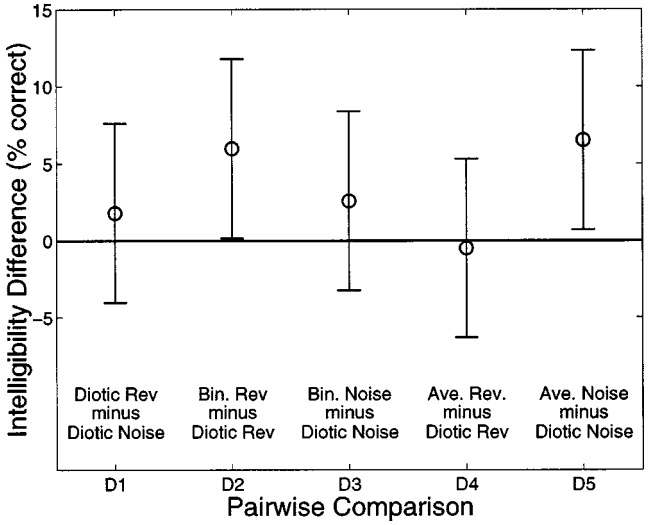

FIG. 5. Pairwise comparisons from the binaural word intelligibility test. Error bars demonstrate the 90% confidence intervals for the family of comparisons shown.

$$\hat{D}_4 = Y_{\ldots 13\cdot} - Y_{\ldots 11\cdot} = \text{L}/2 + \text{R}/2 \text{ reverb.} - \text{L or R reverb,}$$

$$\hat{D}_5 = Y_{\ldots 23\cdot} - Y_{\ldots 21\cdot} = \text{L}/2 + \text{R}/2 \text{ noise} - \text{L or R noise.}$$

The pairwise comparisons $\hat{D}_2$ and $\hat{D}_5$ differ significantly from zero. The above test shows that binaural words are 6.0% more intelligible than diotic when reverberation is present, $T_{60} = 0.6$ s. This result compares to the work done by Nábělek and Robinson (1982), who found a binaural advantage of 4.2% intelligibility for 27 year olds in a reverberant environment with $T_{60} = 0.8$ s.

There is a 6.5% intelligibility advantage from averaging the left and right channels of reverberation-like noise. This advantage is comparable to a prediction based on the diotic experiment. Averaging the two channels results in a SNR improvement of 3.0 dB. This change corresponds to a 6.0% intelligibility difference based on the linear portion of Fig. 4 where the slope is 2.0%/dB.

The analysis is unable to detect differences in the other pairwise comparisons, $\hat{D}_1$, $\hat{D}_3$, and $\hat{D}_4$. The intelligibility differences for these comparisons are either zero or too small to detect, but an analysis of why these differences are small is more enlightening than the significant comparisons.

The intelligibility difference is $\hat{D}_1 = 1.8\%$ for the comparison between diotic (L or R) presentations of words in reverberation to reverberation-like noise. This small difference is expected since the diotic experiment purposed to match the intelligibility for reverberation and reverberation-like noise by adjusting the SNR. These two diotic treatments are control conditions to which other results are compared, so the small difference is accounted for.

The binaural advantage for words in reverberation-like noise results in $\hat{D}_3 = 2.6\%$ intelligibility. Although this difference is not significant, it is likely that a small advantage exists and binaural overlap-masking release is occurring somewhat. Another way of thinking of this comparison is in the framework of the dichotic experiments that measure intelligibility instead of detection. Essentially, the L or R noise treatment and the L&R noise treatment are comparable to S_0N_0 and S_0N_u conditions, respectively. S_0 or N_0 signify that the signal or noise are equivalent at each ear and N_u signifies the noise is uncorrelated. Licklider (1948, page 152) performs an experiment using phonetically balanced 50 word lists in white noise. He measures intelligibility and finds a 4.2% intelligibility advantage for S_0N_u as compared to S_0N_0 at 0 dB SNR. The excess advantage found by Licklider is probably due to his use of white noise as opposed to reverberation-like noise.

Averaging the reverberation reduces its level by 2.9 dB. This is quite similar to the reduction seen for the reverberation-like noise, 3.0 dB. However, intelligibility scores do not reflect this similarity. The difference due to averaging the reverberation channels is insignificant, $\hat{D}_4 = -0.5\%$ intelligibility.

IV. ANALYSIS

A. Reverberation as signal

The present document refers to reverberation and reverberation-like noise as detrimental to speech, this is not entirely true. Reverberant intelligibility will almost always be worse than anechoic intelligibility provided the overall levels are balanced, but this does not imply that the reverberation functions only as interference. It seems apparent that listeners use reverberation itself to identify speech. Hodgson and Nosal (2002) predict reverberation increases signal levels and reduces masking of uncorrelated noise when noise sources are in close proximity to the listener. The relative increase in signal to noise permits speech understanding because the reverberation contains enough clues to identify the speech. The importance of reverberation is easily demonstrated by listening to reverberation without the direct arrival or any of the early echoes. This is a realistic situation, similar to listening to a speaker in an adjacent room. It reduces intelligibility, but not as severely as one might imagine.

The binaural test supports the notion that reverberation is used to identify words. Averaging the reverberation-like noise improves intelligibility as one expects based on the 3.0 dB of noise reduction associated with the averaging. In contrast, averaging two channels of reverberation does not provide an intelligibility benefit, although the reverberant energy is reduced by 2.9 dB, similar to reverberation-like noise. This result is qualitatively observed in the work of Koenig (1950), who notes that adding two channels recorded in a room is less beneficial than listening binaurally. The fact that averaging reverberation offers no improvement suggests that the reverberation itself is being used for understanding. A reduction in its level, 2.9 dB, relative to the direct signal does nothing to improve intelligibility. This result shows that the reverberation itself can be used for word identification.

The diotic experiment provides evidence that the reverberation-like noise is used for word identification similar to reverberation. The test was not able to show a significant change in intelligibility for SNR levels less than or equal to −6 dB. It seems likely that when the energy in the

anechoic signal is low, the reverberation-like noise is being identified and the anechoic signal is unimportant. This implies that reverberation-like noise is intelligible without a direct arrival.

There is a discrepancy between overall intelligibility of reverberation and reverberation-like noise when the SRR and SNR levels are matched. This may be a result of temporal smearing. The 93 ms window used for randomizing the phase may cause additional smearing beyond that associated with reverberation, $T_{60}=600$ ms. In addition, the relative phase of frequency components may reduce the overall intelligibility. The relative phasing of frequency components and harmonics is jumbled beyond that normally associated with reverberation. Traunmüller (1987) shows the relative phase of the harmonics and formants within critical bands affects the perception of vowels. Nonetheless, the reverberation-like noise can still be used to identify the word.

B. Binaural analysis

The second experiment shows that the binaural intelligibility advantage in reverberation-like noise is not as large as in reverberation. It demonstrates that binaural overlap-masking release accounts for only a portion of the total binaural intelligibility advantage. The subjects are exploiting reverberant information between the two channels that has been lost in producing the noise. The reverberation contains localization cues so it seems likely that a binaural listener uses some of the echo location information that exists in reverberation.

Another possibility is that higher neurological centers process binaurally, for example, channel selection or switching based on likelihood estimates for the speech (Miyata *et al.*, 1991). The binaural advantage associated with high level processing might also be referred to as binaural self-masking release. It is tempting to rule out this alternative since reverberation-like noise could be handled through the same high level process. However, the data show that the binaural advantage is less for reverberation-like noise. The brain may be able to distinguish between the two types of stimuli and make a decision for higher level processing. It could send reverberation to a high level binaural process and speech with noise to a single channel process. The most likely source for this distinction lies in the relative phase of spectral components within critical bands (Traunmüller, 1987) or across channels. These clues may be sufficient to distinguish reverberation from reverberation-like noise and toggle the neurological process, resulting in a high level advantage for binaural reverberation not seen with reverberation-like noise. The present experiments do not distinguish binaural localization processing from a higher level processing, and the comments in this paragraph are speculative.

V. CONCLUSIONS AND FUTURE WORK

Reverberation-like noise can be created by randomizing the phase of recorded reverberation. Words are 10.7% less intelligible with this noise than with the original reverberation as recorded in a small room. Evidence shows that the direct signal is not critical for word identification. Words with reverberation-like noise are equally intelligible for signal to noise ratios less than or equal to -6 dB, indicating that reverberation-like noise is being used for word identification. Moreover, no intelligibility improvement is observable when the reverberation level is reduced by 2.9 dB while the direct signal is held constant. These results indicate subjects use reverberation to identify words when the signal to reverberation ratio is approximately -12 dB, and possibly higher.

The binaural word intelligibility advantage for reverberation is 6.0% for normal listeners. This is in contrast to the 2.6% advantage for anechoic words in reverberation-like additive noise. This shows that binaural overlap-masking release from noise cannot be completely responsible for the intelligibility advantage seen in reverberation. Echo localization may provide information to reduce the effects of reverberation. This reduction might explain the differences in binaural intelligibility advantages since reverberation-like noise contains no localization information and reverberation does. An alternative hypothesis is that higher level processing is responsible. The test does not distinguish these explanations and new experiments would be necessary to dissociate these alternatives.

In conclusion, binaural processing differs for reverberant words and words with noise. This is based on the conclusion that binaural overlap-masking release is *not* solely responsible for the binaural intelligibility advantage.

In future work, it may be possible to overcome uncertainties associated with the mechanism of binaural processing. Rooms simulated with modified image sources are capable of removing all localization cues without severely affecting the relative phase of spectral components. Alternatively, the phase randomization procedure could be performed in limited frequency bands to alleviate concern that the processing might cause degradation at high frequencies. Applying the reverberation-like noise randomization procedure to regions below 1.5 kHz would isolate the contribution of masking level differences to intelligibility where the effect is believed to occur, and separate processing artifacts of the reverberation-like noise above 1.5 kHz.

Future work could be conducted with several variations to improve and expand the results. Increasing the number of subjects and treatment repetitions for each subject is advised for future work. This may improve the confidence intervals in the analysis. In addition, phoneme scores could be counted to produce confusion matrices. This would better identify the types of errors that occur.

[1]Correlation is used in this paper to mean that signals are similar in spectral content and phase. This is different from coherence, which typically does not include phase. Both correlation and coherence are computed for the 1200 words used in the binaural experiment. The mean correlation coefficient between channels of reverberation is 0.04 without the direct path. The reverberation-like noise has a correlation coefficient of 0.03. The standard error for reverberation is 0.24 and for reverberation-like noise it is 0.09. Perfect correlation is unity and random noise has a correlation of zero. The low correlation explains why averaging the left and right channels reduces the amplitude of these signals by nearly 3 dB.

The coherence is calculated using MATLAB's implementation ''cohere·m.'' This is based on the magnitude of the cross-spectral density,

uses a 4096 point hanning window with 2048 points of overlap, and does not include zero padding. The coherence is weighted and averaged across frequencies. The weighting is determined from the spectral energy of all the words. The coherence between the left and right channels is 0.34 for reverberation and 0.18 for reverberation-like noise with standard errors of 0.05 and 0.04 respectively. Perfect coherence is unity and random noise has a coherence of 0.05. These data may be interpreted to mean that there are differences in the spectral energy between each ear's signal. Furthermore, the slightly lower value for reverberation-like noise implies that temporal smearing occurs as a result of the phase randomization window.

[2]Monaural advantages have been found in approximately 8 out of 30 other listeners in previous tests. These tests are similar in that they use recorded reverberation presented diotically and binaurally without additive noise. In most cases, these monaural advantages are small and analysis of variance is unable to show a significant difference from zero. The tests would require more repetitions per subject in order to be confident in individual advantages. Analysis results will differ if subjects were confidently grouped as those with and without a binaural advantage.

Allen, J. B., and Berkley, D. A. (**1979**). ''Image method for efficiently simulating small-room acoustics,'' J. Acoust. Soc. Am. **65**, 943–950.

Allen, J. B., Berkley, D. A., and Blauert, J. (**1977**). ''Multimicrophone signal-processing technique to remove room reverberation from speech signals,'' J. Acoust. Soc. Am. **62**, 912–915.

ANSI (1989). *S3.2, American National Standard Method for Measuring the Intelligibility of Speech over Communication Systems* (Acoustical Society of America, New York).

Arai, T., Kinoshita, K., Hodoshima, N., Kusumoto, A., and Kitamura, T. (**2002**). ''Effects of suppressing steady-state portions of speech on intelligibility in reverberant environments,'' Acoust. Sci. Technol **23**, 229–232.

Bloom, P. J., and Cain, G. D. (**1982**). ''Evaluation of two-input speech dereverberation techniques,'' IEEE Trans. Acoust., Speech, Signal Process. **7**, 164–167.

Bolt, R. H., and MacDonald, A. D. (**1949**). ''Theory of speech masking by reverberation,'' J. Acoust. Soc. Am. **21**, 577–580.

Bronkhorst, A. W. (**2000**). ''The cocktail party phenomenon: A review of research on speech intelligibility in multiple-talker conditions,'' Acustica **86**, 117–128.

Colburn, H. S. (**1996**). *Auditory Computation* (Springer, New York), Chap 8, pp. 332–400.

Drullman, R., Festen, J. M., and Plomp, R. (**1994**). ''Effect of temporal envelope smearing on speech reception,'' J. Acoust. Soc. Am. **95**, 1053–1064.

Flanagan, J. L., and Lummis, R. C. (**1970**). ''Signal processing to reduce multipath distortion in small rooms,'' J. Acoust. Soc. Am. **47**, 1475–1481.

Gelfand, S. A., and Silman, S. (**1979**). ''Effects of small room reverberation upon the recognition of some consonant features,'' J. Acoust. Soc. Am. **66**, 22–29.

Hodgson, M., and Nosal, E.-M. (**2002**). ''Effect of noise and occupancy on optimal reverberation times for speech intelligibility in classrooms,'' J. Acoust. Soc. Am. **111**, 931–939.

Hodoshima, N., Inoue, T., Arai, T., Kusumotoy, A., and Kinoshitaz, K. (**2004**). ''Suppressing steady-state portions of speech for improving intelligibility in various reverberant environments,'' Acoust. Sci. Technol. **25**, 58–60.

Janssen, J. H. (**1957**). ''A method for the calculation of the speech intelligibility under conditions of reverberation and noise,'' Acustica **7**, 305–310.

Jovicic, S. T. (**1990**). ''Dichotic integration of speech-envelope information,'' Acustica **71**, 140–146.

Kidd, G., Mason, C. R., and Arbogast, T. L. (**2002**). ''Similarity, uncertainty, and masking in the identification of nonspeech auditory patterns,'' J. Acoust. Soc. Am. **111**, 1367–1376.

Koenig, A. H., Allen, J. B., Berkley, D. A., and Curtis, T. H. (**1977**). ''Determination of masking-level differences in a reverberant environment,'' J. Acoust. Soc. Am. **61**, 1374–1376.

Koenig, W. (**1950**). ''Subjective effects in binaural hearing,'' J. Acoust. Soc. Am. **22**, 61–62.

Kruger, K., Gough, K., and Hill, P. (**1991**). ''A comparison of subjective speech intelligibility tests in reverberant environments,'' Can. Acoust. **19**, 23–24.

Kulkarni, A., and Colburn, H. S. (**2000**). ''Variability in the characterization of the headphone transfer-function,'' J. Acoust. Soc. Am. **107**, 1071–1074.

Levitt, H. (**1971**). ''Transformed up-down methods in psychoacoustics,'' J. Acoust. Soc. Am. **49**, 467–477.

Levitt, H., and Rabiner, L. R. (**1967a**). ''Binaural release from masking for speech and gain in intelligibility,'' J. Acoust. Soc. Am. **42**, 601–608.

Levitt, H., and Rabiner, L. R. (**1967b**). ''Use of a sequential strategy in intelligibility testing,'' J. Acoust. Soc. Am. **42**, 609–612.

Licklider, J. C. R. (**1948**). ''The influence of interaural phase relations upon the masking of speech by white noise,'' J. Acoust. Soc. Am. **20**, 150–159.

Lochner, J. P. A., and Burger, J. F. (**1958**). ''The subjective masking of short time delayed echoes by their primary sounds and their contribution to the intelligibility of speech,'' Acustica **8**, 1–10.

Lochner, J. P. A., and Burger, J. F. (**1964**). ''The influence of reflections on auditorium acoustics,'' J. Sound Vib. **1**, 426–454.

Loven, F. C., and Collins, M. J. (**1988**). ''Reverberation, masking, filtering, and level effects on speech recognition performance,'' J. Speech Hear. Res. **31**, 681–695.

Miyata, H., Nomura, H., and Houtgast, T. (**1991**). ''Speech intelligibility and subjective MTF under diotic and dichotic listening conditions in reverberant sound fields,'' Acustica **73**, 200–207.

Moncur, J. P., and Dirks, D. D. (**1967**). ''Binaural and monaural speech intelligibility in reverberation,'' J. Speech Hear. Res. **10**, 186–195.

Moore, B. C. J., and Vickers, D. A. (**1997**). ''The role of spread excitation and suppression in simultaneous masking,'' J. Acoust. Soc. Am. **102**, 2284–2290.

Náběelek, A. K., Letowski, T. R., and Tucker, F. M. (**1989**). ''Reverberant overlap- and self-masking in consonant identification,'' J. Acoust. Soc. Am. **86**, 1259–1265.

Náběelek, A. K., and Mason, D. (**1981**). ''Effect of noise and reverberation on binaural and monaural word identification by subjects with various audiograms,'' J. Speech Hear. Res. **24**, 375–383.

Náběelek, A. K., Ovchinnikov, A., Czyzewski, Z., and Crowley, H. J. (**1996**). ''Cues for perception of synthetic and natural diphthongs in either noise or reverberation,'' J. Acoust. Soc. Am. **99**, 1742–1753.

Náběelek, A. K., and Robinette, L. (**1978**). ''Reverberation as a parameter in clinical testing,'' Audiology **17**, 239–259.

Náběelek, A. K., and Robinson, P. K. (**1982**). ''Monaural and binaural speech perception in reverberation for listeners of various ages,'' J. Acoust. Soc. Am. **71**, 1242–1248.

Peutz, V. M. A. (**1971**). ''Articulation loss of consonants as a criterion for speech transmission in a room,'' J. Audio Eng. Soc. **19**, 915–919.

Pierce, A. D. (**1991**). *Acoustics, and Introduction to Its Physical Principles and Applications* (Acoustical Society of America, Woodbury, NY), Chap. 6, pp. 250–312.

Russotti, J. S., Santoro, T. P., and Haskell, G. B. (**1988**). ''Proposed technique for earphone calibration,'' J. Audio Eng. Soc. **36**, 643–650.

Soulodre, G. A., Popplewell, N., and Bradley, J. S. (**1989**). ''Combined effects of early reflections and background noise on speech intelligibility,'' J. Sound Vib. **135**, 123–133.

Steinberg, J. C. (**1929**). ''Effects of distortion upon the recognition of speech sounds,'' J. Acoust. Soc. Am. **1**, 121–137.

Takata, Y., and Náběelek, A. K. (**1990**). ''English consonant recognition in noise and in reverberation by Japanese and American listeners,'' J. Acoust. Soc. Am. **88**, 663–666.

Traunmüller, H. (**1987**). *The Psychophysics of Speech Perception* (Martinus Nijhoff, Hingham, MA), pp. 377–384.

Wallach, H., Newman, E. B., and Rosenzweig, M. R. (**1949**). ''The precedence effect in sound localization,'' Am. J. Psychol. **62**, 315–336.

Watkins, A. J., and Holt, N. J. (**2000**). ''Effects of a complex reflection on vowel indentification,'' Acustica **86**, 532–542.

Wittkop, T., Albani, S., Hohmann, V., Peissig, J., Woods, W. S., and Kollmeier, B. (**1997**). ''Speech processing for hearing aids: Noise reduction motivated by models of binaural interaction,'' Acustica **83**, 684–699.

Zwicker, E., and Fastl, H. (**1999**). *Psychoacoustics, Facts and Models* (Springer, Berlin), Chap. 4, pp. 61–110.

Hearing-aid automatic gain control adapting to two sound sources in the environment, using three time constants

Peter Nordqvist[a] and Arne Leijon
Sound and Image Processing laboratory, KTH Signals, Sensors, and Systems, Osquldas v. 10, Royal Institute of Technology, 100 44 Stockholm, Sweden

(Received August 15 2003; accepted for publication 7 July 2004)

A hearing aid AGC algorithm is presented that uses a richer representation of the sound environment than previous algorithms. The proposed algorithm is designed to (1) adapt slowly (in approximately 10 s) between different listening environments, e.g., when the user leaves a single talker lecture for a multi-babble coffee-break; (2) switch rapidly (about 100 ms) between different dominant sound sources within one listening situation, such as the change from the user's own voice to a distant speaker's voice in a quiet conference room; (3) instantly reduce gain for strong transient sounds and then quickly return to the previous gain setting; and (4) not change the gain in silent pauses but instead keep the gain setting of the previous sound source. An acoustic evaluation showed that the algorithm worked as intended. The algorithm was evaluated together with a reference algorithm in a pilot field test. When evaluated by nine users in a set of speech recognition tests, the algorithm showed similar results to the reference algorithm. © *2004 Acoustical Society of America.*
[DOI: 10.1121/1.1793207]

PACS numbers: 43.71.Ky, 43.66.Ts [DOS] Pages: 3152–3155

I. INTRODUCTION

A few different approaches on how to design a compression system with as few disadvantages as possible have been presented in previous work. One attempt is to use a short attack time in combination with an adaptive release time. The analog K-Amp circuit is an example using this technique (Killion, 1993). Another way to implement adaptive release time is to use multiple level detectors, as in the dual front-end compressor (Stone *et al.*, 1999). The release time is short for intense sounds with short duration. For intense sounds with longer duration the release time is longer. Such a hearing aid can rapidly decrease the gain for short intense sounds and then quickly increase the gain after the transient. For a longer period of intense sounds, e.g., a conversation, the release time increases which reduces pumping effects during pauses in the conversation. The dual front-end compressor is used as a reference algorithm in this work.

The significant advantage of the approach presented here is that the algorithm eliminates more compression system disadvantages than previous algorithms have done. The system presented here is essentially a slow automatic volume control (AVC) system, but it stores knowledge about the environment in several internal state variables that are nonlinearly updated using three different time constants. Compared to the dual-front end system, the system presented here has one extra feature allowing the processor to switch focus, between two dominant sound sources at different levels within a listening environment, e.g., a conversation between the hearing aid user and another person. While switching focus to the second source, the system still remembers the characteristics for the previous source. The proposed system reduces pumping effects, because it does not increase its gain during pauses in the conversation.

The new proposed hearing aid is designed to (1) adapt slowly (in approximately 10 s) between different listening environments, e.g., when the user leaves a single talker lecture for a multi-babble coffee-break; (2) switch rapidly (about 100 ms) between different dominant sound sources within one listening situation, such as the change from the user's own voice to a distant speaker's voice in a quiet conference room; (3) instantly reduce gain for strong transient sounds and then quickly return to the previous gain setting; and (4) not change the gain in silent pauses but instead keep the gain setting of the previous sound source.

II. METHODS

The test platform was an experimental hearing aid system (Audallion) supplied by the hearing aid company GN ReSound. The system consists of a wearable digital hearing aid and an interface program to communicate with the hearing aid. The sampling frequency of the wearable digital hearing aid is 15 625 Hz and the analog front end has a compression limiter with a threshold at 80 dB SPL to avoid overload in the analog to digital conversion. The DUAL-HI version of the dual front-end AGC system (Stone *et al.*, 1999) was implemented as a reference system for a pilot field test. The KTH algorithm has a similar purpose to the reference AGC algorithm. Common to both is the slow acting compressor system with transient reduction for sudden intensive sounds. The difference is that the KTH AGC algorithm can handle two dominant sources within a listening environment, e.g., two people speaking at different levels, and then switch between the two target gain-curves relatively quickly without introducing pumping effects. The two algorithms were implemented in the same wearable digital hearing aid and evaluated in a pilot field test and in a set of laboratory speech

[a]Electronic mail: nordq@s3.kth.se

recognition tests. The KTH AGC algorithm was also implemented off-line in order to evaluate the algorithm behavior in more detail for well-specified sound environments. Unfortunately it was not possible to do similar detailed measurements with the reference algorithm.

A. KTH AGC algorithm

All compressor systems can be described using a set of basis functions or components, defining the possible variations of the gain-frequency response (Bustamante and Braida, 1987; White, 1986). First a target gain vector, $\mathbf{T}_r$, for the current time frame r, is calculated as a function of the spectrum of the 4 ms blocked input signal samples in this frame. The details of this calculation depend on the chosen fitting rule and are not relevant for this presentation. The elements of $\mathbf{T}_r$ represent gain values (in dB) at a sequence of frequencies equidistantly sampled along an auditory frequency scale. The target gain vector is then approximated by a sum of a fixed gain response $\mathbf{T}_0$ and a linear combination of a set of predefined gain-shape functions (Bustamante and Braida, 1987)

$$\mathbf{T}_r \approx \hat{\mathbf{T}}_r = \mathbf{T}_0 + a_r(0)\mathbf{b}_0 + \cdots + a_r(K-1)\mathbf{b}_{K-1}. \tag{1}$$

The fixed gain curve $\mathbf{T}_0$ represents the on-average most common gain frequency response, and the linear combination of the set of predetermined gain shape basis vectors $\mathbf{b}_k$ represents the response deviations. This implementation used $K=4$ nearly orthogonal basis vectors, representing the overall gain level, the slope of the gain-frequency response, etc. All target gain deviations from $\mathbf{T}_0$ are then defined by the shape vector $\mathbf{a}_r = [a_r(0) \cdots a_r(K-1)]^T$. The shape vector $\mathbf{a}_r$ is calculated with the minimum square method,

$$\mathbf{a}_r = (\mathbf{B}^T\mathbf{B})^{-1}\mathbf{B}^T(\mathbf{T}_r - \mathbf{T}_0), \tag{2}$$

where $\mathbf{B} = [\mathbf{b}_0 \cdots \mathbf{b}_{K-1}]$. The matrix $(\mathbf{B}^T\mathbf{B})^{-1}\mathbf{B}^T$ is computed once and then stored. The shape vector $\mathbf{a}_r$ can vary rapidly with r, indicating a new target gain vector for each new input data frame r.

The algorithm stores its knowledge about the environment in three state vectors $\overline{\mathbf{a}}_r$, $\hat{\mathbf{a}}_r$, $\check{\mathbf{a}}_r$, and a so-called focus variable d_r as illustrated in Fig. 1. The average state $\overline{\mathbf{a}}_r$ represents the long-term characteristics of the current listening environment. This state vector is used to prevent the algorithm from adapting to silent pauses in the speech or to low-level background noises. The high-gain state $\hat{\mathbf{a}}_r$ indicates the gain response needed for the stronger segments of a relatively weak sound source in this environment. The low-gain state $\check{\mathbf{a}}_r$ represents the gain needed for the stronger segments of a relatively strong sound source. The focus variable d_r is used to switch the AGC focus rapidly and smoothly between $\hat{\mathbf{a}}_r$ and $\check{\mathbf{a}}_r$. Normally, when no strong transient sounds are encountered, the actually used gain parametrization $\mathbf{c}_r$ is interpolated between $\hat{\mathbf{a}}_r$ and $\check{\mathbf{a}}_r$ as

$$\mathbf{c}_r = d_r\hat{\mathbf{a}}_r + (1-d_r)\check{\mathbf{a}}_r, \tag{3}$$

Thus, when $d_r=1$, the output gain shape is defined by the high-gain state as $\mathbf{c}_r = \hat{\mathbf{a}}_r$, and when $d_r=0$, the low-gain state is used. The average state $\overline{\mathbf{a}}_r$ is updated for every frame according to

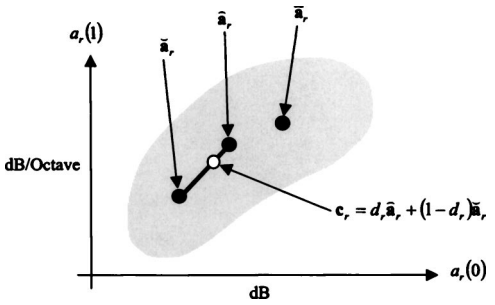

FIG. 1. State vectors of the KTH AGC algorithm illustrated in the plane defined by the first two elements of the state vector. The shaded area represents the variability of the stream of unfiltered gain-shape vectors calculated from the input signal. The average state $\overline{\mathbf{a}}_r$ represents the long-term characteristics of the current sound environment. The high-gain state $\hat{\mathbf{a}}_r$ defines the gain response needed for the stronger segments of relatively weak sound sources. The low-gain state $\check{\mathbf{a}}_r$ represents the gain needed for the stronger segments of relatively strong sound sources. The focus variable d_r is used to switch the gain setting rapidly and smoothly between $\hat{\mathbf{a}}_r$ and $\check{\mathbf{a}}_r$.

$$\overline{\mathbf{a}}_r = \alpha\overline{\mathbf{a}}_{r-1} + (1-\alpha)\mathbf{a}_r, \tag{4}$$

where α is chosen for a time constant of about 10 s. The other state variables $\hat{\mathbf{a}}_r$ and $\check{\mathbf{a}}_r$ are updated together with the focus variable d_r as

$$\begin{aligned}
&\text{if } a_r(0) < (\hat{a}_{r-1}(0) + \check{a}_{r-1}(0))/2 \text{ then}\\
&\check{\mathbf{a}}_r = \beta\check{\mathbf{a}}_{r-1} + (1-\beta)\mathbf{a}_{r-1}, \quad d_r = \max(0, d_{r-1} - \delta)\\
&\text{else if } (a_r(0) < \overline{a}_{r-1}(0)) \text{ then}\\
&\hat{\mathbf{a}}_r = \beta\hat{\mathbf{a}}_{r-1} + (1-\beta)\mathbf{a}_{r-1}, \quad d_r = \min(1, d_{r-1} + \delta)
\end{aligned} \tag{5}$$

Here, β is chosen for a time constant of about 10 s. The step size δ is chosen so that a complete shift in the focus variable takes about 100 ms. In this implementation the update equations are controlled only by the overall gain needed for the current frame defined by the first element $a_r(0)$ in the shape vector $\mathbf{a}_r$. If the sound pressure level in the current frame is low, the overall gain parameter $a_r(0)$ is greater than $\overline{a}_r(0)$ and no update is done. If the power in the current frame generates an overall gain $a_r(0)$ lower than the average of the high-gain state $\hat{\mathbf{a}}_r$ and the low-gain state $\check{\mathbf{a}}_r$, the low gain state is updated and the focus variable is decreased one step size. If the power in the current frame generates an overall gain $a_r(0)$ higher than the same average, the high gain state is updated and the focus variable is increased one step size. Finally, the actual AGC gain parameter vector $\mathbf{c}_r$ is updated to include transient reduction as

$$\begin{aligned}
&\text{if } a_r(0) < (\check{a}_r(0) - L) \text{ then } \mathbf{c}_r = \mathbf{a}_r \text{ else}\\
&\mathbf{c}_r = d_r\hat{\mathbf{a}}_r + (1-d_r)\check{\mathbf{a}}_r,
\end{aligned} \tag{6}$$

The threshold L for transient reduction is adjusted during the fitting so that strong input sound, e.g., porcelain clatter, is reduced by the transient reduction system.

Finally, the desired filter gain function $\mathbf{G}_r$ for frame r is obtained as

$$\mathbf{G}_r = \mathbf{T}_0 + c_r(0)\mathbf{b}_0 + \cdots + c_r(K-1)\mathbf{b}_{K-1}, \tag{7}$$

where the sequence of AGC parameter vectors $\mathbf{c}_r = [c_r(0) \cdots c_r(K-1)]^T$ is the filtered version of the se-

quence of shape vectors $\mathbf{a}_r$. The actual filtering is implemented by a FIR filter redesigned for each time frame.

B. Evaluation

Three different simulated sound environments were used in the off-line evaluation. The first listening situation consisted of conversation in quiet between two people standing relatively close to each other, one speaking at 75 dB SPL RMS and the other speaking at 69 dB SPL RMS, as measured at the hearing aid microphone input. The other listening situation was a conversation in quiet between two people standing far away from each other, one speaking at 75 dB SPL RMS and the other speaking at 57 dB SPL RMS. In the two listening situations, each alternation between the talkers is separated by 2 s of silence. The purpose of these two tests was to investigate if the algorithm can adapt separately to the two dominating sources both when they are close to each other and when they are far away from each other. Sections of silence should not cause the algorithm to increase the gain. Instead, the aid should keep the settings for the previous sound source and wait for higher input levels. The algorithm was fitted to a hypothetical user with mild to moderate hearing loss. To evaluate the transient reduction, the sound from a porcelain coffee cup was recorded and mixed with continuous speech at 60 dB SPL RMS. The peak level of the transient was 110 dB SPL at the microphone.

The algorithm was also evaluated in a pilot field test including subjects with a symmetric mild to moderate sensorineural hearing loss who were experienced hearing aid users. Nine candidates were chosen from one of the main hearing clinics in Stockholm. The reference algorithm was fitted for each individual as recommended by Stone *et al.* (1999), and the KTH AGC algorithm was fitted to achieve approximately normal loudness density, i.e., normal loudness contributions calculated for primary excitation in frequency bands with normal auditory equivalent rectangular bandwidths (ERBs) (Moore and Glasberg, 1997).

III. RESULTS AND DISCUSSION

The behavior of the algorithm is illustrated in Figs. 2 and 3. Subplot (a) in the two figures shows that the low-gain state and the high-gain state are well separated by 3 and 5 dB for the two test recordings. The behavior of the focus variable is illustrated in subplot (b) in the two pictures. The variation in the focus variable is well synchronized with the switching in sound pressure level when the talkers are alternating in the conversation. During silent sections in the material, the focus variable remains nearly constant as desired. The resulting average insertion gain frequency responses, for the high-gain state and the low-gain state, are illustrated in subplot (c). Since the prescription method was designed to restore normal loudness density, the insertion gain was relatively high at high frequencies.

Because the time constant of the focus variable was chosen as short as 100 ms, the algorithm gives a slight degree of syllabic compression, as the focus variable varies slightly between speech sounds within segments of running speech from each speaker.

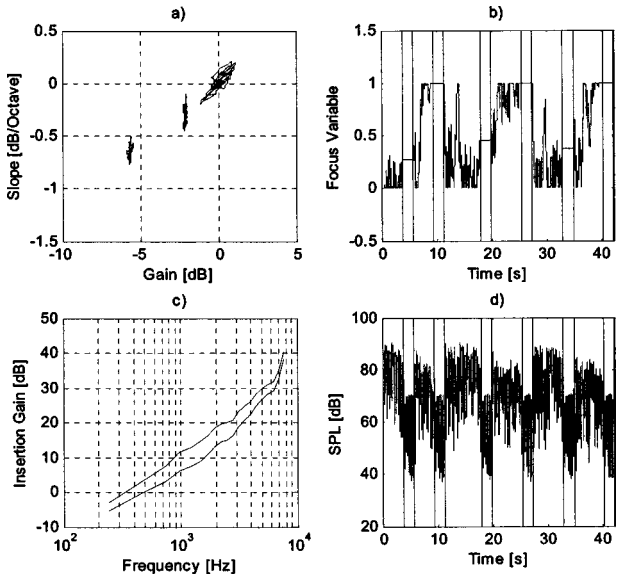

FIG. 2. Behavior of the KTH AGC algorithm in a conversation in quiet between two people standing close to each other, one at 75 dB SPL rms and the other person at 69 dB SPL RMS, with 2s pauses between each utterance. (a) Scatter plot of the first two elements of the state variables, $\check{\mathbf{a}}_r$, $\hat{\mathbf{a}}_r$, and $\bar{\mathbf{a}}_r$, from left to right. (b) The focus variable d_r. (c) The average insertion gain for the high gain state $\hat{\mathbf{a}}_r$ and the low gain state $\check{\mathbf{a}}_r$. (d) Sound input level at the microphone. The time instances when there was a true shift between speakers and silence are marked with vertical lines.

Figure 4 illustrates the transient suppression behavior of the KTH AGC algorithm. Subplot (a) shows the insertion gain at 2.5 kHz as a function of time and subplot (b) shows the sound input level at the microphone, as measured in the input signal. The AGC gain parameters react instantly by reducing the gain when the transient is present and then rapidly return after the transient, to the same gain as before the transient sound. The transient sound includes modulation and this causes some fast modulation in the transient response. The compression ratio in the current system can be estimated

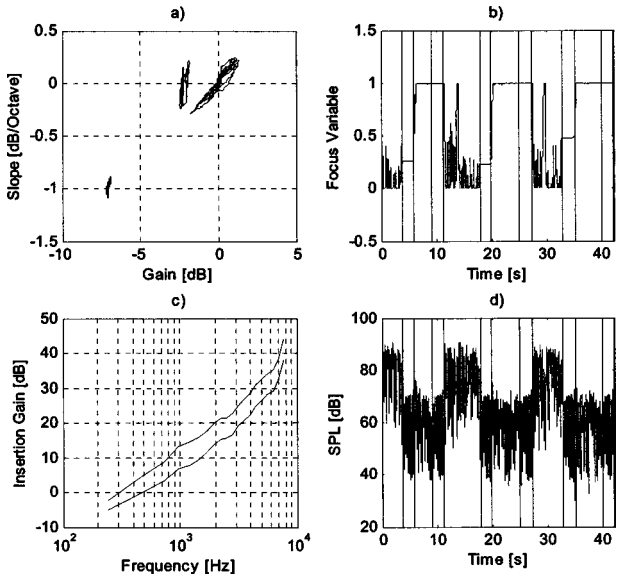

FIG. 3. Behavior of the KTH AGC algorithm, illustrated in the same way as in Fig. 2, for a conversation in quiet between two people standing far away from each other, one at 75 dB SPL RMS and the other person at 57 dB SPL RMS, with 2-s pauses between each utterance.

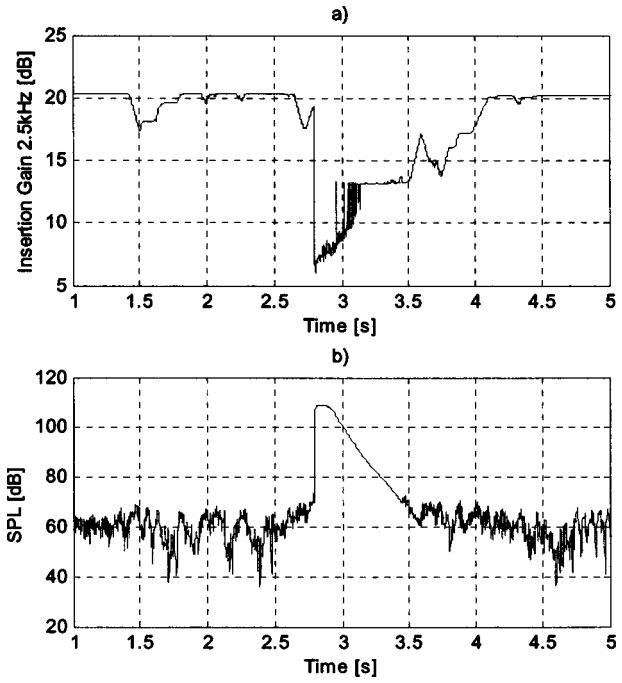

FIG. 4. Transient suppression behavior of the KTH AGC algorithm. A transient sound obtained by striking a coffee cup with a spoon is mixed with continuous speech. Subplot (a) shows the insertion gain at 2.5 kHz as a function of time and subplot (b) shows the sound input level at the microphone, as measured in the blocked input signal.

from Fig. 4. The compression ratio is approximately 1.3 in this implementation.

A wide range of speech presentation levels is necessary in order to test compression algorithms (Moore *et al.*, 1992). Among the field test participants, the average monosyllabic word recognition score in quiet with the KTH AGC algorithm was 68% for speech at 50 dB SPL RMS and 94% for speech at 80 dB SPL RMS, respectively. The corresponding scores for the reference algorithm were 60% and 82%. The average signal to noise threshold (for 40% recognition), with Hagerman's sentences (Hagerman, 1982) at 70 dB SPL RMS in steady noise, was −4.6 dB for the KTH algorithm and −3.8 dB for the reference algorithm, respectively. The signal-to-noise threshold with the modulated noise version of Hagerman's sentences at 60 dB SPL RMS was −14.6 dB for the KTH algorithm and −15.0 dB for the reference algorithm. Thus, in this test the reference system performed slightly better compared to the KTH algorithm. Otherwise there was a tendency towards slightly better results with the KTH algorithm for the other three tests. However, this tendency was statistically significant (Wilcoxon paired-difference rank test 0.05) only for the monosyllabic words in quiet, at 80 dB SPL RMS presentation level. Among the nine persons who completed the field test, five preferred the KTH algorithm, three preferred the reference algorithm, and one could not state a clear preference.

In addition to the reference system, the KTH AGC algorithm includes slow adaptation of two target-gain settings for two different dominant sound sources in a listening environment, allowing rapid switching between them when needed.

IV. CONCLUSION

A hearing aid algorithm is presented that (1) can adapt the hearing aid frequency response slowly, to varying sound environments; (2) can adapt the hearing aid frequency response rapidly, to switch between two different dominant sound sources in a given sound environment; (3) can adapt the hearing aid frequency response instantly, to strong transient sounds; and (4) does not increase the gain in periods of silence but instead keeps the gain setting of the previous sound source in the listening situation. The acoustic evaluation showed that the algorithm worked as intended. When evaluated by nine users in a set of speech recognition tests, the KTH AGC algorithm showed similar results as the dual-front end reference algorithm (Stone *et al.*, 1999). There was no clear overall preference for either algorithm.

ACKNOWLEDGMENT

This work was sponsored by GN ReSound.

Bustamante, D. K., and Braida, L. D. (**1987**). "Principal-component amplitude compression for the hearing impaired," J. Acoust. Soc. Am. **82**, 1227–1242.

Hagerman, B. (**1982**). "Sentences for testing speech intelligibility in noise," Scand. Audiol. **11**, 79–87.

Killion, M. C. (**1993**). "The K-Amp hearing aid: An attempt to present high fidelity for the hearing impaired," Am. J. Audiol. **2(2)**, 52–74.

Moore, B. C., Johnson, J. S., Clark, T. M., and Pluvinage, V. (**1992**). "Evaluation of a dual-channel full dynamic range compression system for people with sensorineural hearing loss," Ear Hear. **13**, 349–370.

Moore, B. C. J., and Glasberg, B. R. (**1997**). "A model of loudness perception applied to cochlear hearing loss," Aud. Neurosci. **3**, 289–311.

Stone, M. A., Moore, B. C. J., Alcantara, J. I., and Glasberg, B. R. (**1999**). "Comparison of different forms of compression using wearable digital hearing aids," J. Acoust. Soc. Am. **106**, 3603–3619.

White, M. W. (**1986**). "Compression Systems for Hearing Aids and Cochlear Prostheses," J. Rehabil. Res. Dev. **23**, 25–39.

Envelope-onset asynchrony as a cue to voicing in initial English consonants[a)]

Hanfeng Yuan,[b)] Charlotte M. Reed, and Nathaniel I. Durlach
Research Laboratory of Electronics, Massachusetts Institute of Technology, Cambridge, Massachusetts 02139

(Received 8 January 2004; revised 16 August 2004; accepted 17 August 2004)

An acoustic cue for voicing is proposed based on the underlying processes associated with the production of the voicing contrast. This cue is based on the time asynchrony between the onsets of two amplitude-envelope signals derived from different bands of speech (i.e., envelopes derived from a lowpass-filtered band at 350 Hz and from a highpass-filtered band at 3000 Hz). Acoustic measurements made on the envelope signals of a set of 16 initial consonants represented through multiple tokens of C_1VC_2 syllables indicate that the onset-timing difference between the low- and high-frequency envelopes (Envelope-Onset Asynchrony or EOA) provides a reliable and robust cue for distinguishing voiced from voiceless consonants. This cue, which is simply derived in real-time, has applications to the design of sensory aids for persons with profound hearing impairments (e.g., as a supplement to lipreading), as well as to automatic speech recognition. © *2004 Acoustical Society of America.* [DOI: 10.1121/1.1804626]

PACS numbers: 43.71.Ky, 43.71.Ma, 43.72.Ar [KWG] Pages: 3156–3167

I. INTRODUCTION

For many persons with hearing impairments, lipreading is an important means of obtaining information about speech, either through lipreading alone or in conjunction with a sensory aid (e.g., a hearing aid, tactual aid, or cochlear implant). Lipreading is based largely on the visibility of various lip features that arise during articulation of speech. Information from lipreading can divide the phonemes into several groups with identical or highly similar visible articulation movements (visemes), but is insufficient for complete speech perception for most lipreaders. Among the various important features of speech, voicing is poorly perceived through lipreading alone (Heider and Heider, 1940; Erber, 1974; Walden *et al.*, 1977; Bratakos *et al.*, 2001). By providing information on voicing as a supplement to lipreading, the viseme groups can be reduced to smaller groups, thereby leading to improved speech reception.

Grant *et al.* (1998) used Braida's (1991) Pre-Labelling model of integration to predict the performance of a hypothetical hearing-impaired observer on a consonant-recognition task for various auditory–visual (A–V) conditions. One such A–V case assumed (1) an auditory condition where only voicing information is available to the subject and is perfectly received (i.e., no confusions are made between voiced and voiceless sounds), and (2) a visual condition consisting of the signal available through lipreading alone where the rate of accuracy and patterns of confusion correspond to those of an average lipreader. Under these assumptions, the model predicts a substantial improvement in the performance of the hypothetical observer under the combined A–V condition compared to either modality alone. Performance was estimated to be roughly 12%-correct under the auditory condition alone, 38%-correct for lipreading alone, and 71%-correct for the combined A–V condition, thus effectively demonstrating the power of voicing information as a supplement to lipreading. Auer and Bernstein (1996) also provide a demonstration of the utility of voicing information in conjunction with lipreading. They estimated the effects of the addition of consonantal voicing information on word recognition and found that consonantal voicing leads to fewer word confusions and to a greater percentage of uniquely identified words.

Voicing is a distinctive feature in the production of English obstruent consonants (i.e., stops, fricatives, and affricatives) and is related to the presence (voiced) or absence (voiceless) of vocal-fold vibration. Three conditions are required for vocal-fold vibration (Stevens, 1998): the first is that there is sufficient transglottal pressure, the second is that the vocal folds are placed together, and the third is that the vocal folds are slack. Production of the voicing contrast consists of a sequence of articulatory and aerodynamic events, each of which has multiple acoustic manifestations. Acoustic cues associated with voicing in English obstruent consonants have been examined, both through measurements of naturally spoken utterances and through the study of edited natural speech or synthetic stimuli in which different acoustic parameters are manipulated. A variety of acoustic cues have been found to provide information for the distinction of voicing between pairs of obstruent consonants produced at the same place in the vocal tract in various contexts.

One of the most highly studied of these cues is voice onset time—VOT (Lisker and Abramson, 1964; Zue, 1976), which applies to initial stop consonants. VOT is the duration of time between the release of a stop closure and the beginning of vocal-fold vibration. In English, VOTs for the voiced stops are in general less than 20 ms or even negative, and greater than this value for voiceless stops (Zue, 1976; Kiefte, 2003). This acoustic property of VOT is regarded as a pho-

[a)]A portion of this work was presented at the 145th meeting of the Acoustical Society of America, 2003, Nashville, Tennessee.
[b)]Electronic mail: hfyuan@mit.edu

netic anchor associated with the feature voicing. It serves as a measure to categorize voicing in stop consonants: stops with long VOT are classified as voiceless, while those with short VOT as voiced.

Cues related to the voicing of fricative consonants include the presence of vocal-fold activity during the fricative noise interval (Stevens *et al.*, 1992), frication duration (Baum and Blumstein, 1987; Behrens and Blumstein, 1988; Crystal and House, 1988; Stevens *et al.*, 1992; Jongman *et al.*, 2000); formant transitions (Liberman *et al.*, 1958; Stevens and Klatt, 1974; Hillenbrand *et al.*, 1984); F0 perturbations (House and Fairbanks, 1953; Ohde, 1984; Whalen *et al.*, 1993); vowel duration (Denes, 1955; House, 1961; Raphael, 1972); amplitude of the first harmonic (Stevens *et al.*, 1992; Pirello *et al.*, 1997); and harmonic structure (Choi, 1999). Each cue can be explained reasonably well by the underlying articulatory, aerodynamic, or linguistic conditions that form the basis for the production of the voicing contrast. Each cue, however, has limitations either in its range of applicability (e.g., VOT is applicable only to stop consonants, frication duration is applicable only to fricatives, and vowel duration is applicable only to consonants in final position) or in the complexity of its derivation (e.g., formant transitions and F0 perturbations are relatively difficult to derive from the speech signal).

Signal-processing algorithms for the automatic detection of voicing have been developed using various acoustic measurements and their statistical properties including F0, F1, harmonic-amplitude differences, and durational properties (e.g., see Choi, 1999; Ali *et al.*, 2001a, 2001b). Although these algorithms have demonstrated good performance in the detection of voicing (e.g., the algorithm of Ali *et al.*, 2001a led to performance of 93%-correct in prevocalic fricatives extracted from the TIMIT database), their success is dependent on prior knowledge of the manner of production. In the current class of mainstream automatic speech-recognition (ASR) systems, relatively high rates of confusion are observed along the voicing dimension (Ramesh and Wilpon, 1992; Lee *et al.*, 1996; Niyogi and Ramesh, 2003). The Hidden Markov Model (HMM) framework (Rabiner and Juang, 1993) of these systems, which is based on a representation of the speech waveform through spectral properties and statistical relations, has inherent difficulties in capturing temporal properties of speech such as VOT. Recently, improvements to performance of HMM-based schemes have been made through the addition of specific voicing-detection algorithms (Niyogi and Ramesh, 2003; Thomson and Chengalvarayan, 2002).

The current research investigated a simply-derived real-time acoustic cue to voicing in the initial consonant of C_1VC_2 syllables. This cue (Envelope-Onset Asynchrony, or EOA) is defined as the time asynchrony between the onsets of two amplitude-envelope signals derived from two different bands of speech (i.e., the onset time of an envelope derived from a lowpass-filtered band at 350 Hz minus the onset time of an envelope derived from a highpass-filtered band at 3000 Hz). It is a relative measurement of the difference between the onset time of two separate bands: thus, it is independent of any overall delays in the system. The real-time measurement of this cue is quite straightforward and more easily derived than measurements of VOT.

Previous studies (e.g., Breeuwer and Plomp, 1984; Grant *et al.*, 1994) have demonstrated substantial benefits to lipreading for the auditory presentation of a similar type of two-band amplitude-envelope cue in normal-hearing listeners. Breeuwer and Plomp (1984) created envelope cues that were derived from bands of speech with center frequencies of 500, 1600, and 3160 Hz (with 1- or 1/3-oct bandwidth), and with a 20-Hz smoothing filter. The envelopes then modulated a tone at the center frequency of the prefilter. The maximal benefit for a two-band envelope signal was achieved with two 1-oct bands at 500 and 3160 Hz, where the mean number of correctly perceived syllables in conversational sentences was 86.7% compared to 22.8% for lipreading alone. Grant *et al.* (1994) investigated the benefits to lipreading provided by simultaneous auditory presentation of amplitude-envelope cues across two different frequency regions (using octave bands of speech centered around 500 and 3150 Hz, a 50-Hz smoothing filter, and carrier signals at or below the center frequency of the prefilter). Aided lipreading scores for sentences with two-band envelopes were superior to single-band performance only when the carrier frequencies of the two-band cues were close to the center frequencies from which the envelopes were derived. Optimal performance was achieved with the two-channel envelope condition when the center frequencies were equal to the center frequencies of each of the two octave bands of speech (500 and 3150 Hz, respectively). For the reception of words in conversational sentences, this condition resulted in an aided lipreading score of 90%-correct compared to 40% for lipreading alone.

Although these previous studies have demonstrated substantial benefits for auditory presentation of envelope-based supplements to lipreading, the nature of the acoustic cues responsible for these benefits has never been adequately determined. These studies were mainly concerned with the selection of frequency regions to derive the envelopes and with the presentation of such envelope cues to maximize speech perception for aided lipreading. The current research is concerned with examining a potential cue to voicing derived from such a two-band amplitude-envelope cue. Different patterns of spectral energy are observed for voiced versus voiceless consonants (independent of their place or manner of production). The voiceless consonants tend to have significant energy above 3000 Hz, and less energy below 350 Hz. The voiced consonants, on the other hand, tend to exhibit significant energy below 350 Hz (at least during part of their production). The low-frequency energy is associated with the presence of vocal-fold vibration, while the high-frequency energy is associated with aspiration or frication. The timing of the onset of high-frequency energy relative to low-frequency energy tends to differ for voiced versus voiceless consonants. Typically, for initial voiceless consonants, the onset of the high-frequency energy occurs before the onset of the low-frequency energy. For initial voiced consonants, on the other hand, the onset of the high-frequency energy either follows or occurs almost simultaneously with the low-frequency energy. Therefore, the onset asynchrony of the two

envelopes is expected to be a good indicator of the voicing distinction.

II. METHODS

A. Stimuli

The materials used in the current study were audiovisual recordings of C_1VC_2 nonsense syllables that were balanced for C_1. The current study examined syllables with 16 values of C_1=/p t k b d g f θ s ʃ v ð z ʒ tʃ dʒ/ and 16 values of V =/i ɪ ɛ æ ʌ ɑ ɔ ɚ ʊ u eɪ aɪ aʊ oʊ ɔɪ ar/. The final consonant C_2 was selected randomly for each syllable from a set of 21 consonants: /p t k b d g f θ s ʃ v ð z ʒ tʃ dʒ m n ŋ r l/.

The speakers for these recordings were two females, SR and RK, both of whom were teachers of the deaf and approximately 30 years of age at the time of the recordings. Each talker recorded two lists of syllables containing one representation of each C_1V combination. The total corpus consists of 1024 C_1VC_2 syllables representing 64 tokens of each of the 16 values of C_1.

The materials were originally recorded on 1-in. U-matic videotapes. Two audio channels were recorded on the tapes: (1) the acoustic speech signal through a Lavalier microphone and (2) a laryngograph signal. The current study is concerned only with measurements of the acoustic speech signal.

B. Procedures for digitizing speech materials

The recorded C_1VC_2 nonsense syllables were digitized for real-time signal processing. The audio-visual stimuli, originally recorded on videotape, were digitized using the Pinnacle DV500 Plus system and then stored in individual files on a host computer. The audio signal was initially sampled at a rate of 48 000 Hz with 16-bit resolution.

The resulting digitized files were then edited by the Adobe Premiere 6.0, a professional digital video-editing software package. The files were decomposed into a video track and an audio track and the two tracks were saved into separate files in the Timeline window of Adobe Premiere for separate processing. The audio signal was filtered at 11 kHz by an antialiasing FIR filter to eliminate a 16-kHz noise (presumably an artifact of the recording process) and downsampled at 22 kHz. The sound level of each file was normalized to remove overall level differences between the two speakers as well as within the same speaker across different recording sessions. In the normalization, the sound level of each file was adjusted proportionally to maintain the same maximum sound level across files (i.e., the maximum sample value of each file was set to 0.95, and all other sample values were adjusted by the ratio 0.95/maximum sample value of the given file). The filtering, sampling-rate conversion, and sound-level normalization of the digitized audio signals were carried out using MATLAB software. The video track and the processed audio track were combined into one file using the Timeline window of Adobe Premiere.

These processed files were then segmented into individual files each of which contained one token of all the C_1VC_2 syllables. Segmentation was carried out using the video track and was based on lip opening and lip closure: the lips always move from a closed to an open state at the initiation of an utterance and from an open to a closed state at the end of an utterance. The following criteria were used to segment the utterances. The starting point of the file was specified at a location roughly two to four frames prior to the initiation of lip opening. The end point of the file was specified as roughly two to four frames following complete lip closure. The number of frames for each segment of the C_1VC_2 syllables averaged approximately 50 corresponding to a duration of roughly 1.67 s, and the average file size was approximately 6 Mbytes.

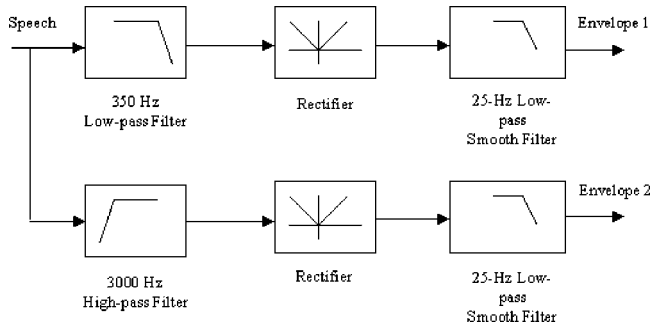

FIG. 1. Block diagram of the envelope-extraction system.

To reduce their size, the segmented files were compressed using the Sorenson Video compressor and converted to QuickTime format. The video was cut to 440×480 from the original 720×480, the audio was set to 22 050 samples/s (16-bit per sample), and the key frame was set to every 60 frames.

C. Acoustic measurements

1. Envelope extraction

Two envelopes (a low-frequency energy envelope and a high-frequency energy envelope) that are believed to carry voicing information were extracted from the acoustic speech signals, as shown in the block diagram of Fig. 1. This envelope extraction procedure uses the basic algorithm described by Horii *et al.* (1971).

The function of the 350-Hz low-pass filter and 3-kHz high-pass filter in Fig. 1 is to extract the speech signal in the frequency bands of interest. A second-order low-pass Butterworth filter with cutoff frequency 350 Hz was used for the low-frequency energy envelope, and a second-order high-pass Butterworth filter with cutoff frequency 3000 Hz was used for the high-energy envelope. Each filter is followed by rectification to invert the negative input to positive output in order to retain only the level information of the selected speech spectrum. The rectified signals are then passed through a smoothing filter to reduce the fluctuations in the envelope. The smoothing filter in each channel is a second-order low-pass Butterworth filter with a cutoff frequency of 25 Hz. This value was selected to preserve only the slow fluctuations within a particular frequency region of speech (see Van Tasell *et al.*, 1987 and Grant *et al.*, 1991 for further discussion of the effects of the smoothing filter).

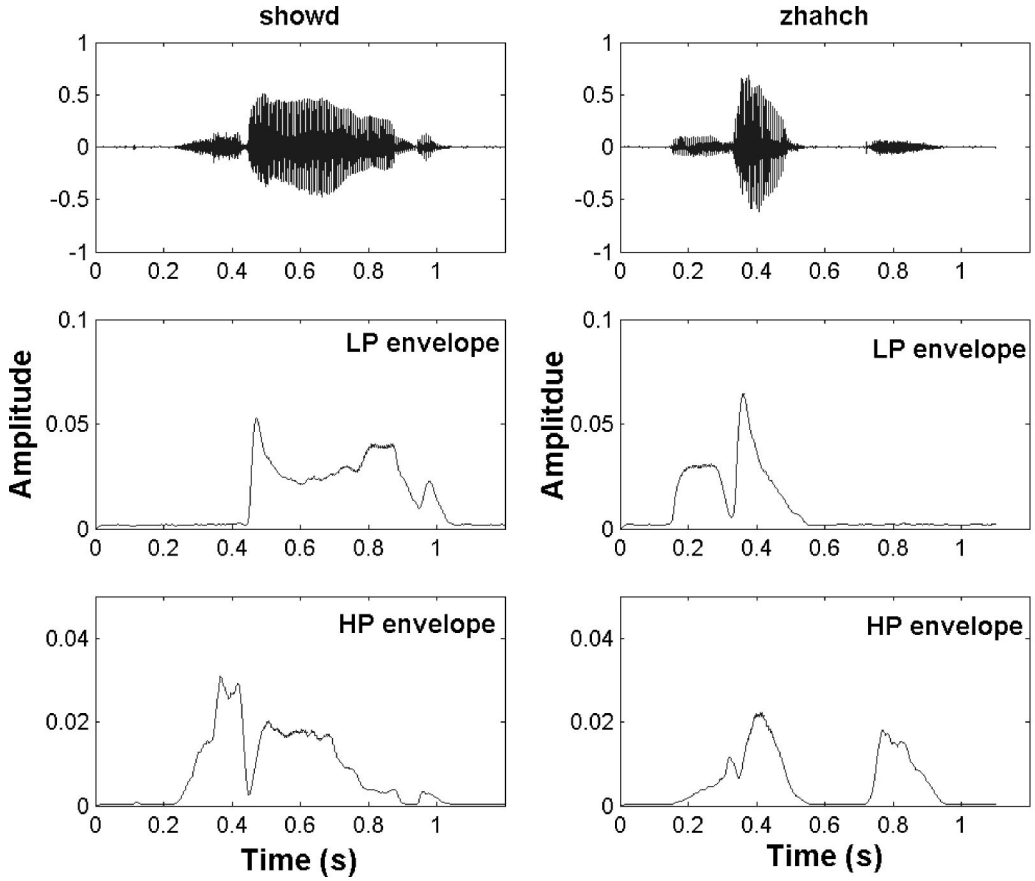

FIG. 2. An illustration of EOA measurements for two syllables. The upper trace is the original speech signal, the middle trace is the low-pass band envelope, and the lower trace is the high-pass band envelope. In each plot, the amplitude (on a scale from 0 to 1) is plotted as a function of time in seconds. In the labels of the plots, sh stands for /ʃ/, zh for /ʒ/, ch for /tʃ/, ow for /aʊ/, and ah for /ɑ/.

2. Measurement of envelope-onset asynchrony

In order to measure the asynchrony of the two envelopes, a threshold must be selected to define the onset of the envelope. In general, there is less energy in the high-frequency band than in the low-frequency band, leading to a corresponding amplitude difference between the two envelopes. A threshold of 0.02 (on a scale from 0 to 1) was selected for the low-frequency energy envelope and a threshold of 0.002 (on a scale from 0 to 1) for the high-frequency energy envelope. The values were selected by visual examination of tokens representing each phoneme category from each talker. The thresholds were chosen (a) to exceed the envelope of the noise floor within the spectral region of each envelope and, at the same time, (b) to capture the onset of the energy within the spectral region of each envelope. The same threshold values were used for all stimuli in the set.[1] The onset time for each envelope was defined as the point in time at which the amplitude of that envelope first exceeds the threshold value.

Envelope-Onset Asynchrony (EOA) is defined as the difference in time between the onset of the high-frequency envelope and the onset of the low-frequency envelope: $\mathrm{EOA} = OnsetTime_L - OnsetTime_H$. For the voiceless consonants, the onset of the high-frequency energy tends to lead the onset of the low-frequency energy; therefore, the EOA of voiceless consonants is typically positive. In contrast, for the voiced consonants, the onset of the low-frequency energy either leads or is nearly simultaneous with the onset of the high-frequency energy; thus, the EOA of voiced consonants is typically negative or approximately zero.

An illustration of the measurement procedure is shown in Fig. 2 for two C_1VC_2 syllables: /ʃaʊd/ (voiceless initial consonant /ʃ/) and /ʒɑtʃ/ (voiced initial consonant /ʒ/). For the syllable /ʃaʊd/ (left panel of Fig. 2), the low-frequency energy envelope exceeds the threshold of 0.02 at roughly 0.455 s (defining its onset). The high-frequency energy envelope exceeds the threshold of 0.002 at roughly 0.252 s (defining its onset). Therefore, the EOA is EOA $= 0.455 - 0.252 = 0.203$ s. Similarly, for the syllable /ʒɑtʃ/ (right panel of Fig. 2), the onsets of the low-frequency energy envelope and high-frequency energy envelope are 0.168 and 0.203 s, respectively. Thus, in this case the EOA is EOA $= 0.168 - 0.203 = -0.035$ s.

III. RESULTS

A. Distribution of the EOA values

The EOA was measured for each of the 64 tokens (2 lists $\times$ 2 speakers $\times$ 16 vowels) of each initial consonant from the nonsense-syllable database. The measurement of EOA was made automatically by a computer program.

The distribution of the EOA values for each consonant was derived by dividing the total range of the EOA for that consonant into equal duration intervals. The number of to-

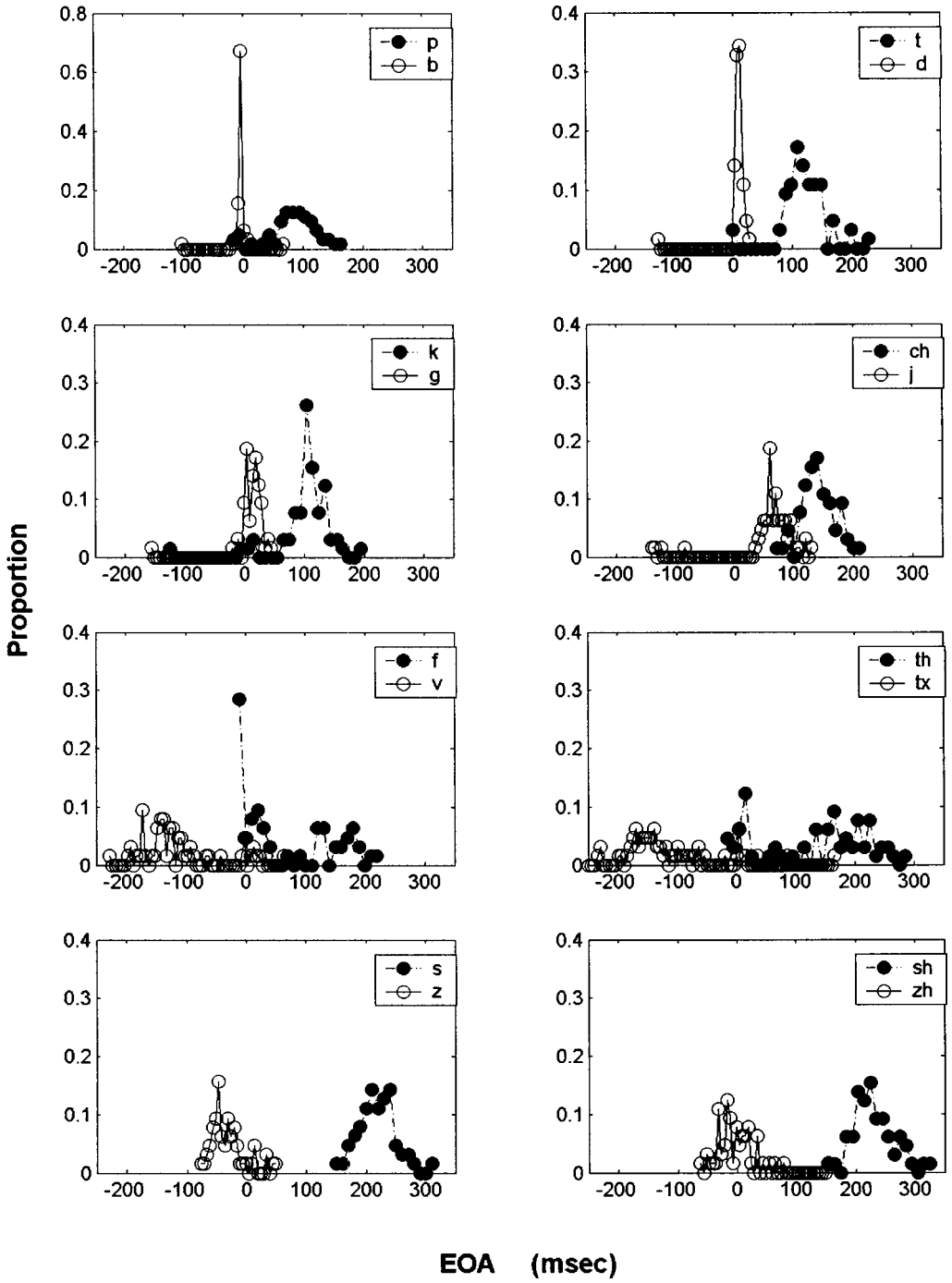

FIG. 3. Probability distributions of EOA for the eight pairs of voicing contrasts. In each plot, measurements are based on 64 tokens of each of the 2 consonants contrasting in voicing. In the labels of the plots, ch stands for /tʃ/, j for /dʒ/, th for /θ/, tx for /ð/, sh for /ʃ/, and zh for /ʒ/.

kens with EOA within each given interval was then tabulated. Finally, the proportion of occurrences within each interval was obtained by dividing the number of counts in each interval bin by the total number of tokens for each consonant. Since the range of EOA of the voiceless stops is larger than that of the voiced stops, a bin size of 10 ms was selected for displaying the EOA of the voiceless consonants, whereas a bin size of 5 ms for the voiced consonants was used to obtain sufficient sample points.

The probability distribution functions (pdfs) of EOA are shown in Fig. 3 for the eight pairs of voiced-voiceless contrasts. The upper four panels show the EOA distributions for the three plosive contrasts (/p b/, /t d/, /k g/) and for the affricate contrast (/tʃ dʒ/). The lower four panels show the EOA distributions for the four fricative contrasts (/f v/, /θ ð/, /s z/, /ʃ ʒ/). Two observations may be made from these plots. First, there appears to be very little overlap in the EOA values for voiced and voiceless contrasts. Second, there appears to be greater variability associated with the EOA value of voiceless compared to voiced consonants.

The probability distribution functions of all EOA values for the two major categories ''voiced'' and ''voiceless'' are

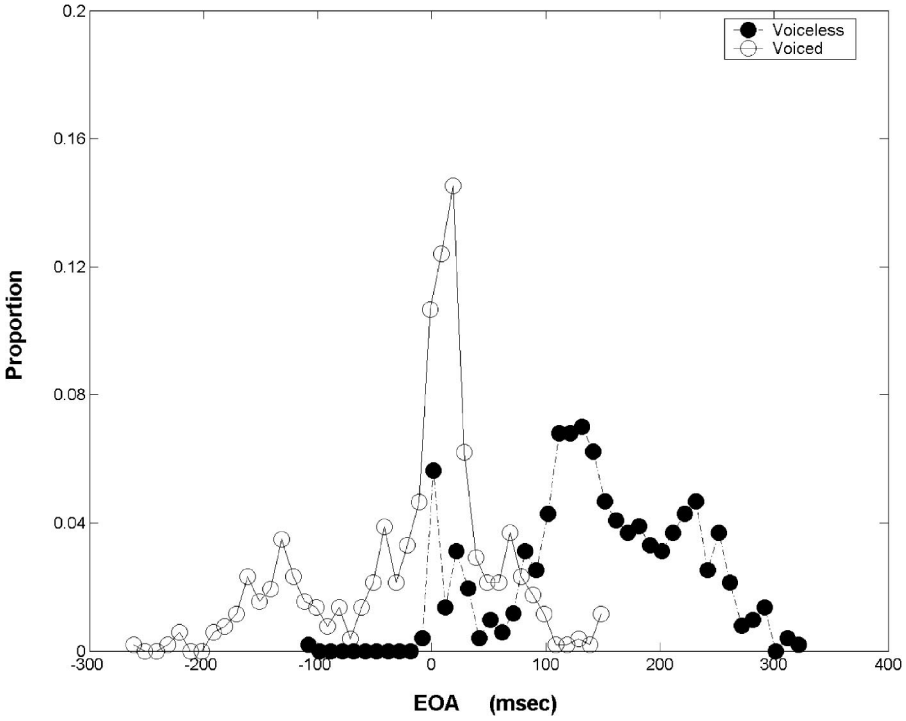

FIG. 4. Probability distribution of EOA for two categories of consonants: Voiceless versus Voiced. Within the Voiceless category, measurements were made on 512 tokens pooled across the 8 voiceless consonants. Likewise, 512 tokens were used in measurements within the Voiced category.

shown in Fig. 4. To construct this figure, the data for the eight voiced consonants /b d g v ð z ʒ dʒ/ were pooled together for the ''voiced'' category and the data for the eight voiceless consonants /p t k f θ s ʃ tʃ/ were pooled together for the ''voiceless'' category. All 16 vowels and both speakers are represented, leading to a total of 512 tokens in each category. The data plotted in Fig. 4 indicate that, across different manners and places of consonant production and in a variety of vowel contexts, there is little overlap between the pdfs for the two general categories ''voiced'' and ''voiceless.''

B. Cumulative distribution functions of EOA values and their Gaussian fittings

A cumulative distribution function (cdf) of EOA was derived for each consonant from the pdf of EOA values by summing the proportions below a given criterion. Cumulative distribution functions for the eight pairs of consonants are shown in Fig. 5 by empty circles (voiced) and filled circles (voiceless).

A Gaussian fit to the cdf of EOA values of the consonants in each of the eight pairs is shown by the solid lines in Fig. 5. The mean and standard deviation of the best Gaussian fit for each consonant were chosen to minimize the sum of squares of the difference between the observed cdf and the predicted cdf at the sample points. The mean and standard deviation of the best Gaussian fit, as well as the percentage error for the fit of each consonant, are listed in Table I. For the voiceless category, the mean values of EOA of the eight consonants ranged from 54.6 to 233.5 ms. For the voiced category, the mean values ranged from −122.4 to 68.6 ms. The values of standard deviation ranged from 2.6 to 36.2 ms for most consonants except for the weak fricatives /f v θ ð/, whose standard deviations ranged from 60.6 to 107.5 ms. The standard deviations for the voiceless consonants were always larger than for their voiced cognates. The Gaussian fits of the cdfs of EOA values generally exhibited error rates less than 7% for most consonants, with the exception of the weak fricatives and the voiced affricate /dʒ/, which have error rates of roughly 10%.

The cdfs for the two general categories of all voiceless and voiced consonants are shown in Fig. 6 by the empty circles (voiced) and filled circles (voiceless). The cdfs, for the two categories pooled across all consonants, are quite separable for voiced compared to voiceless consonants, as is the case for individual pairs of voicing contrasts. The Gaussian fits for all consonants in each of the two categories are shown in Fig. 6 by the solid curves.

The results of the best Gaussian fits of the two categories are provided in the final row of Table I. The mean EOA for the voiceless consonants was 142.5 ms compared to −12.4 ms for the voiced consonants and the standard deviations of the two categories were similar. The function for voiced consonants is less well fit than that for voiceless consonants, especially in the range of −100 to −200 ms.

The goodness-of-fit of each normal distribution to the empirical distribution of each consonant was evaluated using the Kolmogorov–Smirnov (KS) test (DeGroot and Schervish, 2002). The KS test statistic D is the largest absolute deviation between the Gaussian distribution function and the observed cumulative distribution function. The D-statistic values for each consonant are shown in Table II, as well as the D-statistic values for the two overall categories of voiceless versus voiced consonants (provided in the final row). For a significance level of 0.01, the model will not be rejected if the D statistic is less than $1.63/\sqrt{N}$, where N is the sample size provided in Table II. (Sample size, N, varies across consonants due to the binning procedure described earlier in Sec. III A.) Thus, in order not to reject the model, the D statistic must satisfy $D<1.63/\sqrt{N}$ for each case. When

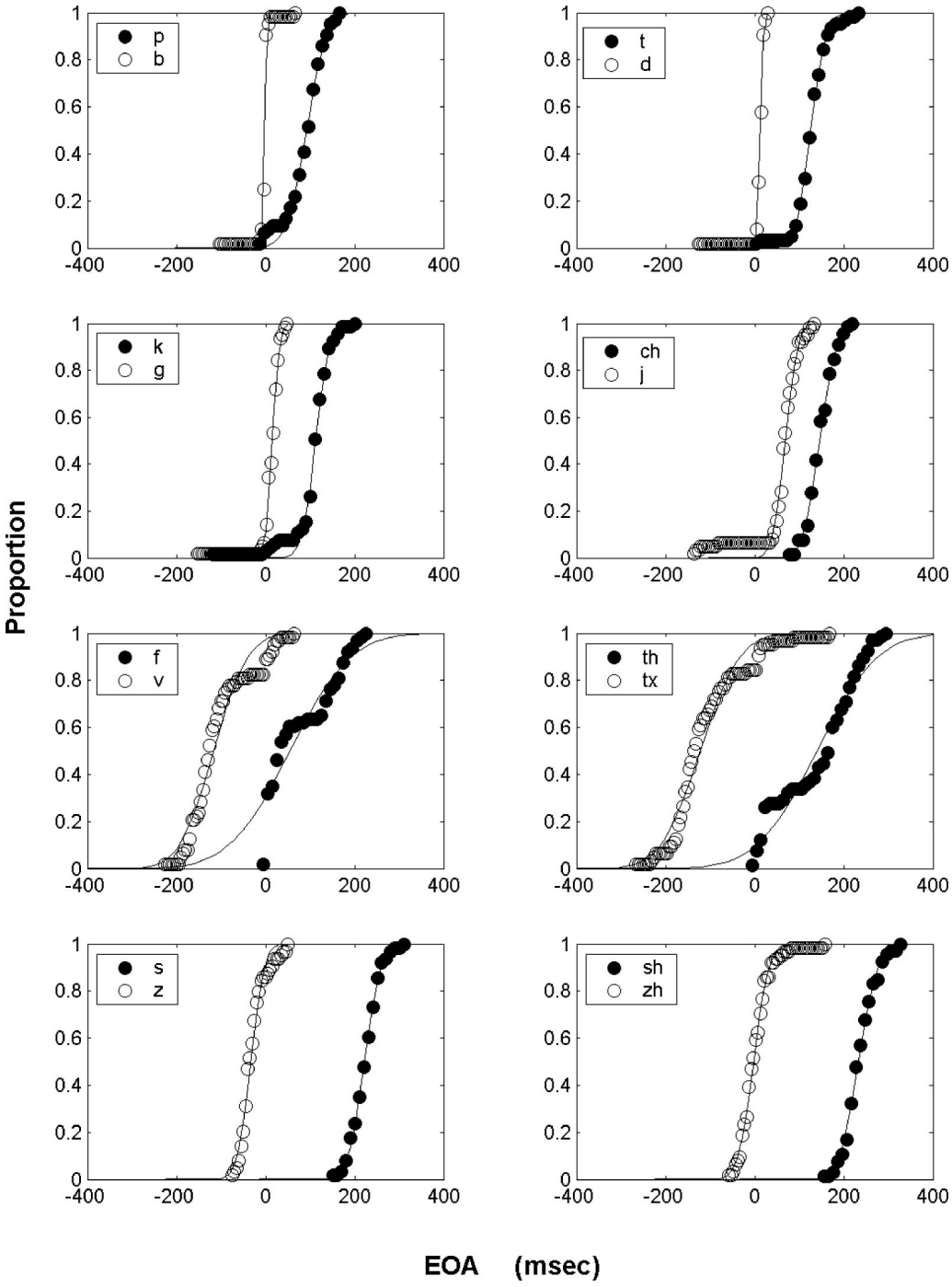

FIG. 5. Cumulative distribution functions of EOA for the eight pairs of voicing contrasts and their Gaussian fittings. Data points for voiceless sounds are shown by filled circles and for voiced sounds by unfilled circles. The Gaussian fit to each cdf is shown by the solid lines. In the labels of the plots, ch stands for /tʃ/, j for /dʒ/, th for /θ/, tx for /ð/, sh for /ʃ/, and zh for /ʒ/.

this criterion is compared with the D statistics shown in Table II, it can be seen that the normal distributions with mean and standard deviation estimated using least-mean-square error are not rejected at a significance level of 0.01 for all cases.

C. Performance of an ideal observer

Using the EOA as a perceptual-distance measurement, we can calculate the performance of an ideal observer in making the voiced-voiceless distinction with sensitivity (d'), a measure widely used in Signal Detection Theory (see Green and Swets, 1966; Durlach, 1968; Macmillan, 1990). Signal detection theory analyzes decision-making in the presence of uncertainty. Its application in sensory experiments provides a way to separate the underlying sensory processing of the stimuli from the subjective decision process. Sensitivity (d') for two Gaussian distributions of equal variances σ^2 is defined as

$$d' = (m_1 - m_2)/\sigma, \tag{1}$$

where m_1 and m_2 are the means of the two Gaussian distributions, respectively.

TABLE I. A summary of the results of the best Gaussian fit to the cdf of EOA values for each of the 16 consonants and for the two general categories: ''Voiceless'' and ''Voiced.'' For consonant or category, mean and standard deviation (STD) of the best fit are given in ms, along with the percentage error of the fit (see the text for a definition).

		Mean (ms)	STD (ms)	Error (%)		Mean (ms)	STD (ms)	Error (%)
Stops	/p/	91.9	36.2	6.4	/b/	−2.0	2.6	3.4
	/t/	126.1	26.8	3.8	/d/	12.8	5.7	5.1
	/k/	112.8	24.9	7.3	/g/	15.5	12.9	5.2
Affricates	/tʃ/	146.0	29.6	3.5	/dʒ/	68.6	21.9	10.3
Fricatives	/f/	54.6	107.5	11.4	/v/	−116.8	60.6	9.9
	/θ/	140.0	106.8	11.1	/ð/	−122.4	69.8	7.0
	/s/	222.4	29.8	1.8	/z/	−33.3	23.7	6.3
	/ʃ/	233.5	33.8	4.0	/ʒ/	−2.6	27.7	2.8
All	Voiceless	142.5	77.2	3.8	Voiced	−12.4	66.5	9.8

The calculation of d' based on the experimental results derived from the stimulus–response confusion matrix in a one-interval two-alternative forced-choice paradigm shown in Table III, is given by

$$d' = z(H) - z(F), \tag{2}$$

where the hit rate H is the proportion of presentations of stimulus S1 to which the subject responds S1, calculated by

$$H = N(\text{Hits})/(\text{N(Hits)} + N(\text{Misses})); \tag{3}$$

and the false-alarm rate F is the proportion of presentations of stimulus S2 to which the subject responds S1, calculated by

$$F = N(\text{False alarms})/(N(\text{False alarms}) + N(\text{Correct rejections})); \tag{4}$$

and z is the inverse of the normal distribution function that converts a hit or false-alarm rate to a z score.

The above method of calculating d' assumes that the decision variables (EOA) have Gaussian distributions of equal variances (or variables that can be transformed by a monotonic function into Gaussian distributions of equal variances). The values of standard deviation provided in Table I, however, indicate that the two distributions for pairs of consonants contrasting in voicing tend to have different variances. This inequality of variances negates the direct application of Eq. (1). There are at least three approaches that could be applied to overcome this problem: (1) using monotonic transfer functions to transform the two variables from unequal variance to equal variance, (2) applying formulas for d' under an assumption of unequal variance (Macmillan and Creelman, 1990), and (3) employing a two-interval two-alternative forced choice (2I, 2AFC) procedure. Our approach for calculating d' for the ideal observer is based on this final option, i.e., the use of a 2I, 2AFC procedure.

In a 2I, 2AFC paradigm, both alternatives (S1, S2) are

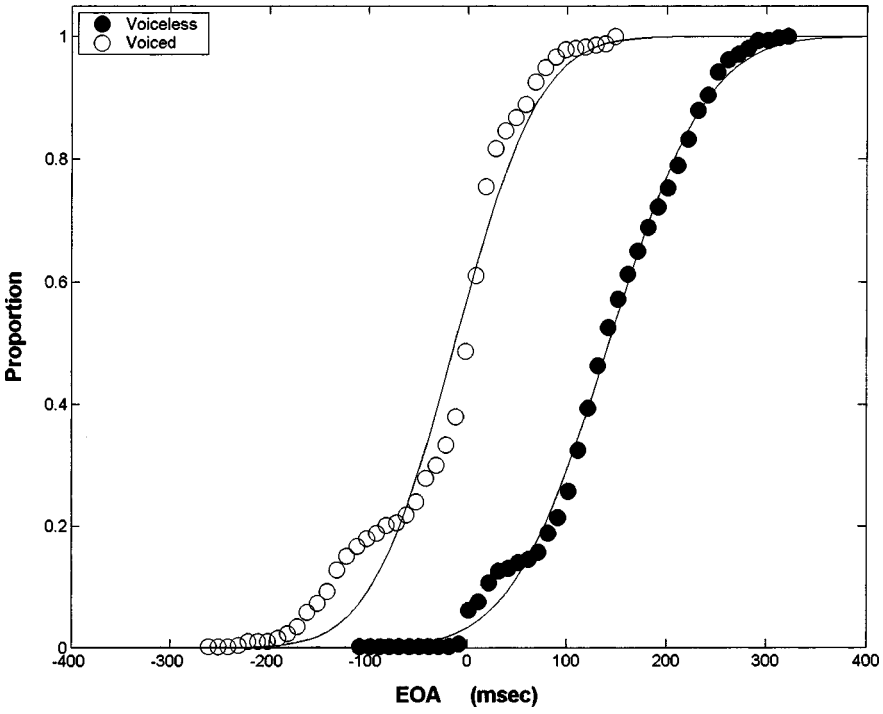

FIG. 6. Cumulative distributions of EOA for two categories of consonants: Voiceless (filled circles) versus Voiced (unfilled circles), and their Gaussian fittings (shown by the solid lines).

TABLE II. D-statistic values for each of the 16 consonants and for the two general categories "Voiceless" and "Voiced." For $D<1.63/\sqrt{N}$, the Gaussian assumption is not rejected at a 0.01 level of significance. The Gaussian assumption is not rejected for any of the cases.

C_1	Sample number	$\frac{1.63}{\sqrt{N}}$	D statistic
/p/	19	0.3739	0.0748
/b/	35	0.2755	0.0728
/t/	24	0.3327	0.0487
/d/	32	0.2881	0.0307
/k/	33	0.2837	0.0763
/g/	41	0.2546	0.0660
/tʃ/	15	0.4209	0.0515
/dʒ/	55	0.2198	0.0625
/f/	24	0.3327	0.2738
/v/	59	0.2122	0.1421
/θ/	31	0.2928	0.1225
/ð/	88	0.1738	0.1212
/s/	17	0.3953	0.0275
/z/	26	0.3197	0.0768
/ʃ/	15	0.4209	0.0552
/ʒ/	55	0.2198	0.0449
Voiceless	44	0.2457	0.0528
Voiced	42	0.2515	0.1329

presented on each trial in the random order of two possibilities: [S1, S2] or [S2, S1]. The decision variable in a 2I, 2AFC experiment is formed by subtracting the EOA value in the first interval from that in the second interval. Thus, the probability distribution functions for the two possible cases ([S1, S2] or [S2, S1]) are symmetric about the origin and have the same variance. The sensitivity d' can be calculated using Eq. (1) (Macmillan and Creelman, 1990). Performance

TABLE III. Confusion matrix derived from the one-interval two-alternative paradigm experiment.

		Response	
		R1	R2
Stimulus	S1	*N*(*Hits*)	*N*(*Misses*)
	S2	*N*(*False alarms*)	*N*(*Correct rejections*)

in 2I, 2AFC is typically scaled by a factor of $1/\sqrt{2}$ to be equivalent to that which would be achieved in a standard 1I, 2AFC procedure.

A simulation procedure was employed to obtain the distribution of the difference between the EOAs of each pair of voiced–voiceless consonants, as well as their cumulative distributions. This procedure was conducted by (1) randomly selecting one token representing the initial voiced consonant of a given pair, (2) randomly selecting another token representing its voiceless cognate, and (3) calculating the difference between the two EOAs. This procedure was repeated for 5000 trials. The same Gaussian fitting procedure was used as described in Sec. III B above. The pdf (top panels) and cdf (bottom panels) of the EOA difference are shown in Fig. 7 for the consonant pair /s-z/: EOA of /z/ minus EOA of /s/ (the left panel of Fig. 7) and EOA of /s/ minus EOA of /z/ (the right panel of Fig. 7). The Gaussian fit to the cdf of the EOA difference is shown by the solid lines in Fig. 7. The absolute values of the mean and the standard deviation of the best Gaussian fit, which are the same for the two distributions, are 254 and 39 ms, respectively. According to Eq. (1), the value of $d'=(254-(-254))/39=13.0$.

The d' values computed for each of the eight pairs in 2I,

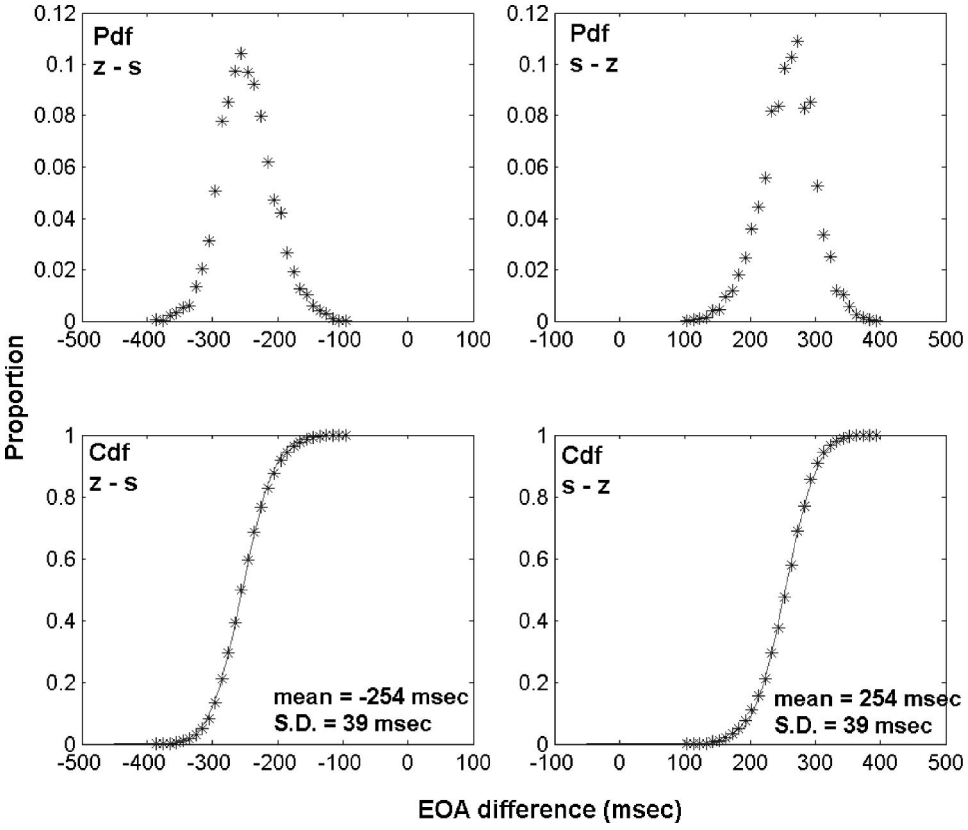

FIG. 7. Probability distributions (pdfs) and cumulative distributions (cdfs) of the EOA difference for the pair /s-z/: /z/ minus /s/ (left panel) and /s/ minus /z/ (right panel). The two panels in the top row show the pdfs and the two panels in the bottom row shown are their cdfs. The Gaussian fit to each cdf is shown by the solid lines.

TABLE IV. Values of d′ for eight pairs in the 2I, 2AFC experiment.

Pair	/p b/	/t d/	/k g/	/tʃ dʒ/	/f v/	/θ ð/	/s z/	/ʃ ʒ/	Overall
d′	5.1	8.1	6.8	3.9	3.5	4.0	13.0	10.6	3.0

2AFC are provided in Table IV, as well as the d' value for the two overall categories. The values of d' cover a range from 3.5 (for /f v/) to 13.0 for /s z/. These results indicate excellent sensitivity: in terms of percent-correct the results fall in the range 96% to 100% correct.

IV. DISCUSSION

Acoustic measurements of EOA in C_1VC_2 syllables indicate that EOA provides a reliable and robust cue for initial consonant voicing across a variety of vowel contexts for two different speakers. The cue is independent of manner and place of production of the consonants. Our results, however, are limited to obstruent consonants in initial position and in isolated syllables. Its applicability to other contexts (such as syllable-final position or consonant clusters), to continuous speech, to noisy speech, and to larger intertalker variability, remains to be examined.

The EOA cue may be easily transferred to certain contexts, such as consonants in syllable-final position. Although a full set of measurements has yet to be obtained, the offset times of the two envelopes appear to provide reliable information for voicing discrimination at least for certain contrasts. Extensions to multiple talkers may also be handled satisfactorily based on the consistency of the measurements across the two different talkers in the current study. The cue may be less reliable in noisy speech. For broadband stationary noise, the thresholds may need to be adjusted according to the noise level and the cue will not be effective under extremely noisy conditions because the envelopes will be masked by the envelope of the noise. Problems become more difficult with speech-like maskers due to the competing onsets from nontarget components.

EOA and VOT for English stops are closely related to each other in two aspects: (1) the burst and the following frication and aspiration of a voiceless stop are composed of high-frequency energy; and (2) the vocal-fold vibration is usually composed of low-frequency energy. Although the energy onsets of the high-and low-frequency bands selected for envelope processing do not coincide with the timing of the burst and the onset of vocal-fold vibration, respectively, they are nonetheless good indicators of the two events in production. Niyogi and Ramesh (2003) examined the VOT distribution of English plosives in initial position followed by a stressed vowel on two different databases of continuous speech. Four observations can be made by comparing the VOT measurements (Niyogi and Ramesh, 2003) with the EOA measurements of the current study for each of the three pairs of English plosives that contrast in voicing. First, both VOT and EOA provide excellent separation of the voiced and voiceless pairs with only small regions of overlap. In general, voiceless plosives have higher VOT and EOA than their voiced counterparts. Second, the variances of both VOT and EOA measurements are smaller for voiced compared to the voiceless plosives. Third, the mean values of EOA measurements for voiceless plosives are larger than the mean values of VOT. Fourth, the values of VOT are always positive (i.e., the onset of burst precedes the onset of the vocal fold vibration); however, the values of EOA can be negative for voiced plosives (i.e., the onset of low-frequency energy can precede the onset of high-frequency energy).

The real-time measurement of VOT, however, is relatively difficult. It requires the real-time detection of the burst that corresponds to the release of the plosives, and the onset of glottal vibration from the speech waveform, as well as prior identification of manner of production. In contrast, the real-time measurement of EOA is quite straightforward in its derivation of the envelopes of two different frequency bands, regardless of the manner of production. Despite difficulties in obtaining accurate and automatic measurements of VOT, two recent studies (Ali *et al.*, 2001b; Niyogi and Ramesh, 2003) have demonstrated good performance in voicing recognition using algorithms for the automatic measurement of VOT in pre-labeled stop consonants.

The reliability and simplicity of the derivation of EOA makes this cue a good candidate as a source of information to be integrated into an automatic speech recognition system. It could be used directly as an individual module for voicing detection in a knowledge-based (rule-based) recognition system that emulates the human ability in speech recognition. The EOA cue could also be used as an additional input to the currently dominant speech recognition systems that exploit the inherent statistical properties of the speech sounds (such as HMMs). Although speech-recognition systems based on statistical models usually employ phonemes as the minimum units instead of the features associated with the phonemes such as voicing, the EOA cue can be used as a supplement combined with the statistical model in an appropriate way.

The EOA cue described here is applicable to the design of speech-communication aids for persons with profound hearing impairment. For example, this cue may be encoded through a simple two-channel display in which the amplitude envelopes of the high- and low-frequency bands are delivered to separate channels of the display. The temporal-onset-order difference between the two channels would provide the user of the display with a cue to voicing. Such a display, which could be presented through any of the modalities of audition, vision, or touch (given the specific modality has sufficient temporal resolution to discriminate the EOA patterns associated with voicing), has the potential to provide substantial improvements to the information available through lipreading alone. Previous studies of temporal order discrimination (Hirsh, 1959; Hirsh and Sherrick, 1961; Craig and Baihua, 1990) suggest that thresholds ranging from 20–70 ms, independent of sensory modality, are sufficient for resolving EOA differences associated with voicing. For voiceless consonants, the high-frequency envelope tends to precede the low-frequency envelope by roughly 50–200 ms, depending on the particular consonant; for voiced consonants, on the other hand, the low-frequency envelope tends to precede the high-frequency envelope by values of −70 to 120 ms, depending on the consonant. It is possible that the benefits observed by Breeuwer and Plomp (1984) and Grant

et al. (1994) may have been derived, at least in part, from the temporal cue described in the current set of measurements.

V. CONCLUSIONS AND FUTURE DIRECTIONS

Acoustic measurements of initial consonants in C_1VC_2 syllables indicate that the envelope-onset asynchrony (EOA) of two bands of speech (a low-pass band and a high-pass band) serves as a reliable acoustic cue for distinguishing voiced from voiceless consonants. The measurements of EOA reported here are applicable to obstruent consonants (regardless of manner or place of production) in the initial position of isolated syllables. This cue is capable of distinguishing pairs of voiced/voiceless consonants at a rate of roughly 96% to 100% correct. This performance compares favorably with that reported for voicing-detection algorithms developed for incorporation into ASR schemes. Further research is warranted to determine the applicability of the EOA cue to additional contexts (including syllable-final and medial positions and consonant clusters), to the coarticulation encountered in continuous speech, to speech under noisy environments, and to larger intertalker variability.

Future work will also be concerned with the development of speech-communication aids for persons with profound hearing impairment or deafness to present the EOA cue through visual or tactual displays or through displays using residual auditory function. Evaluations of these displays will include perceptual studies of the discriminability of pairs of voiced–voiceless consonants (for comparison with the performance of the ideal observer reported here) as well as studies examining the benefits of the EOA cue as a supplement to lipreading.

ACKNOWLEDGMENTS

This research was supported by Research Grant No. R01-DC00126 from the National Institute on Deafness and Other Communication Disorders, National Institutes of Health. The authors wish to thank Lou Braida and Ken Stevens for their contributions to this research. They also wish to thank Ken Grant and two anonymous reviewers for their helpful comments on previous versions of this paper.

[1]The two threshold values that were selected may not be optimal in the sense of obtaining the maximum separation between the EOA distributions of the two sounds within a given voiced–voiceless pair. The precise locations of the threshold values influence the absolute values of EOA of both sounds in a pair: the sharper the onset slope of the envelope, the larger the effect. Changing the threshold values essentially amounts to a shift in the distribution of EOA for both sounds. However, the difference in EOA between the two sounds in a pair remains fairly constant for threshold values changing over a factor of 2–3 and leads to a relatively constant value of d'.

Ali, A. M. A., Van der Spiegel, J., and Mueller, P. (**2001a**). "Acoustic-phonetic features for the automatic classification of fricatives," J. Acoust. Soc. Am. **109**, 2217–2235.

Ali, A. M. A., Van der Spiegel, J., and Mueller, P. (**2001b**). "Acoustic-phonetic features for the automatic classification of stop consonants," IEEE Trans. Speech Audio Process. **9**, 833–841.

Auer, E. T., and Bernstein, L. E. (**1996**). "Lipreading supplemented by voice fundamental frequency: To what extent does the addition of voicing increase lexical uniqueness for the lipreader?," in *ICSLP'96 Proceedings*, Philadelphia, PA, 3–6 October 1996, pp. 86–93.

Baum, S. R., and Blumstein, S. E. (**1987**). "Preliminary observations on the use of duration as a cue to syllable-initial fricative consonant voicing in English," J. Acoust. Soc. Am. **82**, 1073–1077.

Behrens, S. J., and Blumstein, S. E. (**1988**). "Acoustic characteristics of English voiceless fricatives: A descriptive analysis," J. Acoust. Soc. Am. **16**, 295–298.

Braida, L. D. (**1991**). "Crossmodal integration in the identification of consonant segments," Q. J. Exp. Psychol. **43**, 647–677.

Bratakos, M. S., Reed, C. M., Delhorne, L. A., and Denesvich, G. (**2001**). "A single-band envelope cue as a supplement to speechreading of segmentals: A comparison of auditory versus tactual presentation," Ear Hear. **22**, 225–235.

Breeuwer, M., and Plomp, R. (**1984**). "Speechreading supplemented with frequency-selective sound-pressure information," J. Acoust. Soc. Am. **76**, 686–691.

Choi, J. Y. (**1999**). "Detection of consonant voicing: A module for a hierarchical speech recognition system," Ph.D dissertation, Massachusetts Institute of Technology, Cambridge, MA.

Craig, J. C., and Baihua, X. (**1990**). "Temporal order and tactile patterns," Percept. Psychophys. **47**, 22–34.

Crystal, T. H., and House, A. S. (**1988**). "Segmental durations in connected-speech signals—Current results," J. Acoust. Soc. Am. **83**, 1553–1573.

DeGroot, M. H., and Schervish, M. J. (**2002**). *Probability and Statistics* (Addison-Wesley, Boston).

Denes, P. (**1955**). "Effect of duration on the perception of voicing," J. Acoust. Soc. Am. **27**, 761–764.

Durlach, N. I. (**1968**). "A decision model for psychophysics," Communication Biophysics Group, Research Laboratory of Electronics, Massachusetts Institute of Technology, Cambridge, MA.

Erber, N. P. (**1974**). "Visual perception of speech by deaf children—Recent developments and continuing needs," J. Acoust. Soc. Am. **39**, 178–185.

Grant, K. W., Braida, L. D., and Renn, R. J. (**1991**). "Single band amplitude envelope cues as an aid to speechreading," Q. J. Exp. Psychol. A **43**, 621–645.

Grant, K. W., Braida, L. D., and Renn, R. J. (**1994**). "Auditory supplements to speechreading—Combining amplitude envelope cues from different spectral regions of speech," J. Acoust. Soc. Am. **95**, 1065–1073.

Grant, K. W., Walden, B. E., and Seitz, P. F. (**1998**). "Auditory-visual speech recognition by hearing-impaired subjects: Consonant recognition, sentence recognition, and auditory-visual integration," J. Acoust. Soc. Am. **103**, 2677–2690.

Green, D. M., and Swets, J. A. (**1966**). *Signal Detection Theory and Psychophysics* (Wiley, New York).

Heider, F., and Heider, G. M. (**1940**). "An experimental investigation of lipreading," Psychol. Monogr. **52**, 124–133.

Hillenbrand, J., Ingrisano, D. R., Smith, B. L., and Flege, J. E. (**1984**). "Perception of the voiced–voiceless contrast in syllable-final stops," J. Acoust. Soc. Am. **76**, 18–26.

Hirsh, I. J. (**1959**). "Auditory perception of temporal order," J. Acoust. Soc. Am. **31**, 759–767.

Hirsh, I. J., and Sherrick, C. E. (**1961**). "Perceived order in different sensory modalities," J. Exp. Psychol. **62**, 423–432.

Horii, Y., House, A. S., and Hughes, G. W. (**1971**). "A masking noise with speech-envelope characteristics for studying intelligibility," J. Acoust. Soc. Am. **49**, 1849–1856.

House, A. S., and Fairbanks, G. (**1953**). "The influence of consonant environment upon the secondary acoustical characteristics of vowels," J. Acoust. Soc. Am. **25**, 105–114.

House, A. S. (**1961**). "On vowel duration in English," J. Acoust. Soc. Am. **33**, 1174–1178.

Jongman, A., Wayland, R., and Wong, S. (**2000**). "Acoustic characteristics of English fricatives," J. Acoust. Soc. Am. **108**, 1252–1263.

Kiefte, M. (**2003**). "Temporal information in gated stop consonants," Speech Commun. **40**, 315–333.

Lee, C. H., Juang, B. H., Chou, W., and Molina-Perez, J. J. (**1996**). "A study on task independent subword selection and modeling for speech recognition," in *ICSLP'96 Proceedings*, Philadelphia, PA, 3–6 October, 1996, pp. 1816–1819.

Liberman, A. M., Delattre, P. C., and Cooper, F. S. (**1958**). "Some cues for the distinction between voiced and voiceless stops in initial position," Lang. Speech **1**, 153–167.

Lisker, L., and Abramson, A. S. (**1964**). "A cross-language study of voicing in initial stops: Acoustical measurements," Word **20**, 384–422.

Macmillan, N. A., and Creelman, C. D. (**1990**). *Detection Theory: A User's Guide* (Cambridge University Press, London).
Niyogi, P., and Ramesh, P. (**2003**). ''The voicing feature for stop consonants: Recognition experiments with continuously spoken alphabets,'' Speech Commun. **41**, 349–367.
Ohde, R. N. (**1984**). ''Fundamental-frequency as an acoustic correlate of stop consonant voicing,'' J. Acoust. Soc. Am. **75**, 224–230.
Pirello, K., Blumstein, S. E., and Kurowski, K. (**1997**). ''The characteristics of voicing in syllable-initial fricatives in American English,'' J. Acoust. Soc. Am. **101**, 3754–3765.
Rabiner, L. R., and Juang, B. H. (**1993**). *Fundamentals of Speech Recognition* (Prentice–Hall, Englewood Cliffs, NJ).
Ramesh, P., and Wilpon, J. G. (**1992**). ''Modeling state durations in hidden Markov models for automatic speech recognition,'' in *Proceedings of ICASSP*, pp. 381–384.
Raphael, L. J. (**1972**). ''Preceding vowel duration as a cue to the perception of the voicing characteristic of word-final consonants in American English,'' J. Acoust. Soc. Am. **51**, 1296–1303.
Stevens, K. N., and Klatt, D. H. (**1974**). ''Role of formant transitions in the voiced–voiceless distinction for stops,'' J. Acoust. Soc. Am. **55**, 653–659.
Stevens, K. N., Blumstein, S. E., Glicksman, L., Burton, M., and Kurowski, K. (**1992**). ''Acoustic and perceptual characteristics of voicing in fricatives and fricative clusters,'' J. Acoust. Soc. Am. **91**, 2979–3000.
Stevens, K. N. (**1998**). *Acoustic Phonetics* (MIT Press, Cambridge).
Thomson, D. L., and Chengalvarayan, R. (**2002**). ''Use of voicing features in HMM-based speech recognition,'' Speech Commun. **37**, 197–211.
Van Tasell, D. J., Soli, S. D., Kirby, V. M., and Widen, G. P. (**1987**). ''Speech waveform envelope cues for consonant recognition,'' J. Acoust. Soc. Am. **82**, 1152–1161.
Walden, B. E., Prosek, R. A., Montgomery, A. A., Scherr, C. K., and Jones, C. J. (**1977**). ''Effects of training on visual recognition of consonants,'' J. Speech Hear. Res. **20**, 130–145.
Whalen, D. H., Abramson, A. S., Lisker, L., and Mody, M. (**1993**). ''F0 gives voicing information even with unambiguous voice onset times,'' J. Acoust. Soc. Am. **93**, 2152–2159.
Zue, V. W. (**1976**). ''Acoustic characteristics of stop consonants: A controlled study,'' Ph.D. dissertation, Massachusetts Institute of Technology, Cambridge, MA.

Geometry of locating sounds from differences in travel time: Isodiachrons

John L. Spiesberger
Department of Earth and Environmental Science, 240 S. 33rd St., University of Pennsylvania, Philadelphia, Pennsylvania 19104-6316

(Received 2 June 2004; revised 15 August 2004; accepted 16 August 2004)

Calling animals may be located from measurements of the differences in acoustic travel time at pairs of receivers. For inhomogeneous fields of speed, locations can be made with better accuracy when the location algorithm allows the speed to vary from path to path. A new geometrical shape, called an isodiachron, is described. It is the locus of points corresponding to a constant difference in travel time along straight paths between the animal and two receivers. Its properties allow an interpretation for locations when the speed differs from path to path. An algorithm has been developed for finding the location of calling animals by intersecting isodiachrons from data collected at pairs of receivers. When the sound speed field is spatially homogeneous, isodiachrons become hyperboloids. Unlike a hyperboloid that extends to infinity, an isodiachron is confined to a finite region of space when the speeds differ between the animal and each of two receivers. Its shape is significantly different than a hyperboloid for cases of practical interest. Isodiachrons can be used to better understand locations of calling animals and other sounds in the sea, Earth, and air. © *2004 Acoustical Society of America.* [DOI: 10.1121/1.1804625]

PACS numbers: 43.80.Ev [WWA] Pages: 3168–3177

I. INTRODUCTION

Differences in the travel time of acoustic and electromagnetic waves are commonly used to locate objects. Applications include the global positioning system[1] (GPS) and the passive location of calling animals.[2–9] When the speed of the signal is constant, the difference in travel times can be converted to the difference in distances by multiplying the difference in travel times by the speed. Then the method of location is usually interpreted using hyperboloids[10,11] because the hyperboloid is the locus of points whose difference in distance from two points is constant. The hyperbola may have been discovered by the ancient Greek mathematician Menaechmus (circa 350 B.C.) (p. 280-281, Vol II, Ref. 12), but this is not certain as most original writings have been lost. Other geometrical interpretations of location have also been found.[11,13,14]

The single-speed approximation is good enough for some but not all applications. For greater accuracy, methods are used that allow the speed to differ from path to path, while still maintaining the picture of signals traversing straight line segments. Scientists have developed these approaches for application to acoustic navigation in the sea,[15–17] and to the passive location of calling animals in the sea and air.[9,18] Then the question arises as to whether there is a geometrical shape, which cannot be a hyperbola, that can be used to interpret such locations when a constant speed is not used.

The purpose of this paper is to show that such a shape exists and to use it to interpret these methods of location. The shape appears to have not been shown previously in the scientific or mathematical literature, except for a paper that gives its definition without showing its shape or describing its properties.[18] It is therefore necessary to use simple calculations to describe the properties of this shape, called an ''isodiachron,'' from the Greek words ''iso'' for same, ''dia'' for difference, and ''chron'' for time. It is the locus of points along which the difference in *travel time* is constant. It reduces to a hyperboloid when the average speed of the signal is the same on both paths. The isodiachron is the natural shape to intersect to find the location of an animal when the speed differs from path to path. In fact, the algorithm in Ref. 18 yields a probability density function for location using isodiachrons.

Unless noted otherwise, the phrase ''effective speed'' is defined to be the time for the acoustic or electromagnetic signal to propagate from the animal to the receiver divided by the Euclidean distance. Thus the effective speed includes all spatially and temporally varying effects including those due to refraction, diffraction, and, for acoustic signals, advection such as that due to winds or currents. Because of advection, the effective speed from the animal to the receiver can be different than from the receiver to the animal. The word ''speed'' will not include effects from advection.

Section II reviews some of the reasons and methods that have been used to infer location when the effective speed is spatially inhomogeneous. There must be other methods that have been used as well, and the list of examples here is not intended to be complete. What is important about this section is that it highlights some of the pitfalls in hyperbolic location methods in situations where the effective speed is not constant from path to path. Section III provides the calculations that define the isodiachron and its behavior. The paper ends with a short summary, and provides a speculation as to why the ancient Greek mathematicians did not apparently contemplate an isodiachron.

II. HYPERBOLIC LOCATION IS LESS ACCURATE AND SOMETIMES INCORRECT

A. Underwater navigation

Hydrophones are sometimes lowered from a ship to the seafloor to locate acoustic emissions from a variety of objects. There is considerable interest in determining the position of each hydrophone on the bottom so that locations of acoustic emissions can be made accurately.

Quite often, the positions of the hydrophones are estimated by towing an accurately located source from the ship while the hydrophones on the bottom pick up these calibration signals. Suppose the clock for the hydrophone time series has an unknown offset with respect to the clock governing the towed source. The unknown clock offset is removed from the problem by working with differences of signal travel time at the hydrophone. The travel times change primarily because the source transmits from different locations. Until recently, this was usually treated as a standard hyperbolic location problem.

In the sea, the effective speed of sound between the source and hydrophone varies with source location.[15–17] To explain why, assume for simplicity that the speed of sound varies with depth only. The actual time for sound to reach a hydrophone on the bottom from the surface depends on the speed of sound along a ray path, which is not straight because it bends due to refraction. If the ray path were straight, the effective speed of sound would be the same for all source locations at the surface. But the bending changes the effective speed of sound. For cases of interest, this effective speed can be pre-computed in a table of speed versus slant angle to and depth of the receiver.[15,17] This table can be accessed by a location algorithm.[15,16]

The equations relating location to differences in travel time are nonlinear.[15,16] When these equations are linearized about a good initial guess for hydrophone location, a least-squares problem for hydrophone location and clock offset between the source and hydrophone can be solved by iterating the linearized equations to minimize the residuals in a determined or overdetermined problem.[15,16] The method, called the ''inhomogeneous algorithm'' here, allows one to assume that different paths have the same or different effective speeds. The inhomogeneous algorithm looks up the effective speed along each path as it iterates for the location of the hydrophone on the bottom.[15,16] An estimate of the error obtained from hyperbolic location has been investigated as follows.

Using a realistic profile of sound speed in the Atlantic, a simulated hydrophone at 1600 m depth is estimated to have a depth error of about 3 m when located using hyperbolic methods (Table I, case 5, Ref. 16). When the effective speed of sound is allowed to vary from path to path from a precomputed database, the inhomogeneous algorithm yields the correct depth for the hydrophone (Table I, Case 6, Ref. 16). For real data with a similar geometry, the hyperbolic location algorithm yields a 3 m error compared with the inhomogeneous location algorithm (Cases 2 and 4 in Table 2.3 of Ref. 15). There are situations where 3 m errors in hydrophone locations are significant. Errors in the locations of receivers often translate to much larger errors in source location.[11,19]

B. Solutions for animal location in air

Naturalists, biologists, acousticians, and others estimate locations of sounds from differences of travel time on widely separated microphones in air.[20–25] Problems with hyperbolic location are highlighted by considering a geometry where an animal is located at Cartesian coordinate (20,100,7) m and its signals are monitored at five microphones at (0,0,0), (25,0,3), (50,3,5), (30,40,9), and (1,30,4) m respectively. For definiteness, assume the animal's call has a rms. bandwidth of 1000 Hz and, following the cross correlation of the signal between each pair of microphones, the peak signal-to-noise ratio is 20 dB. The lag of this peak has a standard deviation of 16 μs (Ref. 26), where the lag is the difference in the travel time of sound between the animal and two receivers. Such accuracy can be achieved in practice.

A sequential nonlinear Monte Carlo technique is used to estimate the probability density function for location from simulated lags.[18] The technique can accommodate spatially homogeneous or inhomogeneous effective speeds, and allows one to account for errors in the locations of the microphones. Realistic *prior* distributions of errors are permitted for all variables. Distributions of location can be compared with the same statistical assumptions except for the fact that in one case the effective speed is spatially homogeneous, and in the other, spatially inhomogeneous. Other algorithms may also be suitable for generating realistic location distributions, but it does not seem prudent to summarize or compare such techniques because the main point of this paper is not centered on a review of techniques.

Simulated lags are computed without noise for a speed of sound of 330 m/s and for a horizontal wind blowing at 10 m/s toward the positive y Cartesian axis. *A priori* distributions of the remaining variables are taken to be Gaussian but truncated at two standard deviations (Table I). The accurate locations of the receivers are typical for those surveyed optically. It is necessary to accommodate the effects of wind for hyperbolic location without allowing the effective speed to vary from path to path. This can be done in two ways, neither of which is satisfying.

The first accommodation is to let the necessarily spatially homogeneous effective speed vary by an amount equal to the variations from path to path, i.e., a standard deviation of 10 m/s (Table I, Hyperbolic Location 1). The second accommodation is to artificially increase the measured error in the difference in travel times from 16 μs to that which would be due to the change in lag due to path speed variations of $\delta c = \pm 10$ m/s over distances of the acoustic paths. An order-of-magnitude estimate of this effect can be obtained by using equal path lengths, L, given by the length scale of the array. The effect is

$$\sigma_\tau \approx \sqrt{(L\,\delta c/c^2)^2 + (L\,\delta c/c^2)^2}, \tag{1}$$

where to first order, the variation in travel time for one path is $L\,\delta c/c^2$ and σ_τ denotes the standard deviation of the difference in acoustic travel time between the animal and two

TABLE I. *A priori* distributions of independent variables involved in determining the location of a calling animal in air via hyperbolic and isodiachronic methods. Both methods yield distributions for animal location from the differences in simulated arrival times at five microphones. Hyperbolic location requires the effective speed to be the same for each acoustic path whereas isodiachronic location does not. Distributions (probability density functions) are Gaussian with indicated means and standard deviations except all are truncated at two standard deviations. "True" indicates a variable's mean is error-less. The *y* component of the wind is modeled for isodiachronic location but cannot be modeled in hyperbolic location. Instead, this wind is accounted for by including a variation of 10 m/s for the standard deviation of effective sound speed in hyperbolic location (method 1) or by artificially increasing the measured error in the lag from 16 μs to 0.006 49 s (method 2) via Eq. (1). *A priori* errors are zero for receiver one, the *y* and *z* coordinates of receiver two, and the *z* coordinate for receiver three. These coordinates merely define the origin and orientation of the coordinate system.

		A Priori distributions					
		Hyperbolic location 1		Hyperbolic location 2		Isodiachronic location	
Variable	Symbol	Mean	Std. Dev.	Mean	Std. Dev.	Mean	Std. Dev.
Cartesian	$r_i(x)$	True	0.02 m	True	0.02 m	True	0.02 m
Receiver	$r_i(y)$	"	"	"	"	"	"
Coordinate	$r_i(z)$	"	"	"	"	"	"
Cartesian	$u(x)$	0	0	0	0	0	0
Wind	$u(y)$	0	0	0	0	0	10
Component	$u(z)$	0	0	0	0	0	0
Sound speed	c	330	10	330	0	330	0
Lag	τ_{ij}	True	16 μs	True	0.006 49 s	True	16 μs

receivers. For $L=50$ m, $\delta c=10$ m/s, and $c=330$ m/s, we get $\sigma_\tau=0.00649$ s. This artificial increase is about two orders of magnitude greater than the 16 μs accuracy that can be obtained for the signal limited by noise (Table I, Hyperbolic Location 2).

There is no difficulty accommodating inhomogeneous effective speeds with isodiachronic location. In this case, the speed of sound has zero variation about the mean of 330 m/s, and the *y* component of the wind is given a standard deviation of 10 m/s about a mean of 0 m/s (Table I, Isodiachronic Location).

Following application of the sequential nonlinear Monte Carlo algorithm, incorrect animal locations are obtained when the effective speed is assumed to be spatially homogeneous (Table I, Hyperbolic Location 1). Indeed, the animal's 100% confidence limits for *y* are 102.0 to 108.1 m, but its actual *y* coordinate is 100 m. The 100% limits do not extend to infinity because the *a priori* distributions of error are truncated at two standard deviations. So given *a priori* distributions of receiver locations, travel time differences, and environmental variations, this hyperbolic location method always yields incorrect answers for the location of the animal.

If the second hyperbolic location model is used with large errors in the lags (Table I, Hyperbolic Location 2), the 100% confidence limits are: *x* between -312 and $+207$ m, *y* between 55 and 12 000 m, and *z* between -1200 and $+410$ m. These bounds contain the correct location of the animal, but they are so large as to be useless. The 95% confidence limits are: *x* between 13 and 33 m, *y* between 57 and 540 m, and *z* between -66 and $+15$ m. These bounds are about the same scale as the array itself, and still quite large and probably not useful.

With isodiachronic location, 95% confidence limits for the animal are x:16.6–20.5 m, y:98.8–101.7 m, z:3.5–40.5 m. These are statistically consistent with the correct location at (20,100,7) m. The large variation in *z* stems from the fact that the animal and receivers are nearly coplanar. Other confidence limits could be given but they are not shown because the point is that isodiachronic location yields a correct answer at a stringent confidence of 95%, and therefore at 100% confidence as well. This demonstrates that hyperbolic methods yield incorrect or useless locations whereas the isodiachronic method yields useful and statistically correct locations.

C. Global positioning system

The GPS is used to locate receivers from differences of travel time from synchronized emissions of electromagnetic waves from satellites. One of the largest sources of location error is the variation of the group speed of electromagnetic waves for different paths through the ionosphere.[1] If one uses a GPS receiver that monitors only the single L1 frequency, the typical residual after correcting for the GPS-broadcasted ionospheric correction is 4 m, but could be many times that amount.[27] These errors translate to location errors of about 30 m both horizontally and vertically. If one assumes locations are obtained using a hyperbolic technique, no accommodation can be made for the differences in effective speed from path to path, and these errors would be difficult to suppress without further information. In this situation, one could use an algorithm for location that accommodates variations in the effective speed on a path-by-path basis. Such algorithms would yield more accurate estimates of location than hyperbolic algorithms.

III. GEOMETRY OF ISODIACHRONS

Since there is a need for locating signals with high accuracy in spatially inhomogeneous fields of effective speed, it would be desirable to develop a geometrical interpretation of the problem as has been done when the effective speed is spatially homogeneous.[10,11,13,14]

A hyperboloid is the locus of points **s** whose difference in distance, d_{ij}, from two points is constant. These points satisfy

$$\|\mathbf{r}_i-\mathbf{s}\|-\|\mathbf{r}_j-\mathbf{s}\|=d_{ij}, \tag{2}$$

where the coordinates of the points (receivers here) are $\mathbf{r}_i$ and $\mathbf{r}_j$. Let t_i and t_j denote the time for sound to travel between the source and each receiver, respectively, and de-

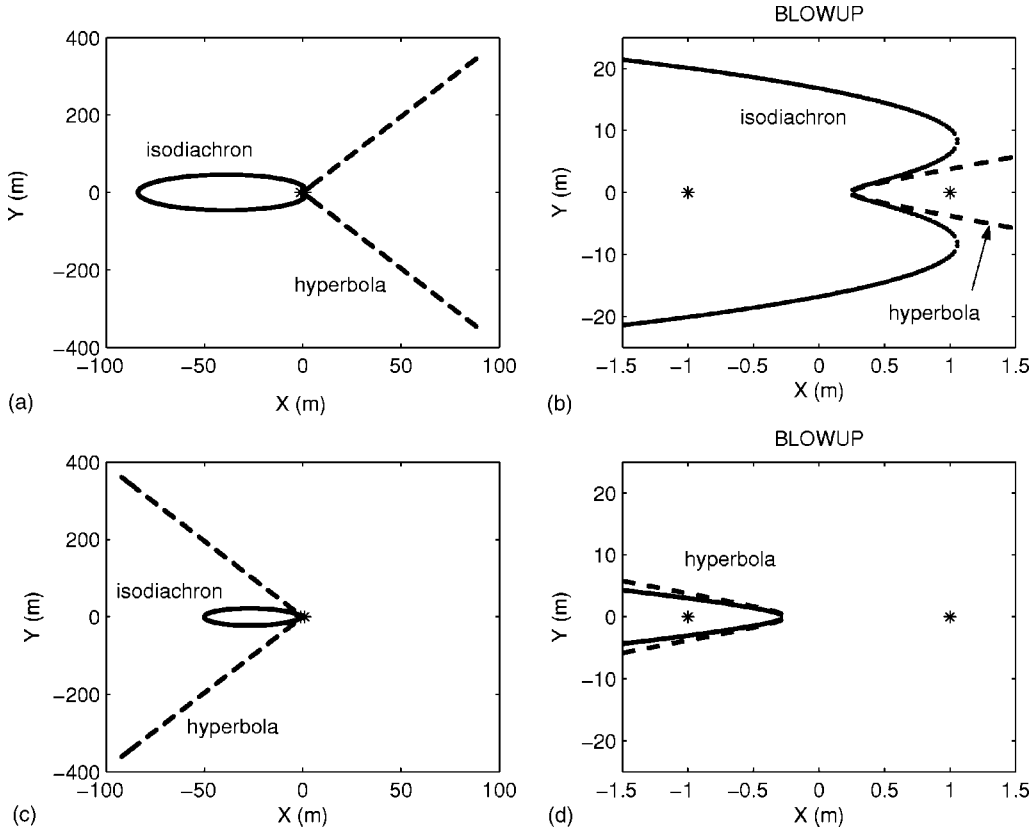

FIG. 1. A, B: Two-dimensional hyperbola (dashed) compared with two-dimensional isodiachron (solid). Locations of the two receivers (asterisks) are at Cartesian coordinates $(-1,0)$ and $(1,0)$. The effective speeds of sound between the calling animal and receivers one and two are 330 and 340 m s^{-1}, respectively. The lag, τ_{12}, is $+0.0015$ s. The hyperbola is computed for an effective speed of 330 m s^{-1}. C, D: Same except the lag is -0.0015 s.

fine the lag as $\tau_{ij} \equiv t_i - t_j$. When the effective speed is c, Eq. (2) is the same as

$$\|\mathbf{r}_i - \mathbf{s}\| - \|\mathbf{r}_j - \mathbf{s}\| = c\,\tau_{ij}, \tag{3}$$

which is described in Cartesian coordinates with a polynomial of degree two.

An isodiachron is defined to be the locus of points satisfying

$$t_i - t_j = \tau_{ij}, \tag{4}$$

where the effective speed depends on the spatial coordinates of the paths. Then Eq. (4) is

$$\frac{\|\mathbf{r}_i - \mathbf{s}\|}{c_i(\mathbf{s})} - \frac{\|\mathbf{r}_j - \mathbf{s}\|}{c_j(\mathbf{s})} = \tau_{ij}, \tag{5}$$

where $c_i(\mathbf{s})$ and $c_j(\mathbf{s})$ denote the effective speeds to receivers i and j, respectively, as a function of $\mathbf{s}$.

In some of what follows, it is useful to consider isodiachrons where $c_i(\mathbf{s})$ and $c_j(\mathbf{s})$ do not depend on location $\mathbf{s}$. This is called a ''class one isodiachron.'' Isodiachrons of other classes are those given by Eq. (5) for which $c_i(\mathbf{s})$ and $c_j(\mathbf{s})$ depend on $\mathbf{s}$. Paradoxically, class one isodiachrons are useful for estimating probability density functions for the location of an animal in all realistic situations where $c_i(\mathbf{s})$ and $c_j(\mathbf{s})$ *do* depend on $\mathbf{s}$ because of another algorithm that uses class one isodiachrons in a particular way.[18] This paradox is resolved in Sec. III A.

The two-dimensional isodiachron approximates a hyperbola in a limited region (Fig. 1). Unlike a hyperbola, isodiachrons contain no points at infinity when $c_i(\mathbf{s})$ is unequal to $c_j(\mathbf{s})$ and when the receivers are separated by a finite distance. Instead, the assumption that the difference in propagation time be constant and that the effective speeds differ, constrains such isodiachrons to finite regions of space (Fig. 1). The proof which follows is true for isodiachrons of *all* classes and for all realistic effective speeds as long as $c_i(\mathbf{s})$ and $c_j(\mathbf{s})$ differ.

We write the definition of an isodiachron

$$\tau_{ij} \equiv t_i - t_j = \frac{d_i}{c_i(\mathbf{s})} - \frac{d_j}{c_j(\mathbf{s})}, \tag{6}$$

where d_i and d_j are the distances between the animal and receivers i and j, respectively. By assumption, $c_i(\mathbf{s})$ is unequal to $c_j(\mathbf{s})$. For all points in space we have

$$d_i = d_j + \Delta, \tag{7}$$

where Δ must be less than or equal to the distance between the receivers, so

$$\Delta \leqslant |\mathbf{r}_i - \mathbf{r}_j| < \infty, \tag{8}$$

since the receiver separation, $|\mathbf{r}_i - \mathbf{r}_j|$, is finite. Substitute Eq. (7) into Eq. (6) and simplify to get

$$\tau_{ij} = d_j\left(\frac{1}{c_i(\mathbf{s})} - \frac{1}{c_j(\mathbf{s})}\right) + \frac{\Delta}{c_i(\mathbf{s})}. \tag{9}$$

All measured lags, τ_{ij}, are finite and the only way to obtain these finite values for $c_i(\mathbf{s}) \neq c_j(\mathbf{s})$ is to demand that d_j be

finite because Δ is finite [Eq. (8)]. Therefore, all points on an isodiachron are a finite distance from the receivers when $c_i(\mathbf{s}) \neq c_j(\mathbf{s})$.

Several facts concerning class one isodiachrons are useful. We derive an expression for $y(x)$, the locations of their x intercepts, and the bounds for their lags. Some of the more complicated algebraic expressions were obtained from a symbolic mathematical software program.

When the effective speeds, c_i and c_j, do not depend on $\mathbf{s}$, the isodiachron can be expressed in Cartesian coordinates with a polynomial of degree four.[18] The polynomial coefficients of degree three and four go to zero when c_i and c_j approach the same value c, leaving a second degree polynomial describing a hyperbola. For class one isodiachrons in two spatial dimensions, Eq. (5) reduces to

$$a_1 y^4 + a_2 y^2 + a_3 = 0, \tag{10}$$

where

$$a_1 \equiv \frac{c_j^4 - 2c_i^2 c_j^2 + c_i^4}{c_i^4 c_j^4}, \tag{11}$$

$$\begin{aligned} a_2 \equiv & 2(c_i^4 c_j^4)^{-1}(c_j^4 x^2 + c_j^4 x_0^2 + c_i^4 x^2 + c_i^4 x_0^2 - 2c_j^2 x^2 c_i^2 \\ & + 2c_j^4 x x_0 - 2c_j^2 c_i^2 x_0^2 - c_j^4 \tau_{ij}^2 c_i^2 - \tau_{ij}^2 c_i^4 c_j^2 - 2c_i^4 x x_0), \end{aligned} \tag{12}$$

$$\begin{aligned} a_3 \equiv & x^4(c_j^4 - 2c_i^2 c_j^2 + c_i^4)/(c_i^4 c_j^4) + (c_i^4 c_j^4)^{-1}(c_j^4 x_0^4 \\ & + 4c_j^4 x^3 x_0 + 6c_j^4 x^2 x_0^2 + 4c_j^4 x x_0^3 - 2c_j^2 x_0^4 c_i^2 + \tau_{ij}^4 c_i^4 c_j^4 \\ & - 4c_i^4 x^3 x_0 + 6c_i^4 x^2 x_0^2 - 4c_i^4 x x_0^3 - 2c_j^4 x^2 \tau_{ij}^2 c_i^2 \\ & + 4c_j^2 x^2 c_i^2 x_0^2 - 4c_j^4 x x_0 \tau_{ij}^2 c_i^2 - 2c_j^4 x_0^2 \tau_{ij}^2 c_i^2 + c_i^4 x_0^4 \\ & - 2\tau_{ij}^2 c_i^4 c_j^2 x^2 + 4\tau_{ij}^2 c_i^4 c_j^2 x x_0 - 2\tau_{ij}^2 c_i^4 c_j^2 x_0^2), \end{aligned} \tag{13}$$

where the receivers are at Cartesian coordinates $(-x_0,0)$ and $(x_0,0)$ and $x_0 > 0$. The solution for y in terms of x can be simplified by substituting $z = y^2$ in Eq. (10) which yields a quadratic equation in z. If z is real valued and non-negative, solutions for y are given by $\pm\sqrt{z}$ for a given value of x. Equation (10) describes a hyperbola when $c_i = c_j$.

The intersection of a class one isodiachron with the x axis occurs when y is zero in Eq. (5) which yields

$$c_j|x + x_0| - c_i|x - x_0| = c_i c_j \tau_{ij}, \tag{14}$$

where x is the x coordinate of $\mathbf{s}$. The solutions are

$$x = \frac{c_i c_j \tau_{ij} + (c_i + c_j)x_0}{c_i - c_j}; \quad x < -x_0, \tag{15}$$

$$x = \frac{c_i c_j \tau_{ij} + (c_i - c_j)x_0}{c_i + c_j}; \quad -x_0 \leq x \leq x_0, \tag{16}$$

$$x = \frac{c_i c_j \tau_{ij} - (c_i + c_j)x_0}{c_j - c_i}; \quad x_0 < x. \tag{17}$$

We now investigate the possible values for τ_{ij} given x_0, c_i and c_j. These are derived from Eqs. (15)–(17)

$$\tau_{ij} = \frac{-c_j(x + x_0) + c_i(x - x_0)}{c_i c_j}; \quad x < -x_0, \tag{18}$$

$$\tau_{ij} = \frac{c_j(x + x_0) + c_i(x - x_0)}{c_i c_j}; \quad -x_0 \leq x \leq x_0, \tag{19}$$

$$\tau_{ij} = \frac{c_j(x + x_0) - c_i(x - x_0)}{c_i c_j}; \quad x_0 < x. \tag{20}$$

For the first case ($x < -x_0$), τ_{ij} equals $-2x_0/c_j$ as $x \to -x_0$. For $x < -x_0$

$$\frac{\partial \tau_{ij}}{\partial x} = \frac{c_i - c_j}{c_i c_j}; \quad x < -x_0, \tag{21}$$

so when $c_i < c_j$

$$-2x_0/c_j \leq \tau_{ij} < \infty; \quad x < -x_0; \quad c_i < c_j. \tag{22}$$

Similarly when $c_i > c_j$

$$-\infty < \tau_{ij} \leq -2x_0/c_j; \quad x < -x_0; \quad c_i > c_j. \tag{23}$$

For the second case ($-x_0 \leq x \leq x_0$), τ_{ij} equals $-2x_0/c_j$ and $+2x_0/c_i$ at x equal to $-x_0$ and x_0, respectively. In between, we have

$$\frac{\partial \tau_{ij}}{\partial x} = 1/c_i + 1/c_j; \quad -x_0 \leq x \leq x_0, \tag{24}$$

which is positive. Thus the values of τ_{ij} increase linearly in this line segment and

$$-2x_0/c_j \leq \tau_{ij} \leq 2x_0/c_i; \quad -x_0 \leq x \leq x_0. \tag{25}$$

For the third case ($x_0 < x$), τ_{ij} equals $2x_0/c_i$ at $x = x_0$. For $x_0 < x$

$$\frac{\partial \tau_{ij}}{\partial x} = \frac{c_j - c_i}{c_i c_j}; \quad x_0 < x. \tag{26}$$

So when $c_i < c_j$,

$$2x_0/c_i < \tau_{ij} < \infty; \quad x_0 < x; \quad c_i < c_j \tag{27}$$

and when $c_i > c_j$

$$-\infty < \tau_{ij} < 2x_0/c_i; \quad x_0 < x; \quad c_i > c_j. \tag{28}$$

We see that τ_{ij} has a minimum value of $-2x_0/c_j$ when $c_i < c_j$ and that the x axis is crossed twice except when τ_{ij} is the minimum value in which case the class one isodiachron touches the x axis once at $-x_0$ (Fig. 2). Similarly, τ_{ij} has a maximum value of $2x_0/c_i$ when $c_i > c_j$, and the isodiachron crosses the x axis twice except when τ_{ij} is maximum in which case the isodiachron touches the x axis once at x_0 (Fig. 3).

We now prove that the lag bounds on the x axis ($\tau_{ij} \geq -2x_0/c_j$ for $c_i < c_j$ and $\tau_{ij} \leq 2x_0/c_i$ for $c_i > c_j$) are the bounds for all points on a class one isodiachron. This can be proved by showing that all such isodiachrons intersect the x axis because then the lag is constant everywhere on an isodiachron. We know that all class one isodiachrons are symmetric about the x axis because all class one isodiachrons have values of y given by $\pm\sqrt{z}$ [see sentences following Eq. (13)]. The isodiachron is a continuous function in $y(x)$ because it is a polynomial. For two points on an isodiachron given by $\pm y(x)$, there must then either be a curve joining them through infinity (which is impossible as shown above), or the curve must join them through finite values and thus

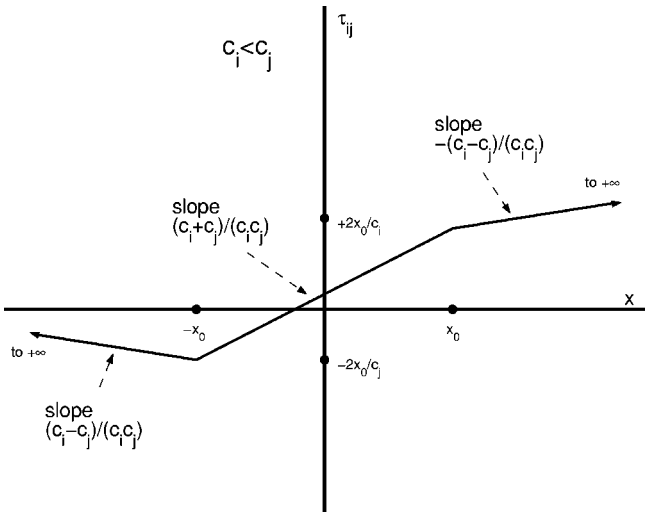

FIG. 2. The lags, τ_{ij}, for isodiachrons as a function of their x intercepts. Receivers i and j are at Cartesian (x,y) coordinates $(-x_0,0)$ and $(x_0,0)$, respectively. The effective speeds of the signal between receivers i and j and the isodiachron are c_i and c_j, respectively, and $c_i<c_j$. $\tau_{ij}=t_i-t_j$ where the times for the signal to travel between the isodiachron and receivers i and j are t_i and t_j respectively. Note that the lags must occur in the interval $-2x_0/c_j \leqslant \tau_{ij} < \infty$ [Eqs. (22), (25), and (27)].

cross the x axis at a value given by Eqs. (15–17). Thus the lag bounds given for class one isodiachrons on the x axis are valid for all class one isodiachrons because all class one isodiachrons touch the x axis.

A three-dimensional isodiachron can be formed by rotating the two-dimensional isodiachron around the x axis (Fig. 1). The closed form solution for isodiachronic location can yield four solutions from four receivers. This can be understood geometrically as follows. The first pair of receivers constrains the source to a class one isodiachron. A third receiver introduces a second isodiachron which can intersect the first one along two different closed curves (e.g., in the region between x between 0.5 and 1 in panel B of Fig. 1). A fourth receiver introduces a third isodiachron which can intersect the two closed curves at at most four points. In this case, a fifth receiver is needed to determine which of the four points is correct.

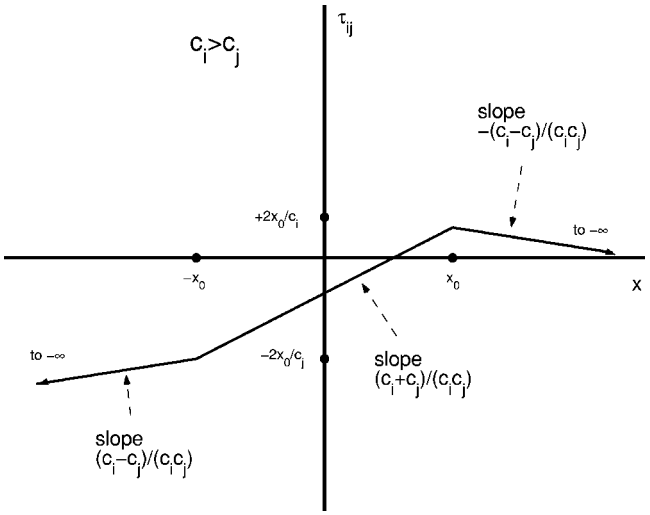

FIG. 3. Same as Fig. 2 except $c_i>c_j$. In this case all isodiachrons have lags $\tau_{ij} \leqslant 2x_0/c_i$ [Eqs. (23), (25), and (28)].

Because class one isodiachronic and hyperbolic surfaces can deviate significantly from one another in the vicinity of the receivers, hyperbolic locations can yield incorrect answers while isodiachronic locations are correct, even when accounting for errors.

A. Class one isodiachrons are useful when the effective speed is spatially inhomogeneous

The paradox is that class one isodiachrons are useful for estimating the probability density function for an animal's location when the effective speed varies in any realistic manner, including effects from advection. Understanding the paradox comes from the way this isodiachron is used by a Monte Carlo algorithm.[18]

A constellation is the minimum number of receivers needed to yield unambiguous solutions for location. For three-dimensional locations without prior knowledge of the animal's location, the constellation consists of four or five receivers, depending on the location of the animal.[18]

An analytical solution for the animal's location is available for any constellation.[18] The solution requires (1) the effective speeds between the animal and each receiver, (2) locations of the receivers, and (3) the values of the lags. When the effective speed includes advective effects, the algorithm needs to do an extra step because the effective speed depends on the location of the animal, but one does not initially know the location of the animal without using the analytical solution. A solution to this problem is given later, but for now it is important to state that no first guess for the animal's location is made by any hyperbolic location technique. The relevant part of the Monte Carlo algorithm is explained next.[18]

When the effective speeds are unaffected by advection, the Monte Carlo algorithm adopts any realistic *prior* probability density functions for (1) the effective speed between the animal and each receiver, (2) the errors in the Cartesian coordinate of each receiver in the constellation, and (3) the measured lags. A sample is drawn from each of the distributions yielding a set called a ''configuration.'' A configuration that does not yield at least one real-valued solution for location is discarded because the samples could not have jointly occurred. A ''valid configuration'' is one where there is at least one real-valued analytical solution for location. Each real-valued analytical solution for location is a point at which class one isodiachrons from all possible receiver pairs intersect. The Monte Carlo algorithm has established one set of effective speeds between the animal and each receiver in the constellation from the valid configuration. The Monte Carlo algorithm continues to find a sufficient number of valid configurations such that convergence is obtained for the probability distribution of the animal's location. The collection of effective speeds from all Monte Carlo runs provides an estimate for all the effective speeds that are consistent with the data, the cloud of possible animal locations, and the clouds of possible receiver locations.

Class one isodiachrons are a mathematically and computationally convenient and efficient means for obtaining the

distribution of the animal's location because they accommodate an analytical solution for location when the effective speed differs from path to path and they accommodate models for sound speed and advection that are realistic when used with the Monte Carlo algorithm.[18] More specifically, the analytical solution for location is derived[18] by using the fact that $\|\mathbf{r}_i-\mathbf{s}\|^2=c_i^2t_i^2$, and then subtracting the equation for $i=1$ from the equations for $i>1$ where c_i is a specified effective speed that is independent of the animal's location. When the equation for $i=1$ is subtracted from any other equation for $i>1$, the resulting equation specifies that the animal resides somewhere on the locus of points for which the difference in travel time to receivers $i>1$ and $i=1$ is a constant. This is a class one isodiachron. With a constellation, one has enough difference equations to yield an analytical solution for location.[18]

Consider an effective speed that is affected by advection, such as wind. A configuration is drawn from prior distributions of the (1) wind, (2) speeds, (3) receiver coordinates, (4) lags, and (5) the location of the animal, **s**. This configuration contains draws from the *prior* wind and source distributions. These were not drawn when advection was unimportant. One can always form a prior distribution for the location of the animal because one can use a uniform distribution in space with boundaries that are so large as to encompass every possible location. For example, one could know that sounds from a cricket would originate within 200 m of a receiver. Next, the effective speed between the animal and each receiver is obtained from

$$c_i=C_i+\mathbf{U}\circ(\mathbf{s}-\mathbf{r}_i)/d_i, \tag{29}$$

where C_i is the draw from the speed distribution (the scalar field), **U** is the draw from the vector wind distribution and the open circle denotes dot product. Note that this draw for the effective speed depends on a random guess for the location of the animal. The analytical solution for location is now obtained as before, yielding location $\mathbf{s}_1$. The closest real-valued solution, $\mathbf{s}_1$, to the randomly chosen location for the animal, **s**, is accepted if

$$|\mathbf{s}_1-\mathbf{s}|<\epsilon, \tag{30}$$

where ϵ is some small value such as 0.1 m. If all analytical solutions, $\mathbf{s}_1$, are complex, they are discarded and a fresh draw is made for a configuration. Otherwise, the effective speed is updated from Eq. (29) using $\mathbf{s}_1$ in place of **s**. This procedure iterates a maximum number of times. On each iteration the analytical solution for location is accepted if the difference between the analytical solution for **s** and the most recent guess for **s** is less than ϵ. We then have a valid configuration. The configuration is discarded if the maximum allowed number of iterations is exceeded, and one starts with fresh draws for the five categories of variables until one has sufficient numbers of valid configurations to yield accurate estimates of the distribution of the animal's location. Because effects from advection are incorporated into the effective speed, the geometrical interpretation for the analytical solution for location is based on class one isodiachrons as before. We see that realistic variations of advection and sound speed are accounted for in the probability distribution of the animal's location.

B. Example in air

Consider a two-dimensional geometry where five receivers are located at Cartesian coordinates (0,0), (25,0), (50,3), (30,40), and (5,30) m (Fig. 4). An animal is located at (22,2) m. The speed of sound is assumed to be a typical 330 m/s, and a wind is blowing in the positive y direction at 10 m/s. With R receivers there are

$$N_\tau=R(R-1)/2, \tag{31}$$

possible lags $(\tau_{ij}, i=1,\ldots,R-1; j=i+1,\ldots,R)$ so for $R=5$, we get $N_\tau=10$. All ten lags are computed without error and, for each, the isodiachron and hyperbola are drawn. The hyperbolas are drawn for an effective speed of 330 m/s. Some of the hyperbolas look like the isodiachrons and others do not (Fig. 5). Isodiachrons all intersect the animal location exactly, but the hyperbolas do not, as it is impossible for them to accommodate variations in effective speed from path to path with the hyperbolic assumption. No attempt has been made to find a single effective speed that minimizes the residuals from a central intersection point, but this is not important to do in this context because the hyperbolas would not intersect at a point anyway, and some of their shapes are quite different than the isodiachrons (Fig. 5).

The location of the animal in Fig. 4 coincides with the point of intersection of the isodiachrons because this example uses error-less values for the variables that determine location (lags, receiver locations, and effective speeds). The presence of errors dictates that there are an infinite number of possible animal locations consistent with measurements. With truncated prior distributions of error for the pertinent variables (lags, receiver locations, and effective speeds), the infinite number of possible locations can be confined to a finite region. The nonlinear Monte Carlo algorithm[18] draws from the prior distributions of these variables to find animal locations for which all ten isodiachrons intersect at one point. These locations form clouds of feasible locations of the animal. The feasible locations near the animal have sets of 10 isodiachrons that look like those in Fig. 4.

C. Example in ocean

Consider a two-dimensional geometry where five receivers are located at Cartesian coordinates (0,0), (4000,0), (1500,3000), $(-50,-2000)$, and $(2000,-3000)$ m (Fig. 6). Suppose these receivers are located near a zonal front where the speed of sound is 1500 m/s to the south and 1525 m/s to the north of the x axis (Fig. 6). Suppose a whale calls at $(3960,-20)$ m. Then the effective speed of sound is 1500 m/s for all receivers except the one at (1500,3000) m where it is 1524.8 m/s because the signal crosses the front to the north. Hyperbolic locations assume the effective speed is 1512.5 m/s. This is the average of the speeds on either side of the front. Isodiachrons and hyperbolas are drawn without data error.

Some of the hyperbolas look like isodiachrons, and others do not (Fig. 6). When isodiachronic location[18] is used to

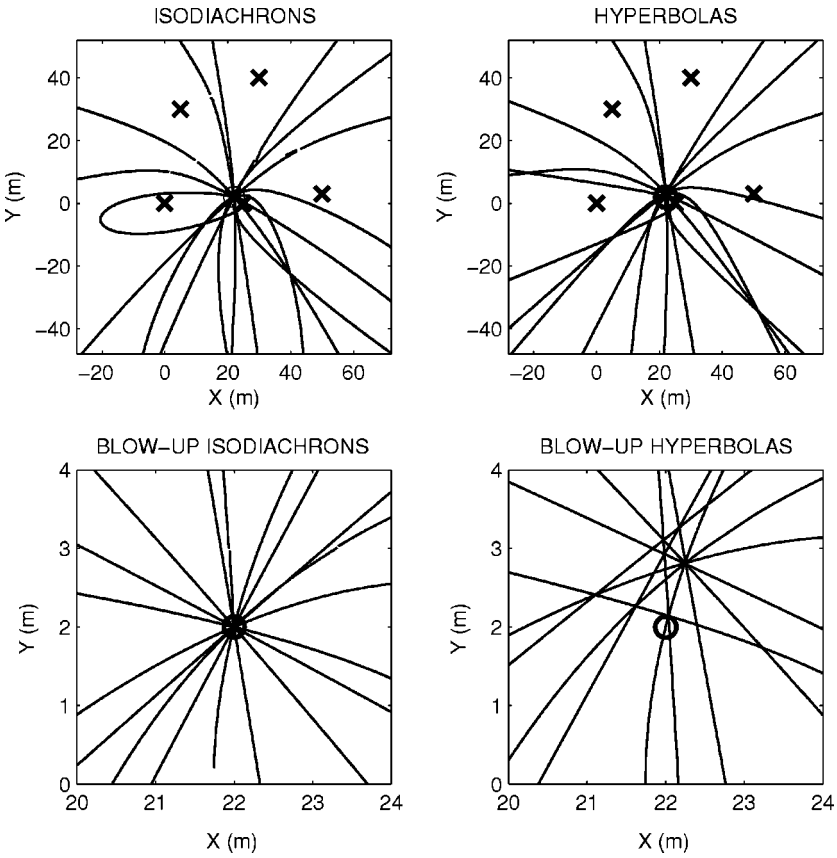

FIG. 4. *Left column*: The ten isodiachrons corresponding to the ten lags derived from an animal at Cartesian coordinate (22,2) m (circle) in air and recorded at five receivers (X's). One of the receivers at (25,0) m is close to the animal so its X is not resolved but is visible in Fig. 5. The bottom shows the isodiachrons within a few meters of the animal. *Right column*: Same except these are the ten hyperbolas. The speed of sound is 330 m/s and a spatially homogeneous wind is blowing in the positive *y* direction at 10 m/s. The hyperbolas are derived by assuming the effective speed of sound is 330 m/s. Note the hyperbolas do not intersect at the same point nor do they intersect the animal (bottom right). Some of the isodiachrons are similar to the hyperbolas, and some are quite different (Fig. 5).

locate the whale, the $N_\tau = 10$ isodiachrons always intersect at the same point. The hyperbolas can never intersect at the same point, and their mismatches indicate the inability of hyperbolic geometry to find a correct location when the effective speed differs from path to path. Even when one accounts for errors in the effective speeds, the lags, and the locations of the hydrophones, isodiachrons always intersect at the same point and hyperbolas do not.[18]

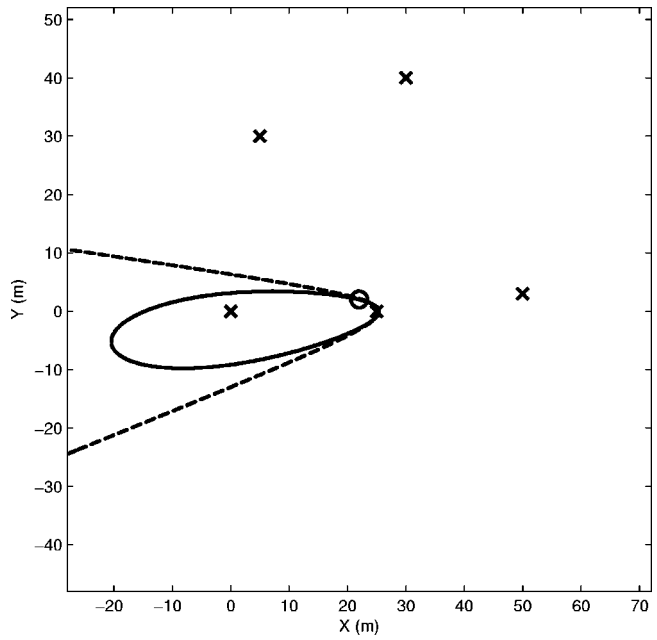

FIG. 5. Same as Fig. 4 except only the isodiachron (solid) and hyperbola (dashed) corresponding to one particular lag are shown.

D. Other examples

Isodiachrons could be used to locate animals when the effective speeds are greatly different from path to path. For example, a modeling study[28] indicates that low-frequency sounds from a fin whale could travel to hydrophones through different paths. Some receivers close to the whale could pick up only the first acoustic path through the sea, while other distant receivers could pick up only the acoustic path that propagates below the sea floor because the paths through the water could be blocked by seamounts. The effective speed through the water and solid Earth can differ by more than a factor of 2.[28]

There are other possibilities. Sounds created by some animals can reach receivers through both the air and the solid Earth.[29,30] Seals flap their flippers on the surface and the sound propagates in air and water to distant receivers.[31] All these animals could be located with isodiachrons.

IV. CONCLUSION

When one seeks accurate locations for a calling animal from measurements of the time differences of signals, consideration must be paid to the differences in effective speed along different paths if such differences exist. Differences in effective speed are significant enough in air and water to have led researchers to adopt models for location that allow the effective speeds to differ from path to path.[15–18] Path-to-path variations in effective speed are inconsistent with a geometrical interpretation based on a hyperbola. Instead, one can visualize a new geometrical shape, called an isodiachron, to interpret location in this situation. The isodiachron is the

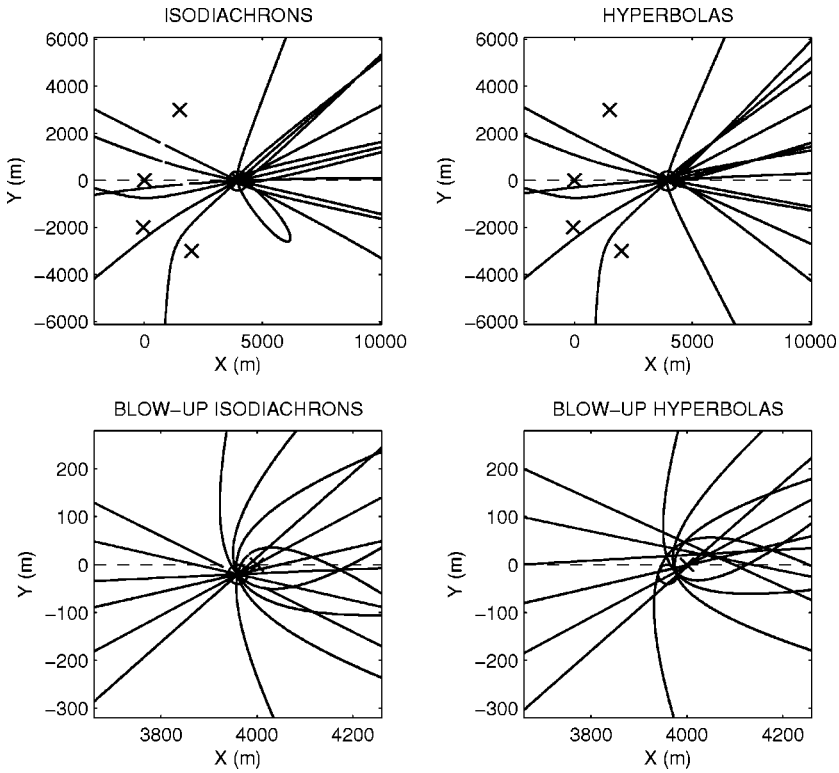

FIG. 6. *Left column*: The ten isodiachrons corresponding to the ten lags derived from a simulated call at Cartesian coordinate $(3960,-20)$ m (circle) in water and recorded at five hydrophones (X's). One of the hydrophones at (4000,0) m is close to the animal and can barely be made out on the bottom row where the isodiachrons are shown within a few hundreds of meters of the animal. *Right column*: Same except these are the ten hyperbolas. The speed of sound is 1500 and 1525 m/s on the lower and upper regions of the figures, respectively. The frontal region separating these speeds occurs at $y=0$ (dashed). The hyperbolas are derived by assuming the effective speed of sound is 1512.5 m/s, the average of the speeds on either side of the front. Note the hyperbolas do not intersect at the same point nor do they intersect the animal (bottom right). Some of the isodiachrons are similar to the hyperbolas, and some are quite different.

locus of points corresponding to a constant difference in travel time along straight paths between the animal and two receivers. Isodiachrons differ significantly in shape from hyperboloids for many problems of practical interest (Figs. 4–6).

It seems interesting to speculate why ancient Greek mathematicians did not think about isodiachrons. The hyperbola was discovered by them (pp. 280, 281, Vol II, Ref. 12). Why did they conceive of hyperbolas? Perhaps the answer to this question is not currently known due to the loss of ancient documents. But something is known about the motivation for geometry and in the use of a hyperbola during these times. The word ''geometry'' comes from the Greek words geo for Earth and metron which means to measure. The emphasis on measuring the Earth was a principal motivation for the Greek's development of this branch of mathematics.[12]

The earliest known written reference to a hyperbola mentions Menaechmus who used it to solve the problem of how long to make the side of a cube so as to double its volume, a problem that today is solved by knowing how to compute a cube root of a number (pp. 280, 281, Vol. II, Ref. 12). There are two ancient documents describing the origin of this problem. The first explains that God asked the Delians via an oracle to double the size of an altar to rid themselves of a plague (p. 257, Vol. I, Ref. 12). The workman did not know how to double a volume, and asked Plato for help, who himself did not know the method of solution. The second document explains that an ancient tragic poet portrayed Minos preparing a tomb for Glaucus in the shape of a cube whose sides were a hundred feet in length. There was a desire to double the volume as to be more suitable for royal burial (pp. 257–259, Vol. I, Ref. 12). Thus the hyperbola's first known reference occurs in the context of solving a practical problem.

The idea of measuring location from the propagation time of signals is conveniently done using electronic equipment developed in the modern age. It is plausible that ancient Greeks would not consider the isodiachron because it would perhaps have been too distant from the problems of their day, though they may have had the mathematical tools needed to derive the geometrical shape.

Besides allowing a general physical interpretation for location in spatially inhomogeneous media of effective speed, isodiachrons are the geometrical shapes that are intersected for an analytical solution for location[18] (Figs. 4, 6). Isodiachrons revert to hyperboloids when the effective speed is spatially homogeneous.

ACKNOWLEDGMENTS

I thank my family, Mary, Ari, and Maia, for their love and in giving me time to pursue this paper. I thank Andrew Jacobson, Eugene Terray, and the reviewers, Magnus Wahlberg and the anonymous reviewer, for their comments which greatly improved its content.

[1] *Global Positioning System: Theory and Applications, Volume I*, edited by B. W. Parkinson and J. J. Spilker, Jr. (American Institute of Aeronautics and Astronautics, Washington, DC, 1996), Vol. 163, p. 781.
[2] R. A. Walker, ''Some intense, low frequency, underwater sounds of wide geographic distribution, apparently of biological origin,'' J. Acoust. Soc. Am. **35**, 1816–1824 (1963).
[3] W. A. Tyrrell, ''Design of acoustic systems,'' in *Marine Bioacoustics*, edited by W. N. Tavolga (Pergamon, Oxford, 1964), pp. 65–86.
[4] W. A. Watkins and W. E. Schevill, ''Four hydrophone array for acoustic three-dimensional location,'' Woods Hole Oceanographic Technical Report No. 71-60, 1971.
[5] W. A. Watkins and W. E. Schevill, ''Listening to Hawaiian Spinner Porpoises, *STENELLA CV. LONGIROSTRIS.* with a three-dimensional hydrophone array,'' J. Mammal. **55**, 319–328 (1974).
[6] W. C. Cummings and D. V. Holliday, ''Passive acoustic location of bow-

head whales in a population census off Point Barrow, Alaska,'' J. Acoust. Soc. Am. **78**, 1163–1169 (1985).
[7] C. Clark, W. T. Ellison, K. Beeman, ''Acoustic tracking of migrating bowhead whales,'' *Oceans 86* (IEEE Oceanic Eng. Soc., New York, 1986), pp. 341–346.
[8] B. Mohl, M. Wahlberg, P. T. Madsen, L. A. Miller, and A. Surlykke, ''Sperm whale clicks: Directionality and source level revisited,'' J. Acoust. Soc. Am. **107**, 638–648 (2000).
[9] C. O. Tiemann and M. B. Porter, ''A comparison of model-based and hyperbolic localization techniques as applied to marine mammal calls,'' J. Acoust. Soc. Am. **114**, 2406 (2003).
[10] N. Marchand, ''Error distributions of best estimate of position from multiple time difference hyperbolic networks,'' IEEE Trans. Aerosp. Navigational Electron. **11**, 96–100 (1964).
[11] R. O. Schmidt, ''A new approach to geometry of range difference location,'' IEEE Trans. Aerosp. Electron. Syst. **AES-8**, 821–835 (1972).
[12] I. Thomas, *Greek Mathematical Works, Vols. I and II, Aristarchus to Tappus of Alexendria* (Harvard University Press, Cambridge, 1939).
[13] H. C. Schau and A. Z. Robinson, ''Passive source localization employing intersecting spherical surfaces from time-of-arrival differences,'' IEEE Trans. Acoust., Speech, Signal Process. **ASSP-35**, 1223–1225 (1987).
[14] J. Hoshen, ''The GPS equations and the problem of Apollonius,'' IEEE Trans. Aerosp. Electron. Syst. **32**, 1116–1124 (1996).
[15] H. T. Vincent ''Models, algorithms, and measurements for underwater acoustic positioning,'' Ph.D. dissertation, University of Rhode Island, Kingston, RI, 2001.
[16] H. T. Vincent and Sau-Lon J. Hu, ''Geodetic position estimation for underwater acoustic sensors,'' US Patent No. 6,028,823 (22 Feb., 2000).
[17] H. T. Vincent and Sau-Lon J. Hu, ''Method and system for determining underwater effective sound velocity,'' US Patent No. 6,388,948 (14 May, 2002).
[18] J. L. Spiesberger and M. Wahlberg, ''Probability density functions for hyperbolic and isodiachronic location,'' J. Acoust. Soc. Am. **112**, 3046–3052 (2002).
[19] M. Wahlberg, B. Mohl, and P. Madsen, ''Estimating source position accuracy of a large-aperture hydrophone array for bioacoustics,'' J. Acoust. Soc. Am. **109**, 397–406 (2001).
[20] I. Magyar, W. M. Schleidt, and D. Miller, ''Localization of sound producing animals using the arrival time differences of their signals at an array of microphones,'' Experientia **34**, 676–677 (1978).
[21] S. Mitchell and J. Bower, ''Localization of animal calls via hyperbolic methods,'' J. Acoust. Soc. Am. **97**, 3352–3353 (1995).
[22] J. M. Burt, ''Use of a radio microphone array to study banded-wren song interactions at the neighborhood level,'' J. Acoust. Soc. Am. **108**, 2583 (2000).
[23] M. Wahlberg, J. Tougaard, and B. Mohl, ''Localizing bitterns Botaurus stellaris with an array of non-linked microphones,'' Bioacoustics **13**, 233–245 (2003).
[24] M. Wahlberg, G. Ramos-Fernandez, F. Ugarte, B. Mohl, and M. Rasch, ''Recording spider monkeys (*Ateles geoffroyi*) with a microphone array,'' PhD. dissertation, Chapter IX, Centre for Sound Communication, Institute of Biology, U. Southern Denmark, 2002.
[25] M. S. Dantzker, G. B. Deane, and J. W. Bradbury, ''Directional acoustic radiation in the strut display of male Sage Grouse *Centrocercus Urophasianus*,'' J. Exp. Biol. **202**, 2893–2909 (1999).
[26] C. W. Helstrom, *Statistical Theory of Signal Detection* (Pergamon, New York, 1975), pp. 276, 470.
[27] Global Positioning System standard positioning service performance standard, OASD(C31)/ ODASD (C3ISR)/Space Systems, Attn: Assistant for GPS, Positioning and Navigation, 6000 Defense Pentagon, Washington, DC 20301-6000, p. 54. Oct. 2001.
[28] V. Premus and J. L. Spiesberger, ''Can acoustic multipath explain finback *B. physalus* 20-Hz doublets in shallow water?,'' J. Acoust. Soc. Am. **101**, 1127–1138 (1997).
[29] P. M. Narins, ''Frog communication,'' Sci. Am. **263**, 78–83 (1995).
[30] T. Reuter, S. Nummela, and S. Hemilä, ''Elephant hearing,'' J. Acoust. Soc. Am. **104**, 1122–1123 (1998).
[31] M. Wahlberg, S. G. Lunneryd, and H. Westerberg, ''The source level of harbour seal flipper slaps,'' Aquatic Mammals **28.1**, 90–92 (2002).

The effect of recording and analysis bandwidth on acoustic identification of delphinid species

Julie N. Oswald[a)]
Scripps Institution of Oceanography, University of California, San Diego, La Jolla, California 92093

Shannon Rankin and Jay Barlow
National Marine Fisheries Service, Southwest Fisheries Science Center, La Jolla, California 92037

(Received 16 March 2004; revised 13 August 2004; accepted 16 August 2004)

Because many cetacean species produce characteristic calls that propagate well under water, acoustic techniques can be used to detect and identify them. The ability to identify cetaceans to species using acoustic methods varies and may be affected by recording and analysis bandwidth. To examine the effect of bandwidth on species identification, whistles were recorded from four delphinid species (*Delphinus delphis, Stenella attenuata, S. coeruleoalba*, and *S. longirostris*) in the eastern tropical Pacific ocean. Four spectrograms, each with a different upper frequency limit (20, 24, 30, and 40 kHz), were created for each whistle ($n=484$). Eight variables (beginning, ending, minimum, and maximum frequency; duration; number of inflection points; number of steps; and presence/absence of harmonics) were measured from the fundamental frequency of each whistle. The whistle repertoires of all four species contained fundamental frequencies extending above 20 kHz. Overall correct classification using discriminant function analysis ranged from 30% for the 20-kHz upper frequency limit data to 37% for the 40-kHz upper frequency limit data. For the four species included in this study, an upper bandwidth limit of at least 24 kHz is required for an accurate representation of fundamental whistle contours. © *2004 Acoustical Society of America.*
[DOI: 10.1121/1.1804635]

PACS numbers: 43.80.Ka [WWA] Pages: 3178–3185

I. INTRODUCTION

Shipboard cetacean abundance surveys have traditionally relied on visual line transect methods (Holt, 1987; Wade and Gerrodette, 1993; Barlow, 1995; Jaramillo-Legorreta *et al.*, 1999; Carretta *et al.*, 2000; Jefferson, 2000; Buckland *et al.*, 2001; Hammond *et al.*, 2002). Visual detection and identification of cetaceans can be challenging as these animals spend most of their lives completely under water. Many cetacean species produce characteristic calls that propagate well under water (Richardson *et al.*, 1995), and therefore acoustic techniques can be used to detect and identify them. Because of this, towed hydrophone arrays are becoming increasingly common elements of cetacean abundance surveys (Thomas *et al.*, 1986; Leaper *et al.*, 1992; Clark and Fristrup, 1997; Goold 1998; Norris *et al.*, 1999; Gordon *et al.*, 2000; Oswald *et al.*, 2003).

The ability to identify cetaceans to species using acoustic methods varies. Many large whales, including blue whales [*Balaenoptera musculus* (Thompson *et al.*, 1996; Stafford *et al.*, 1999)], fin whales [*Balaenoptera physalus* (Thompson *et al.*, 1992)], and sperm whales [*Physeter macrocephalus* (Weilgart and Whitehead, 1993; Goold and Jones, 1995)], produce stereotyped calls that are easily recognized. The calls produced by many dolphin species are more variable, making acoustic identification of these species difficult (Oswald *et al.*, 2003).

Time and frequency characteristics measured from spectrograms have been used to classify delphinid whistles to species in several studies (Steiner, 1981; Wang *et al.*, 1995; Matthews *et al.*, 1999; Rendell *et al.*, 1999; Oswald *et al.*, 2003). These studies have had varying degrees of success, ranging from 28% correct classification of ten species (Matthews *et al.*, 1999) to 70% correct classification of five species (Steiner, 1981). These correct classification scores are significantly higher than expected by chance, but are lower than the usual standards applied to visual identification during shipboard surveys (i.e., near certainty).

The bandwidth with which sounds are recorded and analyzed may have an effect on the ability to classify them to species. Analysis bandwidths vary among studies and are not always reported. Steiner (1981) reported an analysis bandwidth of 0–32 kHz, Wang *et al.* (1995) an analysis bandwidth of 0–25 kHz, and Oswald *et al.* (2003) an analysis bandwidth of 20 Hz to 20 kHz. These bandwidths may not be sufficient to provide complete, accurate representations of vocal repertoires because ultrasonic frequencies (above 20 kHz) are produced by many odontocete species. Whistles with fundamental frequencies extending into the ultrasonic range have been reported for several delphinid species, including spinner dolphins (*Stenella longirostris*) and Atlantic spotted dolphins [*S. frontalis* (Lammers *et al.*, 1997, 2003)], and white-beaked dolphins [*Lagenorhynchus albirostris* (Rasmussen and Miller, 2002)]. Thus, classification errors may be due to inaccurate whistle measurements resulting from bandwidth limitations.

The objectives of this study are twofold: (1) to evaluate the extent to which four delphinid species recorded in the eastern tropical Pacific ocean produce whistles with funda-

a)Electronic mail: joswald@ucsd.edu

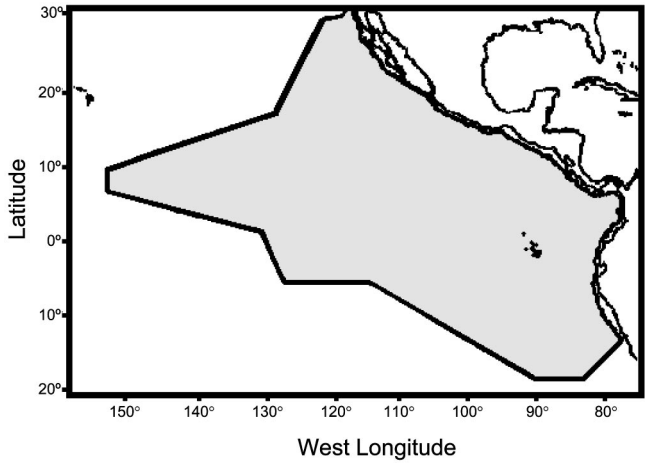

FIG. 1. Eastern tropical Pacific ocean study area for ''*Stenella* Abundance Research'' (STAR2000) survey.

mental frequencies extending into the ultrasonic range, and (2) to examine the effect of increasing bandwidth on acoustic species identification.

II. METHODOLOGY

Recordings were made during the ''*Stenella* Abundance Research'' (STAR2000) survey conducted in the eastern tropical Pacific ocean from 28 July to 9 December 2000. The study area extended from the United States/Mexico border southward to the territorial waters of Peru, and from the continental shores of the Americas to the longitude of Hawaii (Fig. 1). Visual line-transect methods were used to survey all cetaceans encountered in the study area (Kinzey *et al.*, 2001).

A hydrophone array was towed at a depth of 4-6 m approximately 200 m behind the NOAA ship *McArthur* while traveling at a survey speed of 10 kt. The depth of the array was periodically monitored using a *Suunto Solution Nitrox* dive computer. Two calibrated arrays were used during the survey: (1) a five-element array (flat frequency response ± 4 dB from 2 to 45 kHz at -132 dB *re* 1v/μPa after internal amplification), and (2) a three-element array (flat frequency response ± 3 dB from 2 to 120 kHz at -164 dB *re* 1v/μPa after internal amplification). The three-element array was used during 2 of the 29 recording sessions that were included in the analysis. A total of 17 whistles from these two encounters were included in the analysis (versus 467 whistles from 27 recording sessions using the five-element array). Any differences in sensitivity between the two arrays are therefore not likely to have had a significant effect on the results. Also, the selection of whistles was based on a signal-to-noise ratio, which did not differ between the two arrays. An acoustic technician monitored signals from two hydrophones in the array using a stereo headset and custom-written software that displayed real-time scrolling spectrograms. Recordings were made using custom software that recorded signals directly to computer hard drive via an analog-to-digital conversion card (*Data Translation DT-3809*). Recordings were made using sampling rates between 100 and 200 kilo-samples/second. Anti-aliasing filters were applied prior to recording.

Based on sample sizes of acoustic recordings made during the survey, whistles of four delphinid species were chosen for analysis: short-beaked common dolphins, *Delphinus delphis*; pantropical spotted dolphins, *Stenella attenuata*; striped dolphins, *S. coeruleoalba*; and spinner dolphins. Only recordings of groups that had been visually identified to species and observed to contain only one species were included in the analysis. Because it is possible that some recordings identified as ''single species'' may contain faint vocalizations produced by other species in the area, only ''loud and clear'' whistles were analyzed. Whistles were considered to be ''loud and clear'' if they were at least 9 dB louder than background noise.

Richardson *et al.* (1995) suggest that the maximum detection range for many delphinid species is on the order of 1 km. To be conservative, we assumed that whistles detected within 3 km of the array would be of sufficient quality for analysis. To avoid including whistles produced by dolphins other than those being observed and recorded, recordings made within 3 km of any other delphinid groups were excluded from the analysis. Distance was calculated between the location of the ship at the beginning of the recording session in question and the location of the initial sighting of the next group of dolphins encountered (based on angle and reticle measurements read from binoculars). Distance was also calculated between the location of the ship at the beginning of the recording session in question and the location of the previous group of dolphins encountered when they were last seen. Any recording session that occurred within 3 km of either the next or previous sighting was excluded from the analysis.

Fifty percent of the loud and clear whistles recorded during each acoustic encounter were randomly selected for analysis, up to a maximum of 30 whistles per encounter. It

TABLE I. Number of recording sessions and number of whistles included in the analysis (n) for each species. Percentages of whistles containing at least one off-scale variable when measured with an upper bandwidth limit of 20, 24, 30, and 40 kHz are given in the last four columns.

Species	No. of recording sessions	n	20 kHz	24 kHz	30 kHz	40 kHz
Short-beaked common dolphin	11	163	28%	8%	1%	0%
Spotted dolphin	5	100	43%	9%	3%	0%
Striped dolphin	9	104	11%	0%	0%	0%
Spinner dolphin	4	117	27%	4%	0%	0%

TABLE II. Descriptive statistics (means, with standard deviations in parentheses underneath) for measured whistle variables. Maximum frequency and ending frequency increased significantly with increasing upper bandwidth limit for all species except striped dolphins (one-way ANOVA, $\alpha = 0.05$). Significant P-values are underlined.

Species	Upper bandwidth limit (kHz)	Beginning frequency (kHz)	Ending frequency (kHz)	Minimum frequency (kHz)	Maximum frequency (kHz)	Duration (s)	No. of inflection points	No. of steps
Short-beaked common dolphin	20	11.8	12.4	8.7	15.4	0.68	1.7	1.2
		(3.8)	(4.8)	(2.3)	(2.7)	(0.43)	(1.5)	(1.6)
	24	12.3	13.8	8.7	16.7	0.70	1.8	1.2
		(4.3)	(4.8)	(2.3)	(3.5)	(0.42)	(1.5)	(1.7)
	30	12.6	14.1	8.6	17.5	0.75	1.8	1.2
		(4.7)	(5.4)	(2.3)	(4.4)	(0.44)	(1.5)	(1.8)
	40	12.9	14.1	8.6	17.7	0.75	1.8	1.2
		(5.2)	(5.4)	(2.3)	(4.6)	(0.44)	(1.5)	(1.7)
	P	0.31	0.003	0.99	<0.001	0.55	0.84	0.93
Spotted dolphin	20	10.3	13.9	9.0	16.0	0.56	1.1	2.3
		(4.4)	(4.9)	(3.9)	(3.6)	(0.42)	(1.9)	(2.6)
	24	10.4	15.6	9.0	18.4	0.60	1.2	2.7
		(4.5)	(5.1)	(3.9)	(4.1)	(0.40)	(1.8)	(3.3)
	30	10.4	16.1	9.0	18.9	0.62	1.2	2.8
		(4.5)	(5.6)	(3.9)	(4.4)	(0.40)	(1.8)	(3.4)
	40	10.4	16.8	9.0	19.4	0.63	1.2	2.8
		(4.5)	(6.4)	(3.9)	(5.2)	(0.40)	(1.8)	(3.4)
	P	0.99	0.01	1.0	<0.001	0.59	0.86	0.77
Striped dolphin	20	10.4	12.5	8.6	15.1	0.61	1.6	1.6
		(3.4)	(3.9)	(2.1)	(2.5)	(0.36)	(1.8)	(2.0)
	24	10.6	12.8	8.5	15.9	0.64	1.7	1.7
		(3.8)	(3.5)	(2.1)	(3.3)	(0.37)	(1.8)	(2.1)
	30	10.6	12.8	8.5	15.9	0.64	1.7	1.7
		(3.8)	(3.5)	(2.1)	(3.3)	(0.37)	(1.8)	(2.1)
	40	10.6	12.8	8.5	15.9	0.64	1.7	1.7
		(3.8)	(3.5)	(2.1)	(3.3)	(0.37)	(1.8)	(2.1)
	P	0.97	0.70	0.99	0.17	0.92	0.96	0.94
Spinner dolphin	20	12.8	13.0	10.8	15.8	0.55	1.8	0.87
		(3.9)	(4.9)	(3.1)	(3.1)	(0.46)	(3.8)	(1.5)
	24	13.5	14.6	11.1	17.4	0.66	2.0	0.98
		(4.5)	(4.7)	(3.7)	(4.0)	(0.49)	(3.8)	(1.7)
	30	13.7	15.0	11.1	17.8	0.67	2.0	0.98
		(4.7)	(5.1)	(3.7)	(4.4)	(0.49)	(3.8)	(1.7)
	40	13.7	15.0	11.1	17.8	0.67	2.0	0.98
		(4.7)	(5.1)	(3.7)	(4.4)	(0.49)	(3.8)	(1.7)
	P	0.52	0.003	0.87	0.001	0.26	0.73	0.99

was assumed that this degree of subsampling would allow a sufficient sample size to be obtained while minimizing the risk of over-sampling groups or individuals (which can lead to non-independence of data). Overlapping whistles were only included in the data set if each individual whistle contour could be discerned without question.

Four spectrograms (512-point FFT), each with a different upper frequency limit (20, 24, 30, and 40 kHz), were created for each whistle using commercially available sound analysis software, ''*SpectraPlus*.'' Eight variables were measured from the fundamental frequency of each whistle: (1) beginning frequency (Hz), (2) ending frequency (Hz), (3) minimum frequency (Hz), (4) maximum frequency (Hz), (5) duration (ms), (6) number of inflection points (defined as a change from positive to negative or negative to positive slope), (7) number of steps (defined as a sudden jump in frequency over a short time period), and (8) presence/absence of harmonics (a binary variable).

Following Oswald *et al.* (2003), multivariate discriminant function analysis (DFA) was used to classify whistles to species based on spectrographic measurements. Prior to running DFA, continuous variables (frequency variables, duration, and number of steps and inflection points) were tested for normality and were square-root or log transformed as necessary. The binary variable (presence/absence of harmonics) was coded as dummy variables. Discriminant function analysis classifies whistles to prespecified groups based on orthogonal linear functions derived from the measured variables. Some whistles were missing measurements for one or more variables because a portion of the whistle extended beyond the upper bandwidth limit. These whistles were excluded from the DFA, resulting in different sample sizes for the different upper bandwidth limit data sets.

A modified jackknife, or cross-validation, method was used to calculate correct classification scores for DFAs. Each recording session was omitted from the total sample and new

TABLE III. Classification results of discriminant function analysis for the 20-kHz upper bandwidth limit data. Percentages of whistles correctly classified for each species are in bold. Correct classification scores that are significantly different (χ^2 test, $\alpha=0.05$) than expected by chance alone are underlined and P-values are given in the sixth column. The number of whistles included in the analysis for each species (n) is given in the last column. Overall, 30% of whistles were classified to the correct species. This is significantly greater ($P=0.02$) than the 25% that would be expected by chance alone.

	Predicted species					
Actual species	Short-beaked common dolphin	Spotted dolphin	Striped dolphin	Spinner dolphin	P	n
Short-beaked common dolphin	**37%**	16%	20%	27%	0.003	118
Spotted dolphin	21%	**23%**	32%	24%	0.76	56
Striped dolphin	24%	32%	**16%**	28%	0.05	93
Spinner dolphin	19%	18%	21%	**42%**	<0.001	85

discriminant functions were calculated for classification of the omitted whistles. The discriminant functions calculated using this method were therefore created from data independent of the whistles being classified. This helped ensure that whistles were classified based on species-specific characteristics rather than group- or individual-specific characteristics. To evaluate correct classification scores, it is necessary to compare them to what would be expected by chance alone. Chi-square was used to test whether correct classification was significantly greater than expected by chance alone. Statistical significance was evaluated at $\alpha=0.05$ without corrections for multiple testing.

III. RESULTS

A total of 484 whistles from 29 different recording sessions were included in the analysis (Table I). Some whistle variables could not be determined if a portion of the fundamental frequency of the whistle extended beyond the upper limit of the analysis bandwidth. These variables were labeled as ''off-scale'' variables. The percent of whistles with off-scale variables ranged from 11% for striped dolphins to 43% for spotted dolphins when the upper bandwidth limit was 20 kHz (Table I). When the upper bandwidth limit was increased to 24 kHz, the percent of whistles with at least one off-scale variable decreased for every species, ranging from 0% for striped dolphins to 9% for spotted dolphins. An additional 6 kHz increase in upper bandwidth limit reduced the percent of whistles with off-scale variables even further. No whistles had off-scale variables when the upper bandwidth limit was 40 kHz.

Descriptive statistics (means and standard deviations) for all bandwidth limit data are given in Table II. Only maximum and ending frequency showed significant differences with increasing upper bandwidth limit (one-way ANOVA, $\alpha=0.05$). Maximum and ending frequency increased significantly with increasing upper bandwidth limit in all species except striped dolphins.

Results of the DFAs are given in Tables III–VI. For all bandwidths, both overall percent correct classification (30%–37%) and percent correct classification of spinner dolphin whistles (37%–42%) were significantly greater than the 25% expected by chance alone (χ^2 tests; overall, $P<0.05$; spinner dolphins, $P<0.003$). When the upper bandwidth limit was 20 kHz, percent correct classification was not significantly different than chance for spotted dolphins (23%, χ^2 test, $P=0.76$) and was significantly less than chance for striped dolphins (16%, χ^2 test, $P=0.05$). For both species, percent correct classification increased to significantly greater than chance when the upper bandwidth limit was increased to 24 kHz (χ^2 tests; spotted dolphins, 40%, $P=0.002$; striped dolphins, 36%, $P=0.01$), and remained significantly greater than chance at all subsequent bandwidths. In contrast, the percent of short-beaked common dolphin whistles that were correctly classified was significantly greater than chance (37%, χ^2 test, $P=0.003$) when the upper

TABLE IV. Classification results of discriminant function analysis for the 24-kHz upper bandwidth limit data. Percentages of whistles correctly classified for each species are in bold. Correct classification scores that are significantly different (χ^2 test, $\alpha=0.05$) than expected by chance alone are underlined and P-values are given in the sixth column. The number of whistles included in the analysis for each species (n) is given in the last column. Overall, 37% of whistles were classified to the correct species. This is significantly greater ($P<0.001$) than the 25% that would be expected by chance alone.

	Predicted species					
Actual species	Short-beaked common dolphin	Spotted dolphin	Striped dolphin	Spinner dolphin	P	n
Short-beaked common dolphin	**32%**	19%	30%	19%	0.06	150
Spotted dolphin	15%	**40%**	25%	20%	0.002	91
Striped dolphin	22%	23%	**36%**	19%	0.01	104
Spinner dolphin	19%	15%	24%	**42%**	<0.001	112

TABLE V. Classification results of discriminant function analysis for the 30-kHz upper bandwidth limit data. Percentages of whistles correctly classified for each species are in bold. Correct classification scores that are significantly different (χ^2 test, $\alpha=0.05$) than expected by chance alone are underlined and P-values are given in the sixth column. The number of whistles included in the analysis for each species (n) is given in the last column. Overall, 36% of whistles were classified to the correct species. This is significantly greater ($P<0.001$) than the 25% that would be expected by chance alone.

	Predicted species					
Actual species	Short-beaked common dolphin	Spotted dolphin	Striped dolphin	Spinner dolphin	P	n
Short-beaked common dolphin	**29%**	20%	31%	20%	0.27	161
Spotted dolphin	13%	**42%**	25%	20%	<0.001	96
Striped dolphin	19%	21%	**40%**	20%	<0.001	104
Spinner dolphin	21%	15%	27%	**37%**	0.003	117

bandwidth limit was 20 kHz and decreased to not significantly different than chance when the upper bandwidth limit was increased to 24 kHz (32%, χ^2 test, $P=0.06$), 30 kHz (29%, χ^2 test, $P=0.27$), and 40 kHz (30%, χ^2 test, $P=0.21$).

IV. DISCUSSION

The production of clicks containing ultrasonic components is common in several dolphin species (Au, 1980; Kamminga and Wiersma, 1981; Wiersma, 1982; Dawson, 1991; Au, 1993; Lammers *et al.*, 2003), and delphinid whistles often have harmonic components that extend well above 20 kHz (Lammers *et al.*, 2003). In contrast, the production of whistles with fundamental frequencies extending into the ultrasonic range has been documented for few species (Lammers *et al.*, 1997; Au *et al.*, 1999; Rasmussen and Miller, 2002; Lammers *et al.*, 2003). The whistle repertoires of all four species examined in this study contained whistles with fundamental frequencies extending into the ultrasonic range. While all species produced high-frequency whistles, some used high frequencies more often than others. For example, 43% of spotted dolphin whistles had fundamental frequencies that extended beyond 20 kHz, compared to only 11% of striped dolphin whistles (Table I).

The presence of whistles with fundamental frequencies extending beyond the upper limit of the analysis bandwidth can lead to inaccurate representations of whistle contours and have an adverse effect on the ability to classify whistles to species. For example, the spotted dolphin whistle shown in Fig. 2 has an ending frequency of 39 kHz. When this whistle was analyzed using an upper bandwidth limit of less than 40 kHz, it was impossible to determine not only ending frequency, but also maximum frequency and whistle duration. This whistle also has harmonics that were completely missed when the upper bandwidth limit was less than 30 kHz.

In addition to this loss of information, the presence of off-scale variables can lead to misrepresentations of whistles. The fundamental contour of the striped dolphin whistle shown in Fig. 3 appears to be entirely below 20 kHz when the upper bandwidth limit is 20 kHz [Fig. 3(a)]. When the upper bandwidth limit is increased to 24 kHz it becomes apparent that this contour does contain energy above 20 kHz [Fig. 3(b)]. For this whistle, duration, beginning frequency, and maximum frequency were all underestimated when the upper bandwidth limit was 20 kHz. This whistle also has a harmonic component that was missed when the upper bandwidth limit was 20 kHz.

Overall, for the species in this study, loss of information and misrepresentation had the greatest effect on measurements of maximum and ending frequency. Both variables increased significantly with increasing upper bandwidth limit for every species except striped dolphins (Table II).

Increased accuracy of whistle measurements resulting from increasing bandwidth led to greater overall success in acoustic species identification. Overall correct classification increased from 30% to 37% when the upper bandwidth limit was increased from 20 to 24 kHz, and varied only slightly when bandwidth was increased further (Tables III–VI). More substantial increases were evident in some individual species percent correct classification scores. Percent correct classification of spotted and striped dolphin whistles increased from not significantly different than chance (spotted dolphins) or significantly less than chance (striped dolphins) to significantly greater than chance when the upper bandwidth limit was increased from 20 to 24 kHz. Classification success for both species increased further with subsequent increases in bandwidth, but the most sizeable increases occurred between 20 and 24 kHz.

In contrast, percent correct classification of short-beaked common and spinner dolphin whistles decreased as bandwidth increased. Even with these decreases, classification success for spinner dolphin whistles remained significantly greater than chance at all bandwidths. Percent correct classification of short-beaked common dolphin whistles decreased from significantly greater than chance at 20 kHz upper bandwidth limit to not significantly different than chance at all other upper bandwidth limits. This was an unexpected result as both species had a relatively high percentage of off-scale whistles when the upper bandwidth limit was 20 kHz and relatively low percentages of off-scale whistles at higher upper bandwidth limits. Also, average maximum frequency and average ending frequency increased significantly with increasing bandwidth for both species.

Fewer off-scale whistles and more accurate whistle measurements should lead to more complete representations of whistles at higher upper bandwidth limits. It was expected

TABLE VI. Classification results of discriminant function analysis for the 40-kHz upper bandwidth limit data. Percentages of whistles correctly classified for each species are in bold. Correct classification scores that are significantly different (χ^2 test, $\alpha = 0.05$) than expected by chance alone are underlined and P-values are given in the sixth column. The number of whistles included in the analysis for each species (n) is given in the last column. Overall, 37% of whistles were classified to the correct species. This is significantly greater ($P < 0.001$) than the 25% that would be expected by chance alone.

	Predicted species					
Actual species	Short-beaked common dolphin	Spotted dolphin	Striped dolphin	Spinner dolphin	P	n
Short-beaked common dolphin	**30%**	20%	31%	19%	0.21	163
Spotted dolphin	13%	**44%**	23%	20%	<0.001	100
Striped dolphin	19%	19%	**42%**	20%	<0.001	104
Spinner dolphin	20%	16%	26%	**38%**	0.001	117

that this would lead to greater classification success, but as illustrated in the cases of short-beaked common and spinner dolphins, this was not always true. In addition, striped dolphins had the lowest percentage of off-scale whistles when the upper bandwidth limit was 20 kHz and their whistle variables did not change significantly with increasing bandwidth, yet striped dolphin correct classification scores increased markedly with increasing bandwidth. Thus, classification success was not directly related to the percentage of off-scale whistles or changes in mean whistle variables with increasing bandwidth.

To further explore trends in classification success, patterns of misclassification were examined. When the upper bandwidth limit was increased from 20 to 24 kHz, the percent of short-beaked common dolphin whistles that were correctly classified decreased. At the same time, the percent of short-beaked common dolphin whistles that were misclassified as striped dolphins increased (Tables III and IV). It was hypothesized that the additional whistles being misclassified as striped dolphins by the 24-kHz upper bandwidth limit DFA were those that had been excluded from the 20-kHz upper bandwidth limit DFA (recall that whistles with off-scale variables were excluded from the DFA). This hypothesis was rejected because, of the 33 short-beaked common dolphin whistles that were missing from the 20-kHz upper bandwidth limit data set, only one was misclassified as a striped dolphin whistle when included in the 24-kHz upper bandwidth limit DFA. Many ($n = 15$) of the missing short-beaked common dolphin whistles were misclassified as spotted dolphins and one third were correctly classified. This suggests that the observed changes in patterns of classification were not caused directly by the added whistles, but were more likely caused indirectly by the influence of additional whistles on the calculation of discriminant functions. Discriminant functions are orthogonal linear functions derived from the measured variables and will be affected by the relationship of whistle variables to one another as well as the values of the whistle variables themselves. Consequently, when evaluating the benefits of increasing bandwidth, it is not sufficient to examine the percent of off-scale whistle variables or changes in whistle variables with changes in bandwidth for individual species. It is also necessary to consider the ways in which representations of whistles change in relation to whistles of other species.

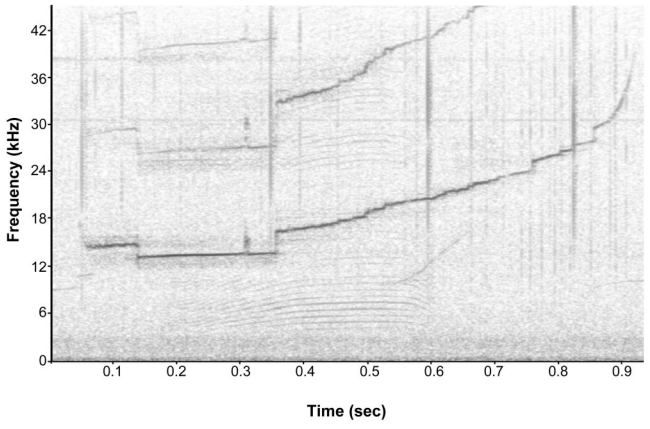

FIG. 2. Spotted dolphin whistle (512 point FFT). Maximum frequency, ending frequency, and duration were impossible to measure when the whistle was analyzed using an upper bandwidth limit less than 40 kHz. Harmonics were completely missed when the upper bandwidth limit was less than 30 kHz.

It is important to note that although percent correct classification of short-beaked common and spinner dolphin whistles did decrease with increasing bandwidth, the decreases (5% for spinner dolphins and 8% for short-beaked common dolphins) were minor compared to the 21% (spotted dolphin) and 26% (striped dolphin) increases in correct classification that were observed.

Even with sufficient bandwidth, classification success was lower than desirable for use as a field identification tool. Classification was based on eight variables that could be measured relatively easily and reliably in the field. These variables, however, do not provide complete representations of whistles and may miss whistle characteristics that carry species-specific information. Fristrup and Watkins (1993) measured variables such as amplitude, median frequency, and mode frequency (frequency corresponding to the largest energy value in the spectrum) from the vocalizations of 53 marine mammal species (including mysticetes, odontocetes, and pinnipeds). They devised a number of statistical measures to quantify the relationships among time, amplitude, and frequency. When tree-based classification models were applied to these variables, 66% of the vocalizations were classified to the correct species. Another approach to whistle

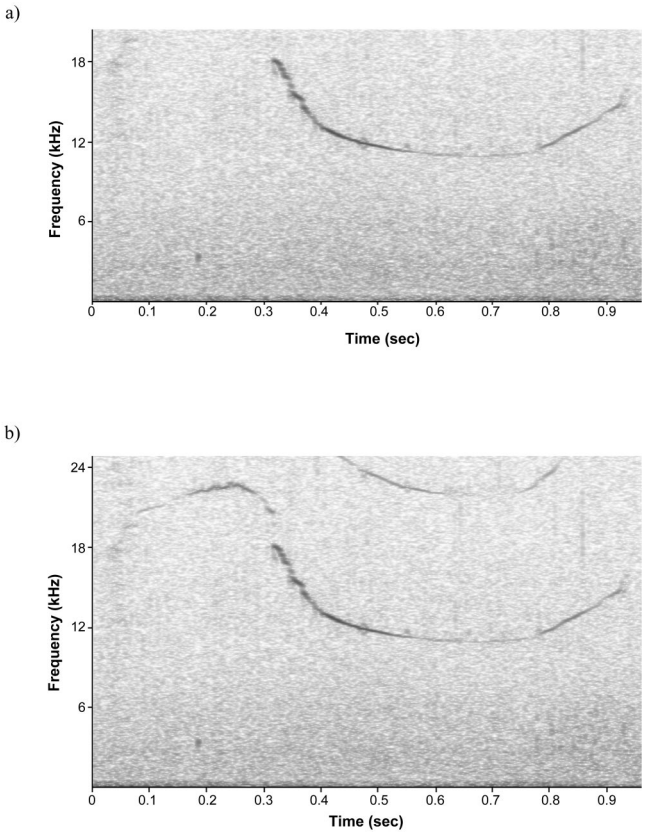

FIG. 3. Striped dolphin whistle (512 point FFT). (a) Upper bandwidth limit = 20 kHz. (b) Upper bandwidth limit = 24 kHz. Beginning frequency, maximum frequency, and duration were underestimated and harmonic was missed when the whistle was analyzed using an upper bandwidth limit less than 24 kHz.

classification was taken by Buck and Tyack (1993) and McCowan (1995). In these studies, overall whistle contours were compared rather than specific acoustic parameters. Different variables and approaches such as these could increase the accuracy of delphinid species identification.

Another cause of the lower than desirable correct classification scores could be that classification decisions were based on one whistle at time. This may be analogous to asking a visual observer to determine species from a single random surfacing of a single individual. Determining species based on several whistles may prove more reliable than classifying one whistle at a time.

The results of this study suggest that for the four species included, an upper bandwidth limit of at least 24 kHz is required for an accurate representation of the fundamental frequencies of their whistles and for optimizing the ability of computerized statistical techniques such as DFA to classify these whistles to species. The percentage of off-scale whistles, mean maximum and ending frequencies, and overall percent correct classification scores showed marked differences when the upper bandwidth limit was increased from 20 to 24 kHz. Increasing the upper bandwidth limit beyond 24 kHz did result in fewer off-scale whistles as well as changes in whistle variables and percent correct classification scores; however, these changes were minor compared to the changes occurring between 20 and 24 kHz.

Many acoustic research projects involve the use of DAT recorders, which typically have the capability to sample at either 44 100 or 48 000 kilo-samples/second. The results of this study suggest that the use of DAT recorders is sufficient for examinations of the fundamental frequencies of most dolphin whistles, however care should be taken to sample at 48 000 kilo-samples/second. If alternate equipment is available, advantages can be gained by recording and analyzing dolphin whistles at higher sampling rates.

ACKNOWLEDGMENTS

We would like to extend our thanks to Xenia Brobeil, Ann Chen, Megan Ferguson, and Tom Norris for their many hours spent at sea recording whistles. We gratefully acknowledge the patience and cooperation of the scientists and crew aboard the NOAA ship *McArthur*. This project could not have been completed without the aid of skilled visual observers: Eric Archer, Lisa Ballance, Isabel Beasley, James Carretta, James Cotton, Anne Douglas, Michael Force, Tim Gerrodette, Chris Hoefer, Kathy Hough, Brett Jarrett, Doug Kinzey, Erin LaBrecque, Sarah Mesnick, Laura Morse, Paula Olson, Richard Rowlett, Juan Carlos Salinas, Ernesto Vázquez, and Suzanne Yin. Many thanks are due to Michael Oswald, Tonya Huff, Marc Lammers, and one anonymous reviewer for insightful and helpful suggestions on drafts of this manuscript.

Au, W. W. L. (**1980**). "Echolocation signals of the Atlantic bottlenose dolphin (*Tursiops truncatus*) in open waters," in *Animal sonar systems*, edited by R. G. Busnel and J. F. Fish (Plenum, New York).

Au, W. W. L. (**1993**). *The Sonar of Dolphins* (Springer-Verlag, New York), pp. 32–35.

Au, W. W. L., Lammers, M. O., and Aubauer, R. (**1999**). "A portable broadband data acquisition system for field studies in bioacoustics," Marine Mammal Sci. **15**, 526–530.

Barlow, J. (**1995**). "The abundance of cetaceans in California waters. Part I: Ship surveys in summer and fall of 1991," Fish. Bull. **93**, 1–14.

Buck, J. R., and Tyack, P. L. (**1993**). "A quantitative measure of similarity for *Tursiops truncatus* signature whistles," J. Acoust. Soc. Am. **94**, 2497–2506.

Buckland, S. T., Anderson, D. R., Burnham, K. P., Laake, J. L., Borchers, D. L., and Thomas, L. (**2001**). *Distance Sampling: Estimating Abundance of Biological Populations* (Oxford U.P. Oxford).

Carretta, J. V., Taylor, B. L., and Chivers, S. J. (**2000**). "Abundance and depth distribution of harbor porpoise (*Phocoena phocoena*) in northern California determined from a 1995 ship survey," Fish. Bull. **99**, 29–39.

Clark, C. W., and Fristrup, K. M. (**1997**). "Whales '95: a combined visual and acoustic survey of blue and fin whales off Southern California," Rept. Int. Whal. Comm. **47**, 583–600.

Dawson, S. M. (**1991**). "Clicks and communication: the behavioural and social contexts of Hector's dolphin vocalizations," Ethology **88**, 265–276.

Fristrup, K. M., and Watkins, W. A. (**1993**). "Marine animal sound classification," Woods Hole Oceanographic Institution Technical Report WHOI-94-13.

Goold, J. C. (**1998**). "Acoustic assessment of populations of common dolphin off the west Wales coast, with perspectives from satellite infrared imagery," J. Mar. Biol. Assoc. U.K. **78**, 1353–1364.

Goold, J. C., and Jones, S. E. (**1995**). "Time and frequency domain characteristics of sperm whale clicks," J. Acoust. Soc. Am. **98**, 1279–1291.

Gordon, J. C. D., Matthews, J. N., Panigada, S., Gannier, A., Borsani, J. F., and Di Sclara, G. Notarbartolo (**2000**). "Distribution and relative abundance of striped dolphins in the Ligurian Sea Cetacean Sanctuary: Results from an acoustic collaboration," J. Cet. Res. **2**, 27–36.

Hammond, P. S., Berggren, P., Benke, H., Borchers, D. L., Collet, A., Heide-Jorgensen, M. P., Heimlich, S., Hiby, A. R., Leopold, M. F., and Oien, N. (**2002**). "Abundance of harbour porpoise and other cetaceans in the North Sea and adjacent waters," J. Appl. Ecol. **39**, 361–376.

Holt, R. S. (**1987**). ''Estimating density of dolphin schools in the eastern tropical Pacific ocean by line transect methods,'' Fish. Bull. **85**, 419–434.
Jaramillo-Legorreta, A. M., Rojas-Bracho, L., and Gerrodette, T. (**1999**). ''A new abundance estimate for vaquitas: first step for recovery,'' Marine Mammal Sci. **15**, 957–973.
Jefferson, T. J. (**2000**). ''Population biology of the Indo-Pacific humpbacked dolphin in Hong Kong waters,'' Wildlife Monogr. **144**, 1–65.
Kamminga, C., and Wiersma, H. (**1981**). ''Investigations on cetacean sonar II. Acoustical similarities and differences in odontocete sonar signals,'' Aq. Mamm. **8**, 41–62.
Kinzey, D., Gerrodette, T., Dizon, A., Perryman, W., Olson, P., and Rankin, S. (**2001**). ''Marine mammal data collected during a survey in the eastern tropical Pacific ocean aboard the NOAA ships *McArthur and David Starr Jordan*, July 28–December 9, 2000,'' Southwest Fisheries Science Center Technical Memorandum NOAA-TM-NMFS-SWFSC-303.
Lammers, M. O., Au, W. W. L., and Aubauer, R. (**1997**). ''Broadband characteristics of spinner dolphin (*Stenella longirostris*) social acoustic signals,'' J. Acoust. Soc. Am. **102**, 3122.
Lammers, M. O., Au, W. W. L., and Herzing, H. L. (**2003**). ''The broadband social acoustic signaling behavior of spinner and spotted dolphins,'' J. Acoust. Soc. Am. **114**, 1629–1639.
Leaper, R., Chappell, O., and Gordon, J. (**1992**). ''The development of practical techniques for surveying sperm whale populations acoustically,'' Rept. Int. Whal. Comm. **42**, 549–560.
Matthews, J. N., Rendell, L. E., Gordon, J. C. D., and MacDonald, D. W. (**1999**). ''A review of frequency and time parameters of cetacean tonal calls,'' Bioacoustics **10**, 47–71.
McCowan, B. (**1995**). ''A new quantitative technique for categorizing whistles using simulated signals and whistles from captive bottlenose dolphins (Delphinidae, *Tursiops truncatus*),'' Ethology **100**, 177–193.
Norris, T. F., McDonald, M., and Barlow, J. (**1999**). ''Acoustic detections of singing humpback whales (*Megaptera novaeangliae*) in the eastern North Pacific during their northbound migration,'' J. Acoust. Soc. Am. **106**, 506–514.
Oswald, J. N., Barlow, J., and Norris, T. F. (**2003**). ''Acoustic identification of nine delphinid species in the eastern tropical Pacific ocean,'' Marine Mammal Sci. **19**, 20–37.
Rasmussen, M. H., and Miller, L. A. (**2002**). ''Whistles and clicks from white-beaked dolphins, *Lagenorhynchus albirostris*, recorded in Faxafloi Bay, Iceland,'' Aq. Mamm. **28**, 78–89.
Rendell, L. E., Matthews, J. N., Gill, A., Gordon, J. C. D., and MacDonald, D. W. (**1999**). ''Quantitative analysis of tonal calls from five odontocete species, examining interspecific and intraspecific variation,'' J. Zool. **249**, 403–410.
Richardson, W. J., Green, C. R., Malme, C. I., and Thomson, D. H. (**1995**). *Marine Mammals and Noise* (Academic, San Diego).
Stafford, K. M., Nieukirk, S. L., and Fox, C. G. (**1999**). ''An acoustic link between blue whales in the eastern tropical Pacific and the northeast Pacific,'' Marine Mammal Sci. **15**, 1258–1268.
Steiner, W. W. (**1981**). ''Species-specific differences in pure tonal whistle vocalizations of five western north Atlantic dolphin species,'' Behav. Ecol. Sociobiol. **9**, 241–246.
Thomas, J. A., Fisher, S. A., and Ferm, L. M. (**1986**). ''Acoustic detection of cetaceans using a towed array of hydrophones,'' Rept. Int. Whal. Comm. Spec. Iss. **8**, 139–148.
Thompson, P., Findley, L. T., and Vidal, O. (**1992**). ''20 Hz pulses and other vocalizations of fin whales, *Balaenoptera physalus*, in the Gulf of California, Mexico,'' J. Acoust. Soc. Am. **92**, 3051–3057.
Thompson, P., Findley, L., Vidal, O., and Cummings, W. (**1996**). ''Underwater sounds of blue whales, *Balaenoptera musculus*, in the Gulf of California, Mexico,'' Marine Mammal Sci. **12**, 288–292.
Wade, P. R., and Gerrodette, T. (**1993**). ''Estimates of cetacean abundance and distribution in the eastern tropical Pacific,'' Rept. Int. Whal. Commn. **43**, 477–493.
Wang, D., Wursig, B., and Evans, W. (**1995**). ''Comparisons of whistles among seven odontocete species,'' in *Sensory Systems of Aquatic Mammals*, edited by R. A. Kastelein, J. A. Thomas, and P. E. Nachtigall (De Spil, Woerden), pp. 299–323.
Weilgart, L., and Whitehead, H. (**1993**). ''Coda vocalizations in sperm whales (*Physeter macrocephalus*) off the Galapagos Islands,'' Can. J. Zool. **71**, 744–752.
Wiersma, H. (**1982**). ''Investigations on cetacean sonar IV. A comparison of wave shapes of odontocete sonar signals,'' Aq. Mamm. **9**, 57–66.

Measurement of an individual silver perch *Bairdiella chrysoura* sound pressure level in a field recording

Mark W. Sprague[a)]
Department of Physics, East Carolina University, Greenville, North Carolina 27858 USA

Joseph J. Luczkovich[b)]
Department of Biology and Institute for Coastal and Marine Resources, East Carolina University, Greenville, North Carolina 27858 USA

(Received 27 February 2004; revised 6 August 2004; accepted 9 August 2004)

Simultaneous audio and video were recorded of a silver perch *Bairdiella chrysoura* producing its characteristic drumming sound in the field. The background noise contribution to the total sound pressure level is estimated using sounds that occurred between the pulses of the silver perch sound. This background contribution is subtracted from the total sound to give an estimate of the sound pressure level of the individual fish. A silver perch source level in the range 128–135 dB (*re*: 1 μPa) is obtained using an estimate of the distance between the fish and the hydrophone. The maximum distance at which an individual silver perch could be detected depends on the background sound level as well as the propagation losses. Under the conditions recorded in this study, the maximum detection distance would be 1–7 m from the hydrophone. © *2004 Acoustical Society of America.* [DOI: 10.1121/1.1802651]

PACS numbers: 43.80.Ka [WWA] Pages: 3186–3191

I. INTRODUCTION

A. Fish sound production

Many fishes produce species-specific sounds (Fine *et al.* 1977; Fish and Mowbray 1970; Mann *et al.* 1997; Myrberg 1981; Myrberg *et al.* 1965) associated with aggression, aggregation, fright, and reproductive behaviors (Winn 1964). The males of Family Sciaenidae (drums and croakers) produce species-specific courtship ''drumming'' sounds at spawning sites (Connaughton and Taylor 1995, 1996; Fish and Mowbray, 1970; Luczkovich *et al.*, 1999b; Mok and Gilmore 1983). These spawning-related sounds have been used by scientists and fisheries managers to delineate areas where spawning occurs (Luczkovich *et al.* 2000, 1999a, b). Luczkovich *et al.* (1999a, b) demonstrated that the sound pressure levels of silver perch *Bairdiella chrysoura* and weakfish *Cynoscion regalis* drumming each correlate with densities of fertilized conspecific eggs in the water column. Although information about egg production is important, scientists and fisheries managers would like a technique for estimating fish populations, especially spawning populations. Individual source levels are required in order to use passive acoustics for fish population estimates.

B. Measurement of fish sound pressure levels

Fish sounds have been measured both in nature (Luczkovich *et al.* 1999b) and in captivity (Guest and Lasswell 1978; Sprague *et al.* 2000), but the source level of an individual in the natural environment has never been precisely determined. In captivity, reflections from tank walls complicate the relationship between measured individual source levels and those produced in nature (Akamatsu *et al.* 2002). Connaughton *et al.* (1997, 2000) avoided the complications of tank reflections by measuring disturbance sounds produced by captive weakfish in air and found that the sound levels increased significantly with fish size, temperature, and sonic muscle condition. Most sciaenid fishes live in turbid waters and spawn at night. In this low-visibility environment, it is often difficult to determine important parameters such as the distance to and identity of a sound-producing fish. Luczkovich *et al.* (1999b) report that the maximum sound pressure level they recorded for an ''individual'' silver perch sound was 136 dB and assumed that the individual producing the sound was very near their hydrophone, although there was no confirmation of this assumption. The maximum sound pressure level measured during that study was 147 dB, but this was for a chorus of weakfish and silver perch together with background noise. Individual fish could not be distinguished in that recording (Luczkovich *et al.* 1999b).

In North Carolina (USA) waters, where sciaenids are acoustically dominant, fish sound production begins just before sunset and lasts into the night (Sprague *et al.* 2000). Sounds produced by large aggregations of drumming sciaenids blend together obscuring individual calls. Even when an individual fish sound is identifiable, it must be separated from the background noise in order to determine its sound pressure level.

C. Sound and video recording

On May 5, 2001 we obtained audio and video of a silver perch producing its drumming sounds at Wallace Channel in Ocracoke Inlet, North Carolina. In this paper we analyze the

a)Electronic mail: spraguem@mail.ecu.edu; http://personal.ecu.edu/spraguem
b)Electronic mail: luczkovichj@mail.ecu.edu; http://drjoe.biology.ecu.edu

audio and video to estimate the background sound pressure level and estimate the sound pressure level of the individual fish.

II. THEORY

A. Combining sounds from incoherent sources

Sound pressures measured by a sound meter are given by

$$p_{\mathrm{rms}}(t)=\left[\frac{1}{t_c}\int_{-\infty}^{t}p^2(t')e^{(t'-t)/t_c}dt\right]^{1/2}, \tag{1}$$

where $p_{\mathrm{rms}}(t)$ is the rms pressure read on the meter at time t, $p(t')$ the instantaneous pressure at time t', and t_c the time constant of the meter. Equation (1) can be approximated for a sound discretely sampled at frequency f_0 as

$$(p_n)_{\mathrm{rms}}=\left[\frac{1}{f_0 t_c}\sum_{k=1}^{n}p_k^2\exp\left(\frac{k-n}{f_0 t_c}\right)\right]^{1/2}, \tag{2}$$

where the $(p_n)_{\mathrm{rms}}$ represents the rms pressure at the time of sample n and p_k the acoustic pressure at the time of sample k.

We assume that each fish in an aggregation produces sound independently from the others (i.e., there is no fixed phase relationship between each sound source). Hence, each sound source is approximately incoherent. The time average pressure-squared is the sum of the pressures-squared for each mutually incoherent source (Pierce 1989). With an individual fish can be heard over a background, the total average pressure-squared is

$$p_{\mathrm{av}}^2=(p_f^2)_{\mathrm{av}}+(p_{\mathrm{bg}}^2)_{\mathrm{av}}, \tag{3}$$

where p_f is the acoustic pressure of the individual fish and p_{bg} the acoustic pressure of the background sound. The subscript ''av'' in Eq. (3) indicates a time average. The time average pressure-squared p_{av}^2 is approximated by the square of the rms pressure measured by a sound meter.

B. Sound pressure levels and source levels

The sound pressure level in decibels is a logarithmic measure of sound pressure, given by

$$L=20\log_{10}\frac{p_{\mathrm{rms}}}{p_0}, \tag{4}$$

where p_0 is the reference pressure (1 μPa for underwater measurements and throughout this paper). Sound pressure levels in decibels must be converted to pressure units before using them in Eq. (3). Pierce (1989) introduced a background correction factor C_{bg} for computing sound pressure levels when incoherent background noise is present. Using the notation in Pierce (1989), the sound pressure level of the individual fish L_f can be represented as

$$L_f=L-C_{\mathrm{bg}}(L-L_{\mathrm{bg}}), \tag{5}$$

where L is the total sound pressure level, and L_{bg} the sound pressure level of the background sound. The function C_{bg} is the background correction factor, which is

$$C_{\mathrm{bg}}(\Delta L)=-10\log_{10}(1-10^{-\Delta L/10}), \tag{6}$$

where $\Delta L=L-L_{\mathrm{bg}}$ is the difference between the total and background sound pressure levels. Equations (5) and (6) can be used to obtain the fish sound pressure level L_f if the total sound pressure level L and the background sound pressure level L_{bg} can be measured.

The source level is defined as the sound pressure level at a distance of one meter from the sound source under free-field conditions. Since sound spreads spherically at distances smaller than the water depth (Urick 1983), we can use the spherical spreading model,

$$p_{\mathrm{rms}}(r)=r_0\frac{p_s}{r}, \tag{7}$$

to determine the source level. In Eq. (7), $p_{\mathrm{rms}}(r)$ is the rms acoustic pressure at distance r, r_0 the reference distance (1 m), and p_s the rms acoustic pressure at distance r_0 from the source. Using Eqs. (4) and (7), the source level is

$$L_s=20\log_{10}\frac{p_s}{p_0}=20\log_{10}\left[\frac{rp_{\mathrm{rms}}(r)}{r_0 p_0}\right]. \tag{8}$$

C. Maximum detection distance

The maximum detection distance r_{max} for a sound depends on the background sound level as well as the propagation losses as the sound travels between the source and receiver. A sound can be accurately detected above the incoherent background when its sound level is greater than or equal to the background sound level (Pierce 1989). The propagation losses in shallow water depend on many parameters including water depth, bottom type, variations in sound speed, and water currents with depth and horizontal position. Precise measurements of propagation losses are particular to the properties of a given location, but estimates of minimum propagation loss can be made using geometrical spreading laws. Sound spreads spherically at distances less than the water depth [see Eq. (7)] and cylindrically at distances much greater than the water depth (Urick 1983). Solving Eqs. (4) and (7) for the distance at which the sound level is equal to that of the background under spherical spreading conditions

$$r_{\mathrm{max,sph}}=r_0 10^{(L_s-L_{\mathrm{bg}})/20}. \tag{9}$$

The cylindrical spreading model is

$$p_{\mathrm{rms}}(r)=\sqrt{r_0}\frac{p_s}{\sqrt{r}}. \tag{10}$$

Solving Eqs. (4) and (10) for the distance at which the sound level is equal to that of the background under cylindrical spreading conditions

$$r_{\mathrm{max,cyl}}=r_0 10^{(L_s-L_{\mathrm{bg}})/10}. \tag{11}$$

The predicted value for r_{max} is $r_{\mathrm{max,sph}}$ for distances less than the water depth and $r_{\mathrm{max,cyl}}$ for distances much greater than the water depth. There is a transition region at distances close to the water depth at which the propagation losses are between those predicted by spherical spreading and those predicted by cylindrical spreading (Urick 1983). At these distances r_{max} is between $r_{\mathrm{max,sph}}$ and $r_{\mathrm{max,cyl}}$.

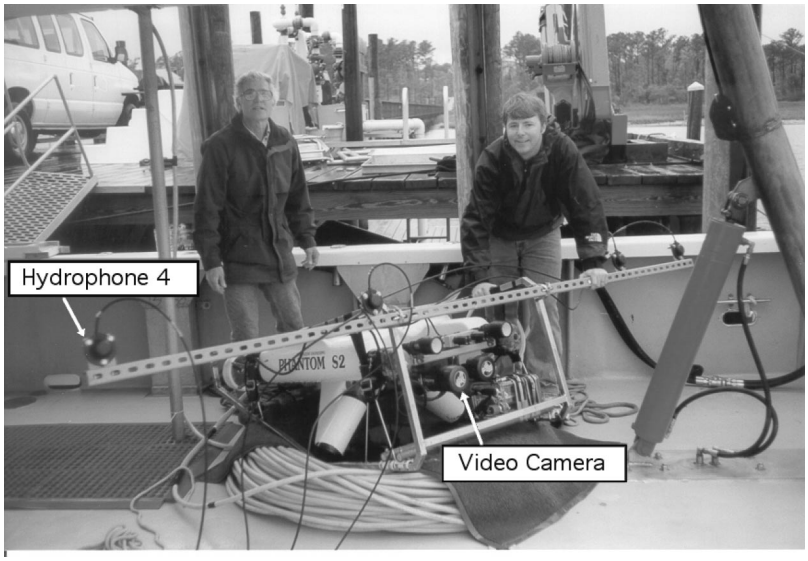

FIG. 1. Phantom S2 ROV with hydrophone boom. The audio signal was recorded by Hydrophone 4 on the starboard side of the vehicle as indicated in the figure, and the video was recorded by the video camera on the body of the ROV. Pictured are the ROV pilot (Glenn Taylor, left) and the one of the authors (Mark W. Sprague, right). Photo by Joseph J. Luczkovich.

III. METHOD

We recorded simultaneous sound and video using a hydrophone (ITC, Model 4066) mounted on a Phantom S2 remote operated vehicle (ROV) with on-board low-light video cameras. (See Fig. 1.) The hydrophone signal was recorded onto the left channel of an audio-cassette recorder (Sony model CFS-1055) while commentary recorded using a microphone on the research vessel was recorded onto the right channel. The video signal was recorded to a VHS recorder which also inserted a time display on the recording. Electrical problems on the research vessel prevented us from recording the hydrophone signal directly onto the audio track without 60-Hz interference or analyze all four hydrophone signals simultaneously, but we were able to match the sound recording from Hydrophone 4 with the video recording to within ~0.5 s by announcing the time recorded on the video track onto the commentary recording.

The ROV was deployed in Wallace Channel (lattitude: 35° 04′ 21.814″ N, longitude: 76° 02′ 59.325″ W) in 10–11-m deep water at a location we had previously documented as silver perch spawning site (Luczkovich *et al.* 1999a). Due to large tidal currents in the inlet, the ROV could not maneuver effectively with its motors. We used a 20-kg downweight attached to the bridle to anchor the ROV to the seafloor for use as an audio and video platform.

We calibrated the sound recording system by comparing it to a calibrated hydrophone system (Inner Ocean902). We placed the calibrated hydrophone less than 1 cm from the measurement hydrophone, and played a sequence of tones over the frequency range of interest (300–5000 Hz) recording the signals from both hydrophone systems. There was little variation between the two systems over the entire frequency range. We used the calibration value from the peak frequency range of the silver perch sound (700–1200 Hz) to calibrate the measurement system.

We digitized the sound recording at a sampling frequency of 24 kHz using an analog–to–digital board (National Instruments NB-2150F) connected to a Macintosh computer. A sonogram was computed from the digitized sound file using a 1024-point Hanning-windowed fast Fourier transform (FFT) with each window overlapping the previous window by 512 sample points.

We computed sound pressure levels for the entire sound recording using Eq. (2) and used Eq. (5) to obtain the fish sound pressure level during the peak of each pulse in the silver perch sound. We estimated the background level using the sound pressure level between the pulses of the silver perch sound. Local maxima of background sound pressure level were used to construct an interpolated maximum background sound pressure level. Similarly, local minima of the background sound pressure level were used to construct an interpolated minimum background sound pressure level. We used the interpolated maximum and minimum background sound pressure levels to determine minimum and maximum values (respectively) for L_f in Eq. (5) for each silver perch pulse.

IV. RESULTS

We began recording audio at 20:25 local time and recorded continuously until 22:36 local time. Although we heard silver perch in the background during the two-hour recording, we only heard an individual silver perch (i.e., an individual fish sound distinguishable above the background noise from fish aggregations) during one segment. We observed a silver perch swim in front of the ROV toward Hydrophone 4 on the starboard side and, at the same time, recorded audio of the silver perch sound on Hydrophone 4. The fish entered the video at time 6 s (22:18:07 local time) and swam off the right of the screen at time 10 s (22:18:11 local time). The silver perch sound pressure level reached a maximum between times 15–18 s (22:18:16–22:18:19 local time) when the fish swam by Hydrophone 4. A sonogram (Fig. 2) shows that the silver perch pulses, seen as dark lines from 700–1200 Hz, are loudest between times 15.75 and 17.50 s. Figure 3 shows a plot of the total sound pressure level, maximum and minimum background noise estimates, and estimates of the maximum silver perch sound pressure level for each sound pulse. The maximum silver perch received sound pressure level in the entire recording of 128 dB, using the estimated maximum background sound pres-

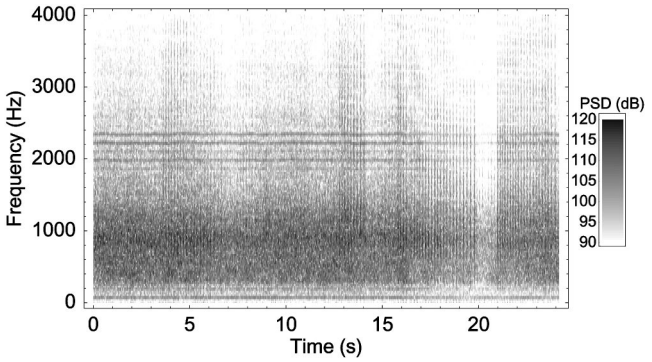

FIG. 2. Sonogram of silver perch recording from Hydrophone 4. Each power spectrum was computed from a 1024-sample Hanning window which overlapped the previous power spectrum by 512 sample points.

sure level and 129 dB using the estimated minimum background sound pressure level occurred at time 15.85 s in the recording. All of the other pulses from 15.75–17.50 s had silver perch received sound pressure levels from 127–129 dB.

V. DISCUSSION

In order to know the silver perch source level precisely, we must know its distance from the hydrophone. Our encounter with the silver perch was a fortuitous event. Although we were not able to determine the exact distance between the silver perch and the hydrophone, the video allows us to confirm its proximity. We can say with reasonable confidence that the fish was within 1–2 m of Hydrophone 4 when we recorded the sound. This allows us to establish a minimum source level of 128 dB for an individual silver perch in field conditions. If the silver perch were 2 m from the hydrophone the source level could be as high as 135 dB (assuming spherical spreading and minimum background noise). The sound pressure level that we have measured with our calibrated hydrophone system on the ROV at Wallace Channel in 2001 corresponds well with levels for individual

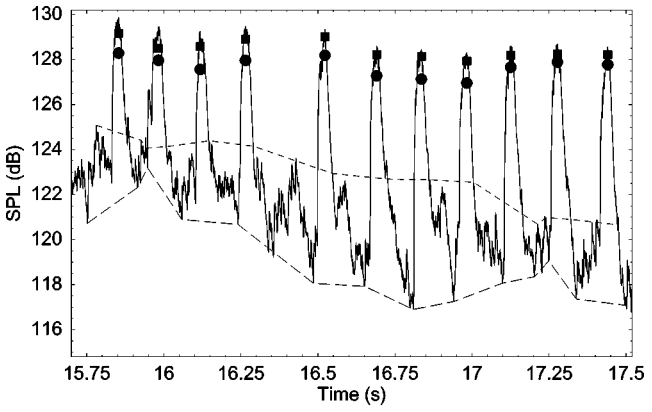

FIG. 3. Sound pressure levels computed from the silver perch recording from Hydrophone 4. The black curve is the total sound pressure level computed with a time constant of 0.01 s. The short-dash and long-dash curves are estimates of the maximum and minimum background sound pressure levels, respectively. The circles and squares represent the estimated peak silver perch sound pressure level for each pulse computed using the maximum and minimum background sound pressure levels (respectively) in Eq. (5).

silver perch that were an unknown distance from the hydrophone as reported by Luczkovich *et al.* (1999b). Those authors measured a maximum of 136 dB on 13 recordings made at similar inlet locations in 1997. However, the result obtained here was for a single fish. We have no estimate of variability for silver perch that are a known distance from the hydrophone. Nonetheless, this result is important because nobody has ever measured the source level of a sciaenid fish calling *in situ*.

We do not have conclusive proof that the silver perch observed on the video was the fish producing the sound. However, it is highly unlikely that another fish produced the sound, because we never recorded another individual silver perch on audio or video near the ROV at Wallace Channel, even though we recorded continuously for over two hours on May 5th. Additionally, we recorded with the ROV's video and audio at a nearby station on May 2nd–4th for nearly two hours in the evening, at Wallace Channel on May 4th for two hours in the evening, and for a total of 56 min on May 8th, with 12 short recordings made at hourly intervals through an entire tidal cycle (from 11:25 until 23:18 local time), without encountering an individual silver perch near the ROV. We conclude that the co-occurrence of the very loud silver perch sounds with the appearance of a silver perch swimming into the video cameras viewing area strongly implicates it as the sound producer in this recording. Further work using hydrophone arrays to localize the source of the sound producers and determine the spatial distribution of these fishes on the spawning grounds is needed.

An important application of these data is the maximum distance $r_{\max}$ at which a fish can be detected above the background level. The background levels during our recording session varied between 118 and 125 dB. The maximum distance at which an individual silver perch could be detected above the background noise in this environment would depend on the background sound pressure level (see Table I). When the background sound is loud (125 dB), $r_{\max}$ is less than the water depth (10 m), and spherical spreading dominates. When the background sound is quiet (110 dB), $r_{\max}$ is much greater than the water depth and cylindrical spreading dominates. At midlevel background noise (118 dB), $r_{\max}$ is likely between the spherical and cylindrical spreading distances.

The biological significance of these computations is that both what a fisheries biologist can detect and what another fish or predator can detect will be affected by background sound. For example, an individual silver perch calling with source level between 128 and 135 dB will be heard above the background by a biologist doing a passive acoustic survey with hydrophone similar to ours at between 1.4 and 3.2 m away ($r_{\max}$), assuming spherical spreading and a maximum background level of 125 dB. This distance will vary with background levels at the location and the sound spreading model (cylindrical or spherical) used, as shown in Table I. Thus, the estimates of $r_{\max}$ provided by Luczkovich *et al.* (1999b), which assumed an individual weakfish (*Cynoscion regalis*) calling at 127 dB, cylindrical spreading and 110 dB as a background level, were relatively large (50 m). However, a more typical situation for the biologist doing a pas-

TABLE I. Maximum detection distance for an individual sound, r_{max}.

Estimated source level	Spreading model and background level					
	Spherical			Cylindrical		
	110 dB	118 dB	125 dB	110 dB	118 dB	125 dB
128 dB (minimum)	7.9 m	3.2 m	1.4 m	63 m	10 m	2.0 m
135 dB (maximum)	18 m	7.1 m	3.2 m	316 m	50 m	10 m

sive acoustic survey will be a recording made with other fish calling in the background (118–125 dB), resulting in r_{max} distances that are relatively small (1–7 m for spherical spreading model and 2–50 m for the cylindrical model). In shallow water (~10 m), the choice of model will depend on the background sound at the site, with spherical model being favored at high background levels and cylindrical model at low background levels. Thus, at our measured background levels (118–125 dB caused by other fish chorusing) an individual fish calling could only be detected above the background chorus at 1–7 m range. On a quiet morning, when background levels are 110 dB (Luczkovich *et al.* 1999b), an individual calling at 135 dB could be heard at an r_{max} of 316 m. For the loudest background level recorded in this area, 147 dB (Luczkovich *et al.* 1999b), an individual silver perch 1 m from the hydrophone would be undetectable. These calculations provide an upper and lower bound for r_{max} under conditions measured in actual field situations that will be encountered by biologists, and thus provide a basis for developing calibrated passive acoustic survey techniques.

We can now set a threshold for sound detection of an individual silver perch that is close to an autonomous recording system, so the system can be automatically triggered when it exceeds the level described here. That is, if a sound is detected that is 128 dB or louder and has similar spectral properties to silver perch sounds (Sprague *et al.* 2000), then the system can be automatically triggered to photograph or record the sound producer. Such a remote sensing system is achievable with current technology and can be deployed in multiple locations, saving money and time associated with surveying fish populations. This approach, with similar source level measurements, could be used to remotely sense cod *Gadus morhua*, sturgeon *Acipenser* sp., red drum *Sciaenops ocellatus*, or any soniferous species.

Additionally, the female silver perch would only be likely to hear a calling male at this range (r_{max}). Obviously, males that called louder than the background would be more likely to be heard by biologists, female silver perch, and bottlenose dolphin (*Turisops truncatus*), one of their major predators that also use sound to detect their prey (Luczkovich *et al.* 2000). So there are trade-offs for the fish to consider when calling, and the fish may modulate their sounds to be not too much louder than the background. We have no data on this, but note that some choruses seem to increase and decrease in sound pressure level (Luczkovich *et al.* 2000).

An aggregation of silver perch can be heard at a much larger distance than an individual. In this study, the sound of other silver perch was likely to be an aggregation at some distance away. The maximum distance that an aggregation can be detected depends on how many fish are in the aggregation and their spatial distribution as well as the variation in water depth and properties. It is beyond the scope of this study to model the properties of silver aggregations until we have better information on these parameters, but our calculations provides a first step toward this ultimate goal.

VI. CONCLUSION

We measured simultaneous audio and video of a calling silver perch in the field and determined its maximum sound pressure level by estimating the background noise. Using an estimated distance between the fish and our hydrophone, we calculate the silver perch source level between 128 and 135 dB. This information is useful for modeling distributions of fishes and developing algorithms of automatic detection of sound-producing fishes by autonomous sound recorders.

ACKNOWLEDGMENTS

This work was supported by the National Undersea Research Center at the University of North Carolina at Wilmington and the East Carolina University Institute for Coastal and Marine Resources and Departments of Biology, Physics, and Geology. The authors would like to thank Glenn Taylor and James Watson for their assistance in data collecting.

Akamatsu, T., Okumura, T., Novarini, N., and Yan, H. Y. (**2002**). ''Empirical refinements applicable to the recording of fish sounds in small tanks,'' J. Acoust. Soc. Am. **112(6)**, 3073–3082.

Connaughton, M. A., Fine, M. L., and Taylor, M. H. (**1997**). ''The effects of seasonal hypertrophy and atrophy on fiber morphology, metabolic substrate concentration and sound characteristics of the weakfish sonic muscle,'' J. Exp. Biol. **200**, 2449–2457.

Connaughton, M. A., and Taylor, M. H. (**1995**). ''Seasonal and daily cycles in sound production associated with spawning in weakfish, *Cynoscion regalis*,'' Environ. Biol. Fish. **42**, 233–240.

Connaughton, M. A., and Taylor, M. H. (**1996**). ''Drumming, courtship, and spawning behavior in captive weakfish, *Cynoscion regalis*,'' Copeia **1996(1)**, 195–199.

Connaughton, M. A., Taylor, M. H., and Fine, M. L. (**2000**). ''Effects of fish size and temperature on weakfish disturbance calls: implications for the mechanism of sound generation,'' J. Exp. Biol. **203**, 1503–1512.

Fine, M. L., Winn, H. E., and Olla, B. L. (**1977**). ''Communication in fishes,'' in *How Animals Communicate*, edited by T. A. Sebeok (Indiana University Press, Bloomington, IN), pp. 472–518.

Fish, M. P., and Mowbray, W. H. (**1970**). *Sounds of the Western North Atlantic Fishes* (Johns Hopkins Press, Baltimore, MD).

Guest, W. C., and Lasswell, J. L. (**1978**). ''A note on courtship behavior and sound production of red drum,'' Copeia **1978(2)**, 337–338.

Luczkovich, J. J., Daniel, H. J. III, Hutchinson, M., Jenkins, T., Johnson, S. E., Pullinger, R. C., and Sprague, M. W. (**2000**). ''Sounds of sex and death in the sea: Bottlenose dolphin whistles suppress mating choruses of silver perch,'' Bioacoustics **10(4)**, 323–334.

Luczkovich, J. J., Daniel, H. J., III, Sprague, M. W., Johnson, S. E., Pullinger, R. C., Jenkins, T., and Hutchinson, M. (**1999**a). ''Characterization of critical spawning habitats of weakfish, spotted seatrout and red drum in

Pamlico Sound using hydrophone surveys,'' Tech. Rep., North Carolina Dept. of Environmen. and Natural Resources, Division of Marine Fisheries, Morehead City, NC.
Luczkovich, J. J., Sprague, M. W., Johnson, S. E., and Pullinger, R. C. (**1999b**). ''Delimiting spawning areas of weakfish *Cynoscion regalis* (family Sciaenidae) in Pamlico Sound, North Carolina using passive hydroacoustic surveys,'' Bioacoustics **10(2)**, 143–160.
Mann, D. A., Bowers-Altman, J., and Rountree, R. A. (**1997**). ''Sounds produced by the striped cusk-eel *Ophidion marginatum* (Ophidiidae) during courtship and spawning,'' Copeia **1997(3)**, 610–612.
Mok, H.-K., and Gilmore, R. G. (**1983**). ''Analysis of sound production in estuarine fish aggregations of *Pogonias cromis*, *Bairdiella chrysoura*, and *Cynoscion nebulosus* (Sciaenidae),'' Bull. Inst. Zool. Acad. Sinica **22**, 157–186.
Myrberg, A. A. (**1981**). ''Sound communication and interception in fishes,'' in *Hearing and Sound Communication in Fishes*, edited by W. N. Tavolga, A. N. Popper, and R. R. Fay (Springer-Verlag, New York), pp. 395–425.
Myrberg, A. A., Kramer, E., and Heinecke, P. (**1965**). ''Sound production by cichlid fishes,'' Science **149**, 555–558.
Pierce, A. D. (**1989**). *Acoustics an Introduction to its Physical Principals and Applications* (Acoustical Society of America, Woodbury, NY).
Sprague, M. W., Luczkovich, J. J., Pullinger, R. C., Johnson, S. E., Jenkins, T., and Daniel, H. J., III. (**2000**). ''Using spectral analysis to identify drumming sounds of some North Carolina fishes in the family Sciaenidae,'' J. Elisha Mitchell Scientific Society **116(2)**, 124–145.
Urick, R. J. (**1983**). ''Propagation of sound in the sea: Transmission loss, I,'' in *Principles of Underwater Sound* (McGraw-Hill, New York), Chap. 5. 3rd. ed., pp. 99–146.
Winn, H. E. (**1964**). ''The biological significance of fish sounds,'' in *Marine Bio-Acoustics*, edited by W. N. Tavolga (Macmillan, New York), pp. 213–231.

How to measure information carried by a modulated vocal signature?

Amanda Searby[a] and Pierre Jouventin
Behavioural Ecology Group, CEFE-CNRS UPR 9056, 1919 Route de Mende F-34293 Montpellier Cedex 5, France

(Received 1 October 2003; revised 12 May 2004; accepted 2 June 2004)

Acoustic signaling systems that permit individual recognition are described in an increasing number of species. Evolutionary logic predicts that the efficiency of these signatures is related to the possibilities for confusion. To test this ''signature adaptation'' hypothesis, one needs a standardized method to estimate and compare the efficiency of different signatures. Beecher [Am. Zool. **22**, 477–490 (1989)] developed such a method by comparing scalar parameters extracted from the signals. However, vocal signatures frequently consist in the evolution of one parameter against one other, which are not comparable through Beecher's method. Here we present a method to estimate the efficiency of modulated signatures. A signature's efficiency is given by its information capacity (H_m), derived from Shannon's information theory. The measure of H_m is based on an analysis of variance and uses the Euclidian distances between the signature's contours in the population. To validate our method, simulated datasets of modulated contours were used. The predicted efficiency of those signatures, estimated from H_m, was strongly correlated to its actual efficiency given by two classification methods: a discriminant analysis and a classification by human observers. Being also untied to sample size, H_m therefore allows comparing objectively vocal, but also visual and olfactory signatures. © *2004 Acoustical Society of America.* [DOI: 10.1121/1.1775271]

PACS numbers: 43.80.Lb, 43.66.Gf, 43.60.Ek [WWA] Pages: 3192–3198

I. INTRODUCTION

Individual recognition systems are favored in conditions when confusion between individuals might result in a decrease of one's fitness. When individuals aggregate in dense colonies or are highly mobile, parent–offspring recognition, for example, is necessary to allow well-directed parental care. As an adaptive behavior, parent–offspring recognition should be more efficient in species where the probability of misdirected care is increased, due for example to high densities or to an important mobility of the young. More generally, the ''signature'' adaptation hypothesis predicts that a given signature system, which is the set of signals by which individuals are recognized, would be more efficient in conditions where the risks for confusion are higher (Beecher, 1989).

While a large literature exists on individual recognition [reviewed in Falls (1982); Colgan (1983); Halpin (1991); e.g., in penguins: Aubin and Jouventin (2002); Searby *et al.* (2004); swallows: Medvin *et al.* (1993); amphibians: Bee and Gerhardt (2002); pinnipeds: Charrier *et al.* (2003); cetaceans: Sayigh *et al.* (1999); rodents: Hurst *et al.* (2001); bats: Balcombe (1990); primates: Parr *et al.* (2000); other mammals: Goldman *et al.* (1995); Searby and Jouventin (2003); Frommolt *et al.* (2003)], to date very few studies have actually compared the efficiencies of individual recognition systems in different contexts. Most studies have only focused on the presence or absence of individual recognition in different species. This lack of quantitative analyses was underlined by Beecher (1989; 1982) who provided a method for measuring the efficiency of a given signature system. Beecher used an information theory approach to develop an information capacity measure (H_s) of a signature, essentially based on an analysis of variance made on the signature's components. This information estimate is then directly translatable into the efficiency of the signature system. It potentially enables comparisons across species and across recognition cue modalities.

Since the omnidirectionnal properties of acoustic signals make them more reliable than other sensory cues in dense environments, acoustic recognition systems are frequent in situations where the risk of confusion is increased. As acoustic signals are also easier to record and to measure, acoustic signature systems constitute good models to compare individual recognition systems. Beecher's team applied the information capacity method to compare the acoustic signature systems of two species of swallows. Their results confirmed the signature adaptation hypothesis, as they found more efficient signature systems associated with higher risks of confusion (Medvin *et al.* 1993). However, the method developed by Beecher presents some limitations. First, the measurement of the information capacity is made from a set of predetermined scalar variables measured on the sounds. This provides a bias in the measurement of the similarity between sounds, as the decision of which parameters should be considered and how they should be weighted is made arbitrarily by the investigator. Second, together with many other sound measurement methods, this analysis only considers monodimensional parameters. Since a sound is defined in three dimensions, frequency, amplitude, and time, only the three-dimensional values do fully characterize it. It is therefore highly restrictive to consider only one dimension at a time.

[a]Electronic mail: searby@cefe.cnrs-mop.fr

This excludes in particular the modulations of one parameter against one other, such as frequency and amplitude modulations over time, or the spectrum of the sound represented by the distribution of amplitude among the frequencies. Those bi-dimensional variables are necessary to get at least a good definition of a given sound, and may constitute significant sources of information within a signature system. This problem has been solved previously by restricting the modulations to several representative parameters such as the minima and maxima of the considered values over time. Here again this method is highly subjective as it is dependent on the choice made by the observer of which parameters to consider. Any approach that does not consider the modulation pattern may omit important elements used in the signature.

In this paper we propose a new method to measure objectively the information capacity of modulated signatures, based on the information theory analysis developed by Beecher. In the first part of this paper, we develop the algorithms used to measure the information capacity of a modulated signature. An example, based on a data set created by simulation, is then presented to illustrate features of the information analysis. In the second part, our method is validated by comparing the theoretical efficiency of different signature systems as predicted by the information capacity values, and their actual efficiency, measured by a classification error rate. For a separate validation of our approach, we provide two classification methods, one performed by human observers and the other by a mathematical method, here the discriminant function analysis.

II. THEORY

The mechanisms of individual identification rely on a signature system, where a signature refers to a combination of individually distinctive traits. The efficiency of a signature system can be measured in terms of stereotypy, defined as the ratio between intraindividual and interindividual variation of the signatures. Using information theory (Shannon and Weaver, 1949), Beecher developed an information analysis method that computes the information capacity of a scalar parameter measured within a set of signatures (Beecher, 1982, 1989). The information content of one variable (H_s) is a measure of the stereotypy of this variable in the considered population. H_s is derived from the F-value found in the ANOVA, but, unlike F, does not vary with sample size. Information capacity measurements are therefore more reliable to compare variables and samples. H_s, measured in bits/signal, represents the number of binary decisions necessary to discriminate among N objects. For a given variable, H_s is expressed as

$$H_s = \log_2 \sqrt{\frac{\sigma_B^2 + \sigma_W^2}{\sigma_W^2}} = \log_2 \sqrt{\frac{F+n-1}{n}}, \tag{1}$$

where n is the number of measures per individual, σ_B^2 is the between-individual variation, and σ_W^2 is the within-individual variation. The higher the values of H_s, the more potential the parameter has for encoding individual identity. According to the mathematical significance of H_s, 2^{Hs} gives a theoretical estimate of the number of potential signatures achievable on the basis of the considered parameter (Beecher, 1982). This information analysis does not require that the signal systems be compared in the same units (Beecher, 1989). The unitless nature of the information measures derives from standardizing the variables by dividing through by the within-individual standard variation.

The model developed by Beecher applies to signatures that consist of several intercorrelated scalar variables. To measure the global information of a vocal signature, a principal component transformation of the data allows adding the information capacity of the independent components to give the total information amount. It is clear from this method that the resulting information capacity varies according to which parameters of the sound are at first selected subjectively by the investigator. We propose a method that solves this selection problem by considering the sounds as a whole. A sound is produced by periodical oscillations of air pressure. Any sound is therefore fully described by the three following parameters: the amplitude of the vibrations, the frequency of the vibrations, and the evolution of amplitude and frequency with time. The analysis of an acoustic signal therefore requires to consider three dimensions: frequency, amplitude, and time. A full description of a sound is consequently given by the corresponding three-dimensional matrix. Such a 3-D representation is, however, difficult to apprehend. In a slightly more reductive way, we can describe a given sound by means of three bi-dimensional parameters: frequency and amplitude modulations over time, and amplitude distribution over the frequencies, which is the spectrum of the call. Our method proposes a comprehensive analysis of the sounds using these three parameters, which can also be referred to as modulated parameters. Because these measurements are vectorial and not scalar, it is however not possible to measure their information capacity as proposed in Beecher's method.

Here we compute a new estimate of their information capacity using another assessment of their stereotypy. The similarity between two vectorial variables is measured by the Euclidian distance d_{Aij} between the two curves. d_{Aij} is expressed as the square distance between two given vectors of measurements $A_i(t)$ and $A_j(t)$:

$$d_{Aij} = \frac{1}{N_{\min}} \sum_{k=1}^{N_{\min}} (A_j(k) - A_i(k))^2, \tag{2}$$

$N_{\min}$ being the shortest length of the two vectors.

If we consider a group of k observations, the sum of distance indices between all pairs of observations (*dist*) can be estimated using the sum of square SS as:

$$dist = \sum_{i,j} d_{Aij} = k \cdot \sum_j (A_j - \overline{A})^2 = k \cdot SS. \tag{3}$$

Consequently, the information capacity H_m for g groups with n observations per group was estimated as follows:

$$H_m = \log_2 \sqrt{\frac{F_{est}+n-1}{n}}, \tag{4}$$

where

$$F_m = \frac{n-1}{g-1}\left(\frac{dist_T - g \cdot dist_W}{dist_W}\right), \quad (5)$$

$dist_T$ being the sum of distance indices between all pairs of calls, and $dist_W$ the sum of distance indices between pair of calls within each group.

III. VALIDATION

A. Methods

To validate our method, we performed the described information analysis on randomly computed data sets simulating more or less efficient modulated signatures. We compared the resulting estimated efficiencies H_m to their actual efficiencies obtained from actual classifications of the simulated signatures.

Illustrative data sets were created on this purpose by simulation using MATLAB software. Simulated signatures were designed to resemble frequency-modulated contours, which are frequently used as vocal signatures [cetaceans: Sayigh *et al.* (1999); bats: Balcombe (1990); seals: Charrier *et al.* (2002); penguins: Aubin and Jouventin (2002)]. A signature was represented by a vector of 25 independent, normally distributed variables calculated as in Beecher (1989): each variable was the sum of two independent variables, B_i and W_{ij}, where $\sigma_t^2 = \sigma_B^2 + \sigma_W^2 = 1$ and σ_B^2/σ_W^2 took different values, according to the series of contours considered (Table I). All means were zero. A given data set consisted in ten series of contours, assimilated to ten different population samplings. Each of the ten ''populations'' consisted in N contours divided into g subgroups (or ''individuals'') of N/g contours each. This data set was designed to resemble usual data sets obtained in real conditions. Each ''population'' was given a specific σ_B^2/σ_W^2 ratio, resulting in a specific H_m value. An example of contours for three individuals from the same population ($\sigma_B^2/\sigma_W^2 = 2$) is shown in Fig. 1.

In a second step, we checked our model by comparing predicted and actual classification error rates. Accordingly, we first needed to assess predicted classification error rates as a function of H_m values. The proportion of correct classifications corresponds to the probability of correctly attributing a given signature to the right individual. It equals the ratio of the number of signatures actually used within the population, by the number of individuals. According to the information theory, 2^{Hm} is proportional to the number of signatures available for the population (Beecher, 1982). However, the actual number of signatures is always smaller than the number of available signatures. Consider randomly picking four balls in a bag where three different colors are available. The four picked balls might only be of one or two colors. As the mathematical expression giving the number of signatures actually used as a function of the number of available signatures is not directly computable, we chose to run a simulation on MATLAB instead. This simulation predicted the proportions of correct classifications as a function of the number of available signatures, proportional to $m = 2^{Hm}$. It consisted in attributing 50 signatures to 50 individuals, the signatures being randomly picked from a set of m different signatures (m varied between 1 and 400). Here signatures were represented by integers ranging from one to m. Accordingly, some individuals may share the same signature. Each individual was then picked in turn and, according to its signature, was randomly attributed to one of the k individuals sharing the same signature. This attribution was performed six times for each individual to imitate the jackknifed classification protocol performed by the upcoming discriminant analysis, with six contours for each individual. At the end of these 300 attributions, we computed the proportion of correct classifications, as in a jackknifed classification matrix. This simulation run was performed 50 times for each value of m. The final expected proportion of correct classifications was calculated for each m value as the mean of the 50 corresponding rates.

Actual classifications of the signatures were then achieved following two different procedures: a discriminant function analysis and a classification by human observers. The choice of a human observer's classification follows Janik's comparison of contours classification methods (Janik, 1999), which established human observer classifications as reliable when compared to other computer methods. For the discriminant analysis classification, we computed 20 datasets (i.e., populations) of $g = 50$ ''individuals'' and $n = 6$ signatures per ''individual.'' The σ_B^2/σ_W^2 ratio ranged from 1 to 2, according to the population (Table I). The proportion of cor-

TABLE I. Parameters for data sets obtained by simulation

Population	σ_B^2	σ_W^2	σ_T/σ_W	H_m	2^{Hm}
Data sets for discriminant analysis (50 individuals, 300 signatures per population):					
1	0.00	1.00	1.00	0.01	1.01
2	0.07	0.93	1.04	0.05	1.03
3	0.13	0.87	1.07	0.09	1.06
4	0.19	0.81	1.11	0.17	1.13
5	0.24	0.76	1.15	0.21	1.16
6	0.29	0.71	1.19	0.25	1.19
7	0.34	0.66	1.23	0.33	1.26
8	0.38	0.62	1.27	0.38	1.30
9	0.43	0.57	1.32	0.43	1.35
10	0.46	0.54	1.37	0.49	1.40
11	0.50	0.50	1.41	0.51	1.43
12	0.53	0.47	1.46	0.54	1.45
13	0.56	0.44	1.52	0.57	1.48
14	0.59	0.41	1.57	0.64	1.56
15	0.62	0.38	1.62	0.73	1.66
16	0.65	0.35	1.68	0.77	1.71
17	0.67	0.33	1.74	0.85	1.80
18	0.69	0.31	1.80	0.87	1.83
19	0.71	0.29	1.87	0.88	1.84
20	0.73	0.27	1.93	0.98	1.97
Data sets for human observers (10 individuals, 60 signatures per population):					
1	0.00	1.00	1.00	0.01	1.00
2	0.50	0.50	1.41	0.45	1.37
3	0.65	0.35	1.68	0.70	1.63
4	0.75	0.25	2.00	0.96	1.94
5	0.82	0.18	2.38	1.21	2.32
6	0.88	0.13	2.83	1.47	2.76
7	0.91	0.09	3.36	1.72	3.30
8	0.94	0.06	4.00	1.98	3.93
9	0.97	0.03	5.66	2.48	5.58
10	0.98	0.02	8.00	2.99	7.92

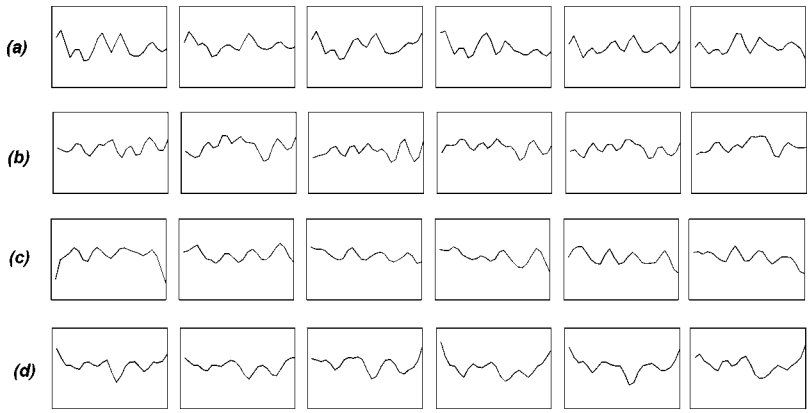

FIG. 1. An example of the simulated contours that were used for classification. Each line (a,b,c,d) corresponds to a different individual (six contours per individual). Here $\sigma_B^2/\sigma_W^2=2$.

rect classification was measured from a jackknifed classification matrix for each of the ten populations corresponding to different σ_B^2/σ_W^2 ratios. To increase the number of data, this operation was repeated three times. For the human observer's classifications, a smaller dataset was used for practical reasons. It consisted in ten populations of $g=10$ ''individuals,'' $n=6$ signatures per ''individual.'' The σ_B^2/σ_W^2 ratio ranged from 1 to 6, according to the population. For each population, all 60 contours were printed on separate sheets and seven observers were asked to classify contours independently by their shape into ten groups of six contours. To standardize the procedure, observers were asked to compute their classification in 20 min regardless of the σ_B^2/σ_W^2 ratio of the population. Each observer carried out ten tests to classify the ten populations in random order. To prevent habituation, no more than two tests a day were performed per observer. The proportions of correct classifications were then directly computed from their classifications using MATLAB software.

For each simulated population in the two experiments, we calculated the information capacity H_m using our method and deduced the corresponding excepted and compared the H_m values to the observed proportions of correct classifications (Fig. 2). Expected and observed correct classification rates were compared using nonlinear regressions and SigmaPlot 2001 software.

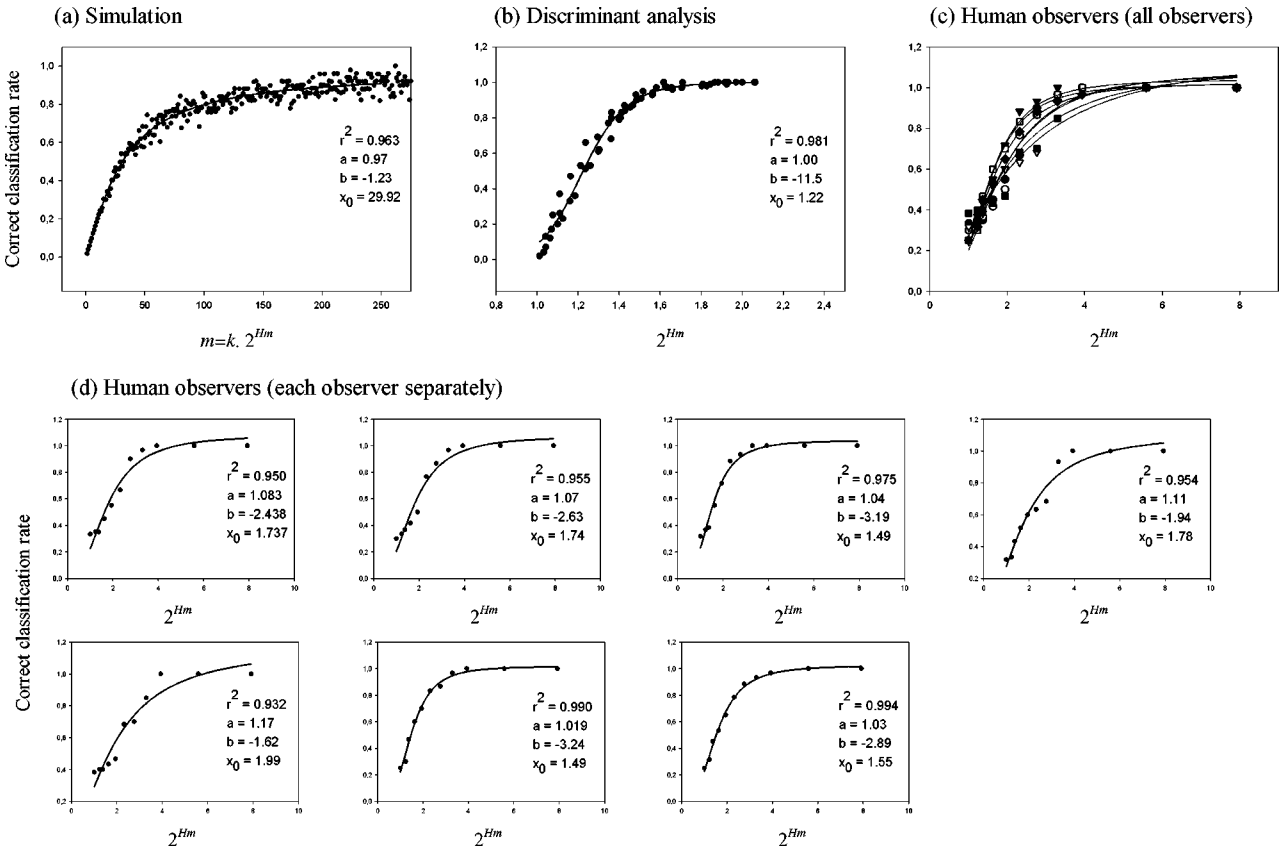

FIG. 2. Expected and observed rates of correct classification of our datasets. (a) Expected rates as predicted from our simulation; (b) observed classification rates obtained from discriminant function analysis; (c) observed classification rates obtained from all human observers; and (d) observed classification rates obtained from each human observer separately. Each curve fits a three-parameters logistic curve, $y=a/[1+(x/x_0)^b]$.

B. Results

Expected rates of correct classification are shown in Fig. 2(a). Observed classification rates obtained from discriminant function analysis and from human observers are shown on Figs. 2(b) and (c). The three curves show the same profile. Direct comparison of the curves was not possible as classification efficiencies differed according to the classification method. Comparison was therefore performed through regressions. Nonlinear regressions confirm that each curve fits a three-parameters logistic curve, whose equation is

$$y = \frac{a}{1 + (x/x_0)^b}.$$

To account for human observer's effect, regressions were made separately on each observer's curve [Fig. 2(d)]. Regression curves and regression coefficients are given in Fig. 2 ($r^2 > 0.93$ for all regressions).

IV. GENERAL DISCUSSION

This paper provides for the first time a method to predict the efficiency of modulated signatures in individual recognition. Our prediction is validated twice, by visual inspection and by discriminant analysis of the signatures, as observed and expected classification rates are similar in both cases. Our algorithm therefore represents a reliable tool to investigate individual signatures. It is of interest to note that we did not aim here to establish a classification method for signatures, as such methods already exist (e.g., in McCowan, 1995; Janik, 1999). Our point was not to classify, but to predict the difficulty in classification. By measuring the efficiency of the signals as individual signatures, one gets for the first time a quantitative assessment of the potential value of a signature system. This constitutes a new tool to study such a complex behavior as the use of signatures from an evolutionary point of view, as the efficiency of signature systems may have direct consequences on fitness, and are here directly comparable between species.

Several studies have used discriminant function analysis to quantify the usefulness of a signature's traits for individual identification (Hafner *et al.*, 1979; Smith *et al.*, 1982; Gelfand and McCracken, 1986; Galeotti and Pavan, 1991; Scherrer and Wilkinson, 1993; Lengagne, 2001; Frommolt *et al.*, 2003; Phillips and Stirling, 2000). Both methods use the same logic and provide a global measure of the classification efficiency. However, discriminant analysis results are tied to the sample size, which is not the case for information capacity (Beecher, 1989). Hence discriminant analysis cannot be applied to compare different signature datasets. Our use of artificial datasets with a unique sample size allowed us here to verify that our information analysis method provides the same results as a discriminant function analysis.

All previous estimations of the efficiency of individual signatures were made from a set of predetermined scalar variables measured on the sounds (Medvin *et al.*, 1993; Stoddard and Beecher, 1983; Scherrer and Wilkinson, 1993; Leonard *et al.*, 1997). Our method proposes a different way to extract information from the signal, which does not induce arbitrary choices on the relevant informative parameters. While the former approach is probably more convenient to study the encoding of information in signatures that share a similar acoustic structure, it lacks the necessary objectivity for a comparative study of more different vocal signals. Moreover, our method is based on a vectorial analysis of modulated contours, as opposed to an analysis of several scalar variables extracted from the signals. Information in modulated signatures may indeed be extracted from the modulation pattern as a whole, and not only from a few measurements such as the positions of maxima and minima. This is clearly illustrated by the contours shown in Fig. 1, where the shape of the contour greatly varies within and between individuals. In this case, manual extraction of the relevant parameters could fail in extracting all the information in the signal. Our method has therefore the advantages of being utterly objective, as no parameters are selected prior to the analysis, exhaustive, and fast, due to the automation provided through computer programming. It offers a standardized way to compare all kinds of signatures and may represent a significant advance for future comparative analyses.

Since the computed dataset we used as an example here consists of artificial modulated signals, our method can be applied to any kind of modulation. For example, frequency modulation is common in animal sounds. Encoding information within a frequency contour is actually a widespread method, as it is the case for individual signatures in bats (Scherrer and Wilkinson, 1993), dolphins (Sayigh *et al.*, 1990), king penguins (Lengagne *et al.*, 2001), and gulls (Charrier *et al.*, 2001), but also for other kinds of information such as in the territorial songs of passerine birds (Catchpole and Slater, 1995) or in the alarm calls of primates (Zuberbuhler *et al.*, 1997). The algorithm we provide here is, however, reliable only in the case of a high level of temporal consistency between calls. Contours might actually be subjected to considerable temporal variation within or between individuals, as it is the case in bottlenose dolphins whistles, for example. Buck and Tyack (1993) have provided a solution by using a nonuniform time dilation algorithm to provide a measure of similarity between contours. The combination of both algorithms might then constitute a more complete tool to assess the efficiency of such signatures.

Apart from frequency modulations, our method can also be applied to compare any modulations within an acoustic signal, such as amplitude modulations over time and amplitude modulations over frequencies, i.e., the spectra of different sounds. It is of interest to note that a given sound is entirely represented by those three modulations. By assessing the information capacity H_m of those three modulations within a given vocal signature, different kinds of information are provided. First, high H_m values would indicate whether one of those modulations actually forms a proper signature of identity. Theoretically, information can be extracted from an acoustic signal using two main processes (Okanoya and Dooling, 1991): integration in the frequency domain, using a power spectral profile, or integration in the temporal domain. In a second step, comparing the three H_m values would then assess the relative importance of frequency and temporal domains in identity coding. The information capacity H_m is

used here as a way to understand how information is encoded within a vocal signature. Finally, the three values taken together would give a global measure of the efficiency of the modulated signature, allowing comparisons between species. As it only measures bi-dimensional parameters, our method, however, does not include signals where the power spectral profile also varies with time, providing a tridimensional parameter. Such vocal signals are probably harder to perform, as the power spectral profile often depends on morphological constraints and is thus difficult to modulate. However variation in the power spectral profile is a critical feature of communication in animals that change the filter characteristics of the vocal tract—certainly including primates, but may be more widespread. The combined 3D analysis of all three values, frequency, amplitude, and time, would be very useful and should be the next step in development of this analysis.

As mentioned in the Introduction, acoustic signals have often been favored in the study of individual signatures over visual or olfactory ones, as they are easier to record, playback, or measure. By providing a new tool to analyze contour profiles, our method, however, extends the analysis of signatures to any kind of signal:vocal, visual, or olfactory. It enables comparisons of signatures such as spectrographic or spectrometry profiles obtained from color or odor analysis. Moreover, the unitless nature of our information measure allows comparisons across those different sensory modalities. Such disparate comparisons may prove highly helpful in comparing different methods used to encode individual distinctiveness across species. Interesting evolutionary convergences might for example be found between olfactory signatures in mammals and acoustic signatures in birds. Multimodal individual recognition can also be studied by comparing the relative efficiencies of olfactory and acoustic recognition within one given species, as it is the case in sheep or fur seal for example (Charrier *et al.*, 2002; Searby and Jouventin, 2003). In brief, the method we propose here constitutes a powerful tool to better understand the evolutionary mechanisms underlying the emergence of different signature systems.

ACKNOWLEDGMENTS

We are grateful to Francesco Bonadonna, Olivier Boutard, Joël Bried, Rachel Julien, Marion Nicolaus, James Searby and Mara Villafane for their useful help with contour classifications. Many thanks to James Searby for constructive comments on early drafts of the manuscript. This research was supported by the Centre National de la Recherche Scientifique (CNRS).

Aubin, T., and Jouventin, P. (**2002**). ''How to vocally identify kin in a crowd: the penguin model,'' Adv. Study Behav. **31**, 243–277.

Balcombe, J. P. (**1990**). ''Vocal recognition of pups by mother Mexican free-tailed bats, *Tadarida brasiliensis mexicana*,'' Anim. Behav. **39**, 960–966.

Bee, M. A., and Gerhardt, H. C. (**2002**). ''Individual voice recognition in a territorial frog (*Rana catesbeiana*),'' Proc. R. Soc. London, Ser. B **269**, 1443–1448.

Beecher, M. D. (**1982**). ''Signature systems and kin recognition,'' Am. Zool. **22**, 477–490.

Beecher, M. D. (**1989**). ''Signalling systems for individual recognition: an information theory approach,'' Anim. Behav. **18**, 465–482.

Buck, J. R., and Tyack, P. L. (**1993**). ''A quantitative measure of similarity for *Tursiops truncatus* signature whistles,'' J. Acoust. Soc. Am. **94**, 2497–2506.

Catchpole, C. K., and Slater, P. J. B. (**1995**). *Bird Song: Biological Themes and Variation* (Cambridge U.P., Cambridge).

Charrier, I., Mathevon, N., and Jouventin, P. (**2002**). ''How does a fur seal mother recognize the voice of her pup? An experimental study of *Arctocephalus tropicalis*,'' J. Exp. Biol. **205**, 603–612.

Charrier, I., Mathevon, N., and Jouventin, P. (**2003**). ''Vocal signature recognition of mothers by fur seal pups,'' Anim. Behav. **65**, 543–550.

Charrier, I., Mathevon, N., Jouventin, P., and Aubin, T. (**2001**). ''Acoustic communication in a black-headed gull colony: how do chicks identify their parents?'' Ethology **107**, 961–974.

Colgan, P. (**1983**). *Comparative Social Recognition* (Wiley, New York).

Falls, J. B. (**1982**). ''Individual recognition by sounds in birds,'' in *Acoustic Communication in birds, Vol. 2*, edited by D. E. Kroodsma and E. H. Miller (Academic, New York), pp. 237–278.

Frommolt, K.-H., Goltsman, M. E., and Macdonald, D. W. (**2003**). ''Barking foxes, Alopex lagopus: field experiments in individual recognition in a territorial mammal,'' Anim. Behav. **65**, 509–518.

Galeotti, P., and Pavan, G. (**1991**). ''Individual Recognition of Male Tawny Owls (Strix-Aluco) Using Spectrograms of Their Territorial Calls,'' Ethol. Ecol. Evol. **3**, 113–126.

Gelfand, D. L., and McCracken, G. F. (**1986**). ''Individual variation in the isolation calls of Mexican free-tailed bat pups (*Tadarida brasiliensis mexicana*),'' Anim. Behav. **34**, 1078–1086.

Goldman, J. A., Phillips, D. P., and Fentress, J. C. (**1995**). ''An acoustic basis for maternal recognition in timber wolves (*Canis lupus*),'' J. Acoust. Soc. Am. **97**, 1970–1973.

Hafner, G. W., Hamilton, C. L., Steiner, W. W., Thompson, T. J., and Winn, H. E. (**1979**). ''Signature information in the song of the humpback whale,'' J. Acoust. Soc. Am. **66**, 1–6.

Halpin, Z. T. (**1991**). ''Kin recognition cues of vertebrates,'' in *Kin Recognition*, edited by P. G. Hepper (Univ. of Cambridge, Cambridge), pp. 220–258.

Hurst, J. L., Payne, C. E., Nevison, C. M., Marie, A. D., Humphries, R. E., Robertson, D. H. L., Cavaggioni, A., and Beynon, R. J. (**2001**). ''Individual recognition in mice mediated by major urinary proteins,'' Nature (London) **414**, 631–634.

Janik, V. M. (**1999**). ''Pitfalls in the categorization of behaviour: a comparison of dolphin whistle classification methods,'' Anim. Behav. **57**, 133–143.

Lengagne, T. (**2001**). ''Temporal stability in the individual features in the calls of eagle owls (*Bubo bubo*),'' Behaviour **138**, 1407–1419.

Lengagne, T., Lauga, J., and Aubin, T. (**2001**). ''Intra-syllabic acoustic signatures used by the king penguin in parent-chick recognition: an experimental approach,'' J. Exp. Biol. **204**, 663–672.

Leonard, M. L., Horn, A. G., Brown, C. R., and Fernandez, N. J. (**1997**). ''Parent-offspring recognition in tree swallows, *Tachycineta bicolor*,'' Anim. Behav. **54**, 1107–1116.

McCowan, B. (**1995**). ''A new quantitative technique for categorizing whistles using simulated signals and whistles from captive bottlenose dophins (Dephinidae, *Tursiops truncatus*),'' Ethology **100**, 177–193.

Medvin, M. B., Stoddard, P. K., and Beecher, M. D. (**1993**). ''Signals for parent-offspring recognition: a comparative analysis of the begging calls of cliff swallows and barn swallows,'' Anim. Behav. **45**, 841–850.

Okanoya, K., and Dooling, R. J. (**1991**). ''Detection of species-specific calls in noise by zebra finches *Poephila guttata* and budgerigars *Melopsittacus undulatus*: time or frequency domain?'' Bioacoustics **3**, 163–172.

Parr, L. A., Winslow, J. T., Hopkins, W. D., and de Waal, F. B. M. (**2000**). ''Recognizing facial cues: individual discrimination by chimpanzees (*Pan troglodytes*) and rhesus monkeys (*Macaca mulatta*),'' J. Comp. Psychol. **114**, 47–60.

Phillips, A. V., and Stirling, I. (**2000**). ''Vocal individuality in mother and pup South American fur seals, *Arctocephalus australis*,'' Marine Mammal Sci. **16**, 592–616.

Sayigh, L. S., Tyack, P. L., Wells, R. S., and Scott, M. D. (**1990**). ''Signature whistles of free-ranging bottlenose dolphins *Tursiops truncatus*: stability and mother-offspring comparisons,'' Behav. Ecol. Sociobiol. **26**, 247–260.

Sayigh, L. S., Tyack, P. L., Wells, R. S., Solow, A. R., Scott, M. D., and

Irvine, A. B. (**1999**). ''Individual recognition in wild bottlenose dolphins: a field test using playback experiments,'' Anim. Behav. **57**, 41–50.
Scherrer, J. A., and Wilkinson, G. S. (**1993**). ''Evening bat isolation calls provide evidence for heritable signatures,'' Anim. Behav. **46**, 847–860.
Searby, A., and Jouventin, P. (**2003**). ''Mother-lamb acoustic recognition in sheep: a frequency coding,'' Proc. R. Soc. London, Ser. B **270**, 1765–1771.
Searby, A., Jouventin, P., and Aubin, T. (**2004**). ''Acoustic recognition in macaroni penguins: an original signature system,'' Anim. Behav. **67**, 615–625.
Shannon, C. E., and Weaver, W. (**1949**). *The Mathematical Theory of Communication* (Univ. of Illinois, Urbana).
Smith, H. J., Newman, J. D., Hoffman, H. J., and Fetterly, K. (**1982**). ''Statistical discrimination among vocalizations of individual squirrel monkeys (*Saimiri sciureus*),'' Folia Phoniatr. **37**, 267–279.
Stoddard, P. K., and Beecher, M. D. (**1983**). ''Parental recognition of offspring in the cliff swallow *Hirundo pyrrhonota*,'' Auk **100**, 795–799.
Zuberbuhler, K., Noe, R., and Seyfarth, R. M. (**1997**). ''Diana monkey long-distance calls: messages for conspecifics and predators,'' Anim. Behav. **53**, 589–604.

Drilling and operational sounds from an oil production island in the ice-covered Beaufort Sea

Susanna B. Blackwell[a] and Charles R. Greene, Jr.
Greeneridge Sciences, Inc., 1411 Firestone Road, Goleta, California 93117

W. John Richardson
LGL Ltd., Environmental Research Associates, 22 Fisher Street, P.O. Box 280, King City, Ontario L7B 1A6, Canada

(Received 8 August 2003; revised 14 July 2004; accepted 14 July 2004)

Recordings of sounds underwater and in air, and of iceborne vibrations, were obtained at Northstar Island, an artificial gravel island in the Beaufort Sea near Prudhoe Bay (Alaska). The aim was to document the levels, characteristics, and range dependence of sounds and vibrations produced by drilling and oil production during the winter, when the island was surrounded by shore-fast ice. Drilling produced the highest underwater broadband (10–10 000 Hz) levels (maximum=124 dB *re*: 1 μPa at 1 km), and mainly affected 700–1400 Hz frequencies. In contrast, drilling did not increase broadband levels in air or ice relative to levels during other island activities. Production did not increase broadband levels for any of the sensors. In all media, broadband levels decreased by ~20 dB/tenfold change in distance. Background levels underwater were reached by 9.4 km during drilling and 3–4 km without. In the air and ice, background levels were reached 5–10 km and 2–10 km from Northstar, respectively, depending on the wind but irrespective of drilling. A comparison of the recorded sounds with harbor and ringed seal audiograms showed that Northstar sounds were probably audible to seals, at least intermittently, out to ~1.5 km in water and ~5 km in air. [DOI: 10.1121/1.1806147]

PACS numbers: 43.80.Nd, 43.50.Rq [WWA] Pages: 3199–3211

I. INTRODUCTION

During the winter of 1999–2000, BP Exploration (Alaska) Inc. began construction of the Northstar oil production island (position 70.49 °N, 148.70 °W) in the shallow (12 m), near-shore waters of the Alaskan Beaufort Sea, northwest of Prudhoe Bay (Fig. 1). The area is inhabited year-round by numerous ringed seals (*Phoca hispida*) that maintain breathing holes through the land-fast ice during the winter and spring. During the ice-covered season, these seals spend time on the ice, in lairs under the snow, and in the water below the ice. Ice-based and aerial surveys have shown that ringed seals have continued to overwinter near Northstar during island construction (Moulton *et al.*, 2002, 2003b) and initial production (Moulton *et al.*, 2003a). Ringed seals around Northstar have also shown tolerance toward specific construction activities such as the driving of pipes in late spring (Blackwell *et al.*, 2004). In order to help interpret the data on the occurrence of ringed seals near Northstar during winter and early spring, measurements were needed of underwater and airborne sounds and of iceborne vibrations.

The main island-construction work took place during early 2000. By March 2001, when the first of the acoustic measurements reported here were obtained, construction of the island itself was nearly completed, permanent living quarters and diesel generators had been installed, the pipelines to shore had been completed, and drilling had begun [Fig. 2(a)]. During summer 2001, a sealift brought modular buildings, gas turbine generators, and other equipment needed to complete the construction of the oil processing facilities on the island. The first oil was produced on 31 October 2001, although drilling of additional wells continued thereafter. During February–March 2002, when additional acoustic measurements were obtained, both oil production and drilling were underway.

Sounds associated with the initial island construction work in early 2000 are briefly described by Moulton *et al.* (2003b). Here we describe and compare winter sounds during the later stages of construction (early 2001) and initial oil production (early 2002). The specific objective of the present work was to measure and document the levels, frequency characteristics, and range dependence of sounds and vibrations produced by Northstar-related industrial activities (mainly drilling and oil production) occurring during the winter–early spring of 2001 and 2002. The approach involved making recordings of sounds in air and in the water below the ice, along with recordings of vibrations in the ice, at a series of increasing distances from Northstar Island. The collected data would allow us to estimate the sound levels to which seals living in the area were exposed, and the audibility range of these industrial sounds. We report broadband values, but because the auditory sensitivity of seals depends strongly on frequency (e.g., Terhune and Ronald, 1975; Richardson *et al.*, 1995; Kastak and Schusterman, 1998), we also report one-third-octave data, since these allow frequency weighting appropriate to the animals of concern.

II. METHODS

Recordings were obtained on 6, 8, and 9 March 2001, and 28 February and 1 March 2002 (Fig. 1). All recordings

[a]Corresponding author; electronic-mail: susanna@greeneridge.com

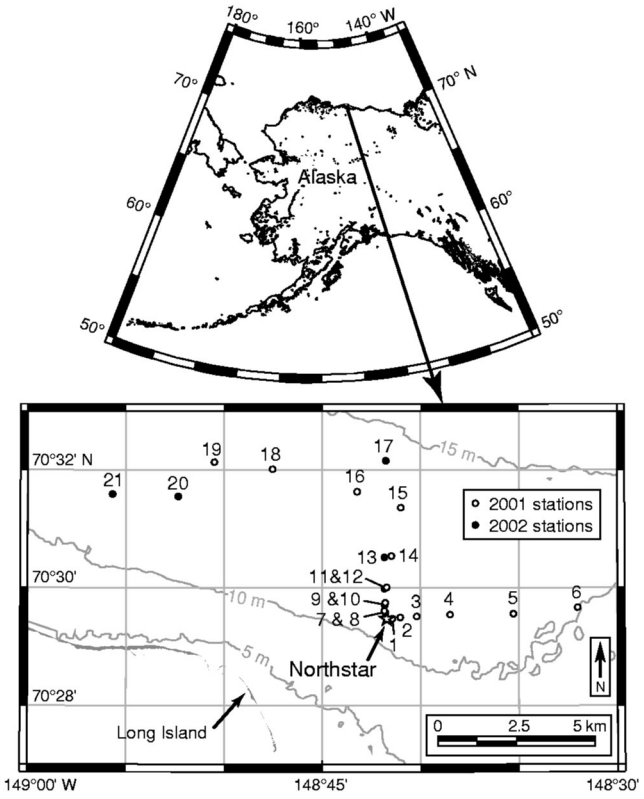

FIG. 1. The location of the study area close to Northstar Island, Beaufort Sea, Alaska, showing acoustic recording locations sampled during March 2001 plus February and March 2002. Northstar is indicated by the star.

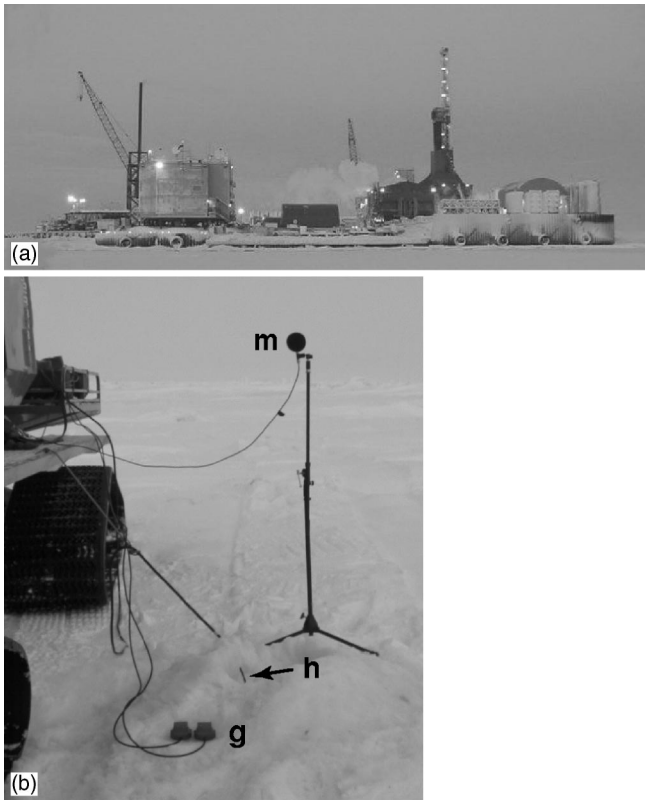

FIG. 2. (a) Northstar Island surrounded by land-fast ice, seen from the south in early February 2001. The drill rig is the tallest structure on the right side of the picture. (b) Recording setup next to an all-terrain vehicle during the 2002 measurements. m=microphone and wind shield; h=hydrophone cable disappearing into the augered hole in the ice; g=geophones planted in the ice (one was used as a backup).

were made at stations on the land-fast ice. Stations were accessed using an all-terrain vehicle for the transport of equipment and personnel (Hägglunds in 2001, Tucker Sno-Cat 1600 Terra in 2002), and a Blue Bird all-terrain vehicle equipped with a powered ice auger to drill the holes through which underwater recordings were made (Table I).

A. Equipment

The sensors included a hydrophone, a microphone, and a 3-axis geophone [Fig. 2(b)], all calibrated. The hydrophone was an International Transducer Corporation (ITC) model 6050C, which includes a low-noise preamplifier next to the sensor and a 30 m cable. The hydrophone cable was attached with cable-ties to a fairing to minimize strumming. Prior to recording, the hydrophone signals were amplified with an adjustable-gain postamplifier. In 2001, the omnidirectional microphone was an ACO model 7013 condenser microphone with a 4012 preamplifier. In 2002, we used a G.R.A.S. Sound and Vibration 1/2 in. prepolarized free-field microphone model 40AE with an ICP preamplifier model TMS426C01. The three-axis geophone was a GeoSpace model 20 with critical damping on the two horizontal axes (H_1 and H_2, perpendicular to each other) and the vertical axis (V). The geophone provided separate data for the three channels; signals were amplified with an adjustable-gain postamplifier.

Hydrophone, geophone (three channels), and microphone signals were recorded on five channels of a SONY model PC208Ax instrumentation-quality digital audiotape (DAT) recorder at a sampling rate of 24 kHz. Quantization was 16 bits, providing a dynamic range of >80 dB between an overloaded signal and the quantization noise. A memo channel on the tape recorder was used for voice announcements, and the date and time were recorded automatically.

B. Field procedures

In late February and early March of 2001 and 2002, Northstar Island [Fig. 2(a)] was surrounded by land-fast ice 1.4–1.5 m thick. Near the island and on the ice road south of the island, the ice had been artificially thickened and sometimes exceeded 2.5 m in depth. The recording procedure was identical on all days of recording. The first measurements were made as close as possible to Northstar, with subsequent recordings at progressively increasing distances, either eastward (6 and 8 March 2001) or north and northwestward (9 March 2001, 28 February, and 1 March 2002; see Fig. 1). In both years, a pressure ridge 3.5–5 km north of the island prevented us from making all our recordings in a straight northward line; instead we followed the pressure ridge to the west (Fig. 1). The decision to make recordings north and northwest of the island was based mainly on the fact that water depth increases in those directions. More seals were expected to occur there than to the south and west, where shallower water, barrier islands, and land occur (Fig. 1; cf. Moulton *et al.*, 2002). The drill rig was located on the eastern side of the island [Fig. 2(a)] but drilling was directional and oriented toward the northwest.

TABLE I. Circumstances of recordings, including distance from the drill rig tower, water depth, ice thickness, mean wind speed, and wind direction for all acoustic recording locations on the ice, 6–9 March 2001 and 28 February–1 March 2002. The general direction of the recordings in relation to Northstar, and the recording times (local), are given in parentheses.

2001					
				Wind	
Station	Dist. (m)	Water depth (m)	Ice thickness (m)	Speed (m/s)	Direction
6 March (East, 16:00-17:00)					
1	200	11.5	2.1	4.5	NE
2	460	11.5	1.2	″	″
8 March (East, 11:00-16:00)					
1	200	11.0	2.1	7.6	ENE
2	460	11.8	1.2	″	″
3	990	11.5	1.7	7.8	″
4	2030	11.3	1.4	″	″
5	4020	10.0	1.4	8.0	″
6	6050	9.0	1.5	″	″
9 March (North & Northwest, 8:45-15:45)					
8	260	11.8	2.0	6.3	ENE
10	490	11.8	1.5	″	″
12	990	11.5	1.4	7.3	″
14	1990	12.0	1.4	″	″
15	3530	12.8	1.4	8.4	″
16	4100	13.6	1.4	″	″
18	5910	14.0	1.4	9.4	″
19	7320	14.0	1.5	″	″

2002					
				Wind	
Station	Dist. (m)	Water depth (m)	Ice thickness (m)	Speed (m/s)	Direction
28 Feb. (North & Northwest, 11:16-15:14)					
9	470	12.0	1.3	0.6	E
11	970	12.5	1.5	0.1	E
13	1970	13.5	1.5	1.3	SE
17	5000	11.2	1.6	1.0	SSE
20	7620	13.7	1.4	0.8	SE
1 March (North & Northwest, 8:46-14:13)					
7	220	12.0	1.5	2.0	SSW
9	470	12.0	1.3	4.7	SW
11	970	12.5	1.5	3.8	SW
13	1970	13.5	1.5	4.3	WSW
17	5000	11.2	1.6	1.7	W
20	7620	13.7	1.4	1.7	W
21	9400	13.5	1.5	0.7	SSW

Suitable recording locations were chosen and their distances from Northstar were determined using a hand-held GPS receiver (Garmin model 12XL) or, for close distances (<800 m), a laser rangefinder (Bushnell model #20-0880). The drill rig tower [the tallest structure in Fig. 2(a)] was used as the reference at all stations. The Blue Bird augered a 30 cm (12 in.) hole through the ice, after which it moved at least 500 m away (but generally >1 km) from the recording site and remained idling (this was a mandatory safety requirement). In a comparable recording situation, Greene and McLennan (2000) did not find any differences in sound levels or spectra with and without a rolligon (a larger version of the Blue Bird we used) idling 460 m from their recording site.

The recording equipment was set up in the all-terrain vehicle. The hydrophone was lowered through the ice hole and was positioned about 1 m above the bottom. The geophone was planted in the ice and positioned with H_1 pointing directly toward Northstar. After the geophone was properly positioned, water was poured around the ''foot'' to freeze it in place. The microphone was placed 1.5–2 m above the ice with an unobstructed path to the island. It was fitted with a windscreen and, when necessary, it was shielded from the wind by the all-terrain vehicle [see Fig. 2(b)]. Recordings from all sensors commenced after all sound-generating devices on the all-terrain vehicle (engine and heater) had been turned off. An average of 5.7 min of recordings were obtained at each station, for a total of 2 h 45 min.

In 2001, the hourly wind speed and direction were obtained from the Northstar weather station, accessed on the website http://www.resdat.com/mms. In 2002, the wind speed and direction were recorded over a period of 5 min at each station with a Kestrel 2000 Pocket Thermo Wind Meter (Nielsen Kellerman, Chester, PA, 19013). This allowed us to keep better track of variations between recording stations, which were averaged out in the hourly means from the weather station.

C. Island activities during recordings

After each day of recording, island personnel provided us with detailed records of the drilling activities that took place on the island. The Nabors rig 33E on Northstar Island uses a Varco brand top-drive (250 rpm max, 1000 hp continuous). The rig is either powered by its own five diesel electric generators or by the island's power supply (see below). On one recording day each year (6 March 2001 and 28 February 2002), no drilling took place. On the other days the drill rig was operational, which included several procedures that likely varied in the amount of sound they produced. Therefore, the category ''drilling,'' as presented in this paper, includes only periods of time during which the drill bit was boring through the ground. Activities such as adding 27.5 m (90 ft) of drill pipe at the surface of the wellbore are included in the ''no drilling'' category. Oil production had not begun in March 2001, but took place on both days of recording in 2002. The term ''production,'' as used in this paper, is the pumping of crude oil while gas is being injected into the formations.

In 2001, two diesel electric generators (4-cycle, 16-cylinder engines running at 1800 rpm, cylinder firing rate =240 Hz, shaft rate=30 Hz) provided the island's power. In 2002 these had been replaced by three Solar gas-turbine-powered generators and three compressors for gas injection. Of those, the following units were functioning during the 2002 acoustic recordings: (1) ''Solar'' generator ''B,'' with a 13 000 hp=9700 kW gas turbine rated at 10 780 rpm and operating at 9500 rpm; (2) high-pressure compressor ''B,'' with a GE model LM-2500 gas-turbine engines of 30 000 hp=22 370 kW, rated at 10 000 rpm and operating at 9000–9400 rpm, the speed varying with the gas injection rate; (3) low-pressure compressor driven by a 5000 hp (3730 kW) electric motor, running at a constant speed of 3600 rpm.

Other activities that took place during recordings in both years included flooding of the island perimeter and ice road to thicken the ice, the transport of goods and personnel (in SUVs, crew-cab pick-up trucks, vans, and buses), and some hauling of mud and cuttings from the drilling activities. No flaring of gas, pile-driving, or helicopter flights occurred during the recording periods in either year.

D. Signal analysis

The recorded, digitized hydrophone signals were transferred directly to a computer hard drive as time series. They were then equalized and calibrated in units of sound pressure with flat frequency response over the data bandwidth, 4–500 Hz for the geophone, 4–10 000 Hz for the hydrophone, and 10–10 000 Hz for the microphone. Analyses were done using MATLAB (The MathWorks, 3 Apple Hill Drive, Natick, MA 01760-2098) routines and custom programs. For each recording, a sound-pressure time series (waveform) was generated, and the sound was played via a speaker to help the analyst match notes from the field with the recorded sounds. The sound waveform was used to select representative samples for further analysis. If the overall sound-pressure levels (SPLs) varied little with time, at least three 8.5-s segments of time were selected from the recording and analyzed (these segments were evenly spaced throughout the recording). If the sound waveform showed fluctuations in the SPL, then segments were taken from both the stronger and the weaker sections of the recording.

Frequency composition was determined by calculating the sound-pressure (or particle velocity for the geophone data) spectral density by Fourier analysis, using the Blackman–Harris minimum three-term window (Harris, 1978). The averaging time for such measurements was 8.5 s. The transform length was one second. With windowing, the spectral resolution was 1.7 Hz with 1-Hz bin separation. Transforms were overlapped by 50% and therefore 16 power spectral densities were averaged for each 8.5-s measurement.

To show how received levels varied with distance from the activity, root-mean-square (rms) broadband sound-pressure and vibration levels were plotted against range from the dominant source. An interpretation of these data is complicated by variability of the sources within and between recordings, and by the possible presence of sound from more than one sound source. Nevertheless, the ''received level versus range'' plots give an estimate of the range of levels received at several distances during the activity studied. A tone was identified when the sound-pressure spectral density level (SPSDL) for a given frequency was greater than the SPSDL for both adjacent frequencies, and at least 5 dB above the nearest minimum SPSDL at a lower frequency. The detection range for a band or tone was the distance beyond which SPLs for that band or tone remained constant (within $\sim\pm 2$ dB).

Microphone and geophone data were transferred to disk files and analyzed in the same way as hydrophone data; values for all sensors in this paper were unweighted. The three-axis geophone senses particle velocity in three orthogonal directions; results from these three channels are presented separately. Microphone data are expressed in dB *re*: 20 μPa and geophone data are expressed in dB *re*: 1 pm/s (picometer per second).

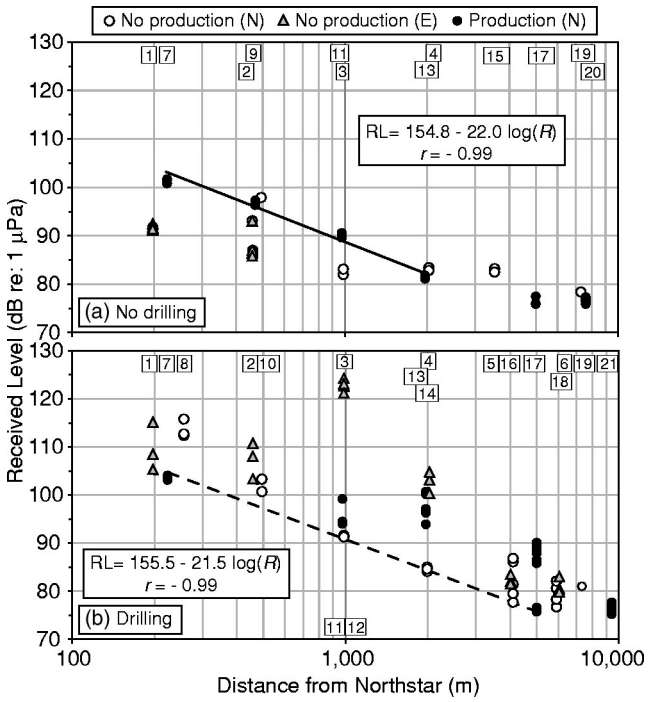

FIG. 3. Broadband (10–10 000 Hz) levels of underwater sound as a function of distance from the drill rig tower on Northstar Island, for conditions of (a) no drilling, with and without production; and (b) drilling, with and without production. Data collected on 6, 8, and 9 March 2001, plus 28 February and 1 March 2002, north (N) and east (E) of Northstar. Station numbers are indicated above their respective datasets (Fig. 1, Table I). Also shown are the logarithmic spreading loss models (see the text for details).

When appropriate, a propagation model was fitted to the broadband data in order to characterize the propagation loss underwater, in air, and through the ice. The model used was based on logarithmic spreading loss, appropriate for describing sound loss versus distance when used within the range of distances for which measurements were obtained:

$$\text{Received Level } (\mathbf{RL}) = A - B \cdot \log(R), \tag{1}$$

where R is the range in m. **RL** is in dB *re*: 1 μPa underwater, dB *re*: 20 μPa in air, and dB *re*: 1 pm/s in the ice. When fitting the model to the data, recordings at increasing distances from the sound source were included until the broadband levels reached a minimum and remained constant (to within $\sim\pm 2$ dB).

III. RESULTS

A. Underwater sound

1. Broadband levels

Received broadband (10–10 000 Hz) levels of underwater sound are shown in Fig. 3 for four sets of recording conditions: *No drilling, no production* and *No drilling, with production* [Fig. 3(a)]; *Drilling, no production* and *Drilling, with production* [Fig. 3(b)]. The highest broadband SPL (124 dB *re*: 1 μPa) was recorded during drilling, 1 km east of Northstar. The lowest broadband SPLs ($\sim$75 dB *re*: 1 μPa) were reached at stations 5–8 km northwest of Northstar, both

during and without drilling, and correspond to background levels. The sound propagation model represented by Eq. (1) was fitted by least-squares to the recordings obtained during production but no drilling, for which four stations of data were available, exclusive of distant stations where received levels had apparently reached background values. The resulting regression line and equation are shown in Fig. 3(a). The spreading loss term, B in Eq. (1), was 22.0 dB/tenfold change in distance. Received levels during drilling [Fig. 3(b)] tended to be higher, but were extremely variable. It was therefore not possible to fit the sound propagation model to a complete dataset in a reasonable way. Instead, for purposes of comparison, we fitted the model to the lowest broadband level recorded at each northern station during both years (ranges 220, 490, 990, 1990, 4100, and 5000 m), regardless of whether production was taking place or not [Fig. 3(b)]. This allowed us to estimate propagation loss of underwater sound associated with baseline island activities despite large variations in SPLs that were likely due to varying activities at Northstar. The spreading loss term obtained was 21.5 dB/tenfold change in distance.

Based on the data shown in Fig. 3(a), we can infer that the distance at which broadband values reached a minimum in the absence of drilling was 3–4 km during oil production at Northstar. Without production SPLs were unchanged 1–4.5 km from the island, beyond which they dropped another 5 dB. During drilling [Fig. 3(b)], these values were ~4–6 km without production and 5–9.4 km with production taking place.

2. Spectral characteristics

Figure 4 shows mean underwater one-third-octave band levels for three sets of recording conditions: (a) Without drilling or oil production; (b) without drilling but with oil production; and (c) with both drilling and oil production taking place. Elevated and range-dependent received levels are evident at frequencies below 100 Hz in all three plots. These likely can be attributed to baseline island sounds such as power generation. The infrasonic peak centered at 6–8 Hz was present in the majority of underwater recordings during both years. Another peak at 125–160 Hz is only prominent in the data recorded in 2002 [Figs. 4(b) and 4(c)] and may therefore be linked to oil production and/or the operation of gas turbines. Finally, a peak centered at 1 kHz was associated with drilling activity in most cases, and was rarely found in the absence of drilling [Fig. 4(c)]. However, the association with drilling was not perfect. For example, during recordings at stations 13 and 17 (2 and 5 km, during drilling) the peak was present in 16 of 17 segments. In contrast, in the absence of drilling at station 20 (7.6 km) it was seen in only 1 of 8 segments.

In summary, it is likely that the peak centered at 1 kHz was caused by some machinery normally, but not always, used during drilling. According to the drilling records, the drilling activities performed during recordings at stations 13, 17, and 21 (2, 5, and 9.4 km) were the same, but none of the segments at the farthest station contained a 1 kHz peak [Fig. 4(c)]. It is therefore likely that the peak was no longer detectable at 9.4 km.

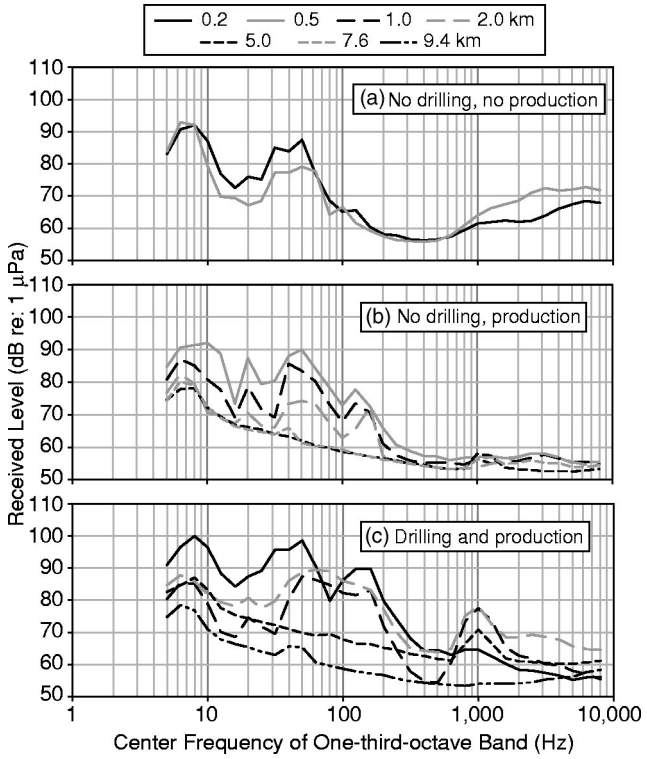

FIG. 4. Received underwater sound-pressure levels in one-third-octave bands (5–8000 Hz center frequencies), for conditions of (a) no drilling, no production; (b) no drilling, with production; and (c) drilling and production. Data collected on 6 March 2001 in (a), 28 February 2002 in (b), and 1 March 2002 in (c).

The ''drilling peak'' near 1 kHz is emphasized in Fig. 5, which compares narrowband spectra (5–10 000 Hz) of underwater sound with and without drilling. These data represent two 8.5-s segments recorded in 2002 at station 13, 2 km from the drill rig, on two consecutive days: one with and one without drilling. Oil production was taking place on both occasions. During drilling, received levels were markedly higher for the 60–250 and 650–1400 Hz bands. The 1 kHz ''drilling peak'' was also found in drilling segments from 2001, without production taking place.

The presence in Fig. 5 of tones at 20, 30, 40, 50, and 60

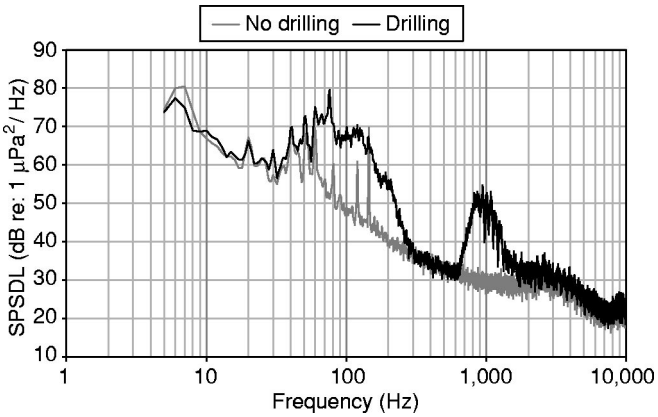

FIG. 5. Narrowband spectra (5–10 000 Hz) of underwater sound recorded from the same location (station 13, 2 km from the drill rig) on two consecutive days in 2002, one with drilling and one without. Oil production was occurring at both times. SPSDL=sound-pressure spectral density level.

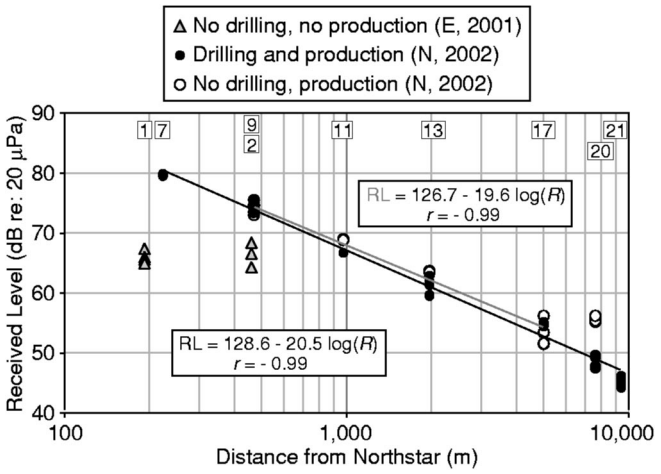

FIG. 6. Broadband (10–10 000 Hz, unweighted) levels of airborne sound as a function of drilling, production, and distance from the drill rig tower on Northstar Island. Data collected on 6 March 2001 (eastward, gray triangles), and 28 February and 1 March 2002 (northward, open, and filled circles, respectively). Station numbers are indicated above their respective datasets. Also shown are the logarithmic spreading loss models (see the text for details).

Hz, both during and without drilling, indicates that these tones are probably related to power generation on the island. The same set of tones was seen during and without drilling in 2001, with diesel rather than gas-turbine generators. The 60 Hz power generation tone was found out to distances of 2–3.5 km during both years.

Overall, the tones produced by generators, turbines and compressors on Northstar could not be identified reliably in the water. In 2001, a 30 Hz tone was detectable up to 6 km from Northstar. This corresponds to the shaft rate of the diesel electric generators, but the presence of the tone in 2002 indicates multiple sources, since the diesel generators had then been decommissioned. In 2002, tones expected from the turbines (i.e., in the 150–158 Hz range) were detected at all stations on 28 February, but only in two segments (at stations 7 and 21) on 1 March. However, the SPLs of these tones varied independently of their distance from Northstar. Finally, the shaft rate for the low-pressure compressor (60 Hz) could not be distinguished from a power generation source.

B. In-air sound

1. Broadband levels

Received broadband (10–10 000 Hz, unweighted) levels of airborne sound are shown in Fig. 6. To minimize wind contamination in the data, only recordings obtained with wind speeds <5 m/s were used. This eliminated all recordings from 8 and 9 March 2001. Both the highest (80 dB re: 20 μPa) and lowest (44 dB re: 20 μPa) broadband levels were obtained in 2002, at the closest (220 m) and farthest (9.4 km) stations, respectively (Fig. 6). Broadband levels east of the island in 2001, before oil production had started, were 10–15 dB lower than levels north of the island in 2002, despite the generally lower wind speeds in 2002.

The sound propagation model represented by Eq. (1) was fitted by least squares to the 2002 data (during production) with and without drilling, and the resulting regression lines and equations are shown in Fig. 6. Spreading loss terms (20.5 vs 19.6 dB/tenfold change in distance, respectively) and constant terms [A in Eq. (1), 128.6 vs 126.7 dB re: 20 μPa, respectively] were very similar for both situations. On 1 March 2002, which included all the recordings during drilling, broadband levels continued decreasing until the farthest station, 9.4 km from Northstar. On 28 February 2002, the day with the least wind and also a day with no drilling, Northstar was still faintly audible to the field crew at the 5 km station.

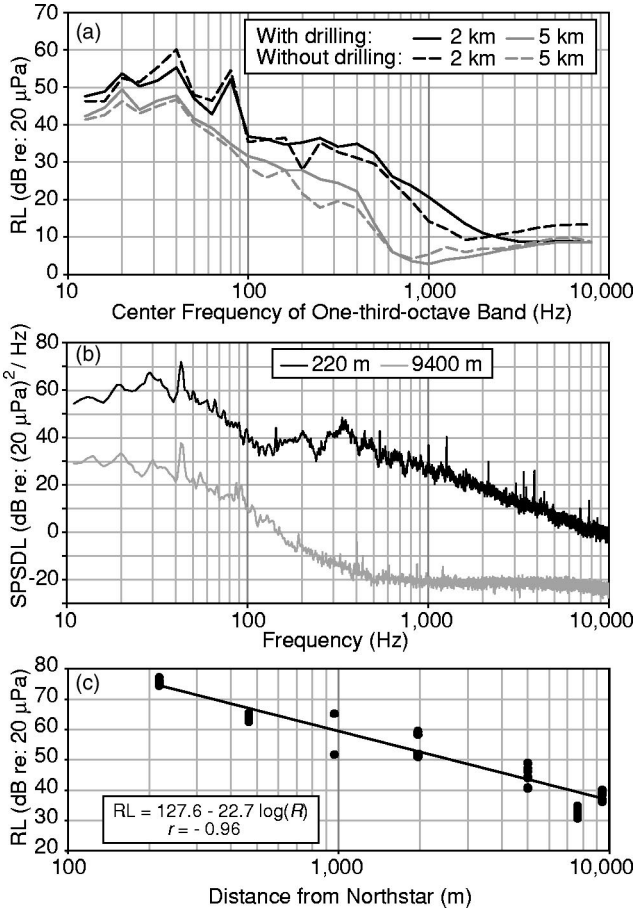

FIG. 7. Spectra and received levels of airborne sounds as a function of distance to the source. (a) One-third-octave band levels (12.5–8000 Hz center frequencies) for two stations where recordings were made on two consecutive days, one with and one without drilling (28 February and 1 March 2002; production occurring at all times). (b) Narrowband spectra (11–10 000 Hz) from the closest (0.2 km) and farthest (9.4 km) stations on 1 March 2002, during drilling and production. One representative 8.5-s segment was chosen from each station. SPSDL=sound-pressure spectral density level. (c) Unweighted received SPL for the 42–45 Hz tone on 28 February and 1 March 2002, as a function of distance from Northstar. RL =received level.

2. Spectral characteristics

Figure 7(a) compares one-third-octave band levels for two stations at which recordings were made on two consecutive days, with and without drilling. These data were obtained in 2002, while production was taking place. Band levels were similar with versus without drilling, consistent with the close similarity found in broadband levels with versus

without drilling (see Fig. 6). Distinct peaks can be seen at the one-third-octave bands centered at 40 and 80 Hz; these peaks are present at 2 km both with and without drilling. Higher frequencies (>2 kHz) leveled off 2–5 km from Northstar, whereas lower frequencies (<630 Hz) continued decreasing out to the farthest station, 9.4 km from Northstar.

A tone at 42–45 Hz accounts for the peak in the one-third-octave band centered at 40 Hz [Fig. 7(a)]. This tone was evident at 11 out of 12 stations sampled in 2002; the only location at which it was absent was 7.6 km from Northstar on 28 February. The tone was found in 53 of 65 segments analyzed (82%) and can be seen in Fig. 7(b), showing narrowband spectra from the closest and farthest stations on 1 March 2002 (during drilling). This tone is likely part of the island's power generation. The sound propagation model [Eq. (1)] was fitted by least-squares to the SPL for the tone as received at every station over both days [Fig. 7(c)]. The spreading loss term was 22.7 dB/tenfold change in distance. The greatest difference between the two spectra, about 60 dB, was found at about 350 Hz [Fig. 7(b)]. The 60 Hz power frequency tone was only detected in a few (5%) segments at two stations.

A tone at 81 Hz was the cause of the peak in the one-third-octave band centered at 80 Hz, and was only found in three recordings: on 28 February at the 1 and 2 km stations (#11 and 13, respectively) and on 1 March at the 2 km station (#13). In the latter case, the peak was present in only part of the recording, suggesting that it may be linked to a particular activity or piece of machinery. Activities reported at the rig during these three recordings did not shed any light on the possible origin of the tone.

C. Iceborne vibrations

1. Broadband levels

Mean broadband (10–500 Hz) particle velocity (PV) levels, as recorded by the geophone channels, are shown in Fig. 8(a) in the absence of drilling, and in Fig. 8(b) during drilling. Both plots display 2002 data. In 2001, geophone measurements were only made on 9 March. Those recordings were affected by wind and showed high variability, particularly for the vertical and H_2 channels. The less-affected H_1 data are shown in Fig. 8(b) for comparison with 2002. Broadband levels for the H_1 channel during drilling were very similar in 2001 with no production [gray filled circles in Fig. 8(b)] and in 2002 with production (black circles). However, in 2001 the H_1 values stopped decreasing at 2 km. Beyond that distance, wind probably became the dominant source. In 2002, H_1 broadband levels continued to decrease until the farthest station, at 9.4 km.

The sound propagation model represented by Eq. (1) was fitted by least squares to the 2002 data for H_1, with [Fig. 8(b)] and without [Fig. 8(a)] drilling. As for the in-air data, the spreading loss terms (19.2 vs 19.6 dB/tenfold change in distance) and constant terms (159.6 vs 160.5 dB re: 1 pm/s) were nearly identical with and without drilling. Spreading loss terms of $\sim 20\log(R)$, where R is distance (in m) from Northstar Island, suggest that the island was the dominant source of the measured iceborne vibrations.

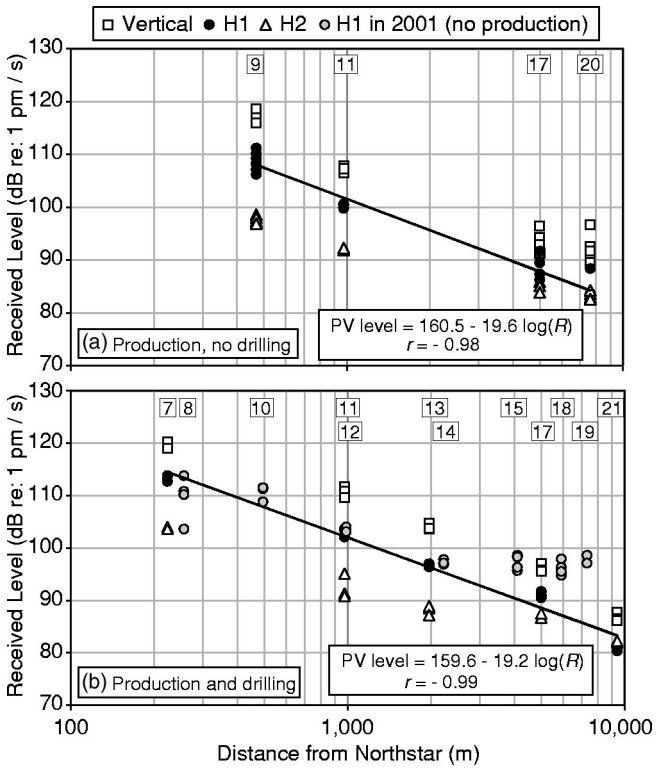

FIG. 8. Mean broadband (10–500 Hz) particle velocity levels as a function of distance from the drill rig, for all three geophone channels and two production and drilling conditions in 2002 [(a) 28 February and (b) 1 March]. Values for channel H_1 in 2001 (9 March, during drilling but no production) are also shown in (b). Station numbers are indicated above their respective datasets. Also shown are the logarithmic spreading loss models (see the text for details). PV=particle velocity.

2. Spectral characteristics

Figure 9 presents mean one-third-octave band levels for the H_1 geophone channel (pointing toward the sound source) for three sets of recording conditions: (a) Drilling but no production; (b) production but no drilling; and (c) production and drilling. All three plots show elevated values in the one-third-octave bands centered at 20–40 Hz, but the peak is more distinct and more closely related to range from Northstar during production [Figs. 9(b) and 9(c)]. During drilling and production, this peak is small but still evident 9.4 km from the island [Fig. 9(c)]. During production [Figs. 9(b) and 9(c)] there is also an increase in received one-third-octave levels with increasing frequency above 100 Hz, particularly for the closer stations.

Figure 10 shows narrowband spectra (5–400 Hz) for the geophone vertical channel at four distances on 1 March 2002, during drilling and production. The largest peaks, at ~27 and 43 Hz, were present in all four recordings. Though the received levels diminished with increasing range, both peaks remained relatively prominent out to the farthest station, 9.4 km from Northstar. A smaller range-dependent peak at ~60 Hz could also be distinguished out to 9.4 km. Above 200 Hz, differences in received levels at 1 and 9.4 km were small, on average <6 dB. Received levels at ~7 Hz were the same at 0.5, 1, and 9.4 km. A peak at this frequency has been noted in most of our underwater recordings since the beginning of Northstar construction. It did not seem to vary as a

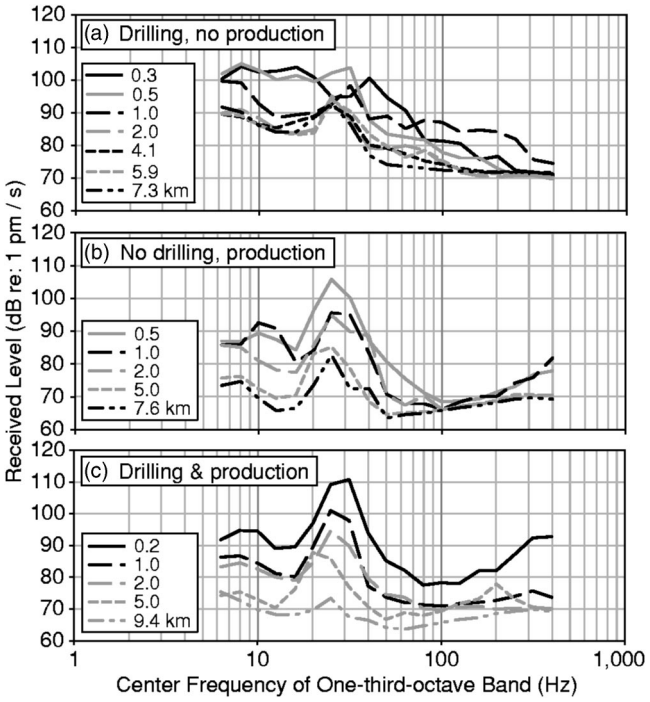

FIG. 9. Received iceborne H_1 particle velocity levels for one-third-octave bands (6.3–400 Hz center frequencies), for three sets of production and drilling conditions. Data collected on 9 March 2001 in (a) and 28 February and 1 March 2002 in (b) and (c).

function of distance to the island or the activity taking place, and has been noted independently by other observers (i.e. Shepard *et al.*, 2001).

The main results for all three sensors are summarized in Table II.

IV. DISCUSSION

A. Sounds during drilling

Drilling sounds were readily identifiable underwater (see Fig. 5) and drilling resulted in marked increases in level for the frequency bands 60–250 Hz and 650–1400 Hz. The higher-frequency peak was still clearly detectable 5 km from the drill rig, but had fallen to background values by the 9.4 km station [Fig. 4(c)]. The lower-frequency peak straddled the range of frequencies involved in power generation on the

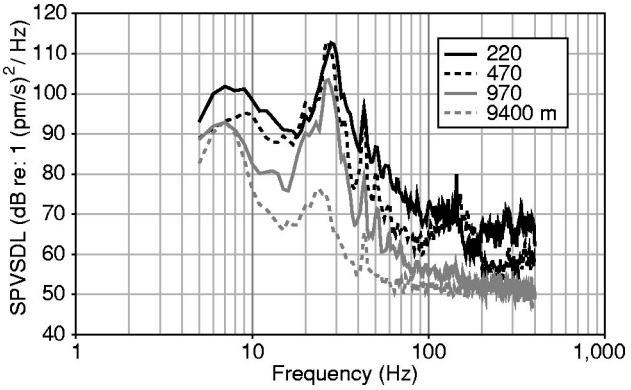

FIG. 10. Narrowband spectra (5–400 Hz) for geophone vertical channel at four different distances from Northstar, during drilling and production. SPVSDL=sound particle velocity spectral density level.

island—60 Hz and multiples thereof. However, power generation is most likely also responsible for peaks at 10 Hz and its harmonics (i.e., 20, 30, 40, 50, 70, 80, and 90 Hz), which have been common in recordings since the beginning of construction at Northstar (see Greene and McLennan, 2000). During drilling it is reasonable to expect an increase in the level of sound and vibration from any equipment having to work harder, including the machinery used for power generation as well as that directly involved in drilling.

In air it was not possible to distinguish drilling sounds from overall island sounds based on broadband levels (Fig. 6) or on spectral characteristics [Fig. 7(a)]. The logarithmic spreading loss models obtained with and without drilling were nearly identical and had very high associated r values. There was no temporal variation in broadband SPLs within stations during drilling on 1 March 2002 (Fig. 6), unlike what was seen in the underwater recordings [Fig. 3(b)]. In addition, the field crew could not distinguish drilling sounds from overall island sounds by listening in the field, even at the stations closest to Northstar (220–470 m away). A tone at 42–45 Hz was present both with and without drilling, and in quiet conditions it was detectable in air at the farthest station (9.4 km). Production was occurring at these times, but the specific origin of the tone is unknown.

Similar results were found for geophone channel H_1. Broadband levels of iceborne vibrations with or without drilling were indistinguishable (Fig. 8). However, the levels for one-third-octave bands centered at 20–40 Hz were elevated during production, and were the same or only marginally higher during drilling plus production as for production alone [Fig. 9(b) vs 9(c)].

Thus, the results (see Table II) show that drilling did not increase the broadband levels of airborne sound or iceborne vibrations originating from Northstar. In contrast, underwater broadband levels were notably higher during drilling. Spectral analyses revealed that, for all three sensors, tones or peaks in frequency believed to originate at the island could still be detected at the farthest station (9.4 km) but it was unclear whether these were related to drilling.

Previous studies of underwater (i.e., under-ice) noise from winter drilling on icebound gravel islands and ice pads have indicated that drilling noise is clearly detectable at close ranges, but is generally confined to low frequencies and has low received levels. Drilling sounds transmit poorly from the drill rig machinery through gravel into the water (Richardson *et al.*, 1995). Malme and Mlawski (1979) measured the underwater sound associated with drilling rigs operating on two icebound gravel islands (one natural and one man-made) near Prudhoe Bay during the month of March. They found that most drilling sound was below 200 Hz and that broadband levels reached ambient values ~1.5 km from the islands; with low ambient noise, low-frequency tones were measurable to ~9.5 km, but with high ambient noise they were undetectable beyond ~1.5 km. Richardson *et al.* (1990) reported broadband (20–1000 Hz) drilling sounds from a rotary-table drill rig on an ice pad grounded in very shallow water (6–7 m). Again, drilling sounds were confined to low frequencies, <350 Hz. At 2 km, drilling sounds reached 85 dB re: 1 μPa and were barely detectable; this is equivalent

TABLE II. Summary of the main results: highest broadband value recorded and distance (in m) at which it was recorded; broadband value at 1000 m from the source; ''background'' (i.e., lowest) value and distance at which this background value was reached; center frequency of the main peaks in the one-third-octave and narrow band data; spreading loss terms, when available. Underlined center frequencies are the more important ones.

	Broadband received levels				
	Highest level recorded (distance)	Lowest level at 1000 m	''Background'' level (closest distance with that level)[d]	Center frequency of peak(s)	Spreading loss term (dB/tenfold change in distance)
Underwater sound (in dB *re*: 1 μPa)[a]					
No drilling, no production (N)	98 (500 m)	83		7, 40	
No drilling, production	102 (220 m)	91	76 (3–4 km)	7, 20, 50, 125	22.0
Drilling, no production (N)	116 (250 m)	92	77 (4–6 km)		
Drilling, no production (E)	124 (1000 m)	124	80 (5 km)		
Drilling and production	104 (220 m)	99	76 (5–9.4 km)	7, 50, 125, 1 k	21.5
In-air sound (in dB *re*: 20 μPa)[b]					
No drilling, production	74 (470 m)	69	52 (5 km)	20, 40, 80	19.6
Drilling and production	80 (220 m)	67	44 (9.4 km)	20, 40, 80	20.5
Iceborne vibrations (H_1) (in dB *re*: 1 pm/s)[c]					
Drilling, no production	114 (250 m)	104	95 (2–4 km)	25–40	
No drilling, production	111 (470 m)	100	82 (5 km)	25	19.6
Drilling and production	114 (220 m)	102	80 (9.4 km)	20–31.5	19.2

[a]Bandwidth 5–10 000 Hz for underwater sound (unweighted).
[b]Bandwidth 10–10 000 Hz for in-air sound (unweighted).
[c]Bandwidth 5–500 Hz for iceborne vibrations (unweighted).
[d]Note that broadband levels of in-air sound and iceborne vibrations did not differ with versus without drilling or production, and the variation in the distance to background levels is due entirely to the variation in recording conditions. Similarly, only drilling affected underwater levels of broadband sound (see the text).

to the values obtained in the present study during drilling with a top-drive rig and no production [Fig. 3(a)]. Finally, Greene (1997) measured sounds during February from a rotary-table drilling operation on Tern Island, an artificial gravel island in the Liberty Prospect, east of Prudhoe Bay. Again water depth was 6–7 m, shallower than at Northstar. A comparison of spectra from the two sites, obtained during drilling 1160 m from Tern Island and 970 from Northstar, showed them to be very similar, despite the different types of drilling rigs. Sound-pressure levels in the Northstar recording were a few dB higher, particularly at low frequencies, but both spectra displayed prominent tones at 20, 40, 50, 60, and 120 Hz and heightened levels at ~30–200 Hz.

Results from the present study indicate that winter drilling can increase underwater sound levels at somewhat higher frequencies, i.e., 650–1400 Hz. Recording conditions were unusually quiet (low wind speeds) in 2002, when the ''drilling peak'' centered at ~1 kHz was detectable up to at least 5 km from Northstar. An inspection of unpublished higher-frequency data from Tern Island (from the work of Greene, 1997) showed that the spectrum there also contained a ''drilling peak'' at 800–2000 Hz, similar to the results from Northstar (Fig. 5).

Sound levels from drilling on icebound caissons with concrete or metal sides have not been documented very extensively, but are expected to be somewhat higher than those from gravel islands given the (presumed) better coupling to the bottom and water. The CIDS (Concrete Island Drilling System) is a self-contained floatable concrete structure that is ballasted down onto the bottom. Hall and Francine (1991) made under-ice recordings of the sounds produced by the CIDS during winter drilling with a rotary-table rig. Broadband (20–1000 Hz) levels 1370 m from the source were ~90 dB *re*: 1 μPa, which is ~2 and 4 dB above values obtained in this study with and without drilling, respectively, for the same frequency band. However, Hall and Francine found that CIDS also produced a much stronger infrasonic tone at 1.375–1.5 Hz, outside the bandwidth considered during this and other studies of drilling sound. They attributed the infrasonic tone to the rotary table drill rig aboard CIDS, which turned at 75–110 rpm (1.25–1.83 Hz).

Of all the offshore drilling operations in the Arctic, drillships and their support vessels apparently produce the highest sound levels. The drillship hull contains generators, the drill rig and other machinery, and is well coupled to the water. Also, support vessels are usually present near drillships. Greene (1987) measured sounds during drilling from the ice-strengthened drillships *Explorer II* and *Kulluk* (with a number of support ships present). Broadband (20–1000 Hz) levels 1, 2, and 5 km from the *Explorer II* and *Kulluk* were nearly 40 and 50 dB higher, respectively, than levels recorded at the same distances during drilling at Northstar.

A number of variables during drilling can potentially account for some of the temporal variation in broadband levels that is visible in Fig. 3(b). These include (1) composition of the layer being drilled through, which was gravel on 8 March 2001 and clay on 9 March 2001; (2) depth of the drill bit, which varied by an order of magnitude during our measurements (255–2880 m); (3) bit torque and rotation rate, the latter ranging from 0 to 150 rpm; (4) the rate of penetration,

ranging from 6 to 150 m per hour during our measurements; and (5) bathymetry, which was shallower east than north of the island. In addition, other sources of sound were operating on the island and in the Prudhoe Bay area, and could contribute to overall SPLs. Activities started, stopped, or changed in an uncontrolled manner within and between our recordings at different distances. On the island itself, the type and identity of the generators and turbines involved in power generation varied on a daily—and sometimes hourly—basis. Nevertheless, despite this variation in the data, fitting a logarithmic propagation loss model to the minimum values recorded during drilling resulted in a spreading loss term very close to that obtained with no drilling, i.e., about 20 dB/tenfold change in distance.

B. Sounds during production

Production operations were underway in early 2002 but not in early 2001. There was little evidence that oil production at Northstar during wintertime led to higher levels of underwater sound. Underwater broadband levels recorded north of the island were similar with and without production, whether or not there was simultaneous drilling (Fig. 3). Although the broadband underwater levels did not seem to be affected appreciably by the occurrence of production, one-third-octave analysis (Fig. 4) revealed a peak at 125–160 Hz that could be due to production. This peak was no longer detectable 5 km from the island, either with [Fig. 4(c)] or without [Fig. 4(b)] simultaneous drilling. Thus, oil production at Northstar did not cause any substantial increase in overall broadband levels of underwater sound relative to the levels in the absence of production. However, production probably caused a change in frequency composition. This was to be expected for two reasons: (1) ''No production'' recordings were obtained while diesel generators provided the island's power source (2001), whereas ''production'' recordings were obtained after the island had shifted to gas turbines (2002); (2) production implies the use of compressors, which were an additional sound source.

There were not enough good quality in-air recordings to determine the effect of oil production on airborne levels. In the absence of drilling, measurements made *north* of the island with production (open circles in Fig. 6) had higher broadband levels than did measurements at similar distances *east* of the island with no production (gray triangles in Fig. 6). Although consistent with the expectation that in-air sounds would be stronger with than without production, the apparent difference is more likely a function of the recording location.

There was no evidence that ice vibration levels, on a broadband (10–500 Hz) basis, were affected by the start of oil production or the associated change in power source. Geophone recordings north of the island during 2001 and 2002 yielded nearly identical values up to 2 km from Northstar [Fig. 8(b); gray versus black circles]. At 2 km, particle velocity levels reached a minimum (~97 dB re: 1 pm/s) in 2001, most likely because of the higher wind speeds during those recordings. Sounds of snow blowing on the ice surface were distinct on the geophone recordings. Levels in the bands centered at 25–40 Hz were slightly elevated with drilling and no production [Fig. 9(a)], but increased with production and drilling combined [Fig. 9(c)]. This was probably a result, at least in part, of the increased demand for power generation during these activities; indeed, a peak centered at 25 Hz was still evident 9.4 km from Northstar [Figs. 9(c) and 10].

C. Sounds from power generation

The electric power source at Northstar Island consisted of diesel generators during acoustical measurements in early 2001 and gas turbine generators in early 2002. Also, gas turbine compressors were in use in 2002 to compress and inject natural gas. Overall, the transition from diesel to gas turbine power did not seem to result in detectable changes in broadband levels of island sounds in the water or in the ice. In-air sound recordings obtained before and after the transition were not directly comparable because of different recording locations (N vs E). Tones expected underwater from the generators and turbines variously could not be found, or appeared unpredictably in time and space, or were multiples of the 60 Hz power generation tone and were therefore not distinguishable. In both years, the 60 Hz tone could not be detected beyond 3.5 km underwater and was unusual in air. Tones at frequencies of 42–45 Hz were detectable in air at all stations, but their origin was unknown. The sounds from power generation were low frequency in nature and contained a number of tones (as well as their harmonics) at frequencies below 100 Hz. Tones in the 10 Hz family (e.g., 10, 20, 30 Hz, etc.) are attributed to vibrations in the diesel–electric power generation. These tones have been prevalent in all recordings (during both winter and summer) since the first utility generator was installed on Northstar in August 2000.

D. Background levels

Underwater background levels, as recorded at the farthest stations, were 77 dB re: 1 μPa in 2001 and 76 dB in 2002 (broadband, 10–10 000 Hz band). The spectrum levels of these background sounds were well below the Knudsen *et al.* (1948) sea state 0 curve, and fall within the range of other under-ice ambient noise measurements made away from anthropogenic sound sources (e.g., Greene and Buck, 1964; Milne and Ganton, 1964).

In-air sound levels recorded during drilling and production (filled circles in Fig. 6) decreased to as low as 44 dB re: 20 μPa (broadband, 10–10 000 Hz) at the farthest station (9.4 km). Because the values never reached a minimum, we cannot state with certainty that these were background levels. If A-weighted, these data convert to broadband levels of 20 dBA re: 20 μPa. This value falls at the lower range of the Kinsler *et al.* (2000) ''wilderness'' category (given in dBA), corresponding to some of the quietest environments found in nature. They are also the lowest in-air broadband levels we have recorded in the area since Northstar construction began in 2000.

In 2002, broadband (10–500 Hz) PV levels measured in the ice during drilling and production for geophone axis H_1 (pointing toward Northstar) continued decreasing until the

farthest station (9.4 km), reaching a low of 80 dB *re*: 1 pm/s. Greene and Buck (1964) reported spectrum levels of vertical velocity (25–1000 Hz band) as received by a seismometer (geophone) in thin (38 cm) ice far offshore in the Beaufort Sea. Recording conditions during our measurements were exceptionally quiet, so we compared vertical data from our most distant station (9.4 km from Northstar, Fig. 10; ice thickness 1.5 m), with the lowest values found by Greene and Buck (1964). Broadband levels 9.4 km from Northstar were probably close to background values. Minimum values measured by Greene and Buck (1964) were about 5 dB lower than those in the present study at 25 Hz, but higher by 9–11 dB at 50, 100, 200, and 400 Hz. The Greene and Buck measurements were made during April in the central Arctic ice pack, a more dynamic environment (in terms of ice movement) than the shore-fast ice of our study. This could explain their higher values at frequencies above 30 Hz. Also, their study area was completely removed from industrial activity, whereas our measurements 9.4 km from Northstar still contain evidence of industry-related vibrations, such as the peaks at 24 and 43 Hz (Fig. 10).

The shallow water depth around Northstar will tend to limit the transmission of low frequencies. This results in a ''dip'' in received levels, mainly below 20 or 30 Hz, which can be seen in data from both the hydrophone (Fig. 5) and the geophone (Fig. 10). Low-frequency cut-off in propagation could therefore explain the lower received levels in the 10–30 Hz frequency range.

E. Detection ranges

The ranges at which Northstar sounds reached background levels varied among the three media (water, air, and ice) and are summarized in Table II. These ranges are strictly the distances at which broadband levels stopped decreasing; stronger frequency peaks or tones produced by Northstar were detectable beyond these distances. It is important to point out that the ranges were also a function of the recording conditions, determined principally by wind speed. Wind affected all sensors in 2001, but particularly the microphone and the geophone. The detection ranges at times with the best recording conditions and the highest source levels yield conservative (high) estimates of island audibility. Therefore we mainly based our ranges on data collected in 2002, during production and when recording conditions were the quietest. Northstar sounds then reached background levels underwater by 10 km with drilling and 3–4 km without. In air, background levels were reached 5–10 km from Northstar, depending on the wind, irrespective of drilling. In the ice, background vibration levels were reached 2–10 km from the island, depending on the geophone channel and the wind speed. At times with high background noise (e.g., windy periods), Northstar sounds disappeared below ambient levels at closer distances.

Northstar is located in shallow Arctic waters and was surrounded by land-fast ice during this study in early 2001 and early 2002. The island was also mainly in a drilling and/or production phase, rather than an active construction phase. We conclude that the sounds produced during the activities studied here, and for all three sensors, reached background levels by 10 km in quiet ambient conditions, and by 2–5 km in noisier ambient conditions. Drilling produced a wide range of SPLs, depending on the type of drilling activity. Overall, sound levels from Northstar during drilling and production were low in comparison with drill ships or drilling from caissons, and comparable to drilling from grounded ice pads or other artificial islands. Sounds recorded from all three types of sensors showed a very consistent spreading loss of about 20 dB/tenfold change in distance over the range of distances studied (0.2–9.4 km).

F. Audibility by seals

The maximum detection distances presented above are based on data extending, on a unweighted basis, from 10 to 10 000 Hz for underwater and airborne sounds, and from 10 to 500 Hz for iceborne vibrations. However, seals do not have equal hearing sensitivity at all frequencies (Richardson *et al.*, 1995; Kastak and Schusterman, 1998). The auditory sensitivity of ringed seals, which occupy the land-fast ice near Northstar, has been documented only at frequencies $\geqslant$1 kHz underwater (Terhune and Ronald, 1975), and not at all in air. More information exists for harbor seals, *Phoca vitulina* (Møhl, 1968; Terhune and Turnbull, 1995; Kastak and Schusterman, 1998; Schusterman *et al.*[1]), which are close relatives of ringed seals. To assess the audibility of Northstar sounds to seals, we compared one-third-octave band levels of recorded sounds to available audiogram data for both species, both underwater [Fig. 11(a)] and in air [Fig. 11(b)]. (The detectability of ice vibrations to seals cannot at this point be discussed, as we are not aware of any publications on that topic.) These comparisons assume that the critical bandwidth (CBW) for ringed and harbor seal hearing is approximately one-third-octave, and that detection occurs when the signal level in one or more one-third-octave bands exceeds the auditory threshold at the corresponding frequencies.

These assumptions seemed more reasonable to us than adding critical ratios (CRs) to spectrum levels of industrial sound, in a case where the signal spectrum contains tones or is otherwise far from flat (see, for example, Fig. 5). For ringed seals, CBWs underwater were estimated by Terhune and Ronald (1975) using Fletcher's (1940) equal power method. At frequencies below 1 kHz the CBW decreased with increasing frequency but was centered at about one-third-octave. Terhune and Turnbull (1995) made the same type of estimate for harbor seals underwater, and found much narrower CBWs below 1 kHz, close to one-twelfth octave. Recent studies on auditory masking have suggested that directly measured critical bandwidths in some seal species may be narrower than one-third-octave (i.e., Southall *et al.*, 2003a) and that Fletcher's (1940) equal power method may be of limited accuracy, at least in humans (Zwicker *et al.*, 1957; Patterson, 1976). Finally, Southall *et al.* (2003b) showed that directly measured CBWs in a harbor seal in air are much wider than previously estimated based on CRs and are very close to one-third-octave. Given this information, plus the limited available data on auditory sensitivity of seals, especially at low frequencies, our comparisons should

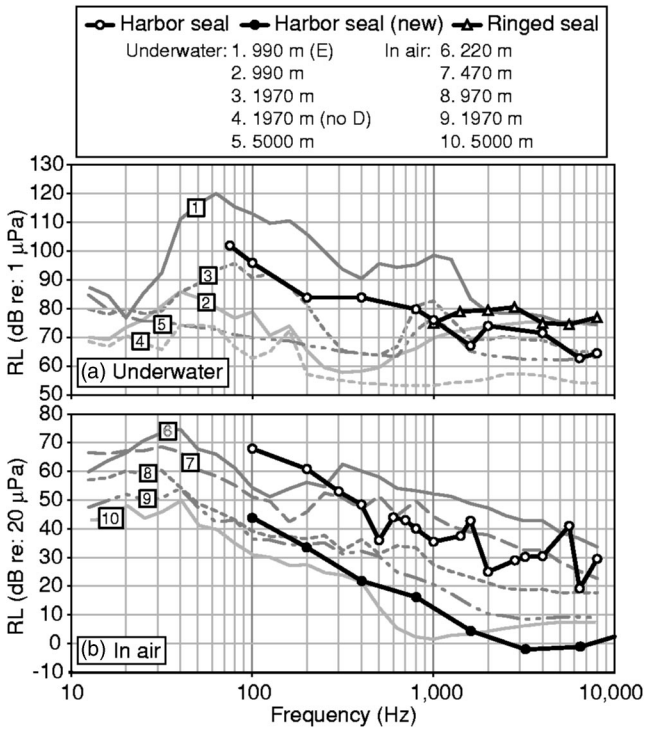

FIG. 11. A comparison of one-third-octave band levels of industrial sound with hearing threshold levels for harbor and ringed seals. (a) Underwater: ringed seal audiogram (open triangles) from Terhune and Ronald (1975); ''composite'' audiogram (open circles) for harbor seals based on three sets of measurements (Møhl 1968; Terhune and Turnbull, 1995; Kastak and Schusterman, 1998). (b) In air: ''composite'' audiogram (open circles) for harbor seals based on the same studies as in (a); recent unpublished data (closed circles) from Schusterman *et al.* (see Endnote 1). D=drilling, E=east, RL=received level.

be recognized as first approximations. In the discussion below we have assumed a CBW of one-third-octave, but discuss the implications if it is narrower.

All underwater and in-air samples shown in Fig. 11 were collected north of Northstar during drilling, except where otherwise stated. **Underwater** received one-third-octave band levels ~200 m from Northstar (not shown) were generally above auditory thresholds. Sample 1 (990 m E of Northstar) had a broadband level of 124 dB *re* 1 μPa (see Fig. 3), one of the highest received levels during drilling. For this sample, received levels at all frequencies were at or above threshold levels for both ringed and harbor seals. In contrast, sample 2, obtained at the same distance but north of the island, had levels either at the auditory threshold or well below it. Samples 3 and 4 were obtained 1970 m from Northstar, with and without ongoing drilling, respectively. One-third-octave band levels were below threshold, except for frequencies near the ''drilling peak'' (~1 kHz) in sample 3. Sample 5, at 5 km, was also below threshold levels. The maximum detection distance for a seal would therefore be particularly variable during drilling, but in most cases close to ~2 km. **In air**, received levels were compared with two different sets of threshold levels for harbor seals: (1) a ''composite'' audiogram based on three published studies [open circles in Fig. 11(b)]; and (2) recent unpublished audiometric data by Schusterman *et al.*[1] [filled circles in Fig. 11(b)].

(i) A comparison with the composite (older) audiogram data shows that received levels at 220 and 470 m (samples 6 and 7) were above the harbor seal thresholds for at least some frequencies, whereas levels beyond 970 m (samples 8–10) were below threshold at all measured frequencies. The maximum detection distance based on these data would be ~0.75 km.

(ii) In contrast, one-third-octave band levels at most frequencies remained above the more recent audiogram out to a distance of ~2 km (sample 9). At the 5 km station (sample 10) received levels were above the more recent harbor seal hearing threshold only for frequencies above 1.6 kHz. However, near and above 1.6 kHz, one-third-octave levels were identical at the 5, 7.6, and 9.4 km stations (not shown), indicating that island sounds were no longer contributing measurably to these frequencies and the seals were unlikely to hear components of island sound above 1.6 kHz.

Using this method of comparison, island sounds were probably audible to seals, at least intermittently, out to ~2 km in water and nearly 5 km in air (using the more recent Schusterman *et al.*[1] data). However, given the wide variation in received levels, the sounds would not always be audible to seals this far away. For example, sounds recorded underwater 990 m north of the island during production and drilling [Fig. 11(a), sample 2] would have been barely audible to a seal at that location, whereas those recorded 990 m east of Northstar with production and drilling (sample 1) were likely quite audible. In addition, during February and March ringed seals spend much of their time on the ice inside snow lairs (Smith and Stirling, 1975). Snow has an important dampening effect on in-air sounds, on the order of ~40 dB (broadband) per meter of snow thickness (Blix and Lentfer, 1992). This would reduce considerably the range of detectability of in-air sounds to a ringed seal in its lair.

If we assume a critical bandwidth for ringed seal hearing that is closer to one-twelfth octave, rather than one-third-octave, then the audiogram data in Fig. 11 would have to be compared to one-twelfth octave levels of industrial sound. These would be lower than one-third-octave levels, consequently decreasing the audibility ranges of Northstar sounds to seals.

There is no standardized procedure for comparing sounds with audiogram data the way we attempted in Fig. 11. Since audiogram data are based on the perception of pure tones whereas the industrial sound we compare them to is anything but pure tones, another possible method is to recalculate the pure tone detection thresholds into flat signal spectrum levels across each band of the same bandwidth as the industrial sound. Doing this with the data in Fig. 11 lowers the audiogram threshold levels compared to the sound spectral density levels of Northstar sound, and consequently increases the audibility ranges. Determining the correct procedure for these types of comparisons will be an important step when attempting to gauge the effect of industrial sound on marine mammals or other animals.

ACKNOWLEDGMENTS

This study was funded by BP Exploration (Alaska) Inc. to fulfill BP's policy of documenting and minimizing environmental impacts and to satisfy monitoring requirements associated with the Northstar oil development. We thank J. Leavitt (LGL Alaska) and A. Seitz (Greeneridge Sciences) for help in the field, and B. Dunbar, D. Otton, C. Hermans, and C. Lester with Alaska Interstate Construction (AIC) for being our all-terrain vehicle drivers. M. Williams, S. Schwenn, and C. Perham (LGL Alaska) helped with logistics. For logistical support and problem solving at Northstar we thank J. Huey (BP), R. Greenway, and R. Vogel (AIC), and W. Cullor and A. Erickson (Oasis Environmental). J. Huey provided the picture of Northstar in Fig. 2. G. Kidd, J. Polya, J. McDade, S. Carboy, and M. Johns provided us with information on drilling activities and machinery schedules. Dr. W. Burgess (Greeneridge Sciences) helped with Fig. 1. We thank Dr. R. Schusterman for permission to use the recent harbor seal audiometric data. Dr. B. Southall reviewed the manuscript and greatly improved the section on audibility by seals. Finally, we thank Dr. R. Jakubczak, Dr. W. Streever (BP), and D. Trudgen (Oasis Environmental) for their support, and Dr. W. Streever, R. Suydam, and an anonymous reviewer for their critical review.

[1]Schusterman, R. J., Kastak, D., Southall, B. L., Reichmuth Kastak, C., and Holt, M. M. ''Noise-induced temporary threshold shift in pinnipeds: effects of exposure medium, intermittence, duration, and intensity,'' Presentation at ECOUS (Environmental Consequences Of Underwater Sound) meeting, 12–16 May 2003, San Antonio, TX.

Blackwell, S. B., Lawson, J. W., and Williams, M. T. (**2004**). ''Tolerance by ringed seals (*Phoca hispida*) to impact pipe-driving and construction sounds at an oil production island,'' J. Acoust. Soc. Am. **115**, 2346–2357.

Blix, A. S., and Lentfer, J. W. (**1992**). ''Noise and vibration levels in artificial polar bear dens as related to selected petroleum exploration and developmental activities,'' Arctic **45**, 20–24.

Fletcher, H. (**1940**). ''Auditory patterns,'' Rev. Mod. Phys. **12**, 47–65.

Greene, Jr., C. R. (**1987**). ''Characteristics of oil industry dredge and drilling sounds in the Beaufort Sea,'' J. Acoust. Soc. Am. **82**, 1315–1324.

Greene, Jr., C. R. (**1997**). ''Underice drillrig sound, sound transmission loss, and ambient noise near Tern Island, Foggy Island Bay, Alaska, February 1997,'' report from Greeneridge Sciences Inc., Santa Barbara, CA, and LGL Alaska Research Associates Inc., Anchorage, AK, for BP Explor. (Alaska) Inc., Anchorage, AK, p. 24.

Greene, Jr., C. R., and Buck, B. M. (**1964**). ''Arctic Ocean ambient noise,'' J. Acoust. Soc. Am. **36**, 1218–1220.

Greene, Jr., C. R., and McLennan, M. W., with Blaylock, R. W. (**2000**). ''Sound and vibration measurements during Northstar construction in early 2000,'' p. 4-1 to 4-31 in ''Monitoring of ringed seals and sounds during construction of BP's Northstar oil development, Alaskan Beaufort Sea, winter and spring 1999–2000: 90-day report,'' LGL Rep. TA2426-1. Rep. from LGL Ltd., King City, Ont., and LGL Alaska Res. Assoc. Inc., Anchorage, AK, for BP Explor. (Alaska) Inc., Anchorage, AK, and Nat. Mar. Fish. Serv., Anchorage, AK, and Silver Spring, MD, edited by W. J. Richardson and M. T. Williams, p. 107.

Hall, J. D., and Francine, J. (**1991**). ''Measurements of underwater sounds from a concrete island drilling structure located in the Alaskan sector of the Beaufort Sea,'' J. Acoust. Soc. Am. **90**, 1665–1667.

Harris, F. J. (**1978**). ''On the use of windows for harmonic analysis with the discrete Fourier transform,'' Proc. IEEE **66**, 51–83.

Kastak, D., and Schusterman, R. J. (**1998**). ''Low-frequency amphibious hearing in pinnipeds: methods, measurements, noise, and ecology,'' J. Acoust. Soc. Am. **103**, 2216–2228.

Kinsler, L. E., Frey, A. R., Coppens, A. B., and Sanders, J. V. (**2000**). *Fundamentals of Acoustics*, 4th ed. (Wiley, New York, NY), pp. 360–361.

Knudsen, V. O., Alford, R. S., and Emling, J. W. (**1948**). ''Underwater ambient noise,'' J. Mar. Res. **7**, 410–429.

Malme, C. I., and Mlawski, R. (**1979**). ''Measurements of underwater acoustic noise in the Prudhoe Bay area,'' BBN Tech. Memo, 513, Rep. from Bolt Beranek & Newman Inc., Cambridge, MA, for Exxon Prod. Res. Co., Houston, TX, p. 74.

Milne, A. R., and Ganton, J. H. (**1964**). ''Ambient noise under Arctic-sea ice,'' J. Acoust. Soc. Am. **36**, 855–863.

Møhl, B. (**1968**). ''Auditory sensitivity of the common seal in air and water,'' J. Aud Res. **8**, 27–38.

Moulton, V. D., Richardson, W. J., McDonald, T. L., Elliott, R. E., and Williams, M. T. (**2002**). ''Factors influencing local abundance and haulout behaviour of ringed seals (*Phoca hispida*) on landfast ice of the Alaskan Beaufort Sea,'' Can. J. Zool. **80**, 1900–1917.

Moulton, V. D., Richardson, W. J., McDonald, T. L., Elliott, R. E., Williams, M. T., and Nations, C. (**2003a**). ''Effects of Northstar on local abundance and distribution of ringed seals (*Phoca hispida*) of the Alaskan Beaufort Sea,'' p. 5-1 to 5-23, in ''Monitoring of industrial sounds, seals, and bowhead whales near BP's Northstar Oil Development, Alaskan Beaufort Sea, 1999–2002,'' LGL Rep. TA2702-3, Rep. from LGL Ltd., King City, Ont., and Greeneridge Sciences Inc., Santa Barbara, CA, for BP Explor (Alaska) Inc., Anchorage, AK, and Nat. Mar. Fish. Serv., Anchorage, AK, and Silver Spring, MD, edited by W. J. Richardson and M. T. Williams.

Moulton, V. D., Richardson, W. J., Williams, M. T., and Blackwell, S. B. (**2003b**). ''Ringed seal densities and noise near an icebound artificial island with construction and drilling,'' Acoust. Res. Lett. Online **4**, 112–117.

Patterson, R. D. (**1976**). ''Auditory filter shapes derived with noise stimuli,'' J. Acoust. Soc. Am. **59**, 640–654.

Richardson, W. J., Greene, Jr., C. R., Koski, W. R., Malme, C. I., Miller, G. W., Smultea, M. A., and Würsig, B. (**1990**). ''Acoustic effects of oil production activities on bowhead and white whales visible during spring migration near Pt. Barrow, Alaska-1989 phase,'' OCS Study MMS 90-0017; LGL Rep. TA848-4. Rep. from LGL Ltd., King City, Ont., for U.S. Minerals Manage. Serv., Herndon, VA, p. 284 NTIS PB91-105486.

Richardson, W. J., Greene, Jr., C. R., Malme, C. I., and Thomson, D. H. (**1995**). *Marine Mammals and Noise* (Academic, San Diego, CA.), pp. 127–132 and 207–218.

Shepard, G. W., Krumhansl, P. A., Knack, M. L., and Malme, C. I. (**2001**). ''ANIMIDA phase I: ambient and industrial noise measurements near the Northstar and Liberty sites during April 2000,'' BBN Tech. Memo. 1270; OCS Study MMS 2001-0047. Rep. from BBN Technologies Inc., Cambridge, MA, for U.S. Minerals Manage. Serv., Anchorage, AK, p. 66.

Smith, T. G., and Stirling, I. (**1975**). ''The breeding habitat of the ringed seal (*Phoca hispida*). The birth lair and associated structures,'' Can. J. Zool. **53**, 1297–1305.

Southall, B. L., Schusterman, R. J., and Kastak, D. (**2003a**). ''Acoustic communication ranges for northern elephant seals (*Mirounga angustirostris*),'' Aquat. Mamm. **29**, 202–213.

Southall, B. L., Schusterman, R. J., and Kastak, D. (**2003b**). ''Auditory masking in three pinnipeds: aerial critical ratios and direct critical bandwidth measurements,'' J. Acoust. Soc. Am. **114**, 1660–1666.

Terhune, J. M., and Ronald, K. (**1975**). ''Underwater hearing sensitivity of two ringed seals (*Pusa hispida*),'' Can. J. Zool. **53**, 227–231.

Terhune, J., and Turnbull, S. (**1995**). ''Variation in the psychometric functions and hearing thresholds of a harbour seal,'' in *Sensory Systems of Aquatic Mammals*, edited by R. A. Kastelein, J. A. Thomas, and P. W. Nachtigall (De Spil, Woerden, the Netherlands), pp. 81–93.

Zwicker, E., Flottorp, G., and Stevens, S. S. (**1957**). ''Critical bandwidth in loudness summation,'' J. Acoust. Soc. Am. **29**, 548–557.

Improved scatterer property estimates from ultrasound backscatter for small gate lengths using a gate-edge correction factor

Michael L. Oelze[a] and William D. O'Brien, Jr.
Bioacoustics Research Laboratory, Department of Electrical and Computer Engineering, University of Illinois, 405 North Mathews, Urbana, Illinois 61801

(Received 2 March 2004; revised 2 August 2004; accepted 4 August 2004)

Backscattered rf signals used to construct conventional ultrasound B-mode images contain frequency-dependent information that can be examined through the backscattered power spectrum. The backscattered power spectrum is found by taking the magnitude squared of the Fourier transform of a gated time segment corresponding to a region in the scattering volume. When a time segment is gated, the edges of the gated regions change the frequency content of the backscattered power spectrum due to truncating of the waveform. Tapered windows, like the Hanning window, and longer gate lengths reduce the relative contribution of the gate-edge effects. A new gate-edge correction factor was developed that partially accounted for the edge effects. The gate-edge correction factor gave more accurate estimates of scatterer properties at small gate lengths compared to conventional windowing functions. The gate-edge correction factor gave estimates of scatterer properties within 5% of actual values at very small gate lengths (less than 5 spatial pulse lengths) in both simulations and from measurements on glass-bead phantoms. While the gate-edge correction factor gave higher accuracy of estimates at smaller gate lengths, the precision of estimates was not improved at small gate lengths over conventional windowing functions. [DOI: 10.1121/1.1798353]

PACS numbers: 43.80.Qf, 43.80.Vj [FD] Pages: 3212–3223

I. INTRODUCTION

A conventional ultrasound B-mode image relates the envelope of each backscattered radio-frequency (rf) time signal to a gray-scale value. A conventional ultrasound B-mode image is made up of adjacently spaced axial time signals that have, in general, been envelope detected. Each envelope-detected time signal is a series of echoes backscattered from structures in the interrogated medium.

In a conventional ultrasound B-mode image, the frequency-dependent information in a rf time signal is not utilized. The frequency-dependent information in a rf time signal has been hypothesized to be related to the tissue microstructure (structures less than the ultrasound wavelength).[1–13] Parametrization of the frequency dependence of backscattered signals from tissues has allowed the characterization of tissues. Several researchers have used quantitative ultrasound (QUS) information about the shape of the spectrum of backscattered ultrasound to classify tissue microstructure and identify disease.[2,9,11–16] Other researchers have been able to estimate the size, shape, and internal make-up of scatterers in tissues from (QUS) models.[3,5–7,9–11,16]

Scattering from tissues is often modeled using the Born approximation (no multiple scattering).[17] Regions of interest (ROIs) are chosen from interrogated volumes, and the spectral properties of the rf signal corresponding to the ROIs are quantified and related to models of tissue scattering. Tissue scattering often represents a stochastic process with incoherent and coherent scattering.[17–19] The incoherent scattering includes information about the size, shape, density, and mechanical properties of the scatterers.[19] If a model accurately describes the incoherent part of the scattered spectrum, then estimates of scatterer properties can be made. If the spatial arrangement of the scatterers is regular or periodic, a coherent component is introduced into the backscattered signal. For truly random or diffuse scattering, the coherent part of the spectrum appears as noise to the incoherent part of the spectrum.

If the total interrogated volume is not homogeneous but is suspected of having a distribution of nonuniform scatterers, i.e., tissues, then taking large ROIs in the volume may not give the same average structural information as that of smaller ROIs. In the case of tissue interrogation, smaller ROIs are chosen within the interrogated volume to resolve changing structure within the interrogated volume. The smaller ROIs are then assumed to have a distribution of uniform scatterers within a larger volume composed of a possible larger distribution of different scatterers. Typically, an ROI is constructed from several rf time signal realizations axially gated to a particular length. If the gate length used to make spectral estimates is too small, a bias is introduced (the estimates are less accurate).[20] There exists a trade-off between the smaller ROI size (better axial resolution) and the ability to make accurate and precise scatterer property estimates in media characterized by randomly spaced scatterers. This trade-off has been expressed in terms of the stability–time–bandwidth product.[21] Reducing the size of gated time signal increases the bias of estimates in the spectral domain and causes more distortion of the spectrum.[22] Tapered win-

[a]Electronic mail: oelze@uiuc.edu

dows decrease sidelobe contribution that reduces the bias. However, the broader main lobe correlates consecutive frequency values increasing noise in variance of estimates.[21]

Numerous studies have examined the effects of the axial gate length and windowing function on the accuracy and precision of scatterer property estimates in the context of ultrasound. One study showed that when the gated length was not large (5 times the wavelength at the center frequency) the measured backscattered power spectrum did not fit the theoretical power spectrum well no matter what windowing function was used.[23] As the size of the gated length increased, the measured backscattered power spectrum fit the theoretical power spectrum better. Further, a better fit to the theoretical power spectrum occurred at a gate length of 12.5 times the wavelength at the center frequency when a Hanning window was used over that of a rectangular window. Other studies showed that as the length of the axial gate was larger than the spatial pulse length (SPL), the contribution of the coherent spectrum was reduced, improving the accuracy and precision of scatterer property estimates.[18,24] As the size of the axial gate length was reduced to the SPL, it was noted that the effects of the pulse needed to be incorporated.[25] Attempts were made with limited success to correct for the small gate truncation errors using a deconvolution method.[26] If the edge effects of gated time segments can be corrected, then the axial resolution, at which accurate estimates of scatterer properties are made, may be improved further. However, the precision of estimates of scatterer properties may not be improved by correcting for the edge effects.

In another study, axial resolution for ROIs was optimized to a length of 10 times the wavelength of interrogation.[15] In that study, a line was fit to the backscattered power spectrum versus gated axial length using a Hanning window. The 10-wavelength ROI was chosen at the point where the slope estimates from the best-fit line first converged. The study examined the accuracy of slope estimates versus axial length and did not consider the precision in making estimates versus axial length.

In the study reported herein, the accuracy of scatterer property estimates of smaller gate lengths is improved, and the bias is removed, by developing and using a gate-edge correction factor. The analysis assumes that the scatterers are randomly spaced and that the coherent component of the backscattered spectrum is small relative to the incoherent component. The approach is unique in that it applies physical principles of the scatterers rather than purely signal-processing techniques to reduce bias in spectral estimates. The gate-edge correction factor allows the axial resolution to be enhanced beyond typical gating techniques that involve conventional windowing functions. Section II describes the theory behind backscattering from weakly scattering volumes and the development of the gate-edge correction factor. Section III details the construction of simulations and measurements from physical phantoms with randomly spaced glass beads. Section IV presents the results of the simulations and physical phantom measurements and compares the different gating functions with the gate-edge correction factor. The final section (Sec. V) provides some conclusions about the study.

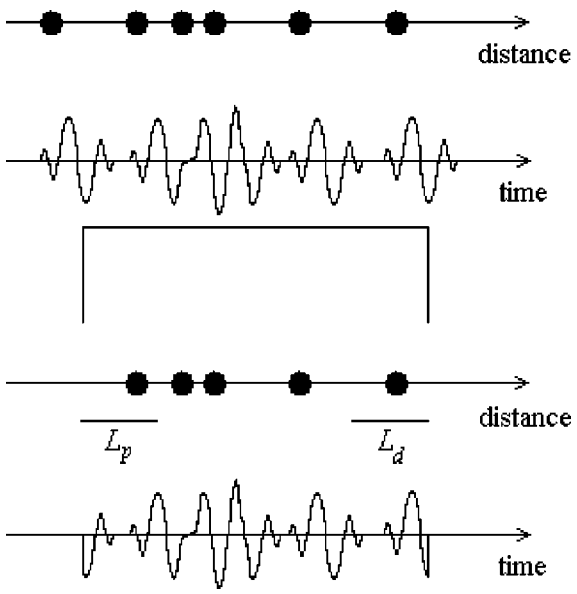

FIG. 1. Comparison between scatterers located at variable distances from a source and the time signal associated with the position of each scatterer and the gated signal.

II. THEORY

Consider a medium filled with random scatterers. A pulse is propagated from a source into the scattering medium and each scatterer reradiates the incident pulse and modifies its frequency content, giving an echo signal. Figure 1 represents a simple case of a few scatterers randomly spaced in the scattering medium. Each scatterer has an echo signal associated with it in time and these echo signals are summed back at the source to form a backscatter wavetrain.

The echo signals from the scatterers contain frequency-dependent information that is related to the size, shape, and mechanical properties of the scatterers. The frequency-dependent information can be determined by gating out a portion of the backscattered wavetrain and taking the Fourier transform of the gated time signal. QUS models then relate the backscattered power spectrum, which is the magnitude squared of the Fourier spectrum, to properties of the scatterers.

The gating of time signals allows estimates of scattering properties to be related to distinct ROIs in the volume under interrogation. However, the gating process also adds unwanted frequency content into the backscattered power spectrum. The unwanted frequency content leads to inaccurate estimates of scatterer properties. The reason that the gating adds unwanted frequency content into the spectrum can be illustrated. In Fig. 1 the time signal is gated using a rectangular window. When the signal is gated, inevitably echo signals will be abruptly truncated at the edges of the gate, leading to added higher frequency content in the backscattered power spectrum.

A couple of ways exist to reduce the effects of the gate edges. One way is to apply windows that taper at the edges, i.e., the Hanning window. The tapered windows reduce the high-frequency content added into the gated time signal by making the edges more continuous. Another way to reduce the effects of the gate edge is to make the total gate length

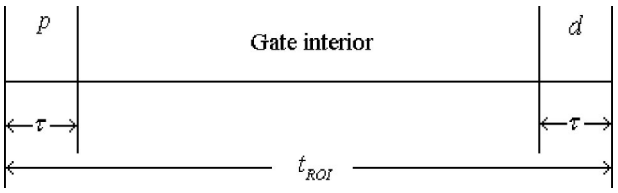

FIG. 2. The different regions of a gated signal where p denotes the proximal region, d denotes the distal region, τ denotes the temporal pulse length, and t_{ROI} denotes the total temporal gate length of the ROI.

longer. When the gate is longer, the effects of the echo signals truncated at the gate edge are minimized relative to the larger number of unaffected echo signals located in the middle of the gate. The longer the gate length, the better the accuracy of the estimates of scatterer properties at the expense of spatial resolution.[20]

The gated region can be broken into a middle region (gate interior) and two edge regions (Fig. 2). The edge regions are the size of the backscattered echo signal pulse (1 SPL) and the edge regions represent the time durations from where truncated echo signals will originate. The length of a backscattered echo signal pulse will depend on the initial excitation pulse and the type of scatterer in the interrogated medium. The middle portion of the gated region represents the region from where unaltered echo signals originate. The time signal from a gated region, $r(t)$, can be represented as the sum of N' identical scatterers in the gated volume by[27]

$$r(t)=s(t+t_1)+s(t+t_2)+\cdots+s(t+t_N)+s_{p1}(t+t_{p1})+\cdots+s_{pN_p}(t+t_{pN_p})+s_{d1}(t+t_{d1})+\cdots+s_{dN_d}(t+t_{dN_d}), \tag{1}$$

where $N'=N+N_p+N_d$, $s(t+t_i)$ represents the echo signal from a single scatterer located temporally at time $t+t_i$, and s_p and s_d represent echo signals that have been truncated at different points by the proximal and distal gate edges, respectively.

Figure 1 schematically demonstrates that the time signal contains truncated echo signals from scatterers not actually contained in the ROI volume, $L_{\mathrm{ROI}}A$, where L_{ROI} is the length of the gated segment and A is the cross-sectional area of the beam (in most cases defined by the -6-dB beamwidth). For example, the left-most echo signal in Fig. 1 that originates from a scatterer outside the ROI becomes a truncated echo signal that is included inside the proximal gate edge of the time segment corresponding to the ROI. In other words, there exists some proximal length, L_p, of the ROI that includes truncated echo signals from scatterers that are completely or partially outside of the ROI. Thus, the proximal length is defined as the SPL of an echo signal from a scatterer, L_{SPL}. Furthermore, the right-most echo signal in Fig. 1 that originates from a scatterer inside the ROI contains a truncated echo signal that is included inside the distal gate edge of the ROI. In other words, there exists some distal length, L_d, of the ROI that includes truncated echo signals from scatterers that are completely or partially inside of the ROI. Thus, the distal length is also defined as the SPL of an echo signal from a scatterer. Therefore, $L_{\mathrm{SPL}}=L_p=L_d$, the axial length of an echo signal from a scatterer. In the case of elastic scatterers where shear waves are supported, resonances can occur that elongate the SPL appreciably over the excitation pulse for large ka values. In soft tissues, shear waves are not supported so that the SPL will be very close to the size of the excitation pulse. In this analysis, either small ka values ($\leqslant 1$) or scatterers that did not support shear waves were considered.

If the number density of scatterers is given by $\overline{n}$, then, in the middle region, the number of scatterers $N=\overline{n}(L_{\mathrm{ROI}}-L_{\mathrm{SPL}})A$, where only L_{SPL} needs to be subtracted from the full gated length, L_{ROI}, to get the total number of scatterers in the middle region of the ROI because the proximal scatterers are not included in the physical ROI.

If the time gate is large, then $N \gg N_p$, N_d and the contribution of the s_p and s_d scatterers is negligible relative to the $s(t)$ echo signals of the middle gate region. When gate lengths are small, the contributions of the echo signals near the edge are not negligible and will change the frequency content of the backscattered power spectrum from that of the scatterers in the middle region.

Assuming that there is a uniform density of scatterers in the ROI, then $N_p \simeq N_d \simeq N_{\mathrm{res}}$, where N_{res} represents the number of scatterers in a resolution cell (defined as the SPL times the cross-sectional area of the beam of the ultrasound source as defined by the beamwidth at half maximum), with

$$N_{\mathrm{res}}=\overline{n}L_{\mathrm{SPL}}A. \tag{2}$$

Further, assuming the echo signals are approximately identical backscattered pulses and loss is negligible within the ROI, then $s_p \simeq s_d$ and

$$r(t)\simeq \sum_{n=1}^{N} s(t+t_n)+\sum_{j=1}^{2N_p} s_{p_j}(t+t_{p_j}). \tag{3}$$

The Fourier transform of Eq. (3) gives

$$R(f)\simeq S(f)\sum_{n=1}^{N} e^{-i2\pi f t_n}+\sum_{j=1}^{2N_p} S_{p_j}(f)e^{-i2\pi f t_{p_j}}. \tag{4}$$

The power spectrum is obtained by taking the magnitude squared of Eq. (4). The power spectrum can be divided into incoherent (like terms) and coherent components (cross terms). Assuming that the scatterers are randomly placed (no periodic structure), then the coherent component is small relative to the incoherent. The incoherent spectrum is used for estimating the frequency dependence of scattering, and its normalized backscattered power spectrum of Eq. (4) is given by

$$W(f)=N|S(f)|^2+\sum_{j=1}^{2N_p}|S_{p_j}(f)|^2. \tag{5}$$

To characterize the backscatter and obtain accurate scatterer property estimates, the first term of Eq. (5) is sought. For long gate lengths

$$W(f)\cong N|S(f)|^2. \tag{6}$$

However, when the gate lengths are small, significant contribution is made from the second term of Eq. (5). Smaller gate

lengths are desired to obtain better axial resolution for scatterer property estimates.

To improve the accuracy of scatterer property estimates from small gated segments, the edge terms of Eq. (5) can be corrected. The edge terms are corrected by determining the additional frequency content added to the power spectrum from the truncated echo signals. In the edge terms, the exact frequency contribution from each truncated echo signal cannot be explicitly determined. In order to determine the contribution from each truncated echo signal in the edge region, the exact location of each scatterer in the cutoff regions would need to be known. Instead, the frequency contribution of the truncated echo signals in the edge region can be calculated ranging from where almost the whole echo signal is in the edge region to where almost the whole echo signal has been truncated.

The average frequency contribution from truncated echo signals in the gate edges can be calculated by

$$\langle S'(f)\rangle = \frac{1}{t_p}\int_0^{t_p}\int_{-\infty}^{\infty} s(t)g(t,t')e^{-i2\pi ft}dt\,dt', \tag{7}$$

where t_p is the time duration of the echo signal, $s(t)$ is approximated from the excitation pulse and from some simple assumptions about the scatterers, and $g(t,t')$ is a rectangular gate function given by

$$g(t,t') = \begin{cases} 1 & 0 \leqslant t \leqslant t' \\ 0 & t > t' \end{cases}. \tag{8}$$

The efficacy of the simple assumptions about the scatterers will be examined later in the context of real tissue scattering. Equation (5) represents the normalized backscattered power spectrum from a realization from a single time segment. Spatially averaging several power spectra from the different time segments that make up an ROI yields

$$\langle W(f)\rangle_s = N\langle |S(f)|^2\rangle_s + \left\langle \sum_{j=1}^{2N_p} |S_{p_j}(f)|^2 \right\rangle_s. \tag{9}$$

Replacing

$$\left\langle \sum_{j=1}^{2N_p} |S_{p_j}(f)|^2 \right\rangle_s$$

in Eq. (9) with average frequency contribution from the truncated echo signals in the gate edges from Eq. (7), $2N_{\text{res}}|\langle S'(f)\rangle|^2$, gives

$$\langle W(f)\rangle_s \simeq N\langle |S(f)|^2\rangle_s + 2N_{\text{res}}|\langle S'(f)\rangle|^2. \tag{10}$$

There exists some function $\beta(f)$ defined as

$$\beta(f) = \frac{|\langle S'(f)\rangle|^2}{\langle |S(f)|^2\rangle_s}, \tag{11}$$

such that

$$2N_{\text{res}}|\langle S'(f)\rangle|^2 = \beta(f)\left(\frac{2N_{\text{res}}}{N}\right)N\langle |S(f)|^2\rangle_s = \beta(f)\left(\frac{2L_{\text{SPL}}}{L_{\text{ROI}}-L_{\text{SPL}}}\right)N\langle |S(f)|^2\rangle_s. \tag{12}$$

Substituting Eq. (12) into Eq. (10) gives

$$\langle W(f)\rangle_s = \left[1+\beta(f)\frac{2L_{\text{SPL}}}{L_{\text{ROI}}-L_{\text{SPL}}}\right]N\langle |S(f)|^2\rangle_s. \tag{13}$$

Solving for the scattered spectrum

$$N\langle |S(f)|^2\rangle_s = \left[1+\beta(f)\frac{2L_{\text{SPL}}}{L_{\text{ROI}}-L_{\text{SPL}}}\right]^{-1}\langle W(f)\rangle_s = \phi(f)\langle W(f)\rangle_s, \tag{14}$$

where

$$\phi(f) = \frac{1}{1+\beta(f)\dfrac{2L_{\text{SPL}}}{L_{\text{ROI}}-L_{\text{SPL}}}}, \tag{15}$$

and $\phi(f)$ is always positive, assuming that the total gate length is greater than or equal to the SPL. As the size of the ROI becomes large relative to the SPL, $\phi(f)$ approaches unity. The function, $\phi(f)$, acts as a corrective filter due to windowing of signals at small gate lengths relative to the SPL. Application of $\phi(f)$ adjusts the frequency dependence of the backscattered power spectrum from smaller gate lengths to be the same as for larger gate lengths.

If $\phi(f)$ can be determined, then the backscattered power spectrum can be approximated for any gated length with the effects of the gate edges reduced. However, the functional form of $\beta(f)$ is unknown because both $|\langle S'(f)\rangle|^2$ and $\langle |S(f)|^2\rangle_s$ are unknowns. Therefore, Eq. (11) is approximated as

$$\beta(f) = \frac{|\langle S'_{\text{app}}(f)\rangle|^2}{\langle |S_{\text{app}}(f)|^2\rangle_s}, \tag{16}$$

where $\langle |S_{\text{app}}(f)|^2\rangle$ and $|\langle S'_{\text{app}}(f)\rangle|^2$ represent approximate backscattered power spectra by making some simple assumptions about the scatterers.

The function $\phi(f)$ can be explicitly defined only if the excitation pulse, the frequency-dependent attenuation (including both total and local attenuation within the ROI), and the frequency-dependent backscatter from the scatterers are known. The excitation pulse and frequency-dependent attenuation can be quantified independently from the backscatter. The attenuation can be incorporated into the gate-edge correction factor by

$$\langle S'(f)\rangle = \frac{1}{t_p}\int_0^{t_p}\int_{-\infty}^{\infty} s(t)g(t,t')e^{-\alpha(f)x_0}e^{-i2\pi ft}dt\,dt', \tag{17}$$

where $\alpha(f)$ is the frequency-dependent attenuation coefficient and x_0 is the distance from the beginning of the interrogated medium to the front edge of the gated region. If the product of the gate length and attenuation is small, then the effects of attenuation over the length of the ROI can be neglected.

What is not quantified, apart from the backscatter, is the frequency-dependent information about the scatterers in the interrogated medium. The goal is to estimate the true frequency dependence of the backscatter. However, in terms of ultrasonic scattering, certain assumptions about the scatterers

can be made and further information about the scatterers can be obtained from initial results by iteration. For example, if the scatterers are assumed to be point scatterers (Rayleigh scatterers), then

$$|S(f)|^2 \propto f^4. \tag{18}$$

The reference (excitation) pulse can then be used to construct an echo signal scattered from a point scatterer. Essentially

$$\langle |S_{\text{app}}(f)|^2 \rangle = |S_{f^4}(f)|^2 = f^4 |R_{\text{ref}}(f)|^2, \tag{19}$$

where $|R_{\text{ref}}(f)|^2$ is the reference pulse power spectrum. We can take our original excitation pulse and scatter it from a single-point scatterer to get a model for the echo signal, $s(t)$. From the approximate echo signal we can then use Eqs. (16) and (17) to calculate the function $\phi(f)$, Eq. (15).

In ultrasound backscatter data acquisition, point scatterers occur when the $ka \ll 1$, where k is the acoustic wave number and a is the radius of the scatterer. Often, frequency ranges are chosen so that $ka \sim 1$. In this case, the frequency dependence of the backscattered power spectrum is more complicated than a simple f^4 dependence given by point scatterers. The frequency dependence of the backscattered power spectrum can be described by[16]

$$W(f) = C f^4 F(f), \tag{20}$$

where C is a constant (depending on the beam characteristics, the gate length, the size of the scatterers, and the concentration of scatterers) and $F(f)$ is called the form factor and depends on the size, shape, and mechanical properties of the scatterers. When $ka \sim 1$, it is possible to estimate the average scatterer size from the form factor. As the ka value increases, the form factor becomes increasingly small for most scatterers and estimates become increasingly difficult to obtain from large ka values. In numerous studies, estimates of the scatterer size from the normalized backscattered power spectrum have been used to characterize and diagnose tissues ultrasonically.[5–8,10–13,16,28] Initial estimates of scatterer size from the backscattered power spectrum can be made by using the $\phi(f)$ correction factor for the f^4 dependence to create an echo signal, $s(t)$, for a point scatterer. Then, a new echo signal, $s(t)$, and a new correction factor, $\phi(f)$, can be constructed based on the initial corrected estimates of the average scatterer diameter.

III. SIMULATION AND EXPERIMENTAL METHODS

Several simulations and tissue-mimicking phantom measurements were made to examine the utility of the new gate-edge correction factor for obtaining accurate estimates of scattering properties when small gate lengths are used. The simulations consisted of software phantoms interacting with an acoustic source containing randomly spaced scatterers of different kinds and with different number densities.

The software phantoms were constructed in MATLAB (The Mathworks Inc., Natick, MA) as discussed in a previous study.[28] A large-volume matrix was constructed 10 mm in depth by 20 mm parallel to the transducer face and 2 mm in height. The source was placed 50 mm from the front edge of the scattering volume. The excitation pulse of the simulated source had a 10-MHz center frequency and a pulse length of approximately 1.5 cycles. The beamwidth (−6 dB) was 600 μm for the source, assuming a Gaussian beamwidth for an $f/4$ aperture. Scatterers were randomly spaced in the volume matrix using randomization functions from MATLAB. Care was taken to prevent scatterers from overlapping. In the case of the Gaussian scatterers, the minimum separation distance between scatterers was the −6-dB fall-off of the Gaussian function describing the scatterers.

The first set of simulations consisted of software phantoms containing point scatterers with different number densities. The attenuation in the software phantom was set to 0.5 dB $\text{MHz}^{-1}\,\text{cm}^{-1}$ and the speed of sound was 1540 m/s. Four software phantoms were constructed with relative number densities of 1.1, 3.6, 5.5, and 9.8 scatterers per resolution cell. The scatterers were point scatterers that had an f^4 dependence in the backscattered power spectrum. The power dependence of the scattering was estimated using the correction factor for point scatterers, Eqs. (15) and (19). Each estimate was made by spatially averaging the backscattered power spectra from 30 adjacent rf time signal echoes, each separated by 100 μm. Estimates were made over different gate lengths using a rectangular window, a Hanning window, and a rectangular window using the gate-edge correction factor. A total of 60 estimates was made for each simulation and these estimates were averaged. The standard deviation for the average of the 60 estimates was also calculated to determine the precision of the estimation techniques.

The second set of software phantoms was constructed using spherical Gaussian scatterers with a ka value of 1.0 at the center frequency of the acoustic excitation pulse.[5] Therefore, the scatterers had a more complicated frequency dependence than that of point scatterers. The correction factor, Eq. (15), was calculated with the appropriate form factor model, Eq. (20), from initial estimates of the scatterer diameter assuming a correction factor for a point scatterer. The attenuation was varied (0.0, 0.5, and 1.0 dB $\text{MHz}^{-1}\,\text{cm}^{-1}$). The utility of the gate-edge correction was examined in terms of spherical Gaussian scatterers and different values for attenuation. A total of 60 estimates of the scatterer diameter was made for each simulation using the linear least-squares fit estimator, and these estimates were averaged.[29] Each estimate was made by spatially averaging the backscattered power spectra from 30 adjacent rf time signal echoes, each separated by 100 μm. The standard deviation for the average of the 60 estimates was also calculated to determine the precision of the estimation techniques.

The third set of software phantoms was constructed using spherical Gaussian scatterers with ka values of 0.5, 1.0, and 2.0 based on the center frequency of the excitation pulse and the size of the scatterers. In all cases, the scatterers had a more complicated frequency dependence than that of point scatterers. The correction factor, Eq. (15), was calculated with the appropriate form factor model, Eq. (20), from initial estimates of the scatterer diameter assuming a correction factor for a point scatterer. The attenuation was 0.5 dB $\text{MHz}^{-1}\,\text{cm}^{-1}$.

A fourth set of software phantoms was constructed using a distribution of spherical Gaussian scatterers with different diameters rather than a single diameter. A distribution of

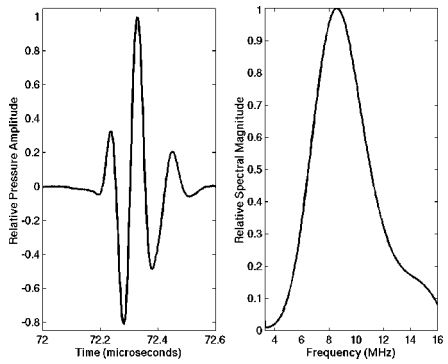

FIG. 3. Time pulse (left) and the magnitude of the frequency spectrum (right) of ultrasound signal reflected from a plexiglas plate reflector located at the focus of the transducer used in the physical phantom measurements.

scatterer diameters is more like the situation that might be found in real soft-tissue scattering. The diameters had an equal number of scatterer diameters between 35 and 65 μm and between 20 and 80 μm. The average scatterer diameter was 50 μm. The correction factor, Eq. (15), was calculated with the appropriate form factor model, Eq. (20), from initial estimates of the scatterer diameter assuming a correction factor for a point scatterer. The attenuation was set to 0.0 $\mathrm{dB\,MHz^{-1}\,cm^{-1}}$.

Finally, measurements were made on two tissue-mimicking phantoms containing randomly placed glass-bead scatterers of diameter 45–53 μm.[30] The phantom measurements were made with a single-element weakly focused transducer ($f/4$) that had an 8.5-MHz center frequency as measured (resulting in a $ka \sim 0.83$ at the center frequency). The -6-dB pulse/echo bandwidth of the transducer was 6.5 MHz and the -6-dB pulse/echo beamwidth at the focus was measured to be 670 μm using the wire method.[31] Figure 3 shows an example of the incident pulse reflected from a Plexiglas® plate centered at the focus. The pulse reflected from the Plexiglas® was used as a reference pulse.[5,6,17]

In a measurement, the transducer's beam axis was perpendicular to the face of the phantom so that the ultrasound would propagate normal to the surface. Phantom A had a measured attenuation of approximately 0.5 $\mathrm{dB\,MHz^{-1}\,cm^{-1}}$ over the frequency range of 5–12 MHz (ka range 0.5 to 1.2) using an insertion loss method and a number density of scatterers approximately twice that of the second phantom (B).[30] The hydrophone used for the attenuation measurements was a 1-mm spot size polyvinylidene diflouride hydrophone (Sonic Technologies model 804-010, Hatboro, PA). In the insertion loss method, the pulse from the transducer was measured through a water path using the hydrophone. The phantom was then placed in the path between the transducer and hydrophone and a new pulse was measured with the hydrophone. The attenuation was calculated by dividing the power spectrum of the initial pulse by the power spectrum of the pulse through the phantom and by the thickness of the phantom. Phantom B had a measured attenuation of approximately 0.64 $\mathrm{dB\,MHz^{-1}\,cm^{-1}}$ over the frequency range of 5–12 MHz using an insertion loss method. A 2-cm-length lateral scan was performed along the surface of the phantoms with a step size of 100 μm between each scan line. A scattered pulse was created by simulating the scattering of the measured excitation pulse (Fig. 3) by a glass-bead scatterer based on the theory of Faran over the analysis bandwidth.[32] The final estimate of the diameter of the glass bead was based on initial estimates using a correction factor for point scatters. The subsequent scattered pulse was used in Eqs. (15) and (20) to create the correction factor for the glass-bead scatterers. Each estimate was made by spatially averaging the backscattered power spectrum from 33 consecutive rf echoes separated by 100 μm. For each acquired echo, the backscattered signal was temporally averaged for 300 realizations to reduce any electronic noise associated with the measurement. Estimates of glass-bead diameter were made versus different gate lengths using a rectangular window, a Hanning window, and a rectangular window using the gate-edge correction factor. A total of 60 estimates was made for each phantom and these estimates were averaged. The standard deviation for the average of the 60 estimates was also calculated to determine the precision of the estimation techniques.

IV. SIMULATION AND EXPERIMENTAL RESULTS

When a time sequence is gated with a conventional windowing function, the frequency content of the main lobe and sidelobes is modified. Tapered windows, i.e., the Hanning window, are often used because they reduce the sidelobe levels in the frequency spectrum more than a rectangular window. Figure 4 shows the effects of rectangular and Hanning windows on the spectral main lobe and sidelobes as a function of the SPL. In Fig. 4 an ideal power spectrum from a pulse scattered from a single-point scatterer (f^4 dependence) is divided by a windowed wavetrain of echo signals scattered from randomly spaced point scatterers. The excitation pulse was a Gaussian pulse with a 10-MHz center frequency and an 8-MHz -6-dB bandwidth (analysis bandwidth of 6–14 MHz). The spectra were normalized by the number of scatterers so that the relative magnitude of the two spectra was equal at the center frequency. If the ratio of the two spectra were a perfect horizontal line, then the frequency dependence of the two spectra would be identical and perfect estimates of scatterer properties could be made.

For short gate lengths [gate lengths of 2 SPLs, Figs. 4(a) and (c)], both rectangular and Hanning windowed spectra had markedly different frequency dependencies than the ideal spectrum. In both cases the main lobe was broader in the windowed functions and the sidelobes had either shifted in position or were larger than the ideal scattered power spectrum. When the gate length was increased [Figs. 4(b) and (d)], a horizontal line could be fit to both the rectangular and Hanning windowed functions over the analysis bandwidth. Therefore, scatterer property estimates made over the analysis bandwidth for the larger gated segments tend to be more accurate than estimates made at shorter gate lengths. Superior matching occurred for the spectral ratios (ratio closer to unity) with the Hanning gated spectrum over that of the rectangular gated spectrum at larger gated lengths due to the smaller sidelobes of the Hanning window and a wider main lobe.

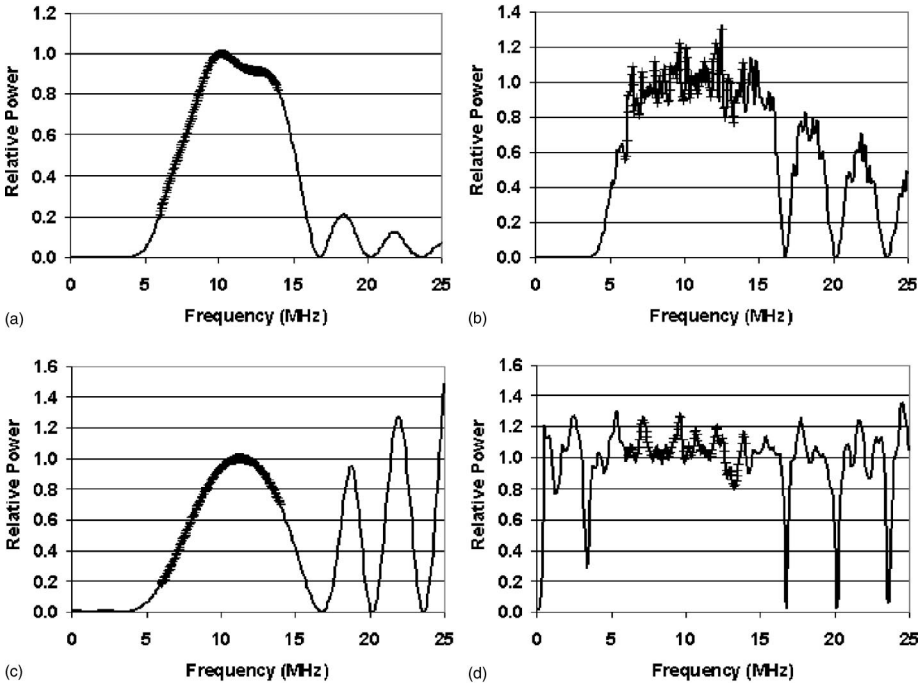

FIG. 4. Normalized ratio of an ideal scattered power spectrum from a single-point scatterer to the power spectrum from a windowed wavetrain of pulses scattered from randomly spaced scatterers with (a) rectangular windowed segment of length 2 SPLs; (b) rectangular windowed segment of 20 SPLs; (c) Hanning windowed segment of 2 SPLs; and (d) Hanning-windowed segment of 20 SPLs. The rectangular- and Hanning-windowed spectra represent the average of 30 independent realizations. The analysis bandwidth is denoted on the curves by the superimposed "+" signs.

The correction factor [Eq. (15) combined with Eq. (19)] was applied to the rectangular gated window and then the ideal spectrum was divided by the rectangular gated spectrum using the gate-edge correction factor. At both the short and long gate length [Figs. 5(a) and (b), respectively] the corrected spectra appeared to match the ideal spectrum over the analysis bandwidth and at frequencies well above the analysis bandwidth. Even at small gate lengths, accurate estimates of the scatterer properties could be made. The gate-edge correction factor did not appear to correct for frequencies lower than the analysis bandwidth. The correction factor may enable a larger analysis bandwidth to be used because higher frequency components can be included in the analysis bandwidth. The gate-edge correction factor corrected for the spectral main and sidelobe modifications at frequencies in or above the analysis bandwidth introduced by the windowing functions.

The frequency dependence of the correction factor depends on the gate length relative to the SPL. Figure 6(a) shows a representative time sequence from a medium with randomly spaced Gaussian scatterers. Figures 6(b) and (c) show the measured form factor (Gaussian) and the correction factor, Eq. (15), that would be applied to the measured power spectrum for gate lengths of different size. The smallest gate length has the largest frequency variance. As the gate length gets larger, the overall correction becomes flatter so that the frequency dependence in the analysis bandwidth is barely changed by the correction factor.

For point scatterers, the frequency dependence of the backscattered power spectrum is proportional to f^4. One method of characterizing a scattering medium is to estimate the exponent of the frequency dependence in the normalized backscattered power spectrum. Figure 7 shows the results of estimating the exponent from a medium containing randomly spaced point scatterers. The results were plotted versus the size of the total gate length in SPLs. In each case the estimation of the exponent of the frequency dependence using the gate-edge correction factor yielded better accuracy (less bias in the estimate) than using rectangular and Hanning windowed time gates. The largest improvement in accuracy using the gate-edge correction factor occurred at the smaller gate lengths. The magnitude of the gate-edge correction factor was largest when the gate length was small [as the gate length increased, $\phi(f) \rightarrow 1$]. Good agreement (less than 5 percent error) between the actual frequency dependence and the estimated frequency dependence occurred at all gate lengths for the gate-edge correction estimates. The number of scatterers per resolution cell did not seem to affect the effectiveness of the gate-edge correction factor.

The next set of simulations examined non-point scatter-

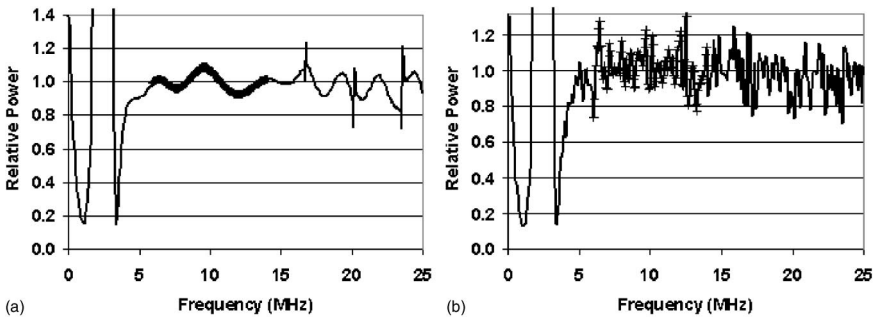

FIG. 5. Normalized ratio of an ideal scattered power spectrum from a single-point scatterer to the power spectrum from a rectangular windowed wavetrain of pulses scattered from randomly spaced scatterers using the gate-edge correction factor with (a) a windowed segment of length 2 SPLs and (b) a windowed segment of 20 SPLs. The windowed spectra represent the average of 30 independent realizations. The analysis bandwidth is denoted on the curves by the superimposed "+" signs.

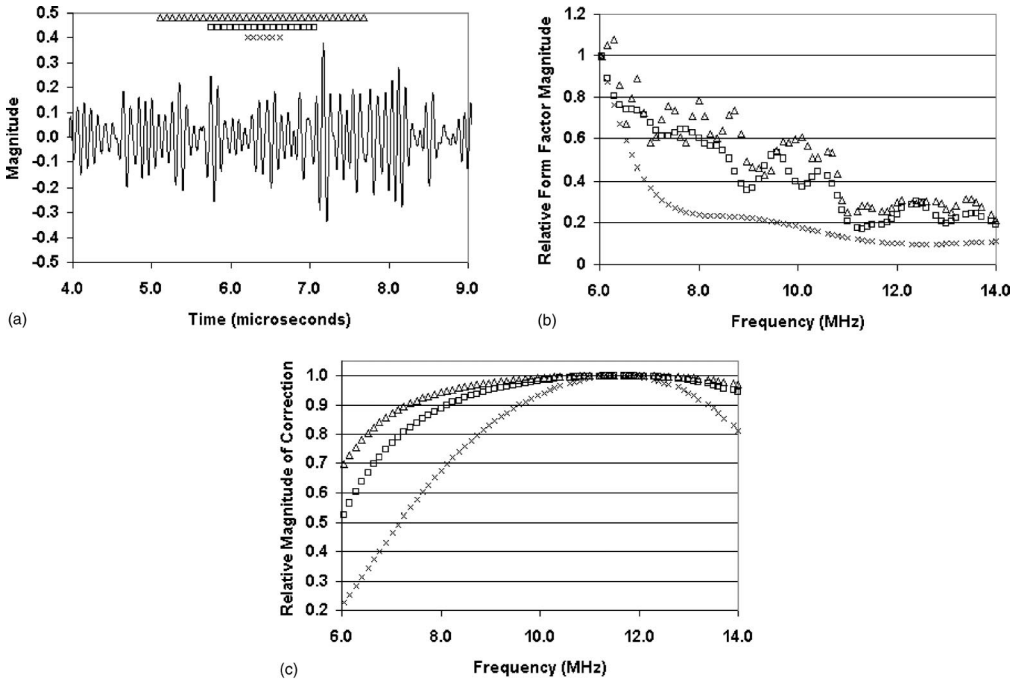

FIG. 6. (a) Representative time sequence of backscatter from randomly spaced Gaussian scatterers with (b) subsequent measured form factor and (c) corresponding correction factor for gate lengths of △, 7.5 SPLs; □, 3.7 SPLs; and ×, 2 SPLs.

ers (spherical Gaussian scatterers with radii sizes chosen so that the $ka \sim 1.0$ at the center frequency of operation) in volumes having variable attenuation. The average scatterer diameter was estimated using the rectangular window, the Hanning window, and the gate-edge correction factor, and then compared. An initial estimate of the scatterer size was made using the gate-edge correction factor for point scatterers, and then a new estimate of the scatterer diameter was made using the initial scatterer diameter estimate. Figure 8 indicates that increasing attenuation did not affect the ability of the gate-edge correction factor to obtain more accurate estimates at small gate lengths as compared to rectangular and Hanning windowed estimates. As the attenuation increased, the rectangular and Hanning windowed estimates

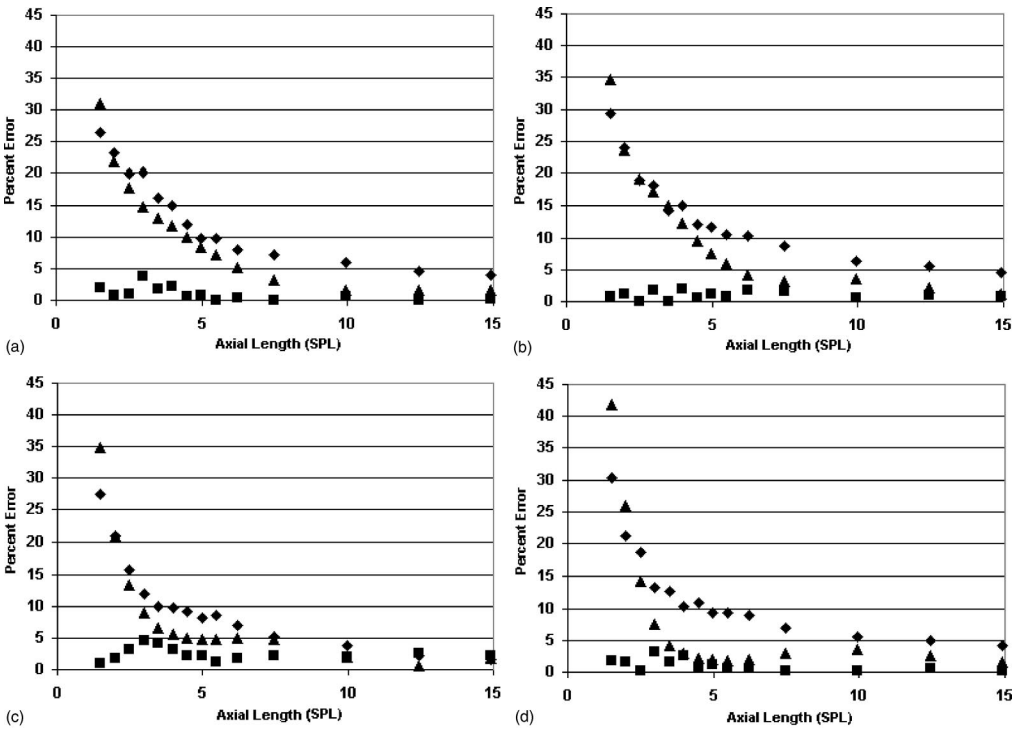

FIG. 7. Percent error between estimates of the frequency exponent dependencies of point scatterers versus gate length in SPLs for ■, gate-edge correction factor; ◆, rectangular window; ▲, Hanning window for a number density of (a) 1.1 scatterers per resolution cell; (b) 3.6 scatterers per resolution cell; (c) 5.8 scatterers per resolution cell; and (d) 9.1 scatterers per resolution cell.

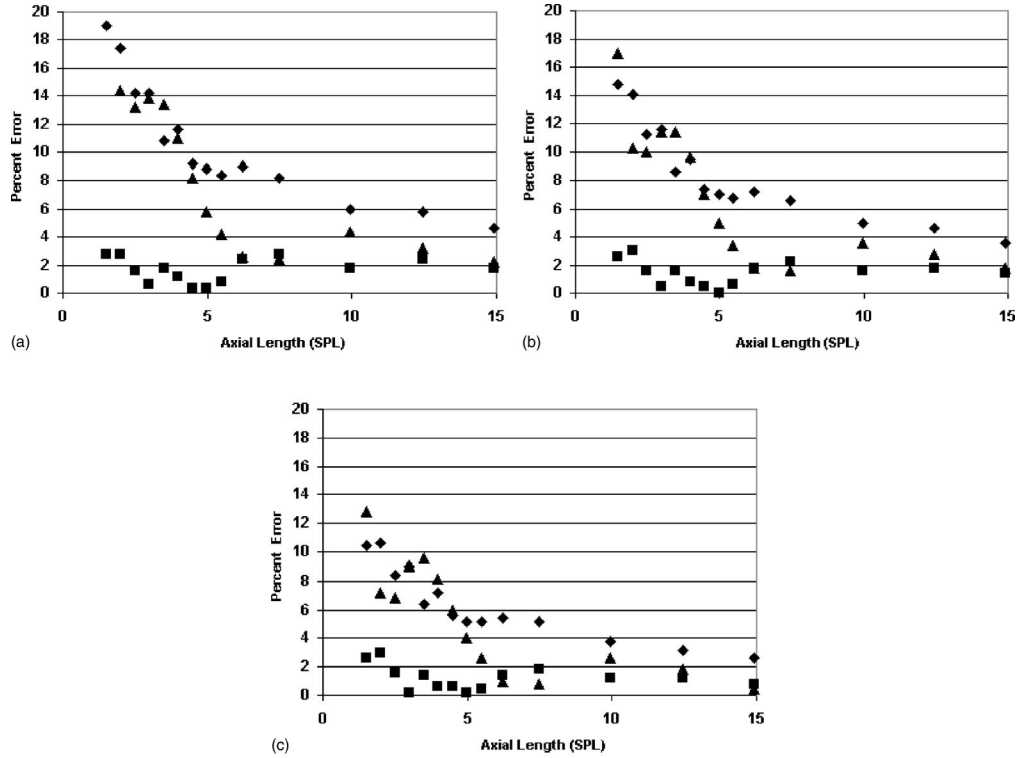

FIG. 8. Percent error between estimates of the average diameter for spherical Gaussian scatterers versus gate length in SPLs for ■, gate-edge correction factor; ♦, rectangular window; ▲, Hanning window and an attenuation of (a) 0.0 dB MHz^{-1} cm^{-1}; (b) 0.5 dB MHz^{-1} cm^{-1}; and (c) 1.0 dB MHz^{-1} cm^{-1}.

improved in accuracy at smaller gate lengths, but were still less accurate estimates than using the gate-edge correction factor. Figure 9 shows the average standard deviation of the estimates of the average diameter of the spherical Gaussian scatterers from the simulation. The standard deviation was best with the rectangular gated estimates and worst overall with the Hanning window. While the accuracy of the estimates was increased using the gate-edge correction factor relative to rectangular and Hanning windows, the precision at smaller gate lengths was not improved. However, the precision did not grow markedly worse using the gate-edge correction factor as opposed to standard windowing functions.

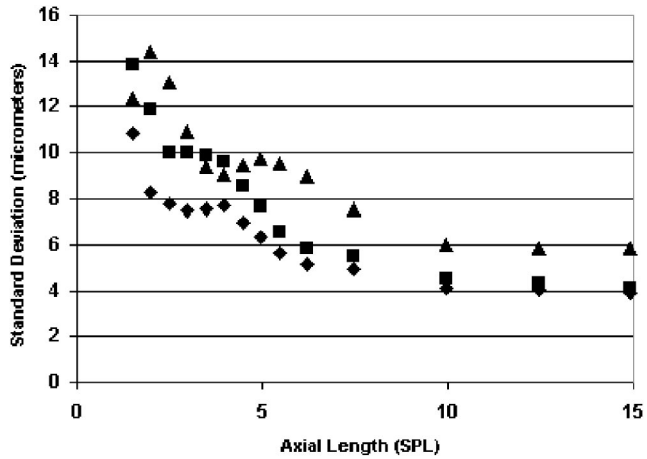

FIG. 9. Standard deviation of the estimates of the average diameter for spherical Gaussian scatterers versus gate length in SPLs for ■, gate-edge correction factor; ♦, rectangular window; ▲, Hanning window. The attenuation was 0.5 dB MHz^{-1} cm^{-1}.

Similar trends were seen in the other simulations and measurements.

The third set of simulations examined spherical Gaussian scatterers with ka values of 0.5, 1.0, and 2.0 based on the center frequency of the excitation pulse. Accurate estimates of scatterer diameters are made when the ka value is greater than 0.5.[6] Below this ka value, it is difficult to differentiate the scatterers from point scatterers.[33] Furthermore, if the ka value is too large, the measured form factor has a small magnitude leading to less accurate estimates. Figure 10 shows the percent error in estimates made of the average scatterer diameter compared with the actual scatterer diameter using the gate-edge correction, the rectangular window, and the Hanning window. The gate-edge correction showed marked improvement in the accuracy of the estimate over the other windowing schemes for each case. For small ka the accuracy of the estimates was very poor for each method used. The largest improvement in the estimate accuracy from the gate-edge correction occurred when the $ka \sim 1.0$ at the center frequency of operation.

The fourth set of simulations examined the effectiveness of the correction factor when a distribution of scatterers was interrogated. Figure 11 shows the percent error in estimates made of the average scatterer diameter compared with a diameter of 50 μm [Fig. 11(a)] and 53 μm [Fig. 11(b)] using the gate-edge correction, the rectangular window, and the Hanning window. An equal number of scatterers of diameters ranging from 35 to 65 μm [Fig. 11(a)] or 20 to 80 μm [Fig. 11(b)] were randomly spaced within a scattering volume with an average scatterer diameter of 50 μm. For the simulation in Fig. 11(b), the estimate of scatterer diameter con-

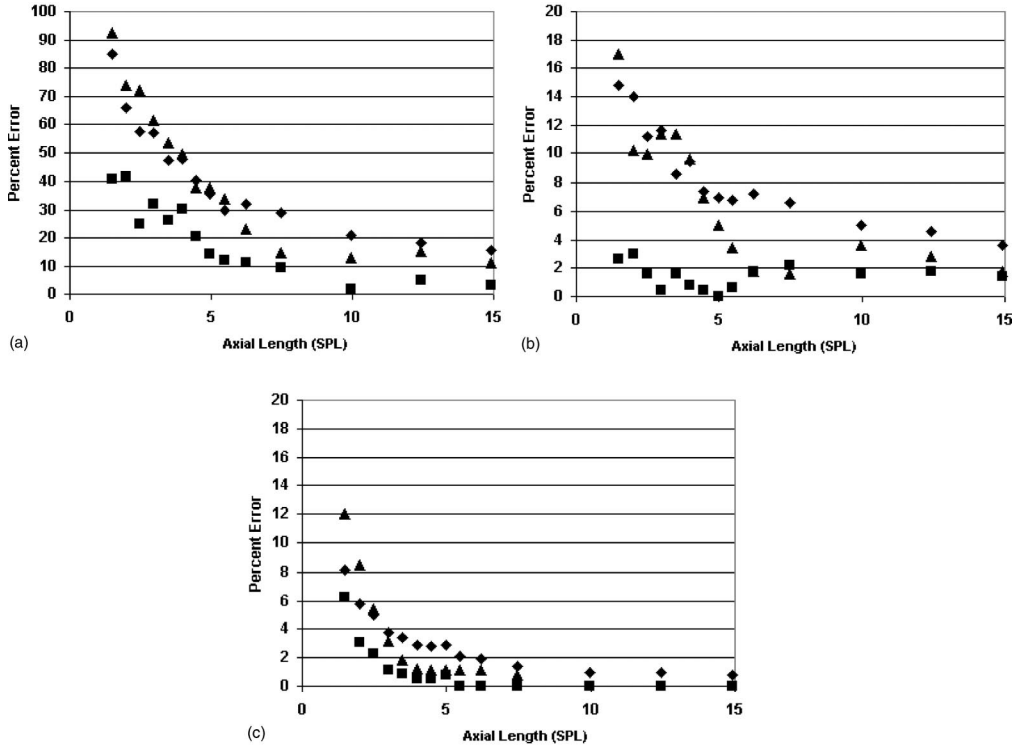

FIG. 10. Percent error between estimates of the average diameter for spherical Gaussian scatterers versus gate length in SPLs for ■, gate-edge correction factor; ♦, rectangular window; ▲, Hanning window and a *ka* value at the center frequency of operation of (a) 0.5; (b) 1.0; and (c) 2.0.

verged to about 53 μm at long gate length for all window types rather than 50 μm. The larger distribution of scatterers appeared to bias the estimate of average scatterer diameter to a larger scatterer diameter. The gate-edge correction showed marked improvement in obtaining estimates closer to the long gate length limit over the other windowing schemes for each case. The reason that the larger distribution biased the results to a larger estimate of scatterer diameter is because the backscattered power spectrum is proportional to the radius to the sixth power.[5] Larger scatterers will contribute more to the backscattered signal than will smaller scatterers, pushing the estimate of the average scatterer diameter towards the larger scatterers.

The final set of estimates was made from tissue-mimicking phantoms containing glass beads with scatterer diameters of 45–53 μm but with different concentrations and attenuation values. Figure 12 shows the estimates versus gate length using the rectangular window, the Hanning window, and the rectangular window using gate-edge correction factor. The gate-edge correction factor estimates gave improved accuracy at small gate lengths over the rectangular and Hanning windowed estimates. The most improvement over the conventional windowed estimates came from phantom A, which had the smaller attenuation and the smaller concentration of scatterers. Figure 13 shows the absolute standard deviation of the estimates from the physical phantoms. Small differences in the precision were seen using the different methods. The precision of the Hanning window estimates was worse than the precision using the other methods. However, the correction factor estimates appeared to have slightly worse precision over the simple rectangular window. The reason for the loss of precision over the rectangular gated estimates may be due to amplification of noise by the application of the correction factor. The gate-edge correction fac-

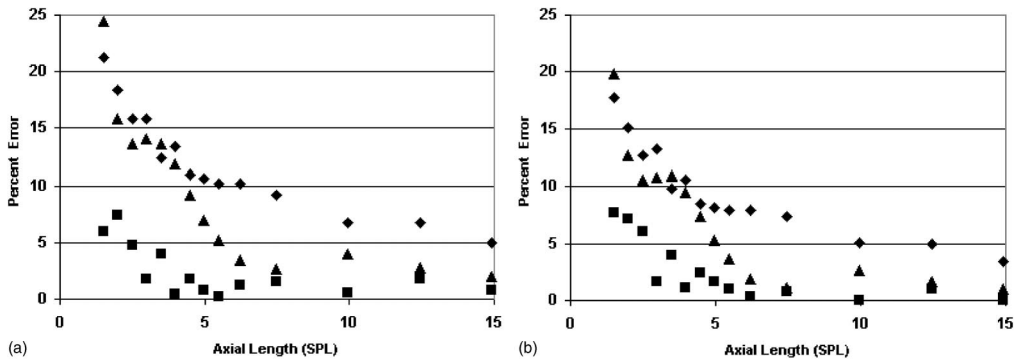

FIG. 11. Percent error between estimates of the average diameter for spherical Gaussian scatterers versus gate length in SPLs for ■, gate-edge correction factor; ♦, rectangular window; ▲, Hanning window with an equal distribution of scatterers from (a) 35 to 65 μm and (b) 20 to 80 μm.

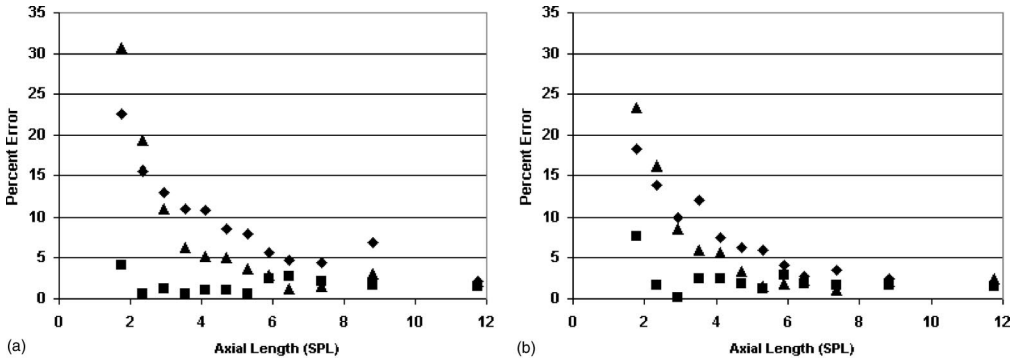

FIG. 12. Percent error between estimates of the average diameter for glass beads in tissue-mimicking phantoms versus gate length in SPLs for ■, gate-edge correction factor; ♦, rectangular window; ▲, Hanning window in (a) phantom A; and (b) phantom B.

tor improved the accuracy of the estimates (reduced or eliminated the bias) but did not improve the precision of the estimates at small gate lengths.

V. CONCLUSION

For QUS imaging of tissues utilizing scatterer property estimates, it is important to improve the accuracy of estimates while minimizing the size of the ROIs necessary to obtain good estimates. Minimizing the ROIs amounts to improving the spatial resolution of QUS images utilizing scatterer property estimates. One of the factors that decreases the accuracy of estimates (increases the estimate bias) is the gating of the rf signals used to obtain the scatterer property estimates. The gating effects are diminished as the size of the gate length is increased because error is introduced from the edges of the gate. As the gate length is increased the contribution of the gate edges is decreased relative to the larger, undisturbed middle region of the gate. A gate-edge correction factor was introduced that partially accounted for the edge effects prevalent in smaller gated segments.

Estimates of scatterer properties using the gate-edge correction factor were compared with estimates using conventional windowing functions. In all cases, the gate-edge correction factor yielded more accurate size estimates for smaller gate lengths than the conventional windowing functions. In almost all cases, the size estimates from the gate-edge correction factor were within 5% of the actual values (for an ensemble average from 60 estimates) for the scatterer properties examined. While the gate-edge correction factor improved the accuracy of the estimates at small gate lengths, the precision of estimates was not improved above conventional windowing techniques. The lack of improvement in precision in many applications for QUS imaging techniques may be a limiting factor in using small gate lengths where estimates come from a few echo segments.

In specific cases, the conventional windowing functions gave improved results for small gate lengths but not greater than estimates using the gate-edge correction factor. For large number density of scatterers, the Hanning window appeared to approach the gate-edge correction estimates at gate lengths larger than 3 SPLs. Furthermore, larger attenuation appeared to improve the accuracy of size estimates from the conventional windowing function estimates, but not above the accuracy of estimates obtained using the gate-edge correction factor. The improvement may have resulted from the fact that the distal gate edge was more highly attenuated and thus contributed less to the overall frequency dependence.

When the $ka \sim 0.5$ (as measured at the center frequency) the difference between real and estimated diameter using the gate-edge correction factor was 10% or greater when the gate length was less than 10 SPLs. However, diameter estimates from the gate-edge correction factor were still better relative to the conventional windowing function estimates at small gate lengths. Further research is required to determine the reason that the gate-edge correction factor failed to give as good improvement for the low ka case.

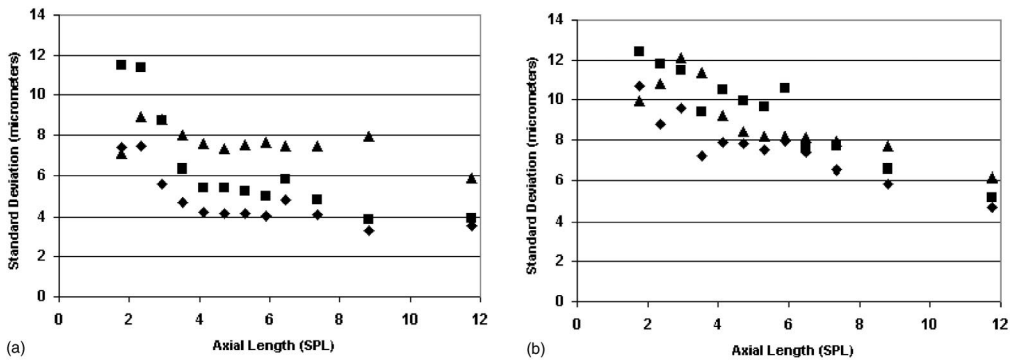

FIG. 13. Standard deviation of the scatterer diameter estimates for glass beads versus gate length in SPLs for ■, gate-edge correction factor; ♦, rectangular window; ▲, Hanning window in (a) phantom A; and (b) phantom B.

ACKNOWLEDGMENT

Supported by NIH F32 CA96419 to M.L.O.

[1] D. Nicholas, ''Evaluation of backscattering coefficients for excised human tissues: Results, interpretation, and associated measurements,'' Ultrasound Med. Biol. **8**, 17–28 (1982).
[2] E. J. Feleppa, F. L. Lizzi, D. J. Coleman, and M. M. Yaremko, ''Diagnostic spectrum analysis in ophthalmology: A physical perspective,'' Ultrasound Med. Biol. **12**, 623–631 (1986).
[3] F. L. Lizzi, M. Ostromogilsky, E. J. Feleppa, M. C. Rorke, and M. M. Yaremko, ''Relationship of ultrasonic spectral parameters to features of tissue microstructure,'' IEEE Trans. Ultrason. Ferroelectr. Freq. Control **33**, 319–329 (1986).
[4] D. K. Nassiri and C. R. Hill, ''The use of angular scattering measurements to estimate structural parameters of human and animal tissues,'' J. Acoust. Soc. Am. **87**, 179–192 (1990).
[5] M. F. Insana, R. F. Wagner, D. G. Brown, and T. J. Hall, ''Describing small-scale structure in random media using pulse–echo ultrasound,'' J. Acoust. Soc. Am. **87**, 179–192 (1990).
[6] M. F. Insana and T. J. Hall, ''Parametric ultrasound imaging from backscatter coefficient measurements: Image formation and interpretation,'' Ultrason. Imaging **12**, 245–267 (1990).
[7] M. F. Insana, J. G. Wood, and T. J. Hall, ''Identifying acoustic scattering sources in normal renal parenchyma from the anisotropy in acoustic properties,'' Ultrasound Med. Biol. **18**, 587–599 (1992).
[8] K. K. Shung and G. A. Thieme, *Ultrasonic Scattering in Biological Tissues* (CRC Press, Boca Raton, 1993).
[9] M. F. Insana, T. J. Hall, J. G. Wood, and Z.-Y. Yan, ''Renal ultrasound using parametric imaging techniques to detect changes in microstructure and function,'' Invest. Radiol. **28**, 720–725 (1993).
[10] M. F. Insana, ''Modeling acoustic backscatter from kidney microstructure using an anisotropic correlation function,'' J. Acoust. Soc. Am. **97**, 649–655 (1995).
[11] T. J. Hall, M. F. Insana, L. A. Harrison, and G. G. Cox, ''Ultrasonic measurement of glomerular diameters in normal adult humans,'' Ultrasound Med. Biol. **22**, 987–997 (1996).
[12] E. J. Feleppa, T. Liu, A. Kalisz, M. C. Shao, N. Fleshner, and V. Reuter, ''Ultrasonic spectral-parameter imaging of the prostate,'' Int. J. Imaging Syst. Technol. **8**, 11–25 (1997).
[13] F. L. Lizzi, M. Astor, T. Liu, C. Deng, D. J. Coleman, and R. H. Silverman, ''Ultrasonic spectrum analysis for tissue assays and therapy evaluation,'' Int. J. Imaging Syst. Technol. **8**, 3–10 (1997).
[14] R. M. Golub, R. E. Parsons, B. Sigel, E. J. Feleppa, J. Justin, H. A. Zaren, M. Rorke, J. Sokil-Melgar, and H. Kimitsuki, ''Differentiation of breast tumors by ultrasonic tissue characterization,'' J. Ultrasound Med. **12**, 601–608 (1993).
[15] K. A. Topp, J. F. Zachary, and W. D. O'Brien, Jr., ''Quantifying B-mode images of *in vivo* rat mammary tumor with frequency dependence of backscatter,'' J. Ultrasound Med. **20**, 605–612 (2001).
[16] M. L. Oelze, J. F. Zachary, and W. D. O'Brien, Jr., ''Parametric imaging of rat mammary tumors *in vivo* for the purposes of tissue characterization,'' J. Ultrasound Med. **21**, 1201–1210 (2002).
[17] F. L. Lizzi, M. Greenbaum, E. J. Feleppa, M. Elbaum, and D. J. Coleman, ''Theoretical framework for spectrum analysis in ultrasonic tissue characterization,'' J. Acoust. Soc. Am. **73**, 1366–1373 (1983).
[18] E. L. Madsen, M. F. Insana, and J. A. Zagzebski, ''Method of data reduction for accurate determination of acoustic backscatter coefficients,'' J. Acoust. Soc. Am. **76**, 913–923 (1984).
[19] J. F. Chen, E. L. Madsen, and J. A. Zagzebski, ''A method for determination of frequency-dependent effective number density,'' J. Acoust. Soc. Am. **95**, 77–85 (1994).
[20] H. J. Huisman and J. M. Thijssen, ''Precision and accuracy of acoustospectrographic parameters,'' Ultrasound Med. Biol. **22**, 855–871 (1996).
[21] S. L. Marple, Jr., *Digital Spectral Analysis* (Prentice-Hall, Englewood Cliffs, NJ, 1987).
[22] G. M. Jenkins and D. G. Watts, *Spectral Analysis and Its Applications* (Holden-Day, San Francisco, 1968).
[23] J. F. Chen, J. A. Zagzebski, and E. L. Madsen, ''Tests of backscatter coefficient measurement using broadband pulses,'' IEEE Trans. Ultrason. Ferroelectr. Freq. Control **40**, 603–607 (1993).
[24] M. F. Insana, E. L. Madsen, T. J. Hall, and J. A. Zagzebski, ''Tests of the accuracy of a data reduction method for determination of acoustic backscatter coefficients,'' J. Acoust. Soc. Am. **79**, 1230–1236 (1986).
[25] M. Ueda and Y. Ozawa, ''Spectral analysis of echoes for backscattering coefficient measurement,'' J. Acoust. Soc. Am. **77**, 38–47 (1985).
[26] M. Akita and M. Ueda, ''The effect of windowing on spectral estimation of echoes scattered by a random medium,'' J. Acoust. Soc. Am. **83**, 1243–1248 (1988).
[27] K. A. Wear, R. F. Wagner, M. F. Insana, and T. J. Hall, ''Application of autoregressive spectral analysis to cepstral estimation of mean scatterer spacing,'' IEEE Trans. Ultrason. Ferroelectr. Freq. Control **40**, 50–58 (1993).
[28] M. L. Oelze and W. D. O'Brien, Jr., ''Defining optimal axial and lateral resolution for estimating scatterer properties from volumes using ultrasound backscatter,'' J. Acoust. Soc. Am. **115**, 3226–3234 (2004).
[29] M. L. Oelze, J. F. Zachary, and W. D. O'Brien, Jr., ''Characterization of tissue microstructure using ultrasonic backscatter: Theory and technique for optimization using a Gaussian form factor,'' J. Acoust. Soc. Am. **112**, 1202–1211 (2002).
[30] E. L. Madsen, F. Dong, G. R. Frank, B. S. Garra, K. A. Wear, T. Wislon, J. A. Zagzebski, H. L. Miller, K. Shung, S. H. Wang, E. J. Feleppa, T. Liu, W. D. O'Brien, Jr., K. A. Topp, N. T. Sanghvi, A. V. Zaitsev, T. J. Hall, J. B. Fowlkes, O. D. Kripfgans, and J. G. Miller, ''Interlaboratory comparison of ultrasonic backscatter, attenuation, and speed measurements,'' J. Ultrasound Med. **18**, 615–631 (1999).
[31] K. Raum and W. D. O'Brien, Jr., ''Pulse–echo field distribution measurement technique for high-frequency ultrasound sources,'' IEEE Trans. Ultrason. Ferroelectr. Freq. Control **44**, 810–815 (1997).
[32] J. J. Faran, Jr., ''Sound scattering by solid cylinders and spheres,'' J. Acoust. Soc. Am. **23**, 405–418 (1951).
[33] T. Hosokawa, B. Sigel, J. Machi, H. Kitamura, R. V. Kolecki, J. R. Justin, E. J. Feleppa, G. Tuszynski, and T. Kakegawa, ''Experimental assessment of spectrum analysis of ultrasonic echoes as a method for estimating scatterer properties,'' Ultrasound Med. Biol. **20**, 463–470 (1994).

Erratum: "A phenomenological model for the responses of auditory-nerve fibers: II. Nonlinear tuning with a frequency glide" [J. Acoust. Soc. Am. 114, 2007–2020 (2003)]

Qing Tan
Boston University Hearing Research Center, Department of Biomedical Engineering, Boston University, 44 Cummington Street, Boston, Massachusetts 02215

Laurel H. Carney[a)]
Boston University Hearing Research Center, Department of Biomedical Engineering, Boston University, 44 Cummington Street, Boston, Massachusetts 02215; and Department of Bioengineering and Neuroscience, Institute for Sensory Research, 621 Skytop Road, Syracuse University, Syracuse, New York 13244[b)]

(Received 7 July 2004; revised 19 July 2004; accepted 20 July 2004)

[DOI: 10.1121/1.1791873]

PACS numbers: 43.64.Bt, 43.64.Pg, 43.10.Vx [WPS]

The schematic diagram and text erroneously omitted a component of the auditory-nerve model. A first-order low-pass filter with a cutoff frequency of 500 Hz was included in the feedback path within the model's control-path, as shown here (LP2, Fig. 1); a scalar K with a value of 10 followed the low-pass filter in the feedback path. This low-pass filter was included in some but not all of the simulations shown in the original paper, as clarified below. The inclusion of LP2 did not significantly affect responses to pure tone stimuli (Tan and Carney, 2003, Figs. 7–9,11,12) or to broadband noise (Tan and Carney, 2003, Figs. 4,10). The low-pass filter (LP2) mainly affected responses to two-tone stimuli, and in particular was responsible for introducing the differences in growth of suppression for tones below or above CF. Figure 13 in Tan and Carney (2003) did *not* include LP2; Fig. 2 here illustrates the effect of its inclusion. Figure 14 in Tan and Carney (2003) *did* include LP2; the effects of its inclusion are illustrated here in Fig. 3.

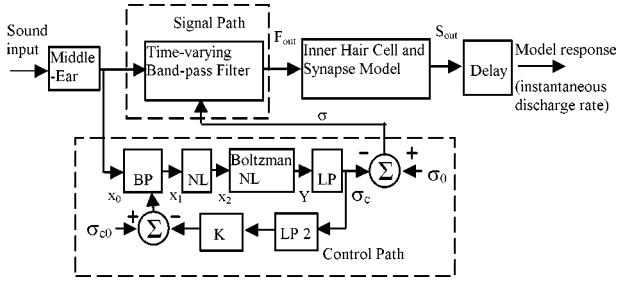

FIG. 1. Corrected schematic diagram of the AN model. The block labeled LP2 is a first-order low-pass filter with cutoff frequency of 500 Hz. The associated scalar, K, had a value of 10. This low-pass filter was omitted from the figure and text in Tan and Carney (2003), but was included in some of the simulations.

The parameter values for Z_0 and Z_1 in Eq. (13) (Table I) were used in all results shown in Tan and Carney (2003), but these values are not consistent with the fit shown in Fig. 5(d). The values used were varied to adjust the amount of glide in the impulse responses. Values of $Z_0=1.572$ and $Z_1=0.564$ provide a better fit to Fig. 5(d) and result in better filter shapes at high CFs.

Finally, Eq. 18 should read $G_{\text{control}}=(10^{(0.5732\ \log10\ (\text{CF})+1.522)}-10^{(0.4\ \log10\ (\text{CF})+1.9)})/0.3357$.

[a)]Author to whom correspondence should be addressed. Electronic mail: Lacarney@syr.edu
[b)]Address for correspondence.

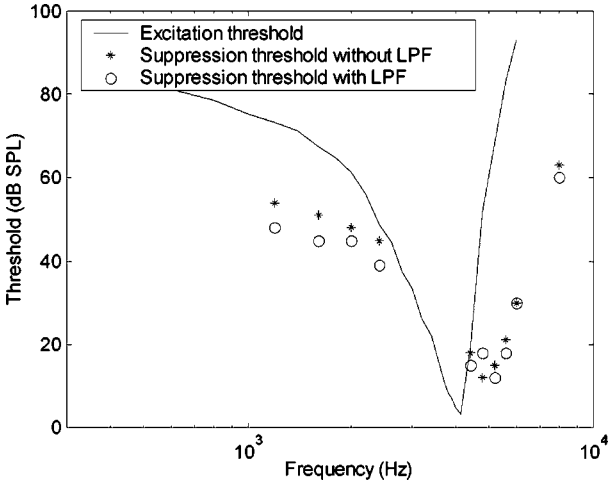

FIG. 2. The solid line illustrates the model's tuning curve with CF at 4000 Hz. The stars indicate the suppression threshold illustrated in Tan and Carney (2003), *without* LP2 in the control path. Circles indicate suppression thresholds *with* LP2 in the control path. Suppression threshold was defined as the suppressor tone SPL that decreases the response to CF tone by 10 spike/sec.

Tan, Q., and Carney, L. (**2003**). ''A phenomenological model for the responses of auditory-nerve fibers: II. Nonlinear tuning with a frequency glide,'' J. Acoust. Soc. Am. **114**, 2007–2020.

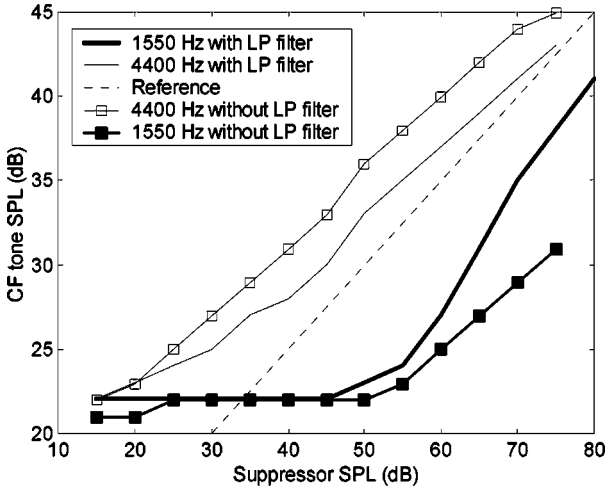

FIG. 3. Suppression growth functions measured for a CF of 3500 Hz, with suppressors at 1550 Hz (below CF) or 4400 Hz (above CF). The CF tone SPL was adjusted to maintain a response rate that was two-thirds of the maximum response rate at each suppressor SPL. The dotted line indicates a growth with slope of 1 (dB/dB). The thin and thick solid lines without symbols are responses of the model *with* LP2 in the control path (same as in Fig. 14 of Tan and Carney, 2003). The lines with symbols show the effects of *removal* of LP2. *Without* LP2, the suppression growth functions for suppressors above and below CF have the same slope.